

STRUCTURE AND SOLVATION OF CONFINED WATER AND ALKANOLS IN  
ZEOLITE ACID CATALYSIS

A Dissertation

Submitted to the Faculty

of

Purdue University

by

Jason S. Bates

In Partial Fulfillment of the

Requirements for the Degree

of

Doctor of Philosophy

December 2019

Purdue University

West Lafayette, Indiana



**THE PURDUE UNIVERSITY GRADUATE SCHOOL**  
**STATEMENT OF DISSERTATION APPROVAL**

Dr. Rajamani Gounder, Chair

Charles D. Davidson School of Chemical Engineering

Dr. Fabio H. Ribeiro

Charles D. Davidson School of Chemical Engineering

Dr. Jeffrey Greeley

Charles D. Davidson School of Chemical Engineering

Dr. Christopher Uyeda

Department of Chemistry

**Approved by:**

Dr. John Morgan

Head of the School Graduate Program

“Reading is like thinking, like praying, like talking to a friend, like expressing your ideas, like listening to other people’s ideas, like listening to music (oh yes), like looking at the view, like taking a walk on the beach.”

—Roberto Bolaño, *2666*

## ACKNOWLEDGMENTS

To Raj Gounder, who always seemed more than anyone to be confident in my potential as a researcher. Thank you for your tireless mentorship in virtually all aspects of my professional development, including reading the literature, writing clearly and concisely, and teaching effectively, for emphasizing an approach to heterogeneous catalysis research that centers quantitative kinetics, for teaching me how to ask the right scientific questions, and how to seek their answers in a consistent manner. To Fabio Ribeiro, whose vision and dedication to catalysis research at Purdue and in the broader scientific community underpins the success of many. Thank you for providing me with a strong foundation to follow the path of kinetics, active sites, and turnover rates. To Jeff Greeley, whose theory-based viewpoint significantly impacted my work and perspective on experimental-theoretical collaboration. Thank you for being a thoughtful mentor and collaborator, and always having an interesting question to ask. To Chris Uyeda, for reminding me to keep cultivating my chemical intuition, and encouraging me to pursue future opportunities in chemistry. To Nick Delgass, for providing an inspiring example of the joy that can be found in the pursuit of science; I hope that I will always be tinkering with my own mosaic as you do.

Profound thanks are due to Brandon Bukowski, for countless hours spent discussing the science of catalysis, for making experimental hypotheses a beautiful computational reality that often challenged my thinking, and for sharing in “weird” lunches and attending concerts where instruments were lit on fire. To Jamie Harris, whose tireless work ethic and enthusiasm for science encouraged me as a first-year student to pursue similar research and career goals. Thank you for talking science, tennis, music, and more with me both on- and offline, and the many hours spent pursuing these interests with me in the lab and in our free time, and for setting

the bar high with your achievements in the Gounder group and beyond. Thanks to Phil Kester and Juan Carlos Vega-Vila, collectively for growing alongside me in the group and encouraging one another through the years, and respectively, for helping me maintain a focus on kinetics with your impressive pursuit of the perfect alkane dehydrogenation rate measurement, and for inspiring me with your creative synthetic approaches. John Di Iorio and Ravi Joshi also deserve special mention for their patient and thoughtful mentorship starting in the early years of the Gounder group.

I want to thank the entire Gounder group for holding each other to the highest standards in our field and working together to solve difficult problems. Thanks specifically to Michael Cordon, Claire Nimlos, Trevor Lardinois, Laura Wilcox, Casey Jones, et al. for your contributions both to my growth as a researcher and to the well-being of the group. Thanks also to Rohan Dighe for sticking it out with me as an undergraduate researcher for over two years and maintaining both enthusiasm and a good sense of humor throughout. Thanks to the Purdue Catalysis Center as a whole, whose members together comprise a world-class group of heterogeneous catalysis researchers and have contributed to the broadening of my knowledge beyond the narrow purview of zeolite catalysis. I am also grateful to all the ChE staff members who enable us to focus on research by making sure everything runs smoothly; special thanks to Yury Zvinevich, whose skill with instrumentation is unparalleled, and also to Jeff Valley and Nick Humphrey who really keep the lights on in Forney. Specific technical contributions are also acknowledged in each chapter.

Each stage of growth in life would also be incomplete without the friends and family who travelled through it alongside me. A certain group of friends at Purdue deserves special mention: Phil Kester, Scott McClary, Robert Warburton, and Adam Wingate. Thanks for reminding me not to take myself too seriously, and for being great pizza-eaters, concert-goers, roommates (Phil), jokers, and multi-instrumentalist jammers. Shred til yer dead. Thanks to my family, Mom, Dad, and Emily, whose earliest and continued support and encouragement have enabled me to pursue my interests. Finally, I owe an abundance of the happiness I have experienced over the

last four years to Jenna Beckley. Thank you for supporting me through stressful times and laughing with me through the joyful ones. This thesis concludes a chapter in a longer story that I am thrilled to continue writing with you.

## TABLE OF CONTENTS

	Page
LIST OF TABLES . . . . .	xiii
LIST OF FIGURES . . . . .	xviii
ABSTRACT . . . . .	lxiii
1 Introduction . . . . .	1
2 First Principles, Microkinetic, and Experimental Analysis of Lewis Acid Site Speciation During Ethanol Dehydration on Sn-Beta Zeolites . . . . .	11
2.1 Introduction . . . . .	11
2.2 Methods . . . . .	14
2.2.1 Computational Methods . . . . .	14
2.2.2 Catalyst Synthesis and Characterization . . . . .	16
2.2.3 Ethanol Dehydration Kinetics . . . . .	18
2.3 Results and Discussion . . . . .	19
2.3.1 T-sites in Sn-Beta . . . . .	19
2.3.2 Sn site speciation . . . . .	20
2.3.3 DEE formation mechanisms . . . . .	22
2.3.4 Ethene formation mechanisms . . . . .	32
2.3.5 Ethanol Dehydration Kinetics . . . . .	35
2.4 Conclusions . . . . .	45
2.5 Acknowledgements . . . . .	47
2.6 Supporting Information . . . . .	47
2.6.1 Binding Energies of key intermediates at different acid sites . . . . .	47
2.6.2 Electronic Structure characterization of open sites . . . . .	49
2.6.3 Water shuttling mechanism . . . . .	51
2.6.4 Paired Sn DEE formation . . . . .	52
2.6.5 Complete list of elementary steps in microkinetic model of ethanol dehydration reaction network. . . . .	53
2.6.6 Effect of site normalization on turnover rates . . . . .	55
2.6.7 Additional mechanisms considered . . . . .	56
2.6.8 Construction of microkinetic model . . . . .	57
2.6.9 Additional adsorbate configurations . . . . .	59
2.6.10 Calculation of entropy using mode decompositions and AIMD . . . . .	62
2.6.11 Functional comparison for ethanol monomer and ethanol-ethanol dimer adsorption energies. . . . .	65

	Page
2.6.12 Correlated error analysis . . . . .	66
2.6.13 Derivation of simplified kinetic equation . . . . .	67
3 Influence of Confining Environment Polarity on Ethanol Dehydration Catalysis by Lewis Acid Zeolites . . . . .	69
3.1 Introduction . . . . .	69
3.2 Methods . . . . .	72
3.2.1 Zeolite Synthesis . . . . .	72
3.2.2 Characterization of Zeolites . . . . .	74
3.2.3 Gas-phase ethanol dehydration kinetic studies . . . . .	79
3.3 Results and Discussion . . . . .	81
3.3.1 Kinetic and mechanistic details of bimolecular ethanol dehydration	81
3.3.2 Spectroscopic and kinetic interrogation of active Sn identity . .	88
3.3.3 Influence of framework polarity on ethanol dehydration catalysis	93
3.3.4 Influence of framework polarity on coverages of polar intermediates	99
3.4 Conclusions . . . . .	104
3.5 Acknowledgements . . . . .	106
3.6 Supporting Information . . . . .	106
3.6.1 Supplementary Discussion . . . . .	106
3.6.2 Supplementary Figures . . . . .	113
3.6.3 Supplementary Tables . . . . .	133
4 Distinct Catalytic Reactivity of Sn Substituted in Framework Locations and at Defect Grain Boundaries in Sn-Zeolites . . . . .	135
4.1 Introduction . . . . .	135
4.2 Experimental Section . . . . .	140
4.2.1 Zeolite synthesis and post-synthetic treatments . . . . .	140
4.2.2 Characterization of zeolites . . . . .	144
4.2.3 <i>In situ</i> pyridine titration during ethanol dehydration catalysis	145
4.2.4 Theoretical modeling . . . . .	147
4.3 Results and Discussion . . . . .	149
4.3.1 <i>In situ</i> pyridine titration of Lewis acidic Sn sites during ethanol dehydration catalysis . . . . .	149
4.3.2 Probing structural features that lead to Sn <sub>2316</sub> sites . . . . .	163
4.3.3 Computational modeling of ethanol dehydration at stacking fault defect-open sites . . . . .	184
4.3.4 Dominant active site structures for ethanol dehydration and glucose isomerization catalysis . . . . .	189
4.4 Conclusions . . . . .	193
4.5 Acknowledgements . . . . .	196
4.6 Supporting Information . . . . .	197
4.6.1 Supplementary Discussion . . . . .	197
4.6.2 Supplementary Figures . . . . .	207

	Page
4.6.3 Supplementary Tables . . . . .	250
5 Deactivation of Sn-Beta Zeolites Caused by Structural Transformation of Hydrophobic to Hydrophilic Micropores during Aqueous-Phase Glucose Isomerization . . . . .	271
5.1 Introduction . . . . .	271
5.2 Experimental methods . . . . .	274
5.2.1 Catalyst synthesis and preparation . . . . .	274
5.2.2 Catalyst characterization . . . . .	276
5.2.3 Glucose isomerization kinetic studies . . . . .	278
5.3 Results and discussion . . . . .	280
5.3.1 Effect of hot water pretreatment of Sn-Beta on glucose isomerization kinetics . . . . .	280
5.3.2 Characterization of Sn sites in Sn-Beta as a function of water exposure . . . . .	287
5.3.3 Characterization of silanol densities in Sn-Beta as a function of water exposure duration . . . . .	292
5.3.4 Origin of the aqueous-phase deactivation phenomena on hydrophobic Sn-Beta . . . . .	295
5.3.5 Speculations on the origin of the activation phenomena on hydrophobic Sn-Beta . . . . .	299
5.4 Conclusions . . . . .	301
5.5 Acknowledgements . . . . .	303
5.6 Supporting Information . . . . .	304
5.6.1 Bulk structural and Lewis acid site characterization of Sn-Beta zeolites . . . . .	304
5.6.2 Rate constant and free energy measurements on Sn-Beta samples	309
5.6.3 Bulk characterization of Sn-Beta-F-116 after controlled hot (373 K) water exposure . . . . .	310
5.6.4 Bulk characterization of Sn-Beta-F-100 after NMe <sub>4</sub> OH treatment	315
5.6.5 Supplemental figures on kinetic and mechanistic details of activation and fructose formation on Sn-Beta samples . . . . .	317
6 The Dominant Role of Entropy in Stabilizing Sugar Isomerization Transition States within Hydrophobic Zeolite Pores . . . . .	325
6.1 Introduction . . . . .	325
6.2 Materials and Methods . . . . .	328
6.2.1 Catalyst Synthesis . . . . .	328
6.2.2 Characterization of Bulk Catalyst Properties . . . . .	330
6.2.3 Transmission Infrared Spectroscopy . . . . .	331
6.2.4 Glucose Isomerization Kinetic Studies . . . . .	334
6.2.5 Computational Methods . . . . .	336
6.2.6 ATR-IR Spectroscopy with MES-PSD MCR-ALS . . . . .	338

	Page
6.2.7 X-Ray Absorption Spectroscopy (XAS) Measurements . . . . .	340
6.3 Results and Discussion . . . . .	341
6.3.1 Bulk Structural and Lewis Acid Site Characterization of Ti-Beta Zeolites . . . . .	341
6.3.2 Characterization of Hydrophobic Properties of Ti-Beta Zeolites	345
6.3.3 Aqueous-Phase Glucose Isomerization Mechanisms and Kinetic Measurements . . . . .	351
6.3.4 Characterization of Active Site Complexes in First-Order and Zero-Order Kinetic Regimes . . . . .	359
6.3.5 Enthalpic and Entropic Consequences of Hydrophobic Reaction Pockets for Aqueous-Phase Glucose Isomerization . . . . .	365
6.4 Conclusions . . . . .	377
6.5 Acknowledgements . . . . .	380
6.6 Supporting Information . . . . .	385
6.6.1 Bulk structural and Lewis acid site characterization of Ti-Beta zeolites . . . . .	385
6.6.2 Characterization of the hydrophobic properties of Ti-Beta zeolites	404
6.6.3 Glucose isomerization mechanisms and kinetic measurements .	410
6.6.4 Characterization and kinetic effects of bound surface species in first-order and zero-order regimes . . . . .	417
6.6.5 Enthalpic and entropic contributions of hydrophobic reaction pockets for aqueous-phase glucose isomerization . . . . .	428
7 Defect-Mediated Ordering of Condensed Water Structures in Microporous Zeolites . . . . .	451
7.1 Introduction . . . . .	451
7.2 Results and Discussion . . . . .	453
7.3 Conclusions . . . . .	460
7.4 Acknowledgements . . . . .	461
7.5 Supporting Information . . . . .	462
7.5.1 Methodology . . . . .	462
7.5.2 Supplementary Discussions . . . . .	471
7.5.3 Supplementary Figures . . . . .	479
7.5.4 Supplementary Tables . . . . .	506
8 Structure and Solvation of Confined Water within Microporous Brønsted Acids and its Influence on Ethanol Dehydration Kinetics . . . . .	507
8.1 Introduction . . . . .	507
8.2 Results and Discussion . . . . .	511
8.2.1 Kinetics of Brønsted Acid-catalyzed Ethanol Dehydration and Water Inhibition in Zeolites . . . . .	511
8.2.2 Characterization of Intracrystalline Water Structures . . . . .	521

	Page
8.2.3 Theoretical Calculations of Solvated Ethanol Dehydration Reaction Coordinates . . . . .	533
8.2.4 Mechanistic Implications of Solvation by Condensed Water Structures . . . . .	541
8.2.5 Effects of Pore Topology on Solvation Effects . . . . .	546
8.3 Conclusions . . . . .	551
8.4 Experimental Section . . . . .	552
8.4.1 Zeolite Synthesis and Post-synthetic Treatments . . . . .	552
8.4.2 Characterization of Zeolites . . . . .	554
8.4.3 Ethanol Dehydration Kinetics . . . . .	556
8.4.4 Theoretical Methods . . . . .	557
8.5 Acknowledgements . . . . .	559
8.6 Supporting Information . . . . .	560
8.6.1 Supplementary Methods . . . . .	560
8.6.2 Supplementary Discussion . . . . .	563
8.6.3 Supplementary Figures . . . . .	572
8.6.4 Supplementary Tables . . . . .	629
REFERENCES . . . . .	633
A Bimolecular Dehydration of Ethanol-methanol Mixtures as a Probe of Intrapore Alkanol Structure in Brønsted Acid Zeolites . . . . .	671
A.1 Motivation . . . . .	671
A.2 Results and Discussion . . . . .	671
A.3 Supporting Information . . . . .	680
A.3.1 Derivation of DME/MEE rate ratio expression . . . . .	680
A.3.2 Alkoxide-mediated DEE and MEE formation . . . . .	681
B Effects of Proton Proximity on Ethanol Dehydration Catalysis in CHA and MFI Zeolites . . . . .	683
B.1 Motivation . . . . .	683
B.2 Results and Discussion . . . . .	684
B.2.1 Ethanol dehydration is not sensitive to H <sup>+</sup> proximity in MFI zeolites . . . . .	684
B.2.2 Ethanol dehydration is sensitive to H <sup>+</sup> proximity in CHA zeolites	689
VITA . . . . .	696

## LIST OF TABLES

Table	Page
2.1 Sn contents, micropore volumes, and acid site counts for Sn-Beta catalysts. [151] . . . . .	17
2.2 Kinetic barriers for DEE formation on different Sn sites. . . . .	32
2.3 Selected entropy comparisons for surface-bound intermediates. . . . .	37
2.4 Selected generalized DRC for reactive intermediates and transition states. Level of theory includes HSE06-D3 and AIMD entropy scheme. . . . .	43
2.5 Binding energy of water and ethanol monomers at each T site in the Beta framework, in addition to water dissociation energies to form hydroxy open sites. The reference state is the corresponding gas phase species (water or ethanol) and the empty framework. . . . .	48
2.6 Oxygen Bader charges [150] calculated for closed and open sites. . . . .	49
2.7 COHP [149, 167] bonding energies calculated from VASP wavefunctions using the Lobster code. . . . .	50
2.8 0K intrinsic potential energy barriers (in eV) for the $S_N2$ and $S_{Ni}$ pathways for bimolecular dehydration of ethanol to form DEE. . . . .	56
2.9 . . . . .	66
3.1 Sn contents, micropore volumes, and $CD_3CN$ Lewis acid site distributions for Beta materials. . . . .	82
3.2 Lewis acid site densities of Sn-Beta-F-187 and Sn-Beta-OH-187 after air treatment, ethanol exposure, and reoxidation, as determined by $CD_3CN$ IR (303 K). . . . .	89
3.3 Sample-averaged rate and equilibrium constants for Sn-Beta-F and Sn-Beta-OH. . . . .	95
3.4 Regressed rate and equilibrium constants for each Sn-Beta sample. . . .	133
3.5 Sample-averaged rate and equilibrium constants for Sn-Beta-F and Sn-Beta-OH, assuming $(L) = (\text{mol Open Sn})$ . . . . .	133
3.6 Sample-averaged rate and equilibrium constants for Sn-Beta-F and Sn-Beta-OH, assuming $(L) = (\text{mol Closed Sn})$ . . . . .	133

Table	Page
3.7 Ethanol and water uptakes from two-component breakthrough adsorption measurements <sup>a</sup> . . . . .	134
4.1 Sn contents, micropore volumes, and CD <sub>3</sub> CN Lewis acid site distributions for Beta materials used for <i>in situ</i> pyridine titration experiments. . . . .	150
4.2 Turnover rates and site densities of predominant (A) and secondary (B) sites on Sn-zeolite materials determined by <i>in situ</i> pyridine titration during ethanol dehydration catalysis (404 K, 8 kPa C <sub>2</sub> H <sub>5</sub> OH, 0.1 kPa H <sub>2</sub> O). . . . .	153
4.3 Apparent activation enthalpies and entropies for bimolecular ethanol dehydration at sites A and B on Sn-Beta-F-153 (404–438 K, 8 kPa C <sub>2</sub> H <sub>5</sub> OH, 0.1 kPa H <sub>2</sub> O) using the data in Figure 4.4. . . . .	158
4.4 Quantification <sup>a</sup> of saturated CD <sub>3</sub> CN IR spectra adsorbed on Sn-Beta-F-169 in as-made form and after treatment in 21% O <sub>2</sub> at 853 K to determine densities of Sn Lewis acid sites, extra-framework SnO <sub>2</sub> , and Si-OH groups. . . . .	168
4.5 Quantification of Sn content, micropore volume, and Sn Lewis acid site densities <sup>a</sup> on Sn-Beta-F-110 as a function of NH <sub>4</sub> F treatment time. . . . .	177
4.6 Quantification of Sn content, micropore volume, and Sn Lewis acid site densities <sup>a</sup> on Sn-Beta-F and Si-Beta@Sn-Beta-F samples. . . . .	180
4.7 Turnover rates and site densities of predominant (A) and secondary (B) sites on Sn-Beta-F-153 between 404–438 K, determined by <i>in situ</i> pyridine titration during ethanol dehydration catalysis (8 kPa C <sub>2</sub> H <sub>5</sub> OH, 0.1 kPa H <sub>2</sub> O). . . . .	250
4.8 Effect of different apparent reaction orders ( $\alpha$ ) on apparent activation entropies and free energies for sites A and B on Sn-Beta-F-153 (404–438 K, 8 kPa C <sub>2</sub> H <sub>5</sub> OH, 0.1 kPa H <sub>2</sub> O) determined by <i>in situ</i> pyridine titration. Activation enthalpies are the same as in Table 4.3 in the main text. . . . .	251
4.9 Quantification of Sn Lewis acid site densities on Sn-Beta-F samples before and after NMe <sub>4</sub> OH treatments to remove fluorine. . . . .	252
4.10 Micropore volumes and Sn Lewis acid site densities of Sn-Beta-F samples as a function of crystallization time at fixed gel composition. . . . .	252
4.11 Dehydrated (523 K) DRUV characterization of Sn-Beta-F samples as a function of crystallization time at fixed gel composition. . . . .	253
4.12 Micropore volumes and Sn Lewis acid site densities of Sn-zeolite samples and their siliceous analogs. . . . .	254
4.13 T-sites in Beta zeolites arranged in order of decreasing mean deviations from tetrahedral. . . . .	256

Table	Page
4.14 T-sites in CHA zeolites arranged in order of decreasing mean deviations from tetrahedral. . . . .	259
4.15 T-sites in MFI zeolites arranged in order of decreasing mean deviations from tetrahedral. . . . .	259
4.16 T-sites in STT zeolites arranged in order of decreasing mean deviations from tetrahedral. . . . .	263
4.17 T-sites in BEC zeolites arranged in order of decreasing mean deviations from tetrahedral. . . . .	268
4.18 Apparent activation enthalpies, entropies, and Gibbs free energies (404 K) for bimolecular ethanol dehydration at stacking fault defect-open Sn sites in Beta zeolites covered by different MARI species. . . . .	269
4.19 Ethanol adsorption energies at arbitrarily numbered T-site locations in stacking fault Beta. The T4 location denotes the Sn location used in the provided structural model. The total range in binding energy across all sites is 0.22 eV . . . . .	269
4.20 Differential dispersion energies calculated by the method of Grimme [139] using the optimized geometries of E# at the stacking fault site and E* at the closed site. . . . .	270
4.21 Distances between Sn and O or H belonging to the proximal Si-OH group in the stacking fault defect-open site and the hydrolyzed-open site reported in Bukowski et al. [180] . . . . .	270
5.1 Characterization data on Sn-Beta-F and Sn-Beta-OH zeolites . . . . .	284
5.2 First-order glucose-fructose isomerization rate constants (373 K) and extents of activation after exposure to hot (373 K) water exposure or NMe <sub>4</sub> OH treatment . . . . .	285
6.1 Active Site and Structural Characterization Data for Ti-Beta Samples . .	381
6.2 Semi-Quantitative Measurements of the Hydrophobic Properties of Microporous Voids in Ti-Beta-F and Ti-Beta-OH materials . . . . .	382
6.3 Relative Concentrations <sup>a</sup> of MARI and Minor Species during Modulation of Liquid-Phase Glucose Activity (~3000–3750 mol glucose m <sup>-3</sup> ) at 373 K followed by Processing by PSD and MCR-ALS. . . . .	383
6.4 Apparent Enthalpies and Entropies for First-Order and Zero-Order Rate Constants describing Fructose and Sorbose Formation on Ti-Beta-F-155 and Ti-Beta-OH-46 . . . . .	384

Table	Page	
6.5	Edge energies of Ti-Beta samples after exposure to ambient conditions, dehydrated, and rehydrated in wet He flow. Band maxima correspond to the primary UV-Vis F(R) peaks after dehydration shown in Figure 6.14 above. . . . .	394
6.6	E (1605 cm <sup>-1</sup> ) values determined for four separate Ti-Beta samples by sequentially dosing pyridine at 423 K. . . . .	400
6.7	Surface-area-to-volume (SA/V) ratios and silanol defect densities for selected Ti-Beta-F and Ti-Beta-OH samples normalized to Ti-Beta-F-155. . . . .	403
6.8	Ti energies, coordination numbers, and bond distances determined from Ti XAS. . . . .	427
6.9	Apparent enthalpies and entropies for first- and zero-order rate constants describing fructose and sorbose formation on Ti-Beta-F-155 and Ti-Beta-OH-46 derived from single rate measurements at 5 and 50 wt% corresponding to first-order and zero-order rates. Differences in apparent activation enthalpies ( $\Delta\Delta H_{app}$ ) and entropies ( $\Delta\Delta S_{app}$ ) are listed as the difference between Ti-Beta-F-155 and Ti-Beta-OH-46. . . . .	449
7.1	Al contents, micropore volumes, and water uptakes of zeolite Beta samples in this work. . . . .	506
7.2	Self-diffusion coefficients calculated from the TRAVIS package at representative low and high water densities per unit cell for each defect identity. . . . .	506
8.1	Elemental compositions, micropore volumes, and H <sup>+</sup> densities of H-Al-Beta-F zeolites and their dealuminated analogs. . . . .	513
8.2	Elemental compositions, micropore volumes, H <sup>+</sup> densities, and topological descriptors of Brønsted acidic solids. . . . .	547
8.3	Ethanol dehydration rate and equilibrium constants on H-Al-Beta zeolites quantified in the absence of co-fed water at 373 K. . . . .	629
8.4	Ethanol dehydration rate and equilibrium constants on H-Al-Beta zeolites quantified at 373 K in the water pressure regime described by Equation 6 in the main text (~0.02–10 kPa). . . . .	629
8.5	Ethanol dehydration rate and equilibrium constants on H-Al-Beta-F(1.2) quantified in the water pressure regime described by Equation 6 in the main text. . . . .	629
8.6	Data used to estimate H <sub>2</sub> O/H <sup>+</sup> on H-Al-Beta-F zeolites from volumetric adsorption isotherms at P/P <sub>0</sub> =0.2. . . . .	630

Table	Page
8.7 Data used to estimate $\text{H}_2\text{O}/\text{H}^+$ on H-Al-Beta-F zeolites from volumetric adsorption isotherms at $P/P_0=0.1$ . . . . .	630
8.8 Data used to estimate $\text{H}_2\text{O}/(\text{Si-OH nest})$ on deAl-Beta-F zeolites from volumetric adsorption isotherms at $P/P_0=0.1$ . . . . .	631
8.9 Data used to estimate $\text{H}_2\text{O}/(\text{Si-OH nest})$ on deAl-Beta-F zeolites from volumetric adsorption isotherms at $P/P_0=0.2$ . . . . .	631
8.10 $\text{H}_2\text{O}$ coverages quantified by <i>in situ</i> IR at 373 K on H-Al-Beta-F(2.0). . .	632
A.1 Rate expressions for bimolecular dehydration products given the series of elementary steps in Figure A.2 and different MARI species. . . . .	674
A.2 Rate parameters used to fit the data in Figure A.1 using the expressions in Table A.1. . . . .	675
B.1 H-CHA and H-MFI zeolites studied. <sup>a</sup> . . . . .	684
B.2 Regressed ethanol dehydration rate and equilibrium constants on H-MFI zeolites. <sup>a</sup> . . . . .	687
B.3 Regressed ethanol dehydration rate and equilibrium constants on H-CHA zeolites. . . . .	691

## LIST OF FIGURES

Figure	Page
1.1 Possible framework Sn active site configurations during gas-phase ethanol dehydration catalysis. . . . .	4
2.1 Hydroxy open site formation conformations corresponding to the lowest energy structures. $W^*$ refers to water adsorbed on the closed site, $W_x^*$ refers to the hydroxy open site where water has dissociated to form a hydroxyl ligand. TS refers to transition state, and the numbering (TS2) corresponds to the free energy diagram in Figure 2.4. . . . .	20
2.2 Ethoxy open site conformations corresponding to the lowest energy structures. $E^*$ refers to ethanol adsorbed on the closed site, $E_x^*$ refers to the ethoxy open site where ethanol has dissociated to form an ethoxy ligand. TS refers to transition state, and the numbering (TS3) corresponds to the free energy diagram in Figure 5. . . . .	21
2.3 Condensed DEE reaction network, showing interconversion of closed tin sites and both hydroxy-open and ethoxy-open sites, with subsequent adsorption of ethanol and formation of DEE. Nomenclature for different Sn sites is defined in the figure. A full list of elementary steps considered is provided in the Supporting Information 2.6.5. . . . .	23
2.4 Closed site reaction mechanism and selected adsorbate geometries. Free energies are evaluated at 404 K and 1 bar. For clarity, the pore wall is not shown in the TS1 diagram, and diethyl ether is referred to as D in the reaction diagrams. Nomenclature for the other reaction intermediates and Sn sites is found in Figure 2.3. . . . .	24
2.5 Ethoxy open site reaction mechanism and selected adsorbate geometries. Free energies are evaluated at 404 K and 1 bar. For clarity, the pore wall is truncated in the TS4 diagram, and diethyl ether is referred to as D in the reaction diagrams. Nomenclature for the other reaction intermediates and Sn sites is found in Figure 2.3. . . . .	27
2.6 Hydroxy open site reaction mechanism and selected adsorbate geometries. Free energies are evaluated at 404 K and 1 bar. For clarity, the pore wall is truncated in the TS4 diagram, and diethyl ether is referred to as D in the reaction diagrams. Nomenclature for the other reaction intermediates and Sn sites is found in Figure 2.3. . . . .	30

Figure	Page
2.7 Lumped DEE formation mechanisms with different Sn site speciations. Free energies are evaluated at 404 K and 1 bar. Black – closed site, blue – hydroxy open site, red – ethoxy open site. . . . .	31
2.8 Lumped ethene formation mechanisms with transition state geometries. Free energies are evaluated at 404 K and 1 bar. Ethene formation on closed sites (TS7), ethene formation on ethoxy open sites (TS8), and ethene formation on hydroxy open sites (TS9). The pore wall is truncated for clarity.	34
2.9 A) Ethanol reaction orders at 404 K, 0.1 kPa water partial pressure. Rate predictions at increasing levels of theoretical treatment are provided which include purely harmonic oscillator entropies (short dashed lines), mode decomposition method using AIMD-derived diffusion distances (long dashed lines), and the full entropy treatment with anharmonic integrated entropies (solid line). B) Surface coverages at 404K and 0.1 kPa water partial pressure at the full quasi-harmonic level. Ethanol monomer E* (solid line), ethanol dimer EE* (short dashed line), empty site * (long dashed line), ethanol-water dimer EW* (dotted line). . . . .	40
2.10 A) Water reaction orders at 404 K and 20 kPa ethanol partial pressure (short dashed line and open squares for theory and experiment), 8 kPa ethanol partial pressure (long dashed line and filled squares for theory and experiment), 0.5 kPa ethanol partial pressure (solid line and filled diamonds for theory and experiment). B) Surface coverages are at 404K and 8 kPa ethanol partial pressure. Ethanol monomer E* (solid line), ethanol dimer EE* (short dashed line), empty site * (long dashed line), ethanol-water dimer EW* (dotted line). All calculations at full integrated VDOS level. . . . .	44
2.11 Simplified reaction mechanism derived from the generalized degree of rate control. Steps 1, 2, and 3 are quasi-equilibrated. Step 4 is the rate-limiting bimolecular dehydration on closed Sn sites. . . . .	44
2.12 Electron localization function for hydroxy open site calculated in VASP. . . . .	49
2.13 Potential and free energy diagrams (404 K, 1 bar) for the full water-assisted opening process, as well as images of the transition state for both ethoxy and hydroxy open sites. . . . .	51
2.14 DEE formation on paired Sn sites identified by Bare et al. [108]. . . . .	52
2.15 Bimolecular ethanol dehydration turnover rate to form DEE (a) per Lewis acidic Sn or (b) per open Sn, (b) at $P_{EtOH}=8$ kPa, $P_{H_2O}=0.1$ kPa as a function of the total Sn content for the six Sn-Beta-OH catalysts described in Table 2.1. Dashed lines represent averages of the data. . . . .	55

Figure	Page
2.16 Images correspond to the $S_{Ni}$ conformation ( $S_{N2}$ provided in main text). Surrounding pore environment is truncated for clarity. . . . .	56
2.17 a) ethanol monomer, ethoxy open site, water monomer, hydroxy open site	59
2.18 b) ethanol-water dimer, water on ethoxy open site, water on hydroxy open site . . . . .	60
2.19 c) ethanol-ethanol dimer, ethanol on ethoxy open site, ethanol on hydroxy open site . . . . .	60
2.20 d) ethene-water dimer, ethene-water-water trimer, DEE-water-water-trimer, DEE-water dimer, DEE on hydroxy open site . . . . .	61
2.21 e) water-water on hydroxy open site, water on ethoxy open site, water on hydroxy open site, ethanol-ethene-water trimer . . . . .	61
2.22 Functional comparison for ethanol monomer and ethanol-ethanol dimer adsorption energies. . . . .	65
2.23 Simplified reaction mechanism derived from the generalized degree of rate control. Steps 1, 2, and 3 are quasi-equilibrated. Step 4 is the rate-limiting bimolecular dehydration on closed Sn sites. . . . .	67
3.1 Diethyl ether site-time yield (per Sn) at 404 K on Sn-Beta-OH-84 (a) as a function of ethanol pressure at constant 0.1 kPa $H_2O$ , with ( $\Delta$ ) and without ( $\blacksquare$ ) 0.2 Pa co-fed DEE, and (b) as a function of water pressure at constant 20 kPa $C_2H_5OH$ ( $\blacksquare$ ), and 8 kPa $C_2H_5OH$ ( $\square$ ). Dashed lines represent regressed best fits to Eq. 3.2. . . . .	83
3.2 (a) Interconversion of Sn sites in zeolites and parallel pathways that form diethyl ether, adapted from Bukowski et al. [180]. DFT-optimized struc- tures from [180] are shown in (b). . . . .	84
3.3 Simplified series of elementary steps for bimolecular ethanol dehydration. Steps 1–3 correspond to steps 3, 5 and 9 in Figure 3.2. Product desorption is kinetically-irrelevant and lumped into step 4 (step 7 in Figure 3.2) for clarity. . . . .	86
3.4 IR difference spectra (normalized by T-O-T overtone peak area) of $CD_3CN$ adsorbed at saturation coverages on Sn-Beta-F-187 at 303 K, after initial air treatment at 823 K (solid), after 3 h under 6 kPa ethanol flow (long dash), and after re-treating in air at 803 K (short dash). . . . .	89

Figure	Page
3.5 Apparent rate constants ( $k_{app}$ in Eq. 3.2) for bimolecular ethanol dehydration (per Lewis acidic Sn) at 404 K and 0.1 kPa H <sub>2</sub> O (3–35 kPa C <sub>2</sub> H <sub>5</sub> OH) on Sn-Beta-F (●) and Sn-Beta-OH (□) as a function of Sn content. Dashed lines represent average values among the series of Sn-Beta-F or Sn-Beta-OH samples. . . . .	93
3.6 Bimolecular ethanol dehydration turnover rate (per Lewis acidic Sn) at 404 K on Sn-Beta-OH-84 (□) and Sn-Beta-F-116 (●) (a) as a function of ethanol pressure at constant 0.1 kPa H <sub>2</sub> O, and (b) as a function of water pressure at constant 20 kPa C <sub>2</sub> H <sub>5</sub> OH. . . . .	94
3.7 Reaction coordinate free energy diagram for bimolecular ethanol dehydration on Sn-Beta-F (solid line) and Sn-Beta-OH (dashed line), using predictions from DFT [180] for E* in Sn-Beta-F, and the average values of K <sub>2</sub> , K <sub>3</sub> , and k <sub>4</sub> reported in Table 3 for EE*, EW*, and ‡. The depicted adsorbate and transition state geometries were calculated via DFT (BEEF-vdW) [180]. Gas-phase ethanol and water molecules are present in the free energies for E* (E(g)+W(g)), EE* (W(g)), EW* (E(g)), and ‡ (W(g)), but omitted for clarity in the scheme. . . . .	97
3.8 Single-component adsorption isotherms (302 K) of (a) H <sub>2</sub> O and (b) C <sub>2</sub> H <sub>5</sub> OH on Si-Beta-OH (□) and Si-Beta-F (●). The volume adsorbed is normalized in (a) by the volume of H <sub>2</sub> O that would fill the micropore volume (determined by N <sub>2</sub> adsorption) at its bulk liquid density, and in (b) by the volume of ethanol that fills the pores as determined by the minimum in $\partial V_{ads}/\partial \log(P/P_0)$ . The shaded regions reflect the range of gas-phase P/P <sub>0</sub> accessed during kinetic measurements (at 404 K). . . . .	99
3.9 Ratio of the equilibrium uptake of ethanol to water ( $\Gamma$ ) on Si-Beta-OH (□) and Si-Beta-F (●) at 5.8 kPa C <sub>2</sub> H <sub>5</sub> OH and 2.3 kPa H <sub>2</sub> O as estimated from single-component adsorption isotherms, two-component breakthrough adsorption measurements, and kinetic equilibrium constants ( $\Gamma_{x,k} = K_2 P_{C_2H_5OH} (K_3 P_{H_2O})^{-1}$ ). Dashed line indicates no preference for ethanol or water ( $\Gamma = 1$ ). . . . .	102
3.10 XRD patterns of Beta zeolites after air treatment (853 K, 10 h), normalized by maximum intensity. * denotes an artifact from the sample holder. XRD patterns of Sn-Beta-OH samples are reported in [151]. . . . .	113
3.11 N <sub>2</sub> adsorption isotherms (77 K) on Si-Beta-OH (▲), Si-Beta-F (■), Sn-Beta-F-187 (◆), Sn-Beta-F-153 (▼), Sn-Beta-F-116 (●), Sn-Beta-F-181 (×), and Sn-Beta-OH-187 (◇). Isotherms are offset by multiples of 100 cm <sup>3</sup> g <sup>-1</sup> (STP) for clarity. Isotherms on the other Sn-Beta-OH samples are reported in [151] . . . . .	114

Figure	Page
3.12 DRUV spectra of Sn-Beta-F-203 under ambient conditions (thin line), dehydrated at 523 K for 0.5 h under flowing helium (thick line), and rehydrated by cooling under H <sub>2</sub> O-saturated (ambient temperature) helium flow to 303 K (dashed line). . . . .	114
3.13 DRUV spectra of Sn-Beta-F-187 under ambient conditions (thin line), dehydrated at 523 K for 0.5 h under flowing helium (thick line), and rehydrated by cooling under H <sub>2</sub> O-saturated (ambient temperature) helium flow to 303 K (dashed line). . . . .	115
3.14 DRUV spectra of Sn-Beta-F-116 under ambient conditions (thin line), dehydrated at 523 K for 0.5 h under flowing helium (thick line), and rehydrated by cooling under H <sub>2</sub> O-saturated (ambient temperature) helium flow to 303 K (dashed line). . . . .	115
3.15 Normalized relative abundances of possible ethanol dehydration products at $m/z = 2$ to 75, from NIST [205]. . . . .	116
3.16 Site-time yields (per Sn) of diethyl ether (□) and ethene (■) on Sn-Beta-F-181 at 8 kPa CH <sub>3</sub> OH, 0.1 kPa H <sub>2</sub> O, and a constant site-contact time of 0.39 s (mol Sn) (mol total feed) <sup>-1</sup> over the temperature range 404–528 K, after stabilization for 12 h on stream at 404 K. . . . .	117
3.17 Diethyl ether (DEE) site-time yield (404 K, per Sn) on Sn-Beta-OH-41 as a function of time-on-stream, with initial conditions of 8 kPa CH <sub>3</sub> OH and 0.1 kPa H <sub>2</sub> O. Discontinuities represent changes in the inlet pressures. Open symbols are data points measured upon return to initial inlet conditions, and were used to extrapolate the measured data in (a) to initial times to correct for intervening deactivation and give the corrected site time yields reported in (b). . . . .	118
3.18 Parity plot of diethyl ether (DEE) site-time yields (404 K, per total Sn) measured experimentally on Sn-Beta-OH-84 and predicted by best-fit regression to Eq. 3.2 using Athena Visual Studio. . . . .	119
3.19 IR difference spectra of CD <sub>3</sub> CN (303 K) on air-treated (823 K) Sn-Beta-F-187 (relative to the vacant surface), with increasing coverage 0.2–2.3 CD <sub>3</sub> CN/Sn, and after evacuation to remove gas-phase CD <sub>3</sub> CN (bold spectrum). . . . .	119
3.20 IR difference spectra of ethanol dosing (relative to the vacant surface, dotted lines) from 0.08–80 C <sub>2</sub> H <sub>5</sub> OH/Sn on Sn-Beta-F-187 at 488 K followed by dynamic vacuum for 300 s (solid lines). . . . .	120

Figure	Page
3.21 (a) Baseline-corrected infrared spectrum of 0.4 kPa gas-phase ethanol in flowing helium through an empty IR cell at 298 K, and (b) IR difference spectrum of Sn-Beta-F-187 (relative to the vacant surface) under flowing 6 kPa C <sub>2</sub> H <sub>5</sub> OH after 3 h of reaction at 488 K. Both spectra are normalized by the maximum absorbance in the 1300–3800 cm <sup>-1</sup> range. . . . .	121
3.22 Site-time yields (488 K, per total Sn) of diethyl ether (□) and ethene (■), and turnover number (●), on Sn-Beta-F-187 at 8 kPa CH <sub>3</sub> OH and no co-fed water, as a function of time on stream. . . . .	122
3.23 IR difference spectrum of Sn-Beta-F-187 (relative to the vacant surface) at 488 K, after 3 h of ethanol reaction, 0.5 h helium purge, and 0.25 h dynamic vacuum. . . . .	122
3.24 (a) IR difference spectra of Sn-Beta-OH-187 (relative to the vacant surface) after 11 h under flowing C <sub>2</sub> H <sub>5</sub> OH (5 kPa) at 403 K (dashed), followed by 0.5 h purging in flowing helium and 0.25 h of dynamic vacuum (ca. 10 Pa) (solid). (b) Normalized (by T-O-T overtone peak area) IR difference spectra (relative to the vacant surface) of initial doses of CD <sub>3</sub> CN (303 K, 0.2–1.0 CD <sub>3</sub> CN/Sn) after the treatments described in (a). Dashed lines indicate peaks at 2308 cm <sup>-1</sup> and 2282 cm <sup>-1</sup> . (c) IR difference spectra (relative to the vacant surface, normalized by T-O-T overtone peak area) of CD <sub>3</sub> CN adsorbed on Sn-Beta-OH-187 at 303 K, fresh (solid), after 11 h under 5 kPa ethanol flow at 404 K (long dash), and after treating in air at 823 K (short dash). . . . .	123
3.25 Temperature programmed desorption in flowing helium (1.67 cm <sup>3</sup> s <sup>-1</sup> ) of ethanol reacted on Sn-Beta-F-116 at 404 K for 8 h, followed by purging in flowing helium (1.67 cm <sup>3</sup> s <sup>-1</sup> ) for (a) 0.5 h, (b) 1.0 h, (c) 2.0 h, and (d) 16 h. Traces correspond to ethene (m/z=28, thick black), water (m/z=18, thin black), and ethanol (m/z=31, gray). . . . .	124
3.26 Ethene evolved per Sn as a function of purge time during temperature programmed desorption in flowing helium (1.67 cm <sup>3</sup> s <sup>-1</sup> ) of ethanol reacted on Sn-Beta-F-116 at 404 K for 8 h, followed by purging in flowing helium (1.67 cm <sup>3</sup> s <sup>-1</sup> ). . . . .	125
3.27 Apparent rate constant for bimolecular ethanol dehydration normalized by open Sn (a) or closed Sn (b) at 404 K, and 0.1 kPa H <sub>2</sub> O (P <sub>EtOH</sub> =3–35 kPa) derived from empirical power rate law expressions (r <sub>DEE</sub> =k <sub>app</sub> P <sub>EtOH</sub> <sup>α</sup> ) on Sn-Beta-F (●) and Sn-Beta-OH (□) as a function of Sn content. Dashed lines represent averages within all Sn-Beta-F and Sn-Beta-OH samples. Vertical arrows indicate the minimum-to-maximum variation in the Sn-Beta-OH samples. . . . .	126

Figure	Page
3.28 DFT-optimized geometry of the ethanol monomer ( $E^*$ ) from Bukowski et al. [180] illustrating the Sn-O(H)C <sub>2</sub> H <sub>5</sub> distance (235 pm), and the minimum distance (320 pm) between the oxygen atom of C <sub>2</sub> H <sub>5</sub> OH in $E^*$ and a next-nearest-neighbor framework oxygen atom, as an approximation of the O-O distance between $E^*$ and the nearest possible framework Si-OH.	127
3.29 DFT-optimized geometry of the ethanol-ethanol dimer ( $EE^*$ ) from Bukowski et al. [180] illustrating O-O distance between ethanol molecules (270 pm), the Sn-O(H)C <sub>2</sub> H <sub>5</sub> distance for the strongly-bound ethanol (229 pm) and the weakly-bound ethanol (433 pm), and the minimum distance between the oxygen atom of the weakly-bound C <sub>2</sub> H <sub>5</sub> OH and a framework oxygen atom (292 pm), as an approximation of the O-O distance between it and the nearest framework Si-OH.	128
3.30 DFT-optimized geometry of the ethanol-water dimer ( $EW^*$ ) from Bukowski et al. [180] illustrating O-O distance between ethanol and water (275 pm), the Sn-O(H)C <sub>2</sub> H <sub>5</sub> distance (227 pm), the Sn-OH <sub>2</sub> distance (422 pm), and the minimum distance between the oxygen atom of H <sub>2</sub> O and a framework oxygen atom (324 pm), as an approximation of the O-O distance between it and the nearest framework Si-OH.	129
3.31 Linear-scale single-component adsorption isotherms (302 K), reported in Figure 3.8 of the main text, of (a) H <sub>2</sub> O and (b) C <sub>2</sub> H <sub>5</sub> OH on Si-Beta-OH ( $\square$ ) and Si-Beta-F ( $\bullet$ ). The volume adsorbed is normalized in (a) by the volume of H <sub>2</sub> O that would fill the micropore volume (determined by N <sub>2</sub> adsorption) at its bulk liquid density, and in (b) by the volume of ethanol that fills the pores as determined by the minimum in $\partial V_{\text{ads}}/\partial \log(P/P_0)$ .	130
3.32 Semi-log derivative ethanol adsorption isotherms on (a) Si-Beta-F and (b) Si-Beta-OH. Open circles indicate the local minima corresponding to the micropore filling transitions.	131
3.33 Two-component breakthrough adsorption measurements of ethanol (5.8 kPa, black) and water (2.3 kPa, gray) on (a) Si-Beta-F at 303 K, (b) Si-Beta-F at 403 K, (c) Si-Beta-OH at 303 K, and (d) Si-Beta-OH at 403 K.	132
4.1 Structurally distinct configurations of Sn Lewis acid sites in zeolites proposed in the literature.	137

Figure	Page
4.2 (a) Diethyl ether site-time yield (404 K, 8 kPa C <sub>2</sub> H <sub>5</sub> OH, 0.1 kPa H <sub>2</sub> O, per Sn) on Sn-Beta-OH-187 during approach to quasi-steady state, after introduction of 0.5 Pa pyridine at time point t <sub>1</sub> , and after removal of pyridine titrants from the reactant stream at time point t <sub>2</sub> . (b) Diethyl ether formation rate (per g catalyst) as a function of pyridine uptake on Sn-Beta-OH-187 during catalysis. The solid line represents regressed two-site poisoning model, and the dashed line indicates the regressed value of the number of sites A per total Sn. Inset: site B titration region (○) demonstrating reversible pyridine adsorption/desorption from site B after titrant removal from the stream (▲). . . . .	151
4.3 Bimolecular ethanol dehydration turnover rate (404 K, 8 kPa C <sub>2</sub> H <sub>5</sub> OH, 0.1 kPa H <sub>2</sub> O, per site quantified by <i>in situ</i> pyridine titration) on site A (●,○) and site B (■,□) of Sn-Beta-F (●,■) and Sn-Beta-OH (○,□) samples. Dashed lines represent average values for all sites A and for all sites B. . . . .	154
4.4 Eyring plot to determine apparent activation parameters (404–438 K, 8 kPa C <sub>2</sub> H <sub>5</sub> OH, 0.1 kPa H <sub>2</sub> O) on Sn-Beta-F-153 at sites A (■) and B (○) derived from independent <i>in situ</i> pyridine titration experiments with sample re-oxidation in between each experiment (see Figure 4.25), and by steady-state kinetic measurements (404 K, 437 K, 5–35 kPa C <sub>2</sub> H <sub>5</sub> OH, 0.1 kPa H <sub>2</sub> O) after irreversible titration of sites A (◇). . . . .	156
4.5 DFT-calculated geometries of adsorbed intermediates and transition states for bimolecular ethanol dehydration at closed Sn sites reported by Bukowski et al. [180] of the species involved in overall reaction steps to the bimolecular dehydration transition state (‡) from different MARI species described by Eq. 4.9–4.11, and the resulting apparent activation parameters and reaction orders in ethanol (α <sub>E</sub> ). Gas-phase species are above the geometries of the adsorbed intermediates and transition states. E* = ethanol monomer, EE* = ethanol-ethanol dimer, EW* = ethanol-water dimer. . . . .	157
4.6 Parity of sites titrated by pyridine <i>in situ</i> (corrected to initial time on stream) with (a) Sn <sub>2316</sub> sites or (b) Sn <sub>2308</sub> sites quantified <i>ex situ</i> by CD <sub>3</sub> CN IR on seven Sn-Beta-OH samples (□), four Sn-Beta-F (●) samples, Sn-MFI-F-129 (△), and Sn-Ge-BEC-F (◇). Dashed lines represent parity, while solid lines represent best-fit linear regressions to the data. . . . .	161

Figure	Page
4.7 Sn <sub>2308</sub> /Sn <sub>2316</sub> molar ratio (grey bars, left axis) determined from saturated CD <sub>3</sub> CN IR spectra, and position of the peak center for the first dose of adsorbed CD <sub>3</sub> CN (<0.3 CD <sub>3</sub> CN/Sn, $\diamond$ , right axis) on Sn within various zeolite frameworks or after post-synthetic treatments. The dark grey and light grey shaded regions represent the ranges of the Sn <sub>2308</sub> / Sn <sub>2316</sub> molar ratio, and the position of the first-dose peak center, respectively, that indicate predominant Sn <sub>2316</sub> sites on a sample. Parenthetical values after sample names indicate the number of independent samples averaged to give the Sn <sub>2308</sub> /Sn <sub>2316</sub> value, with error bars representing the 95% confidence interval. Otherwise, labels indicate a single sample with error bar of 20%.	164
4.8 (a) Baseline-corrected IR spectra (normalized by T-O-T overtone peak area) of Sn-Beta-F-169 in the $\nu$ (O-H) region at 303 K under vacuum, in the as-made form after treating at 473 K under dynamic vacuum for 1 h (bottom), or in the air-treated form (853 K, flowing air) after treating at 823 K under dynamic vacuum (top). (b) IR difference spectra of CD <sub>3</sub> CN (normalized by T-O-T overtone peak area) adsorbed at saturation coverages (303 K) on Sn-Beta-F-169 (thick line) and as-made Sn-Beta-F-169 (thin line).	167
4.9 (a) Composite building units of Beta, MFI, CHA, STT, and BEC zeolites [142]. The number of crystallographically distinct T sites for each framework is provided in parentheses. (b) Mean deviation from tetrahedral (O-T-O 109.47°, Eq. 4.12) for each of the T-sites in the pure-silica analogs of the Sn-zeolite frameworks synthesized in this work, as determined with the zeoTsites program [245], and listed by T-site in Table 4.13–Table 4.17.	171
4.10 IR difference spectra of CD <sub>3</sub> CN adsorbed at saturation coverages (303 K) on Sn-Beta-F-116-2 (lower thin line), Si-Beta@Sn-Beta-F-116-2 (lower thick line), Sn-Beta-F-169 (upper thin line), and Si-Beta@Sn-Beta-F-169 (upper thick line), normalized by T-O-T overtone peak area and Sn content (mol g <sup>-1</sup> ).	181
4.11 (a) High-resolution TEM image of double-pore stacking fault defects in zeolite Beta, and (b) tiling of zeolite Beta structural building units in polymorph B (left) and polymorph A (right) to meet at a stacking fault and form a defective pore structure. Adapted with permission from Wright et al. [235] Copyright 2005 American Chemical Society. (c) View of the stacking fault defect model developed in this work, with Sn substitution in the defect-open configuration, and (d) view rotated 90° to show periodicity in one direction, with the unit cell enclosed in the gray box. Blue = Si, Red = O, Gray = Sn, White = H.	183

Figure	Page
4.12 (a) Gibbs free energies of adsorbed intermediates and transition states calculated by DFT, referenced to two gas-phase ethanol molecules, for bimolecular ethanol dehydration at closed framework Sn sites (*) via a concerted pathway (pink, calculated by Bukowski et al. [180]), and at stacking fault defect-open sites (#) via a concerted pathway (orange) or a sequential pathway (black). Product desorption steps are omitted from the stacking fault defect-open pathways for clarity. The gas-phase species at each position along the reaction coordinate are included above the plot area. (b) Transition state geometries for bimolecular dehydration at the closed site (TS1), and the stacking fault defect-open sites via the concerted pathway (TS2) and the sequential pathway (TS4). Intermediate geometries are provided in Figure 4.72. . . . .	185
4.13 Structures, spectroscopic signatures ( $^{119}\text{Sn}$ NMR reported in ref. [68,106]; TMPO $^{31}\text{P}$ NMR reported in ref. [105]), and features of reactivity that distinguish defect-open and framework Sn sites in Sn-zeolites. . . . .	191
4.14 Comparison of pyridine titration data (a) <i>in situ</i> during ethanol dehydration catalysis (404 K, 8 kPa $\text{C}_2\text{H}_5\text{OH}$ , 0.1 kPa $\text{H}_2\text{O}$ ) on Sn-Beta-F-116-1, and (b) <i>ex situ</i> before measurement of initial glucose isomerization rates (373 K, 1 % (w/w) glucose) on Sn-Beta-F-110, reported in Harris et al. [56] The number of defect-open sites per Sn ( $\diamond$ , $\text{Sn}_{2316}$ ) and closed sites per Sn ( $\square$ , $\text{Sn}_{2308}$ ) are plotted on the x-axis. Dashed lines indicate the number of predominant sites titrated by pyridine. . . . .	192
4.15 Diethyl ether formation rate (per g catalyst, 404 K, 8 kPa $\text{C}_2\text{H}_5\text{OH}$ , 0.1 kPa $\text{H}_2\text{O}$ ) as a function of pyridine uptake (1 Pa pyridine) on Sn-Beta-F-181 during catalysis. Solid line represents regressed two-site poisoning model. . . . .	207
4.16 Diethyl ether formation rate (per g catalyst, 404 K, 8 kPa $\text{C}_2\text{H}_5\text{OH}$ , 0.1 kPa $\text{H}_2\text{O}$ ) as a function of pyridine uptake (0.4 Pa pyridine) on Sn-Beta-F-153(14 d) during catalysis. Solid line represents regressed two-site poisoning model. . . . .	208
4.17 Diethyl ether formation rate (per g catalyst, 404 K, 8 kPa $\text{C}_2\text{H}_5\text{OH}$ , 0.1 kPa $\text{H}_2\text{O}$ ) as a function of pyridine uptake (0.4 Pa pyridine) on Sn-Beta-F-180(3 d) during catalysis. Solid line represents regressed two-site poisoning model. . . . .	208
4.18 Diethyl ether formation rate (per g catalyst, 404 K, 8 kPa $\text{C}_2\text{H}_5\text{OH}$ , 0.1 kPa $\text{H}_2\text{O}$ ) as a function of pyridine uptake (0.5 Pa pyridine) on Sn-Beta-F-116-1 during catalysis. Solid line represents regressed two-site poisoning model. . . . .	209

Figure	Page
4.19 Diethyl ether formation rate (per g catalyst, 404 K, 8 kPa C <sub>2</sub> H <sub>5</sub> OH, 0.1 kPa H <sub>2</sub> O) as a function of pyridine uptake (0.5 Pa pyridine) on Sn-Beta-OH-84 during catalysis. Solid line represents regressed two-site poisoning model. . . . .	209
4.20 Diethyl ether formation rate (per g catalyst, 404 K, 8 kPa C <sub>2</sub> H <sub>5</sub> OH, 0.1 kPa H <sub>2</sub> O) as a function of pyridine uptake (0.5 Pa pyridine) on Sn-Beta-OH-80 during catalysis. Solid line represents regressed two-site poisoning model. . . . .	210
4.21 Diethyl ether formation rate (per g catalyst, 404 K, 8 kPa C <sub>2</sub> H <sub>5</sub> OH, 0.1 kPa H <sub>2</sub> O) as a function of pyridine uptake (0.5 Pa pyridine) on Sn-Beta-OH-95 during catalysis. Solid line represents regressed two-site poisoning model. . . . .	210
4.22 Diethyl ether formation rate (per g catalyst, 404 K, 8 kPa C <sub>2</sub> H <sub>5</sub> OH, 0.1 kPa H <sub>2</sub> O) as a function of pyridine uptake (0.6 Pa pyridine) on Sn-Beta-OH-46 during catalysis. Solid line represents regressed two-site poisoning model. . . . .	211
4.23 Diethyl ether formation rate (per g catalyst, 404 K, 8 kPa C <sub>2</sub> H <sub>5</sub> OH, 0.1 kPa H <sub>2</sub> O) as a function of pyridine uptake (0.1 Pa pyridine) on Sn-Beta-OH-41 during catalysis. Solid line represents regressed two-site poisoning model. . . . .	211
4.24 Diethyl ether formation rate (per g catalyst, 404 K, 8 kPa C <sub>2</sub> H <sub>5</sub> OH, 0.1 kPa H <sub>2</sub> O) as a function of pyridine uptake (0.5 Pa pyridine) on Sn-Beta-OH-30 during catalysis. Solid line represents regressed two-site poisoning model. . . . .	212
4.25 (a) Diethyl ether formation rate on Sn-Beta-F-153 (per g, 8 kPa C <sub>2</sub> H <sub>5</sub> OH, 0.1 kPa H <sub>2</sub> O) measured at 421 K after treating in 5% O <sub>2</sub> /He at 813 K, 2 h (○), then after repeated re-oxidation treatments (5% O <sub>2</sub> /He at 813 K, 2 h) after each rate measurement and pyridine titration, in the order 421 K (●), 404 K (■), 413 K (▲), 438 K (◇). (b) Eyring plot for the deactivation process measured over the 60 ks interval in (a), assuming exponential decay.	212
4.26 (a) Number of sites A (●) and B(■) per total Sn, and (b) their sum, quantified by <i>in situ</i> pyridine titration (404–438 K, 8 kPa C <sub>2</sub> H <sub>5</sub> OH, 0.1 kPa H <sub>2</sub> O) as a function of the extent of initial deactivation. The solid line represents the best fit to the data points. . . . .	213
4.27 Diethyl ether formation rate (per g catalyst, 421 K, 8 kPa C <sub>2</sub> H <sub>5</sub> OH, 0.1 kPa H <sub>2</sub> O) as a function of pyridine uptake (0.4 Pa pyridine) on Sn-Beta-F-153 during catalysis. Solid line represents regressed two-site poisoning model. . . . .	213

Figure	Page
4.28 Diethyl ether formation rate (per g catalyst, 421 K, 8 kPa C <sub>2</sub> H <sub>5</sub> OH, 0.1 kPa H <sub>2</sub> O) as a function of pyridine uptake (0.4 Pa pyridine) on Sn-Beta-F-153 during catalysis, after re-oxidation (5% O <sub>2</sub> /He at 813 K, 2 h). Solid line represents regressed two-site poisoning model. . . . .	214
4.29 Diethyl ether formation rate (per g catalyst, 413 K, 8 kPa C <sub>2</sub> H <sub>5</sub> OH, 0.1 kPa H <sub>2</sub> O) as a function of pyridine uptake (0.4 Pa pyridine) on Sn-Beta-F-153 during catalysis, after re-oxidation (5% O <sub>2</sub> /He at 813 K, 2 h). Solid line represents regressed two-site poisoning model. . . . .	214
4.30 Diethyl ether formation rate (per g catalyst, 438 K, 8 kPa C <sub>2</sub> H <sub>5</sub> OH, 0.1 kPa H <sub>2</sub> O) as a function of pyridine uptake (0.4 Pa pyridine) on Sn-Beta-F-153 during catalysis, after re-oxidation (5% O <sub>2</sub> /He at 813 K, 2 h). Solid line represents regressed two-site poisoning model. . . . .	215
4.31 Diethyl ether formation rate (per g catalyst, 404 K, 8 kPa C <sub>2</sub> H <sub>5</sub> OH, 1 kPa H <sub>2</sub> O) at higher water pressure as a function of pyridine uptake (0.4 Pa pyridine) on Sn-Beta-F-153 during catalysis. Solid line represents regressed two-site poisoning model. . . . .	215
4.32 (a) Diethyl ether formation rate (404 K, 8 kPa C <sub>2</sub> H <sub>5</sub> OH, 0.1 kPa H <sub>2</sub> O, per g) on Sn-Beta-F-153 during approach to quasi-steady state, after introduction of 0.4 Pa pyridine at time point t <sub>1</sub> , and after removal of pyridine titrants from the reactant stream at time point t <sub>2</sub> (○). Filled squares (■) are rate data from a separate catalyst loading (see Figure 4.25). (b) Diethyl ether formation rate as a function of pyridine uptake during catalysis, as quantified in plot (a). The solid line represents regressed two-site poisoning model, and the regressed parameters are reported in the plot area. The dashed line represents the new quasi-steady-state rate value after desorption of reversibly adsorbed pyridine at B sites. (c) TOR <sub>B</sub> values quantified after pyridine poisoning of A sites on Sn-Beta-F-153 as a function of ethanol pressure (with 0.1 kPa H <sub>2</sub> O) at 404 K (●) and 437 K (○). (d) Diethyl ether formation rate (404 K, 0.1 kPa H <sub>2</sub> O, per g) on Sn-Beta-F-153 measured previously [227] (○), after pyridine poisoning of A sites (●), and the difference between the two (◆). . . . .	216
4.33 Parity of A sites titrated by pyridine <i>in situ</i> (without correcting to initial time-on-stream) with (a) Sn <sub>2316</sub> or (b) Sn <sub>2308</sub> quantified <i>ex situ</i> by CD <sub>3</sub> CN IR on seven Sn-Beta-OH (□) and four Sn-Beta-F (●) samples. Dashed lines represent parity, while solid lines represent best-fit linear regressions to the data. . . . .	217

Figure	Page
4.34 Parity of the total number of A sites titrated by pyridine <i>in situ</i> (a) with and (b) without correcting to initial time-on-stream, with a factor $\alpha$ multiplied by $\text{Sn}_{2308}$ quantified <i>ex situ</i> by $\text{CD}_3\text{CN}$ IR on seven Sn-Beta-OH ( $\square$ ) and four Sn-Beta-F ( $\bullet$ ) samples to minimize the deviation from parity. The dashed lines represent parity, while the solid lines represent the best-fit linear regressions to the data. . . . .	218
4.35 Parity of B sites titrated by pyridine <i>in situ</i> (without correcting to initial time-on-stream) with (a) $\text{Sn}_{2316}$ or (b) $\text{Sn}_{2308}$ quantified <i>ex situ</i> by $\text{CD}_3\text{CN}$ IR on seven Sn-Beta-OH ( $\square$ ) and four Sn-Beta-F ( $\bullet$ ) samples. Dashed lines represent parity, while solid lines represent best-fit linear regressions to the data. . . . .	219
4.36 Parity of the total number of A+B sites titrated by pyridine <i>in situ</i> (without correcting to initial time-on-stream) with (a) $\text{Sn}_{2316}$ or (b) $\text{Sn}_{2308}$ quantified <i>ex situ</i> by $\text{CD}_3\text{CN}$ IR on seven Sn-Beta-OH ( $\square$ ) and four Sn-Beta-F ( $\bullet$ ) samples. Dashed lines represent parity, while solid lines represent best-fit linear regressions to the data. . . . .	220
4.37 (a) Diethyl ether site-time yield (404 K, 8 kPa $\text{C}_2\text{H}_5\text{OH}$ , 0.1 kPa $\text{H}_2\text{O}$ , per Sn) on Sn-MFI-F-129 during approach to quasi-steady state, after introduction of 0.4 Pa pyridine at time point $t_1$ , and after removal of pyridine titrants from the reactant stream at time point $t_2$ . (b) Diethyl ether formation rate (per g catalyst) as a function of pyridine uptake on Sn-MFI-F-129 during catalysis. The solid line represents regressed two-site poisoning model, and the dashed line indicates the regressed value of the number of sites A per total Sn. Inset: site B titration region ( $\circ$ ) demonstrating reversible pyridine adsorption/desorption from site B after titrant removal from the stream ( $\blacktriangle$ ). . . . .	221
4.38 (a) Diethyl ether site-time yield (404 K, 8 kPa $\text{C}_2\text{H}_5\text{OH}$ , 0.1 kPa $\text{H}_2\text{O}$ , per Sn) on Sn-Ge-BEC-F during approach to quasi-steady state, after introduction of 0.5 Pa pyridine at time point $t_1$ , and after removal of pyridine titrants from the reactant stream at time point $t_2$ . (b) Diethyl ether formation rate (per g catalyst) as a function of pyridine uptake on Sn-Ge-BEC-F during catalysis. The solid line represents regressed two-site poisoning model, and the dashed line indicates the regressed value of the number of sites A per total Sn. Inset: site B titration region ( $\circ$ ) demonstrating reversible pyridine adsorption/desorption from site B after titrant removal from the stream ( $\blacktriangle$ ). . . . .	222

Figure	Page
4.39 Diethyl ether site-time yield (404 K, 8 kPa C <sub>2</sub> H <sub>5</sub> OH, 0.1 kPa H <sub>2</sub> O, per Sn), and cumulative pyridine adsorbed (per Sn), on Sn-CHA-F-60 during approach to quasi-steady-state, after introduction of 0.7 Pa pyridine at time point t <sub>1</sub> , and after removal of pyridine titrants from the reactant stream at time point t <sub>2</sub> . . . . .	223
4.40 Parity of sites titrated by pyridine <i>in situ</i> (corrected to initial time on stream) with (a) Sn <sub>2316</sub> or (b) Sn <sub>2308</sub> quantified <i>ex situ</i> by CD <sub>3</sub> CN IR on seven Sn-Beta-OH samples (□), four Sn-Beta-F (●) samples, without Sn-MFI-F-129 and Sn-Ge-BEC-F. Dashed lines represent parity, while solid lines represent best-fit linear regressions to the data. . . . .	223
4.41 Sn <sub>2308</sub> /Sn <sub>2316</sub> molar ratios quantified from CD <sub>3</sub> CN IR spectra at saturation coverages on ten Sn-Beta-F (black) and seven Sn-Beta-OH (white) zeolites. Data for Sn-Beta-OH zeolites are reported in [151, 227], and Sn-Beta-F zeolites in this work and [56, 227] . . . . .	224
4.42 IR difference spectra of CD <sub>3</sub> CN adsorbed at saturation coverages (303 K) on Sn-Beta-F-100 (lower thin line), Sn-Beta-F-100-NMe <sub>4</sub> OH (lower thick line), Sn-Beta-F-181 (upper thin line), and Sn-Beta-F-181-NMe <sub>4</sub> OH (upper thick line), normalized by T-O-T overtone peak area. . . . .	225
4.43 IR difference spectra of CD <sub>3</sub> CN adsorbed (303 K) at saturation coverages (thick lines) and first doses (<0.3 CD <sub>3</sub> CN/Sn, thin lines) on Sn-Beta-F samples as a function of crystallization time, normalized by T-O-T overtone peak area. Spectra are offset for clarity. . . . .	226
4.44 IR difference spectra of CD <sub>3</sub> CN adsorbed (303 K) at saturation coverages (thick lines) and first doses (thin lines) on Sn-CHA-F-70 (bottom) and Sn-CHA-F-60 (top), normalized by T-O-T overtone peak area. Spectra are offset for clarity. The first dose spectrum on Sn-CHA-F-70 is multiplied by 5 (CD <sub>3</sub> CN/Sn<0.3); the CD <sub>3</sub> CN/Sn in the first dose to Sn-CHA-F-60 was 1.3/Sn. . . . .	227
4.45 IR difference spectra of CD <sub>3</sub> CN adsorbed (303 K) at saturation coverages (thick lines) and first doses (thin lines) on Sn-MFI-F-192 (bottom) and Sn-MFI-F-129 (top), normalized by T-O-T overtone peak area. Spectra are offset for clarity. The first dose spectrum on Sn-MFI-F-192 is multiplied by 5 (CD <sub>3</sub> CN/Sn<0.3); the CD <sub>3</sub> CN/Sn in the first dose to Sn-MFI-F-129 was 0.4/Sn. . . . .	228
4.46 IR difference spectra of CD <sub>3</sub> CN adsorbed (303 K) at saturation coverage (thick line) and first dose (<0.3 CD <sub>3</sub> CN/Sn, thin line) on Sn-STT-F-151, normalized by T-O-T overtone peak area. . . . .	228

Figure	Page
4.47 IR difference spectra of CD <sub>3</sub> CN adsorbed (303 K) at saturation coverage (thick line) and first dose (<0.3 CD <sub>3</sub> CN/Sn, thin line) on Sn-Ge-BEC-F, normalized by T-O-T overtone peak area. . . . .	229
4.48 IR difference spectra of the first (thin lines) and second (thick lines) doses of CD <sub>3</sub> CN (<0.3 CD <sub>3</sub> CN/Sn) adsorbed (303 K) on Si-Beta@Sn-Beta-F-169 (bottom) and Si-Beta@Sn-Beta-F-116-2 (top), normalized by T-O-T overtone peak area. . . . .	229
4.49 IR difference spectra of CD <sub>3</sub> CN adsorbed (303 K) at saturation coverages (thick lines) and first doses (<0.3 CD <sub>3</sub> CN/Sn, thin lines) on Sn-Beta-F-110 as a function of NH <sub>4</sub> F treatment time, normalized by T-O-T overtone peak area. Spectra are offset for clarity. . . . .	230
4.50 XRD patterns of Sn-Beta-F samples synthesized with varying crystallization times. . . . .	231
4.51 XRD patterns of air-treated (853 K) Sn-MFI-129 and Sn-MFI-F-192, normalized to maximum intensity. . . . .	231
4.52 XRD patterns of air-treated (853 K) Si-STT-F and as-synthesized Sn-STT-F, (a) normalized to maximum intensity and (b) normalized to maximum intensity at $2\theta > 9^\circ$ . . . . .	232
4.53 XRD patterns of (a) as-synthesized Ge-BEC-F, (b) as-synthesized Sn-Ge-BEC-F, Sn-Ge-BEC-F (c) 26 days and (d) 520 days after air treatment, and (e) Ge-BEC-F 524 days after air treatment, normalized to maximum intensity. . . . .	232
4.54 XRD patterns of (a) Sn-Beta-F-116-2, (b) Si-Beta@Sn-Beta-F-116-2, (c) Sn-Beta-F-169, and (d) Si-Beta@Sn-Beta-F-169. . . . .	233
4.55 XRD patterns of (a) Sn-Beta-F-110, (b) Sn-Beta-F-NH <sub>4</sub> F-0.083h, (c) Sn-Beta-F-NH <sub>4</sub> F-0.33h, and (d) Sn-Beta-F-NH <sub>4</sub> F-1h. . . . .	233
4.56 N <sub>2</sub> adsorption isotherms (77 K) on Sn-Beta-F samples synthesized with varying crystallization times. Isotherms are offset by 100 units for clarity. . . . .	234
4.57 N <sub>2</sub> adsorption isotherms (77 K) on Sn-MFI-F-192 (▲), Sn-MFI-F-129 (■), Si-STT-F (◆), Sn-STT-F (●), Ge-BEC-F (○), and Sn-Ge-BEC-F (□). Isotherms are offset by 100 units for clarity. . . . .	235
4.58 N <sub>2</sub> adsorption isotherms (77 K) on Sn-Beta-F-116-2 (■), Si-Beta@Sn-Beta-F-116-2 (□), Sn-Beta-F-169 (●), and Si-Beta@Sn-Beta-F-169 (○). Isotherms are offset by 100 units for clarity. . . . .	235

Figure	Page
4.59 N <sub>2</sub> adsorption isotherms (77 K) on Sn-Beta-F-110 (●), Sn-Beta-F-NH <sub>4</sub> F-0.08h (■), Sn-Beta-F-NH <sub>4</sub> F-0.08h (◆), and Sn-Beta-F-NH <sub>4</sub> F-0.08h (▲). Open symbols are for desorption data points. Isotherms are offset by 100 units for clarity. . . . .	236
4.60 Diffuse reflectance UV-Visible spectra of Sn-Beta-F samples synthesized with varying crystallization times collected after dehydration treatments (523 K). . . . .	237
4.61 Tauc plots for Sn-Beta-F samples with varying crystallization times from DRUV spectra collected after dehydration treatments (523 K). . . . .	238
4.62 (a) Thermogravimetric analysis of as-made Sn-Beta-F materials with varying crystallization times. Curves are offset by intervals of one for clarity. The weight loss associated with combustion of organic TEA <sup>+</sup> was quantified in the range of 530–730 K. Derivative weight loss curves showing the peak for this combustion event are shown in (b). . . . .	239
4.63 (a) Thermogravimetric analysis of as-made Ge-BEC-F and Sn-Ge-BEC-F materials. Curves are offset by intervals of one for clarity. The weight loss associated with combustion of organic SDA was quantified in the range of 530–730 K. Derivative weight loss curves showing the peaks for these combustion events are shown in (b). . . . .	240
4.64 Normalized baseline-corrected IR spectra of the framework vibrations of (a) Ge-BEC-F, (b) Sn-Ge-BEC-F, (c) Sn-Beta-F-181 as 1–5 wt% mixtures in KBr, and (d) Sn-Beta-F from Courtney et al. [110] measured by ATR-IR. Shaded regions and dashed lines represent Si-O-Si (light gray) $\nu_{AS}$ (1225 cm <sup>-1</sup> , 1100 cm <sup>-1</sup> , 1050 cm <sup>-1</sup> ) and $\nu_S$ (800 cm <sup>-1</sup> ), Si-O-Ge $\nu_{AS}$ (medium gray, 1000 cm <sup>-1</sup> ), and Ge-O-Ge (dark gray) $\nu_{AS}$ (890 cm <sup>-1</sup> ), in D4R (570 cm <sup>-1</sup> ) [248]. Dashed line at 720 cm <sup>-1</sup> is for extraframework GeO <sub>2</sub> . . . . .	241
4.65 <sup>19</sup> F NMR spectra, normalized by sample mass, of (top to bottom) Sn-Beta-F-100, Sn-Beta-F-100-NMe <sub>4</sub> OH, Sn-Beta-F-181, and Sn-Beta-F-181-NMe <sub>4</sub> OH. Spinning sidebands are marked by asterisks. . . . .	242
4.66 SEM images at varying magnifications of (a) Sn-Beta-F-110 after treatment in 40 wt% NH <sub>4</sub> F (323 K) for (b) 0.083 h, (c) 0.33 h, and (d) 1.0 h. . . . .	243
4.67 SEM images of representative crystals of (a) Sn-Beta-F-110 after treatment in 40 wt% NH <sub>4</sub> F (323 K) for (b) 0.083 h, (c) 0.33 h, and (d) 1.0 h. . . . .	244
4.68 Position of the peak center for the first dose of adsorbed CD <sub>3</sub> CN (<0.3 CD <sub>3</sub> CN/Sn) as a function of the mean deviation from tetrahedral averaged among all T-sites in Beta, MFI, CHA, STT, and BEC. . . . .	246

Figure	Page
4.69 Position of the peak center for the first dose of adsorbed CD <sub>3</sub> CN (<0.3 CD <sub>3</sub> CN/Sn) as a function of the mean deviation from tetrahedral for the minimum-valued T-sites in Beta, MFI, CHA, STT, and BEC. . . . .	246
4.70 Position of the peak center for the first dose of adsorbed CD <sub>3</sub> CN (<0.3 CD <sub>3</sub> CN/Sn) as a function of the mean deviation from tetrahedral for the maximum-valued T-sites in Beta, MFI, CHA, STT, and BEC. . . . .	247
4.71 Position of the peak center for the first dose of adsorbed CD <sub>3</sub> CN (<0.3 CD <sub>3</sub> CN/Sn) as a function of the mean deviation from tetrahedral for the arbitrarily-selected T-sites in Beta, MFI, CHA, STT, and BEC that give the best correlation. . . . .	247
4.72 Geometries of adsorbed intermediates (and TS3 to form E <sub>x</sub> # from E#) for the concerted pathway and sequential pathways at the stacking fault defect-open site. .XYZ files for each adsorbate are available online. . . .	248
4.73 Transition state (TS5) for DEE formation by the sequential pathway at the stacking fault defect-open site, starting from EE <sub>x</sub> # without H <sub>2</sub> O assistance, as discussed in the main text. . . . .	248
4.74 Transition state for DEE formation previously calculated [180] at the hydrolyzed-open site in Sn-Beta (T8). . . . .	249
5.1 A) Measured first-order glucose isomerization rates (per open Sn, 373 K) on Sn-Beta-F-116 after liquid water exposure for various durations (0–24 h, 373 K). B) Measured first-order glucose isomerization rates (per open Sn, 373 K) on Sn-Beta-F-100 (■), Sn-Beta-F-110 (◆), Sn-Beta-F-116 (×), Sn-Beta-F-172 (▲), Sn-Beta-F-220 (●), Sn-Beta-OH-80 (○), Sn-Beta-OH-84 (△), and Sn-Beta-OH-94 (◇) after liquid water exposure for various durations (0–24 h, 373 K). The inset shows rate constants measured after short liquid water exposure times (0–1 h). . . . .	282
5.2 <sup>19</sup> F NMR spectra collected on Sn-Beta-F samples before liquid water exposure, after liquid water exposure, and after NMe <sub>4</sub> OH treatment. The resonance centered at -135 ppm is marked with an arrow (* denotes spinning sidebands). . . . .	290
5.3 Silanol densities (per gram zeolite) on Sn-Beta-F-116 (●) and Sn-Beta-F-220 (○) as a function of liquid water exposure time. . . . .	292
5.4 <sup>29</sup> Si MAS NMR spectra of Sn-Beta-F-100 before liquid water exposure and after 0.5 h of liquid water exposure, and <sup>29</sup> Si CPMAS NMR (contact time of 2 ms) after water exposure. . . . .	293

Figure	Page
5.5 A) Vapor-phase methanol adsorption (293 K) isotherms collected on untreated Sn-Beta-F-116 (■) and on Sn-Beta-F-116 after 0.5 (◆), 3 (▲), 6 (×), and 24 (●) h of hot (373 K) liquid water exposure time. B) Vapor-phase water adsorption (293 K) isotherms collected on untreated Sn-Beta-F-116 (■) and on Sn-Beta-F-116 after 0.5 (◆), 3 (▲), 6 (×), and 24 (●) h of hot (373 K) liquid water exposure time. . . . .	294
5.6 Measured first-order glucose isomerization rate constants (373 K) on Sn-Beta-F samples prior to liquid water exposure (●), Sn-Beta-F samples after 24 h of liquid water exposure (○), Sn-Beta-OH samples prior to liquid water exposure (■), and Sn-Beta-OH samples after 24 h of liquid water exposure (□). . . . .	296
5.7 A) Observed activation extents (373 K, 1 wt%) as a function of initial silanol density on Sn-Beta-F (●) and Sn-Beta-OH (○) zeolites. B) Observed activation extents (373 K, 1 wt%) as a function of initial hydrophilic site density on Sn-Beta-F (●) and Sn-Beta-OH (○) zeolites. Hydrophilic sites represent the linear combination of silanol defects and Lewis acidic Sn centers on a given sample. . . . .	299
5.8 Powder XRD patterns of Sn-Beta samples studied in this work. . . . .	304
5.9 N <sub>2</sub> adsorption isotherms (77 K) of Sn-Beta samples studied in this work. Isotherms are offset by 200 cm <sup>3</sup> g <sup>-1</sup> for clarity. . . . .	305
5.10 Tauc plots of Sn-Beta samples studied in this work after treatment in flowing He at 523 K for 1800 s. Edge energies are summarized in Table 5.1.305	
5.11 Dehydrated UV-Vis spectra (523 K, 1800 s) of Sn-Beta samples studied in this work. . . . .	306
5.12 IR spectra collected on CD <sub>3</sub> CN-saturated Sn-Beta samples studied in this work. Spectra were normalized by combination and overtone modes for Si—O—Si stretches prior to the subtraction of spectra collected before CDCN adsorption. Dashed lines are drawn at 2308 cm <sup>-1</sup> (CD <sub>3</sub> CN bound to closed Sn), 2316 cm <sup>-1</sup> (CD <sub>3</sub> CN bound to open Sn), and 2275 cm <sup>-1</sup> (CD <sub>3</sub> CN bound to silanols). . . . .	307
5.13 Vapor-phase water adsorption isotherms (293 K) on Sn-Beta samples studied in this work. Isotherms are offset by 100 cm <sup>3</sup> g <sup>-1</sup> for clarity. . . . .	308
5.14 Vapor-phase methanol adsorption isotherms (293 K) on Sn-Beta samples studied in this work. Isotherms are offset by 100 cm <sup>3</sup> g <sup>-1</sup> for clarity. . . . .	308
5.15 Powder XRD patterns of Sn-Beta-F-116 samples after various (0-24 h) amounts of hot (373 K) water exposure time. . . . .	310

Figure	Page
5.16 N <sub>2</sub> adsorption isotherms (77 K) of Sn-Beta-F-116 after 0 (diamond), 0.5 (circle), 3 (square), and 24 h (triangle) of hot (373 K) water exposure time.	311
5.17 SEM images of Sn-Beta-F-116 (a) before and (b) after 24 h of hot (373 K) water exposure time. . . . .	311
5.18 Sn density (A), Lewis acidic Sn fraction (B), and SnO <sub>x</sub> fraction (C) on Sn-Beta-F-116 as a function of liquid water exposure time. Site densities on untreated materials are plotted at 1 min of water exposure. . . . .	312
5.19 Tauc plots collected after treatment in flowing He at 523 K for 1800 s on Sn-Beta samples after various (0-24 h) amounts of hot (373 K) water exposure time. . . . .	313
5.20 Dehydrated UV-Vis spectra (523 K, 1800 s) of Sn-Beta samples after various (0-24 h) amounts of hot (373 K) water exposure time. . . . .	314
5.21 Open (◦) and closed Sn density (●) per mol Lewis acidic Sn on Sn-Beta-F-116 as a function of liquid water exposure time. Site densities on untreated materials are plotted at 1 min of water exposure. . . . .	314
5.22 Powder XRD patterns of Sn-Beta-F-100 samples before and after NMe <sub>4</sub> OH treatment. . . . .	315
5.23 IR spectra collected on CD <sub>3</sub> CN-saturated Sn-Beta-F-100 samples before and after NMe <sub>4</sub> OH treatment. Spectra were normalized by combination and overtone modes for Si–O–Si stretches prior to the subtraction of spectra collected before CD <sub>3</sub> CN adsorption. Dashed lines are drawn at 2308 cm <sup>-1</sup> (CD <sub>3</sub> CN bound to closed Sn), 2316 cm <sup>-1</sup> (CD <sub>3</sub> CN bound to open Sn), and 2275 cm <sup>-1</sup> (CD <sub>3</sub> CN bound to silanols). . . . .	316
5.24 Water uptakes at P/P <sub>0</sub> = 0.2 (373 K) after rigorously subtracting off two water molecules per Lewis acid site counted from CD <sub>3</sub> CN titration plotted against bulk silanol defect density from CD <sub>3</sub> CN titration measurements. The solid line is a best fit line forced through the origin to guide the eye.	317
5.25 Measured first-order glucose isomerization rates (per Lewis acidic Ti, 373 K) on Ti-Beta-F-155 after hot (373 K) liquid water exposure (0-24 h). Characterization data on Ti-Beta-F-155 is reported in Ref. [57]. . . . .	318
5.26 Observed activation extents (373 K, 1 wt%) as a function of initial open Sn density on Sn-Beta-F (closed) and Sn-Beta-OH (open) zeolites. Observed activation extents are defined as the ratio of the highest measured first-order glucose isomerization rate constant per sample normalized by the measured first-order rate constant on the unexposed Sn-Beta sample. . .	319

Figure	Page
5.27 Observed activation extents (373 K, 1 wt%) as a function of initial closed Sn density on Sn-Beta-F (closed) and Sn-Beta-OH (open) zeolites. Observed activation extents are defined as the ratio of the highest measured first-order glucose isomerization rate constant per sample normalized by the measured first-order rate constant on the unexposed Sn-Beta sample.	320
5.28 Observed activation extents (373 K, 1 wt%) as a function of initial initial open-to-closed ratio on Sn-Beta-F (closed) and Sn-Beta-OH (open) zeolites. Observed activation extents are defined as the ratio of the highest measured first-order glucose isomerization rate constant per sample normalized by the measured first-order rate constant on the unexposed Sn-Beta sample. . . . .	321
5.29 Observed activation extents (373 K, 1 wt%) as a function of initial Lewis acidic Sn density on Sn-Beta-F (closed) and Sn-Beta-OH (open) zeolites. Observed activation extents are defined as the ratio of the highest measured first-order glucose isomerization rate constant per sample normalized by the measured first-order rate constant on the unexposed Sn-Beta sample.	322
5.30 Observed activation extents (373 K, 1 wt%) as a function of initial SnO <sub>x</sub> density on Sn-Beta-F (closed) and Sn-Beta-OH (open) zeolites. Observed activation extents are defined as the ratio of the highest measured first-order glucose isomerization rate constant per sample normalized by the measured first-order rate constant on the unexposed Sn-Beta sample. . .	323
5.31 Solution-phase <sup>1</sup> H NMR of fructose products formed after contacting 1 wt% glucose solutions (373 K) with Sn-Beta-F samples. A fructose standard is given for direct comparison. . . . .	324
6.1 CD <sub>3</sub> CN IR spectra of the $\nu$ (C $\equiv$ N) stretching region with increasing coverage of CD <sub>3</sub> CN on Ti-Beta-F-155 (0.013, 0.026, 0.065, 0.170, and 0.235 CD <sub>3</sub> CN/Ti, light-to-dark). Dashed vertical lines correspond to 2308 and 2275 cm <sup>-1</sup> for $\nu$ (C $\equiv$ N) stretching vibrations of CD <sub>3</sub> CN bound to Lewis acidic Ti sites and silanol groups, respectively. The inset shows the integrated area of the 2308 cm <sup>-1</sup> peak multiplied by the cross-sectional area of the IR wafer, plotted against the moles of CD <sub>3</sub> CN adsorbed at Lewis acidic Ti sites for Ti-Beta-F-155 (●), Ti-Beta-F-135 (■), and Ti-Beta-OH-38 (▲). The dashed line in the inset is the best fit line through all data, with the slope representing the integrated molar extinction coefficient for CD <sub>3</sub> CN adsorbed onto Lewis acidic Ti sites. . . . .	342

Figure	Page	
6.2	Baseline-corrected difference IR spectra of adsorbed water on Ti-Beta-F-155 (top, magnified for clarity) and Ti-Beta-OH-46 (bottom) at 298 K for (a) $\delta(\text{HOH})$ scissoring modes in the water bending region and (b) the $\nu(\text{O-H})$ water stretching region. Difference spectra reflect the subtraction of spectrum measured on the sample under vacuum prior to water flow and corrected for background water adsorption onto the IR cell. Spectra for each sample displayed from bottom-to-top correspond to $P/P_0=0.1, 0.2, 0.5,$ and $0.75$ . The insets display the change in (a) the water bending peak area and (b) the water stretching peak maximum with increasing water concentration for Ti-Beta-F-155 ( $\bullet$ ) and Ti-Beta-OH-46 ( $\blacktriangle$ ). . . . .	348
6.3	Free energy (373 K, 1 bar) reaction coordinate diagram for the formation of fructose from glucose on closed-form Ti Lewis acid sites. Reaction arrows with overlaid circles indicate quasi-equilibrated events or the formation of transition states from relevant precursors. Relative enthalpies are given near inset images. . . . .	352
6.4	Initial first-order (a) fructose and (b) sorbose formation rates (373 K, pH 4) normalized per total Ti content as a function of Ti/Si ratio, for Ti-Beta-F ( $\bullet$ ) and Ti-Beta-OH samples ( $\blacktriangle$ ). Data on Ti-Beta-F ( $\times$ ) and Ti-Beta-OH ( $\blacksquare$ ) samples reported previously in Ref. [307] are plotted for comparison. Dashed lines correspond to average values within the series of Ti-Beta-F and Ti-Beta-OH samples. . . . .	356
6.5	Dependence of initial glucose isomerization rates (373 K, pH 4) for fructose (filled) and sorbose (open) formation on Ti-Beta-F-155 ( $\bullet, \circ$ ) and Ti-Beta-OH-46 ( $\blacktriangle, \triangle$ ) as a function of initial glucose thermodynamic activity (corresponding to 1–50 wt% initial glucose concentration). Solid lines represent fits of the experimental data to the rate equation (Eq. 6.9) using activation enthalpies and entropies given in Table 6.4. The inset shows initial glucose isomerization rates at low glucose thermodynamic activities, highlighting the first-order kinetic regime. . . . .	357

Figure	Page
6.6 (a) ATR-IR spectra of MARI (top, water derived) and minor (bottom, glucose derived) intermediates on Ti-Beta-F-155 (black) and Ti-Beta-OH-46 (gray) that oscillate with aqueous-phase glucose activity (0–700 mol m <sup>-3</sup> ) at 373 K. Glucose spectra are normalized by the peak at ~1030 cm <sup>-1</sup> and water spectra are normalized by the peak at ~1630 cm <sup>-1</sup> . Spectra reflecting aqueous-phase glucose (330 mol m <sup>-3</sup> ) flowing over the ZnSe crystal is overlaid on the glucose spectra (dashed). Dashed vertical lines at 1630 and 3400 cm <sup>-1</sup> indicate water bending and stretching vibrational modes, respectively. (b) ATR-IR spectra of the MARI (bottom four) and minor (top four) species that oscillate with aqueous-phase glucose activity (~3000–3750 mol glucose m <sup>-3</sup> , 373 K, normalized by the maximum feature at ~1030 cm <sup>-1</sup> ) over Ti-Beta-F-155, Ti-Beta-OH-46, Si-Beta-F, and blank ZnSe crystal from top to bottom, respectively. The inset depicts difference spectra between aqueous-phase glucose flowing over the ZnSe crystal and the MARI (black) or minor species (gray) species observed on Ti-Beta-OH-46 (top) and Ti-Beta-F-155 (bottom) spectra from modulating aqueous-phase glucose activity (~3000–3750 mol glucose m <sup>-3</sup> ) at 373 K after normalization by the peak centered at ~1030 cm <sup>-1</sup> ; dashed lines indicate the baseline. All spectra are obtained during MES experiments and isolated by processing through PSD and MCR-ALS. . . . .	361
6.7 Plausible Glucose Isomerization Mechanism for Fructose and Sorbose formation on Lewis Acidic Ti Sites. Modified from Ref. [307] and shown in greater detail in Figures 6.3 and 6.33, Supp. Info. Quasi-equilibrated glucose adsorption (Step 1) forms reactive bound glucose intermediates (R* <sub>F</sub> and R* <sub>S</sub> ) which form bound fructose (Step 2a) or sorbose (Step 2b) isomers through the formation of kinetically relevant hydride shift transition states. Quasi-equilibrated fructose (Step 3,F) and sorbose (Step 3,S) desorption phenomena release the product into the liquid phase. Quasi-equilibrated water adsorption onto Lewis acidic active sites (Steps 4 and 5) inhibits isomerization rates at low glucose coverages. . . . .	366
6.8 Dependence of initial fructose formation rates (pH 3) on Ti-Beta-F-155 on initial glucose thermodynamic activity (corresponding to 1–50 wt% glucose concentration) at 368 (■), 373 (×), 378 (▲), and 383 K (●). Solid lines represent regression of the data to the rate equation (Eq. 6.9) using activation enthalpies and entropies given in Table 6.4. The inset shows initial glucose isomerization rates at low glucose thermodynamic activities, highlighting the first-order kinetic regime. . . . .	369
6.9 Powder XRD patterns of Ti-Beta-F (A) Ti-Beta-OH (B) samples studied in this work. Weak signals around 9–10° reflect an artifact from the sample holders used to collect XRD patterns. . . . .	385

Figure	Page
6.10 N <sub>2</sub> adsorption isotherms (77 K) of Ti-Beta-F (A) Ti-Beta-OH (B) samples studied in this work. Isotherms are offset by 200 cm <sup>3</sup> g <sup>-1</sup> for clarity. . . .	386
6.11 SEM images of selected Ti-Beta-F samples: (a) Ti-Beta-F-135, (b) Ti-Beta-F-155, and (c) Ti-Beta-F-180. Bulk sample uniformity is assumed based on images for (d) Ti-Beta-F-135, (e) Ti-Beta-F-155, and (f) Ti-Beta-F-180. Larger crystal aggregates reflect Si-Beta-F seeds used to nucleate the formation of Ti-Beta-F. . . . .	387
6.12 SEM images of selected Ti-Beta-OH samples: (a) Ti-Beta-OH-46, (b) Ti-Beta-OH-34, and (c) Ti-Beta-OH-71. Bulk sample uniformity is assumed based on images for (d) Ti-Beta-OH-46, (e) Ti-Beta-OH-34, and (f) Ti-Beta-OH-71 which show larger agglomerates of small crystals. . . . .	388
6.13 SEM images of Ti-Beta-OH-34 at various steps of the synthesis procedure: (a) Al-Beta parent material, (b) after nitric acid treatment for dealumination, and (c) after TiCl <sub>4</sub> grafting to form Ti-Beta-OH-34. Bulk sample uniformity is assumed based on images for (d) Al-Beta parent material, (e) after nitric acid treatment for dealumination, and (f) after TiCl <sub>4</sub> grafting to form Ti-Beta-OH-34. All show larger agglomerates of small crystals. . .	389
6.14 Hydrated UV-Vis spectra of (A) Ti-Beta-F and (B) Ti-Beta-OH samples studied in this work collected prior to dehydration at 523 K. . . . .	390
6.15 Dehydrated UV-Vis spectra (523 K, 1800 s) of (A) Ti-Beta-F and (B) Ti-Beta-OH samples studied in this work. . . . .	391
6.16 Tauc plots of (A) Ti-Beta-F and (B) Ti-Beta-OH samples studied in this work prior to heating and sample dehydration (“hydrated” samples). Edge energies are summarized in Table 6.5. . . . .	392
6.17 Tauc plots of (A) Ti-Beta-F and (B) Ti-Beta-OH samples studied in this work after treatment in flowing He at 523 K for 1800 s. Edge energies are summarized in Table 6.5. . . . .	393
6.18 IR spectra on Ti-Beta-OH-46 after progressive titration of CD <sub>3</sub> CN at 303 K (CD <sub>3</sub> CN/Ti = 0.002-2.34). Dashed lines are drawn at 2308 cm <sup>-1</sup> (CD <sub>3</sub> CN bound to Lewis acidic Ti) and 2275 cm <sup>-1</sup> (CD <sub>3</sub> CN hydrogen bound to silanols). Note that the peak center shifts slightly to lower wavenumbers with increasing adsorbed CD <sub>3</sub> CN concentrations. . . . .	395

Figure	Page
6.19 CD <sub>3</sub> CN-saturated IR spectra for Ti-Beta-F-155. The thickest solid line reflects the measured spectra upon saturation with CD <sub>3</sub> CN while thinner lines indicate constitute peaks associated with CD <sub>3</sub> CN bound to Lewis acidic Ti sites (2308 cm <sup>-1</sup> ), CD <sub>3</sub> CN bound to silanols (2275 cm <sup>-1</sup> ), and gas phase physisorbed CD <sub>3</sub> CN (2265 cm <sup>-1</sup> ). The dashed line represents the modeled spectra from combining deconvoluted peaks. . . . .	396
6.20 IR spectra collected on (A) CD <sub>3</sub> CN-saturated Ti-Beta-F and (B) CD <sub>3</sub> CN-saturated Ti-Beta-OH samples studied in this work. Dashed lines are drawn at 2308 cm <sup>-1</sup> (CD <sub>3</sub> CN bound to Lewis acidic Ti) and 2275 cm <sup>-1</sup> (CD <sub>3</sub> CN bound to silanols). . . . .	397
6.21 IR spectra measured (a) after the first four doses of pyridine on Ti-Beta-F-135 (0.015–0.058 mol pyridine (mol Ti) <sup>-1</sup> ) and (b) after saturation of Ti-Beta-F-135 with pyridine (1.05 mol pyridine (mol Ti) <sup>-1</sup> ). The components included in the deconvolution are shown (thin solid lines) with the resulting fit envelope (dotted line) and the measured spectra (thick solid line). . .	399
6.22 (A) Integrated peak area normalized by wafer cross-sectional areas for the IR feature centered at 1605 cm <sup>-1</sup> as a function of moles pyridine adsorbed onto Ti-Beta-F-155 (◆), Ti-Beta-F-135 (●), Ti-Beta-F-170 (▲), and Ti-Beta-OH-46 (■). Dashed lines indicate best fit lines through the origin for each sample with slopes equal to integrated molar extinction coefficients as listed in Table 6.7. (B) Integrated peak area normalized by wafer cross-sectional areas for the IR feature centered at 1605 cm <sup>-1</sup> as a function of moles pyridine adsorbed onto Ti-Beta-F-155, Ti-Beta-F-135, Ti-Beta-F-170, and Ti-Beta-OH-46 as a single data set (●). The dashed line indicates the best fit line through the origin for the combined data set with the slope equal to the average integrated molar extinction coefficient. . . . .	400
6.23 Lewis acid site densities determined from pyridine-saturation IR experiments plotted against Lewis acid site densities determined from CD <sub>3</sub> CN-saturation IR experiments. The dashed line is a parity line drawn to guide the eye. . . . .	401
6.24 Vapor-phase water adsorption isotherms at 293 K on Ti-Beta-F samples studied in this work. Isotherms are offset by 100 cm <sup>3</sup> g <sup>-1</sup> for clarity. . . .	404
6.25 Vapor-phase water adsorption isotherms at 293 K on Ti-Beta-OH samples studied in this work. Isotherms are offset by 100 cm <sup>3</sup> g <sup>-1</sup> for clarity. . . .	405
6.26 Water uptakes at P/P <sub>0</sub> = 0.2 (373 K) after subtracting two moles of water molecules per mol Ti Lewis acid site (quantified by CD <sub>3</sub> CN IR) as a function of the bulk silanol defect density (quantified by CD <sub>3</sub> CN IR). The solid line is a best fit line drawn through the origin to guide the eye. . . . .	405

Figure	Page
6.27 Vapor-phase methanol adsorption isotherms at 293 K on Ti-Beta-F samples studied in this work. Isotherms are offset by $100 \text{ cm}^3 \text{ g}^{-1}$ for clarity. .	406
6.28 Vapor-phase methanol adsorption isotherms at 293 K on Ti-Beta-OH samples studied in this work. Isotherms are offset by $100 \text{ cm}^3 \text{ g}^{-1}$ for clarity. .	406
6.29 Differential, subtracted, normalized, cell-corrected IR spectra of adsorbed $\text{H}_2\text{O}$ at $P/P_0=0.1, 0.2, 0.5,$ and $0.75$ (lightest to darkest, 298 K) on (A) Ti-Beta-F-155 and (B) Ti-Beta-OH-46. Differential spectra are spectral changes between a given $P/P_0$ value and the previous relative pressure spectra, isolating changes in spectral features due only to increasing water partial pressure. . . . .	407
6.30 Vapor-phase water adsorption isotherms at 298 K on Ti-Beta-F-155 ( $\bullet$ ) and Ti-Beta-OH-46 ( $\square$ ). . . . .	408
6.31 Subtracted IR spectra of the OH stretching region as a function of increased relative pressure of water on (A) Ti-Beta-F-155 and (B) Ti-Beta-OH-46. . . . .	409
6.32 Solution phase $^{13}\text{C}$ NMR of monosaccharide solutions after contacting 5 wt% glucose solutions with Ti-Beta-F-133, Ti-Beta-F-155, and Ti-Beta-OH-46. Glucose, fructose and sorbose standards are given for direct comparison. . . . .	410
6.33 Free energy (373 K, 1 bar) reaction coordinate diagram for the formation of sorbose from glucose on closed-form Ti Lewis acid sites. Reaction arrows with overlaid circles indicate quasi-equilibrated events or the formation of transition states from relevant precursors. Relative enthalpies are given near inset images. . . . .	411
6.34 First-order fructose ( $\bullet, \blacktriangle$ ) and sorbose ( $\circ, \triangle$ ) formation rate constants (373 K, pH 4) normalized per total Lewis acidic Ti content (measured from $\text{CD}_3\text{CN}$ IR) as a function of Lewis acidic Ti density for (A) Ti-Beta-F and (B) Ti-Beta-OH samples. . . . .	414
6.35 Dependence of initial glucose isomerization rates (373 K, pH 4) for fructose (filled) and sorbose (open) formation on Ti-Beta-F-155 ( $\bullet, \circ$ ) and Ti-Beta-OH-46 ( $\blacktriangle, \triangle$ ) as a function of initial glucose concentration (1–50 wt%). Solid lines represent fits of the experimental data to the rate equation (Eq. 6.25 of the main text) using activation enthalpies and entropies given in Table 6.4. . . . .	416

Figure	Page
6.36 a) Time-resolved infrared spectra obtained <i>in situ</i> during reactions of glucose and water over Ti-Beta-F-155 while modulating glucose concentrations (42–50 wt%) with a period length of 250 s at 373 K. b) Phase resolved spectra that result from phase sensitive detection of the time resolved spectra in (a). Coloring indicates absorbance intensity. . . . .	419
6.37 Dependence of fructose-to-sorbose selectivity (373 K, pH 4) on Ti-Beta-F-155 (●) and Ti-Beta-OH-46 (▲) as a function of initial glucose thermodynamic activity. Relatively constant product selectivities support the identification of the secondary bound glucose species being a bound intermediate which is not directly responsible for sorbose formation as relative coverages of MARI and secondary bound species observed from ATR-IR are affected by changes in initial glucose activity. . . . .	420
6.38 Ti K edge XANES of water exchanged Ti-Beta-OH-46 zeolite after dehydration at 523 K in He (solid) and under ambient conditions (dashed). The increase in intensity of the pre-edge peak is consistent with a decrease in coordination number from 6 to 4 upon dehydration. . . . .	421
6.39 Magnitude of the Fourier transform of the $k^2$ -weighted Ti K edge EXAFS of water exchanged Ti-Beta-OH-46 zeolite under ambient conditions (solid) and after dehydration at 523 K in He (dashed). . . . .	422
6.40 Magnitude of the Fourier transform of the $k^2$ -weighted Ti K edge EXAFS of water exchanged Ti-Beta-OH-46 zeolite after dehydration at 523 K in He (solid) and $\Delta$ EXAFS of the hydrated and dehydrated water exchanged catalyst (dashed). The $\Delta$ EXAFS spectrum was obtained by subtracting the $k^0$ -weighted EXAFS of the sample after dehydration from the $k^0$ -weighted EXAFS of the sample under ambient conditions and is representative of the water adsorbed on Ti under ambient conditions. . . . .	423
6.41 Ti K edge XANES of water (dashed) and glucose (solid) exchanged Ti-Beta-OH-46 zeolite under ambient conditions. The spectra are identical within experimental error indicating Ti has equivalent coordination environments in the two samples. The intensity of the pre-edge peak is consistent with a coordination number of 6. . . . .	424
6.42 Ti K edge XANES of Ti-Beta-OH-46 zeolite: solid – glucose exchanged under ambient conditions, long dashes – glucose exchanged after treatment at 523 K in He, and short dashes – water exchanged after treatment at 523 K in He. The intensity of the pre-edge peak in the glucose exchanged sample after treatment in He at 523 K is consistent with a coordination number of 5 and suggests glucose adsorbed through a single oxygen. . . .	425

Figure	Page
6.43 Plausible glucose isomerization mechanism for fructose and sorbose formation on Lewis acidic Ti sites, modified from Ref. [53]. Quasi-equilibrated glucose adsorption (Steps 1a, 1b) forms bound glucose intermediates which form bound fructose (Step 2a) or sorbose (Step 2b) isomers through kinetically relevant hydride shifts. Quasi-equilibrated fructose (Step 3a) and sorbose (Step 3b) desorption phenomena release the product into the liquid phase. Quasi-equilibrated water adsorption onto Lewis acidic active sites (Steps 4 and 5) inhibits isomerization rates at low glucose coverages.	429
6.44 Dependence of initial sorbose formation rates (pH 3) on Ti-Beta-F-155 on initial glucose thermodynamic activity (corresponding to 1–50 wt% initial glucose concentration) at 368 (■), 373 (×), 378 (▲), and 383 K (●). Solid lines for all data represent modeled regressions of the experimental data to the overall rate equation given in Eq. 6.16 in the main text using activation enthalpies and entropies given in Table 6.4. . . . .	436
6.45 Dependence of initial fructose formation rates (pH 3) on Ti-Beta-OH-46 on initial glucose thermodynamic activity (corresponding to 1–50 wt% initial glucose concentration) at 368 (■), 373 (×), 378 (▲), and 383 K (●). Solid lines for all data represent modeled regressions of the experimental data to the overall rate equation given in Eq. 6.16 in the main text using activation enthalpies and entropies given in Table 6.4. . . . .	437
6.46 Dependence of initial sorbose formation rates (pH 3) on Ti-Beta-OH-46 on initial glucose thermodynamic activity (corresponding to 1–50 wt% initial glucose concentration) at 368 (■), 373 (×), 378 (▲), and 383 K (●). Solid lines for all data represent modeled regressions of the experimental data to the overall rate equation given in Eq. 6.16 in the main text using activation enthalpies and entropies given in Table 6.4. . . . .	438
6.47 Dependence of initial fructose formation rates (pH 3) on Ti-Beta-F-155 on initial glucose and osmotic thermodynamic activity ratio (corresponding to 1–50 wt% initial glucose concentration) at 368 (■), 373 (×), 378 (▲), and 383 K (●). Solid lines for all data represent modeled regressions of the experimental data to the overall rate equation given in Eq. 6.16 in the main text using activation enthalpies and entropies given in Table 6.4. . . . .	439
6.48 Dependence of initial sorbose formation rates (pH 3) on Ti-Beta-F-155 on initial glucose and osmotic thermodynamic activity ratio (corresponding to 1–50 wt% initial glucose concentration) at 368 (■), 373 (×), 378 (▲), and 383 K (●). Solid lines for all data represent modeled regressions of the experimental data to the overall rate equation given in Eq. 6.16 in the main text using activation enthalpies and entropies given in Table 6.4. . . . .	440

Figure	Page
6.49 Percent residual plot of fructose formation rates on Ti-Beta-F-155 as a function of initial glucose thermodynamic activity (corresponding to 1–50 wt% initial glucose concentration) at 368 (■), 373 (×), 378 (▲), and 383 K (●) comparing experimental rate measurements with modeled rate behavior from Eq. 6.16 from the main text. Percent residuals were obtained from Eq. 6.72. . . . .	442
6.50 Percent residual plot of sorbose formation rates on Ti-Beta-F-155 as a function of initial glucose thermodynamic activity (corresponding to 1–50 wt% initial glucose concentration) at 368 (■), 373 (×), 378 (▲), and 383 K (●) comparing experimental rate measurements with modeled rate behavior from Eq. 6.16 from the main text. Percent residuals were obtained from Eq. 6.72. . . . .	443
6.51 Percent residual plot of fructose formation rates on Ti-Beta-OH-46 as a function of initial glucose thermodynamic activity (corresponding to 1–50 wt% initial glucose concentration) at 368 (■), 373 (×), 378 (▲), and 383 K (●) comparing experimental rate measurements with modeled rate behavior from Eq. 6.16 from the main text. Percent residuals were obtained from Eq. 6.72. . . . .	444
6.52 Percent residual plot of sorbose formation rates on Ti-Beta-OH-46 as a function of initial glucose thermodynamic activity (corresponding to 1–50 wt% initial glucose concentration) at 368 (■), 373 (×), 378 (▲), and 383 K (●) comparing experimental rate measurements with modeled rate behavior from Eq. 6.16 from the main text. Percent residuals were obtained from Eq. 6.72. . . . .	445
6.53 Arrhenius plot for apparent first-order fructose (A) and sorbose (B) formation rate constants (368–383 K, 5 wt%) on Ti-Beta-F-155 (●) and Ti-Beta-OH-46 (○). Solid lines represent the results of the regression of Eq. 6.16 and dashed lines represent regressions using rate measurements at 5 wt% on Ti-Beta-F-155 (black) and Ti-Beta-OH-46 (gray). Both regression lines follow the Eyring equation with activation enthalpies and entropies given in Table 6.4 of the main text and Table 6.9, respectively. . . . .	447
6.54 Arrhenius plot for apparent zero-order fructose (A) and sorbose (B) formation rate constants (368–383 K, 50 wt%) on Ti-Beta-F-155 (●) and Ti-Beta-OH-46 (○). Solid lines represent the results of the regression of Eq. 6.16 and dashed lines represent regressions using rate measurements at 50 wt% on Ti-Beta-F-155 (black) and Ti-Beta-OH-46 (gray). Both regressions follow the Eyring equation with activation enthalpies and entropies given in Table 6.4 of the main text and Table 6.9, respectively. . . . .	448

Figure	Page
6.55 DFT-calculated glucose adsorption energies (a) and effective first- (b) and zero-order (c) energy barriers for glucose-fructose isomerization. Enthalpies (■) and free energies (●) are shown in $\text{kJ mol}^{-1}$ and entropies (◆) in $\text{J mol}^{-1} \text{K}^{-1}$ (373 K). The intrapore water molecule density was assumed to remain constant during glucose adsorption and reaction for first-order analyses yet water molecules were allowed to reorient into lowest energy configurations in all cases. . . . .	450
7.1 Zeolite Beta with intersecting pore structures (a,b). Water physisorbed in Si-Beta exploring parallel and perpendicular pore structures (c). Closed Sn (d), hydrolyzed open Sn (SnOH) (e), and silanol nests ( $\text{OH}_4$ ) (f) in the Si-Beta framework. Oxygen is red, silicon is blue, tin is grey, and hydrogen is green (at defects) or white (in water). . . . .	452
7.2 Time-averaged low (8 $\text{H}_2\text{O}$ per cell) and high (23 $\text{H}_2\text{O}$ per cell) densities in each Beta model, as viewed along the [010] plane. Intensities are normalized to the highest intensity of each simulation and are not directly comparable between images. Approximate location of the defects are indicated by blue circles. Orthogonal direction views are provided in the SI (section 7.5.3.2). . . . .	454
7.3 (a) Clustering coefficients, (b) potential energy, (c) entropy, and (d) free energy, defined as the calculated Helmholtz energy, minus the chemical potential of an external water reservoir multiplied by the number of water molecules (see text for details), as a function of water density for each considered defect in zeolite Beta. Blue squares are Si-Beta, red triangles denote Sn-Beta, purple circles correspond to SnOH-Beta, and orange diamonds are ( $\text{OH}$ ) <sub>4</sub> -Beta. . . . .	456
7.4 Difference infrared spectra of water adsorbed on low-defect Si-Beta-F (a,d; red) and high-defect Si-Beta-OH (b,e; blue) zeolites. Subtracted spectra are relative to the sample before water adsorption, and differential spectra are relative to the next-lowest $\text{H}_2\text{O}$ pressure. Measured OH stretching peak centers versus $\text{H}_2\text{O}$ adsorption (f), including AIMD-predicted OD peak shifts (f). . . . .	460
7.5 Representative snapshots of water structures obtained during production runs at varying density in Si-Beta. . . . .	480
7.6 Representative snapshots of water structures obtained during production runs at varying density in Sn-Beta. . . . .	481
7.7 Representative snapshots of water structures obtained during production runs at varying density in SnOH-Beta. . . . .	482

Figure	Page
7.8 Representative snapshots of water structures obtained during production runs at varying density in (OH) <sub>4</sub> -Beta. . . . .	483
7.9 Time averaged density plot for Si-Beta along the [010] and [100] planes at low (8) and high (23) water densities (water unit cell <sup>-1</sup> ). . . . .	484
7.10 Time averaged density plot for Sn-Beta along the [010] and [100] planes at low (8) and high (23) water densities (water unit cell <sup>-1</sup> ). . . . .	484
7.11 Time averaged density plot for SnOH-Beta along the [010] and [100] planes at low (8) and high (23) water densities (water unit cell <sup>-1</sup> ). . . . .	485
7.12 Time averaged density plot for (OH) <sub>4</sub> -Beta along the [010] and [100] planes at low (8) and high (23) water densities (water unit cell <sup>-1</sup> ). . . . .	485
7.13 Supercell of bulk water simulated as a reference state. . . . .	486
7.14 Fluctuations in the potential energy predicted per water molecule for Si-beta (blue), Sn-Beta (red), SnOH-Beta (orange), and (OH) <sub>4</sub> -Beta (purple) at 19 ps and 20 ps. . . . .	487
7.15 Fluctuations in the entropy predicted per water molecule for Si-beta (blue), Sn-Beta (red), SnOH-Beta (orange), and (OH) <sub>4</sub> -Beta (purple) at 19 ps and 20 ps. . . . .	487
7.16 Fluctuations in the potential energy predicted per water molecule for Si-beta (blue), Sn-Beta (red), SnOH-Beta (orange), and (OH) <sub>4</sub> -Beta (purple) at 19 ps and 20 ps. . . . .	488
7.17 Calculated OD stretching peaks in Si-Beta. Spectra have been offset and normalized for clarity. Inset Xw denotes X number of water molecules per unit cell. . . . .	489
7.18 Calculated peak centers in Si-Beta. . . . .	489
7.19 Calculated OD stretching peaks in Sn-Beta. Spectra have been offset and normalized for clarity. Inset Xw denotes X number of water molecules per unit cell. . . . .	490
7.20 Calculated peak centers in Sn-Beta. . . . .	490
7.21 Calculated OD stretching peaks in SnOH-Beta. Spectra have been offset and normalized for clarity. Inset Xw denotes X number of water molecules per unit cell. . . . .	491
7.22 Calculated peak centers in SnOH-Beta. . . . .	491

Figure	Page
7.23 Calculated OD stretching peaks in (OH) <sub>4</sub> -Beta. Spectra have been offset and normalized for clarity. Inset Xw denotes X number of water molecules per unit cell. . . . .	492
7.24 Calculated peak centers in SnOH-Beta. . . . .	492
7.25 Hydrogen bonding graphs showing time averaged hydrogen bond frequency between water pairs in Si-Beta. . . . .	493
7.26 Hydrogen bonding graphs showing time averaged hydrogen bond frequency between water pairs in Sn-Beta. . . . .	494
7.27 Hydrogen bonding graphs showing time averaged hydrogen bond frequency between water pairs in SnOH-Beta. . . . .	495
7.28 Hydrogen bonding graphs showing time averaged hydrogen bond frequency between water pairs in (OH) <sub>4</sub> -Beta. . . . .	496
7.29 VDOS spectra of the Si-Beta framework at water densities of 0 (blue), 12 (red), and 45 (black) waters per unit cell. . . . .	497
7.30 XRD patterns of (a) Si-Beta-F, (b) H-Al-Beta-F, and (c) Si-Beta-OH, normalized to maximum intensity. . . . .	498
7.31 N <sub>2</sub> adsorption isotherms (77 K) on Si-Beta-F (●) and Si-Beta-OH (■). Isotherms are offset by 200 units for clarity. . . . .	499
7.32 H <sub>2</sub> O adsorption isotherms (293 K) on Si-Beta-F (●) and Si-Beta-OH (■). . . . .	500
7.33 Illustration of processing of spectra under flowing H <sub>2</sub> O, using Si-Beta-F at P/P <sub>0</sub> = 0.5 (293 K) as an example. (a) The signal from vapor-phase H <sub>2</sub> O in the empty cell is subtracted from the signal for Si-Beta-F under flowing vapor-phase H <sub>2</sub> O to yield a cell-corrected spectrum, then (b) the spectrum of the zeolite in flowing He before H <sub>2</sub> O adsorption is subtracted from this to give the difference after adsorption. . . . .	501
7.34 Differential subtracted IR spectra of H <sub>2</sub> O adsorbed at 293 K on Si-Beta-F (left) and Si-Beta-OH (right) at P/P <sub>0</sub> values of 0.1–0.75. Si-Beta-F spectra are multiplied by 3 for clarity. . . . .	502
7.35 Correlation of $\delta(\text{O-H})$ bending area (1630 cm <sup>-1</sup> ) quantified from subtracted IR spectra in the range of P/P <sub>0</sub> = 0.1–0.75 with the amount of adsorbed H <sub>2</sub> O quantified at the same P/P <sub>0</sub> value in volumetric adsorption isotherms on Si-Beta-F (●) and Si-Beta-OH (■). . . . .	503

Figure	Page
7.36 Grand potential energies referenced to the Helmholtz energy of water (" $\mu_{\text{ref}}$ ", at $P/P^\circ = 0.05$ and 300 K) for each defect. The curves shift systematically as the chemical potential is changed, with the mathematical dependence discussed in section 7.5.2.2. At any given value of the chemical potential, the value of N that minimizes the grand free energy corresponds to the thermodynamic equilibrium of the system. Blue, Si-Beta; red, Sn-Beta; purple, SnOH; orange, $(\text{OH})_4$ -Beta. . . . .	504
7.37 Fluctuations in total energy for Si-Beta at a unit cell energy of 23 $\text{H}_2\text{O}$ u.c. <sup>-1</sup> . . . . .	505
7.38 Fluctuations in temperature for Si-Beta at a unit cell energy of 23 $\text{H}_2\text{O}$ u.c. <sup>-1</sup> . . . . .	505
8.1 (a) Bimolecular ethanol dehydration turnover rate (per $\text{H}^+$ , 373 K) as a function of $\text{C}_2\text{H}_5\text{OH}$ pressure, without co-fed $\text{H}_2\text{O}$ , on H-Al-Beta-F(1.2) ( $\bullet$ ), H-Al-Beta-F(2.0) ( $\blacksquare$ ), and H-Al-Beta-OH(1.7) ( $\blacktriangledown$ ). Solid lines represent regression to Eq. 8.1. (b) Bimolecular ethanol dehydration turnover rate (per $\text{H}^+$ , 373 K) on H-Al-Beta-F(2.0) as a function of the $\text{C}_2\text{H}_5\text{OH}/\text{H}_2\text{O}$ pressure ratio, in the range 2–10 kPa $\text{H}_2\text{O}$ ( $\blacksquare$ ), and at 40 kPa $\text{H}_2\text{O}$ ( $\blacksquare$ ), 50 kPa $\text{H}_2\text{O}$ ( $\blacksquare$ ), and 75 kPa $\text{H}_2\text{O}$ ( $\square$ ). . . . .	514
8.2 Series of elementary steps describing associative bimolecular ethanol dehydration at $\text{H}^+$ sites in zeolites (steps 1–3), and the adsorption of water to form inhibitory ethanol-water dimers (step 4). Kinetically irrelevant DEE and water desorption steps are omitted for brevity. . . . .	515
8.3 (a) Apparent first-order bimolecular ethanol dehydration rate constant (per $\text{H}^+$ , 373 K) and (b) rate deviation ( $\chi$ ) from the functional dependence of Eq. 8.7, as a function of $\text{H}_2\text{O}$ pressure on H-Al-Beta-F(0.16) ( $\triangle$ ), H-Al-Beta-F(1.2) ( $\bullet$ , $\bullet$ at 423 K), H-Al-Beta-F(2.0) ( $\blacksquare$ ), and H-Al-Beta-OH(1.7) ( $\blacktriangledown$ ). Solid lines reflect regression to the functional form of Eq. 8.7. . . . .	519
8.4 (a) Volumetric $\text{H}_2\text{O}$ adsorption isotherms (293 K) on H-Al-Beta-F samples and their dealuminated analogs, with $\text{H}^+$ (or Si-OH nest) u.c. <sup>-1</sup> = 0.11 ( $\blacklozenge$ ), 0.16 ( $\triangle$ ), 0.57 ( $\blacktriangle$ ), 0.78 ( $\circ$ ), 1.2 ( $\bullet$ ), 1.4 ( $\square$ ), 2.0 ( $\blacksquare$ ), and Si-Beta-F ( $\diamond$ ); and (b) after subtraction of Si-Beta-F isotherm and normalizing by $\text{H}^+$ (or Si-OH nest). (c) Isothermic heat of adsorption of $\text{H}_2\text{O}$ as a function of coverage on Si-Beta-F ( $\diamond$ ) and deAl-Beta-F(2.0) ( $\blacksquare$ ), determined in the range 283–302 K. deAl-Beta-F isotherms are offset for clarity by 300 units in (a) and 60 units in (b). . . . .	523

- 8.5 (a, b) Baseline-corrected difference IR spectra of H<sub>2</sub>O adsorbed at 293 K on Si-Beta-F (bottom,  $\times 10$  for clarity), H-Al-Beta-F(2.0) (middle), and deAl-Beta-F(2.0) (top) at P/P<sub>0</sub> values of 0.1, 0.2, 0.5, and 0.75 in (a) the  $\nu(\text{OH})$  stretching region and (b) the  $\delta(\text{HOH})$  scissoring region. Difference spectra reflect the subtraction of the spectrum of the dehydrated sample under flowing He prior to H<sub>2</sub>O adsorption, and the spectrum of H<sub>2</sub>O adsorbed within an empty IR cell. All spectra are normalized to the T–O–T overtone peak area (1750–2100 cm<sup>-1</sup>) prior to adsorption. (c) Correlation of  $\delta(\text{HOH})$  area quantified from subtracted spectra on all H-Al-Beta-F ( $\blacktriangle$ ) and siliceous Beta samples (deAl-Beta-F, Si-Beta-F,  $\blacksquare$ ) found in Table 8.1 with the amount of H<sub>2</sub>O adsorbed at the same P/P<sub>0</sub> in volumetric isotherms (Figure 8.4). Solid line reflects line-of-best-fit. (d, e) Correlation of the  $\nu(\text{OH})$  peak center with the amount of H<sub>2</sub>O adsorbed on (d) H-Al-Beta-F ( $\blacktriangle$ ) and (e) siliceous Beta samples (deAl-Beta-F, Si-Beta-F,  $\blacksquare$ ).528
- 8.6 (a, b) Baseline-corrected difference IR spectra of adsorbed species on H-Al-Beta-F(2.5) at H<sub>2</sub>O P/P<sub>0</sub> values of 0.1, 0.2, 0.5, and 0.75 at 293 K (bottom), 373 K (middle), and 373 K with co-fed C<sub>2</sub>H<sub>5</sub>OH (top, C<sub>2</sub>H<sub>5</sub>OH/H<sub>2</sub>O = 0.005 (10, 20 kPa H<sub>2</sub>O) and 0.03 (50, 75 kPa H<sub>2</sub>O)) in (a) the  $\nu(\text{OH})$  stretching region and (b) the  $\delta(\text{HOH})$  scissoring region. Difference spectra reflect the subtraction of the spectrum of the dehydrated sample under flowing He prior to adsorption, and the spectrum of species adsorbed within an empty IR cell. All spectra are normalized to the T–O–T overtone peak area (1750–2100 cm<sup>-1</sup>) prior to adsorption. (c) Amount of H<sub>2</sub>O adsorbed determined from  $\delta(\text{HOH})$  scissoring areas and the correlation in Figure 8.5c at 293 K ( $\bullet$ ), 373 K ( $\blacktriangle$ ), and 373 K with co-fed C<sub>2</sub>H<sub>5</sub>OH ( $\blacksquare$ ). Dashed line corresponds to the volumetric adsorption isotherm of H<sub>2</sub>O at 293 K (Figure 8.4). (d) Variation in  $\nu(\text{CH})$  peak area with C<sub>2</sub>H<sub>5</sub>OH pressure on H-Al-Beta-F(2.5) at 373 K with co-fed H<sub>2</sub>O at 10, 20, 50, and 75 kPa. Dashed line represents the average value. (e) Correlation of the  $\nu(\text{OH})$  peak center with the amount of H<sub>2</sub>O adsorbed on H-Al-Beta-F(2.5) at 293 K ( $\bullet$ ), 373 K ( $\blacktriangle$ ), and 373 K with co-fed C<sub>2</sub>H<sub>5</sub>OH (0.05–4.6 kPa) ( $\blacksquare$ ).534
- 8.7 (a) Gibbs free energies of adsorbed intermediates and transition states within H-Al-Beta calculated by DFT, referenced to two gas-phase ethanol molecules and one water molecule, for diethyl ether formation through the dissociative pathway (black), the associative pathway (pink), and the associative pathway with one co-adsorbed H<sub>2</sub>O molecule (orange). (b) Geometries of adsorbed intermediates and transition states. . . . . 536

Figure	Page
8.8 (a) Gibbs free energies of adsorption (373 K) of ethanol monomer and dimer species with 1–6 co-adsorbed H <sub>2</sub> O molecules calculated by <i>ab initio</i> molecular dynamics, referenced to gas-phase ethanol and the zeolite with the same number of adsorbed H <sub>2</sub> O molecules. (b) Gibbs free energy landscape (373 K) calculated by metadynamics, as a function of the collective variables which are the distances between the C <sub>α</sub> the ethanol molecule bound at H <sub>3</sub> O <sup>+</sup> in the EW <sub>5</sub> * cluster within H-Al-Beta (A), and the two O atoms that are involved in the nucleophile and leaving group at the transition state (B). The minimum free energy path including the transition state and representative images along the reaction coordinate are shown below. . . . .	538
8.9 Series of elementary steps for ethanol dehydration catalyzed by solvated hydronium ions, and free energy diagram illustrating the effects of solvation by extended hydrogen-bonded H <sub>2</sub> O networks. . . . .	542
8.10 (a) Apparent first-order bimolecular ethanol dehydration rate constant (per H <sup>+</sup> , 373 K) and (b) activity coefficient ratio ( $\chi = \gamma_{\text{EWn}}/\gamma_{\ddagger}$ ) from the functional dependence of Eq. 8.7, as a function of H <sub>2</sub> O pressure on H-Al-Beta-F(2.0) (■), H-Al-TON (▲), H-Al-FAU (◆), H-Al-MFI (●), H-Al-AEI (□), H-Al-CHA (○), and HPW/Si-MCM-41 (◉). Solid lines in (a) reflect regression of measured rate constants to Eq. 8.7. Inset (a): dependence of k <sub>3</sub> K <sub>2</sub> K <sub>4</sub> <sup>-1</sup> values on the largest included sphere diameter of zeolite pores. Inset (b): slopes of the data sets in (b) in the high water pressure limit, as a function of the channel undulation parameter (d <sub>PL</sub> /d <sub>LC</sub> ). Solid lines in both insets are to guide the eye. . . . .	549
8.11 Left: XRD patterns of (a) H-Al-Beta-OH(1.7), (b) Si-Beta-F, and H-Al-Beta-F with H <sup>+</sup> u.c. <sup>-1</sup> = (c) 0.11, (d) 0.16, (e) 0.57, (f) 0.78, (g) 1.2, (h) 1.4, (i) 2.0. Right: dealuminated analogs (deAl-Beta-F) of the samples at left. All XRD patterns are normalized to their highest peak intensity. . .	572
8.12 NH <sub>3</sub> -TPD profiles for H-Al-Beta-F zeolites with Si/Al = (a) 23, (b) 34, (c) 45, (d) 65, (e) 93, (f) 220, (g) 500. Offset by 0.5 units for clarity. . . .	573
8.13 NH <sub>3</sub> -TPD profiles for (a) H-Al-MFI, (b) H-Al-TON, (c) H-Al-FAU, (d) H-Al-Beta-OH(1.7). Offset by 0.5 units for clarity. . . . .	574
8.14 Diethyl ether formation rate (per g catalyst, 378 K, 5 kPa C <sub>2</sub> H <sub>5</sub> OH, 1 kPa H <sub>2</sub> O) as a function of 2,6-di- <i>tert</i> -butylpyridine uptake (0.6 Pa DTBP) on H-Al-Beta-F(2.0) during catalysis. Solid line represents linear regression. . . . .	575
8.15 Diethyl ether formation rate (per g catalyst, 378 K, 0.7 kPa C <sub>2</sub> H <sub>5</sub> OH, 30 kPa H <sub>2</sub> O) as a function of 2,6-di- <i>tert</i> -butylpyridine uptake (1.4 Pa DTBP) on H-Al-Beta-F(2.0) during catalysis. Solid line represents linear regression. . . . .	575

Figure	Page
8.16 Diethyl ether formation rate (per g catalyst, 378 K, 4.5 kPa C <sub>2</sub> H <sub>5</sub> OH, 1 kPa H <sub>2</sub> O) as a function of 2,6-di- <i>tert</i> -butylpyridine uptake (1.8 Pa DTBP) on H-Al-Beta-F(1.2) during catalysis. Solid line represents linear regression.	576
8.17 Diethyl ether formation rate (per g catalyst, 378 K, 4.5 kPa C <sub>2</sub> H <sub>5</sub> OH, 1 kPa H <sub>2</sub> O) as a function of 2,6-di- <i>tert</i> -butylpyridine uptake (0.5 Pa DTBP) on H-Al-Beta-F(0.16) during catalysis. Solid line represents linear regression.	576
8.18 Diethyl ether formation rate (per g catalyst, 378 K, 4.4 kPa C <sub>2</sub> H <sub>5</sub> OH, 1 kPa H <sub>2</sub> O) as a function of 2,6-di- <i>tert</i> -butylpyridine uptake (1.9 Pa DTBP) on H-Al-Beta-OH(1.7) during catalysis. Solid line represents linear regression. . . . .	577
8.19 Diethyl ether formation rate (per g catalyst, 373 K, 4.7 kPa C <sub>2</sub> H <sub>5</sub> OH, 1 kPa H <sub>2</sub> O) as a function of 2,6-di- <i>tert</i> -butylpyridine uptake (0.9 Pa DTBP) on H-Al-FAU during catalysis. Solid line represents linear regression. . .	577
8.20 Diethyl ether formation rate (per g catalyst, 378 K, 4.5 kPa C <sub>2</sub> H <sub>5</sub> OH, 1 kPa H <sub>2</sub> O) as a function of 2,6-di- <i>tert</i> -butylpyridine uptake (0.4 Pa DTBP) on HPW/Si-MCM-41 during catalysis. Solid line represents linear regression.	578
8.21 (a) Fractional conversion of C <sub>2</sub> H <sub>5</sub> OH as a function of site-contact time at 0.008 kPa C <sub>2</sub> H <sub>5</sub> OH on H-Al-Beta-F(2.0) (■), and at 0.04 kPa and 0.002 kPa C <sub>2</sub> H <sub>5</sub> OH on H-Al-Beta-OH(1.7) (▼), collected without co-fed H <sub>2</sub> O at 373 K. (b) provides a better view of the data points near the origin in (a) at 0.04 kPa C <sub>2</sub> H <sub>5</sub> OH on H-Al-Beta-OH(1.7) (▼). . . . .	579
8.22 First-order ( $k_3K_2 / \text{mol} (\text{mol H}^+)^{-1} \text{kPa}^{-1} \text{s}^{-1}$ ) and zero-order ( $k_3 / \text{mol} (\text{mol H}^+)^{-1} \text{s}^{-1}$ ) dehydration rate constants (per H <sup>+</sup> , 373 K) quantified on H-Al-Beta-F(1.2) (●), H-Al-Beta-F(2.0) (■), and H-Al-Beta-OH(1.7) (▼) as a function of H <sup>+</sup> density. Dashed line represents the average value. Because intracrystalline transport limitations would lead to lower k <sub>3</sub> values at higher H <sup>+</sup> densities, these data are consistent with kinetically limited rates as described by the Madon-Boudart criterion [196]. . . . .	580
8.23 Bimolecular ethanol dehydration turnover rate (per H <sup>+</sup> , 373 K) as a function of C <sub>2</sub> H <sub>5</sub> OH pressure, without co-fed H <sub>2</sub> O, on H-Al-MFI. Solid line represents regression to Eq. 8.1 (Main Text). . . . .	581
8.24 Bimolecular ethanol dehydration turnover rate (373 K, per H <sup>+</sup> ) on H-Al-Beta-F(2.0) as a function of ethanol pressure at water pressures of 0.02, 0.05, 0.2, 0.6, 2, 5, 7, 10, 14, 20, 30, 40, 50, 75 kPa. Squares, triangles, and circles were measured in separate experiments. Solid lines reflect linear regression to data points in first-order regimes. . . . .	582

Figure	Page
8.25 Bimolecular ethanol dehydration turnover rate (373 K, per H <sup>+</sup> ) on H-Al-Beta-F(1.2) as a function of ethanol pressure at water pressures of 0.02, 0.2, 2, 10, 14, 20, 30, 40, 50, 75 kPa. Solid lines reflect linear regression to data points in first-order regimes. . . . .	583
8.26 Bimolecular ethanol dehydration turnover rate (373 K, per H <sup>+</sup> ) on H-Al-Beta-F(0.16) as a function of ethanol pressure at water pressures of 10, 14, 20, 30, 40, 50, 75 kPa. Solid lines reflect linear regression to data points in first-order regimes. . . . .	584
8.27 Bimolecular ethanol dehydration turnover rate (373 K, per H <sup>+</sup> ) on H-Al-Beta-OH(1.7) as a function of ethanol pressure at water pressures of 0.05, 0.2, 0.6, 1, 2, 5, 10, 14, 20, 30, 40, 50, 75 kPa. Squares and circles were measured in separate experiments. Solid lines reflect linear regression to data points in first-order regimes. . . . .	585
8.28 Apparent first-order rate constant for bimolecular ethanol dehydration (per H <sup>+</sup> , 373 K) on H-Al-Beta samples as a function of H <sub>2</sub> O pressure (10–75 kPa) and H <sup>+</sup> density (quantified by <i>in situ</i> 2,6-di- <i>tert</i> -butylpyridine titration). Dashed lines represent averages at each H <sub>2</sub> O pressure. . . . .	586
8.29 Mears criterion values calculated as a function of ethanol and water pressure on H-Al-Beta-F(2.0) at 373 K. Shaded regions correspond to Mears criterion values that fall in the range of values specified by the scale bar. . . . .	586
8.30 Bimolecular ethanol dehydration turnover rate (423 K, per H <sup>+</sup> ) on H-Al-Beta-F(1.2) (boxes) as a function of ethanol pressure at water pressures between 2.5–75 kPa (see color legend in bottom right). Bimolecular 1-propanol dehydration turnover rates (423, per H <sup>+</sup> ) on H-Al-MFI reported by Zhi et al. [177] are adapted from Figure 8.4S in their manuscript's Supporting Information, where the filled circles were collected at 2.5 kPa H <sub>2</sub> O, and the open circles were collected at 0.53 kPa H <sub>2</sub> O. . . . .	587
8.31 Bimolecular ethanol dehydration turnover rate (373 K, per H <sup>+</sup> ) on H-Al-FAU as a function of ethanol pressure at water pressures of 2, 5, 10, 14, 20, 30, 40, 60 kPa. Solid lines reflect linear regression to data points in first-order regimes. . . . .	588
8.32 Bimolecular ethanol dehydration turnover rate (373 K, per H <sup>+</sup> ) on H-Al-TON as a function of ethanol pressure at water pressures of 1, 2, 5, 10, 14, 20, 30, 40, 50, 75 kPa. Solid lines reflect linear regression to data points in first-order regimes. . . . .	589

Figure	Page
8.33 Bimolecular ethanol dehydration turnover rate (373 K, per H <sup>+</sup> ) on H-Al-CHA as a function of ethanol pressure at water pressures of 0.2, 0.6, 5, 10, 14, 20, 30, 40, 50 kPa. Solid lines reflect linear regression to data points in first-order regimes. . . . .	590
8.34 Bimolecular ethanol dehydration turnover rate (373 K, per H <sup>+</sup> ) on H-Al-AEI as a function of ethanol pressure at water pressures of 0.6, 1, 2, 5, 10, 14, 20, 30, 40, 50, 75 kPa. Solid lines reflect linear regression to data points in first-order regimes. . . . .	591
8.35 Bimolecular ethanol dehydration turnover rate (373 K, per H <sup>+</sup> ) on H-Al-MFI as a function of ethanol pressure at water pressures of 0.02, 0.2, 2, 10, 14, 20, 30, 40, 50, 75 kPa. Solid lines reflect linear regression to data points in first-order regimes. . . . .	592
8.36 Bimolecular ethanol dehydration turnover rate (373 K, per H <sup>+</sup> ) on HPW/Si-MCM-41 as a function of ethanol pressure at water pressures of 0.1, 0.2, 0.6, 1, 2, 5, 10, 20, 40, 50 kPa. Solid lines reflect linear regression to data points in the first-order regime. . . . .	593
8.37 Dependence of activity coefficient ratios ( $\chi = \gamma_{\text{EW}_n}/\gamma_{\ddagger}$ ) on P <sub>H<sub>2</sub>O</sub> in the high water pressure limit, on H-Al-Beta-F(2.0) (■), H-Al-TON (▲), H-Al-FAU (◆), H-Al-AEI (□), H-Al-CHA (○), and HPW/Si-MCM-41 (●), as a function of the diameter of the largest included sphere within the pore topology (d <sub>LC</sub> ). . . . .	594
8.38 Volumetric N <sub>2</sub> adsorption isotherms (77 K) measured on H-Al-Beta-F samples (a) and their dealuminated analogs (b), with H <sup>+</sup> (or Si-OH nest) per unit cell = 0 (◇), 0.11 (◆), 0.16 (△), 0.57 (▲), 0.78 (○), 1.2 (●), 1.4 (□), and 2.0 (■), and on H-Al-Beta-OH(1.7) (×). Isotherms are offset by 100 units for clarity. . . . .	595
8.39 (a) Volumetric N <sub>2</sub> adsorption isotherms (77 K) measured on Si-MCM-41 (■) and HPW/Si-MCM-41 (●), and (b) NLDFIT-based pore-size distributions derived from the data. . . . .	596
8.40 (a) Volumetric H <sub>2</sub> O adsorption isotherms (293 K) on H-Al-Beta-F(0.57) (orange squares) and Na-Al-Beta-F(0.57) (black circles). (b) Difference between H-Al-Beta-F(0.57) and Na-Al-Beta-F(0.57) isotherms in (a), normalized by the Al density. Dashed line represents approximate plateau value between P/P <sub>0</sub> = 0.2–0.6, which implies that (H <sup>+</sup> )(H <sub>2</sub> O) <sub>n</sub> clusters are saturated at P/P <sub>0</sub> = 0.2, and that they contain 2 more H <sub>2</sub> O molecules than (Na <sup>+</sup> )(H <sub>2</sub> O) <sub>n</sub> clusters. . . . .	597

Figure	Page
8.41 (a) H <sub>2</sub> O adsorption isotherms (293 K) on H-Al-FAU (pink), H-Al-TON (orange), H-Al-CHA (light blue), H-Al-AEI (purple), HPW/Si-MCM-41 (dark blue), and H-Al-Beta-F(1.2) (red), for comparison. (b) Calculated H <sub>2</sub> O adsorbed per H <sup>+</sup> on H-zeolite samples. H <sub>2</sub> O adsorbed within Si-Beta-F or any other siliceous analogs is not subtracted in this case, as it is in the main text on H-Al-Beta-F samples. . . . .	598
8.42 (a) Volumetric adsorption isotherms of H <sub>2</sub> O on Si-Beta-F at 283 K (■), 288 K (◆), 293 K (▲), 298 K (●), and 302 K (◦), with low-coverage data shown in (b) for clarity. . . . .	599
8.43 (a) Volumetric adsorption isotherms of H <sub>2</sub> O on deAl-Beta-F(2.0) at 283 K (■), 288 K (◆), 293 K (▲), and 298 K (●), with low-coverage data shown in (b) for clarity. . . . .	599
8.44 (a) Normalized (to T–O–T overtone peak area (1750–2100 cm <sup>-1</sup> )) IR spectra of Si-Beta-F and deAl-Beta-F zeolites at 293 K after treatment in flowing He to 823 K for 1 h. Grey traces represent deconvoluted signal for Si-OH nest peak areas. (b) Correlation of Si-OH nest $\nu(\text{O-H})$ peak area with the number of Si-OH nests u.c. <sup>-1</sup> generated by removal of framework Al. . . . .	600
8.45 Illustration of processing of spectra under flowing H <sub>2</sub> O, using Si-Beta-F at P/P <sub>0</sub> = 0.5 (293 K) as an example. (a) The signal from vapor-phase H <sub>2</sub> O in the empty cell is subtracted from the signal for Si-Beta-F under flowing vapor-phase H <sub>2</sub> O to yield a cell-corrected spectrum, then (b) the spectrum of the zeolite in flowing He before H <sub>2</sub> O adsorption is subtracted from this to give the difference after adsorption. . . . .	601
8.46 (a) Baseline-corrected difference IR spectra of H <sub>2</sub> O adsorbed at 293 K on Si-Beta-F at P/P <sub>0</sub> values of 0.1 (red), 0.2 (green), 0.5 (blue), and 0.75 (orange). Difference spectra reflect the subtraction of the spectrum of the dehydrated sample under flowing He prior to H <sub>2</sub> O adsorption, and the spectrum of H <sub>2</sub> O adsorbed within an empty IR cell. (b) Differential-subtracted spectra reflect the difference between the spectrum at the given P/P <sub>0</sub> value and the next-lowest P/P <sub>0</sub> value. All spectra are normalized to the T–O–T overtone peak area (1750–2100 cm <sup>-1</sup> ) prior to adsorption. The spectra on Si-Beta-F were originally reported in Ref. [406]. . . . .	602

Figure	Page
8.47 (a) Baseline-corrected difference IR spectra of H <sub>2</sub> O adsorbed at 293 K on deAl-Beta-F(2.0) at P/P <sub>0</sub> values of 0.1 (red), 0.2 (green), 0.5 (blue), and 0.75 (orange). Difference spectra reflect the subtraction of the spectrum of the dehydrated sample under flowing He prior to H <sub>2</sub> O adsorption, and the spectrum of H <sub>2</sub> O adsorbed within an empty IR cell. (b) Differential-subtracted spectra reflect the difference between the spectrum at the given P/P <sub>0</sub> value and the next-lowest P/P <sub>0</sub> value. All spectra are normalized to the T–O–T overtone peak area (1750–2100 cm <sup>-1</sup> ) prior to adsorption. . .	603
8.48 (a) Baseline-corrected difference IR spectra of H <sub>2</sub> O adsorbed at 293 K on deAl-Beta-F(1.4) at P/P <sub>0</sub> values of 0.1 (red), 0.2 (green), 0.5 (blue), and 0.75 (orange). Difference spectra reflect the subtraction of the spectrum of the dehydrated sample under flowing He prior to H <sub>2</sub> O adsorption, and the spectrum of H <sub>2</sub> O adsorbed within an empty IR cell. (b) Differential-subtracted spectra reflect the difference between the spectrum at the given P/P <sub>0</sub> value and the next-lowest P/P <sub>0</sub> value. All spectra are normalized to the T–O–T overtone peak area (1750–2100 cm <sup>-1</sup> ) prior to adsorption. . .	604
8.49 (a) Baseline-corrected difference IR spectra of H <sub>2</sub> O adsorbed at 293 K on deAl-Beta-F(1.2) at P/P <sub>0</sub> values of 0.1 (red), 0.2 (green), 0.5 (blue), and 0.75 (orange). Difference spectra reflect the subtraction of the spectrum of the dehydrated sample under flowing He prior to H <sub>2</sub> O adsorption, and the spectrum of H <sub>2</sub> O adsorbed within an empty IR cell. (b) Differential-subtracted spectra reflect the difference between the spectrum at the given P/P <sub>0</sub> value and the next-lowest P/P <sub>0</sub> value. All spectra are normalized to the T–O–T overtone peak area (1750–2100 cm <sup>-1</sup> ) prior to adsorption. . .	605
8.50 (a) Baseline-corrected difference IR spectra of H <sub>2</sub> O adsorbed at 293 K on deAl-Beta-F(0.78) at P/P <sub>0</sub> values of 0.1 (red), 0.2 (green), 0.5 (blue), and 0.75 (orange). Difference spectra reflect the subtraction of the spectrum of the dehydrated sample under flowing He prior to H <sub>2</sub> O adsorption, and the spectrum of H <sub>2</sub> O adsorbed within an empty IR cell. (b) Differential-subtracted spectra reflect the difference between the spectrum at the given P/P <sub>0</sub> value and the next-lowest P/P <sub>0</sub> value. All spectra are normalized to the T–O–T overtone peak area (1750–2100 cm <sup>-1</sup> ) prior to adsorption. . .	606
8.51 (a) Baseline-corrected difference IR spectra of H <sub>2</sub> O adsorbed at 293 K on deAl-Beta-F(0.57) at P/P <sub>0</sub> values of 0.1 (red), 0.2 (green), 0.5 (blue), and 0.75 (orange). Difference spectra reflect the subtraction of the spectrum of the dehydrated sample under flowing He prior to H <sub>2</sub> O adsorption, and the spectrum of H <sub>2</sub> O adsorbed within an empty IR cell. (b) Differential-subtracted spectra reflect the difference between the spectrum at the given P/P <sub>0</sub> value and the next-lowest P/P <sub>0</sub> value. All spectra are normalized to the T–O–T overtone peak area (1750–2100 cm <sup>-1</sup> ) prior to adsorption. . .	607

Figure	Page
8.52 (a) Baseline-corrected difference IR spectra of H <sub>2</sub> O adsorbed at 293 K on deAl-Beta-F(0.16) at P/P <sub>0</sub> values of 0.1 (red), 0.2 (green), 0.5 (blue), and 0.75 (orange). Difference spectra reflect the subtraction of the spectrum of the dehydrated sample under flowing He prior to H <sub>2</sub> O adsorption, and the spectrum of H <sub>2</sub> O adsorbed within an empty IR cell. (b) Differential-subtracted spectra reflect the difference between the spectrum at the given P/P <sub>0</sub> value and the next-lowest P/P <sub>0</sub> value. All spectra are normalized to the T–O–T overtone peak area (1750–2100 cm <sup>-1</sup> ) prior to adsorption. . .	608
8.53 (a) Baseline-corrected difference IR spectra of H <sub>2</sub> O adsorbed at 293 K on deAl-Beta-F(0.11) at P/P <sub>0</sub> values of 0.1 (red), 0.2 (green), 0.5 (blue), and 0.75 (orange). Difference spectra reflect the subtraction of the spectrum of the dehydrated sample under flowing He prior to H <sub>2</sub> O adsorption, and the spectrum of H <sub>2</sub> O adsorbed within an empty IR cell. (b) Differential-subtracted spectra reflect the difference between the spectrum at the given P/P <sub>0</sub> value and the next-lowest P/P <sub>0</sub> value. All spectra are normalized to the T–O–T overtone peak area (1750–2100 cm <sup>-1</sup> ) prior to adsorption. . .	609
8.54 (a) Baseline-corrected difference IR spectra of H <sub>2</sub> O adsorbed at 293 K on H-Al-Beta-F(2.0) at P/P <sub>0</sub> values of 0.1 (red), 0.2 (green), 0.5 (blue), and 0.75 (orange). Difference spectra reflect the subtraction of the spectrum of the dehydrated sample under flowing He prior to H <sub>2</sub> O adsorption, and the spectrum of H <sub>2</sub> O adsorbed within an empty IR cell. (b) Differential-subtracted spectra reflect the difference between the spectrum at the given P/P <sub>0</sub> value and the next-lowest P/P <sub>0</sub> value. All spectra are normalized to the T–O–T overtone peak area (1750–2100 cm <sup>-1</sup> ) prior to adsorption. . .	610
8.55 (a) Baseline-corrected difference IR spectra of H <sub>2</sub> O adsorbed at 293 K on H-Al-Beta-F(1.4) at P/P <sub>0</sub> values of 0.1 (red), 0.2 (green), 0.5 (blue), and 0.75 (orange). Difference spectra reflect the subtraction of the spectrum of the dehydrated sample under flowing He prior to H <sub>2</sub> O adsorption, and the spectrum of H <sub>2</sub> O adsorbed within an empty IR cell. (b) Differential-subtracted spectra reflect the difference between the spectrum at the given P/P <sub>0</sub> value and the next-lowest P/P <sub>0</sub> value. All spectra are normalized to the T–O–T overtone peak area (1750–2100 cm <sup>-1</sup> ) prior to adsorption. . .	611
8.56 (a) Baseline-corrected difference IR spectra of H <sub>2</sub> O adsorbed at 293 K on H-Al-Beta-F(1.2) at P/P <sub>0</sub> values of 0.1 (red), 0.2 (green), 0.5 (blue), and 0.75 (orange). Difference spectra reflect the subtraction of the spectrum of the dehydrated sample under flowing He prior to H <sub>2</sub> O adsorption, and the spectrum of H <sub>2</sub> O adsorbed within an empty IR cell. (b) Differential-subtracted spectra reflect the difference between the spectrum at the given P/P <sub>0</sub> value and the next-lowest P/P <sub>0</sub> value. All spectra are normalized to the T–O–T overtone peak area (1750–2100 cm <sup>-1</sup> ) prior to adsorption. . .	612

Figure	Page
8.57 (a) Baseline-corrected difference IR spectra of H <sub>2</sub> O adsorbed at 293 K on H-Al-Beta-F(0.78) at P/P <sub>0</sub> values of 0.1 (red), 0.2 (green), 0.5 (blue), and 0.75 (orange). Difference spectra reflect the subtraction of the spectrum of the dehydrated sample under flowing He prior to H <sub>2</sub> O adsorption, and the spectrum of H <sub>2</sub> O adsorbed within an empty IR cell. (b) Differential-subtracted spectra reflect the difference between the spectrum at the given P/P <sub>0</sub> value and the next-lowest P/P <sub>0</sub> value. All spectra are normalized to the T–O–T overtone peak area (1750–2100 cm <sup>-1</sup> ) prior to adsorption. . .	613
8.58 (a) Baseline-corrected IR spectra of H <sub>2</sub> O adsorbed at 293 K on H-Al-Beta-F(0.57) at P/P <sub>0</sub> values of 0.1 (red), 0.2 (green), 0.5 (blue), and 0.75 (orange). A small leak in the system led to H <sub>2</sub> O entering the system during cooling to 293 K, and adsorbing at some of the H <sup>+</sup> in 1:1 hydrogen-bonded complexes, evident in the A, B, C triplet seen in the grey spectrum, so difference spectra were not analyzed. (b) Differential-subtracted spectra reflect the difference between the spectrum at the given P/P <sub>0</sub> value and the next-lowest P/P <sub>0</sub> value. All spectra are normalized to the T–O–T overtone peak area (1750–2100 cm <sup>-1</sup> ) prior to adsorption. . . . .	614
8.59 (a) Baseline-corrected difference IR spectra of H <sub>2</sub> O adsorbed at 293 K on H-Al-Beta-F(0.16) at P/P <sub>0</sub> values of 0.1 (red), 0.2 (green), 0.5 (blue), and 0.75 (orange). Difference spectra reflect the subtraction of the spectrum of the dehydrated sample under flowing He prior to H <sub>2</sub> O adsorption, and the spectrum of H <sub>2</sub> O adsorbed within an empty IR cell. (b) Differential-subtracted spectra reflect the difference between the spectrum at the given P/P <sub>0</sub> value and the next-lowest P/P <sub>0</sub> value. All spectra are normalized to the T–O–T overtone peak area (1750–2100 cm <sup>-1</sup> ) prior to adsorption. . .	615
8.60 (a) Baseline-corrected difference IR spectra of H <sub>2</sub> O adsorbed at 293 K on H-Al-Beta-F(0.11) at P/P <sub>0</sub> values of 0.1 (red), 0.2 (green), 0.5 (blue), and 0.75 (orange). Difference spectra reflect the subtraction of the spectrum of the dehydrated sample under flowing He prior to H <sub>2</sub> O adsorption, and the spectrum of H <sub>2</sub> O adsorbed within an empty IR cell. (b) Differential-subtracted spectra reflect the difference between the spectrum at the given P/P <sub>0</sub> value and the next-lowest P/P <sub>0</sub> value. All spectra are normalized to the T–O–T overtone peak area (1750–2100 cm <sup>-1</sup> ) prior to adsorption. . .	616
8.61 Baseline-corrected, gas-phase-corrected IR spectra of 16:8:1 D <sub>2</sub> O:HOD:H <sub>2</sub> O mixtures adsorbed at 303 K on (a) deAl-Beta-F(2.0) and (b) Si-Beta-F, at P/P <sub>0</sub> values of 0.1 (red), 0.2 (green), and 0.5 (blue). All spectra are normalized to the T–O–T overtone peak area (1750–2100 cm <sup>-1</sup> ) prior to adsorption. (c) and (d) show subtracted IR spectra of the δ(HOD) peaks under the same conditions described for (a), (b) on (c) deAl-Beta-F(2.0) and (d) Si-Beta-F. . . . .	618

Figure	Page
8.62 $\delta(\text{HOD})$ peak areas quantified from Figure 8.61c,d correlated with the $\delta(\text{HOH})$ peak areas quantified from Figure 8.46 and Figure 8.47 on Si-Beta-F ( $\bullet$ ) and deAl-Beta-F(2.0) ( $\circ$ ) at the same $P/P_0$ conditions (0.1, 0.2, 0.5). . . . .	619
8.63 (a) Baseline-corrected difference IR spectra of $\text{H}_2\text{O}$ adsorbed at 373 K on H-Al-Beta-F(2.0) at $\text{H}_2\text{O}$ pressures of 10 (red), 20 (green), 30 (blue), and 75 kPa (orange) ( $P/P_0 = 0.1\text{--}0.75$ ). Difference spectra reflect the subtraction of the spectrum of the dehydrated sample under flowing He prior to $\text{H}_2\text{O}$ adsorption, and the spectrum of $\text{H}_2\text{O}$ adsorbed within an empty IR cell. (b) Differential-subtracted spectra reflect the difference between the spectrum at the given $P/P_0$ value and the next-lowest $P/P_0$ value. All spectra are normalized to the T–O–T overtone peak area ( $1750\text{--}2100\text{ cm}^{-1}$ ) prior to adsorption. . . . .	620
8.64 (a) Baseline-corrected difference IR spectra of $\text{H}_2\text{O}/\text{C}_2\text{H}_5\text{OH}$ mixtures adsorbed at 373 K on H-Al-Beta-F(2.0) at $\text{H}_2\text{O}$ pressures of 10 (red), 20 (green), 30 (blue), and 75 kPa (orange) ( $P/P_0 = 0.1\text{--}0.75$ ). The colors shown in the legend correspond to $\text{C}_2\text{H}_5\text{OH}/\text{H}_2\text{O}$ ratios of 0.005 (red, green) and 0.03 (blue, orange), and the lighter blue and orange spectra correspond to a $\text{C}_2\text{H}_5\text{OH}/\text{H}_2\text{O}$ ratio of 0.06. Difference spectra reflect the subtraction of the spectrum of the dehydrated sample under flowing He prior to $\text{H}_2\text{O}$ adsorption, and the spectrum of $\text{H}_2\text{O}$ adsorbed within an empty IR cell. (b) Differential-subtracted spectra reflect the difference between the spectrum at the given $P/P_0$ value and the next-lowest $P/P_0$ value. All spectra are normalized to the T–O–T overtone peak area ( $1750\text{--}2100\text{ cm}^{-1}$ ) prior to adsorption. . . . .	621
8.65 (a) Baseline-corrected difference IR spectra of $\text{H}_2\text{O}$ adsorbed at 373 K on H-Al-FAU at $\text{H}_2\text{O}$ pressures of 2 (red), 4 (green), 10 (blue), 34 (grey), and 68 kPa (orange) ( $P/P_0 = 0.02\text{--}0.75$ ). Difference spectra reflect the subtraction of the spectrum of the dehydrated sample under flowing He prior to $\text{H}_2\text{O}$ adsorption, and the spectrum of $\text{H}_2\text{O}$ adsorbed within an empty IR cell. (b) Differential-subtracted spectra reflect the difference between the spectrum at the given $P/P_0$ value and the next-lowest $P/P_0$ value. All spectra are normalized to the T–O–T overtone peak area ( $1750\text{--}2100\text{ cm}^{-1}$ ) prior to adsorption. . . . .	622

Figure	Page
8.66 (a) Baseline-corrected difference IR spectra of H <sub>2</sub> O adsorbed at 373 K on H-Al-TON at H <sub>2</sub> O pressures of 2 (red), 4 (green), 10 (blue), 20 (grey), 50 (purple) and 75 kPa (orange) (P/P <sub>0</sub> = 0.02–0.75). Difference spectra reflect the subtraction of the spectrum of the dehydrated sample under flowing He prior to H <sub>2</sub> O adsorption, and the spectrum of H <sub>2</sub> O adsorbed within an empty IR cell. (b) Differential-subtracted spectra reflect the difference between the spectrum at the given P/P <sub>0</sub> value and the next-lowest P/P <sub>0</sub> value. All spectra are normalized to the T–O–T overtone peak area (1750–2100 cm <sup>-1</sup> ) prior to adsorption. . . . .	623
8.67 (a) Baseline-corrected difference IR spectra of H <sub>2</sub> O adsorbed at 373 K on H-Al-AEI at H <sub>2</sub> O pressures of 1 (red), 2 (green), 10 (blue), 20 (grey), 50 (purple) and 75 kPa (orange) (P/P <sub>0</sub> = 0.02–0.75). Difference spectra reflect the subtraction of the spectrum of the dehydrated sample under flowing He prior to H <sub>2</sub> O adsorption, and the spectrum of H <sub>2</sub> O adsorbed within an empty IR cell. (b) Differential-subtracted spectra reflect the difference between the spectrum at the given P/P <sub>0</sub> value and the next-lowest P/P <sub>0</sub> value. All spectra are normalized to the T–O–T overtone peak area (1750–2100 cm <sup>-1</sup> ) prior to adsorption. . . . .	624
8.68 (a) Baseline-corrected difference IR spectra of H <sub>2</sub> O adsorbed at 373 K on H-Al-CHA at H <sub>2</sub> O pressures of 2 (red), 4 (green), 10 (blue), 20 (grey), 50 (purple) and 75 kPa (orange) (P/P <sub>0</sub> = 0.02–0.75). Difference spectra reflect the subtraction of the spectrum of the dehydrated sample under flowing He prior to H <sub>2</sub> O adsorption, and the spectrum of H <sub>2</sub> O adsorbed within an empty IR cell. (b) Differential-subtracted spectra reflect the difference between the spectrum at the given P/P <sub>0</sub> value and the next-lowest P/P <sub>0</sub> value. All spectra are normalized to the T–O–T overtone peak area (1750–2100 cm <sup>-1</sup> ) prior to adsorption. . . . .	625
8.69 (a) Baseline-corrected difference IR spectra of H <sub>2</sub> O adsorbed at 373 K on HPW/Si-MCM-41 at H <sub>2</sub> O pressures of 1 (red), 2 (green), 10 (blue), 20 (grey), 50 (purple) and 75 kPa (orange) (P/P <sub>0</sub> = 0.02–0.75). Difference spectra reflect the subtraction of the spectrum of the dehydrated sample under flowing He prior to H <sub>2</sub> O adsorption, and the spectrum of H <sub>2</sub> O adsorbed within an empty IR cell. (b) Differential-subtracted spectra reflect the difference between the spectrum at the given P/P <sub>0</sub> value and the next-lowest P/P <sub>0</sub> value. All spectra are normalized to the T–O–T overtone peak area (1750–2100 cm <sup>-1</sup> ) prior to adsorption. . . . .	626

Figure	Page
8.70 (a) Relative rates of dissociative and associative pathways to form diethyl ether (373 K) in the absence of co-fed water as a function of ethanol pressure on H-Al-Beta zeolites predicted from their DFT-calculated free energy barriers (Eq. 8.25), plotted as the fraction of the total rate ( $r_{\text{total}} = r_{\text{dissoc}} + r_{\text{assoc}}$ ). (b) Predicted coverage of ethanol monomers at $\text{H}^+$ in H-Al-Beta at 373 K as a function of ethanol pressure, based on the DFT-calculated adsorption free energy (Eq. 8.26–8.27). In both plots, the range of possible values introduced by a $\pm 10 \text{ kJ mol}^{-1}$ error in free energies is shown as the unfilled circles. . . . .	627
8.71 Gibbs free energies of adsorbed intermediates and transition states within H-Al-Beta calculated by DFT, referenced to two gas-phase ethanol molecules and one water molecule, for diethyl ether formation through the dissociative pathway with one co-adsorbed $\text{H}_2\text{O}$ molecule (black) and the associative pathway with one co-adsorbed $\text{H}_2\text{O}$ molecule (orange). . . . .	628
A.1 (a) DME (square), MEE (triangle), and DEE (circle) turnover rates (per $\text{H}^+$ , 373 K) on H-CHA (Si/Al = 15, 0% Al in 6-MR pairs) as a function of the ethanol/methanol pressure ratio, at constant $P_{\text{CH}_3\text{OH}} = 4 \text{ kPa}$ . Solid lines represent fits to the rate expressions in Table A.1. (b) Etherification rate ratios calculated from the data in the left graph. Blue: $r_{\text{MEE}}/r_{\text{DME}}$ , orange: $r_{\text{DEE}}/r_{\text{DME}}$ , red: $r_{\text{DEE}}/r_{\text{MEE}}$ , with fits to data from $\alpha = 0.01\text{--}0.06$ in the inset. . . . .	672
A.2 (a) Series of elementary steps to form DME, MEE, and DEE by associative mechanisms through transition states involving dimeric surface intermediates with no co-adsorbed spectator alcohol molecules. (b) Additional plausible elementary steps to rationalize high-pressure methanol inhibition of DME and MEE turnover rates. . . . .	673
A.3 (a) (blue circles) DME turnover rate (373 K, per $\text{H}^+$ ) on H-CHA (Si/Al = 15) as a function of methanol pressure, at constant (M)/(E) ratio = 100. (red squares) DME turnover rate (403 K, per $\text{H}^+$ ) measured by Di Iorio et al. [452] without co-fed ethanol. (b) The same data as in (a), but as a function of the $\text{CH}_3\text{OH}$ Gibbs free energy, $RT\ln(P/P_{\text{sat}}^{-1})$ [452]. . . . .	674
A.4 DME/MEE rate ratio as a function of the $P_{\text{CH}_3\text{OH}}/P_{\text{C}_2\text{H}_5\text{OH}}$ ratio ( $\alpha^{-1}$ ) on H-CHA (Si/Al = 15) at 373 K at methanol pressures between 0.1–50 kPa. Solid lines obtained by linear regression constrained to go through the origin.	677
A.5 Dependence of $r_{\text{DME}}/r_{\text{MEE}}\alpha\chi^{-1}$ (373 K, as quantified according to Equation A.1 at $\alpha^{-1}$ values between 50–200 in Figure A.4) on the $\text{CH}_3\text{OH}$ pressure. Solid line obtained by linear regression. . . . .	679

Figure	Page
B.1 DEE turnover rate (415 K, per H <sup>+</sup> ) as a function of ethanol pressure on H-MFI(0.12) (▲), H-MFI(0.23) (●), H-MFI(0.39) (◆), and H-MFI(0.46) (■) on a linear scale (a) and a semi-log scale (b). Solid lines represent regression to Equation B.2. Unfilled data points are adapted from Chiang and Bhan [218] (409 K, H-MFI Si/Al = 43, Zeolyst CBV8014). . . . .	685
B.2 Plausible series of elementary steps (1–3) that describe the dependence of DEE formation rates on ethanol pressure on H-MFI and H-CHA zeolites. Below the dashed line, steps (4–5) are proposed to describe EY formation rates on H-CHA zeolites. . . . .	686
B.3 First-order ( $k_{\text{DEE}}K_{\text{dimer}}$ , ■, right axis) and zero-order ( $k_{\text{DEE}}$ , ●, left axis) rate constants to form DEE on MFI zeolites as a function of proximal H <sup>+</sup> fraction (titrated by Co <sup>2+</sup> ). . . . .	688
B.4 EY STY (415 K, per H <sup>+</sup> ) as a function of ethanol pressure on H-CHA(0) (●), H-CHA(0.23) (■), and H-CHA(0.44) (▲) on a linear scale (a) and a semi-log scale (b). Solid lines represent regression to Equation B.5. . . .	689
B.5 DEE STY (415 K, per H <sup>+</sup> ) as a function of ethanol pressure on H-CHA(0) (●), H-CHA(0.23) (■), and H-CHA(0.44) (▲) on a linear scale (a) and a semi-log scale (b). Solid lines represent regression to Equation B.1. . . .	690
B.6 Ratio of DEE / EY formation rates (415 K, per H <sup>+</sup> ) as a function of ethanol pressure on H-CHA(0) (●), H-CHA(0.23) (■), and H-CHA(0.44) (▲). Solid lines represent regression to Equations B.1 and B.5. . . . .	692
B.7 (a) First-order ( $k_{\text{DEE}}K_{\text{dimer}}$ , ■, right axis) and zero-order ( $k_{\text{DEE}}$ , ●, left axis) rate constants to form DEE on CHA zeolites as a function of paired H <sup>+</sup> fraction. (b) Intrinsic rate constants to form ethene from ethanol monomer precursors ( $k_{\text{EY,m}}$ , ●, left axis) and ethanol-ethanol dimer precursors ( $k_{\text{EY,d}}$ , ■, right axis) on CHA zeolites as a function of paired H <sup>+</sup> fraction. Solid symbols were fit by regression of Equations B.1 and B.5 to data on collected on each sample, and the solid lines represent a linear regression to the solid symbols. Unfilled symbols and their associated error bars represent regression of the entire data set to the same rate equation as a function of paired H <sup>+</sup> fraction (Equations B.6 and B.7). . . . .	694

## ABSTRACT

Bates, Jason S. Ph.D., Purdue University, December 2019. Structure and Solvation of Confined Water and Alkanols in Zeolite Acid Catalysis. Major Professor: Rajamani Gounder.

Brønsted and Lewis acid sites located within microporous solids catalyze a variety of chemical transformations of oxygenates and hydrocarbons. Such reactions occur in condensed phases in envisioned biomass and shale gas upgrading routes, motivating deeper fundamental understanding of the reactivity-determining interactions among active sites, reactants, and solvents. The crystalline structures of zeolites, which consist of  $\text{SiO}_4$  tetrahedra with isomorphously-substituted  $\text{M}^{4+}$  (e.g.,  $\text{Sn}^{4+}$ ,  $\text{Ti}^{4+}$ ) as Lewis acid sites, or  $\text{Al}^{3+}$  with charge-compensating extraframework  $\text{H}^+$  as Brønsted acid sites, provide a reasonably well-defined platform to study these interactions within confining voids of molecular dimension. In this work, gas-phase probe reactions that afford independent control of solvent coverages are developed and used to interpret measured rate data in terms of rate and equilibrium constants for elementary steps, which reflect the structure and stability of kinetically relevant transition states and reactive intermediates. The foundational role of quantitative kinetic information enables building molecular insights into the mechanistic and active site requirements of catalytic reactions, when combined with complementary tools including synthetic approaches to prepare active sites and surrounding environments of diverse and intended structure, quantitative methods to characterize and titrate active sites and functional groups in confining environments, and theoretical modeling of putative active site structures and plausible reaction coordinates.

Bimolecular ethanol dehydration to diethyl ether was developed as a gas-phase catalytic probe reaction for Lewis acid zeolites. A detailed mechanistic understanding of

the identities of reactive intermediates and transition states on Sn-Beta zeolites was constructed by combining experimental kinetic measurements with density functional theory treatments. Microkinetic modeling demonstrated that Sn active site configurations undergo equilibrated interconversion during catalysis (404 K, 0.5–35 kPa C<sub>2</sub>H<sub>5</sub>OH, 0.1–50 kPa H<sub>2</sub>O) from hydrolyzed-open configurations ((HO)-Sn-(OSi≡)<sub>3</sub>--HO-Si) to predominantly closed configurations (Sn-(OSi≡)<sub>4</sub>), and identified the most abundant productive (ethanol-ethanol dimer) and inhibitory (ethanol-water dimer) reactive intermediates and kinetically relevant transition state (S<sub>N</sub>2 at closed sites). Mechanism-based interpretations of bimolecular ethanol dehydration turnover rates (per Lewis acidic Sn, quantified by CD<sub>3</sub>CN IR) enabled measuring chemically significant differences between samples synthesized to contain high or low densities of residual Si-OH defects (quantified by CD<sub>3</sub>CN IR) within microporous environments that confine Sn active sites. Hydrogen-bonding interactions with Si-OH groups located in the vicinity of Sn active sites in high-defect Sn-Beta zeolites stabilize both reactive and inhibitory intermediates, leading to differences in reactivity within polar and non-polar micropores that reflect solely the different coverages of intermediates at active sites. The ability of confining microporous voids to discriminate among reactive intermediates and transition states on the basis of polarity thus provides a strategy to mitigate inhibition by water and to influence turnover rates by designing secondary environments of different polarity via synthetic and post-synthetic techniques.

Despite the expectation from theory that Sn active sites adopt the same closed configurations after high-temperature (823 K) oxidation treatments, distinct Sn sites can be experimentally identified and quantified by the  $\nu(\text{C}\equiv\text{N})$  infrared peaks of coordinated CD<sub>3</sub>CN molecules, and a subset of these sites are correlated with first-order rate constants of aqueous-phase glucose-fructose isomerization (373 K). In contrast, *in situ* titration of active sites by pyridine during gas-phase ethanol dehydration catalysis (404 K) on a suite of Sn-zeolites of different topology (Beta, MFI, BEC) quantified the dominant active site to correspond to a different subset of Sn sites than those dominant in glucose-fructose isomerization. An extensive series of synthetic

and post-synthetic routes to prepare Sn-zeolites containing Sn sites hosted within diverse local coordination environments identified a subset of Sn sites located in defective environments such as grain boundaries, which are more pronounced in Beta crystallites comprised of intergrowths of two polymorphs than in zeolite frameworks with un-faulted crystal structures. Sn sites in such environments adopt defect-open configurations ((HO)-Sn-(OSi≡)<sub>3</sub>) with proximal Si-OH groups that do not permit condensation to closed configurations, which resolves debated spectroscopic assignments to hydrolyzed-open site configurations. Defect-open Sn sites are dominant in glucose-fructose isomerization because their proximal Si-OH groups stabilize kinetically relevant hydride shift transition states, while closed framework Sn sites are dominant in alcohol dehydration because they stabilize S<sub>N</sub>2 transition states via Sn site opening in the kinetically relevant step and re-closing as part of the catalytic cycle. The structural diversity of real zeolite materials, whose defects distinguish them from idealized crystal structures and allows hosting Lewis acid sites with distinct local configurations, endows them with the ability to effectively catalyze a broad range of oxygenate reactions.

During aqueous-phase catalysis, high extra-crystalline water chemical potentials lead to intra-pore stabilization of H<sub>2</sub>O molecules, clusters, and extended hydrogen-bonded networks that interact with adsorbed intermediates and transition states at Lewis acid sites. Glucose-fructose isomerization turnover rates (373 K, per defect-open Sn, quantified by CD<sub>3</sub>CN IR) are higher when Sn sites are confined within low-defect, non-polar zeolite frameworks that effectively prevent extended water networks from forming; however, increasing exposure to hot (373 K) liquid water generates Si-OH groups via hydrolysis of siloxane bridges and leads to lower turnover rates commensurate with those of high-defect, polar frameworks. Detailed kinetic, spectroscopic, and theoretical studies of polar and non-polar titanosilicate zeolite analogs indicate that extended water networks entropically destabilize glucose-fructose isomerization transition states relative to their bound precursors, rather than influence the competitive adsorption of water and glucose at active sites. Infrared spectra sup-

port the stabilization of extended hydrogen-bonded water networks by Si-OH defects located within Si- and Ti-Beta zeolites, consistent with *ab initio* molecular dynamics simulations that predict formation of distinct thermodynamically stable clustered and extended water phases within Beta zeolites depending on the external water chemical potential and the nature of their chemical functionality (closed vs. hydrolyzed-open Lewis acid site, or silanol nest defect). The structure of water confined within microporous solids is determined by the type and density of intracrystalline polar binding sites, leading to higher reactivity in aqueous media when hydrogen-bonded networks are excluded from hydrophobic micropores.

Aluminosilicate zeolites adsorb water to form  $(\text{H}_3\text{O}^+)(\text{H}_2\text{O})_n$  clusters that mediate liquid-phase Brønsted acid catalysis, but their relative contributions to the solvation of reactive intermediates and transition states remain unclear. Bimolecular ethanol dehydration turnover rates (per  $\text{H}^+$ , quantified by  $\text{NH}_3$  temperature-programmed desorption and *in situ* titrations with 2,6-di-*tert*-butylpyridine) and transmission infrared spectra measured on Brønsted acid zeolites under conditions approaching intrapore  $\text{H}_2\text{O}$  condensation (373 K, 0.02–75 kPa  $\text{H}_2\text{O}$ ) reveal the formation of clustered, solvated  $(\text{C}_2\text{H}_5\text{OH})(\text{H}^+)(\text{H}_2\text{O})_n$  intermediates, which are stabilized to greater extents than bimolecular dehydration transition states by extended hydrogen-bonded water networks. Turnover rates deviate sharply below those predicted by kinetic regimes in the absence of extended condensed water networks because non-ideal thermodynamic formalisms are required to account for the different solvation of transition states and MARI. The condensation of liquid-like phases within micropores that stabilize reaction intermediates and transition states to different extents is a general phenomenon for Brønsted acid-catalyzed alcohol dehydration within zeolites of different topology (CHA, AEI, TON, FAU), which governs the initial formation and structure of clustered hydronium-reactant and water-protonated transition state complexes. Systematic control of liquid-phase structures within confined spaces by gas-phase measurements around the point of intrapore condensation enables more detailed mechanistic and structural insights than those afforded by either kinetic measurements in the

liquid phase, or structural characterizations of aqueous systems in the absence of reactants.



## 1. INTRODUCTION

Zeolites are crystalline, microporous ( $< 2$  nm pore diameter), inorganic solids broadly applied in adsorption [1,2] separation [3,4], and catalysis [5]. Their diverse structures (248 synthesized [6],  $>2.6$  million predicted [7,8]) are built from  $\text{TO}_4$  units, where T is a tetrahedral atom and O atoms bridge two T-atoms, leading to neutrally-charged frameworks when  $\text{T} = \text{Si}^{4+}$  [9,10]. Substitution of  $\text{Al}^{3+}$  at T-sites leads to negatively-charged frameworks which, when compensated by  $\text{H}^+$ , are solid Brønsted acids ubiquitous in hydrocarbon catalysis such as fluid catalytic cracking [11,12]. Substitution of  $\text{M}^{4+}$  ( $\text{M} = \text{Ti}, \text{Sn}, \text{Zr}, \text{Hf}$ ) at T-sites yields Lewis acid sites, which have found large-scale application in selective oxidations of organic molecules with  $\text{H}_2\text{O}_2$  [13–15]. Efforts to devise new routes to fuels and chemicals from biomass-derived feedstocks [16–21] and from hydrocarbons under conditions that lead to condensed phases [22–25] motivate ongoing research in catalysis by both Lewis and Brønsted acid zeolites in liquid reaction media.

New applications of zeolites in liquid-phase reactions motivate studying the fundamentals of solvation within pores of molecular dimension. Zeolites have long been recognized as shape-selective catalysts that exclude reactants from active sites occluded within their pores on the basis of size and shape [26–29]. Beyond size exclusion, the voids that confine active sites provide a solvating environment that influences the free energies of reaction intermediates and transition states through van der Waals interactions [30–33]. Introducing intraporous functional groups through synthesis and post-synthetic modifications such as Si-OH defects [34,35] or organic moieties [36] adds the potential for specific bonding interactions to discriminate among reactants and solvents of different polarity. Thus, the microporous environments of diverse size, shape, and polarity possessed by zeolites can be modified to prefer a given guest

molecule or transition state; however, the effects of co-adsorbed solvent molecules on such reactant-framework interactions are difficult to predict.

The fundamental concepts of chemical kinetics require that a complete picture of solvation effects in zeolite catalysis must consider solvating molecules and solid host environments from the perspective of the transition states and the prevalent configurations adopted by reactant and solvent ensembles at active sites. Detailed studies of water confined in nanoscale environments indicate that its structure [37, 38] and dynamics [24, 39, 40] are drastically different from those of liquid water and depend strongly on confining environment dimensions [38, 41] and the functional groups within them [37, 42, 43]. Measured rates of zeolite-catalyzed reactions in the liquid phase differ from those catalyzed homogeneously in bulk liquid phases [44–46], depend on the identity of solvent or solvent mixtures [47–51], and are affected by the hydrophobicity of zeolite frameworks [52–58] and their pore structures [47, 59–61]. The degree to which observed rate differences are connected to the molecular structures of confined solvents and reactants on a mechanistic basis is often limited; strengthening these structural and mechanistic connections would enable designing with higher fidelity microporous reaction environments for liquid-phase heterogeneous catalysis.

Although solvents may occupy the entire microporous channel networks of zeolites, catalysis occurs at active sites [62] associated with specific collections of atoms in the zeolite lattice. Identifying the different configurations adopted by active sites and quantifying their numbers is essential for accurate comparisons among samples with diverse structural motifs and different catalytic behavior in terms of their turnover rates [63, 64]. The interactions of solvents with active sites lead to additional complexities in determining their chemical identity because solvents can modify the local coordination of active sites to the zeolite framework, their coordination to solvent ligands, and the chemical interactions afforded by their secondary environments, or irreversibly deactivate some fraction of them. Liquid water at elevated temperatures ( $>373$  K) has been shown to leach framework heteroatoms from zeolites [65, 66] and in some cases cause collapse of porous structures [67]. Framework Lewis acid sites ( $M-(OSi\equiv)_4$ )

can adopt different local configurations after partial hydrolysis by water molecules ((HO)-M-(OSi≡)<sub>3</sub>---HO-Si), which have been calculated to stabilize glucose-fructose isomerization transition states with their proximal Si-OH group [68–70]. Brønsted acidic H<sup>+</sup> associated with framework AlO<sub>4</sub><sup>-</sup> tetrahedra become solvated by water as (H<sub>3</sub>O<sup>+</sup>)(H<sub>2</sub>O)<sub>n</sub> clusters that locate H<sup>+</sup> more distant from framework Al [71–73], and which have structures [73] and catalytic behavior [44–46] different from analogous homogeneous clusters. The changing solvated configurations of solid Lewis and Brønsted acid sites within micropores lead to different solvation of adsorbed reactants and transition states.

Fundamental insights into the active sites and reactivity of heterogenous catalysts have often been driven by the kinetics of probe reactions. A probe reaction is characterized by the ability to quantify kinetic rate constants based on a mechanistic understanding of turnover rates, accurately normalized by the number of active sites, and measured on a suite of catalysts with systematically varying properties [74]. For instance, the foundational concept of the structure-sensitivity [75] of reactions catalyzed by metal nanoparticles and alloys bearing different active site ensembles was elegantly demonstrated by Sinfelt using dehydrogenation and hydrogenolysis as probe reactions [76, 77]. In the realm of acid catalysis, alcohol dehydration was studied by Iglesia and coworkers as a probe reaction to understand the strength of solid Brønsted acids [74, 78–83] and the consequences of confinement of H<sup>+</sup> within zeolites for catalysis [81, 84, 85]. In this work, alcohol dehydration is adapted to study Brønsted acid catalysis by zeolites in regimes characterized by condensed intrapore liquid phases, and is developed as a gas-phase probe reaction for Lewis acid zeolites, taking inspiration from the mechanistic insights of prior studies of alcohol dehydration on Lewis acidic  $\gamma$ -Al<sub>2</sub>O<sub>3</sub> surfaces [86–90]. The liquid-phase reactivity of Lewis acid zeolites is interrogated by aqueous-phase glucose isomerization, which has a well-understood mechanism [91, 92] and kinetic interpretation of rate data [53].

Measured rates (404 K, per total Sn) of gas-phase bimolecular ethanol dehydration to form diethyl ether on Sn-Beta zeolites depend on ethanol and water concentrations

(0.5–35 kPa ethanol, 0.1–50 kPa water) with non-integer reaction orders, consistent with multiple prevalent surface intermediates and/or competing reaction pathways [88,90]. After framework Sn sites in closed configurations ( $\text{Sn}-(\text{OSi}\equiv)_4$ , Figure 1.1b) react with ethanol or water to adopt new hydrolyzed-open ( $(\text{HO})\text{-Sn}-(\text{OSi}\equiv)_3\text{---HO-Si}$ , Figure 1.1a) or ethoxy-open ( $(\text{CH}_3\text{CH}_2\text{O})\text{-Sn}-(\text{OSi}\equiv)_3\text{---HO-Si}$ , Figure 1.1c) configurations, they can adsorb ethanol molecules to stabilize distinct bimolecular dehydration transition states in parallel reaction pathways that are indistinguishable to experimental reaction order measurements. In Chapter 2, density functional theory

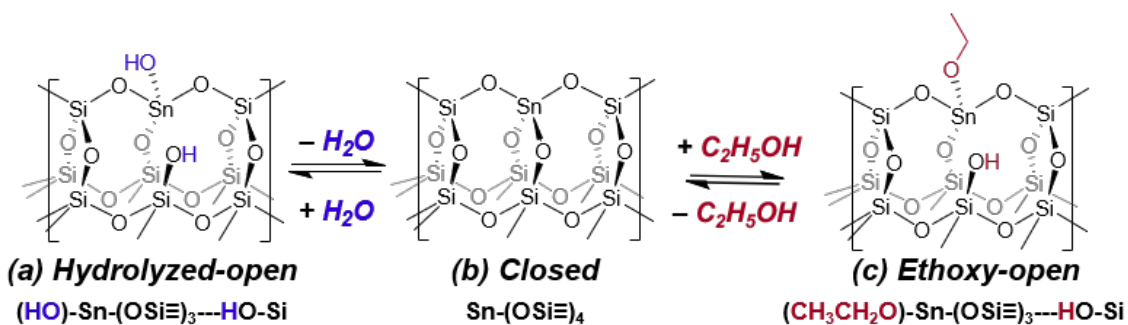


**Figure 1.1:** Possible framework Sn active site configurations during gas-phase ethanol dehydration catalysis.

(DFT) calculations are combined with experimental bimolecular ethanol dehydration kinetics to identify the relative catalytic contributions of these pathways through microkinetic modeling. Accurate evaluation of adsorbate entropies for kinetically and thermodynamically sensitive intermediates identified by degree-of-rate-control (DRC) analyses requires more precise theoretical techniques that employ quasi-harmonic densities of states methods to account for anharmonicity of vibrational modes, and result in rate and equilibrium constants that agree with measured reaction orders in ethanol and water. Site balances and DRC analyses of the microkinetic modeling data indicate that quasi-equilibrated interconversion among closed, hydrolyzed-open, and ethoxy-open sites results in adoption of predominantly closed Sn configurations during catalysis (404 K, 0.5–35 kPa  $\text{C}_2\text{H}_5\text{OH}$ , 0.1–50 kPa  $\text{H}_2\text{O}$ ), that these closed sites

are covered by most abundant reactive intermediate (MARI) species consisting of ethanol monomers, productive ethanol-ethanol dimers, and inhibitory ethanol-water dimers, and that diethyl ether is formed in a sole kinetically relevant step through an  $S_N2$ -like bimolecular substitution transition state at closed Sn sites.

The mechanistic insight into bimolecular ethanol dehydration detailed in Chapter 2 enables it to be used as a probe reaction of the structure and function Lewis acid zeolites, and thus to learn detailed molecular information from measured ethanol dehydration rate and equilibrium constants quantified from kinetic data. Turnover rates of bimolecular ethanol dehydration to diethyl ether (per Lewis acidic Sn, 404 K, 0.5–35 kPa  $C_2H_5OH$ , 0.1–50 kPa  $H_2O$ ) are presented in Chapter 3 on a suite of Sn-Beta zeolites with either high or low densities of Si-OH defects within secondary environments that confine structurally similar Sn active sites. Adsorption equilibrium constants to form both productive and inhibitory dimeric surface intermediates are 3–4 $\times$  higher in polar Sn-Beta zeolites due to hydrogen-bonding interactions with Si-OH groups surrounding Sn active sites, resulting in more extensive  $H_2O$  inhibition than in non-polar frameworks, and consistent with their relative adsorption preferences derived from single-component (302 K) and two-component (303 K, 403 K) ethanol and water adsorption measurements. Similar measured values of intrinsic rate constants indicate that differences in reactivity within polar and non-polar secondary environments are solely a consequence of different abundances of intermediates at active sites that result from the higher stabilities of these MARI when interacting with Si-OH groups by hydrogen bonding. The sensitivity of reaction intermediates to the polarity of their surrounding environment provides a mechanism to mitigate solvent inhibition by designing reaction pockets that preferentially stabilize reactant molecules over solvent molecules.

Sn sites in distinct configurations are distinguished by infrared spectra detecting the  $\nu(C\equiv N)$  frequency of adsorbed  $CD_3CN$  at 2316  $cm^{-1}$  ( $Sn_{2316}$ ) and 2308  $cm^{-1}$  ( $Sn_{2308}$ ), yet Sn sites are spectroscopically indistinguishable after ethanol dehydration catalysis (404 K) because they are covered by structurally similar reaction interme-

diates, and they revert to their initial configurations quantitatively after regenerative oxidation treatments (21% O<sub>2</sub>, 803 K). The recovery of distinct structural configurations after catalysis and regeneration indicates that underlying structural features of the zeolite host determine the configurations of Sn Lewis acid sites. The different reactivities and structural features that distinguish Sn<sub>2316</sub> and Sn<sub>2308</sub> sites are probed in Chapter 4 using *in situ* pyridine titrations during ethanol dehydration catalysis (404–438 K) and CD<sub>3</sub>CN IR on Sn-zeolites with diverse local coordination environments generated by synthesis (Beta, BEC, MFI, CHA, STT) and post-synthetic treatments to Sn-Beta. *In situ* pyridine titrations identify two types of Sn sites with bimolecular ethanol dehydration turnover rates (404 K) that differ by more than one order of magnitude (>20×). Apparent activation entropies to form substitution transition states from sites predominantly covered by ethanol monomers are less negative ( $\Delta\Delta S_{\text{app}}^{\ddagger} = 48 \pm 22 \text{ J mol}^{-1} \text{ K}^{-1}$ ) at the more reactive subset of Sn sites, which are present in amounts equivalent to 17–26% of Sn<sub>2308</sub> sites, but not correlated with Sn<sub>2316</sub> sites. Post-synthetic treatments to Sn-Beta in HF and NH<sub>4</sub>F solutions, which preferentially dissolve zeolites at their grain boundaries, indicated that Sn<sub>2316</sub> sites are preferentially located at stacking faults generated by the intergrowth of the two polymorphs that comprise Beta crystallites. Stacking faults lead to Sn<sub>2316</sub> sites in defect-open configurations ((HO)-Sn-(OSi≡)<sub>3</sub>) with proximal Si-OH groups that are not able to condense with Sn-OH groups to form closed configurations. A computational model of stacking fault defect-open sites predicts apparent activation free energies for ethanol dehydration that are 65–74 kJ mol<sup>-1</sup> higher than at framework closed sites, consistent with their low reactivity determined by *in situ* pyridine titrations. Closed Sn sites stabilize S<sub>N</sub>2 transition states by adopting open configurations along the reaction coordinate of bimolecular alcohol dehydration reactions, while the proximal Si-OH groups of defect-open Sn sites stabilize hydride shift transition states involved in glucose-fructose isomerization. Zeolite frameworks impart different local configurations to Lewis acid sites, which enables stabilizing transition states that require unique chemical functionality of reaction environments.

The catalysis of oxygenates in envisioned biomass upgrading pathways occurs in liquid phases, which necessitates understanding the effects of solvents on the structural evolution of active sites and their surrounding environments, and therefore on the stability of reaction intermediates and transition states. The effects of hot (373 K) liquid water pretreatments on the reactivity of Sn-Beta zeolites synthesized with polar and non-polar frameworks is discussed in Chapter 5 as an analogy to extended solvent exposure in continuous reactors, independent of competing deactivation mechanisms associated with reactant conversion. Hot (373 K) liquid water exposure does not alter the measured distribution of active Sn sites between closed and defect-open configurations quantified *ex situ* by CD<sub>3</sub>CN IR, but systematically increases the density of Si-OH defects in initially non-polar frameworks with increasing exposure time until they are commensurate with those of polar frameworks after ~24 h, which is accompanied by a concomitant systematic decrease in measured glucose-fructose isomerization turnover rates (373 K, per defect-open Sn). This study highlights the need for continuous aqueous-phase processes to minimize irreversible siloxane bridge hydrolysis that forms Si-OH groups and decreases glucose-fructose isomerization turnover rates (373 K).

Lower first-order glucose-fructose isomerization rate constants within polar Sn-Beta and Ti-Beta zeolites have been attributed to their ability to preferentially stabilize adsorbed water molecules relative to non-polar micropores [53,56], but without disentangling the relative contributions of the stability of adsorbed intermediates, water molecules, and transition states. In Chapter 6, glucose isomerization turnover rates (368–383 K, per Lewis acidic Ti) are quantified on Ti-Beta zeolites in both first-order and zero-order regimes that reflect Ti sites covered either by bound water molecules or bound glucose MARI, consistent with *in situ* attenuated total reflectance IR spectra (373 K). Isomerization rate constants, regardless of the MARI species, are 3–12× higher within non-polar Ti-Beta than polar Ti-Beta not because of competitive adsorption of glucose and water, but because isomerization transition states are entropically destabilized relative to their bound precursors by extended

hydrogen-bonded water structures found within polar frameworks, as detected by *in situ* transmission IR. Here, using glucose isomerization as an aqueous-phase probe reaction highlights the gradual changes in the polarity of confining environments during exposure to hot (373 K) liquid water, which lowers reactivity when polar micropores stabilize extended solvent structures.

The varied catalytic effects of adsorbed solvents within micropores of different polarity motivates studying the individual contributions of different types of intracrystalline functional groups to the local structure of adsorbed water. In Chapter 7, the structure and thermodynamics of water within Beta zeolites are investigated by *ab initio* molecular dynamics (AIMD) simulations (293 K) across a wide range of adsorbed water loadings (1–23 per unit cell) in the presence of silanol nest defects, closed Sn sites, and hydrolyzed-open Sn sites (one per unit cell). Pure-SiO<sub>2</sub> zeolite Beta with minimal intracrystalline Si-OH defects was synthesized using fluoride as the mineralizer [35], and compared with pure-SiO<sub>2</sub> Beta with one silanol nest per unit cell generated by complete dealumination of a fluoride-mediated Al-Beta-F zeolite initially containing one Al per unit cell and minimal residual Si-OH defects [93]. Transmission IR spectra of water adsorbed within these model samples possess  $\nu(\text{OH})$  peak centers that shift to lower wavenumbers as higher amounts of water are adsorbed at silanol nest defects and form extended hydrogen-bonded water networks, validating AIMD simulations that show these extended networks form in a periodic Beta unit cell containing one Si-OH nest, but not within defect-free Si-Beta. Thermodynamic and clustering analyses of AIMD simulations indicate that distinct liquid-like phases are formed within Sn-Beta zeolites where Lewis acidic Sn sites stabilize localized clusters in their vicinity, whereas silanol nest defects assist in stabilizing the extended hydrogen-bonded networks implicated in destabilizing glucose isomerization transition states.

Aqueous-phase reactions catalyzed by Brønsted acid zeolites are accompanied by solvent-active site interactions distinct from those of Lewis acid zeolites because confined water molecules transform isolated H<sup>+</sup> associated with the framework to

$(\text{H}_3\text{O}^+)(\text{H}_2\text{O})_n$  clusters. The zeolite-confined structures of  $(\text{H}_3\text{O}^+)(\text{H}_2\text{O})_n$  are beginning to be understood in detail [71–73]; however, the catalytic consequences of adsorption and reaction of organic molecules interacting with  $\text{H}_3\text{O}^+$  and the associated clustered  $\text{H}_2\text{O}$  molecules that solvate them still remain under investigation. The liquid-phase probe reactions that have been studied (e.g., cyclohexanol dehydration [45, 46, 94], carbohydrate dehydration [44, 51] and isomerization [50], phenol alkylation [95–97]) limit the ability to systematically vary solvent structures independent of the reactant or a co-solvent. This limitation is addressed by gas-phase probe reaction in Chapter 7, where ethanol dehydration turnover rates (373 K, per  $\text{H}^+$ ) measured across a wide range of co-fed water pressures (0.02–75 kPa) enable systematic control of intrapore water structures into regimes that include condensed liquid-like intrapore water. Here, measured turnover rates on a suite of H-Al-Beta-F zeolites with systematically varying  $\text{H}^+$  densities (0.16–2.0  $\text{H}^+$  per unit cell) but minimal Si-OH defects deconvolute the effects of  $\text{H}^+$  and Si-OH groups on intrapore water structure. First-order rate constants in ethanol pressure ( $k_{first}$ ) for bimolecular ethanol dehydration (373 K, per  $\text{H}^+$ ) reflect surfaces saturated with  $(\text{C}_2\text{H}_5\text{OH})(\text{H}^+)(\text{H}_2\text{O})_n$  MARI, and exhibit a  $-1$  order dependence on water pressure (2–10 kPa  $\text{H}_2\text{O}$ ) because one water coordinated in MARI species must be displaced by ethanol to form the  $\text{S}_{\text{N}}2$  transition state that eliminates diethyl ether. Water inhibition of ethanol dehydration rates becomes more severe at higher  $\text{H}_2\text{O}$  pressures (10–75 kPa  $\text{H}_2\text{O}$ ,  $P/P_0 = 0.1$ –0.75), reflected in  $k_{first}$  values with an apparent  $\text{H}_2\text{O}$  order more negative than  $-1$ . *In situ* IR spectra of adsorbed water (293 K and 373 K,  $P/P_0=0.1$ –0.75) possess  $\nu(\text{OH})$  peak centers that shift to lower wavenumbers with increasing water coverage, indicating that extended hydrogen-bonded water networks form around clustered  $(\text{H}_3\text{O}^+)(\text{H}_2\text{O})_n$  or at Si-OH nests within H-Al-Beta-F and deAl-Beta-F materials, respectively. The different solvation of kinetically relevant MARI and transition states requires non-ideal thermodynamic formalisms, which show that extended hydrogen-bonded water networks stabilize transition states less effectively than MARI, leading to stronger water inhibition. These effects are ubiquitous in Brønsted acid zeolites of

different topology (CHA, AEI, TON, FAU), which influences the onset and severity of water inhibition by extended hydrogen-bonded networks.

## 2. FIRST PRINCIPLES, MICROKINETIC, AND EXPERIMENTAL ANALYSIS OF LEWIS ACID SITE SPECIATION DURING ETHANOL DEHYDRATION ON SN-BETA ZEOLITES

### 2.1 Introduction

Microporous Lewis acids formed through isomorphous metal atom substitution into siliceous zeolite frameworks are shape selective heterogeneous catalysts that facilitate a broad range of oxygenate reactions [16], including Baeyer-Villiger oxidation [98], Meerwein-Ponndorf Verley carbonyl reduction and Oppenauer oxidation of alcohols (MPVO) [99], and sugar isomerization [100]. A central question in the elucidation of elementary reaction networks in solid Lewis acids is the nature of active site heteroatom speciation. Tin heteroatoms, for example, adopt at least two distinct framework configurations: either tetra-coordinate to the framework (denoted as “closed”) or tri-coordinate to the framework with an additional hydroxyl ligand (denoted as “open”). Open configurations are proposed to be the dominant active sites for glucose isomerization [56, 101] and MPVO [102–104], while both open and closed sites catalyze aldol condensation [105]. The structure of these different Sn sites has been studied with density functional theory (DFT), as well as experimental spectroscopies such as  $^{119}\text{Sn}$  nuclear magnetic resonance (NMR) [68, 106, 107], infrared upon adsorption of probe molecules (e.g., pyridine, deuterated acetonitrile) [56, 102], extended X-ray adsorption fine structure (EXAFS) [108], and diffuse reflectance UV-visible (DRUV) [102, 109]. DFT studies have proposed multiple structures for defect configurations of framework heteroatom sites, such as penta-coordinated Sn centers with a hydroxy ligand and protonated framework oxygen [110, 111], “open” tri-coordinate sites with a hydroxyl ligand and an adjacent framework silanol [68, 69, 101], and “defect open” sites where a proximal silicon vacancy creates a nest of silanol de-

fects [111,112]. In addition, the adsorption and subsequent dissociation of water at heteroatom sites to form the hydroxyl ligand and proximal silanol group has been discussed in previous studies [113,114]. In spite of these advances in understanding the pathways that interconvert these active site structures, the dynamics of their interconversion, and the resulting effects on observed reaction kinetics, have not been quantitatively analyzed.

To obtain fundamental, molecular-level understanding of how Sn sites interconvert under reaction conditions, ethanol dehydration is chosen as a model gas-phase probe reaction. This choice is motivated by the fact that liquid phase reactions are difficult to model accurately with DFT due to explicit solvent interactions between intermediates and transition states [115], and, DFT studies are limited in terms of the number and size of molecules that can be effectively treated in reaction networks, as the search space of relevant molecular configurations that must be analyzed increases rapidly with system complexity. Furthermore, reactive intermediate coverages are difficult to control in experiment due to the ubiquity of the solvent, and rapid deactivation in continuous liquid flow reactors [116,117] precludes analysis of site dynamics. Ethanol dehydration therefore provides a more suitable probe of site interconversion and its effect on reaction kinetics, and it is known to proceed on Lewis acidic sites in  $\gamma$ -Al<sub>2</sub>O<sub>3</sub> [87] via both unimolecular and bimolecular pathways [88,118] to form ethene and diethyl ether (DEE), respectively. Since reaction mechanisms on both closed and open Sn sites form DEE, computational insights are essential to understand the interconversion of active sites and its impact on the rate and selectivity of alternate dehydration pathways.

To model the ethanol dehydration reaction network, a total of 25 elementary steps and 19 reactive intermediates are first considered using DFT at the generalized gradient approximation (GGA) level. It is found that rates and reaction orders predicted from GGA-level calculations, along with entropies derived using the harmonic oscillator approximation, are insufficient to permit reliable interpretation of experimental kinetic data measured under differential conditions at which DEE is the only product

formed. To enhance model fidelity, a generalized degree of rate control (DRC) [119] analysis is therefore used to identify kinetically relevant transition states and reaction intermediates, which are subjected to density functional and entropy treatments that are systematically refined. The hybrid density functional HSE06 includes a fraction of screened exact Hartree-Fock exchange [120], which improves calculated lattice constants in zeolite frameworks because it favors shorter cation-oxygen bonds [121–123]. More importantly, the confining pore environment introduces entropic contributions that are fundamentally distinct from similar effects on terraces of supported metal nanoparticles, because numerous anharmonic molecular interactions make harmonic partition functions problematic for low frequency modes, resulting in errors in calculated free energies on the order of 0.1–0.2 eV [124, 125]. The modes that deviate from harmonicity correspond to delocalized rotational and translational degrees of freedom and require more robust sampling of the potential energy surface (PES). The full PES can be sampled using semi-empirical force fields with Monte Carlo free-energy integrations [126], but direct use of such methods at the *ab-initio* level is limited by the speed of current computational resources. To overcome this limitation, Piccini and Sauer developed an algorithm in curvilinear normal mode coordinates to efficiently sample anharmonic features of the PES of methane adsorption in the proton form of chabazite [124]. Alternatively, Alexopoulos et al. sampled the PES of ethanol adsorption in H-MFI [127] by integrating the rotational and vibrational density of states from *ab-initio* molecular dynamics (AIMD). Both methods incorporate anharmonic corrections but are impractical to perform for an extensive reaction network. For simplicity, it may be possible, in some cases, to replace harmonic modes that have calculated frequencies below an arbitrarily chosen threshold with a higher frequency harmonic mode that approximates some aspects of rotational or translational freedom [128]. However, Jørgensen and Gronbeck have recently compared harmonic oscillator partition functions, free translational partition functions, hindered translational partition functions, and complete potential energy sampling (CPES) methods and have demonstrated that, even for CO oxidation on simple Pt(111) surfaces [129],

there are non-negligible deficiencies of the harmonic oscillator approach relative to hindered translational partition function analyses and CPES sampling. The advanced partition function methods represent an improvement over simple harmonic analyses but do not explicitly include the effects of mode-mode coupling, thus motivating judicious use of CPES sampling or AIMD-related methods [130].

In this work, a tiered approach to kinetic model development is proposed, wherein partition function methods are used for the majority of the reaction intermediates, while a higher accuracy AIMD method is used for the kinetically sensitive intermediates determined by the DRC analysis. These intermediates, in turn, are identified using a generalized degree of rate control (GDRC) analysis [131]. Apparent reaction orders in water and ethanol are then determined from the fully converged model and are compared with experimental measurements to obtain a simplified rate expression derived from elementary steps. Finally, conclusions concerning the Sn site speciation that dominates reactivity are drawn.

## 2.2 Methods

### 2.2.1 Computational Methods

All calculations are performed using self-consistent, periodic density functional theory (DFT) with the Vienna Ab-initio Simulation Package (VASP) [132–136]. The Bayesian error estimation functional (BEEF-vdw) [137], which self-consistently includes dispersion interactions, is employed. In addition to this generalized-gradient approximation (GGA) functional, a hybrid functional, HSE06 [120, 138], using a screened coulombic interaction with additional semi-empirical dispersion corrections via the Grimme approach [139, 140], is employed for selected calculations. Pseudopotentials are constructed in the projector augmented wave (PAW) framework for PBE functionals [136, 141]. The Beta unit cell is obtained from the International Zeolite Database [142]. The defect-free Beta framework is relaxed to final lattice vectors 12.66 Å, 12.66 Å, 26.54 Å. For HSE06-D3 calculations, unit cell vectors are reopti-

mized to 12.58 Å, 12.58 Å, 26.36 Å. The optimized cell volumes are within 1.9% and 0.2% of the IZA values for BEEF-vdW and HSE06-D3, respectively. For geometry optimizations, a plane wave cutoff of 520 eV is employed, along with a single gamma point to sample reciprocal space. Geometry convergence is performed to a force criterion of 20 meV/Å. All calculations are spin polarized. Gaussian smearing of the Fermi surface with a width of 10 meV is used due to the large band gap in the zeolite material.

Transition state geometries are obtained through the climbing-image nudged elastic band (CI-NEB) method [143,144]. A total of 9 images are generated between initial and final states, and the Image Dependent Pair Potential pre-optimizer is employed to generate initial configurations [145]. A Lanczos diagonalization [146] scheme is used, which converges rapidly for zeolite transition states when starting from a partially converged NEB pathway. For all transition states and reaction intermediates, a partial hessian vibrational calculation of the adsorbed structure is performed. Harmonic vibrational states are used for zero-point vibrational energy corrections ( $E_{ZPVE}$ ) and also form the basis for entropy calculations. Free energies are approximated as

$$G = E_0 + E_{ZPVE} - TS \quad (2.1)$$

where  $E_0$  is the ground state potential energy obtained through DFT. Adsorption energies in the framework ( $E_{ads}$ ) are considered relative to the doped framework and gas phase molecule

$$E_{ads} = E_{ZA} - E_Z - E_A \quad (2.2)$$

where A is the adsorbate and Z is the doped zeolite framework.

To facilitate the identification of stable adsorbate geometries, AIMD simulations at the same level of theory (BEEF-VdW) are performed. Stable configurations obtained from initial geometry optimizations are heated to 400K and then equilibrated using a Nosé-Hoover thermostat and 0.5 fs timestep. Geometries are extracted from the equilibrated simulation and then quenched to provide additional adsorbate configurations.

This process is performed for selected monomolecular intermediates, including ethanol and water, as well as for some dimeric intermediates, including ethanol-ethanol dimers and ethanol-water dimers.

Rate constants for surface processes are evaluated using transition state theory, where the preexponential factor is assumed to correspond to the harmonic saddle mode. For molecular adsorption and desorption, collision theory is employed, as these processes not activated. To simulate reaction rates, a differential reactor model, similar to that developed by Gokhale et al. [147] and by Choksi and Greeley [148], is used. Numerical solution of the reactor and site balance equations is accomplished with a custom python-based solver. While the rate equations are relatively straightforward to integrate numerically, the large number of elementary steps and surface intermediates results in poor convergence of nonlinear equation solvers without the reasonable initial guesses provided by a coarse-grained differential equation solution. Thus, the scheme uses an initial transient differential equation solver to approximately locate local steady state solutions, which are then input into a nonlinear equation solver for further refinement. A rate sensitivity analysis is performed using the generalized degree of rate control [119] to identify thermodynamically and kinetically sensitive intermediates and transition states. A detailed discussion of entropy calculations, elementary steps of the reaction, the microkinetic model construction, adjustments, and error analysis can be found in the Supporting Information.

Crystal Orbital Hamiltonian Population (COHP) analysis in semiconductors and insulators has seen success in qualitatively explaining the bonding structure of these materials by localizing a periodic wavefunction onto Gaussian orbitals. The LOBSTER [149] code, which employs COHP, is used for wavefunction localization, along with a Bader analysis [150], to determine charge transfer and Sn oxidation states.

## 2.2.2 Catalyst Synthesis and Characterization

The Sn-Beta zeolites in this study are a subset of the samples reported by Vega-Vila et al. [151]. In brief, Sn-Beta zeolites were prepared by post-synthetic grafting

of stannic chloride into dealuminated Beta frameworks in dichloromethane reflux. The zeolite topology was identified from powder X-ray diffraction patterns and N<sub>2</sub> adsorption isotherms (77 K) that gave micropore volumes characteristic of the Beta structure (0.21 cm<sup>3</sup> g<sup>-1</sup>). The total Sn content was measured by atomic absorption spectroscopy (AAS). The bulk Sn coordination was assessed from diffuse reflectance UV-Visible spectroscopy after dehydration treatments at 523 K under flowing dry helium, which revealed ligand-to-metal charge transfer bands centered at ~190–200 nm characteristic of tetrahedral Sn sites in framework locations [152, 153]. Infrared spectroscopic bands for CD<sub>3</sub>CN adsorbed at open (2316 cm<sup>-1</sup>) and closed (2308 cm<sup>-1</sup>) Sn sites were quantified according to the methods developed by Harris et al. [56]. These data are summarized in Table 2.1 for the samples used in this study. The reader

**Table 2.1:** Sn contents, micropore volumes, and acid site counts for Sn-Beta catalysts. [151]

Catalyst	Si/Sn (Sn wt%) <sup>a</sup>	V <sub>micro</sub> (cm <sup>3</sup> g <sup>-1</sup> ) <sup>b</sup>	LAS/Sn <sup>c</sup>	Open/Sn <sup>c</sup>	Closed/Sn <sup>c</sup>
Sn-Beta-OH-30 <sup>d</sup>	30 (6.08)	0.16	0.72	0.18	0.54
Sn-Beta-OH-41 <sup>d</sup>	41 (4.60)	0.19	1.32	0.50	0.82
Sn-Beta-OH-46 <sup>d</sup>	46 (4.10)	0.19	0.92	0.22	0.70
Sn-Beta-OH-95 <sup>d</sup>	95 (2.00)	0.22	1.22	0.49	0.73
Sn-Beta-OH-80 <sup>e</sup>	80 (2.39)	0.22	1.01	0.42	0.59
Sn-Beta-OH-84 <sup>f</sup>	84 (2.29)	0.20	1.20	0.24	0.96

<sup>a</sup>Determined by AAS

<sup>b</sup>Determined by N<sub>2</sub> adsorption minimum in  $\partial V_{\text{ads}}/\partial \log(P/P_0)$

<sup>c</sup>LAS = Lewis acidic Sn sites, from CD<sub>3</sub>CN IR, errors  $\pm 20\%$

<sup>d</sup>Parent Si/Al = 19 <sup>e</sup>Parent Si/Al = 29 <sup>f</sup>Parent Si/Al = 54

is referred to the original study by Vega-Vila et al. for a complete description of the synthetic protocols and characterization techniques [151]. All samples are labeled as Sn-Beta-X-Y, where X denotes the synthesis method used (“OH” for post-synthetic grafting) and Y denotes the Si/Sn ratio determined by AAS.

### 2.2.3 Ethanol Dehydration Kinetics

Sn-Beta samples (0.010–0.050 g) were pelleted, crushed, and sieved to retain aggregates between 180–250  $\mu\text{m}$  and supported between two plugs of acid-washed quartz wool (W.R. Grace, 1 M  $\text{HNO}_3$  for 16 h) in a tubular quartz reactor (7 mm ID). The catalyst temperature was measured using a K-type thermocouple (Omega) placed in contact with the outside of the quartz tube at the level of the catalyst bed, and was maintained using a three-zone furnace (Applied Test Systems) and Watlow controllers (EZ-ZONE). The catalyst was heated to 803 K ( $0.0167 \text{ K s}^{-1}$ ) under flowing 5%  $\text{O}_2/\text{He}$  (UHP, Indiana Oxygen,  $16.67 \text{ cm}^3 \text{ s}^{-1} (\text{g catalyst})^{-1}$ ), held at 803 K for 2 h, then cooled to 404 K ( $0.0333 \text{ K s}^{-1}$ ) and held under flowing He (UHP, Indiana Oxygen,  $16.67 \text{ cm}^3 \text{ s}^{-1} (\text{g catalyst})^{-1}$ ) for 1.5 h before starting the reaction. Liquid ethanol (Sigma Aldrich, anhydrous, >99.5%) and deionized water (18.2 M $\Omega$ ) were introduced using syringe pumps (KD Scientific Legato 100) into separate heated transfer lines (>383 K) containing flowing He streams and mixed upstream of the reactor. A stream of 25%  $\text{CH}_4/\text{Ar}$  (Indiana Oxygen,  $0.0167 \text{ cm}^3 \text{ s}^{-1}$ ) was mixed with the He stream as an internal standard prior to mixing with ethanol. Reactant and product concentrations were measured by gas chromatography (Agilent 6890) using a HP-PLOT-Q capillary column (30 m  $\times$  530  $\mu\text{m}$   $\times$  40  $\mu\text{m}$ ) and flame ionization detector.

Prior to reaction, the composition of the feed stream was determined from reactor bypass injections. Frequent sojourns to a reference condition (typically, 8 kPa  $\text{C}_2\text{H}_5\text{OH}$ , 0.1 kPa  $\text{H}_2\text{O}$ , 404 K) were used to correct for deactivation by extrapolating rates to initial time assuming first-order deactivation. First-order deactivation rate constants varied between  $2 \times 10^{-3}$ – $1 \times 10^{-2} \text{ ks}^{-1}$ . A period of 5 h on stream was allowed at a given condition to reach steady state. Ethanol pressures were varied from 0.5–35 kPa, and  $\text{H}_2\text{O}$  pressures were varied from 0.10–50 kPa. The site-contact time (total Sn per total moles fed basis) was held constant at 0.39 s (mol Sn) (mol fed) $^{-1}$ . Minor background contributions to DEE formation by quartz wool and other background sources were measured using a reactor packed with only quartz wool as a function of

ethanol pressure at 404 K, and corrected from all rates measured in the presence of a catalyst. Additionally, background rates on Si-Beta-F (on a per g basis) were measured at 404 K, and were  $<10\times$  lower than all rates measured on Sn-Beta samples. Measured ethanol dehydration rates and deactivation profiles on Sn-Beta catalysts could be reversibly recovered by treating in air, as described above, after intervening deactivation occurred over a period of  $>30$  ks on stream.

## 2.3 Results and Discussion

### 2.3.1 T-sites in Sn-Beta

The specific distribution of Sn among crystallographically distinct tetrahedral site (T-site) locations in the Beta framework remains a topic of continued discussion [107, 108, 111], and the local structure of Si-O bonds around each T-site may influence the energies of transition states and intermediates in the ethanol dehydration reaction network. To determine the sensitivity of adsorbate energies to Sn T-site location in Beta, the energetics of two key intermediates (water, ethanol) and one reaction step (water dissociation to form open sites) at closed sites are examined. A single Sn atom is placed in one of nine crystallographically distinct T-sites per unit cell to simulate a Si:Sn ratio of 63:1. The range in ethanol and water adsorption energies, and water dissociation energies, among these 9 T-sites is less than 0.2 eV (Supporting Information, 2.6.1). In a study of site stabilities in Sn-Beta, Josephson et al. report a similar narrow distribution of energies, and the wide variation of stable tin sites reported in literature are likely due to functional choice and kinetic energy cutoff, producing energy fluctuations commensurate with a multiplicity of lowest energy Sn sites [154]. For convenience, therefore, we choose the T8 site [142] for all Sn substitutions, as it has the most exothermic ethanol binding energy. However, we do not anticipate the T-siting of Sn atoms to influence the binding energies of intermediates beyond the standard error of periodic DFT calculations, which is typically

around  $\sim 0.1$  eV and is similar to the distribution of ethanol binding energies across all T-sites.

### 2.3.2 Sn site speciation

Partially hydrolyzed open sites are formed by dissociation of water or alkanols [113] on closed Sn sites, yielding a hydroxyl ligand on the Sn center (stannanol) and a corresponding silanol on a framework oxygen. Water adsorption on the closed site ( $W^*$ , Figure 2.1) is exergonic by  $-0.12$  eV at ethanol dehydration conditions of 404 K, and dissociation on an adjacent oxygen site proceeds with an activation free energy barrier of  $0.75$  eV (TS2, Figure 2.1). This adjacent oxygen site is a metastable

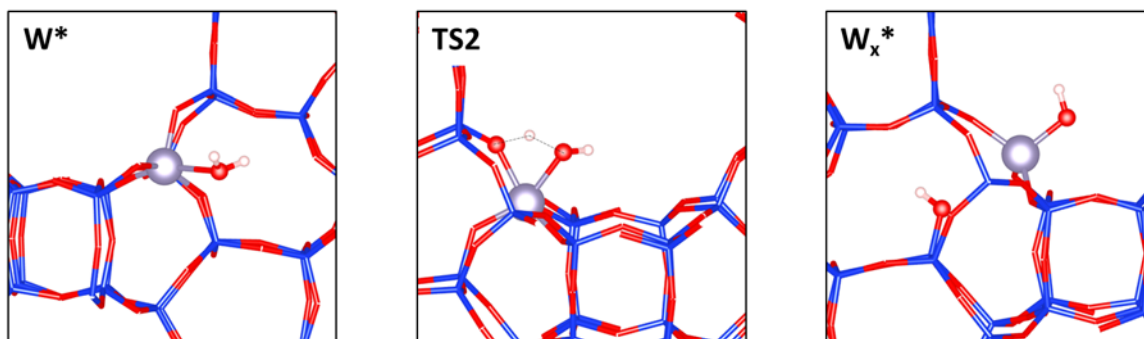


**Figure 2.1:** Hydroxy open site formation conformations corresponding to the lowest energy structures.  $W^*$  refers to water adsorbed on the closed site,  $W_x^*$  refers to the hydroxy open site where water has dissociated to form a hydroxyl ligand. TS refers to transition state, and the numbering (TS2) corresponds to the free energy diagram in Figure 2.4.

location for the proton, which migrates to a more stable location at an oxygen *anti* to the stannanol ( $W_x^*$ , Figure 2.1) with an HO-Sn-OH coordination angle of  $160.5^\circ$ , adopting a structure similar to that reported by Josephson et al. [154]. The energy difference between the *syn* and *anti* configurations is  $0.12$  eV. From the electron localization function and Crystal Orbital Hamiltonian Population (COHP) analysis, no significant orbital overlap exists between the framework silanol and Sn center, consistent with full cleavage of the framework Sn-O bond (Supporting Information,

2.6.2). A Bader charge analysis shows that the  $4^+$  oxidation state of Sn is preserved in its closed and open states (Supporting Information, 2.6.2). Water or ethanol carriers facilitate a low barrier (0.3 eV) proton shuttling mechanism that transfers the silanol proton to the most stable *anti* conformation, as further described in the Supporting Information 2.6.3. Open site energies and geometries will be referenced to this most stable conformation ( $W_x^*$ ), and thus the reaction free energy of water dissociation to form open sites is 0.37 eV at 404 K.

An alternative pathway for open site formation involving dissociative adsorption of ethanol is also considered based on experimental evidence by Yakimov et al. that dissociative adsorption of (secondary) alcohols is possible [155]. The free energy of ethanol adsorption (-0.31 eV) at the closed site is stronger than that of water (-0.12 eV), and results in the alkyl group facing the channel ( $E^*$ , Figure 2.2). In

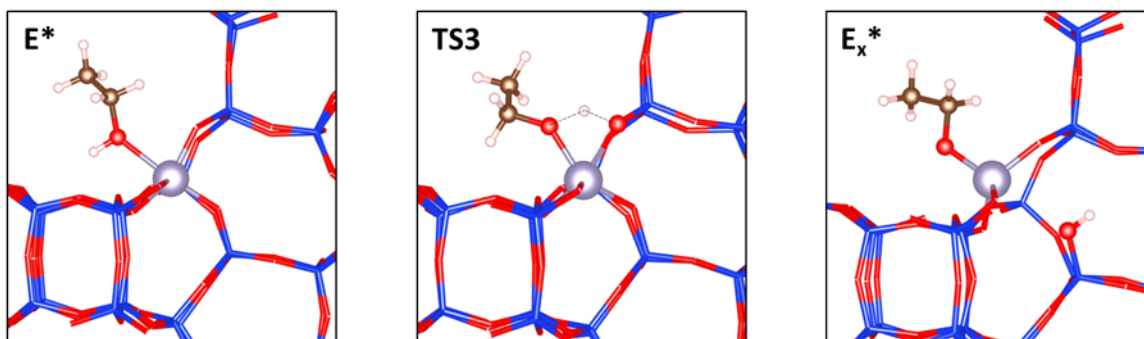


**Figure 2.2:** Ethoxy open site conformations corresponding to the lowest energy structures.  $E^*$  refers to ethanol adsorbed on the closed site,  $E_x^*$  refers to the ethoxy open site where ethanol has dissociated to form an ethoxy ligand. TS refers to transition state, and the numbering (TS3) corresponds to the free energy diagram in Figure 5.

a mechanism analogous to site opening by water, the adsorbed ethanol dissociates to form an ethoxy open site ( $E_x^*$ , Figure 2). The activation free energy barrier (TS3, Figure 2.2) for ethanol dissociation (0.80 eV) is comparable to that of water dissociation (0.75 eV). A proton shuttling mechanism similar to that described above is necessary to access the most stable silanol location *anti* to the ethoxy ligand,

with an EtO-Sn-OH coordination angle of  $159.7^\circ$  ( $E_X^*$ , Figure 2.2). The energy difference between the syn and *anti* configurations is 0.16 eV. The reaction free energy of ethanol dissociation is 0.41 eV, endergonic relative to adsorbed ethanol. As in the case of the open site formed through water dissociation, there is no orbital overlap between the protonated framework oxygen and Sn, and Bader charge analysis on Sn indicates that the oxidation state remains  $4^+$  after opening with ethanol. For clarity, in what follows, open sites will be described according to their ligand identity as either hydroxy open sites or ethoxy open sites. We note that the formation of open sites by molecular dissociation of both water and alcohols has been described previously [113], but the effects of reaction conditions on their speciation and relative populations during steady-state catalysis are not well understood.

### 2.3.3 DEE formation mechanisms

Direct formation of DEE involves adsorption of an ethanol dimer that subsequently undergoes bimolecular rearrangement to form DEE and water, as proposed by Christiansen et al. [89] on the Lewis acid sites of  $\gamma$ -Al<sub>2</sub>O<sub>3</sub> surfaces. A second mechanism for bimolecular dehydration involves reaction of a dissociated ethanol and an adjacent adsorbed ethanol, as also considered by Christiansen et al. [89]. Although ethanol reaction mechanisms on  $\gamma$ -Al<sub>2</sub>O<sub>3</sub> provide conceptual analogies for candidate mechanisms on zeolite Beta, a crucial structural difference exists between the two classes of catalysts. On the  $\gamma$ -Al<sub>2</sub>O<sub>3</sub> surface, bimolecular ethanol dehydration requires neighboring aluminum Lewis acid sites. In contrast, tin sites in the Beta framework in the elemental composition range studied here (1–2 per unit cell) are unlikely to be paired, and although Bare et al. [108] have provided evidence for Sn site pairing in Beta frameworks, reaction barriers at paired Sn sites are higher by  $>0.25$  eV than at isolated Sn sites (Supporting Information, 2.6.4). Therefore, our analysis of DEE formation will be restricted to isolated Sn sites in at the T8 position in closed, hydroxy open, and ethoxy open configurations.

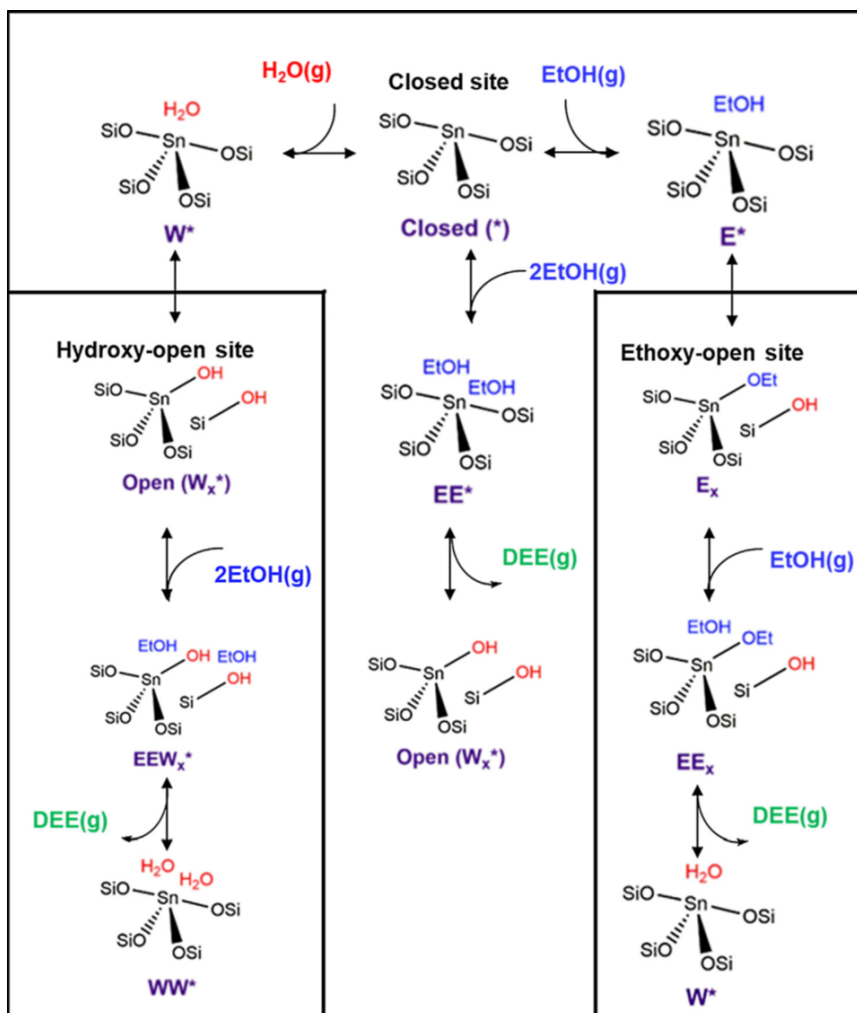


**Figure 2.3:** Condensed DEE reaction network, showing interconversion of closed tin sites and both hydroxy-open and ethoxy-open sites, with subsequent adsorption of ethanol and formation of DEE. Nomenclature for different Sn sites is defined in the figure. A full list of elementary steps considered is provided in the Supporting Information 2.6.5.

### 2.3.3.1 Closed site mediated mechanism

DEE formation on the closed site must first involve adsorption of two ethanol molecules to form an ethanol-ethanol dimer ( $EE^*$ , Figure 2.4). As stated above, the

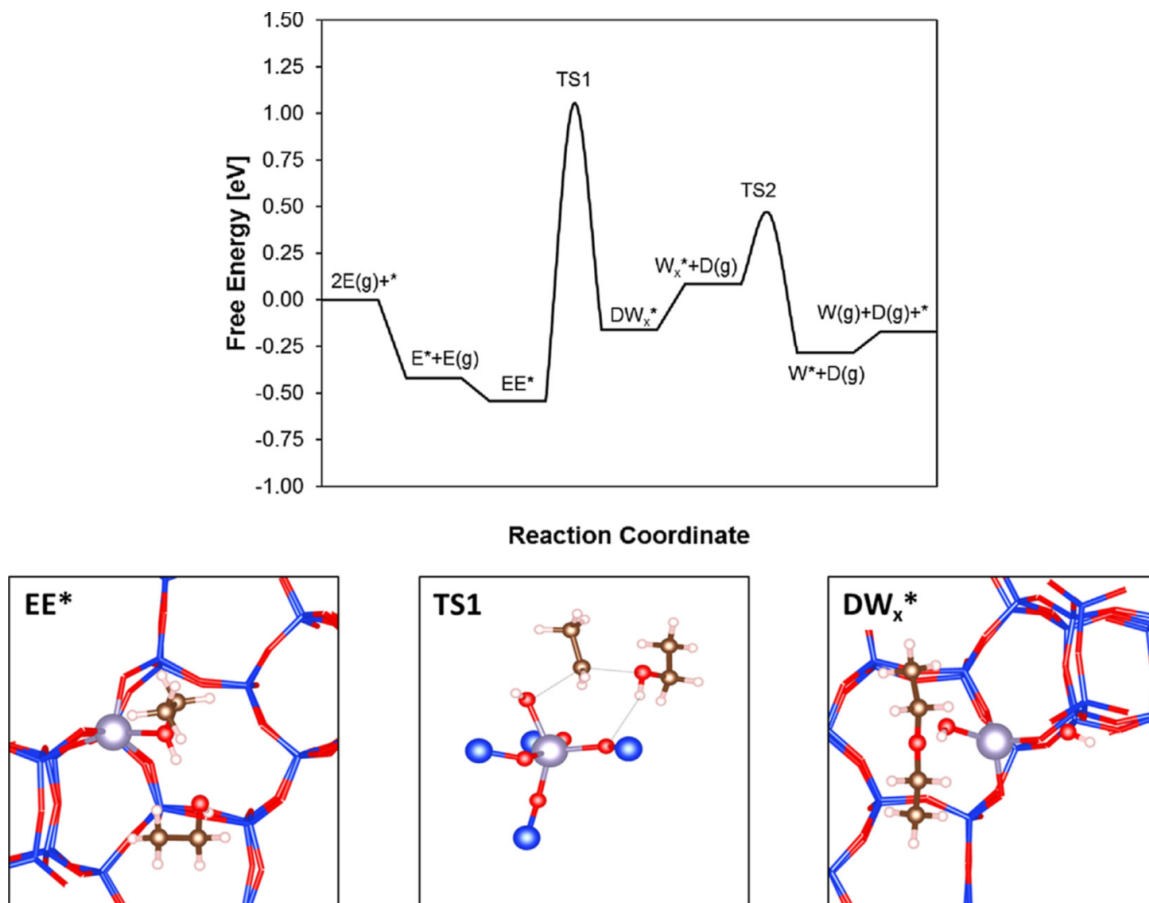


**Figure 2.4:** Closed site reaction mechanism and selected adsorbate geometries. Free energies are evaluated at 404 K and 1 bar. For clarity, the pore wall is not shown in the TS1 diagram, and diethyl ether is referred to as D in the reaction diagrams. Nomenclature for the other reaction intermediates and Sn sites is found in Figure 2.3.

adsorption free energy of the first ethanol molecule is -0.31 eV, while the differential adsorption free energy of the second ethanol is -0.16 eV. For comparison, the differential adsorption energy of a water to form an ethanol-water dimer is -0.20 eV. This second ethanol is denoted “vdW-ethanol”, as its adsorption is largely dictated by van der Waals interactions through the hydroxyl group in the primary ethanol.

The interatomic distance between the protic hydrogen of the primary ethanol and the hydroxyl group oxygen of the vdW-ethanol is 1.72 Å, which, together with the magnitude of the differential binding energy, confirms that a hydrogen bond is formed (Figure 2.4).

We note that the binding energy of the second ethanol in the ethanol-ethanol dimer is referenced to that of a gas-phase ethanol molecule. However, the specific ethanol precursor that forms the dimer may originate from a weakly physisorbed state within the zeolite framework, such as that at a silanol defect. As physisorbed ethanol is in equilibrium with the gas phase, and there are no indications of internal mass transfer limitations (Supporting Information 2.6.6), the barriers to intracrystallite diffusion are assumed to be low. Such barriers do not, therefore, affect the reaction kinetics, although they might be relevant for those describing alternative reactions.

At the subsequent nucleophilic substitution transition state for DEE formation (TS1, Figure 2.4), the oxygen atom of the vdW-ethanol acts as the nucleophile, attacking the alpha carbon of the primary ethanol, while its C-O bond to the leaving group (OH) is cleaved. The angle of attack between the stannanol leaving group, the ethyl electrophile, and the vdW-ethanol nucleophile is 154.6°, which deviates from the expected angle of 180° for gas phase S<sub>N</sub>2 reactions that maximizes overlap of the vdW-ethanol oxygen lone pair and the C-O antibonding orbital of the primary ethanol. This deviation may be influenced by the confining pore geometry, which would strain the transition state geometry away from the most favorable angle. The distance between the stannanol group and the ethyl electrophile is 2.24 Å, while the distance from the ethyl electrophile to the nucleophilic vdW-ethanol is 2.04 Å, and the distance from the nucleophilic vdW-ethanol ethyl group to the nearest pore wall oxygen atom is 4.04 Å. The O-H bond of the nucleophilic ethanol is fully formed at the transition state and is similar in length as in the coadsorbed dimer. The protic hydrogen transfers from the vdW-ethanol to an adjacent framework oxygen to form a silanol defect.

The lowest energy final state ( $DW_X^*$ , Figure 2.4) is comprised of the hydroxyl open site and adsorbed DEE. The most stable adsorption configuration for DEE is on the stannanol group, with a distance of 1.76 Å between the stannanol hydrogen and the ether oxygen. The preference for adsorption at the stannanol is slight, however, as the differential binding energy of DEE adsorbed instead to the framework silanol is only 0.05 eV higher. The intrinsic activation free energy for DEE formation from a coadsorbed ethanol dimer is 1.59 eV, and the reaction free energy is endergonic by 0.38 eV.

An alternative DEE formation mechanism is an  $S_Ni$ -type reaction where the nucleophilic attack is constrained to be retentive, and necessitates a frontside attack [156]. This type of transition state has been observed for a set of glycosyltransferase enzymes [157] and involves a hydrogen bonding interaction between the leaving group and the nucleophile. As the classical  $S_N2$  angle of attack, described above, may be restricted by the geometry of the confining pore, the frontside attack mechanism could be a plausible transition state configuration. In the  $S_Ni$  mechanism, the protic hydrogen of the nucleophilic vdW-ethanol is transferred to the stannanol leaving group, directly forming an adsorbed water molecule. The distance from the methyl group of the vdW-ethanol to the nearest pore wall oxygen atom is 5.38 Å, corresponding to a more tightly bound transition state complex than for the  $S_N2$  case. The intrinsic barrier for the  $S_Ni$  mechanism is higher by 0.66 eV (Supporting Information, 2.6.7). Thus, the enthalpic penalty of straining the  $S_N2$  transition state complex is less severe than that incurred by adopting the frontside nucleophilic attack angle.

### 2.3.3.2 Ethoxy open site mediated mechanism

Beginning with an ethoxy open site formed by ethanol dissociation, other DEE formation mechanisms are possible. Adsorption of molecular ethanol on the ethoxy open site ( $EE_X^*$ , Figure 2.5) is exergonic at -0.33 eV and is mediated by hydrogen bonding with the framework silanol. The interaction distance between the proton of the framework silanol and the hydroxyl oxygen of the adsorbed ethanol is 1.84

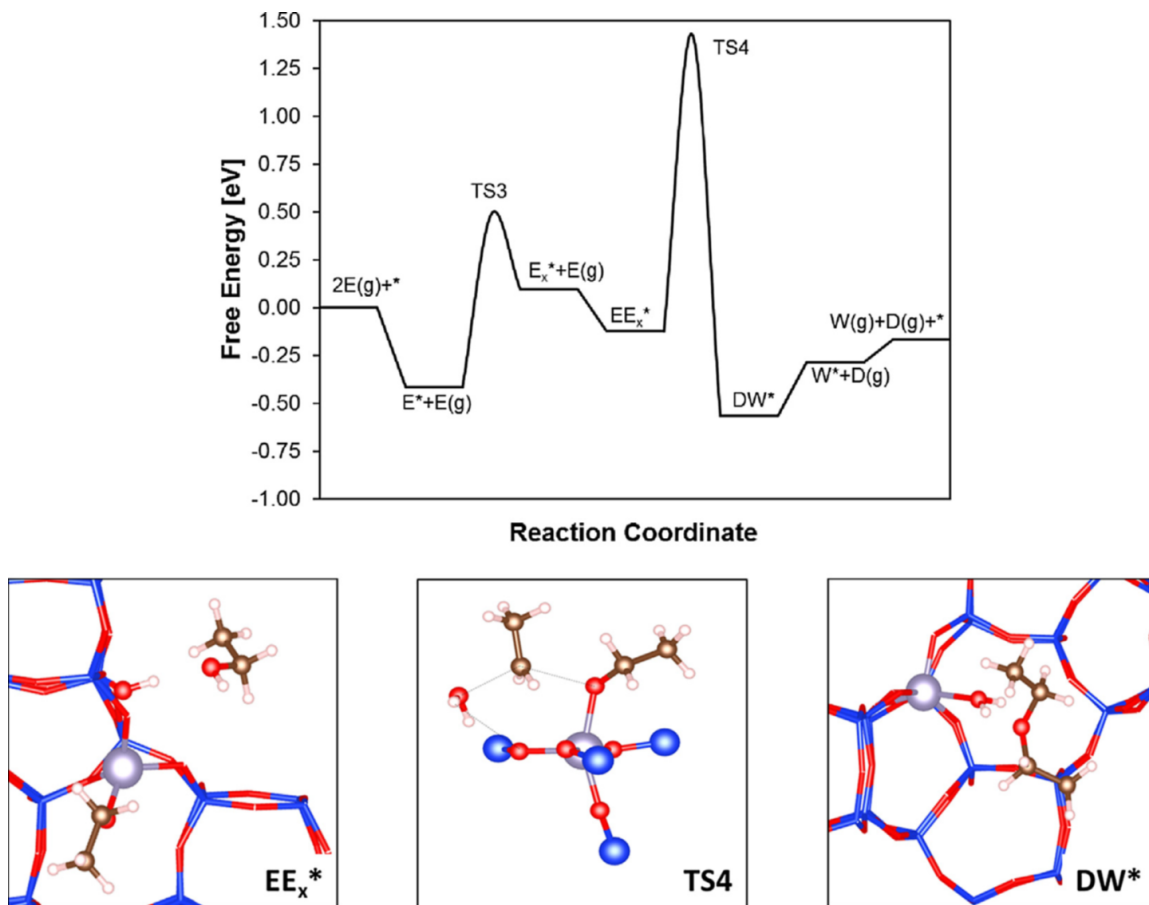


**Figure 2.5:** Ethoxy open site reaction mechanism and selected adsorbate geometries. Free energies are evaluated at 404 K and 1 bar. For clarity, the pore wall is truncated in the TS4 diagram, and diethyl ether is referred to as D in the reaction diagrams. Nomenclature for the other reaction intermediates and Sn sites is found in Figure 2.3.

Å. DEE forms via nucleophilic substitution, where the ethoxy ligand behaves as the nucleophile. In a concerted step, the adsorbed ethanol is protonated by the framework silanol, forming water as a stable leaving group, while the ethyl electrophile is attacked by the nucleophilic ethoxy ligand (TS4, Figure 2.5). The bond angle between the leaving group (water), electrophile (ethyl), and nucleophile (ethoxy) is  $150.6^\circ$ . The distance to the nearest oxygen atom in the opposite pore wall is greater than 5 Å, indicating minimal steric interaction based on atomic distances. The distance between the nucleophile and electrophile is 2.40 Å, while the distance from the electrophile to

the water leaving group is 2.02 Å. The free energy of activation is 1.66 eV, and the reaction free energy is exergonic at -0.33 eV. The ethoxy open site is closed in the process of protonating the leaving group to form the closed Sn site and coadsorbed DEE and water. The most stable final state configuration involves adsorption of water on the Sn and a hydrogen bonding interaction between water and DEE (DW\*, Figure 2.5). The interaction distance between the hydrogen from water and the etheric oxygen is 1.73 Å.

The possibility of forming a retentive S<sub>Ni</sub>-type transition state from the ethoxy-ethanol dimer was considered as an alternative to the backside attack S<sub>N2</sub> mechanism presented above. Here, the ethoxy ligand again behaves as the nucleophile. The nucleophilic ethoxy ligand attacks the ethanol in a concerted mechanism where the hydroxyl leaving group forms a bond to Sn, yielding a hydroxy ligand (Supporting Information, 2.6.7). An ethyl fragment is once again the electrophile, forming DEE and breaking the ethoxy-Sn bond. The silanol is not necessary to protonate the leaving group, therefore this mechanism behaves as a ligand transfer process in which the ethoxy ligand is replaced with a stannanol to preserve the structure of the silanol and form DEE. The free energy of activation for the ligand transfer mechanism is higher than that of the S<sub>N2</sub>-type mechanism by 0.2 eV.

The S<sub>N2</sub> mechanism on the ethoxy open site is analogous to a Brønsted acid-like dehydration mechanism mediated by protonation of the ethanol. The Lewis acid-mediated mechanism differs from the Brønsted acid-mediated one, however, because the electronic structure of the nucleophile is modulated by the strength of the interaction with Sn. There is a cooperative effect of the Sn and the framework silanol in stabilizing the nucleophile and the leaving group, which lowers the activation barrier compared to a case involving direct ligand transfer in which Sn must stabilize the nucleophile and electrophile simultaneously. On an oxide surface such as  $\gamma$ -Al<sub>2</sub>O<sub>3</sub>, adjacent Lewis acid sites stabilize the leaving group and nucleophile separately, as described by Christiansen et al. [89]. Here, the framework silanol that is formed when

Sn is opened by ethanol acts as a second site that stabilizes the leaving group, while Sn stabilizes the nucleophile.

### 2.3.3.3 Hydroxy open site mediated mechanism

The hydroxy open site can adsorb an ethanol-ethanol dimer, introducing an additional distinct mechanism for bimolecular DEE formation. Coadsorption of two ethanol molecules onto a hydroxy open site can be described by multiple adsorption geometries. One ethanol can form a hydrogen bond with the stannanol while the second forms a hydrogen bond with the framework silanol. Either of these ethanol molecules may alternatively form a hydrogen bond with the other ethanol rather than the stannanol or silanol, generating two additional possibilities. The most stable configuration is the former, with one ethanol on each OH site ( $EEW_x^*$ , Figure 2.6). As discussed above, the binding energy for the first ethanol that makes up the dimer is -0.07 eV, and the differential binding energy for the second ethanol is -0.24 eV.

At the transition state (TS6, Figure 2.6), the ethanol adsorbed on the framework silanol is protonated in a concerted step while the ethanol adsorbed on the stannanol acts as the nucleophile. The protic hydrogen of the nucleophilic ethanol can transfer to the stannanol, forming water and closing the active site. The attack angle is  $155^\circ$  and deviates from the expected  $180^\circ$ , suggesting that additional electrostatic interactions with the surrounding pore stabilize this alternate configuration. The distance between the water leaving group and the ethyl electrophile is  $2.07 \text{ \AA}$ , and the distance from the electrophile to nucleophilic ethanol is  $2.22 \text{ \AA}$ . The most stable final state involves a trimeric adsorbed complex of two water molecules and DEE ( $DWW^*$ , Figure 2.6). A hydrogen bonding network is formed involving a strongly bound water molecule, a weakly coadsorbed water molecule, and the ether oxygen in DEE. The distance from the strongly bound water to the ether oxygen is  $1.76 \text{ \AA}$ , and that from the strongly bound water to weakly bound water is  $1.79 \text{ \AA}$ . The intrinsic activation free energy for this process is 1.67 eV with a reaction free energy of -0.30 eV. We note that this mechanism of DEE formation bears some resemblance

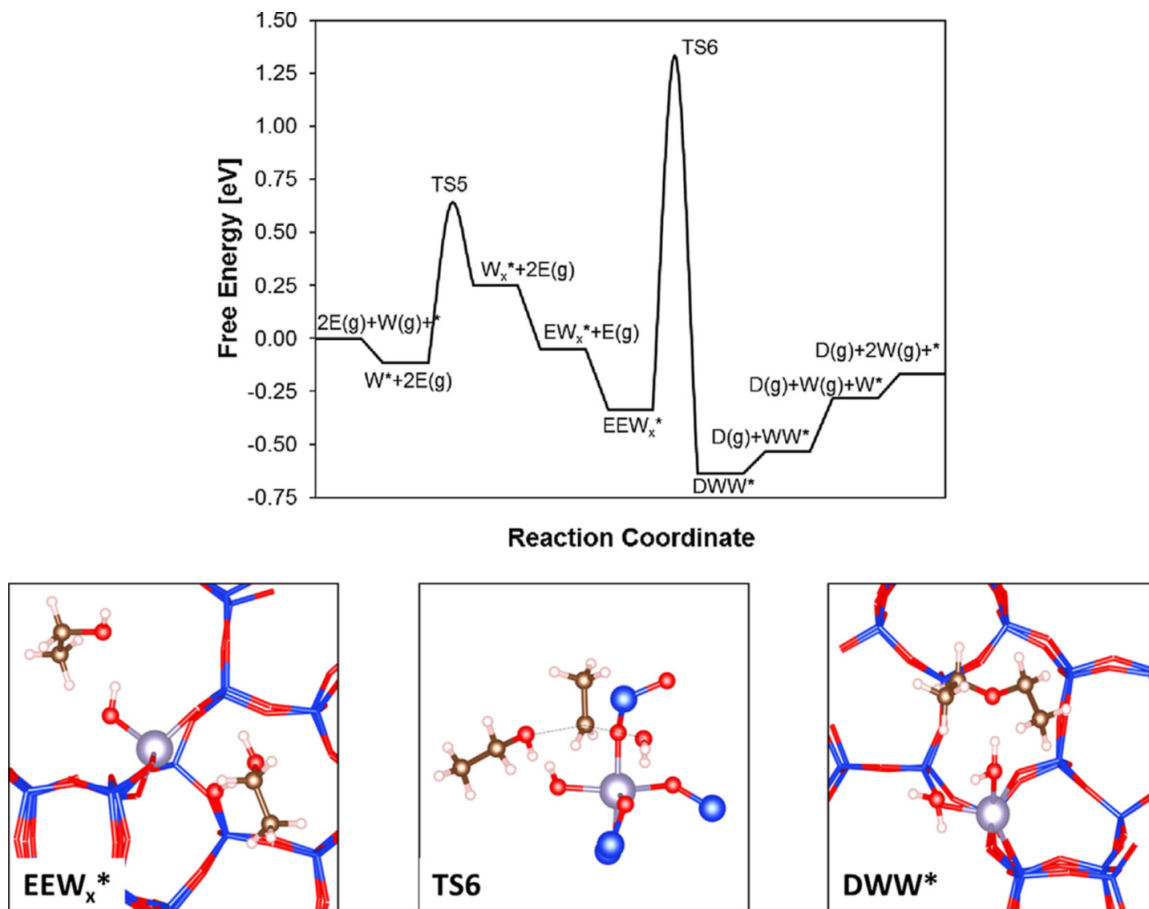


**Figure 2.6:** Hydroxy open site reaction mechanism and selected adsorbate geometries. Free energies are evaluated at 404 K and 1 bar. For clarity, the pore wall is truncated in the TS4 diagram, and diethyl ether is referred to as D in the reaction diagrams. Nomenclature for the other reaction intermediates and Sn sites is found in Figure 2.3.

to a mechanism proposed by Knaeble and Iglesia [158], in which a Brønsted acidic hydroxyl group on a polyoxometallate (POM) cluster protonates ethanol, while the nucleophilic ethanol transfers its proton to a different oxygen site.

Intriguingly, the tin center does not directly influence the electronic structure of the hydroxy open site pathway since protonation of the nucleophile occurs through the framework silanol. The Brønsted acidic character of this silanol has been discussed by Josephson et al [154]. The silanol, in turn, has no electronic overlap with Sn,

as shown from the COHP analysis for hydroxy open sites (Supporting Information, 2.6.2). Hence, the Lewis acidic character of Sn appears to influence dehydration transition state energies more weakly than the deprotonation energy (DPE) of the framework silanol, as the metal atom predominantly affects the energy needed to close the open site. The DPE, in turn, is a probe-independent descriptor of the intrinsic strength of Brønsted acids that correlates with the intrinsic activation barriers of reactions mediated by ion-pair transition states [33, 74, 80]. Additionally, since there is no electronic interaction between the framework silanol and the Sn center, the DPE of framework silanols formed through site opening will likely be similar for different Lewis acidic heteroatoms.

Figure 2.7 compares the free energy profiles for the various site-specific pathways (closed, hydroxy open, ethoxy open), with all pathways placed on a common energy reference of stoichiometric reactant gases and a closed Sn site. Adsorption, desorption,

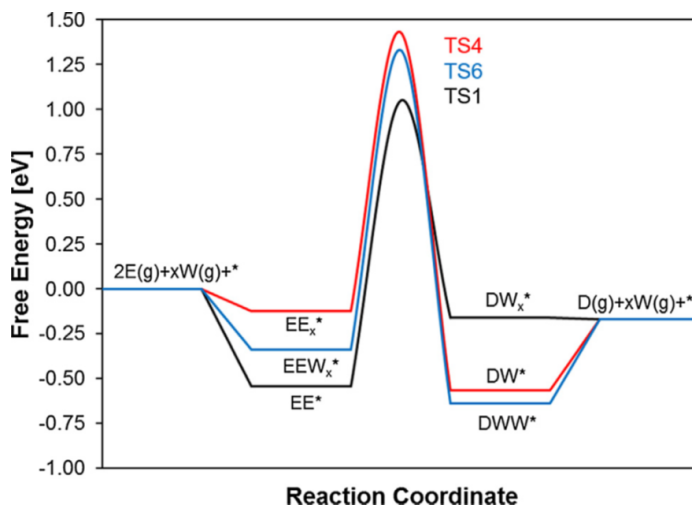


**Figure 2.7:** Lumped DEE formation mechanisms with different Sn site speciations. Free energies are evaluated at 404 K and 1 bar. Black – closed site, blue – hydroxy open site, red – ethoxy open site.

and site opening elementary steps have been lumped for clarity, highlighting the distribution of intrinsic and apparent activation barriers relative to the gas phase (see also Table 2.2).

**Table 2.2:** Kinetic barriers for DEE formation on different Sn sites.

Sn site	Intrinsic barrier (eV)	Activation barrier relative to gas phase (eV)
Closed	1.59	1.05
Hydroxy open	1.67	1.33
Ethoxy open	1.66	1.43

The apparent activation barrier relative to gas phase for the closed site mechanism is 0.28 eV lower than the barrier for the hydroxy open site mechanism, and 0.38 eV lower than that of the ethoxy open site mechanism. This result may relate to the observation that the formation of hydroxy and ethoxy open sites from closed sites is endergonic, and the free energies of ethanol-ethanol dimer species adsorbed on these sites are hence penalized relative to the ethanol-ethanol dimer adsorption on closed Sn sites. The relative stability of the closed sites may, in turn, be due to the low chemical potentials of gas phase ethanol and water and to the local structure of the beta framework. These results suggest that DEE formation will be primarily mediated by closed Sn sites, but this conclusion depends on the relative populations of the various sites during reaction conditions. These populations may, in turn, be influenced by factors that are not described by the free energy diagrams, such as the coproduction of water and associated hydroxyl open site formation. Therefore, catalytically-relevant site populations can only be quantified through the development of a detailed microkinetic model.

#### 2.3.4 Ethene formation mechanisms

While the primary focus of this study is on ethanol dehydration at conditions where DEE is the only product formed, consideration of the monomolecular dehydration products (ethene) permits prediction of selectivity at other reaction conditions. The experimental DEE formation rate per mole of Sn at 404 K is at least two orders of magnitude greater than that of ethene (ethene was formed below the experimental

detection limit). Thus, an additional test of the accuracy of a microkinetic model is to verify that DEE formation is preferred when ethene formation mechanisms are also included. Inclusion of these additional mechanisms also permits extension of the microkinetic model to higher temperatures where ethene formation may be favored.

On a Sn closed site, the formation of ethene requires C<sub>α</sub>-O and C<sub>β</sub>-H scission, which may be either concerted or sequential. The concerted pathway proceeds with a lower overall barrier, as ethanol can form a 6-member ring transition state. In this transition state, an OH ligand is transferred to the Sn, while a hydrogen from the β carbon is transferred simultaneously to a framework oxygen forming a hydroxy open site. The methyl hydrogen must be transferred to an oxygen adjacent to the stannanol, which is metastable compared to silanol formation *anti* to the hydroxy ligand. As discussed above, a proton shuttling mechanism mediated by water or ethanol allows the hydroxy open site to adopt its most favorable configuration. At the transition state, the C<sub>α</sub>-O bond of ethanol elongates to 2.21 Å, and the C<sub>β</sub>-H bond elongates by 0.33 Å as the hydrogen lies equidistant between the C<sub>β</sub> and framework oxygen. The free energy of activation for this process is 1.96 eV with an endergonic free energy of reaction of 0.67 eV.

Ethene can also form through a bimolecular mechanism starting from ethanol adsorbed onto an ethoxy open site. The ethoxy ligand acts as a base to break the C<sub>β</sub>-H bond by a classical E2 mechanism. Simultaneously, the framework silanol protonates the adsorbed ethanol to form water. The C<sub>α</sub>-O bond of the adsorbed ethanol elongates to 2.23 Å, while the C<sub>β</sub>-H bond increases to 1.26 Å, with a distance of 1.43 Å to the ethoxy ligand. The intrinsic activation free energy for this mechanism is 1.83 eV, with an exergonic free energy of reaction of -0.14 eV. The most favorable final state configuration is an ethanol-ethene-water trimer with ethanol bound to the Sn site at a distance of 2.27 Å. Water forms a hydrogen bond 1.80 Å away from ethanol, while ethene lies 3.46 Å from the ethanol C<sub>α</sub>.

Ethene formation on the hydroxy open site is closely related to that on the ethoxy open site. Instead of ethoxy behaving as a base to remove the C<sub>β</sub>-H, however, the

stannanol acts as a base. The C-O bond elongation is 2.25 Å, differing by 0.02 Å compared to the ethoxy open site pathway. The C<sub>β</sub>-H bond elongates to 1.27 Å, and the transferred hydrogen is 1.41 Å from the stannanol. The C<sub>β</sub>-H distance is within 0.01 Å, and the distance to the base is within 0.03 Å of the ethoxy open site pathway. The intrinsic activation free energy for this process is 1.51 eV, with an exergonic free energy of reaction of -0.13 eV. The lumped ethene formation free energy diagram (Figure 2.8) shows higher intrinsic activation energies than for DEE formation (Figure 2.7), suggesting selectivity toward DEE. As mentioned above, however, this conclusion

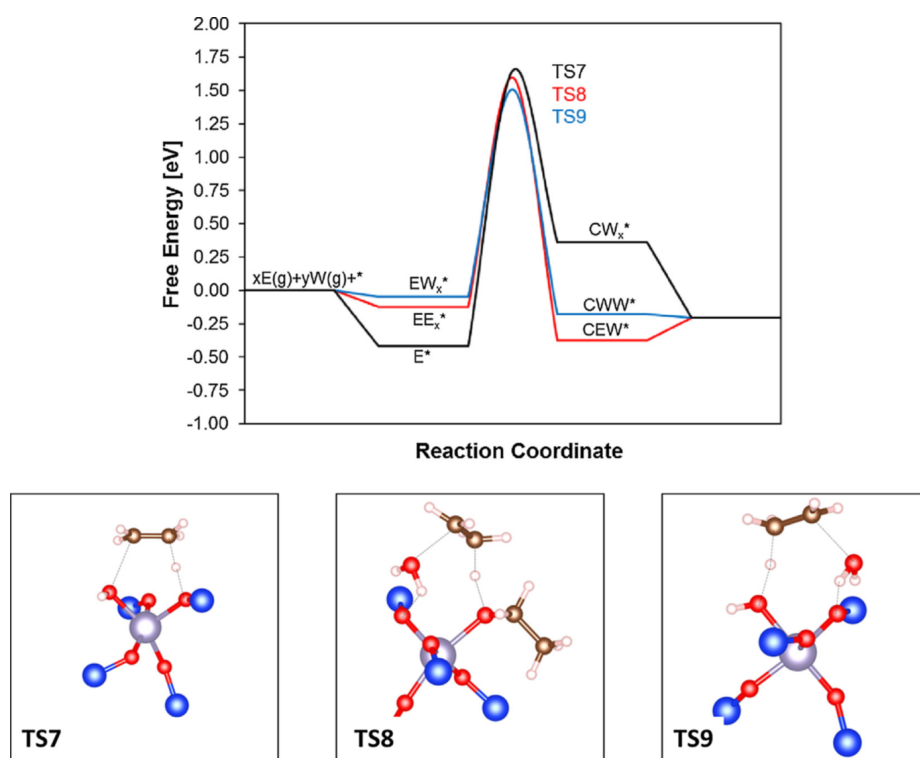


**Figure 2.8:** Lumped ethene formation mechanisms with transition state geometries. Free energies are evaluated at 404 K and 1 bar. Ethene formation on closed sites (TS7), ethene formation on ethoxy open sites (TS8), and ethene formation on hydroxy open sites (TS9). The pore wall is truncated for clarity.

is sensitive to the population of the various types of Sn sites, which will be further elucidated via microkinetic modeling.

### 2.3.5 Ethanol Dehydration Kinetics

Free energy diagrams of reaction pathways and transition state structural characterization are useful for defining the space of plausible catalytic elementary steps. However, direct comparison with experimental kinetic measurements, which is necessary to verify mechanistic predictions, is not possible without microkinetic modeling. An accurate microkinetic model can, in turn, provide information that may be inaccessible to experiment, such as the identities of the most abundant surface intermediates (MASI) and kinetically relevant steps, and these fundamental kinetic insights may ultimately be used to develop trend-based descriptions of how reaction conditions and heteroatom identity influence reaction rates and selectivities.

#### 2.3.5.1 Microkinetic model development

To develop and optimize the microkinetic model, we introduce a self-consistent method of model calibration in which sensitive parameters are identified and subsequently treated at higher levels of theoretical accuracy [148,159,160], including hybrid functional calculations for potential energies and molecular dynamics simulations for entropies. To identify sensitive parameters, the generalized Degree of Rate Control (GDRC) [119] is calculated for every reactive intermediate and transition state, normalized by the total DEE formation rate. The first iteration of the microkinetic model is constructed using BEEF-vdW rate constants with harmonic oscillator-derived entropies for adsorbates and standard partition function methods for entropies of gas phase species. A more detailed discussion of the microkinetic model construction, as well as structures of all intermediates, is included in the Supporting Information sections 2.6.8 and 2.6.9.

Once rate-controlling intermediates are identified, hybrid functional calculations with HSE06 and improved entropy analyses are performed. A mode decomposition method for calculating adsorbate entropies was developed, where low frequency modes are visualized and replaced with translational and rotational degrees of freedom, as

appropriate (Supporting Information, 2.6.10). In the zeolite framework, free translational diffusion of adsorbates is not possible due to site isolation. Despite this, AIMD calculations of molecular adsorbates show localized translational motion around the adsorption sites, which indicates highly anharmonic potential energy wells. A 1-D square potential is used to approximate these wells, where the width of the square well is estimated from AIMD calculations. Rotational modes, both with and without hindering potentials, are treated with classical partition function methods. Finally, higher frequency modes that cannot be identified as localized translations or rotations are treated using harmonic vibrational partition functions.

Although unfeasible for every reaction intermediate, the entropies of kinetically and thermodynamically sensitive intermediates are calculated using integration of the Vibrational Density of States (VDOS) obtained from atomic trajectories [127]. Atomic trajectories are determined through AIMD with a NVT thermostat at 404 K, and a 0.5 fs timestep is used for 10 ps of equilibration followed by a 15 ps production run. The atomic velocities are then analyzed according to the method by Lin et al. [161, 162] by decomposing the VDOS into ideal gas, rotational, and vibrational degrees of freedom.

A comparison of entropy calculations at 404 K for ethanol monomers and dimers is provided in Table 2.3, including the standard quantum harmonic oscillator method, the Campbell-Sellers relationship [163], which is a semi-empirical correlation for weakly-bound surface intermediates whose entropies are dominated by two dimensional quasi-translational modes, the mode-decomposition method, and the AIMD/VDOS approach. The standard quantum harmonic oscillator underestimates entropies of adsorbed intermediates relative to the Campbell-Sellers approximation, which accounts for translational degrees of freedom. The inclusion of these translational degrees of freedom, in turn, was determined to be important, as translation was observed in AIMD simulations of adsorbed monomers and in visualization of the low frequency harmonic modes. However, the use of the Campbell-Sellers entropy for coadsorbed dimers does not account for the mutual exclusion of identical ethanol molecules, mo-

**Table 2.3:** Selected entropy comparisons for surface-bound intermediates.

Adsorbate	Harmonic entropy <sup>a</sup> (J mol <sup>-1</sup> K <sup>-1</sup> )	Campbell-Sellers entropy (J mol <sup>-1</sup> K <sup>-1</sup> )	Mode-decomposition entropy (J mol <sup>-1</sup> K <sup>-1</sup> )	AIMD entropy (J mol <sup>-1</sup> K <sup>-1</sup> )
Ethanol (E <sup>*</sup> )	141	177	169	195
Water (W <sup>*</sup> )	63	111	109	-
Ethanol-ethanol (EE <sup>*</sup> )	319	354 <sup>b</sup>	348	372
Ethanol-water (EW <sup>*</sup> )	205	288 <sup>c</sup>	282	390 <sup>d</sup>
Ethoxy open (E <sub>x</sub> <sup>*</sup> )	151	-	182	-
Hydroxy open (W <sub>x</sub> <sup>*</sup> )	59	-	105	-
DEE-water (DW <sup>*</sup> )	294	-	362	-

<sup>a</sup>Imaginary frequencies replaced with a 20 cm<sup>-1</sup> mode, similar to [164]

<sup>b</sup>Referenced to uncorrelated gas phase ethanol

<sup>c</sup>Referenced to uncorrelated gas phase ethanol and water

<sup>d</sup>Sum of ethanol and water contributions

tivating the exploration of mode decomposition approaches. Based on the localized translational character observed in AIMD simulations, the explicit mode decomposition method used particle-in-a-box translation partition functions with diffusion lengths derived from short 5ps AIMD simulations. The mode-decomposed entropies are within 10 J mol<sup>-1</sup>K<sup>-1</sup> of the Campbell-Sellers entropies, as adsorbates were observed to have two localized degrees of translational freedom. While the Campbell-Sellers approximation is valid for closed-shell molecular adsorbates on different Sn speciations, the entropy change of dissociation to form defect sites involves open-shell species. To improve estimates of the ethoxy- and hydroxy-open sites, therefore, the mode decomposition method is applied with mode assignments being made based on visualization of harmonic modes. The AIMD/VDOS approach is particularly useful for ethanol monomers and dimers, as it provides a more accurate entropy treatment than the mode decomposition method by including the coupling between anharmonic rotations and vibrations, albeit at a much higher computational cost. With this ap-

proach, for example, the entropy of the ethanol-ethanol dimer is found to be  $24 \text{ J mol}^{-1}\text{K}^{-1}$  less than the weakly interacting mode-decomposition method.

We note that both the mode decomposition and AIMD/VDOS methods are expected to perform better than the purely harmonic mode approximation, which excessively localizes the molecular adsorbates. In the case of the ethanol-water dimer, AIMD predicts a strongly bound ethanol with entropy similar to the ethanol monomer, and a weakly bound water with entropy similar to an ideal gas state. This delocalization of adsorbate water is not represented in the harmonic mode approximation, which thus greatly underestimates the entropy of the ethanol-water dimer. However, we additionally note that while the mode decomposition entropy is expected to provide a better approximation than the harmonic entropy, the AIMD method is necessary to properly predict experimentally observed kinetic behavior, as is discussed further below. Since AIMD calculations are expensive due to their duration, we suggest first using a mode decomposition method, with short-duration AIMD of a few picoseconds to observe translation lengths, and finally perform a full 15ps or longer AIMD run to obtain anharmonic entropies for the most sensitive intermediates, as determined by the DRC.

In addition to improving the entropic contributions to the free energy, the electronic structure of intermediates can be improved by hybrid DFT functionals, such as HSE06. These constitute a natural progression toward higher computational accuracy in potential energy calculations because of the exact-exchange contributions that properly localize electron density. The excessive delocalization of electron density by typical GGA-level functionals produces systematic errors in non-conducting oxides [165], and some of this error can be corrected through use of hybrid functionals. HSE06 does not, however, treat long range dispersion interactions, as shown in the Supporting Information 2.6.11, and thus a Grimme D3-type semi-empirical dispersion correction is added [139, 140]. To quantify the effects of these factors on adsorption energetics, focusing on dimeric species due to their rate-sensitivity, a hypothetical reference state is established corresponding to two adsorbates at separate Sn sites

that are non-interacting. The energy of this configuration can then be compared to the corresponding energy of a dimeric adsorbate and an empty Sn site as shown in Equation 2.3. The difference in potential energy between these two states will be referred to as the dimerization energy, which only includes the energy of reorganization of the adsorbates and additional dispersion interactions gained through dimerization.



With this metric, it is found that the ethanol-ethanol and ethanol-water dimers have lower energies when treated with BEEF-vdW as opposed to HSE06-D3 (optimized geometries of these intermediates, however, show no significant differences between BEEF-vdW and HSE06-D3). To compensate for this excess dimer stabilization in BEEF-vdW, differential binding energies are adjusted by +0.12 and +0.15 for the ethanol-ethanol dimer and water-ethanol dimer in subsequent iterations of the microkinetic model, as discussed further below. A full figure of binding energies comparing BEEF-vdW, PBE, PBE-D3, HSE06, and HSE06-D3 is available in the Supporting Information 2.6.11.

### 2.3.5.2 Microkinetic model refinement and mechanistic analysis

The generalized degree of rate control for intermediates and transition states based on mode decomposition entropies and BEEF-VdW energies implies that the reaction rate is sensitive to adsorption energies of ethanol monomers, ethanol-water dimers, and ethanol-ethanol dimers, which have the largest GDRC values of  $-1.66 \times 10^{-2}$ ,  $-1.14 \times 10^{-5}$ ,  $-9.83 \times 10^{-1}$ . These energies then become the focus for two additional tiers of model accuracy, as described above. The results of the three tiers are summarized in Figure 2.9, first using a purely quantum harmonic oscillator entropy description and BEEF-VdW energies, second using the mode decomposition method with BEEF-VdW energies, and third with AIMD entropies and HSE06-D3 corrected dimerization energies. Using a purely harmonic oscillator entropy for all adsorbed intermediates,

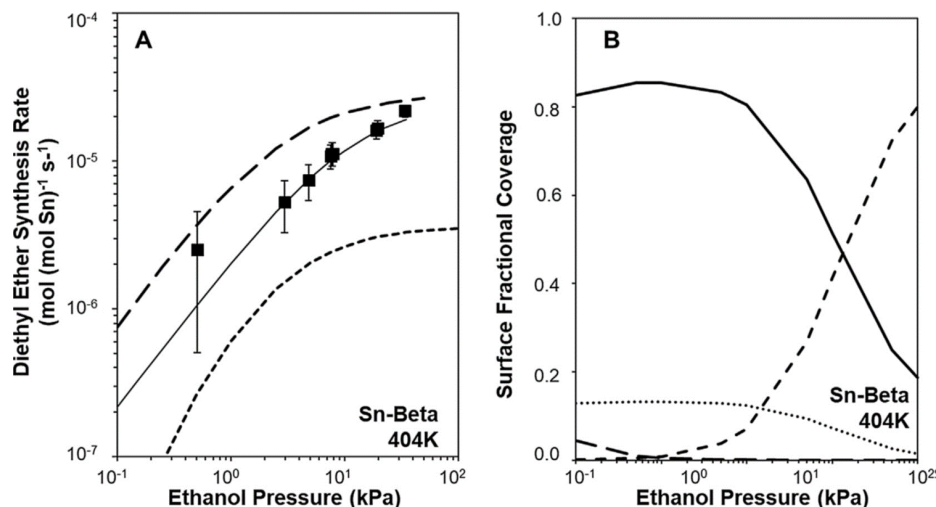


**Figure 2.9:** A) Ethanol reaction orders at 404 K, 0.1 kPa water partial pressure. Rate predictions at increasing levels of theoretical treatment are provided which include purely harmonic oscillator entropies (short dashed lines), mode decomposition method using AIMD-derived diffusion distances (long dashed lines), and the full entropy treatment with anharmonic integrated entropies (solid line). B) Surface coverages at 404K and 0.1 kPa water partial pressure at the full quasi-harmonic level. Ethanol monomer E\* (solid line), ethanol dimer EE\* (short dashed line), empty site \* (long dashed line), ethanol-water dimer EW\* (dotted line).

the ethanol reaction order approaches zero at lower ethanol partial pressures than is observed experimentally, suggesting that the harmonic oscillator approach underestimates the entropy of adsorbed ethanol monomers. The ethanol reaction order of zero is likely due to a convoluted effect of differential binding energies between the ethanol monomer and dimer species as evidenced by the HSE06-D3 dimerization energies, as well as the presence of coupled anharmonic entropic modes in the dimer. Without the HSE06-D3 dimerization energy correction, ethanol orders are zero at ethanol partial pressures above approximately 5 kPa. When applying the mode decomposition (MDE) approximation for entropies and dimerization correction, the ethanol orders remain nonzero over the entire experimental pressure range studied (0.5 kPa – 35 kPa ethanol).

Better agreement with the experimental orders is achieved, however, when replacing the ethanol monomer, ethanol dimer, and ethanol-water dimer entropies with

the full AIMD/VDOS integrated entropies. Water reaction orders agree well with experiment at this level of treatment, and the DEE rate and selectivity are nearly quantitatively consistent with the measurements. The ethanol reaction order is higher (still sub-unity), however, than what is measured in experiment. This modest discrepancy is likely because the ethanol-ethanol dimer binds too weakly when incorporating the HSE06-D3 energies and AIMD integrated entropy. A small reduction of the binding energy (0.06 eV) is sufficient to remove this discrepancy, and this is the only fit parameter in the entire model. The model is also robust against numerical uncertainties; propagation of a 0.1 eV error centered on the calculated free energies of adsorbates and transition states had a negligible change on the generalized degree of rate control (Supporting Information, 2.6.12). These results highlight the usefulness of tiered treatments of microkinetic parameters using both theoretical DRC analysis and comparisons to experimental reaction orders and rates. The iterated DRC analysis captures trends and provides semiquantitative agreement with experimental orders and rates; achieving quantitative agreement with all measurable quantities requires a small residual parameter adjustment.

The site interconversion steps are found to have DRC values more than three orders of magnitude below those of the bimolecular rearrangement steps, demonstrating that site equilibration is achieved under reaction conditions. Effectively, open and closed sites readily interconvert to achieve their equilibrium distribution, which in turn depends only on the chemical potentials of ethanol and water. Significantly, this result demonstrates that the numbers of open and closed Sn sites determined *ex-situ* or after specific gaseous pre-treatment steps cannot be directly correlated with reaction rates under steady-state conditions. Additional evidence for this conclusion is provided by our kinetic measurements. Experimental turnover rates are similar when normalized by the total number of Sn sites (within a factor of  $\sim 2$  at 404 K) among six samples with varying Sn contents ( $2\text{--}5 \times 10^{-4}$  mol Sn g<sup>-1</sup>, or Si/Sn=30–95), but normalization of rates by the number of open Sn sites quantified *ex situ* increases the scatter in turnover rate measurements among these six samples (Supporting In-

formation, 2.6.6). In fact, this phenomenon can be directly simulated by seeding the reactor model with variable initial populations of open sites, similar to a catalyst sample containing a non-equilibrated distribution of open sites under *ex-situ* conditions. Similar equilibrium coverages of open sites are obtained at steady-state in all cases.

The reactive intermediates with surface coverages identified by the generalized DRC to be rate-controlling include ethanol monomers, ethanol-ethanol dimers, ethanol-ethoxy dimers, and water-ethanol dimers. Figure 2.9 displays DEE rates and surface coverages over an ethanol pressure range of three orders of magnitude (0.1 kPa H<sub>2</sub>O, 404 K). As discussed above, the optimized microkinetic treatment captures experimental trends quite well. At conditions where experimental data are available, the ethanol order is sub-unity, and the surface contains a mixture of ethanol monomer, ethanol-ethanol dimer, and ethanol-water dimer species. As the ethanol pressure increases beyond 100 kPa, the ethanol order approaches zero, and the surface becomes covered in ethanol-ethanol dimers.

At low ethanol partial pressures, below 1 kPa, the coverage of empty Sn sites begins to increase, which might eventually lead to an ethanol order greater than unity at ethanol partial pressures much lower than what we can access experimentally. However, as the adsorption of ethanol is highly exothermic, few vacant Sn sites are present at the relevant pressures. This fact, coupled with the presence of a non-negligible coverage of ethanol-water dimers resulting from competitive adsorption of water, leads to ethanol reaction orders less than unity (see section 3.5.3 for additional discussion).

Under reaction conditions, the abundance of vacant ethoxy and hydroxy open sites is predicted to be below 1%. The contribution to DEE formation from the closed site mechanism is 99% of the total DEE formation rate, with the ethoxy open site accounting for slightly less than 1% of the total rate and the hydroxy open site mechanism having a negligible contribution to the total DEE formation rate. This higher turnover rate from the closed site mechanism is due to both the negligible cov-

erage of open sites under reaction conditions and the lower kinetic barrier, relative to the gas phase species, of the closed site mechanism (Figure 2.7). These results demonstrate that open sites contribute only marginally to ethanol dehydration turnovers on Sn-Beta.

**Table 2.4:** Selected generalized DRC for reactive intermediates and transition states. Level of theory includes HSE06-D3 and AIMD entropy scheme.

Adsorbate	Generalized DRC
Ethanol ( $E^*$ )	-0.55
Ethanol-ethanol ( $EE^*$ )	-0.37
Ethanol-water ( $EW^*$ )	-0.08
Closed site TS ( $TS1$ )	0.99

Water orders and coverages are calculated at fixed ethanol partial pressure and fixed conversion and shown in Figure 2.10. At low water partial pressures, the water order approaches zero, and at higher partial pressures, the water order approaches -1, consistent with measured reaction rates and kinetic inhibition by water. Indeed, the dominant water intermediate at high water pressure is found to be the ethanol-water dimer. This result is fully consistent with DRC analyses that give a modest negative value for ethanol-water dimers (-0.11), indicative of an inhibitory species.

### 2.3.5.3 Simplified mechanism and rate expression

Using the generalized degree of rate control analysis and knowledge that the kinetically relevant pathway is mediated by the closed site, a simplified rate expression for ethanol dehydration can be derived. Over the range of reaction conditions studied, the intermediates with an appreciable degree of rate control and surface coverage are ethanol monomers ( $E^*$ ), ethanol-ethanol dimers ( $EE^*$ ), and ethanol-water dimers ( $EW^*$ ). All adsorption and desorption steps are quasi-equilibrated, and there is site equilibration between closed and open sites regardless of ligand identity. From these

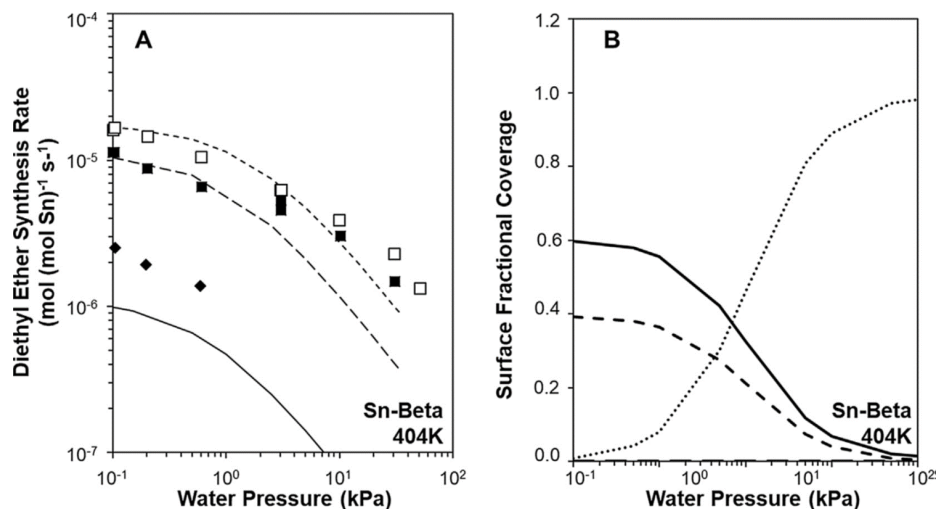


**Figure 2.10:** A) Water reaction orders at 404 K and 20 kPa ethanol partial pressure (short dashed line and open squares for theory and experiment), 8 kPa ethanol partial pressure (long dashed line and filled squares for theory and experiment), 0.5 kPa ethanol partial pressure (solid line and filled diamonds for theory and experiment. B) Surface coverages are at 404K and 8 kPa ethanol partial pressure. Ethanol monomer E\* (solid line), ethanol dimer EE\* (short dashed line), empty site \* (long dashed line), ethanol-water dimer EW\* (dotted line). All calculations at full integrated VDOS level.

observations, the mechanism can be reduced to three intermediates, three quasi-equilibrated elementary steps, and one rate determining step (Figure 2.11).

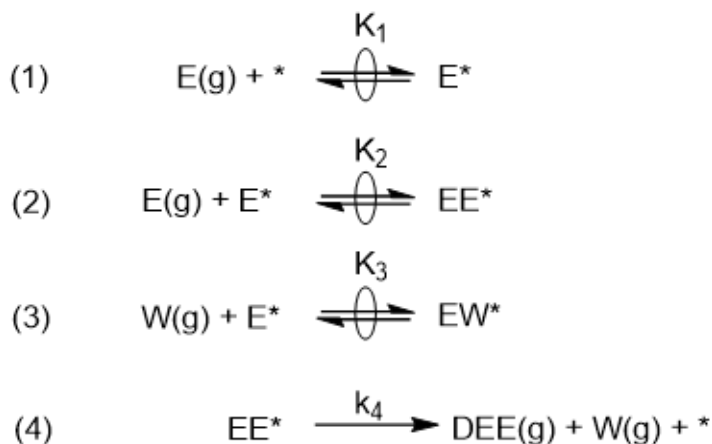


**Figure 2.11:** Simplified reaction mechanism derived from the generalized degree of rate control. Steps 1, 2, and 3 are quasi-equilibrated. Step 4 is the rate-limiting bimolecular dehydration on closed Sn sites.

The mechanism in Figure 2.4 can be used to derive a rate expression of DEE formation per active site in terms of ethanol and water partial pressures, as well as rate and equilibrium constants of the elementary steps:

$$\frac{r_{DEE}}{L} = \frac{k_4 K_1 K_2 P_E^2}{1 + K_1 P_E + K_1 K_2 P_E^2 + K_1 K_3 P_E P_W} \quad (2.4)$$

where  $r_{DEE}$  is the rate per unit surface area, “L” denotes the total number of catalytic Sn sites, and  $\theta$  denotes the fractional coverage of a given reactive intermediate. However, since the coverage of vacant sites is negligible, the unity term in the denominator can be neglected, yielding

$$\frac{r_{DEE}}{L} = \frac{k_4 K_2 P_E}{1 + K_2 P_E + K_3 P_W} \quad (2.5)$$

A detailed derivation is provided in the Supporting Information 2.6.13. Equation 2.5 predicts ethanol reaction orders of between zero and unity, depending upon the relative partial pressures of ethanol and water, in agreement with our experimental results. We note, however, that equation 2.5 will not hold in the limit of extremely low ethanol partial pressures (below what we have accessed experimentally) where the coverage of empty sites becomes relevant and where the ethanol order could approach two. In general, this simplified rate expression provides a model that can be used to extract intrinsic rate and equilibrium constants from measured kinetic data. In addition, future computational searches over zeolites with different topologies or Lewis heteroatom identities could be more rapidly performed by focusing on these key descriptors of the reacting molecules.

## 2.4 Conclusions

A mechanistic study of ethanol dehydration to diethyl ether in Sn-substituted zeolite Beta was performed using a combination of DFT calculations and experimental kinetic measurements, which were linked through microkinetic modeling. The

kinetic modeling results at the level of GGA functionals and harmonic oscillator-derived entropies compare poorly with experimentally measured rates and reaction orders. Although performing hybrid functional calculations and AIMD entropies for all reactive intermediates is infeasible, a hierarchical scheme of microkinetic model development that employs higher accuracy methods for kinetically sensitive intermediates provides an efficient approach to capture the critical physicochemical features of the ethanol dehydration reaction network. Here, the generalized degree of rate control is used both as a criterion for distinguishing rate-determining pathways and as a criterion for employing higher accuracy methods. The BEEF-vdW functional, used for its self-consistent van der Waals correlation, overbinds ethanol-water (EW\*) and ethanol-ethanol (EE\*) dimers in comparison to HSE06-D3, perhaps due to imprecise descriptions of hydrogen bonding interactions that dominate many of the differential binding energies in this study. For kinetically sensitive intermediates, an AIMD-based integration scheme treats the long-range anharmonic framework interactions, and further improves agreement with experimentally measured orders. The model allowed for rationalization of experimentally observed reaction orders and identifies ethanol-water dimers as the dominant inhibitory surface species. Methods such as these can be broadly applied to microkinetic models requiring higher accuracy methods for a subset of intermediates.

Closed and open sites are found to interconvert in quasi-equilibrated processes under reaction conditions, and distinct mechanisms for dehydration on each site are considered. Dehydration transition states at each type of site show similar intrinsic barriers, and the dominant pathway is mediated by closed Sn sites. Indeed, under experimentally studied reaction conditions (404 K, 0.5–35kPa ethanol, 0.1–50 kPa water), the relative coverages of ethoxy and hydroxy open sites were less than 1%, with the dominant surface intermediates being ethanol monomers and ethanol-ethanol dimers. Mechanisms considered on the hydroxy-open site show a concerted transition state involving both the Lewis acidic character of the tin center in addition to the weak Brønsted acidic character of the adjacent framework silanol, via a transition state

geometry reminiscent of that in ethanol dehydration previously studied on Brønsted solid acids.

The dynamic conversion of tin sites of different coordination under reaction conditions introduces additional possibilities for influencing the reactivity of Lewis acid zeolite catalysts. Depending on the applied chemical potential of water or other alkanols, the equilibrium distribution of sites under reaction conditions can be controlled. This opens an avenue to influence selectivity by preferentially enhancing rates of specific pathways that may be catalyzed on different heteroatom coordinations. These findings show how the relative stability of different active site structures under reaction conditions must be understood to gain a mechanistic understanding of reactions catalyzed by Lewis acid zeolites and to provide additional strategies for tuning the catalytic properties of these materials.

## 2.5 Acknowledgements

R.G. and J.B. acknowledge financial support from the Ralph W. and Grace M. Showalter Research Trust and a 3M Non-Tenured Faculty Award. B.B. and J.G. acknowledge support from the National Science Foundation's program for Designing Materials to Revolutionize and Engineer our Future, DMREF (CBET-1437219). Use of the Center for Nanoscale Materials, a U.S. Department of Energy, Office of Science, Office of Basic Energy Sciences User Facility under Contract No. DE-AC02-06CH11357, and of computational resources from the National Energy Research Scientific Computing Center, are gratefully acknowledged. We thank Professor Chris Uyeda for helpful technical discussions.

Reprinted with permission from *Journal of Catalysis*. 365 (2018) 261–276. Copyright (2018) Elsevier.

## 2.6 Supporting Information

### 2.6.1 Binding Energies of key intermediates at different acid sites

**Table 2.5:** Binding energy of water and ethanol monomers at each T site in the Beta framework, in addition to water dissociation energies to form hydroxy open sites. The reference state is the corresponding gas phase species (water or ethanol) and the empty framework.

reference state $^*+X(g)$	T1	T2	T3	T4	T5	T6	T7	T8	T9	maximum deviation
H <sub>2</sub> O Binding Energy (eV)	-0.60	-0.58	-0.56	-0.51	-0.44	-0.47	-0.58	-0.58	-0.55	0.16
H <sub>2</sub> O Dissociation Energy (eV)	-0.19	-0.19	-0.27	-0.21	-0.24	-0.17	-0.22	-0.22	-0.16	0.11
EtOH Binding Energy (eV)	-0.84	-0.81	-0.85	-0.71	-0.70	-0.72	-0.82	-0.88	-0.79	0.18

## 2.6.2 Electronic Structure characterization of open sites

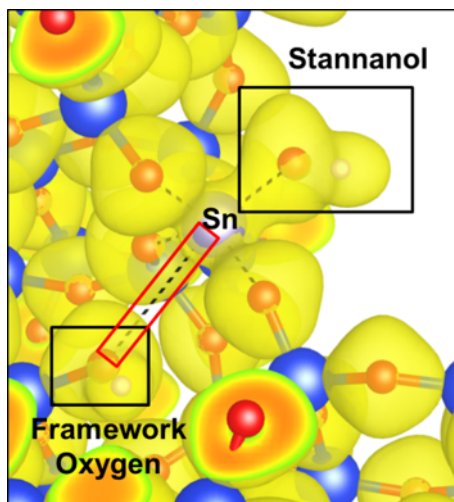


**Figure 2.12:** Electron localization function for hydroxy open site calculated in VASP.

Electron localization function for hydroxy open site calculated in VASP shows no overlap of electron density between the protonated framework oxygen and Sn heteroatom [166]. The remaining three framework oxygen atoms and Stannanol ligand have electronic overlap with the Sn heteroatom. Bader charges show Sn maintains the

**Table 2.6:** Oxygen Bader charges [150] calculated for closed and open sites.

Sn speciation	Unscaled Sn Bader charge ( $e^-$ )
closed site (*)	1.67
hydroxy open site ( $Wx^*$ )	1.69
ethoxy open site ( $Ex^*$ )	1.71

same oxidation state upon dissociation. COHP [149,167] bonding energies calculated from VASP wavefunctions using the Lobster code show only 4 total Sn bonds upon formation of an open site. The framework oxygen which is protonated loses its bond to Sn, while Sn forms a bond to the ligand, maintaining the  $4^+$  oxidation state. Additionally, orbital energies for OEt and OH ligands are similar to those of Sn-O<sub>f</sub> bonds.

**Table 2.7:** COHP [149,167] bonding energies calculated from VASP wavefunctions using the Lobster code.

Oxygen local environment <sup>a</sup>		ICOHP occupation (eF)	Bond distance (Å)
Closed site (*)	Sn-O <sub>f</sub>	-5.72	1.937
	Sn-O <sub>f</sub>	-5.72	1.937
	Sn-O <sub>f</sub>	-5.50	1.950
	Sn-O <sub>f</sub>	-5.49	1.953
Hydroxy open site (W <sub>x</sub> *)	Sn-O <sub>f</sub>	-5.45	1.947
	Sn-O <sub>f</sub>	-5.59	1.945
	Sn-O <sub>f</sub>	-5.40	1.955
	Sn-OH	-5.75	1.969
Ethoxy open site (E <sub>x</sub> *)	Sn-O <sub>f</sub>	-5.54	1.947
	Sn-O <sub>f</sub>	-5.51	1.950
	Sn-O <sub>f</sub>	-5.15	1.974
	Sn-OEt	-5.80	1.966

<sup>a</sup>O<sub>f</sub> denotes a Sn-O bond to the framework.

### 2.6.3 Water shuttling mechanism

Water shuttling allows for a *syn* open site with adjacent ligand and silanol to adopt a more thermodynamically stable *anti* open site. Barriers are similar for ethoxy (TS2) and hydroxy (TS4) open sites, 0.33 eV and 0.37 eV, respectively. Shown in Figure 2.13 are potential and free energy diagrams (404 K, 1 bar) for the full water-assisted opening process, as well as images of the transition state for both ethoxy and hydroxy open sites.

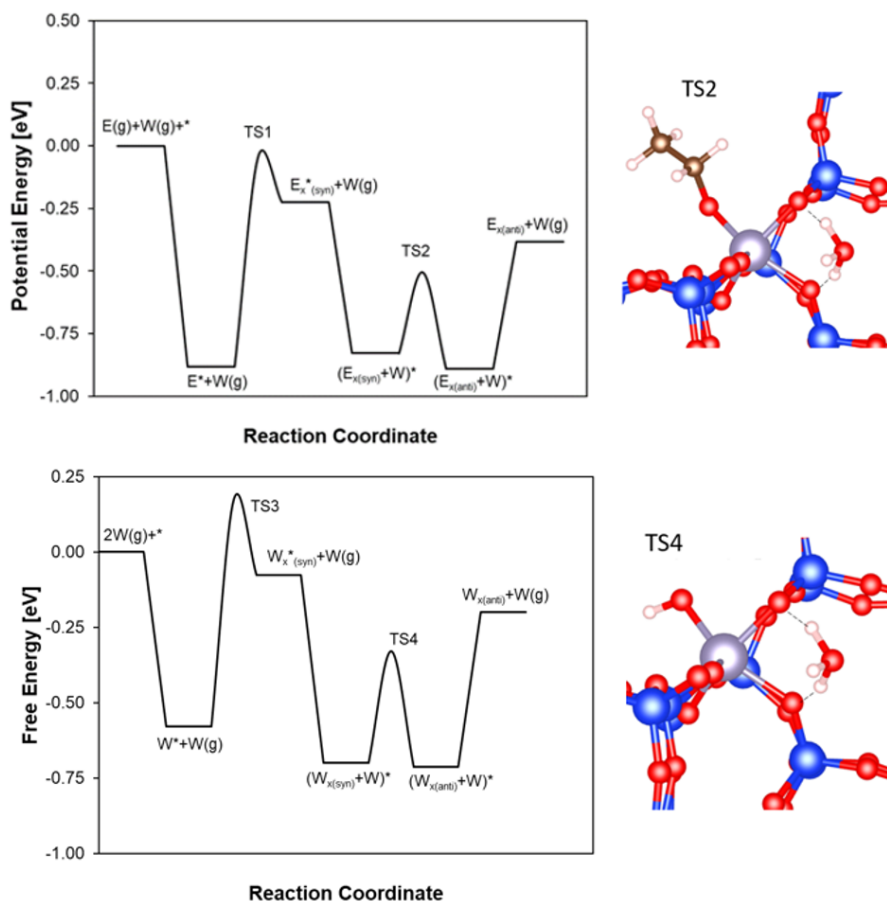


**Figure 2.13:** Potential and free energy diagrams (404 K, 1 bar) for the full water-assisted opening process, as well as images of the transition state for both ethoxy and hydroxy open sites.

#### 2.6.4 Paired Sn DEE formation

DEE formation on paired Sn sites identified by Bare et al. [108]. The 0K intrinsic potential energy barrier (referenced to  $EE_{x^*}$ , where here  $E_{x^*}$  denotes a paired Sn site) is higher than single Sn-site Beta  $SN_2$  mechanisms. The left-most Sn site adsorbs molecular ethanol while the right-most Sn site is functionalized with an ethoxy open site with framework silanol circled for clarity. This configuration is thematically similar to the lowest barrier transition state found by Christiansen [89] for ethanol dehydration on  $\gamma\text{-Al}_2\text{O}_3$ .

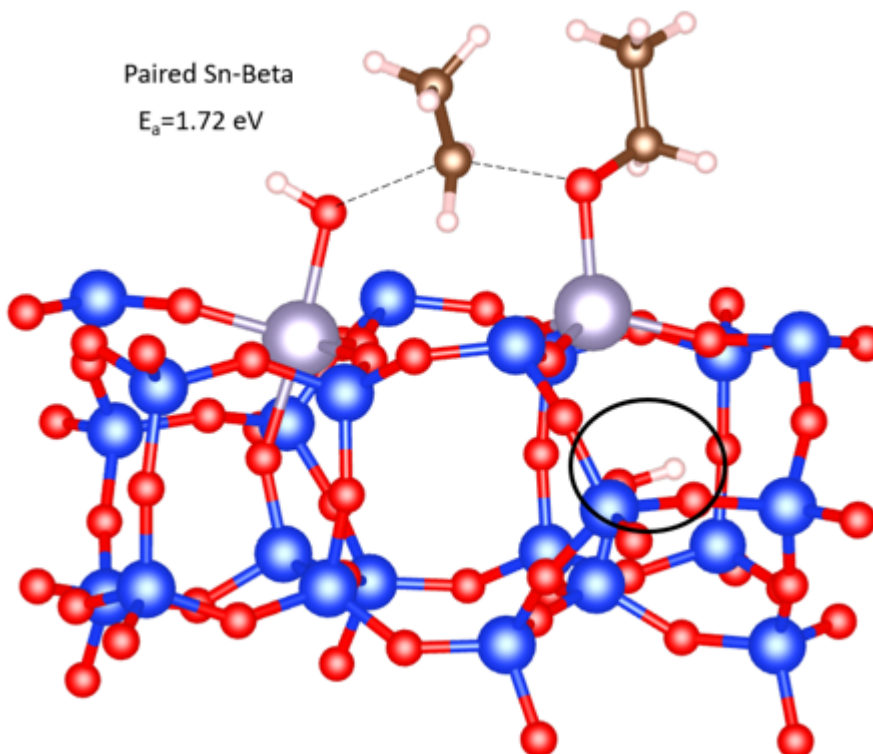
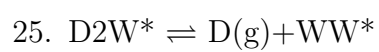
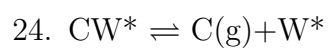
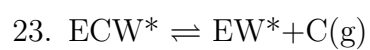
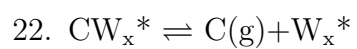
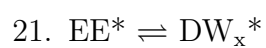
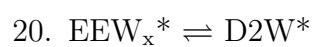
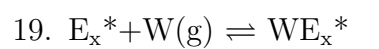


**Figure 2.14:** DEE formation on paired Sn sites identified by Bare et al. [108].

2.6.5 Complete list of elementary steps in microkinetic model of ethanol dehydration reaction network.

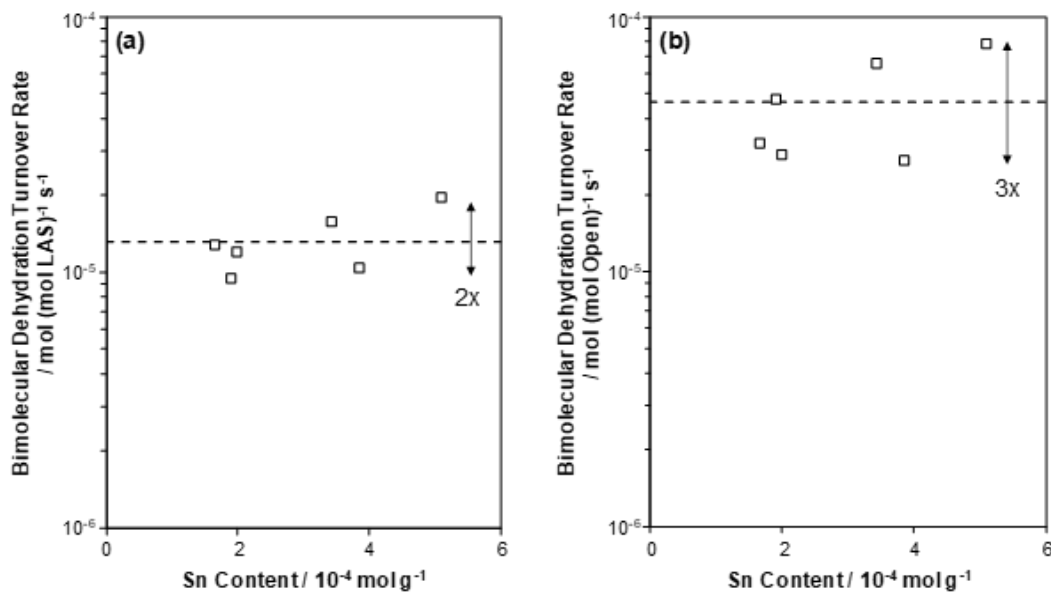
Here “C” denotes the monomolecular dehydration product, ethene.

1.  $WW^* \rightleftharpoons W(g)+W^*$
2.  $DW^* \rightleftharpoons D(g)+W^*$
3.  $C2W^* \rightleftharpoons CW^*+W(g)$
4.  $E(g)+^* \rightleftharpoons E^*$
5.  $E(g)+E^* \rightleftharpoons EE^*$
6.  $EE_x^* \rightleftharpoons ECW^*$
7.  $C2W^* \rightleftharpoons C(g)+WW^*$
8.  $W^* \rightleftharpoons W_x^*$
9.  $EE_x^* \rightleftharpoons DW^*$
10.  $W^* \rightleftharpoons W(g)+^*$
11.  $E(g)+EW_x^* \rightleftharpoons EEW_x^*$
12.  $E(g)+W_x^* \rightleftharpoons EW_x^*$
13.  $E^* \rightleftharpoons CW_x^*$
14.  $EW_x^* \rightleftharpoons C2W^*$
15.  $E^*+W(g) \rightleftharpoons EW^*$
16.  $E_x^*+E(g) \rightleftharpoons EE_x^*$
17.  $E^* \rightleftharpoons E_x^*$
18.  $DW_x^* \rightleftharpoons D(g)+W_x^*$



### 2.6.6 Effect of site normalization on turnover rates

The standard deviations of the data in Figure 2.15(a) and (b), normalized to their respective averages, are 0.28 (a) and 0.46 (b).

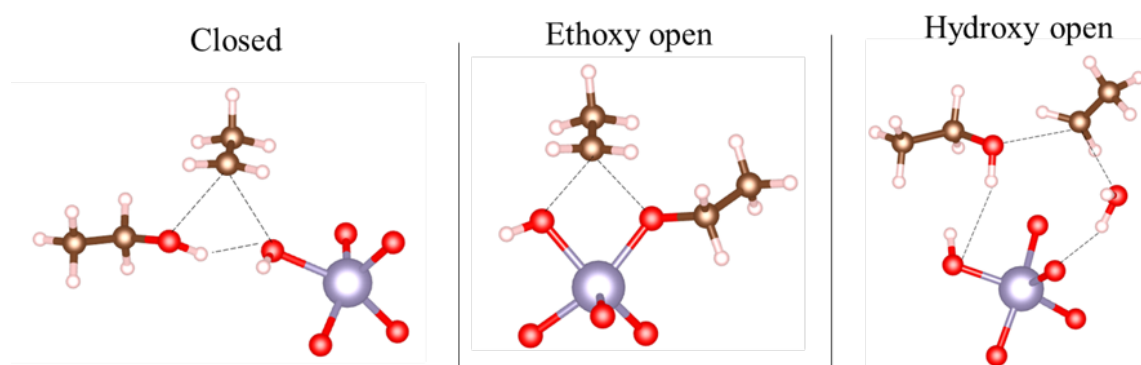


**Figure 2.15:** Bimolecular ethanol dehydration turnover rate to form DEE (a) per Lewis acidic Sn or (b) per open Sn, (b) at  $P_{\text{EtOH}}=8$  kPa,  $P_{\text{H}_2\text{O}}=0.1$  kPa as a function of the total Sn content for the six Sn-Beta-OH catalysts described in Table 2.1. Dashed lines represent averages of the data.

## 2.6.7 Additional mechanisms considered

**Table 2.8:** 0K intrinsic potential energy barriers (in eV) for the  $S_N2$  and  $S_{Ni}$  pathways for bimolecular dehydration of ethanol to form DEE.

	$S_{N2}$	$S_{Ni}$
closed (*)	1.47	2.20
hydroxy open ( $W_x^*$ )	1.32	2.31
ethoxy open ( $E_x^*$ )	1.41	1.92

**Figure 2.16:** Images correspond to the  $S_{Ni}$  conformation ( $S_{N2}$  provided in main text). Surrounding pore environment is truncated for clarity.

### 2.6.8 Construction of microkinetic model

Rate constants for gas phase adsorption are approximated using collision theory. This approximation is the most accurate for gas collisions on a flat surface. The inside pores of a zeolite are clearly not planar, but the flux of gas particles in the pore striking isolated Sn atoms is likely not significantly different. The rate constant of adsorptive processes is described by

$$k_{ads} = \frac{A_0\Lambda}{(2\pi kT)^2} \quad (2.6)$$

where  $A_0$  is the area of a surface site and  $\Lambda$  is an adsorption sticking probability, which will be assumed to be one. Rate constants for surface reactions are described as

$$k = \frac{kT}{h} e^{-\frac{(G_{TS}-G)}{kT}} \quad (2.7)$$

Here, transition state theory has been applied to relate the free energy change from the transition state of an elementary step to the forward rate constant with a frequency factor approximated as the fundamental mode. Note that potential energy and entropy effects have been included in the free energy.

Equilibrium constants for each step are defined by the standard relationship

$$K_{eq} = e^{-\frac{(G_{products}-G_{reactants})}{kT}} \quad (2.8)$$

The reverse rate constants can be obtained from the forward rate and equilibrium constant with a pressure conversion term. For purely surface reactions, the reverse rate is the forward rate divided by the equilibrium constant.

Once rate and equilibrium constants for all elementary steps have been determined, a CSTR reactor model can be established for an isothermal well-mixed reactor.

Mass balance equations for each species are developed. For a gas phase species, the mass balance takes the form

$$\frac{dF}{dt} = a(F_0 - F - b(rate)) \quad (2.9)$$

where the rate term contains the rate expression involving gas phase species and  $F$  denotes the gas flowrate in molar units. The parameters  $a$  and  $b$  determine the reactor parameters, with ‘ $a$ ’ relating to the reactor conversion and  $b$  relating to the site normalization. To compare with experimental measurements, the rates are normalized by the number of Sn sites in the same catalyst. Intrinsic rates for the reaction are very low, and reactor conversion can be constrained below 1% by consistent choice of parameter  $a$ .

For surface coverages, the rate of change is described by the expression

$$\frac{d\theta_a}{dt} = rate \quad (2.10)$$

where the coverage of an intermediate is expressed by the sum of the rates of elementary steps. In the microkinetic code, a stoichiometric matrix is formed which can be used to identify rates of each elementary steps in an organized manner. The number of sites is constrained by the site balance, resulting in a set of differential equations numbering the total reaction species. An inert is included to maintain pressure in the reactor. Initial gas flowrates can be calculated to match experimental data, and the set of differential equations are integrated in time until steady state is achieved. At steady state, the coverages and pressures can be used to evaluate the rates of each elementary step. The total rate of product formation is defined as the total flowrate of DEE produced from desorption.

As the overall rate of an elementary step involves the subtraction of a forward and reverse rate, rounding errors can become large for steps with low overall rate. Thus, the solution from the differential equation solver is fed into a nonlinear algebraic solver

to achieve better numerical accuracy. Usage of the nonlinear solver alone is difficult, however, since for a complex reaction network there may be many local roots.

Degree of rate control calculations are made by systematically varying each free energy and reevaluating the rate and equilibrium constants. A differential change is made to the free energy, and a least squares regression is made of the resultant rate constant vs. rate plot. The least squares regression is useful to determine whether the size of the differential perturbation is sufficient to maintain linearity in the numerical derivative.

### 2.6.9 Additional adsorbate configurations

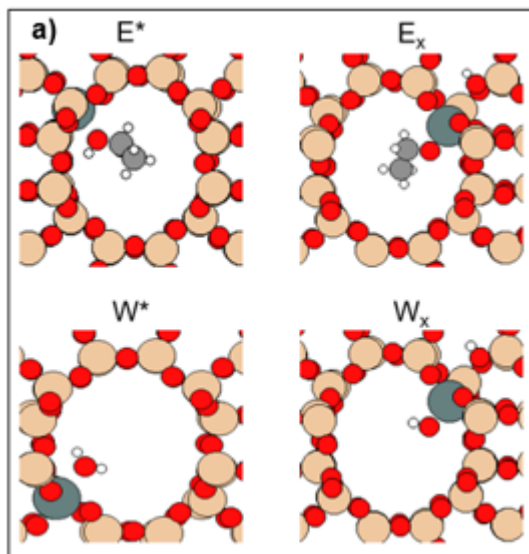


**Figure 2.17:** a) ethanol monomer, ethoxy open site, water monomer, hydroxy open site

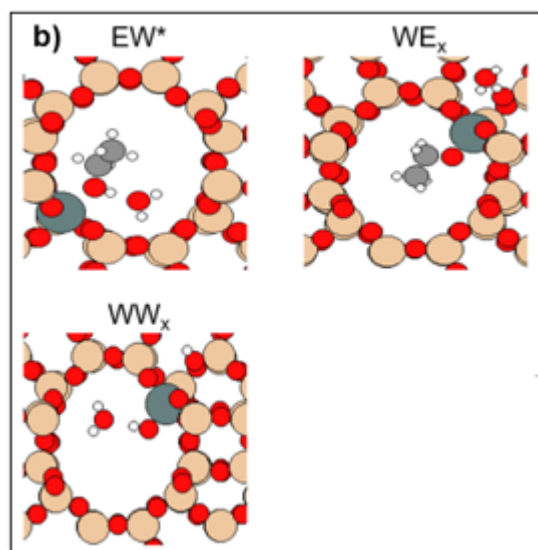


**Figure 2.18:** b) ethanol-water dimer, water on ethoxy open site, water on hydroxy open site

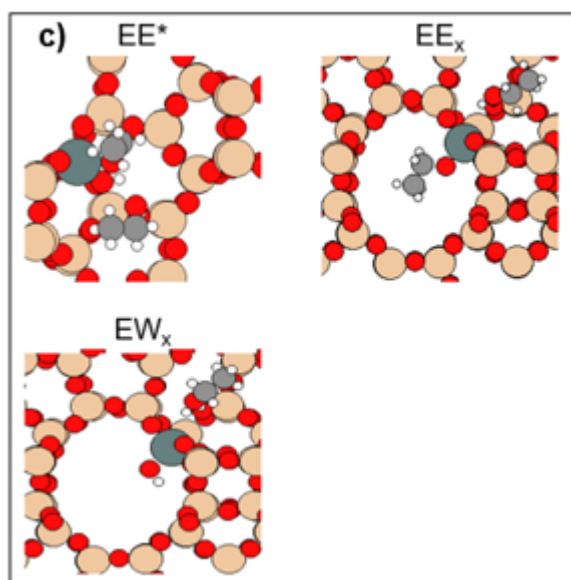


**Figure 2.19:** c) ethanol-ethanol dimer, ethanol on ethoxy open site, ethanol on hydroxy open site

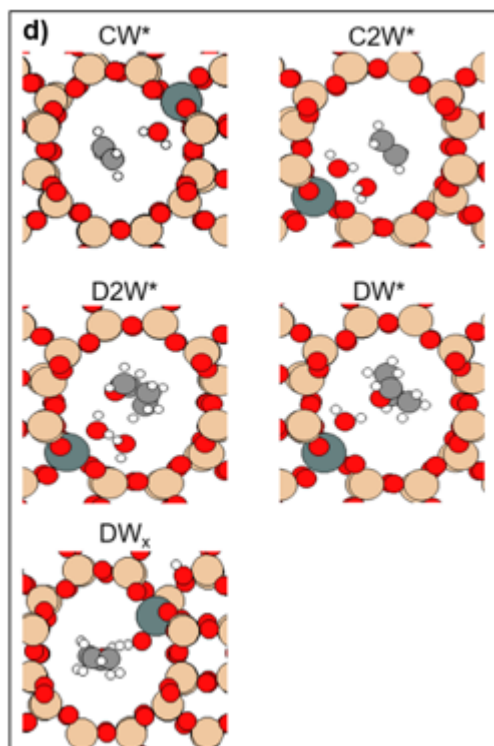


**Figure 2.20:** d) ethene-water dimer, ethene-water-water trimer, DEE-water-water-trimer, DEE-water dimer, DEE on hydroxy open site

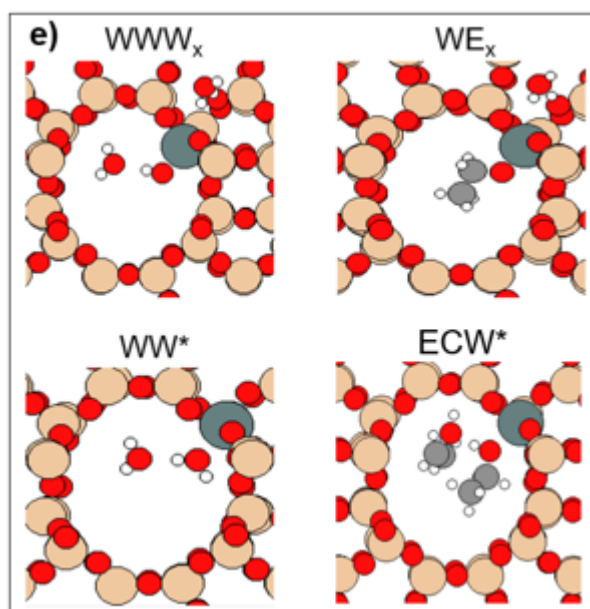


**Figure 2.21:** e) water-water on hydroxy open site, water on ethoxy open site, water on hydroxy open site, ethanol-ethene-water trimer

### 2.6.10 Calculation of entropy using mode decompositions and AIMD

Harmonic vibrational modes for each adsorbate and transition state was calculated, and the modes are visualized to determine contributions to different idealized partition functions for each respective mode. These partition functions are either the quantum harmonic oscillator, the free or hindered rotor, or translation in an infinite square potential. This choice of translational partition function is motivated by the particular characteristics of adsorbates in zeolites. Through inspection of the lowest frequency modes and AIMD simulations, adsorbates are found to translate around the Sn atom, but they cannot diffuse to a nearby site due to isolation of the T site. Thus, instead of using a full free translational partition function or a hindered translator, an infinite potential well is approximated around the Sn atom.

Entropies determined from the respective partition functions, as used in the microkinetic code, are provided below for each such partition function:

1. Harmonic oscillator:

$$S_{vib} = \frac{\frac{E}{kT}}{e^{\frac{E}{kT}} - 1} - \ln \left( 1 - e^{-\frac{E}{kT}} \right) \quad (2.11)$$

where E denotes the energy of the vibrational mode

2. Hindered rotators: hindered rotational modes are dependent on the free rotor partition function and the magnitude of the rotational barrier. The entropy is expressed for each rotational degree of freedom. The corresponding free rotor partition functions are

$$Q_{rot} = \frac{\sqrt{\pi}}{\sigma} \left( \frac{8\pi^2 I_{ii} kT}{h^2} \right)^{0.5} \quad (2.12)$$

which require knowledge of the symmetry factor and principle moments of inertia. The hindering potential is expressed by

$$E_{hind} = \frac{E}{2kT} \quad (2.13)$$

and the hindered rotational partition function is expressed as

$$Q_{hind} = Q_{rot} e^{-E_{hind}} J_0(iE_{hind}) \quad (2.14)$$

where  $J_0$  is the zeroth order Bessel function. The entropy corresponding to each degree of freedom is then evaluated as

$$S_{rot} = k \left( \ln(Q_{hind}) + \frac{1}{2} \right) \quad (2.15)$$

If the hindering potential is 0, the entropy corresponds to a free rotor about the specified principle moment of inertia. Any hindering potential reduces the entropy of the mode.

### 3. Translation in infinite square potential wells:

For localized translational modes, the characteristic translational length,  $L$ , is used to establish an infinite square potential. The translational partition function per degree of freedom is expressed as

$$Q_{trans} = \left( \frac{2\pi mkTL^2}{h^2} \right)^{\frac{1}{2}} \quad (2.16)$$

The entropy is then expressed as

$$S_{trans} = k \left( \ln(Q_{trans}) + \frac{1}{2} \right) \quad (2.17)$$

To obtain accuracy beyond that of mode-decomposed partition functions, entropies and free energies for adsorbed species are estimated from the two-phase thermodynamic method developed by Lin, Blanco, and Goddard [161,162]. The crux of this method is usage of molecular trajectories from AIMD to calculate the vibrational density of states (VDOS). This calculation is performed using a python code which directly generates the VDOS from the molecular velocities. This is the same method recommended by Lin et al. and involves projecting ideal gas translational, rotational,

and vibrational contributions from the VDOS. The degrees of freedom corresponding to the zeolite framework are projected out. The TRAVIS code [168,169] is used for its ability to sort and organize molecular trajectories.

### 2.6.11 Functional comparison for ethanol monomer and ethanol-ethanol dimer adsorption energies.

Lattice constants for the framework were individually relaxed for each functional, and a full geometry relaxation to a force constant of  $20 \text{ meV}/\text{\AA}$  was performed for each functional considered. Free energies are calculated at 404 K and 1 bar.

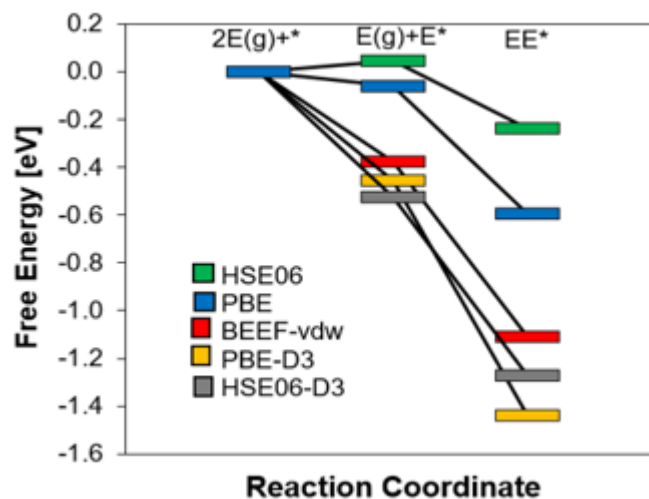


**Figure 2.22:** Functional comparison for ethanol monomer and ethanol-ethanol dimer adsorption energies.

## 2.6.12 Correlated error analysis

A centered 0.1 eV (+/- 0.05 eV maximum deviation) error was propagated through the optimized microkinetic model, which includes first and second order correlations in each reactive intermediate and transition state, as described in the text. The table below reports the generalized degree of rate control for the unchanged model, the change in DRC at the maximum DEE formation rate allowed by the error bounds, and the change in DRC at the minimum DEE formation rate. These changes did not introduce any additional rate-sensitive intermediates or alter the rate determining step determined from the model.

**Table 2.9**

GDRC	unchanged	maximum DEE formation rate	minimum DEE formation rate
Closed site TS	0.99	0.98	0.98
E*	-0.55	-0.24	-0.83
EE*	-0.37	-0.62	-0.14
EW*	-0.08	-0.15	-0.03

## 2.6.13 Derivation of simplified kinetic equation

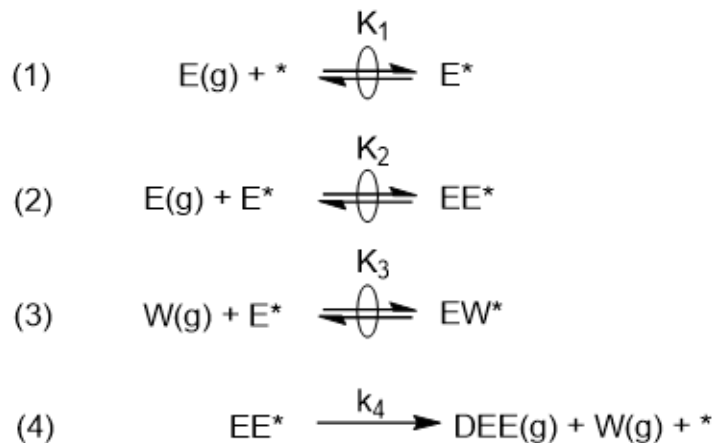


**Figure 2.23:** Simplified reaction mechanism derived from the generalized degree of rate control. Steps 1, 2, and 3 are quasi-equilibrated. Step 4 is the rate-limiting bimolecular dehydration on closed Sn sites.

Assumptions based on microkinetic modeling results:

1. Steps 1, 2, and 3 are quasi-equilibrated
2. Step 4 is irreversible and rate-determining
3. The relevant surface intermediates at the conditions studied are ethanol monomers, ethanol-ethanol dimers, and ethanol-water dimers. The coverage of empty sites is negligible.

The overall reaction rate per Sn site is therefore:

$$\frac{r_{DEE}}{L} = k_4 \theta_{EE} \quad (2.18)$$

where  $r_{DEE}$  is the rate per unit surface area, “L” denotes the total number of catalytic Sn sites, and  $\theta$  denotes the fractional coverage of a given reactive intermediate. Applying the quasi-equilibrium hypothesis on steps 1,2, and 3 yields:

$$\theta_E = K_1 P_E \theta_* \quad (2.19)$$

$$\theta_{EE} = K_1 K_2 P_E^2 \theta_* \quad (2.20)$$

$$\theta_{EW} = K_1 K_3 P_E P_W \theta_* \quad (2.21)$$

where P is a gas-phase partial pressure, and \* is the coverage of empty sites. We can write the total balance of sites L as:

$$1 = \theta_E + \theta_{EE} + \theta_{EW} \quad (2.22)$$

$$1 = (1 + K_2 P_E + K_3 P_W) K_1 P_E \theta_* \quad (2.23)$$

as the coverage of empty sites under the conditions studied is negligible. Therefore:

$$\frac{r_{DEE}}{L} = \frac{k_4 K_1 K_2 P_E^2}{(1 + K_2 P_E + K_3 P_W) K_1 P_E} \quad (2.24)$$

$$\frac{r_{DEE}}{L} = \frac{k_4 K_2 P_E}{(1 + K_2 P_E + K_3 P_W)} \quad (2.25)$$

Which is as presented in equation 2.5 of the main text.

### 3. INFLUENCE OF CONFINING ENVIRONMENT POLARITY ON ETHANOL DEHYDRATION CATALYSIS BY LEWIS ACID ZEOLITES

#### 3.1 Introduction

Catalytic reactivity in heterogeneous solids originates from the surface sites that bind reactive intermediates and stabilize transition states [62], and the secondary environments that confine them. Microporous structures in zeolites influence the free energies of intermediates and transition states through van der Waals contacts that depend on the sizes and shapes of confining environments and reacting moieties [30, 31, 33]. Co-adsorbed solvent or condensed phases that exist within microporous and mesoporous voids during catalysis also provide solvating environments, with analogous consequences for the free energies of intermediates that participate in productive catalytic turnovers [44, 46, 50, 170] and unproductive deactivation paths [23]. Pure-silica zeolite frameworks are composed of siloxane bonds that provide a non-polar and hydrophobic solvating environment, which becomes more polar and hydrophilic as the density of framework silanol defects (Si-OH) increases [171]. Silanol defects originate during zeolite crystallization when framework siloxy defects (Si-O<sup>-</sup>) balance cationic charges in occluded structure directing agents (SDA) and become Si-OH groups after SDA removal [35]; hence, their formation is suppressed during crystallization when fluoride (F<sup>-</sup>) serves as an alternative charge-balancing anion [172, 173]. Silanol defect groups, which are structural features inherent to microporous silica frameworks, comprise a solvating environment similar in function to that provided by co-adsorbed solvent phases, by influencing reactivity and stability against inhibition or deactivation.

One consequence of zeolite framework polarity has been recognized by the preferential adsorption of molecules at locations that encourage favorable intermolecular in-

teractions between polar or non-polar moieties. Water clusters are stabilized at polar groups (e.g., Si-OH, H<sup>+</sup>) within dealuminated MOR [171], MFI [174] and Beta [175] zeolites, and calorimetrically-measured water adsorption enthalpies are more exothermic at Ti sites confined within high-defect than low-defect Beta zeolites [52] and on SiO<sub>2</sub> surfaces with higher Si-OH densities [176]. The resulting consequences of framework polarity for catalysis appear to manifest as the inhibition observed during glucose-fructose isomerization [54] and Baeyer-Villiger oxidation [55] on Sn-Beta zeolites in polar solvents, which has motivated prescriptions to choose weakly-interacting solvents [54] or to optimize defect density to favor reactant adsorption [55]. The use of low-defect Ti-MFI (TS-1) zeolites results in higher initial epoxidation rates (308 K) for non-polar than for polar alkenes in the presence of competing polar solvents [47], although interactions between co-adsorbed solvent and reacting molecules also lead to residual differences in reactivity [48, 49]. Similarly, aqueous-phase phenol alkylation proceeds at higher turnover rates (per H<sup>+</sup>, 523 K) as Brnsted acidic H-MFI zeolites become more hydrophobic with increasing Si/Al ratio, solely because of increases in phenol adsorption constants [95]. Beyond influencing adsorption phenomena during catalysis, energetically favorable pathways involving the participation of adsorbed water molecules have been reported for glucose-fructose isomerization [70] and 1-propanol dehydration [177], further convoluting the inhibitory effects of competitive adsorption with the potential benefits of solvent-mediated elementary steps. Additionally, theoretical simulations predict different structures for condensed solvent phases within polar and non-polar confining environments [37, 178], which have been proposed to cause differences in stabilization of glucose-fructose isomerization transition states within polar and non-polar Sn-Beta zeolites [56, 151].

Lewis acidic Sn sites are formed by isomorphous substitution of Sn<sup>4+</sup> for Si<sup>4+</sup> in siliceous zeolite frameworks, and can adopt closed configurations with four framework bonds (Sn-(OSi≡)<sub>4</sub>) or open configurations with one hydrolyzed framework bond resulting in neighboring stannanol ((HO)-Sn-(OSi≡)<sub>3</sub>) and silanol groups. Open and closed Sn sites are detected spectroscopically by infrared (IR) peaks for C≡N stretches

in adsorbed  $\text{CD}_3\text{CN}$  centered at  $2316\text{ cm}^{-1}$  and  $2308\text{ cm}^{-1}$ , respectively, which are assignments supported by their relative vibrational frequencies calculated by density functional theory (DFT) [102] and by their respective correlation to  $^{119}\text{Sn}$  NMR resonances centered at  $-420\text{ ppm}$  and  $-443\text{ ppm}$ , only the former of which cross-polarizes with a proton [68]. Open Sn sites in Sn-Beta zeolites have been identified as dominant active sites for glucose-fructose isomerization by experiment using *ex situ* poisoning techniques ( $\text{Na}^+$  [106],  $\text{NH}_3$  [106], pyridine [56]), and by DFT-calculated barriers to form intramolecular 1,2-hydride shift transition states that are lower at open Sn sites [68, 69, 101]. Experimental studies have focused on interpreting initial turnover rates measured in batch reactors using Sn site configurations measured *ex situ*, because of the deactivation typical of Sn-Beta in condensed water [116, 117, 179], resulting in a dearth of information about the influence of reaction conditions on Sn site configurations *in situ*. The reconfiguration of Sn structure during catalysis in aqueous media seems plausible, however, considering that theoretical studies have described the interconversion of open and closed sites via reversible hydrolysis of Sn-O-Si bonds by adsorbed  $\text{H}_2\text{O}$  [113, 180], and  $^{119}\text{Sn}$  NMR experiments have provided evidence for such interconversion [114, 155]. Hence, more complete descriptions of framework polarity effects on catalysis require considering the coverages of adsorbed species and extended solvent structures, and their involvement in facilitating elementary steps and structural changes to Lewis acidic binding sites.

Here, we study ethanol dehydration as a gas-phase probe of the reactivity of Lewis acidic Sn sites to examine its sensitivity to the polarity of confining secondary environments, while circumventing complications from analogous assessments in liquid water that arise from limited ranges of accessible surface coverages and from rapid deactivation. Ethanol dehydration occurs on Lewis acid sites and has been studied extensively on  $\gamma\text{-Al}_2\text{O}_3$  [86, 87], although the nature of active site ensembles that catalyze ethanol dehydration remains debated [181]. Thus, we choose to probe ethanol dehydration at site-isolated Lewis acidic Sn centers in Sn-Beta zeolites, which provide better-defined structures to clarify the interpretation of experimental kinetic measurements

and of spectroscopic observations for active site restructuring upon ethanol exposure. Ethanol dehydration can proceed through unimolecular pathways to form ethene or bimolecular pathways to form diethyl ether, generating a rich pool of surface intermediates [88,90,158] that vary in size and polarity, including monomeric and dimeric combinations of ethanol and water. Ethanol-ethanol dimers form diethyl ether, while intermediates containing water molecules inhibit ether formation [88], providing kinetic responses in the form of turnover rates and apparent reaction orders that can be related to changes in surface coverages of reactive and inhibitory intermediates. The synthesis of low-defect (Sn-Beta-F) and high-defect (Sn-Beta-OH) molecular sieve analogs provides a strategy to confine Sn centers within secondary environments of different polarity. Mechanistic interpretations of measured rate data, supported by DFT-based microkinetic modeling [180], enable rigorous assessments of the effects of framework polarity on the stabilities of transition states and adsorbed intermediates in ethanol dehydration catalysis.

## 3.2 Methods

### 3.2.1 Zeolite Synthesis

Si-Beta-F was synthesized hydrothermally in fluoride media according to the literature [106]. Tetraethyl ammonium fluoride hydrate (TEAF, Alfa Aesar, 98%) was dissolved in deionized water (18.2 M $\Omega$  cm) in a perfluoroalkoxy alkane (PFA) container (Savillex Corp.) followed by addition of tetraethylorthosilicate (TEOS, Sigma Aldrich, 98%). Then, the mixture was covered and stirred overnight at ambient conditions to completely hydrolyze TEOS. The mixture was uncovered to completely evaporate ethanol, and partially evaporate water to achieve the desired molar composition of 1 SiO<sub>2</sub>/0.55 TEAF/6.7 H<sub>2</sub>O. The gel was transferred into a Teflon-lined stainless steel autoclave and heated statically in an isothermal oven at 413 K for 11 days. The solids were recovered by centrifugation and washed thoroughly with deionized water and acetone, then dried overnight in a 373 K oven. The dried material was

treated at 853 K ( $0.0167 \text{ K s}^{-1}$ ) for 10 h in air (Ultra Zero Grade, Indiana Oxygen,  $1.67 \text{ cm}^3 \text{ s}^{-1} (\text{g zeolite})^{-1}$ ) in a muffle furnace (Nabertherm LE 6/11).

Sn-Beta-F zeolites were synthesized hydrothermally in fluoride media. TEOS was dissolved in tetraethylammonium hydroxide (TEAOH, Sachem, 35%) by stirring in a PFA container until homogeneous. Tin(IV) chloride pentahydrate (Sigma Aldrich, 98%) was dissolved in deionized water and added dropwise to the mixture. The gel was covered and stirred overnight to completely hydrolyze TEOS, then uncovered to completely evaporate ethanol and partially evaporate water to the desired molar ratio. Finally, a hydrofluoric acid solution (Sigma Aldrich, 48%) was added and stirred with a PTFE spatula to give a thick gel with molar composition  $1 \text{ SiO}_2/0.54 \text{ TEAOH}/0.54 \text{ HF}/x \text{ SnCl}_4/7.5 \text{ H}_2\text{O}$  (where  $x = 0.005$  or  $0.0077$  for target solid Si/Sn ratios of 200 and 130, respectively). (Caution: when working with hydrofluoric acid, use appropriate personal protective equipment, ventilation, and other engineering controls.) The gel was transferred into a Teflon-lined stainless steel autoclave, seeded with 0.25 g of dealuminated Beta (Sn-Beta-F-187, Sn-Beta-F-181;  $x = 0.005$ ) or 0.25 g of Si-Beta-F (Sn-Beta-F-116;  $x = 0.0077$ ), and heated in an isothermal rotating oven at 413 K for 14 days (Sn-Beta-F-187, Sn-Beta-F-181) or 28 days (Sn-Beta-F-116). Sn-Beta-F-153 was synthesized according to the above with  $x = 0.005$ , but without seeds and  $\text{H}_2\text{O}/\text{SiO}_2 = 6.8$  in 14 days, as suggested by Yakimov et al. [182]. The solids were recovered by centrifugation and washed thoroughly with deionized water and acetone, then dried overnight in a 373 K oven. The dried material was treated at 853 K ( $0.0167 \text{ K s}^{-1}$ ) for 10 h in air ( $1.67 \text{ cm}^3 \text{ s}^{-1} (\text{g zeolite})^{-1}$ ) in a muffle furnace.

Al-Beta-OH was synthesized hydrothermally in hydroxide media and subsequently dealuminated as reported in the literature [151,183]. Tetraethylammonium hydroxide (Sigma-Aldrich, 35%) and Ludox HS-30 colloidal silica (Sigma Aldrich, 30%) were added to a PFA container and stirred covered for 1 h at ambient conditions. Then, sodium hydroxide (NaOH, Avantor, 98%) was dissolved in deionized water, and this mixture was added to the gel, followed by aluminum isopropoxide (Sigma Aldrich, 98%). The gel was stirred covered for 24 h at ambient conditions, then uncovered

to completely evaporate isopropanol, and partially evaporate water to achieve the desired molar composition of  $1 \text{ SiO}_2/x \text{ Al}_2\text{O}_3/13.24 \text{ H}_2\text{O}/0.18 \text{ TEAOH}/0.014 \text{ Na}_2\text{O}$  (where  $x$  was 0.0165, 0.01, and 0.005 for target solid Si/Al ratios of 30, 50, and 100, respectively). The gel was transferred into a Teflon-lined stainless steel autoclave and heated statically in an isothermal oven at 413 K for 7 days. The solids were recovered by centrifugation and washed thoroughly with deionized water and acetone, then dried overnight in a 373 K oven. The dried material was treated at 853 K ( $0.0167 \text{ K s}^{-1}$ ) for 10 h in air ( $1.67 \text{ cm}^3 \text{ s}^{-1} (\text{g zeolite})^{-1}$ ) in a muffle furnace.

Air-treated Al-Beta-OH zeolites were dealuminated in concentrated nitric acid ( $\text{HNO}_3$ , Avantor, 69%). The zeolite was added to a PFA container, followed by  $\text{HNO}_3$  ( $25 \text{ cm}^3 (\text{g zeolite})^{-1}$ ), then the container was covered and stirred for 16 h at 353 K. The solids were recovered by centrifugation and washed thoroughly with deionized water until the pH of the supernatant was constant, then dried overnight in a 373 K oven.

Sn-Beta-OH zeolites were prepared by post-synthetic grafting of Sn precursors into dealuminated Beta in dichloromethane reflux. All but one of the Sn-Beta-OH samples used in this study are a subset of the samples reported in Vega-Vila et al. [151], and the details of their synthesis and complete characterization can be found there. Sn-Beta-OH-187 was synthesized using the same procedures, after dealumination of the parent Al-Beta-OH (synthesized at a Si/Al of 34).

In this study, all samples are denoted as Sn-Beta-X-Y, where X refers to the preparation method used (F = fluoride-assisted hydrothermal synthesis; OH = post-synthetic Sn insertion into dealuminated Beta) and Y is the Si/Sn ratio determined by atomic absorption spectroscopy.

### 3.2.2 Characterization of Zeolites

Powder X-ray diffraction (XRD) patterns were collected using a Rigaku Smartlab X-ray diffractometer with a  $\text{Cu K}\alpha$  X-ray source in the range of  $2\theta = 4\text{--}40^\circ$  with a step size of  $0.01^\circ$  and scan speed of  $0.005^\circ \text{ s}^{-1}$ .

Vapor-phase  $\text{N}_2$ ,  $\text{H}_2\text{O}$ , and  $\text{C}_2\text{H}_5\text{OH}$  adsorption isotherms were collected using a Micromeritics ASAP 2020 instrument. Samples were pelleted and sieved to retain 180–250  $\mu\text{m}$  aggregates, and 0.010–0.040 g were degassed by heating to 393 K for 2 h then 623 K for 10 h under dynamic vacuum ( $<0.67$  Pa) prior to adsorption measurements.  $\text{N}_2$  isotherms were collected at 77 K, while  $\text{H}_2\text{O}$  and  $\text{C}_2\text{H}_5\text{OH}$  were collected at 302 K.  $\text{H}_2\text{O}$  and  $\text{C}_2\text{H}_5\text{OH}$  (Sigma Aldrich, anhydrous,  $>99.5\%$ ) liquids were degassed by three freeze-pump-thaw cycles and supplied at their respective vapor pressures at 313 K. For adequate resolution at low pressures and to avoid errors associated with residual adsorbed gas, samples were held under dynamic vacuum ( $<0.67$  Pa) on the analysis port up until the point of filling the dosing manifold with adsorbate prior to collecting the first data point. This procedure, coupled with dosing a fixed amount of vapor, was necessary for accurate  $\text{C}_2\text{H}_5\text{OH}$  adsorption measurements on Si-Beta-OH. The volume of adsorbate that filled zeolite micropores was determined at the uptake corresponding to the minimum value of  $\partial V_{\text{ads}}/\partial \log(P/P_0)$ .

The bulk mass fraction of Al or Sn in zeolite samples was obtained by atomic absorption spectroscopy (AAS). 0.030 g of powder were digested with 2 g of hydrofluoric acid (Sigma Aldrich, 48%) overnight, then diluted with 50 g of deionized water. Calibration standards were prepared by diluting a stock solution of each metal (Sigma Aldrich,  $1000 \pm 4$  ppm) with deionized water. A PerkinElmer AAnalyst 300 instrument equipped with lamps for Sn (396.2 nm) and Al (284.0 nm) was used to measure the absorbance of the standards and digested samples. Si/M ratios were calculated assuming the unit cell formula of zeolite Beta.

Diffuse reflectance UV-Visible (DRUV) spectra were collected on a Varian-Cary 5000 spectrometer using a Harrick Praying Mantis *in situ* cell. Background spectra were collected prior to zeolite spectra at all conditions with poly(tetrafluoroethylene) (PTFE, Sigma Aldrich, 1  $\mu\text{m}$ ), and used to transform absorption spectra with the Kubelka-Munk function. Spectra were collected of samples under flowing dry He (UHP, Indiana Oxygen,  $4.17 \text{ cm}^3 \text{ s}^{-1}$  (g zeolite) $^{-1}$ ) at ambient temperature, and after

dehydration for 0.5 h at 523 K ( $0.5 \text{ K s}^{-1}$ ), then after rehydration by cooling in He ( $4.17 \text{ cm}^3 \text{ s}^{-1} (\text{g zeolite})^{-1}$ ) saturated with deionized water at ambient conditions.

Infrared spectroscopy of adsorbed  $\text{CD}_3\text{CN}$  was used to identify the type and number of Sn species in Sn-Beta catalysts as a function of reaction and post-reaction treatments. A 0.030 g zeolite sample (Sn-Beta-F-187) was pressed into a self-supporting wafer with a 0.9 cm radius and loaded into a custom-built quartz IR cell [184] with  $\text{CaF}_2$  windows, equipped with six cartridge heaters (Chromalox) and encased in an insulated brass block within an alumina silicate cover. Wafer temperatures were measured within 2 mm of each side of the wafer by K-type thermocouples (Omega). IR spectra were collected on a Nicolet 4700 spectrometer with a Hg-Cd-Te (MCT, cooled to 77 K by liquid  $\text{N}_2$ ) detector by averaging 64 scans at  $2 \text{ cm}^{-1}$  resolution in the  $4000\text{--}400 \text{ cm}^{-1}$  range and were taken relative to an empty cell background reference collected under dynamic vacuum ( $<0.1 \text{ Torr}$ ) at 303 K. The  $\text{CD}_3\text{CN}$  (Sigma Aldrich, 99.96 atom% D) and ethanol (Sigma Aldrich, 200 proof) adsorbates were purified by three freeze-pump-thaw cycles. The wafer was treated in flowing air ( $0.33 \text{ cm}^3 \text{ s}^{-1}$ ), purified by an FTIR purge gas generator (Parker Balston,  $<1 \text{ ppm CO}_2$ , 200 K  $\text{H}_2\text{O}$  dew point), to 723 K ( $0.083 \text{ K s}^{-1}$ ) for 1 h. The wafer was then held under dynamic vacuum at 723 K for 1 h, then cooled to 303 K under dynamic vacuum.  $\text{CD}_3\text{CN}$  was introduced into to the cell in sequential doses until the sample was saturated, then the sample was exposed to dynamic vacuum for 0.25 h. The spectrum collected before dosing was subtracted from all subsequent spectra. The subtracted spectrum after dosing and then reaching dynamic vacuum was deconvoluted using CasaXPS (Casa Software Ltd) with Gauss-Lorentzian lineshapes with a 50% Lorentzian correction (SGL(50)) to determine the areas of peaks centered at  $2316 \text{ cm}^{-1}$  (open Sn),  $2308 \text{ cm}^{-1}$  (closed Sn),  $2287 \text{ cm}^{-1}$  (nanosized  $\text{SnO}_x$ ),  $2275 \text{ cm}^{-1}$  (SiOH), and  $2265 \text{ cm}^{-1}$  (physisorbed  $\text{CD}_3\text{CN}$ ). Integrated molar extinction coefficients reported by Harris et al. [56] were used to quantify the number of each species according to the equation:

$$\text{Site density } (\mu\text{mol g}^{-1}) = \left( \frac{\text{Integrated Peak Area } (\text{cm}^{-1})}{E (\text{cm } \mu\text{mol}^{-1})} \right) \left( \frac{a_{CS} (\text{cm}^2)}{m(\text{g})} \right) \quad (3.1)$$

Subsequently, the cell was slowly returned to ambient pressure by allowing ambient air to leak in, and the wafer was treated under flowing air ( $0.33 \text{ cm}^3 \text{ s}^{-1}$ ) at 803 K ( $0.0167 \text{ K s}^{-1}$ ) for 2 h, then cooled to 488 K ( $0.0333 \text{ K s}^{-1}$ ). Ethanol was introduced into the cell in sequential doses of progressively increasing amounts ( $7 \times 10^{-6} \text{ mol g}^{-1} - 1 \times 10^{-3} \text{ mol g}^{-1}$  per dose). After a cumulative amount of  $7 \times 10^{-3} \text{ mol g}^{-1}$  ( $80 \text{ mol C}_2\text{H}_5\text{OH (mol Sn)}^{-1}$ ) was dosed, the sample was exposed to dynamic vacuum for 300 s, after which spectra did not change further. Next, the wafer was vented with He (UHP, Indiana Oxygen) up to ambient pressure. Then, the wafer was held under a flowing He ( $0.233 \text{ cm}^3 \text{ s}^{-1}$ ) stream that was passed through a saturator containing ethanol (Sigma Aldrich, 200 proof, for molecular biology) at ambient temperature (ca. 294 K), to introduce ethanol flow at ca. 6 kPa and a site-contact time of 0.39 s ( $\text{mol Sn}$ ) ( $\text{mol total feed}$ ) $^{-1}$ . The wafer was treated for 3 h under flowing ethanol in He at 488 K. During this treatment, spectra were collected every 300 s, and were essentially invariant and dominated by gas-phase ethanol. Following ethanol reaction, the He flow was directed to bypass the saturator for 0.5 h to purge gas-phase ethanol and physisorbed species, then the cell was evacuated and held under dynamic vacuum for 0.25 h (spectra were invariant with time after this point). The sample was then cooled to 303 K under dynamic vacuum, and a  $\text{CD}_3\text{CN}$  dosing experiment was performed as described previously. Next, the sample was heated to 803 K ( $0.167 \text{ K s}^{-1}$ ) under dynamic vacuum and held at 803 K for 0.33 h. Then, ambient air was introduced to the sample at 803 K by gradually leaking through the cell outlet. Flowing air ( $0.33 \text{ cm}^3 \text{ s}^{-1}$ ) was introduced to the cell for 0.25 h, and spectra were collected every 180 s. The wafer was left under dynamic vacuum for 12 h and then allowed to cool to 303 K. Then, a third  $\text{CD}_3\text{CN}$  dosing experiment was performed as described above.

Temperature programmed desorption (TPD) was performed to gain additional insight into the chemical species present on Sn sites after ethanol dehydration catalysis. 0.04–0.10 g of sample were pelleted, crushed, and sieved to retain 180–250  $\mu\text{m}$  aggregates, placed between two quartz wool plugs in a U-tube reactor, and connected to a Micromeritics Autochem II 2920 Analyzer equipped with an Agilent 5973N mass

selective detector (MSD). Samples were treated in flowing air (Zero grade, Indiana Oxygen,  $0.833 \text{ cm}^3 \text{ s}^{-1}$ ) at 803 K ( $0.0167 \text{ K s}^{-1}$ ) for 2 h, then cooled to 404 K. Ethanol (Sigma Aldrich, anhydrous, >99.5%) was introduced into a flowing He (UHP, Indiana Oxygen,  $1.67 \text{ cm}^3 \text{ s}^{-1}$ ) stream via a saturator held at 303 K, with all transfer lines heated to >383 K to prevent condensation, and reacted over the catalyst for 8 h. Then, any ethanol that was weakly adsorbed or in the transfer lines was purged with flowing He ( $1.67 \text{ cm}^3 \text{ s}^{-1}$ ) for 0.5–16 h, and the TPD was performed by heating to 530 K ( $0.167 \text{ K s}^{-1}$ ). The MSD was used to monitor desorbing species at  $m/z = 18$  ( $\text{H}_2\text{O}$ ), 28 ( $\text{C}_2\text{H}_4$ ), 31 ( $\text{C}_2\text{H}_5\text{OH}$ ), 44 ( $\text{C}_2\text{H}_4\text{O}$ ), and 59 ( $(\text{C}_2\text{H}_5)_2\text{O}$ ), selected based on standard fragmentation patterns (Figure 3.15, Supporting Information). Ethene was calibrated in a separate experiment by mixing two streams of Ar (UHP, Indiana Oxygen) and  $\text{C}_2\text{H}_4$  (UHP, Indiana Oxygen) at a total flow rate of  $0.833 \text{ cm}^3 \text{ s}^{-1}$  and varying  $\text{C}_2\text{H}_4$  mole fraction (0.1–0.9) to fill a sample loop ( $0.5 \text{ cm}^3$ ) that was injected into a He stream ( $0.833 \text{ cm}^3 \text{ s}^{-1}$ ) and sent to the MSD (Ar  $m/z = 40$ ,  $\text{C}_2\text{H}_4$   $m/z = 28$ ). The integrated area of the  $\text{C}_2\text{H}_4$  signal was referenced to the area of the Ar signal using this calibration, and a pure Ar pulse was measured following each TPD experiment to correct for any drift in the instrument. The integrated Ar pulse area (units of s) and mass of sample (units of g) were used to normalize ion signals (resulting units  $\text{s}^{-1} \text{ g}^{-1}$ ) such that integration of this signal in time and multiplication by the calibrated response factor would give the total moles of  $\text{C}_2\text{H}_4$  ( $\text{g sample}^{-1}$ ), to compare samples on a similar scale (Figure 3.25, Supporting Information).

Breakthrough adsorption measurements of two-component mixtures consisting of  $\text{C}_2\text{H}_5\text{OH}$  and  $\text{H}_2\text{O}$  were conducted on the same unit as described for the TPD experiments. Si-Beta-OH (0.090 g) and Si-Beta-F (0.364 g) were pelleted, crushed, and sieved to retain 180–250  $\mu\text{m}$  aggregates, and loaded into the U-tube reactor between two quartz wool plugs. Samples were pretreated in flowing air (Zero grade, Indiana Oxygen,  $0.833 \text{ cm}^3 \text{ s}^{-1}$ ) to 803 K ( $0.0167 \text{ K s}^{-1}$ ) for 2 h, then cooled to the adsorption temperature (303 K or 403 K) under flowing He (UHP, Indiana Oxygen,  $0.833 \text{ cm}^3 \text{ s}^{-1}$ ) with all transfer lines heated to >383 K. After reaching the adsorption temperature,

the samples were held under flowing He ( $0.167 \text{ cm}^3 \text{ s}^{-1}$ ) and the effluent was analyzed using the MSD to obtain baseline signals for  $\text{C}_2\text{H}_5\text{OH}$  ( $m/z = 31$ ),  $\text{H}_2\text{O}$  ( $m/z = 18$ ), and Ar ( $m/z = 40$ ). Concurrently, a flowing Ar stream (UHP, Indiana Oxygen,  $0.167 \text{ cm}^3 \text{ s}^{-1}$ ) was passed through a saturator held at 303 K that contained a mixture of 52 mol%  $\text{C}_2\text{H}_5\text{OH}$  and 48 mol%  $\text{H}_2\text{O}$  to give 5.8 kPa  $\text{C}_2\text{H}_5\text{OH}$  and 2.3 kPa  $\text{H}_2\text{O}$  in the feed. After 0.5 h, a 4-port valve was switched to direct the saturated stream to the sample (time = 0). The breakthrough adsorption was considered complete when the ion signals of  $\text{C}_2\text{H}_5\text{OH}$ ,  $\text{H}_2\text{O}$ , and Ar reached steady values, indicating that equilibrium was reached. First, the baseline values obtained in flowing He prior to adsorption were subtracted from the ion signals, then the expected gas-phase signal was estimated by linear regression to the steady-state signal after adsorption, and extrapolated back through the adsorption period. The baseline-corrected ion signals were then normalized by their gas-phase signals, and the normalized ion signal for Ar was subtracted from these to correct for the residence time in the system. These signals represented the  $\text{C}_2\text{H}_5\text{OH}$  and  $\text{H}_2\text{O}$  that broke through the sample, and were converted to an adsorption rate assuming a value of one corresponded to an adsorption rate of zero, and a value of zero corresponded to an adsorption rate equal to the flow rate of the component in the feed. The adsorption rate ( $\text{mol s}^{-1}$ ) is plotted against the adsorption time normalized by sample mass ( $\text{ks g}^{-1}$ ) in Figure 3.30 (Supporting Information), such that the area under the curve is proportional to the amount adsorbed per sample mass.

### 3.2.3 Gas-phase ethanol dehydration kinetic studies

Zeolite samples (0.010–0.050 g) were pelleted, crushed, and sieved to retain aggregates between 180–250  $\mu\text{m}$  and supported between two plugs of acid-washed quartz wool (W.R. Grace, washed with 1 M  $\text{HNO}_3$  for 16 h, ambient temperature) in a tubular quartz reactor (7 mm ID). The bed temperature was measured using a K-type thermocouple (Omega) in contact with the side of the quartz tube at the level of the bed and kept constant using a three-zone furnace (Applied Test Systems) and Wat-

low controllers (EZ-ZONE). The catalyst was heated to 803 K ( $0.0167 \text{ K s}^{-1}$ ) under flowing 5%  $\text{O}_2/\text{He}$  (UHP, Indiana Oxygen,  $16.67 \text{ cm}^3 \text{ s}^{-1} (\text{g catalyst})^{-1}$ ), held at 803 K for 2 h, then cooled to 404 K ( $0.0333 \text{ K s}^{-1}$ ) and held under flowing He (UHP, Indiana Oxygen,  $16.67 \text{ cm}^3 \text{ s}^{-1} (\text{g catalyst})^{-1}$ ) for 1.5 h before beginning reaction. Liquid ethanol (Sigma Aldrich, anhydrous, >99.5%) and deionized water were introduced via heated lines (>383 K) into separate He streams flowing at approximately equal rates using syringe pumps (KD Scientific Legato 100), and mixed at a tee upstream of the reactor. Reactant and product concentrations were measured by gas chromatography (Agilent 6890) using a HP-PLOT-Q capillary column ( $30 \text{ m} \times 530 \mu\text{m} \times 40 \mu\text{m}$ ) and flame ionization detector. Prior to reaction, the composition of the feed stream was verified from bypass injections. The catalyst was stabilized at 8 kPa  $\text{C}_2\text{H}_5\text{OH}$  and 0.1 kPa  $\text{H}_2\text{O}$  for 8–12 h on stream before measuring reaction orders. Frequent sojourns to a reference condition (typically, 8 kPa  $\text{C}_2\text{H}_5\text{OH}$ , 0.1 kPa  $\text{H}_2\text{O}$ , 404 K) were used to correct for deactivation by extrapolating rates to initial time assuming first-order deactivation. Deactivation rate constants ranged from  $6 \times 10^{-4}$ – $3 \times 10^{-2} \text{ ks}^{-1}$ . A period of 3–5 h was allowed at a given condition to reach steady state, and reported rates represent an average of 1.5 h at the end of this time period (6 data points). Ethanol pressure was varied from 0.5–35 kPa, and  $\text{H}_2\text{O}$  pressure was varied from 0.1–50 kPa. Site-contact time (on a total Sn per total moles feed basis) was held constant at  $0.39 \text{ s} (\text{mol Sn}) (\text{mol feed})^{-1}$ , except under conditions ( $P_{\text{C}_2\text{H}_5\text{OH}} + P_{\text{H}_2\text{O}} > 50 \text{ kPa}$ ) that required higher He flow rates to stay above the minimum that could be reliably supplied by the mass flow controllers used (ca.  $0.0667 \text{ cm}^3 \text{ s}^{-1}$ , per MFC). Minor background contributions to DEE formation by quartz wool and other reactor internals were assessed using a reactor packed with only quartz wool as a function of ethanol pressure at 404 K, and subtracted from all experimental flow rates with catalyst. Additionally, the background reactivity of Si-Beta-F (on a per g basis) was assessed at 404 K over time and rates that are reported herein were  $>10\times$  that of Si-Beta-F. Estimation of rate and equilibrium constants was performed by Bayesian

nonlinear regression in Athena Visual Studio (v14.2, Athena Visual Software, Inc.). Reported uncertainties represent 95% marginal highest posterior density intervals.

### 3.3 Results and Discussion

#### 3.3.1 Kinetic and mechanistic details of bimolecular ethanol dehydration

Alcohols dehydrate at Lewis acid sites via unimolecular pathways to form alkenes and water, and bimolecular pathways to form ethers and water [86,87]. Diethyl ether (DEE) was the dominant product formed on Sn-Beta zeolites in the temperature range studied here (>80% molar selectivity, 404-528 K), and ethene was not detected below 455 K under the typical reaction conditions studied here (8 kPa C<sub>2</sub>H<sub>5</sub>OH, 0.1 kPa H<sub>2</sub>O, Figure 3.16, Supporting Information). Thus, ethanol dehydration rates measured on Sn-Beta zeolites at 404 K reflect solely bimolecular pathways to form diethyl ether. DEE site-time yields (404 K, per Sn) were measured as a function of time-on-stream (Figure 3.17, Supporting Information) and decay transiently to a quasi-steady-state value during the timescale of one catalytic turnover (8–12 h). Afterwards, the partial pressures of ethanol and water were varied to measure apparent kinetic orders, and frequent sojourns to a reference condition (typically, 8 kPa C<sub>2</sub>H<sub>5</sub>OH, 0.1 kPa H<sub>2</sub>O) were used to assess the extent of deactivation and correct all data points by extrapolation to initial time on stream (as illustrated in Figure 3.17, Supporting Information).

The kinetic details of ethanol dehydration to DEE were examined at 404 K over the pressure range of 0.1–50 kPa H<sub>2</sub>O and 0.5–35 kPa C<sub>2</sub>H<sub>5</sub>OH on Sn-Beta-OH-84, and are plotted as DEE site-time yields (404 K, per Sn) in Figure 3.1. Under these conditions, the apparent reaction order with respect to ethanol is ca. 0.5, and the apparent reaction order with respect to water varies monotonically from ca. -0.4 at low water pressures (0.1–3 kPa) to ca. -1.0 at high water pressures (>30 kPa). Ethanol reaction orders that are sub-unity reflect active Sn sites that are not vacant, but partially covered with reactive intermediates that contain at least one ethanol-

**Table 3.1:** Sn contents, micropore volumes, and CD<sub>3</sub>CN Lewis acid site distributions for Beta materials.

Catalyst	Si/M (M wt%) <sup>a</sup>	$V_{micro}$ (cm <sup>3</sup> g <sup>-1</sup> ) <sup>b</sup>	Sn <sub>LA</sub> /Sn <sup>c</sup>	Open/Sn <sup>c</sup>	Closed/Sn <sup>c</sup>
Si-Beta-F	–	0.21	–	–	–
Al-Beta-OH	22 (1.88) <sup>d</sup>	0.24	–	–	–
Si-Beta-OH	–	0.10	–	–	–
Sn-Beta-F-116	116 (1.66)	0.23	1.21	0.45	0.76
Sn-Beta-F-153	153 (1.27)	0.23	0.61	0.13	0.48
Sn-Beta-F-187	187 (1.04)	0.21	0.75	0.21	0.54
Sn-Beta-F-181	181 (1.08)	0.21	1.13	0.44	0.70
Sn-Beta-OH-30 <sup>e,f</sup>	30 (6.08)	0.16	0.72	0.18	0.54
Sn-Beta-OH-41 <sup>e,f</sup>	41 (4.60)	0.19	1.32	0.50	0.82
Sn-Beta-OH-46 <sup>e,f</sup>	46 (4.10)	0.19	0.92	0.22	0.70
Sn-Beta-OH-95 <sup>e,f</sup>	95 (2.00)	0.22	1.22	0.49	0.73
Sn-Beta-OH-80 <sup>e,g</sup>	80 (2.39)	0.22	1.01	0.42	0.59
Sn-Beta-OH-84 <sup>e,h</sup>	84 (2.29)	0.20	1.20	0.24	0.96
Sn-Beta-OH-187 <sup>i</sup>	187 (1.04)	0.23	1.26	0.29	0.97

<sup>a</sup>Determined by AAS<sup>b</sup>Determined by N<sub>2</sub> adsorption minimum in  $\partial V_{ads}/\partial \log(P/P_0)$ <sup>c</sup>Sn<sub>LA</sub> = Lewis acidic Sn sites, from CD<sub>3</sub>CN IR, errors  $\pm 20\%$ <sup>d</sup>Determined by EDS in SEM<sup>e</sup>Data reported in Vega-Vila et al. [151]<sup>f</sup>Parent Si/Al = 19 <sup>g</sup>Parent Si/Al = 29 <sup>h</sup>Parent Si/Al = 54 <sup>i</sup>Parent Si/Al = 34

derived moiety, since kinetically-relevant bimolecular dehydration steps require rates that are second-order in ethanol pressure when sites are unoccupied by ethanol (rate derivation in Section 3.6.1.1, Supporting Information). The fractional ethanol order suggests that more than one surface intermediate is present on Sn sites under these conditions, most likely ethanol monomers and ethanol-ethanol dimers, as proposed on Lewis acid sites on  $\gamma$ -Al<sub>2</sub>O<sub>3</sub> surfaces by DeWilde et al. [88]. Negative fractional water orders indicate that another surface intermediate containing water is present at active sites, which becomes the sole most abundant reactive intermediate (MARI) at high water pressures (>30 kPa) that lead to apparent water orders of  $-1$ , consistent with

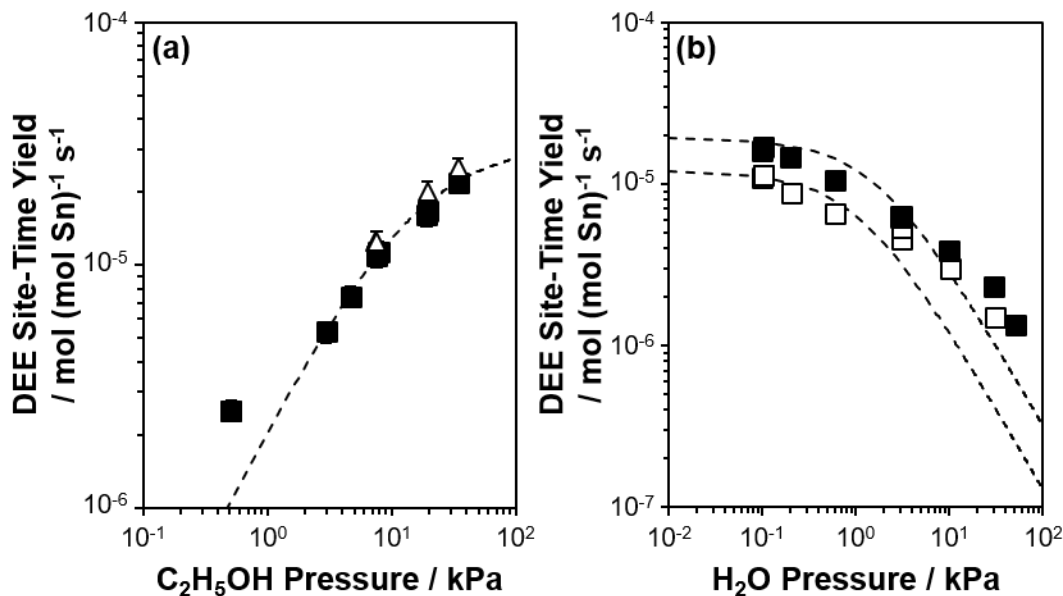


**Figure 3.1:** Diethyl ether site-time yield (per Sn) at 404 K on Sn-Beta-OH-84 (a) as a function of ethanol pressure at constant 0.1 kPa H<sub>2</sub>O, with (△) and without (■) 0.2 Pa co-fed DEE, and (b) as a function of water pressure at constant 20 kPa C<sub>2</sub>H<sub>5</sub>OH (■), and 8 kPa C<sub>2</sub>H<sub>5</sub>OH (□). Dashed lines represent regressed best fits to Eq. 3.2.

inhibition of bimolecular dehydration by ethanol-water dimers [88]. Furthermore, ethanol dehydration rates are insensitive to co-fed DEE (0.2 Pa, 20–90% of the amount formed catalytically, Figure 3.1), indicating that adsorbed DEE or its derivatives are not MARI. Coverage of Sn sites with dimeric intermediates is consistent with hexacoordinated Sn detected in <sup>119</sup>Sn NMR spectra of hydrated samples [68]. These experimental observations must be described by the functional form of the bimolecular ethanol dehydration rate equation, after simplifying assumptions about kinetically-relevant steps and MARI are applied to a general rate equation derived from a series of plausible elementary steps.

Elementary steps for bimolecular ethanol dehydration are proposed in Figure 3.2 and account for open and closed Sn site configurations and ethoxy as an intermediate, as described by Bukowski et al. [180]. Closed sites (\*) may adsorb water (W\*, step 1) and undergo framework bond hydrolysis to form an open site (W<sub>x</sub>\*) with a neighbor-

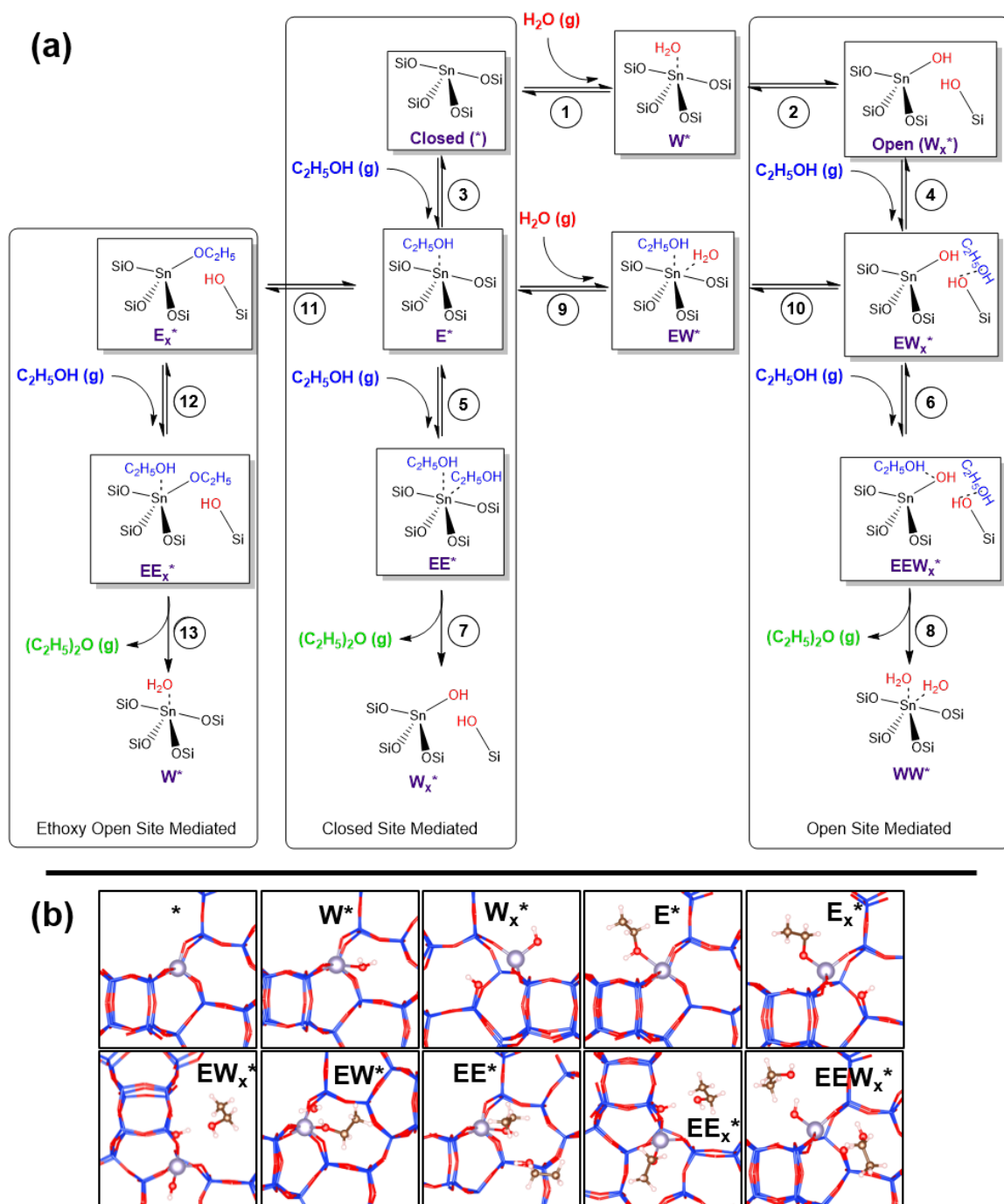


**Figure 3.2:** (a) Interconversion of Sn sites in zeolites and parallel pathways that form diethyl ether, adapted from Bukowski et al. [180]. DFT-optimized structures from [180] are shown in (b).

ing silanol group (step 2), a process that has been detected experimentally using  $^{119}\text{Sn}$  NMR spectroscopy [155] and computed on a variety of metals substituted in zeolite frameworks [113]. In analogous pathways, adsorption of gaseous ethanol onto closed or open sites forms ethanol monomers ( $\text{E}^*$  or  $\text{EW}_x^*$  in steps 3 and 4, respectively), and is followed by adsorption of a second gaseous ethanol to form ethanol-ethanol dimers ( $\text{EE}^*$  or  $\text{EEW}_x^*$  in steps 5 and 6, respectively). Ethanol-ethanol dimer species at closed or open sites ( $\text{EE}^*$  or  $\text{EEW}_x^*$ ) can subsequently undergo kinetically-relevant nucleophilic substitution (steps 7 and 8, respectively) to form adsorbed diethyl ether and water followed by quasi-equilibrated desorption of both products to regenerate the active site. Adsorption of water onto ethanol monomers ( $\text{E}^*$  or  $\text{EW}_x^*$ ) forms an unreactive ethanol-water dimer species ( $\text{EW}^*$ , steps 9 and 10) that inhibits DEE formation rates. In a third parallel pathway, ethanol monomers adsorbed at a closed site ( $\text{E}^*$ ) dissociate in a manner analogous to water dissociation at a closed site that forms open sites (step 2), forming a bound ethoxy group and neighboring silanol group (step 11). This open site configuration is denoted  $\text{E}_x^*$ , and can subsequently react with gaseous ethanol (step 12) to form a co-adsorbed ethoxy-ethanol complex ( $\text{EE}_x^*$ ), which undergoes nucleophilic substitution to form adsorbed DEE (step 13) that desorbs in a quasi-equilibrated step. The parallel pathways and surface intermediates that form DEE, as presented in Figure 3.2, are indistinguishable from steady-state kinetic measurements alone, prompting the use of theoretical modeling to determine which among them contribute to measured DEE formation rates.

DFT-based microkinetic modeling of the ethanol dehydration reaction pathways presented in Figure 3.2 on Sn sites in Beta frameworks is reported elsewhere [180]. Additional steps not shown in Figure 3.2 were included in the microkinetic model (e.g. ethene formation, ethanol-water dimers on open sites) [180], but identified as kinetically-irrelevant under the conditions studied here. This modeling was performed using rigorous entropy treatments that included anharmonicity, and accurately described the experimental rate data presented in Figure 3.1. Degree of rate control analyses, which determine the sensitivity of the product formation rate to the free en-

ergy of a transition state [119], indicated that DEE is formed via only one kinetically-relevant pathway through the ethanol-ethanol dimer on closed sites ( $EE^*$ , step 7), throughout the range of reaction conditions studied here (0.5–35 kPa  $C_2H_5OH$ , 0.1–50 kPa  $H_2O$ , 404 K). In addition, calculated surface coverages revealed that ethanol monomers ( $E^*$ , formed in step 3), ethanol-ethanol dimers ( $EE^*$ , formed in step 5), and ethanol-water dimers ( $EW^*$ , formed in step 9) were MARI in the range of ethanol and water pressures studied here [180]. These assumptions result in a reduced reaction mechanism involving the four steps shown in Figure 3.3, which taken together with the quasi-equilibrium assumption for adsorption steps (Figure 3.3, steps 1–3) give the simplified rate expression in Eq. 3.2 (complete derivation in Section 3.6.1.1, Supporting Information):

$$r_{DEE} = \frac{k_4 K_2(E)}{1 + K_2(E) + K_3(W)}(L) \quad (3.2)$$

Eq. 3.2 accurately describes the rate data in Figure 3.1 (parity plot shown in Figure 3.18, Supporting Information), and captures the fractional order dependences on ethanol and water pressure via the relative coverage terms of  $E^*$ ,  $EE^*$ , and  $EW^*$  surface intermediates. The equilibrium constant  $K_2$  reflects the free energy of the

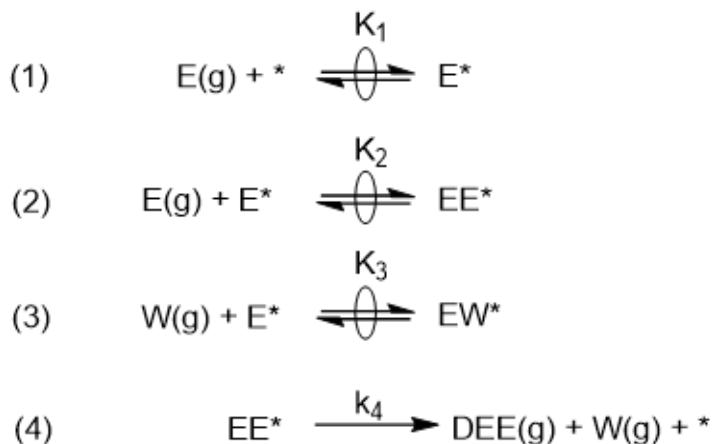


**Figure 3.3:** Simplified series of elementary steps for bimolecular ethanol dehydration. Steps 1–3 correspond to steps 3, 5 and 9 in Figure 3.2. Product desorption is kinetically-irrelevant and lumped into step 4 (step 7 in Figure 3.2) for clarity.

ethanol-ethanol dimer ( $EE^*$ ), relative to the ethanol monomer ( $E^*$ ) and gaseous ethanol. Similarly,  $K_3$  reflects the free energy of the ethanol-water dimer ( $EW^*$ ), relative to the ethanol monomer ( $E^*$ ) and gaseous water. The intrinsic rate constant  $k_4$  represents the free energy difference between the bimolecular ethanol dehydration transition state ( $\ddagger$ ) on closed Sn sites and its precursor, the ethanol-ethanol dimer ( $EE^*$ ) (derivation in Section 3.6.1.2, Supporting Information). The values of these thermodynamic equilibrium constants ( $K_2$ ,  $K_3$ ) and the intrinsic rate constant ( $k_4$ ) provide information about the stability of dimeric intermediates and transition states, relative to specific precursors, at Sn sites within zeolite frameworks.

Rigorous application of Eq. 3.2 to estimate intrinsic rate constants  $k_4$  among Sn-Beta samples requires quantification of the number of active sites ( $L$ ) that turn over during catalysis. Framework Sn atoms adopt both open and closed configurations and can interconvert via elementary steps involving water molecules (Figure 3.2, steps 1 and 2). Sn sites in these two configurations have been quantified by *ex situ* spectroscopy of adsorbed probe molecules ( $CD_3CN$  IR [56], trimethylphosphine oxide  $^{31}P$  NMR [105]), and detected by  $^{119}Sn$  NMR [68,155]. Previous studies suggest that open sites are the dominant active site for glucose isomerization [56] and Baeyer-Villiger oxidation [102] by correlating rates measured at initial times in a batch reactor with open sites quantified by *ex situ*  $CD_3CN$  IR. Here, quasi-steady-state ethanol dehydration rate measurements reflect the reactivity of Sn sites in quasi-equilibrium with reactant and product gas mixtures, rather than their configurations determined *ex situ* that may be present at initial times. Previous microkinetic modeling results imply that Sn sites interconvert and equilibrate to a distribution of open and closed configurations that is dictated by reaction conditions [180], regardless of their *ex situ* structures, suggesting that ( $L$ ) in Eq. 3.2 should represent the total number of framework Sn sites. We next experimentally probe the hypothesis that all framework Sn sites behave catalytically equivalent during ethanol dehydration, prior to interpreting rate and equilibrium constant differences among Sn-Beta samples determined from turnover rate data.

### 3.3.2 Spectroscopic and kinetic interrogation of active Sn identity

Deuterated acetonitrile ( $\text{CD}_3\text{CN}$ ) is a Lewis base that binds through its nitrogen lone pair to Lewis acidic Sn sites, which perturbs IR-active  $\nu(\text{C}\equiv\text{N})$  stretches in the 2265–2350  $\text{cm}^{-1}$  range [56, 185–187]. Here,  $\text{CD}_3\text{CN}$  was used to probe structural changes to Sn sites after they catalyze at least one ethanol dehydration turnover (at 488 K). A representative Sn-Beta-F sample (Sn-Beta-F-187) was exposed to a high-temperature oxidation treatment (823 K), followed by exposure to  $\text{CD}_3\text{CN}$  (303 K) at increasing surface coverages (0.2–2.3  $\text{CD}_3\text{CN}/\text{Sn}$ ) and collection of IR spectra (Figure 3.19, Supporting Information). The IR spectrum acquired after the first dose (ca. 0.2  $\text{CD}_3\text{CN}/\text{Sn}$ ) shows predominantly one peak centered at 2316  $\text{cm}^{-1}$ , which has been assigned to  $\text{CD}_3\text{CN}$  adsorbed at open framework Sn sites [56]. This peak is accompanied by a shoulder for  $\text{CD}_3\text{CN}$  adsorbed at small  $\text{SnO}_x$  domains at 2287  $\text{cm}^{-1}$  [188]. After dosing to saturation coverages and evacuating to remove gaseous species (Figure 3.4, solid trace), these two peaks are convoluted with three other peaks for  $\text{CD}_3\text{CN}$  adsorbed at closed Sn sites (2308  $\text{cm}^{-1}$ ), at silanol groups (2275  $\text{cm}^{-1}$ ), and physisorbed  $\text{CD}_3\text{CN}$  (2265  $\text{cm}^{-1}$ ). Deconvolution into these five component peaks, and quantification using integrated molar extinction coefficients reported elsewhere [56], estimated a total of  $0.79 \pm 0.16$  Lewis acid sites (per total Sn) on Sn-Beta-F-187, which is composed of  $0.23 \pm 0.05$  open sites (per total Sn) and  $0.56 \pm 0.11$  closed sites (per total Sn) (Table 3.2).

After removal of  $\text{CD}_3\text{CN}$  by oxidative treatment at 803 K, Sn-Beta-F-187 was cooled to 488 K to investigate the nature of adsorbed intermediates at open and closed Sn sites formed upon ethanol exposure. Initial doses of ethanol (0.1–0.3  $\text{C}_2\text{H}_5\text{OH}/\text{Sn}$ , Figure 3.20, Supporting Information) were partially adsorbed on the sample, consistent with the rapid growth of gas-phase ethanol peaks in the spectra ( $\nu_{\text{OH}}$ : 3655  $\text{cm}^{-1}$ , 3680  $\text{cm}^{-1}$ ;  $\nu_{\text{CH}}$ : 2983  $\text{cm}^{-1}$ , 2974  $\text{cm}^{-1}$ , 2904  $\text{cm}^{-1}$ ; Figure 3.21, Supporting Information). Ethanol adsorption results in negative peaks corresponding to isolated silanol groups at external crystallite surfaces (3745  $\text{cm}^{-1}$ ), and to isolated internal

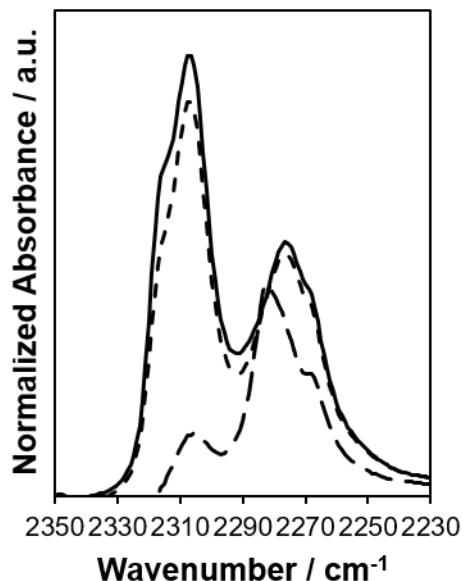


**Figure 3.4:** IR difference spectra (normalized by T-O-T overtone peak area) of  $\text{CD}_3\text{CN}$  adsorbed at saturation coverages on Sn-Beta-F-187 at 303 K, after initial air treatment at 823 K (solid), after 3 h under 6 kPa ethanol flow (long dash), and after re-treating in air at 803 K (short dash).

**Table 3.2:** Lewis acid site densities of Sn-Beta-F-187 and Sn-Beta-OH-187 after air treatment, ethanol exposure, and reoxidation, as determined by  $\text{CD}_3\text{CN}$  IR (303 K).

Sample	Treatment	$\text{Sn}_{LA}/\text{Sn}$	Open/Sn	Closed/Sn
Sn-Beta-F-187	Air, 823 K	$0.79 \pm 0.16$	$0.23 \pm 0.05$	$0.56 \pm 0.11$
	$\text{C}_2\text{H}_5\text{OH}$ (6 kPa), 488 K, 3 h	$0.08 \pm 0.02$	n.d. <sup>a</sup>	$0.08 \pm 0.$
	Air, 803 K	$0.67 \pm 0.13$	$0.16 \pm 0.03$	$0.51 \pm 0.10$
Sn-Beta-OH-187	Air, 823 K	$1.26 \pm 0.25$	$0.29 \pm 0.06$	$0.97 \pm 0.19$
	$\text{C}_2\text{H}_5\text{OH}$ (5 kPa), 403 K, 11 h	$0.39 \pm 0.08$	$0.03 \pm 0.01$	$0.36 \pm 0.07$
	Air, 823 K	$1.13 \pm 0.23$	$0.33 \pm 0.07$	$0.81 \pm 0.16$

<sup>a</sup>n.d.; not detected

silanol groups ( $3735 \text{ cm}^{-1}$ ) [189] generated by the faulted intergrowth of zeolite Beta polymorphs (BEA, BEB) [190] and as part of hydrolyzed-open Sn sites. A broad positive peak at  $3000\text{--}3500 \text{ cm}^{-1}$  also appears, corresponding to perturbed hydroxyl

stretches in silanol groups or ethanol molecules and water molecules that are present. After exposure to excess ethanol ( $>30 \text{ C}_2\text{H}_5\text{OH}/\text{Sn}$ ) and subsequent evacuation, a sharper fraction of the perturbed hydroxyl stretching peak remains centered at ca.  $3445 \text{ cm}^{-1}$  for perturbed silanol groups [189] (Figure 3.20, Supporting Information). These vibrations, taken together with the negative  $3745$  and  $3735 \text{ cm}^{-1}$  peaks and persistent C-H stretches after evacuation, suggest that intermediates derived from ethanol interact with surface hydroxyl groups.

Next, the sample was exposed to flowing ethanol (6 kPa, 488 K) over 3 h at the site-contact time used in flow reactor experiments ( $0.39 \text{ s (mol Sn) (mol total feed)}^{-1}$ ), during which the turnover number is estimated to reach ca. 1.4 (Figure 3.22, Supporting Information). IR spectra showed predominantly gas-phase ethanol peaks after exposure to flowing ethanol (Figure 3.21, Supporting Information), and the subtracted spectrum after subsequent purge and evacuation (Figure 3.23, Supporting Information) showed the same features that appeared during the ethanol dosing experiments described above. When  $\text{CD}_3\text{CN}$  was adsorbed on the sample after these treatments (Figure 3.4, long dash), contributions from open Sn sites were undetectable and those from closed Sn sites were nearly fully suppressed ( $0.08$  closed sites per Sn, Table 3.2). A new IR peak centered at  $2282 \text{ cm}^{-1}$  was observed and attributed to  $\text{CD}_3\text{CN}$  adsorbed at Sn sites containing ethanol-derived intermediates, consistent with the persistent C-H stretches and perturbed O-H stretches after reaction and evacuation (Figure 3.23, Supporting Information), and reminiscent of the  $2280 \text{ cm}^{-1}$  peak for  $\text{CD}_3\text{CN}$  adsorbed at Na-poisoned Sn sites in Sn-Beta-F [106]. Regenerative oxidative treatments (803 K) followed by  $\text{CD}_3\text{CN}$  titration (303 K, Figure 3.4, short dash), resulted in IR spectra that gave an open ( $0.16 \pm 0.03$  per Sn) and closed ( $0.51 \pm 0.10$  per Sn) site distribution identical, within error, to the initial distribution (Table 3.2). The recovery of the initial open-to-closed distribution after Sn sites were converted to a spectroscopically indistinguishable configuration suggests that these initial open and closed site configurations are determined by structural or geometric constraints related to the position of Sn atoms in the zeolite lattice or

their local environment. Similar site reconstruction behavior was also observed on a representative Sn-Beta-OH sample (Sn-Beta-OH-187; Figure 3.24, Supporting Information), with the site quantification shown in Table 3.2. The near-quantitative consumption of open and closed sites, the appearance of the 2282  $\text{cm}^{-1}$  peak, and the reversibility of these changes are consistent with the dynamic interconversion and participation of all Sn sites during ethanol dehydration catalysis [180], regardless of their initial configurations.

The species adsorbed on Sn sites after ethanol dehydration at 403 K, and a subsequent purge step in flowing helium, were probed using on-line mass spectrometry to monitor gaseous products formed during temperature programmed desorption (TPD). Minor amounts of physisorbed ethanol unassociated with Sn sites desorbed at low temperature ( $<500$  K), but this amount decreased with increasing purge time until it was eliminated (16 h). Ethene and water were the predominant species that desorbed from Sn-Beta-F-116 (Figure 3.25, Supporting Information); however, no diethyl ether was observed because the purge step had effectively eliminated ethanol-ethanol dimers as surface species. Desorption of ethene and water is consistent with unimolecular dehydration events that convert adsorbed ethanol monomers ( $\text{E}^*$ ) to ethene and water. Species associated with Sn sites desorbed predominantly as ethene at high temperature (600–800 K), although caution should be taken when interpreting the positions of TPD peak maxima [191–193], which are influenced by re-adsorption during egress from tortuous pores, and bed-scale and particle-scale transport effects. The number of ethene molecules evolved per Sn was 0.9 (at 0.5 and 1.0 h purge times), numbers larger than expected from intermediates covering solely open sites (0.45 per Sn) or closed sites (0.76 per Sn), yet smaller than the total number of Sn sites, consistent with the minority fraction of closed Sn sites (0.08 per Sn) on Sn-Beta-F-187 that could bind  $\text{CD}_3\text{CN}$  even after ethanol exposure (Figure 3.4). These TPD experiments corroborate the IR data and indicate that nearly all Sn sites in Sn-Beta are converted to a common intermediate structure during catalysis, suggesting that (L) in Eq. 3.2 represents the total number of Lewis acidic Sn sites. We note, however, that these

TPD and IR data do not rigorously exclude the possibility that a subset of all Sn sites are responsible for the majority of observed reactivity.

Turnover rates provide quantitative comparisons among samples with different active site densities and framework polarities, and facilitate identifying differences in catalytic behavior among materials [63] and benchmarking of catalytic data measured in different studies [194]. Site-time yields represent rates averaged over the catalyst bed, and are rigorously turnover rates when gradients in reactant and product coverages are differential throughout the bed [195]. In practice, this requirement is met by (i) low conversions (<1%), and either (ii) co-feeding products or (iii) verifying lack of product inhibition. Here, (i) is satisfied in all reported data, (ii) is accomplished by co-feeding H<sub>2</sub>O in excess of the amount produced by reaction, and (iii) was verified for DEE (Figure 3.1a). Bimolecular dehydration turnover rates (404 K, per Sn<sub>LA</sub>) were fit at constant 0.1 kPa H<sub>2</sub>O and 0.5–35 kPa C<sub>2</sub>H<sub>5</sub>OH to obtain an empirical apparent rate constant, according to:

$$r_{DEE,app} = k_{app} P_{C_2H_5OH}^\alpha \quad (3.3)$$

This apparent rate constant (404 K, per Sn<sub>LA</sub>) is invariant within a factor of 3 ( $\Delta G_{app} < 4 \text{ kJ mol}^{-1}$ ) within the series of three Sn-Beta-F samples, and within the series of seven Sn-Beta-OH samples, studied here across a wide range of Sn contents (Figure 3.5), consistent with measured rates that are kinetically-limited according to the Madon-Boudart criterion [196]. Normalization of turnover rates by either the open or closed Sn site densities (CD<sub>3</sub>CN IR, 303 K) does not reduce the variation in  $k_{app}$  values within the Sn-Beta-F or Sn-Beta-OH series (Figure 3.27, Supporting Information), consistent with IR spectra and TPD measurements that suggest all framework Sn sites interconvert to common configurations during catalysis. Although apparent rate constants measured at 0.1 kPa H<sub>2</sub>O imply that Sn-Beta-OH is more reactive than Sn-Beta-F, a broader survey of experimental conditions and mechanistic interpretations (Eq. 3.2) are required to assess whether these differences reflect variations

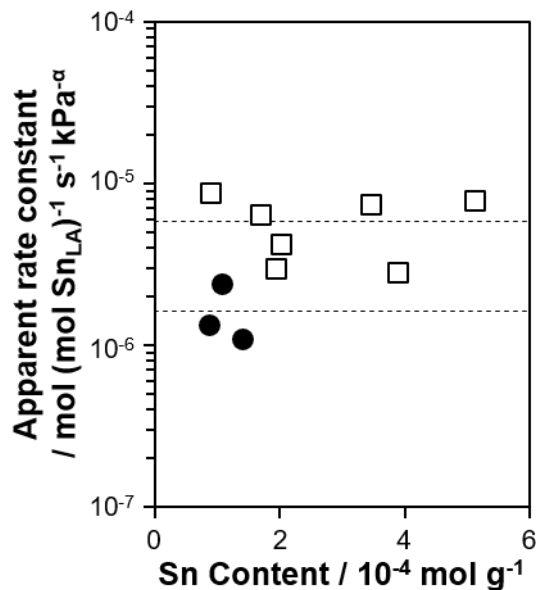


**Figure 3.5:** Apparent rate constants ( $k_{\text{app}}$  in Eq. 3.2) for bimolecular ethanol dehydration (per Lewis acidic Sn) at 404 K and 0.1 kPa  $\text{H}_2\text{O}$  (3–35 kPa  $\text{C}_2\text{H}_5\text{OH}$ ) on Sn-Beta-F (●) and Sn-Beta-OH (□) as a function of Sn content. Dashed lines represent average values among the series of Sn-Beta-F or Sn-Beta-OH samples.

in intermediate surface coverages via equilibrium constants or in transition state stabilities via reaction rate constants.

### 3.3.3 Influence of framework polarity on ethanol dehydration catalysis

Ethanol and water reaction orders reflect the relative coverages of ethanol monomers ( $\text{E}^*$ ), ethanol-ethanol dimers ( $\text{EE}^*$ ), and ethanol-water dimers ( $\text{EW}^*$ ); hence, differences in these orders between Sn-Beta-F and Sn-Beta-OH samples indicate differing extents to which the polarity of the confining environment affects reactive intermediate coverages. Figure 3.6 shows the bimolecular ethanol dehydration turnover rates (per  $\text{Sn}_{\text{LA}}$ ) as a function of ethanol pressure (at 0.1 kPa  $\text{H}_2\text{O}$ ) and water pressure (at 8 and 20 kPa  $\text{C}_2\text{H}_5\text{OH}$ ) on two representative samples, Sn-Beta-F-116 and Sn-Beta-OH-84. The turnover rate is higher on Sn-Beta-OH than on Sn-Beta-F, and the magnitude of the difference depends on both the water and ethanol pressures.

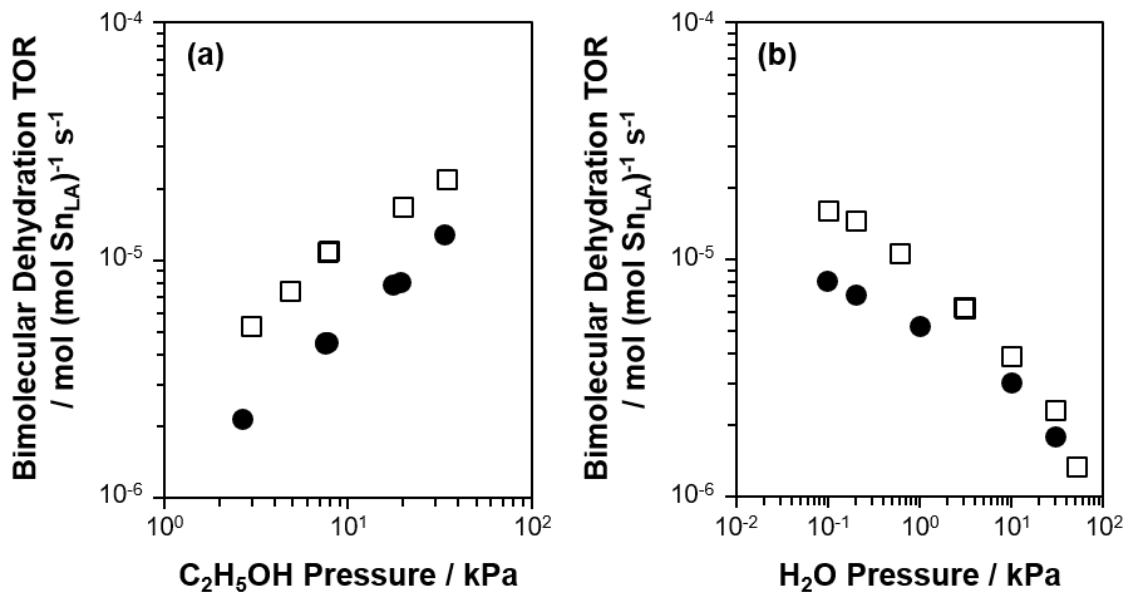


**Figure 3.6:** Bimolecular ethanol dehydration turnover rate (per Lewis acidic Sn) at 404 K on Sn-Beta-OH-84 (□) and Sn-Beta-F-116 (●) (a) as a function of ethanol pressure at constant 0.1 kPa H<sub>2</sub>O, and (b) as a function of water pressure at constant 20 kPa C<sub>2</sub>H<sub>5</sub>OH.

At high water pressures, the apparent reaction order in water is less negative on Sn-Beta-F (−0.5 between 10–30 kPa) than Sn-Beta-OH (−0.6 between 10–30 kPa sharply falling to −1.0 above 30 kPa), suggesting that the ethanol-water dimer is more stable in polar Sn-Beta-OH frameworks under these conditions. Furthermore, at high ethanol pressures (20–35 kPa), the apparent reaction order in ethanol is less positive on Sn-Beta-OH (0.4) than on Sn-Beta-F (0.6), indicating a higher coverage of ethanol-ethanol dimers in polar Sn-Beta-OH frameworks under these conditions. These reaction orders suggest that the framework polarity influences reactivity by changing the coverages of reactive and inhibitory intermediates, but cannot determine whether differences in intrinsic kinetic rate constants also influence measured turnover rate differences. Mechanistic interpretations of measured turnover rates using Eq. 3.2 allow separating the contributions of kinetic rate constants and adsorption equilibrium constants.

Regression of rate data (404 K) measured on four Sn-Beta-OH samples and two Sn-Beta-F samples (0.5–35 kPa C<sub>2</sub>H<sub>5</sub>OH, 0.1–50 kPa H<sub>2</sub>O, 24–33 data points per sample) to Eq. 3.2 allowed estimating two thermodynamic adsorption constants (K<sub>2</sub>, K<sub>3</sub>) and the intrinsic kinetic rate constant (k<sub>4</sub>) on each sample (Table 3.4, Supporting Information). Values of K<sub>2</sub>, which represent equilibrium constants to form ethanol-ethanol dimers from ethanol monomers (Figure 3.3), were higher on Sn-Beta-OH samples ( $6.6\text{--}11 \times 10^{-2}$  kPa<sup>-1</sup>) than on Sn-Beta-F samples ( $2.8\text{--}3.7 \times 10^{-2}$  kPa<sup>-1</sup>). Values of K<sub>3</sub>, which represent equilibrium constants to form ethanol-water dimers from ethanol monomers (Figure 3.3), were also higher on Sn-Beta-OH samples ( $4.3\text{--}16 \times 10^{-1}$  kPa<sup>-1</sup>) than on Sn-Beta-F samples ( $2.5\text{--}2.7 \times 10^{-1}$  kPa<sup>-1</sup>). In general, values of K<sub>3</sub> are an order of magnitude larger than K<sub>2</sub>, regardless of framework polarity, consistent with the prevalence of EW\* intermediates that inhibit turnover rates even at high C<sub>2</sub>H<sub>5</sub>OH pressures (20 kPa, Figure 4). Values of k<sub>4</sub> were similar on both Sn-Beta-OH samples ( $2.6\text{--}10 \times 10^{-5}$  mol (mol Sn<sub>LA</sub>)<sup>-1</sup> s<sup>-1</sup>) and Sn-Beta-F samples ( $2.6\text{--}4.7 \times 10^{-5}$  mol (mol Sn<sub>LA</sub>)<sup>-1</sup> s<sup>-1</sup>).

The effects of framework polarity on rate and equilibrium constants in bimolecular ethanol dehydration were assessed by averaging values of K<sub>2</sub>, K<sub>3</sub>, and k<sub>4</sub> among low-defect (Sn-Beta-F) or high-defect (Sn-Beta-OH) samples of similar polarity, to give the values reported in Table 3.

**Table 3.3:** Sample-averaged rate and equilibrium constants for Sn-Beta-F and Sn-Beta-OH.

Parameter/Catalyst	Sn-Beta-F <sup>a</sup>	Sn-Beta-OH <sup>b</sup>	OH/F Ratio
K <sub>2</sub> / 10 <sup>-2</sup> kPa <sup>-1</sup>	3.3 ± 1.4	8.6 ± 3.3	3
K <sub>3</sub> / 10 <sup>-1</sup> kPa <sup>-1</sup>	2.6 ± 1.0	10 ± 4	4
k <sub>4</sub> / 10 <sup>-5</sup> mol (mol Sn <sub>LA</sub> ) <sup>-1</sup> s <sup>-1</sup>	3.7 ± 0.8	4.6 ± 0.8	1.3

<sup>a</sup>Average of Sn-Beta-F-181 and Sn-Beta-F-153

<sup>b</sup>Average of Sn-Beta-OH-80, Sn-Beta-OH-84, Sn-Beta-OH-41, and Sn-Beta-OH-187

Sample-averaged values of K<sub>2</sub> and K<sub>3</sub> are larger by 3× and 4×, respectively, on Sn sites within high-defect frameworks than low-defect frameworks (Table 3). The higher

$K_2$  and  $K_3$  values on Sn-Beta-OH than Sn-Beta-F are consistent with observed reaction orders in similar ethanol and water pressure regimes (Figure 3.6), which indicate that Sn-Beta-OH catalysts stabilize higher coverages of ethanol-ethanol dimers, yet are more susceptible to inhibition by ethanol-water dimers. In contrast, the sample-averaged value of  $k_4$  is identical within error on Sn-Beta-F and Sn-Beta-OH samples. We note that higher values of  $K_2$  and  $K_3$  on Sn-Beta-OH than on Sn-Beta-F samples, and the identical values of  $k_4$  on the two sets of samples, are independent of the active site type (open, closed, or total Lewis acidic Sn) used to normalize rate data (Tables S.3, S.4, Supporting Information). This kinetic analysis indicates that differences in observed catalytic behavior between polar Sn-Beta-OH and non-polar Sn-Beta-F samples solely reflect differences in the coverages of reactive and inhibitory dimers.

The Gibbs free energy differences (at 404 K) corresponding to differences in sample-averaged values of  $K_2$ ,  $K_3$ , and  $k_4$  are summarized on the reaction coordinate diagram in Figure 3.7, using Eqs. 3.16–3.25 and DFT-predicted values for  $\Delta G_{E^*}$  [180] (Step 1, Figure 3.3). For clarity, Figure 3.7 was constructed assuming that  $G_{E^*}$  is the same value in both polar and non-polar frameworks, which seems reasonable given that the adsorbed ethanol molecule is closely associated with the Sn atom (235 pm distance between Sn and O(H)C<sub>2</sub>H<sub>5</sub> [180], Figure 3.28, Supporting Information), precluding hydrogen bonding (typical O-O distances <300 pm [197,198]) with the nearest potential framework silanol groups at next-nearest-neighbor O atoms (>300 pm from the O atom in C<sub>2</sub>H<sub>5</sub>O(H)-Sn, Figure 3.28, Supporting Information). Formation of the ethanol-water dimer (EW\*) is 7–8 kJ mol<sup>-1</sup> more exergonic than formation of the ethanol-ethanol dimer (EE\*) in either framework ( $K_3/K_2 = 8$ –12, Eq. 3.19), which is qualitatively consistent with DFT-predicted reaction free energies of these elementary steps (13 kJ mol<sup>-1</sup>, BEEF-vdW and AIMD-based entropy [180]). Both dimeric intermediates (EE\* and EW\*) are 3–5 kJ mol<sup>-1</sup> lower in Gibbs free energy (404 K, Eq. 3.22–3.23) within Sn-Beta-OH, consistent with stabilization of the second adsorbed ethanol or water molecule by hydrogen bonding with framework silanol groups. This proposal seems reasonable because the second ethanol molecule in EE\* and the wa-

ter molecule in  $EW^*$  are more distant from the Sn atom than the first ethanol (433 pm distance between Sn and  $O(H)C_2H_5$ , Figure 3.29, Supporting Information; 422 pm distance between Sn and  $OH_2$ , Figure S.21, Supporting Information). These free energies reflect the ability of polar frameworks to stabilize polar adsorbates (either ethanol or water) that form dimeric intermediates with prevalent ethanol monomer species ( $E^*$ ).

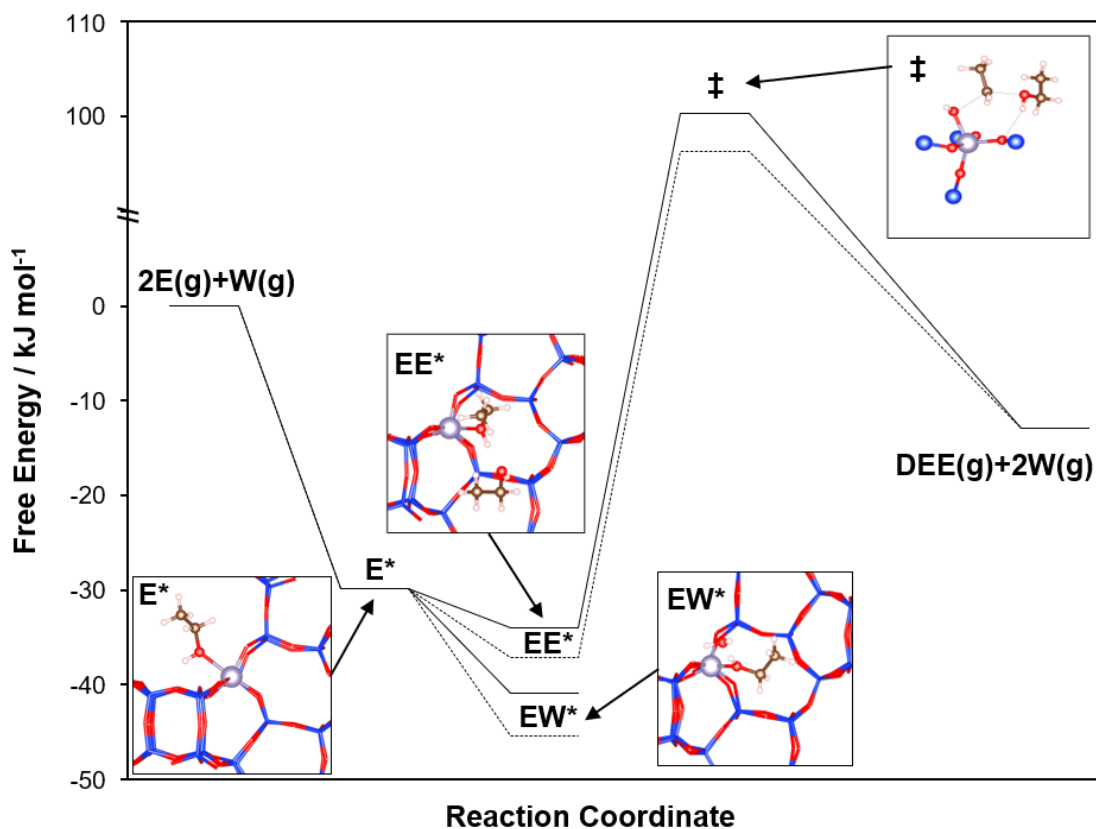


**Figure 3.7:** Reaction coordinate free energy diagram for bimolecular ethanol dehydration on Sn-Beta-F (solid line) and Sn-Beta-OH (dashed line), using predictions from DFT [180] for  $E^*$  in Sn-Beta-F, and the average values of  $K_2$ ,  $K_3$ , and  $k_4$  reported in Table 3 for  $EE^*$ ,  $EW^*$ , and  $\ddagger$ . The depicted adsorbate and transition state geometries were calculated via DFT (BEEF-vdW) [180]. Gas-phase ethanol and water molecules are present in the free energies for  $E^*$  ( $E(g)+W(g)$ ),  $EE^*$  ( $W(g)$ ),  $EW^*$  ( $E(g)$ ), and  $\ddagger$  ( $W(g)$ ), but omitted for clarity in the scheme.

The estimated intrinsic free energy barrier (404 K,  $\Delta G_{\ddagger}$ , Eq. 3.18) to form diethyl ether is the same within polar and non-polar frameworks at ca. 130 kJ mol<sup>-1</sup>, and in reasonable agreement with the DFT-calculated value of 150 kJ mol<sup>-1</sup> [180]. The similarity of intrinsic free energy barriers in polar and non-polar environments implies (via Eq. 3.25) that the transition state is stabilized to a similar extent as the ethanol-ethanol dimeric precursor within the two environments. Thus, the apparent free energy barrier to form the transition state (404 K, relative to E(g) + E\*) is ca. 3 kJ mol<sup>-1</sup> lower within polar Sn-Beta-OH frameworks, and turnover rates are consequently higher, in kinetic regimes corresponding to dilute dimer coverages (Figure 3.6, low H<sub>2</sub>O pressures). In contrast, apparent free energy barriers (404 K) to form the transition state (141 kJ mol<sup>-1</sup>, Sn-Beta-F; 142 kJ mol<sup>-1</sup>, Sn-Beta-OH) are similar, and turnover rates approach similar values on Sn-Beta-F and Sn-Beta-OH, in kinetic regimes wherein ethanol-water dimers (EW\*) become MARI at high water pressures (Figure 3.6b). In this regime, the free energy penalty to desorb water (in EW\*) from polar environments is nearly commensurate with the free energy benefit to adsorb ethanol (forming EE\*) within them. Hence, polar silanol defect groups influence turnover rates through preferential stabilization of reactive (EE\*) and inhibitory (EW\*) dimers, resulting in higher turnover rates at low water pressures within polar frameworks, but which also become more rapidly inhibited as water pressures increase.

We conclude from this kinetic analysis that bimolecular ethanol dehydration rate differences between Sn-Beta samples of different framework polarity result solely from differences in the stabilization of polar ethanol and water molecules that form inhibitory and reactive dimer species within confining environments of different polarity. Next, we use single-component and two-component adsorption measurements on non-catalytic Si-Beta-F and Si-Beta-OH materials to independently probe the influence of framework polarity on the coverages of polar molecules, and to corroborate conclusions drawn from kinetic measurements on catalytic Sn-Beta-F and Sn-Beta-OH materials.

### 3.3.4 Influence of framework polarity on coverages of polar intermediates

Single-component vapor-phase adsorption isotherms (302 K) of water and ethanol were measured on Si-Beta-F and Si-Beta-OH to probe preferences for polar adsorbates introduced by the higher density of silanol defect groups within Si-Beta-OH than Si-Beta-F, absent of adsorption or catalytic effects introduced by Sn heteroatoms. Adsorption isotherms are plotted on a semi-log scale (Figure 3.8) to facilitate comparisons across all relative pressures ( $P/P_0 = 10^{-4}$ – $10^0$ ; linear scale provided in Figure 3.31, Supporting Information). Water adsorption isotherms on each sample (Figure

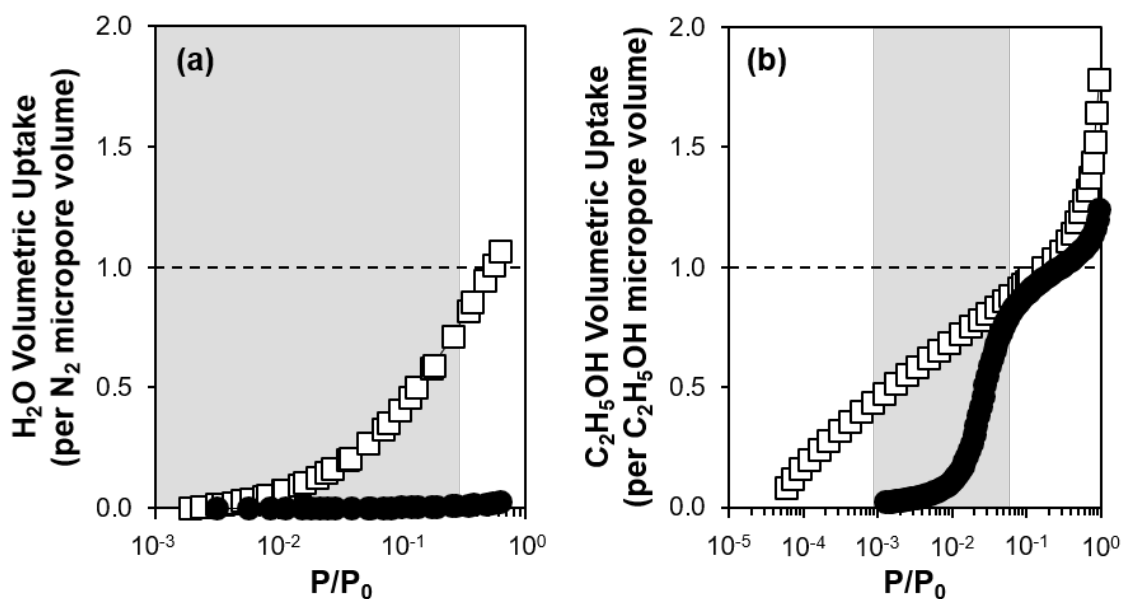


**Figure 3.8:** Single-component adsorption isotherms (302 K) of (a) H<sub>2</sub>O and (b) C<sub>2</sub>H<sub>5</sub>OH on Si-Beta-OH (□) and Si-Beta-F (●). The volume adsorbed is normalized in (a) by the volume of H<sub>2</sub>O that would fill the micropore volume (determined by N<sub>2</sub> adsorption) at its bulk liquid density, and in (b) by the volume of ethanol that fills the pores as determined by the minimum in  $\partial V_{\text{ads}}/\partial \log(P/P_0)$ . The shaded regions reflect the range of gas-phase  $P/P_0$  accessed during kinetic measurements (at 404 K).

3.8a) are normalized by the liquid volume of H<sub>2</sub>O (302 K) that would be equivalent to the micropore volume measured by N<sub>2</sub> at 77 K (Table 3.1), to provide a reference value for the total water uptake that would be nominally commensurate with mi-

cropore filling. On hydrophobic, non-polar Si-Beta-F, the water adsorption isotherm is characteristic of weak adsorbate-adsorbent interactions (Type III), and water uptakes are much lower than the available micropore volume. On hydrophilic, polar Si-Beta-OH, the water adsorption isotherm is characteristic of stronger adsorbate-adsorbent interactions (Type II) [199]. Higher water uptake values on Si-Beta-OH than Si-Beta-F ( $40\times$  at  $P/P_0=0.2$ ) reflect the ability of silanol groups to stabilize water clusters [171], and the higher values than available micropore volume likely reflect contributions from adsorption at defects in external crystallite surfaces.

In contrast to water, ethanol fills the micropore volume of both Si-Beta-OH and Si-Beta-F (Figure 3.8b), evidenced by local minima in semi-log derivative isotherms ( $\partial V_{\text{ads}}/\partial \log(P/P_0)$ , Figure 3.32, Supporting Information) that occur at  $P/P_0$  values of 0.17 and 0.28, respectively. The lower reduced pressure corresponding to ethanol micropore filling reflects the more facile condensation of ethanol within the high-defect Si-Beta-OH framework. Assuming that ethanol occupies the equivalent micropore volume measured by liquid  $N_2$  at 77 K (Table 3.1), these data indicate that ethanol pore filling of Si-Beta-OH and Si-Beta-F occurs at 65% and 88% of its liquid density at 302 K, respectively (Section 3.6.1.6, Supporting Information). Geometric constraints provided by confining micropores are responsible for the inability of ethanol to pack at its liquid density [200], which prevent optimal hydrogen-bonding interactions with other ethanol molecules as occurs in bulk liquid phases. Here, it appears that Si-OH groups that hydrogen bond with adsorbed ethanol molecules further inhibit the efficiency of intermolecular ethanol interactions that are otherwise present in its bulk liquid structure.

Although ethanol fills the pores of both hydrophobic, low-defect Si-Beta-F and hydrophilic, high-defect Si-Beta-OH, notable differences in adsorption behavior are revealed at low relative pressures (Figure 5b). At low  $P/P_0$  values, ethanol forms hydrogen bonds at polar silanol groups within Si-Beta-OH to fill available micropore volume via strong adsorbate-adsorbent interactions (Type I). In contrast, ethanol initially adsorbs within Si-Beta-F via dispersive interactions at non-polar siloxane

bonds, consistent with ethanol adsorption enthalpies at low coverage that are less negative on thermally-treated low-defect silica than on hydroxylated silica [176]. At higher ethanol reduced pressures, non-polar micropores in Si-Beta-F become filled with ethanol in adsorption processes driven by adsorbate-adsorbate hydrogen-bonding interactions (Type V). Comparisons of the single-component adsorption isotherms in the  $P/P_0$  ranges corresponding to ethanol dehydration kinetic measurements (0.5–35 kPa  $C_2H_5OH$ , 0.1–50 kPa  $H_2O$ ,  $P_0$  values at 404 K give the shaded regions in Figure 3.8) suggests that polar Si-Beta-OH frameworks stabilize higher intrapore concentrations of ethanol and water molecules than non-polar Si-Beta-F frameworks under conditions relevant to catalysis. Although single-component adsorption measurements near ambient (302 K) qualitatively indicate that polar silanol groups provide favorable hydrogen-bonding interactions for polar adsorbates, they do not accurately reflect the prevalent intrapore coverages of two-component ethanol-water mixtures, nor the elevated temperatures of catalysis (404 K).

Two-component breakthrough adsorption measurements were performed on Si-Beta-F and Si-Beta-OH at 303 K and 403 K (5.8 kPa  $C_2H_5OH$ , 2.3 kPa  $H_2O$ , Figure 3.33, Supporting Information) to provide additional evidence for the enhanced uptake of polar molecules within polar frameworks under ethanol dehydration reaction conditions. Ethanol uptakes in competitive adsorption experiments at 303 K approached those measured in single-component isotherms at 302 K ( $V_{ads}/V_{micro} = 0.45$ – $0.69$ , Table 3.7, Supporting Information), but were lower because co-adsorbed water occupied some of the micropore volume. The water uptake on Si-Beta-F was nearly  $4\times$  higher than in the single-component case, because ethanol molecules adsorbed within the pores provided hydrogen-bonding interactions for water co-adsorption. These ethanol and water uptakes on Si-Beta-F at 303 K ( $0.16\text{ cm}^3\text{ g}^{-1}\text{ C}_2\text{H}_5\text{OH}$ ,  $0.02\text{ cm}^3\text{ g}^{-1}\text{ H}_2\text{O}$ ) also closely resemble those previously reported using two-component breakthrough measurements on Sn-Beta-F ( $0.14\text{ cm}^3\text{ g}^{-1}\text{ C}_2\text{H}_5\text{OH}$ ,  $0.02\text{ cm}^3\text{ g}^{-1}\text{ H}_2\text{O}$ , 293 K, 1 kPa  $C_2H_5OH$ , 1.7 kPa  $H_2O$  [54]), providing independent verification of these measurements.

The ratio of adsorbed ethanol to water from equilibrium measurements, denoted as  $\Gamma_{x,y}$  ( $x$  = sample type (F, OH),  $y$  = number of components in the measurement (1, 2) or 'k' for kinetics), is taken here as a quantitative descriptor for framework polarity, for which a value of unity indicates no preference for ethanol or water at the chosen reference condition (5.8 kPa  $\text{C}_2\text{H}_5\text{OH}$ , 2.3 kPa  $\text{H}_2\text{O}$ ).  $\Gamma$  values are shown for low-defect (-F, filled bars) and high-defect (-OH, open bars) Beta zeolite samples in Figure 3.9.  $\Gamma_{x,1}$  values estimated from single-component isotherms measured at

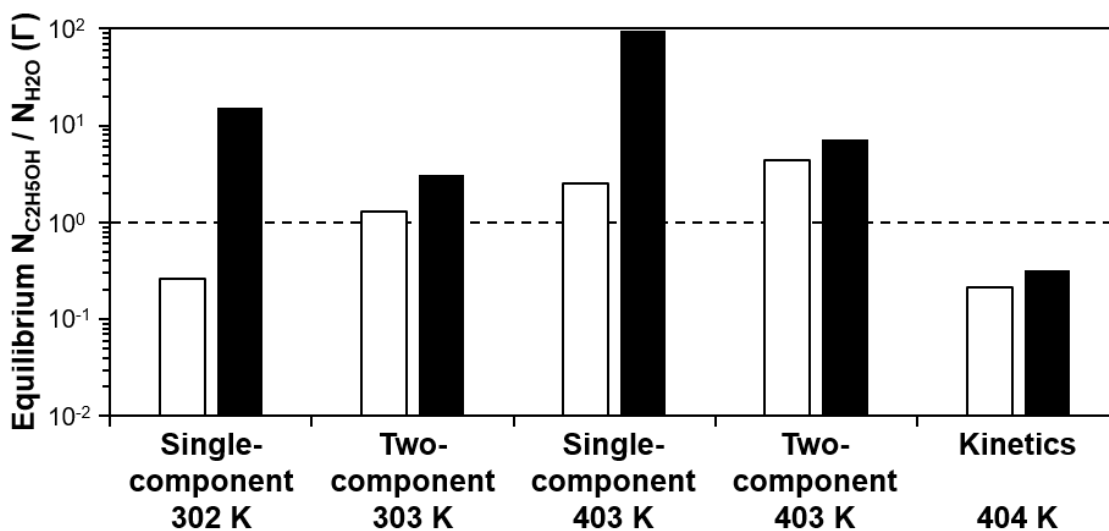


**Figure 3.9:** Ratio of the equilibrium uptake of ethanol to water ( $\Gamma$ ) on Si-Beta-OH ( $\square$ ) and Si-Beta-F ( $\bullet$ ) at 5.8 kPa  $\text{C}_2\text{H}_5\text{OH}$  and 2.3 kPa  $\text{H}_2\text{O}$  as estimated from single-component adsorption isotherms, two-component breakthrough adsorption measurements, and kinetic equilibrium constants ( $\Gamma_{x,k} = K_2 P_{\text{C}_2\text{H}_5\text{OH}} (K_3 P_{\text{H}_2\text{O}})^{-1}$ ). Dashed line indicates no preference for ethanol or water ( $\Gamma = 1$ ).

302 K ( $\text{C}_2\text{H}_5\text{OH } P/P_0 = 0.59$ ,  $\text{H}_2\text{O } P/P_0 = 0.49$ ) indicate that polar frameworks prefer water ( $\Gamma_{\text{OH},1} = 0.26$ ) while non-polar frameworks prefer ethanol ( $\Gamma_{\text{F},1} = 15$ ). The single-component uptakes were adjusted to the reaction temperature (404 K) by recalculating the saturation pressure and comparing uptakes measured at 302 K at corrected  $P/P_0$  values ( $\text{C}_2\text{H}_5\text{OH } P/P_0 = 0.0099$ ,  $\text{H}_2\text{O } P/P_0 = 0.0082$ ), which predict an enhanced preference for ethanol in both frameworks at 404 K ( $\Gamma_{\text{F},1} = 96$ ,  $\Gamma_{\text{OH},1} =$

2.5). Independent of the reference temperature chosen, non-polar frameworks prefer ethanol over water to a greater extent than their polar analogs, which reflects both the lack of hydrogen-bonding interactions for water at non-polar siloxane bridges, and the favorable dispersive contacts for ethyl groups provided by them.

The measured two-component  $\Gamma_{x,2}$  values (Figure 3.9) indicate that the non-polar framework prefers ethanol more than the polar framework, at both 303 K ( $\Gamma_{F,2} = 3.1 > \Gamma_{OH,2} = 1.3$ ) and 403 K ( $\Gamma_{F,2} = 7.3 > \Gamma_{OH,2} = 4.4$ ). Consistent with single-component predictions, both frameworks prefer ethanol to a greater extent at higher temperatures ( $\Gamma_{F,2}$ :  $7.3 > 3.1$ ;  $\Gamma_{OH,2}$ :  $4.4 > 1.3$ ). In contrast to single-component predictions,  $\Gamma_{x,2}$  values are closer to unity, because ethanol-water interactions attenuate adsorbate-adsorbent effects that are more prominent in single-component systems. In the case of Si-Beta-F, co-adsorbed ethanol molecules provide additional hydrogen bonds for adsorbed water that attenuate the preference for ethanol ( $\Gamma_{F,1} = 15$   $\Gamma_{F,2} = 3.1$ ). In the case of Si-Beta-OH, ethanol molecules more effectively compete with water for hydrogen bonding at Si-OH groups ( $\Gamma_{OH,1} = 0.26$   $\Gamma_{OH,2} = 1.3$ ). Despite attenuation of adsorbate-adsorbent interactions in two-component mixtures, the  $\Gamma_{F,2} > \Gamma_{OH,2}$  trend indicates that framework polarity influences the coverages of polar molecules at catalytically-relevant temperatures (403 K).

Furthermore, this trend is consistent with that predicted from kinetically-measured equilibrium constants at 404 K ( $\Gamma_{x,k} = K_2P_{C_2H_5OH} (K_3P_{H_2O})^{-1}$ ;  $\Gamma_{F,k} = 0.32 > \Gamma_{OH,k} = 0.21$ ).  $\Gamma_{x,k}$  values less than unity indicate a greater preference for water over ethanol in kinetic measurements at 404 K, in contrast to breakthrough adsorption measurements ( $\Gamma_{x,2} > 1$ ) at 403 K. This difference seems reasonable because  $\Gamma_{x,2}$  values represent an integral co-adsorption of both ethanol and water molecules within zeolite frameworks absent of Sn sites, while  $\Gamma_{x,k}$  are calculated using equilibrium constants that represent elementary steps in which gas-phase ethanol or water molecules adsorb within zeolite frameworks and associate with an ethanol monomer already adsorbed at a Sn site ( $E^*$ ). Thus,  $\Gamma_{x,k}$  values reflect not only the relative preference of polar and non-polar frameworks for ethanol and water adsorption, but also the relative preference for ad-

sorbing a second molecule (ethanol or water, to form EW\* or EE\*, respectively) at an ethanol preadsorbed at the active Sn site (E\*). Differences in  $\Gamma_{x,k}$  among polar and non-polar frameworks reflect their relative preference for ethanol and water adsorption. The higher  $\Gamma_{F,k}$  than  $\Gamma_{OH,k}$  values estimated from kinetic data (404 K), and the higher values measured in breakthrough adsorption measurements ( $\Gamma_{x,2}$ , 403 K) in the absence of metal site effects, provide quantitative evidence that framework polarity changes the coverages of intermediates during catalysis.

### 3.4 Conclusions

The influence of confining environment polarity on Lewis acid catalysis was probed by studying the kinetics of bimolecular ethanol dehydration on Sn-Beta zeolites with high and low silanol defect densities. Selecting this gas-phase probe reaction avoided complications introduced by molecules present in condensed phases that mediate elementary steps [70], form extended solvating environments [56, 151], or cause rapid deactivation [116, 117, 179]. Gas-phase ethanol and water facilitated interconversion among Sn site configurations during catalysis, as detected by infrared spectroscopy of adsorbed CD<sub>3</sub>CN after reaction and consistent with predictions from theory [180]. Although this evidence does not preclude the existence of a subset of more reactive sites, as reported for other catalytic reactions [56, 68, 102], the conclusions drawn here regarding the effects of framework polarity on ethanol dehydration catalysis do not depend on the choice of active site configuration used to normalize rate data. Turnover rates (per Sn<sub>LA</sub>) measured between 0.5–35 kPa of ethanol and 0.1–50 kPa of water at 404 K were accurately described by a mechanism-derived rate expression supported by DFT-based microkinetic modeling [180], and comparisons among ten different samples with varying Sn contents (Si/Sn = 30–187) were used to eliminate transport corruptions. These treatments enabled assigning chemical significance to turnover rates in the form of regressed rate ( $k_4$ ) and equilibrium ( $K_2$ ,  $K_3$ ) constants, which had characteristic values on samples with different defect densities imparted by synthetic control (post-synthetic, -OH; hydrothermal, -F).

Regressed thermodynamic equilibrium constants were 3–4× higher on Sn sites within polar frameworks, while kinetic rate constants were similar regardless of framework polarity, leading to differences in turnover rates between polar Sn-Beta-OH and non-polar Sn-Beta-F samples. Therefore, the polarity of the confining environments surrounding Sn sites influence ethanol dehydration catalysis by changing the prevalent coverages of the MARI, whose adsorption free energies are sensitive to hydrogen-bonding interactions with silanol defects present in secondary confining environments. The identity of MARI species as productive ethanol-ethanol dimers or inhibitory ethanol-water dimers gave rise to predictable differences in measured reaction orders in ethanol and water pressures on samples with different framework polarity. Furthermore, these framework polarity effects during ethanol dehydration catalysis were corroborated using single-component and two-component adsorption measurements on non-catalytic Si-Beta materials. Changes in equilibrium uptakes on these non-catalytic materials, which differed solely in their framework polarity, were similar to changes in coverages predicted by kinetically-derived equilibrium constants, consistent with analogous polarity effects present during catalysis at Lewis acidic Sn sites.

The sensitivity of reaction intermediates to the polarity of their surrounding environment provides a mechanism to enhance turnover rates when productive and inhibitory intermediates differ in polarity. During ethanol dehydration at low water pressures, turnover rates are higher at Sn sites confined within polar surroundings because coverages of reactive ethanol-ethanol dimers are enhanced, but also decrease more sharply with increasing water pressure because such environments stabilize inhibitory ethanol-water dimers. Hydrophobic, non-polar reaction environments attenuate this inhibition by ethanol-water dimers, which has been recognized as one underlying feature characteristic of water-tolerant Lewis acids [173, 201]. Besides destabilizing inhibitory intermediates by selecting confining environments with incompatible polarity, these results also highlight the benefit of stabilizing productive intermediates within environments of compatible polarity, as suggested in Sn-Beta, [55] TS-1 [47],

and increasingly complex co-solvent systems [50]. Here, studying a gas-phase probe reaction on well-defined catalysts using mechanistic interpretations of rate data and corroborating adsorption measurements gave chemical insights into the role of confining secondary environment polarity, which influenced intermediate coverages and thereby reactivity and the extent of water inhibition, on active sites of similar local structure. The conceptual framework used to interpret these catalytic effects can be extended to probe and predict the behavior of other reactions within microporous materials synthesized with different framework polarity.

### 3.5 Acknowledgements

We acknowledge financial support from the Ralph W. and Grace M. Showalter Research Trust and a 3M Non-Tenured Faculty Award. We thank Juan Carlos Vega-Vila for synthesis of Sn-Beta-OH samples, Dr. James Harris for assistance with IR experiments, and Brandon Bukowski for providing DFT-calculated geometries of ethanol dehydration intermediates. Finally, we thank Brandon Bukowski, Prof. Jeffrey Greeley, Dr. James Harris, and John Di Iorio for technical discussions and feedback on this manuscript.

Reprinted with permission from Journal of Catalysis. 365 (2018) 213–226. Copyright (2018) Elsevier.

### 3.6 Supporting Information

#### 3.6.1 Supplementary Discussion

##### 3.6.1.1 Derivation of bimolecular ethanol dehydration rate equation

Elementary steps refer to Figure 3.3 in the main text.

Assuming the MARI are  $E^*$ ,  $EE^*$ , and  $EW^*$ , the site balance is:

$$(L) = (E^*) + (EE^*) + (EW^*) \quad (3.4)$$

Assuming quasi-equilibrated adsorption steps,

$$(E^*) = K_1(E)(*) \quad (3.5)$$

$$(EE^*) = K_2(E^*)(E) = K_1K_2(E)^2(*) \quad (3.6)$$

$$(EW^*) = K_3(E^*)(W) = K_1K_3(E)(W)(*) \quad (3.7)$$

Therefore,

$$(*) = (L) [K_1(E) + K_1K_2(E)^2 + K_1K_3(E)(W)]^{-1} \quad (3.8)$$

Assuming DEE is formed in the sole kinetically relevant step 4,

$$r_{DEE} = r_4 = k_4(EE^*) \quad (3.9)$$

$$r_{DEE} = k_4K_1K_2(E)^2(*) \quad (3.10)$$

Substituting the site balance gives:

$$r_{DEE} = \frac{k_4K_1K_2(E)^2}{K_1(E) + K_1K_2(E)^2 + K_1K_3(E)(W)}(L) \quad (3.11)$$

which can be simplified to the form:

$$r_{DEE} = \frac{k_4K_2(E)}{1 + K_2(E) + K_3(W)}(L) \quad (3.12)$$

We note that if vacant sites are included in the MARI, then the rate expression becomes:

$$r_{DEE} = \frac{k_4K_1K_2(E)^2}{1 + K_1(E) + K_1K_2(E)^2 + K_1K_3(E)(W)}(L) \quad (3.13)$$

which implies a second-order dependence on ethanol pressure under conditions where \* is the sole MARI:

$$r_{DEE} = k_4K_1K_2(E)^2(L) \quad (3.14)$$

Including quasi-equilibrated elementary steps that lead to water dimers ( $WW^*$ ) as the sole MARI will also lead to a second-order dependence on ethanol pressure:

$$r_{DEE} = \frac{k_4 K_1 K_2}{K_{W^*} K_{WW^*} (W)^2} (E)^2 (L) \quad (3.15)$$

We note that  $WW^*$  are not MARI species under the experimental conditions studied here. As seen in Figure 3.1(b) in the main text, the reaction order in  $H_2O$  at high  $H_2O$  pressures is close to  $-1$ , inconsistent with  $WW^*$  as the sole MARI, which would give rise to a reaction order of  $-2$  (Eq. 3.15). This is also consistent with the microkinetic modeling results of Bukowski et al. which predict  $E^*$ ,  $EE^*$ , and  $EW^*$  are the MARI [180].

### 3.6.1.2 Relation of rate and equilibrium constants to thermodynamic quantities

The adsorption equilibrium constants as derived above have units of inverse pressure. To relate them to free energies, the standard state pressure is required ( $P^\circ = 1$  bar) [202]:

$$K_{2,thermodynamic} = K_2 P^\circ = \exp\left(-\frac{\Delta G_2}{RT}\right) = \exp\left(-\frac{G_{EE^*} - G_{E^*} - G_{E(g)}}{RT}\right) \quad (3.16)$$

$$K_{3,thermodynamic} = K_3 P^\circ = \exp\left(-\frac{\Delta G_3}{RT}\right) = \exp\left(-\frac{G_{EW^*} - G_{E^*} - G_{W(g)}}{RT}\right) \quad (3.17)$$

$k_4$  is readily interpreted as a thermodynamic quantity according to transition state theory, when rates are normalized by the number of active sites ( $L$ ):

$$k_4 = \frac{k_B T}{h} \exp\left(-\frac{\Delta G_\ddagger}{RT}\right) = \frac{k_B T}{h} \exp\left(-\frac{G_\ddagger - G_{EE^*}}{RT}\right) \quad (3.18)$$

The ratio of  $K_2/K_3$  reflects the relative free energy changes of adsorption steps:

$$\frac{K_2}{K_3} = \exp\left(-\frac{\Delta G_2 - \Delta G_3}{RT}\right) = \exp\left(-\frac{G_{EE^*} - G_{EW^*} + G_{E(g)} - G_{W(g)}}{RT}\right) \quad (3.19)$$

Rate and equilibrium constants may also be compared between high-defect and low-defect frameworks:

$$\frac{K_{2,OH}}{K_{2,F}} = \exp\left(-\frac{\Delta G_{2,OH} - \Delta G_{2,F}}{RT}\right) = \exp\left(-\frac{G_{EE^*,OH} - G_{EE^*,F} + G_{E^*,F} - G_{E^*,OH}}{RT}\right) \quad (3.20)$$

$$\frac{K_{3,OH}}{K_{3,F}} = \exp\left(-\frac{\Delta G_{3,OH} - \Delta G_{3,F}}{RT}\right) = \exp\left(-\frac{G_{EW^*,OH} - G_{EW^*,F} + G_{E^*,F} - G_{E^*,OH}}{RT}\right) \quad (3.21)$$

And if  $G_{E^*,OH} = G_{E^*,F}$ :

$$\frac{K_{2,OH}}{K_{2,F}} = \exp\left(-\frac{G_{EE^*,OH} - G_{EE^*,F}}{RT}\right) \quad (3.22)$$

$$\frac{K_{3,OH}}{K_{3,F}} = \exp\left(-\frac{G_{EW^*,OH} - G_{EW^*,F}}{RT}\right) \quad (3.23)$$

Comparing rate constants between high- and low-defect frameworks:

$$\frac{k_{4,OH}}{k_{4,F}} = \exp\left(-\frac{\Delta G_{\ddagger,OH} - \Delta G_{\ddagger,F}}{RT}\right) = \exp\left(-\frac{G_{\ddagger,OH} - G_{\ddagger,F} + G_{EE^*,F} - G_{EE^*,OH}}{RT}\right) \quad (3.24)$$

And using Eq. 3.21,

$$\frac{k_{4,OH}}{k_{4,F}} = \frac{K_{2,F}}{K_{2,OH}} \exp\left(-\frac{G_{\ddagger,OH} - G_{\ddagger,F}}{RT}\right), \text{ or } \frac{k_{4,OH}}{k_{4,F}} \frac{K_{2,OH}}{K_{2,F}} = \exp\left(-\frac{G_{\ddagger,OH} - G_{\ddagger,F}}{RT}\right) \quad (3.25)$$

The derived equations allow comparison of free energies of adsorbed intermediates and transition states between Sn-Beta-F and Sn-Beta-OH catalysts, as illustrated in Figure 3.7, main text.

### 3.6.1.3 Synthesis and characterization of zeolites

Si-Beta-F and dealuminated Beta (denoted Si-Beta-OH) were synthesized to compare the effects of framework defects on adsorption in the absence of a heteroatom. Sn-Beta-F and Sn-Beta-OH samples were synthesized to compare the effects of framework defects on catalysis. Table 3.1 in the main text summarizes the range of Sn

loadings and micropore volumes for these samples. Successful synthesis was confirmed from micropore volumes near  $0.21 \text{ cm}^3 \text{ g}^{-1}$ , together with XRD patterns (Figure 3.10) that possess reflections at  $8^\circ$  and  $22.4^\circ 2\theta$ , characteristic of the Beta topology. The micropore volume of Si-Beta-OH was  $0.10 \text{ cm}^3 \text{ g}^{-1}$  and a significant decrease in XRD peak intensity was observed, consistent with partial destruction of the framework by dealumination treatment, and generation of mesopores, seen in the increase in adsorbed volume at high  $P/P_0$  values (Figure 3.11).

Sn sites were predominantly incorporated within the Beta framework as confirmed by diffuse reflectance UV-Visible (DRUV) spectra (Figure S.3–Figure 3.14) and IR of adsorbed  $\text{CD}_3\text{CN}$  (Figure 3.19, and Table 3.1, main text). Ambient DRUV spectra showed bands centered around  $\sim 230 \text{ nm}$  that shifted toward  $190\text{--}210 \text{ nm}$  upon dehydration, then returned to their ambient position upon rehydration. These shifts are consistent with ligand-to-metal charge transfer for  $\text{Sn}^{4+}$  in octahedral coordination (with  $\text{H}_2\text{O}$ ), and tetrahedral coordination upon dehydration [68, 152]. Sn incorporation within the framework is corroborated by values of the number of Lewis acid sites per Sn atom near unity, quantified by IR spectroscopy of adsorbed  $\text{CD}_3\text{CN}$  [56]. The dehydrated DRUV spectra for Sn-Beta-F-187 (Figure 3.13) and Sn-Beta-OH-30 [151] show broad features centered around  $250\text{--}260 \text{ nm}$  for small  $\text{SnO}_2$  particles, consistent with Lewis acid sites per Sn atom counted  $<1$ . These data indicate that Sn atoms are incorporated in tetrahedral configuration within the Beta framework.

#### 3.6.1.4 IR Spectroscopy of $\text{CD}_3\text{CN}$ after ethanol dehydration catalysis on Sn-Beta-OH-187

The IR spectra from an experiment similar to that described in the main text on Sn-Beta-F-187 are shown in Figure 3.24, and quantified in Table 2 (main text). The details of this experiment are the same, except ethanol treatment occurred at  $403 \text{ K}$  for  $11 \text{ h}$  ( $5 \text{ kPa C}_2\text{H}_5\text{OH}$ ), and the initial ethanol dosing was omitted. Subtracted spectra after treating in flowing ethanol, purging in flowing helium, and exposure to dynamic vacuum (Figure 3.24a) possess the same features discussed in the main text (C-H

stretches, perturbed O-H stretch) that correspond to adsorbed intermediates. Initial doses of CD<sub>3</sub>CN (Figure 3.24b) adsorbed at ethanol-modified Sn sites (2282 cm<sup>-1</sup>), consistent with spectra showing this peak on Sn-Beta-F in the main text. This peak is not prominent in saturated spectra (Figure 3.24c) because the Si-OH peak (2275 cm<sup>-1</sup>) overlaps with it and is present in higher densities ( $6.8 \times 10^{-4}$  mol g<sup>-1</sup>) on Sn-Beta-OH-187 than on Sn-Beta-F-187 ( $8.1 \times 10^{-5}$  mol g<sup>-1</sup>). Quantification of these spectra (Table 3.2, main text) indicates that reoxidation of Sn sites restores the initial open-to-closed distribution, within error, after ethanol treatment quantitatively consumed the open sites, and reduced the closed site density by ca. 60%. This is consistent with the spectra reported on Sn-Beta-F-187, where all open sites (2316 cm<sup>-1</sup>) were consumed after ethanol reaction, but some closed sites (2308 cm<sup>-1</sup>, 0.08 closed/Sn) remained. Some closed sites are detected by CD<sub>3</sub>CN likely because reaction intermediates may desorb from Sn sites during the He purge step (0.5 h) and dynamic vacuum treatment (0.25 h), prior to cooling to 303 K for CD<sub>3</sub>CN adsorption. Furthermore, gas-phase H<sub>2</sub>O transiently present within micropores as a reaction product may also displace some reaction intermediates from Sn sites.

### 3.6.1.5 Temperature programmed desorption after ethanol reaction as a function of purge time

All sites are covered by intermediates during ethanol dehydration catalysis, but when the feed is switched to He purge, the resulting transients in ethanol and water concentration in the gas phase allow water to displace the small number of adsorbed ethanol molecules needed to close the site balance to 1.0 (Figure 3.25). After a 16 h purge, 0.58 ethene per Sn were quantified, indicating some adsorbed ethanol can desorb during the purge step at 404 K.

### 3.6.1.6 Calculation of C<sub>2</sub>H<sub>5</sub>OH density at micropore filling

The micropore filling transition for single-component C<sub>2</sub>H<sub>5</sub>OH isotherms (302 K) on Si-Beta-F and Si-Beta-OH is given by the minimum of  $\partial V_{\text{ads}}/\partial \log(P/P_0)$ , shown

in Figure 3.32. These values were 1.13 mmol g<sup>-1</sup> and 3.12 mmol g<sup>-1</sup> on Si-Beta-OH and Si-Beta-F, respectively. Dividing by the N<sub>2</sub> micropore volume values (Table 3.1, main text), and converting mmol C<sub>2</sub>H<sub>5</sub>OH to g gave the value of the density of C<sub>2</sub>H<sub>5</sub>OH within the micropores: 0.51 g cm<sup>-3</sup> (Si-Beta-OH) and 0.69 g cm<sup>-3</sup> (Si-Beta-F). This was compared with the value for bulk C<sub>2</sub>H<sub>5</sub>OH, 0.78 g cm<sup>-3</sup>.

### 3.6.1.7 Assessment of intraparticle transport corruptions

Intraparticle transport corruptions were ruled out using the Mears criterion [203]. Measured reaction rates are kinetically limited when they are significantly lower than the estimated diffusion rate per catalyst particle:

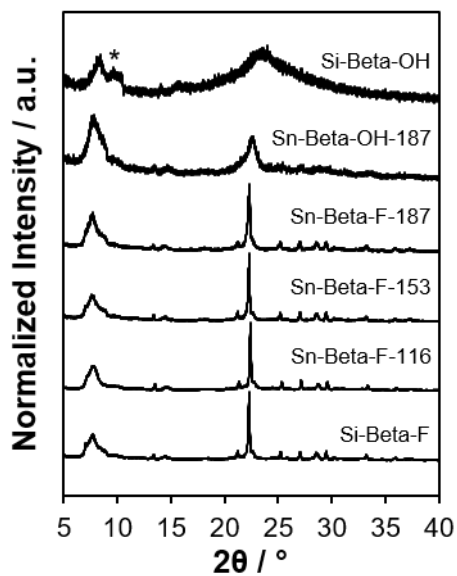
$$\frac{Rr_p^2}{C_s D_e} < \frac{1}{|n|} \quad (3.26)$$

where R is the reaction rate (per particle volume) for an n<sup>th</sup> order reaction (R=kC<sub>s</sub><sup>n</sup>), r<sub>p</sub> is the particle radius, C<sub>s</sub> is the reactant concentration at the external surface of the particle, and D<sub>e</sub> is the effective diffusivity of the reactant within the particle.

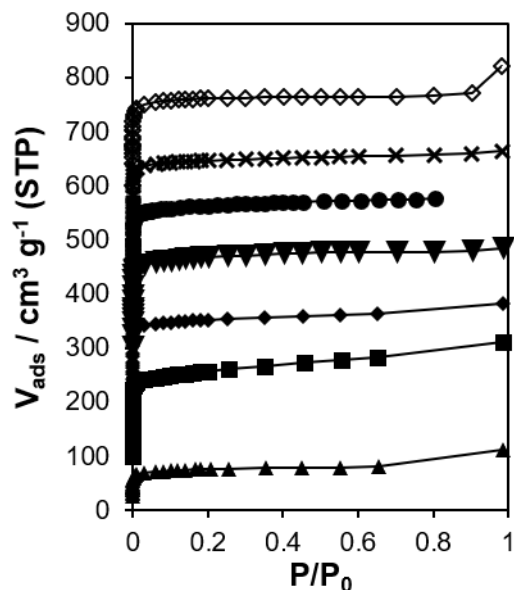
The highest reaction rate per particle volume was measured on Sn-Beta-OH-30 at 35 kPa C<sub>2</sub>H<sub>5</sub>OH, which has a site-time yield of 3×10<sup>-5</sup> mol (mol Sn)<sup>-1</sup> s<sup>-1</sup>. Using the Sn site density of 5.12×10<sup>-4</sup> mol Sn g<sup>-1</sup> and 1.53×10<sup>6</sup> g m<sup>-3</sup> (estimated from the \*BEA unit cell formula), the reaction rate per crystallite volume is R = 2.4×10<sup>-2</sup> mol m<sup>-3</sup> s<sup>-1</sup>. A conservative estimate for the particle radius of 1×10<sup>-6</sup> m was chosen, which is twice the typical radius observed for Sn-Beta-F samples in SEM images [56]. Sn-Beta-OH crystallites are expected to be smaller than this (ca. 250 nm in radius estimated from SEM images [151]). The surface concentration of C<sub>2</sub>H<sub>5</sub>OH was taken as the bulk fluid concentration (10 mol m<sup>-3</sup>), because interparticle gradients are not expected (particles were sieved to 180–250 μm). The effective diffusivity was estimated to be similar to the self-diffusivity of C<sub>2</sub>H<sub>5</sub>OH within FAU zeolites calculated using molecular dynamics simulations at 300 K [204], which is conservative

for the reaction temperature of 404 K. Using these estimates, the left-hand side of Eq. 3.26 was approximately  $8 \times 10^{-6}$ , ruling out intraparticle diffusion corruptions of measured reaction rates.

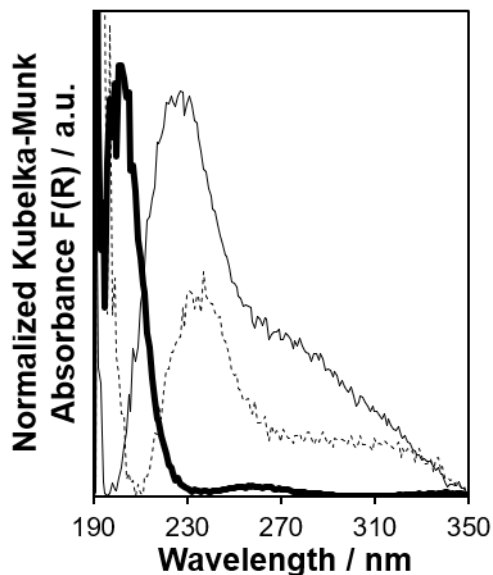
### 3.6.2 Supplementary Figures



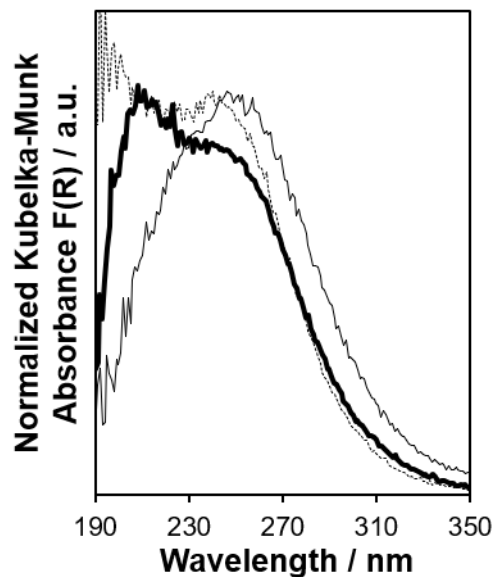
**Figure 3.10:** XRD patterns of Beta zeolites after air treatment (853 K, 10 h), normalized by maximum intensity. \* denotes an artifact from the sample holder. XRD patterns of Sn-Beta-OH samples are reported in [151].



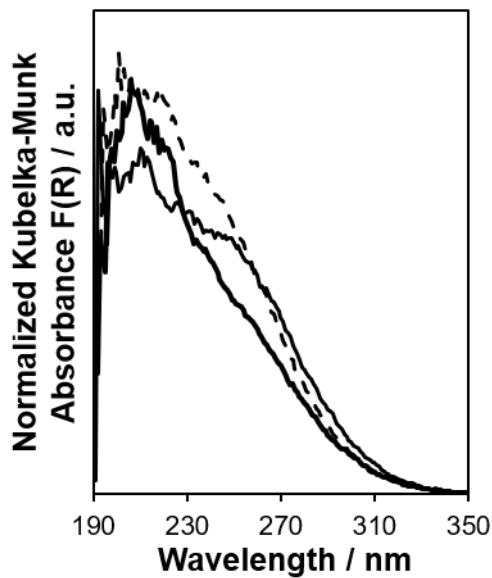
**Figure 3.11:**  $N_2$  adsorption isotherms (77 K) on Si-Beta-OH ( $\blacktriangle$ ), Si-Beta-F ( $\blacksquare$ ), Sn-Beta-F-187 ( $\blacklozenge$ ), Sn-Beta-F-153 ( $\blacktriangledown$ ), Sn-Beta-F-116 ( $\bullet$ ), Sn-Beta-F-181 ( $\times$ ), and Sn-Beta-OH-187 ( $\diamond$ ). Isotherms are offset by multiples of  $100 \text{ cm}^3 \text{ g}^{-1}$  (STP) for clarity. Isotherms on the other Sn-Beta-OH samples are reported in [151]



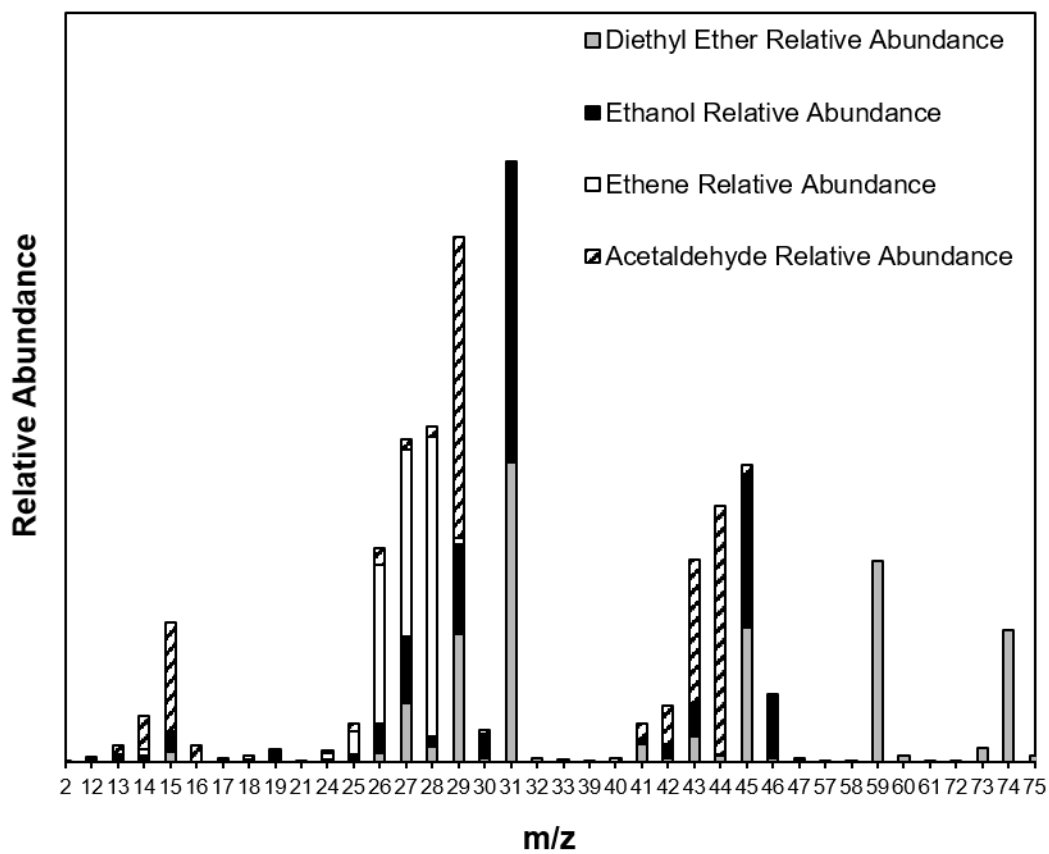
**Figure 3.12:** DRUV spectra of Sn-Beta-F-203 under ambient conditions (thin line), dehydrated at 523 K for 0.5 h under flowing helium (thick line), and rehydrated by cooling under  $H_2O$ -saturated (ambient temperature) helium flow to 303 K (dashed line).



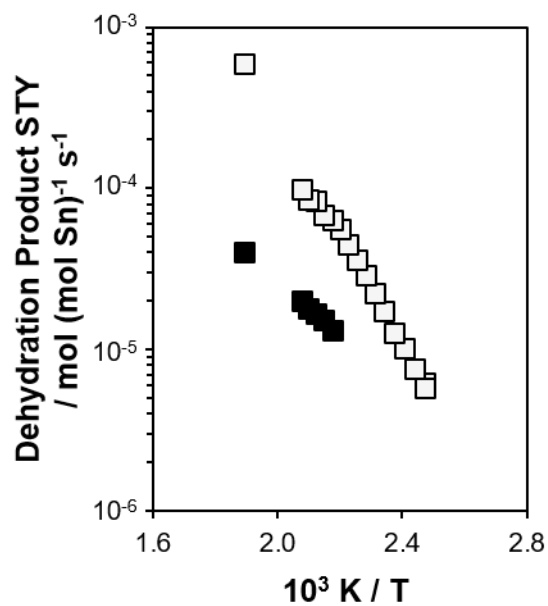
**Figure 3.13:** DRUV spectra of Sn-Beta-F-187 under ambient conditions (thin line), dehydrated at 523 K for 0.5 h under flowing helium (thick line), and rehydrated by cooling under H<sub>2</sub>O-saturated (ambient temperature) helium flow to 303 K (dashed line).



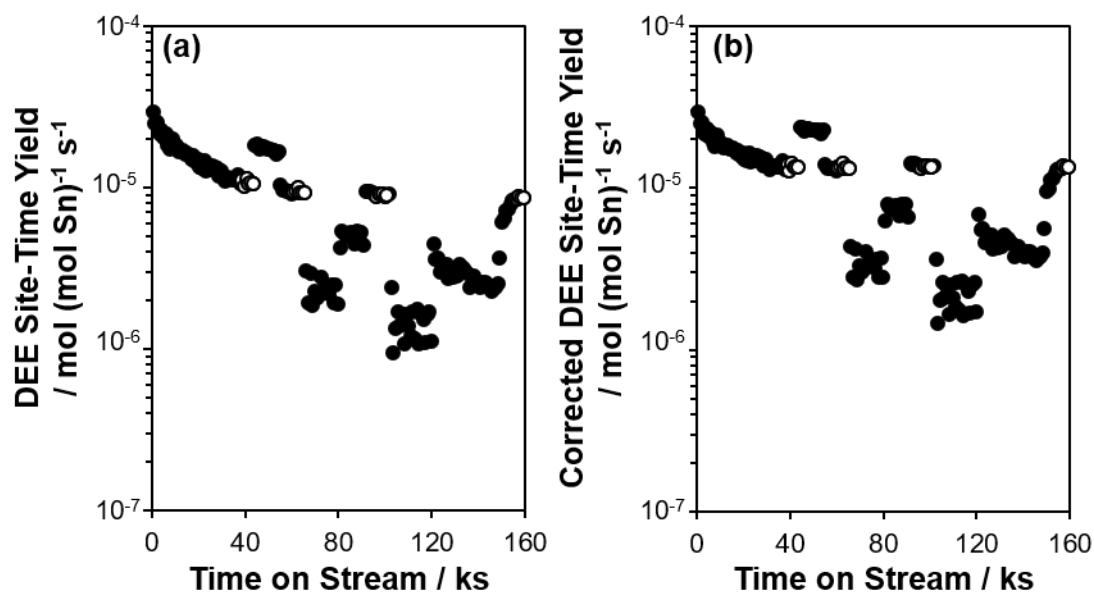
**Figure 3.14:** DRUV spectra of Sn-Beta-F-116 under ambient conditions (thin line), dehydrated at 523 K for 0.5 h under flowing helium (thick line), and rehydrated by cooling under H<sub>2</sub>O-saturated (ambient temperature) helium flow to 303 K (dashed line).



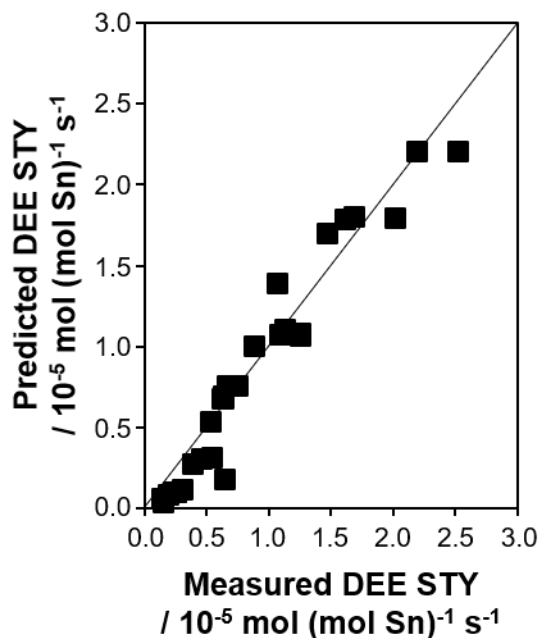
**Figure 3.15:** Normalized relative abundances of possible ethanol dehydration products at  $m/z = 2$  to 75, from NIST [205].



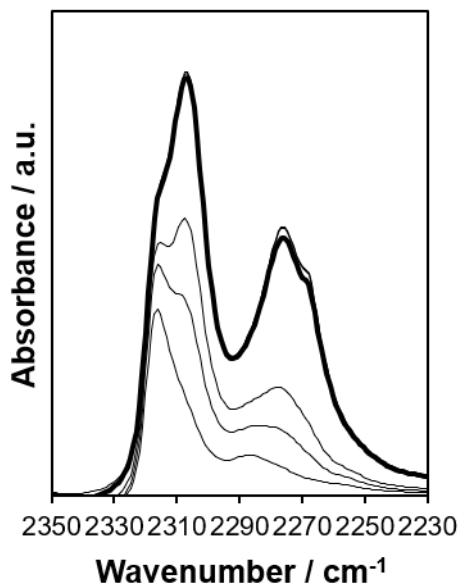
**Figure 3.16:** Site-time yields (per Sn) of diethyl ether ( $\square$ ) and ethene ( $\blacksquare$ ) on Sn-Beta-F-181 at 8 kPa  $\text{CH}_3\text{OH}$ , 0.1 kPa  $\text{H}_2\text{O}$ , and a constant site-contact time of 0.39 s  $(\text{mol Sn}) (\text{mol total feed})^{-1}$  over the temperature range 404–528 K, after stabilization for 12 h on stream at 404 K.



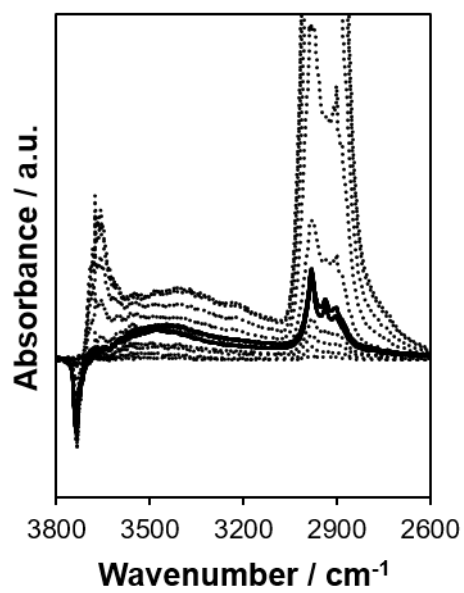
**Figure 3.17:** Diethyl ether (DEE) site-time yield (404 K, per Sn) on Sn-Beta-OH-41 as a function of time-on-stream, with initial conditions of 8 kPa  $\text{CH}_3\text{OH}$  and 0.1 kPa  $\text{H}_2\text{O}$ . Discontinuities represent changes in the inlet pressures. Open symbols are data points measured upon return to initial inlet conditions, and were used to extrapolate the measured data in (a) to initial times to correct for intervening deactivation and give the corrected site time yields reported in (b).



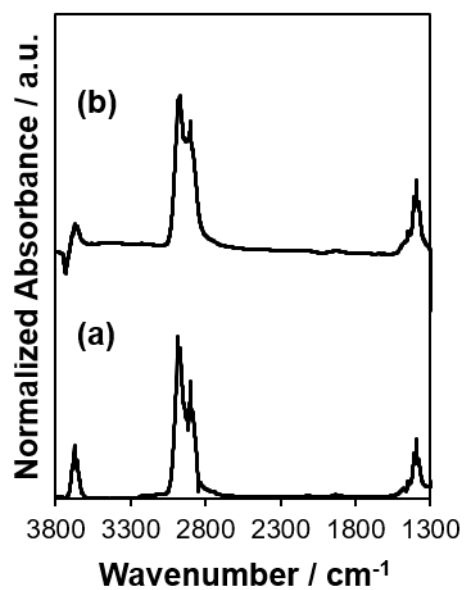
**Figure 3.18:** Parity plot of diethyl ether (DEE) site-time yields (404 K, per total Sn) measured experimentally on Sn-Beta-OH-84 and predicted by best-fit regression to Eq. 3.2 using Athena Visual Studio.



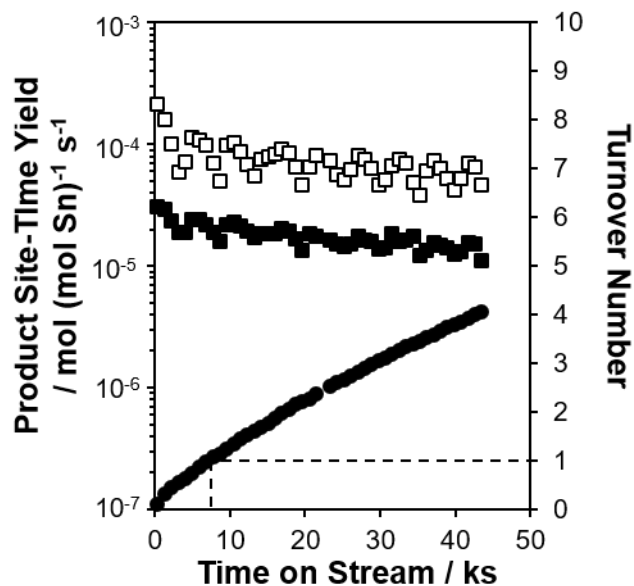
**Figure 3.19:** IR difference spectra of  $\text{CD}_3\text{CN}$  (303 K) on air-treated (823 K) Sn-Beta-F-187 (relative to the vacant surface), with increasing coverage 0.2–2.3  $\text{CD}_3\text{CN}/\text{Sn}$ , and after evacuation to remove gas-phase  $\text{CD}_3\text{CN}$  (bold spectrum).



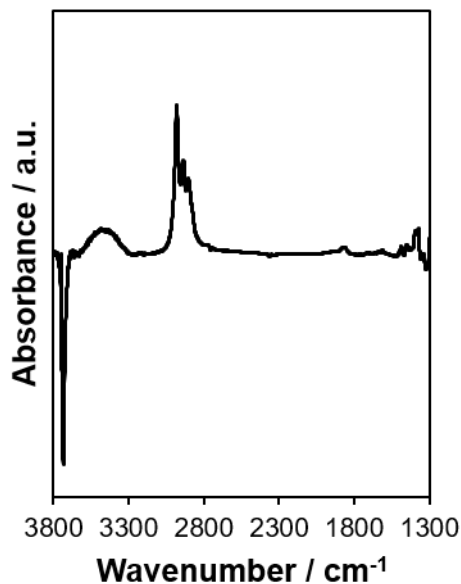
**Figure 3.20:** IR difference spectra of ethanol dosing (relative to the vacant surface, dotted lines) from 0.08–80 C<sub>2</sub>H<sub>5</sub>OH/Sn on Sn-Beta-F-187 at 488 K followed by dynamic vacuum for 300 s (solid lines).



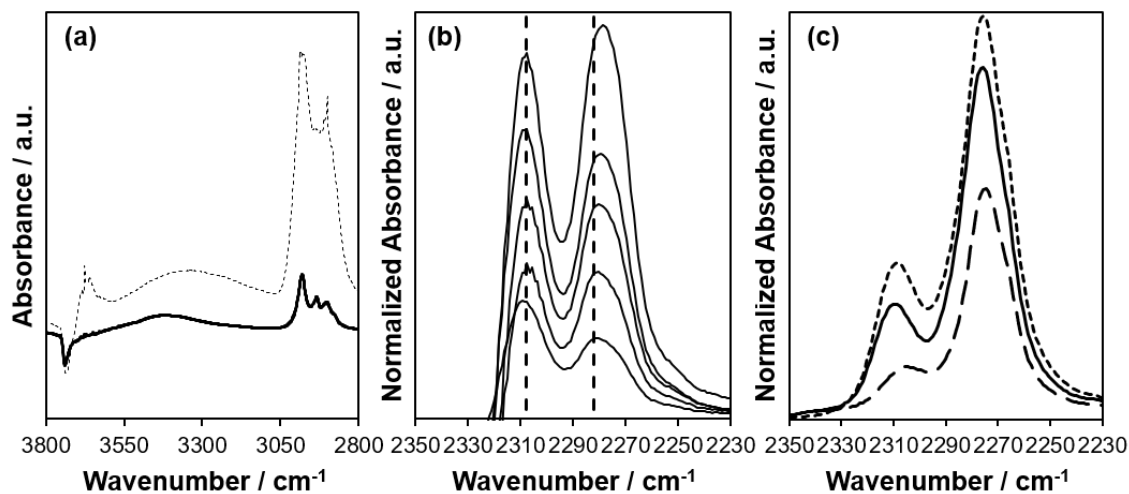
**Figure 3.21:** (a) Baseline-corrected infrared spectrum of 0.4 kPa gas-phase ethanol in flowing helium through an empty IR cell at 298 K, and (b) IR difference spectrum of Sn-Beta-F-187 (relative to the vacant surface) under flowing 6 kPa C<sub>2</sub>H<sub>5</sub>OH after 3 h of reaction at 488 K. Both spectra are normalized by the maximum absorbance in the 1300–3800 cm<sup>-1</sup> range.



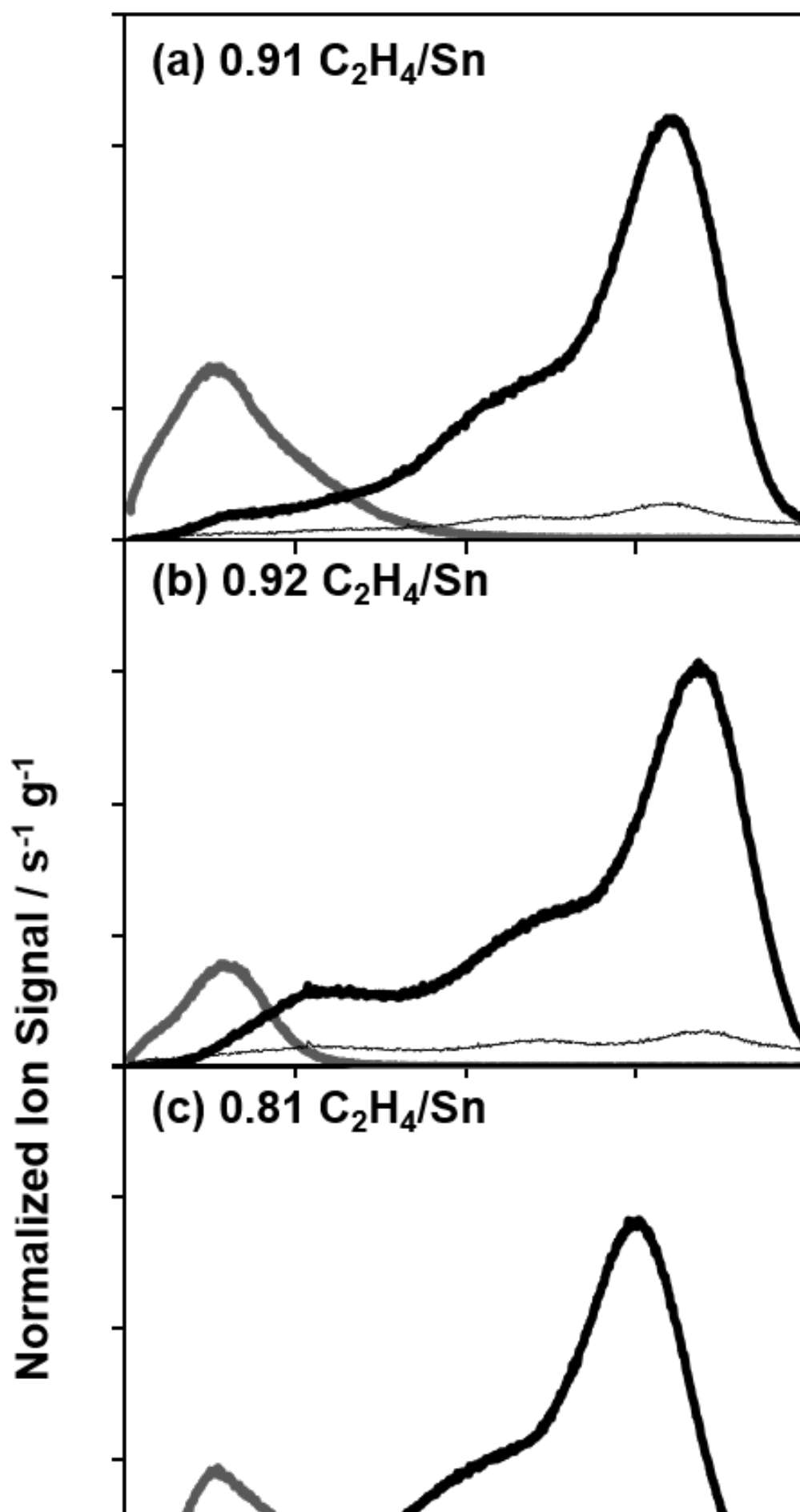
**Figure 3.22:** Site-time yields (488 K, per total Sn) of diethyl ether ( $\square$ ) and ethene ( $\blacksquare$ ), and turnover number ( $\bullet$ ), on Sn-Beta-F-187 at 8 kPa  $\text{CH}_3\text{OH}$  and no co-fed water, as a function of time on stream.



**Figure 3.23:** IR difference spectrum of Sn-Beta-F-187 (relative to the vacant surface) at 488 K, after 3 h of ethanol reaction, 0.5 h helium purge, and 0.25 h dynamic vacuum.



**Figure 3.24:** (a) IR difference spectra of Sn-Beta-OH-187 (relative to the vacant surface) after 11 h under flowing  $\text{C}_2\text{H}_5\text{OH}$  (5 kPa) at 403 K (dashed), followed by 0.5 h purging in flowing helium and 0.25 h of dynamic vacuum (ca. 10 Pa) (solid). (b) Normalized (by T-O-T overtone peak area) IR difference spectra (relative to the vacant surface) of initial doses of  $\text{CD}_3\text{CN}$  (303 K, 0.2–1.0  $\text{CD}_3\text{CN}/\text{Sn}$ ) after the treatments described in (a). Dashed lines indicate peaks at  $2308\text{ cm}^{-1}$  and  $2282\text{ cm}^{-1}$ . (c) IR difference spectra (relative to the vacant surface, normalized by T-O-T overtone peak area) of  $\text{CD}_3\text{CN}$  adsorbed on Sn-Beta-OH-187 at 303 K, fresh (solid), after 11 h under 5 kPa ethanol flow at 404 K (long dash), and after treating in air at 823 K (short dash).



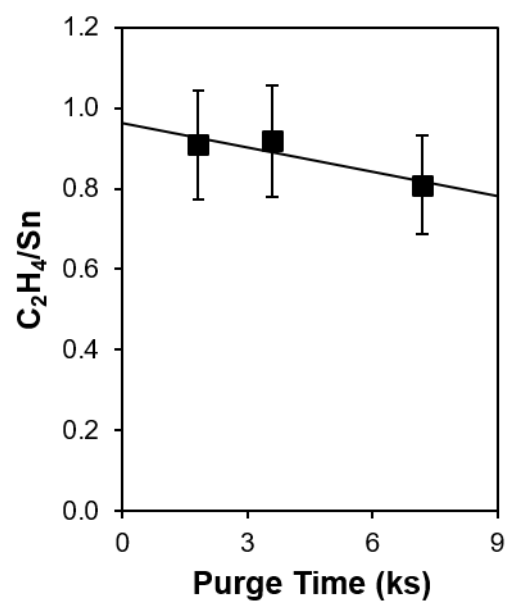


**Figure 3.26:** Ethene evolved per Sn as a function of purge time during temperature programmed desorption in flowing helium ( $1.67 \text{ cm}^3 \text{ s}^{-1}$ ) of ethanol reacted on Sn-Beta-F-116 at 404 K for 8 h, followed by purging in flowing helium ( $1.67 \text{ cm}^3 \text{ s}^{-1}$ ).

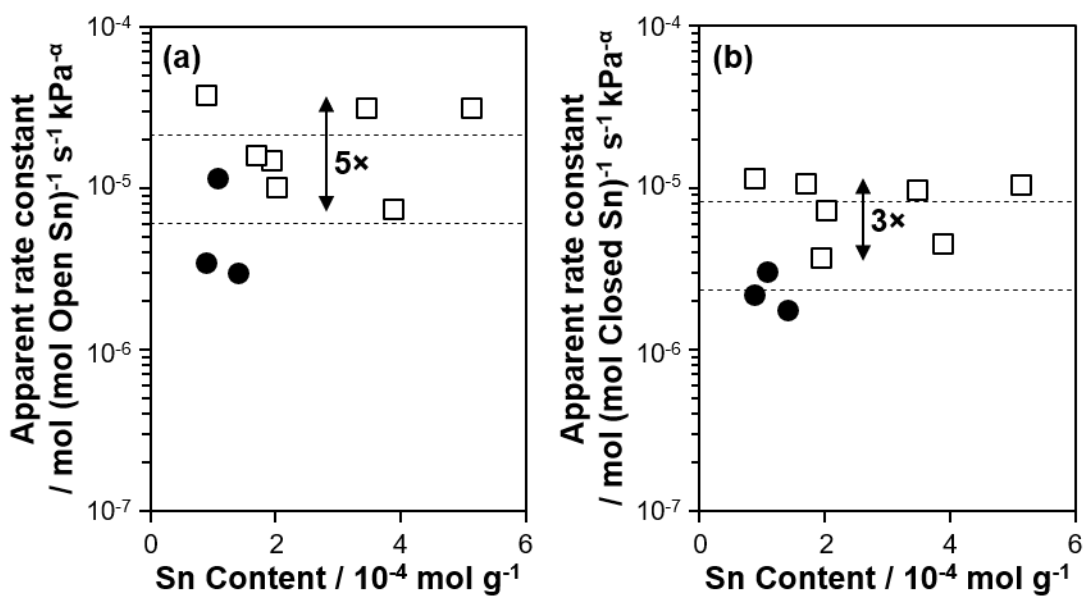


**Figure 3.27:** Apparent rate constant for bimolecular ethanol dehydration normalized by open Sn (a) or closed Sn (b) at 404 K, and 0.1 kPa  $\text{H}_2\text{O}$  ( $P_{\text{EtOH}}=3\text{--}35 \text{ kPa}$ ) derived from empirical power rate law expressions ( $r_{\text{DEE}}=k_{\text{app}}P_{\text{EtOH}}^\alpha$ ) on Sn-Beta-F (●) and Sn-Beta-OH (□) as a function of Sn content. Dashed lines represent averages within all Sn-Beta-F and Sn-Beta-OH samples. Vertical arrows indicate the minimum-to-maximum variation in the Sn-Beta-OH samples.

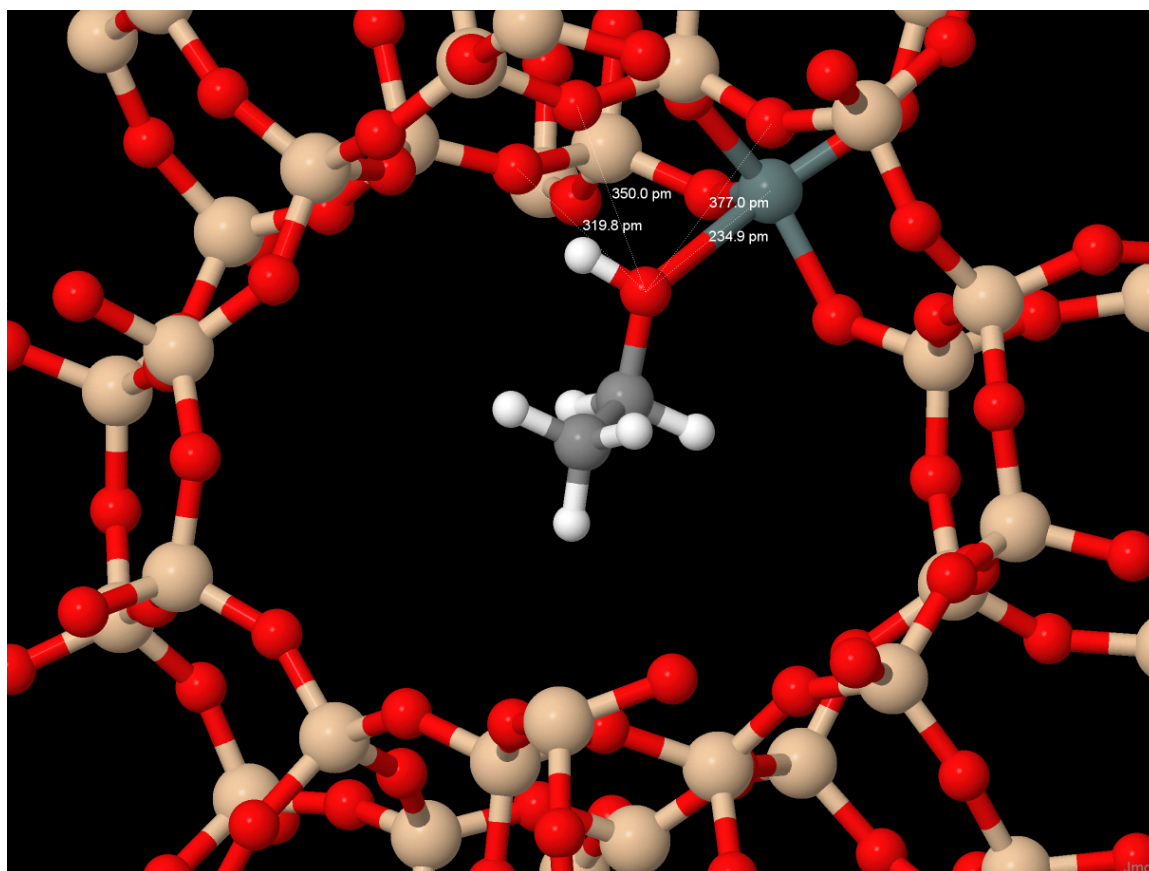


**Figure 3.28:** DFT-optimized geometry of the ethanol monomer ( $E^*$ ) from Bukowski et al. [180] illustrating the Sn-O(H) $C_2H_5$  distance (235 pm), and the minimum distance (320 pm) between the oxygen atom of  $C_2H_5OH$  in  $E^*$  and a next-nearest-neighbor framework oxygen atom, as an approximation of the O-O distance between  $E^*$  and the nearest possible framework Si-OH.

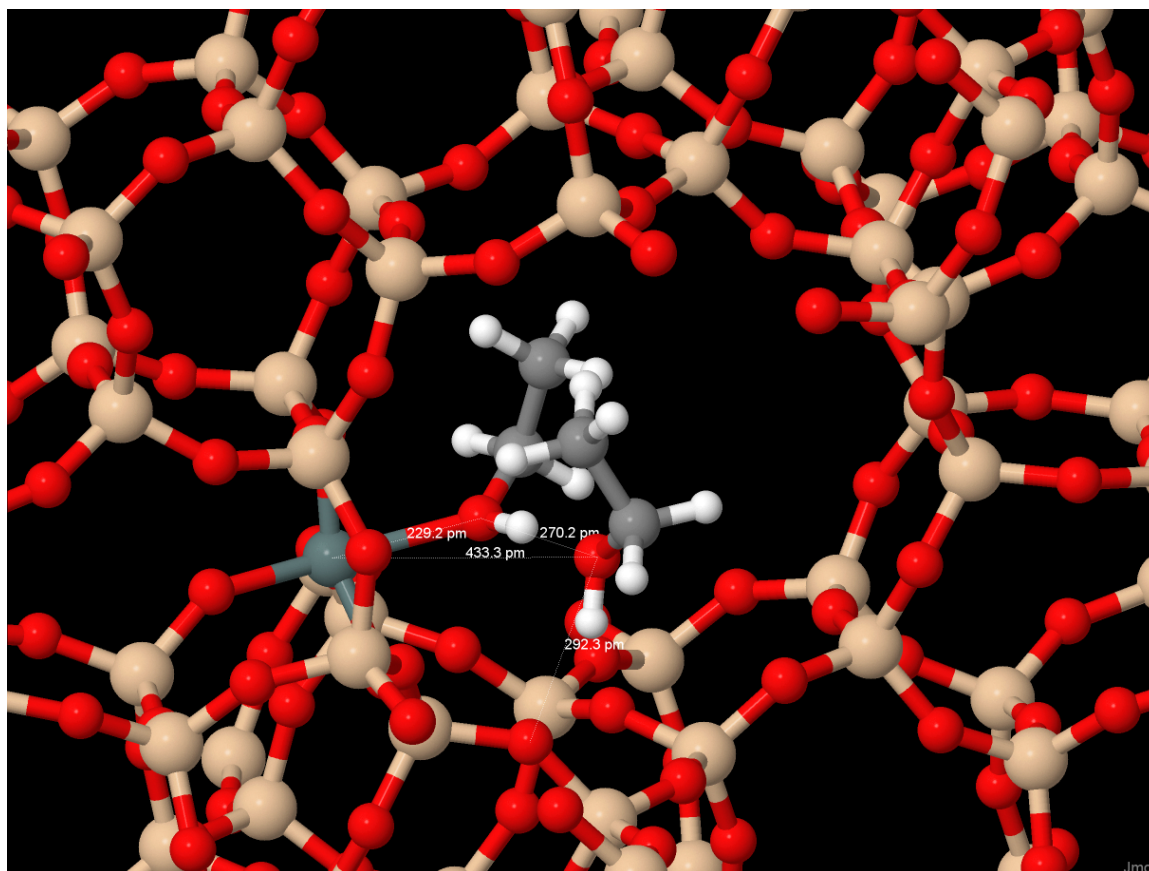


**Figure 3.29:** DFT-optimized geometry of the ethanol-ethanol dimer (EE\*) from Bukowski et al. [180] illustrating O-O distance between ethanol molecules (270 pm), the Sn-O(H)C<sub>2</sub>H<sub>5</sub> distance for the strongly-bound ethanol (229 pm) and the weakly-bound ethanol (433 pm), and the minimum distance between the oxygen atom of the weakly-bound C<sub>2</sub>H<sub>5</sub>OH and a framework oxygen atom (292 pm), as an approximation of the O-O distance between it and the nearest framework Si-OH.

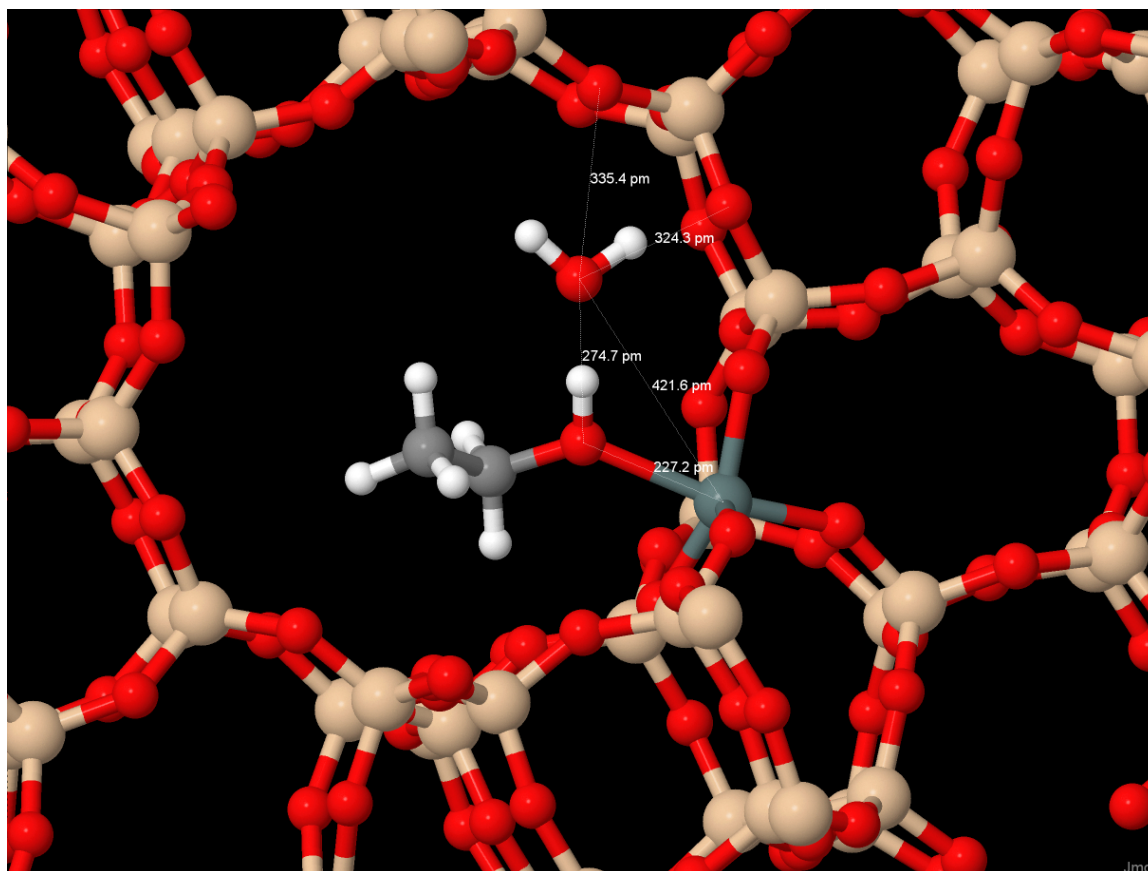


**Figure 3.30:** DFT-optimized geometry of the ethanol-water dimer (EW\*) from Bukowski et al. [180] illustrating O-O distance between ethanol and water (275 pm), the Sn-O(H)C<sub>2</sub>H<sub>5</sub> distance (227 pm), the Sn-OH<sub>2</sub> distance (422 pm), and the minimum distance between the oxygen atom of H<sub>2</sub>O and a framework oxygen atom (324 pm), as an approximation of the O-O distance between it and the nearest framework Si-OH.

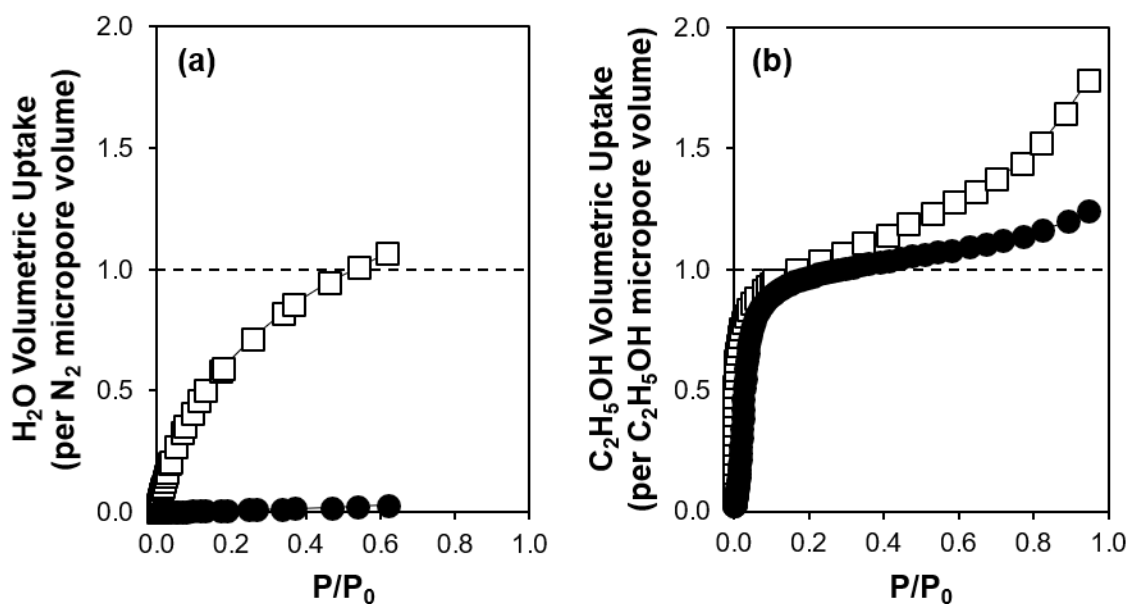


**Figure 3.31:** Linear-scale single-component adsorption isotherms (302 K), reported in Figure 3.8 of the main text, of (a) H<sub>2</sub>O and (b) C<sub>2</sub>H<sub>5</sub>OH on Si-Beta-OH ( $\square$ ) and Si-Beta-F ( $\bullet$ ). The volume adsorbed is normalized in (a) by the volume of H<sub>2</sub>O that would fill the micropore volume (determined by N<sub>2</sub> adsorption) at its bulk liquid density, and in (b) by the volume of ethanol that fills the pores as determined by the minimum in  $\partial V_{\text{ads}}/\partial \log(P/P_0)$ .

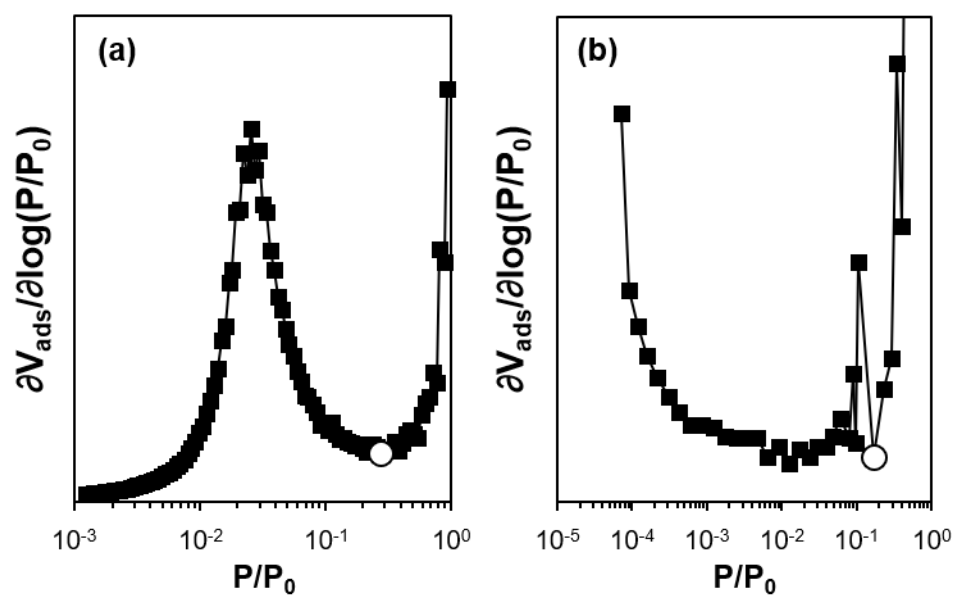


**Figure 3.32:** Semi-log derivative ethanol adsorption isotherms on (a) Si-Beta-F and (b) Si-Beta-OH. Open circles indicate the local minima corresponding to the micropore filling transitions.

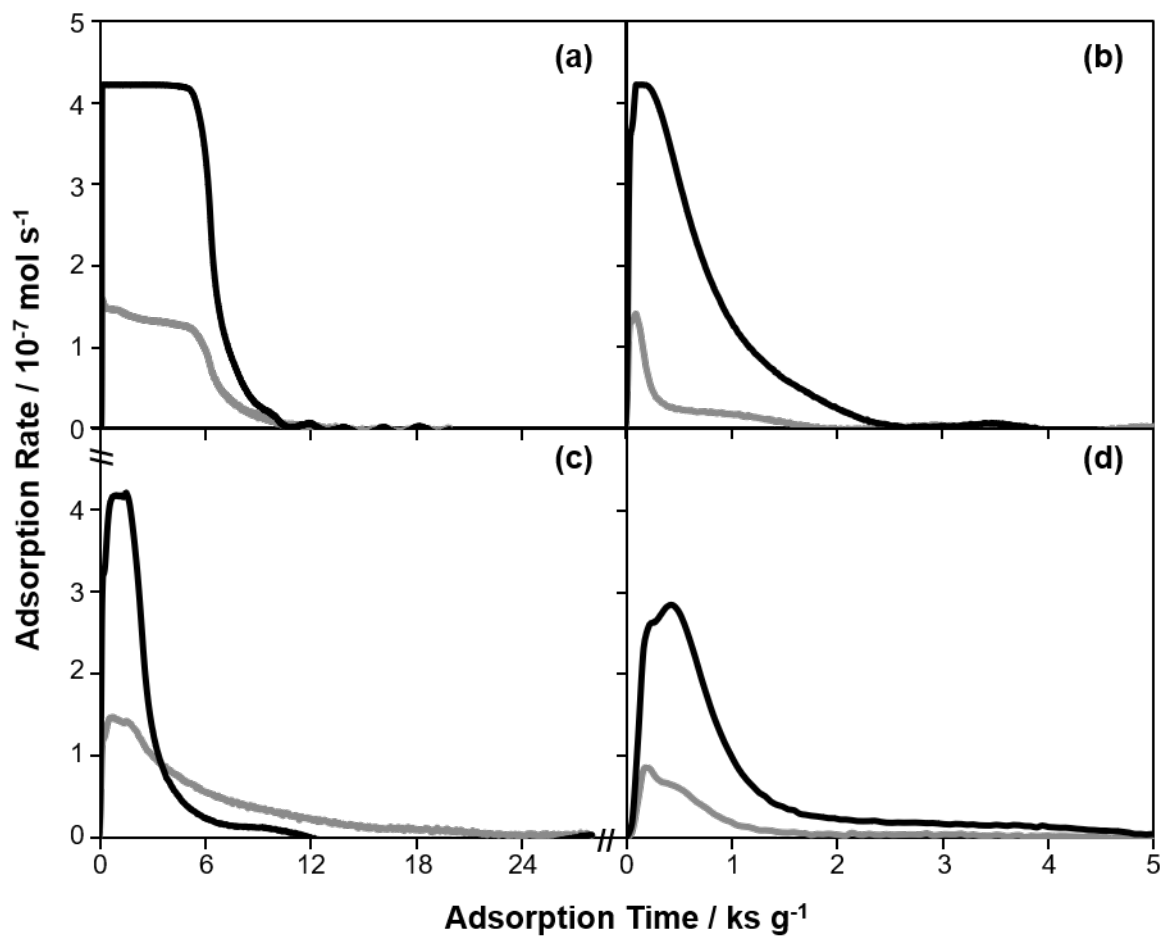


**Figure 3.33:** Two-component breakthrough adsorption measurements of ethanol (5.8 kPa, black) and water (2.3 kPa, gray) on (a) Si-Beta-F at 303 K, (b) Si-Beta-F at 403 K, (c) Si-Beta-OH at 303 K, and (d) Si-Beta-OH at 403 K.

## 3.6.3 Supplementary Tables

**Table 3.4:** Regressed rate and equilibrium constants for each Sn-Beta sample.

Catalyst	$K_2 / 10^{-2} \text{ kPa}^{-1}$	$K_3 / 10^{-1} \text{ kPa}^{-1}$	$k_4 / 10^{-5} \text{ mol (mol Sn}_{LA})^{-1} \text{ s}^{-1}$
Sn-Beta-F-153	$3.7 \pm 1.4$	$2.7 \pm 1.0$	$4.7 \pm 0.9$
Sn-Beta-F-181	$2.8 \pm 1.3$	$2.5 \pm 1.1$	$2.6 \pm 0.7$
Sn-Beta-OH-41	$9.5 \pm 3.6$	$16 \pm 5$	$2.7 \pm 0.4$
Sn-Beta-OH-80	$11 \pm 3$	$6.7 \pm 2.1$	$3.1 \pm 0.3$
Sn-Beta-OH-84	$7.9 \pm 4.0$	$15 \pm 8$	$2.6 \pm 0.6$
Sn-Beta-OH-187	$6.6 \pm 2.7$	$4.3 \pm 1.9$	$10 \pm 2$

**Table 3.5:** Sample-averaged rate and equilibrium constants for Sn-Beta-F and Sn-Beta-OH, assuming (L) = (mol Open Sn).

Parameter	Sn-Beta-F <sup>a</sup>	Sn-Beta-OH <sup>b</sup>	OH/F Ratio
$K_2 / 10^{-2} \text{ kPa}^{-1}$	$3.3 \pm 1.4$	$8.6 \pm 3.3$	3
$K_3 / 10^{-1} \text{ kPa}^{-1}$	$2.6 \pm 1.0$	$10 \pm 4$	4
$k_4 / 10^{-4} \text{ mol (mol Open Sn)}^{-1} \text{ s}^{-1}$	$1.5 \pm 0.3$	$1.8 \pm 0.3$	1.2

<sup>a</sup>Average of Sn-Beta-F-181 and Sn-Beta-F-153<sup>b</sup>Average of Sn-Beta-OH-80, Sn-Beta-OH-84, Sn-Beta-OH-41, and Sn-Beta-OH-187**Table 3.6:** Sample-averaged rate and equilibrium constants for Sn-Beta-F and Sn-Beta-OH, assuming (L) = (mol Closed Sn).

Parameter	Sn-Beta-F <sup>a</sup>	Sn-Beta-OH <sup>b</sup>	OH/F Ratio
$K_2 / 10^{-2} \text{ kPa}^{-1}$	$3.3 \pm 1.4$	$8.6 \pm 3.3$	3
$K_3 / 10^{-1} \text{ kPa}^{-1}$	$2.6 \pm 1.0$	$10 \pm 4$	4
$k_4 / 10^{-5} \text{ mol (mol Closed Sn)}^{-1} \text{ s}^{-1}$	$6.5 \pm 1.0$	$5.1 \pm 1.2$	1.3

<sup>a</sup>Average of Sn-Beta-F-181 and Sn-Beta-F-153<sup>b</sup>Average of Sn-Beta-OH-80, Sn-Beta-OH-84, Sn-Beta-OH-41, and Sn-Beta-OH-187

**Table 3.7:** Ethanol and water uptakes from two-component breakthrough adsorption measurements<sup>a</sup>.

Sample	Temperature (K)	$\Gamma_{x,2}^b$	$V_{EtOH}/V_{micro}^c$	$V_{H2O}/V_{micro}^d$
Si-Beta-F	303	3.1	0.69	0.07
Si-Beta-OH	303	1.3	0.45	0.11
Si-Beta-F	403	7.3	0.11	0.0041
Si-Beta-OH	403	4.4	0.12	0.0079

<sup>a</sup>5.8 kPa C<sub>2</sub>H<sub>5</sub>OH, 2.3 kPa H<sub>2</sub>O

<sup>b</sup> $N_{EtOH}/N_{H2O}$  adsorbed, x = F or OH, 2 denotes two-component

<sup>c</sup>Assuming ethanol liquid density at 303 K and 403 K

<sup>d</sup>Assuming water liquid density at 303 K and 403 K

## 4. DISTINCT CATALYTIC REACTIVITY OF SN SUBSTITUTED IN FRAMEWORK LOCATIONS AND AT DEFECT GRAIN BOUNDARIES IN SN-ZEOLITES

### 4.1 Introduction

The concepts of active sites [62] and their turnover rates [63] are foundational to understanding the reactivity of heterogeneous catalysts; yet, *a priori* knowledge of the structure of active sites is difficult to obtain [64]. Site-time yields (STYs) often serve as a starting point for kinetic analysis, wherein initial assumptions of active site identity can lead to preliminary mechanistic insights that suggest new experiments to refine the structural descriptions of active sites [206]. Even for catalytic solids containing sites that are presumed to be “well-defined,” such as those associated with single atoms, heterogeneous structural features often lead to differences in reactivity. Single metal atoms hosted on supports such as CeO<sub>2</sub> [207], graphene [208], and N-doped carbons [209, 210] enable maximum dispersion of active metals [211], yet potassium thiocyanate [209] and benzoic acid [210] titrations of Fe and Co atoms in N-doped carbons reveal that <30% of the metals are the most reactive sites, in the case of Fe because of their local N-coordination environments [209]. Metal-organic frameworks that host coordinatively-unsaturated “open” metal sites [212] provide well-defined local structures; however, defects caused by missing organic linkers are prevalent [213] and catalytically relevant, such as for two-defect Zr<sub>6</sub> nodes in UiO-66 with lower intrinsic activation energies for bimolecular ethanol dehydration [214]. Brønsted acidic zeolites were once the canonical example of single-site heterogeneous catalysts [215], but their protons exhibit different reactivity either when confined within different-sized void environments, such as in 8-MR side pockets of MOR [216–218] or near

extraframework Al species [84, 219], or when protons are in close proximity with one another [220–222].

Heterogeneous distributions of framework Lewis acid sites in zeolites have similarly been identified and characterized by spectroscopic techniques with and without probe molecules. Boronat et al. [102] first identified two distinct Sn configurations in Sn-Beta zeolites that bind  $\text{CD}_3\text{CN}$  differently so as to perturb IR-active  $\nu(\text{C}\equiv\text{N})$  stretches to either  $2316\text{ cm}^{-1}$  ( $\text{Sn}_{2316}$ ) or  $2308\text{ cm}^{-1}$  ( $\text{Sn}_{2308}$ ) from the gas-phase frequency of  $2265\text{ cm}^{-1}$ , and correlated Baeyer-Villiger oxidation rates (363 K, per g) with the number of  $\text{Sn}_{2316}$  sites. The Davis [68] and Ivanova [155, 223] groups also identified two distinct tetrahedral Sn sites in dehydrated Sn-Beta samples associated with  $^{119}\text{Sn}$  NMR chemical shifts at ca.  $-420\text{ ppm}$  and  $-440\text{ ppm}$ , and the  $-420\text{ ppm}$  peak was correlated with  $\text{Sn}_{2316}$  sites by  $\text{NH}_3$  poisoning experiments [106]. Harris et al. [56] quantified integrated molar coefficients (IMECs) for  $\text{CD}_3\text{CN}$  IR peaks at  $2316\text{ cm}^{-1}$  and  $2308\text{ cm}^{-1}$ , allowing quantitative comparisons with the number of sites titrated *ex situ* by pyridine before glucose isomerization catalysis to provide further evidence that  $\text{Sn}_{2316}$  sites are correlated with the predominant active sites for glucose-fructose isomerization. Lewis et al. [105] dosed trimethylphosphine oxide (TMPO) onto Sn-Beta and identified  $^{31}\text{P}$  NMR resonances at  $55.8$  and  $54.9\text{ ppm}$  that appeared concomitantly as the  $-420\text{ ppm}$   $^{119}\text{Sn}$  NMR resonance shifted to that characteristic of penta-coordinated Sn ( $-582\text{ ppm}$ ) and that correlated with glucose-fructose isomerization STY values (358 K, per mole Sn), while distinct Sn sites with  $^{31}\text{P}$  resonances at  $58.6\text{ ppm}$  and  $57.2\text{ ppm}$  instead correlated with benzaldehyde-acetone aldol condensation STY values (383 K, per mole Sn). In summary, spectroscopic characterizations of Sn-Beta zeolites after dehydration treatments detect a distinct tetrahedral Sn site ( $2316\text{ cm}^{-1}$   $\text{CD}_3\text{CN}$  IR,  $-420\text{ ppm}$   $^{119}\text{Sn}$  NMR,  $55.8/54.9\text{ ppm}$  TMPO  $^{31}\text{P}$  NMR) whose quantity correlates with reaction rates of Baeyer-Villiger oxidation [102] and glucose-fructose isomerization [56, 105], while other sites ( $58.6/57.2\text{ ppm}$  TMPO  $^{31}\text{P}$  NMR) correlate with rates of aldol condensation, but their precise structures and mechanistic origins of their different reactivity still remain incompletely understood.

Various structures for Sn sites in zeolites have been postulated in prior work, the most common of which are depicted in Figure 4.1. Closed Sn sites ( $\text{Sn}-(\text{OSi}\equiv)_4$ ,

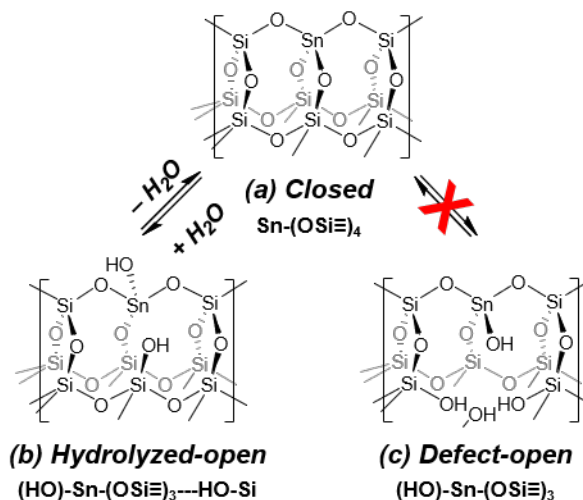


**Figure 4.1:** Structurally distinct configurations of Sn Lewis acid sites in zeolites proposed in the literature.

Figure 4.1a) are generated by isomorphous substitution of  $\text{Sn}^{4+}$  into framework positions occupied by  $\text{Si}^{4+}$  in pure- $\text{SiO}_2$  zeolite crystal structures. Water may react with closed Sn to hydrolyze one Sn-O-Si bond and generate a hydrolyzed-open site ( $(\text{HO})-\text{Sn}-(\text{OSi}\equiv)_3\text{---HO-Si}$ , Figure 4.1b) with a proximal Si-OH group. DFT-calculated activation enthalpies for glucose-fructose isomerization were lower by  $30 \text{ kJ mol}^{-1}$  at hydrolyzed-open Sn sites than at closed Sn sites [68], which is attributed to participation of the proximal Si-OH group in the kinetically-relevant intramolecular 1,2-hydride shift step [69, 70]. Treating Sn-Beta-F zeolites in aqueous  $\text{NaNO}_3$  solutions, which was intended to exchange Na for proximal Si-OH group protons at hydrolyzed-open Sn sites, decreased glucose-fructose isomerization conversion values, consistent with the involvement of a proximal Si-OH group in this reaction [106].  $^1\text{H}$  cross-polarized (CP)  $^{119}\text{Sn}$  NMR spectra (pretreated at 393 K under vacuum) that detect only the -420 ppm peak provided evidence that these are hydrolyzed-open Sn sites [68], but later studies report disappearance of this CP peak after high-temperature ( $>523 \text{ K}$ ) dehydration treatments under vacuum [155]. In addition, interconversion among

hydrolyzed-open and closed sites is thermodynamically accessible according to DFT calculations [113, 180], and has been observed by two-dimensional proton-detected  $^1\text{H}/^{119}\text{Sn}$  correlation NMR [224]. Characterizations that detect multiple site configurations (e.g.,  $\text{CD}_3\text{CN}$  IR,  $^{119}\text{Sn}$  NMR) performed after high-temperature treatments under vacuum therefore would not sample hydrolyzed-open sites because they become equilibrated to closed configurations, supporting proposals for an additional site configuration called “defect-open” (Figure 4.1c) on the basis of  $^{119}\text{Sn}$  DNP NMR and DFT calculations [111], wherein deletion of a neighboring Si atom generates an open site  $(\text{HO})\text{-Sn}\text{-(OSi}\equiv\text{)}_3$  and three additional Si-OH groups that are not sufficiently proximal to the stannanol to re-close the site. A defect-open cluster model was also used in DFT calculations by Boronat et al. [102] to rationalize the frequency shift of the  $2316\text{ cm}^{-1}$  peak in  $\text{CD}_3\text{CN}$  IR; however, it is unclear how defect-open sites are formed during crystallization, and there is a dearth of definitive experimental evidence for their existence. 2D  $^{119}\text{Sn}$  NMR has been used to propose that distinct Sn configurations exist at different T-sites in Beta frameworks [111, 225], and multi-shell EXAFS fittings have invoked additional site configurations such as 3-coordinate Sn with a nearby charge-balancing  $\text{SiO}^-$  as a frustrated Lewis pair [226], and paired Sn sites at T5/T6 sites in 6-MR [108]; however, these site proposals have not yet been verified by quantitative characterization and catalytic data. Identifying probe reactions sensitive to distinct site configurations is integral to this effort, as in the connections made between glucose-fructose isomerization turnover rates and  $\text{Sn}_{2316}$  sites identified by  $\text{CD}_3\text{CN}$  IR [56].

In our previous work [180, 227] studying the gas-phase bimolecular ethanol dehydration reactivity of Sn-Beta, theory and experiment together suggested that all Lewis acidic Sn sites, if speciated in the closed form, contribute to measured turnover rates. DFT calculations and microkinetic modeling indicated that interconversion between closed and hydrolyzed-open framework Sn sites was quasi-equilibrated during ethanol dehydration catalysis (404 K, 0.5–35 kPa  $\text{C}_2\text{H}_5\text{OH}$ , 0.1–50 kPa  $\text{H}_2\text{O}$ ), and that the most abundant reactive intermediate (MARI) species at steady-state were adsorbed

monomeric and dimeric intermediates at closed Sn sites, which accurately described measured STYs (per total Sn) and reaction orders in both H<sub>2</sub>O and C<sub>2</sub>H<sub>5</sub>OH [180]. After ethanol dehydration catalysis, CD<sub>3</sub>CN titrants detected Sn sites predominantly covered by indistinguishable MARI species ( $\nu(\text{C}\equiv\text{N}) = 2282 \text{ cm}^{-1}$ ), whereas distinct Sn sites (Sn<sub>2316</sub>, Sn<sub>2308</sub>) were present in equivalent quantities before catalysis and after regenerative oxidation treatments (823 K) in flowing air [227]. Complete coverage by indistinguishable MARI after ethanol dehydration is consistent with both types of Lewis acidic Sn contributing to measured turnover rates, as was assumed previously [227]; however, as noted previously, this does not preclude the existence of a subset of intrinsically more reactive sites. The recovery of initial Sn configurations after catalysis indicates their distinct structural identities are retained and perhaps related to distinct local coordination environments.

Here, the choice of gas-phase ethanol dehydration as a catalytic probe reaction of Lewis acid zeolites enables performing *in situ* pyridine titrations to quantify the densities of dominant active sites during catalysis on a suite of eleven Sn-Beta-F (i.e., hydrophobic, hydrothermally crystallized in fluoride media) and Sn-Beta-OH (i.e., hydrophilic, prepared via post-synthetic grafting of Sn into dealuminated supports) zeolites. Approximately 5–35% of the total Sn sites were found to contribute 70–90% of the overall bimolecular ethanol dehydration STY (404 K, per Sn) on Sn-Beta, prompting more detailed kinetic analyses and examination of hypotheses for structural features that lead to distinct sites (Sn<sub>2316</sub>) in Sn-zeolites. Targeted syntheses of different Sn-zeolite frameworks (CHA, MFI, STT, BEC) and post-synthetic treatments were used to test and eliminate hypotheses that Sn<sub>2316</sub> sites were correlated with residual fluorine coordinated to Sn sites, Sn sites located at external crystallite surfaces, Sn located in minority amorphous regions of predominantly crystalline materials, and heterogeneities resulting from crystallographically-unique T-site positions. After ruling out these possibilities, we propose that Sn<sub>2316</sub> sites are defect-open Sn sites that are preferentially located at stacking fault grain boundaries in Sn-Beta, consistent with post-synthetic treatments with NH<sub>4</sub>F and HF that preferentially de-

crease the number of  $\text{Sn}_{2316}$  sites and etch zeolites at grain boundaries [228, 229]. We develop a computational model of stacking fault defect-open sites based on a  $2 \times 2 \times 1$  Beta supercell in order to compare their ethanol dehydration reactivity with that of closed sites [180], and show that the apparent activation free energy for bimolecular ethanol dehydration (referenced to the ethanol monomer) is 65–74  $\text{kJ mol}^{-1}$  higher at stacking fault-defect open sites than at closed sites, because the former are unable to interconvert between open and closed configurations, thus requiring the reaction mechanism to proceed through higher energy transition states. The experimental and theoretical evidence indicate that the dominant active sites for ethanol dehydration are not the defect-open Sn sites ( $\text{Sn}_{2316}$ ), in contrast to glucose isomerization, and instead comprise 17–26% of the closed sites ( $\text{Sn}_{2308}$ ) as indicated by *in situ* pyridine titration of a diverse range of Sn-zeolites.

## 4.2 Experimental Section

### 4.2.1 Zeolite synthesis and post-synthetic treatments

Sn-Beta-F zeolites were crystallized for different lengths of time starting from a single gel prepared following the procedure of Yakimov et al. [182] A Sn-MFI-F sample was synthesized following “method D” of Mal et al. [230] A second Sn-MFI-F sample was synthesized by modifying a procedure to synthesize Sn-MFI-OH from Boronat et al. [231] Full descriptions of these previously reported hydrothermal synthesis procedures are found in Section 4.6.1.1, Supporting Information.

Si-STT-F was synthesized according to Cambor et al. [232], and used as seed material for a Sn-STT-F crystallization under similar conditions. Tetraethyl orthosilicate (TEOS, Sigma Aldrich, 98%) was dissolved in an aqueous solution of N,N,N-trimethyl-1-adamantylammonium hydroxide (TMAdaOH, Sachem, 25 wt%) in a perfluoroalkoxy alkane (PFA) container, and covered and stirred for 0.5 h. In the case of Sn-STT-F, a solution of  $\text{SnCl}_4 \cdot 5\text{H}_2\text{O}$  (Sigma Aldrich, 98%) in deionized water was added dropwise. The mixture was covered and stirred overnight at ambient conditions

to completely hydrolyze TEOS. The mixture was uncovered to evaporate ethanol and partially evaporate water to achieve the desired water content. Aqueous HF (Sigma Aldrich, 48%) was added and the mixture was stirred with a PTFE spatula, yielding a thick gel with molar composition  $1 \text{ SiO}_2/0.50 \text{ TMAOH}/0.50 \text{ HF}/x \text{ SnCl}_4/15 \text{ H}_2\text{O}$ , where  $x = 0$  for Si-STT-F and  $x = 0.005$  for Sn-STT-F. (Caution: when working with hydrofluoric acid, use appropriate personal protective equipment, ventilation, and other engineering controls.) For Sn-STT-F, air-treated Si-STT-F was added to the mixture (5 wt% of  $\text{SiO}_2$  contributed by TEOS) as seed. The gel was loaded into a PTFE liner, sealed within a stainless-steel autoclave (Parr Instruments), and heated in an isothermal tumbling oven ( $\sim 60$  rpm, Yamato DKN-402C) at 423 K for 35 days (Si-STT-F) or 31 days (Sn-STT-F). Attempts to crystallize Sn-STT-F without seeds were abandoned when materials were amorphous after 95 days.

Ge-BEC-F and Sn-Ge-BEC-F were synthesized according to the report of Zhang et al. [233] TEOS was dissolved in an 11.5 wt% aqueous solution of N-isobutyl-N-methylpyrrolidinium hydroxide (iButOH, synthesis described in Section 4.6.1.3, Supporting Information), in a PFA container, and stirred covered for 0.5 h. Germanium oxide (Sigma Aldrich, 99.99%) was added to the gel and allowed to homogenize while stirring. In the case of Sn-Ge-BEC-F, a solution of  $\text{SnCl}_4 \cdot 5\text{H}_2\text{O}$  in deionized water ( $18.2 \text{ M}\Omega \text{ cm}$ ) was added dropwise. Then, the mixture was covered and stirred overnight at ambient conditions to completely hydrolyze TEOS. The mixture was uncovered to evaporate ethanol and partially evaporate water to achieve the desired water content. Aqueous HF (48%) was added and the mixture was stirred with a PTFE spatula, yielding a thick gel with molar composition  $1 \text{ SiO}_2/0.20 \text{ GeO}_2/0.50 \text{ iButOH}/0.65 \text{ HF}/x \text{ SnCl}_4/5 \text{ H}_2\text{O}$ , where  $x = 0$  for Ge-BEC-F and  $x = 0.007$  for Sn-Ge-BEC-F. The gel was loaded into a PTFE liner, sealed within a stainless-steel autoclave, and heated without agitation in an isothermal oven at 448 K for 38 hours.

As-made Sn-Beta-F zeolites were used as seed material for Si-Beta-F syntheses with the intent to grow a Si-Beta shell around Sn-Beta. Briefly, a gel of composition  $1 \text{ SiO}_2/0.54 \text{ TEAOH}/0.54 \text{ HF}/7.5 \text{ H}_2\text{O}$  was prepared following the same procedure

described for Sn-Beta-F zeolites. Then, as-made Sn-Beta-F (Sn-Beta-F-116-2, Sn-Beta-F-169) was added to the gel as 30% of the mass of SiO<sub>2</sub> contributed by TEOS and the gel was homogenized with a PTFE spatula. The gel was loaded into a PTFE liner, sealed within a stainless-steel autoclave, and heated in an isothermal tumbling oven (~60 rpm) at 413 K for 21 days (Sn-Beta-F-169) or 25 days (Sn-Beta-F-116-2). These samples are denoted Si-Beta@Sn-Beta-F.

After all hydrothermal zeolite syntheses, the solids were recovered by centrifugation and washed thoroughly with deionized water and acetone, then dried overnight in an oven at 373 K. The dried materials were then treated at 853 K (0.0167 K s<sup>-1</sup>) for 10 h in air (UHP, 99.999%, Indiana Oxygen, 1.67 cm<sup>3</sup> s<sup>-1</sup> (g zeolite)<sup>-1</sup>) in a muffle furnace (Nabertherm LE 6/11). These samples are denoted M-ZEO-X-Y, where M is the metal incorporated within the siliceous framework (Sn, Ge, or Si if pure-SiO<sub>2</sub>), ZEO is the 3-letter code of the framework topology according to the International Zeolite Association (IZA) [142] (“Beta” is written as such because its topology is ill-defined as an intergrowth of two polymorphs A and B), X is the mineralizing agent in the gel (F, OH), and Y is the Si/M ratio quantified by atomic absorption spectroscopy. In one case, a final number (-1, -2) is added to distinguish separate zeolites with the same Sn content. Some of each sample was not subjected to the final air-treatment step, and is denoted “as-made” for any other necessary characterizations (e.g., thermogravimetric analysis). We note here that Sn-Ge-BEC-F and Ge-BEC-F frameworks after air treatments to remove SDA were not stable when stored in ambient conditions for >1 year, because of hydrolysis of Si-O-Ge bonds after hydration by ambient moisture [234], as indicated by semi-crystalline XRD patterns after 520 days (Figure 4.56 patterns (d) and (e)). Relevant characterizations of Sn-Ge-BEC-F (CD<sub>3</sub>CN IR, N<sub>2</sub> adsorption) were performed <2 weeks after the air treatment.

Fluorine that remained on Sn-Beta-F samples after air treatments (853 K) was removed by anion exchange with tetramethylammonium hydroxide (NMe<sub>4</sub>OH). A 1 mol dm<sup>-3</sup> solution of NMe<sub>4</sub>OH (Sigma Aldrich, 25 wt%) was prepared in a PFA jar by mixing NMe<sub>4</sub>OH with deionized water to give a total solution volume of 25 cm<sup>3</sup>.

Glacial acetic acid (Avantor, 99.7%) was added dropwise during continuous stirring until the pH was 12. The sample (0.1–0.25 g) was added to this solution and heated to 353 K for 4 h under continuous stirring (300 rpm). After cooling, the solids were recovered by centrifugation, washed four times with deionized water ( $\sim 30 \text{ cm}^3$  per wash), and dried in an oven at 373 K. Samples were treated in a muffle furnace in flowing air ( $16.7 \text{ cm}^3 \text{ s}^{-1} (\text{g zeolite})^{-1}$ ) at 853 K ( $0.0167 \text{ K s}^{-1}$ ) for 10 h, and are denoted Sn-Beta-F-100-NMe<sub>4</sub>OH and Sn-Beta-F-181-NMe<sub>4</sub>OH.

A Sn-Beta-F-110 sample (characterization data reported in Harris et al. [56]) was treated with NH<sub>4</sub>F following the procedure reported by Qin et al. [229] In three separate PFA containers, 1.6 g of NH<sub>4</sub>F (Sigma Aldrich, 98%) were added to 2.4 g of deionized water to prepare 40 wt% NH<sub>4</sub>F solutions. To these solutions were added 0.2 g of Sn-Beta-F-110 ( $\text{g solution} (\text{g zeolite})^{-1} = 20$ ), and the slurries were heated by immersion in oil baths pre-heated to 323 K for 0.0833, 0.33, and 1.0 h while stirring at 300 rpm. The timer was started immediately after immersion in the oil bath. After the desired time period, each slurry was removed from its oil bath and immersed in an ice-water bath to rapidly cool. The cooled slurries were kept on ice for at most 0.25 h before washing  $5\times$  with ca.  $35 \text{ cm}^3$  portions of deionized water at ambient temperature, then dried overnight in a 353 K oven. The mass of solids recovered after this procedure was 0.165 g (0.0833 h), 0.156 g (0.33 h), and 0.125 g (1.0 h), indicating greater loss of solids at longer treatment times, likely because of sample dissolution. The samples were loaded into quartz boats in a horizontal-flow quartz tube within a three-zone furnace (Applied Test Systems), with each zone controlled independently (Watlow EZ-ZONE), and treated in flowing air ( $22 \text{ cm}^3 \text{ g}^{-1} \text{ s}^{-1}$ ) at 373 K ( $0.0167 \text{ K s}^{-1}$ ) for 1 h, then at 823 K ( $0.0167 \text{ K s}^{-1}$ ) for 4 h to ensure removal of any residual NH<sub>4</sub>F. These samples are denoted Sn-Beta-F-NH<sub>4</sub>F-Zh, where Z is the NH<sub>4</sub>F treatment time in hours.

Synthetic details and characterization of Sn-Beta-OH zeolites [151] and Sn-CHA-F zeolites [114] have been described previously.

#### 4.2.2 Characterization of zeolites

Routine characterizations (powder X-ray diffraction, thermogravimetric analysis, nitrogen adsorption, atomic absorption spectroscopy, diffuse reflectance UV-Visible, and scanning electron microscopy) are described in Section S.1.2, Supporting Information.

Infrared spectroscopy of adsorbed  $\text{CD}_3\text{CN}$  was used to quantify the Lewis acidic Sn sites on Sn-zeolites. Sn-zeolite samples (0.020–0.050 g) were pressed into self-supporting wafers with a 0.9 cm radius and loaded into a custom-built quartz IR cell [184] with  $\text{CaF}_2$  windows. The cell was housed inside an insulated brass block within an alumina silicate cover, and heated with six cartridge heaters (Chromalox). Wafer temperatures were measured within 2 mm of each side of the wafer by K-type thermocouples (Omega). IR spectra were collected on a Nicolet 4700 spectrometer with a Hg-Cd-Te (MCT, cooled to 77 K by liquid  $\text{N}_2$ ) detector by averaging 64 scans at  $2\text{ cm}^{-1}$  resolution in the  $4000\text{--}400\text{ cm}^{-1}$  range and were taken relative to an empty cell background reference collected under dynamic vacuum ( $<13\text{ Pa}$ ) at 303 K. Sn-zeolite wafers were treated in flowing air ( $6.67\text{--}16.7\text{ cm}^3\text{ (g zeolite)}^{-1}\text{ s}^{-1}$ ) purified by an FTIR purge gas generator (Parker Balston,  $<1\text{ ppm CO}_2$ , 200 K  $\text{H}_2\text{O}$  dew point), to 823 K ( $0.083\text{ K s}^{-1}$ ) for 1 h. The cell was evacuated and held under dynamic vacuum at 823 K for 1 h, then cooled to 303 K under dynamic vacuum. The cell was isolated under static vacuum, and  $\text{CD}_3\text{CN}$  (Sigma Aldrich, 99.96 atom% D) was purified by three freeze-pump-thaw cycles. A spectrum was collected, then  $\text{CD}_3\text{CN}$  was admitted into the cell in sequential doses (typically,  $<0.3\text{ CD}_3\text{CN/Sn}$ ) from a calibrated volume ( $22\text{ cm}^3$ ), and a spectrum was collected after 180 s of equilibration. The spectrum collected before dosing was subtracted from all spectra collected after dosing. Dosing was continued until the sample was saturated by  $\text{CD}_3\text{CN}$ , as evidenced by the appearance of a peak at  $2267\text{ cm}^{-1}$  in the subtracted spectra for physisorbed or gas-phase  $\text{CD}_3\text{CN}$ . Then, the sample was exposed to dynamic vacuum until the measured pressure in the cell was  $<13\text{ Pa}$ , returned to static vacuum, and a spectrum

was collected. This spectrum was treated as the spectrum for the CD<sub>3</sub>CN-saturated sample. Spectra were deconvoluted using CasaXPS (Casa Software Ltd) with Gauss-Lorentzian lineshapes with a 50% Lorentzian correction (SGL(50)) to determine the areas of peaks centered at 2316 cm<sup>-1</sup> (Sn Lewis acid site), 2308 cm<sup>-1</sup> (Sn Lewis acid site), 2287 cm<sup>-1</sup> (SnO<sub>x</sub>), 2275 cm<sup>-1</sup> (SiOH), and 2265 cm<sup>-1</sup> (physisorbed CD<sub>3</sub>CN). Integrated molar extinction coefficients (IMECs) reported by Harris et al. [56] were used to quantify the number of each species according to the equation:

$$\text{Site density } (\mu\text{mol g}^{-1}) = \left( \frac{\text{Integrated Peak Area (cm}^{-1}\text{)}}{E \text{ (cm } \mu\text{mol}^{-1}\text{)}} \right) \left( \frac{a_{CS}(\text{cm}^2)}{m(\text{g})} \right) \quad (4.1)$$

#### 4.2.3 *In situ* pyridine titration during ethanol dehydration catalysis

The number of active Sn Lewis acid sites was quantified during ethanol dehydration catalysis by *in situ* titrations with pyridine in a reactor system described previously [227]. Air-treated zeolite samples (0.030–0.050 g) were pelleted, crushed, and sieved to retain 180–250 μm aggregates, and loaded into a tubular quartz reactor (7 mm ID) supported between two plugs of acid-washed quartz wool (W. R. Grace, washed with 1 M HNO<sub>3</sub> at ambient temperature for 16 h). The quartz tube was mounted in down-flow configuration in a three-zone furnace (Applied Test Systems) equipped with Watlow controllers (EZ-ZONE), and the bed temperature was measured with a K-type thermocouple (Omega) in contact with the quartz tube at the level of the bed. Zeolites were pre-treated in flowing 5% O<sub>2</sub>/He (UHP, Indiana Oxygen, 16.67 cm<sup>3</sup> (g zeolite)<sup>-1</sup> s<sup>-1</sup>) at 813 K (0.0167 K s<sup>-1</sup>) for 2 h, then cooled to reaction temperature, typically 404 K (0.0333 K s<sup>-1</sup>), in flowing He (UHP, Indiana Oxygen, 16.67 cm<sup>3</sup> (g zeolite)<sup>-1</sup> s<sup>-1</sup>). Before starting the pre-treatment, a 20 cm<sup>3</sup> solution of C<sub>2</sub>H<sub>5</sub>OH (Sigma Aldrich, anhydrous, >99.5%) and deionized water was prepared with C<sub>2</sub>H<sub>5</sub>OH/H<sub>2</sub>O molar ratio of 80. Separately, a 1 wt% solution of pyridine (Avantor, 99%) in C<sub>2</sub>H<sub>5</sub>OH was prepared. Several drops (0.03–0.10 g) of this C<sub>5</sub>H<sub>5</sub>N/C<sub>2</sub>H<sub>5</sub>OH solution were added to a 10 cm<sup>3</sup> portion of the C<sub>2</sub>H<sub>5</sub>OH/H<sub>2</sub>O solution to give a C<sub>5</sub>H<sub>5</sub>N/C<sub>2</sub>H<sub>5</sub>OH/H<sub>2</sub>O solution with molar composition 80 C<sub>2</sub>H<sub>5</sub>OH/1

$\text{H}_2\text{O}/x \text{C}_5\text{H}_5\text{N}$ , where  $x = 0.001\text{--}0.01$ . This solution, and the  $\text{C}_2\text{H}_5\text{OH}/\text{H}_2\text{O}$  solution, were loaded separately into  $10 \text{ cm}^3$  glass syringes (Hamilton 1000 series) and delivered by syringe pumps (KD Scientific Legato 100) into separate stainless-steel lines heated to  $>383 \text{ K}$  to prevent condensation. The vapor was mixed with flowing He (UHP, Indiana Oxygen) to achieve pressures of  $8 \text{ kPa C}_2\text{H}_5\text{OH}$  and  $0.1 \text{ kPa H}_2\text{O}$  in both lines, and additionally  $0.1\text{--}1 \text{ Pa}$  of  $\text{C}_5\text{H}_5\text{N}$  in the second reactant line. These reactant or reactant/titrant mixture flows were allowed to stabilize in a bypass line during pre-treatment. After the reactor was held at reaction temperature (typically,  $404 \text{ K}$ ) for  $1 \text{ h}$ , the reactant stream ( $8 \text{ kPa C}_2\text{H}_5\text{OH}$ ,  $0.1 \text{ kPa H}_2\text{O}$ ) was introduced.  $\text{C}_2\text{H}_5\text{OH}$ ,  $(\text{C}_2\text{H}_5)_2\text{O}$ , and  $\text{C}_5\text{H}_5\text{N}$  concentrations were quantified by gas chromatography (Agilent 6890) with a HP-PLOT-Q capillary column ( $30 \text{ m} \times 530 \mu\text{m} \times 40 \mu\text{m}$ ) and flame ionization detector. No other products were detected under the conditions studied, because the higher intrinsic barrier for monomolecular dehydration to  $\text{C}_2\text{H}_4$  [180] leads to rates below detection limits on Sn-Beta zeolites until temperatures above  $450 \text{ K}$  (at  $8 \text{ kPa C}_2\text{H}_5\text{OH}$ ,  $0.1 \text{ kPa H}_2\text{O}$ ) [227]. After the start of reaction, the bypass stream was maintained with  $8 \text{ kPa C}_2\text{H}_5\text{OH}$ ,  $0.1 \text{ kPa H}_2\text{O}$ , and  $0.1\text{--}1 \text{ Pa C}_5\text{H}_5\text{N}$ , and the pressure drop in this stream was equalized with that of the reactor-to-GC stream with a metering valve in the bypass line. At  $4 \text{ h}$  and  $10 \text{ h}$  times-on-stream, a 4-way valve after the reactor was switched to sample the bypass stream in the GC for  $2 \text{ h}$  periods to verify the concentrations of  $\text{C}_2\text{H}_5\text{OH}$  and  $\text{C}_5\text{H}_5\text{N}$  in the stream. After  $16 \text{ h}$  on stream, the second reactant stream was introduced to the reactor, and the cumulative uptake of  $\text{C}_5\text{H}_5\text{N}$  on the zeolite was quantified by its disappearance relative to its measured bypass concentration. After suppression of measured rates, and measured  $\text{C}_5\text{H}_5\text{N}$  concentration values returned to near their bypass values, the  $\text{C}_5\text{H}_5\text{N}$ -free stream was re-directed to the reactor to probe the reversibility of titration and quantify desorbed  $\text{C}_5\text{H}_5\text{N}$ . In a separate experiment, the initial  $\text{C}_2\text{H}_5\text{OH}/\text{H}_2\text{O}$  ratio of the  $20 \text{ cm}^3$  solution was adjusted to  $8$  to achieve pressures of  $8 \text{ kPa C}_2\text{H}_5\text{OH}$ ,  $1 \text{ kPa H}_2\text{O}$ , and  $0.4 \text{ kPa C}_5\text{H}_5\text{N}$ . In a series of experiments to determine the apparent activation parameters on Sn-Beta-F-153,

5% O<sub>2</sub>/He pretreatments and titration procedures were performed repeatedly with identical conditions on the same catalyst bed, where only the bed temperature during titration was varied between 404–438 K. Temperatures were varied in random order and the same temperature (421 K) was visited twice to verify reproducibility.

#### 4.2.4 Theoretical modeling

Periodic, self-consistent density functional theory (DFT) calculations with the Vienna Ab-initio Simulation Package (VASP) [132, 133, 135] were employed for all electronic structure calculations at stacking fault defect-open Sn sites. The computational parameters were chosen to be consistent with our previous work on ethanol dehydration in Sn-Beta to allow for comparisons among calculations at both closed and hydrolyzed-open Sn sites in Beta (“framework sites”), and stacking fault sites. For all calculations, the Bayesian error estimation functional (BEEF-vdw) [137] was used with projector augmented wave (PAW) pseudopotentials [136, 141] along with a plane wave cutoff of 520 eV. All calculations were performed spin-polarized.

The stacking fault model is provided with the online version of this manuscript to facilitate benchmarking [194] and reproducible computational studies on similar structures. The model was constructed based on TEM images of stacking fault defects in Beta zeolites [235]. A 1-D periodic cell was built by first tiling polymorph A and polymorph B bridged by three “bea” composite building units (CBUs). Individual mor, bea, and mtw CBUs were then manipulated to form a natural tiling and link the two polymorphs at the double-pore region. The resulting structure consisted of 422 oxygen atoms and 202 silicon atoms. Domains of polymorph A or B in Beta crystals typically continue for multiple nanometers between stacking faults [190, 235], so the model was terminated following a single A and B repetition and capped with hydrogen atoms, to maintain a similar strain on the structure as if it were repeated. Along the plane parallel to the double pore, periodicity was maintained as an infinite stacking of A and B polymorphs. This direction of periodicity provides well-needed structural rigidity to the model and allows calculation of van der Waals energies of

guest molecules in the double-pore region that include interactions along the length of the pore. This structure was then relaxed to a force criterion of  $30 \text{ meV } \text{\AA}^{-1}$ . The sizeable memory requirements demanded by this model in VASP 5.3.5 necessitate careful selection of an appropriate number of computer nodes and band parallelization for the researcher's specific hardware. Initial geometric relaxations were performed without spin polarization, and spin polarization was included in a subsequent relaxation.

Nudged elastic band (NEB) calculations were performed in the stacking fault model with the climbing image method (CI-NEB) [143, 144]. CI-NEB calculations were converged to a force criterion of  $75 \text{ meV } \text{\AA}^{-1}$ , which is higher than previously used by us for framework sites in Beta [180]. This force criterion is needed because of the large unit cell size, and poor convergence of the CI-NEB algorithm for systems with multiple low-frequency modes [124, 180]. The Lanczos diagonalization method, which is typically successful for refining transition states to force convergence criteria of  $30 \text{ meV } \text{\AA}^{-1}$ , is computationally demanding, and slow to converge for a system of this size. Despite the less stringent force criteria employed for stacking fault sites compared to the traditional framework models for Beta, transition state energies can still be compared between the models due to the otherwise identical calculation parameters. The faulted intergrowth of the A and B polymorphs in the double pore leads to seven distinct tetrahedral locations with the configuration (HO)-Si-(OSi $\equiv$ )<sub>3</sub>, and no Si-OH groups are sufficiently proximal to allow condensation. Sn substitutions were considered at all seven locations to yield defect-open sites with the configuration (HO)-Sn-(OSi $\equiv$ )<sub>3</sub>. C<sub>2</sub>H<sub>5</sub>OH binding energies at all seven defect-open sites were within 0.20 eV, suggesting that they are chemically similar. The *ab initio* molecular dynamics (AIMD) adsorption configuration sampling methods used previously [180] were inaccessible due to the model size, requiring manual selection of adsorbate configurations. Free energy calculations in the stacking fault model required unique assumptions because of the large unit cell. Zero-point energy corrections were assumed to be equivalent to those calculated previously for analogous adsorbates at standard framework Sn sites (hydrolyzed-open or ethoxy-open [180]) because of their

similar adsorbate structures and active site ligands. In addition, vibrational and rotational entropies of each adsorbate were considered equivalent to those at standard framework Sn sites. The translational entropy of adsorbates in stacking fault sites was calculated by replacing the low-frequency translational modes with localized free particle diffusion constants by adjusting the accessible diffusion length. Without AIMD trajectories to calculate the accessible diffusion length [180], the lengths were adjusted to account for the  $\sim 2\times$  larger accessible pore volume surrounding stacking fault sites. Edge lengths for ethanol monomer species were increased from 3 Å to 6 Å, corresponding to a  $10 \text{ J mol}^{-1} \text{ K}^{-1}$  increase in entropy. An entropy increase of  $23 \text{ J mol}^{-1} \text{ K}^{-1}$  for ethanol-ethanol dimers corresponded to changing the accessible diffusion length from 5 Å to 10 Å. Ethoxy intermediates had similar entropies at both defect-open sites and framework sites because the degrees of freedom as a ligand on the Sn site are assumed to be similar for both types of sites.

### 4.3 Results and Discussion

#### 4.3.1 *In situ* pyridine titration of Lewis acidic Sn sites during ethanol dehydration catalysis

The number of catalytically relevant active sites in four Sn-Beta-F zeolites and seven Sn-Beta-OH zeolites (characterization data reported in Table 4.1) was assessed with *in situ* pyridine titrations during catalytic bimolecular ethanol dehydration to diethyl ether (DEE) at 404 K (8 kPa  $\text{C}_2\text{H}_5\text{OH}$  and 0.1 kPa  $\text{H}_2\text{O}$ ), as illustrated on Sn-Beta-OH-187 in Figure 4.2. This suite of samples has no Brønsted acid sites detectable by IR after adsorption of pyridine [56, 151], and their ethanol dehydration reactivity can therefore be attributed to Lewis acidic Sn sites [180, 227]. The conversion of closed Sn sites to hydrolyzed-open configurations by water has been suggested to impart Brønsted acid character to the sites [154, 236], but DFT-based microkinetic modeling indicates that such dynamically formed open sites have a negligible contribution to measured rates under the conditions studied here [180]. The reaction conditions were selected to provide a surface predominantly covered by ethanol

**Table 4.1:** Sn contents, micropore volumes, and CD<sub>3</sub>CN Lewis acid site distributions for Beta materials used for *in situ* pyridine titration experiments.

Sample	Si/Sn (Sn wt%) <sup>a</sup>	V <sub>micro</sub> <sup>b</sup> / cm <sup>3</sup> g <sup>-1</sup>	Sn <sub>LA</sub> /Sn <sup>c</sup>	Sn <sub>2316</sub> /Sn <sup>c</sup>	Sn <sub>2308</sub> /Sn <sup>c</sup>
Sn-Beta-OH-84 <sup>d</sup>	84 (2.29)	0.20	1.20	0.24	0.96
Sn-Beta-OH-80 <sup>d</sup>	80 (2.39)	0.22	1.01	0.42	0.59
Sn-Beta-OH-95 <sup>d</sup>	95 (2.00)	0.22	1.22	0.49	0.73
Sn-Beta-OH-46 <sup>d</sup>	46 (4.10)	0.19	0.92	0.22	0.70
Sn-Beta-OH-41 <sup>d</sup>	41 (4.60)	0.19	1.32	0.50	0.82
Sn-Beta-OH-30 <sup>d</sup>	30 (6.08)	0.16	0.72	0.18	0.54
Sn-Beta-OH-187 <sup>e</sup>	187 (1.04)	0.23	1.26	0.29	0.97
Sn-Beta-F-181 <sup>e</sup>	181 (1.08)	0.21	1.13	0.44	0.70
Sn-Beta-F-153 <sup>e</sup>	153 (1.27)	0.23	0.61	0.13	0.48
Sn-Beta-F-180 <sup>f</sup>	180 (1.08)	0.14	0.66	0.11	0.55
Sn-Beta-F-116-1 <sup>e</sup>	116 (1.66)	0.23	1.21	0.45	0.76

<sup>a</sup>Quantified by AAS<sup>b</sup>Determined by N<sub>2</sub> adsorption minimum in  $\partial V_{\text{ads}}/\partial \log(P/P_0)$ <sup>c</sup>Sn<sub>LA</sub> = Lewis acidic Sn sites, from CD<sub>3</sub>CN IR using reported IMECs [56], errors  $\pm 20\%$ ; Sn<sub>LA</sub> = Sn<sub>2316</sub> + Sn<sub>2308</sub><sup>d</sup>Data reported by us in Vega-Vila et al. [151]<sup>e</sup>Data reported by us in Bates and Gounder [227]<sup>f</sup>Partially crystalline 3-day Sn-Beta-F (see Section 4.3.2.3 and Table 4.10)

monomer species (60–80%, Section 4.6.1.4, Supporting Information) and similar STYs (per Sn, within 2 $\times$ ) on Sn-Beta-F and Sn-Beta-OH materials. DEE site-time yields (STY) stabilized to quasi-steady-state values after an initial deactivation transient (50–90% of initial STY at quasi-steady state). Pyridine titrants (0.1–1 Pa; typically, 0.5 Pa) were then introduced to the reactant stream ( $t_1$ , Figure 4.2a), causing DEE site-time yields to become suppressed to <10% of their quasi-steady-state values. After pyridine titrants were removed from the reactant stream ( $t_2$ , Figure 4.2a), site-time yields did not recover to their initial quasi-steady-state values (at  $t_1$ ), reflecting irreversible titration of the predominant active sites by pyridine.

DEE formation rates (per g) decreased sharply and linearly with increasing cumulative amount of adsorbed pyridine (per total Sn) (Figure 1b), consistent with

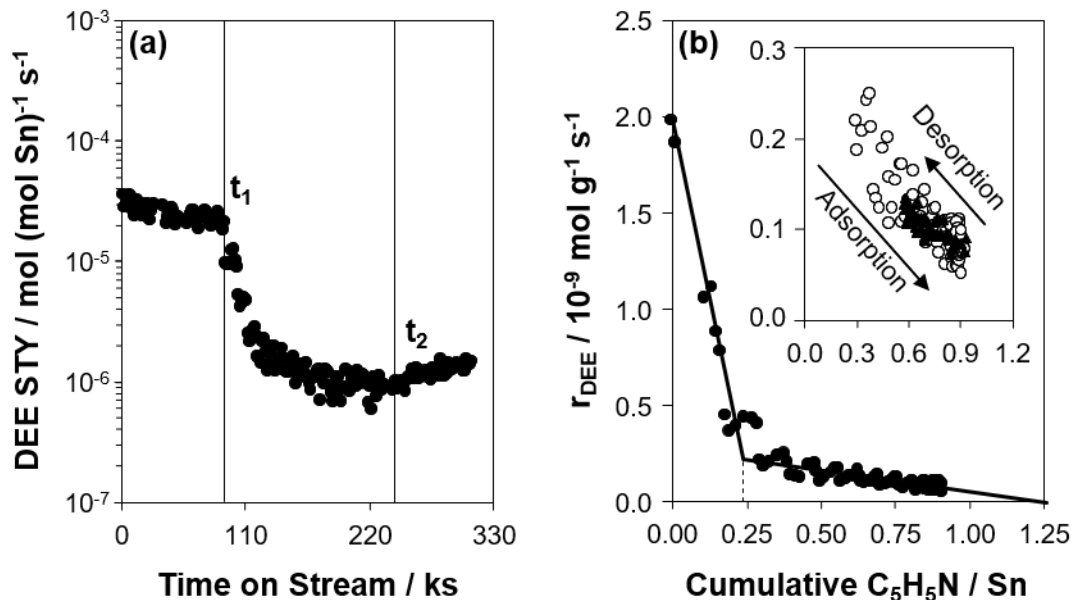


**Figure 4.2:** (a) Diethyl ether site-time yield (404 K, 8 kPa  $\text{C}_2\text{H}_5\text{OH}$ , 0.1 kPa  $\text{H}_2\text{O}$ , per Sn) on Sn-Beta-OH-187 during approach to quasi-steady state, after introduction of 0.5 Pa pyridine at time point  $t_1$ , and after removal of pyridine titrants from the reactant stream at time point  $t_2$ . (b) Diethyl ether formation rate (per g catalyst) as a function of pyridine uptake on Sn-Beta-OH-187 during catalysis. The solid line represents regressed two-site poisoning model, and the dashed line indicates the regressed value of the number of sites A per total Sn. Inset: site B titration region ( $\circ$ ) demonstrating reversible pyridine adsorption/desorption from site B after titrant removal from the stream ( $\blacktriangle$ ).

preferential titration of the most reactive subset of Sn sites present, and then decreased more gradually as a second subset of less-reactive Sn sites became titrated by pyridine. This pyridine poisoning behavior can be described according to Eq. 4.2–4.3:

$$r_{\text{DEE}} = (n_{A1} - n_{\text{Py},A}) \text{TOR}_A + (n_{B1} - n_{\text{Py},B}) \text{TOR}_B \quad (4.2)$$

$$n_{\text{Py}} = n_{\text{Py},A} + n_{\text{Py},B} \quad (4.3)$$

where  $n_{i1}$  is the amount of site  $i$  in the sample at  $t_1$  ( $\text{mol g}^{-1}$ ),  $n_{\text{Py},i}$  is the amount of pyridine adsorbed at site  $i$  ( $\text{mol g}^{-1}$ ),  $\text{TOR}_i$  is the turnover rate at site  $i$  ( $\text{s}^{-1}$ ), and  $r_{\text{DEE}}$  is the measured bimolecular dehydration rate ( $\text{mol g}^{-1} \text{s}^{-1}$ ). Upon removal of

pyridine titrants from the reactant stream, pyridine desorption from the catalyst bed was detected with concomitant increases in DEE formation rates (Figure 4.2b inset, ▲). The rate data during pyridine desorption is in quantitative agreement with rate data measured during the titration regime for adsorption at the less-reactive subset of Sn sites (Figure 4.2b inset, ○).

Taken together, these observations are consistent with preferential and irreversible titration by pyridine of a more-reactive subset of Lewis acidic Sn sites (A), followed by the weaker and reversible titration of a less-reactive subset of Lewis acidic Sn sites (B). This assumption defines the terms in Eq. 4.2–4.3 according to:

$$n_{Py,A} = \begin{cases} n_{Py}, & n_{Py} < n_{A1} \\ n_{A1}, & n_{Py} \geq n_{A1} \end{cases} \quad (4.4)$$

$$n_{Py,B} = \begin{cases} 0, & n_{Py} < n_{A1} \\ n_{Py} - n_{A1}, & n_{Py} \geq n_{A1} \end{cases} \quad (4.5)$$

where  $n_{Py}$  is the total measured pyridine uptake ( $\text{mol g}^{-1}$ ), A is the predominant site, and B is the secondary, reversibly-titrated site. The data in Figure 4.2b were regressed to Eq. 4.2–4.5, with the additional constraint:

$$r_{DEE,1} = n_{A1}TOR_A + n_{B1}TOR_B \quad (4.6)$$

where  $r_{DEE,1}$  denotes the rate at the start of the titration ( $t_1$  in Figure 4.2a). This ensures the regressed  $TOR_i$  values accurately reflect the measured rate at each site type before titration. The regressed fit is represented by the solid line in Figure 4.2b, where the slopes in the regions that correspond to titration of each site type  $i$  reflect the values of  $TOR_i$  (Eq. 4.2). The regression also gives values for the amounts (per total Sn) of sites A ( $x_{A1}$ , dashed line in Figure 4.2b) and B ( $x_{B1}$ , x-intercept of solid line in Figure 4.2b less the number of A sites) of 0.24 and 1.0, respectively, with  $TOR_A/TOR_B = 34$ . These values are consistent with the total number of Sn Lewis acid sites in the material quantified by  $CD_3CN$  IR *ex situ* ( $1.26 \text{ Sn}_{LA}/\text{Sn}$ , Table

4.1). Thus, the population of more-reactive A sites on the Sn-Beta-OH-187 sample accounts for 89% of the measured bimolecular ethanol dehydration rate (per g).

The same *in situ* pyridine titration procedures were used to quantify the densities of A and B sites, and their individual turnover rates, on the same suite of eleven Sn-Beta-F and Sn-Beta-OH samples (Table 4.1) comprising a wide range of Sn densities ( $>5\times$ , 0.9–5.1 mol g<sup>-1</sup>), as shown in Figure S1–Figure 4.24 and summarized in Table 4.2. The value of  $x_{A1}$  varied from 0.05–0.24, while  $x_{B1}$  varied from 0.29–1.0. Values

**Table 4.2:** Turnover rates and site densities of predominant (A) and secondary (B) sites on Sn-zeolite materials determined by *in situ* pyridine titration during ethanol dehydration catalysis (404 K, 8 kPa C<sub>2</sub>H<sub>5</sub>OH, 0.1 kPa H<sub>2</sub>O).

Sample	TOR <sub>A</sub> / 10 <sup>-5</sup> s <sup>-1</sup>	TOR <sub>B</sub> / 10 <sup>-6</sup> s <sup>-1</sup>	TOR <sub>A</sub> /TOR <sub>B</sub>	$x_{A1}$ <sup>a</sup>	$x_{B1}$ <sup>b</sup>	$r_1/r_0$	$x_{A0}$ <sup>c</sup>
Sn-Beta-OH-84	3.4	2.1	16	0.15	0.82	0.65	0.25
Sn-Beta-OH-80	3.7	3.1	12	0.08	0.33	0.58	0.16
Sn-Beta-OH-95	5.7	1.9	30	0.11	0.65	0.62	0.19
Sn-Beta-OH-46	6.9	3.9	18	0.09	0.38	0.53	0.19
Sn-Beta-OH-41	5.4	6.8	8	0.12	0.29	0.57	0.24
Sn-Beta-OH-30	10	4.1	25	0.06	0.38	0.57	0.11
Sn-Beta-OH-187	8.5	2.5	34	0.24	1.0	0.69	0.35
Sn-Beta-F-181	13	1.4	89	0.07	0.91	0.92	0.08
Sn-Beta-F-180	6.8	5.2	13	0.05	0.31	0.73	0.08
Sn-Beta-F-116-1	4.7	1.7	28	0.06	0.61	0.59	0.11
Sn-Beta-F-153	4.2	3.1	14	0.05	0.28	0.75	0.08
Sn-Beta-F-153 <sup>d</sup>	3.2	2.4	13	0.06	0.25	0.85	0.08
Sn-MFI-F-192	32	7	47	0.09	0.36	0.68	0.14
Sn-Ge-BEC-F	16	15	11	0.04	0.21	0.56	0.08

<sup>a</sup>Sites A (per total Sn) at the start of pyridine titration ( $t_1$ )

<sup>b</sup>Sites B (per total Sn) at the start of pyridine titration ( $t_1$ )

<sup>c</sup>Sites A (per total Sn) extrapolated to initial time-on-stream ( $t_0$ )

<sup>d</sup>Titration performed at 1 kPa H<sub>2</sub>O, all other conditions the same

of TOR<sub>A</sub> and TOR<sub>B</sub> on each Sn-Beta sample are plotted as a function of Sn content in Figure 4.3, and are scattered about average values of TOR<sub>A,avg</sub> = 6.7×10<sup>-5</sup> s<sup>-1</sup> and TOR<sub>B,avg</sub> = 3.1×10<sup>-6</sup> s<sup>-1</sup> (TOR<sub>A,avg</sub>/TOR<sub>B,avg</sub> = 22) without a systematic decreasing

dependence on site density, consistent with the absence of transport limitations per the Madon-Boudart criterion [196], and the Mears criterion [203] as determined previously [227]. These  $\text{TOR}_A$  and  $\text{TOR}_B$  values indicate 70–90% of the overall bimolecular

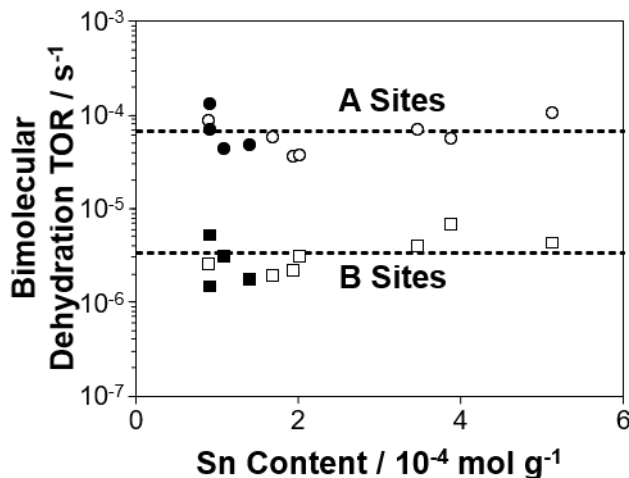


**Figure 4.3:** Bimolecular ethanol dehydration turnover rate (404 K, 8 kPa  $\text{C}_2\text{H}_5\text{OH}$ , 0.1 kPa  $\text{H}_2\text{O}$ , per site quantified by *in situ* pyridine titration) on site A ( $\bullet, \circ$ ) and site B ( $\blacksquare, \square$ ) of Sn-Beta-F ( $\bullet, \blacksquare$ ) and Sn-Beta-OH ( $\circ, \square$ ) samples. Dashed lines represent average values for all sites A and for all sites B.

dehydration STY (404 K, per Sn) is accounted for at A sites. Higher values of  $\text{TOR}_A$  than  $\text{TOR}_B$  ( $\text{TOR}_A/\text{TOR}_B = 8\text{--}89$ , Table 4.2) on all samples indicate that a common active site motif (A) is present in Sn-Beta zeolites that leads to turnover rates that are an order of magnitude higher than those at the remaining sites (B) under the conditions studied here (404 K, 8 kPa  $\text{C}_2\text{H}_5\text{OH}$ , 0.1 kPa  $\text{H}_2\text{O}$ ). Such  $\text{TOR}_A/\text{TOR}_B$  ratios correspond to lower apparent Gibbs free energies of activation (404 K) at site A of 7–15  $\text{kJ mol}^{-1}$ , which can be decomposed into entropic and enthalpic components, as we discuss next.

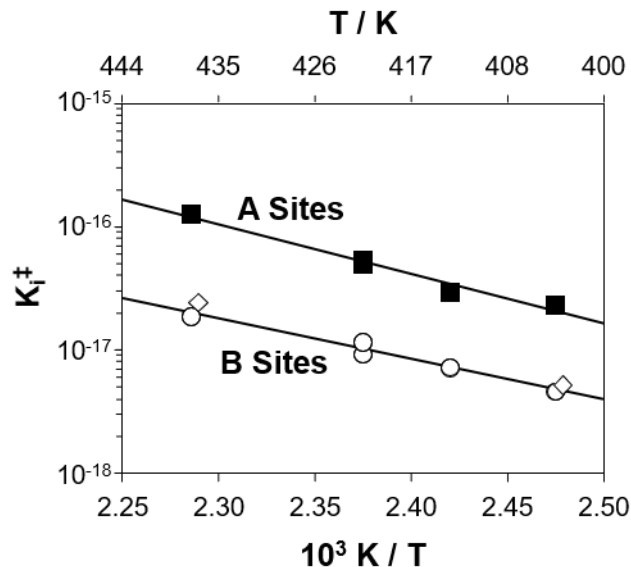
A representative sample, Sn-Beta-F-153, was subjected to additional *in situ* pyridine titrations at different temperatures (404–438 K) to probe the entropic and enthalpic components of activation Gibbs free energies at sites A and B. Between each titration experiment, the sample was regenerated in an oxidative environment (5%  $\text{O}_2/\text{He}$ , 813 K, 2 h) intended to remove pyridine from active sites, as verified by the

recovery of initial deactivation transients upon exposure to ethanol dehydration conditions (rate data at 421 K measured from 0–60 ks time on stream before and after oxidation treatments shown in Figure 4.25a, and discussed in Section 4.6.1.5, Supporting Information). Initial deactivation transients may also be used to estimate the number of A sites at initial time on stream ( $x_{A0}$ , Table 4.2, and Section 4.6.1.5, Supporting Information). Similar numbers of both  $x_{A1}$  (0.01–0.06 per total Sn) and  $x_{B1}$  (0.26–0.31 per total Sn) were quantified on Sn-Beta-F-153 at different temperatures (Figure 4.26), indicating that  $TOR_i$  values quantified by *in situ* pyridine titration correspond to the same two pools of sites at each temperature, and in turn can be used to estimate apparent activation barriers at each site type. Eyring plots in the range 404–438 K are shown in Figure 4.4 for sites A and B, and give  $\Delta H_{i,app}^\ddagger$  and  $\Delta S_{i,app}^\ddagger$  values according to transition state theory:

$$TOR_i = \frac{k_B T}{h} K_{i,app}^\ddagger P_E^{\alpha_E} \quad (4.7)$$

$$K_{i,app}^\ddagger = \exp \left( -\frac{\Delta H_{i,app}^\ddagger}{RT} + \frac{\Delta S_{i,app}^\ddagger}{R} \right) \quad (4.8)$$

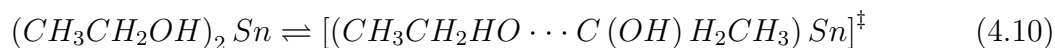
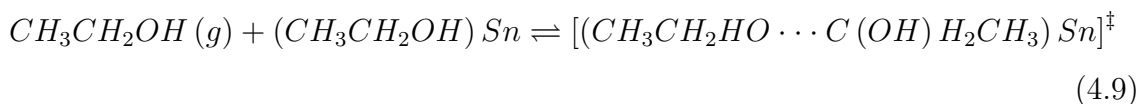
where  $k_B$  is Boltzmann's constant,  $h$  is Planck's constant,  $T$  is the temperature (K),  $K_{i,app}^\ddagger$  is the transition-state equilibrium constant at site  $i$ ,  $P_E$  is the ethanol pressure (bar),  $\alpha_E$  is the apparent reaction order in ethanol, and  $\Delta H_{i,app}^\ddagger$  and  $\Delta S_{i,app}^\ddagger$  are the apparent enthalpy and entropy of activation at site  $i$ , respectively. The value of  $\alpha_E$  at B sites is 1.0 as quantified by steady-state rate measurements (404 K, 437 K) after irreversible titration of the A sites (Figure 4.32, Supporting Information). The value of  $\alpha_E$  of 1.0 at B sites, together with the previously measured [227] ethanol reaction order of 0.7 on un-poisoned Sn-Beta-F materials (404 K) and the measured  $TOR_i$  values, enable estimating an  $\alpha_E$  value of 0.6 at A sites (Section 4.6.1.6, Supporting Information). Variations in the value of  $\alpha_E$  do not change the sign of  $\Delta\Delta S_{A-B,app}^\ddagger$  in this analysis (Table 4.8;  $\Delta\Delta S_{A-B,app}^\ddagger = \Delta S_{A,app}^\ddagger - \Delta S_{B,app}^\ddagger$ ). The quantity  $K_{i,app}^\ddagger$  reflects equilibrium between the bimolecular ethanol dehydration transition state and

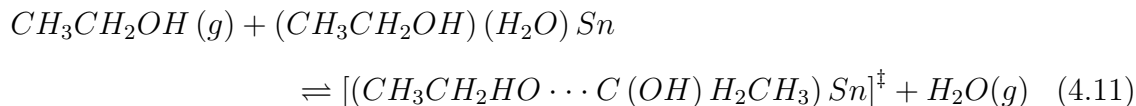


**Figure 4.4:** Eyring plot to determine apparent activation parameters (404–438 K, 8 kPa C<sub>2</sub>H<sub>5</sub>OH, 0.1 kPa H<sub>2</sub>O) on Sn-Beta-F-153 at sites A (■) and B (○) derived from independent *in situ* pyridine titration experiments with sample re-oxidation in between each experiment (see Figure 4.25), and by steady-state kinetic measurements (404 K, 437 K, 5–35 kPa C<sub>2</sub>H<sub>5</sub>OH, 0.1 kPa H<sub>2</sub>O) after irreversible titration of sites A (◇).

the most abundant reactive intermediate (MARI) species at sites A or B, and gas-phase species needed to co-adsorb with the MARI and form the transition state.

DFT-based microkinetic modeling and experimental reaction order measurements [180, 227] indicate there is not a sole MARI species at A sites under the conditions studied here (8 kPa C<sub>2</sub>H<sub>5</sub>OH, 0.1 kPa H<sub>2</sub>O, 404 K), but that ethanol monomers account for ~70% of surface intermediates, with ~20% present as ethanol-ethanol dimers, and ~10% present as ethanol-water dimers. Thus, the measured  $\Delta H_{i,app}^{\ddagger}$  and  $\Delta S_{i,app}^{\ddagger}$  values reflect contributions from the steps:





which are depicted in Figure 4.5, and serve as limiting cases for the apparent activation parameters in different coverage regimes. Values of  $\Delta H_{A,app}^\ddagger$  and  $\Delta H_{B,app}^\ddagger$

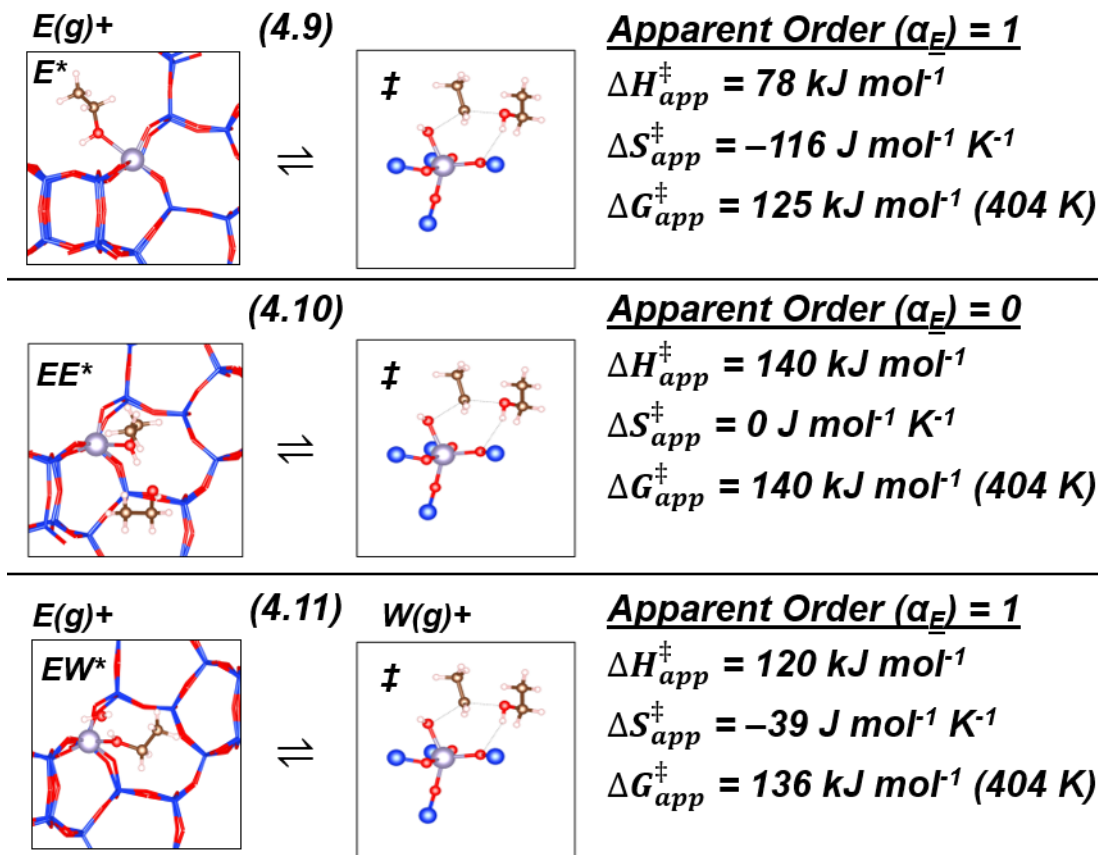


**Figure 4.5:** DFT-calculated geometries of adsorbed intermediates and transition states for bimolecular ethanol dehydration at closed Sn sites reported by Bukowski et al. [180] of the species involved in overall reaction steps to the bimolecular dehydration transition state ( $\ddagger$ ) from different MARI species described by Eq. 4.9–4.11, and the resulting apparent activation parameters and reaction orders in ethanol ( $\alpha_E$ ). Gas-phase species are above the geometries of the adsorbed intermediates and transition states.  $E^*$  = ethanol monomer,  $EE^*$  = ethanol-ethanol dimer,  $EW^*$  = ethanol-water dimer.

were  $77 \pm 7 \text{ kJ mol}^{-1}$  and  $63 \pm 6 \text{ kJ mol}^{-1}$ , respectively (Table 4.3), which are in

reasonable agreement with the apparent enthalpy of activation calculated with the ethanol monomer as the sole MARI species by Bukowski et al. [180] (78 kJ mol<sup>-1</sup>, Figure 4.5), but not those for ethanol-ethanol dimers or ethanol-water dimers as sole MARI (140 kJ mol<sup>-1</sup> and 120 kJ mol<sup>-1</sup>, respectively, Figure 4.5). Similarly, values

**Table 4.3:** Apparent activation enthalpies and entropies for bimolecular ethanol dehydration at sites A and B on Sn-Beta-F-153 (404–438 K, 8 kPa C<sub>2</sub>H<sub>5</sub>OH, 0.1 kPa H<sub>2</sub>O) using the data in Figure 4.4.

	Site A	Site B	$\Delta\Delta$ Quantity <sub>A-B</sub>
$\Delta H_{i,app}^\ddagger$ <sup>a</sup> / kJ mol <sup>-1</sup>	77 ± 7	63 ± 6	14 ± 9
$\Delta S_{i,app}^\ddagger$ <sup>a</sup> / J mol <sup>-1</sup> K <sup>-1</sup>	-129 ± 17	-177 ± 14	48 ± 22
$\Delta G_{i,app}^\ddagger$ (404 K) / kJ mol <sup>-1</sup>	129	134	-5

<sup>a</sup>Errors are from linear regression

of  $\Delta S_{A,app}^\ddagger$  and  $\Delta S_{B,app}^\ddagger$  were  $-129 \pm 17$  J mol<sup>-1</sup> K<sup>-1</sup> and  $-177 \pm 14$  J mol<sup>-1</sup> K<sup>-1</sup>, respectively, resembling calculated apparent activation entropies for ethanol monomer MARI species of  $-116$  J mol<sup>-1</sup> K (Figure 4.5 [180]). Taken together, the measured values of apparent activation enthalpies and entropies are consistent with dominant pathways through the ethanol monomer MARI species, and some contribution from ethanol-ethanol dimer species, reflected in  $\alpha_E$  values between 0.6–1.0.

The value of  $\Delta\Delta H_{A-B,app}^\ddagger$  was  $14 \pm 9$  kJ mol<sup>-1</sup>, while the value of  $\Delta\Delta S_{A-B,app}^\ddagger$  was  $48 \pm 22$  J mol<sup>-1</sup> K<sup>-1</sup> (Table 4.3). Given that  $\Delta\Delta H_{A-B,app}^\ddagger$  is positive, the higher reactivity of site A is attributed solely to its more positive apparent activation entropy ( $\Delta\Delta S_{A-B,app}^\ddagger > 0$ ) that compensates for the higher enthalpic barrier. Such differences can be explained mechanistically by differences in the relative abundances of the MARI species at sites A and B that are the precursors to similar transition states, consistent with sub-first-order kinetics at A sites and first-order kinetics at B sites that reflect partial coverage by ethanol-ethanol dimers at A sites and B sites that are otherwise covered by ethanol monomer species; however, differences in transition state structures, and therefore entropies, between the sites may also contribute to

$\Delta\Delta S_{A-B,app}^\ddagger$  values. In this case, the value of  $\Delta\Delta S_{A-B,app}^\ddagger$  ( $48 \text{ J mol}^{-1} \text{ K}^{-1}$ ) could plausibly reflect changes in either rotational or vibrational degrees of freedom at the transition state.

Given that degree of rate control analyses in DFT-based microkinetic modeling indicate that reaction pathways at closed Sn sites dominate measured rates over those at hydrolyzed-open sites [180], we first probed whether less-reactive hydrolyzed-open and more-reactive closed Sn configurations could account for the observed reactivity and distributions of A sites and B sites by measuring *in situ* pyridine titration data at a higher  $\text{H}_2\text{O}$  pressure that should shift Sn distributions toward hydrolyzed-open via  $\text{H}_2\text{O}$ -mediated hydrolysis. *In situ* titration data were collected on Sn-Beta-F-153 at a higher  $\text{H}_2\text{O}$  pressure (1 kPa  $\text{H}_2\text{O}$ , 8 kPa  $\text{C}_2\text{H}_5\text{OH}$ , 404 K). The titration occurred with the same two regimes for A sites and B sites common among all samples at 0.1 kPa  $\text{H}_2\text{O}$  (Figure 4.31), enabling estimation of  $x_{A1}$ ,  $x_{B1}$ ,  $x_{A0}$ ,  $\text{TOR}_A$ , and  $\text{TOR}_B$  according to Eq. 4.2–4.6 (Table 4.2, third-to-last entry). The values of  $x_{A1}$ ,  $x_{B1}$ , and  $x_{A0}$  were in reasonable agreement (within 0.03) with those measured at 0.1 kPa  $\text{H}_2\text{O}$ . In addition, DFT calculations and microkinetic modeling of bimolecular ethanol dehydration (404 K, 0.5–35 kPa  $\text{C}_2\text{H}_5\text{OH}$ , 0.1–50 kPa  $\text{H}_2\text{O}$ ) indicate a negligible coverage of less-reactive hydrolyzed-open sites under similar conditions [180], which is inconsistent with less-reactive B sites in hydrolyzed-open configurations. The values of  $\text{TOR}_A$  and  $\text{TOR}_B$  decrease from 0.1–1 kPa  $\text{H}_2\text{O}$ , with a calculated  $\text{H}_2\text{O}$  reaction order of -0.1 at both A and B sites, consistent with measured reaction orders of -0.1 based on overall diethyl ether site-time yields (per total Sn) on Sn-Beta-F between 0.1–1 kPa  $\text{H}_2\text{O}$  [227]. Similar  $\text{H}_2\text{O}$  reaction orders are consistent with turnovers at sites A and B through the same mechanistic pathways, wherein ethanol-water dimers at sites inhibit turnover rates, and inconsistent with  $\text{H}_2\text{O}$ -mediated site hydrolysis, which would result in a different functional dependence of  $\text{TOR}_A$  and  $\text{TOR}_B$  on  $\text{H}_2\text{O}$  pressure (Section 4.6.1.7, Supporting Information). *In situ* pyridine titration data at 0.1–1 kPa  $\text{H}_2\text{O}$  indicates that a configurational difference between A and B sites unrelated to site hydrolysis underlies their different reactivity, as dictated by the more

positive apparent activation entropy at A sites. Therefore, we next sought to link the numbers of A and B sites to quantitative probes of site configuration.

The structurally distinct configurations of sites A and B determined by *in situ* pyridine titration were probed by comparing their densities with those of structurally distinct Sn<sub>2316</sub> sites and Sn<sub>2308</sub> sites quantified by *ex situ* CD<sub>3</sub>CN titration. These *ex situ* quantifications were performed on samples with treatment histories (823 K, 21% O<sub>2</sub>/N<sub>2</sub>) more analogous to initial times on stream (803 K, 5% O<sub>2</sub>/He), rather than after the initial deactivation transient (60 ks on stream) experienced before *in situ* pyridine titration. Thus, the initial density of site A was estimated by extrapolation to initial times on stream ( $n_{A0}$ ) using the values of  $r_1/r_0$  and TOR<sub>i</sub> assuming irreversible deactivation of site A and no deactivation of site B (Section 4.6.1.5, Supporting Information); hence,  $n_{A0}$  represents an upper bound on the number of A sites present on Sn-Beta zeolites. Parity plots comparing  $n_{A0}$  values with the densities of Sn<sub>2316</sub> sites and Sn<sub>2308</sub> sites are presented in Figure 4.6, and those comparing  $n_{A1}$  values (without extrapolation to initial time-on-stream) in Figure 4.33. When compared to either the density of Sn<sub>2316</sub> sites or Sn<sub>2308</sub> sites,  $n_{A0}$  values provide closer agreement to parity than do  $n_{A1}$  values, and improve linearity. Better agreement with parity is observed for Sn<sub>2316</sub> sites with a best-fit slope ( $m = 0.46$ ) that is closer to a value of unity than for Sn<sub>2308</sub> sites ( $m = 0.28$ ), although these comparisons indicate that Sn<sub>2316</sub> site densities are  $\sim 2\times$  higher than those of pyridine-titrated  $n_{A0}$  sites, with a lower degree of linearity than Sn<sub>2308</sub> sites ( $R^2 = 0.74 < 0.92$ ).

A slope of 0.5 could indicate that Sn<sub>2316</sub> sites quantified *ex situ* by CD<sub>3</sub>CN are  $2\times$  the number of sites quantified by *in situ* pyridine titration because of a 2:1 binding stoichiometry of CD<sub>3</sub>CN at Sn sites, or that each adsorbed pyridine poisons two Sn<sub>2316</sub> sites during catalysis because of their close proximity. The former possibility, a 2:1 CD<sub>3</sub>CN:Sn stoichiometry, is unlikely given that the integrated molar extinction coefficients for CD<sub>3</sub>CN adsorbed at Sn<sub>2316</sub> sites and Sn<sub>2308</sub> sites were determined from low-coverage dosing IR experiments for which 1:1 CD<sub>3</sub>CN:Sn stoichiometry is expected, and Lewis acidic Sn densities quantified at saturation by CD<sub>3</sub>CN IR are

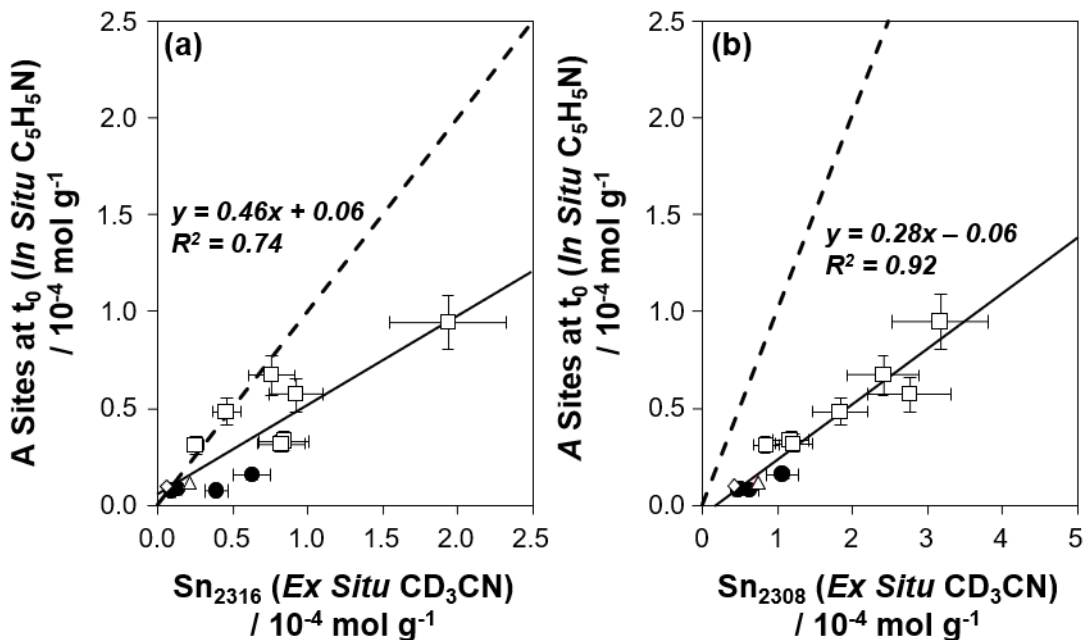


**Figure 4.6:** Parity of sites titrated by pyridine *in situ* (corrected to initial time on stream) with (a)  $\text{Sn}_{2316}$  sites or (b)  $\text{Sn}_{2308}$  sites quantified *ex situ* by  $\text{CD}_3\text{CN}$  IR on seven Sn-Beta-OH samples ( $\square$ ), four Sn-Beta-F ( $\bullet$ ) samples, Sn-MFI-F-129 ( $\triangle$ ), and Sn-Ge-BEC-F ( $\diamond$ ). Dashed lines represent parity, while solid lines represent best-fit linear regressions to the data.

in agreement with those quantified by *ex situ* pyridine IR, which adsorbs at 1:1 stoichiometry [56, 237]. Additionally, penta-coordinate Sn, but not hexa-coordinate Sn, is detected by  $^{119}\text{Sn}$  NMR across a wide range of  $\text{CD}_3\text{CN}$  coverages (0.5–4.0  $\text{CD}_3\text{CN}/\text{Sn}$ ) on a Sn-Beta-F zeolite with  $\text{Si}/\text{Sn} = 200$  [155]. It is also unlikely that Sn sites are located in close proximity across such a wide range of Sn densities (0.3–2 Sn per unit cell), although such proximal sites have been hypothesized previously based on multi-shell fitting of Sn K-edge EXAFS data on one Sn-Beta-F zeolite with  $\text{Si}/\text{Sn} = 120$  [108]. The linearity is improved when deactivation-corrected A sites are correlated with  $\text{Sn}_{2308}$  sites ( $R^2 = 0.92$ , Figure 4.6b), but with an even sharper deviation from parity ( $m = 0.28$ ) that would indicate that  $\text{Sn}_{2308}$  sites quantified *ex situ* by  $\text{CD}_3\text{CN}$  are  $4\times$  the pyridine value determined from *in situ* titration.

The data in Figure 4.6 suggest that the predominant sites (A) for ethanol dehydration detected by *in situ* pyridine titration are distinct from both Sn<sub>2316</sub> sites and Sn<sub>2308</sub> sites, but could be a subset of one or the other type of site either because of further structural differences, or inaccurate quantitative corrections for deactivation phenomena, which we have attempted to do within reason. The linear relationship with Sn<sub>2308</sub> sites is consistent with 17–26% of Sn<sub>2308</sub> sites as the most reactive sites (Figure 4.34), but this constant fraction of active sites seems unlikely given the range of samples with diverse Sn contents ( $0.9\text{--}5\times 10^{-4}$  mol Sn g<sup>-1</sup>) and synthetic provenance (-F, -OH). On the other hand, Sn<sub>2316</sub> sites have been identified previously as the predominant active sites for glucose isomerization [56,105,106] and Baeyer-Villiger oxidation [102], while sites other than Sn<sub>2316</sub> are reactive for aldol condensation [105]. Attempts were also made, albeit less successfully, to correlate B sites (at t<sub>1</sub>, Figure 4.35) or the total A+B sites (at t<sub>1</sub>, Figure 4.36) with either Sn<sub>2316</sub> sites or Sn<sub>2308</sub> sites. A reasonable agreement of A+B sites with Sn<sub>2308</sub> sites may be noted (Figure 4.36b), although with outliers that make the best-fit trendline deviate from parity. Such quantitative ambiguity would be further dispelled by complimentary approaches to probe the identity of Sn<sub>2316</sub> sites and Sn<sub>2308</sub> sites.

Samples with Lewis acidic Sn in different zeolite frameworks (Sn-MFI-F and Sn-Ge-BEC-F) were examined by the same *in situ* titration procedures to understand the generality of the correlations in Figure 4.6. Titration data are reported in Figure 4.37 (Sn-MFI-F-129) and Figure 4.38 (Sn-Ge-BEC-F), and summarized in the last two lines of Table 4.2. Sn-MFI-F-129 and Sn-Ge-BEC-F exhibited similar deactivation behavior ( $r_1/r_0 = 0.56\text{--}0.68$ ) before titrations, and titration curves could be fit by Eq. 2–6, with reversible titration of B sites second after A sites. TOR<sub>A</sub>/TOR<sub>B</sub> values between 11–47 were similar to those quantified on Sn-Beta (8–89), and the fraction of total Sn as A sites extrapolated to initial time ( $x_{A0}$ ) was 0.08–0.14, a consistent subset of Sn sites as was quantified on Sn-Beta. Including their n<sub>A0</sub> values on the parity plot in Figure 4.6 does not change the best-fit lines (plots without these points are shown in Figure 4.40), providing evidence that the 17–26% fraction of Sn<sub>2308</sub> sites

as A sites is independent of zeolite topology in the samples studied. Taken together with the better linearity of the correlation with Sn<sub>2308</sub> sites ( $R_2 = 0.92$ ) than with Sn<sub>2316</sub> sites ( $R^2 = 0.74$ ), the insensitivity of A and B sites to H<sub>2</sub>O pressure (0.1–1 kPa), and TOR<sub>A</sub> and TOR<sub>B</sub> values that differ in activation entropy ( $\Delta\Delta S_{A-B,app}^\ddagger = 48 \pm 22 \text{ J mol}^{-1} \text{ K}^{-1}$ ), we conclude that the predominant sites A for bimolecular ethanol dehydration are 17–26% of Sn<sub>2308</sub> sites, which are structurally distinct from the remaining Sn<sub>2308</sub> sites, and from Sn<sub>2316</sub> sites. Identifying the structural features responsible for these sites can enable quantitative theoretical predictions of their ethanol dehydration reactivity to further support this finding.

One-site models that predict identical ethanol dehydration reactivity of framework Sn sites (i.e., [L] = total Sn in rate expressions), via quasi-equilibrated interconversion of closed and hydrolyzed-open Sn sites, are not sufficient to describe the data presented here, because they do not account for the structural features that result in higher reactivity of a subset of Sn sites. Simultaneously, potentially distinct structural features must also account for the higher reactivity of a subset of Sn sites for glucose isomerization, and for ethanol dehydration. Different structural features of Sn sites must persist after ethanol dehydration catalysis and regenerative oxidation treatments, as discussed previously [227], and result in a distinct CD<sub>3</sub>CN IR peak at 2316 cm<sup>-1</sup>. These two criteria led us to hypothesize and systematically investigate several structural features that could lead to Sn<sub>2316</sub> sites.

#### 4.3.2 Probing structural features that lead to Sn<sub>2316</sub> sites

A range of post-synthetic treatments and targeted hydrothermal syntheses were performed to alter the relative amounts of Sn<sub>2316</sub> sites and Sn<sub>2308</sub> sites in Sn-Beta and related Sn-containing zeolites. The influence of each bulk structural change on the relative abundance of Sn<sub>2316</sub> sites was assessed by CD<sub>3</sub>CN IR spectra, monitoring both spectra collected after initial CD<sub>3</sub>CN doses (<0.3 CD<sub>3</sub>CN/Sn) that result in preferential population of Sn<sub>2316</sub> sites on Sn-Beta-F samples [56, 102], and those collected at saturation CD<sub>3</sub>CN coverages to estimate the final distribution of Sn<sub>2316</sub>

sites and Sn<sub>2308</sub> sites. The Sn<sub>2308</sub>/Sn<sub>2316</sub> molar ratio at saturation CD<sub>3</sub>CN coverages varied between 2–5 on ten Sn-Beta-F zeolites, and between 2–4 on seven Sn-Beta-OH zeolites (Figure 4.17) [56, 151, 227], which leads to similar values of  $2.6 \pm 1.0$  after averaging within both sample types (Figure 4.7), where the error of 1.0 represents the 95% confidence interval of the data sets. Sn<sub>2316</sub> sites are predominant active sites for

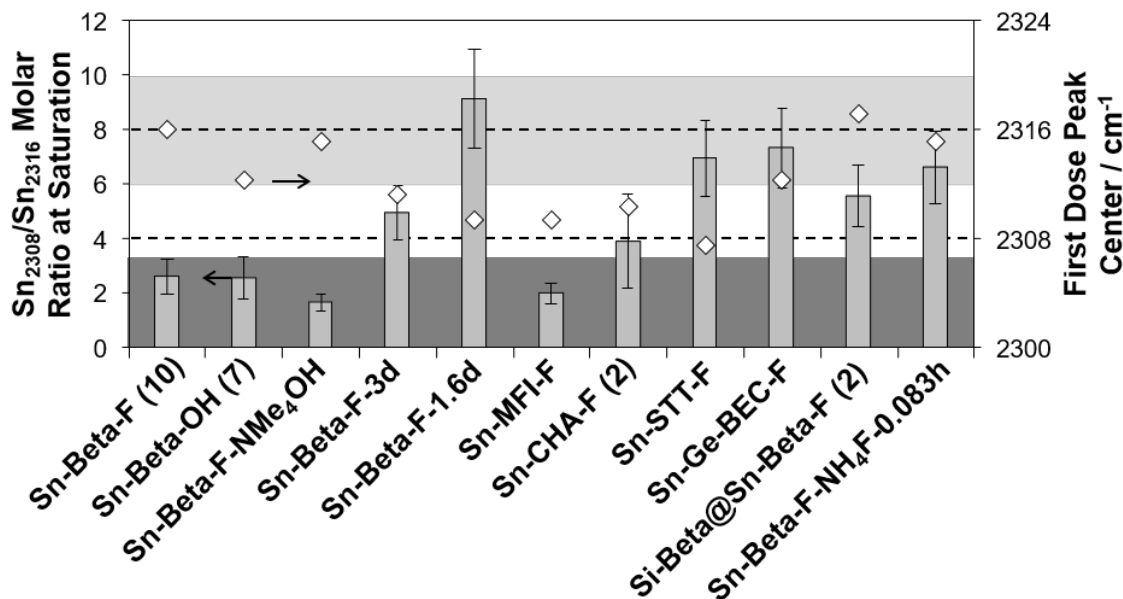


**Figure 4.7:** Sn<sub>2308</sub>/Sn<sub>2316</sub> molar ratio (grey bars, left axis) determined from saturated CD<sub>3</sub>CN IR spectra, and position of the peak center for the first dose of adsorbed CD<sub>3</sub>CN ( $<0.3$  CD<sub>3</sub>CN/Sn,  $\diamond$ , right axis) on Sn within various zeolite frameworks or after post-synthetic treatments. The dark grey and light grey shaded regions represent the ranges of the Sn<sub>2308</sub>/Sn<sub>2316</sub> molar ratio, and the position of the first-dose peak center, respectively, that indicate predominant Sn<sub>2316</sub> sites on a sample. Parenthetical values after sample names indicate the number of independent samples averaged to give the Sn<sub>2308</sub>/Sn<sub>2316</sub> value, with error bars representing the 95% confidence interval. Otherwise, labels indicate a single sample with error bar of 20%.

glucose isomerization on Sn-Beta-F [56] and Sn-Beta-OH [151] zeolites according to *ex situ* pyridine titrations before glucose isomerization catalysis [56], and first-order isomerization rate constants (373 K) do not vary systematically with Sn density when normalized by Sn<sub>2316</sub> [56, 151], which provides evidence that this suite of samples pos-

sess distinct structural features that lead to  $\text{Sn}_{2316}$  sites. Therefore, we conclude that Sn-zeolite samples with structural features that lead to  $\text{Sn}_{2316}$  sites should contain  $\text{Sn}_{2308}/\text{Sn}_{2316}$  molar ratios at saturation  $\text{CD}_3\text{CN}$  coverages characteristic of Sn-Beta ( $2.6 \pm 1.0$ ), or ratios of  $\leq 3.6$  that are denoted by the dark grey shaded region in Figure 4.7. A value of 3.6 represents the upper bound on  $\text{Sn}_{2308}/\text{Sn}_{2316}$  molar ratio values when averaged among ten Sn-Beta zeolites; therefore, values above 3.6 were taken as indication that a given sample contains different structural features that are uncharacteristic of Sn-Beta so as to result in a minority of  $\text{Sn}_{2316}$  sites.

This first criterion is necessary, but insufficient, to identify structural features that lead to  $\text{Sn}_{2316}$  sites, because deconvolution of the broad peaks present in IR spectra collected at saturation  $\text{CD}_3\text{CN}$  coverages may result in quantification of a larger fraction of  $\text{Sn}_{2316}$  sites than actually present. Boronat et al. [102] reported initial detection of  $\text{Sn}_{2316}$  sites by exposing Sn-Beta-F samples to small doses of  $\text{CD}_3\text{CN}$ , which initially adsorbed at Sn with a peak center at  $2316 \text{ cm}^{-1}$  and then gradually populated  $\text{Sn}_{2308}$  sites. Harris et al. [56] used similar low-coverage  $\text{CD}_3\text{CN}$  dosing procedures to unambiguously identify  $2316 \text{ cm}^{-1}$  peaks and quantify their integrated molar extinction coefficients by ensuring that the deconvolution parameters employed captured the changing experimental spectra as a function of  $\text{CD}_3\text{CN}$  coverage across a series of Sn-Beta samples. Here, we use the peak center of the first dose of  $\text{CD}_3\text{CN}$  ( $< 0.3 \text{ CD}_3\text{CN}/\text{Sn}$ ) as a second, necessary criterion to identify the presence of  $\text{Sn}_{2316}$  sites on a given sample. First-dose peak centers of  $2316 \text{ cm}^{-1}$  and  $2312 \text{ cm}^{-1}$  are observed on Sn-Beta-F and Sn-Beta-OH samples, respectively, and is used as a heuristic range to identify the presence of  $\text{Sn}_{2316}$  sites ( $2312\text{--}2320 \text{ cm}^{-1}$ , light grey shaded region in Figure 4.7).

With these two criteria, we assess the effects of various structural changes on the relative abundance of  $\text{Sn}_{2316}$  sites in Sn-Beta and other Sn-containing zeolites. To summarize, a sample has structural features that lead to  $\text{Sn}_{2316}$  sites if its first-dose peak center is within the  $2312\text{--}2320 \text{ cm}^{-1}$  range (light grey shaded region in Figure

4.7), and the molar ratio of  $\text{Sn}_{2308}/\text{Sn}_{2316}$  is  $\leq 3.6$  at saturation  $\text{CD}_3\text{CN}$  coverages (dark grey shaded region in Figure 4.7).

#### 4.3.2.1 Sn bound to residual fluorine

We first hypothesized that residual fluorine left on Sn-Beta-F samples after calcination could coordinate to Sn, changing its electronic properties and leading to the distinct IR peak at  $2316\text{ cm}^{-1}$ . Fluoride ions preferentially incorporate within confined spaces in zeolites during hydrothermal synthesis, such as in double-four-membered ring or  $[4^3\ 5^4]$  cage structures [238], and can remain occluded in these locations after high-temperature air treatments [239]. To test this hypothesis, we used tetramethylammonium hydroxide ( $\text{NMe}_4\text{OH}$ ) treatments reported by Tatsumi and co-workers [240] ( $1.0\text{ mol dm}^{-3}$ ,  $353\text{ K}$ ,  $4\text{ h}$ ) to remove F from a Sn-Beta-F-100 sample that retained F after high-temperature air treatment ( $853\text{ K}$ ), as reported in our previous paper [241], and denoted Sn-Beta-F- $\text{NMe}_4\text{OH}$  in Figure 4.7. Complete F removal was confirmed by  $^{19}\text{F}$  NMR (Figure 4.65), and coincided with an increase in the number of  $\text{Sn}_{2316}/\text{Sn}$  from  $0.13\pm 0.03$  to  $0.26\pm 0.05$ , while  $\text{Sn}_{2308}/\text{Sn}$  remained constant within error (Table 4.9), which corresponds to a decrease in  $\text{Sn}_{2308}/\text{Sn}_{2316}$  from 2.8 to 1.7 (Figure 4.7). In addition, treating a Sn-Beta-F-181 sample with  $\text{NMe}_4\text{OH}$  that did not initially have occluded F (Figure S51) did not affect the number of Sn sites within error but did increase the density of Si-OH groups quantified from  $\text{CD}_3\text{CN}$  IR peaks centered at  $2275\text{ cm}^{-1}$  (Table 4.9), confirming that such treatments remove F from Sn-Beta samples and can also increase the number of Si-OH groups by hydrolysis of Si-O-Si bonds, a process observed during treatments in liquid water at elevated temperature ( $373\text{ K}$ ) [241]. These observations indicate that residual fluorine occluded within Sn-Beta-F samples after calcination does not lead to  $\text{Sn}_{2316}$  sites, but instead may bind to Sn Lewis acid sites and restrict binding of  $\text{CD}_3\text{CN}$  titrants, consistent with  $^{119}\text{Sn}\{^{19}\text{F}\}$  CPMAS NMR that detected F in the vicinity of Sn in Sn-Beta-F [242], or also bind at locations unrelated to framework Sn. In Figure 4.7, Sn-Beta-F- $\text{NMe}_4\text{OH}$  falls within the acceptable values of  $\text{Sn}_{2308}/\text{Sn}_{2316}$  and

first-dose peak center for samples with structural features that lead to  $\text{Sn}_{2316}$  sites, so alternative hypotheses related to local Sn environments were examined.

#### 4.3.2.2 Sn at external crystallite surfaces

The possibility that Lewis acidic Sn sites could be preferentially located at external crystallite surfaces in Sn-Beta was probed by  $\text{CD}_3\text{CN}$  IR on an as-made Sn-Beta-F-169 sample, whose pores were filled with the organic structure-directing agent tetraethylammonium ( $\text{TEA}^+$ ) [93], rendering Sn sites within micropores inaccessible to  $\text{CD}_3\text{CN}$  titrants. This sample was treated at 473 K for 1 h under dynamic vacuum to remove adsorbed  $\text{H}_2\text{O}$  from crystallite surfaces, confirmed by the absence of  $\nu(\text{O-H})$  peaks for adsorbed  $\text{H}_2\text{O}$  at Si-OH groups ( $\sim 3400\text{ cm}^{-1}$ ) [57] as shown in Figure 4.8a. Peaks were observed for isolated Si-OH groups ( $3745\text{ cm}^{-1}$ ) [189] and

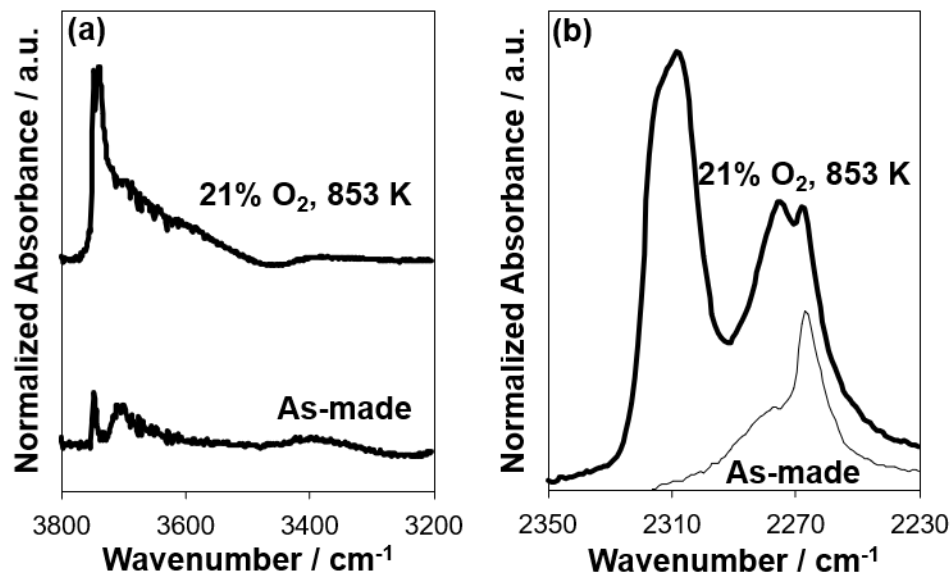


**Figure 4.8:** (a) Baseline-corrected IR spectra (normalized by T-O-T overtone peak area) of Sn-Beta-F-169 in the  $\nu(\text{O-H})$  region at 303 K under vacuum, in the as-made form after treating at 473 K under dynamic vacuum for 1 h (bottom), or in the air-treated form (853 K, flowing air) after treating at 823 K under dynamic vacuum (top). (b) IR difference spectra of  $\text{CD}_3\text{CN}$  (normalized by T-O-T overtone peak area) adsorbed at saturation coverages (303 K) on Sn-Beta-F-169 (thick line) and as-made Sn-Beta-F-169 (thin line).

hydrogen-bonded Si-OH nests ( $\sim 3500\text{--}3700\text{ cm}^{-1}$ ) [189], with a total area comprising 21% of that observed on the same sample after high-temperature air treatments (853 K, 10 h) to remove  $\text{TEA}^+$  (Table 4.4), indicating more Si-OH groups reside within Sn-Beta-F crystallites than on their surfaces. Such intracrystalline Si-OH groups in

**Table 4.4:** Quantification<sup>a</sup> of saturated  $\text{CD}_3\text{CN}$  IR spectra adsorbed on Sn-Beta-F-169 in as-made form and after treatment in 21%  $\text{O}_2$  at 853 K to determine densities of Sn Lewis acid sites, extra-framework  $\text{SnO}_2$ , and Si-OH groups.

	$\nu(\text{OH})$ Area <sup>b</sup>	$\text{Sn}_{2316}$ / $10^{-5}\text{ mol g}^{-1}$	$\text{Sn}_{2308}$ / $10^{-5}\text{ mol g}^{-1}$	$\text{SnO}_x$ / $10^{-6}$ $\text{mol g}^{-1}$	Si-OH / $10^{-4}\text{ mol g}^{-1}$
Sn-Beta-F-169 as-made	0.06	0	0	6.6	0.35
Sn-Beta-F-169 air-treated	0.30	3.3	7.0	9.4	1.3
Fraction of extra-crystalline sites <sup>c</sup>	0.21	0	0	0.70	0.28

<sup>a</sup>IMEC values for  $\text{CD}_3\text{CN}$  determined by Harris et al. [56]

<sup>b</sup>Quantified in the range  $\sim 3400\text{--}3800\text{ cm}^{-1}$  from spectra before  $\text{CD}_3\text{CN}$  exposure (303 K) under static vacuum ( $<15\text{ Pa}$ ).

<sup>c</sup>Quantified as the ratio of the values quantified on the as-made sample to that of the air-treated sample.

Sn-Beta-F likely exist at grain boundaries within crystals generated by the faulted intergrowth of polymorphs A and B of zeolite Beta [190, 235]. After saturation with  $\text{CD}_3\text{CN}$  (Figure 4.8b), the predominant peaks observed corresponded to  $\text{CD}_3\text{CN}$  that was physisorbed ( $2267\text{ cm}^{-1}$ ) [186], adsorbed at Si-OH groups ( $2275\text{ cm}^{-1}$ ) [186], and at nanocrystalline  $\text{SnO}_2$  ( $2287\text{ cm}^{-1}$ ) [188], but not at Lewis acidic Sn ( $2316\text{ cm}^{-1}$ ,  $2308\text{ cm}^{-1}$ ) [56, 102]. The density of Si-OH groups quantified by adsorbed  $\text{CD}_3\text{CN}$  was 28% that of the air-treated (853 K) material (Table 4.4), consistent with  $\nu(\text{O-H})$  peak areas, indicating 70–80% of Si-OH groups are within crystallites. The density of  $\text{SnO}_2$  nanoparticles, however, was 70% that of the air-treated (853 K) material, indicating they reside predominantly outside crystallites (Table 4.4). No Lewis acidic Sn sites are detected, indicating all these sites are within crystallites and inaccessible

to  $\text{CD}_3\text{CN}$  because  $\text{TEA}^+$  remains occluded within micropores. This conclusion is consistent with measured first-order glucose isomerization rate constants (398 K, per total Sn) on amorphous Sn-xerogel materials (amorphous Sn-silicates with isolated Sn sites [243] that are four orders of magnitude lower than on Sn-Beta [114], because these rate constants are a kinetic probe of  $\text{Sn}_{2316}$  sites, indicating Sn-xerogel materials do not host them. The unconfined sites of Sn-xerogel ( $\sim 8$  nm average pore diameter [114]) serve as a structural analog for Sn sites at external surfaces of Beta zeolites, and therefore these sites are not  $\text{Sn}_{2316}$ . Discounting this hypothesis, we next investigate the relevance of different intracrystalline and zeolite framework structural heterogeneities.

#### 4.3.2.3 Sn located in amorphous regions

Distinct Sn configurations could reside within amorphous regions of the solid that are undetectable by standard techniques to verify bulk crystallinity such as XRD or micropore volume measurements. For instance, Kots et al. observed that Zr does not incorporate into tetrahedral framework positions in Zr-Beta zeolites synthesized hydrothermally without seeding until ca. 5 days after fully crystalline products have formed [244], suggesting non-classical mechanisms of Lewis acidic metal atom incorporation within Beta zeolites and the presence of amorphous Zr-silicate species even after apparently crystalline products have been formed. To test the hypothesis that Sn species in amorphous regions lead to distinct Lewis acid site configurations, we performed a similar study of crystallization time of Sn-Beta-F zeolites at a fixed gel composition, without seeding. A gel with a composition of  $\text{Si}/\text{Sn} = 200$  and  $\text{H}_2\text{O}/\text{Si} = 6.8$  was separated and crystallized for 1.6, 3, 7, 14, and 21 days. Consistent with prior reports [182], Sn-Beta-F samples were crystalline after seven days, according to XRD patterns (Figure 4.50) and micropore volumes consistent with the Beta topology ( $0.21 \text{ cm}^3 \text{ g}^{-1}$ , Table 4.10). The  $\text{Sn}_{2308}/\text{Sn}_{2316}$  molar ratio was relatively invariant from 7–21 days (Table 4.10), suggesting no reorganization of Sn sites takes place after crystalline Beta frameworks are formed, in contrast to Zr-Beta zeolites [244].

Before seven days, however, mixtures of crystalline Beta zeolites and amorphous solids were recovered from synthesis gels, as indicated by systematically decreasing XRD peak intensities (Figure 4.50), micropore volumes, and organic contents in as-made solids (Table 4.10) with decreasing crystallization times (1.6, 3 d) that were below those expected for crystalline Beta zeolites. The Si/Sn ratio is invariant ( $\sim 180$ ) as these structural changes are taking place, and diffuse reflectance UV-visible peak centers (206–210 nm) and edge energies (4.15–5.06 eV, Table 4.11) are characteristic of Sn atoms in tetrahedral configurations throughout. These data indicate that Sn precursors in synthesis gels are incorporated tetrahedrally within amorphous silicate units that eventually form crystalline Beta frameworks. Lower fractions of Lewis acidic Sn accessible to  $\text{CD}_3\text{CN}$  titrants after shorter crystallization times (0.42  $\text{Sn}_{\text{LA}}/\text{Sn}$  at 1.6 d and 0.66  $\text{Sn}_{\text{LA}}/\text{Sn}$  at 3 d) are consistent with this interpretation, because agglomeration of amorphous precursor nanoparticles during air treatments at 853 K can occlude Sn atoms within inaccessible domains. The  $\text{Sn}_{2308}/\text{Sn}_{2316}$  molar ratio systematically decreases from 9.1 (1.6 days) to 5.0 (3 days) as Sn atoms are incorporated within crystalline domains (Figure 4.7), until values between 2–4 are attained at full crystallinity (Table 4.10, 7–21 days), inconsistent with the hypothesis that  $\text{Sn}_{2316}$  sites are located in amorphous regions. Instead, Sn sites require placement within crystalline domains of zeolite frameworks to exist in configurations that give rise to the  $2316\text{ cm}^{-1}$  peak. These sites are more pronounced in Beta zeolites compared with other frameworks, as we discuss next in the context of their local structure.

#### 4.3.2.4 Sn at T-sites with different local structure

Various Sn-zeolite frameworks (CHA, MFI, STT, BEC) were synthesized to explore the effects of the local structure and bond angles surrounding Lewis acidic Sn on their speciation. The composite building units (CBUs) that each of these frameworks possess are summarized in Figure 4.9a, and serve as a basis for identifying commonalities between T-atom local environments among frameworks. The selected

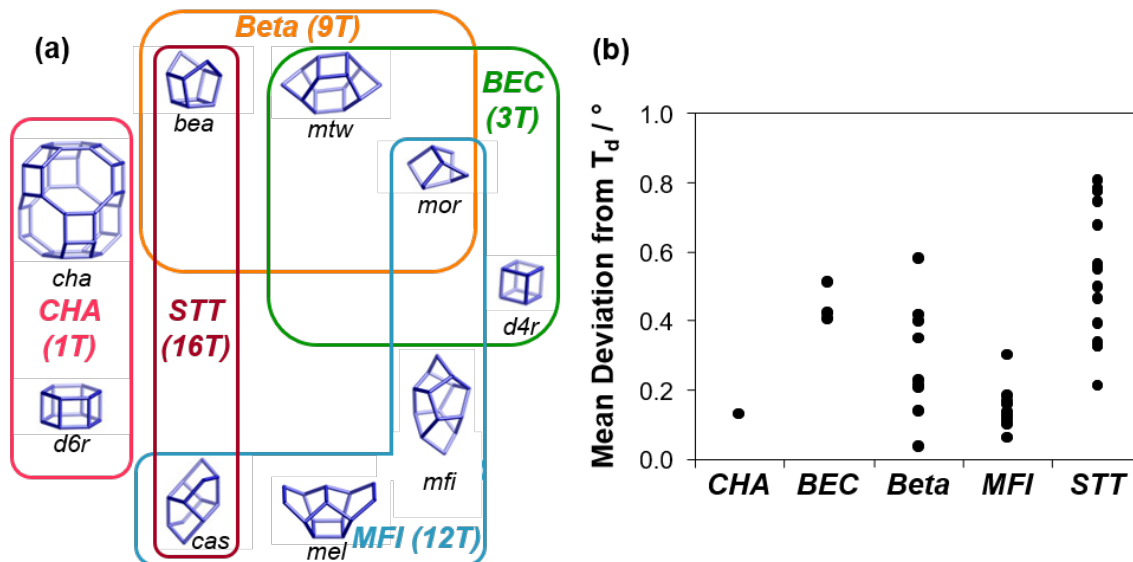


**Figure 4.9:** (a) Composite building units of Beta, MFI, CHA, STT, and BEC zeolites [142]. The number of crystallographically distinct T sites for each framework is provided in parentheses. (b) Mean deviation from tetrahedral (O-T-O 109.47°, Eq. 4.12) for each of the T-sites in the pure-silica analogs of the Sn-zeolite frameworks synthesized in this work, as determined with the zeoTsites program [245], and listed by T-site in Table 4.13–Table 4.17.

frameworks provide a diverse range of CBU structures that have varying degrees of commonality with those of Beta, ranging from none (CHA), to nearly all (BEC) of the same CBUs. The number of crystallographically-distinct T-sites for each framework is given parenthetically in Figure 4.9a, and describes the maximum number of chemical environments for Sn within a zeolite crystal because some T-sites may have similar bond angles and bond lengths, despite being crystallographically distinct. A quantitative way to compare the chemical environments around T-sites is to compute the distortion of their bond angles away from tetrahedral. The zeoTsites program of Sastre and Gale [245] was used to obtain all O-Si-O bond angles for the pure-SiO<sub>2</sub>

forms of each framework, and then the mean deviation from tetrahedral ( $109.47^\circ$ ) was computed for each T-site (Figure 4.9b) according to Eq. 4.12:

$$\text{Mean Deviation from } T_d = \sqrt{\frac{\sum_j N_j (\theta_{O-Si-O,j} - 109.47^\circ)^2}{\sum_j N_j}} \quad (4.12)$$

where  $N_j$  is the multiplicity of bond angle  $j$  in the extended unit cell used by zeoT-sites, as summarized in Table S7–Table 4.17. Mean deviations ranged from  $0.04$ – $0.58^\circ$  for Beta, and from  $0.06$ – $0.81^\circ$  for the other four frameworks, indicating these frameworks should encompass the range of possible Sn coordination environments in Beta. Specifically, CHA and MFI primarily sample low mean deviations, STT samples medium-high mean deviations, and BEC samples high mean deviations, relative to Beta. We note that the precise T-site locations of Sn in the zeolite frameworks synthesized here are unknown and difficult to accurately determine with currently available techniques [108, 111, 225], and thus acknowledge the implicit assumption in this discussion that Sn heteroatoms are substituted randomly among the distinct T-site locations in each of the frameworks synthesized.

Sn-CHA-F has been hydrothermally synthesized by our group previously [114], and serves as a good starting point for this discussion because it has one T-site, low tetrahedral distortion ( $0.13^\circ$ ), no common CBUs with Beta, and an abundance of prior characterization data. In brief, the previous study concluded through  $\text{CD}_3\text{CN}$  and pyridine IR and  $^{119}\text{Sn}$  DNP NMR, that Sn-CHA-F samples possessed defect-open sites and framework Sn sites that can interconvert between hydrolyzed-open and closed configurations, and that some of these sites (ca. 20%) are located within mesopores. The latter conclusion was corroborated here on the Sn-CHA-F-60 sample by *in situ* pyridine titrations during ethanol dehydration catalysis (Figure 4.39), where  $0.15 \text{ C}_5\text{H}_5\text{N}/\text{Sn}$  were adsorbed, suppressing the diethyl ether site-time yield by only  $\sim 30\%$ . The majority of the Sn is within the framework where access is limited by  $4 \text{ \AA}$  windows that prevent pyridine intrusion, and thus accounts for the majority of the  $\text{CD}_3\text{CN-Sn}_{\text{LA}}$  peak that is detected in IR spectra. These spectra (Figure 4.44) may

be deconvoluted into 2316  $\text{cm}^{-1}$  and 2308  $\text{cm}^{-1}$  components ( $\text{Sn}_{2308}/\text{Sn}_{2316} = 2$ ), but the peak center of the first dose (Figure 4.7) at 2309  $\text{cm}^{-1}$  does not indicate there are distinct  $\text{Sn}_{2316}$  sites. This is consistent with either T-sites with greater deviations from tetrahedral, or structural features unrelated to local T-site geometry as the dominant factor that leads to  $\text{Sn}_{2316}$  sites.

Sn-MFI-F zeolites were synthesized to provide a wider range T-sites with low-moderate deviations from tetrahedral ( $0.06\text{--}0.30^\circ$ ), and a single CBU in common with Beta ( $[5^4]$  cage, or “mor”, Figure 7a). Different sources of Si (TEOS, fumed  $\text{SiO}_2$ ) and  $\text{F}^-$  (HF,  $\text{NH}_4\text{F}$ ) were used, and in both cases yielded crystalline materials with MFI topology (Figure 4.51, Figure 4.57, Table 4.12). Similar to Sn-CHA-F samples, their IR spectra (Figure 4.45) can be deconvoluted into 2316  $\text{cm}^{-1}$  and 2308  $\text{cm}^{-1}$  components ( $\text{Sn}_{2308}/\text{Sn}_{2316} = 3.9$ ), but the peak center of the first dose (Figure 4.7) at 2310  $\text{cm}^{-1}$  does not indicate the presence of distinct  $\text{Sn}_{2316}$  sites. Together with Sn-CHA-F samples, these observations are inconsistent with  $\text{Sn}_{2316}$  sites located at T-sites with low mean deviations from tetrahedral ( $<0.15^\circ$ ), which include Beta T-sites T9 ( $0.04^\circ$ ) and T1 ( $0.14^\circ$ ). Such low distortions do not give rise to the 2316  $\text{cm}^{-1}$   $\text{CD}_3\text{CN}$  IR peak center in Sn-Beta, as indicated by structurally-similar lattice sites in Sn-CHA-F and Sn-MFI-F that do not lead to this 2316  $\text{cm}^{-1}$   $\text{CD}_3\text{CN}$  IR peak.

A Sn-STT-F sample was synthesized because the STT framework encompasses a higher range of tetrahedral deviations ( $0.21\text{--}0.81^\circ$ ) relative to Beta and shares the  $[4^35^4]$  cage CBU (“bea”, Figure 4.9a) with Beta. Incorporating Sn within the STT framework required a seed-assisted crystallization with Si-STT-F and yielded a solid product with STT topology (Figure 4.52) and a lower  $\text{N}_2$  micropore volume ( $0.15 \text{ cm}^3 \text{ g}^{-1}$ ) than the siliceous analog ( $0.18 \text{ cm}^3 \text{ g}^{-1}$ ), indicating some amorphous solids may be present. Quantifying  $\text{CD}_3\text{CN}$ -saturated IR spectra (Figure 4.46) gave 0.33  $\text{Sn}_{\text{LA}}/\text{Sn}$  on Sn-STT-F-151 (Table 4.12), indicating more than half of the Sn was present as extra-framework  $\text{SnO}_2$  species or within inaccessible regions of amorphous solids. We conclude from these observations ( $\text{Sn}_{\text{LA}}/\text{Sn} < 0.5$ , seed-assisted crystallization necessary) that it is difficult to incorporate Sn within STT frameworks, similar

to hydrothermal Sn-Beta-F syntheses that are unable to incorporate more framework Sn than approximately  $\text{Si}/\text{Sn}_{\text{LA}} = 100$  [107]. Despite this low Sn incorporation ( $\text{Si}/\text{Sn}_{\text{LA}} \sim 450$ ), the  $\text{CD}_3\text{CN}-\text{Sn}_{\text{LA}}$  peak can be deconvoluted into  $2316 \text{ cm}^{-1}$  and  $2308 \text{ cm}^{-1}$  peaks to give  $\text{Sn}_{2308}/\text{Sn}_{2316} = 6.9$  (Figure 5). The peak for the first  $\text{CD}_3\text{CN}$  dose is also centered at  $2307 \text{ cm}^{-1}$ , suggesting the small deconvoluted  $2316 \text{ cm}^{-1}$  peak (0.04 sites per Sn, Table 4.12) is not necessary to accurately describe the spectrum. Assuming Sn distributes randomly among the 16 T-sites in the STT framework, this result would appear to also exclude the remaining range of tetrahedral deviations that could explain  $\text{Sn}_{2316}$  sites in Beta that are not excluded by the prior discussion of MFI and CHA ( $>0.30^\circ$ ). On the other hand, preferential siting at locations with lower tetrahedral deviations in STT (T3, T10, T13, T16  $< 0.35^\circ$ , Table 4.16) is possible and could allow that  $\text{Sn}_{2316}$  sites are located at T-sites with higher tetrahedral deviations in Beta (T3, T4, T5, T8  $> 0.35^\circ$ , Table 4.13). To further explore the possibility that T-siting in locations with high tetrahedral deviations leads to  $\text{Sn}_{2316}$  sites, we synthesized a Sn-Ge-BEC-F sample, which has fewer T-sites (three) with a narrow range of higher tetrahedral deviations ( $0.41\text{--}0.51^\circ$ ).

Sn-Ge-BEC-F and Ge-BEC-F samples were synthesized hydrothermally with *N*-isobutyl-*N*-methyl-pyrrolidinium hydroxide (iButOH) as structure-directing agent following Zhang et al. [233] XRD patterns (Figure 4.53) were consistent with the BEC topology, while micropore volumes ( $0.15 \text{ cm}^3 \text{ g}^{-1}$ , Table 4.12) were lower than expected ( $0.21 \text{ cm}^3 \text{ g}^{-1}$ ) [246], but consistent with Zhang et al. [233] Two iButF per unit cell were quantified by TGA of as-made samples (Figure 4.63), consistent with prior reports that fluoride ions are located within double four-membered ring (D4R) cages in BEC [247], and are charge-balanced by  $\text{iBut}^+$  [233]. Infrared peaks for T-O-T stretching vibrational modes in the  $400\text{--}1400 \text{ cm}^{-1}$  range (KBr intrapellet mixture, Figure 4.64) were benchmarked with a Sn-Beta-F-181 sample and were consistent with previously-reported ATR-IR spectra [110], and on Sn-Ge-BEC-F and Ge-BEC-F samples indicated Ge incorporation through stretching peaks for Si-O-Ge ( $1000 \text{ cm}^{-1}$ ), Ge-O-Ge ( $890 \text{ cm}^{-1}$ ), and Ge in D4R units ( $570 \text{ cm}^{-1}$ ) [248]. Since Ge prefer-

entially incorporates into D4R units [249] (composed of T1 sites), it is likely that Sn incorporates elsewhere in “mtw” or “mor” CBUs, at T2 and T3 sites with mean tetrahedral deviations of  $0.41^\circ$  and  $0.51^\circ$ , respectively. Quantifying the  $\text{CD}_3\text{CN}$ -saturated IR spectrum on Sn-Ge-BEC-F (Figure 4.47) gave a value of 0.44  $\text{Sn}_{\text{LA}}/\text{Sn}$ , indicating a large fraction of Sn was present as  $\text{SnO}_2$ . The peak for  $\text{CD}_3\text{CN}$  bound to framework Sn could be deconvoluted to give a  $\text{Sn}_{2308}/\text{Sn}_{2316}$  molar ratio of 7.3, with a first-dose peak center of  $2312\text{ cm}^{-1}$  (Figure 4.7). While this peak center is closer to  $2316\text{ cm}^{-1}$  than those of CHA, MFI, and STT zeolites, the  $\text{Sn}_{2308}/\text{Sn}_{2316}$  molar ratio indicates BEC frameworks do not possess structural features that give rise to distinct  $\text{Sn}_{2316}$  sites.

The synthesis of zeolite frameworks with a diverse range of CBUs and T-site bonding environments failed to identify any framework other than Beta with distinct  $\text{Sn}_{2316}$  sites in  $\text{CD}_3\text{CN}$  IR spectra, according to the criteria of the peak center of the first dose ( $2312\text{--}2320\text{ cm}^{-1}$ ), and the  $\text{Sn}_{2308}/\text{Sn}_{2316}$  molar ratio at saturation ( $\leq 3.6$ ). This result is consistent either with the conclusion that  $\text{Sn}_{2316}$  sites are unrelated to geometric heterogeneities among different T-site locations, or that the specific T-site structure in Beta is not properly reproduced in the CHA, MFI, STT, and BEC samples studied here. We have discussed the latter possibility in the context of the range of deviations from tetrahedral bond angles available to Sn heteroatoms within each zeolite structure (Figure 4.9b). CHA, MFI, STT, and BEC encompass the range of deviations from tetrahedral ( $0.06\text{--}0.81^\circ$ ) available within Beta zeolites ( $0.04\text{--}0.58^\circ$ ) and assuming a random distribution of Sn among the various T-sites in these frameworks, should have led to at least one of them possessing  $\text{Sn}_{2316}$  sites, yet they do not. Attempts to correlate the first-dose peak center with different Sn siting models including a random distribution, the lowest mean tetrahedral deviation, and the highest mean tetrahedral deviation did not lead to satisfactory correlations, although a reasonable correlation could be forced by arbitrary choices of specific T-sites in each framework (Section S.2.10, Supporting Information). Yet, attempts to determine the T-site locations of Sn by  $^{119}\text{Sn}$  NMR have not uncovered a preferred

site for Sn in Beta [107, 225], and are not consistent with preferential siting at T8 sites, as needed for the correlation with tetrahedral deviations in Figure 4.71. In this case, the parsimonious explanation is that T-siting does not explain the identity of Sn<sub>2316</sub> sites, but we cannot fully exclude it as a possibility based on these data alone [250]. Additional computational screening coupled with a suitable kinetic and structural probe may provide additional information, since T-site location can be controlled precisely unlike in experiments. With the exhaustion of this and the other hypotheses discussed above, we postulate that the pronounced Sn<sub>2316</sub> sites in Sn-Beta samples is a consequence of the uniquely faulted structure of Beta zeolites.

#### 4.3.2.5 Sn at stacking fault grain boundaries

Qin et al. reported that HF and NH<sub>4</sub>F solutions preferentially dissolve heteroatoms located at grain boundaries in  $\sim 1 \mu\text{m}$  MFI crystals by observing the etching process with SEM, TEM, and electron tomography [228, 229], and suggested that this phenomenon can be generalized to other zeolite frameworks [229]. We thus hypothesized that NH<sub>4</sub>F treatments would preferentially remove Sn<sub>2316</sub> sites from Sn-Beta, if these sites were located at grain boundaries. A Sn-Beta-F-110 sample was treated in 40 wt% NH<sub>4</sub>F at 323 K for 0.083 h, 0.33 h, and 1 h as reported by Qin et al. [229]. Samples treated in NH<sub>4</sub>F at shorter timescales (0.083–0.33 h) retained their bulk crystal structures according to XRD patterns (Figure 4.55), micropore volumes (0.18–20 cm<sup>3</sup> g<sup>-1</sup>, Table 4.5) and similar Sn contents as the parent sample (Si/Sn = 105–115, Table 4.5), while the sample treated for one hour was partially destroyed according to decreased XRD peak intensities (Figure S41), lower micropore volume (0.09 cm<sup>3</sup> g<sup>-1</sup>, Table 4.5), and a higher Sn content (Si/Sn = 84, Table 4.5) that suggests preferential removal of dissolved SiO<sub>2</sub> relative to SnO<sub>x</sub> species during treatment and washing.

**Table 4.5:** Quantification of Sn content, micropore volume, and Sn Lewis acid site densities<sup>a</sup> on Sn-Beta-F-110 as a function of NH<sub>4</sub>F treatment time.

NH <sub>4</sub> F treatment time <sup>b</sup> / h	Si/Sn <sup>c</sup>	V <sub>micro</sub> <sup>d</sup> / cm <sup>3</sup> g <sup>-1</sup>	Sn <sub>2316</sub> /Sn	Sn <sub>2308</sub> /Sn	Sn <sub>LA</sub> /Sn	Sn <sub>2308</sub> /Sn <sub>2316</sub>	Si-OH / 10 <sup>-4</sup> mol g <sup>-1</sup>
0	110	0.23	0.35 ± 0.07	0.65 ± 0.13	1.0 ± 0.20	1.9	0.9
0.083	115	0.20	0.08 ± 0.02	0.52 ± 0.10	0.60 ± 0.12	6.6	1.3
0.33	105	0.18	0.11 ± 0.02	0.45 ± 0.09	0.56 ± 0.11	4.0	2.2
1.0	84	0.09	0.04 ± 0.01	0.48 ± 0.10	0.52 ± 0.10	11	3.6

<sup>a</sup>IMEC values for CD<sub>3</sub>CN determined by Harris et al. [56]

<sup>b</sup>Conditions: 40 wt% NH<sub>4</sub>F, 323 K, 300 rpm, 20 g solution (g zeolite)<sup>-1</sup>

<sup>c</sup>Quantified by AAS

<sup>d</sup>Determined by N<sub>2</sub> adsorption minimum in  $\partial V_{\text{ads}}/\partial \log(P/P_0)$

Hysteresis loops in the N<sub>2</sub> adsorption/desorption isotherms ( $P/P_0 > 0.5$ ) on the 0.083 h and 0.33 h samples are also consistent with generation of mesopores by fluoride etching, while the lack of hysteresis and gradually increasing isotherm on the 1 h sample is characteristic of multilayer adsorption in the macropores of amorphous solids [199] generated by partial framework destruction. These XRD and N<sub>2</sub> adsorption characterizations are consistent with retention of bulk crystallinity reported by Qin et al. [229] for Al-MFI zeolites treated under similar conditions (0.083–1 h), and preferential dissolution of crystals at grain boundaries was observed by Qin et al. on these same samples by SEM and tomography. By extension, we therefore conclude that NH<sub>4</sub>F treatments preferentially dissolved Sn-Beta-F crystals at their grain boundaries while preserving their crystallinity (0.083–0.33 h), and at longer times led to partial destruction of their frameworks (1 h).

The distribution of Lewis acidic Sn sites and Si-OH defects in NH<sub>4</sub>F-treated Sn-Beta-F samples was quantified by CD<sub>3</sub>CN IR (spectra in Figure 4.49) and summarized in Table 4.5. Systematic and monotonic increases in the density of Si-OH groups quantified by the 2275 cm<sup>-1</sup> CD<sub>3</sub>CN IR peak with NH<sub>4</sub>F treatment time ( $0.9\text{--}3.6 \times 10^{-4}$  mol g<sup>-1</sup>) are consistent with increasing extents of framework dissolution that generate defect-rich mesopores (0.083–0.33 h) and eventually lead to amorphous structures (1.0 h). After 0.083 h of NH<sub>4</sub>F treatment, the Sn<sub>2308</sub>/Sn<sub>2316</sub> molar ratio increased from 1.9 to 6.6, indicating this sample no longer possesses predominant Sn<sub>2316</sub> sites (Figure 4.7). The number of Sn<sub>2308</sub>/Sn did not change, within error ( $0.65 \pm 0.13 \rightarrow 0.52 \pm 0.10$ , Table 4.5), while the number of Sn<sub>2316</sub>/Sn decreased from 0.35 to 0.08, consistent with removal of Sn<sub>2316</sub> sites from grain boundaries after NH<sub>4</sub> etching of Sn-Beta-F. Further framework dissolution between 0.083 and 0.33 h did not impact the distribution of Sn<sub>2316</sub> sites and Sn<sub>2308</sub> sites, within error, and amorphization after 1.0 h increased the Sn<sub>2308</sub>/Sn<sub>2316</sub> molar ratio to 11 (Table 4.5), in agreement with the lack of Sn<sub>2316</sub> sites in amorphous stannosilicate structures (Section 4.3.2.3). The preferential removal of Sn<sub>2316</sub> sites from Sn-Beta-F after NH<sub>4</sub>F treatments is consistent with their location at defect grain boundaries.

Additionally, two Sn-Beta-F samples were treated in HF-containing Si-Beta-F synthesis gels followed by crystallization, initially with the intent to grow a siliceous shell or overlayer around Sn-Beta-F crystallites, but also to preferentially dissolve Sn-Beta-F crystals at grain boundaries before crystallization. Sn-Beta-F crystals were included as seed material in the gels ( $\sim 30$  wt% by  $\text{SiO}_2$ ). The solid products were crystalline Beta zeolites by XRD (Figure 4.54) and micropore volume (Table 4.6), and Si/Sn ratios increased to values ( $\text{Si/Sn} = 840$  and  $410$  for Si-Beta@Sn-Beta-F-169 and 116-2, respectively, Table 4.6) similar to that of the seeded gel ( $\text{Si/Sn}_{\text{gel}} = 670$  and  $510$  for Si-Beta@Sn-Beta-F-169 and 116-2, respectively), consistent with crystallization of Si-Beta at the seeds.

**Table 4.6:** Quantification of Sn content, micropore volume, and Sn Lewis acid site densities<sup>a</sup> on Sn-Beta-F and Si-Beta@Sn-Beta-F samples.

Sample	Si/Sn <sup>b</sup>	$V_{\text{micro}}^c / \text{cm}^3 \text{g}^{-1}$	Sn <sub>2316</sub> /Sn	Sn <sub>2308</sub> /Sn	Sn <sub>LA</sub> /Sn	Sn <sub>2308</sub> /Sn <sub>2316</sub>	Si-OH / $10^{-4} \text{ mol g}^{-1}$
Sn-Beta-F-116-2	116	0.23	0.36 ± 0.07	0.64 ± 0.13	1.01 ± 0.20	1.8	1.0
Si-Beta@Sn-Beta-F-116-2	410	0.22	0.17 ± 0.03	0.70 ± 0.14	0.87 ± 0.17	4.1	2.0
Sn-Beta-F-169	169	0.21	0.34 ± 0.07	0.72 ± 0.14	1.06 ± 0.21	2.2	1.3
Si-Beta@Sn-Beta-F-169	840	0.21	0.09 ± 0.02	0.63 ± 0.13	0.72 ± 0.14	7.1	0.65

<sup>a</sup>IMEC values for CD<sub>3</sub>CN determined by Harris et al. [56]

<sup>b</sup>Quantified by AAS

<sup>c</sup>Determined by N<sub>2</sub> adsorption minimum in  $\partial V_{\text{ads}} / \partial \log(P/P_0)$

The first doses of  $\text{CD}_3\text{CN}$  adsorbed at more Si-OH groups in Si-Beta@Sn-Beta-116-2 than at Sn sites (Figure 4.48), consistent with encapsulation within a siliceous shell, because first doses on typical Sn-Beta-F zeolites adsorb solely at Sn sites (e.g., in Figure 4.43). The first doses of  $\text{CD}_3\text{CN}$  adsorbed at more Sn sites than Si-OH groups on Si-Beta@Sn-Beta-F-169, suggesting incomplete encapsulation within a siliceous shell.

The  $\text{CD}_3\text{CN}$ -saturated IR spectra for the Si-Beta@Sn-Beta-F samples (thick lines) and their parent Sn-Beta-F samples (thin lines) are plotted in Figure 4.10, normalized to total Sn content for clarity to compare  $\text{CD}_3\text{CN-Sn}_{\text{LA}}$  peaks. The shapes of

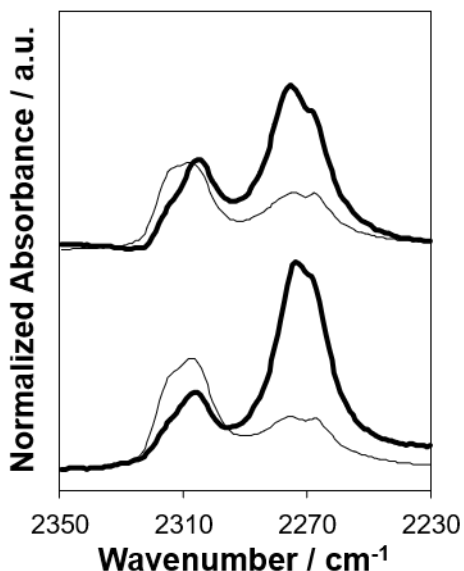


**Figure 4.10:** IR difference spectra of  $\text{CD}_3\text{CN}$  adsorbed at saturation coverages (303 K) on Sn-Beta-F-116-2 (lower thin line), Si-Beta@Sn-Beta-F-116-2 (lower thick line), Sn-Beta-F-169 (upper thin line), and Si-Beta@Sn-Beta-F-169 (upper thick line), normalized by T-O-T overtone peak area and Sn content ( $\text{mol g}^{-1}$ ).

the peaks indicate there are fewer  $\text{Sn}_{2316}$  sites after treating in Si-Beta gels, reflected after deconvolution in the average  $\text{Sn}_{2308}/\text{Sn}_{2316}$  molar ratio of 5.6 (Figure 5), which suggests that the structural features that lead to  $\text{Sn}_{2316}$  sites in the parent samples are diminished after treatment in a Si-Beta-F synthesis gel. Quantifying saturated  $\text{CD}_3\text{CN}$  spectra on a per Sn basis (Table 4.6) indicates that  $\text{Sn}_{2308}$  sites were unaf-

fects during the treatment process, because all values are the same within error, while the number of  $\text{Sn}_{2316}/\text{Sn}$  decreased to  $\sim 25\text{--}50\%$  of its value before treatment. Selective consumption of  $\text{Sn}_{2316}$  sites, but without loss of total Sn, is consistent either with blockage of these sites to prevent the access of  $\text{CD}_3\text{CN}$ , or their removal from the framework and conversion to  $\text{SnO}_2$  species. It is more likely the latter, because HF in the synthesis gel may react with framework Si and Sn in the seed materials to extract it into solution. Once Sn heteroatoms are removed from the framework, they can aggregate and form  $\text{SnO}_2$  after calcination.

Based on the evidence that treatment in  $\text{NH}_4\text{F}$  and HF solutions preferentially removes  $\text{Sn}_{2316}$  sites from Sn-Beta-F, that these treatments preferentially dissolve zeolite grain boundaries [228, 229], and the exclusion of the other structural features discussed above, we conclude that  $\text{Sn}_{2316}$  sites are defect-open sites (Figure 4.1c) that are preferentially located at stacking fault grain boundaries in Beta crystallites. These stacking faults occur because of interruptions in the stacking sequence of tertiary building unit layers that form chiral polymorph A and achiral polymorph B [190]. The mixture of these polymorphs (typically, 50-60% polymorph B) leads to the well-known broad XRD peak centered at  $7.8^\circ$  [190], with stacking faults that occur frequently at distances  $< 8$  nm, as detected by TEM [190, 251, 252] and Raman spectroscopy [253]. This highly faulted structure is unique to Beta among the other frameworks studied (CHA, MFI, STT, BEC), and thus provides an alternative explanation other than T-siting for the distinct  $\text{CD}_3\text{CN-Sn}$  peak at  $2316\text{ cm}^{-1}$ . The lack of predominant  $\text{Sn}_{2316}$  sites in Sn-Ge-BEC-F is particularly illustrative, given its similarity to the Beta structure, but absence of stacking faults, as evidenced by its two well-resolved low-angle XRD peaks (Figure 4.53). High-resolution TEM images of stacking faults in Beta [235] reveal a double-pore structure  $1.5\text{--}2\times$  as large as the 12-MR pores of Beta (Figure 4.11a), with several  $\text{Q}^3$  Si atoms terminated by Si-OH groups. Sn atoms located within these stacking fault structures would adopt defect-open configurations, and thus retain their Sn-OH group after dehydration treatments that would otherwise cause condensation of proximal silanol and stannanol groups

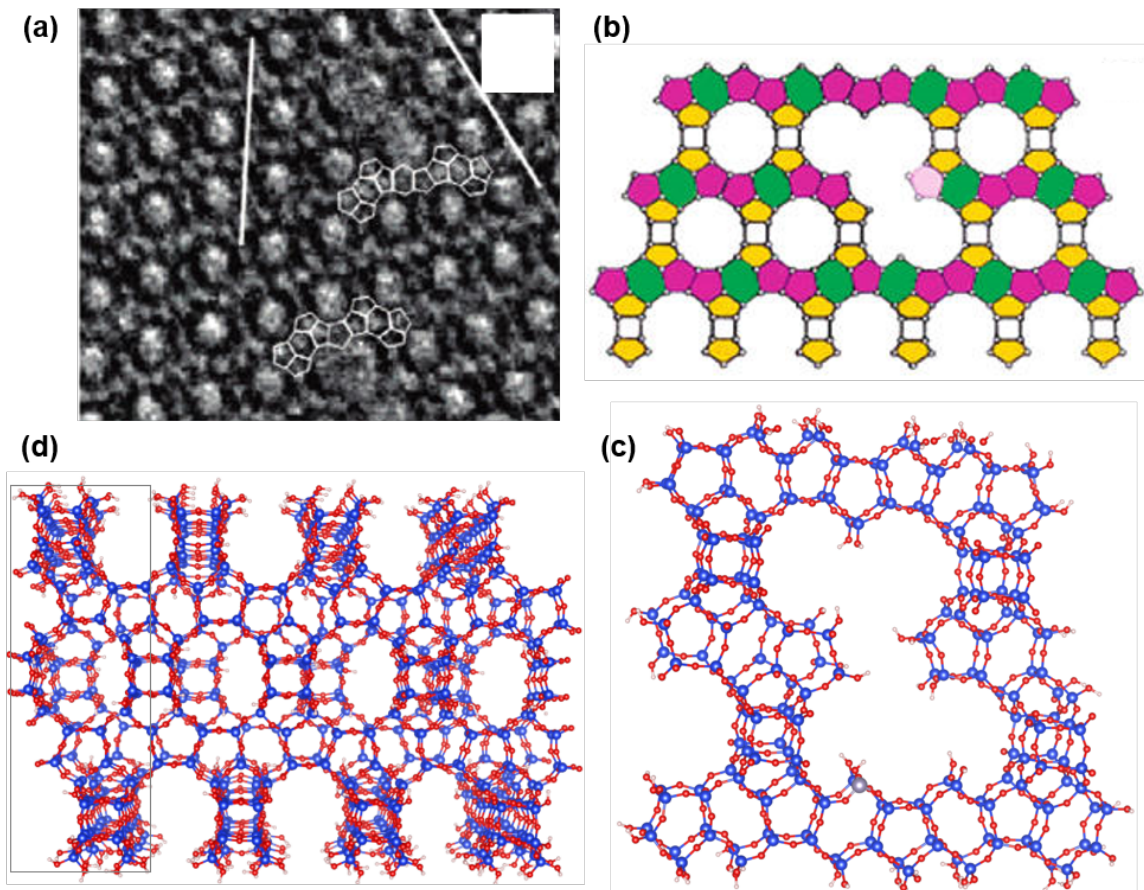


**Figure 4.11:** (a) High-resolution TEM image of double-pore stacking fault defects in zeolite Beta, and (b) tiling of zeolite Beta structural building units in polymorph B (left) and polymorph A (right) to meet at a stacking fault and form a defective pore structure. Adapted with permission from Wright et al. [235] Copyright 2005 American Chemical Society. (c) View of the stacking fault defect model developed in this work, with Sn substitution in the defect-open configuration, and (d) view rotated  $90^\circ$  to show periodicity in one direction, with the unit cell enclosed in the gray box. Blue = Si, Red = O, Gray = Sn, White = H.

in hydrolyzed-open sites to form their corresponding closed configurations. We next develop a structural model for these defect sites at stacking faults, and investigate their different ethanol dehydration reactivity to further explore whether they are the predominant site identified by *in situ* pyridine poisoning experiments.

### 4.3.3 Computational modeling of ethanol dehydration at stacking fault defect-open sites

A computational model of Sn substituted at a stacking fault grain boundary was constructed by following the tiling pattern developed by Wright et al. [235] (Figure 4.11b), where one layer of polymorph A and one of polymorph B meet and form a double-pore structure with seven T-atoms within the pores terminated by hydroxyl groups, depicted in Figure 4.11c. It is periodic in one dimension along the axial direction of the defective pore (Figure 4.11d) to provide structural rigidity. Sn was substituted at one of the locations in the lower part of the defective pore (Figure 4.11c, gray atom), leading to a  $(\text{OH})\text{Sn}(\text{OSi}\equiv)_3$  structure with a stannanol group and no nearby Si-OH that can form a closed site by condensation with the stannanol, which can be described as defect-open [111]. This model differs from previously used defect-open models because they were created by removing a Si T-atom from the otherwise intact crystal structure of polymorph A, resulting in a hydroxyl nest including 3 Si-OH groups and the stannanol [102,111]. Sn at the chosen defect-open location in the stacking fault is representative of any site in the defective pore that prevents forming closed sites, as evidenced by the similar calculated ethanol binding energies among the seven different defect-open locations (Table 4.19, Supporting Information). The model therefore captures the distinct structural features of Lewis acid sites located within defective regions at stacking faults in Beta zeolites and permits comparing their reactivity with traditional models of Lewis acid sites within Sn-Beta, as we discuss below.

The Gibbs free energies of adsorbed intermediates and transition states involved in concerted and sequential bimolecular ethanol dehydration pathways were calculated at the stacking fault defect-open site and compared with previously calculated free energies for the concerted dehydration mechanism at closed sites, which is the sole kinetically-relevant pathway (degree of rate control = 0.99), as determined by microkinetic modeling that included sequential pathways and interconversion between hydrolyzed-open and closed sites [180]. These pathways are compared on a free energy

diagram in Figure 4.12, with the gas-phase species that are involved at each reaction coordinate position listed above the plot. We note that the computational complex-

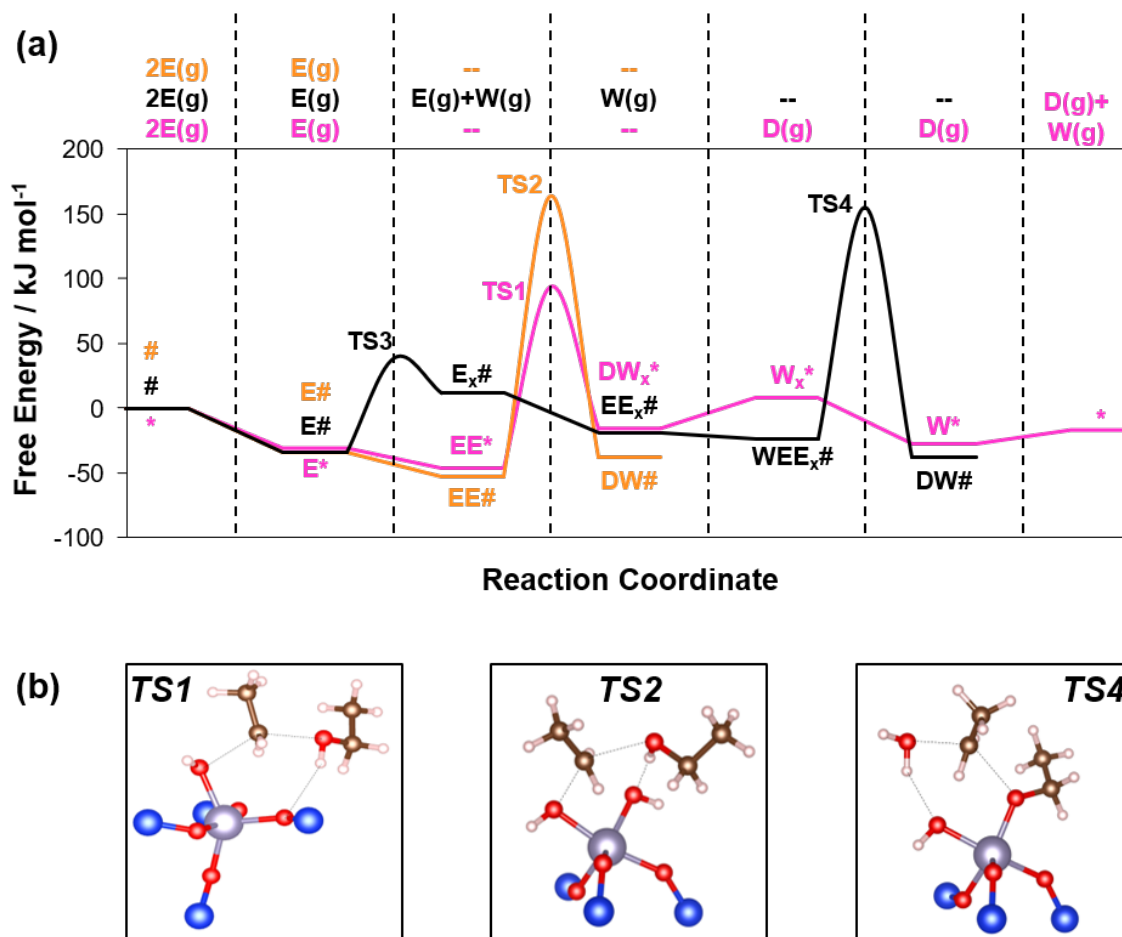


**Figure 4.12:** (a) Gibbs free energies of adsorbed intermediates and transition states calculated by DFT, referenced to two gas-phase ethanol molecules, for bimolecular ethanol dehydration at closed framework Sn sites (\*) via a concerted pathway (pink, calculated by Bukowski et al. [180]), and at stacking fault defect-open sites (#) via a concerted pathway (orange) or a sequential pathway (black). Product desorption steps are omitted from the stacking fault defect-open pathways for clarity. The gas-phase species at each position along the reaction coordinate are included above the plot area. (b) Transition state geometries for bimolecular dehydration at the closed site (TS1), and the stacking fault defect-open sites via the concerted pathway (TS2) and the sequential pathway (TS4). Intermediate geometries are provided in Figure 4.72.

ity of the model prevents vibrational frequency calculations; thus, zero-point energies

(ZPEs) were considered equivalent to the same reactive intermediate at framework sites calculated previously [180], and ZPE changes for transition states were assumed equal to their initial state. These ZPE approximations can introduce errors on the order of 10 kJ mol<sup>-1</sup> in apparent free energy barriers.

The pink pathway corresponds to the concerted mechanism at closed sites (denoted \*) calculated previously [180], where diethyl ether forms via an S<sub>N</sub>2-like transition state (TS1, Figure 4.12b) from a co-adsorbed ethanol-ethanol dimer intermediate (EE\*) with an apparent activation free energy of 125 kJ mol<sup>-1</sup> (referenced to E\* + E(g), because this gives first-order kinetics consistent with experimental measurements). It is worth noting here that the S<sub>N</sub>2 transition state is stabilized by forming a hydrolyzed-open site (W<sub>x</sub>\*), with its stannanol acting as the leaving group, and one framework O atom acting as a Brønsted base [254] to accept the alcohol proton from the nucleophilic ethanol and to begin to form a proximal silanol. This site can then complete the catalytic cycle by kinetically-irrelevant product desorption and site-closing steps, where the stannanol and proximal silanol recombine to form surface-bound water. In contrast, defect-open sites do not have these interconversion pathways available to them because of geometric constraints and so must traverse distinct mechanistic pathways. If defect-open sites are the predominant sites (A) for ethanol dehydration, the activation free energies at these sites, properly referenced to adsorbed intermediates that give first-order kinetic behavior, should be lower than 125 kJ mol<sup>-1</sup>.

A concerted mechanism was calculated on the stacking fault defect-open site (denoted #) and corresponds to the orange pathway in Figure 4.12. Gas-phase ethanol adsorbs at the Sn center to form the ethanol monomer intermediate (E#) with an adsorption free energy of -35 kJ mol<sup>-1</sup>. The similarity of this adsorption free energy to that calculated at closed sites (-31 kJ mol<sup>-1</sup> [180]) reflects compensations among entropies, van der Waals energies [139] and electronic contributions to adsorption that are distinct at the stacking fault defect-open site (Table 4.20, Supporting Information).

A second gas-phase ethanol molecule adsorbs in an octahedral configuration to the Sn to form the ethanol-ethanol dimer intermediate (EE#) with a differential adsorption free energy of  $-19 \text{ kJ mol}^{-1}$  and a differential adsorption enthalpy within  $5 \text{ kJ mol}^{-1}$  of that at the closed site. This similarity reflects compensation between the weaker van der Waals dispersion energy and a stronger adsorption energy at the stacking fault defect-open site. An octahedral configuration was not stabilized at closed Sn sites, which preferred a hydrogen-bonded ethanol-ethanol dimer structure that minimized geometric distortion in the framework and increased the degree of favorable interactions with the confining pore.

Despite a stannanol group bound to Sn, the transition state (TS2, Figure 10b) differs from that previously reported on hydrolyzed-open sites [180] because defect-open sites lack a Brønsted acidic proximal silanol. At the hydrolyzed-open site, the proximal silanol donates its proton to the hydroxyl group of the ethanol being attacked, forming water as a leaving group and simultaneously closing the site by re-forming the Sn-O bond, while the stannanol group accepts a proton from the nucleophilic ethanol to form adsorbed  $\text{H}_2\text{O}$  at the newly-closed site (Figure 4.74, Supporting Information). In TS2, the stannanol serves the same function to deprotonate the nucleophilic ethanol and form water, but the leaving group instead is the hydroxyl group of the second ethanol molecule, which transfers to the Sn atom to re-form the stannanol group at the defect-open site. The hydroxyl leaving group of TS2 is less stable than a  $\text{H}_2\text{O}$  molecule, leading to an intrinsic activation free energy of  $218 \text{ kJ mol}^{-1}$ , or an apparent activation free energy of  $199 \text{ kJ mol}^{-1}$ , when referenced to gas-phase ethanol and the ethanol monomer, which would give first-order kinetics (Table 4.18). This apparent activation free energy is  $74 \text{ kJ mol}^{-1}$  higher than that calculated at the closed site ( $125 \text{ kJ mol}^{-1}$ ), and so this pathway cannot account for the reactivity of the predominant active sites on Sn-Beta. The apparent enthalpic and entropic contributions to the high apparent activation free energy are  $157 \text{ kJ mol}^{-1}$  and  $-103 \text{ J mol}^{-1} \text{ K}^{-1}$ , respectively, indicating that the lower reactivity is a consequence of the enthalpy at the transition state, because the  $\Delta S_{\text{app}}^\ddagger$  value of  $-103 \text{ J mol}^{-1} \text{ K}^{-1}$  is similar to  $-116 \text{ J}$

$\text{mol}^{-1} \text{K}^{-1}$  at the closed site. The higher transition state enthalpy is likely related to the less stable hydroxyl leaving group. With the conclusion that concerted mechanisms are unfavorable at defect-open sites, we explored ethoxide-mediated sequential pathways to broaden the space of potential mechanisms.

The sequential pathway at the stacking fault defect-open site (black line, Figure 4.12) begins like the concerted pathway, with adsorption of gas-phase ethanol to form an ethanol monomer,  $E\#$ . The ethanol monomer then eliminates  $\text{H}_2\text{O}$  to form an ethoxy group at the site ( $E_x\#$ ) and gas-phase water, with a reaction free energy of  $46 \text{ kJ mol}^{-1}$ , and an intrinsic activation free energy of  $74 \text{ kJ mol}^{-1}$  (TS3, Figure 4.72). A second gas-phase ethanol molecule adsorbs at the Sn center to form an ethoxy-ethanol complex ( $EE_x\#$ ), with a differential adsorption free energy of  $-30 \text{ kJ mol}^{-1}$ . The ethoxy-ethanol complex may rearrange to form diethyl ether, but this transition state (TS5, Figure 4.73) is highly geometrically-constrained because the proton of the nucleophilic ethanol molecule must transfer to the O atom of the ethoxy it is attacking to regenerate the stannanol group of the defect-open site, leading to a high intrinsic activation free energy of  $231 \text{ kJ mol}^{-1}$ . Instead, a gas-phase water molecule (perhaps desorbed during the ethoxy formation step) adsorbs to form a water-ethanol-ethoxy complex ( $WEE_x\#$ , Figure 4.72), with a differential adsorption free energy of  $-5 \text{ kJ mol}^{-1}$ . This water molecule lowers the intrinsic activation free energy to  $179 \text{ kJ mol}^{-1}$  by donating a proton to the hydroxyl leaving group of the adsorbed ethanol to form a stable  $\text{H}_2\text{O}$  leaving group, and simultaneously regenerating the defect-open site stannanol group (TS4, Figure 4.12b). The reduction of activation barriers by  $\text{H}_2\text{O}$ -mediated proton transfer pathways has been noted before in theoretical studies of glucose isomerization catalysis [70]. Different MARI species along the water-assisted sequential pathway may give first-order kinetics ( $E\#$ ,  $E_x\#$ ), but the reaction free energy to form  $E_x\#$  is similar to that for forming  $E_x^*$  at framework sites (within  $6 \text{ kJ mol}^{-1}$ ), where previous microkinetic modeling predicted the coverage of  $E_x^*$  was  $<1\%$ . Thus,  $E\#$  is a more plausible MARI species, leading to an apparent activation free energy at defect-open sites of  $190 \text{ kJ mol}^{-1}$ . While this apparent activation free energy

for the sequential pathway may be competitive with that of the concerted pathway at the defect-open sites ( $199 \text{ kJ mol}^{-1}$ ), it is higher than that of the concerted pathway at closed sites ( $125 \text{ kJ mol}^{-1}$ ). Thus, our calculations indicate that defect-open sites are not the predominant sites for ethanol dehydration.

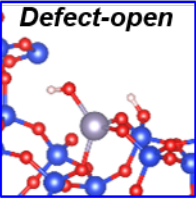
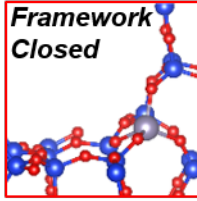
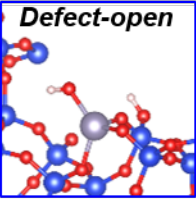
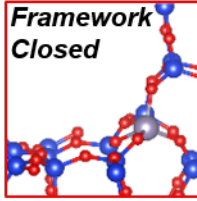
#### 4.3.4 Dominant active site structures for ethanol dehydration and glucose isomerization catalysis

The insights provided by these calculations were used to re-assess the identities of sites A and B that were titrated by pyridine *in situ* during ethanol dehydration catalysis (Section 4.3.1). Assuming  $\text{Sn}_{2316}$  sites are defect-open sites, and because the calculated apparent activation free energy barriers for ethanol dehydration at these sites are at least  $\sim 50 \text{ kJ mol}^{-1}$  higher than those measured at either A sites or B sites, then both A and B sites are a subset of  $\text{Sn}_{2308}$  sites that correspond to framework Sn sites. DFT-calculated apparent activation free energies (404 K, relative to the ethanol monomer) at closed sites consistent with those measured on A sites (Section 4.3.1) are also consistent with their identity as closed framework Sn sites ( $\text{Sn}_{2308}$ ). The density of A+B sites quantified at  $t_1$  (after initial deactivation transients) is in reasonable agreement with parity for  $\text{Sn}_{2308}$  sites (Figure 4.36b), consistent with this assessment. This supports the conclusion that the predominant sites (A) correspond to 17–26% of  $\text{Sn}_{2308}$  sites (Figure 4.34), with B sites accounting for the remaining  $\text{Sn}_{2308}$  sites, and that these sites differ in their reactivity predominantly by their entropies of activation. The generality of this correlation to different Sn-zeolite samples (Sn-MFI-F-129, Sn-Ge-BEC-F) that lack distinct  $\text{Sn}_{2316}$  sites, and its insensitivity to increased  $\text{H}_2\text{O}$  pressures (0.1–1 kPa  $\text{H}_2\text{O}$ ), indicates that this subset of  $\text{Sn}_{2308}$  sites is structurally distinct from the remaining  $\text{Sn}_{2308}$  sites, but that  $\text{CD}_3\text{CN}$  IR is not sensitive to this difference.

Although currently available spectroscopic probes cannot distinguish between A sites and B sites, the ethanol dehydration kinetic probes that distinguish them are sensitive to free energies of ethanol dehydration transition states that involve simulta-

neous Sn site-opening, a salient feature of the DFT-calculated pathways that results in stabilization of transition states at framework closed sites over those at stacking fault defect-open sites. As a result, more-reactive and less-reactive framework Sn sites may be sensitive to the energetics associated with closed-to-open site interconversion during the reaction coordinate, which we speculate may reflect heterogeneities in local structure caused by crystallographically-unique framework T-site locations; such phenomena may be amenable to further detailed examination by DFT calculations that are beyond the scope of the current study. The stacking fault defect-open site model used here provides evidence that such sites do not contribute to measured ethanol dehydration reactivity, and we anticipate it will be useful to accurately model reaction coordinates that do occur at them such as glucose isomerization, which would benefit from the larger void space and nearby hydroxyl groups in the surrounding environment. The defect-open site possesses Si-OH groups that would stabilize hydride shift transition states similar to pathways calculated on hydrolyzed-open sites [69,70] because their Si-OH groups lie within distances sufficiently proximal (Sn-H(O-Si) distance of 4.6 Å compared with 3.5 Å at the hydrolyzed-open site, Table 4.21) to donate hydrogen bonds to glucose or co-adsorbed H<sub>2</sub>O molecules at transition states. Their double-pore structure may also enable facile diffusion of glucose and fructose molecules, as suggested as an explanation for the lower reactivity of Sn-MFI zeolites [70]. The structural diversity of zeolite frameworks that host Sn sites in both framework and defect-open configurations confers reactivity for a broad range of oxygenated molecules [16,105,255,256]. In summary, the salient features that distinguish the spectroscopic signatures, structure, and reactivity of defect-open and framework Sn sites are collected in Figure 4.13.

Here, as in our previous work identifying Sn<sub>2316</sub> sites as the active sites for glucose-fructose isomerization [56], the combination of quantitative site characterization and catalytic rate data enabled identifying the dominant active sites for ethanol dehydration. Pyridine served as the titrant of both closed and defect-open sites in these chemistries, as compared side-by-side in Figure 4.14. In the case of ethanol dehy-

<b>Structure</b>		
	<b>Defect-open</b>	
		
<b>Spectroscopic Signatures</b>		
2316 $cm^{-1}$	<b>CD<sub>3</sub>CN IR</b>	2308 $cm^{-1}$
-420 ppm	<b><sup>119</sup>Sn NMR</b>	-440 ppm
55.8/54.9 ppm	<b>TMPO <sup>31</sup>P NMR</b>	58.6/57.2 ppm
<b>Reactivity</b>		
Possesses proximal Si-OH	<b>Salient Feature</b>	Can open at transition states
Dominant	<b>Glucose Isomerization</b>	Less reactive
Unreactive	<b>Ethanol Dehydration</b>	17–26% (A) dominant; the rest (B) secondary

**Figure 4.13:** Structures, spectroscopic signatures (<sup>119</sup>Sn NMR reported in ref. [68, 106]; TMPO <sup>31</sup>P NMR reported in ref. [105]), and features of reactivity that distinguish defect-open and framework Sn sites in Sn-zeolites.

dration (404 K, 8 kPa C<sub>2</sub>H<sub>5</sub>OH, 0.1 kPa H<sub>2</sub>O), gas-phase operation enabled *in situ* titrations of active Sn sites during catalysis (Figure 4.14a) on a suite of Sn-zeolite samples (Table 4.2), and correlating the predominant active sites with 17–26% of the framework Sn sites (Sn<sub>2308</sub>). In contrast, the aqueous-phase nature of glucose isomerization catalysis required introduction of pyridine titrants to Sn-Beta samples by *ex situ* dosing procedures in an IR cell before initial rate measurements (373 K, 1% (w/w) glucose) in batch reactors (Figure 4.14b). The pyridine uptake corresponding to suppression of the majority of the initial rate correlated with the defect-open sites

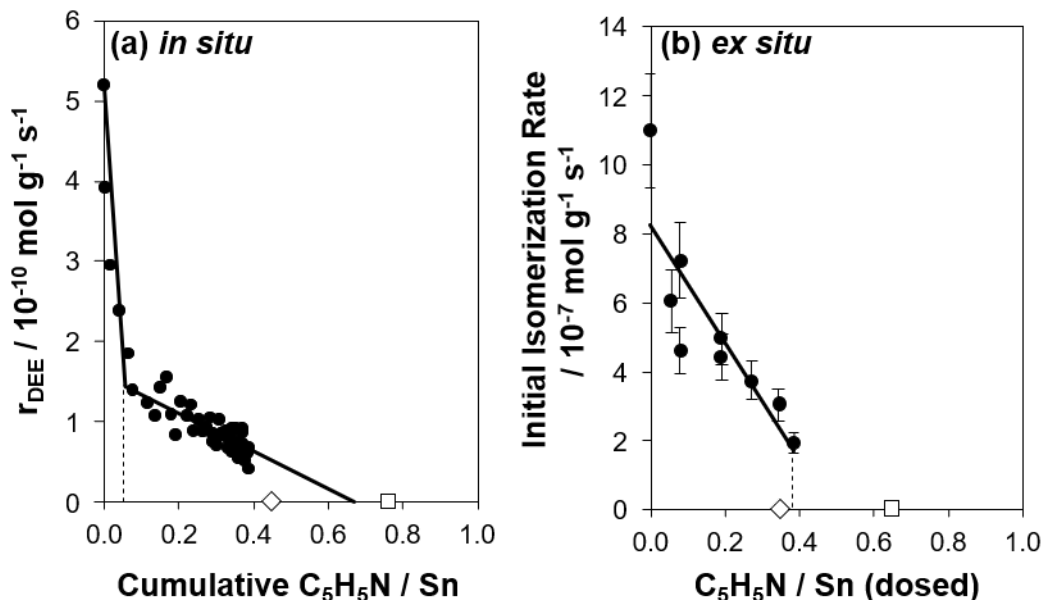


**Figure 4.14:** Comparison of pyridine titration data (a) *in situ* during ethanol dehydration catalysis (404 K, 8 kPa  $C_2H_5OH$ , 0.1 kPa  $H_2O$ ) on Sn-Beta-F-116-1, and (b) *ex situ* before measurement of initial glucose isomerization rates (373 K, 1 % (w/w) glucose) on Sn-Beta-F-110, reported in Harris et al. [56] The number of defect-open sites per Sn ( $\diamond$ ,  $Sn_{2316}$ ) and closed sites per Sn ( $\square$ ,  $Sn_{2308}$ ) are plotted on the x-axis. Dashed lines indicate the number of predominant sites titrated by pyridine.

( $Sn_{2316}$ ) on two samples, consistent with their identity as the dominant active sites for glucose isomerization [56]. The different sites titrated by pyridine dosed onto Sn-Beta *ex situ* under vacuum at 423 K (defect-open sites) and during ethanol dehydration catalysis *in situ* at 404 K in the presence of ethanol and water (framework sites) likely reflect the different conditions of the titrations (Figure 4.14), and highlights the sensitivity of titration procedures to the conditions under which they are conducted, as noted by Lewis et al. [105] who observed changes in  $^{31}P$  NMR signals for TMPO dosed onto Sn-Beta before and after continuous liquid-phase benzaldehyde-acetone condensation catalysis (383 K, toluene solvent). Defect-open sites ( $Sn_{2316}$ ) are typically titrated first in *ex situ*  $CD_3CN$  IR experiments on Sn-Beta-F samples, except on materials prepared to contain a siliceous external shell, as indicated by the concurrent titration of both defect-open sites ( $Sn_{2316}$ ) and Si-OH groups ( $2275 \text{ cm}^{-1}$ ) on

Si-Beta@Sn-Beta-F samples (Section 4.3.2.5). This observation suggests that pyridine titration *ex situ* is non-equilibrated, causing pyridine to bind irreversibly to surface sites in a chromatographic fashion, providing a plausible explanation for the different Sn sites titrated by pyridine *ex situ* under vacuum compared with those titrated *in situ* during ethanol dehydration catalysis wherein titration is likely equilibrated. This phenomenon highlights the need for additional quantitative characterization and kinetic investigations to validate titration data as described here and noted by others [56, 105].

#### 4.4 Conclusions

*In situ* pyridine titrations during ethanol dehydration catalysis (404 K, 8 kPa C<sub>2</sub>H<sub>5</sub>OH, 0.1 kPa H<sub>2</sub>O) on a suite of eleven Sn-Beta-F and Sn-Beta-OH zeolites identified two pools of Sn sites with turnover rates that differ by over an order of magnitude ( $\text{TOR}_{\text{A,avg}}/\text{TOR}_{\text{B,avg}} = 22$ ). The predominant active sites (A) comprised only 5–35% of the total Sn sites, but contributed 70–90% of the overall bimolecular ethanol dehydration STY (404 K, per Sn). Measured apparent activation enthalpies and entropies on a representative Sn-Beta-F-153 sample were consistent with A and B sites covered predominantly by ethanol monomer species [180, 227], and indicated that higher reactivity at A sites is a consequence of less negative apparent activation entropies ( $\Delta\Delta S_{\text{A-B,app}}^\ddagger = 48 \pm 22 \text{ J mol}^{-1} \text{ K}^{-1}$ ). The experimentally measured apparent activation free energy (404 K, diethyl ether formation transition state relative to the adsorbed ethanol monomer and gas-phase ethanol) at A sites (129 kJ mol<sup>-1</sup>) was consistent with the DFT-predicted apparent activation free energy at closed Sn sites (125 kJ mol<sup>-1</sup>). The structural identity of the predominant sites (A) could not be determined solely by comparing their quantities with the densities of Sn Lewis acid sites with CD<sub>3</sub>CN IR peaks at either 2316 cm<sup>-1</sup> (closer agreement to parity, but poor linearity) or 2308 cm<sup>-1</sup> (worse agreement to parity, but good linearity), because the structures of these sites were also not precisely known.

Motivated by widely-recognized but unclear relationships between structure and different reactivity of subsets of Sn sites in Sn-Beta [102, 105], and *in situ* pyridine titrations that detected a subset of more reactive sites during ethanol dehydration catalysis, we used a combined approach of targeted zeolite syntheses and post-synthetic treatments with *ex situ* CD<sub>3</sub>CN IR characterization to identify the underlying Sn structural feature that correlates with the 2316 cm<sup>-1</sup> CD<sub>3</sub>CN IR peak. The influence of residual fluorine bound to Sn sites was excluded by NMe<sub>4</sub>OH treatments to remove F that did not decrease the density of Sn<sub>2316</sub> sites. Lewis acidic Sn was also not detected at external crystallite surfaces on as-made Sn-Beta-F whose micropores are occluded by TEA<sup>+</sup>. Quantifying Sn<sub>2308</sub>/Sn<sub>2316</sub> molar ratios as a function of crystallization time of Sn-Beta-F indicated Sn<sub>2316</sub> sites are not located within amorphous regions of solid products, but require crystalline frameworks. The influence of local T-site geometry was probed by synthesizing Sn-zeolites with varying numbers of common building units with Beta, and with T-sites differing in their mean deviations from tetrahedral geometry, including Sn-CHA-F, Sn-MFI-F, Sn-STT-F, and Sn-Ge-BEC-F, but none of these alternative frameworks possessed distinct Sn<sub>2316</sub> sites, indicating that differences in local T-site structure are unlikely to account for this Sn site configuration. Treating Sn-Beta-F zeolites in NH<sub>4</sub>F solutions reported to preferentially etch zeolites at grain boundaries [228, 229], and in HF-containing Si-Beta synthesis gels to achieve similar dissolution before crystallization, decreased the number of Sn<sub>2316</sub> sites while leaving the number of Sn<sub>2308</sub> sites unchanged, supporting the hypothesis that Sn<sub>2316</sub> sites are located at stacking fault grain boundaries with defect-open configuration in Beta zeolites. Stacking fault defect-open structures are consistent with DFT-calculated CD<sub>3</sub>CN vibrational frequencies of 2316 cm<sup>-1</sup> for similar defect-open structures [102], with their ability to retain open configuration after ethanol dehydration catalysis and regenerative oxidation treatments [227], and with their function as predominant active sites for glucose-fructose isomerization [56] because they provide proximal Si-OH groups that stabilize hydride shift transition states [69, 70]. Sn<sub>2308</sub> sites, therefore, are the remaining tetrahedral framework Sn

sites, which may interconvert among closed and hydrolyzed-open configurations depending on chemical equilibrium. Such sites are closed after high-temperature dehydration treatments under vacuum [155], or during ethanol dehydration catalysis at 404 K [180].

A structural model of stacking fault defect-open sites was developed and enabled assessing their ethanol dehydration reactivity to determine whether they are the predominant sites (A) titrated by pyridine *in situ*. DFT-calculated apparent free energies of activation (404 K, diethyl ether formation transition state relative to the adsorbed ethanol monomer and gas-phase ethanol) for concerted and sequential pathways at stacking fault defect-open sites were higher than at closed Sn sites [180] by 65–74 kJ mol<sup>-1</sup>, indicating these sites do not contribute to ethanol dehydration reactivity at 404 K. Calculated transition state structures at stacking fault defect-open sites are less stable enthalpically because of their constrained geometries and less stable leaving groups, in contrast to transition states at closed sites that adopt less-constrained geometries and stabilize leaving groups by site-opening at the transition state. The predominant sites for bimolecular ethanol dehydration quantified by *in situ* pyridine titrations are therefore consistent with 17–26% of Sn<sub>2308</sub> sites quantified by CD<sub>3</sub>CN, rather than the defect-open sites that give rise to a CD<sub>3</sub>CN IR peak at 2316 cm<sup>-1</sup>. This fraction of framework Lewis acid sites is similar in Sn-Beta-F and Sn-Beta-OH materials with a wide range of Sn contents (0.9–5×10<sup>-4</sup> mol Sn g<sup>-1</sup>) and synthetic provenance (-F, hydrothermal; -OH, post-synthetic), and additionally in Sn-MFI-F and Sn-Ge-BEC-F materials.

In summary, we have identified the structural features that lead to distinct Sn site configurations in Beta zeolites, and reasons for their different reactivity. Defect-open sites (Sn<sub>2316</sub>) are distinguished by their inability to form closed configurations and preserve nearby Si-OH groups, the former feature causing their negligible bimolecular ethanol dehydration reactivity, and the latter resulting in their predominance for glucose-fructose isomerization. Framework Sn sites (Sn<sub>2308</sub>), on the other hand, are distinguished by their ability to interconvert between closed and hydrolyzed-open

configurations during catalysis, a critical feature that facilitates bimolecular ethanol dehydration. The different site requirements of these two probe reactions at Sn Lewis acid sites in Beta zeolites, and the structural diversity of their frameworks that allows them to host different Sn site configurations that catalyze both types of reactions, can rationalize the broad application of Sn-Beta for diverse chemical conversions of oxygenated molecules [16, 105, 255, 256]. This structural diversity in active site coordination afforded by the intergrowth of Beta polymorphs, which contain frequent occurrences of defect grain boundaries at stacking faults that pronounce defect-open site configurations, may also have catalytic consequences for Brønsted acid-catalyzed reactions in H-Al-Beta zeolites, which are applied in a variety of hydrocarbon transformations [257–260]. The approach taken here to reach these conclusions requires synthetic, spectroscopic, and theoretical techniques working in concert, all of which are undergirded and driven by the guiding principles of the turnover rate [63] and its accurate quantification with the aid of chemical titrants under reaction conditions [64].

#### 4.5 Acknowledgements

JB, JH, and RG acknowledge financial support from the Purdue Process Safety and Assurance Center (P2SAC), and a 3M Non-Tenured Faculty Award. BB and JG acknowledge support from the National Science Foundation’s program for Designing Materials to Revolutionize and Engineer our Future, DMREF (CBET-1437219). Use of the Center for Nanoscale Materials, a U.S. Department of Energy, Office of Science, Office of Basic Energy Sciences User Facility under Contract No. DE-AC02-06CH11357, and of computational resources from the National Energy Research Scientific Computing Center.  $^{19}\text{F}$  NMR spectra are courtesy of Dr. Sonjong Hwang (Caltech). We thank Dr. Germán Sastre for help using zeoTsites, Juan Carlos Vega-Vila for synthesis of Sn-Beta-OH samples, and Elizabeth Bickel for collecting SEM images.

Reprinted with permission from ACS Catal. 2019, 9 (7), 6146–6168. Copyright (2019) American Chemical Society.

## 4.6 Supporting Information

### 4.6.1 Supplementary Discussion

#### 4.6.1.1 Hydrothermal syntheses of zeolites

Sn-Beta-F zeolites were crystallized for different lengths of time starting from a single gel. Tetraethyl orthosilicate (TEOS, Sigma Aldrich, 98%) was dissolved in an aqueous solution of tetraethylammonium hydroxide (TEAOH, Sachem, 35 wt%) in a perfluoroalkoxy alkane (PFA) container (Savillex Corp.) and excess deionized water (18.2 M $\Omega$  cm) was added with the intent to promote hydrolysis of TEOS. The solution was covered and homogenized for 0.5 h. Then, a solution of tin(IV) chloride pentahydrate (Sigma Aldrich, 98%) in deionized water was added dropwise, and the mixture was covered and stirred overnight at ambient conditions to completely hydrolyze TEOS. The mixture was uncovered to evaporate ethanol and partially evaporate water to achieve the desired Si/H<sub>2</sub>O molar ratio. During the evaporation step, the H<sub>2</sub>O/Si ratio was allowed to decrease below the desired value to ensure complete evaporation of ethanol, and then deionized water was added to reach the desired H<sub>2</sub>O/Si. Lastly, hydrofluoric acid solution (Sigma Aldrich, 48%) was added and the mixture was stirred with a polytetrafluoroethylene (PTFE) spatula, yielding a thick gel with molar composition 1 SiO<sub>2</sub>/0.54 TEAOH/0.54 HF/0.005 SnCl<sub>4</sub>/6.8 H<sub>2</sub>O, where the total amounts corresponded to 30 g of TEOS. (Caution: when working with hydrofluoric acid, use appropriate personal protective equipment, ventilation, and other engineering controls.) The gel was divided approximately evenly among five 45 cm<sup>3</sup> PTFE liners (6–8 g of gel per liner), sealed within stainless-steel autoclaves (Parr Instruments), and heated to 413 K in an isothermal tumbling oven (~60 rpm, Yamato DKN-402C) for 1.6, 3, 7, 14, and 21 days.

A Sn-MFI-F sample was synthesized with NH<sub>4</sub>F and fumed SiO<sub>2</sub>. 1.23 g of ammonium fluoride (Sigma Aldrich, 98%) were dissolved in 5.98 g of deionized water in a 50 cm<sup>3</sup> centrifuge tube, then 0.071 g SnCl<sub>4</sub>·5H<sub>2</sub>O dissolved in 2.55 g of deionized water was added dropwise, and the mixture was homogenized by vortex mixer (VWR). In

a PFA container, 2.56 g of tetrapropylammonium bromide (TPABr, Sigma Aldrich, 98%) was dissolved in 12.59 g of deionized water. The  $\text{NH}_4\text{F}/\text{SnCl}_4/\text{H}_2\text{O}$  solution was added dropwise to the TPABr solution in the PFA container under continuous stirring, and the mixture stirred for 0.33 h. After this, 2 g of fumed silica (Cab-o-sil, Cabot) were slowly added and the mixture was covered and stirred overnight. The mixture was uncovered and water was allowed to evaporate until the gel composition was 1  $\text{SiO}_2/0.25$  TPABr/1  $\text{NH}_4\text{F}/0.006$   $\text{SnCl}_4/33.4$   $\text{H}_2\text{O}$ . The gel was loaded into a PTFE liner, sealed within a stainless-steel autoclave, and heated without agitation in an isothermal oven at 473 K for six days.

A second Sn-MFI-F sample was synthesized with HF and TEOS. TEOS was dissolved in an aqueous solution of tetrapropylammonium hydroxide (TPAOH, Alfa Aesar, 40 wt%) in a PFA container, and covered and stirred for 0.5 h. A solution of  $\text{SnCl}_4 \cdot 5\text{H}_2\text{O}$  in deionized water was added dropwise, and the mixture was covered and stirred overnight at ambient conditions to completely hydrolyze TEOS. The mixture was uncovered to evaporate ethanol and partially evaporate water to achieve the desired water content. Aqueous HF (48%) was added and the mixture was stirred with a PTFE spatula, yielding a thick gel with molar composition 1  $\text{SiO}_2/0.40$  TPAOH/0.40 HF/0.005  $\text{SnCl}_4/30$   $\text{H}_2\text{O}$  where the total amounts corresponded to 5 g of TEOS. The gel was loaded into a PTFE liner, sealed within a stainless-steel autoclave, and heated without agitation in an isothermal oven at 423 K for 14 days.

#### 4.6.1.2 Characterization of zeolites

Powder X-ray diffraction (XRD) patterns were collected with a Rigaku Smartlab X-ray diffractometer with a  $\text{Cu K}\alpha$  X-ray source in the range of  $2\theta = 4\text{--}40^\circ$  with a step size of  $0.01^\circ$  and scan speed of  $0.005^\circ \text{ s}^{-1}$ .

Thermogravimetric analysis (TGA) of as-made zeolites was performed to determine their SDA contents on a TA Instruments SDT Q600. As-made zeolites (0.01–0.02 g) were heated to 523 K ( $0.167 \text{ K s}^{-1}$ ) in flowing air (UHP, 99.999%, Indiana Oxygen,

83.3–167 cm<sup>3</sup> g<sup>-1</sup> s<sup>-1</sup>), held at 523 K for 0.5 h to desorb H<sub>2</sub>O, then heated to 1073 K (0.167 K s<sup>-1</sup>) to combust structure-directing agent molecules.

Nitrogen adsorption isotherms were collected on a Micromeritics ASAP 2020 instrument. Samples were pelleted and sieved to retain 180–250 μm aggregates, and 0.010–0.040 g were degassed by heating to 393 K for 2 h then 623 K for 10 h under dynamic vacuum (<0.67 Pa) before adsorption measurements. The temperature of the analysis tube was held at 77 K by immersion in a liquid N<sub>2</sub> bath. Micropore volumes were determined at the uptake corresponding to the minimum value of  $\partial V_{\text{ads}}/\partial \log(P/P_0)$ .

The bulk mass fraction of Sn in zeolite samples was obtained by atomic absorption spectroscopy (AAS). 0.03 g of powder were digested with 2 g of HF (Sigma Aldrich, 48%) overnight, then diluted with 50 g of deionized water. Calibration standards were prepared by diluting a stock solution (Sigma Aldrich, 1000±4 ppm Sn) with deionized water. A PerkinElmer AAnalyst 300 instrument equipped with a lamp for Sn (286.3 nm) was used to measure the absorbance of the standards and digested samples. Si/Sn ratios were calculated assuming the unit cell formula of each zeolite.

Diffuse reflectance UV-visible (DRUV) spectra were collected on a Varian-Cary 5000 spectrometer in a Harrick Praying Mantis *in situ* cell. Background spectra were collected before zeolite spectra at all conditions with poly(tetrafluoroethylene) (PTFE, Sigma Aldrich, 1 μm), and used to transform absorption spectra with the Kubelka-Munk function. Spectra were collected of samples under flowing dry He (UHP, Indiana Oxygen, 4.17 cm<sup>3</sup> s<sup>-1</sup> (g zeolite)<sup>-1</sup>) after dehydration for 0.5 h at 523 K (0.5 K s<sup>-1</sup>).

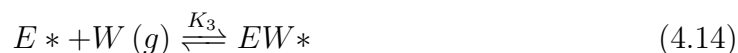
Scanning electron microscopy (SEM) was performed on a NovaNano SEM equipped with an Everhart-Thornlev detector for high-vacuum imaging. SEM micrographs were collected with a spot size of 3 μm and a voltage of 5 kV.

#### 4.6.1.3 Synthesis of N-isobutyl-N-methyl-pyrrolidinium hydroxide (iButOH)

Synthesis of iButOH was carried out following the procedure reported by Zhang et al. [233] In a 500 cm<sup>3</sup> two-neck flask containing a Teflon stir bar, 9.7 g of 1-methylpyrrolidine (Sigma Aldrich,  $\geq 98\%$ ) were mixed with 5.6 g of acetonitrile (Sigma Aldrich,  $\geq 99.9\%$ ) and formed a clear solution after stirring. While stirring, 15.6 g of 1-bromo-2-methylpentane (Sigma Aldrich, 99%) were added dropwise. After addition was complete, one neck of the flask was sealed by a rubber stopper, the second neck was connected to a reflux condenser, and the stirred mixture was heated by a hemispherical heating mantle at 348 K ( $0.0833 \text{ K s}^{-1}$ ) under reflux. After 3 h of reflux at 348 K, the mixture was an amber slurry thick enough to prevent movement of the stir bar, and was allowed to cool to ambient temperature, then washed by filtration with  $\sim 500 \text{ cm}^3$  of cold ( $\sim 273 \text{ K}$ , ice bath) ethyl acetate (Sigma Aldrich, anhydrous, 99.8%), yielding a pale yellow solid (iButBr). The solid was left to dry overnight in a fume hood in an open crystallization dish under ambient atmosphere, and the next morning, the dish contained a pale yellow viscous liquid because the solid adsorbed ambient moisture and dissolved. (Attempts to re-crystallize a solid from this mixture using cold (273 K) ethyl acetate yielded a two-phase liquid mixture and no solid, indicating the solid was dissolved in an aqueous phase. The aqueous phase was recovered by separatory funnel and residual ethyl acetate was evaporated by heating to 333 K ( $0.0833 \text{ K s}^{-1}$ ) for 0.333 h.) The concentrated iButBr solution was further diluted with deionized water (68.1 g H<sub>2</sub>O and 22.6 g of concentrated iButBr solution) in a PFA container. To this container were added 67.8 g of anion exchange resin (Dowex Marathon A), and the slurry was stirred for 20 h. The resin was separated from the solution by filtration, and this procedure was repeated a second time with fresh resin (67.9 g, 23 h stirring). The final iButOH solution was determined to be 11.5 wt% by titration with 0.1 M HCl and phenolphthalein as an indicator.

#### 4.6.1.4 Surface coverages of intermediates during *in situ* pyridine titrations

The coverages of surface intermediates can be estimated for Sn-Beta-F and Sn-Beta-OH zeolites using equilibrium constants measured previously [227], represented by the elementary reactions, assuming no vacant sites:



where  $E^*$  is the ethanol monomer,  $EE^*$  is the ethanol-ethanol dimer, and  $EW^*$  is the ethanol-water dimer, and the equilibrium constants for step 4.13 and 4.14 are  $K_2$  and  $K_3$ , respectively. The numbering of  $K_2$  and  $K_3$  are chosen for consistency with the simplified mechanism derived in our previous papers [180, 227]. Assuming only these three species ( $E^*$ ,  $EE^*$ ,  $EW^*$ ), the expressions for their coverages are:

$$\theta_{E^*} = \frac{1}{1 + K_2 P_E + K_3 P_W} \quad (4.15)$$

$$\theta_{EE^*} = \frac{K_2 P_E}{1 + K_2 P_E + K_3 P_W} \quad (4.16)$$

$$\theta_{EW^*} = \frac{K_3 P_W}{1 + K_2 P_E + K_3 P_W} \quad (4.17)$$

where  $P_E$  and  $P_W$  are the pressures of ethanol and water (kPa), respectively. Taking the measured values [227] of  $K_2$  and  $K_3$  in Sn-Beta-F ( $K_2 = 0.033 \text{ kPa}^{-1}$ ,  $K_3 = 0.26 \text{ kPa}^{-1}$ ) and Sn-Beta-OH ( $K_2 = 0.086 \text{ kPa}^{-1}$ ,  $K_3 = 1 \text{ kPa}^{-1}$ ), we estimate that the coverages on Sn-Beta-F are 78%  $E^*$ , 20%  $EE^*$ , and 2%  $EW^*$ , and in Sn-Beta-OH are 56%  $E^*$ , 38%  $EE^*$ , and 6%  $EW^*$ . Both surfaces are predominantly covered by  $E^*$  intermediates, and together with values of the intrinsic rate constant for diethyl ether formation on Sn-Beta-F ( $k_4 = 3.7 \times 10^{-5} \text{ mol (mol Sn}_{LA})^{-1} \text{ s}^{-1}$ ) and Sn-Beta-OH ( $k_4 = 4.6 \times 10^{-5} \text{ mol (mol Sn}_{LA})^{-1} \text{ s}^{-1}$ ), we estimate that  $r_{DEE} = k_4(EE^*)$  is  $2 \times$  higher

on Sn-Beta-OH than on Sn-Beta-F. This value is within the scatter of  $TOR_i$  values measured by *in situ* pyridine titration.

#### 4.6.1.5 Deactivation of Sn-Beta zeolites before pyridine titrations

Deactivation of Sn-Beta zeolites during approach to quasi-steady-state was modeled as an exponential decay:

$$r(t) = r_0 \exp(-k_d t) \quad (4.18)$$

where  $t$  is the time on stream (ks), and  $r_0$  and  $k_d$  are two fit parameters that are the rate at zero time on stream ( $\text{mol g}^{-1} \text{s}^{-1}$ ) and the deactivation rate constant ( $\text{ks}^{-1}$ ). Values of  $r_0/r_1$  (Figure 4.2, Main Text) were determined by regressing time-on-stream rate data to obtain  $r_0$  and  $k_d$ , then rearranging Eq. 4.18 for the expression  $\frac{r_1}{r_0} = \exp(-k_d t_1)$ , where  $t_1$  is the time the titration started.

To estimate the value of  $x_{A0}$  (A sites per total Sn, at initial time-on-stream) from the measured values of  $TOR_A$ ,  $TOR_B$ ,  $x_{A1}$ ,  $x_{B1}$  and  $r_0/r_1$ , it was assumed that the deactivation process occurring before pyridine titration deactivates solely A sites. This represents an upper bound on the value of  $x_{A0}$ , because relaxing the assumption and allowing the initial number of B sites to be greater at  $t_0$  than at  $t_1$  would decrease the estimated value of  $x_{A0}$  (see equation S.9 below). The value of  $x_{A0}$  was computed according to:

$$\frac{r_0}{r_1} = \frac{TOR_A x_{A0} + TOR_B x_{B0}}{TOR_A x_{A1} + TOR_B x_{B1}} \quad (4.19)$$

Rearranging, we obtain:

$$x_{A0} = \frac{\frac{r_0}{r_1} (TOR_A x_{A1} + TOR_B x_{B1}) - TOR_B x_{B0}}{TOR_A} \quad (4.20)$$

and applying the assumption that  $x_{B0} = x_{B1}$  gives:

$$x_{A0} = \frac{\frac{r_0}{r_1} (TOR_A x_{A1} + TOR_B x_{B1}) - TOR_B x_{B1}}{TOR_A} \quad (4.21)$$

The extents of initial deactivation transients over the course of 60 ks varied with temperature ( $r_1/r_0 = 0.38\text{--}0.75$ , Table 4.7), and the entire range (0–60 ks) can be fit with a first-order deactivation model to obtain deactivation rate constants ( $k_d = 7\text{--}23 \times 10^{-3} \text{ ks}^{-1}$ , Section 4.6.1.5, Supporting Information). The variation in deactivation rate constants with temperature (404–438 K) gives an apparent activation enthalpy of  $47 \pm 2 \text{ kJ mol}^{-1}$  (Figure 4.25b), which resembles calculated values of the apparent barrier to hydrolyze framework Sn-O-Si bonds ( $\sim 60 \text{ kJ mol}^{-1}$ ) [180]. The hydrolyzed-open sites formed could account for deactivation because their DFT-predicted bimolecular dehydration turnover rates are an order of magnitude lower than at closed sites [180], and because these sites can become closed again upon regenerative oxidation treatments. Structural changes to Sn sites are likely the cause of deactivation because Sn sites within both hydrophobic and hydrophilic frameworks deactivate to similar extents ( $r_1/r_0 = 0.59\text{--}0.92$ , Sn-Beta-F;  $r_1/r_0 = 0.53\text{--}0.69$ , Sn-Beta-OH; Table 2), in contrast to deactivation caused by gradual transformation of hydrophobic secondary environments to hydrophilic ones as proposed in liquid water [241] and evidenced in part by lower  $k_{24h}/k_0$  first-order glucose isomerization rate constant ratios on hydrophobic Sn-Beta-F ( $<20\%$ ) than on Sn-Beta-OH ( $\sim 50\%$ ) after 24 hours of hot (373 K) liquid water treatment [241].

#### 4.6.1.6 Kinetic measurements at B sites after poisoning of A sites

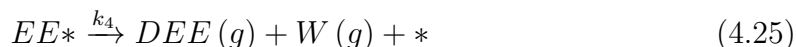
The reaction order in ethanol was measured at B sites on Sn-Beta-F-153 after irreversible titration of the A sites, as summarized in Figure S18. First, *in situ* pyridine titration was performed in the same way as reported in the main text, with injection of pyridine after reaching a quasi-steady-state ethanol dehydration rate. Pyridine was removed from the reactant stream at  $t_2$ , and after a period of  $>100$  ks, the sample reached a new quasi-steady-state rate that was  $<50\%$  of the rate before titration. Quantifying the uptake of pyridine during the titration (Figure 4.32b) gave regressed values of  $x_{A1}$ ,  $x_{B1}$ ,  $\text{TOR}_A$ , and  $\text{TOR}_B$  that agreed well with those reported in Table 4.2 in the main text. The dashed line in Figure 4.32b represents

the value of the quasi-steady-state rate after poisoning of A sites and desorption from B sites ( $1.5 \times 10^{-10} \text{ mol g}^{-1} \text{ s}^{-1}$ ), and is similar to the value predicted using  $x_{B1}$  and  $\text{TOR}_B$  ( $1.1 \times 10^{-10} \text{ mol g}^{-1} \text{ s}^{-1}$ ). Hence, rates measured after this point at different temperatures and ethanol pressures solely reflect turnover rates at B sites, and were quantified as  $\text{TOR}_B = r_{\text{DEE}}/n_{B1}$ , where  $r_{\text{DEE}}$  is the DEE formation rate ( $\text{mol g}^{-1} \text{ s}^{-1}$ ), and  $n_{B1}$  is the density of sites B quantified by the *in situ* pyridine titration ( $4.3 \times 10^{-5} \text{ mol g}^{-1}$ ). Turnover rates at B sites were quantified at 404 K and 437 K as a function of ethanol pressure (at 0.1 kPa  $\text{H}_2\text{O}$ ), were first-order in ethanol pressure in this regime (5–35 kPa  $\text{C}_2\text{H}_5\text{OH}$ , Figure 4.32c), and agreed well with rates quantified at 0.1 kPa  $\text{H}_2\text{O}$  and 8 kPa  $\text{C}_2\text{H}_5\text{OH}$  by separate *in situ* pyridine titrations as compared in Figure 4.4 in the main text. Periodic measurements at this reference condition (8 kPa  $\text{C}_2\text{H}_5\text{OH}$ , 0.1 kPa  $\text{H}_2\text{O}$ , 404 K) confirmed that the A sites remained irreversibly titrated after excursions in temperature and ethanol pressure, and were used to correct for intervening deactivation. In Figure 4.32d, comparing the DEE formation rate (404 K, 0.1 kPa  $\text{H}_2\text{O}$ , per g) at B sites with that measured on an un-poisoned catalyst allows estimating the ethanol reaction order ( $\alpha_E$ ) at A sites, after subtracting the contribution of B sites on the pyridine-poisoned catalyst from the measured rate at both site types on the un-poisoned catalyst. Because the fraction of the total rate contributed by B sites is low (10–30%), this results in a minor correction to the overall apparent reaction order determined when both sites are turning over, lowering it from 0.7 to 0.6 (Figure 4.32d). Thus, values of 0.6 and 1.0 were used to compute transition state formation rate constants ( $K_{i,app}^\ddagger$ ) at A and B sites, respectively in Figure 4.4 of the main text.

#### 4.6.1.7 Consequences of site hydrolysis for ethanol dehydration reaction orders

Including site hydrolysis in mechanisms for bimolecular ethanol dehydration involves expanding rate expressions to include parallel pathways at hydrolyzed-open

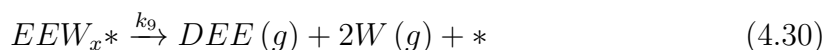
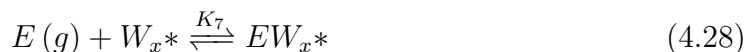
sites. Starting from the simplified series of elementary steps used in our previous papers, for consistency of nomenclature:



we can add additional steps for forming hydrolyzed-open sites ( $W_x^*$ ) after adsorption of  $H_2O$ :



where the site-hydrolysis step is quasi-equilibrated, according to DFT calculations [180]. Hydrolyzed-open sites then form diethyl ether from analogous molecularly-adsorbed intermediates, as detailed previously [180].



With these two parallel pathways, the overall diethyl ether formation rate is:

$$r_{DEE} = k_4(EE*) + k_9(EEW_x*) \quad (4.31)$$

Using the assumption of quasi-equilibrium for all adsorption steps,

$$\frac{r_{DEE}}{(L)} = k_4 K_1 K_2 (E)^2 \frac{(*)}{(L)} + k_9 K_5 K_6 K_7 K_8 (W) (E)^2 \frac{(*)}{(L)} \quad (4.32)$$

If we assume the same MARI species indicated by microkinetic modeling ( $E^*$ ,  $EE^*$ ,  $EW^*$ ), the overall site balance equation is expressed as:

$$(L) = (*) + (E^*) + (EE^*) + (EW^*) \quad (4.33)$$

and using the assumption of quasi-equilibrium for all adsorption steps,

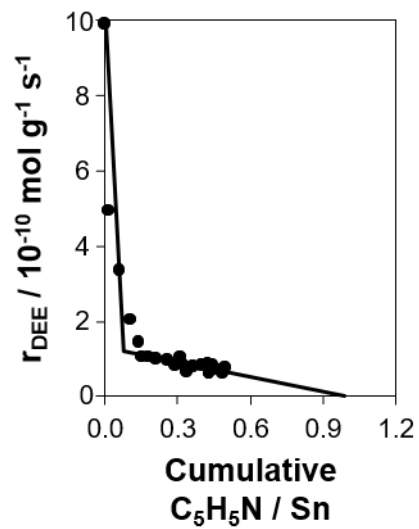
$$\frac{(*)}{(L)} = [K_1(E) + K_1K_2(E)^2 + K_1K_3(E)(W)]^{-1} \quad (4.34)$$

Substituting Eq. 4.34 into Eq. 4.32, and dividing numerator and denominator by  $K_1(E)$  gives

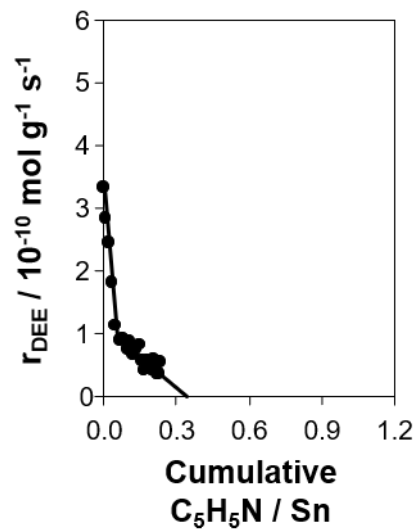
$$\frac{r_{DEE}}{(L)} = \frac{k_4K_2(E) + k_9K_1^{-1}K_5K_6K_7K_8(W)(E)}{1 + K_2(E) + K_3(W)} \quad (4.35)$$

where the two terms in the numerator represent DEE formation via the closed and hydrolyzed-open pathways. The salient feature of these parallel pathways is that the hydrolysis of a closed site by adsorbed  $H_2O$  (Eq. 4.26–Eq. 4.27) leads to a  $(W)$  in the part of the numerator for the hydrolyzed-open site that is not present for the closed site. Hence, if the two pools of sites quantified by *in situ* pyridine titration represented sites traversing these two pathways, then  $TOR_A$  and  $TOR_B$  would have different functional dependences on the water pressure. Therefore, the same  $H_2O$  reaction order of -0.1 measured for  $TOR_A$  and  $TOR_B$  is inconsistent with this interpretation, as discussed in the main text.

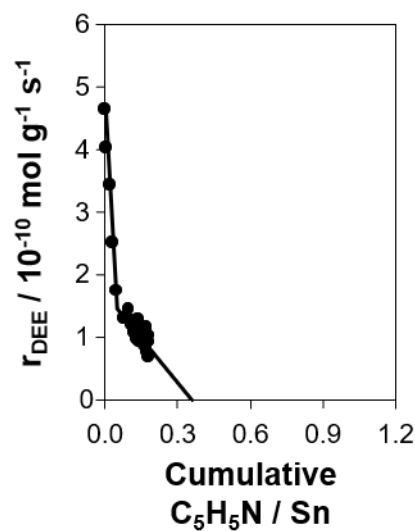
## 4.6.2 Supplementary Figures

4.6.2.1 *in situ* pyridine titration data

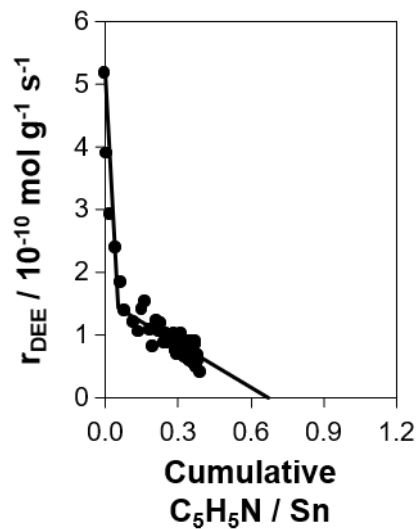
**Figure 4.15:** Diethyl ether formation rate (per g catalyst, 404 K, 8 kPa  $C_2H_5OH$ , 0.1 kPa  $H_2O$ ) as a function of pyridine uptake (1 Pa pyridine) on Sn-Beta-F-181 during catalysis. Solid line represents regressed two-site poisoning model.



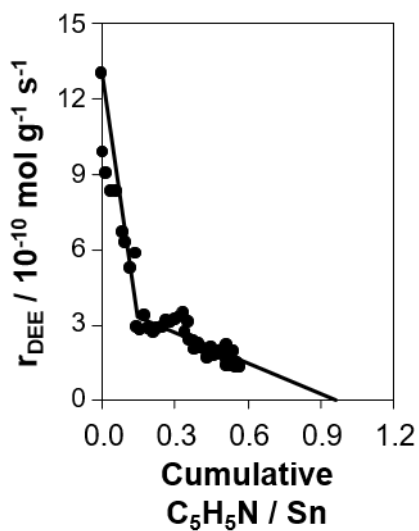
**Figure 4.16:** Diethyl ether formation rate (per g catalyst, 404 K, 8 kPa C<sub>2</sub>H<sub>5</sub>OH, 0.1 kPa H<sub>2</sub>O) as a function of pyridine uptake (0.4 Pa pyridine) on Sn-Beta-F-153(14 d) during catalysis. Solid line represents regressed two-site poisoning model.



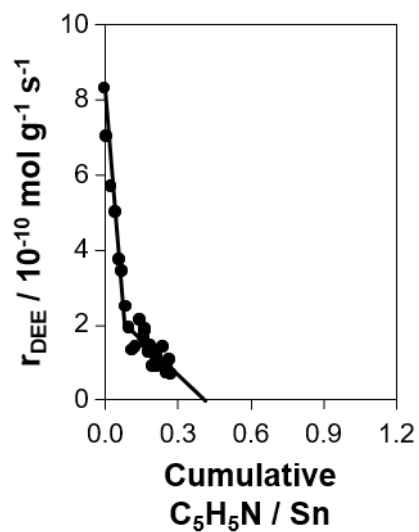
**Figure 4.17:** Diethyl ether formation rate (per g catalyst, 404 K, 8 kPa C<sub>2</sub>H<sub>5</sub>OH, 0.1 kPa H<sub>2</sub>O) as a function of pyridine uptake (0.4 Pa pyridine) on Sn-Beta-F-180(3 d) during catalysis. Solid line represents regressed two-site poisoning model.



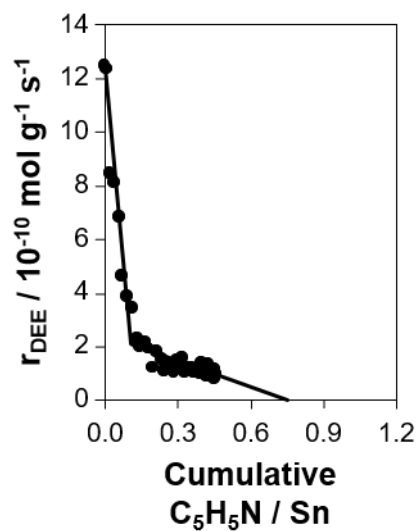
**Figure 4.18:** Diethyl ether formation rate (per g catalyst, 404 K, 8 kPa  $C_2H_5OH$ , 0.1 kPa  $H_2O$ ) as a function of pyridine uptake (0.5 Pa pyridine) on Sn-Beta-F-116-1 during catalysis. Solid line represents regressed two-site poisoning model.



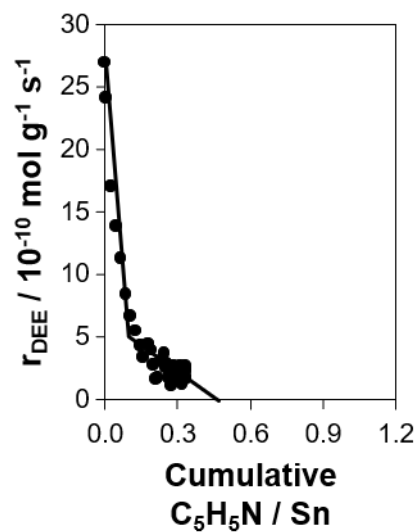
**Figure 4.19:** Diethyl ether formation rate (per g catalyst, 404 K, 8 kPa  $C_2H_5OH$ , 0.1 kPa  $H_2O$ ) as a function of pyridine uptake (0.5 Pa pyridine) on Sn-Beta-OH-84 during catalysis. Solid line represents regressed two-site poisoning model.



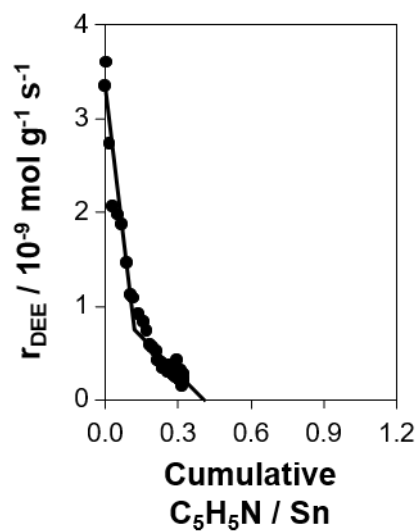
**Figure 4.20:** Diethyl ether formation rate (per g catalyst, 404 K, 8 kPa  $C_2H_5OH$ , 0.1 kPa  $H_2O$ ) as a function of pyridine uptake (0.5 Pa pyridine) on Sn-Beta-OH-80 during catalysis. Solid line represents regressed two-site poisoning model.



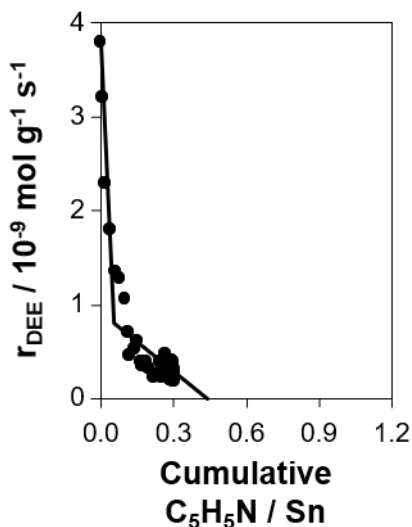
**Figure 4.21:** Diethyl ether formation rate (per g catalyst, 404 K, 8 kPa  $C_2H_5OH$ , 0.1 kPa  $H_2O$ ) as a function of pyridine uptake (0.5 Pa pyridine) on Sn-Beta-OH-95 during catalysis. Solid line represents regressed two-site poisoning model.



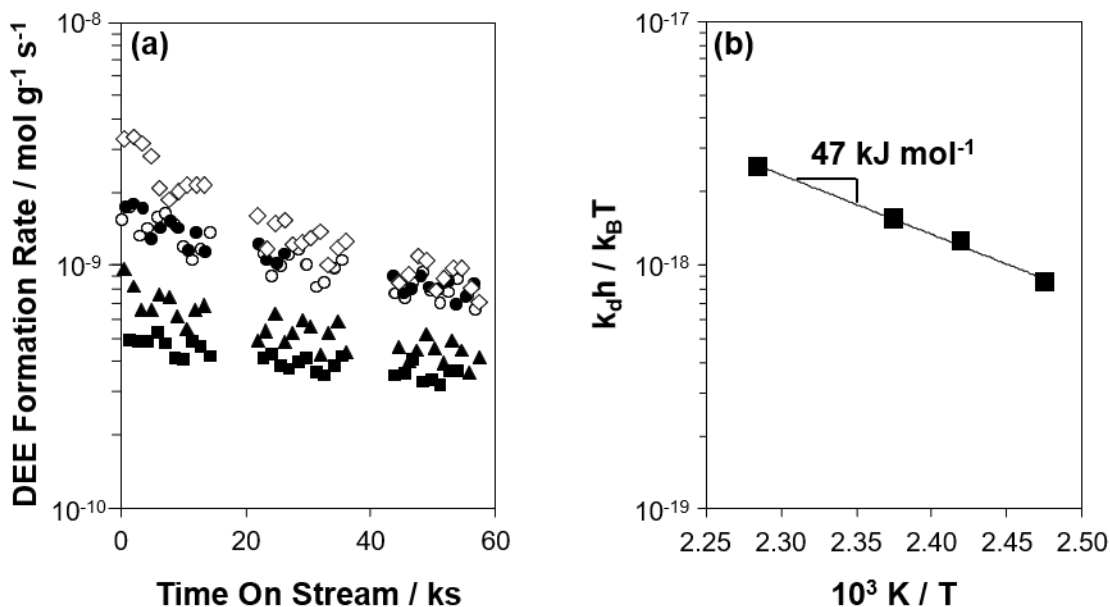
**Figure 4.22:** Diethyl ether formation rate (per g catalyst, 404 K, 8 kPa  $C_2H_5OH$ , 0.1 kPa  $H_2O$ ) as a function of pyridine uptake (0.6 Pa pyridine) on Sn-Beta-OH-46 during catalysis. Solid line represents regressed two-site poisoning model.



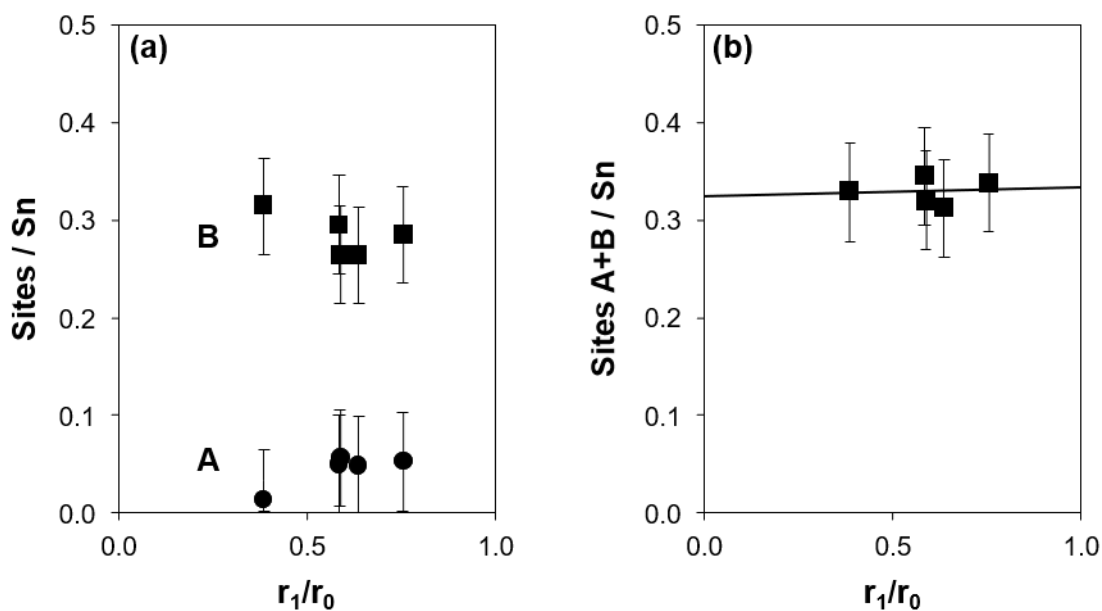
**Figure 4.23:** Diethyl ether formation rate (per g catalyst, 404 K, 8 kPa  $C_2H_5OH$ , 0.1 kPa  $H_2O$ ) as a function of pyridine uptake (0.1 Pa pyridine) on Sn-Beta-OH-41 during catalysis. Solid line represents regressed two-site poisoning model.



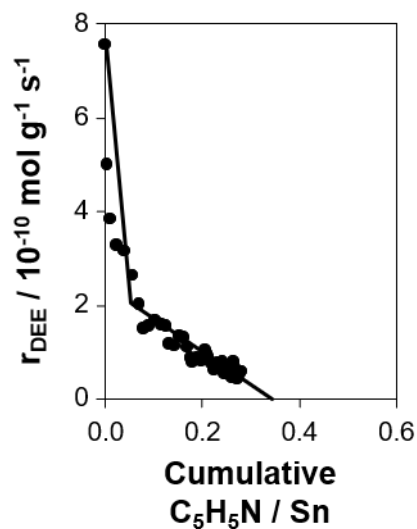
**Figure 4.24:** Diethyl ether formation rate (per g catalyst, 404 K, 8 kPa  $C_2H_5OH$ , 0.1 kPa  $H_2O$ ) as a function of pyridine uptake (0.5 Pa pyridine) on Sn-Beta-OH-30 during catalysis. Solid line represents regressed two-site poisoning model.



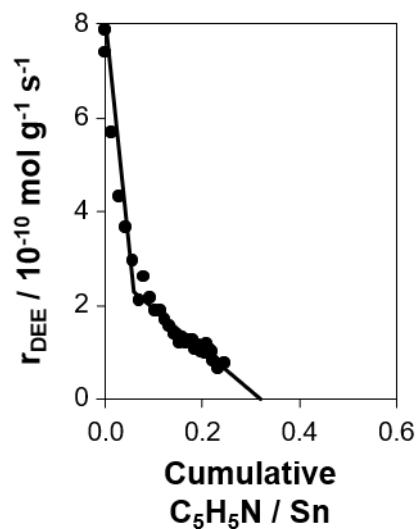
**Figure 4.25:** (a) Diethyl ether formation rate on Sn-Beta-F-153 (per g, 8 kPa  $C_2H_5OH$ , 0.1 kPa  $H_2O$ ) measured at 421 K after treating in 5%  $O_2/He$  at 813 K, 2 h ( $\circ$ ), then after repeated re-oxidation treatments (5%  $O_2/He$  at 813 K, 2 h) after each rate measurement and pyridine titration, in the order 421 K ( $\bullet$ ), 404 K ( $\blacksquare$ ), 413 K ( $\blacktriangle$ ), 438 K ( $\diamond$ ). (b) Eyring plot for the deactivation process measured over the 60 ks interval in (a), assuming exponential decay.



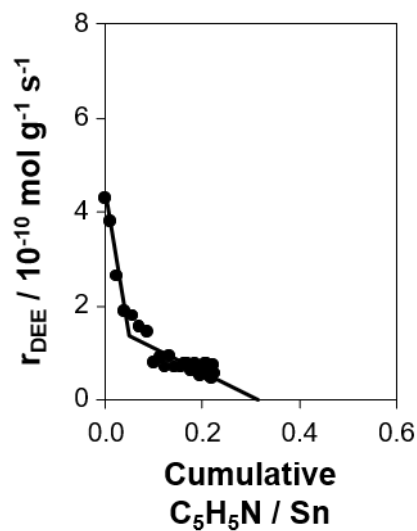
**Figure 4.26:** (a) Number of sites A (●) and B(■) per total Sn, and (b) their sum, quantified by *in situ* pyridine titration (404–438 K, 8 kPa  $C_2H_5OH$ , 0.1 kPa  $H_2O$ ) as a function of the extent of initial deactivation. The solid line represents the best fit to the data points.



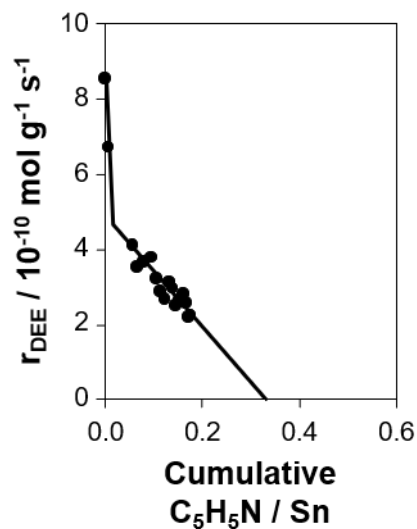
**Figure 4.27:** Diethyl ether formation rate (per g catalyst, 421 K, 8 kPa  $C_2H_5OH$ , 0.1 kPa  $H_2O$ ) as a function of pyridine uptake (0.4 Pa pyridine) on Sn-Beta-F-153 during catalysis. Solid line represents regressed two-site poisoning model.



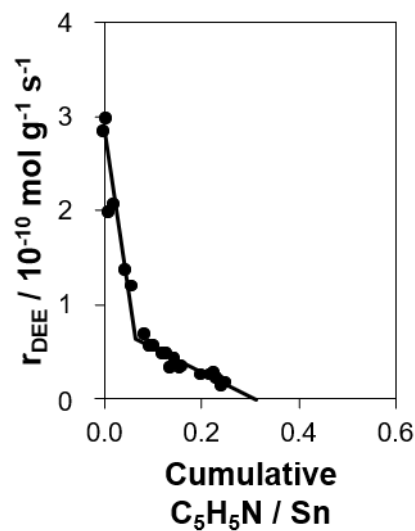
**Figure 4.28:** Diethyl ether formation rate (per g catalyst, 421 K, 8 kPa  $\text{C}_2\text{H}_5\text{OH}$ , 0.1 kPa  $\text{H}_2\text{O}$ ) as a function of pyridine uptake (0.4 Pa pyridine) on Sn-Beta-F-153 during catalysis, after re-oxidation (5%  $\text{O}_2/\text{He}$  at 813 K, 2 h). Solid line represents regressed two-site poisoning model.



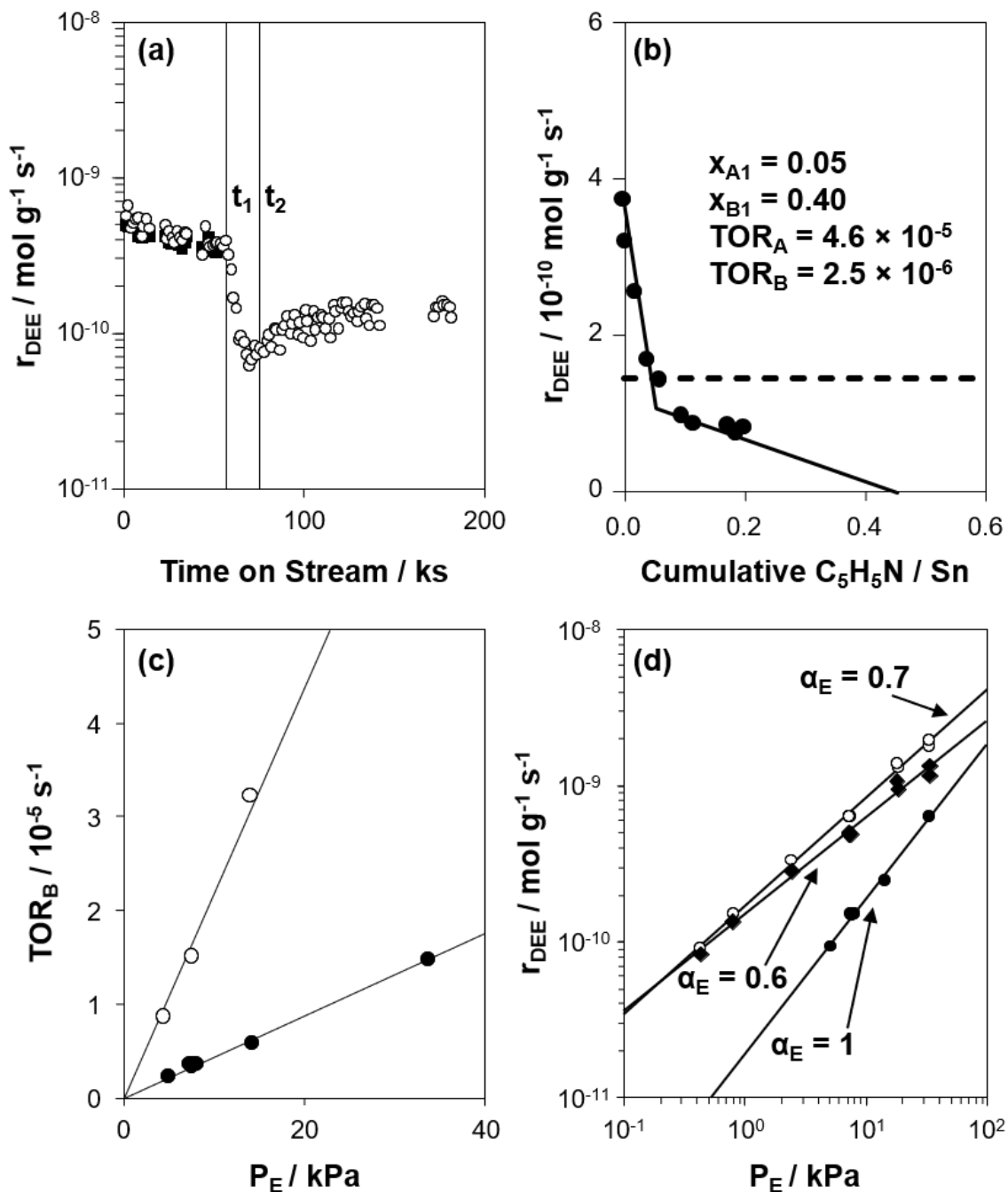
**Figure 4.29:** Diethyl ether formation rate (per g catalyst, 413 K, 8 kPa  $\text{C}_2\text{H}_5\text{OH}$ , 0.1 kPa  $\text{H}_2\text{O}$ ) as a function of pyridine uptake (0.4 Pa pyridine) on Sn-Beta-F-153 during catalysis, after re-oxidation (5%  $\text{O}_2/\text{He}$  at 813 K, 2 h). Solid line represents regressed two-site poisoning model.



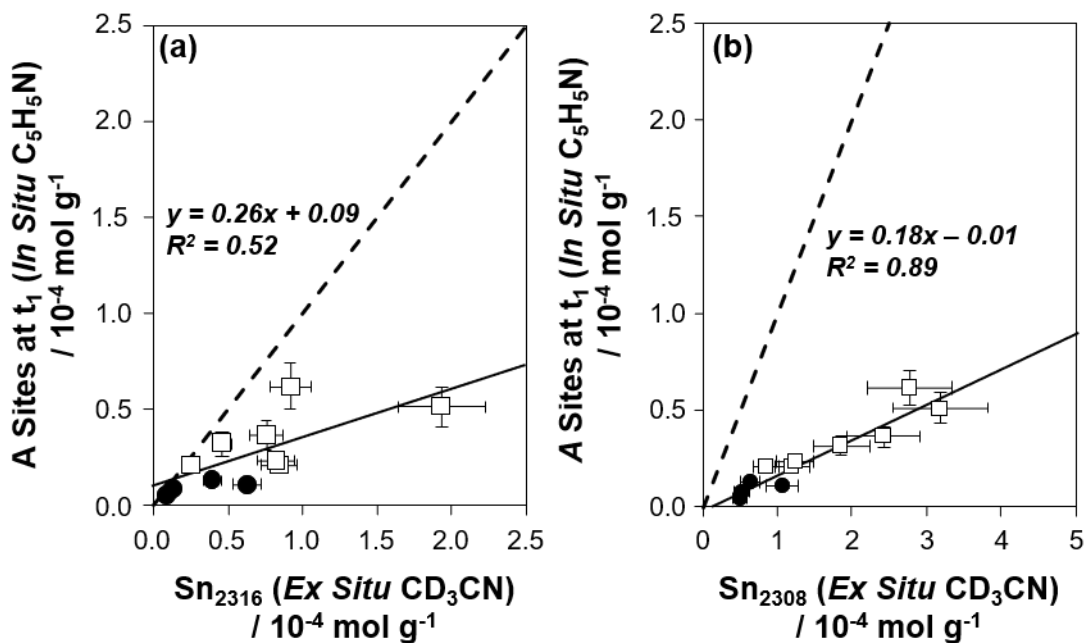
**Figure 4.30:** Diethyl ether formation rate (per g catalyst, 438 K, 8 kPa  $C_2H_5OH$ , 0.1 kPa  $H_2O$ ) as a function of pyridine uptake (0.4 Pa pyridine) on Sn-Beta-F-153 during catalysis, after re-oxidation (5%  $O_2/He$  at 813 K, 2 h). Solid line represents regressed two-site poisoning model.



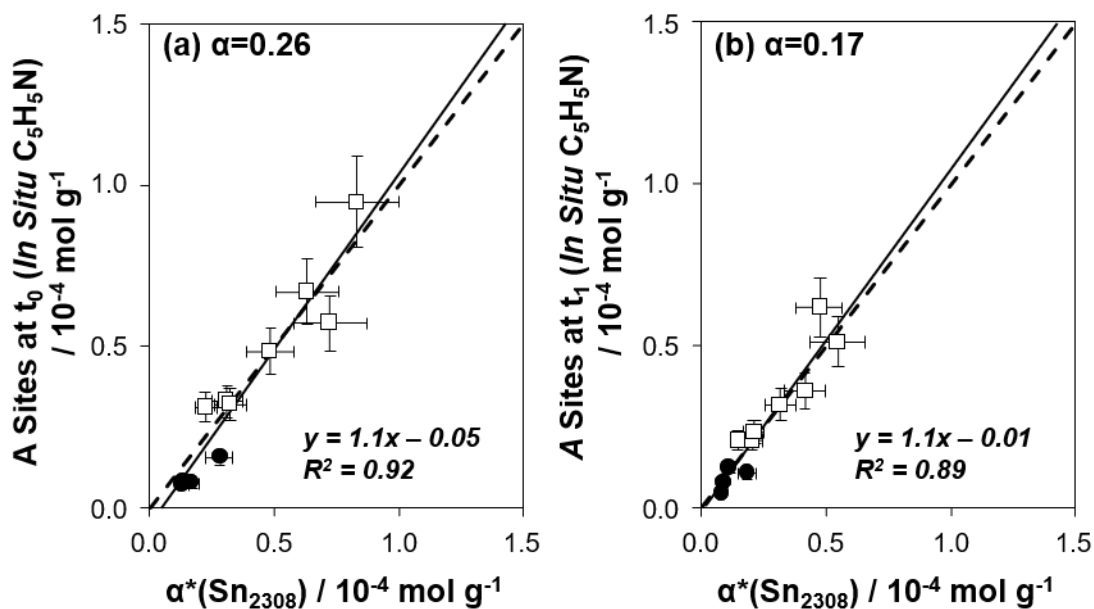
**Figure 4.31:** Diethyl ether formation rate (per g catalyst, 404 K, 8 kPa  $C_2H_5OH$ , 1 kPa  $H_2O$ ) at higher water pressure as a function of pyridine uptake (0.4 Pa pyridine) on Sn-Beta-F-153 during catalysis. Solid line represents regressed two-site poisoning model.



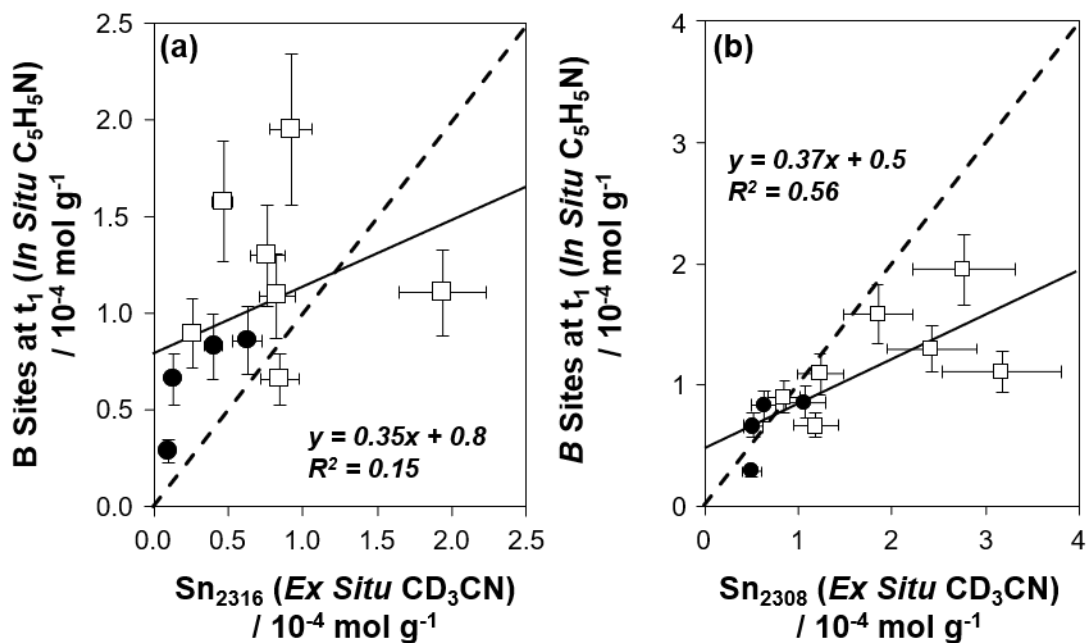
**Figure 4.32:** (a) Diethyl ether formation rate (404 K, 8 kPa  $\text{C}_2\text{H}_5\text{OH}$ , 0.1 kPa  $\text{H}_2\text{O}$ , per g) on Sn-Beta-F-153 during approach to quasi-steady state, after introduction of 0.4 Pa pyridine at time point  $t_1$ , and after removal of pyridine titrants from the reactant stream at time point  $t_2$  ( $\circ$ ). Filled squares ( $\blacksquare$ ) are rate data from a separate catalyst loading (see Figure 4.25). (b) Diethyl ether formation rate as a function of pyridine uptake during catalysis, as quantified in plot (a). The solid line represents regressed two-site poisoning model, and the regressed parameters are reported in the plot area. The dashed line represents the new quasi-steady-state rate value after desorption of reversibly adsorbed pyridine at B sites. (c)  $\text{TOR}_{\text{B}}$  values quantified after pyridine poisoning of A sites on Sn-Beta-F-153 as a function of ethanol pressure (with 0.1 kPa  $\text{H}_2\text{O}$ ) at 404 K ( $\bullet$ ) and 437 K ( $\circ$ ). (d) Diethyl ether formation rate (404 K, 0.1 kPa  $\text{H}_2\text{O}$ , per g) on Sn-Beta-F-153 measured previously [227] ( $\circ$ ), after pyridine poisoning of A sites ( $\bullet$ ), and the difference between the two ( $\blacklozenge$ ).



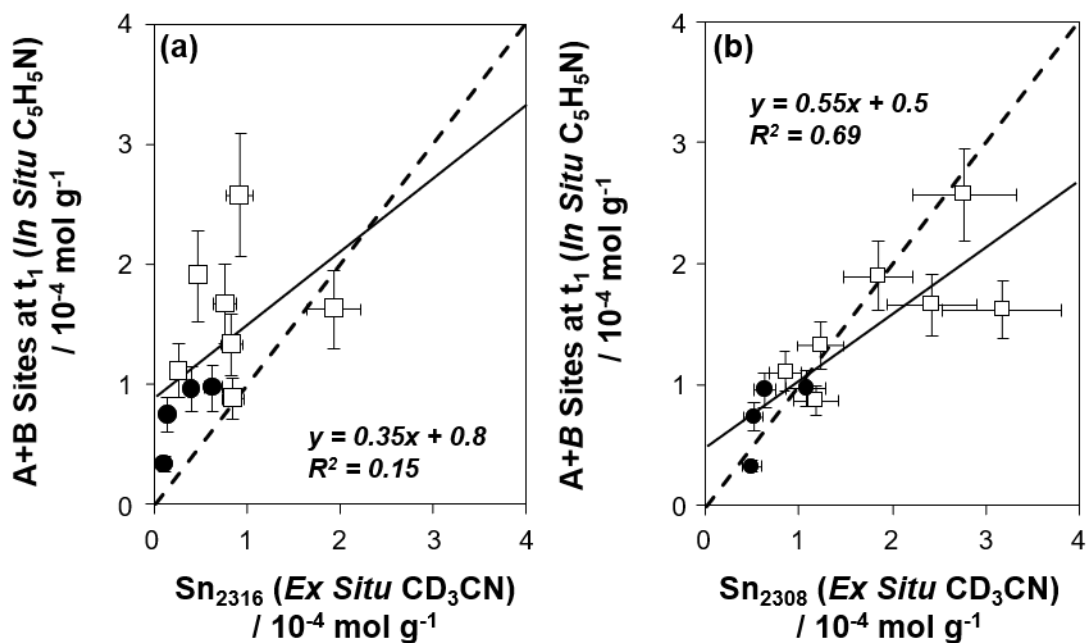
**Figure 4.33:** Parity of A sites titrated by pyridine *in situ* (without correcting to initial time-on-stream) with (a) Sn<sub>2316</sub> or (b) Sn<sub>2308</sub> quantified *ex situ* by CD<sub>3</sub>CN IR on seven Sn-Beta-OH (□) and four Sn-Beta-F (●) samples. Dashed lines represent parity, while solid lines represent best-fit linear regressions to the data.



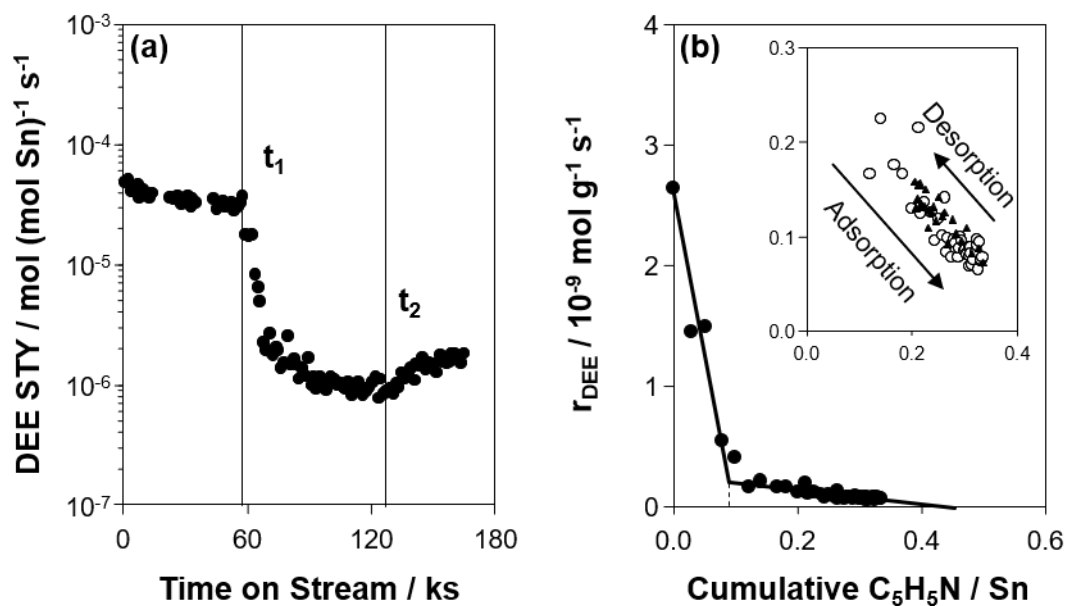
**Figure 4.34:** Parity of the total number of A sites titrated by pyridine *in situ* (a) with and (b) without correcting to initial time-on-stream, with a factor  $\alpha$  multiplied by  $\text{Sn}_{2308}$  quantified *ex situ* by  $\text{CD}_3\text{CN}$  IR on seven Sn-Beta-OH ( $\square$ ) and four Sn-Beta-F ( $\bullet$ ) samples to minimize the deviation from parity. The dashed lines represent parity, while the solid lines represent the best-fit linear regressions to the data.



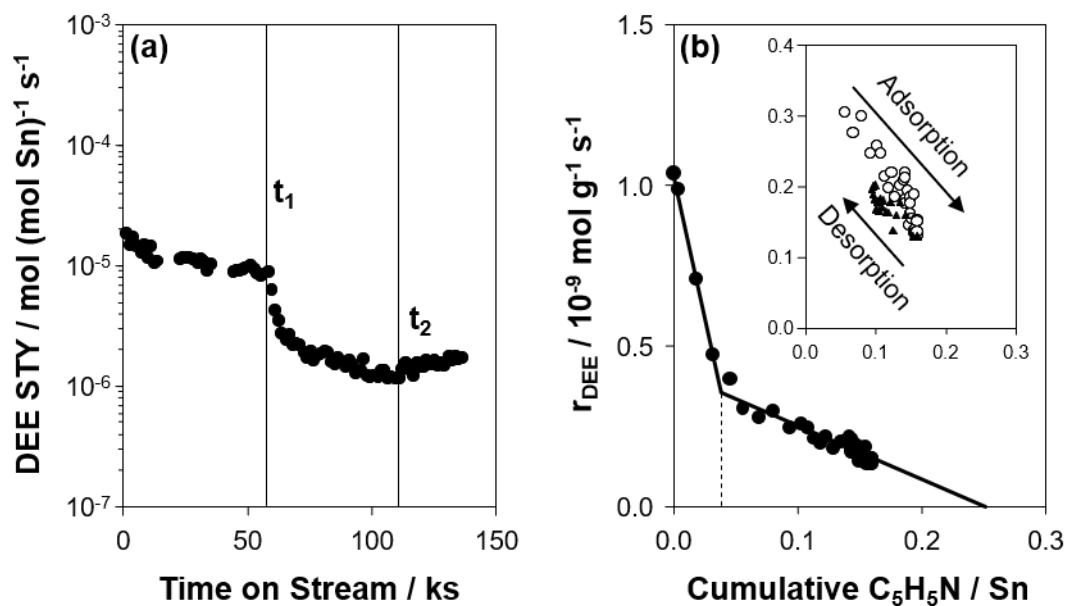
**Figure 4.35:** Parity of B sites titrated by pyridine *in situ* (without correcting to initial time-on-stream) with (a) Sn<sub>2316</sub> or (b) Sn<sub>2308</sub> quantified *ex situ* by CD<sub>3</sub>CN IR on seven Sn-Beta-OH (□) and four Sn-Beta-F (●) samples. Dashed lines represent parity, while solid lines represent best-fit linear regressions to the data.



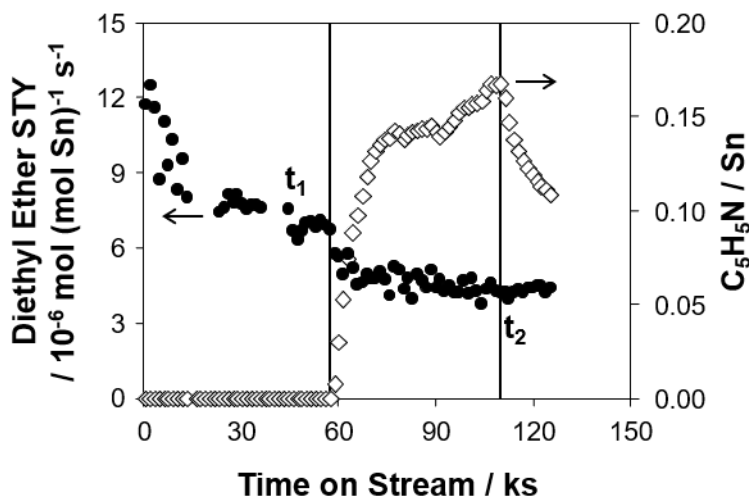
**Figure 4.36:** Parity of the total number of A+B sites titrated by pyridine *in situ* (without correcting to initial time-on-stream) with (a) Sn<sub>2316</sub> or (b) Sn<sub>2308</sub> quantified *ex situ* by CD<sub>3</sub>CN IR on seven Sn-Beta-OH (□) and four Sn-Beta-F (●) samples. Dashed lines represent parity, while solid lines represent best-fit linear regressions to the data.



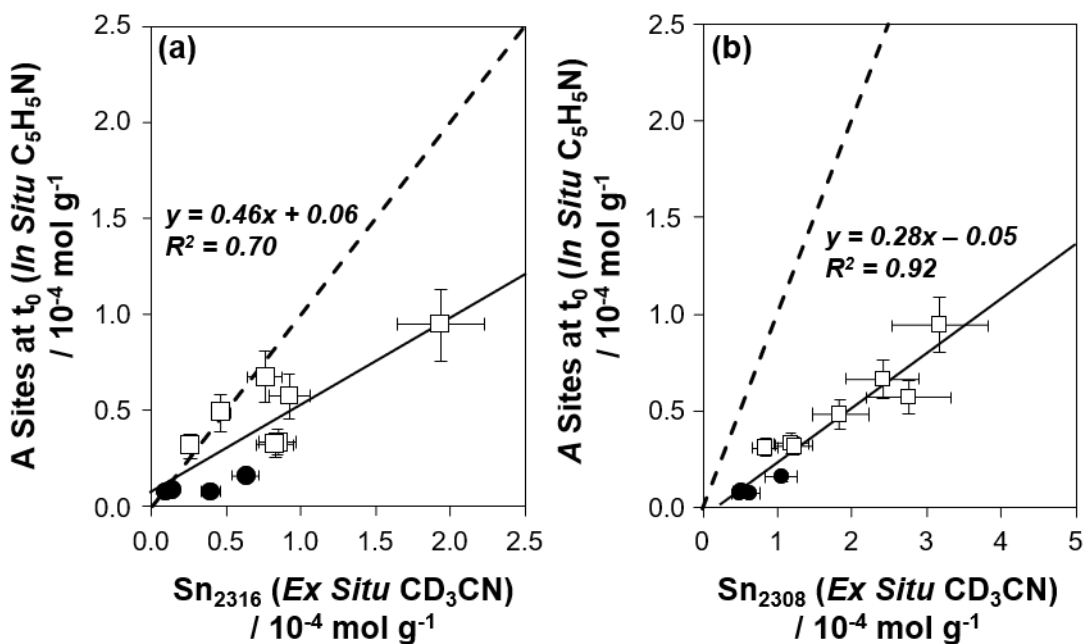
**Figure 4.37:** (a) Diethyl ether site-time yield (404 K, 8 kPa  $\text{C}_2\text{H}_5\text{OH}$ , 0.1 kPa  $\text{H}_2\text{O}$ , per Sn) on Sn-MFI-F-129 during approach to quasi-steady state, after introduction of 0.4 Pa pyridine at time point  $t_1$ , and after removal of pyridine titrants from the reactant stream at time point  $t_2$ . (b) Diethyl ether formation rate (per g catalyst) as a function of pyridine uptake on Sn-MFI-F-129 during catalysis. The solid line represents regressed two-site poisoning model, and the dashed line indicates the regressed value of the number of sites A per total Sn. Inset: site B titration region ( $\circ$ ) demonstrating reversible pyridine adsorption/desorption from site B after titrant removal from the stream ( $\blacktriangle$ ).



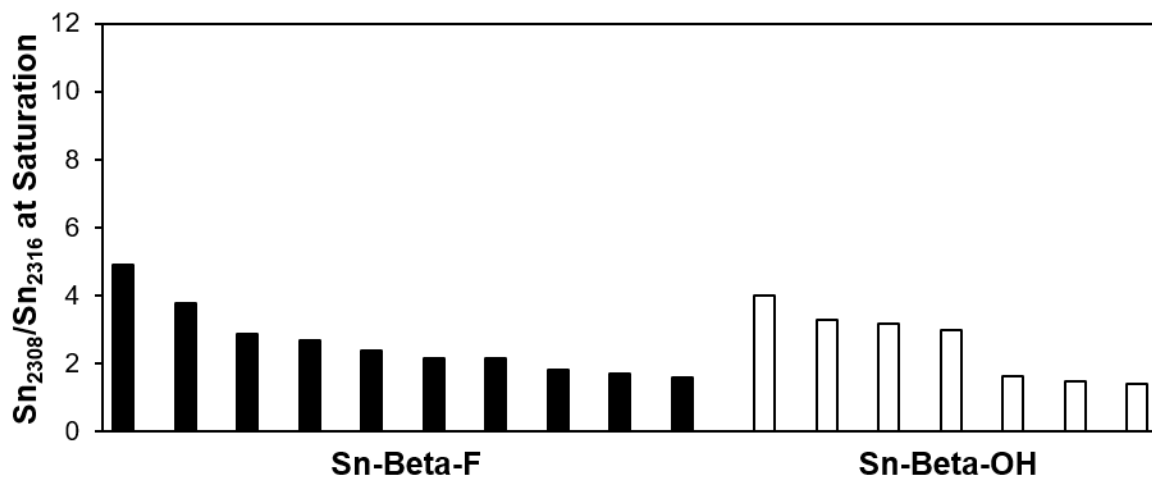
**Figure 4.38:** (a) Diethyl ether site-time yield (404 K, 8 kPa  $\text{C}_2\text{H}_5\text{OH}$ , 0.1 kPa  $\text{H}_2\text{O}$ , per Sn) on Sn-Ge-BEC-F during approach to quasi-steady state, after introduction of 0.5 Pa pyridine at time point  $t_1$ , and after removal of pyridine titrants from the reactant stream at time point  $t_2$ . (b) Diethyl ether formation rate (per g catalyst) as a function of pyridine uptake on Sn-Ge-BEC-F during catalysis. The solid line represents regressed two-site poisoning model, and the dashed line indicates the regressed value of the number of sites A per total Sn. Inset: site B titration region ( $\circ$ ) demonstrating reversible pyridine adsorption/desorption from site B after titrant removal from the stream ( $\blacktriangle$ ).



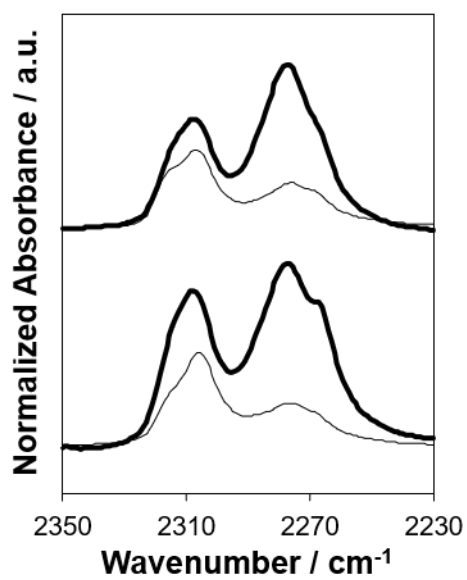
**Figure 4.39:** Diethyl ether site-time yield (404 K, 8 kPa  $C_2H_5OH$ , 0.1 kPa  $H_2O$ , per Sn), and cumulative pyridine adsorbed (per Sn), on Sn-CHA-F-60 during approach to quasi-steady-state, after introduction of 0.7 Pa pyridine at time point  $t_1$ , and after removal of pyridine titrants from the reactant stream at time point  $t_2$ .



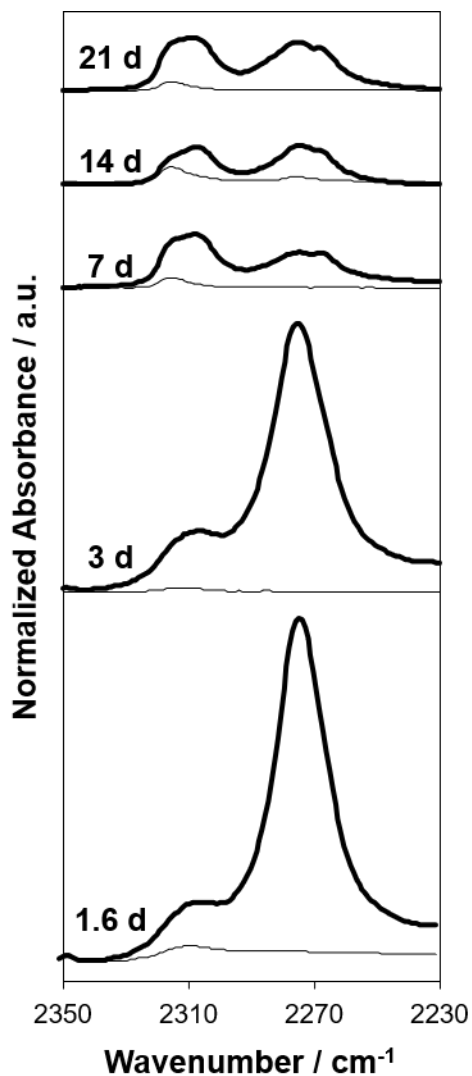
**Figure 4.40:** Parity of sites titrated by pyridine *in situ* (corrected to initial time on stream) with (a)  $Sn_{2316}$  or (b)  $Sn_{2308}$  quantified *ex situ* by  $CD_3CN$  IR on seven Sn-Beta-OH samples ( $\square$ ), four Sn-Beta-F ( $\bullet$ ) samples, without Sn-MFI-F-129 and Sn-Ge-BEC-F. Dashed lines represent parity, while solid lines represent best-fit linear regressions to the data.

4.6.2.2 CD<sub>3</sub>CN IR spectra

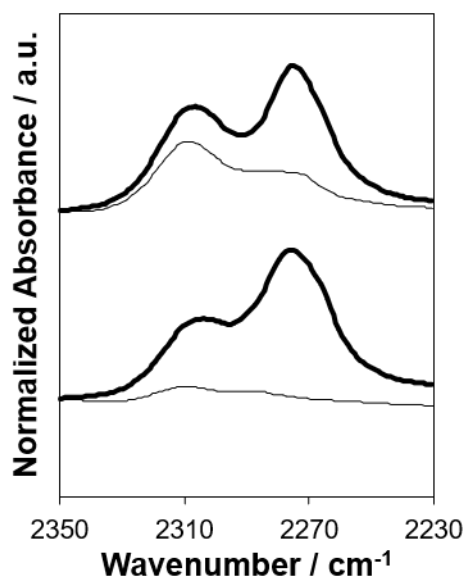
**Figure 4.41:** Sn<sub>2308</sub>/Sn<sub>2316</sub> molar ratios quantified from CD<sub>3</sub>CN IR spectra at saturation coverages on ten Sn-Beta-F (black) and seven Sn-Beta-OH (white) zeolites. Data for Sn-Beta-OH zeolites are reported in [151,227], and Sn-Beta-F zeolites in this work and [56,227]



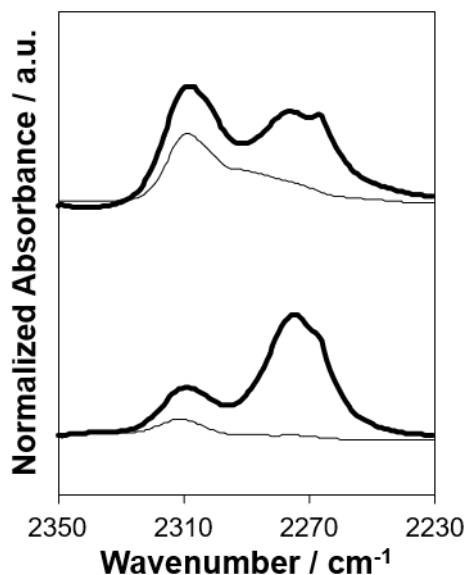
**Figure 4.42:** IR difference spectra of CD<sub>3</sub>CN adsorbed at saturation coverages (303 K) on Sn-Beta-F-100 (lower thin line), Sn-Beta-F-100-NMe<sub>4</sub>OH (lower thick line), Sn-Beta-F-181 (upper thin line), and Sn-Beta-F-181-NMe<sub>4</sub>OH (upper thick line), normalized by T-O-T overtone peak area.



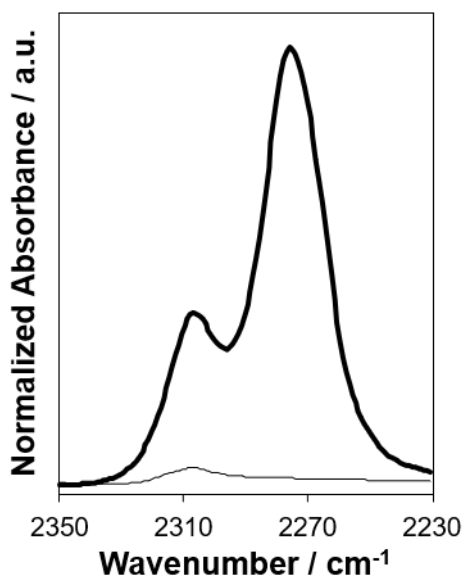
**Figure 4.43:** IR difference spectra of CD<sub>3</sub>CN adsorbed (303 K) at saturation coverages (thick lines) and first doses (<0.3 CD<sub>3</sub>CN/Sn, thin lines) on Sn-Beta-F samples as a function of crystallization time, normalized by T-O-T overtone peak area. Spectra are offset for clarity.



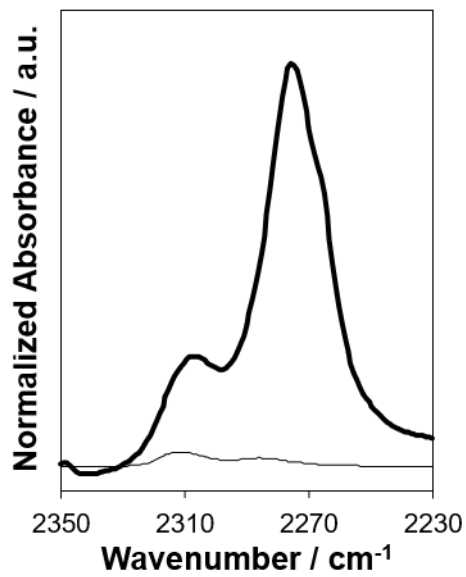
**Figure 4.44:** IR difference spectra of CD<sub>3</sub>CN adsorbed (303 K) at saturation coverages (thick lines) and first doses (thin lines) on Sn-CHA-F-70 (bottom) and Sn-CHA-F-60 (top), normalized by T-O-T overtone peak area. Spectra are offset for clarity. The first dose spectrum on Sn-CHA-F-70 is multiplied by 5 (CD<sub>3</sub>CN/Sn < 0.3); the CD<sub>3</sub>CN/Sn in the first dose to Sn-CHA-F-60 was 1.3/Sn.



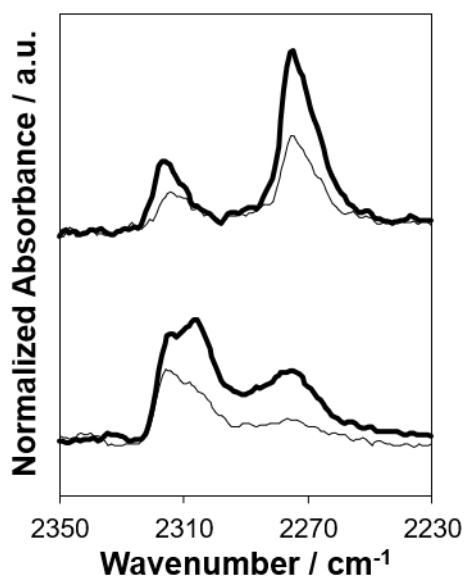
**Figure 4.45:** IR difference spectra of  $\text{CD}_3\text{CN}$  adsorbed (303 K) at saturation coverages (thick lines) and first doses (thin lines) on Sn-MFI-F-192 (bottom) and Sn-MFI-F-129 (top), normalized by T-O-T overtone peak area. Spectra are offset for clarity. The first dose spectrum on Sn-MFI-F-192 is multiplied by 5 ( $\text{CD}_3\text{CN}/\text{Sn} < 0.3$ ); the  $\text{CD}_3\text{CN}/\text{Sn}$  in the first dose to Sn-MFI-F-129 was 0.4/Sn.



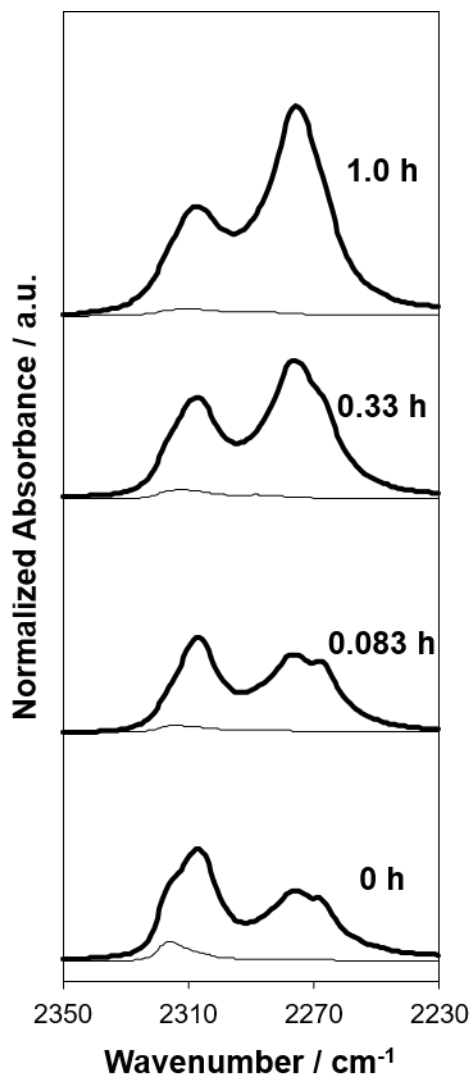
**Figure 4.46:** IR difference spectra of  $\text{CD}_3\text{CN}$  adsorbed (303 K) at saturation coverage (thick line) and first dose ( $< 0.3 \text{ CD}_3\text{CN}/\text{Sn}$ , thin line) on Sn-STT-F-151, normalized by T-O-T overtone peak area.



**Figure 4.47:** IR difference spectra of  $\text{CD}_3\text{CN}$  adsorbed (303 K) at saturation coverage (thick line) and first dose ( $<0.3 \text{ CD}_3\text{CN/Sn}$ , thin line) on Sn-Ge-BEC-F, normalized by T-O-T overtone peak area.

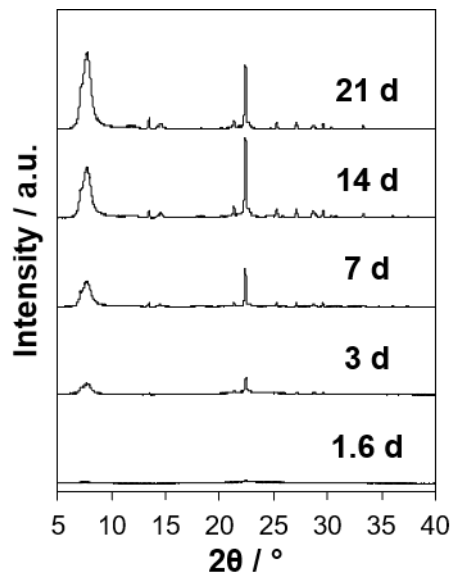


**Figure 4.48:** IR difference spectra of the first (thin lines) and second (thick lines) doses of  $\text{CD}_3\text{CN}$  ( $<0.3 \text{ CD}_3\text{CN/Sn}$ ) adsorbed (303 K) on Si-Beta@Sn-Beta-F-169 (bottom) and Si-Beta@Sn-Beta-F-116-2 (top), normalized by T-O-T overtone peak area.

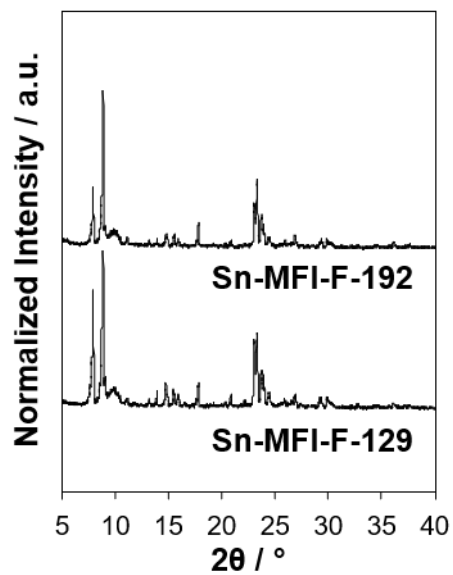


**Figure 4.49:** IR difference spectra of  $\text{CD}_3\text{CN}$  adsorbed (303 K) at saturation coverages (thick lines) and first doses ( $<0.3 \text{ CD}_3\text{CN/Sn}$ , thin lines) on Sn-Beta-F-110 as a function of  $\text{NH}_4\text{F}$  treatment time, normalized by T-O-T overtone peak area. Spectra are offset for clarity.

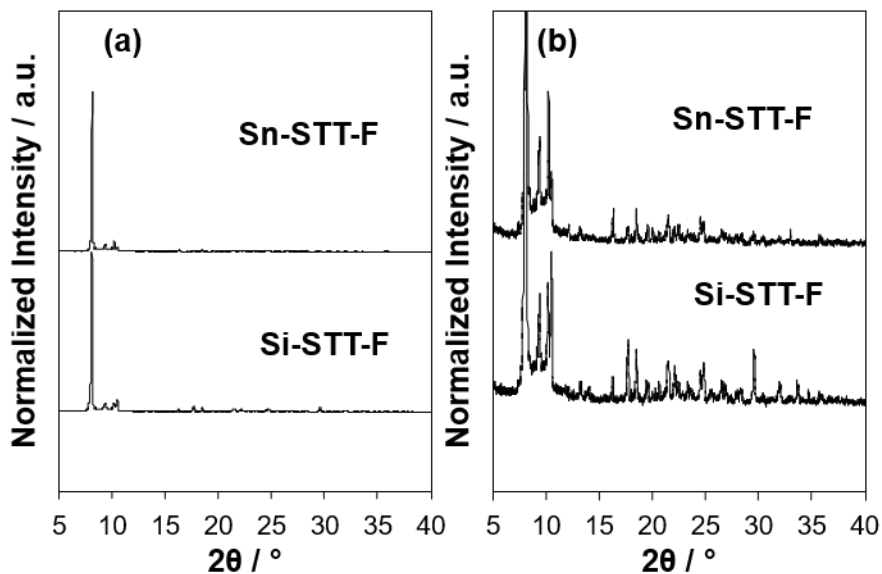
## 4.6.2.3 XRD patterns



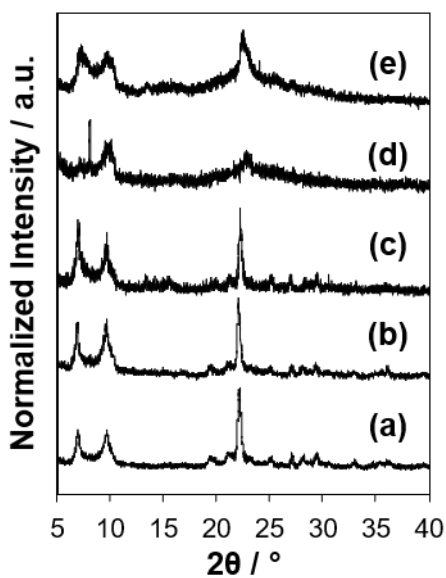
**Figure 4.50:** XRD patterns of Sn-Beta-F samples synthesized with varying crystallization times.



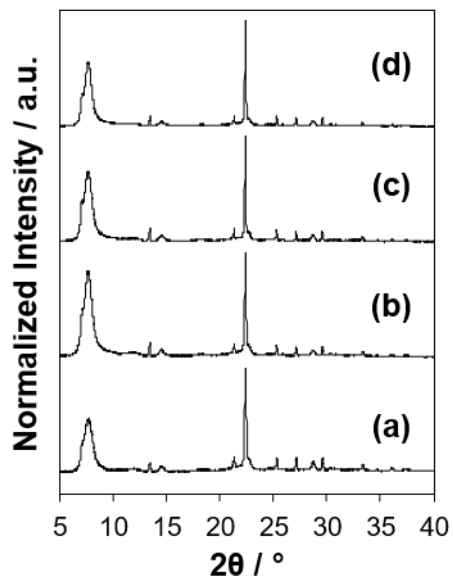
**Figure 4.51:** XRD patterns of air-treated (853 K) Sn-MFI-129 and Sn-MFI-F-192, normalized to maximum intensity.



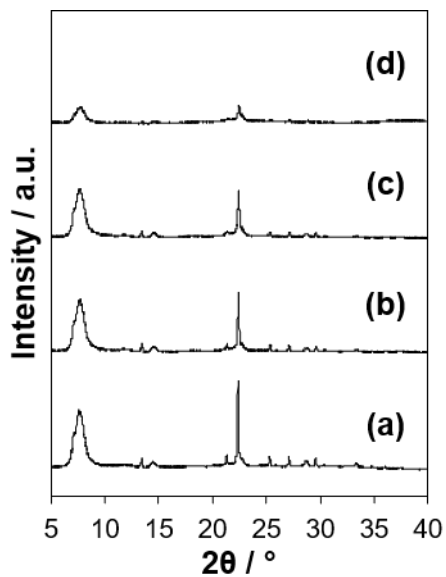
**Figure 4.52:** XRD patterns of air-treated (853 K) Si-STT-F and as-synthesized Sn-STT-F, (a) normalized to maximum intensity and (b) normalized to maximum intensity at  $2\theta > 9^\circ$ .



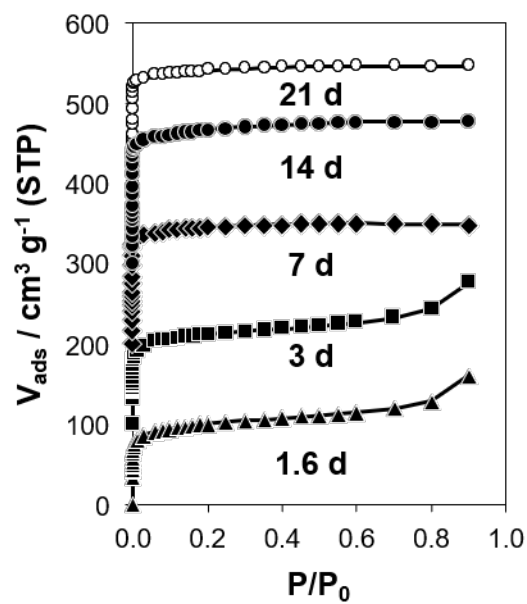
**Figure 4.53:** XRD patterns of (a) as-synthesized Ge-BEC-F, (b) as-synthesized Sn-Ge-BEC-F, Sn-Ge-BEC-F (c) 26 days and (d) 520 days after air treatment, and (e) Ge-BEC-F 524 days after air treatment, normalized to maximum intensity.



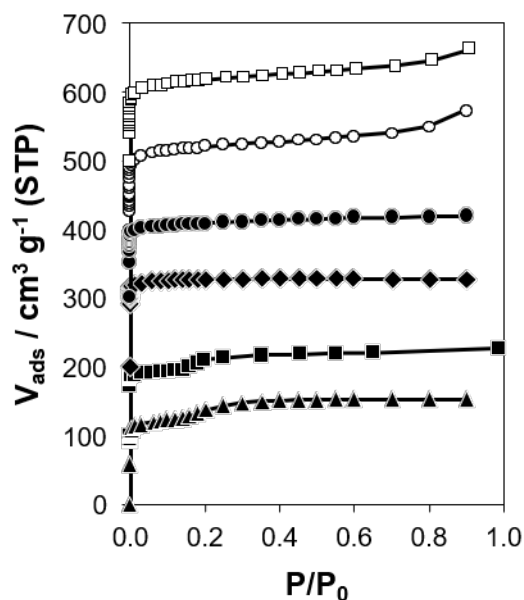
**Figure 4.54:** XRD patterns of (a) Sn-Beta-F-116-2, (b) Si-Beta@Sn-Beta-F-116-2, (c) Sn-Beta-F-169, and (d) Si-Beta@Sn-Beta-F-169.



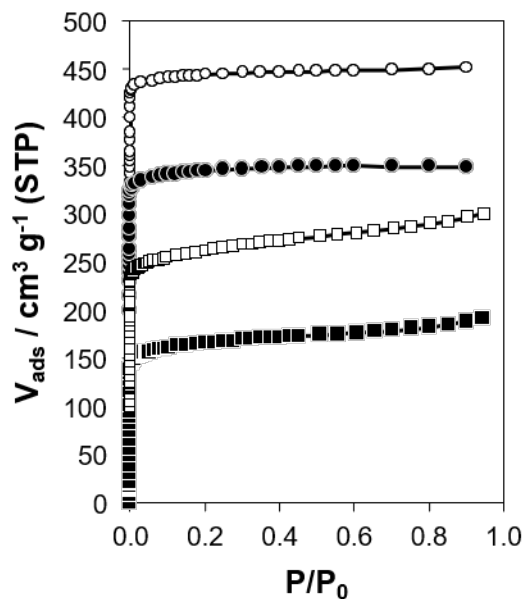
**Figure 4.55:** XRD patterns of (a) Sn-Beta-F-110, (b) Sn-Beta-F-NH<sub>4</sub>F-0.083h, (c) Sn-Beta-F-NH<sub>4</sub>F-0.33h, and (d) Sn-Beta-F-NH<sub>4</sub>F-1h.

4.6.2.4 N<sub>2</sub> adsorption isotherms

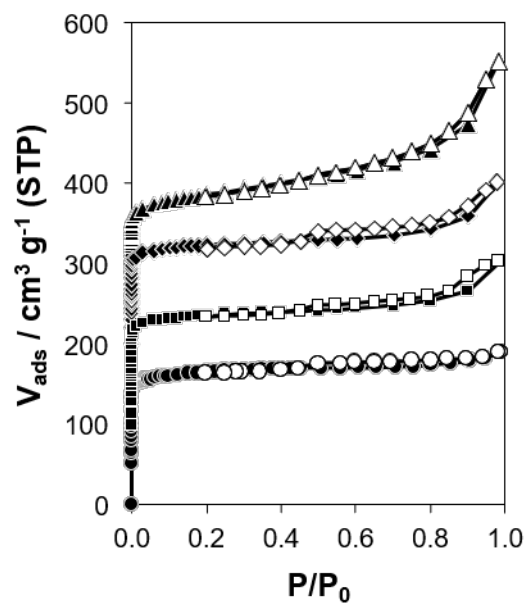
**Figure 4.56:** N<sub>2</sub> adsorption isotherms (77 K) on Sn-Beta-F samples synthesized with varying crystallization times. Isotherms are offset by 100 units for clarity.



**Figure 4.57:**  $\text{N}_2$  adsorption isotherms (77 K) on Sn-MFI-F-192 ( $\blacktriangle$ ), Sn-MFI-F-129 ( $\blacksquare$ ), Si-STT-F ( $\blacklozenge$ ), Sn-STT-F ( $\bullet$ ), Ge-BEC-F ( $\circ$ ), and Sn-Ge-BEC-F ( $\square$ ). Isotherms are offset by 100 units for clarity.

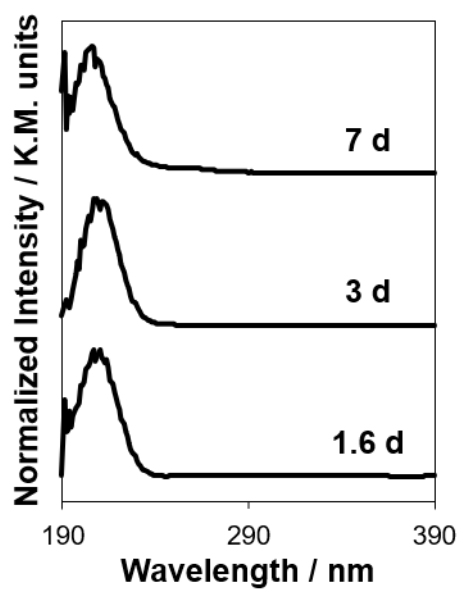


**Figure 4.58:**  $\text{N}_2$  adsorption isotherms (77 K) on Sn-Beta-F-116-2 ( $\blacksquare$ ), Si-Beta@Sn-Beta-F-116-2 ( $\square$ ), Sn-Beta-F-169 ( $\bullet$ ), and Si-Beta@Sn-Beta-F-169 ( $\circ$ ). Isotherms are offset by 100 units for clarity.

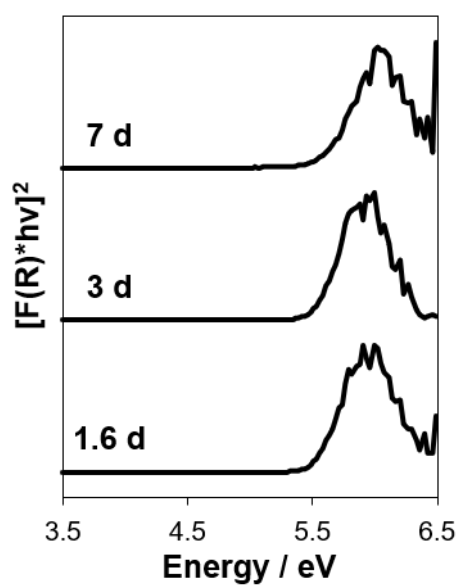


**Figure 4.59:**  $\text{N}_2$  adsorption isotherms (77 K) on Sn-Beta-F-110 (●), Sn-Beta-F-NH<sub>4</sub>F-0.08h (■), Sn-Beta-F-NH<sub>4</sub>F-0.08h (◆), and Sn-Beta-F-NH<sub>4</sub>F-0.08h (▲). Open symbols are for desorption data points. Isotherms are offset by 100 units for clarity.

## 4.6.2.5 Diffuse reflectance UV-Vis spectra

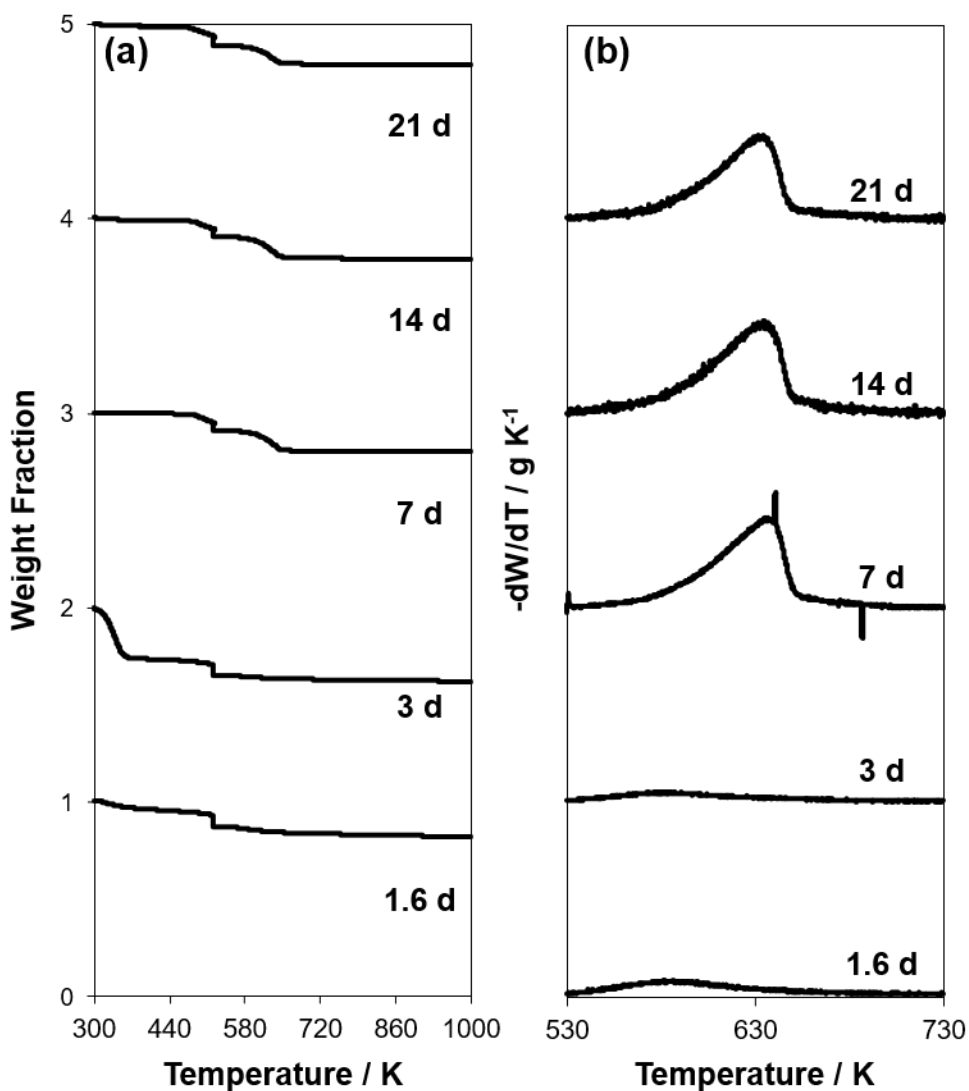


**Figure 4.60:** Diffuse reflectance UV-Visible spectra of Sn-Beta-F samples synthesized with varying crystallization times collected after dehydration treatments (523 K).

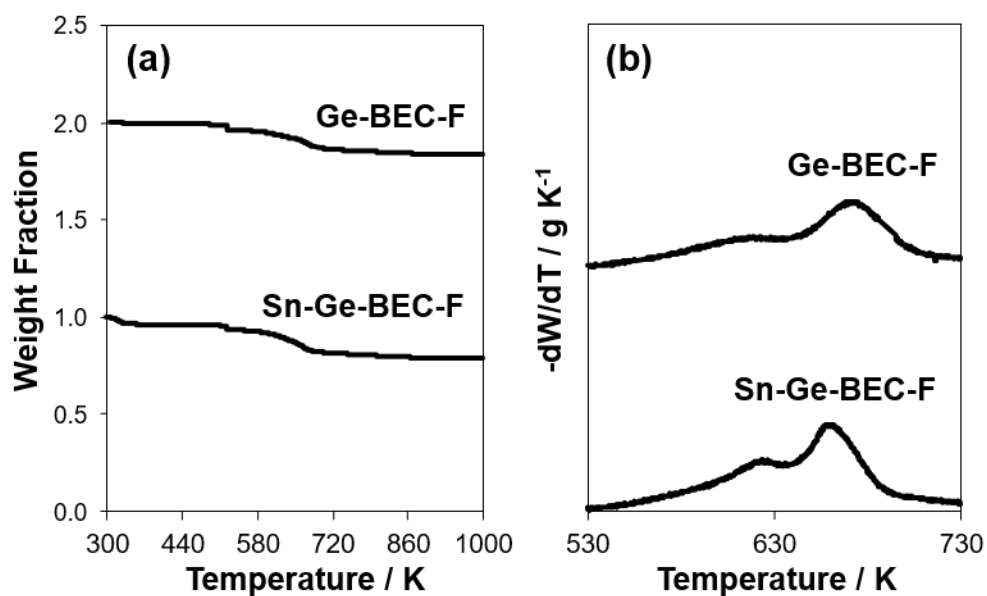


**Figure 4.61:** Tauc plots for Sn-Beta-F samples with varying crystallization times from DRUV spectra collected after dehydration treatments (523 K).

## 4.6.2.6 Thermogravimetric analysis

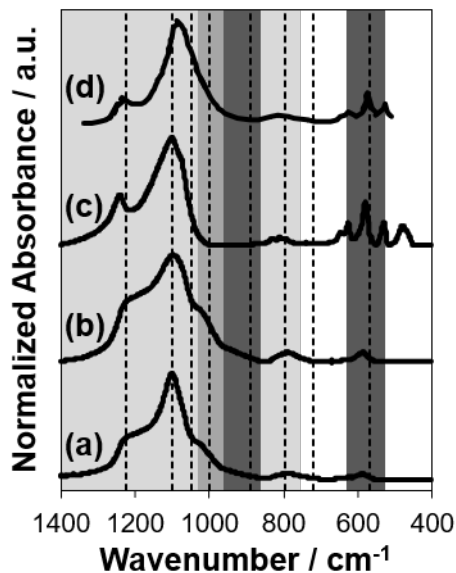


**Figure 4.62:** (a) Thermogravimetric analysis of as-made Sn-Beta-F materials with varying crystallization times. Curves are offset by intervals of one for clarity. The weight loss associated with combustion of organic TEA<sup>+</sup> was quantified in the range of 530–730 K. Derivative weight loss curves showing the peak for this combustion event are shown in (b).

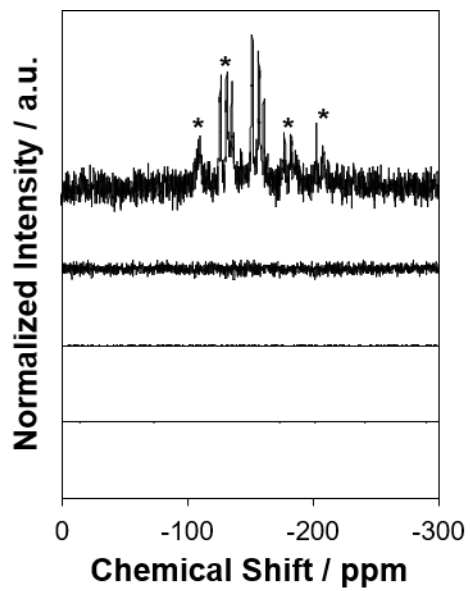


**Figure 4.63:** (a) Thermogravimetric analysis of as-made Ge-BEC-F and Sn-Ge-BEC-F materials. Curves are offset by intervals of one for clarity. The weight loss associated with combustion of organic SDA was quantified in the range of 530–730 K. Derivative weight loss curves showing the peaks for these combustion events are shown in (b).

## 4.6.2.7 IR spectra of zeolite framework vibrations



**Figure 4.64:** Normalized baseline-corrected IR spectra of the framework vibrations of (a) Ge-BEC-F, (b) Sn-Ge-BEC-F, (c) Sn-Beta-F-181 as 1–5 wt% mixtures in KBr, and (d) Sn-Beta-F from Courtney et al. [110] measured by ATR-IR. Shaded regions and dashed lines represent Si-O-Si (light gray)  $\nu_{AS}$  ( $1225\text{ cm}^{-1}$ ,  $1100\text{ cm}^{-1}$ ,  $1050\text{ cm}^{-1}$ ) and  $\nu_S$  ( $800\text{ cm}^{-1}$ ), Si-O-Ge  $\nu_{AS}$  (medium gray,  $1000\text{ cm}^{-1}$ ), and Ge-O-Ge (dark gray)  $\nu_{AS}$  ( $890\text{ cm}^{-1}$ ), in D4R ( $570\text{ cm}^{-1}$ ) [248]. Dashed line at  $720\text{ cm}^{-1}$  is for extraframework  $\text{GeO}_2$ .

4.6.2.8  $^{19}\text{F}$  NMR spectra

**Figure 4.65:**  $^{19}\text{F}$  NMR spectra, normalized by sample mass, of (top to bottom) Sn-Beta-F-100, Sn-Beta-F-100-NMe<sub>4</sub>OH, Sn-Beta-F-181, and Sn-Beta-F-181-NMe<sub>4</sub>OH. Spinning sidebands are marked by asterisks.

## 4.6.2.9 Scanning electron microscopy images

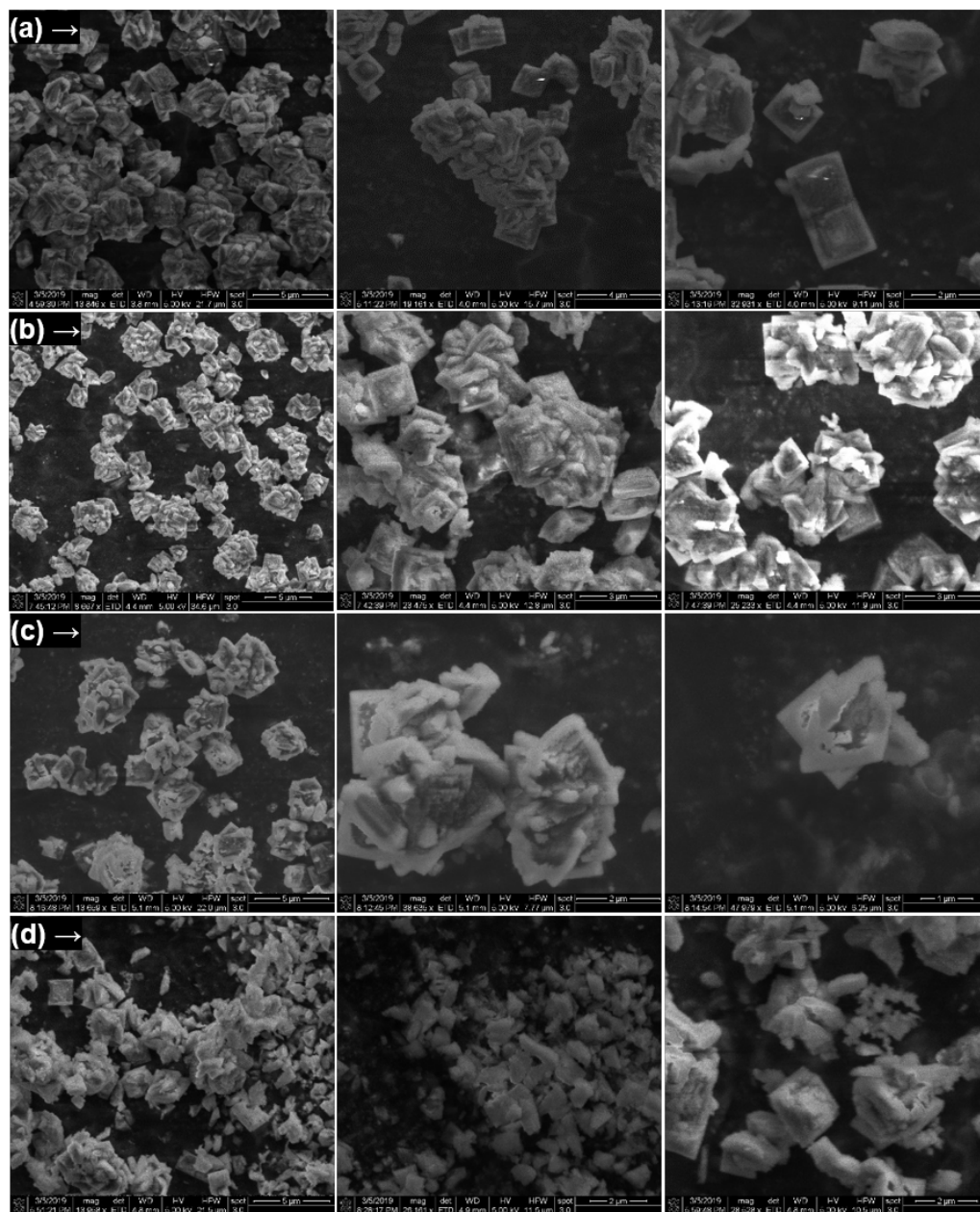


**Figure 4.66:** SEM images at varying magnifications of (a) Sn-Beta-F-110 after treatment in 40 wt%  $\text{NH}_4\text{F}$  (323 K) for (b) 0.083 h, (c) 0.33 h, and (d) 1.0 h.

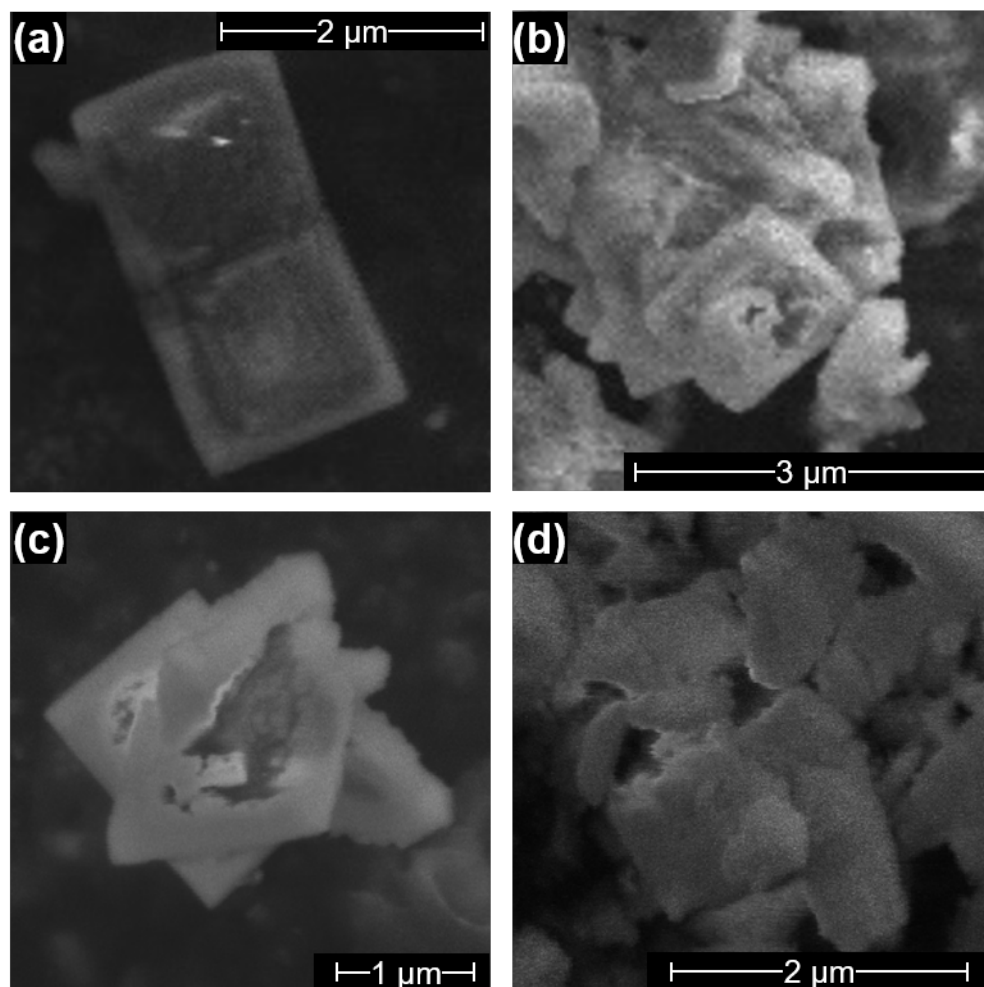


**Figure 4.67:** SEM images of representative crystals of (a) Sn-Beta-F-110 after treatment in 40 wt% NH<sub>4</sub>F (323 K) for (b) 0.083 h, (c) 0.33 h, and (d) 1.0 h.

#### 4.6.2.10 Correlations for mean deviations from tetrahedral among zeolite frameworks

It can be noted that  $\text{CD}_3\text{CN}$  adsorbed at Sn within each framework has different peak centers at low coverage (2307–2316  $\text{cm}^{-1}$ ), and according the T-siting hypothesis, these peak centers would vary monotonically with the tetrahedral deviations of the T-sites where  $\text{CD}_3\text{CN}$  is bound. Random T-siting of Sn within each framework would lead to average values of tetrahedral deviations among all T-sites, but this assumption gives to no correlation with the first-dose peak center (Figure 4.68). The simplest non-random way to preferentially site Sn would be at its thermodynamically most stable location, as theoretical studies have predicted, although with some disagreement [261,262]. Taking these to be the sites with lowest tetrahedral deviations, however, leads to an unsatisfactory correlation with the first-dose peak center (Figure 4.69), as discussed above in reference to CHA T1 and Beta T9. Assuming the opposite, that Sn preferentially sites at locations with maximum tetrahedral deviations, also does not produce a good correlation (Figure S56). A reasonable correlation of first-dose peak center with tetrahedral deviation is possible when certain T-sites are chosen arbitrarily (Beta T8, BEC T2, MFI T2, STT T16, and CHA T1, Figure 4.71), illustrating that variations in T-site bond angles could explain  $\text{Sn}_{2316}$ , but only if Sn siting is highly non-random and preferential to certain T-sites in all frameworks.

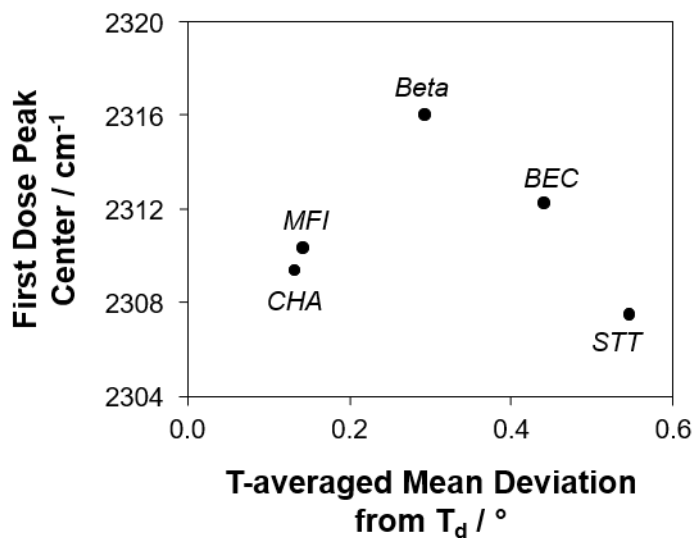


**Figure 4.68:** Position of the peak center for the first dose of adsorbed CD<sub>3</sub>CN (<0.3 CD<sub>3</sub>CN/Sn) as a function of the mean deviation from tetrahedral averaged among all T-sites in Beta, MFI, CHA, STT, and BEC.

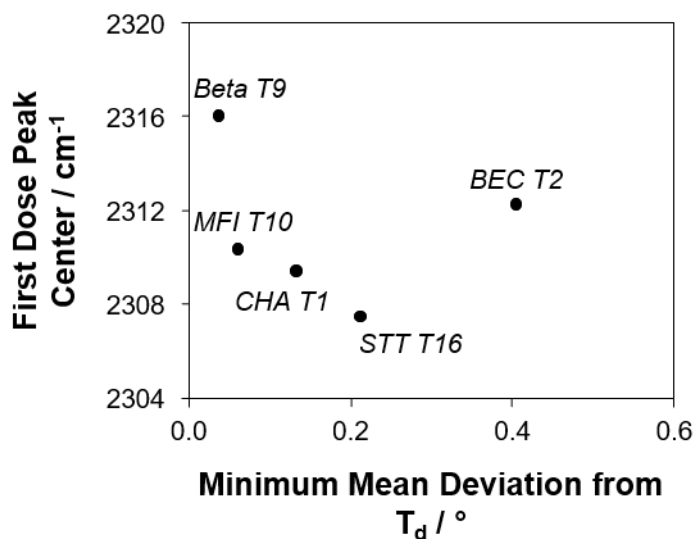


**Figure 4.69:** Position of the peak center for the first dose of adsorbed CD<sub>3</sub>CN (<0.3 CD<sub>3</sub>CN/Sn) as a function of the mean deviation from tetrahedral for the minimum-valued T-sites in Beta, MFI, CHA, STT, and BEC.

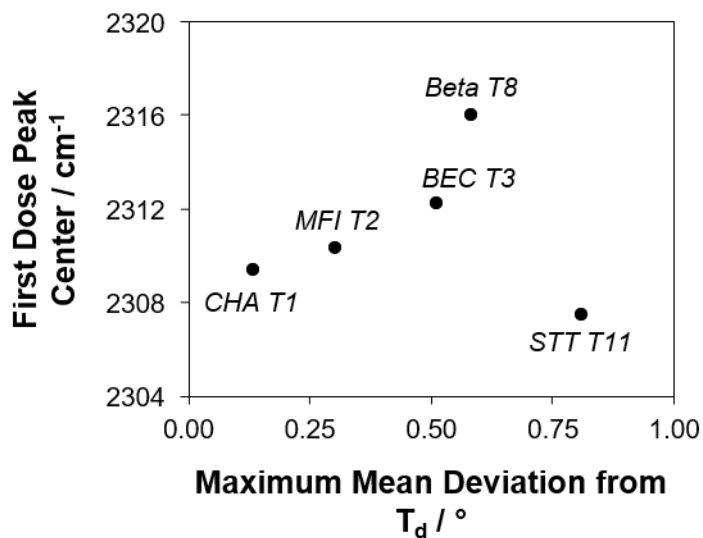


**Figure 4.70:** Position of the peak center for the first dose of adsorbed  $\text{CD}_3\text{CN}$  ( $<0.3$   $\text{CD}_3\text{CN}/\text{Sn}$ ) as a function of the mean deviation from tetrahedral for the maximum-valued T-sites in Beta, MFI, CHA, STT, and BEC.

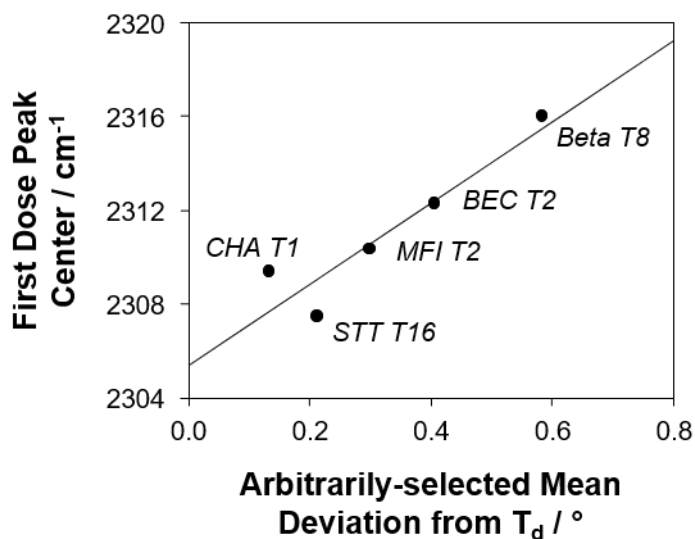


**Figure 4.71:** Position of the peak center for the first dose of adsorbed  $\text{CD}_3\text{CN}$  ( $<0.3$   $\text{CD}_3\text{CN}/\text{Sn}$ ) as a function of the mean deviation from tetrahedral for the arbitrarily-selected T-sites in Beta, MFI, CHA, STT, and BEC that give the best correlation.

## 4.6.2.11 Density functional theory calculations at stacking fault defect-open sites

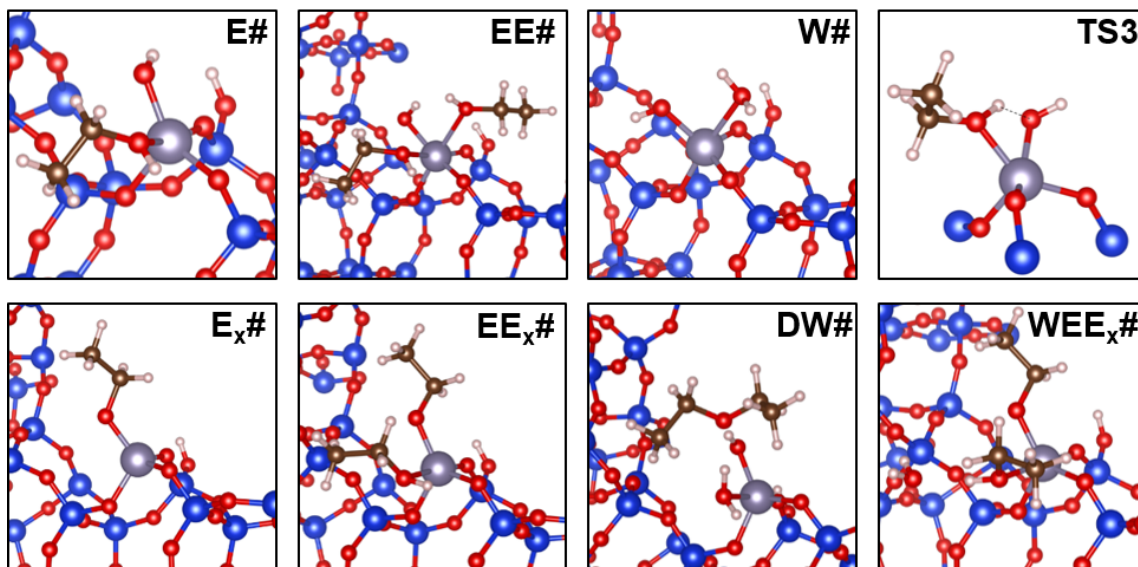


**Figure 4.72:** Geometries of adsorbed intermediates (and TS3 to form  $E_x\#$  from  $E\#$ ) for the concerted pathway and sequential pathways at the stacking fault defect-open site. .XYZ files for each adsorbate are available online.

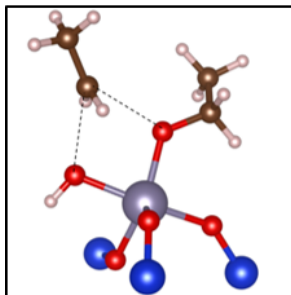


**Figure 4.73:** Transition state (TS5) for DEE formation by the sequential pathway at the stacking fault defect-open site, starting from  $EE_x\#$  without  $H_2O$  assistance, as discussed in the main text.

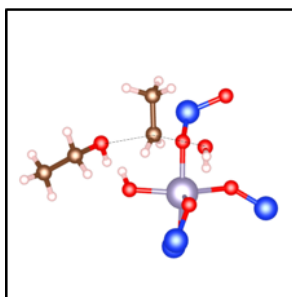


**Figure 4.74:** Transition state for DEE formation previously calculated [180] at the hydrolyzed-open site in Sn-Beta (T8).

## 4.6.3 Supplementary Tables

4.6.3.1 *in situ* pyridine titration data**Table 4.7:** Turnover rates and site densities of predominant (A) and secondary (B) sites on Sn-Beta-F-153 between 404-438 K, determined by *in situ* pyridine titration during ethanol dehydration catalysis (8 kPa C<sub>2</sub>H<sub>5</sub>OH, 0.1 kPa H<sub>2</sub>O).

Reoxidation number <sup>a</sup>	T / K	TOR <sub>A</sub> / 10 <sup>-5</sup> s <sup>-1</sup>	TOR <sub>B</sub> / 10 <sup>-6</sup> s <sup>-1</sup>	TOR <sub>A</sub> /TOR <sub>B</sub>	x <sub>A1</sub> <sup>c</sup>	x <sub>B1</sub> <sup>d</sup>	r <sub>1</sub> /r <sub>0</sub>	x <sub>A0</sub> <sup>e</sup>
0 <sup>b</sup>	421	10	6.5	16	0.05	0.29	0.58	0.09
1	421	9.2	8.1	11	0.06	0.26	0.59	0.10
2	404	4.2	3.1	14	0.05	0.28	0.75	0.07
3	413	5.6	4.9	11	0.05	0.26	0.64	0.08
4	438	25	14	18	0.01	0.31	0.38	0.04

<sup>a</sup>Re-oxidations performed after the previous *in situ* pyridine titration procedure, 5% O<sub>2</sub>/He, 813 K, 2 h

<sup>b</sup>Initial oxidation treatment 5% O<sub>2</sub>/He, 813 K, 2 h

<sup>c</sup>Sites A (per total Sn) at the start of pyridine titration (t<sub>1</sub>)

<sup>d</sup>Sites B (per total Sn) at the start of pyridine titration (t<sub>1</sub>)

<sup>e</sup>Sites A (per total Sn) extrapolated to initial time-on-stream (t<sub>0</sub>)

**Table 4.8:** Effect of different apparent reaction orders ( $\alpha$ ) on apparent activation entropies and free energies for sites A and B on Sn-Beta-F-153 (404–438 K, 8 kPa C<sub>2</sub>H<sub>5</sub>OH, 0.1 kPa H<sub>2</sub>O) determined by *in situ* pyridine titration. Activation enthalpies are the same as in Table 4.3 in the main text.

$\alpha$	Quantity	Site A	Site B	$\Delta\Delta$ Quantity <sub>A-B</sub>
0	$\Delta S_{i,app}^{\ddagger a} / \text{J mol}^{-1} \text{ K}^{-1}$	$-141 \pm 17$	$-198 \pm 14$	$48 \pm 22$
	$\Delta G_{i,app}^{\ddagger} (404 \text{ K}) / \text{kJ mol}^{-1}$	134	143	-8
0.6	$\Delta S_{i,app}^{\ddagger a} / \text{J mol}^{-1} \text{ K}^{-1}$	$-129 \pm 17$	$-185 \pm 14$	$48 \pm 22$
	$\Delta G_{i,app}^{\ddagger} (404 \text{ K}) / \text{kJ mol}^{-1}$	129	137	-8
1.0	$\Delta S_{i,app}^{\ddagger a} / \text{J mol}^{-1} \text{ K}^{-1}$	$-120 \pm 17$	$-177 \pm 14$	$48 \pm 22$
	$\Delta G_{i,app}^{\ddagger} (404 \text{ K}) / \text{kJ mol}^{-1}$	126	134	-8

<sup>a</sup>Errors are from linear regression

We note that even if the values of  $\alpha$  are different at sites A and B, the value of  $\Delta\Delta S_{A-B,app}^{\ddagger}$  is positive and greater than the value of the error. The values of  $\Delta\Delta S_{A-B,app}^{\ddagger} = 35 \pm 22 \text{ J mol}^{-1} \text{ K}^{-1}$  for  $\alpha_A=0, \alpha_B=1$ , and  $\Delta\Delta S_{A-B,app}^{\ddagger} = 77 \pm 22 \text{ J mol}^{-1} \text{ K}^{-1}$  for  $\alpha_A=1, \alpha_B=0$  therefore reflect the extremes of possible coverage regimes.

## 4.6.3.2 Sample characterization data

**Table 4.9:** Quantification of Sn Lewis acid site densities on Sn-Beta-F samples before and after NMe<sub>4</sub>OH treatments to remove fluorine.

Sample	Sn <sub>2316</sub> /Sn	Sn <sub>2308</sub> /Sn	Sn <sub>LA</sub> /Sn	Sn <sub>2308</sub> / Sn <sub>2316</sub>	Si-OH / 10 <sup>-4</sup> mol g <sup>-1</sup>
Sn-Beta-F-100 <sup>a</sup>	0.13 ± 0.03	0.36 ± 0.07	0.49 ± 0.10	2.8	0.6
Sn-Beta-F-100-NMe <sub>4</sub> OH <sup>a</sup>	0.26 ± 0.05	0.44 ± 0.09	0.70 ± 0.14	1.7	2.3
Sn-Beta-F-181	0.44 ± 0.09	0.70 ± 0.14	1.13 ± 0.23	1.6	1.8
Sn-Beta-F-181-NMe <sub>4</sub> OH	0.38 ± 0.08	0.59 ± 0.12	0.96 ± 0.19	1.6	3.4

<sup>a</sup>Data reported in Cordon et al. [241]**Table 4.10:** Micropore volumes and Sn Lewis acid site densities of Sn-Beta-F samples as a function of crystallization time at fixed gel composition.

Crystallization time / days	Si/Sn <sup>a</sup>	V <sub>micro</sub> <sup>b</sup> / cm <sup>3</sup> g <sup>-1</sup>	TEA <sup>+</sup> / u.c. <sup>c</sup>	Sn <sub>2316</sub> /Sn	Sn <sub>2308</sub> /Sn	Sn <sub>LA</sub> /Sn	Sn <sub>2308</sub> / Sn <sub>2316</sub>
1.6	178	0.12	1.2	0.04 ± 0.01	0.38 ± 0.08	0.42 ± 0.08	9.1
3	180	0.14	1.0	0.11 ± 0.02	0.55 ± 0.11	0.66 ± 0.13	5.0
7	169	0.21	3.6	0.34 ± 0.07	0.72 ± 0.14	1.06 ± 0.21	2.2
14	153	0.23	3.9	0.13 ± 0.03	0.48 ± 0.10	0.61 ± 0.12	3.8
21	181	0.20	3.5	0.28 ± 0.06	0.82 ± 0.16	1.10 ± 0.22	2.9

<sup>a</sup>Quantified by AAS<sup>b</sup>Determined by N<sub>2</sub> adsorption minimum in  $\partial V_{\text{ads}}/\partial \log(P/P_0)$ <sup>c</sup>Quantified by TGA

**Table 4.11:** Dehydrated (523 K) DRUV characterization of Sn-Beta-F samples as a function of crystallization time at fixed gel composition.

Crystallization time / days	Peak Center / nm	Edge Energy / eV
1.6	210	5.06
3	207	4.95
7	206	4.15

**Table 4.12:** Micropore volumes and Sn Lewis acid site densities of Sn-zeolite samples and their siliceous analogs.

Sample	Si(+Ge)/Sn <sup>a</sup>	$V_{micro}^b / \text{cm}^3$ $\text{g}^{-1}$	Sn <sub>2316</sub> /Sn <sup>c</sup>	Sn <sub>2308</sub> /Sn <sup>c</sup>	Sn <sub>LA</sub> /Sn <sup>c</sup>	Sn <sub>2308</sub> /Sn <sub>2316</sub>
Sn-CHA-F-70 <sup>d</sup>	70	0.15	0.36 ± 0.07	0.78 ± 0.16	1.14 ± 0.23	2.2
Sn-CHA-F-60 <sup>d</sup>	60	0.16	0.42 ± 0.08	0.76 ± 0.15	1.18 ± 0.24	1.8
Sn-MFI-F-192	192	0.18	0.25 ± 0.05	0.75 ± 0.15	1.00 ± 0.20	3.0
Sn-MFI-F-129	129	0.14	0.18 ± 0.04	0.88 ± 0.18	1.07 ± 0.21	4.8
Si-STT-F	∞	0.18	--	--	--	--
Sn-STT-F-151	151	0.15	0.04 ± 0.01	0.29 ± 0.06	0.33 ± 0.07	6.9
Ge-BEC-F	∞	0.15	--	--	--	--
Sn-Ge-BEC-F	127–142 <sup>e</sup>	0.15	0.05 ± 0.01	0.38 ± 0.08	0.44 ± 0.09	7.3

See next page for footnotes

<sup>a</sup>Quantified by AAS, assuming unit cell formula  $\text{Si}_x\text{Sn}_{1-x}\text{O}_2$ , except for Ge-containing materials<sup>e</sup>

<sup>b</sup>Determined by  $\text{N}_2$  (Ar in the case of CHA) adsorption minimum in  $\partial V_{\text{ads}}/\partial \log(P/P_0)$

<sup>c</sup>Quantified by  $\text{CD}_3\text{CN}$  IR

<sup>d</sup>Reported in Harris et al. [114]

<sup>e</sup>Ge content was not measured; thus, this number represents the range of potential (Si+Ge)/Sn ratios for the measured Sn content, assuming a unit cell formula  $\text{Si}_{1-x-y}\text{Ge}_y\text{Sn}_x\text{O}_2$ , and a Si/Ge ratio ranging from  $(5-\infty)$ ; that is, Ge incorporation at the gel Si/Ge ratio or less).

## 4.6.3.3 Mean tetrahedral deviations

The .xtl files for unit cells of all zeolites in the pure-silica form were used as-provided in the zeoTsites program, with the exception of the STT file. The STT file as-provided had an error where the first 16 Si atoms were repeated. After making this deletion, the .xtl file accurately reflected the STT unit cell, and could be loaded by zeoTsites. We thank Germán Sastre for identifying this discrepancy in the file. The “OTO\_in\_rings\_of\_XXX” (XXX = zeolite three-letter code) file output by zeoTsites was used directly to obtain the four righthand columns of the tables below, and the mean deviation from tetrahedral was computed according to Eq. 4.12 in the main text.

Table 4.13: T-sites in Beta zeolites arranged in order of decreasing mean deviations from tetrahedral.

T-site	Mean deviation from tetrahedral / °	Angle	Ring Size	N <sub>j</sub>	$\theta_{\text{O-Si-O}_j}$
T8	0.58	O11-Si8-O16	6	16	109.68
		O11-Si8-O11	12	28	108.70
		O16-Si8-O16	5	8	109.41
T4	0.42	O5-Si4-O9	4	8	109.08
		O5-Si4-O11	12	48	109.85
		O5-Si4-O12	5	8	109.69
		O9-Si4-O11	5	8	108.52
		O9-Si4-O12	4	8	110.16
		O11-Si4-O12	6	8	109.53
		O11-Si4-O12	12	24	109.53
T3	0.40	O1-Si3-O8	12	24	109.86
		O1-Si3-O9	4	8	109.01
		O1-Si3-O10	5	8	109.79

*continued on next page*

Table 4.13: *continued*

T-site	Mean deviation from tetrahedral / °	Angle	Ring Size	N <sub>j</sub>	$\theta_{\text{O-Si-O}_j}$
		O8-Si3-O9	5	8	109.18
		O8-Si3-O10	6	8	109.90
		O8-Si3-O10	12	24	109.90
		O9-Si3-O10	4	8	109.07
T5	0.35	O13-Si5-O14	5	8	109.32
		O13-Si5-O15	5	16	109.38
		O13-Si5-O10	6	8	109
		O13-Si5-O10	12	16	109
		O14-Si5-O15	5	8	109.66
		O14-Si5-O10	4	8	110.14
		O15-Si5-O10	5	8	109.33
		O15-Si5-O10	12	8	109.33
T2	0.23	O4-Si2-O5	4	8	109.64
		O4-Si2-O6	4	8	109.7
		O4-Si2-O7	5	8	109.71
		O5-Si2-O6	5	8	109.34
		O5-Si2-O7	12	48	109.24
		O6-Si2-O7	5	8	109.21
		O6-Si2-O7	12	8	109.21
T7	0.21	O8-Si7-O13	6	8	109.26
		O8-Si7-O7	12	40	109.33
		O8-Si7-O17	5	8	109.84
		O8-Si7-O17	12	8	109.84
		O13-Si7-O7	5	8	109.22

*continued on next page*

Table 4.13: *continued*

T-site	Mean deviation from tetrahedral / °	Angle	Ring Size	N <sub>j</sub>	$\theta_{\text{O-Si-O}_j}$
		O13-Si7-O7	12	16	109.22
		O13-Si7-O17	5	16	109.51
		O7-Si7-O17	5	8	109.66
T6	0.21	O14-Si6-O16	5	8	109.87
		O14-Si6-O17	5	8	109.62
		O14-Si6-O12	4	8	109.04
		O16-Si6-O17	5	16	109.44
		O16-Si6-O12	6	8	109.34
		O16-Si6-O12	12	16	109.34
		O17-Si6-O12	5	8	109.52
		O17-Si6-O12	12	8	109.52
T1	0.14	O1-Si1-O2	5	8	109.12
		O1-Si1-O3	12	24	109.45
		O1-Si1-O4	4	8	109.55
		O2-Si1-O3	5	8	109.47
		O2-Si1-O3	12	8	109.47
		O2-Si1-O4	4	8	109.65
		O1-Si1-O2	5	8	109.12
T9	0.04	O3-Si9-O15	5	16	109.45
		O3-Si9-O3	12	12	109.46
		O15-Si9-O15	5	8	109.55

Table 4.14: T-sites in CHA zeolites arranged in order of decreasing mean deviations from tetrahedral.

T-site	Mean deviation from tetrahedral / °	Angle	Ring Size	$N_j$	$\theta_{\text{O-Si-O}_j}$
T1	0.13	O4-Si-O2	8	36	109.41
		O4-Si-O3	4	36	109.75
		O4-Si-O1	4	36	109.48
		O2-Si-O3	8	36	109.45
		O2-Si-O1	4	36	109.34
		O3-Si-O1	6	36	109.40

Table 4.15: T-sites in MFI zeolites arranged in order of decreasing mean deviations from tetrahedral.

T-site	Mean deviation from tetrahedral / °	Angle	Ring Size	$N_j$	$\theta_{\text{O-Si-O}_j}$
T2	0.30	O2-Si2-O5	10	24	109.92
		O2-Si2-O6	5	8	109.17
		O2-Si2-O7	5	16	109.29
		O5-Si2-O6	5	8	109.69
		O5-Si2-O7	5	8	109.25
		O5-Si2-O7	10	8	109.25
		O6-Si2-O7	5	8	109.52
T1	0.18	O1-Si1-O2	10	16	109.43
		O1-Si1-O3	6	8	109.62
		O1-Si1-O3	10	8	109.62
		O1-Si1-O4	5	8	109.53

*continued on next page*

Table 4.15: *continued*

T-site	Mean deviation from tetrahedral / °	Angle	Ring Size	N <sub>j</sub>	$\theta_{\text{O-Si-O}_j}$
		O1-Si1-O4	6	8	109.53
		O2-Si1-O3	5	8	109.36
		O2-Si1-O3	10	8	109.36
		O2-Si1-O4	5	16	109.15
		O3-Si1-O4	5	8	109.75
T9	0.16	O19-Si9-O21	6	16	109.27
		O19-Si9-O22	5	8	109.20
		O19-Si9-O15	5	8	109.63
		O19-Si9-O15	10	8	109.63
		O21-Si9-O22	4	8	109.61
		O21-Si9-O15	10	24	109.44
		O22-Si9-O15	5	8	109.68
T12	0.16	O20-Si12-O25	5	8	109.33
		O20-Si12-O26	6	16	109.48
		O20-Si12-O8	5	16	109.28
		O25-Si12-O26	6	16	109.73
		O25-Si12-O8	5	8	109.63
		O25-Si12-O8	10	8	109.63
		O26-Si12-O8	10	16	109.38
T8	0.14	O6-Si8-O17	5	8	109.57
		O6-Si8-O19	5	8	109.44
		O6-Si8-O20	5	8	109.52
		O17-Si8-O19	6	8	109.59
		O17-Si8-O19	10	8	109.59

*continued on next page*

Table 4.15: *continued*

T-site	Mean deviation from tetrahedral / °	Angle	Ring Size	$N_j$	$\theta_{\text{O-Si-O}_j}$
		O17-Si8-O20	5	8	109.49
		O17-Si8-O20	6	8	109.49
		O19-Si8-O20	5	8	109.22
		O19-Si8-O20	6	8	109.22
T11	0.13	O14-Si11-O24	5	8	109.46
		O14-Si11-O25	5	8	109.46
		O14-Si11-O16	5	8	109.42
		O24-Si11-O25	5	8	109.70
		O24-Si11-O25	6	8	109.70
		O24-Si11-O16	6	16	109.47
		O25-Si11-O16	6	8	109.32
		O25-Si11-O16	10	8	109.32
T6	0.13	O7-Si6-O13	5	8	109.26
		O7-Si6-O15	5	8	109.39
		O7-Si6-O15	10	8	109.39
		O7-Si6-O10	5	16	109.47
		O13-Si6-O15	10	24	109.64
		O13-Si6-O10	5	8	109.43
		O13-Si6-O10	10	8	109.43
		O15-Si6-O10	5	8	109.63
T3	0.12	O5-Si3-O8	10	24	109.44
		O5-Si3-O9	5	8	109.45
		O5-Si3-O10	5	8	109.52
		O5-Si3-O10	10	8	109.52

*continued on next page*

Table 4.15: *continued*

T-site	Mean deviation from tetrahedral / °	Angle	Ring Size	N <sub>j</sub>	$\theta_{\text{O-Si-O}_j}$
		O8-Si3-O9	5	8	109.53
		O8-Si3-O10	5	16	109.24
		O9-Si3-O10	5	8	109.64
T4	0.12	O9-Si4-O11	5	8	109.35
		O9-Si4-O12	5	8	109.62
		O9-Si4-O4	5	8	109.55
		O11-Si4-O12	6	8	109.53
		O11-Si4-O12	10	8	109.53
		O11-Si4-O4	5	16	109.50
		O12-Si4-O4	5	8	109.28
		O12-Si4-O4	6	8	109.28
T7	0.11	O16-Si7-O17	10	8	109.30
		O16-Si7-O18	6	16	109.49
		O16-Si7-O11	5	8	109.57
		O16-Si7-O11	6	8	109.57
		O17-Si7-O18	6	16	109.34
		O17-Si7-O11	5	16	109.55
		O18-Si7-O11	10	8	109.58
T5	0.10	O12-Si5-O13	5	8	109.54
		O12-Si5-O13	10	8	109.54
		O12-Si5-O14	5	8	109.48
		O12-Si5-O1	6	16	109.62
		O13-Si5-O14	5	8	109.32
		O13-Si5-O1	10	24	109.38

*continued on next page*

Table 4.15: *continued*

T-site	Mean deviation from tetrahedral / °	Angle	Ring Size	N <sub>j</sub>	$\theta_{\text{O-Si-O}_j}$
		O14-Si5-O1	5	8	109.50
T10	0.06	O22-Si10-O23	4	8	109.56
		O22-Si10-O24	5	8	109.56
		O22-Si10-O3	5	8	109.40
		O23-Si10-O24	6	16	109.42
		O23-Si10-O3	10	16	109.49
		O24-Si10-O3	5	8	109.41
		O24-Si10-O3	6	8	109.41

Table 4.16: T-sites in STT zeolites arranged in order of decreasing mean deviations from tetrahedral.

T-site	Mean deviation from tetrahedral / °	Angle	Ring Size	N <sub>j</sub>	$\theta_{\text{O-Si-O}_j}$
T11	0.81	O29-Si11-O25	5	4	110.20
		O29-Si11-O25	6	4	110.20
		O29-Si11-O22	6	4	110.23
		O29-Si11-O30	5	4	110.36
		O25-Si11-O22	5	8	108.54
		O25-Si11-O30	6	4	108.77
		O22-Si11-O30	6	4	108.69
T14	0.78	O31-Si14-O10	5	4	110.02
		O31-Si14-O25	5	4	109.32
		O31-Si14-O19	7	4	108.80
		O10-Si14-O25	5	4	108.68

*continued on next page*

Table 4.16: *continued*

T-site	Mean deviation from tetrahedral / °	Angle	Ring Size	N <sub>j</sub>	$\theta_{\text{O-Si-O}_j}$
		O10-Si14-O25	6	4	108.68
		O10-Si14-O19	6	4	111.01
		O25-Si14-O19	5	4	108.99
		O25-Si14-O19	6	4	108.99
T1	0.77	O19-Si1-O18	5	4	108.35
		O19-Si1-O18	6	4	108.35
		O19-Si1-O8	7	4	109.37
		O19-Si1-O2	6	4	110.56
		O18-Si1-O8	9	4	109.43
		O18-Si1-O2	5	4	110.04
		O8-Si1-O2	4	4	109.08
T9	0.75	O28-Si9-O24	5	4	110.33
		O28-Si9-O17	4	4	109.84
		O28-Si9-O18	5	4	110.40
		O24-Si9-O17	5	4	108.77
		O24-Si9-O18	6	4	108.73
		O24-Si9-O18	9	4	108.73
		O17-Si9-O18	5	4	108.72
T2	0.68	O14-Si2-O5	4	4	109.05
		O14-Si2-O4	7	4	109.12
		O14-Si2-O2	5	4	109.86
		O5-Si2-O4	9	4	108.56
		O5-Si2-O2	6	4	109.52
		O4-Si2-O2	4	4	110.68

*continued on next page*

Table 4.16: *continued*

T-site	Mean deviation from tetrahedral / °	Angle	Ring Size	N <sub>j</sub>	$\theta_{\text{O-Si-O}_j}$
T12	0.57	O7-Si12-O6	4	4	108.61
		O7-Si12-O3	4	4	109.65
		O7-Si12-O11	5	4	109.35
		O6-Si12-O3	5	4	110.29
		O6-Si12-O11	9	4	108.98
		O3-Si12-O11	5	4	109.94
T5	0.56	O27-Si5-O26	4	4	108.96
		O27-Si5-O8	7	4	109.76
		O27-Si5-O6	4	4	109.83
		O26-Si5-O8	4	4	110.25
		O26-Si5-O6	5	4	108.58
		O8-Si5-O6	9	4	109.45
T6	0.55	O31-Si6-O26	5	4	108.99
		O31-Si6-O20	5	4	109.61
		O31-Si6-O4	7	4	110.00
		O26-Si6-O20	4	4	110.04
		O26-Si6-O4	4	4	108.50
		O20-Si6-O4	9	4	109.68
T15	0.55	O22-Si15-O9	6	4	109.50
		O22-Si15-O32	5	4	109.79
		O22-Si15-O24	5	4	108.74
		O22-Si15-O24	6	4	108.74
		O9-Si15-O32	4	4	109.78
		O9-Si15-O24	9	4	110.16

*continued on next page*

Table 4.16: *continued*

T-site	Mean deviation from tetrahedral / °	Angle	Ring Size	N <sub>j</sub>	$\theta_{\text{O-Si-O}_j}$
		O32-Si15-O24	5	4	108.87
T4	0.50	O17-Si4-O12	5	4	109.66
		O17-Si4-O7	4	4	109.07
		O17-Si4-O1	5	4	109.02
		O12-Si4-O7	4	4	110.13
		O12-Si4-O1	6	4	110.04
		O7-Si4-O1	5	4	108.90
T7	0.47	O27-Si7-O15	4	4	110.15
		O27-Si7-O12	4	4	109.27
		O27-Si7-O13	7	4	108.82
		O15-Si7-O12	5	4	109.88
		O15-Si7-O13	6	4	109.65
		O12-Si7-O13	6	4	109.05
T8	0.39	O21-Si8-O16	4	4	108.96
		O21-Si8-O11	5	4	108.89
		O21-Si8-O5	4	4	109.62
		O16-Si8-O11	5	4	109.80
		O16-Si8-O5	6	4	109.83
		O11-Si8-O5	9	4	109.72
T3	0.34	O23-Si3-O13	6	4	109.59
		O23-Si3-O1	5	4	109.07
		O23-Si3-O14	4	4	109.59
		O13-Si3-O1	6	4	109.19
		O13-Si3-O14	7	4	110.09

*continued on next page*

Table 4.16: *continued*

T-site	Mean deviation from tetrahedral / °	Angle	Ring Size	$N_j$	$\theta_{\text{O-Si-O}_j}$
		O1-Si3-O14	5	4	109.29
T10	0.33	O30-Si10-O16	6	4	109.97
		O30-Si10-O23	6	4	109.86
		O30-Si10-O21	5	4	109.11
		O16-Si10-O23	5	4	109.20
		O16-Si10-O21	4	4	109.26
		O23-Si10-O21	4	4	109.44
T13	0.33	O32-Si13-O20	5	4	109.58
		O32-Si13-O15	5	4	109.70
		O32-Si13-O9	4	4	108.88
		O20-Si13-O15	4	4	109.19
		O20-Si13-O9	9	4	109.80
		O15-Si13-O9	6	4	109.69
T16	0.21	O29-Si16-O28	5	4	109.58
		O29-Si16-O10	6	8	109.48
		O29-Si16-O3	5	4	109.48
		O28-Si16-O10	5	4	109.84
		O28-Si16-O3	4	4	109.37
		O10-Si16-O3	5	4	109.08

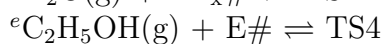
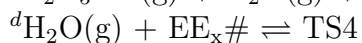
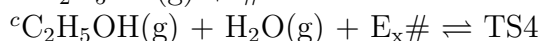
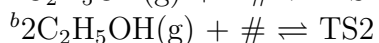
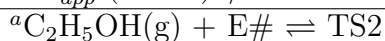
Table 4.17: T-sites in BEC zeolites arranged in order of decreasing mean deviations from tetrahedral.

T-site	Mean deviation from tetrahedral / °	Angle	Ring Size	$N_j$	$\theta_{\text{O-Si-O}_j}$
T3	0.51	O6-Si3-O7	5	16	110.24
		O6-Si3-O5	4	8	109.32
		O7-Si3-O5	6	16	109.00
		O7-Si3-O5	12	48	109.00
		O7-Si3-O7	5	16	109.02
T1	0.42	O2-Si1-O4	6	16	110.09
		O2-Si1-O4	12	32	110.09
		O2-Si1-O1	4	16	109.63
		O2-Si1-O3	4	16	109.36
		O4-Si1-O1	5	16	108.92
		O4-Si1-O3	12	96	109.79
		O1-Si1-O3	4	16	109.04
T2	0.41	O4-Si2-O4	12	40	109.01
		O4-Si2-O7	6	32	109.72
		O7-Si2-O7	5	16	108.96

## 4.6.3.4 Density functional theory calculations at stacking fault defect-open sites

**Table 4.18:** Apparent activation enthalpies, entropies, and Gibbs free energies (404 K) for bimolecular ethanol dehydration at stacking fault defect-open Sn sites in Beta zeolites covered by different MARI species.

Pathway:	Concerted		Sequential (H <sub>2</sub> O-assisted)		
MARI Species:	E# <sup>a</sup>	# <sup>b</sup>	E <sub>x</sub> # <sup>c</sup>	EE <sub>x</sub> # <sup>d</sup>	E# <sup>e</sup>
Expected Ethanol Order	1	2	1	0	1
$\Delta H_{app}^\ddagger / \text{kJ mol}^{-1}$	157	78	19	90	145
$\Delta S_{app}^\ddagger / \text{J mol}^{-1} \text{K}^{-1}$	-103	-214	-310	-209	-110
$\Delta G_{app}^\ddagger (404 \text{ K}) / \text{kJ mol}^{-1}$	199	164	144	174	190

**Table 4.19:** Ethanol adsorption energies at arbitrarily numbered T-site locations in stacking fault Beta. The T4 location denotes the Sn location used in the provided structural model. The total range in binding energy across all sites is 0.22 eV

Stacking fault T-location	$\Delta E_{ads}$ Ethanol / eV
T1	-0.70
T2	-0.63
T3	-0.79
T4	-0.85
T5	-0.76
T6	-0.76
T7	-0.68

**Table 4.20:** Differential dispersion energies calculated by the method of Grimme [139] using the optimized geometries of E# at the stacking fault site and E\* at the closed site.

Species	$\Delta E_{vdW}$ / eV
E*	-40
E#	-31

**Table 4.21:** Distances between Sn and O or H belonging to the proximal Si-OH group in the stacking fault defect-open site and the hydrolyzed-open site reported in Bukowski et al. [180]

Site	Sn-O Distance / Å	Sn-H Distance / Å
Defect-open	4.59	4.63
Hydrolyzed-open	3.20	3.54

## 5. DEACTIVATION OF SN-BETA ZEOLITES CAUSED BY STRUCTURAL TRANSFORMATION OF HYDROPHOBIC TO HYDROPHILIC MICROPORES DURING AQUEOUS-PHASE GLUCOSE ISOMERIZATION

### 5.1 Introduction

Lewis acidic molecular sieves are silica-based microporous materials with some of their framework silicon atoms isomorphously substituted with tetravalent heteroatoms ( $M^{4+} = Sn^{4+}, Ti^{4+}, \text{etc.}$ ), which are useful catalysts for alkene epoxidation [263, 264] and transformations of biomass-derived oxygenates [265]. Active sites in these materials comprise both Lewis acidic binding sites, present because of differences in electronegativity between lattice  $M^{4+}$  and  $Si^{4+}$  centers, and their confining environments [266], which vary in size and polarity among materials of different framework topology and synthetic and treatment history. Active sites within inorganic Lewis acidic molecular sieves catalyze glucose isomerization by an analogous reaction mechanism to that reported for metalloenzymes (e.g., D-xylose isomerase) [267], but are more tolerant to variations in solvent pH, temperature, and impurity concentrations than are immobilized metalloenzymes [268]. One challenge to practical implementation of Lewis acidic molecular sieves, however, is the deactivation typically observed under aqueous-phase conditions [116, 179, 266, 269].

Mechanistic understanding of such deactivation phenomena has been limited by the complexity of in situ quantification of the interactions between liquids and solids [266], although recent research has provided insights on the nature of zeolite degradation in liquid water. Al-Beta zeolites deactivate significantly when treated in hot liquid water (48 h, 433–573 K) because intraporous water facilitates the hydrolysis of framework siloxane bonds and amorphization of crystallites [65, 67, 270]. Silanol defects stabilize water molecules, clusters of water molecules, and extended hydrogen-

bonded networks of water molecules between hydrophobic SiO<sub>2</sub> plates positioned 0.7 nm apart in molecular dynamics simulations (300 K) [37], and these silanol defects decrease zeolite stability during gas-phase water exposure (473 K, 0–24 h) as observed using X-ray diffraction (XRD) to assess crystallinity and diffuse reflectance IR spectroscopy (DRIFTS) to monitor silanol group formation [66]. This amorphization can be suppressed via functionalization of external zeolite surfaces with hydrophobic organosilanes, which hinders direct contact between zeolite crystallites and the aqueous phase [66,271,272] and, in turn, the solvation of intraporous fragments formed upon zeolite framework hydrolysis and their transport to bulk solvent phases [273]. Higher intraporous water densities also accelerate catalyst deactivation and decrease reaction rates for coupled transfer hydrogenation and etherification of 5-hydro-methylfurfural in primary and secondary alcohols on Zr-Beta, Hf-Beta, and Sn-Beta zeolites [179], dihydroxyacetone isomerization in methanol on Sn-Beta, Sn-MOR, and Sn-FAU zeolites [116], aqueous-phase cyclohexanol dehydration on Al-Beta zeolites [65], and liquid-phase glucose-fructose isomerization on Sn-Beta zeolites in both water and methanol [117,274]. These observations are consistent with higher glucose isomerization rates reported on Sn-Beta zeolites when samples are dehydrated before exposure to aqueous reactant solutions [54].

Glucose-fructose isomerization is an aqueous-phase probe reaction for which the reaction mechanism and active sites are commonly accepted, as it is catalyzed over partially-hydrolyzed Lewis acidic open Sn sites (Sn(OSi)<sub>3</sub>OH) on Sn-Beta zeolites [56,68,106], involves the kinetically-relevant intramolecular 1,2-hydride shift [91] with negligible formation of undesired side products at initial reaction times [91,100,153], and is sensitive to confining environment polarity [53,56]. Glucose isomerization over Sn-Beta catalysts proceeds by quasi-equilibrated adsorption of glucose from solution onto the Lewis acid site, followed by quasi-equilibrated ring-opening and deprotonation, and then by kinetically-relevant 1,2-hydride shift to form ring-opened fructose [68]. The 1,2-hydride shift transition state has been identified by isotopically labeling the glucose C<sub>2</sub>-H with D and monitoring the retained D label in fructose

products in the C<sub>1</sub>-D position via <sup>1</sup>H NMR [91]. The involvement of this 1,2-hydride shift transition state in the sole kinetically relevant step has been verified through measurement of the glucose-H<sub>2</sub>/D<sub>2</sub> kinetic isotope effect (KIE) of 2.1 at 373 K [68], and from quantum mechanics/molecular mechanics (QM/MM) calculations on M<sup>4+</sup>-Beta and M<sup>5+</sup>-Beta zeolites [101]. Furthermore, this KIE value of 2.1 (at 373 K) indicates that rate data are uncorrupted by mass transfer artifacts, which in the limit of severe intracrystalline transport restrictions would result in measurement of the square root of the theoretical KIE value (1.4 at 373 K) [53]. Initial rate measurements on Sn-Beta zeolites are first-order in initial glucose concentration (1–10 wt%, 373 K) [56] and reflect free energy differences between 1,2-hydride shift transition states and two water molecules bound to open Sn sites, a reference state that has been observed in diffuse-reflectance UV-visible spectra [56, 151, 230], <sup>119</sup>Sn NMR spectra [112, 153, 155], and X-ray absorption spectra [108, 114, 226]. Further, free energy differences reflected in aqueous-phase glucose isomerization rates are sensitive to intraporous silanol defect density, because silanol groups stabilize co-adsorbed hydrogen bonding networks of water molecules that increase free energy barriers [57] and lead to lower initial isomerization rates on Ti-Beta and Sn-Beta [56, 151].

Here, we investigate systematic changes to Sn site densities and the polarity of microporous confining environments on Sn-Beta zeolites after extended durations (0–24 h) of hot water exposure at 373 K. Aqueous-phase glucose isomerization rates measured in batch reactors, after Sn-Beta zeolites were exposed to hot liquid water for increasing times, are used to simulate the deactivation behavior reported previously during continuous aqueous-flow rate measurements [116, 117, 275]. IR spectra collected after CD<sub>3</sub>CN titration of framework and extraframework Sn sites and silanol defect groups, combined with single-component vapor-phase water and methanol adsorption isotherms and <sup>29</sup>Si and <sup>19</sup>F solid-state NMR spectra are used to monitor and quantify changes in the densities of surface functional groups caused by hot water exposure. These changes in surface species are correlated with observed deactivation and activation phenomena to isolate the role of silanol defects, and the co-adsorbed

water molecules and extended hydrogen bonding networks they stabilize during reaction, on changes to the stability and catalytic reactivity of Sn-Beta zeolites under aqueous-phase reaction conditions.

## 5.2 Experimental methods

### 5.2.1 Catalyst synthesis and preparation

Sn-Beta zeolites were synthesized in fluoride media (Sn-Beta-F) using previously reported methods [56,151,183]. Dealuminated Beta zeolites were used as seed material and were prepared by stirring a mixture of 5 g of H-form Al-Beta (Zeolyst, CP814C, Si/Al = 19) and 125 cm<sup>3</sup> of concentrated nitric acid (HNO<sub>3</sub>, Avantor, 69 wt%) for 16 h at 353 K. Solids were then collected through centrifugation, washed in deionized water (18.2 MΩ, 6 washes, 25 cm<sup>3</sup> (g zeolite)<sup>-1</sup> per wash), and dried at 373 K for 16 h. Preparation of the synthesis gels used to crystallize Sn-Beta-F samples involved mixing 7.67 g of tetraethylammonium hydroxide (TEAOH, Sachem, 35 wt%) with 6.98 g of tetraethylorthosilicate (TEOS, Sigma Aldrich, >98 wt%) in a perfluoroalkoxy (PFA) alkane (Savillex Corp.) container and then stirring for 1 h. Then, a solution containing 0.04–0.12 g of tin(IV) chloride pentahydrate (SnCl<sub>4</sub>·5H<sub>2</sub>O, Sigma-Aldrich, 98 wt%) dissolved in 0.64 g of deionized water was added to the gel prior to sealing the PFA container and stirring for 12 h. The cap was then removed to allow for the evaporation of ethanol and excess water. Then, 0.74 g of hydrofluoric acid (HF, Alfa Aesar, 48%) were added to the solution and stirred manually for 300 s. The resulting gel was loaded into a Teflon-lined stainless steel autoclave (45 cm<sup>3</sup>, Parr Instruments) and 0.085 g of dealuminated Beta zeolite seeds were added. The autoclave was then sealed and placed in an isothermal oven (Yamato DKN-402C) at 413 K for 6–25 d while rotating at 60 RPM. The autoclaves were then cooled to ambient temperature and the resulting solids were washed thoroughly with water and acetone (Sigma Aldrich, >99.5 wt%, 5 washes per solvent, 25 cm<sup>3</sup> (g zeolite)<sup>-1</sup> per wash), separated by centrifugation, and then dried for 16 h at 373 K. The dry powders were heated

in dry air (Ultra Zero Grade, Indiana Oxygen,  $1.67 \text{ cm}^3 \text{ s}^{-1} (\text{g zeolite})^{-1}$ ) to 853 K ( $0.0167 \text{ K s}^{-1}$ ) and held for 10 h in a muffle furnace (Nabertherm LE 6/11 equipped with a P300 controller). Samples are labeled as Sn-Beta-F-X, where X is the Si/Sn ratio determined from atomic absorption spectroscopy (AAS). Some of these samples (Sn-Beta-F-100, Sn-Beta-F-220, Sn-Beta-F-172, and Sn-Beta-F-110) have been studied in our prior publication [56].

Post-synthetic Sn-Beta-OH zeolite samples were synthesized via  $\text{SnCl}_4$  grafting as reported previously in dichloromethane reflux [151]. Briefly, Al-Beta-OH samples were synthesized hydrothermally using previously reported procedures [183] ( $\text{Si}/\text{Al} = 29\text{--}55$ ). Subsequently, the Al-Beta-OH parent materials were dealuminated by stirring in nitric acid (Avantor,  $25 \text{ cm}^3 (\text{g Al-Beta-OH zeolite})^{-1}$ , 69 wt%) at 353 K overnight. The dealuminated Beta obtained was washed thoroughly with water and dried at 373 K overnight in a drying oven. Next, the dealuminated Beta was loaded into a  $500 \text{ cm}^3$  three-neck round-bottom flask with a septum stopper (white rubber, Ace Glass) and connected to a Schlenk line prior to drying under rough vacuum ( $\sim 0.04$  Torr, Oerlikon Trivac 140002E2) at 423 K overnight. Dichloromethane (DCM, Sigma Aldrich, 99.8%) was dried separately in an inert atmosphere (Ar, Indiana Oxygen, 99.999%) over pre-activated molecular sieves (W. R. Grace, Type 3AA, Grade 562, 4–8 mesh) in a separate round bottom flask for 72 h, then transferred via air-free and moisture-free cannula to the round-bottom flask containing the dried dealuminated Beta. Finally, 1 M  $\text{SnCl}_4$  in DCM (Sigma Aldrich,  $0.001\text{--}0.040 \text{ mol Sn (g zeolite)}^{-1}$ ) was transferred via moisture-free cannula to the round-bottom flask containing the dealuminated Beta and DCM, and the mixture was stirred under reflux conditions (333 K) in Ar atmosphere for 7 h. The resulting solids were separated by centrifugation and thoroughly washed with methanol (99.9%, Sigma Aldrich,  $\sim 120 \text{ cm}^3 (\text{g zeolite})^{-1}$ ) to reduce the formation of extraframework Sn oxide [276]. Solids were then dried overnight at 373 K prior to treatments in air ( $1.67 \text{ cm}^3 \text{ s}^{-1} (\text{g zeolite})^{-1}$ ) at 473 K ( $0.05 \text{ K s}^{-1}$ ) for 6 h and then at 823 K ( $0.05 \text{ K s}^{-1}$ ) for 6 h in a muffle furnace. Samples

prepared post-synthetically are subsequently labeled as Sn-Beta-OH-X, where X is the Si/Sn ratio determined from AAS.

Hot (373 K) water treatment of Sn-Beta catalysts were performed by loading  $\sim 0.3$  g of catalyst evenly among three 10 cm<sup>3</sup> thick-walled glass batch reactors (VWR) and adding water adjusted to pH 4 with hydrochloric acid (HCl, Macron, 37 wt%) to each reactor to achieve a 1:50 catalyst to water ratio, which is the same pH and catalyst to solution ratio used in glucose isomerization kinetic studies. The reactors were heated to 373 K and stirred at 750 RPM for variable exposure times (0.08–24 h). After the specified time, the reactors were quenched in an ice bath and the water-treated solids were collected via centrifugation, and then dried overnight in an oven (363 K).

### 5.2.2 Catalyst characterization

Elemental compositions of catalyst samples were determined by atomic absorption spectroscopy (AAS) using a Perkin Elmer AAnalyst 300 atomic absorption spectrometer. Calibration standards for each metal tested were created from 1000 ppm AAS standards (Alfa Aesar, TraceCERT,  $\pm 4$  ppm). Samples were prepared for AAS analyses by dissolving  $\sim 0.02$  g solid in 2.6 g of HF (48 wt%, Alfa Aesar) overnight prior to the addition of 50 g of deionized water. Absorbance values were measured at 396.2 nm and 286.3 nm in an acetylene/nitrous oxide flame for Al and Sn, respectively. Si/Al and Si/Sn ratios were determined from the Al and Sn weight fractions obtained by AAS together with the unit cell formula for zeolite Beta.

Powder X-ray diffraction (XRD) patterns were obtained using a Rigaku Smartlab X-ray diffractometer equipped with an ASC-6 automated sample changer and a Cu K $\alpha$  X-ray source (1.76 kW). Approximately 0.01 g of sample were loaded into low dead volume, zero background sample holders (Rigaku) prior to diffraction pattern collection (4–40°, scan rate of 0.00417° s<sup>-1</sup>, step size of 0.01°). The presence of large (>3 nm) SnO<sub>x</sub> domains, reflected by peaks located at 26.7 and 34°, were not observed in XRD patterns.

Scanning electron microscopy (SEM) images were obtained using a FEI Quanta 3D FEG Dual-beam SEM with an Everhart–Thornley attachment for high vacuum imaging. The focused beam operating mode was used (5 kV, spot size of 4  $\mu\text{m}$ ) to collect SEM micrographs.

Gas-phase nitrogen (77 K), and vapor-phase water (293 K) and methanol (293 K) adsorption isotherms were measured with a Micrometrics ASAP2020 surface area and porosity analyzer.  $\sim 0.03$  g of catalyst were pelleted and sieved to 180–250  $\mu\text{m}$  and loaded for analysis. Sample degas was performed by heating samples to 623 K ( $0.0167 \text{ K s}^{-1}$ ) under vacuum ( $< 0.005$  Torr) for 8 h prior to adsorption measurements. Micropore volumes were determined from a semi-log derivative analysis of nitrogen adsorption isotherms. Water uptakes at a reduced pressure of 0.2 were reported for comparison between samples, and a reduced pressure of 0.2 is a reference pressure associated with completion of micropore filling by cyclohexane (298 K) within hydrophobic zeolites [171].

Diffuse reflectance UV-visible spectroscopy was performed using a Varian Cary 5000 spectrometer with a Harrick Praying Mantis in situ diffuse reflectance cell. Spectra were collected after heating the sample to 523 K ( $\sim 0.5 \text{ K s}^{-1}$ ) under dry He flow ( $4.17 \text{ cm}^3 \text{ s}^{-1} (\text{g zeolite})^{-1}$ ) and holding the sample at 523 K for 0.5 h. Polytetrafluoroethylene (PTFE, 1  $\mu\text{m}$ , Sigma Aldrich) was used as the baseline, 100% reflectance standard. Spectra were processed using the Kubelka–Munk function ( $F(R)$ ).

Infrared spectroscopy experiments were performed in a custom-built IR cell and heating/cooling chamber [184] by first pressing self-supporting wafers of Sn-Beta zeolite samples prior to placing them in a custom quartz cell placed in an insulated brass block. The quartz cell was sealed with custom ultra-Torr fittings equipped with  $\text{CaF}_2$  windows. The IR cell was connected to a custom glass manifold and the wafer was treated in flowing air (Parker Balston,  $< 1$  ppm  $\text{CO}_2$ , 200 K  $\text{H}_2\text{O}$  dew point) at 823 K ( $0.0833 \text{ K s}^{-1}$ ) for 1 h. The wafer was then exposed to vacuum ( $\sim 10^{-2}$  Torr) for 1 h at 823 K then cooled to 303 K. Infrared spectra (64 scans,  $2 \text{ cm}^{-1}$  resolution) were collected using a Nicolet 4700 spectrometer equipped with a HgCdTe detector

cooled with liquid nitrogen (77 K). A spectrum was collected prior to deuterated acetonitrile ( $\text{CD}_3\text{CN}$ ) dosing and was subtracted from spectra collected after each dose. Known quantities of  $\text{CD}_3\text{CN}$  ( $\sim 1.5 \times 10^{-7}$  mol) were prepared in a calibrated volume, dosed into the cell, and allowed to equilibrate for 180 s. Dosing was repeated until saturation as determined from significant pressures ( $>0.4$  Torr) remaining after equilibration, indicating residual  $\text{CD}_3\text{CN}$  vapor. Spectra collected on samples treated in hot (373 K) liquid water were collected in a similar fashion except that the samples were heated to 673 K ( $0.0833 \text{ K s}^{-1}$ ) in dry He flow prior to vacuum exposure (1 h) and cooling to 303 K for dosing.

Infrared spectra were deconvoluted in CasaXPS using a previously reported procedure and integrated peak areas for peaks centered at  $2316 \text{ cm}^{-1}$ ,  $2308 \text{ cm}^{-1}$ ,  $2287 \text{ cm}^{-1}$ , and  $2275 \text{ cm}^{-1}$  were quantified [56]. Integrated molar extinction coefficients ( $E$ ) for each peak were previously reported and were used to convert integrated peak areas into total densities of open and closed Lewis acidic Sn sites, extraframework Sn sites, and silanol groups, respectively [188].

Solid-state magic angle spinning (MAS) and cross-polarization MAS (CPMAS) NMR spectra were collected using a Bruker Avance 500 MHz spectrometer equipped with a Bruker 4 mm MAS probe.  $\sim 75$  mg of Sn-Beta was packed into a 4 mm  $\text{ZrO}_2$  rotor. The operating frequencies were 99.5 and 470.5 MHz for  $^{29}\text{Si}$  and  $^{19}\text{F}$  nuclei, respectively. Spectra were externally referenced to tetramethylsilane (TMS) for  $^{29}\text{Si}$  and  $\text{CFCl}_3$  for  $^{19}\text{F}$ . For  $^{29}\text{Si}$  CPMAS spectra, contact pulse of 62.5 kHz radio-frequency (rf) pulse power was applied while  $^1\text{H}$  contact rf power was adjusted at 54.5 kHz at sample spinning rate of 8 kHz for optimal CPMAS condition.  $^{19}\text{F}$  MAS spectra were recorded under 14 kHz of sample spinning and without  $^1\text{H}$  decoupling pulse.

### 5.2.3 Glucose isomerization kinetic studies

Kinetic studies were performed with 1–2 wt% aqueous D-glucose (Sigma-Aldrich,  $\geq 99.5\%$ ) solutions in  $10 \text{ cm}^3$  thick-walled glass batch reactors (VWR). Reactant solutions were prepared by first lowering the pH of deionized water to 4 with hydrochloric

acid to suppress background glucose isomerization reactivity from hydroxide anions in solution prior to dissolving D-glucose in the pH-adjusted water to obtain the desired concentration. Reactant solutions were then filtered (0.2  $\mu\text{m}$  PTFE filters, VWR) and loaded into 2  $\text{cm}^3$  glass vials capped with a PTFE/silicone septum for pre-heating to reaction temperature. Typically  $\sim 0.01$  g of catalyst were added to the batch reactor and sealed in with a crimp top (PTFE/silicone septum, Agilent). Batch reactors and vials containing reactant solutions were heated separately for 600 s to 373 K in an oil bath atop a digital stirred hotplate (IKA RCT basic). Reactions were initiated by injecting  $\sim 1$   $\text{cm}^3$  of the pre-heated reactant solution into the capped batch reactor. Reactors were held at temperature (373 K, 750 RPM, autogenous pressure) for various reaction times (0.08–1 h) to ensure differential conversions ( $< 6\%$ ). Under these conditions, measured reaction rates are equivalent to initial rate measurements obtained from batch reactor kinetic studies, in which aliquots are taken at multiple time points and measured fructose concentrations are regressed to a reversible batch reactor model in order to extract initial fructose formation rates.

After reaction, batch reactors were quenched in an ice bath and product solutions were collected and filtered through 0.2  $\mu\text{m}$  PTFE filters (VWR). Product solutions were mixed with a 1 wt% aqueous D-mannitol (Sigma Aldrich,  $\geq 98$  wt%) solution as an internal standard for product quantification. A high-performance liquid chromatograph (HPLC, Agilent 1260) equipped with a Hi-Plex Ca column ( $7.7 \times 300$  mm, 8  $\mu\text{m}$  particle size, Agilent) and an aqueous mobile phase (0.01  $\text{cm}^3 \text{ s}^{-1}$ , 353 K) was used to separate isomerization products. Quantification was performed using an evaporative light scattering detector (Agilent 1260 Infinity ELSD) and individual calibration curves for reactant and product compounds.

To collect reaction rates after extended durations of water exposure,  $\sim 0.01$  g of catalyst were loaded into a batch reactor followed by the addition of  $\sim 0.5$   $\text{cm}^3$  of pH-adjusted water, achieving an approximate 1:50 catalyst to water mass ratio. The reactor was then capped with a crimp top and heated (373 K, 750 RPM) in an oil bath for 0.08–24 h. After the desired water exposure time, the reaction was initi-

ated by the injection of  $\sim 0.5 \text{ cm}^3$  of a 2 wt% aqueous glucose solution (heated to 373 K for 600 s prior to injection) to produce a bulk glucose concentration of  $\sim 1$  wt% in the reactant solution. Reaction times were chosen (0.08–1 h) to maintain differential conversions ( $< 6\%$ ). Products were subsequently quantified as described above. Glucose–fructose isomerization rate constants measured on Sn-Beta-F samples immediately after extended water exposure, and those measured on Sn-Beta-F samples dried after hot water exposure prior to the onset of reaction (as performed on untreated Sn-Beta samples), were identical within experimental error.

### 5.3 Results and discussion

#### 5.3.1 Effect of hot water pretreatment of Sn-Beta on glucose isomerization kinetics

Sn-Beta zeolites were synthesized hydrothermally in fluoride media or using post-synthetic methods to graft  $\text{SnCl}_4$  precursors within vacancy defects of dealuminated Beta frameworks in order to obtain hydrophobic Sn-Beta-F and hydrophilic Sn-Beta-OH samples, respectively. Powder X-ray diffraction patterns (Figure 5.8, Supporting Information) and micropore volumes (Table 5.1) derived from  $\text{N}_2$  adsorption isotherms (77 K, Figure 5.9, Supporting Information) of all Sn-Beta samples were consistent with the Beta topology. Higher signal-to-noise ratios in XRD patterns measured for Sn-Beta-F samples reflect larger crystallite sizes than Sn-Beta-OH samples, as previously noted for Sn-Beta [56] and Ti-Beta [57]. Absorption edge energies, estimated from Tauc plots of diffuse reflectance UV-visible spectra measured after dehydration of Sn-Beta-F and Sn-Beta-OH samples (523 K, Figure 5.10 and 5.11, Supporting Information), are listed in Table 5.1 and are characteristic of isolated  $\text{Sn}^{4+}$  centers within zeolite frameworks ( $\geq 4.1 \text{ eV}$ ) on all samples [277]. The number of open Sn sites, closed Sn sites, and silanol groups (per g) are also listed in Table 5.1, as quantified from IR peak areas measured on Sn-Beta samples titrated with  $\text{CD}_3\text{CN}$  to saturation coverages (Figure 5.12, Supporting Information) and previously reported integrated molar extinction coefficients ( $E(2316 \text{ cm}^{-1}) = 1.04 \pm 0.22 \text{ cm } \mu\text{mol}^{-1}$ ,  $E(2308 \text{ cm}^{-1})$

$= 2.04 \pm 0.43 \text{ cm } \mu\text{mol}^{-1}$ ,  $E(2275 \text{ cm}^{-1}) = 0.74 \pm 0.16 \text{ cm } \mu\text{mol}^{-1}$ , respectively) [56]. Vapor-phase water adsorption isotherms (293 K, Figure 5.13, Supporting Information), water uptakes quantified at  $P/P_0 = 0.2$  (Table 5.1), and methanol adsorption isotherms (293 K, Figure 5.14, Supporting Information) on all Sn-Beta-F and Sn-Beta-OH samples [171] are consistent with previously reported data for hydrophobic and hydrophilic Beta zeolites [56]. Taken together, the bulk properties of all Sn-Beta-F and Sn-Beta-OH samples studied here are characteristic of the hydrophobic and hydrophilic Sn-Beta samples reported in our prior work [56, 151, 173].

Figure 5.1A shows measured first-order glucose-fructose isomerization rate constants for Sn-Beta-F-116, normalized by the number of open Sn sites quantified ex situ (Table 5.1), as a function of hot (373 K) water exposure time before the onset of reaction. First-order rate constants are higher (by  $\sim 2\times$ ) on samples exposed to water for short times (0–1 h, Figure 5.1A), but decrease monotonically with increasing water exposure time (6–24 h) and eventually become lower than rate constants measured on untreated samples. First-order isomerization rate constants on Sn-Beta-F-116 are measured from initial reaction time data; therefore, differences in such rate constants reflect activation phenomena that occur at short water exposure times and deactivation phenomena that occur at longer water exposure times, but prior to glucose isomerization catalysis in both cases. Similar activation phenomena have been observed for glucose-fructose isomerization on Sn-Beta catalysts in methanol solvent in initial time-on-stream measurements (0–36 h, 383 K under continuous flow conditions) [117, 274].

Several additional hydrophobic Sn-Beta-F and hydrophilic Sn-Beta-OH samples of varying Sn content ( $\text{Si}/\text{Sn} = 80\text{--}220$ ) were studied in an analogous manner to that used for Sn-Beta-F-116 in order to probe whether similar activation and deactivation phenomena were observed generally on samples of varying composition and synthetic provenance. Figure 5.1B shows measured first-order glucose isomerization rate constants for five hydrophobic Sn-Beta-F samples and three hydrophilic Sn-Beta-OH samples, normalized by the number of open Sn sites quantified ex situ on samples

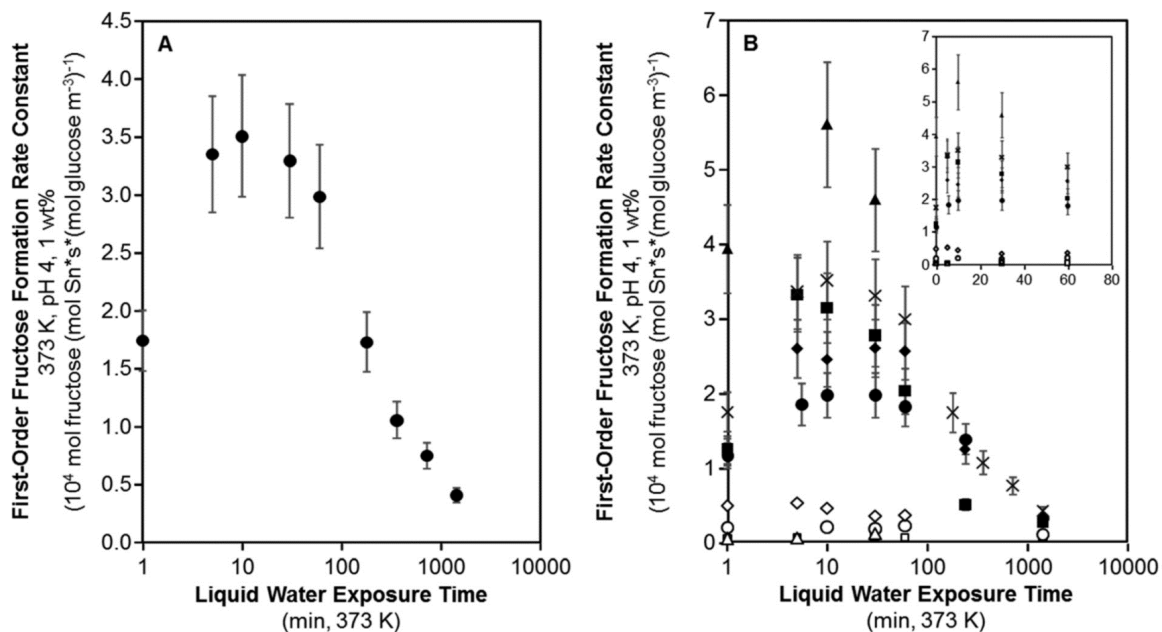


**Figure 5.1:** A) Measured first-order glucose isomerization rates (per open Sn, 373 K) on Sn-Beta-F-116 after liquid water exposure for various durations (0–24 h, 373 K). B) Measured first-order glucose isomerization rates (per open Sn, 373 K) on Sn-Beta-F-100 (■), Sn-Beta-F-110 (◆), Sn-Beta-F-116 (×), Sn-Beta-F-172 (▲), Sn-Beta-F-220 (●), Sn-Beta-OH-80 (○), Sn-Beta-OH-84 (△), and Sn-Beta-OH-94 (◇) after liquid water exposure for various durations (0–24 h, 373 K). The inset shows rate constants measured after short liquid water exposure times (0–1 h).

prior to hot water treatment (Table 5.1), as a function of water exposure time (373 K). Previously reported first-order rate constants vary (by  $\sim 3\times$  at 373 K, per Sn) among Sn-Beta-F samples ( $\text{Si/Sn} = 100\text{--}220$ ) [56], and decrease systematically with increasing Sn content among Sn-Beta-OH samples prepared by post-synthetic grafting of Sn into a dealuminated Beta support [151]. Rates are similar (within  $\sim 3\times$ ) for Sn-Beta-F and for Sn-Beta-OH sample sets when normalized by the number of open Sn sites, and those for Sn-Beta-OH samples no longer depend systematically on Sn content [56]. Among the Sn-Beta-F and the Sn-Beta-OH samples studied here (four of which belong to a larger suite of samples we have studied previously [56]), first-order rate constants (373 K, per open Sn) vary within this factor of  $\sim 3\times$ , which is reasonable agreement considering that there may be residual heterogeneities among the

distribution of reactive environments within these samples, such as that provided by differences in the relative position of silanol groups to open Sn sites. This  $\sim 3\times$  variation of first-order rate constants has also been observed on hydrophobic Ti-Beta-F and hydrophilic Ti-Beta-OH zeolites [57].

**Table 5.1:** Characterization data on Sn-Beta-F and Sn-Beta-OH zeolites

Sample	$V_{\text{ads}}^{\text{a}}$ ( $\text{N}_2$ , 77 K) ( $\text{cm}^3 \text{g}^{-1}$ )	Edge energy <sup>b</sup> (eV)	Open Sn density <sup>c</sup> ( $10^5 \text{ mol Sn}_{\text{LA}} \text{g}^{-1}$ )	Closed Sn density <sup>c</sup> ( $10^5 \text{ mol Sn}_{\text{LA}} \text{g}^{-1}$ )	Silanol density <sup>c</sup> ( $10^5 \text{ mol Sn}_{\text{LA}} \text{g}^{-1}$ )	$V_{\text{ads}}^{\text{d}}$ ( $\text{H}_2\text{O}$ , 293 K) ( $10^3 \text{ cm}^3 \text{g}^{-1}$ , $\text{P}/\text{P}_0 = 0.2$ )
Sn-Beta-F-100	0.24	4.1	2.09	5.97	5.88	6.9
Sn-Beta-F-172	0.21	4.2	1.86	6.36	9.81	7.3
Sn-Beta-F-220	0.22	4.3	2.48	4.44	10.3	5
Sn-Beta-F-116	0.23	4.3	5.09	9.11	12.29	10.5
Sn-Beta-F-110	0.23	4.3	5.14	9.83	9.3	9.5
Sn-Beta-OH-80	0.24	5.5	8.48	11.92	90.9	84.4
Sn-Beta-OH-94	0.17	5.5	10.79	9.07	14.5	23.4
Sn-Beta-OH-84	0.22	5.5	4.62	18.69	73.7	94.6

<sup>a</sup> $\text{N}_2$  volumes at the end of micropore filling transition (77 K). <sup>b</sup>Determined from Tauc plots after dehydration (523 K).

<sup>c</sup>Lewis acidic Sn densities and silanol densities measured from  $\text{CD}_3\text{CN}$  titration IR experiments.

<sup>d</sup>Water uptake at  $\text{P}/\text{P}_0 = 0.2$  (293 K).

**Table 5.2:** First-order glucose-fructose isomerization rate constants (373 K) and extents of activation after exposure to hot (373 K) water exposure or NMe<sub>4</sub>OH treatment

Sample	First-order isomerization rate constant, 0 h water exposure ( $10^{-4}$ mol (mol glucose per m <sup>3</sup> ) <sup>-1</sup> (mol open Sn) <sup>-1</sup> s <sup>-1</sup> )	Extent of activation ( $\chi_{act}$ )	Water exposing time corresponding to maximum rate (h)	First-order isomerization rate constant, 24 h water exposure ( $10^{-4}$ mol (mol glucose per m <sup>3</sup> ) <sup>-1</sup> (mol open Sn) <sup>-1</sup> s <sup>-1</sup> )
Sn-Beta-F-100	1.24	2.7	0.083	0.27
Sn-Beta-F-172	1.21	2.1	0.083	0.25
Sn-Beta-F-220	1.16	1.8	0.17	0.32
Sn-Beta-F-116	1.74	2	0.17	0.41
Sn-Beta-F-110	3.93	1.4	0.17	0.42
<i>Avg. Sn-Beta-F</i>	1.86	2		0.33
Sn-Beta-OH-80	0.19	1.1	0.17	0.09
Sn-Beta-OH-94	0.48	1.1	0.083	n.m. <sup>a</sup>
Sn-Beta-OH-84	0.04	1.4	8.8	0.14
<i>Avg. Sn-Beta-OH</i>	0.24	1.2		0.12
Sn-Beta-F-100 <sup>b</sup>	1.52	2.9		n.m. <sup>a</sup>

<sup>a</sup>n.m.: not measured <sup>b</sup>after NMe<sub>4</sub>OH Treatment

First-order rate constants (373 K, per open Sn) collected on Sn-Beta samples prior to hot water exposure were systematically higher by  $\sim 8\times$  on Sn-Beta-F than on Sn-Beta-OH samples reported here (Table 5.2), similar to the differences (15–50 $\times$ ) in initial rates reported previously [56, 151]. Activation phenomena at short water exposure times and deactivation phenomena at long water exposure times were observed on each of the five Sn-Beta-F samples studied. In contrast, none of the three Sn-Beta-OH samples showed significant activation ( $>25\%$  increase) at short water exposure times (Table 5.2), and all samples showed minimal deactivation ( $>25\%$  decrease) after 24 h of water exposure at 373 K, reflected in rate constants that were similar regardless of water exposure time (Figure 5.1B).

These findings indicate that activation and deactivation upon water exposure (373 K) prior to reaction are general phenomena characteristic of Sn-Beta-F samples, but not Sn-Beta-OH samples. The extent of activation ( $\chi_{\text{act}}$ ), defined as the ratio of the highest isomerization rate constant measured after water exposure (typically 0.08–0.5 h at 373 K) to that on the untreated sample (Table 5.2), varied by 1.4–2.7 $\times$  among the five Sn-Beta-F samples studied, indicating that the changes responsible for catalyst activation occur to different extents on each Sn-Beta-F sample. The increased turnover rates measured in the activation period on each sample are reproducible and outside of the experimental uncertainty for turnover rate measurements on a given sample (within 15%, not subject to sources of uncertainty from sample-to-sample variability responsible for  $\sim 3\times$  differences in rate constants between samples, details in Section 5.6.2, Supporting Information). Sn-Beta-F samples deactivate and show similar isomerization rate constants (within  $\sim 1.5\times$ ) after 24 h of water exposure time. This deactivation behavior does not reflect the degradation of bulk crystalline structural properties, evident in similar powder XRD patterns, micropore volume measurements, and SEM images before and after water exposure at 373 K (Figure 5.15–5.17, Supporting Information).

The preservation of long-range crystalline structure after water treatment times corresponding to activation and deactivation phenomena suggests that hot (373 K)

water exposure influences the local structure of active Sn sites or of their surrounding microporous environments in the case of Sn-Beta-F, but not in the case of Sn-Beta-OH. Dissociative adsorption of water at closed Sn sites ( $\text{Sn}-(\text{OSi})_4$ ) facilitates interconversion of framework Sn between hydrolyzed-open ( $(\text{HO})-\text{Sn}(\text{OSi})_3 + \text{Si}-\text{OH}$ ) and closed configurations as detected experimentally by  $^{119}\text{Sn}$  NMR spectra through changes in Sn coordination from tetrahedral (-420 to -440 ppm) to octahedral (-690 to -720 ppm) upon water adsorption and hydrolysis of Sn-O-Si linkages [114,155], and computationally using density functional theory (DFT) calculations (BEEF-vdW) of water dissociation reactions at closed Sn sites that access both open and closed configurations via quasi-equilibrated steps during ethanol dehydration catalysis (404 K, 0.1–50 kPa  $\text{H}_2\text{O}$ ) [180]. Such changes to Sn structure in the presence of water would influence measured rate constants, given that open Sn sites are dominant active sites for glucose–fructose isomerization [56,68,106]. Dissociative adsorption of water has also been reported to facilitate cleavage of framework siloxane bonds to form silanol defects in neutral or basic solutions [66,278], which could also influence measured rate constants given that hydrophilic confining environments increase apparent activation Gibbs free energies compared to their hydrophobic analogs (Sn-Beta [56], Ti-Beta [53,57]). Given that the number and coordination of framework Lewis acidic Sn sites and residual silanol defects are two structural features that influence glucose–fructose isomerization rate constants in Sn-Beta, we next probe changes in these two properties of Sn-Beta zeolites in response to hot liquid water exposure to determine more precisely the mechanisms underlying the activation and deactivation phenomena observed on Sn-Beta-F samples.

### 5.3.2 Characterization of Sn sites in Sn-Beta as a function of water exposure

The evolution of the number and structure of Sn sites was studied by exposing Sn-Beta-F-116, a representative Sn-Beta-F sample, to hot water (373 K) for various times followed by characterization of the bulk structure and surface sites on the recovered solids. The bulk Sn content determined from elemental analysis does not

vary systematically with water exposure time and is identical (within error) after 24 h of hot water exposure (Figure 5.18A, Supporting Information). This indicates that Sn leaching from the framework into solution is negligible, which is consistent with prior elemental analysis characterization using energy-dispersive X-ray analysis (SEM-EDX) of Sn-Beta after 150 h of continuous aqueous-flow exposure (413 K) [117], and inductively coupled plasma optical emission spectroscopy (ICP-OES) of Sn-Beta after 50 h of continuous aqueous-flow exposure (373 K) [116, 275, 279].

The potential hydrolysis of framework Sn species to form extraframework  $\text{SnO}_x$  domains, which are essentially unreactive for glucose isomerization catalysis in acidic ( $\text{pH} = 4$ ) aqueous solution [153], was probed by measuring IR spectra upon  $\text{CD}_3\text{CN}$  titration of water-treated Sn-Beta-F-116. Adsorption of  $\text{CD}_3\text{CN}$  onto Sn-Beta zeolites results in IR spectra similar to those collected on untreated materials (Figure 5.12, Supporting Information) and contain  $\nu(\text{C}\equiv\text{N})$  peaks centered at 2316, 2308, 2287, and 2275  $\text{cm}^{-1}$ . The  $\nu(\text{C}\equiv\text{N})$  stretching frequency centered at 2287  $\text{cm}^{-1}$  has been assigned to  $\text{CD}_3\text{CN}$  bound to undercoordinated Sn sites located in surfaces of  $\text{SnO}_x$  domains [56, 188], and the  $\nu(\text{C}\equiv\text{N})$  stretching frequencies centered at 2316 and 2308  $\text{cm}^{-1}$  have been assigned to  $\text{CD}_3\text{CN}$  bound to open and closed framework Lewis acid sites [102, 153]. The fractions of Sn present as Lewis acid sites, defined as the sum of open and closed Lewis acidic Sn sites ( $\text{Sn}_{\text{LA}}$ ), and as sites located in surfaces of extraframework  $\text{SnO}_x$  domains ( $\text{Sn}_{\text{EX}}$ ) on Sn-Beta-F-116 as a function of hot water (373 K) exposure time are shown in Figure 5.18 (Supporting Information). Neither  $\text{Sn}_{\text{LA}}$  nor  $\text{Sn}_{\text{EX}}$  varies outside of experimental error or in a systematic manner with increasing hot water exposure time. This observation suggests either that the distribution of Sn within framework locations and in extraframework  $\text{SnO}_x$  domains does not change significantly upon hot water exposure, or that it reverts to a common distribution upon exposure to vacuum (673 K) during the ex situ conditions of the IR measurements. The formation of  $\text{Sn}_{\text{EX}}$  domains upon hot water exposure was further investigated by estimating Sn edge energies determined from Tauc plots (Figure 5.19, Supporting Information) derived from UV-vis spectra measured on dehydrated

samples (523 K, Figure 5.20, Supporting Information) recovered after hot water treatment. Edge energies vary between 3.7 and 4.3 eV regardless of hot water exposure time (edge energies  $>4.1$  eV indicate predominantly isolated framework  $\text{Sn}^{4+}$ ) [280]. On all samples, UV-vis spectra show bands centered around 200–230 nm that do not vary in position with extended water exposure, yet new bands appear at higher wavelengths (340–500 nm) upon hot water exposure (373 K,  $>3$  h), reflecting the formation of some  $\text{Sn}_{\text{EX}}$  domains. Such domains are expected to be small ( $<3$  nm) as peaks for  $\text{SnO}_x$  phases were not observed in powder XRD patterns of samples after extended hot water exposure (Figure 5.15, Supporting Information).

As in the case of the total Lewis acidic Sn density on Sn-Beta-F-116, which does not change upon extended hot (373 K) water exposure, the relative density of open and closed Sn sites (per  $\text{Sn}_{\text{LA}}$ ) also does not change systematically with increasing duration of water exposure (Figure 5.21). This observation is consistent with structural changes in framework Sn coordination, which can occur upon water adsorption at ambient conditions [155] or in situ (404 K, 0.1–50 kPa  $\text{H}_2\text{O}$ , 0.5–35 kPa  $\text{C}_2\text{H}_5\text{OH}$ ) upon hydrolysis of closed Sn sites to form open Sn sites [180, 227], and are reversible upon exposure to the vacuum treatments (823 K) prior to  $\text{CD}_3\text{CN}$  titration. Open and closed Sn site distributions are equilibrated in DFT-based microkinetic modeling simulations of gas-phase ethanol dehydration catalysis that include the free energy barriers for water dissociation reactions at closed Sn sites in Sn-Beta zeolites (404 K, 0.5–35 kPa  $\text{C}_2\text{H}_5\text{OH}$ , 0.1–50 kPa  $\text{H}_2\text{O}$ ) [180]. Therefore, it is likely that an equilibrated distribution of open and closed Sn sites on each Sn-Beta sample is formed in situ, and reverts to a distribution that is different for each Sn-Beta sample upon ex situ vacuum exposure.

The possibility that extraneous anionic ligands at Sn sites, which may interfere with  $\text{CD}_3\text{CN}$  adsorption at such sites and thus with Sn site quantification from IR spectra of Sn-Beta saturated with  $\text{CD}_3\text{CN}$ , was probed by characterizing residual fluoride anions that remain on Sn-Beta-F after the oxidative treatments used to remove organic structure directing agents that are present after hydrothermal synthesis [242].

Fluoride anions are preferentially located within double four membered ring building units, as observed on siliceous zeolites by  $^{19}\text{F}$  MAS NMR ( $-38.5$  ppm), and are covalently bonded to framework tetrahedral atoms [238]. Figure 5.2 shows solid-state  $^{19}\text{F}$  NMR spectra (normalized by sample mass for comparison) collected on Sn-Beta-F-100 and Sn-Beta-F-220 prior to water exposure and after 0.5 h of water exposure at 373 K.

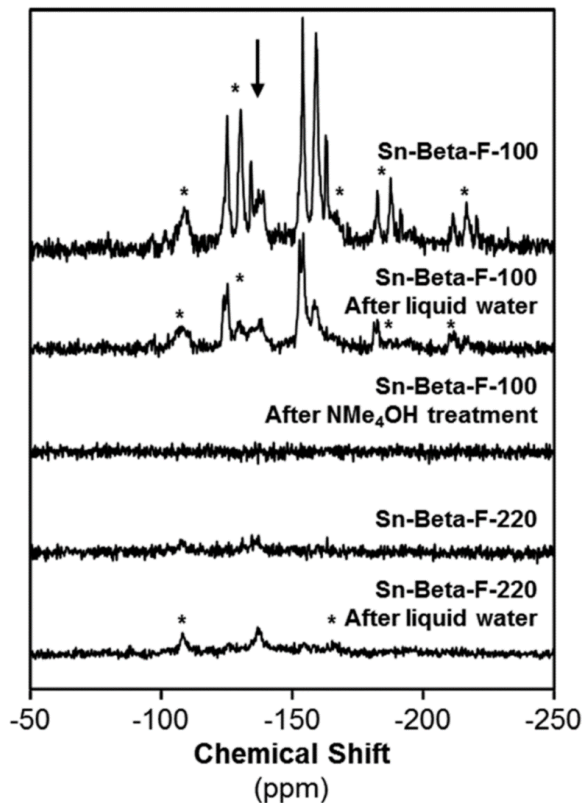


**Figure 5.2:**  $^{19}\text{F}$  NMR spectra collected on Sn-Beta-F samples before liquid water exposure, after liquid water exposure, and after  $\text{NMe}_4\text{OH}$  treatment. The resonance centered at  $-135$  ppm is marked with an arrow (\* denotes spinning sidebands).

A substantial amount of residual F is present in Sn-Beta-F-100, as indicated by resonances between  $-135$  and  $-160$  ppm and their spinning sidebands, which have previously been assigned to fluorine bound to hydrated and dehydrated Lewis acidic Sn sites, respectively [242]. A lower amount of residual F is present on Sn-Beta-F-220 despite the identical hydrofluoric acid content used in the hydrothermal synthesis

of both Sn-Beta-F-220 and Sn-Beta-F-100. After exposure of Sn-Beta-F-100 to hot water for 0.5 h,  $^{19}\text{F}$  resonances remain centered at identical chemical shifts (Figure 5.2) but decrease in intensity (by  $\sim 2\times$ ), reflecting partial defluorination of the solid. Open and closed Sn site densities (per  $\text{Sn}_{\text{LA}}$ ) on Sn-Beta-F-100, however, did not change significantly after partial defluorination, suggesting that the presence of residual fluoride did not interfere with the quantification of Lewis acid sites using  $\text{CD}_3\text{CN}$  IR and that the presence of distinct IR peaks centered at  $2316\text{ cm}^{-1}$  and  $2308\text{ cm}^{-1}$  for  $\text{CD}_3\text{CN}$ -saturated Sn-Beta-F samples likely do not reflect any influence of  $\text{F}^-$  anions on framework Sn sites. This hypothesis was tested further by treating Sn-Beta-F-100 with aqueous  $\text{NMe}_4\text{OH}$ , which has been previously observed to remove all occluded fluorine from hydrophobic Ti-Beta-F zeolites [240]. The NMR spectrum collected on Sn-Beta-F-100 after  $\text{NMe}_4\text{OH}$  treatment (Figure 5.2) shows no  $^{19}\text{F}$  resonances, indicating removal of occluded fluorine without disruption of bulk crystalline properties or Sn site densities (additional details including XRD, UV-vis, and  $\text{CD}_3\text{CN}$  IR in Section 5.6.4, Supporting Information). The extent of activation observed on Sn-Beta-F-100 after  $\text{NMe}_4\text{OH}$  treatment does not change upon F removal (Table 5.2), and a similar  $\chi_{\text{act}}$  value ( $2.9\times$ , Table 5.2) is measured on Sn-Beta-F-220 despite the presence of residual amounts of F before and after water treatment. These findings indicate that the residual F content on a given Sn-Beta-F sample is not related to the activation phenomena observed upon hot (373 K) water treatment.

In summary, these data indicate that Sn site speciation is not significantly affected by hot (373 K) water exposure time. Open and closed Sn densities, and total Lewis acidic Sn densities, remain essentially constant with increasing water exposure time (0–24 h), although  $\text{Sn}_{\text{EX}}$  domains are observable in UV-visible spectra and residual  $\text{F}^-$  anions are removed from the samples into solution. Collectively, this evidence does not suggest that there are significant changes in Sn speciation and location upon extended hot (373 K) water exposure. We next characterize changes in surface polarity as a function of extended hot water exposure by quantifying silanol defect densities.

### 5.3.3 Characterization of silanol densities in Sn-Beta as a function of water exposure duration

Figure 5.3 shows silanol defect densities quantified from gas-phase  $\text{CD}_3\text{CN}$  titration measured on Sn-Beta-F-116 and Sn-Beta-F-220 as a function of hot water exposure time. Silanol densities increase by  $\sim 2.5\times$  and  $\sim 7.5\times$  on Sn-Beta-F-220 and

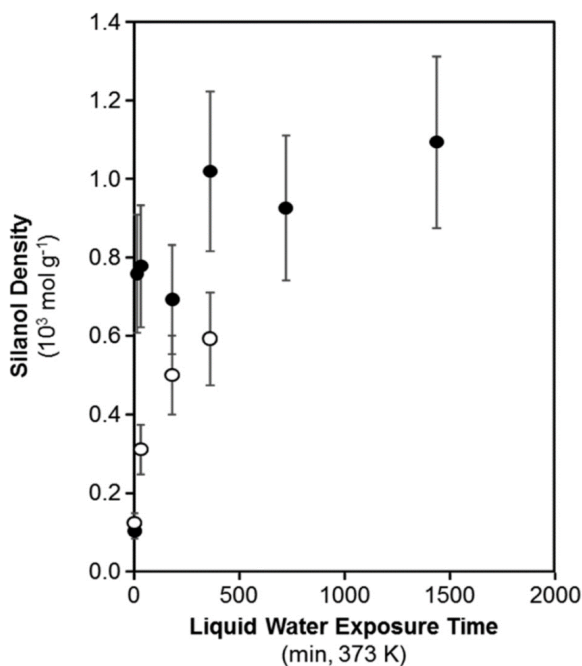


**Figure 5.3:** Silanol densities (per gram zeolite) on Sn-Beta-F-116 (●) and Sn-Beta-F-220 (○) as a function of liquid water exposure time.

Sn-Beta-F-116 even after short water exposure times (0.08–0.5 h, Table 5.1), and continue to increase with longer durations of water exposure. These findings are consistent with qualitative increases in silanol density that are reflected in higher areas for IR peaks centered at  $3740 \text{ cm}^{-1}$ , as previously observed on Sn-Beta zeolites after exposure to aqueous-phase glucose isomerization conditions (373 K) for 6 h [275]. Figure 5.4 shows  $^{29}\text{Si}$  MAS NMR spectra of Sn-Beta-F-100 and  $^{29}\text{Si}$  MAS and CP-MAS NMR spectra of Sn-Beta-F-100 before and after 0.5 h of hot water exposure where the majority of the signal ranges between -109 and -119 ppm, representing  $\text{Q}^4$  silicon sites whose assignments are consistent with  $^{29}\text{Si}$  NMR resonances reported for

pure silica Beta zeolites [281]. After water exposure,  $^{29}\text{Si}$  MAS NMR shows a  $\sim 2.8\times$

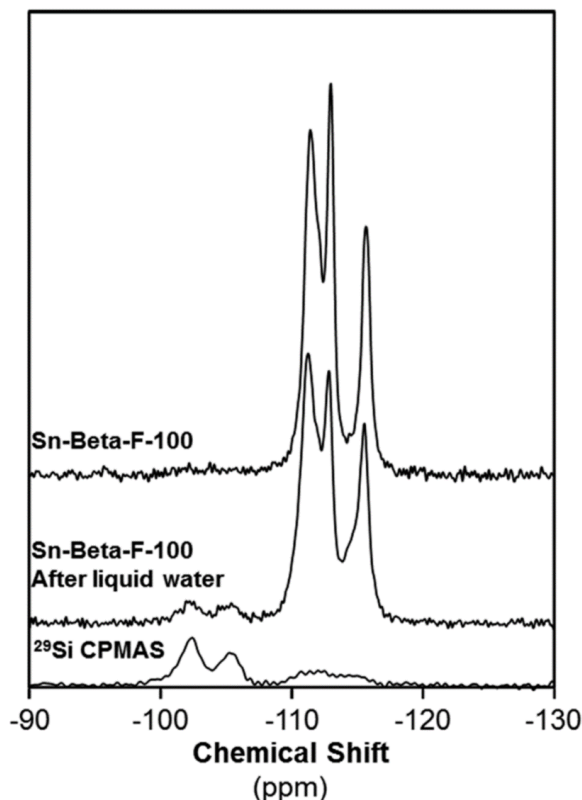


**Figure 5.4:**  $^{29}\text{Si}$  MAS NMR spectra of Sn-Beta-F-100 before liquid water exposure and after 0.5 h of liquid water exposure, and  $^{29}\text{Si}$  CPMAS NMR (contact time of 2 ms) after water exposure.

increase (relative to  $\text{Q}^4$  Si resonance areas) in the areas of  $\text{Q}^3$  Si resonances centered at -102.3 and -105.5 ppm for Si-OH groups, and their presence was further confirmed by  $^{29}\text{Si}$  CPMAS NMR. We thus conclude that extended hot (373 K) water exposure leads to hydrolysis of siloxane linkages and increases the density of silanol defects on Sn-Beta-F samples.

The location of silanol defects within microporous environments can be characterized by vapor-phase methanol and water adsorption isotherms on Sn-Beta-F samples. Figure 5.5A shows methanol adsorption isotherms (293 K,  $P/P_0 = 0-0.3$ ) on Sn-Beta-F-116 as a function of extended hot water exposure time. Methanol adsorption isotherms show type V isotherm behavior on untreated Sn-Beta-F-116

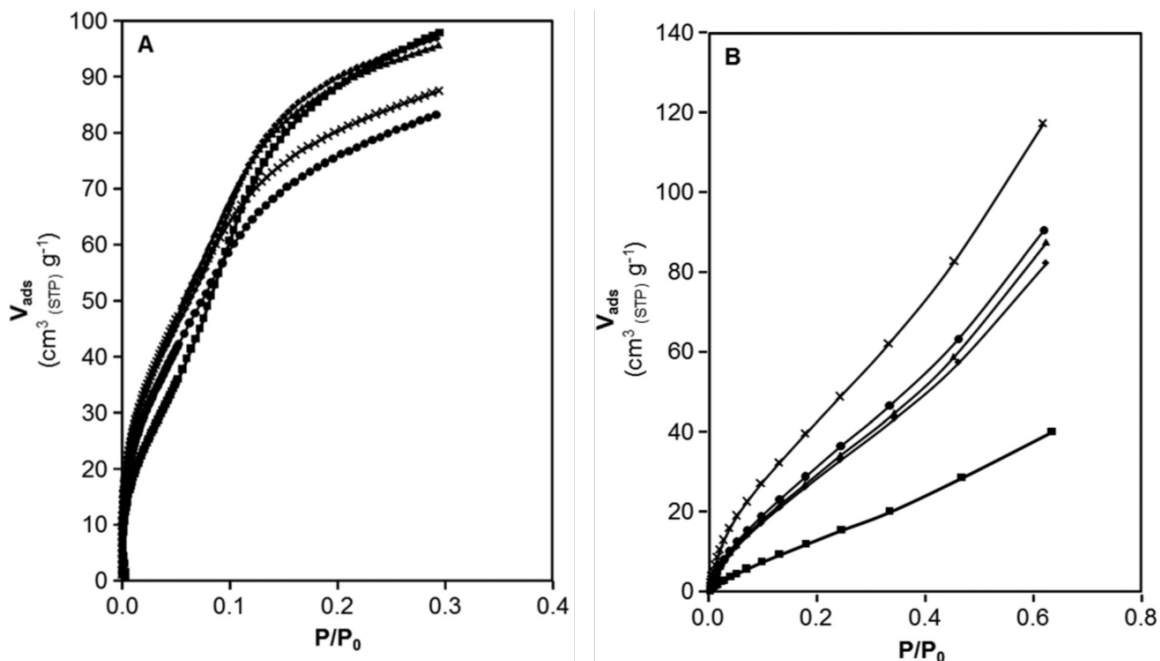


**Figure 5.5:** A) Vapor-phase methanol adsorption (293 K) isotherms collected on untreated Sn-Beta-F-116 (■) and on Sn-Beta-F-116 after 0.5 (◆), 3 (▲), 6 (×), and 24 (●) h of hot (373 K) liquid water exposure time. B) Vapor-phase water adsorption (293 K) isotherms collected on untreated Sn-Beta-F-116 (■) and on Sn-Beta-F-116 after 0.5 (◆), 3 (▲), 6 (×), and 24 (●) h of hot (373 K) liquid water exposure time.

and after short water exposure times (0–3 h), reflecting weak adsorbate–adsorbent interactions that dominate at low relative pressures ( $P/P_0 = 0\text{--}0.06$ ) followed by adsorbate–adsorbate hydrogen-bonding interactions that drive microporous condensation at higher pressures ( $P/P_0 = 0.1\text{--}0.3$ ). This adsorption behavior is consistent with previously reported methanol adsorption isotherms within hydrophobic Sn-Beta-F and Ti-Beta-F zeolites and reflects microporous environments comprising non-polar siloxane linkages incapable of hydrogen bonding with methanol molecules [56, 151, 173, 227]. As Sn-Beta-F-116 is exposed to hot water for longer times, vapor-phase methanol adsorption isotherms increasingly resemble type I isotherms in shape, reflecting strong adsorbate–adsorbent interactions that lead to micropore filling. On average, adsorbate–adsorbent interactions gradually strengthen with increasing hot water exposure time, as evidenced by increased methanol uptakes at low relative

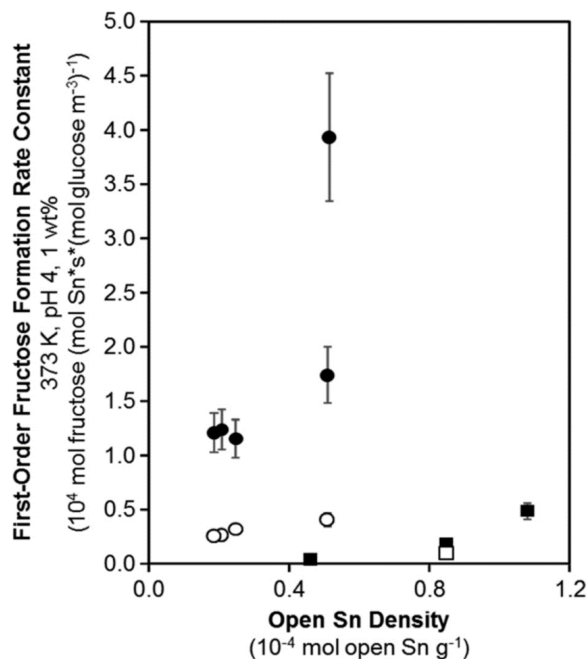
pressures ( $P/P_0 = 0-0.06$ ). Qualitatively, these isotherms gradually shift from type V to type I with increasing water treatment time, and concomitantly with a  $\sim 7.5\times$  increase in silanol defect density. The type I methanol isotherm behavior exhibited by samples exposed to extended hot water treatment (373 K,  $\geq 12$  h) reflects sufficient intraporous silanol densities to result in comparable methanol adsorption behavior to hydrophilic Sn-Beta-OH samples (Figure 5.14, Supporting Information).

Figure 5.5B shows vapor-phase water adsorption isotherms (293 K,  $P/P_0 = 0-0.3$ ) on Sn-Beta-F-116 with varying hot water exposure time. Vapor-phase water adsorption isotherms on Sn-Beta-F-116 prior to hot water exposure are characteristic of hydrophobic Beta zeolites and follow a type I isotherm, indicative of strong adsorbate-adsorbent interactions that result in water adsorption. These strong interactions reflect a combination of water adsorption onto Lewis acid sites and silanol groups. Water uptakes on Sn-Beta-F-116 ( $P/P_0 = 0-0.3$ ) increase monotonically with increasing hot water exposure time and concomitantly with increasing silanol density (Figure 5.24, Supporting Information), as observed previously on Sn-Beta [56] and Ti-Beta [57] samples. These isotherms increasingly resemble water adsorption isotherms collected on Sn-Beta-OH samples (Figure 5.13, Supporting Information), indicating that the initially hydrophobic micropores of Sn-Beta-F have become substantially hydrophilic because of intraporous silanol formation. Having identified and quantified changes to both Lewis acidic site densities and intraporous defect density with increasing water exposure, we next discuss the observed deactivation of Sn-Beta catalysts for aqueous-phase glucose isomerization in the context of site and structural changes to the zeolite samples.

#### 5.3.4 Origin of the aqueous-phase deactivation phenomena on hydrophobic Sn-Beta

Open Sn site densities remain unchanged upon exposure to hot water (Figure 5.21, Supporting Information), indicating that the observed deactivation cannot be ascribed to the loss of active sites. In contrast, intraporous silanol defects increase with water exposure time (Figure 5.3), and such sites can stabilize higher intraporous

water densities (Section 5.3.3). Our prior work has shown that extended solvent structures present under reaction conditions result in lower initial glucose–fructose isomerization rates on hydrophilic Ti-Beta-OH zeolites relative to hydrophobic Ti-Beta-F zeolites [57]. Figure 5.6 shows first-order fructose formation rate constants (per open Sn) on Sn-Beta-F and Sn-Beta-OH samples, both prior to hot water exposure and after 24 h of hot water exposure (373 K). First-order isomerization rate



**Figure 5.6:** Measured first-order glucose isomerization rate constants (373 K) on Sn-Beta-F samples prior to liquid water exposure (●), Sn-Beta-F samples after 24 h of liquid water exposure (○), Sn-Beta-OH samples prior to liquid water exposure (■), and Sn-Beta-OH samples after 24 h of liquid water exposure (□).

constants measured on untreated Sn-Beta-F samples are  $\sim 8\times$  higher than on Sn-Beta-OH samples, yet decrease after 24 h of hot water exposure to values identical to first-order rate constants measured on Sn-Beta-OH materials (within  $\sim 2\times$ , per open Sn).

Hydrophobic Sn-Beta-F materials stabilize significantly lower water densities than hydrophilic Sn-Beta-OH materials (Figure 5.13, Supporting Information), yet the formation of intraporous silanol groups when Sn-Beta-F materials are exposed to hot

liquid water (Figure 5.4) leads to increased intraporous water densities when equilibrated with vapor-phase water (Figure 5.5B) and, in turn, with liquid-phase water. Higher intraporous water densities and increased extents of hydrogen bonding in the co-adsorbed water network, which are measured in situ on Ti-Beta-OH relative to Ti-Beta-F using attenuated total reflectance IR (ATR-IR) and transmission IR spectroscopy [57], entropically destabilize the 1,2-hydrate shift transition states to increase apparent free energy barriers and lower glucose isomerization rates in turn [57]. These findings, extended to Sn-Beta, are consistent with the higher rate constants measured on untreated hydrophobic Sn-Beta-F zeolites than hydrophilic Sn-Beta-OH zeolites (Figure 5.1), and with the formation of additional intraporous silanol defects leading to increased co-adsorbed water densities in Sn-Beta-F and concomitant increases to apparent free energy barriers after extended hot water exposure time (373 K, ~24 h), until co-adsorbed water densities are sufficient to fully occupy microporous reaction environments, as in the case of untreated Sn-Beta-OH. After this point, additional silanol groups do not lead to further changes in co-adsorbed water content nor, in turn, to apparent free energy barriers for glucose–fructose isomerization. Therefore, the deactivation of Sn-Beta-F after extended hot water exposure reflects the formation of intraporous silanol defects to stabilize extended water structures under aqueous-phase reaction conditions and increase apparent free energy barriers for glucose isomerization.

Other proposed deactivation mechanisms for Sn-Beta materials during aqueous-phase oxygenate conversion include Sn leaching from the zeolite framework and the coking or fouling of Lewis acid sites by product or byproduct formation [116,275,279]. Framework Sn leaching, the formation of Sn<sub>EX</sub> species, and irreversible local structural changes to less reactive Sn species (i.e., closed Sn sites) are inconsistent with the data reported here using Sn elemental analysis and Lewis acid site densities quantified by CD<sub>3</sub>CN titrations (Figure 5.18 and 5.21) measured as a function of hot (373 K) water exposure time. Product inhibition of active sites, which would hinder the ability for glucose to adsorb and isomerize, is also negligible under the conditions studied here,

as the addition of small amounts of water (1–10 wt%, 383 K) during continuous flow minimizes the adsorption of other compounds onto Sn sites during glucose isomerization in methanol [274, 282]. Product inhibition also cannot explain the decrease in initial rate measurements because products are absent at initial reaction times. Thus, the findings reported here reveal another mechanism of deactivation reflecting structural changes to intraporous reaction environments, in addition to prior reports indicating that solvent or product inhibition is a deactivation mechanism observed during glucose isomerization in water (373 K) at higher conversions ( $\sim$ 20–50%) and in methanol at high temperatures (383–433 K) [275, 283]. We note that product inhibition may become more prominent at increased glucose concentrations that correspond to regimes in which glucose occupies larger fractions of microporous voids and becomes the most abundant surface intermediate on active sites, in contrast to the conditions studied here that correspond to dilute glucose concentrations that lead to water as the most abundant surface intermediate.

We conclude that the deactivation observed here on Sn-Beta-F under aqueous-phase glucose isomerization conditions is attributed to the conversion of hydrophobic siloxane linkages into hydrophilic silanol defects within microporous voids. These intraporous silanol groups stabilize higher water densities within reactive environments and increase apparent free energy barriers for glucose–fructose isomerization. The formation of silanol defects as the primary aqueous-phase deactivation mechanism would be consistent with the irreversible nature of Sn-Beta deactivation observed previously, despite oxidative treatments (823 K) used to attempt to regenerate these catalysts [117], which may be insufficient to condense silanol pairs. We surmise that higher temperature oxidative treatments ( $>873$  K) may be able to condense larger fractions of intraporous geminal silanol groups [284], potentially resulting in the recovery of more hydrophobic reaction environments and therefore higher initial isomerization rates after regeneration. Next, we discuss the activation phenomena observed at short hot water exposure times (0–3 h) to rationalize the site and surface changes responsible for increased aqueous-phase glucose isomerization rates.

### 5.3.5 Speculations on the origin of the activation phenomena on hydrophobic Sn-Beta

Figure 5.7A shows  $\chi_{\text{act}}$  values measured on all Sn-Beta catalysts as a function of initial silanol density measured on the untreated samples. Values of  $\chi_{\text{act}}$  appear to

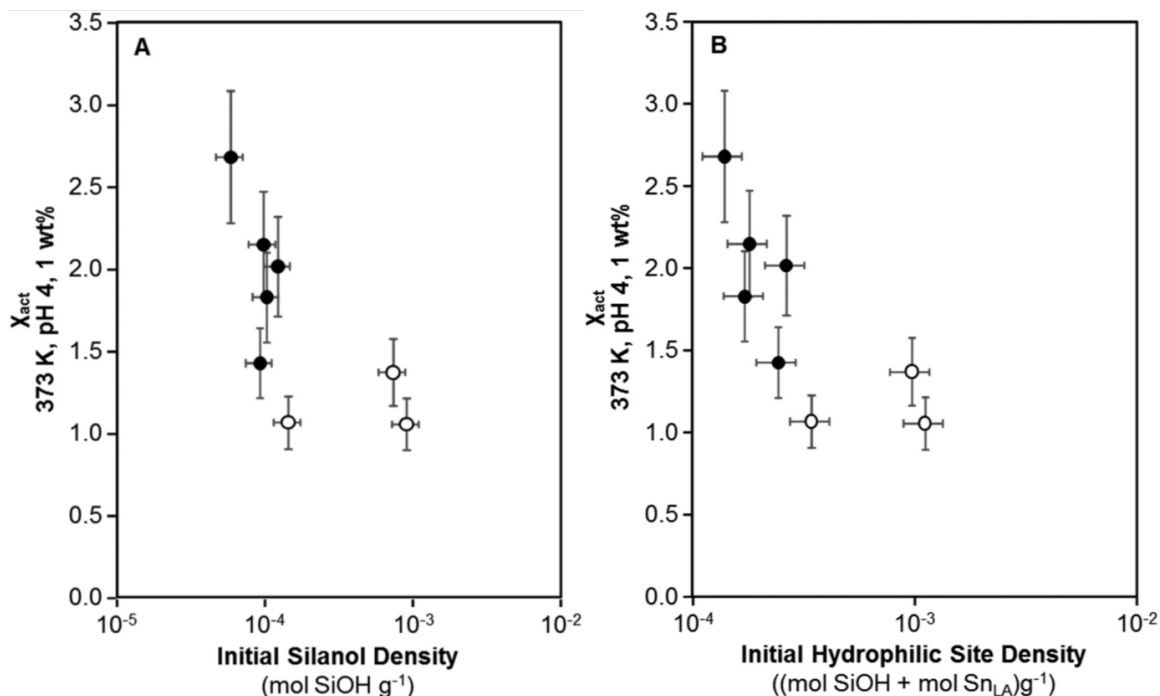


**Figure 5.7:** A) Observed activation extents (373 K, 1 wt%) as a function of initial silanol density on Sn-Beta-F (●) and Sn-Beta-OH (○) zeolites. B) Observed activation extents (373 K, 1 wt%) as a function of initial hydrophilic site density on Sn-Beta-F (●) and Sn-Beta-OH (○) zeolites. Hydrophilic sites represent the linear combination of silanol defects and Lewis acidic Sn centers on a given sample.

decrease systematically with increasing silanol density on Sn-Beta-F samples and are invariant with silanol density on Sn-Beta-OH materials. Further, activation phenomena are only observed on samples that initially contain low silanol densities ( $< 2 \times 10^{-4}$  mol silanol per g), after which higher silanol densities do not significantly impact measured  $\chi_{\text{act}}$  values. This implies that there is a critical density of silanol groups and co-adsorbed water beyond which activation phenomena are not observed under

the conditions studied here. We note that similar activation phenomena to that observed on Sn-Beta-F is also observed on hydrophobic Ti-Beta zeolites (Figure 5.25, Supporting Information), indicating that such activation is not dependent on heteroatom identity, and further suggesting that kinetic observations on Ti-Beta zeolites of varying defect density can be extended to Sn-Beta zeolites.

Water molecules within Ti-Beta zeolites have been reported to lower activation enthalpies by assisting in hydride transfer events [70], despite increasing activation entropies through the frustration of translational and rotational degrees of freedom. DFT-predicted apparent activation enthalpies and entropies both increase systematically with increasing co-adsorbed water density [57]. Given that the exact influences of water on enthalpic barriers are unclear from these literature reports, we surmise that the presence of water molecules or clusters near Lewis acid sites, in a density higher than initially present within low-defect Sn-Beta-F zeolites, results in enthalpy–entropy compromises that lower apparent activation free energies for glucose–fructose isomerization that lead to higher initial measured rates. Further increases of additional intraporous water molecules cause increases to free energy barriers because of entropic destabilization of the 1,2-hydride shift transition state, eventually resulting in lower fructose formation rates [57].

Direct quantification of intraporous water content during reaction (per  $\text{Sn}_{\text{LA}}$ ), and thus of the precise amount of water that minimizes free energy barriers and maximizes initial glucose isomerization rates, is convoluted by at least two factors. First, Lewis acidic Sn sites are capable of binding two water molecules that can stabilize small water clusters. The exact number of water molecules contained within second (or higher) solvation spheres through hydrogen-bonding networks will also depend on the proximity of other hydrophilic binding sites, such as silanol groups or framework Sn sites. Second, glucose adsorption into hydrophobic reaction environments entrains small quantities of water molecules from the solution-phase solvation sphere of glucose, as noted by increased water bending modes in in situ ATR-IR spectra at low glucose concentrations [57]. While these two factors cannot be quantitatively

accounted for with current experimental techniques, Figure 7B shows  $\chi_{\text{act}}$  values as a function of hydrophilic binding site density, which is defined as the sum of the silanol defect density and the Lewis acid site concentration on the untreated Sn-Beta material. Values of  $\chi_{\text{act}}$  decrease systematically with increasing hydrophilic binding site density until approaching values near unity. Differences in the initial density of silanol groups, and their proximity to  $\text{Sn}_{\text{LA}}$  sites, may result in the  $\sim 3\times$  variation in initial isomerization rates on untreated Sn-Beta samples (Figure 5.1B), via differences in co-adsorbed water densities proximal to  $\text{Sn}_{\text{LA}}$  sites that become irrelevant as microporous voids are filled with water. These findings are consistent with continuous-flow glucose isomerization rates in methanol that increase and then deactivate more slowly when small concentrations of water are added to the reaction mixture [274].

We note that  $\chi_{\text{act}}$  values also correlate with ex situ open Sn density, closed Sn density, open-to-closed ratio, Lewis acid site density, and even with the density of  $\text{Sn}_{\text{EX}}$  domains (per Sn, Figure 5.16–5.30, Supporting Information). The correlation with  $\text{Sn}_{\text{EX}}$  density is notable because  $\text{Sn}_{\text{EX}}$  species catalyze glucose–fructose isomerization through a base-catalyzed enolate intermediate [153]; however, these domains are inactive under the conditions studied here, evident from isotopic tracer studies using glucose- $\text{D}_2$  reactants that show formation of only fructose- $\text{D}_1$  products (Figure 5.31, Supporting Information). Therefore, the activation and deactivation phenomena evident in the turnover rate changes caused by hot water exposure, and the free energy differences they reflect, are most likely caused by differences in intraporous water content during catalysis.

#### 5.4 Conclusions

The densities of hydrophilic surface groups and co-adsorbed water within microporous reaction environments influence catalytic turnover rates in aqueous media. The evolution in the number density of surface species, including framework Sn sites, extraframework Sn domains, and silanol defect groups, upon extended exposure to hot liquid water (373 K) were quantified using ex situ characterization techniques on

Sn-Beta materials. Silanol concentrations increased with increasing duration (0–24 h) of hot water exposure, leading to concomitant increases in vapor-phase water uptakes (293 K) and a transition in vapor-phase methanol adsorption behavior (293 K) from type V to type I isotherms, indicating that the silanol groups formed from exposure to hot water are located within microporous reaction environments and can stabilize extended water networks during relevant aqueous-phase reaction conditions.

The catalytic implications of increased intraporous silanol densities and the co-adsorbed water structures they stabilize were probed using aqueous-phase glucose–fructose isomerization on hydrophobic Sn-Beta-F samples, which undergo activation (0–1 h) and eventual deactivation (>3 h) upon extended hot (373 K) water exposure. These activation and deactivation phenomena on Sn-Beta-F zeolites correlated with silanol densities, with low water densities appearing to enthalpically stabilize kinetically-relevant hydride shift transition states and higher water densities forming hydrogen-bonded networks that entropically destabilize hydride shift transition states via crowding effects, consistent with previous reports on Ti-Beta zeolites [57]. Enthalpic stabilization of sugar isomerization transition states by molecular water appears reminiscent of the reaction mechanism that occurs on the D-xylose isomerase enzyme [267], which contains an active site pocket that expels bulk water structures from the reaction environment while retaining molecular water to assist in proton shuttling events for glucose ring-opening and hydride transfer steps [66, 267].

These findings provide guidance for catalyst design strategies to attenuate deactivation of Sn-Beta-F in liquid water by mitigating the formation of intraporous silanol defects. One strategy involves tailoring the solvent mixture to maintain high isomerization rates [44, 50, 51, 285], while mitigating intraporous silanol formation under reaction conditions, as in the case of methanol and water mixtures that maintain hydroxyl ligands on open Sn sites under glucose isomerization reaction conditions and minimize Sn-Beta deactivation [282]. A second strategy involves the modification of external crystallite surfaces using hydrophobic organosilanes, which hinders water diffusion into MFI micropores [286] and results in significant improvements to Beta

z eolite stability in hot water [66,270,272]. Overall, this study shows how combining quantitative ex situ characterization techniques and catalytic probe reactions, on a suite of zeolite samples containing Lewis acid active sites confined within hydrophobic or hydrophilic environments, can be used to understand the structural changes underlying the deactivation of Lewis acid zeolites in liquid water.

## 5.5 Acknowledgements

We acknowledge the financial support provided by the Purdue Process Safety and Assurance Center (P2SAC). We also thank Juan Carlos Vega-Vila for helpful technical discussions and comments on this manuscript. The NMR facility at the California Institute of Technology was supported by the National Science Foundation (NSF) under Grant Number 9724240 and partially supported by the MRSEC Program of the NSF under Award Number DMR-520565.

M. J. Cordon, J. N. Hall, J. W. Harris, J. S. Bates, S. Hwang and R. Gounder, *Catal. Sci. Technol.*, 2019, 9, 1654 - Reproduced by permission of The Royal Society of Chemistry.

## 5.6 Supporting Information

## 5.6.1 Bulk structural and Lewis acid site characterization of Sn-Beta zeolites

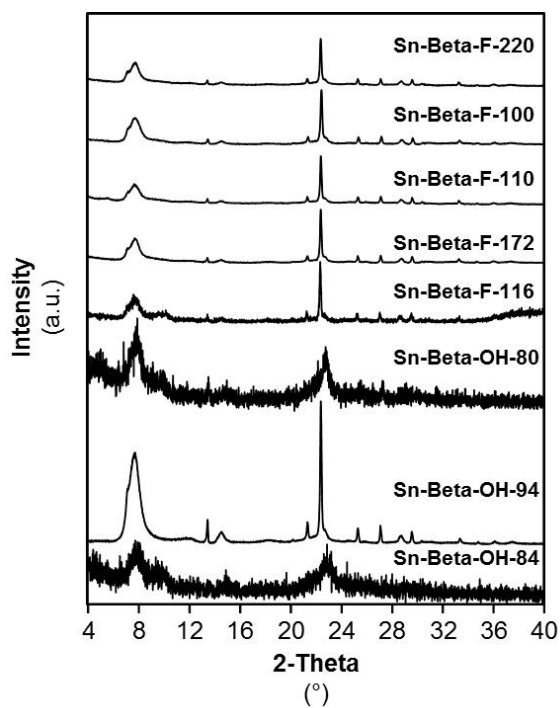


**Figure 5.8:** Powder XRD patterns of Sn-Beta samples studied in this work.

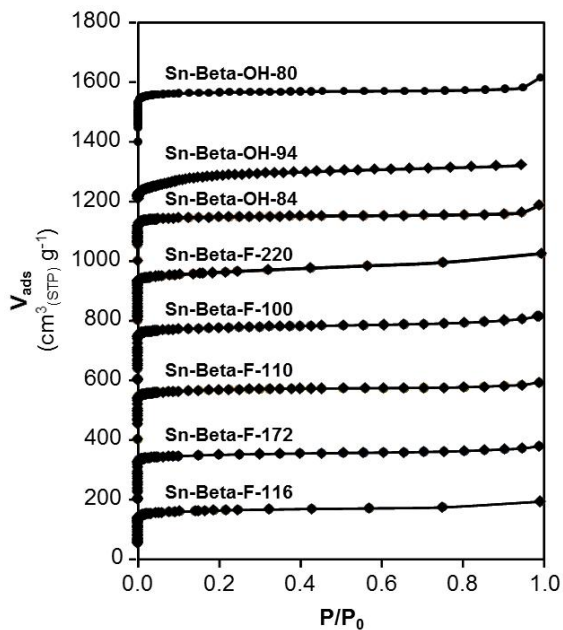


**Figure 5.9:**  $N_2$  adsorption isotherms (77 K) of Sn-Beta samples studied in this work. Isotherms are offset by  $200 \text{ cm}^3 \text{ g}^{-1}$  for clarity.

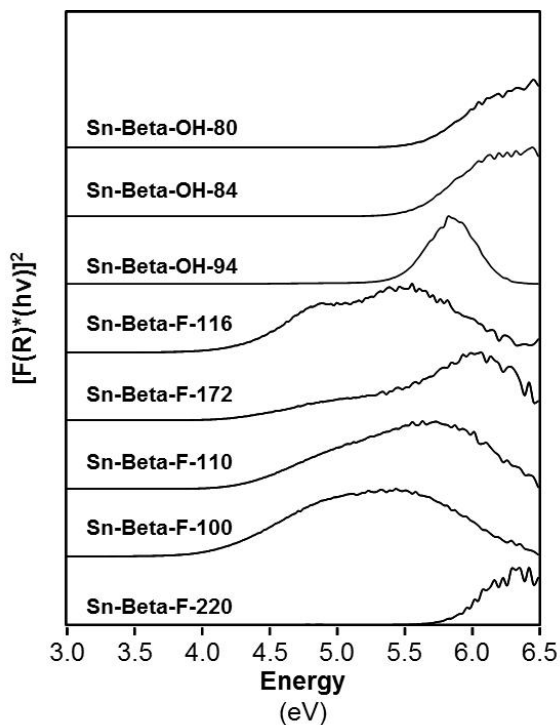


**Figure 5.10:** Tauc plots of Sn-Beta samples studied in this work after treatment in flowing He at 523 K for 1800 s. Edge energies are summarized in Table 5.1.

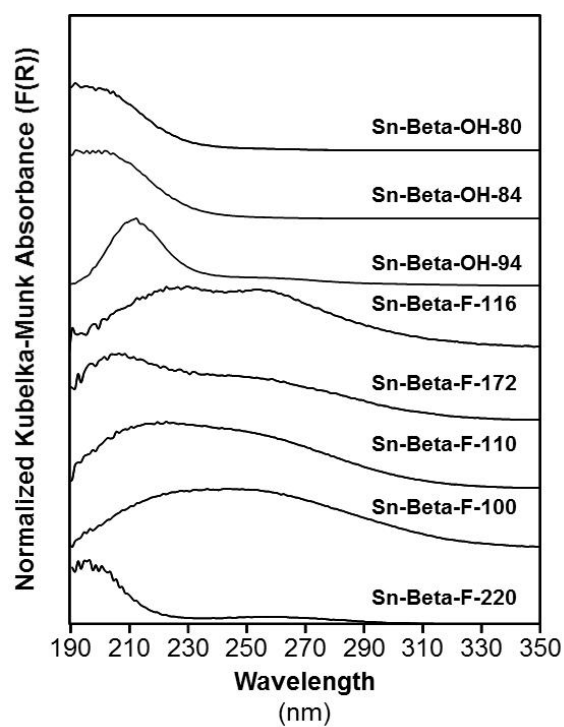


**Figure 5.11:** Dehydrated UV-Vis spectra (523 K, 1800 s) of Sn-Beta samples studied in this work.

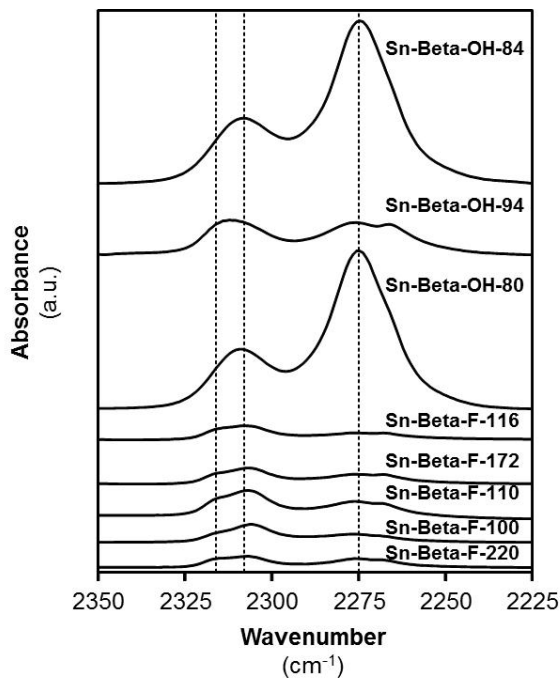


**Figure 5.12:** IR spectra collected on  $\text{CD}_3\text{CN}$ -saturated Sn-Beta samples studied in this work. Spectra were normalized by combination and overtone modes for Si-O—Si stretches prior to the subtraction of spectra collected before  $\text{CD}_3\text{CN}$  adsorption. Dashed lines are drawn at  $2308\text{ cm}^{-1}$  ( $\text{CD}_3\text{CN}$  bound to closed Sn),  $2316\text{ cm}^{-1}$  ( $\text{CD}_3\text{CN}$  bound to open Sn), and  $2275\text{ cm}^{-1}$  ( $\text{CD}_3\text{CN}$  bound to silanols).

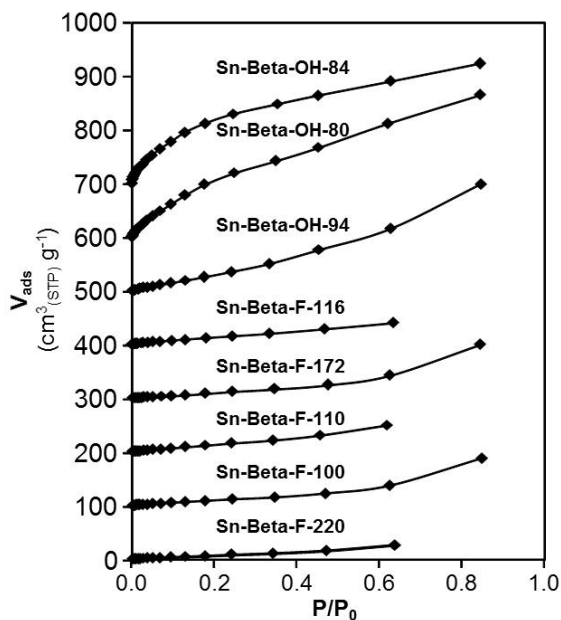


**Figure 5.13:** Vapor-phase water adsorption isotherms (293 K) on Sn-Beta samples studied in this work. Isotherms are offset by  $100 \text{ cm}^3 \text{ g}^{-1}$  for clarity.

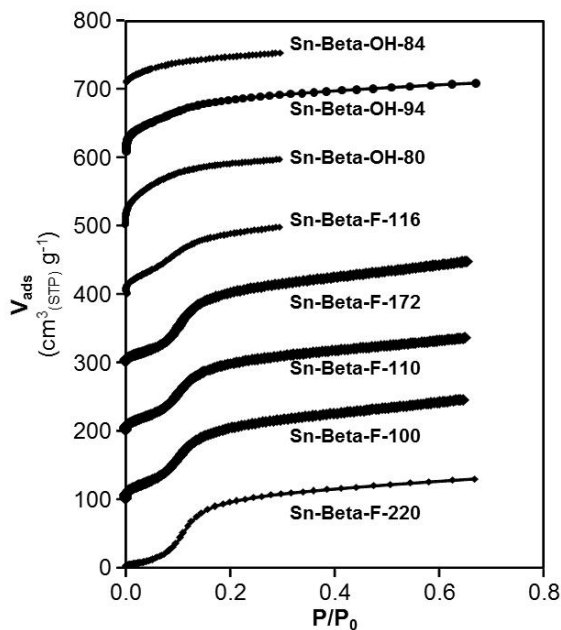
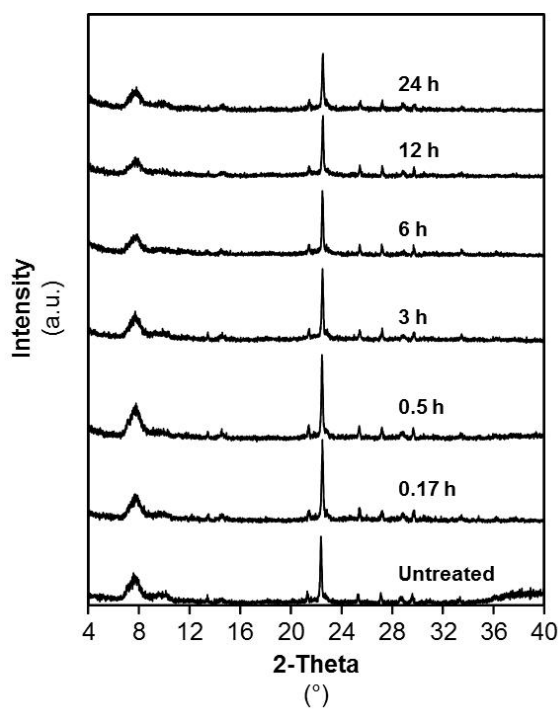


**Figure 5.14:** Vapor-phase methanol adsorption isotherms (293 K) on Sn-Beta samples studied in this work. Isotherms are offset by  $100 \text{ cm}^3 \text{ g}^{-1}$  for clarity.

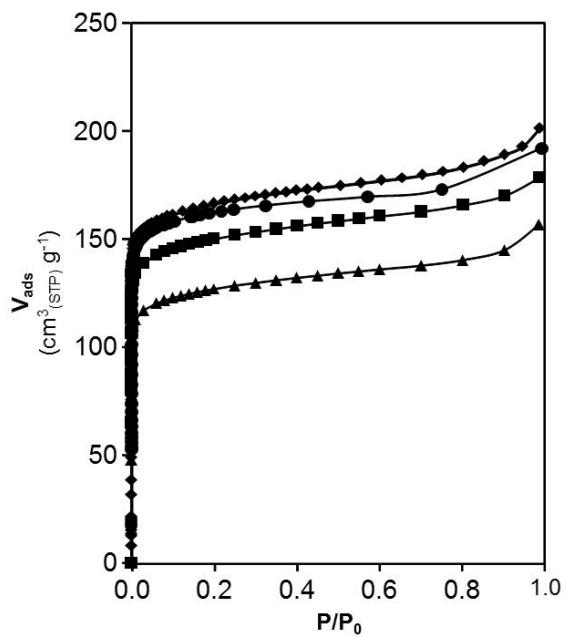
### 5.6.2 Rate constant and free energy measurements on Sn-Beta samples

Apparent first-order glucose-fructose isomerization rate constants (1-10 wt% glucose) measured on Sn-Beta samples free energy differences between 1,2-hydrate shift transition states and two water molecules bound to the Lewis acidic Sn site, the most abundant reactive intermediate (MARI) under aqueous-phase operating conditions [56]. The  $\sim 3$ x difference in first-order rate constants (normalized per open Sn site) reflect small free energy differences ( $\sim 3$  kJ mol<sup>-1</sup>) between the kinetically-relevant transition state and the reference state comprising two bound water ligands at the Sn site. Thus, activation and deactivation phenomena reflect free energy decreases and increases, respectively, which are distinct from the 3 kJ mol<sup>-1</sup> differences between individual samples.

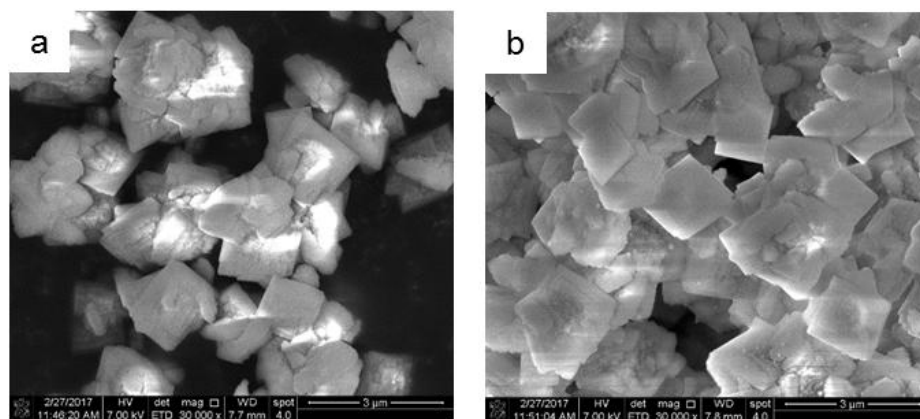
5.6.3 Bulk characterization of Sn-Beta-F-116 after controlled hot (373 K) water exposure



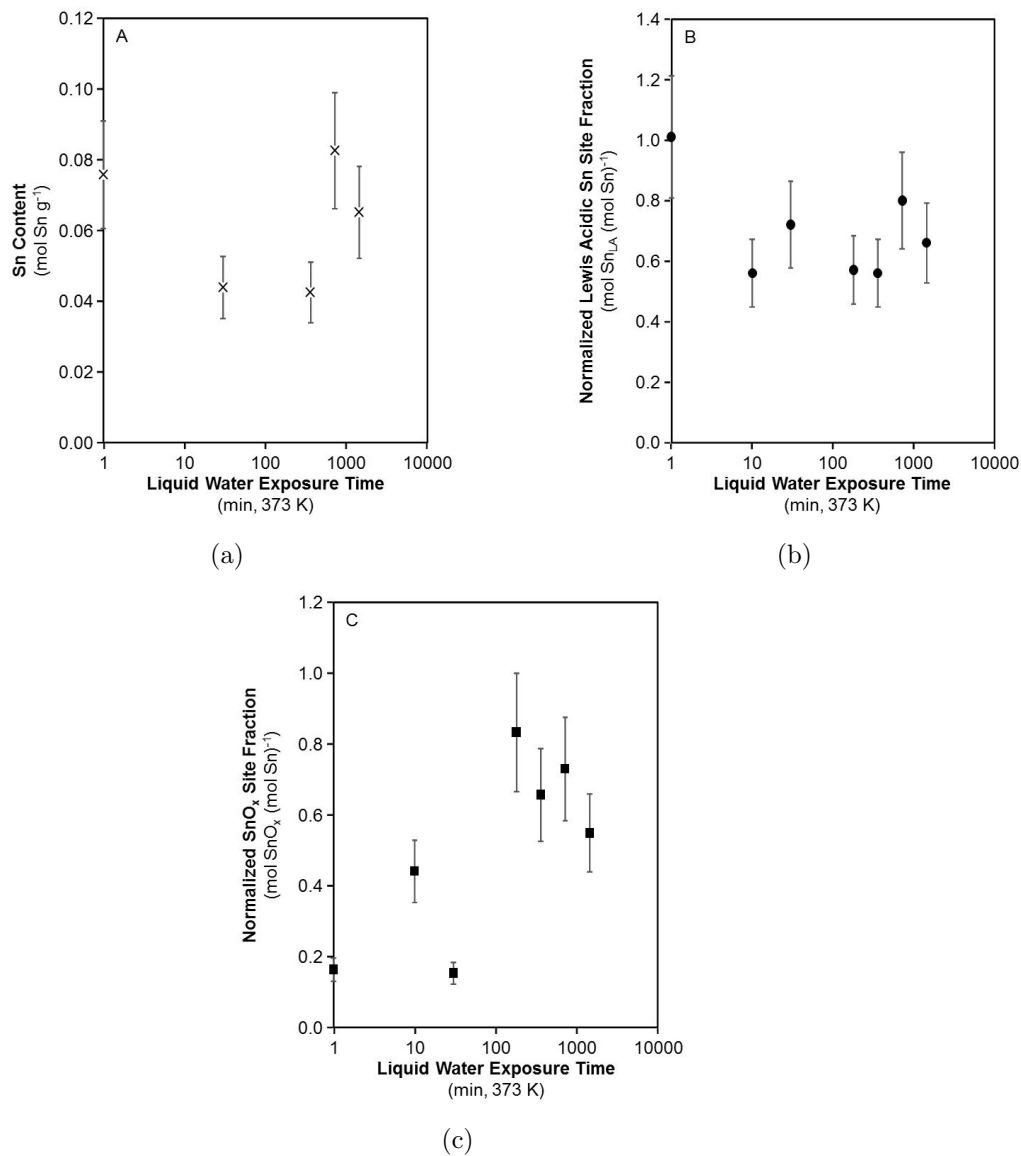
**Figure 5.15:** Powder XRD patterns of Sn-Beta-F-116 samples after various (0-24 h) amounts of hot (373 K) water exposure time.



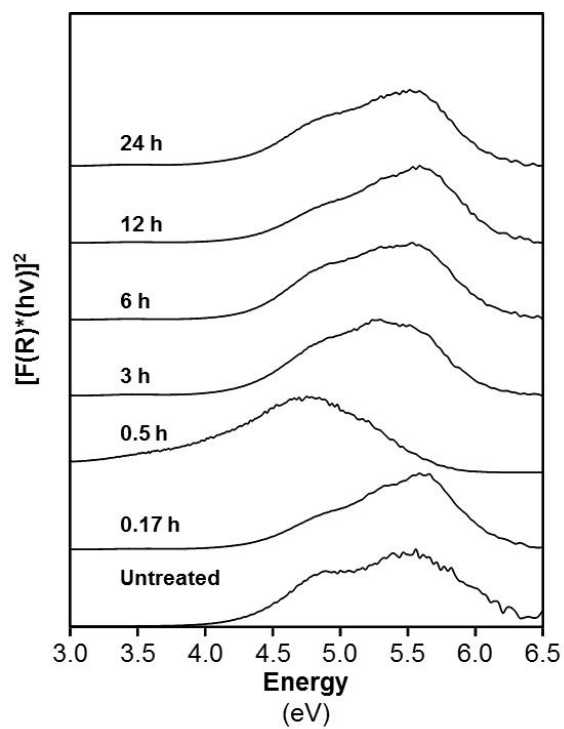
**Figure 5.16:**  $\text{N}_2$  adsorption isotherms (77 K) of Sn-Beta-F-116 after 0 (diamond), 0.5 (circle), 3 (square), and 24 h (triangle) of hot (373 K) water exposure time.



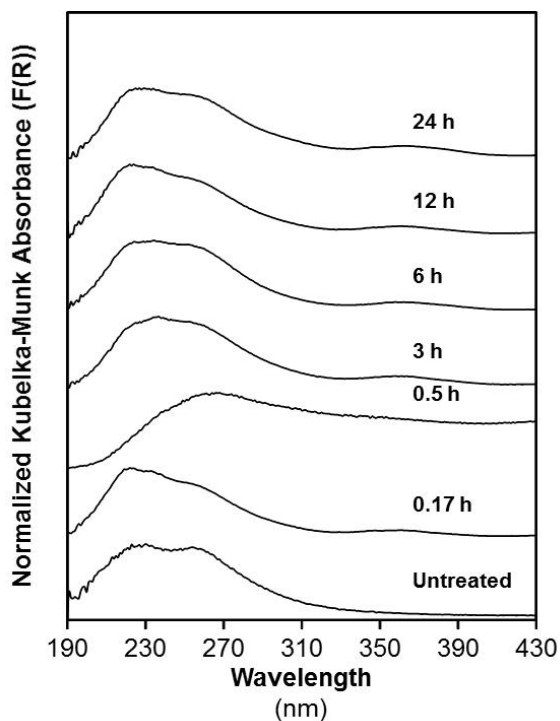
**Figure 5.17:** SEM images of Sn-Beta-F-116 (a) before and (b) after 24 h of hot (373 K) water exposure time.



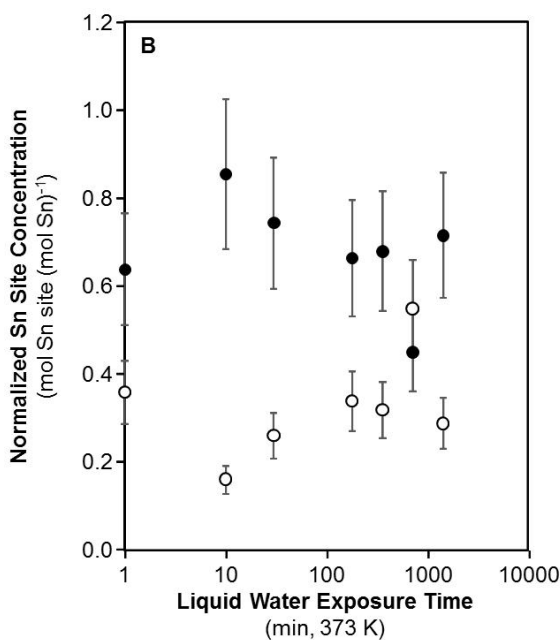
**Figure 5.18:** Sn density (A), Lewis acidic Sn fraction (B), and SnO<sub>x</sub> fraction (C) on Sn-Beta-F-116 as a function of liquid water exposure time. Site densities on untreated materials are plotted at 1 min of water exposure.



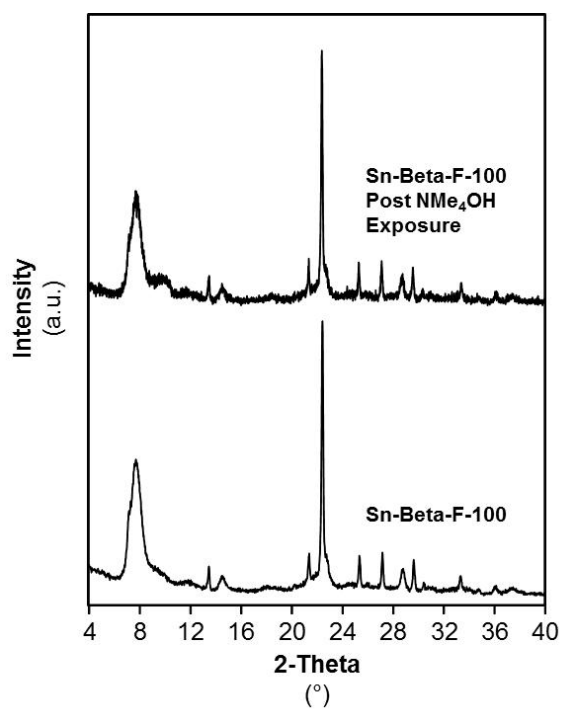
**Figure 5.19:** Tauc plots collected after treatment in flowing He at 523 K for 1800 s on Sn-Beta samples after various (0-24 h) amounts of hot (373 K) water exposure time.



**Figure 5.20:** Dehydrated UV-Vis spectra (523 K, 1800 s) of Sn-Beta samples after various (0-24 h) amounts of hot (373 K) water exposure time.



**Figure 5.21:** Open (○) and closed Sn density (●) per mol Lewis acidic Sn on Sn-Beta-F-116 as a function of liquid water exposure time. Site densities on untreated materials are plotted at 1 min of water exposure.

5.6.4 Bulk characterization of Sn-Beta-F-100 after  $\text{NMe}_4\text{OH}$  treatment

**Figure 5.22:** Powder XRD patterns of Sn-Beta-F-100 samples before and after  $\text{NMe}_4\text{OH}$  treatment.

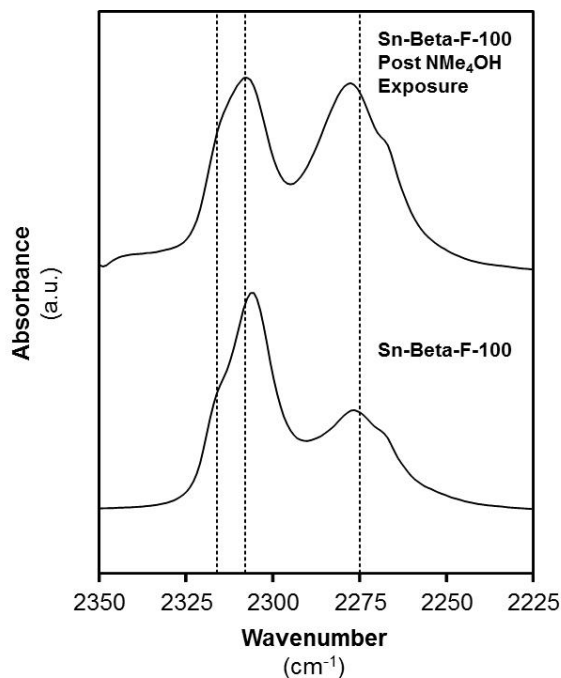


**Figure 5.23:** IR spectra collected on CD<sub>3</sub>CN-saturated Sn-Beta-F-100 samples before and after NMe<sub>4</sub>OH treatment. Spectra were normalized by combination and overtone modes for Si–O–Si stretches prior to the subtraction of spectra collected before CD<sub>3</sub>CN adsorption. Dashed lines are drawn at 2308 cm<sup>-1</sup> (CD<sub>3</sub>CN bound to closed Sn), 2316 cm<sup>-1</sup> (CD<sub>3</sub>CN bound to open Sn), and 2275 cm<sup>-1</sup> (CD<sub>3</sub>CN bound to silanols).

5.6.5 Supplemental figures on kinetic and mechanistic details of activation and fructose formation on Sn-Beta samples

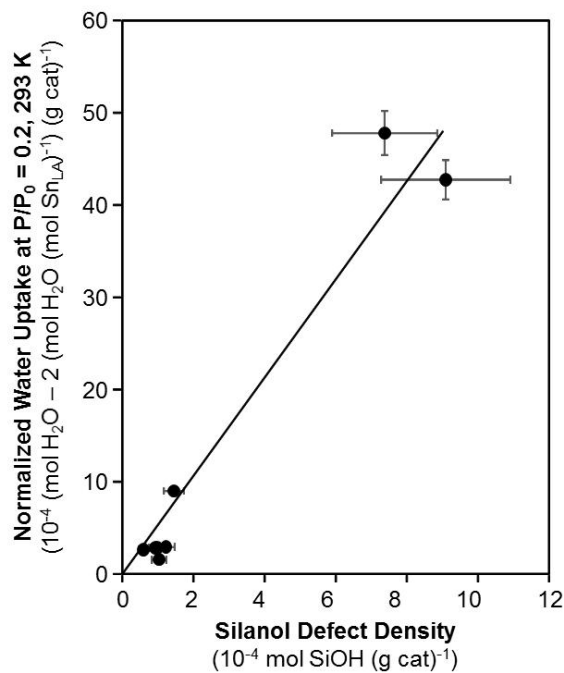


**Figure 5.24:** Water uptakes at  $P/P_0 = 0.2$  (373 K) after rigorously subtracting off two water molecules per Lewis acid site counted from  $\text{CD}_3\text{CN}$  titration plotted against bulk silanol defect density from  $\text{CD}_3\text{CN}$  titration measurements. The solid line is a best fit line forced through the origin to guide the eye.

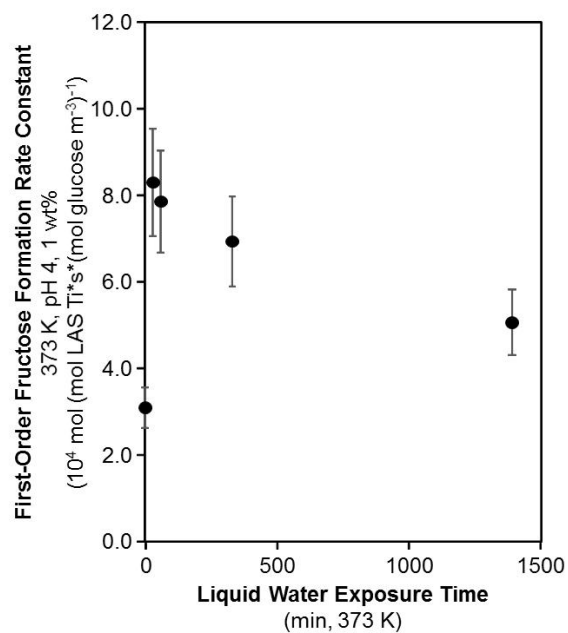


**Figure 5.25:** Measured first-order glucose isomerization rates (per Lewis acidic Ti, 373 K) on Ti-Beta-F-155 after hot (373 K) liquid water exposure (0-24 h). Characterization data on Ti-Beta-F-155 is reported in Ref. [57].

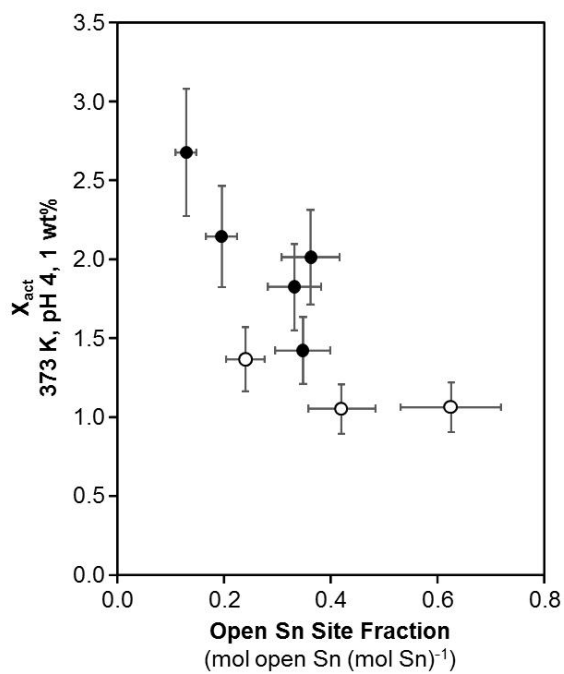


**Figure 5.26:** Observed activation extents (373 K, 1 wt%) as a function of initial open Sn density on Sn-Beta-F (closed) and Sn-Beta-OH (open) zeolites. Observed activation extents are defined as the ratio of the highest measured first-order glucose isomerization rate constant per sample normalized by the measured first-order rate constant on the unexposed Sn-Beta sample.

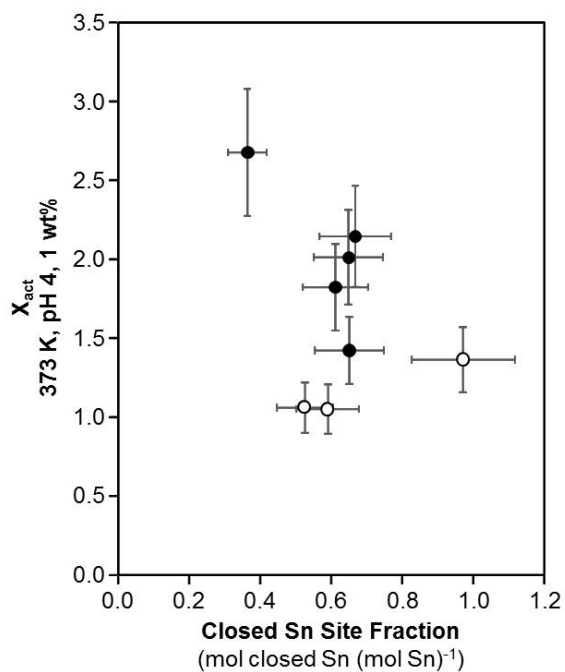


**Figure 5.27:** Observed activation extents (373 K, 1 wt%) as a function of initial closed Sn density on Sn-Beta-F (closed) and Sn-Beta-OH (open) zeolites. Observed activation extents are defined as the ratio of the highest measured first-order glucose isomerization rate constant per sample normalized by the measured first-order rate constant on the unexposed Sn-Beta sample.

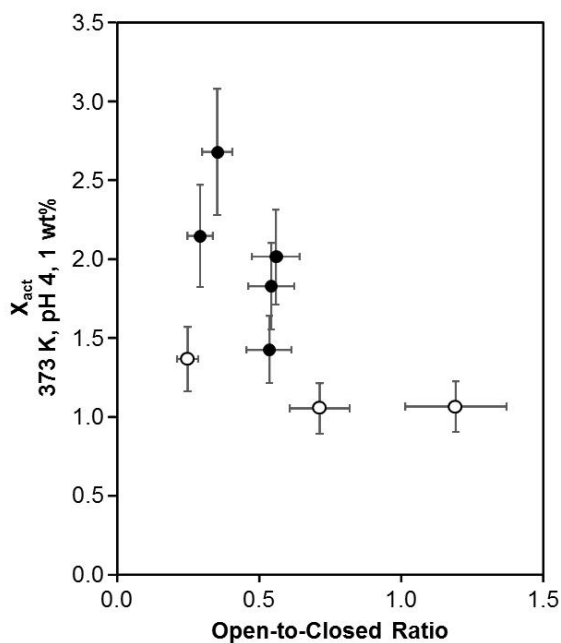


**Figure 5.28:** Observed activation extents (373 K, 1 wt%) as a function of initial open-to-closed ratio on Sn-Beta-F (closed) and Sn-Beta-OH (open) zeolites. Observed activation extents are defined as the ratio of the highest measured first-order glucose isomerization rate constant per sample normalized by the measured first-order rate constant on the unexposed Sn-Beta sample.

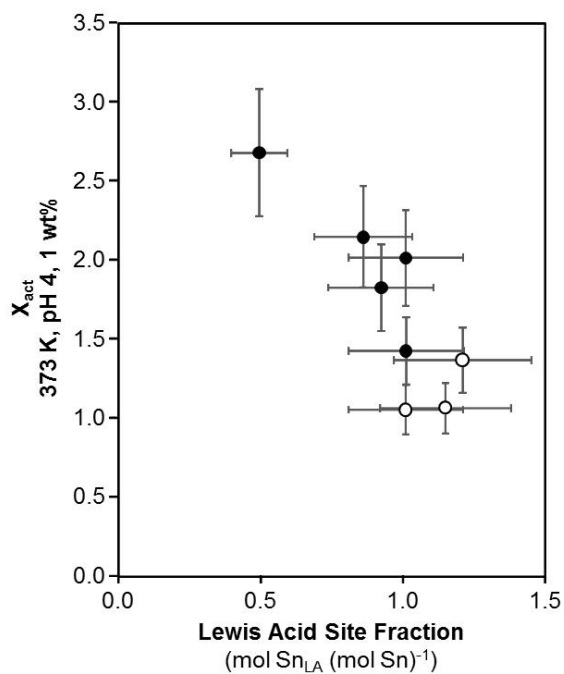


**Figure 5.29:** Observed activation extents (373 K, 1 wt%) as a function of initial Lewis acidic Sn density on Sn-Beta-F (closed) and Sn-Beta-OH (open) zeolites. Observed activation extents are defined as the ratio of the highest measured first-order glucose isomerization rate constant per sample normalized by the measured first-order rate constant on the unexposed Sn-Beta sample.

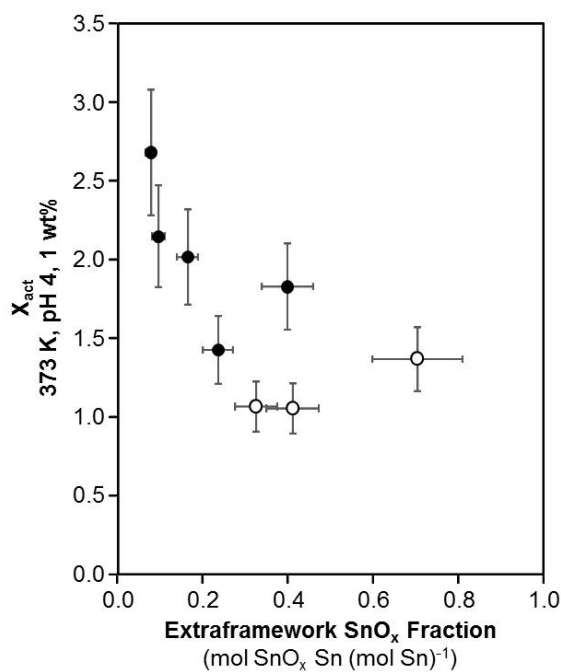


**Figure 5.30:** Observed activation extents (373 K, 1 wt%) as a function of initial SnO<sub>x</sub> density on Sn-Beta-F (closed) and Sn-Beta-OH (open) zeolites. Observed activation extents are defined as the ratio of the highest measured first-order glucose isomerization rate constant per sample normalized by the measured first-order rate constant on the unexposed Sn-Beta sample.

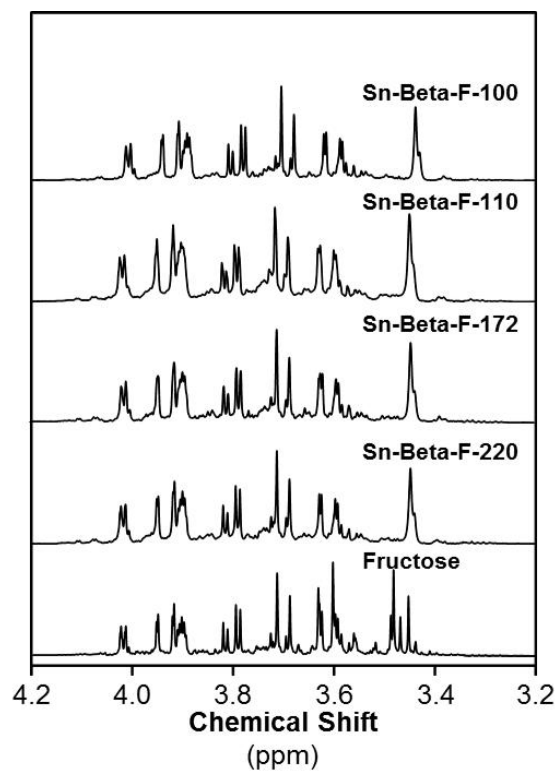


**Figure 5.31:** Solution-phase  $^1\text{H}$  NMR of fructose products formed after contacting 1 wt% glucose solutions (373 K) with Sn-Beta-F samples. A fructose standard is given for direct comparison.

## 6. THE DOMINANT ROLE OF ENTROPY IN STABILIZING SUGAR ISOMERIZATION TRANSITION STATES WITHIN HYDROPHOBIC ZEOLITE PORES

### 6.1 Introduction

Hydrophobic surfaces are characterized by weak hydrogen bonding interactions with water molecules, which cause structural changes to molecular ensembles and extended water networks near surfaces [287] that are referred to collectively as “hydrophobic effects” [288]. At least three distinct hydrophobic effects have been recognized during aqueous-phase reactions catalyzed within metalloenzymes, including hydrophobic side chains that provide contacts that increase free energies to drive water diffusion from binding pockets during protein folding [289], hydrophilic side chains that hydrogen bond with water molecules to preferentially position them within specific locations in binding pockets [267], and hydrophobic and hydrophilic groups that regulate water movement along reaction coordinates to facilitate enthalpy-entropy compromises that moderate reaction free energy landscapes [290–292]. Hydrophobic effects on water adsorption have also been observed at silica surfaces [43], as well as within defect-free carbon nanotubes of sub-nanometer pore diameter [41] and defect-free silica surfaces positioned less than one nanometer apart [37], which lack surface groups capable of hydrogen bonding and lead to the confinement of gas-like water rather than the “ice-like” structures confined within highly-defective and hydrophilic microporous voids. The influence of surrounding environment hydrophobicity on the structure and behavior of confined water has been noted generally in biomolecular recognition [288] and in reports of enhanced water transport in carbon nanotubes for separation and molecular sensing applications [38, 293–295], in addition to applications in catalysis [44, 46].

Within the context of liquid-phase catalysis, hydrophobic pockets within inorganic microporous materials influence the free energies of reactive intermediates and transition states that result in differences in adsorption equilibrium constants and reaction rate constants. Several studies have focused on zeolites, which are crystalline silica-based materials whose microporous surfaces are composed of non-polar and hydrophobic siloxane bonds, but become increasingly hydrophilic with increasing densities of framework heteroatom substituents or of silanol and other hydroxyl groups that donate and accept hydrogen bonds [296–299]. Silanol groups originate from framework siloxy (i.e.,  $\text{SiO}^-$ ) defects that form during hydrothermal synthesis when cationic structure directing agents are not charge balanced either by aliovalent heteroatoms substituted in framework positions (e.g.,  $\text{Al}^{3+}$  [300,301]) or by counteranions occluded within extraframework locations (i.e.,  $\text{F}^-$  [35,302,303]). Silanol groups can also form after synthesis upon hydrolysis of framework siloxane linkages in neutral or basic aqueous media [66, 278], or upon removal of framework heteroatoms (e.g., Al, B) in acidic media [304, 305]. The adsorption of gaseous water on zeolites measured by gravimetry increases with silanol density [52, 173], consistent with higher intraporous water densities that are stabilized with increasing silanol density when zeolites are contacted or equilibrated with liquid water [56]. Higher intraporous water densities have been shown to influence the kinetics of catalytic reactions, such as to cause preferential stabilization of protonated water and propanol clusters during gas-phase propanol dehydration on Brønsted acidic Al-MFI zeolites that enhances rates of bimolecular or trimolecular dehydration pathways over those of monomolecular routes [306]. Hydrophobic channels in Lewis acidic Ti-MFI zeolites increase 1-hexene epoxidation rates relative to hydrophilic  $\text{TiO}_2\text{-SiO}_2$  surfaces by mitigating the formation of bulk water structures near Ti sites [307], while silanol groups near Ti sites in UCB-4 zeotypes lead to increases cyclohexene epoxidation rates [308]. Hydrophobic channels also increase rates for a variety of monomolecular and bimolecular reactions, such as aqueous-phase and biphasic *m*-cresol alkylation with 2-propanol in Al-FAU zeolites [271,273], aqueous-phase 1-hexene epoxidation on

Ti-MWW zeolites [309], hydrogenation and etherification of hydroxymethylfurfural in alcohol solvents on metal-substituted Beta zeolites [179], gas-phase bimolecular ethanol dehydration at high water partial pressures on Sn-Beta zeolites [180, 227], and aqueous-phase Meerwein-Ponndorf-Verley reduction and Oppenauer oxidation (MPVO) reactions in Ti-Beta [53] and Sn-Beta zeolites [56].

Here, we study aqueous-phase glucose isomerization catalysis that proceeds via Lewis acid-mediated intramolecular hydride shift steps on a suite of materials synthesized with site-isolated framework Ti centers ( $\text{Si}/\text{Ti} = 30\text{--}300$ ) and residual silanol defect densities that vary by two orders of magnitude ( $10^{-5}\text{--}10^{-3}$  mol  $\text{g}^{-1}$ ) to isolate the kinetic effects of hydrophobic confining pockets around Ti centers. In prior reports, first-order aqueous-phase glucose isomerization rate constants were higher on hydrophobic Ti-Beta ( $\sim 7\text{--}10\times$ , 373 K) [53] and Sn-Beta ( $\sim 50\times$ , 373 K) [56] zeolites than their hydrophilic analogs, but rate data measured in first-order kinetic regimes are unable to resolve the kinetic contributions of glucose and water competitive adsorption from those of isomerization transition state stabilization. Co-adsorbed water within Sn-Beta micropores has been reported to decrease experimentally measured glucose and 1,3-dihydroxyacetone isomerization rates, which was attributed to the competitive adsorption of water and substrate molecules at Sn sites [54]. In contrast, density functional theory (DFT) studies report that silanol defects in Sn-Beta lower activation barriers to form 1,2-hydride shift transition states during glucose-fructose isomerization [69] and enthalpically stabilize adsorbed deprotonated glucose intermediates [310] via hydrogen bonding interactions, while *ab initio* molecular dynamics (AIMD) simulations indicate that explicit co-adsorbed water molecules lower activation free energies via solvent reorganization and charge redistribution throughout the reaction coordinate [311]. These studies emphasize that understanding the specific structure and density of co-adsorbed water molecules under reaction conditions, and their separate influence on the free energies of reactive intermediates and transition states involved in sugar isomerization, remains a relevant and active area of research.

The incomplete understanding of water density and structure within microporous environments of different polarity precludes more precise definitions of the kinetic and mechanistic effects of hydrophobic reaction pockets on sugar isomerization catalysts. Here, we report a detailed kinetic analysis of initial glucose isomerization turnover rates (normalized per Lewis acid site) on hydrophobic Ti-Beta-F and hydrophilic Ti-Beta-OH zeolites in first-order and zero-order kinetic regimes as a function of temperature (368–383 K), which enables measuring rate constants, activation enthalpies and activation entropies that separate the effects of confining environment polarity on transition state stabilization and water competitive adsorption. The kinetic effects of co-adsorbed solvent molecules on relevant intermediates and transition states are determined from a suite of *ex situ* and *in situ* experimental characterizations and insights from DFT calculations. These combined experimental and computational results highlight the dominant role of hydrophobic pockets to prevent the formation of extended water structures. Such co-adsorbed water structures confer modest enthalpic stabilization, but more severe entropic destabilization, of isomerization transition states that ultimately lead to lower turnover rates.

## 6.2 Materials and Methods

### 6.2.1 Catalyst Synthesis

Ti-Beta-F zeolites were synthesized in fluoride media following a previously reported hydrothermal synthesis method [52]. A gel was prepared by first mixing 4.89 g of tetraethylammonium fluoride (TEAF, Alfa Aesar, 97 wt%) with 7.25 g of deionized water (18.2 M $\Omega$ ) in a perfluoroalkoxy alkane (PFA) container (Savillex Corp.) followed by the addition of 10.0 g of tetraethylorthosilicate (TEOS, Sigma Aldrich, >98 wt%). The resulting gel was stirred for 1 h prior to adding 0.221 g of titanium(IV) isopropoxide (TIPO, Sigma Aldrich, 99.999%). The PFA container was sealed and the contents stirred for 16 h prior to removing the cover to allow ethanol, isopropanol, and excess water to evaporate. The final gel molar composition was 1

$\text{SiO}_2 / x \text{ TIPO} / 0.55 \text{ TEAF} / 7.15 \text{ H}_2\text{O}$  where  $x$  ranged between 0.005 and 0.0087. The gel was then loaded and sealed into a Teflon-lined stainless steel autoclave (45  $\text{cm}^3$ , Parr Instruments) with 0.14 g of Si-Beta-F ( $\sim 5\%$  of Si in the gel) and heated to 413 K while rotating (60 rpm) in an isothermal oven (Yamato DKN-402C) for 25 days. The products were removed from the liner and washed with water and acetone (Sigma Aldrich,  $>99.5 \text{ wt}\%$ , 6 washes each,  $\sim 20 \text{ cm}^3 (\text{g zeolite})^{-1}$  per wash), centrifuged to recover the solid portion, and dried for 16 h at 373 K. The resulting solids were then heated in a muffle furnace (Nabertherm LE 6-11 with P300 controller) in flowing dry air (Indiana Oxygen, Ultra Zero Grade,  $1.67 \text{ cm}^3 \text{ s}^{-1} (\text{g solids})^{-1}$ ) to 853 K ( $0.0167 \text{ K s}^{-1}$ ) for 10 h.

Ti-Beta-OH zeolites were prepared using a previously reported post-synthetic reflux technique [151]. Briefly, Al-Beta zeolites ( $\text{Si}/\text{Al} = 20\text{--}50$ ) were synthesized using a method similar to that reported previously [183] without the aluminosilicate gel filtration step. The recovered solids were washed, centrifuged, dried, and treated in air, as described above for Ti-Beta-F preparation. The resulting Al-Beta samples were dealuminated by stirring with nitric acid (69 wt%  $\text{HNO}_3$ , Avantor, 25  $\text{cm}^3$  of solution per 1 g H-form zeolite) in a covered PFA container for 16 h at 353 K. The solids were then washed thoroughly with water until a constant supernatant pH was observed, isolated via centrifugation, and dried for 16 h at 373 K. Dealuminated Beta samples were then treated in flowing dry air (Indiana Oxygen, Ultra Zero Grade,  $1.67 \text{ cm}^3 \text{ s}^{-1} (\text{g solids})^{-1}$ ) to 853 K ( $0.0167 \text{ K s}^{-1}$ ) for 10 h. On each dealuminated Beta sample, the resulting Si/Al ratio was greater than 1500 as measured by atomic absorption spectroscopy (AAS). Afterward, 2 g of dealuminated Beta were loaded into a 500  $\text{cm}^3$  round bottom flask and dried for 12 h on a Schlenk line under rough vacuum (Oerlikon Trivac 140002E2,  $\sim 0.04 \text{ Torr}$ ). Dichloromethane ( $\text{CH}_2\text{Cl}_2$ , Sigma Aldrich,  $>99.8 \%$ ) was dried over 3A molecular sieves (W. R. Grace, 4–8 mesh, Grade 562) prior to being transferred via moisture-free and air-free cannula to the flask containing the dealuminated Beta zeolites. A solution of titanium (IV) tetrachloride pre-dissolved in  $\text{CH}_2\text{Cl}_2$  (Sigma Aldrich, 1.0 M  $\text{TiCl}_4$  in  $\text{CH}_2\text{Cl}_2$ ) was further diluted

in dry  $\text{CH}_2\text{Cl}_2$  to achieve a concentration of 1 mmol  $\text{TiCl}_4$  per gram of dealuminated Beta prior to cannula transfer to the round-bottom flask containing the dealuminated zeolite sample. This mixture was heated for 7 h under reflux at 333 K. The solids were then collected via centrifugation, washed 6 times ( $\sim 60 \text{ cm}^3$  per wash) with methanol (Sigma Aldrich, >99.9%), dried for 16 h at 373 K, and then thermally treated in air (Indiana Oxygen, Ultra Zero Grade,  $1.67 \text{ cm}^3 \text{ s}^{-1} (\text{g solids})^{-1}$ ) to 473 K ( $0.05 \text{ K s}^{-1}$ ) for 6 h and then at 823 K ( $0.05 \text{ K s}^{-1}$ ) for 6 h in a muffle furnace.

## 6.2.2 Characterization of Bulk Catalyst Properties

Bulk elemental compositions were determined using atomic absorption spectroscopy (AAS) on a Perkin Elmer AAnalyst 300 Atomic Absorption Spectrometer after calibration using standard solutions for each element generated by dilution of 1000 ppm AAS standards (Alfa Aesar, TraceCERT,  $\pm 4$  ppm). Typically, 0.02 g of zeolite samples were dissolved in 2.6 g of HF (48 wt %, Alfa Aesar) and 50 g of deionized water prior to characterization. Extreme caution should be taken when working with hydrofluoric acid, and appropriate personal protective equipment, ventilation, and other engineering controls should be used. Absorbance values were measured in an acetylene/nitrous oxide flame at 396.2, 399.9, and 251.6 nm for Al, Ti, and Si respectively. Samples are denoted as Ti-Beta-X-Y, where X refers to the synthetic history (F = fluoride-mediated hydrothermal synthesis; OH = post-synthetic grafting of dealuminated Al-Beta) and Y reflects the bulk Si/Ti ratio (by AAS).

Powder X-ray diffraction (XRD) patterns were collected using a Rigaku Smartlab X-ray diffractometer with a  $\text{Cu K}\alpha$  source (1.76 kW) and an ASC-6 automated sample changer. Zero background, low dead volume sample holders (Rigaku) were loaded with approximately 0.01 g of sample prior to collecting diffraction patterns from 4–40° at a scan rate of  $0.00417^\circ \text{ s}^{-1}$  with a step size of  $0.01^\circ$ . The presence of  $\text{TiO}_x$  domains larger than 3 nm ( $25.4^\circ$  and  $37.9^\circ$  for anatase,  $27.4^\circ$  and  $35.2^\circ$  for rutile) was not observable in the XRD pattern of any sample studied here.

Nitrogen (77 K), water (293 or 298 K), and methanol (293 K) adsorption isotherms were collected using a Micromeritics ASAP2020 Surface Area and Porosity Analyzer. Typically,  $\sim 0.03$  g of sample were pelleted and sieved to obtain particle diameters between 180 and 250  $\mu\text{m}$ . Samples were degassed prior to analysis by heating to 393 K ( $0.0167 \text{ K s}^{-1}$ ) under vacuum ( $<0.005$  Torr) for 2 h then heating to 623 K ( $0.0167 \text{ K s}^{-1}$ ) under vacuum for 8 h. A semi-log derivative analysis of  $\text{N}_2$  isotherms ( $\partial(V_{\text{ads}}/\text{g})/\partial(\log(P/P_0))$  vs.  $\log(P/P_0)$ ) was used to identify the end of the micropore filling regime, in order to quantify the micropore volume of each sample. Water uptakes are reported at a reduced pressure of 0.2, which has been used previously [171] as a reference pressure corresponding to micropore filling of cyclohexane (298 K) within hydrophobic zeolites.

Scanning electron microscopy (SEM) was performed on a FEI Quanta 3D FEG Dual-beam SEM equipped with an Everhart-Thornlev detector for high vacuum imaging. The focused beam operating mode was used to collect SEM micrographs with a spot size of 4  $\mu\text{m}$  and a voltage of 5 kV.

Diffuse reflectance UV-Vis (DRUV) spectra were collected on a Varian Cary 5000 UV-VIS-NIR equipped with a Harrick Praying Mantis *in situ* diffuse reflectance cell. UV-Vis spectra were collected at ambient conditions prior to thermally treating samples to 523 K (1800 s,  $\sim 0.5 \text{ K s}^{-1}$ ) in dry flowing He ( $4.17 \text{ cm}^3 \text{ s}^{-1} (\text{g solids})^{-1}$ ), at which point spectra of dehydrated samples were collected at 523 K. Spectra were collected at a resolution of 10  $\text{nm s}^{-1}$  using poly(tetrafluoroethylene) (PTFE, Sigma Aldrich, 1  $\mu\text{m}$  powder) as the 100% reflectance standard. Diffuse reflectance spectra were converted into absorbance spectra using the Kubelka-Munk (F(R)) function. Band centers are reported as that corresponding to the highest F(R) intensity on dehydrated samples.

### 6.2.3 Transmission Infrared Spectroscopy

A Nicolet 4700 spectrometer with an Hg-Cd-Te detector (MCT, cooled to 77 K by liquid  $\text{N}_2$ ) was used to collect IR spectra by averaging 64 scans at a resolution

of  $2\text{ cm}^{-1}$  in the  $4000$  to  $400\text{ cm}^{-1}$  range. Spectra were taken relative to an empty cell background reference collected under dynamic vacuum ( $<0.1$  Torr, rotary vane rough pump, Alcatel 2008A) at either  $303\text{ K}$  for deuterated acetonitrile ( $\text{CD}_3\text{CN}$ ) adsorption studies or  $423\text{ K}$  for pyridine adsorption studies. Self-supporting wafers of  $0.01\text{--}0.03\text{ g cm}^{-2}$  were sealed in a custom-built quartz IR cell [184] with  $\text{CaF}_2$  windows positioned within an alumina silicate ceramic chamber (Purdue Research Machining Services) with a mineral-insulated resistive heating coil (ARi Industries). K-type thermocouples (Omega) were positioned within  $2\text{ mm}$  of each side of the wafer. A custom glass vacuum manifold was used for sample pretreatment and for dosing controlled amounts of gaseous titrants into the cell. Wafers were first thermally treated to  $823\text{ K}$  ( $0.083\text{ K s}^{-1}$ ) for  $1\text{ h}$  in flowing dry air ( $6.66\text{ cm}^3\text{ s}^{-1}$  ( $\text{g solids}^{-1}$ )), which was further purified by an FTIR purge gas generator ( $<1\text{ ppm CO}_2$ ,  $200\text{ K}$  water dew point, Parker Balston) prior to each experiment. Wafers were then exposed to dynamic vacuum for  $1\text{ h}$  at  $823\text{ K}$  ( $<0.1$  Torr, rotary vane rough pump, Alcatel 2008A).

For  $\text{CD}_3\text{CN}$  titration experiments, wafers were then cooled under dynamic vacuum to  $303\text{ K}$ .  $\text{CD}_3\text{CN}$  (Sigma Aldrich,  $>99.9\%$ ,  $99.96\text{ atom\% D}$ ) was purified through three freeze-pump-thaw cycles prior to dosing  $\sim 1.5 \times 10^{-7}\text{ mol}$  into the cell (similar procedures for pyridine titration given in Section 6.6.1.2, Supp. Info.). The cell was allowed to equilibrate for  $180\text{ s}$  at a constant final pressure for each dose prior to collecting each IR spectrum. Subsequent doses were introduced until wafer saturation was achieved, which was determined when final pressures  $>0.4\text{ Torr}$  were observed due to residual gaseous titrant within the cell. Wafers were then exposed to dynamic vacuum at the dosing temperature to remove gas phase and weakly-adsorbed species until a final pressure of  $0.0\text{ Torr}$  was measured in the cell. IR spectra were baseline-corrected and normalized to combination and overtone modes of zeolite Si-O-Si stretches ( $1750\text{--}2100\text{ cm}^{-1}$ ) followed by subtraction of the parent spectrum and deconvolution of the  $\text{CD}_3\text{CN}$  IR peaks into their individual components ( $2308$ ,  $2275$ , and  $2265\text{ cm}^{-1}$ ) as reported elsewhere [56]. Peak areas were used in conjunction with

integrated molar extinction coefficients ( $E$ ) to determine site concentrations per gram of zeolite:

$$\text{Site density } (\mu\text{mol g}^{-1}) = \left( \frac{\text{Integrated Peak Area } (\text{cm}^{-1})}{E (\text{cm } \mu\text{mol}^{-1})} \right) \left( \frac{a_{CS}(\text{cm}^2)}{m(\text{g})} \right) \quad (6.1)$$

In the case of  $\text{CD}_3\text{CN}$  adsorbed onto silanol groups ( $2275 \text{ cm}^{-1}$ ), an integrated molar extinction coefficient value ( $E (2275 \text{ cm}^{-1}) = 0.74 \text{ cm } \mu\text{mol}^{-1}$ ) measured on dealuminated Beta was used [56]. In the case of Lewis acidic Ti sites that give rise to the  $\text{CD}_3\text{CN}$  IR peak at  $2308 \text{ cm}^{-1}$ , an integrated molar extinction coefficient was measured following previously reported methods [56]. Briefly, Ti-Beta wafers were pretreated as mentioned above and sequentially dosed with small amounts of  $\text{CD}_3\text{CN}$  in vacuum ( $0.1\text{--}0.3 \mu\text{mol } \text{CD}_3\text{CN}$  per dose) prior to equilibration for 180 s. For these initial doses, the final recorded pressure in the cell was measured to be 0.0 Torr, and all of the  $\text{CD}_3\text{CN}$  dosed into the cell was assumed to be adsorbed onto the sample wafer. IR spectra were collected after each dose, baseline-corrected and normalized, and then deconvoluted into constituent peaks associated with  $\nu(\text{C}\equiv\text{N})$  stretching vibrations for  $\text{CD}_3\text{CN}$  adsorbed onto Lewis acidic Ti sites ( $2308 \text{ cm}^{-1}$ ) and silanols ( $2275 \text{ cm}^{-1}$ ) and for gas-phase or physisorbed  $\text{CD}_3\text{CN}$  ( $2265 \text{ cm}^{-1}$ ) at higher doses. The number of  $\text{CD}_3\text{CN}$  adsorbed onto Lewis acidic Ti sites was determined by quantifying the total amount of adsorbed  $\text{CD}_3\text{CN}$  via equilibrated pressure differences before and after dosing and subtracting contributions from silanol-bound  $\text{CD}_3\text{CN}$ .

For water adsorption experiments, the cell was first assembled without a sample wafer to quantify the contributions of water in the gas phase and adsorbed on cell windows. The cell was treated in flowing He (UHP, Indiana Oxygen,  $0.96 \text{ cm}^3 \text{ s}^{-1}$ ) at  $823 \text{ K}$  ( $0.0833 \text{ K s}^{-1}$ ) for 1 h, then cooled to  $298 \text{ K}$ . The temperature was controlled at  $298 \text{ K}$  ( $\pm 2 \text{ K}$ , the gradient observed between the two thermocouples on either side of the wafer was  $<1.5 \text{ K}$ ) by flowing air free of carbon dioxide and moisture through the cooling channels of the insulated brass block and by resistive heating. A spectrum

was collected at 298 K in flowing He ( $0.96 \text{ cm}^3 \text{ s}^{-1}$ ) and used as the background for all subsequent spectra. Liquid water ( $18.2 \text{ M}\Omega \text{ cm}$ ) was vaporized into the flowing He stream ( $0.96 \text{ cm}^3 \text{ s}^{-1}$ ) from a syringe pump (KD Scientific Legato 100) equipped with a  $1 \text{ cm}^3$  syringe (Hamilton) and delivered to the cell in heated lines ( $>363 \text{ K}$ ). The liquid water flow rate was varied to achieve partial pressures of 0.32, 0.63, 1.58, and 2.37 kPa, corresponding to  $P/P_0=0.10$ , 0.20, 0.50, and 0.75, respectively, at 298 K. Spectra were averaged over 64 scans at  $2 \text{ cm}^{-1}$  resolution in the  $4000\text{--}650 \text{ cm}^{-1}$  range and were monitored over time at each condition until invariant ( $>30 \text{ min}$ ), indicating that equilibrium was reached. After equilibrium was verified, a 640-scan spectrum at  $2 \text{ cm}^{-1}$  resolution was collected to average out temporal variations in gas-phase pressures and temperature.

Next, self-supporting wafers ( $0.015\text{--}0.040 \text{ g}$ ) of Ti-Beta-F-155 and Ti-Beta-OH-46 were pressed and loaded into the cell, and subjected to treatments identical to those described above for the empty cell. Spectra were processed first to remove the contributions of water adsorbed in the cell and gas-phase water by subtracting the respective spectrum of the empty cell measured at the same  $P/P_0$  value. Then, spectra were normalized by the combination and overtone modes of zeolite Si-O-Si stretches ( $1750\text{--}2100 \text{ cm}^{-1}$ ) of the wafer prior to water exposure followed by subtraction of the normalized spectrum for the sample before water adsorption. The resulting difference spectra represent the vibrations of adsorbed water and any differences on the sample induced by this adsorption (e.g., perturbation of silanol groups). These spectra were further baseline-corrected with pivot points at  $4000$ ,  $2400$ , and  $1350 \text{ cm}^{-1}$ , where no absorbance was detected.

#### 6.2.4 Glucose Isomerization Kinetic Studies

Kinetic studies were performed in  $10 \text{ cm}^3$  thick-walled glass batch reactors (VWR) with 1–50 wt% aqueous D-glucose (Sigma-Aldrich,  $\geq 99.5\%$ ) solutions. The reactant solutions were first prepared by adjusting the pH of deionized water ( $18.2 \text{ M}\Omega \text{ cm}$ ) with hydrochloric acid (HCl, Macron, 37 wt%) to 4 for kinetic studies performed

at  $\leq 373$  K, or 3 for kinetic studies performed at  $> 373$  K, in order to suppress contributions from background isomerization reactivity catalyzed by hydroxide anions. The pH-adjusted water was then mixed with D-glucose to the desired concentration, filtered (0.2  $\mu\text{m}$  PTFE filters, VWR), and loaded into 2 mL glass vials capped with a PTFE/silicone septum (Waters) for pre-heating. Catalytic solids ( $\sim 0.01$ – $0.06$  g) were added to a batch reactor and sealed with a crimp top (PTFE/silicone septum, Agilent). The vials containing the reactant solution and the catalyst were heated separately for 600 s to the reaction temperature atop a digital stirred hotplate (IKA RCT basic) prior to injecting  $\sim 1$ – $4$   $\text{cm}^3$  of the pre-heated reactant solution into the capped reactors.

Reactors were maintained at temperature (368–383 K, 750 rpm, autogenous pressure) for various time intervals (300–14400 s) before quenching in an ice bath. Product solutions were filtered (0.2  $\mu\text{m}$ , PTFE), diluted to 1 wt% sugar concentration with deionized water, and then mixed with a 1 wt% aqueous D-mannitol (Sigma Aldrich,  $\geq 98$  wt%) solution as an internal quantification standard. Product separation was performed using an Agilent 1260 high performance liquid chromatograph (HPLC) with an aqueous mobile phase (0.01  $\text{cm}^3 \text{ s}^{-1}$ , 353 K) through a Hi-Plex Ca column (7.7  $\times$  300 mm, 8  $\mu\text{m}$  particle size, Agilent). Quantification was performed using an Agilent 1260 Infinity evaporative light scattering detector (ELSD) using separate calibration curves for each sugar compound. Initial rates were determined by extrapolating transient product formation rates to zero reaction time, a procedure that gave values identical to rate measurements from batch reactors operated at differential conversions ( $< 5\%$ ) upon correcting for approach to equilibrium. Reaction enthalpies and entropies were obtained from Bayesian nonlinear regression in Athena Visual Studio (Athena Visual Software, Inc., v 14.2) and reported errors represent 95% marginal highest posterior density intervals.

Isotopic labeling studies were performed using 1  $\text{cm}^3$  of a 5 wt% aqueous D-glucose- $\text{D}_2$  (Cambridge Isotope Laboratories, 98% 2-D) solution (pH = 4) and 0.01–0.04 g of catalytic solids for variable times (300–3600 s) at 373 K. Reactor contents were

then quenched and products were filtered and separated as described above. Liquid samples containing products and unreacted glucose were collected using an Agilent 1260 Infinity series fraction collector, frozen in liquid N<sub>2</sub> to 77 K, and freeze-dried to remove water using a Labconco FreeZone lyophilizer (<0.01 Torr, 36 h). Afterward, 0.06 cm<sup>3</sup> D<sub>2</sub>O (Cambridge Isotope Laboratories, 99.9%) was added to dissolve dried sugar products prior to loading into NMR tubes (Wilmad LabGlass, 5 mm thin wall, 7 in., 500MHz) for liquid NMR analysis. <sup>13</sup>C NMR spectra were collected on a Bruker ARX500 spectrometer equipped with a 5 mm BBFO Z-gradient probe at ambient temperature and represent the average of 1500 scans acquired at ~0.3 scans per second.

Glucose adsorption experiments were performed using 10 cm<sup>3</sup> of 50 wt% aqueous D-glucose solution (pH = 4) and 0.1 g of catalytic solids for 1800 s at 373 K. Reactor contents were then quenched and centrifuged prior to decanting off the aqueous solution. Solids were dried in ambient flowing air overnight prior to removal from the reactor for XAS analysis.

### 6.2.5 Computational Methods

Periodic planewave-based DFT calculations were carried out using the Vienna ab initio simulation package (VASP) [132–135]. Planewaves were constructed using the projector augmented wave method (PAW) with an energy cutoff of 400 eV [136, 141]. Exchange and correlation energies were computed using the revised Perdew-Burke-Ernzerhof (RPBE) form of the generalized gradient approximation [312–314]. Dispersive interactions were accounted for using the DFT-D3 method with Becke-Johnson damping (D3BJ) [140, 315]. The Brillouin zone was sampled using the  $\Gamma$ -point [316].

Wavefunctions were converged to electronic energies within 10<sup>-6</sup> eV; forces were determined using a fast Fourier transform (FFT) grid with a cutoff equal to twice the planewave cutoff and structures were optimized to forces less than 0.05 eV Å<sup>-1</sup>. Transition state structures were obtained using a two-step method. First, the nudged

elastic band (NEB) method [143,317] was used to approximate the minimum energy pathway using 16 images along the reaction coordinate and converging forces normal to the pathway to less than  $0.5 \text{ eV } \text{\AA}^{-1}$ , while calculating forces using an FFT grid with a cutoff of 1.5 times the planewave cutoff and converging wavefunctions to energies within  $10^{-4} \text{ eV}$ . The approximate pathway generated by this method was used to generate input transition state geometries and reaction trajectories for the dimer method [318], which was then used to determine transition state structures using the same electronic and structural convergence criteria described for optimizations above.

The Beta zeolite was modeled using a fully periodic structure obtained from the IZA-SC database of zeolite structures [142] (tetragonal,  $a = b = 12.632 \text{ \AA}$ ,  $c = 26.186 \text{ \AA}$ ) and is structurally similar to the polymorph A structure of Beta reported elsewhere [190]. Closed Lewis acid sites were created by replacing a framework Si atom (T6 site) with a Ti heteroatom, which are similar to models used in previous studies [310]. The amount of additional intraporous water (0–10 molecules) was varied to determine the effects of intraporous water content on the reaction energetics for glucose isomerization to fructose.

Desorbed glucose was modeled in vacuum and within a crystalline water structure (hexagonal ice, Ih phase). Neither of these desorbed states accurately captures the enthalpy and entropy of glucose within liquid water, but they represent extremes of enthalpic stabilization (ice), entropic stabilization (vapor), and the upper bounds for the glucose free energy, which will be lower in the aqueous phase than in gaseous or ice-like phases at reaction conditions. Inaccuracies in modeling the thermodynamics of the desorbed glucose state may introduce systematic error into the free energy values calculated in this study but will not affect the conclusions regarding the effects of intraporous water, because all reactions modeled at various water contents involve the same number of glucose adsorption events.

Frequency calculations were performed on all states (including transition states) to determine zero-point vibrational energies (ZPVE), vibrational enthalpies ( $H_{\text{vib}}$ ), and free energies ( $G_{\text{vib}}$ ). The finite difference method was used with two displacements

per unconstrained atom to calculate the Hessian matrix and vibrational frequencies of guest species (e.g., glucose, water) within the Beta zeolite in addition to the heteroatom and framework O bound to that heteroatom. Vibrational frequency values  $<60\text{ cm}^{-1}$  are inaccurate from fixed displacement DFT methods but are commonly observed weakly-bound species adsorbed within zeolite pores. In this work, low vibrational frequency modes ( $<60\text{ cm}^{-1}$ ) were replaced with a value of  $60\text{ cm}^{-1}$ , such that frustrated translations and rotations of weakly bound molecules contribute to entropy, while preventing exact values from being inaccurately used. These vibrational frequencies were used, together with VASP-derived electronic energies ( $E_0$ ), to obtain enthalpies:

$$H = E_0 + E_d + ZPVE + H_{vib} + H_{trans} + H_{rot} \quad (6.2)$$

and free energies:

$$G = E_0 + E_d + ZPVE + G_{vib} + G_{trans} + G_{rot} \quad (6.3)$$

for all reactant, product, and transition state structures, where  $E_d$  is the dispersive energy estimated by DFT-D3BJ methods [140, 315]. For gaseous molecules, translational and rotational enthalpies and free energies were computed from statistical mechanics.

### 6.2.6 ATR-IR Spectroscopy with MES-PSD MCR-ALS

*In situ* attenuated total reflectance infrared (ATR-IR) spectroscopy was used to verify the identities of the most abundant reactive intermediates (MARI) and the structures of reactive intermediates that form on Ti-Beta surfaces during reactions with glucose. Untreated samples were ground to a fine powder ( $<200$  mesh), and 0.03 g were suspended in  $5\text{ cm}^3$  of methanol (Macron Chemicals, anhydrous). A ZnSe cylindrical internal reflection element (IRE, International Crystal Labs) was

dipped into the methanol suspension and then dried at ambient temperature. The dip coating procedure was repeated through 10 cycles to evenly coat the IRE with a thin layer of catalyst material. The coated IRE was then loaded into a customized ATR flow cell (Axiom TNL-120) equipped with two liquid inlets and one outlet with a cell volume of 40  $\mu\text{L}$ . The ATR cell was mounted within the sample compartment of a FTIR spectrometer (Bruker, Vertex 70 RapidScan) equipped with a liquid  $\text{N}_2$  cooled HgCdTe detector. Liquid streams of pure water and 50 wt% glucose in water were introduced at controlled flow rates using two high-pressure piston pumps (SSI Series 1), which were controlled using LabVIEW. The cell was heated by a resistive heating cartridge placed within the wall of the cell. A K-type thermocouple (Omega) placed adjacent to the IRE at the center of the z-axis measured the temperature, which was controlled by an electronic temperature controller (Watlow, EZ-Zone). Background scans were obtained under steady-state conditions flowing 1  $\text{cm}^3 \text{min}^{-1}$  of pure deionized water at 373 K after loading the ATR cell. Spectra obtained during transient cutoff experiments were collected at a resolution of 4  $\text{cm}^{-1}$  and averaged over 4 scans. Spectra obtained during modulation experiments were collected at a resolution of 1  $\text{cm}^{-1}$  and averaged over 64 scans. All spectra acquisition was performed using Bruker Corporation's OPUS Spectroscopy Software 7.0.129.

Modulation excitation spectroscopy (MES) is a powerful technique in which a periodic stimulation is applied to the system while acquiring spectra as a function of time. The time domain response is then converted to a phase domain response, and only spectral features that change in synchrony with the applied stimulation are extracted using a phase sensitive detection (PSD) method described by the following equation:

$$A_k(\varphi_k^{\text{PSD}}) = \frac{2}{T} \int_0^T A(t) \sin(k\omega t + \varphi_k^{\text{PSD}}) dt \quad (6.4)$$

Here,  $A(t)$  and  $A_k(\varphi_k^{\text{PSD}})$  are time-domain and phase-domain responses of the measured species, respectively,  $T$  is the period of the applied stimulus in seconds, is the demodulation index and  $\varphi_k^{\text{PSD}}$  is the user defined phase demodulation angle. The application of the MES-PSD technique to FTIR spectra of intermediates on cat-

alytic surfaces reveals spectra that only contain contributions from intermediates that change as a result of the applied stimulus (e.g., changing reactant concentrations) under relevant conditions and, in doing so, simultaneously reduces contributions from random sources of spectral noise [319]. Here, concentrations of glucose and water were modulated sinusoidally by controlling the flow rate of liquid through the two piston pumps and set specifically such that the set points of the pumps were changed in a step-wise manner every 0.5 s to approximate a sine wave with the desired frequency. Recorded time domain spectra were resampled to a single period, and subsequently the spectra of the active species were extracted by PSD using Eq. 6.4. The resultant phase domain spectra reflect contributions from multiple species that oscillate at the same frequency as the applied stimulus, and these chemically distinct species may be separated using principle component analyses that recognize the different phase delays of kinetically distinct groups of species. Multicurve resolution-alternating least squares (MCR-ALS) analysis was performed to extract the spectra and concentration profiles (or surface coverages) of independent species from the phase domain spectra (additional details in Section 6.6.4.1, Supp. Info.) using a recently published MATLAB code [320].

### 6.2.7 X-Ray Absorption Spectroscopy (XAS) Measurements

Ti K-edge (4.966 keV) XAS measurements were performed on the bending magnet beamline of the Materials Research Collaborative Access Team (MRCAT) at the Advanced Photon Source at Argonne National Laboratory. Measurements were taken in step-scan transmission mode with a Ti foil reference spectrum collected simultaneously using a third ion chamber in series for energy calibration. Samples were pressed into a stainless-steel sample holder containing six wells and placed in a quartz reactor tube with Kapton windows. The reactor was purged with He prior to collecting measurements on the hydrated samples to minimize photon absorption by the gas phase. Spectra were collected under ambient conditions prior to heating the samples

in flowing He to 523 K for 30 min. Samples were then cooled to room temperature prior to collection of dehydrated spectra.

XAS data were analyzed using WinXAS 3.2 software [321] for spectra normalization and background subtraction. Coordination parameters were obtained via simultaneous R-space least-squares fits of the magnitude and imaginary component of the  $k^2$ -weighted EXAFS Fourier transform ( $\Delta k = 2.90\text{--}10.0 \text{ \AA}^{-1}$ ). Experimental phase shift and back scattering amplitude fitting functions for Ti-O scattering paths were obtained from the  $\text{TiO}_2$  anatase phase (6 Ti-O bonds at 1.96  $\text{\AA}$ ).

## 6.3 Results and Discussion

### 6.3.1 Bulk Structural and Lewis Acid Site Characterization of Ti-Beta Zeolites

Ti-Beta zeolites were crystallized via direct hydrothermal synthesis in fluoride media (Ti-Beta-F) and via post-synthetic grafting of  $\text{TiCl}_4$  into framework defect vacancies of dealuminated Beta supports (Ti-Beta-OH; residual Si/Al >1500). Relevant structural characterization data on these samples are summarized in Table 6.1.

X-ray diffraction patterns and micropore volumes measured from  $\text{N}_2$  adsorption isotherms (77 K) of all samples were consistent with the Beta topology (Figures 6.9 and 6.10, Supp. Info.). The higher signal-to-noise XRD patterns measured for Ti-Beta-F samples reflect crystallites that are larger ( $\sim 3\text{--}12 \mu\text{m}$ ) than Ti-Beta-OH samples ( $\sim 0.6\text{--}1.2 \mu\text{m}$ ), consistent with average crystallite sizes determined from SEM images (Figures 6.11 and 6.12, Supp. Info.) and as expected from prior reports [173, 322]. Crystallite sizes of all Ti-Beta-OH samples prepared post-synthetically resemble those of their dealuminated and parent Al-Beta samples, which vary with Al content and crystallization time (Figure 6.13, Supp. Info.) [322, 323]. UV-Visible spectra on Ti-Beta-F and Ti-Beta-OH samples (Figure 6.14 and 6.15, Supp. Info.) collected after dehydration treatments (523 K) were used to estimate edge energies (4.2–5.3 eV, Table 6.1) from Tauc plots (Figure 6.16 and 6.17 and Table 6.5, Supp. Info.) that are characteristic of isolated  $\text{Ti}^{4+}$  centers within zeolite frameworks ( $\geq 4.1$

eV) [263]. These bulk characterization data indicate that this suite of Ti-Beta samples contains framework Ti centers of widely varying content ( $\text{Si}/\text{Ti} = 34\text{--}297$ ;  $0.09\text{--}1.36$  Ti per unit cell).

The fraction of  $\text{Ti}^{4+}$  sites that behave as Lewis acid centers was quantified from IR spectra collected after titration by  $\text{CD}_3\text{CN}$  at 303 K. Figure 6.1 shows IR spectra

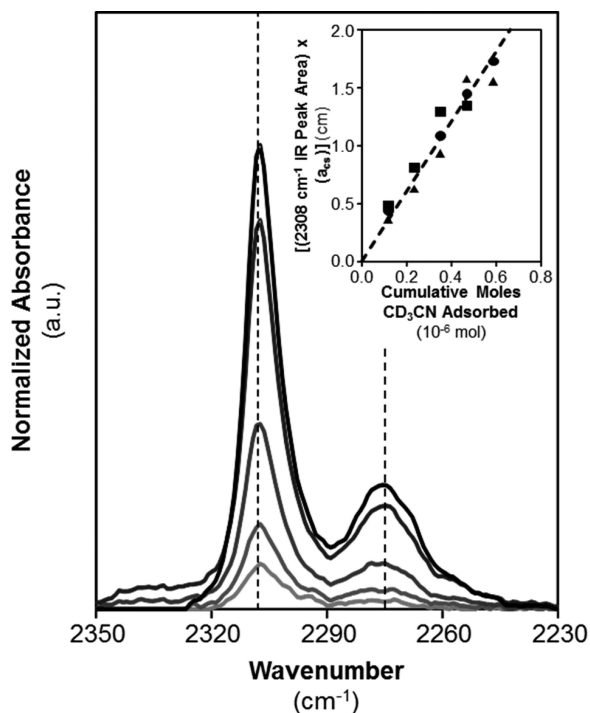


**Figure 6.1:**  $\text{CD}_3\text{CN}$  IR spectra of the  $\nu(\text{C}\equiv\text{N})$  stretching region with increasing coverage of  $\text{CD}_3\text{CN}$  on Ti-Beta-F-155 (0.013, 0.026, 0.065, 0.170, and 0.235  $\text{CD}_3\text{CN}/\text{Ti}$ , light-to-dark). Dashed vertical lines correspond to 2308 and 2275  $\text{cm}^{-1}$  for  $\nu(\text{C}\equiv\text{N})$  stretching vibrations of  $\text{CD}_3\text{CN}$  bound to Lewis acidic Ti sites and silanol groups, respectively. The inset shows the integrated area of the 2308  $\text{cm}^{-1}$  peak multiplied by the cross-sectional area of the IR wafer, plotted against the moles of  $\text{CD}_3\text{CN}$  adsorbed at Lewis acidic Ti sites for Ti-Beta-F-155 (●), Ti-Beta-F-135 (■), and Ti-Beta-OH-38 (▲). The dashed line in the inset is the best fit line through all data, with the slope representing the integrated molar extinction coefficient for  $\text{CD}_3\text{CN}$  adsorbed onto Lewis acidic Ti sites.

for  $\nu(\text{C}\equiv\text{N})$  stretching vibrations on Ti-Beta-F-155 with increasing  $\text{CD}_3\text{CN}$  coverage (spectra of Ti-Beta-OH-46 in Figure 6.18, Supp. Info.). At low  $\text{CD}_3\text{CN}$  coverages ( $\text{CD}_3\text{CN}/\text{Ti} = 0.2\text{--}0.6$ ), a peak centered at 2308  $\text{cm}^{-1}$  for  $\text{CD}_3\text{CN}$  adsorbed at Lewis

acidic Ti sites appears first, followed by peaks for CD<sub>3</sub>CN bound to silanol groups (2275 cm<sup>-1</sup>) and for gas-phase or physisorbed CD<sub>3</sub>CN (2265 cm<sup>-1</sup>) [324], indicating that CD<sub>3</sub>CN preferentially adsorbs onto framework Lewis acidic Ti sites over silanol defects. The 2308 cm<sup>-1</sup> peak increases in area with subsequent CD<sub>3</sub>CN exposure until saturation coverages are reached. Integrated areas for the 2308 cm<sup>-1</sup> peak were quantified from deconvoluting IR spectra into their 2308 cm<sup>-1</sup>, 2275 cm<sup>-1</sup> and 2265 cm<sup>-1</sup> components (Figure 6.19, Supp. Info.), using a previously reported procedure to isolate component peaks for CD<sub>3</sub>CN bound to hydrolyzed-open (Sn(OH)(OSi)<sub>3</sub>, 2316 cm<sup>-1</sup>) and closed (Sn(OSi)<sub>4</sub>, 2308 cm<sup>-1</sup>) Sn sites within Sn-zeolites [56].

The inset of Figure 6.1 shows the integrated area for the 2308 cm<sup>-1</sup> peak as a function of the number of CD<sub>3</sub>CN molecules bound to Lewis acidic Ti sites (Ti<sub>LA</sub>), determined in coverage ranges (CD<sub>3</sub>CN/Ti = 0.2–0.6) that correspond to equimolar titrant-to-site binding stoichiometry. Integrated 2308 cm<sup>-1</sup> peak areas increase linearly with the amount of CD<sub>3</sub>CN adsorbed onto Lewis acidic Ti sites, and in an equivalent proportion for three Ti-Beta samples of different Ti content and synthetic origin (Ti-Beta-F-155, Ti-Beta-F-135, and Ti-Beta-OH-38). This proportion reflects the integrated molar extinction coefficient for this IR peak ( $E(2308\text{ cm}^{-1}) = 3.01 \pm 0.60\text{ cm } \mu\text{mol}^{-1}$ ) via Eq. 6.1. This  $E(2308\text{ cm}^{-1})$  value was then used to quantify Lewis acidic Ti sites on each Ti-Beta sample after saturation with CD<sub>3</sub>CN and deconvolution of IR spectra (Figure 6.20, Supp. Info.). Site quantification values are reported in Table 6.1 as the fraction of Lewis acidic Ti sites titrated by CD<sub>3</sub>CN (per total Ti). Dichloromethane-assisted grafting of TiCl<sub>4</sub> within framework vacancies of dealuminated Beta zeolites formed Ti-Beta-OH samples that generally contained higher fractions of Lewis acidic Ti sites (0.40–1.00, Table 6.1) than fluoride-assisted, hydrothermally synthesized Ti-Beta-F samples (0.24–0.62, Table 6.1). The numbers of Lewis acid sites quantified by CD<sub>3</sub>CN on these Ti-Beta samples are consistent with the numbers quantified by pyridine titration (0.38–1.03 Lewis acid sites per Ti,  $E(1605\text{ cm}^{-1}) = 1.16 \pm 0.23\text{ cm } \mu\text{mol}^{-1}$ , details in Section 6.6.1.2, Supp. Info.). The fraction of Lewis acidic Ti species are below unity for most samples, necessitating

such site quantification techniques to normalize catalytic rate measurements, since residual Ti species reflect small TiO<sub>2</sub> domains that do not contribute to measured glucose-fructose isomerization rates [53].

Exposure to higher CD<sub>3</sub>CN pressures gives rise to IR peaks centered at 2275 cm<sup>-1</sup> that reflect CD<sub>3</sub>CN bound to silanol defects (Figure 6.18, Supp. Info.). Using an integrated molar extinction coefficient ( $E(2275 \text{ cm}^{-1}) = 0.74 \pm 0.16 \text{ cm } \mu\text{mol}^{-1}$ ) determined previously from CD<sub>3</sub>CN IR spectra of a dealuminated Beta sample [56], the total number of silanol defects was estimated for each Ti-Beta sample and listed in Table 6.2.

Silanol groups are present in significantly higher densities ( $\sim 4\text{--}100\times$ ) on Ti-Beta-OH than on Ti-Beta-F samples, as expected for Ti-Beta-OH samples that contain silanol groups formed during the hydrothermal synthesis of the parent Al-Beta zeolite in hydroxide media and silanol nest defects that remain after partial grafting with Ti precursors. CD<sub>3</sub>CN does not discriminate between silanol groups located within microporous voids from those located at extracrystalline surfaces, which may be present in higher concentrations on smaller Ti-Beta-OH crystallites than on larger Ti-Beta-F crystallites ( $\sim 0.9 \mu\text{m}$  vs.  $7.5 \mu\text{m}$ , Figures 6.11–6.13, Supp. Info.). These total silanol concentrations, however, do not correlate with external crystallite surface areas among the Ti-Beta-F and Ti-Beta-OH samples studied here (details in Section 3.6.1.3, Supp. Info.), implying that higher defect densities are present within the microporous channels of Ti-Beta-OH.

From these characterization data, we conclude that the synthesized Ti-Beta-F and Ti-Beta-OH samples are crystalline Beta zeolites that contain varying quantities of Ti atoms located within framework positions and that behave as Lewis acid centers. Furthermore, CD<sub>3</sub>CN titration experiments indicate that Ti-Beta-OH samples contain significantly higher bulk silanol densities than Ti-Beta-F samples. We next use a suite of adsorption and spectroscopic probes that are sensitive to the location of silanol groups within microporous voids, to provide evidence that the density of silanol defects is higher within the microporous voids of Ti-Beta-OH than Ti-Beta-F.

### 6.3.2 Characterization of Hydrophobic Properties of Ti-Beta Zeolites

In this section, we compare the polarity of microporous voids in Ti-Beta-F and Ti-Beta-OH samples by combining semi-quantitative assessments of vapor-phase water and methanol adsorption isotherms with structural assessments of adsorbed water phases from IR spectra collected in the presence of water vapor. Taken together, these data reveal differences in the intraporous density of polar silanol groups within microporous voids of Ti-Beta-F and Ti-Beta-OH and in the structures of water stabilized within these voids.

#### 6.3.2.1 Semi-Quantitative Assessments of Hydrophobicity using Vapor-Phase Adsorption Isotherms

Water adsorption isotherms provide an assessment of the hydrophobic properties of zeolitic surfaces, as bulk water uptakes increase with the density of polar defect sites (e.g., framework heteroatoms, hydroxyl groups) located in otherwise non-polar siloxane frameworks [56,151]. Vapor-phase water adsorption isotherms of Ti-Beta-F samples (Figure 6.24, Supp. Info.) show water uptakes similar to Si-Beta-F (within  $2.5\times$ , 293 K,  $P/P_0 = 0-0.6$ ), suggesting that surfaces with low defect densities are also present within Ti-Beta-F micropores [173]. Table 6.2 summarizes the total water uptake per gram at  $P/P_0 = 0.2$ , a parameter that allows for semi-quantitative comparison of hydrophobicity among samples and which corresponds to the reduced pressure required for micropore filling of cyclohexane within hydrophobic MOR zeolites [171]. Table 6.2 also summarizes the residual water uptakes after subtraction of two water molecules adsorbed per Lewis acid site, a stoichiometry that has been observed experimentally from gravimetric and microcalorimetric studies on Ti-Beta zeolites for water adsorption on isolated framework Ti sites [305]. Water uptakes (per g) at a given reduced pressure are systematically higher on Ti-Beta-F than on Si-Beta-F samples but are similar (within  $1.5\times$ ) after accounting for two water molecules adsorbed onto Lewis acidic Ti site. These low water uptakes ( $V_{\text{ads}}(\text{H}_2\text{O})/V_{\text{ads}}(\text{N}_2) = 0.001-$

0.011, Table 6.2) reflect the hydrophobic nature of intraporous void environments, consistent with water intrusion studies in defect-free siliceous Beta zeolites that require significantly higher water pressures (57 MPa) for pore filling [325]. Hydrophobic channels in Beta zeolites ( $\sim 0.7$  nm diameter) mitigate the formation of bulk water structures under ambient conditions because polar surface groups capable of hydrogen bonding are absent [173], consistent with findings from experimental studies of defect-free carbon nanotubes ( $< 1$  nm diam.) [41] and from computational studies identifying the presence of only vapor-phase water between hydrophobic pure-silica surfaces positioned 0.7 nm apart [37].

Among the Ti-Beta-OH samples studied here, vapor-phase water adsorption isotherms (Figure 6.25, Supp. Info.) showed water uptakes that were  $10\text{--}40\times$  higher than on Ti-Beta-F samples (293 K,  $P/P_0 = 0\text{--}0.6$ ) after accounting for two water molecules adsorbed onto each Lewis acid site (Table 6.2). These order of magnitude higher water uptakes indicate the presence of additional water adsorption sites on Ti-Beta-OH samples, which have  $\sim 4\text{--}100\times$  higher silanol defect densities than Ti-Beta-F as measured by  $\text{CD}_3\text{CN}$  IR (Table 2). Indeed, a linear correlation between total silanol concentration (per g) and water uptake (per g,  $P/P_0 = 0.2$ ) is observed among all Ti-Beta-F and Ti-Beta-OH samples studied (Figure 6.26, Supp. Info.), which has previously been noted among Sn-Beta samples [56] and among H-form FAU, MFI and Beta samples [66]. These findings are qualitatively consistent with computational studies indicating that extended water structures (up to 27 molecules) can be stabilized when two adjacent silanol defects are present between hydrophobic  $\text{SiO}_2$  plates positioned 0.7 nm apart [37]. These water adsorption uptakes and silanol density measurements reflect bulk properties of zeolite samples, however, and do not provide direct information about the density of silanol defects within microporous environments.

In contrast to water, methanol fills microporous voids in both low-defect and high-defect samples, but with distinct adsorption behavior. Methanol adsorption isotherms (293 K) on low-defect Ti-Beta-F samples show Type V isotherm behavior (Figure

6.27, Supp. Info.), reflecting micropore condensation driven by adsorbate-adsorbate interactions that are stronger than adsorbate-adsorbent interactions of methanol with non-polar framework siloxane linkages [151, 173, 227, 326], as observed previously for ethanol within hydrophobic Ti-Beta-F [173] and Si-MFI [327]. In contrast, methanol adsorption isotherms on Ti-Beta-OH materials show Type I isotherm behavior (Figure 6.28, Supp. Info.), reflecting micropore condensation driven by strong adsorbate-adsorbent interactions through methanol hydrogen bonding interactions with specific binding sites located on micropore walls. These adsorption sites are not Lewis acidic Ti sites, evident from the direct comparison of Ti-Beta-F-155 and Ti-Beta-OH-71, which contain similar Lewis acid site densities (0.26 and 0.50 per unit cell, respectively, Table 6.1) but show significant differences in adsorption behavior. The Type I isotherms on Ti-Beta-OH therefore reflect the presence of silanol defects located within microporous channels that hydrogen bond with methanol, while the Type V isotherms on Ti-Beta-F reflect essentially undetectable amounts of silanol groups or other hydrogen bonding moieties located within the microporous channels of Ti-Beta-F [35].

#### 6.3.2.2 Spectroscopic Characterization of Co-adsorbed Water Structures using Transmission IR

Transmission IR spectroscopy was used to probe differences in the vibrational signatures and extended structures of adsorbed water on Ti-Beta-F-155 and Ti-Beta-OH-46, which are representative Ti-Beta-F and Ti-Beta-OH samples from bulk characterization data, Lewis acid site densities, and glucose-fructose isomerization rate measurements (see Tables 6.1 and 6.2 and Section 6.3.3). Figures 2A and 2B show IR spectra collected on Ti-Beta-F-155 and Ti-Beta-OH-46 after removing background contributions for water vapor present in the cell and subtracting the spectrum of dehydrated zeolite samples (full spectra in Figure 6.29, Supp. Info.). Upon equilibration in flowing water, two prominent features appear as positive broad peaks in

the 1500–1750  $\text{cm}^{-1}$  range and the 2600–3700  $\text{cm}^{-1}$  range, while a third negative peak appears centered around 3735–3745  $\text{cm}^{-1}$ .

Figure 6.2A shows the IR peak centered between 1615–1630  $\text{cm}^{-1}$ , which reflects

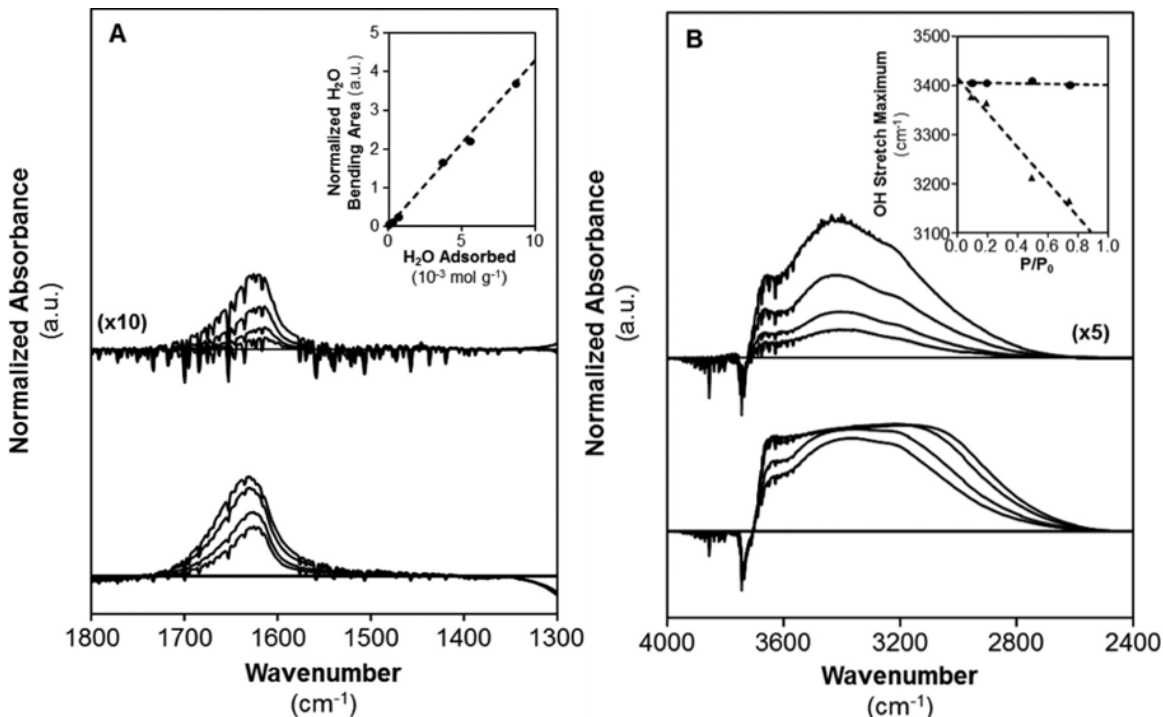


**Figure 6.2:** Baseline-corrected difference IR spectra of adsorbed water on Ti-Beta-F-155 (top, magnified for clarity) and Ti-Beta-OH-46 (bottom) at 298 K for (a)  $\delta(\text{HOH})$  scissoring modes in the water bending region and (b) the  $\nu(\text{O-H})$  water stretching region. Difference spectra reflect the subtraction of spectrum measured on the sample under vacuum prior to water flow and corrected for background water adsorption onto the IR cell. Spectra for each sample displayed from bottom-to-top correspond to  $P/P_0=0.1, 0.2, 0.5,$  and  $0.75$ . The insets display the change in (a) the water bending peak area and (b) the water stretching peak maximum with increasing water concentration for Ti-Beta-F-155 ( $\bullet$ ) and Ti-Beta-OH-46 ( $\blacktriangle$ ).

the  $\delta(\text{H-O-H})$  scissoring mode of adsorbed water [328]. This peak does not significantly change shape or center with increasing water uptake. The integrated area of this peak is proportional to the total water uptake (at equivalent reduced pressures) estimated from vapor-phase adsorption experiments (298 K, Figure 6.30, Supp. Info.), as shown in the inset of Figure 6.2A. The linear relation in the inset of Figure 6.2A

establishes a direct connection between the total water uptake and each IR spectrum as quantified through the integrated area of the 1615–1630  $\text{cm}^{-1}$  peak.

Figure 6.2B shows a negative peak (3735–3745  $\text{cm}^{-1}$ ) on both samples reflecting a convolution of two peaks centered at 3745  $\text{cm}^{-1}$  and 3735  $\text{cm}^{-1}$  for OH stretching modes of external and internal silanol groups, respectively [329]. These features appear as negative peaks because hydrogen bonding interactions between adsorbed water and hydroxyl groups perturb silanol O-H stretches, giving rise to the broad positive peak centered around 3400  $\text{cm}^{-1}$ . Difference spectra on Ti-Beta-OH-46 do not show further changes to the negative peak areas at 3745  $\text{cm}^{-1}$  and 3735  $\text{cm}^{-1}$  at relative water pressures of  $P/P_0 \geq 0.2$ , indicating that the hydroxyl groups are fully perturbed by hydrogen-bonded water by  $P/P_0 = 0.1$  (Figure 6.31, Supp. Info.). Therefore, subsequent adsorption of water above this relative pressure occurs via hydrogen-bonding with other water molecules already present within the channels, rather than through additional adsorption at silanol defects. In contrast, the silanol groups on Ti-Beta-F-155 continue to be perturbed gradually across a wider range of water pressures ( $P/P_0 = 0.1$ – $0.75$ , Figure 6.31, Supp. Info.), indicating that water adsorption continues to occur at silanol defects. These observations are consistent with lower water uptakes from vapor-phase adsorption isotherm experiments, suggesting that water does not fill the micropores of Ti-Beta-F-155 under these conditions. Hence, water adsorbs within Ti-Beta-F at low intraporous densities (0.01–0.16 mol  $\text{H}_2\text{O g}^{-1}$ , Table 6.2) because it predominantly adsorbs at framework Ti sites, but within Ti-Beta-OH with higher intraporous water densities (1.4–4.9 mol  $\text{H}_2\text{O g}^{-1}$ , Table 6.2) because it adsorbs at both framework Ti atoms and silanol defects.

The OH stretching vibrations from adsorbed water molecules are convoluted with the perturbed silanol peak in the 2600–3700  $\text{cm}^{-1}$  range, yet differences regarding the structure of adsorbed water in Ti-Beta-OH-46 and Ti-Beta-F-155 are readily apparent. With increasing water partial pressure ( $P/P_0 = 0.1$ – $0.75$ ), the peak maximum in the OH stretching region monotonically shifts from 3375  $\text{cm}^{-1}$  to 3190  $\text{cm}^{-1}$  on Ti-Beta-OH-46 (Figure 6.2B inset). Shifts in OH stretching frequency to lower wavenumbers

reflect greater extents of hydrogen bonding between water molecules [38, 330], suggesting that adsorbed water molecules within Ti-Beta-OH-46 become arranged in extended hydrogen bonding networks that grow with increasing water partial pressure. In addition, this broad peak for adsorbed water can be deconvoluted into two major components centered in either the  $\sim 3000\text{--}3100\text{ cm}^{-1}$  range or the  $3630\text{--}3665\text{ cm}^{-1}$  range. The latter peak ( $3630\text{--}3665\text{ cm}^{-1}$ ) has been assigned to loosely-bound water in one-dimensional chains which are similar in their extent of hydrogen bonding to vapor-phase water located within non-polar carbon nanotubes ( $<0.8\text{ nm}$  in diameter) [38] similar in size to Beta micropores. Thus, the continued presence of this peak at higher water partial pressures ( $P/P_0 \geq 0.2$ ) indicates that some water molecules are occluded within microporous voids and can plausibly be considered vapor-like. The peak ranging from  $\sim 3000\text{--}3100\text{ cm}^{-1}$  is shifted to lower wavenumbers than that of OH stretches in bulk ice ( $3220\text{--}3250\text{ cm}^{-1}$ ) [331], reflecting contributions of water molecules in extended hydrogen bonding networks. As the water partial pressure increases, this peak becomes more prominent and eventually reflects the hydrogen-bonded structure of the majority of occluded water molecules within the channels of Ti-Beta-OH-46.

The structure of water adsorbed within Ti-Beta-F-155 sharply contrasts that of Ti-Beta-OH-46. First, the water OH stretching peak center remains constant at  $\sim 3400\text{ cm}^{-1}$  in Ti-Beta-F-155 with increasing water partial pressure (Figure 6.2B inset), reflecting weaker contributions from strongly hydrogen bound water stretches in the  $\sim 3000\text{--}3100\text{ cm}^{-1}$  range. This provides evidence that adsorbed water molecules in Ti-Beta-F-155 do not significantly increase their extent of hydrogen bonding with increasing water pressure, nor do they form the extended water structures observed in Ti-Beta-OH-46. Indeed, further adsorption of water perturbs additional silanol groups throughout this partial pressure range, evident in increasingly negative peak area for the peak centered at  $3735\text{--}3745\text{ cm}^{-1}$  and in increasingly positive peak area for the peak centered at  $\sim 3400\text{ cm}^{-1}$  (Figure 6.31, Supp. Info.). A small shoulder present at  $\sim 3100\text{ cm}^{-1}$  in the difference spectra of Ti-Beta-F-155 (Figure 6.2B) increases

in area with increasing water partial pressure, however, indicating that some water molecules adsorb via hydrogen bonding in locations with proximal water molecules, but to a much lesser extent than in Ti-Beta-OH-46. The significantly lower water uptakes (Figure 6.30, Supp. Info.) suggest that the lower silanol defect density in Ti-Beta-F-155 ( $1.9 \times 10^{-4}$  mol SiOH  $\text{g}^{-1}$ , Table 6.2) is insufficient to nucleate the formation of extended hydrogen-bonded water structures within the pores, in contrast to the behavior of water adsorption on Ti-Beta-OH-46 ( $7.0 \times 10^{-4}$  mol SiOH  $\text{g}^{-1}$ , Table 6.2).

From these characterization data in Sections 3.1 and 3.2, we conclude that the series of samples investigated here contain Ti centers isolated within Beta molecular sieve frameworks over a wide range of Ti content ( $\text{Si}/\text{Ti} = 38\text{--}297$ ) and residual silanol defect densities ( $\text{SiOH}/\text{Ti}_{\text{LA}} = 2.0\text{--}10$ , Table 6.2). Water adsorbs preferentially within zeolite Beta micropores at framework Ti atoms, and at surface silanol groups via hydrogen bonding. Methanol adsorption isotherms indicate that Ti-Beta-OH has a significantly higher intrapore silanol defect density than Ti-Beta-F, leading to increased water uptakes and the stabilization of extended hydrogen bonding water structures within their microporous voids. In order to determine the kinetic consequences of these intraporous silanol defects and the extended solvent structures they stabilize, we next interrogate Ti-Beta-F and Ti-Beta-OH samples using aqueous-phase glucose isomerization as a catalytic probe reaction.

### 6.3.3 Aqueous-Phase Glucose Isomerization Mechanisms and Kinetic Measurements

In this section, we combine insights from experiment and theory to elucidate the underlying phenomena that lead to differences in measured reaction kinetics for Lewis acid-catalyzed glucose isomerization in low-defect and high-defect Ti-Beta zeolites. We use a mechanistic model to identify key differences in glucose isomerization reaction coordinates in terms of free energies of reactive intermediates and transition states that are influenced by intrapore silanol defects and the extended solvent structures they stabilize.

## 6.3.3.1 Mechanistic Details of Lewis Acid-Catalyzed Glucose Isomerization

Figure 6.3 shows the free energy reaction coordinate diagram for glucose-fructose

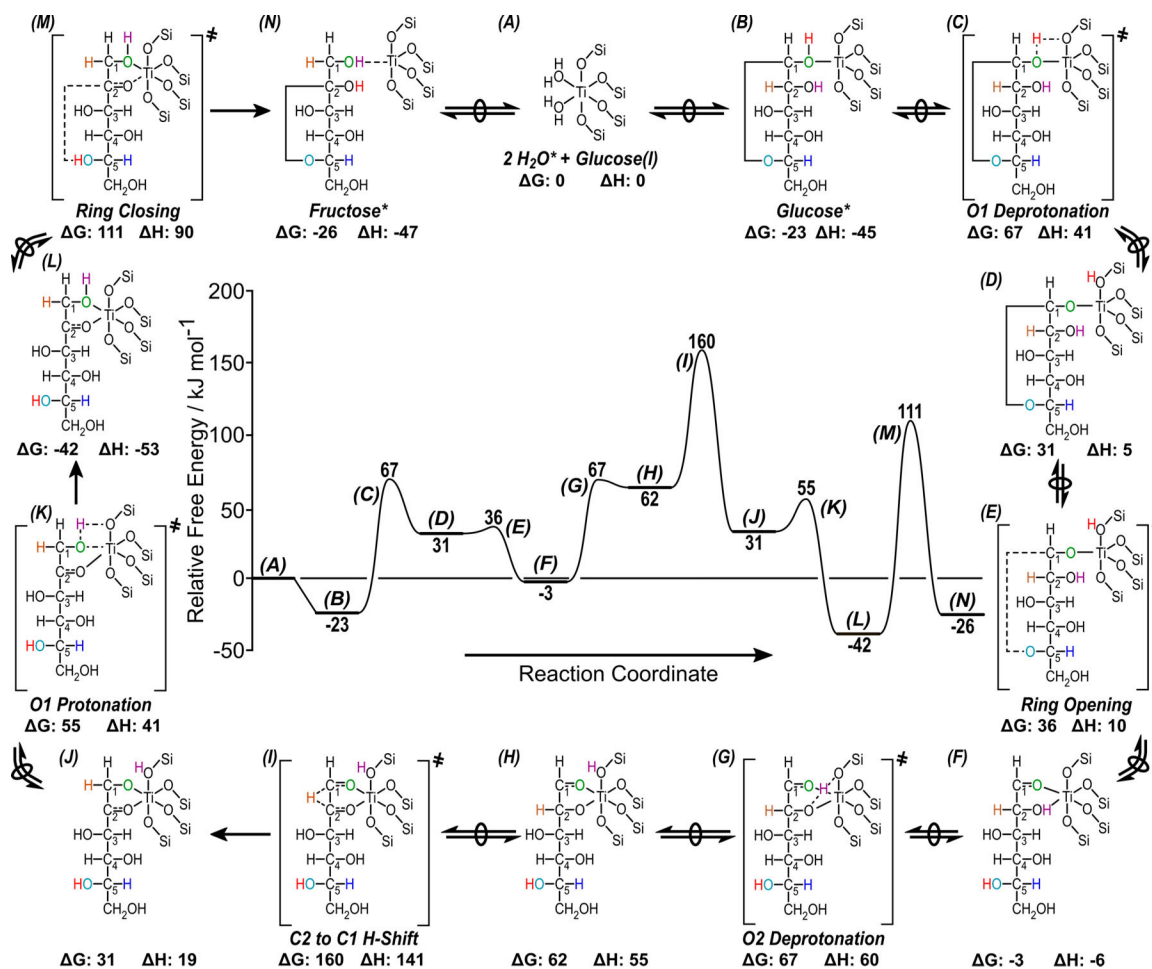


**Figure 6.3:** Free energy (373 K, 1 bar) reaction coordinate diagram for the formation of fructose from glucose on closed-form Ti Lewis acid sites. Reaction arrows with overlaid circles indicate quasi-equilibrated events or the formation of transition states from relevant precursors. Relative enthalpies are given near inset images.

isomerization calculated over a framework coordinated, closed Lewis acidic Ti site at the T6 position in Beta through a mechanism similar to those reported in previous experimental and theoretical studies [68, 310]. Lewis acid-catalyzed glucose isomerization to fructose occurs through quasi-equilibrated adsorption of glucose onto Lewis acid sites through the hemiacetal oxygen (O5), quasi-equilibrated deprotonation of

O1 (States B–D, Figure 6.3), followed by protonation of the ring ether oxygen (O5) to facilitate ring opening to form the acyclic, or open-chain, glucose intermediate bound through the carbonyl moiety (States D–F, Figure 3) [68]. Subsequent deprotonation of the C2 alcohol to a proximal proton acceptor, such as a nearby framework oxygen, generates a glucose intermediate that can bind to the Lewis acid site in a bidentate fashion (States F–H, Figure 6.3). Glucose deprotonation and ring-opening steps have kinetically-irrelevant barriers, consistent with previous findings [68]. The open-chain glucose intermediate then undergoes a kinetically-relevant 1,2-hydride shift to form a bound acyclic fructose intermediate, an elementary step that has the largest computed free energy barrier in the reaction coordinate (States H–J, Figure 6.3) [68,101]. Protonation of the fructose C1 alcohol, ring closure, and desorption of fructose from the Lewis acid site closes the catalytic cycle via kinetically-irrelevant steps. The overall free energy barrier to form fructose from desorbed glucose is  $160 \text{ kJ mol}^{-1}$  (373 K) when using ring-closed glucose in crystalline ice as the reference state for desorbed glucose. The overall free energy barrier from the adsorbed glucose state is  $183 \text{ kJ mol}^{-1}$  (373 K). This Lewis acid-catalyzed intramolecular 1,2-hydride shift mechanism is dominant over the base-catalyzed enolate mechanism under the conditions studied here, as reported in previously published isotopic tracer studies (see Figure 6.32, Supp. Info., for  $^{13}\text{C}$  NMR spectra of monosaccharide products) [91].

Glucose isomerization over Ti-Beta zeolites also forms sorbose, which is a second monosaccharide product formed through a parallel pathway and reaction mechanism analogous to that of fructose formation (free energy reaction coordinate diagram in Figure 6.33, Supp. Info.) [92]. Isomerization to sorbose involves quasi-equilibrated glucose adsorption, deprotonation of the O1 alcohol moiety, and ring opening to form a bidentate-bound glucose-derived intermediate through O1 and O5 (States B–D, Figure 6.33, Supp. Info.). This is followed by a kinetically-relevant 1,5-hydride shift step (States D–F, 6.33, Supp. Info.), as previously observed by isotopic tracer studies on  $^2\text{H}$ - and  $^{13}\text{C}$ -labeled glucose [92] and confirmed in this work (see Figure 6.32, Supp. Info., for  $^{13}\text{C}$  NMR of monosaccharide products). The 1,5-hydride shift transition

state that forms sorbose is analogous to the 1,2-hydride shift that forms fructose, in that both involve six-membered ring structures and a C-H bond scissoring mode along the reaction coordinate. The catalytic cycle for sorbose formation is closed via protonation, ring closure, and desorption (States F–H, H–J, and J–A, respectively, Figure 6.33, Supp. Info.). The overall free energy barrier relative to the desorbed glucose state is  $154 \text{ kJ mol}^{-1}$  (373 K) and suggests that the 1,5-hydride shift is the sole kinetically relevant step, as expected [92]; all other barriers are at least  $25 \text{ kJ mol}^{-1}$  lower. Free energy barriers for fructose and sorbose formation are similar within the error of DFT, as expected for two parallel reactions with reported initial rates within one order of magnitude [53, 92].

While the exact binding coordination [332], adsorption configurations [310], and site requirements [101, 111] associated with glucose isomerization to fructose and sorbose continue to be studied computationally and experimentally, the kinetic relevance of their respective hydride shift transition states can be experimentally detected through measurement of the H/D kinetic isotope effect (KIE) [53, 68]. KIE values reflect differences in the vibrational frequency and zero-point energy upon isotopic substitution of atoms in bonds that are broken along the reaction coordinate (derivation in Section 6.6.3.2, Supp. Info.). Deuteration of the alpha-carbon in glucose reactants results in measured glucose-fructose isomerization H/D KIE values of 2.1–2.3 ( $\pm 0.2$ , 373 K) on both Ti-Beta-F and Ti-Beta-OH samples throughout the range of glucose concentrations studied here (0–50 wt% glucose). These values are consistent with theoretical H/D KIE values expected for transition state reaction coordinates involving C-H bond scissoring ( $\sim 1500 \text{ cm}^{-1}$ ), consistent with the 1,2-hydride shift steps confirmed from isotopic tracer studies [91, 153]. Measured KIE values of 2.1 also indicate that intrazeolitic transport artifacts do not corrupt measured rates, which would otherwise result in measurement of the square root of the theoretical KIE value (details in Section 6.6.3.2, Supp. Info.). Therefore, we conclude that the measured glucose-fructose isomerization rates reported here are uncorrupted by transport artifacts and reflect free energy differences between the kinetically-relevant hydride

shift transition state and the relevant adsorbed reactive intermediates. Next, we measure glucose isomerization turnover rates on a variety of Ti-Beta-F and Ti-Beta-OH samples and across a wide range of initial glucose concentrations, revealing the presence of different kinetic regimes that correspond to changes in reactive intermediate coverages.

### 6.3.3.2 Experimental Measurements of Glucose Isomerization Rate Constants on Hydrophobic and Hydrophilic Ti-Beta Zeolites

Initial glucose isomerization rates were collected on all Ti-Beta-F and Ti-Beta-OH samples at low glucose concentrations (1 wt%, 373 K), which correspond to a first-order kinetic regime in glucose concentration [53]. Apparent first-order glucose isomerization rate constants for fructose and sorbose formation are shown in Figures 6.4A and 6.4B, respectively, as a function of total Ti content for all Ti-Beta samples studied here, and compared to data for Ti-Beta samples reported previously [53] (rate constants plotted as a function of  $Ti_{LA}$  per gram in Figure 6.34, Supp. Info.). On average, first-order rate constants are systematically higher ( $\sim 6\times$ ) on Ti-Beta-F zeolites than on Ti-Beta-OH zeolites across a wide range of Ti content. First-order rate constants vary within  $\sim 3\times$  among all Ti-Beta-F zeolites, and within  $\sim 2\times$  among all Ti-Beta-OH zeolites, which are variations similar to those observed previously among Sn-Beta-F and Sn-Beta-OH zeolites of varying Sn content [56]. Furthermore, rate constants (per Ti) do not depend systematically on Ti content among Ti-Beta-F or Ti-Beta-OH zeolites, consistent with the absence of intracrystalline transport artifacts as expected from measured H/D KIE values of 2.1–2.3 (Section 3.3.1). Next, more detailed kinetic studies are performed on Ti-Beta-F-155 and Ti-Beta-OH-46, which are samples with kinetic behavior representative of the Ti-Beta-F and Ti-Beta-OH series, respectively.

Initial glucose isomerization rates were collected across a wide range of glucose concentrations (1–50 wt%) on both Ti-Beta-F-155 and Ti-Beta-OH-46. Thermodynamic activities for glucose and water are used here to describe rate data at high glu-

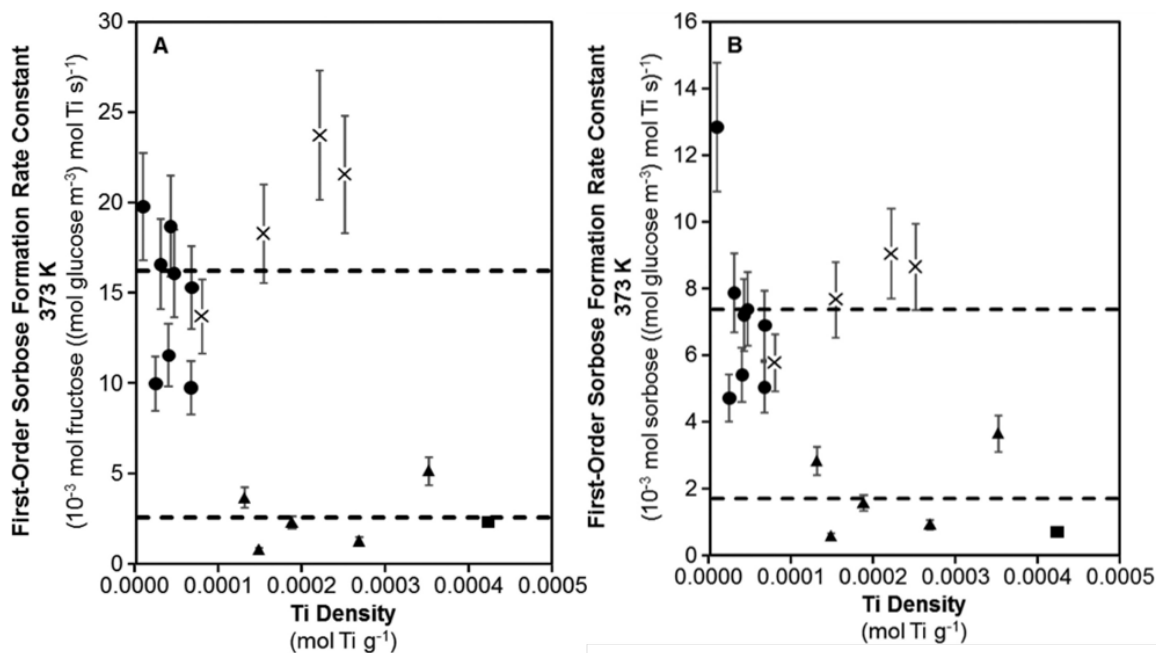


**Figure 6.4:** Initial first-order (a) fructose and (b) sorbose formation rates (373 K, pH 4) normalized per total Ti content as a function of Ti/Si ratio, for Ti-Beta-F (●) and Ti-Beta-OH samples (▲). Data on Ti-Beta-F (×) and Ti-Beta-OH (■) samples reported previously in Ref. [307] are plotted for comparison. Dashed lines correspond to average values within the series of Ti-Beta-F and Ti-Beta-OH samples.

cose concentrations due to expected non-ideal solution behavior that affects reaction rates [333]. Non-ideality was accounted for using solution-phase activity coefficients ( $\gamma_i$ ) which are unity under ideal conditions and diverge from unity at non-dilute glucose concentrations. Activity coefficients for aqueous glucose solutions (1–52 wt%) reported at 298 K [334] were adjusted to reaction temperatures using the following equation (details in Section 6.6.3.3, Supp. Info.) [335]:

$$\frac{-\overline{H}_i^E}{RT^2} = \frac{\delta}{\delta T} \ln \gamma_i \quad (6.5)$$

Here,  $\overline{H}_i^E$  is the excess partial molar enthalpy of species  $i$  in solution and is assumed to be constant with temperature,  $R$  is the universal gas constant, and  $T$  is the absolute temperature in K. Activity coefficients approach unity ( $\gamma_i \rightarrow 1$ ) as temperature

increases or glucose concentrations decrease and solutions approach ideal behavior. Thermodynamic activities ( $a_i$ ) for glucose ( $a_G$ ) and water ( $a_W$ ) were calculated using temperature-dependent and concentration-dependent activity coefficients according to the following equation:

$$a_i = \gamma_i \frac{c_i}{c^0} \quad (6.6)$$

where  $c^0$  is the standard concentration ( $1 \text{ mol m}^{-3}$ ).

The dependence of initial fructose and sorbose formation rates (373 K, per  $\text{Ti}_{\text{LA}}$ ) on the initial aqueous-phase glucose activity is shown in Figure 6.5 for Ti-Beta-F-155 and Ti-Beta-OH-46. Initial isomerization rates are 3–6 $\times$  lower on Ti-Beta-OH-46

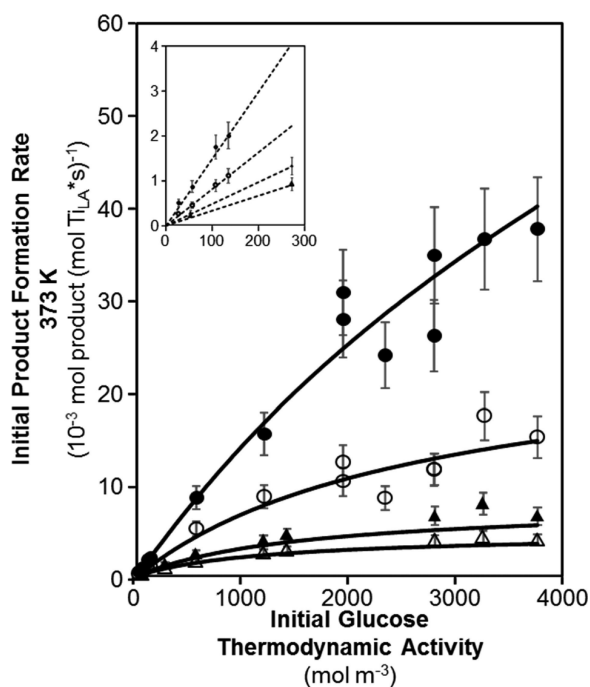


**Figure 6.5:** Dependence of initial glucose isomerization rates (373 K, pH 4) for fructose (filled) and sorbose (open) formation on Ti-Beta-F-155 ( $\bullet$ ,  $\circ$ ) and Ti-Beta-OH-46 ( $\blacktriangle$ ,  $\triangle$ ) as a function of initial glucose thermodynamic activity (corresponding to 1–50 wt% initial glucose concentration). Solid lines represent fits of the experimental data to the rate equation (Eq. 6.9) using activation enthalpies and entropies given in Table 6.4. The inset shows initial glucose isomerization rates at low glucose thermodynamic activities, highlighting the first-order kinetic regime.

than on Ti-Beta-F-155 across the full range of  $a_G$  values studied, consistent with

previously reported rates measured in dilute aqueous glucose solutions (0–1.5 wt%) [173]. Initial glucose-fructose and glucose-sorbose isomerization rates on both Ti-Beta-F and Ti-Beta-OH zeolites show a first-order kinetic dependence on glucose activity at low  $a_G$  values (50–300 mol m<sup>-3</sup>, ~1–5 wt%, Figure 6.5 inset), consistent with previously reported glucose isomerization rates on Ti-Beta [53] and Sn-Beta [56] (isomerization rates shown as a function of glucose concentration in Figure 6.35, Supp. Info.). Glucose-fructose and glucose-sorbose isomerization rates become zero-order in  $a_G$  at high  $a_G$  values (>2700 mol m<sup>-3</sup>), which is a kinetic regime that has not been previously reported to our knowledge for sugar isomerization on Lewis acidic zeolites. The onset of the zero-order kinetic regime in formation rates of both fructose and sorbose products, which are formed in parallel reaction pathways, are consistent with changes in the identities of the most abundant reactive intermediates at Lewis acid active sites and that both products are formed at the same catalytic site.

Modeling multiple kinetic regimes requires consideration of at least two distinct coverage terms, only one of which is first-order in glucose thermodynamic activity, and suggests the presence of two distinct MARI species that are dependent on glucose activities. The general form of such a rate equation is:

$$r_{\text{isom}} = \frac{k_{\text{first}} a_G}{1 + \frac{k_{\text{first}}}{k_{\text{zero}}} a_G} \quad (6.7)$$

In Eq. 6.7,  $r_{\text{isom}}$  is the initial glucose isomerization rate,  $k_{\text{first}}$  and  $k_{\text{zero}}$  are apparent first-order and zero-order rate constants, and  $a_G$  is the initial glucose thermodynamic activity. This rate equation simplifies to first-order and zero-order rate expressions at low and high  $a_G$  values, respectively. We next use spectroscopic techniques to characterize the nature of the bound intermediates as a function of glucose concentration in order to assign chemical significance to the first-order and zero-order kinetic regimes that are predicted by the generalized rate expression (Eq. 6.7).

### 6.3.4 Characterization of Active Site Complexes in First-Order and Zero-Order Kinetic Regimes

#### 6.3.4.1 Characterization of Bound Reactive Intermediates using ATR-IR and Modulation Excitation Spectroscopy (MES)

The competitive adsorption of water solvent, glucose reactants, and glucose isomerization products within microporous voids and at Lewis acidic Ti sites in Ti-Beta-F-155 and Ti-Beta-OH-46 was probed *in situ* with ATR-IR and MES. Figure 6.6A shows spectra corresponding to two independent intermediates extracted by phase sensitive detection (PSD) and multicurve resolution-alternating least squares analysis (MCR-ALS) from experiments with modulated glucose activities within the first-order kinetic regime (0–700 mol m<sup>-3</sup>, 373 K) (time resolved and phase resolved spectra on Ti-Beta-F-155 shown in Figure 6.36, Supp. Info.). These spectra collected on both Ti-Beta-F-155 and Ti-Beta-OH-46 reflect the two independent reactive intermediates observed from interactions between solid surfaces and fluid phases comprised of modulated glucose and water activities. One intermediate (Figure 6.6A, top) is characterized by water bending ( $\delta(\text{O-H})$  at 1630 cm<sup>-1</sup>) [336] and stretching ( $\nu(\text{O-H})$  around 3400 cm<sup>-1</sup>) [336] vibrations, and lacks vibrational modes representative of glucose ( $\nu(\text{C-H})$  at 2900 cm<sup>-1</sup> [337–339]; concerted vibrations at 900–1500 cm<sup>-1</sup> [337–340]), indicating that this intermediate is not derived from glucose. This species is the MARI and, because it is not glucose-derived, spectra were normalized by the water bending resonance at 1630 cm<sup>-1</sup> to facilitate comparison between samples in Figure 6.6A. The minor intermediate (Figure 6.6A, bottom) contains spectral features similar to vibrational modes of glucose, and thus was normalized by the most intense glucose resonance ( $\sim 1030$  cm<sup>-1</sup>). These features do not show significant differences from those of aqueous-phase glucose flowing over the ZnSe crystal (Figure 6.6A, bottom, dashed line), which suggests that such species are not coordinated to Lewis acidic Ti centers on Ti-Beta-F-155 and Ti-Beta-OH-46 and are likely solution-phase glucose. Together, the two species isolated from MES and sequential PSD and MCR-ALS during glucose concentration modulations at low activities ( $\sim 0$ –700 mol

$\text{m}^{-3}$ ) indicate that Ti-Beta zeolite surfaces bind a water-derived MARI species and a minor glucose species that is not coordinated to Lewis acid sites, supporting the mechanistic interpretations of first-order rate measurements at low  $a_G$  values.

Figure 6.6B shows spectra of the MARI species (bottom) and the minor intermediates (top) observed by MES at high glucose activities corresponding to zero-order kinetic regimes ( $\sim 3000\text{--}3750$  mol glucose  $\text{m}^{-3}$ ) on Ti-Beta-F-155, Ti-Beta-OH-46, Si-Beta-F, and the ZnSe crystal. Spectral features between 900 to 1500  $\text{cm}^{-1}$  in spectra of both the MARI and minor species reflect concerted  $\nu(\text{C-O})$ ,  $\nu(\text{C-C})$ ,  $\delta(\text{C-H})$ , and  $\delta(\text{C-O-H})$  [337–341] vibrations of glucose-derived intermediates. Therefore, MARI and minor intermediates are assumed to be related oxygenate structures with identical molar extinction coefficients, such that their integrated areas correlate with their relative surface coverages with MARI species existing in higher abundances in MES experiments. Relative coverages between MARI and minor species are given in Table 6.3, indicating that MARI species are present at coverages that are 1.7–5.3 $\times$  greater than the minority species.

Spectra of isolated species at high glucose activity modulations show relative changes in the quantities of water and glucose present on Ti-Beta-F-155 and Ti-Beta-OH-46 (Figure 6.6B), based on the relative intensities of vibrations from glucose-derived intermediates ( $\nu(\text{C-H})$  at 2900  $\text{cm}^{-1}$  [337–339] and concerted vibrations between 900–1500  $\text{cm}^{-1}$ ) [337–341] and of the  $\delta(\text{O-H})$  water vibrations (1630  $\text{cm}^{-1}$ ) [336]. In hydrophobic Ti-Beta-F-155, the intensity of spectral features attributed to glucose or glucose-derived intermediates (2900  $\text{cm}^{-1}$  [337–339]; 900–1500  $\text{cm}^{-1}$  [337–341]) and the intensity of features attributed to water (1630  $\text{cm}^{-1}$ ) increase concomitantly, indicating that glucose adsorption into hydrophobic Beta pores facilitates co-adsorption of water from its solvation sphere in bulk solution. This observation corroborates previous reports of co-adsorption of water with glucose in both experimental measurements of adsorbed water and glucose content (using TGA-DSC) on Sn-Beta zeolites contacted with aqueous glucose solutions [173] and theoretical Gibbs ensemble Monte Carlo simulations of glucose adsorption from aqueous solutions within hydrophobic

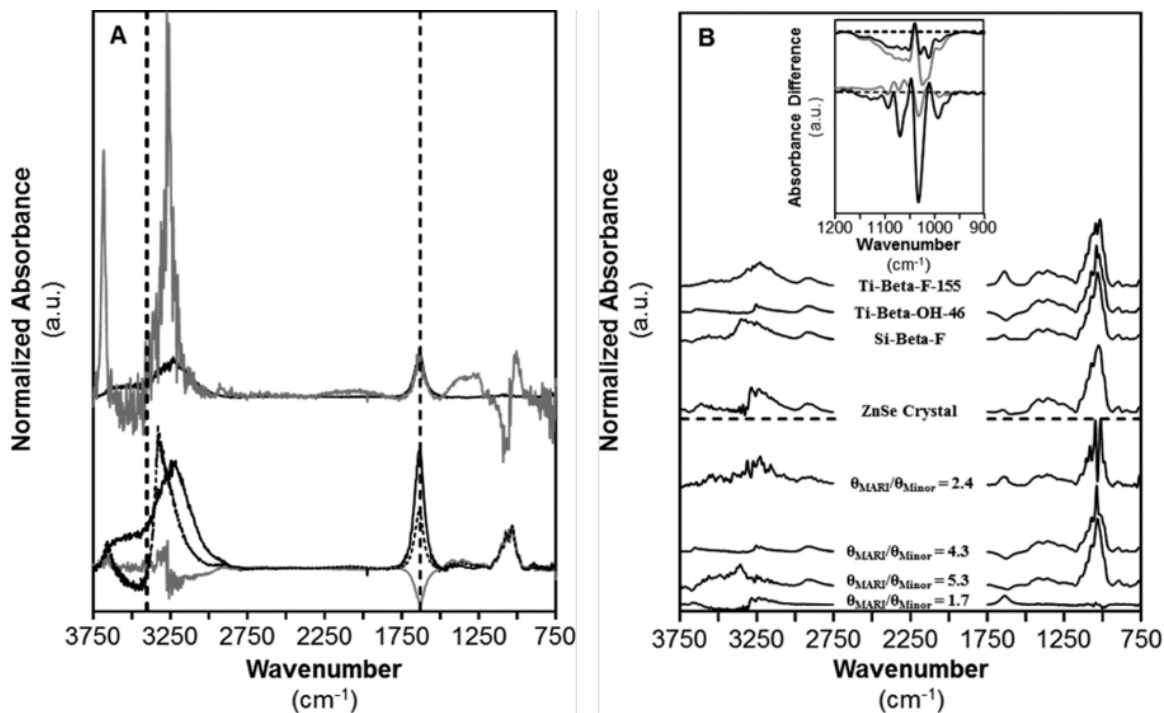


**Figure 6.6:** (a) ATR-IR spectra of MARI (top, water derived) and minor (bottom, glucose derived) intermediates on Ti-Beta-F-155 (black) and Ti-Beta-OH-46 (gray) that oscillate with aqueous-phase glucose activity ( $0\text{--}700\text{ mol m}^{-3}$ ) at  $373\text{ K}$ . Glucose spectra are normalized by the peak at  $\sim 1030\text{ cm}^{-1}$  and water spectra are normalized by the peak at  $\sim 1630\text{ cm}^{-1}$ . Spectra reflecting aqueous-phase glucose ( $330\text{ mol m}^{-3}$ ) flowing over the ZnSe crystal is overlaid on the glucose spectra (dashed). Dashed vertical lines at  $1630$  and  $3400\text{ cm}^{-1}$  indicate water bending and stretching vibrational modes, respectively. (b) ATR-IR spectra of the MARI (bottom four) and minor (top four) species that oscillate with aqueous-phase glucose activity ( $\sim 3000\text{--}3750\text{ mol glucose m}^{-3}$ ,  $373\text{ K}$ , normalized by the maximum feature at  $\sim 1030\text{ cm}^{-1}$ ) over Ti-Beta-F-155, Ti-Beta-OH-46, Si-Beta-F, and blank ZnSe crystal from top to bottom, respectively. The inset depicts difference spectra between aqueous-phase glucose flowing over the ZnSe crystal and the MARI (black) or minor species (gray) species observed on Ti-Beta-OH-46 (top) and Ti-Beta-F-155 (bottom) spectra from modulating aqueous-phase glucose activity ( $\sim 3000\text{--}3750\text{ mol glucose m}^{-3}$ ) at  $373\text{ K}$  after normalization by the peak centered at  $\sim 1030\text{ cm}^{-1}$ ; dashed lines indicate the baseline. All spectra are obtained during MES experiments and isolated by processing through PSD and MCR-ALS.

Si-Beta zeolites [342]. In contrast, spectra collected on Ti-Beta-OH-46 at identical glucose activities and temperature show that water vibrational modes decrease as

glucose vibrational modes increase, suggesting that glucose displaces water molecules previously adsorbed within hydrophilic Beta pores, consistent with the higher gas-phase water uptakes in hydrophilic than hydrophobic materials (Section 6.3.2.2). The differences in relative water and glucose activities present within the hydrophilic and hydrophobic pores indicate that the hydrophobic nature of microporous voids in Beta affect the uptakes of both water and glucose molecules.

At high glucose activities, spectra observed on Ti-Beta-F-155 and Ti-Beta-OH-46 differ from those of the blank ZnSe crystal and Si-Beta-F, indicating that the MARI species on Ti-Beta materials do not reflect solution-phase glucose or physisorbed glucose and instead are glucose-derived intermediates coordinated to Lewis acidic Ti sites within Beta pores. The vibrational features of the MARI observed on Ti-Beta-F-155 at high glucose activities differs significantly from those on Ti-Beta-OH-46 (Figure 6.6B), particularly for  $\nu(\text{C-O})$ ,  $\nu(\text{C-C})$ ,  $\delta(\text{C-H})$ , and  $\delta(\text{C-O-H})$  glucose vibrations ( $900\text{--}1200\text{ cm}^{-1}$ ) [337–341], suggesting that glucose-derived reactive intermediates are structurally distinct on hydrophobic and hydrophilic Ti-Beta zeolites (additional discussion and DFT evidence on the likely and distinct adsorbate configurations is provided in Section 6.6.4.2, Supp. Info.). The inset of Figure 6.6B shows difference spectra for the two intermediates on each Ti-Beta sample relative to those for aqueous glucose on the ZnSe crystal, which show negative features at  $\sim 1030\text{ cm}^{-1}$  that may reflect ring-opened intermediates adsorbed at Ti sites in both Ti-Beta samples. DFT-calculated intermediates that form fructose and sorbose show the loss of the  $\sim 1030\text{ cm}^{-1}$  vibrational mode upon glucose ring opening ( $1029$  and  $1027\text{ cm}^{-1}$ , respectively); however, the ring-opened intermediate that forms sorbose contains a carbonyl group with a resonance at  $1737\text{ cm}^{-1}$  that is not present in any spectra measured on Ti-Beta-F-155 or Ti-Beta-OH-46 (Figure 6.6B). Thus, both the MARI and the minor species on Ti-Beta-F-155 and Ti-Beta-OH-46 likely react to form fructose, which may be expected given the higher selectivity towards fructose over sorbose on both Ti-Beta-F-155 and Ti-Beta-OH-46 at high glucose activities (Figures 6.5 and

6.37, Supp. Info.), yet hydrophobic and hydrophilic pore environments may stabilize different reactive intermediates.

The change in MARI and minor species on both hydrophobic and hydrophilic Ti-Beta samples detected during MES and isolated by PSD and MCR-ALS between low and high glucose activities indicates that the MARI transitions from a water-derived to a glucose-derived intermediate bound to framework Ti atoms, consistent with measured glucose isomerization rates that transition from a first-order to a zero-order kinetic regime with increasing glucose thermodynamic activity (Figure 6.5). Further, the MARI species identified at high  $a_G$  values have distinct binding configurations on Ti-Beta-F and Ti-Beta-OH, which depend on the different solvating environments provided by silanol groups and co-adsorbed water structures in hydrophobic and hydrophilic environments. Next, we use *ex situ* XAS to further characterize the structure of the adsorbed species on Ti-Beta observed after exposure to low and high glucose activities.

#### 6.3.4.2 Ti Structural Characterization using XAS

In order to provide corroborating evidence for the predominant reactive intermediates proposed to exist at low and high glucose thermodynamic activity, we use XAS to determine Ti coordination numbers and Ti-O bond lengths in the presence and absence of adsorbed glucose intermediates. Apparent first-order isomerization rates measured at low glucose activities are consistent with dilute glucose coverages. EXAFS spectra collected on Ti-Beta-OH-46 (a sample with predominantly Lewis acidic Ti sites ( $Ti_{LA}/Ti \sim 1$ )) show that Ti sites are octahedrally coordinated at ambient temperature ( $CN = 6 \pm 0.6$ , Table 6.8 and Figures 6.38–6.40, Supp. Info.) and become tetrahedrally coordinated upon heating to 523 K in flowing helium ( $CN = 4 \pm 0.4$ ), consistent with previous reports on Ti-Beta [52] and the reversible adsorption of water to framework Ti sites upon exposure to ambient conditions. Ti-O bond lengths derived from EXAFS are similar to framework bond distances for dehydrated Lewis acid sites. The loss of two ligands upon heating reflects desorption of two water

molecules from each Lewis acidic Ti site. UV-Visible edge energies derived from Tauc plots also increase upon dehydration (523 K) by 0.22 eV on average (Table 6.6 and Figure 6.15, Supp. Info.), indicative of octahedral to tetrahedral coordination changes of Ti sites. Similar findings from EXAFS spectra [108,226] and UV-Visible edge energies [56] have been reported on Sn-Beta catalysts, in which the shift from octahedral to tetrahedral coordination upon dehydration is corroborated by  $^{119}\text{Sn}$  NMR spectra that show the shift from octahedrally coordinated Sn resonances (685–700 ppm) to tetrahedral Sn resonances (425–445 ppm) upon dehydration at 423 K [68,112]. Thus, we conclude that apparent first-order kinetic regimes measured at low glucose activity correspond to glucose isomerization rates measured on Ti sites covered with two water molecules [68,112], the most abundant reactive intermediate under these reaction conditions [53].

*Ex situ* XANES spectra (Figures 6.41 and 6.42, Supp. Info.) at ambient conditions most closely resemble octahedrally coordinated Ti sites (CN = 6, Table 6.8, Supp. Info.) on glucose-adsorbed Ti-Beta-OH-46. After dehydration treatments in flowing helium (523 K, 30 min), Ti sites became pentahedrally coordinated (CN = 5, Table 6.8, Supp. Info.), indicating the loss of one ligand per Ti site. This may reflect a change from bidentate to monodentate binding modes of glucose or desorption of one water molecule if glucose were originally bound in a monodentate fashion. The presence of pentahedrally coordinated Ti sites that persist after dehydration treatments would be consistent either with complete coverage of all Ti sites with a strongly bound intermediate (e.g., monodentate glucose) or with a mixture of sites in which some remain six-coordinate and populated by a strongly bound bidentate glucose intermediate and others revert to four-coordinate upon desorption of water ligands at 523 K. Although XAS cannot distinguish between these possibilities, the ATR-IR experiments show that Lewis acidic Ti sites in both Ti-Beta-OH-46 and Ti-Beta-F-155 are saturated with bound glucose intermediates at high glucose activities ( $>3000 \text{ mol m}^{-3}$ ) that are characteristic of the zero-order kinetic regime observed in Figure 6.5. Therefore, we propose that the octahedrally coordinated Ti sites observed

after glucose adsorption reflect monodentate-bound glucose and one water ligand, and that the pentahedrally coordinated Ti sites observed after dehydration results from desorption of the water ligand.

Combining insights from *in situ* ATR-IR, *ex situ* XAS and DFT calculations, we conclude that two different reactive species are dominant at low ( $\sim 0\text{--}500\text{ mol m}^{-3}$ ) and high glucose activities ( $>3000\text{ mol m}^{-3}$ ). The most abundant reactive intermediates are two water molecules bound to Lewis acid centers at low glucose activities and bound glucose intermediates (in two different binding configurations) at high glucose activities. The bound glucose intermediates are distinct for Ti-Beta-F and Ti-Beta-OH, evidenced by shifts in IR peak centers and relative peak areas that are likely caused by the presence of extended solvent structures surrounding the adsorbed glucose.

### 6.3.5 Enthalpic and Entropic Consequences of Hydrophobic Reaction Pockets for Aqueous-Phase Glucose Isomerization

In this section, experimentally measured activation enthalpies and entropies on Ti-Beta-F and Ti-Beta-OH are compared with DFT-derived free energies to probe the consequences of intrapore silanol defects, and the co-adsorbed water structures they stabilize, on aqueous-phase glucose isomerization catalysis.

#### 6.3.5.1 Experimentally-Determined Activation Enthalpies and Entropies

A reaction mechanism is shown in Figure 6.7 depicting glucose isomerization pathways to fructose and to sorbose via quasi-equilibrated water adsorption and desorption, glucose adsorption, ring opening, deprotonation, and the kinetically-relevant hydride shift steps, and is adapted from previously published work [53]. Having identified the dominant reactive intermediates at both low and high glucose thermodynamic activities in Section 6.3.4, the following rate equation can be derived from

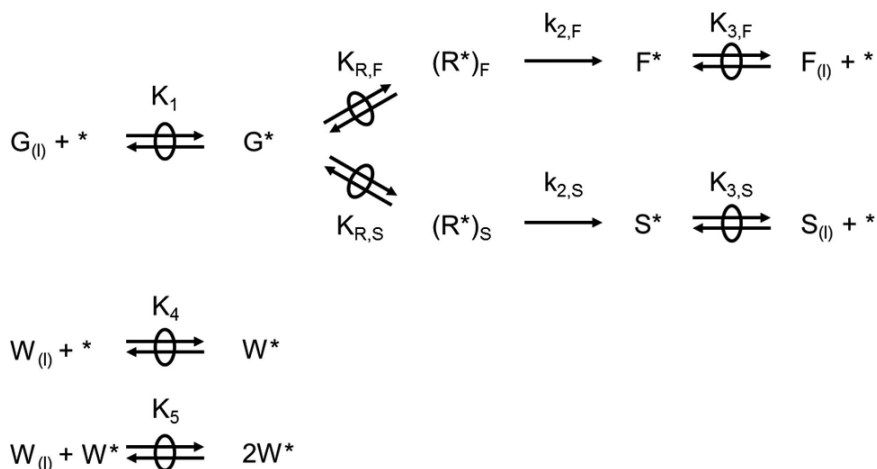


**Figure 6.7:** Plausible Glucose Isomerization Mechanism for Fructose and Sorbose formation on Lewis Acidic Ti Sites. Modified from Ref. [307] and shown in greater detail in Figures 6.3 and 6.33, Supp. Info. Quasi-equilibrated glucose adsorption (Step 1) forms reactive bound glucose intermediates ( $(R^*)_F$  and  $(R^*)_S$ ) which form bound fructose (Step 2a) or sorbose (Step 2b) isomers through the formation of kinetically relevant hydride shift transition states. Quasi-equilibrated fructose (Step 3,F) and sorbose (Step 3,S) desorption phenomena release the product into the liquid phase. Quasi-equilibrated water adsorption onto Lewis acidic active sites (Steps 4 and 5) inhibits isomerization rates at low glucose coverages.

the mechanism in Figure 6.43 to recover both first-order and zero-order dependences on glucose activity (complete derivation in Section 6.6.5.1, Supp. Info.):

$$r_i = \frac{K_1 K_{R,i} k_{2,i} \frac{a_G}{\gamma_{\ddagger,i}} (1 - \eta_i)}{\frac{K_4 K_5 a_W^2}{\gamma_{2W^*}} + \frac{K_1 a_G}{\gamma_{G^*}}} \quad (6.8)$$

In Eq. 6.8,  $i$  stands for fructose or sorbose,  $K_1$  is the lumped equilibrium constant for adsorbing glucose and forming the glucose-derived MARI at the tetrahedral Ti site,  $K_{R,i}$  is the lumped equilibrium constant describing the formation of the structurally distinct intermediates that immediately precede fructose or sorbose formation from the glucose-derived MARI,  $k_{2,i}$  is the rate constant for the kinetically-relevant step that forms the hydride shift transition state from the relevant reactive intermediate, and  $K_4$  and  $K_5$  are equilibrium constants relating the sequential adsorption of two water molecules from the liquid phase to the Lewis acid site; all lumped rate and

equilibrium constants in Eq. 6.8 are identified in Figure 6.43. Additionally,  $\eta_i$  is the approach to equilibrium term, which is rigorously zero for initial isomerization rates extrapolated to zero conversion. Finally,  $\gamma_j$  is the activity coefficient of species  $j$ , where  $j$  denotes two bound water molecules (2W\*), the bound glucose intermediate identified as MARI at high  $a_G$  values (G\*), or the hydride shift transition states that form fructose and sorbose ( $\ddagger, i$ ). This rate equation is the simplest kinetic model that satisfies the requirement of two relevant adsorbed intermediates and accounts for the non-ideality of adsorbed or solution-phase species, which can be reduced to recover first-order and zero-order kinetic regimes at low and high glucose thermodynamic activities. These  $\gamma_j$  values approach unity for ideal solutions and ideal reactive intermediates, in which the ideality of adsorbed intermediates are typically defined as low-coverage and non-interacting species [170]; here, no such co-adsorbate interactions are expected among glucose-derived species and thus  $\gamma_j$  is assumed to be unity for adsorbed species.

Equation 6.8 can be recast in the following form, which was used to regress to initial fructose and sorbose rate data measured on Ti-Beta-F-155 and Ti-Beta-OH-46 as  $a_G/a_W^2$  was varied:

$$r_i = \frac{\frac{K_1}{K_4 K_5} K_{R,i} k_{2,i} \frac{a_G}{a_W^2}}{1 + \frac{K_1}{K_4 K_5} \frac{a_G}{a_W^2}} \quad (6.9)$$

In Eq. 6.9, the apparent zero-order rate constant is defined as:

$$k_{\text{zero},i} = K_{R,i} k_{2,i} \quad (6.10)$$

which describes the formation of the kinetically-relevant hydride shift transition states from the glucose-derived MARI species. Additionally, the competitive adsorption terms for glucose and water can be lumped together into a single apparent equilibrium constant:

$$K_{\text{comp}} = \frac{K_1}{K_4 K_5} \quad (6.11)$$

which describes the adsorption of glucose and concomitant displacement of two water molecules from the Ti site. These two values can be combined to define an apparent first-order rate constant:

$$k_{\text{first},i} = k_{\text{zero},i}K_{\text{comp}} = \frac{K_1K_{R,i}k_{2,i}}{K_4K_5} \quad (6.12)$$

which describes the formation of the kinetically-relevant hydride shift transition state from aqueous-phase glucose and a pair of co-adsorbed waters on the Ti site. Substituting Eqs. 6.10–6.12 into Eq. 6.9 yields the following equation, which follows a Langmuir-Hinshelwood formalism:

$$r_i = \frac{K_{\text{comp}}k_{\text{zero},i}\frac{a_G}{a_W^2}}{1 + K_{\text{comp}}\frac{a_G}{a_W^2}} \quad (6.13)$$

Figure 6.8 shows initial fructose formation rates on Ti-Beta-F-155 as a function of glucose activity ( $a_G \sim 50\text{--}4000 \text{ mol m}^{-3}$ ), water activity ( $a_W \sim 40,000\text{--}50,000 \text{ mol m}^{-3}$ ), and temperature (368–383 K), with similar plots of fructose formation rates on Ti-Beta-OH-46 and sorbose formation rates on both Ti-Beta-F-155 and Ti-Beta-OH-46 available in Figures 6.44–6.46 (Supp. Info.). We note that while water solvent is typically considered to be in excess concentration, water activities vary by  $\sim 20\%$  across the conditions studied here ( $a_W \sim 40,000\text{--}50,000 \text{ mol m}^{-3}$ ) and are accounted for using temperature-dependent activity coefficients and water concentrations following the same procedure used to calculate glucose activities (Section 6.3.3.2). Fructose and sorbose formation rates are plotted as a function of the relevant ratio of glucose and water activities ( $a_G/a_W^2$ ) in Figures 6.47 and 6.48 (Supp. Info.) at each temperature studied. Formation rates of both products on both Ti-Beta-F-155 and Ti-Beta-OH-46 show the kinetic behavior predicted by Langmuir-Hinshelwood formalisms (Eq. 6.13) with a first-order dependence at low  $a_G$  values ( $<500 \text{ mol m}^{-3}$ ) and an approximately zero-order dependence at high  $a_G$  values ( $>2700 \text{ mol m}^{-3}$ ).

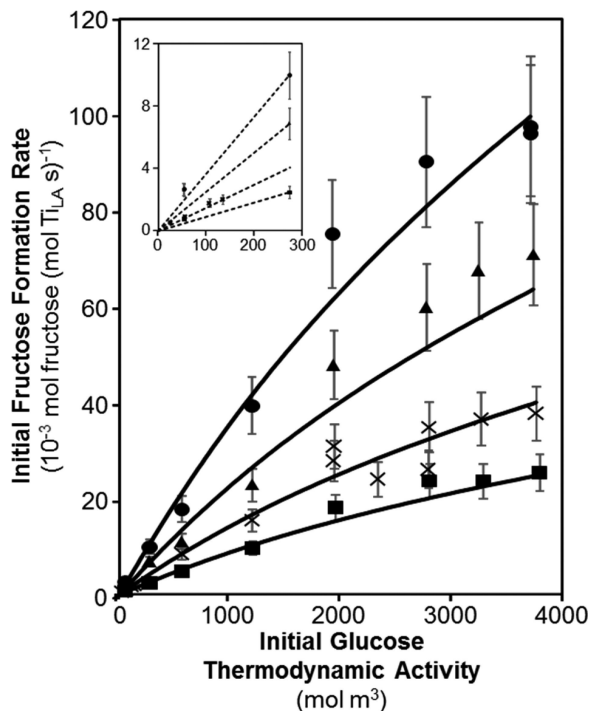


**Figure 6.8:** Dependence of initial fructose formation rates (pH 3) on Ti-Beta-F-155 on initial glucose thermodynamic activity (corresponding to 1–50 wt% glucose concentration) at 368 (■), 373 (×), 378 (▲), and 383 K (●). Solid lines represent regression of the data to the rate equation (Eq. 6.9) using activation enthalpies and entropies given in Table 6.4. The inset shows initial glucose isomerization rates at low glucose thermodynamic activities, highlighting the first-order kinetic regime.

Equations 6.10 and 6.11 can be rewritten in terms of apparent entropic and enthalpic contributions using the Eyring equation:

$$k_{\text{zero},i} = \frac{k_B T}{h} e^{\frac{\Delta S_{\text{zero},i}^\ddagger}{R}} e^{\frac{-\Delta H_{\text{zero},i}^\ddagger}{RT}} \quad (6.14)$$

$$K_{\text{comp}} = e^{\frac{\Delta S_{\text{comp}}}{R}} e^{\frac{-\Delta H_{\text{comp}}}{RT}} \quad (6.15)$$

Here,  $k_B$  is the Boltzmann constant,  $h$  is Planck's constant,  $\Delta S_{\text{zero},i}^\ddagger$  and  $\Delta H_{\text{zero},i}^\ddagger$  are the apparent activation entropy and enthalpy of the hydride shift transition state referenced to the bound glucose MARI, and  $\Delta S_{\text{comp}}$  and  $\Delta H_{\text{comp}}$  are the apparent reaction entropy and enthalpy changes describing the competitive adsorption of glucose relative to water at the Lewis acid sites. We note that the temperature dependence

of any non-unity activity coefficients for adsorbed species and transition state would be convoluted with the temperature dependences of enthalpy terms in eqs 6.14 and 6.15. Substitution of Eqs. 6.14 and 6.15 into Eq. 6.13 yields:

$$r_i = \frac{k_B T}{h} \frac{e^{\frac{\Delta S_{\text{zero},i}^\ddagger + \Delta S_{\text{comp}}}{R}} e^{\frac{-(\Delta H_{\text{zero},i}^\ddagger + \Delta H_{\text{comp}})}{RT}} \frac{a_G}{a_W^2}}{1 + e^{\frac{\Delta S_{\text{comp}}}{R}} e^{\frac{-\Delta H_{\text{comp}}}{RT}} \frac{a_G}{a_W}} \quad (6.16)$$

Table 6.4 lists the apparent activation enthalpies and entropies obtained by regressing Eq. 6.16 to the experimental data for fructose and sorbose formation rates on Ti-Beta-F-155 and Ti-Beta-OH-46 (368–383 K,  $a_G = 50$ –4000,  $a_W = 40,000$ –50,000 mol m<sup>-3</sup>, parity plots available in Figures 6.49–6.52, Supp. Info.). Apparent activation enthalpies for glucose-fructose isomerization on Ti-Beta-F-155 are identical (108 kJ mol<sup>-1</sup>) for both first-order and zero-order rate constants, which measure differences in enthalpy between the same 1,2-hydrate shift transition state and either two bound water molecules or a bound glucose intermediate on the Lewis acid site, respectively. Similarly, apparent activation enthalpies for the parallel glucose-sorbose isomerization reaction on Ti-Beta-F-155 are also identical (121 kJ mol<sup>-1</sup>) for both first-order and zero-order rate constants. Together, these findings indicate that the competitive adsorption of glucose and two water molecules at Ti sites within low-defect Beta frameworks is isenthalpic and depends weakly on temperature in the range studied. This is consistent with glucose heats of adsorption calculated by theory (108 kJ mol<sup>-1</sup>) [342] that are approximately twice that of water heats of adsorption (~50 kJ mol<sup>-1</sup>) measured by experiment from gravimetric and microcalorimetric studies on Ti-Beta-F [52].

In contrast, apparent activation entropies for both glucose-fructose and glucose-sorbose isomerization on Ti-Beta-F-155 are ~120 J mol<sup>-1</sup> K<sup>-1</sup> larger for the first-order rate constant than for the zero-order rate constant. Zero-order activation entropies reflect differences between the relevant hydrate shift transition state and the adsorbed glucose state, while first-order activation entropies reflect differences between the

same transition state and a precursor state involving two adsorbed water molecules at the Lewis acid site and glucose in aqueous solution. As a result, differences in zero-order and first-order activation entropies reflect differences in the entropy of the precursor states describing adsorbed glucose (with two associated water molecules) or two adsorbed water molecules and aqueous-phase glucose. Therefore, the smaller apparent activation entropies measured in zero-order regimes reflect the losses in entropy upon exchange of two bound water molecules with bound glucose, likely dominated by the entropy losses upon glucose adsorption to active sites from aqueous phases. We note that similar apparent enthalpies and entropies are obtained from the first-order and zero-order rate constants modeled by Eq. 6.16 and from the Eyring equation from single rate measurements in the first-order ( $a_G = 275 \text{ mol m}^{-3}$ ) and zero-order ( $a_G \sim 3500 \text{ mol m}^{-3}$ ) kinetic regimes, indicating that the data fitting method used here does not significantly change the measured thermodynamic properties (Table 6.9 and Figures 6.53 and 6.54, Supp. Info.) or the conclusions derived from them.

Apparent activation enthalpies on Ti-Beta-OH-46 are also similar for the first-order and zero-order rate constants for glucose-fructose isomerization (75–86 kJ mol<sup>-1</sup>, Table 6.4) and for glucose-sorbose isomerization (82–93 kJ mol<sup>-1</sup>, Table 4). These data indicate that competitive adsorption of glucose and water onto Lewis acid sites within hydrophilic void environments also depends weakly on temperature in the range studied. Water adsorption has been reported to be  $\sim 7 \text{ kJ mol}^{-1}$  more exothermic within Ti-Beta-OH than Ti-Beta-F from microcalorimetric studies [52], presumably reflecting favorable hydrogen bonding interactions with silanol defects, and similar effects of hydrogen bonding interactions on the adsorption enthalpy of glucose seem reasonable. Indeed, the more exothermic water adsorption enthalpies within hydrophilic channels of Ti-Beta-OH (by  $\sim 7 \text{ kJ mol}^{-1}$ ) resemble the lower apparent activation energies (by 22–39 kJ mol<sup>-1</sup>) for glucose-fructose isomerization on Ti-Beta-OH-46 than Ti-Beta-F-155. As in the case for Ti-Beta-F, apparent activation entropies on Ti-Beta-OH-46 are  $\sim 100 \text{ J mol}^{-1} \text{ K}^{-1}$  higher for the apparent first-order rate constant

than for the zero-order rate constant for both glucose-fructose and glucose-sorbose isomerization. These findings suggest that the polarity of the channel environment, and the associated co-adsorbed water structures they may stabilize, affect the free energy changes associated with water and glucose competitive adsorption to similar extents. Further, DFT calculations with varying intrapore water (2–10 molecules) show scattered glucose adsorption enthalpies with increasing intraporous water content, but do not show a strong increase or decrease in these values (Figure 6.55A, Supp. Info.), indicating that intraporous water has no systematic impact on glucose adsorption and water displacement ( $K_{\text{comp}}$ ).

The kinetic effects of surrounding hydrophobic reaction pockets can be quantified from the difference in apparent activation enthalpies ( $\Delta\Delta H$ ), entropies ( $\Delta\Delta S$ ), and Gibbs free energies ( $\Delta\Delta G$ , 373 K) between Ti-Beta-F-155 and Ti-Beta-OH-46 for each parallel reaction (Table 6.4). For both glucose-fructose and glucose-sorbose isomerization, both first-order and zero-order apparent activation enthalpies are higher (22–39 kJ mol<sup>-1</sup>) on Ti-Beta-F-155 than on Ti-Beta-OH-46, which seems reasonable for enthalpic stabilization of isomerization transition states by an additional hydrogen bonding interaction with silanol groups (or co-adsorbed water) present in more defective pore environments. Despite higher apparent activation enthalpies, initial isomerization rates are higher on Ti-Beta-F-155, reflecting greater apparent activation entropy gains ( $\sim 85$  J mol<sup>-1</sup> K<sup>-1</sup> for fructose,  $\sim 103$  J mol<sup>-1</sup> K<sup>-1</sup> for sorbose) in both first-order and zero-order regimes. Similar findings have been observed for first-order glucose isomerization rates on Sn-Beta (373 K, 5 wt% glucose, per Sn), for which similar apparent activation energies but higher pre-exponential factors are measured on hydrophobic Sn-Beta-F than hydrophilic Sn-Beta-OH [111], although kinetic parameters measured in the first-order regime cannot be separated into individual contributions that affect competitive adsorption and hydride shift transition state formation from the bound glucose MARI species.

For both parallel reactions on Ti-Beta,  $\Delta\Delta H$  and  $\Delta\Delta S$  values are similar for both the first-order and zero-order rate constants, indicating that the dominant ki-

netic effect of the hydrophobic reaction pocket is the entropic stabilization of the hydride shift transition state relative to the bound glucose MARI, and not of the bound water or glucose intermediates. For glucose isomerization reaction coordinates, descriptions of the hydride shift transition state include both the transitory glucose-derived complexes bound at Ti sites and the surrounding solvation environment provided by co-adsorbed water molecules and confining lattice atoms. Solvent reorganization to form cavities near hydrophobic surfaces change the hydrogen bonding structure of water and can result in large entropy losses ( $\sim 80 \text{ J mol}^{-1} \text{ K}^{-1}$ ) [343], and similar entropy losses ( $>70 \text{ J mol}^{-1} \text{ K}^{-1}$ ) have been observed as hydrophobic intermediates became more hydrophilic in nature at transition states for the catalytic formation of  $\text{H}_2\text{O}_2$  on silica-supported Pd clusters [344]. We surmise that the similar ( $\sim 85\text{--}103 \text{ J mol}^{-1} \text{ K}^{-1}$ ) entropy differences measured here for glucose isomerization in Ti-Beta-F and Ti-Beta-OH suggest reorganization of solvating water shells between the kinetically-relevant precursor and transition states, given that both water and glucose-derived moieties are hydrophilic and able to hydrogen bond with the solvating environment. Further, since the stability of the transition state relative to the bound glucose MARI species affects both first-order and zero-order rate constants, comparison between first-order and zero-order rate constants (Table 6.4) indicates that hydrophobic surrounding environments have a weaker effect on water and glucose competitive adsorption equilibrium constants, and a predominant effect on the stability of kinetically-relevant hydride shift transition states relative to the bound glucose MARI species.

In summary, experimental kinetic measurements indicate that the dominant effect of hydrophobic voids in Ti-Beta-F is the entropic stabilization of the hydride shift transition state relative to bound glucose MARI species ( $\Delta\Delta H$  and  $\Delta\Delta S$  values for  $k_{zero}$ , Table 6.4) and not the competitive adsorption of water and glucose ( $\Delta\Delta H$  and  $\Delta\Delta S$  values for  $K_{comp}$  near zero, Table 6.4). As a result, isomerization turnover rates measured in both first-order and zero-order kinetic regimes (per  $\text{Ti}_{LA}$ ) are higher (by similar factors) when active Ti sites are confined within hydrophobic than hydrophilic

voids. Small enthalpic penalties for confining transition states within hydrophobic voids of Ti-Beta-F are compensated by significantly more favorable entropic gains, resulting in higher rate constants than on hydrophilic Ti-Beta-OH. This entropic stabilization of the transition state relative to the adsorbed glucose intermediate is the dominant kinetic effect of confining glucose isomerization reaction coordinates within hydrophobic reaction pockets. In what follows, we assess the effects of hydrophobic and hydrophilic reaction environments on glucose isomerization using DFT calculations that consider the effects of additional water molecules present in reaction environments on glucose isomerization free energy landscapes. These calculations focus primarily on the effects of co-adsorbed water on the stability of the hydride shift transition state, relative to the adsorbed glucose intermediate observed from ATR-IR spectra at high  $a_G$  values.

#### 6.3.5.2 DFT-Derived Activation Enthalpies and Entropies

The kinetic effects of co-adsorbed water on glucose-fructose isomerization were examined by changing the number of intrapore water molecules (2–10) that interact with the transition state for the 1,2-hydride shift step, the adsorbed glucose state, and the desorbed glucose state (the closed Ti site without any organic species present) individually. Additional kinetic effects from proximal silanol groups that may exist in Ti-Beta-OH materials are possible, but cannot be quantified appropriately without more precise definitions of active Ti site structures (e.g., closed, open), which is the subject of ongoing work. Alterations in the nature (e.g., closed, open) of Lewis acidic Sn sites may significantly affect glucose-fructose isomerization activation enthalpies [310]; however, the similar activation enthalpies measured experimentally on Ti-Beta-F and Ti-Beta-OH (Table 6.4) do not suggest that such dramatic differences prevail among active Ti site structures in hydrophobic and hydrophilic Ti-Beta zeolites. Therefore, to isolate the kinetic roles of co-adsorbed water molecules on the stability of hydride shift transition states, the active site model was restricted to a closed Ti site without proximal silanol defects.

The positions of water molecules in these studies were determined by first fully solvating three cases: the 1,2-hydride shift transition state, the adsorbed ring-closed glucose state, and the closed Ti site with a proximal, partially-bound water cluster. Water was systematically removed from each position in these clusters to determine the most weakly bound water molecule, which was then used as the basis for each subsequent water removal. For example, starting with 10 water molecules solvating the 1,2-hydride shift transition state, each individual water molecule was removed to create 10 distinct 9-water arrangements, each of which was optimized into its lowest free energy configuration. The 9-water configuration with the lowest free energy was used to generate 9 distinct 8-water arrangements prior to energy minimization, a process that was repeated until no water molecules remained. The arrangement of water molecules at each discrete water density on the 1,2-hydride shift transition state, the adsorbed glucose state, and the closed Ti site corresponding to the lowest free energy was then used to calculate enthalpy and entropy barriers for the apparent first-order and zero-order rate constants.

The aqueous nature of these reactions prohibits direct assessment of how many water molecules adsorb or desorb over the course of the reaction within hydrophobic and hydrophilic environments. ATR-IR experiments confirm prior reports that glucose adsorption entrains some number of water molecules into hydrophobic channels [173, 342] and indicates that glucose displaces some number of water molecules upon adsorption within hydrophilic channels. Despite these apparent shifts in intrapore water content upon glucose adsorption,  $K_{comp}$  values are nearly identical in Ti-Beta-F and Ti-Beta-OH materials, which correspond to the adsorption of glucose and concomitant desorption of two water molecules. Therefore, the difference in reactivity between Ti-Beta-F and Ti-Beta-OH is directly attributable to changes in the zero-order apparent rate constants, which reflect differences in free energy between hydride shift transition states and the adsorbed glucose MARI state. This reaction event likely causes net-zero changes in the amount of co-adsorbed water within either material.

DFT-predicted apparent zero-order activation enthalpies systematically increase from 165 to 276 kJ mol<sup>-1</sup> and apparent zero-order activation entropies systematically increase from -12 to 49 J mol<sup>-1</sup> K<sup>-1</sup> as the co-adsorbed water density increases from 2–10 molecules (Fig. 6.55C, Supp. Info.). Similar increases in apparent activation enthalpies and entropies with increasing intrapore water content were observed for the first-order regime (Fig. 6.55B, Supp. Info.). These DFT-predicted trends, however, directly contradict the decrease in experimentally measured activation enthalpies ( $\Delta\Delta H_{zero,fructose}$  of 22 kJ mol<sup>-1</sup>) and large decrease in entropies ( $\Delta\Delta S_{zero,fructose}$  of 73 J mol<sup>-1</sup> K<sup>-1</sup>) on Ti-Beta-OH-46 compared to Ti-Beta-F-155 (Table 4) in the zero-order regime.

The inability to directly quantify the water content within the pores prohibits quantitative comparisons between DFT and experiments. Despite overall trends that suggest an increase in activation enthalpy with increasing intraporous water density, certain changes in water content produce statistically insignificant changes in activation enthalpies, such as the shift from 2 to 4 intrapore water molecules that results in a slight decrease in the zero-order activation enthalpy from 165 to 155 kJ mol<sup>-1</sup>, or the shift from 5 to 7 intrapore water molecules that results in a slight increase in the activation enthalpy from 209 to 214 kJ mol<sup>-1</sup>. The overall results from DFT, however, indicate that large increases in the amount of water that directly solvates glucose-derived species cause an increase in activation enthalpies and entropies, suggesting that such large changes are unlikely between hydrophobic and hydrophilic materials. Further, this suggests that adsorbed glucose species may be sufficiently solvated within Ti-Beta-F because of water molecules entrained upon glucose adsorption and the desorbed waters from the Lewis acid site, and that the increase in intrapore water content at other regions within zeolitic voids has little impact on activation enthalpies.

The significant decrease in activation entropy between Ti-Beta-F and Ti-Beta-OH ( $\Delta\Delta S_{zero,fructose}$  of 73 J mol<sup>-1</sup> K<sup>-1</sup>) demonstrates that intrapore water must have an impact on these reactions without a concomitant impact on activation enthalpy, which perhaps indicates that these effects are caused by alterations in the second-

layer solvation shell around glucose-derived intermediates. In other words, glucose adsorption into hydrophobic materials entrains sufficient water molecules to directly solvate itself and the 1,2-hydrate shift transition state that forms fructose, yet these materials lack extended water structures otherwise present in defect-laden hydrophilic materials that restrict the mobility of the first solvation shell of glucose. The net result is a decrease in the entropy of the 1,2-hydrate shift transition state, reflected in a decrease in both first-order and zero-order activation entropies on Ti-Beta-OH. Although the DFT results and entropy treatments used here do not provide straightforward explanations of the experimental findings, they do appear to capture broader effects of intrapore water that can be used to eliminate some possible hypotheses that would otherwise be difficult to assess without DFT. We note that more accurate modeling of this solvated reaction coordinate, using *ab initio* molecular dynamics simulations, may be warranted in future efforts that intend to more closely connect with experimental findings.

#### 6.4 Conclusions

The confinement of binding sites within hydrophobic or hydrophilic micropore environments influences turnover rates of aqueous-phase reactions through effects on the competitive adsorption of solvent and reactant molecules at binding sites, and on the structures of solvent clusters and networks within void spaces that influence Gibbs free energies of transition states and kinetically relevant reactive intermediates. These effects were studied here using aqueous-phase glucose isomerization to fructose and sorbose on Ti-Beta samples comprising varying contents (by 10 $\times$ ) of isolated, active Lewis acidic Ti sites that were synthesized directly or modified post-synthetically in order to obtain suites of materials that confined such sites within hydrophobic (Ti-Beta-F) and hydrophilic (Ti-Beta-OH) samples of widely varying residual silanol defect density (by 100 $\times$ ). Hydrophilic Ti-Beta-OH samples adsorbed 20–25 $\times$  higher amounts of water ( $P/P_0 = 0\text{--}0.2$ , 293 K) than hydrophobic Ti-Beta-F samples and stabilized water in structures characterized by increased extents of hydrogen-bonded

networks than the gas-like molecular structures present within hydrophobic micropores. Initial glucose-fructose and glucose-sorbose isomerization turnover rates (368–383 K, per  $\text{Ti}_{\text{LA}}$ ) are first-order at dilute glucose thermodynamic activities ( $a_G = 50\text{--}300 \text{ mol m}^{-3}$ ) and become zero-order at high glucose thermodynamic activities ( $a_G = 2700\text{--}4000 \text{ mol m}^{-3}$ ), reflecting a change in the MARI at Ti sites from two bound water ligands to adsorbed glucose-derived intermediates. These changes in the identity of the MARI with increasing glucose thermodynamic activity are consistent with shifts in Ti coordination from XANES spectra and are confirmed by spectral identification of intermediate structures using modulation excitation spectroscopy during ATR-IR experiments.

The measurement of first-order and zero-order kinetic behavior enables decoupling the kinetic effects of glucose and water competitive adsorption at active Ti sites from those of kinetically-relevant isomerization transition state stabilization to assess the effects of hydrophilic and hydrophobic reaction environments on adsorption and catalytic phenomena independently. Glucose isomerization rates were  $\sim 6\times$  higher (368–383 K, per  $\text{Ti}_{\text{LA}}$ ) on Ti-Beta-F than on Ti-Beta-OH in both first-order and zero-order kinetic regimes, reflecting both competitive adsorption constants between two waters and one glucose at Ti sites that are essentially insensitive to the polarity of confining reaction environments, and Gibbs free energy differences of kinetically relevant hydride shift transition states relative to their bound glucose precursors that are significantly lower within hydrophobic environments. Lower zero-order activation enthalpies and entropies measured on Ti-Beta-OH than on Ti-Beta-F reflect the effects of higher co-adsorbed water and silanol defect densities that cause modest enthalpic stabilization by hydrogen bonding, but more severe entropic destabilization, of isomerization transition states. Insights from DFT suggest that glucose is solvated within the hydrophobic micropores characteristic of Ti-Beta-F from water molecules entrained upon sugar adsorption and those desorbed from active Ti sites upon formation of ring-opened sugar intermediates; however, the higher water den-

sities present within hydrophilic environments characteristic of Ti-Beta-OH interact with the hydride shift transition state leading to entropic destabilization.

The experimental and theoretical data presented herein provide evidence that silanol defects and associated co-adsorbed water within the microporous reaction pockets of zeolites mediate entropy-enthalpy compromises that influence Gibbs free energies of kinetically-relevant glucose isomerization transition states. Similar entropy-enthalpy compromises have also been observed within metalloenzyme reaction pockets [22, 267]. For example, freeze-trapping X-ray crystallography studies of D-xylose isomerase have shown the migration of water molecules during protein folding and throughout the glucose-fructose isomerization pathway to assist proton shuttling events involved in glucose ring opening and hydride shift steps [267]. Co-adsorbed water is not expelled from the reaction pocket in D-xylose isomerase and continues to interact with bound intermediates, reminiscent of the entrainment of water molecules with glucose upon adsorption within hydrophobic zeolite pores and the influence of such co-adsorbed water to mediate entropy-enthalpy compromises in determining intermediate and transition state stability.

These findings indicate that aqueous-phase sugar isomerization turnover rates on hydrophobic and hydrophilic zeolites are sensitive to the presence of co-adsorbed solvent molecules within the reaction environment. As a result, the density and location of intrapore silanol defects in zeolites, which depend on their synthetic and post-synthetic treatment history, are structural features that influence catalytic rates because they determine the amount and structure of co-adsorbed solvent molecules, clusters, and extended networks within reaction environments. The *in situ* and *ex situ* IR characterization techniques described here are particularly useful for quantifying active site and hydrophilic defect densities, and for probing water structures within hydrophobic and hydrophilic confining environments under both gas-phase and liquid-phase conditions. More accurate modeling of co-adsorbed solvent densities within low-defect and high-defect porous structures promise to help establish stronger connections between computational and experimental studies. While the

polarity of confining environments around binding sites in zeolites have been recognized to influence turnover rates in aqueous-phase catalysis, including several cases for which rate acceleration within hydrophobic confining environments reflect adsorption phenomena, the findings presented herein document an example of rate acceleration that predominantly reflects the influence of hydrophobic confining environments on transition state stability.

## 6.5 Acknowledgements

M.J.C., J.W.H., J.C.V.V., J.B., and R.G. gratefully acknowledge financial support provided by the Purdue Process Safety and Assurance Center (P2SAC) and the Ralph W. and Grace M. Showalter Research Trust, and Jacklyn Hall and Alyssa LaRue for assistance with NMR studies. E.C.W and J.T.M. acknowledge support by the National Science Foundation under Cooperative Agreement No. EEC1647722. Use of the Advanced Photon Source was supported by the U.S. Department of Energy, Office of Basic Energy Sciences, under Contract No. DE-AC02-06CH11357. MR-CAT operations are supported by the Department of Energy and the MRCAT member institutions. M.G., S.K., and D.D.H. acknowledge the Extreme Science and Engineering Discovery Environment (XSEDE) through allocation CTS160041; XSEDE is supported by National Science Foundation grant number ACI-1548562. D.W.F. and M.E.W. acknowledge financial support from the National Science Foundation (CBET-15531377), a National Science Foundation Graduate Research Fellowship Program (DGE-1144245), and the TechnipFMC Educational Fund Fellowship at the University of Illinois, as well as Pranjali Priyadarshini for developing the apparatus and analysis for the MES-PSD experiments.

Reprinted with permission from Journal of the American Chemical Society 2018, 140 (43), 14244–14266. Copyright (2018) American Chemical Society.

**Table 6.1:** Active Site and Structural Characterization Data for Ti-Beta Samples

Sample	$V_{\text{ads}}(\text{N}_2, 77 \text{ K})$ ( $\text{cm}^3 \text{ g}^{-1}$ ) <sup>a</sup>	Edge Energy (eV) <sup>b</sup>	Lewis Acidic Ti Density ( $10^{-5} \text{ mol Ti}_{\text{LA}} \text{ g}^{-1}, \text{CD}_3\text{CN}$ ) <sup>c</sup>	Lewis Acidic Ti Density ( $\text{Ti}_{\text{LA}}$ unit $\text{cell}^{-1}, \text{CD}_3\text{CN}$ ) <sup>d</sup>	Fraction of Lewis Acidic Ti <sup>e</sup>	Lewis Acidic Ti Density ( $10^{-5} \text{ mol Ti}_{\text{LA}} \text{ g}^{-1}, \text{Pyridine}$ ) <sup>f</sup>
Ti-Beta-F-133	0.21	5.3	4.17	0.16	0.34	n.m.
Ti-Beta-F-135	0.19	4.5	3.93	0.15	0.32	6.35
Ti-Beta-F-142	0.20	4.3	6.70	0.26	0.58	8.40
Ti-Beta-F-143	0.21	4.2	4.63	0.18	0.40	6.51
Ti-Beta-F-155	0.20	5.3	6.64	0.26	0.62	4.64
Ti-Beta-F-170	0.20	5.3	2.36	0.09	0.24	4.87
Ti-Beta-F-180	0.22	4.4	2.99	0.12	0.33	n.m.
Ti-Beta-F-282	0.20	5.1	0.89	0.03	0.15	n.m.
Ti-Beta-OH-34	0.22	4.5	18.77	0.72	0.40	16.85
Ti-Beta-OH-38	0.19	4.7	14.80	0.57	0.35	n.m.
Ti-Beta-OH-46	0.23	4.4	35.20	1.36	1.00	36.29
Ti-Beta-OH-71	0.21	4.7	13.08	0.50	0.57	11.79
Ti-Beta-OH-297	0.18	4.5	26.88	1.03	0.32	32.70

<sup>a</sup> $\text{N}_2$  volumes at the end of micropore filling transition (77 K). <sup>b</sup>Determined from Tauc plots after dehydration (523 K).

<sup>c</sup>Lewis acidic Ti densities measured from  $\text{CD}_3\text{CN}$  titration IR experiments.

<sup>d</sup>Lewis acidic Ti densities measured from  $\text{CD}_3\text{CN}$  titration IR experiments normalized per unit cell.

<sup>e</sup>Fraction of total Ti concentration present as Lewis acidic Ti sites measured from  $\text{CD}_3\text{CN}$  titration IR experiments.

<sup>f</sup>Lewis acidic Ti densities measured from pyridine titration IR experiments. <sup>g</sup>n.m.: not measured.

**Table 6.2:** Semi-Quantitative Measurements of the Hydrophobic Properties of Microporous Voids in Ti-Beta-F and Ti-Beta-OH materials

Sample	Silanol Density ( $10^{-4}$ mol SiOH $\text{g}^{-1}$ ) <sup>a</sup>	Silanol Density (mol SiOH mol $\text{Ti}_{\text{LA}}^{-1}$ ) <sup>b</sup>	$V_{\text{ads}}$ ( $\text{H}_2\text{O}$ , 293 K) ( $10^{-3}$ $\text{cm}^3$ $\text{g}^{-1}$ , $\text{P}/\text{P}_0=0.2$ ) <sup>c</sup>	Normalized $V_{\text{ads}}$ ( $\text{H}_2\text{O}$ , 293 K) ( $\text{cm}^3$ $\text{g}^{-1}$ ) <sup>d</sup>	$V_{\text{ads}}$ ( $\text{H}_2\text{O}$ ) / $V_{\text{ads}}$ ( $\text{N}_2$ ) <sup>e</sup>	$V_{\text{ads}}$ ( $\text{CH}_3\text{OH}$ ) ( $\text{cm}^3$ $\text{g}^{-1}$ ) <sup>f</sup>
Ti-Beta-F-133	1.21	2.9	2.31	0.04	0.011	0.062
Ti-Beta-F-135	0.86	2.2	2.02	0.03	0.011	0.072
Ti-Beta-F-142	1.54	2.3	2.53	0.01	0.013	0.083
Ti-Beta-F-143	1.32	2.8	3.52	0.10	0.017	0.080
Ti-Beta-F-155	1.93	2.9	4.48	0.12	0.022	0.051
Ti-Beta-F-170	0.65	2.8	3.10	0.12	0.015	0.082
Ti-Beta-F-180	1.66	5.5	3.88	0.16	0.018	0.062
Ti-Beta-F-282	0.29	3.2	1.33	0.06	0.007	0.035
Ti-Beta-OH-34	6.72	3.6	46.39	2.20	0.211	1.04
Ti-Beta-OH-38	14.79	10.0	93.57	4.90	0.492	0.98
Ti-Beta-OH-46	7.02	2.0	37.93	1.40	0.165	0.33
Ti-Beta-OH-71	7.97	6.1	41.77	2.06	0.199	1.09
Ti-Beta-OH-297	6.28	2.3	53.03	2.41	0.295	1.19
Si-Beta-F	—	—	2.20	2.20	—	—

<sup>a</sup>Silanol densities measured from  $\text{CD}_3\text{CN}$  titration IR experiments. <sup>b</sup>Silanol densities normalized by Lewis acidic

Ti densities measured from  $\text{CD}_3\text{CN}$  titration IR experiments. <sup>c</sup>Water volumes at  $\text{P}/\text{P}_0 = 0.2$  (293 K).

<sup>d</sup>Water volumes at  $\text{P}/\text{P}_0 = 0.2$  (293 K) after normalization by two times the number of Lewis acidic Ti sites determined from  $\text{CD}_3\text{CN}$  titration IR experiments. <sup>e</sup>Fraction of total micropore volume filled by water at  $\text{P}/\text{P}_0 = 0.2$  (293 K).

<sup>f</sup> $\text{CH}_3\text{OH}$  volumes taken at the end of the first adsorption regime (293 K), indicative of adsorbate-adsorbent interactions. This corresponds to low  $\text{P}/\text{P}_0$  values (0.02–0.04) for Type V isotherms on Ti-Beta-F samples and the highest measured  $\text{P}/\text{P}_0$  values (0.6–0.7) on Ti-Beta-OH samples.

**Table 6.3:** Relative Concentrations<sup>a</sup> of MARI and Minor Species during Modulation of Liquid-Phase Glucose Activity ( $\sim 3000\text{--}3750$  mol glucose  $\text{m}^{-3}$ ) at 373 K followed by Processing by PSD and MCR-ALS.

Sample	Relative Concentration <sup>a</sup> ( $\theta_{\text{MARI}} / \theta_{\text{Minor species}}$ )
Ti-Beta-F-155	2.4
Ti-Beta-OH-46	4.3
Si-Beta-F	5.3
ZnSe Crystal	1.7

<sup>a</sup>Relative concentrations assume the equivalent extinction coefficients for glucose vibrations at approximately  $1030\text{ cm}^{-1}$  are between MARI and minor species.

**Table 6.4:** Apparent Enthalpies and Entropies for First-Order and Zero-Order Rate Constants describing Fructose and Sorbose Formation on Ti-Beta-F-155 and Ti-Beta-OH-46

rate constant	$\Delta H_{\text{app}}$ (kJ mol <sup>-1</sup> )		$\Delta S_{\text{app}}$ (J mol <sup>-1</sup> K <sup>-1</sup> )		$\Delta \Delta H_{\text{app}}$ (kJ mol <sup>-1</sup> )		$\Delta \Delta S_{\text{app}}$ (J mol <sup>-1</sup> K <sup>-1</sup> )		$\Delta \Delta G_{\text{app}}$ (kJ mol <sup>-1</sup> )	
	Ti-Beta-F-155	Ti-Beta-OH-46	Ti-Beta-F-155	Ti-Beta-OH-46	(F-OH) <sup>b</sup>	(F-OH) <sup>b</sup>	(F-OH) <sup>b</sup>	(F-OH) <sup>b</sup>	(F-OH) <sup>b</sup>	(F-OH) <sup>b</sup>
$k_{\text{zero,fructose}}$ <sup>a</sup>	108 ± 10	86 ± 9	17 ± 26	-56 ± 25	22	73	-5			
$k_{\text{first,fructose}}$	108	75	133	33	33	100	-4			
$k_{\text{zero,sorbose}}$ <sup>a</sup>	121 ± 7	93 ± 8	46 ± 19	-43 ± 20	28	89	-5			
$k_{\text{first,sorbose}}$	121	82	162	46	39	116	-4			
$K_{\text{comp}}$ <sup>a</sup>	0 ± 0.5	-10 ± 0.5	116	89	11	27	1			

<sup>a</sup>Errors correspond to 95% confidence intervals from regressions. Errors for first-order rate constants are not given as they reflect combined free energy differences for zero-order and competitive adsorption fits.

<sup>b</sup>Differences in apparent activation enthalpies ( $\Delta \Delta H_{\text{app}}$ ), entropies ( $\Delta \Delta S_{\text{app}}$ ), and free energies ( $\Delta \Delta G_{\text{app}}$  at 373 K) are listed as the difference between Ti-Beta-F-155 and Ti-Beta-OH-46.

## 6.6 Supporting Information

## 6.6.1 Bulk structural and Lewis acid site characterization of Ti-Beta zeolites

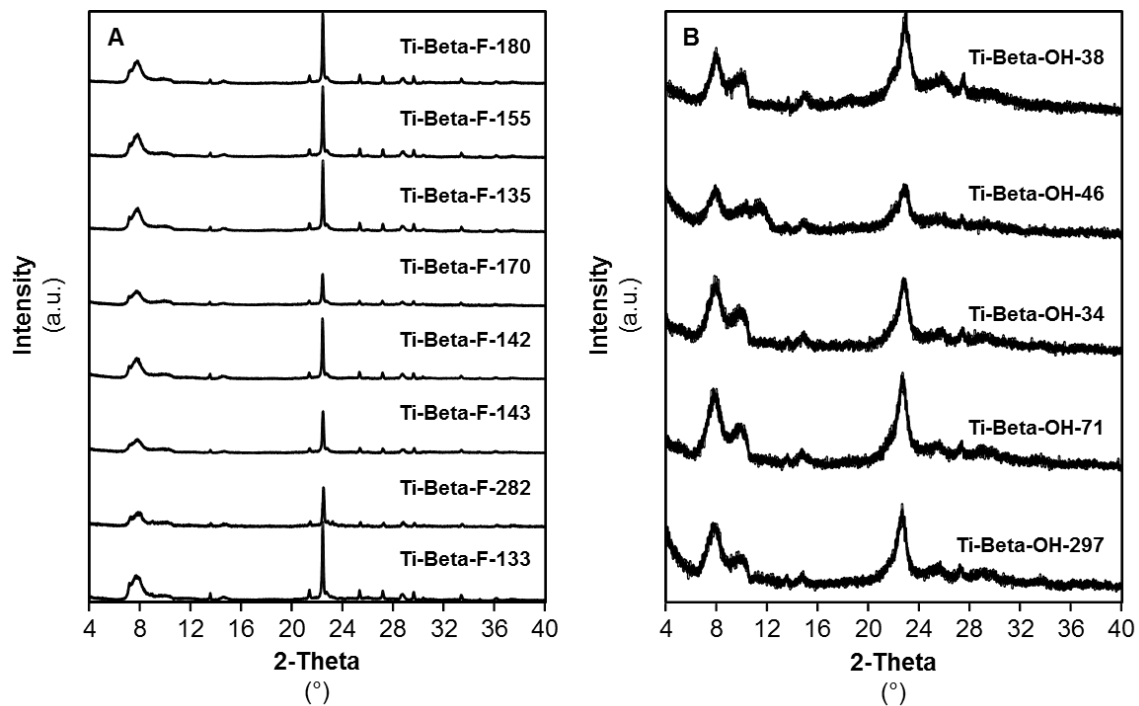


**Figure 6.9:** Powder XRD patterns of Ti-Beta-F (A) Ti-Beta-OH (B) samples studied in this work. Weak signals around 9–10° reflect an artifact from the sample holders used to collect XRD patterns.

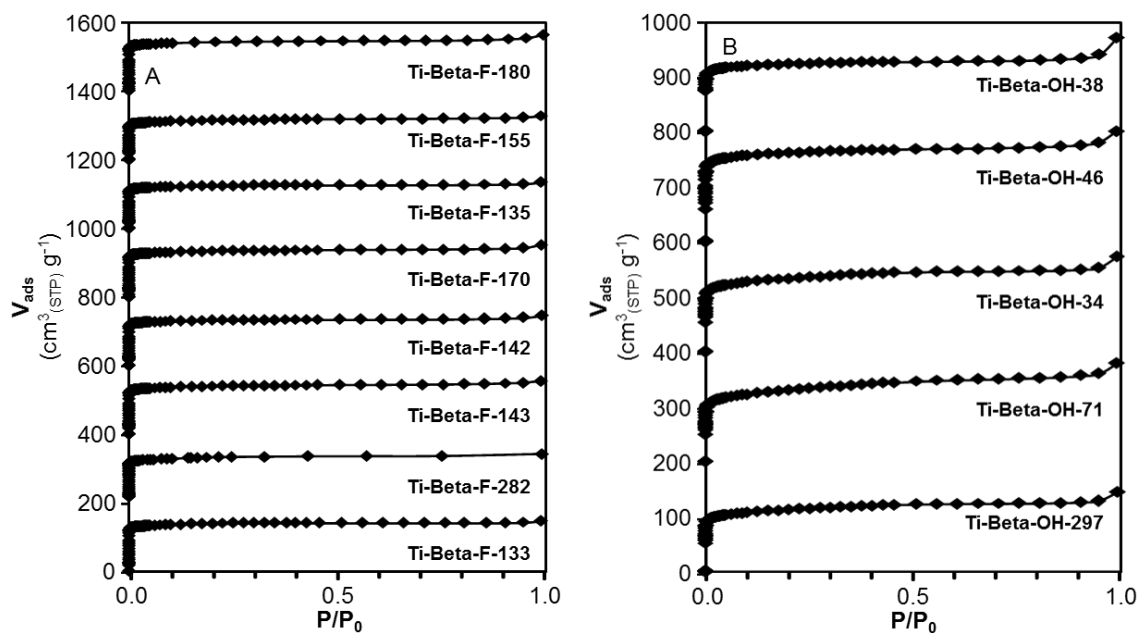


**Figure 6.10:** N<sub>2</sub> adsorption isotherms (77 K) of Ti-Beta-F (A) Ti-Beta-OH (B) samples studied in this work. Isotherms are offset by 200 cm<sup>3</sup> g<sup>-1</sup> for clarity.

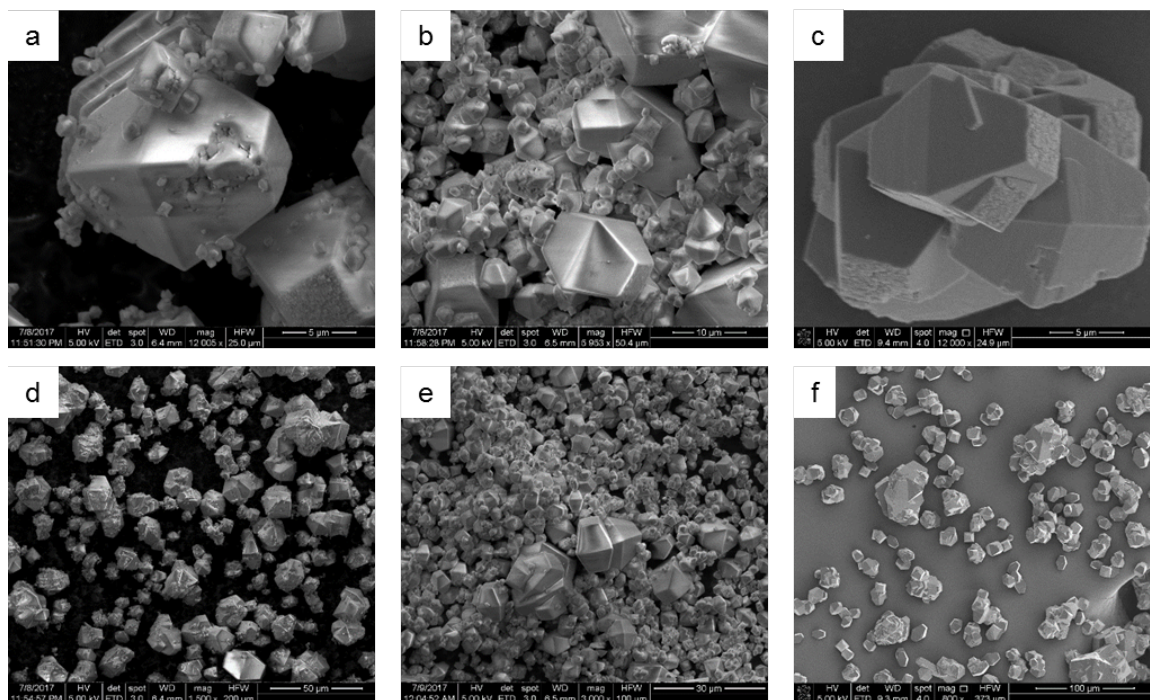


**Figure 6.11:** SEM images of selected Ti-Beta-F samples: (a) Ti-Beta-F-135, (b) Ti-Beta-F-155, and (c) Ti-Beta-F-180. Bulk sample uniformity is assumed based on images for (d) Ti-Beta-F-135, (e) Ti-Beta-F-155, and (f) Ti-Beta-F-180. Larger crystal aggregates reflect Si-Beta-F seeds used to nucleate the formation of Ti-Beta-F.

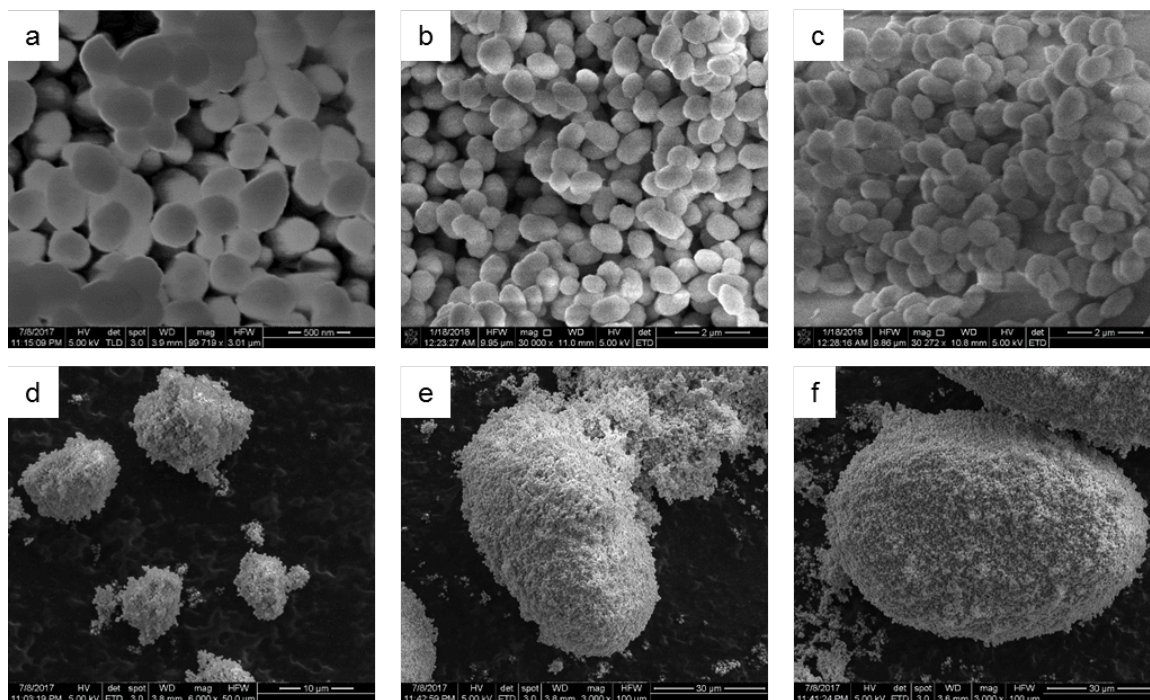


**Figure 6.12:** SEM images of selected Ti-Beta-OH samples: (a) Ti-Beta-OH-46, (b) Ti-Beta-OH-34, and (c) Ti-Beta-OH-71. Bulk sample uniformity is assumed based on images for (d) Ti-Beta-OH-46, (e) Ti-Beta-OH-34, and (f) Ti-Beta-OH-71 which show larger agglomerates of small crystals.

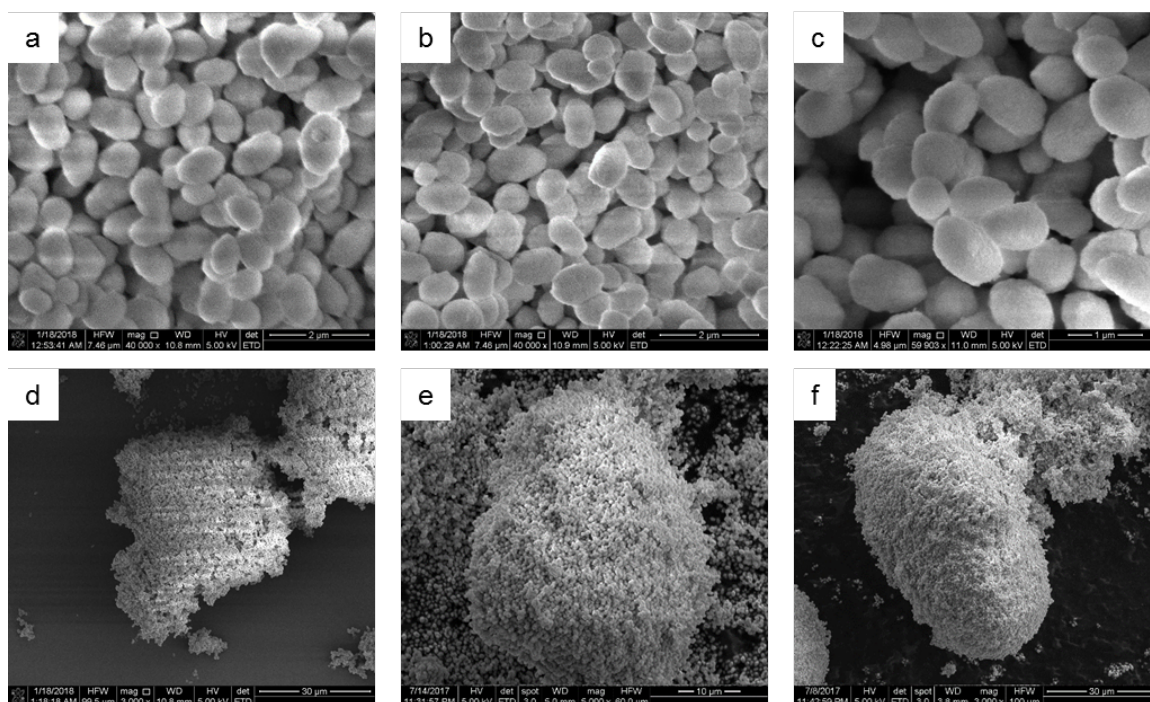


**Figure 6.13:** SEM images of Ti-Beta-OH-34 at various steps of the synthesis procedure: (a) Al-Beta parent material, (b) after nitric acid treatment for dealumination, and (c) after TiCl<sub>4</sub> grafting to form Ti-Beta-OH-34. Bulk sample uniformity is assumed based on images for (d) Al-Beta parent material, (e) after nitric acid treatment for dealumination, and (f) after TiCl<sub>4</sub> grafting to form Ti-Beta-OH-34. All show larger agglomerates of small crystals.

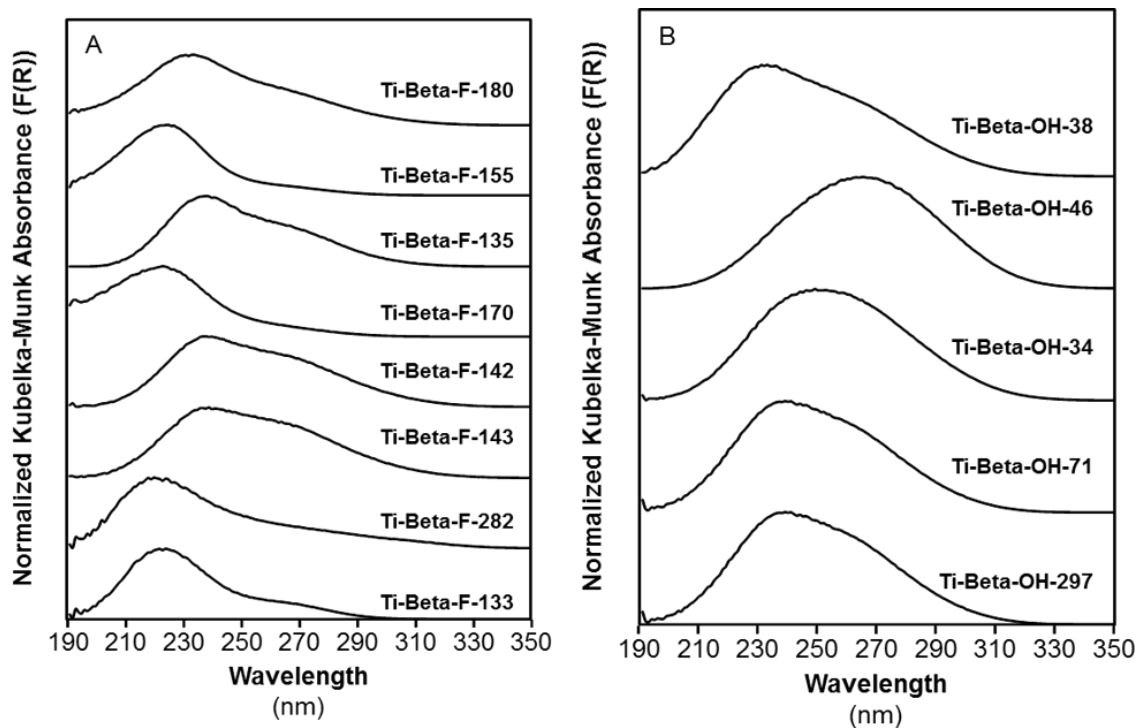


**Figure 6.14:** Hydrated UV-Vis spectra of (A) Ti-Beta-F and (B) Ti-Beta-OH samples studied in this work collected prior to dehydration at 523 K.

Figures 6.14 and 6.15 above show UV-Vis spectra collected before and after the exposure of Ti-Beta samples to heat treatments (523 K, 1800 s). Band maxima do not shift significantly upon dehydration treatments. Tauc plots corresponding to these spectra are shown in Figures 6.16 and 6.17 and edge energies are x-intercept values measured from extrapolating the first linear regions at low energies of Tauc plots. Dehydration of each sample leads to an increase in the edge energy as shown in Table 6.5. These shifts in edge energy upon dehydration corroborate the changes in Ti coordination number observed in XAS measurements detailed below (Section 6.6.4.2).

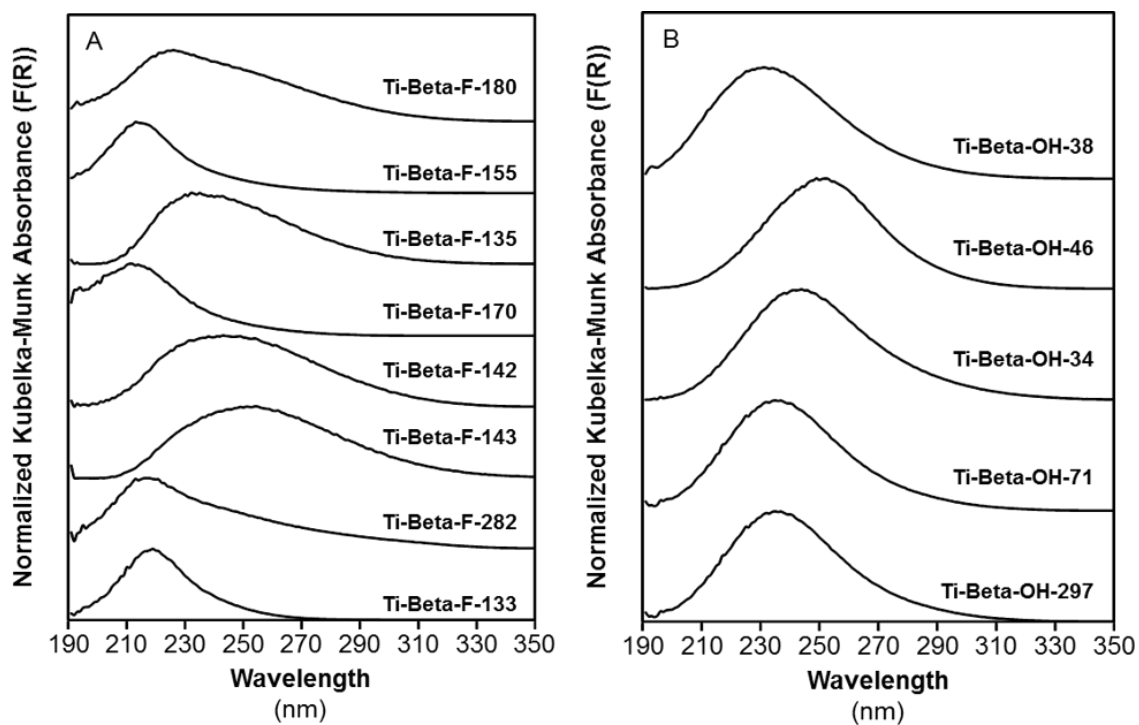


**Figure 6.15:** Dehydrated UV-Vis spectra (523 K, 1800 s) of (A) Ti-Beta-F and (B) Ti-Beta-OH samples studied in this work.

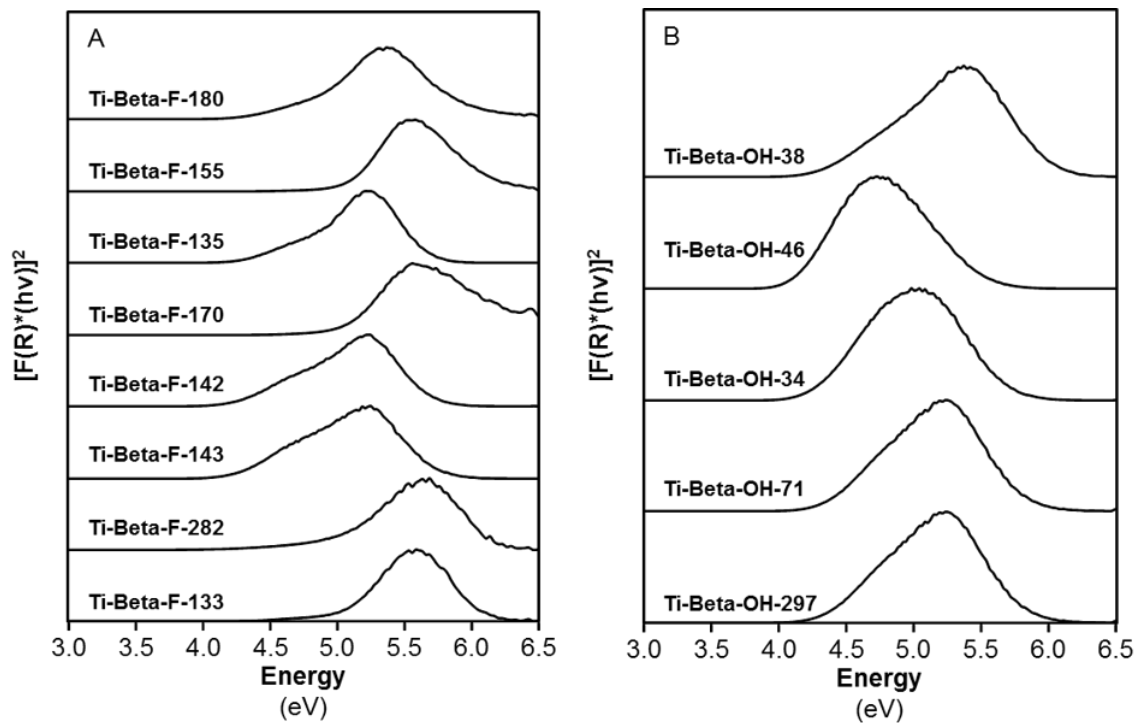


**Figure 6.16:** Tauc plots of (A) Ti-Beta-F and (B) Ti-Beta-OH samples studied in this work prior to heating and sample dehydration (“hydrated” samples). Edge energies are summarized in Table 6.5.

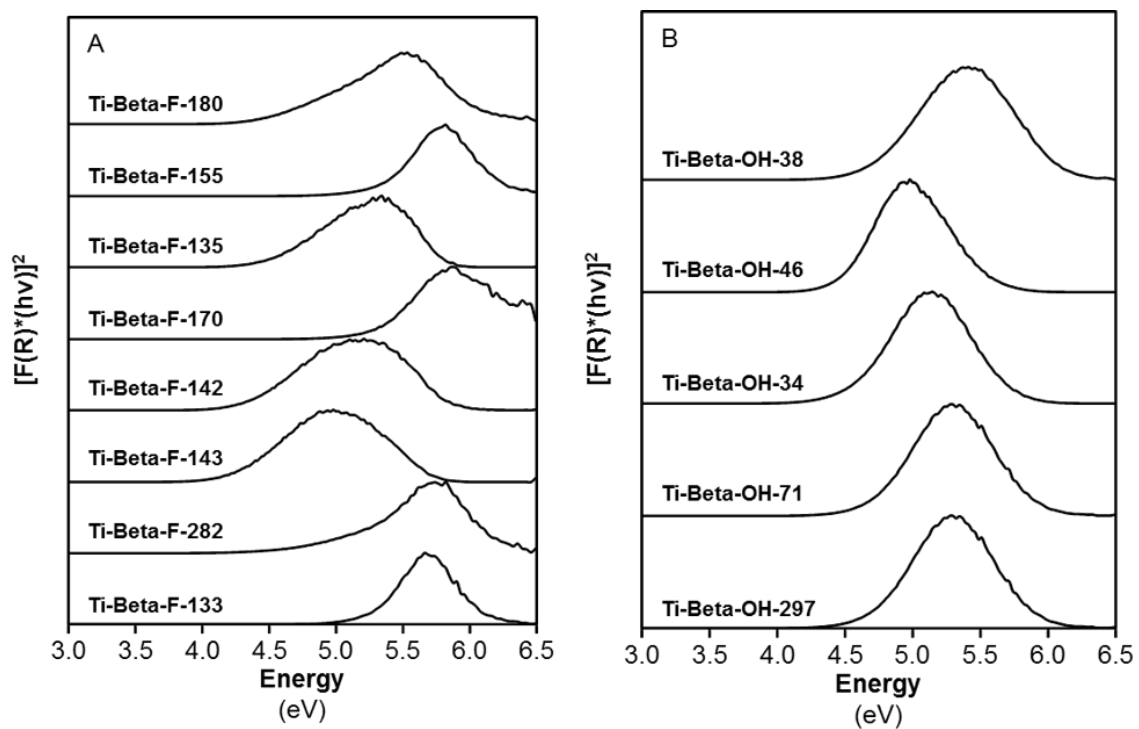


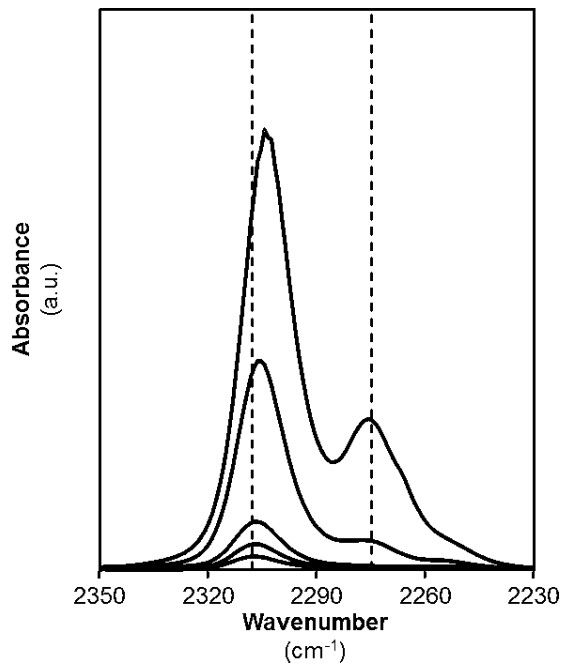
**Figure 6.17:** Tauc plots of (A) Ti-Beta-F and (B) Ti-Beta-OH samples studied in this work after treatment in flowing He at 523 K for 1800 s. Edge energies are summarized in Table 6.5.

**Table 6.5:** Edge energies of Ti-Beta samples after exposure to ambient conditions, dehydrated, and rehydrated in wet He flow. Band maxima correspond to the primary UV-Vis F(R) peaks after dehydration shown in Figure 6.14 above.

Sample	Edge Energies			Band Maximum (nm)
	Ambient (eV)	Dehydrated (eV)	Rehydrated (eV)	
Ti-Beta-F-180	4.4	4.4	4.3	230
Ti-Beta-F-155	5.1	5.3	5.1	216
Ti-Beta-F-135	4.3	4.5	4.3	231
Ti-Beta-F-170	5.1	5.3	5.1	216
Ti-Beta-F-142	4.2	4.3	4.3	246
Ti-Beta-F-143	4.2	4.2	4.2	253
Ti-Beta-F-282	5.0	5.1	5.0	218
Ti-Beta-F-133	5.1	5.3	5.0	219
Ti-Beta-OH-38	4.3	4.7	4.4	234
Ti-Beta-OH-46	4.1	4.4	4.1	253
Ti-Beta-OH-34	4.2	4.5	4.3	246
Ti-Beta-OH-71	4.3	4.7	4.4	235
Ti-Beta-OH-18	4.2	4.5	4.2	235

<sup>a</sup>Dehydration performed in dry flowing He to 523 K and held for 30 min.

<sup>b</sup>Rehydration performed in wet flowing He at ambient temperature.

6.6.1.1 IR characterization of titanosilicate samples using adsorbed  $\text{CD}_3\text{CN}$ 

**Figure 6.18:** IR spectra on Ti-Beta-OH-46 after progressive titration of  $\text{CD}_3\text{CN}$  at 303 K ( $\text{CD}_3\text{CN}/\text{Ti} = 0.002\text{-}2.34$ ). Dashed lines are drawn at  $2308\text{ cm}^{-1}$  ( $\text{CD}_3\text{CN}$  bound to Lewis acidic Ti) and  $2275\text{ cm}^{-1}$  ( $\text{CD}_3\text{CN}$  hydrogen bound to silanols). Note that the peak center shifts slightly to lower wavenumbers with increasing adsorbed  $\text{CD}_3\text{CN}$  concentrations.

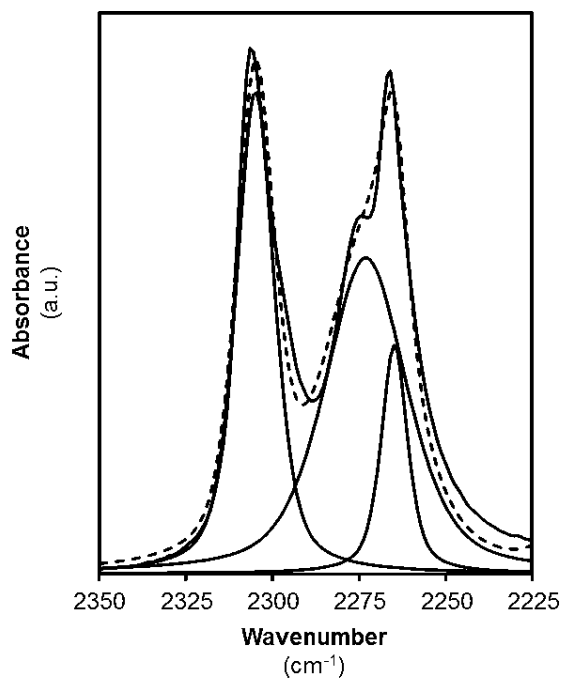


**Figure 6.19:** CD<sub>3</sub>CN-saturated IR spectra for Ti-Beta-F-155. The thickest solid line reflects the measured spectra upon saturation with CD<sub>3</sub>CN while thinner lines indicate constitute peaks associated with CD<sub>3</sub>CN bound to Lewis acidic Ti sites (2308 cm<sup>-1</sup>), CD<sub>3</sub>CN bound to silanols (2275 cm<sup>-1</sup>), and gas phase physisorbed CD<sub>3</sub>CN (2265 cm<sup>-1</sup>). The dashed line represents the modeled spectra from combining deconvoluted peaks.

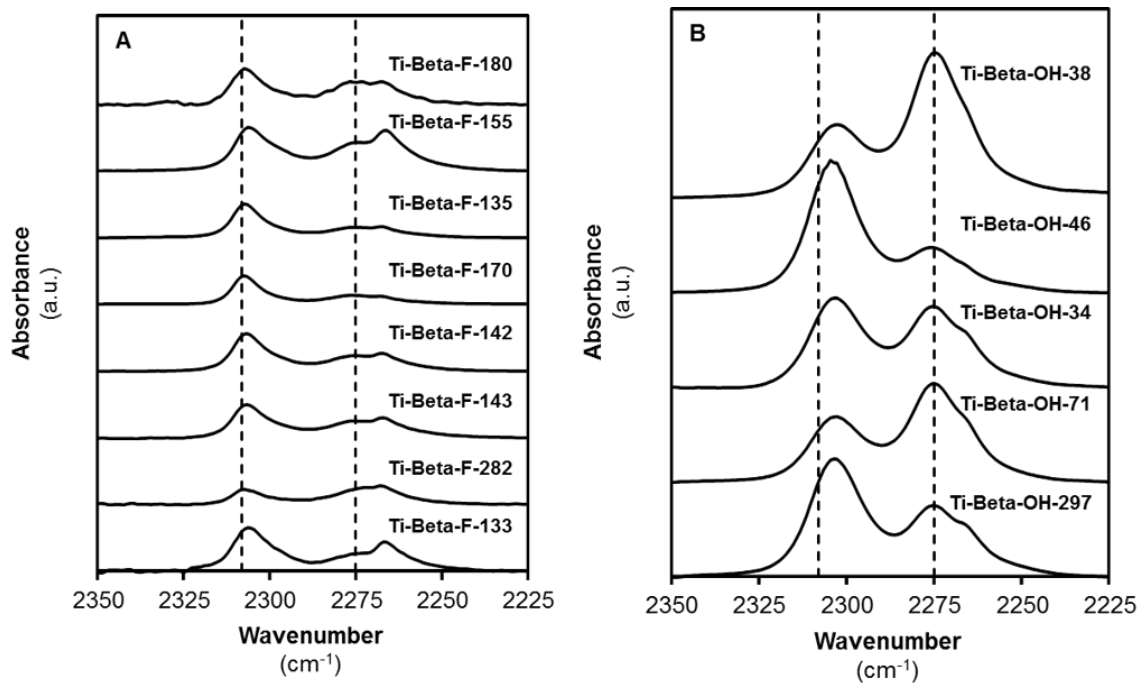


**Figure 6.20:** IR spectra collected on (A) CD<sub>3</sub>CN-saturated Ti-Beta-F and (B) CD<sub>3</sub>CN-saturated Ti-Beta-OH samples studied in this work. Dashed lines are drawn at 2308 cm<sup>-1</sup> (CD<sub>3</sub>CN bound to Lewis acidic Ti) and 2275 cm<sup>-1</sup> (CD<sub>3</sub>CN bound to silanols).

### 6.6.1.2 IR characterization of titanasilicate samples using adsorbed pyridine

Pyridine (Alfa Aesar, >99%) adsorption on self-supporting Ti-Beta wafers was performed following similar procedures to those reported for CD<sub>3</sub>CN titration at 423 K under static vacuum conditions including freeze-pump-thaw cycles, pyridine dosing and equilibration, dynamic vacuum exposure to remove residual gaseous titrant upon saturation, and baseline correction, normalization, and subtraction of parent spectra, resulting in IR spectra similar to those shown in Figure 6.21A. Figure 6.21A shows pyridine adsorption spectra with incremental pyridine doses on Ti-Beta-F-135. IR spectra on pyridine saturated Ti-Beta-F-155 is shown in Figure 6.21B which can be deconvoluted to isolate the peak centered at 1605 cm<sup>-1</sup>.

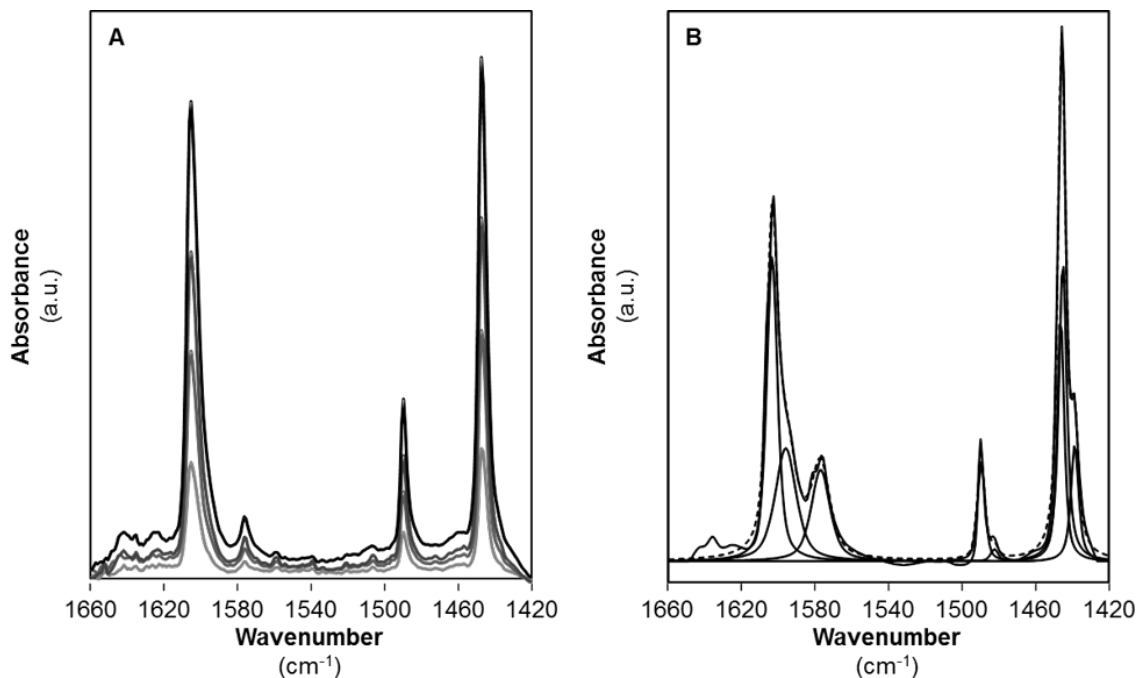


**Figure 6.21:** IR spectra measured (a) after the first four doses of pyridine on Ti-Beta-F-135 ( $0.015\text{--}0.058\text{ mol pyridine (mol Ti)}^{-1}$ ) and (b) after saturation of Ti-Beta-F-135 with pyridine ( $1.05\text{ mol pyridine (mol Ti)}^{-1}$ ). The components included in the deconvolution are shown (thin solid lines) with the resulting fit envelope (dotted line) and the measured spectra (thick solid line).

Marginal increases in integrated area of the feature centered at  $1605\text{ cm}^{-1}$  correlate linearly with marginal increases in adsorbed pyridine. The linear increase can be quantified on four distinct Ti-Beta samples which show similar molar extinction coefficients for pyridine adsorption from identical analyses to those of  $\text{CD}_3\text{CN}$  molar extinction coefficient determination in the main text, as seen in Figure 6.22A and Table 6.6. Averaging the linear increases in  $1605\text{ cm}^{-1}$  peak area at low pyridine doses (Figure 6.20B) yields a single  $E(1605\text{ cm}^{-1})$  value of  $1.16 \pm 0.23\text{ cm } \mu\text{mol}^{-1}$  which can then be used to quantify total Lewis acid density from IR spectra after pyridine saturation on each sample (Table 6.1, Main Text).

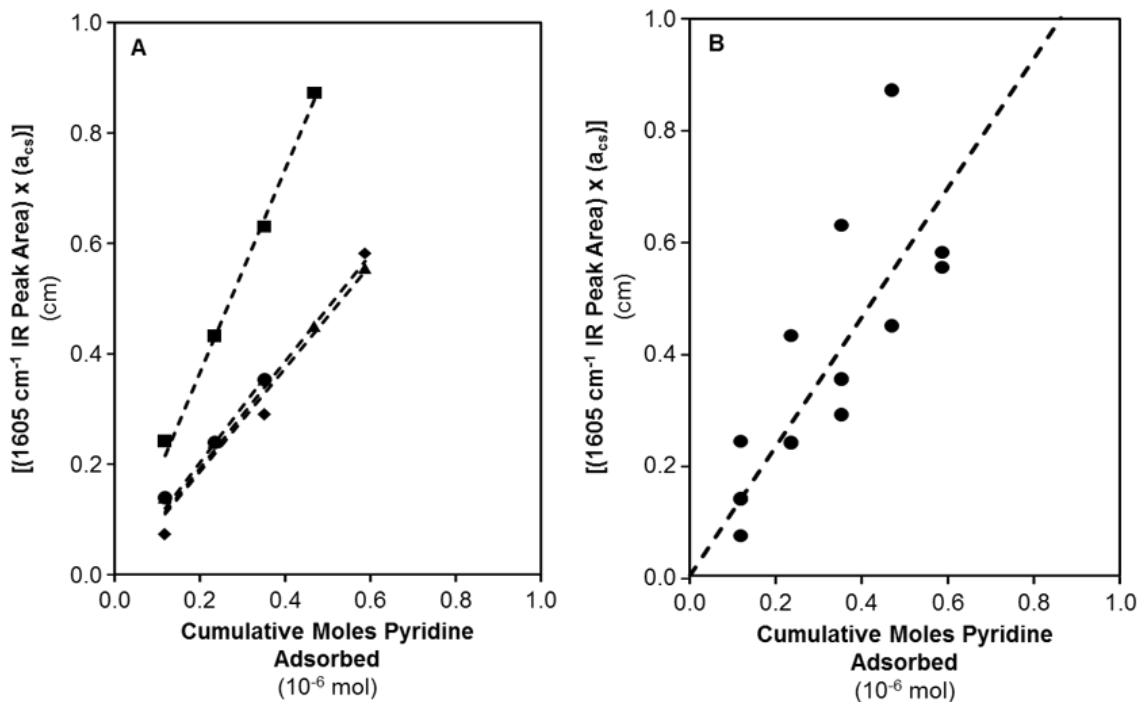


**Figure 6.22:** (A) Integrated peak area normalized by wafer cross-sectional areas for the IR feature centered at  $1605 \text{ cm}^{-1}$  as a function of moles pyridine adsorbed onto Ti-Beta-F-155 ( $\blacklozenge$ , Ti-Beta-F-135 ( $\bullet$ ), Ti-Beta-F-170 ( $\blacktriangle$ ), and Ti-Beta-OH-46 ( $\blacksquare$ ). Dashed lines indicate best fit lines through the origin for each sample with slopes equal to integrated molar extinction coefficients as listed in Table 6.7. (B) Integrated peak area normalized by wafer cross-sectional areas for the IR feature centered at  $1605 \text{ cm}^{-1}$  as a function of moles pyridine adsorbed onto Ti-Beta-F-155, Ti-Beta-F-135, Ti-Beta-F-170, and Ti-Beta-OH-46 as a single data set ( $\bullet$ ). The dashed line indicates the best fit line through the origin for the combined data set with the slope equal to the average integrated molar extinction coefficient.

**Table 6.6:**  $E(1605 \text{ cm}^{-1})$  values determined for four separate Ti-Beta samples by sequentially dosing pyridine at 423 K.

Sample	$E(1605 \text{ cm}^{-1})$ ( $\text{cm } \mu\text{mol}^{-1}$ )
Ti-Beta-F-135	1.84
Ti-Beta-F-170	0.97
Ti-Beta-OH-46	0.93
Ti-Beta-F-155	1.02

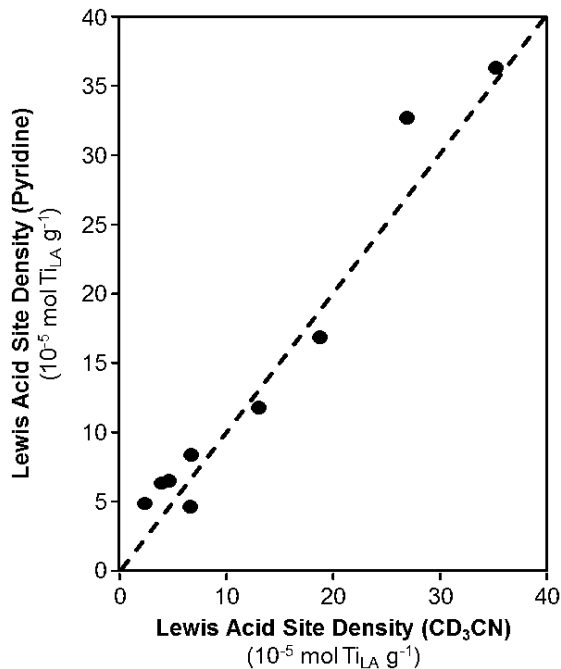


**Figure 6.23:** Lewis acid site densities determined from pyridine-saturation IR experiments plotted against Lewis acid site densities determined from CD<sub>3</sub>CN-saturation IR experiments. The dashed line is a parity line drawn to guide the eye.

Figure 6.23 shows Lewis acid site densities determined from pyridine-saturation infrared experiments plotted against Lewis acid site densities determined from CD<sub>3</sub>CN-saturation infrared experiments from Table 6.2. The two sets of Lewis acid site concentrations linearly correlate with one another, suggesting that they reflect similar site densities.

### 6.6.1.3 Assessing extracrystalline surface areas and normalized silanol densities on titanosilicate samples

Ti-Beta-F crystals exhibit square bipyramidal crystal morphology (Figure 6.11). Characteristic lengths were measured along the plane corresponding to the symmetric crystal center and along the terminal planes and the characteristic height was measured as the distance between those two planes. Characteristic length and height measurements were obtained from SEM images of more than 25 individual crystals selected randomly from multiple locations. Surface area and volume measurements were obtained by treating crystals as square frustums sharing a common base along a symmetrical middle plane.

For Ti-Beta-OH samples, the size of the final material is dependent on the size of the Al-Beta parent material which is maintained after dealumination and grafting as shown in Figure 6.13. Ti-Beta-OH crystals are prolate spheres agglomerated together into large clusters (Figure 6.12). Characteristic lengths were determined in both the  $r$  and  $z$  directions from over 25 individual crystals and averaged to quantify the average surface area and volume per particle.

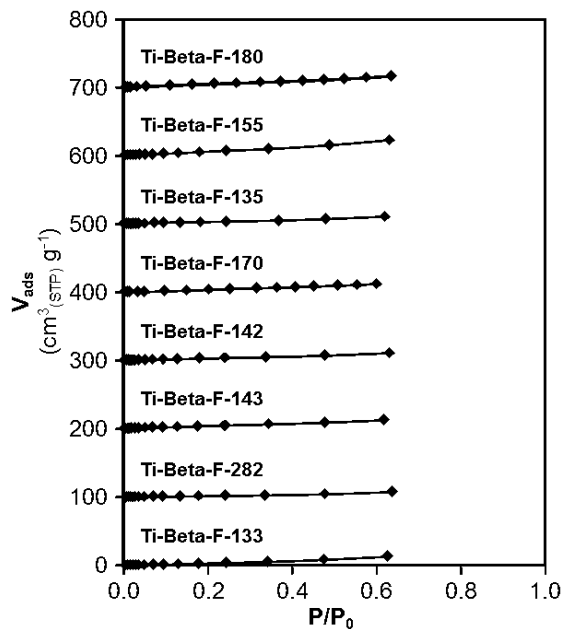
For materials of consistent zeolite topology, the surface-area-to-volume ratio is an adequate proxy for external surface areas. Surface-area-to-volume ratios per particle were normalized to Ti-Beta-F-155, a representative primary Ti-Beta-F sample studied in this work, assuming a consistent particle density between samples. Table 6.7 lists normalized surface-area-to-volume ratios along with normalized silanol densities quantified using IR spectra from  $\text{CD}_3\text{CN}$  titration experiments. A direct correlation between silanol density and external crystal surface area would be expected if all silanols are located only on external crystal surface areas. Silanol densities do not directly scale with surface-area-to-volume ratios, suggesting increased silanol densities present within the microporous environments of Ti-Beta-OH samples.

**Table 6.7:** Surface-area-to-volume (SA/V) ratios and silanol defect densities for selected Ti-Beta-F and Ti-Beta-OH samples normalized to Ti-Beta-F-155.

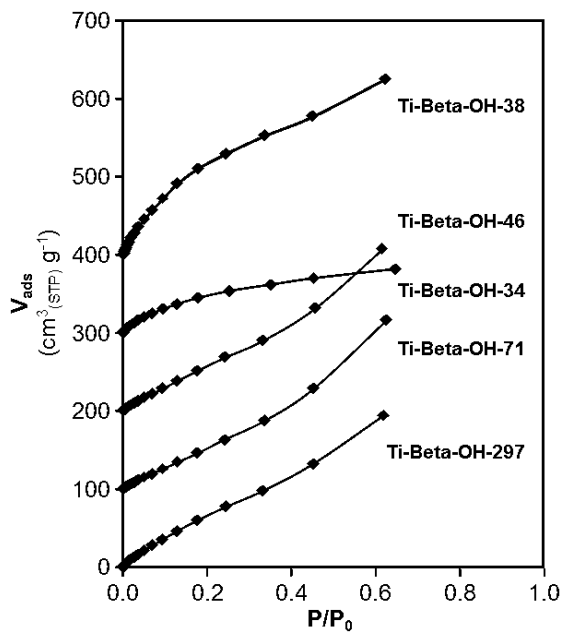
Sample	Normalized SA/V	Normalized Silanol Density
Ti-Beta-F-135	0.5	0.45
Ti-Beta-F-155	1.0	1.0
Ti-Beta-F-180	0.5	0.86
Ti-Beta-OH-46	18	3.6
Ti-Beta-OH-34	10	3.5
Ti-Beta-OH-71	10	4.1

## 6.6.2 Characterization of the hydrophobic properties of Ti-Beta zeolites

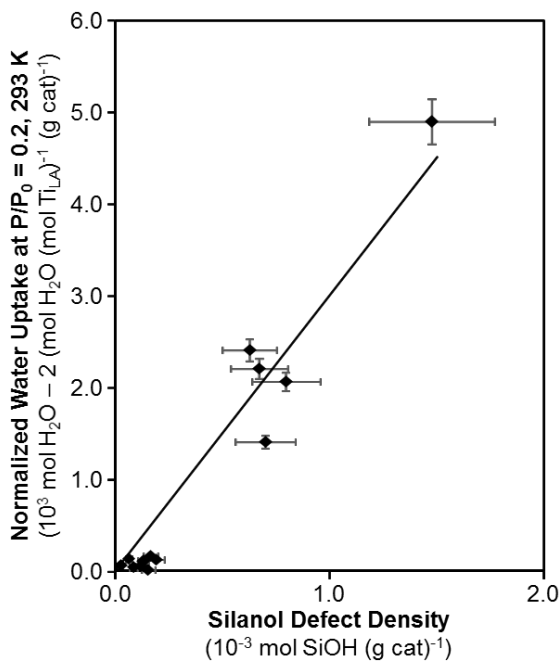
## 6.6.2.1 Vapor-phase adsorption isotherms on titanasilicate samples



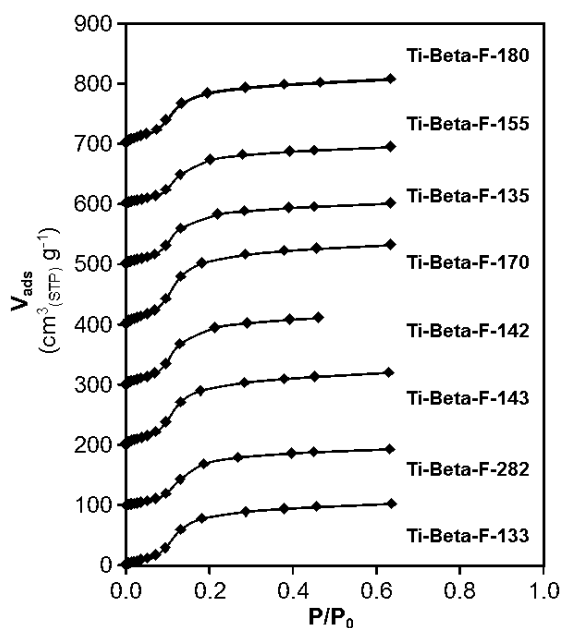
**Figure 6.24:** Vapor-phase water adsorption isotherms at 293 K on Ti-Beta-F samples studied in this work. Isotherms are offset by  $100 \text{ cm}^3 \text{ g}^{-1}$  for clarity.



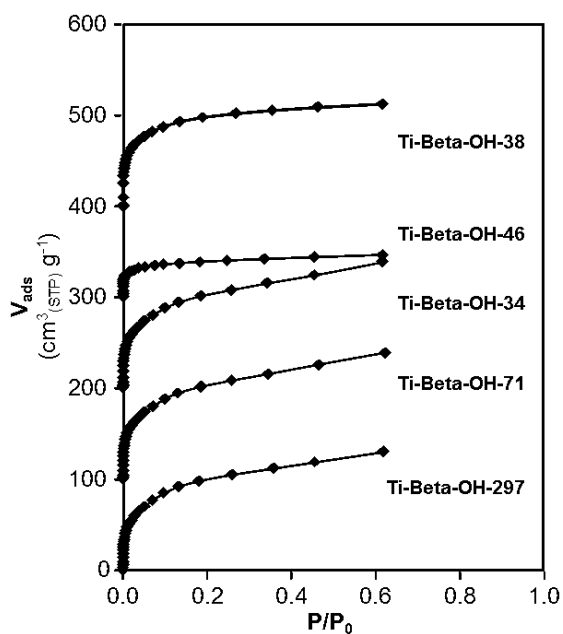
**Figure 6.25:** Vapor-phase water adsorption isotherms at 293 K on Ti-Beta-OH samples studied in this work. Isotherms are offset by  $100 \text{ cm}^3 \text{ g}^{-1}$  for clarity.



**Figure 6.26:** Water uptakes at  $P/P_0 = 0.2$  (373 K) after subtracting two moles of water molecules per mol Ti Lewis acid site (quantified by  $\text{CD}_3\text{CN}$  IR) as a function of the bulk silanol defect density (quantified by  $\text{CD}_3\text{CN}$  IR). The solid line is a best fit line drawn through the origin to guide the eye.



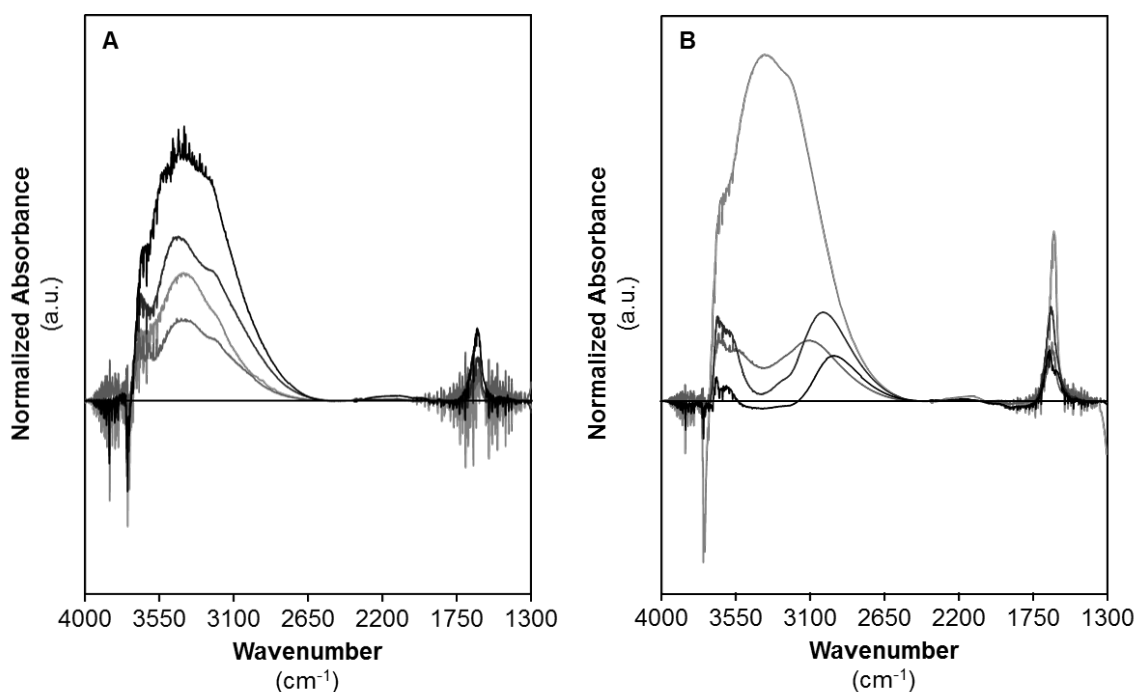
**Figure 6.27:** Vapor-phase methanol adsorption isotherms at 293 K on Ti-Beta-F samples studied in this work. Isotherms are offset by  $100 \text{ cm}^3 \text{ g}^{-1}$  for clarity.



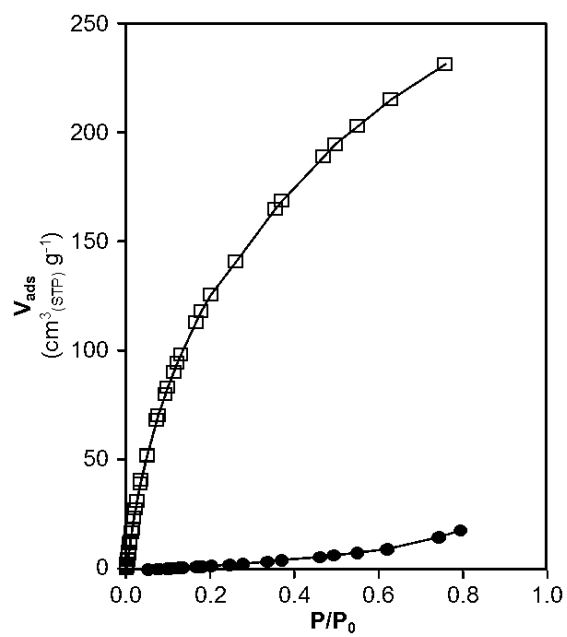
**Figure 6.28:** Vapor-phase methanol adsorption isotherms at 293 K on Ti-Beta-OH samples studied in this work. Isotherms are offset by  $100 \text{ cm}^3 \text{ g}^{-1}$  for clarity.

### 6.6.2.2 Spectroscopic characterization of intraporous water structures using transmission IR

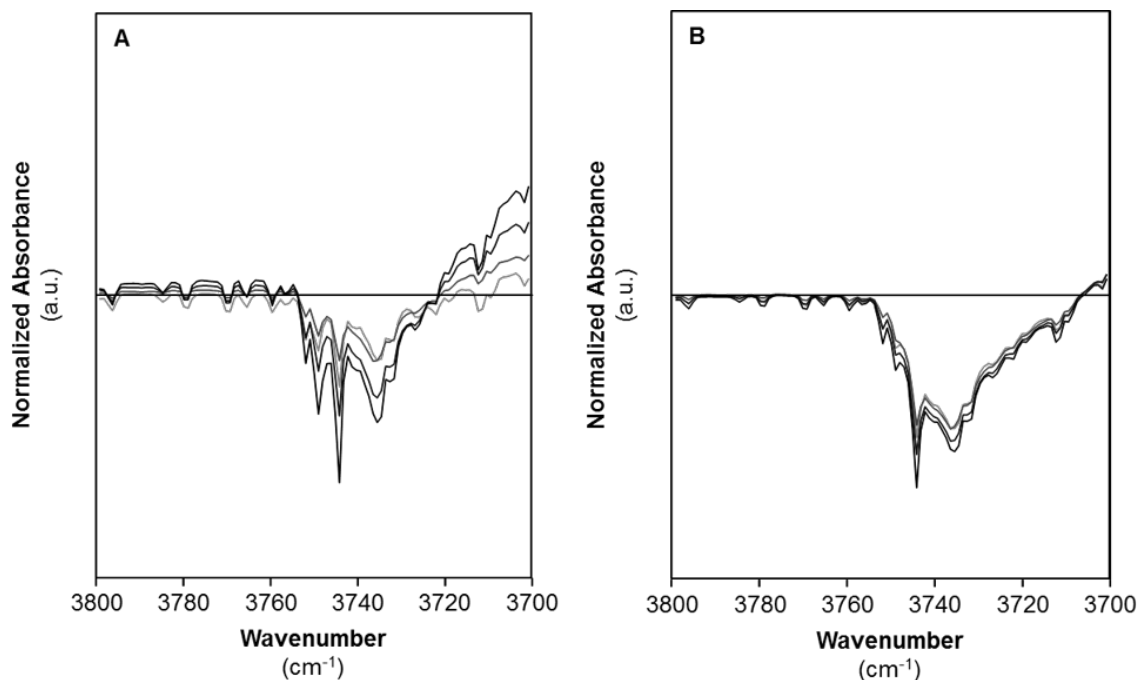
IR spectra of Ti-Beta-F-155 and Ti-Beta-OH-46 with increasing amounts of gas-phase water exposure are shown in Figures 6.29 and 6.31 that correspond to Figures 6.2A and 6.2B in the main text. Peaks centered between  $2700\text{--}3800\text{ cm}^{-1}$  and  $1550\text{--}1750\text{ cm}^{-1}$  increase systematically with increasing water partial pressure which can be equated to an adsorbed water density using the adsorption isotherms given in Figure 6.30.



**Figure 6.29:** Differential, subtracted, normalized, cell-corrected IR spectra of adsorbed  $\text{H}_2\text{O}$  at  $P/P_0=0.1, 0.2, 0.5,$  and  $0.75$  (lightest to darkest, 298 K) on (A) Ti-Beta-F-155 and (B) Ti-Beta-OH-46. Differential spectra are spectral changes between a given  $P/P_0$  value and the previous relative pressure spectra, isolating changes in spectral features due only to increasing water partial pressure.



**Figure 6.30:** Vapor-phase water adsorption isotherms at 298 K on Ti-Beta-F-155 ( $\bullet$ ) and Ti-Beta-OH-46 ( $\square$ ).



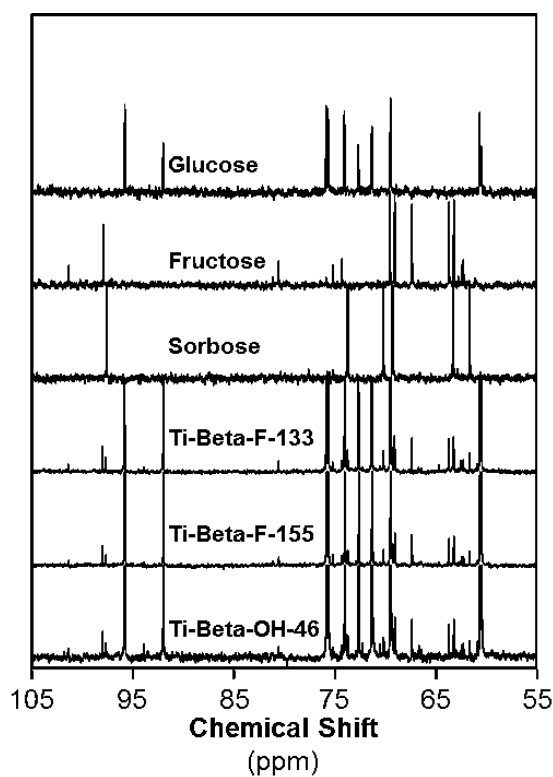
**Figure 6.31:** Subtracted IR spectra of the OH stretching region as a function of increased relative pressure of water on (A) Ti-Beta-F-155 and (B) Ti-Beta-OH-46.

Figure 6.31 shows IR subtraction spectra focusing on the OH stretching region where peaks corresponding to perturbed silanols are observed at 3735 and 3745 cm<sup>-1</sup>. Spectra collected on Ti-Beta-F-155 observe a continuous increase in perturbed silanol peak area while perturbed silanol peaks observed on Ti-Beta-OH-46 are saturated at lower water partial pressures.

### 6.6.3 Glucose isomerization mechanisms and kinetic measurements

#### 6.6.3.1 Identification of fructose and sorbose formed via glucose isomerization on Ti-Beta zeolites

Isomerization product identification was performed using solution phase  $^{13}\text{C}$  NMR as seen in Figure 6.30 on representative Ti-Beta-F and Ti-Beta-OH samples. Glucose, fructose, and sorbose standards are shown for comparison. The resonances at  $\delta = 61.6$  and  $67.3$  ppm are peaks indicative of sorbose and fructose respectively and used to confirm isomerization products formed on all samples.



**Figure 6.32:** Solution phase  $^{13}\text{C}$  NMR of monosaccharide solutions after contacting 5 wt% glucose solutions with Ti-Beta-F-133, Ti-Beta-F-155, and Ti-Beta-OH-46. Glucose, fructose and sorbose standards are given for direct comparison.

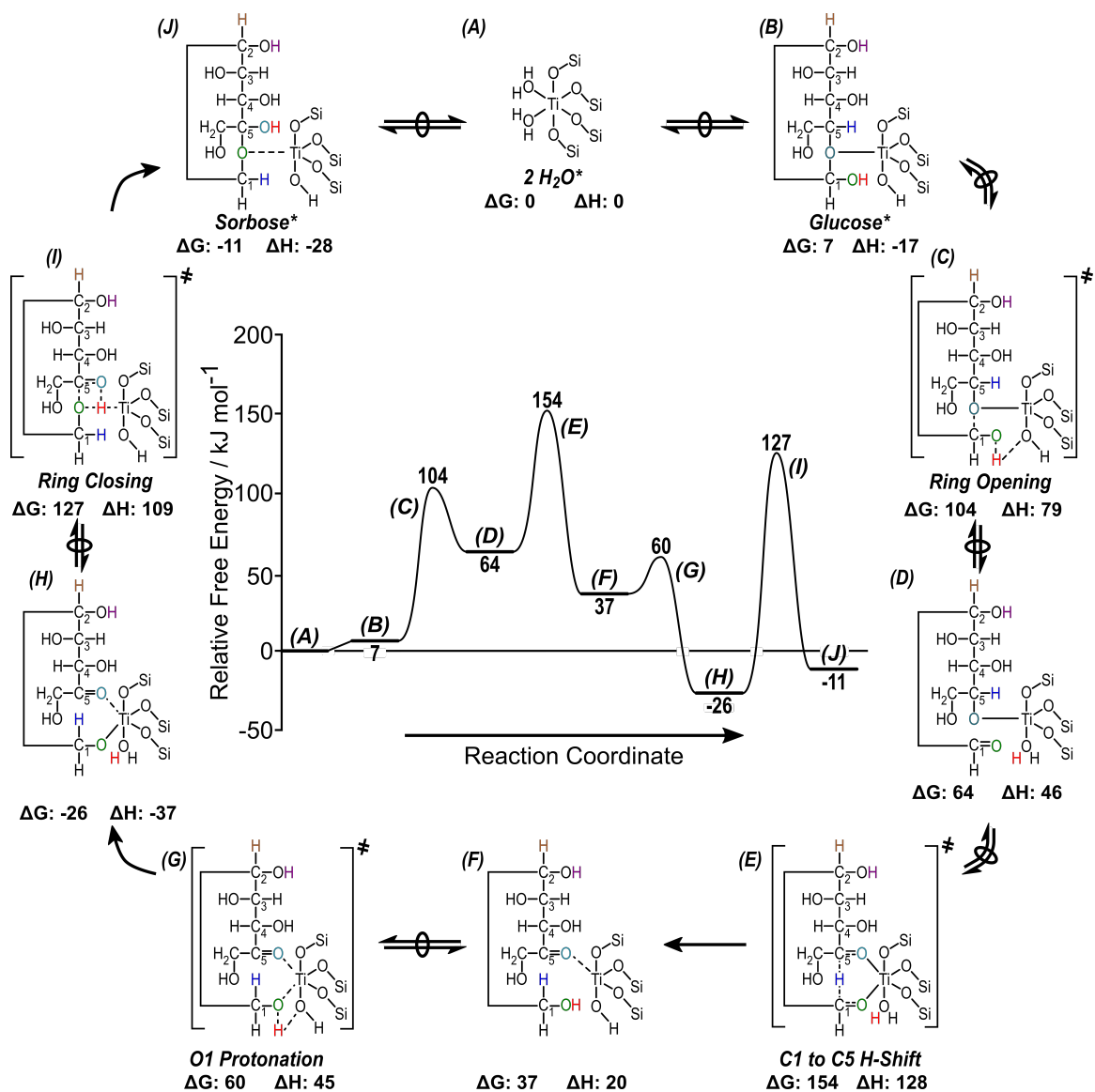


**Figure 6.33:** Free energy (373 K, 1 bar) reaction coordinate diagram for the formation of sorbose from glucose on closed-form Ti Lewis acid sites. Reaction arrows with overlaid circles indicate quasi-equilibrated events or the formation of transition states from relevant precursors. Relative enthalpies are given near inset images.

### 6.6.3.2 H/D KIE derivation as a function of temperature for a general vibrational frequency using zero point energies

The H/D KIE measures the apparent rate constant ratio resulting from isotopically labeling an atom located in a kinetically relevant bond which is the alpha C-H bond in the case of Lewis acid mediated glucose-to-fructose isomerization. The apparent isomerization rate constant in the first-order regime can be written as a series of coupled rate constants which reflects free energy differences between the hydride shift transition state with two free water molecules and the water dimer surface intermediate with a single free glucose molecule in solution as follows:

$$k_{first,i} = \frac{K_1 k_2}{K_4 K_5} = \frac{k_B T}{h} e^{-((\Delta G_{\ddagger}^{\circ} + 2\Delta G_W^{\circ}) - (\Delta G_{G,i}^{\circ} + \Delta G_{2W^*}^{\circ}))/RT} \quad (6.17)$$

Taking the ratio of rate constants, defined as the KIE, for glucose-H2 and glucose-D2 and canceling constants yields the following equation, which relates free energy differences between reaction rates with and without isotopic labeling:

$$KIE = \frac{k_{first,H2}}{k_{first,D2}} = \frac{e^{-((\Delta G_{\ddagger}^{\circ} + 2\Delta G_W^{\circ}) - (\Delta G_{G,H2}^{\circ} + \Delta G_{2W^*}^{\circ}))/RT}}{e^{-((\Delta G_{\ddagger}^{\circ} + 2\Delta G_W^{\circ}) - (\Delta G_{G,D2}^{\circ} + \Delta G_{2W^*}^{\circ}))/RT}} \quad (6.18)$$

Relevant free energy terms can then be separated between water-dependent and water-independent terms, where water-dependent terms are not affected by isotopically labeling the glucose reactant molecule and thus are irrelevant for observed KIEs:

$$KIE = \frac{e^{-((2\Delta G_W^{\circ} + \Delta G_{2W^*}^{\circ}))/RT} e^{-((\Delta G_{\ddagger}^{\circ},H2 - \Delta G_{G,H2}^{\circ}))/RT}}{e^{-((2\Delta G_W^{\circ} + \Delta G_{2W^*}^{\circ}))/RT} e^{-((\Delta G_{\ddagger}^{\circ},D2 - \Delta G_{G,D2}^{\circ}))/RT}} = \frac{e^{-((\Delta G_{\ddagger}^{\circ},H2 - \Delta G_{G,H2}^{\circ}))/RT}}{e^{-((\Delta G_{\ddagger}^{\circ},D2 - \Delta G_{G,D2}^{\circ}))/RT}} \quad (6.19)$$

Similarly, the transition state free energy is not affected by the isotopic label and the associated shift in reduced mass. Therefore, the KIE reflects the free energy difference between the two ground state energies of glucose-D2 and glucose-H2, respectively, which result from differences in zero point energies between C-H and C-D bonds:

$$KIE = e^{(\Delta G_{G,H2}^{\circ} - \Delta G_{G,D2}^{\circ})/RT} = e^{(ZPE_{H2} - ZPE_{D2})/k_B T} \quad (6.20)$$

Here,  $ZPE_i$  is the zero point energy for C-H and C-D bonds and  $k_B$  is the Boltzmann constant ( $1.3806 \times 10^{-23} \text{ m}^2 \text{ kg s}^{-2} \text{ K}^{-1}$ ). Substituting in the definition of the ZPE and accounting for the vibrational frequency shift upon isotopic labeling ( $\nu_D = 0.74\nu_H$ ), the following is derived to define the following generalized KIE equation:

$$\frac{k_{first,H2}}{k_{first,D2}} = e^{(\frac{1}{2}ch\nu_H - \frac{1}{2}ch\nu_D)/k_B T} = e^{(0.13ch\nu_H)/k_B T} \quad (6.21)$$

where  $c$  is the speed of light in a vacuum ( $2.998 \times 10^8 \text{ m s}^{-1}$ ) and  $h$  is the Planck constant ( $6.626 \times 10^{-34} \text{ m}^2 \text{ kg s}^{-1}$ ). This equation yields a KIE value of 2.1 at 373 K for a C-H bond scissoring vibration ( $\nu_H = 1500 \text{ cm}^{-1}$ ) and 4.5 at 373 K for a C-H stretching vibration ( $\sim 3000 \text{ cm}^{-1}$ ) corresponding to the kinetically relevant vibrational mode for the Lewis acid and Lewis base catalyzed transition state, respectively. In the case of severe internal mass transfer limitations, the apparent rate constant ratio is equal to the square root of the intrinsic ratio, yielding lower observed KIE values. In this case, the apparent KIE value for a C-H bond scissoring vibration (intrinsic KIE of 2.1) at 373 K would equal a value of 1.4.

$$\left(\frac{k_{first,H2}}{k_{first,D2}}\right)_{app} = \sqrt{\frac{k_{first,H2}}{k_{first,D2}}} \quad (6.22)$$

The effect of severe internal mass transfer limitations on observed KIEs is independent of the kinetic regime and holds with measured KIE values (2.1-2.3) in both first-order and zero-order regimes.

The apparent lack of mass transfer reflected by experimentally measured KIE values of 2.1 is supported by consistent glucose isomerization rates for fructose and sorbose formation normalized per total Ti content (Figure 6.4, main text) and as a function of Lewis acidic Ti content (Figure 6.34).

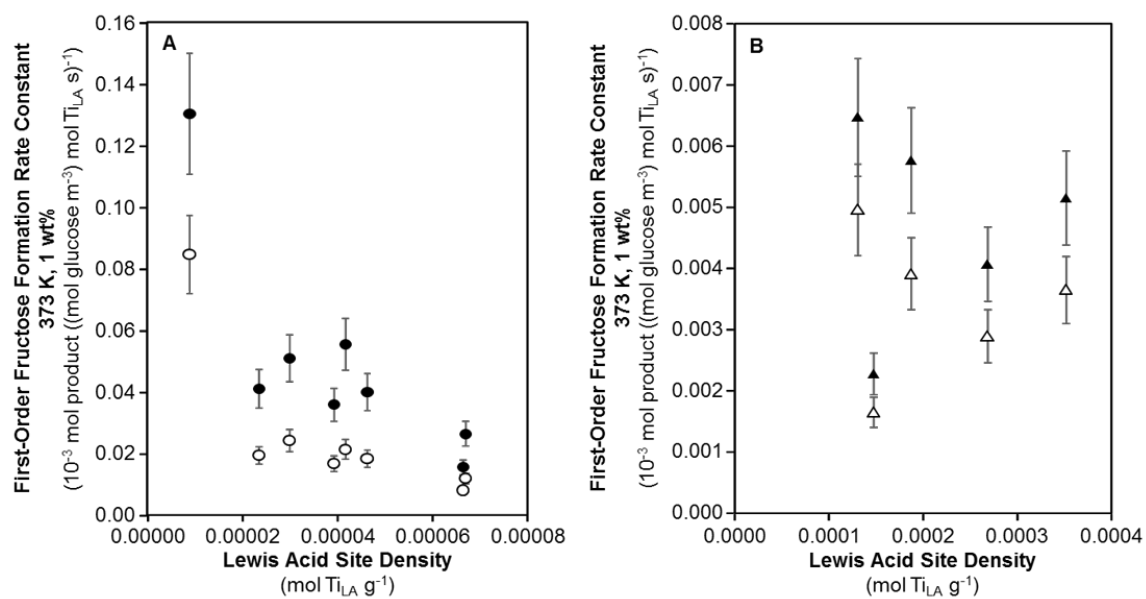


**Figure 6.34:** First-order fructose ( $\bullet$ ,  $\blacktriangle$ ) and sorbose ( $\circ$ ,  $\triangle$ ) formation rate constants (373 K, pH 4) normalized per total Lewis acidic Ti content (measured from  $\text{CD}_3\text{CN}$  IR) as a function of Lewis acidic Ti density for (A) Ti-Beta-F and (B) Ti-Beta-OH samples.

### 6.6.3.3 Bulk solution glucose and osmotic activity coefficient quantification

Standard state glucose activity coefficients (298 K), osmotic coefficients, and excess partial molar enthalpies were linearly interpolated from literature values as a function of glucose mole fraction where activity coefficients vary from unity to 1.329 (298 K) at high glucose concentrations approaching the aqueous room temperature solubility of glucose [334]. Interpolated activity coefficients were then adjusted to reaction temperature using the following thermodynamic relationship [335]:

$$\frac{-\overline{H}_i^E}{RT^2} = \frac{\partial}{\partial T} \ln(\gamma_i) \quad (6.23)$$

Here,  $\overline{H}_i^E$  is the excess partial molar enthalpy of species  $i$  in solution,  $R$  is the universal gas constant,  $T$  is absolute temperature in K, and  $\gamma_i$  is the activity coefficient of species  $i$  in solution which is a function of temperature and the concentration of species  $i$ . Excess partial molar enthalpies are assumed to be independent of temperature across the studied temperature range. Eq. 6.23 can be integrated into:

$$\gamma_i = \gamma_i^0 e^{\frac{\overline{H}_i^E}{R} \left( \frac{1}{T} - \frac{1}{T^0} \right)} \quad (6.24)$$

Here,  $\gamma_i$  and  $\gamma_i^0$  are the activity coefficients of species  $i$  at the reaction temperature and standard temperature (298 K) respectively, and  $T$  and  $T^0$  are the reaction and standard state absolute temperatures respectively. Glucose and osmotic activities at reaction conditions were then calculated from the initial concentrations of glucose and water multiplied by the temperature-adjusted osmotic or activity coefficient as appropriate. We note that all kinetic trends hold constant independent of whether concentrations or thermodynamic activities (using activity coefficients quantified at either 298 K or reaction temperatures, see Figure 6.35 and Section 6.6.5.2 below) are used for glucose and water species. In the main text, temperature-adjusted activities are used as an accurate descriptor in the rate equation models.

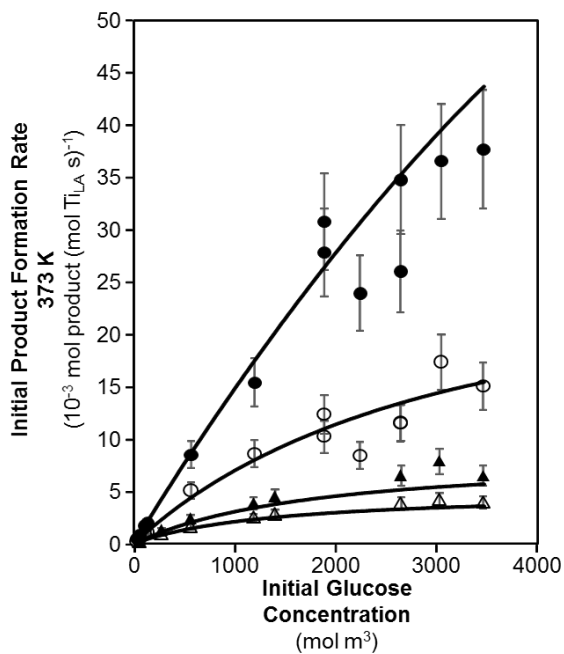


**Figure 6.35:** Dependence of initial glucose isomerization rates (373 K, pH 4) for fructose (filled) and sorbose (open) formation on Ti-Beta-F-155 (●, ○) and Ti-Beta-OH-46 (▲, △) as a function of initial glucose concentration (1–50 wt%). Solid lines represent fits of the experimental data to the rate equation (Eq. 6.25 of the main text) using activation enthalpies and entropies given in Table 6.4.

## 6.6.4 Characterization and kinetic effects of bound surface species in first-order and zero-order regimes

### 6.6.4.1 ATR-IR and modulation excitation spectroscopy quantification for the identification of bound reactive intermediates using MCR-ALS data analysis techniques

The time-resolved FTIR spectra for each Beta material were collected and processed mathematically prior to analyzing spectral features of individual species. The time-domain raw spectra were first averaged into a single period using:

$$A_{\text{average}}(t) = \frac{T}{T_{\text{total}}} \sum_{i=0}^{\frac{T_{\text{total}}}{T}} A(t + iT) \quad (6.25)$$

Here  $A(t + iT)$  is the absorbance at each time point,  $A_{\text{average}}(t)$  is the absorbance after averaging into a single period,  $T$  is the time period of stimulation, and  $T_{\text{total}}$  is the total time for which the experiment was run; therefore,  $\frac{T_{\text{total}}}{T}$  represents the total number of periods measured during a MES experiment. The averaged spectra were then subjected to phase sensitive detection (PSD) using:

$$A_k(\varphi_k^{\text{PSD}}) = \frac{2}{T} \int_0^T A_{\text{average}}(\vartheta, t) \sin(k\omega t + \varphi_k^{\text{PSD}}) dt \quad (6.26)$$

Eq. 6.26 was transformed into a Fourier series by Fourier's theorem for a periodic function gives:

$$A(\vartheta, t) = \sum_{i=1}^N A_{i,0}(\vartheta) + \sum_{i=1}^N \sum_{k=1}^{\infty} (A_{i,k}^{0^\circ}(\vartheta) \cos kt + A_{i,k}^{90^\circ}(\vartheta) \sin kt) \quad (6.27)$$

where  $A_{i,0}$  is the dc component, and  $A_{i,k}^{0^\circ}$  and  $A_{i,k}^{90^\circ}$  are the orthogonal components of the vector.

Each of the above terms in the integral was converted into a single equation using Simpson's Rule:

$$\int_0^T y(t) dt = \frac{\Delta t}{3} (y_0 + 4y_1 + 2y_2 + 4y_3 + \dots + 2y_{n-2} + 4y_{n-1} + y_n) = \frac{\Delta t}{3} \sum_{i=0}^n s_i y_i \quad (6.28)$$

where  $s_i$ , is Simpson's coefficient (where  $n$  must be an even number). A detailed mathematical derivation and implications are discussed in detail elsewhere [345]. A self-developed MATLAB code reported previously [320] was used to resample and average the time resolved spectra and then perform the PSD calculations described in Eqs. 6.27 and 6.28 to yield the phase domain spectra. Figure 6.36 shows an example of the time resolved and phase resolved spectra for Ti-Beta-F-155.

Phase resolved spectra were then subjected to MCR-ALS to extract independent species, including the surface coverages and spectra. Spectra were truncated to contain wavenumbers 3800–2600 and 1800–700  $\text{cm}^{-1}$  and phase angles 1–181° to reduce data set size into MATLAB. Singular value decomposition suggests only two independent species to fully describe the phase resolved spectra. Two sine wave functions were input for the initial guess of the surface coverages and the spectra were constrained to solve for positive features. The MATLAB program iteratively solved for spectra and surface coverages until the convergence criteria were met and the sum of residuals was less than  $10^{-16}$ . The resulting spectra were smoothed with a Fourier Transform filter, baseline corrected, and normalized to the most intense feature between 1000 and 1150  $\text{cm}^{-1}$  using OriginLab's OriginPro 9 software. Initial guesses of three or more species yielded solutions of zero for spectra and surface coverages of all species after two, further indicating that the phase resolved spectra can be completely described by just two independent species.

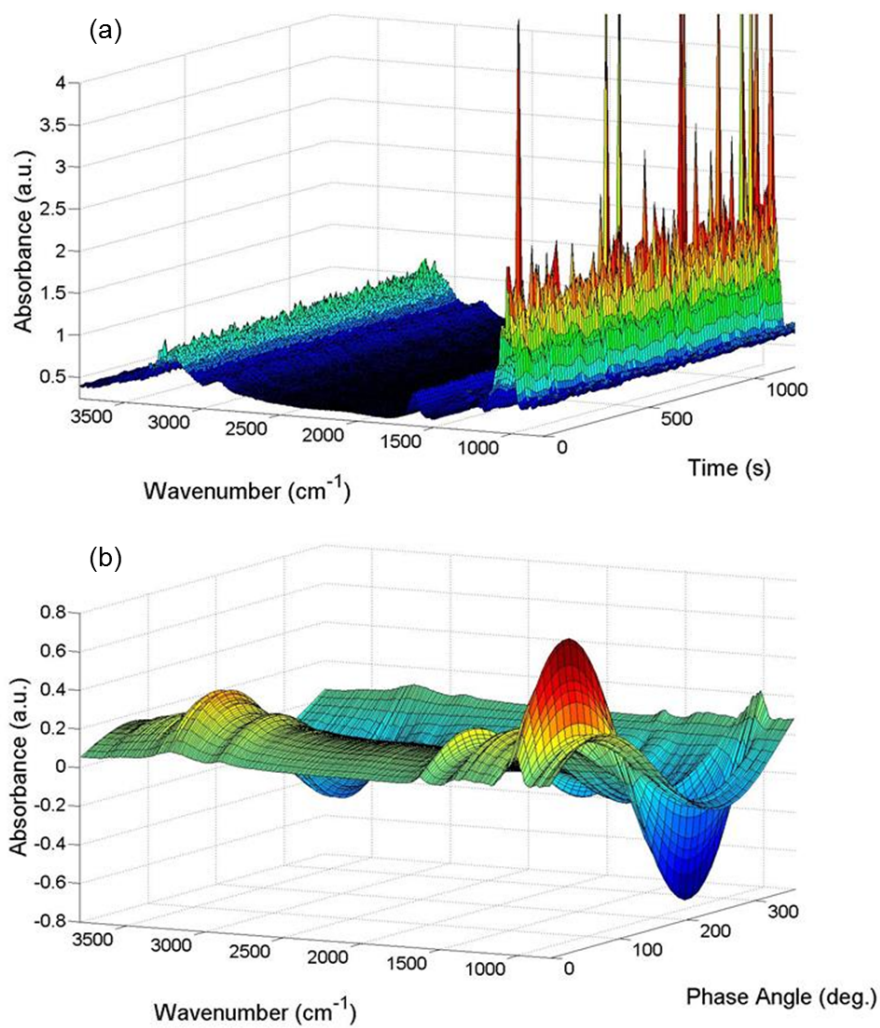


**Figure 6.36:** a) Time-resolved infrared spectra obtained *in situ* during reactions of glucose and water over Ti-Beta-F-155 while modulating glucose concentrations (42–50 wt%) with a period length of 250 s at 373 K. b) Phase resolved spectra that result from phase sensitive detection of the time resolved spectra in (a). Coloring indicates absorbance intensity.

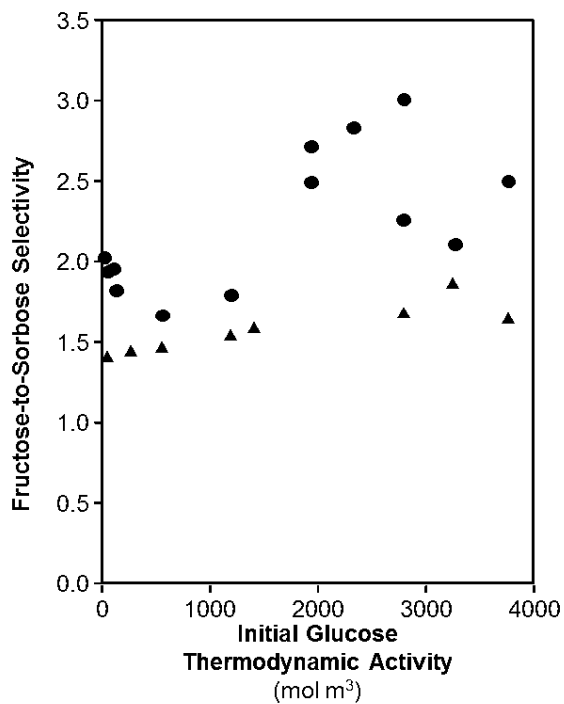


**Figure 6.37:** Dependence of fructose-to-sorbose selectivity (373 K, pH 4) on Ti-Beta-F-155 (●) and Ti-Beta-OH-46 (▲) as a function of initial glucose thermodynamic activity. Relatively constant product selectivities support the identification of the secondary bound glucose species being a bound intermediate which is not directly responsible for sorbose formation as relative coverages of MARI and secondary bound species observed from ATR-IR are affected by changes in initial glucose activity.

## 6.6.4.2 Ti structural characterization using XAS and DFT

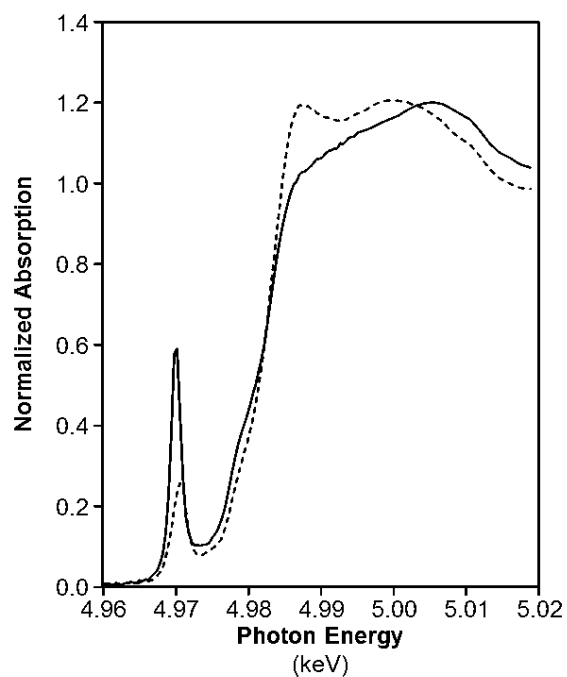


**Figure 6.38:** Ti K edge XANES of water exchanged Ti-Beta-OH-46 zeolite after dehydration at 523 K in He (solid) and under ambient conditions (dashed). The increase in intensity of the pre-edge peak is consistent with a decrease in coordination number from 6 to 4 upon dehydration.

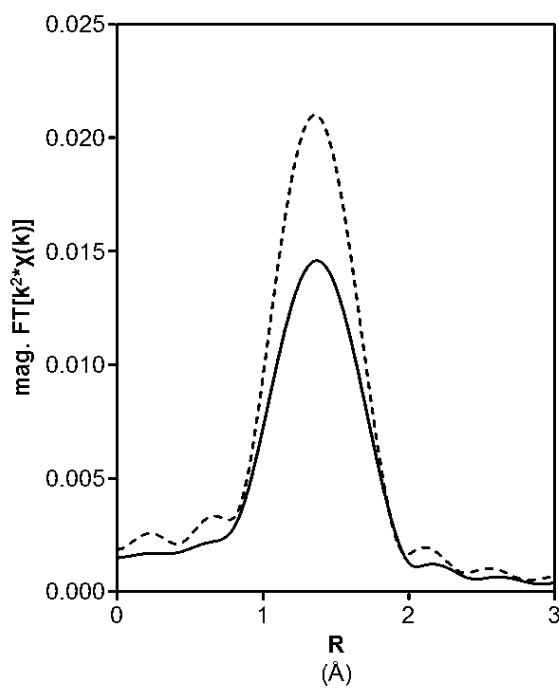


**Figure 6.39:** Magnitude of the Fourier transform of the  $k^2$ -weighted Ti K edge EXAFS of water exchanged Ti-Beta-OH-46 zeolite under ambient conditions (solid) and after dehydration at 523 K in He (dashed).

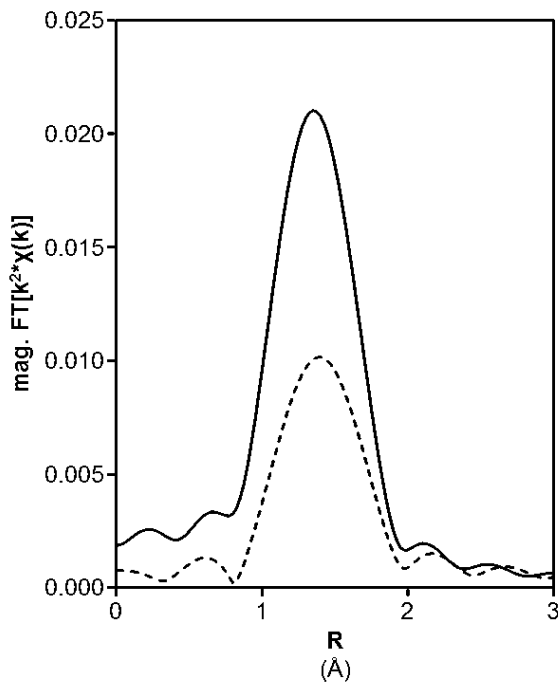


**Figure 6.40:** Magnitude of the Fourier transform of the  $k^2$ -weighted Ti K edge EXAFS of water exchanged Ti-Beta-OH-46 zeolite after dehydration at 523 K in He (solid) and  $\Delta$ EXAFS of the hydrated and dehydrated water exchanged catalyst (dashed). The  $\Delta$ EXAFS spectrum was obtained by subtracting the  $k^0$ -weighted EXAFS of the sample after dehydration from the  $k^0$ -weighted EXAFS of the sample under ambient conditions and is representative of the water adsorbed on Ti under ambient conditions.

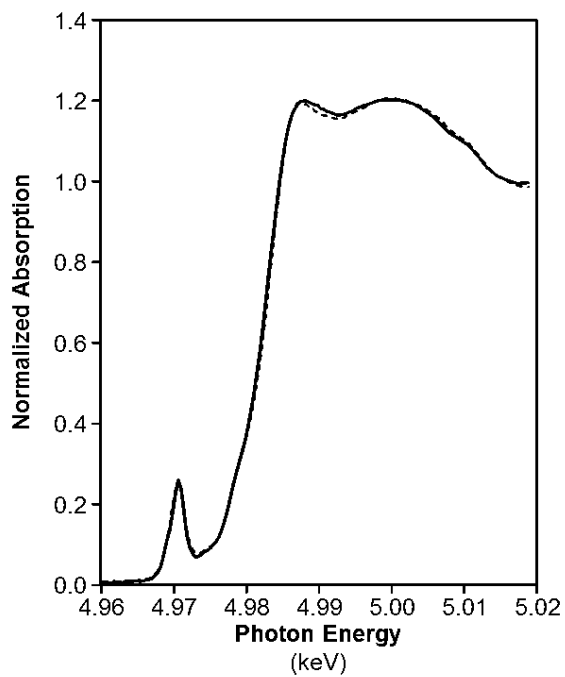


**Figure 6.41:** Ti K edge XANES of water (dashed) and glucose (solid) exchanged Ti-Beta-OH-46 zeolite under ambient conditions. The spectra are identical within experimental error indicating Ti has equivalent coordination environments in the two samples. The intensity of the pre-edge peak is consistent with a coordination number of 6.

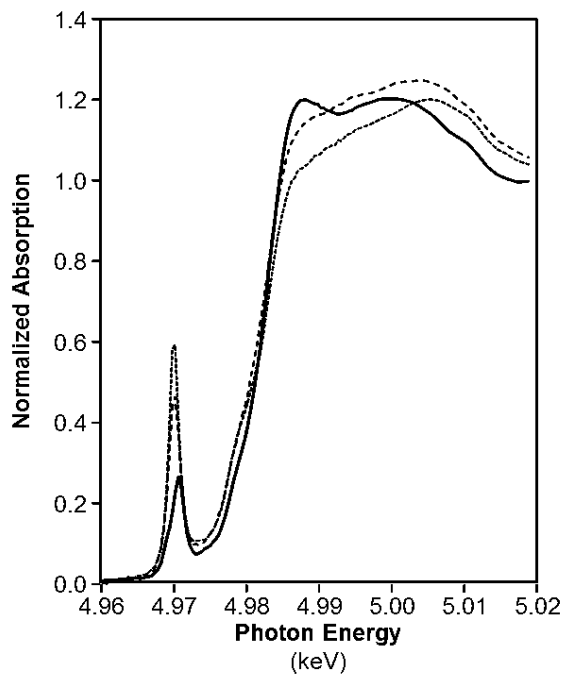


**Figure 6.42:** Ti K edge XANES of Ti-Beta-OH-46 zeolite: solid – glucose exchanged under ambient conditions, long dashes – glucose exchanged after treatment at 523 K in He, and short dashes – water exchanged after treatment at 523 K in He. The intensity of the pre-edge peak in the glucose exchanged sample after treatment in He at 523 K is consistent with a coordination number of 5 and suggests glucose adsorbed through a single oxygen.

The Ti-O coordination number of 4 obtained from fitting the EXAFS of the sample after dehydration is consistent with the intense XANES pre-edge peak at 4.9700 keV and the presence of tetrahedral Ti in the zeolite framework. The pre-edge peak in the hydrated sample is less intense and shifted to higher energy (4.9707 keV) than the hydrated sample and is consistent with a Ti coordination number of 6 [346]. However, the magnitude of the Fourier transform of the  $k^2$ -weighted EXAFS of the hydrated sample is lower than the dehydrated catalyst. Fitting the EXAFS of the hydrated sample with a single Ti-O path gives a coordination number of 3.8, lower than the value of 6 expected from the XANES, and a bond distance of 1.85 Å. Satisfactory fits of the hydrated and dehydrated spectra were obtained with Debye-Waller factors ( $\Delta\sigma^2$ ) of  $1.0 \times 10^{-3}$  and  $-2.0 \times 10^{-3}$  Å<sup>2</sup>, respectively. The higher  $\Delta\sigma^2$  indicates a larger distributions of Ti-O bond distances under ambient conditions than after dehydration. This suggests that the fitted coordination number of 3.8 is a result of destructive interference between Ti-O scattering paths of different distances (i.e. Ti-O<sub>framework</sub> and Ti-O<sub>water</sub>).

To determine the number and bond distance of the adsorbed water, a  $\Delta$ EXAFS spectrum was obtained by taking the difference of the  $k^0$ -weighted EXAFS of the ambient and dehydrated samples. In obtaining the  $\Delta$ EXAFS spectrum it was assumed that the four Ti-O framework bonds in the dehydrated sample are unaffected by the adsorption of water. A Ti-O coordination number of 2 and bond distance of 1.94 Å were obtained from fitting the difference spectrum. Therefore, the total Ti-O coordination number of the hydrated sample is 6, consistent with XANES, at an average bond distance of 1.87 Å, consistent with the single scatter fit of the ambient spectrum.

**Table 6.8:** Ti energies, coordination numbers, and bond distances determined from Ti XAS.

Sample	Pre-edge Energy (keV)	Edge Energy (keV)	Ti-O Coordination Number	Ti-O Bond Distance ( $\text{\AA}$ )	$\Delta\sigma^2$ ( $10^3 \text{\AA}^2$ )	E0 (eV)
Water Exchanged, Dehydrated	4.9700	4.978	4.2	1.83	-2.0	0.3
Water Exchanged, Hydrated (Single scatter fit)	4.9707	4.978	3.8	1.85	1.0	-0.7
$\Delta$ EXAFS (ambient – dehydrated)	–	–	2.1	1.94	-3.0	-12
Water Exchanged, Hydrated	–	–	4.2	1.83	-2.0	0.3
(Total, two scatter fit)	–	–	2.1	1.94	-3.0	-12
Glucose Exchanged, Hydrated	4.9707	4.978	6 <sup>a</sup>	–	–	–
Glucose Exchanged, Dehydrated	4.9702	4.978	5 <sup>a</sup>	–	–	–

<sup>a</sup>Coordination numbers were determined from the intensity of the pre-edge peak of the Ti K edge XANES spectra. Due to poor data quality in the EXAFS region of the absorption spectra reliable fits of these samples could not be obtained.

## 6.6.5 Enthalpic and entropic contributions of hydrophobic reaction pockets for aqueous-phase glucose isomerization

### 6.6.5.1 Derivation of mechanism-based rate expressions for glucose isomerization catalyzed by Lewis acid sites

A reaction pathway for the parallel formation of fructose and sorbose from glucose is given in Figure 6.43, identical to Figure 6.43 from the main text. Here,  $G_{(l)}$ ,  $F_{(l)}$ , and  $S_{(l)}$  stand for glucose, fructose, and sorbose respectively in the liquid phase, \* represents a bare Lewis acid site,  $G^*$  represent the adsorbed glucose intermediate,  $(R^*)_F$  and  $(R^*)_S$  represent the bound glucose precursors leading to fructose and sorbose respectively,  $F^*$  and  $S^*$  represent bound fructose and sorbose respectively, and  $K_i$  is the equilibrium coefficient for Step  $i$ .  $k_{2,i}$  is the rate constant for product formation from the kinetically relevant hydride shift transition state for each product. Sequential water (W) adsorption onto a Lewis acid site forms one ( $W^*$ ) and two ( $2W^*$ ) bound water intermediates (Figure 6.43). This figure and the rate equation derived from it are similar to that reported in Ref. [53].

In Figure 6.43, sequences F and S reflect glucose isomerization to fructose and to sorbose. Net isomerization rates to fructose ( $r_{isom,F}$ ) and sorbose ( $r_{isom,S}$ ) are given by:

$$r_{isom,F} = r_{2,F} - r_{-2,F} \quad (6.29)$$

$$r_{isom,S} = r_{2,S} - r_{-2,S} \quad (6.30)$$

From the law of mass action, reaction rates of elementary steps are proportional to rate constants ( $k_i$ ) and concentrations of kinetically relevant transition states ( $c_{\ddagger,i}$ ). Therefore, net reaction rates can be written as:

$$r_{isom,F} = k_{2,F}c_{\ddagger,F} - k_{-2,F}c_{F^*} \quad (6.31)$$

$$r_{isom,S} = k_{2,S}c_{\ddagger,S} - k_{-2,S}c_{S^*} \quad (6.32)$$



$$r_{isom,S} = \frac{k_{2,S}}{\gamma_{\ddagger,S}} a_{\ddagger,S} \left( 1 - \frac{k_{-2,S} a_{S^*} \gamma_{\ddagger,S}}{k_{2,S} a_{\ddagger,S} \gamma_{S^*}} \right) = \frac{k_{2,S}}{\gamma_{\ddagger,S}} a_{\ddagger,S} \left( 1 - \frac{a_{S^*} \gamma_{\ddagger,S}}{K_{2,S} a_{\ddagger,S} \gamma_{S^*}} \right) \quad (6.37)$$

or:

$$r_{isom,F} = \frac{k_{2,F}}{\gamma_{\ddagger,F}} a_{\ddagger,F} (1 - \eta_F) \quad (6.38)$$

$$r_{isom,S} = \frac{k_{2,S}}{\gamma_{\ddagger,S}} a_{\ddagger,S} (1 - \eta_S) \quad (6.39)$$

Here,  $\eta_F$  and  $\eta_S$  are the approach-to-equilibrium terms for Steps 2F and 2S respectively (Figure 6.43).

The 1,2-hydride shift (or 1,5-hydride shift) step is kinetically relevant for fructose (or sorbose) formation as determined from H/D kinetic isotope effect measurements and isotopic tracer studies [91]. Steps 1F, 1S, 3F, 3S, 4 and 5 are then assumed to be quasi-equilibrated and the following equilibrium expressions are derived to relate thermodynamic activities of reactant and product species:

$$K_1 = \frac{a_{G^*}}{a_G a_*} \quad (6.40)$$

$$K_{3,F} = \frac{a_F a_*}{a_{F^*}} \quad (6.41)$$

$$K_{3,S} = \frac{a_S a_*}{a_{S^*}} \quad (6.42)$$

$$K_4 = \frac{a_{W^*}}{a_W a_*} \quad (6.43)$$

$$K_5 = \frac{a_{2W^*}}{a_W a_{W^*}} \quad (6.44)$$

In addition, the kinetically relevant bound glucose intermediates leading to fructose,  $(R^*)_F$ , or sorbose,  $(R^*)_S$ , formation are quasi-equilibrated with the respective hydride shift transition state as follows:

$$K_{R,F} = \frac{a_{\ddagger,F}}{a_{G^*}} \quad (6.45)$$

$$K_{R,S} = \frac{a_{\ddagger,S}}{a_{G^*}} \quad (6.46)$$

Eqs. 6.45 and 6.46 couple together the formation of the kinetically relevant bound glucose intermediate from the adsorbed glucose intermediate with the subsequent formation of the hydride shift transition state into a single equilibrium coefficient,  $K_{R,i}$ . Solving Eqs. 6.45 and 6.46 for  $a_{\ddagger,F}$  and  $a_{\ddagger,S}$ , isomerization rates can then be expressed as:

$$r_{isom,F} = \frac{k_{2,F}}{\gamma_{\ddagger,F}} K_{R,F} a_{G^*} (1 - \eta_F) \quad (6.47)$$

$$r_{isom,S} = \frac{k_{2,S}}{\gamma_{\ddagger,S}} K_{R,S} a_{G^*} (1 - \eta_S) \quad (6.48)$$

And further expressed using Eq. 6.40 as:

$$r_{isom,F} = \frac{k_{2,F}}{\gamma_{\ddagger,F}} K_{R,F} K_1 a_G a_* (1 - \eta_F) \quad (6.49)$$

$$r_{isom,S} = \frac{k_{2,S}}{\gamma_{\ddagger,S}} K_{R,S} K_1 a_G a_* (1 - \eta_S) \quad (6.50)$$

Eqs. 6.49 and 6.50 can be rewritten in terms of activity coefficients ( $\gamma_i$ ) and concentrations ( $c_i$ ):

$$r_{isom,F} = \frac{k_{2,F}}{\gamma_{\ddagger,F}} K_{R,F} K_1 \gamma_G \gamma_* c_G c_* (1 - \eta_F) \quad (6.51)$$

$$r_{isom,S} = \frac{k_{2,S}}{\gamma_{\ddagger,S}} K_{R,S} K_1 \gamma_G \gamma_* c_G c_* (1 - \eta_S) \quad (6.52)$$

Total Lewis acid site concentrations ( $c_{*,tot}$ ) are related to the concentrations of unoccupied sites ( $c_*$ ) and sites with bound monosaccharide or solvent molecules from Figure 6.43 through the following site balance:

$$c_{*,tot} = c_* + c_{G^*} + c_{R,F} + c_{R,S} + c_{F^*} + c_{S^*} + c_{W^*} + c_{2W^*} \quad (6.53)$$

Eq. 6.53 can be rewritten using Eqs. 6.40–6.46:

$$c_{*,tot} = c_* + \frac{K_1 a_G \gamma_* c_*}{\gamma_{G^*}} + \frac{K_1 K_{R,F} a_G \gamma_* c_*}{\gamma_{R,F}} + \frac{K_1 K_{R,S} a_G \gamma_* c_*}{\gamma_{R,S}} + \frac{a_F \gamma_* c_*}{K_{3,F} \gamma_{F^*}} + \frac{a_S \gamma_* c_*}{K_{3,S} \gamma_{S^*}} + \frac{K_4 a_W \gamma_* c_*}{\gamma_{W^*}} + \frac{K_4 K_5 a_W^2 \gamma_* c_*}{\gamma_{2W^*}} \quad (6.54)$$

$c_*$  can be factored out of the right-hand side of Eq. 6.47 leading to the following equation:

$$c_{*,tot} = c_* \left( 1 + \frac{K_1 a_G \gamma_*}{\gamma_{G^*}} + \frac{K_1 K_{R,F} a_G \gamma_*}{\gamma_{R,F}} + \frac{K_1 K_{R,S} a_G \gamma_*}{\gamma_{R,S}} + \frac{a_F \gamma_*}{K_{3,F} \gamma_{F^*}} + \frac{a_S \gamma_*}{K_{3,S} \gamma_{S^*}} + \frac{K_4 a_W \gamma_*}{\gamma_{W^*}} + \frac{K_4 K_5 a_W^2 \gamma_*}{\gamma_{2W^*}} \right) \quad (6.55)$$

Eq. 6.55 can then be rewritten in terms of fractional coverages ( $\theta_i$ ) of each bound adsorbate:

$$c_{*,tot} = c_* (\theta_* + \theta_{G^*} + \theta_{R^*,F} + \theta_{R^*,S} + \theta_{F^*} + \theta_{S^*} + \theta_{W^*} + \theta_{2W^*}) \quad (6.56)$$

These fractional coverage terms are located in the isomerization rate expression denominator prior to establishing the most abundant surface intermediates.

From spectroscopic evidence discussed in the main text and both first-order and zero-order kinetic behavior in initial glucose activity, the most abundant surface intermediates are the Lewis acid site with two bound water molecules at dilute glucose concentrations ( $<1200 \text{ mol m}^{-3}$ ) and the Lewis acid site with adsorbed glucose at high glucose concentrations ( $>2700 \text{ mol m}^{-3}$ ). Eq. 6.55 can then be reduced to:

$$c_{*,tot} = c_* \left( \frac{K_1 a_G \gamma_*}{\gamma_{G^*}} + \frac{K_4 K_5 a_W^2 \gamma_*}{\gamma_{2W^*}} \right) \quad (6.57)$$

Substitution of Eq. 6.57 into Eqs. 6.51 and 6.52 and yields expressions for isomerization turnover rates per total Lewis acid site in terms of initial glucose thermodynamic activity:

$$\frac{r_{isom,F}}{C_{*,tot}} = \frac{\frac{k_{2,F}}{\gamma_{\ddagger,F}} K_{R,F} K_1 a_G (1 - \eta_F)}{\left( \frac{K_4 K_5 a_W^2}{\gamma_{2W*}} + \frac{K_1 a_G}{\gamma_{G*}} \right)} \quad (6.58)$$

$$\frac{r_{isom,S}}{C_{*,tot}} = \frac{\frac{k_{2,S}}{\gamma_{\ddagger,S}} K_{R,S} K_1 a_G (1 - \eta_S)}{\left( \frac{K_4 K_5 a_W^2}{\gamma_{2W*}} + \frac{K_1 a_G}{\gamma_{G*}} \right)} \quad (6.59)$$

This expression matches the rate equation labeled Eq. 6.8 in the main text and can be rearranged to follow a Langmuir Hinshelwood format which holds for either product:

$$r_i = \frac{\gamma_{G*} \frac{K_1 \gamma_{2W*}}{K_4 K_5 \gamma_{G*}} K_{R,i} k_{2,i} \frac{a_G}{a_W^2} (1 - \eta_i)}{\gamma_{\ddagger,i} \left( 1 + \frac{K_1 \gamma_{2W*}}{K_4 K_5 \gamma_{G*}} \frac{a_G}{a_W^2} \right)} \quad (6.60)$$

Apparent first-order and zero-order rate constants can then be defined as per the main text:

$$k_{app,first,i} = \frac{K_1 K_{R,F} k_{2,F} \gamma_{2W*}}{K_4 K_5 \gamma_{\ddagger,F}} \quad (6.61)$$

$$k_{app,zero,i} = K_{R,i} k_{2,i} \frac{\gamma_{G*}}{\gamma_{\ddagger,i}} \quad (6.62)$$

The equilibrium coefficient corresponding to the competitive adsorption of glucose and water is not dependent on the product formed and can be defined as:

$$K_{app,comp} = \frac{k_{app,first,i}}{k_{app,zero,i}} = \frac{K_1 \gamma_{2W*}}{K_4 K_5 \gamma_{G*}} \quad (6.63)$$

Eq. 6.60 can then be rewritten using Eqs. 6.61–6.63 into:

$$r_i = \frac{k_{app,zero,i} K_{app,comp} \frac{a_G}{a_W^2} (1 - \eta_i)}{1 + K_{app,comp} \frac{a_G}{a_W^2}} \quad (6.64)$$

Rate and equilibrium constants from Eqs. 6.40–6.46 reflect free energy differences between transition states, reactants, and solvent molecules:

$$K_1 = e^{-(\Delta G_{G^*}^0 - \Delta G_G^0 - \Delta G_{G^*}^0)/RT} \quad (6.65)$$

$$K_{R,F} = e^{-(\Delta G_{R,F}^0 - \Delta G_{G^*}^0)/RT} \quad (6.66)$$

$$K_{R,S} = e^{-(\Delta G_{R,S}^0 - \Delta G_{G^*}^0)/RT} \quad (6.67)$$

$$k_{2,F} = \frac{k_B T}{h} e^{-(\Delta G_{\ddagger,F}^0 - \Delta G_{R,F}^0)/RT} \quad (6.68)$$

$$k_{2,S} = \frac{k_B T}{h} e^{-(\Delta G_{\ddagger,S}^0 - \Delta G_{R,S}^0)/RT} \quad (6.69)$$

$$K_4 = e^{-(\Delta G_{W^*}^0 - \Delta G_W^0 - \Delta G_{G^*}^0)/RT} \quad (6.70)$$

$$K_5 = e^{-(\Delta G_{2W^*}^0 - \Delta G_{W^*}^0 - \Delta G_{W^*}^0)/RT} \quad (6.71)$$

Rewriting apparent first-order rate constants,  $k_{app,first,F}$  and  $k_{app,first,S}$ , from Eqs. 6.61 and 6.62 in terms of free energies using Eqs. 6.65–6.71 gives the following expressions:

$$k_{app,first,F} = \frac{K_1 K_{R,F} k_{2,F} \gamma_{2W^*}}{K_4 K_5 \gamma_{\ddagger,F}} = \frac{k_B T}{h} e^{-(\Delta G_{\ddagger,F}^0 + 2\Delta G_W^0 - (\Delta G_G^0 + \Delta G_{2W^*}^0))/RT} \quad (6.72)$$

$$k_{app,first,S} = \frac{K_1 K_{R,S} k_{2,S} \gamma_{2W^*}}{K_4 K_5 \gamma_{\ddagger,S}} = \frac{k_B T}{h} e^{-(\Delta G_{\ddagger,S}^0 + 2\Delta G_W^0 - (\Delta G_G^0 + \Delta G_{2W^*}^0))/RT} \quad (6.73)$$

These apparent first-order rate constants depend on the free energy of the bound glucose isomerization transition state with two liquid phase solvent molecules relative to two bound water molecules with one liquid phase glucose molecule. Similarly, measured zero-order rate constants depend on the free energy of the hydride shift transition state relative to the adsorbed glucose intermediate:

$$k_{zero,F} = \frac{k_B T}{h} e^{-(\Delta G_{\ddagger,F}^0 - \Delta G_{G^*}^0)/RT} \quad (6.74)$$

$$k_{zero,S} = \frac{k_B T}{h} e^{-(\Delta G_{\ddagger,S}^0 - \Delta G_{G^*}^0)/RT} \quad (6.75)$$

Eqs. 6.72–6.75 therefore reflect the free energy differences reflected in first-order and zero-order rate constants quantified from initial rate measurements at low and high glucose activities.

## 6.6.5.2 Initial glucose isomerization rates and enthalpy and entropy determination

Figures 6.44–6.46 show the raw data for sorbose formation rates on Ti-Beta-F-155 and both fructose and sorbose formation rates on Ti-Beta-OH-46 which forms the complete set of measured rates on Ti-Beta-F-155 and Ti-Beta-OH-46 when combined with the data presented in Figure 6.8 from the main text.

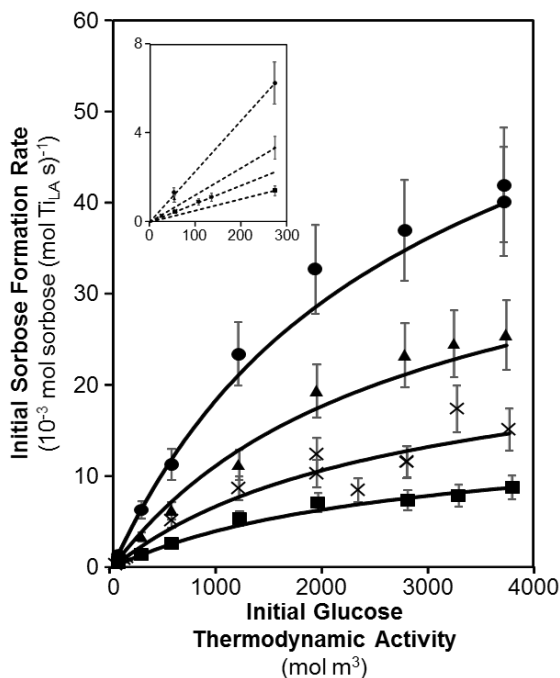


**Figure 6.44:** Dependence of initial sorbose formation rates (pH 3) on Ti-Beta-F-155 on initial glucose thermodynamic activity (corresponding to 1–50 wt% initial glucose concentration) at 368 (■), 373 (×), 378 (▲), and 383 K (●). Solid lines for all data represent modeled regressions of the experimental data to the overall rate equation given in Eq. 6.16 in the main text using activation enthalpies and entropies given in Table 6.4.

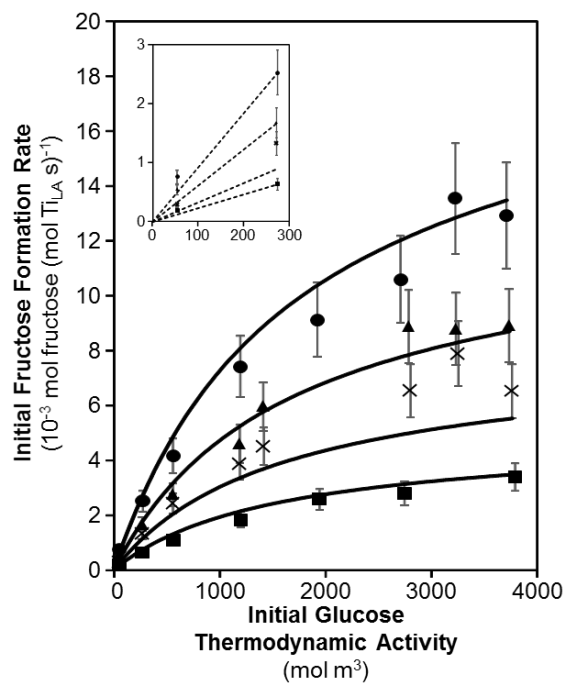


**Figure 6.45:** Dependence of initial fructose formation rates (pH 3) on Ti-Beta-OH-46 on initial glucose thermodynamic activity (corresponding to 1–50 wt% initial glucose concentration) at 368 (■), 373 (×), 378 (▲), and 383 K (●). Solid lines for all data represent modeled regressions of the experimental data to the overall rate equation given in Eq. 6.16 in the main text using activation enthalpies and entropies given in Table 6.4.

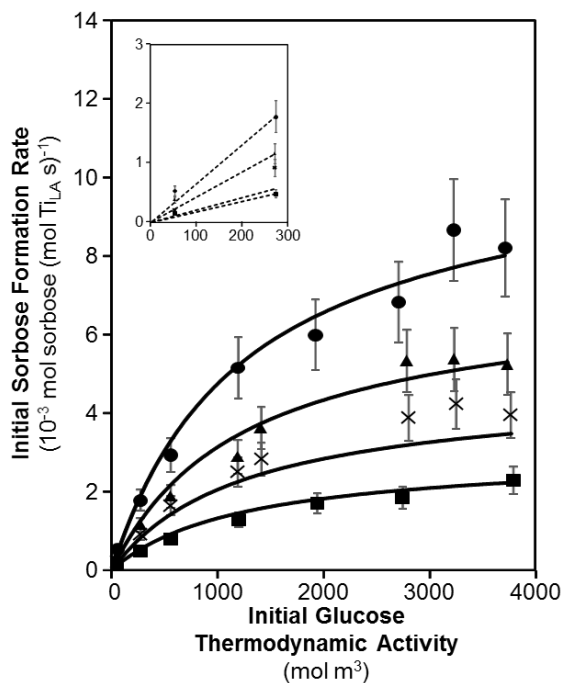


**Figure 6.46:** Dependence of initial sorbose formation rates (pH 3) on Ti-Beta-OH-46 on initial glucose thermodynamic activity (corresponding to 1–50 wt% initial glucose concentration) at 368 (■), 373 (×), 378 (▲), and 383 K (●). Solid lines for all data represent modeled regressions of the experimental data to the overall rate equation given in Eq. 6.16 in the main text using activation enthalpies and entropies given in Table 6.4.

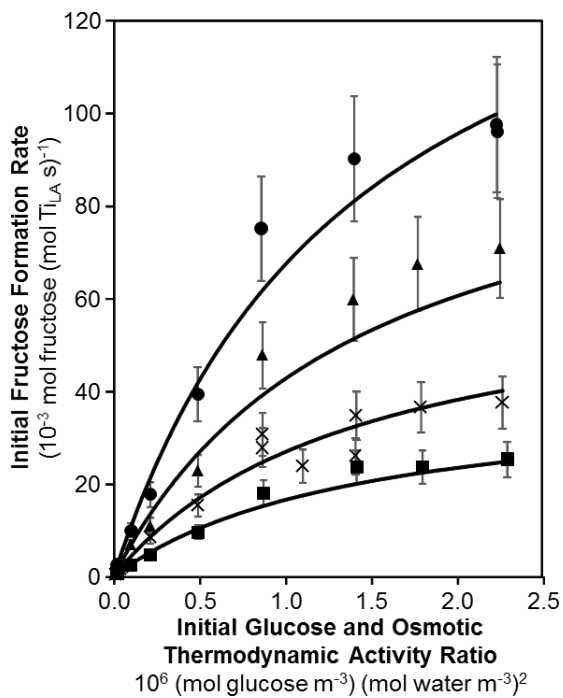


**Figure 6.47:** Dependence of initial fructose formation rates (pH 3) on Ti-Beta-F-155 on initial glucose and osmotic thermodynamic activity ratio (corresponding to 1–50 wt% initial glucose concentration) at 368 (■), 373 (×), 378 (▲), and 383 K (●). Solid lines for all data represent modeled regressions of the experimental data to the overall rate equation given in Eq. 6.16 in the main text using activation enthalpies and entropies given in Table 6.4.

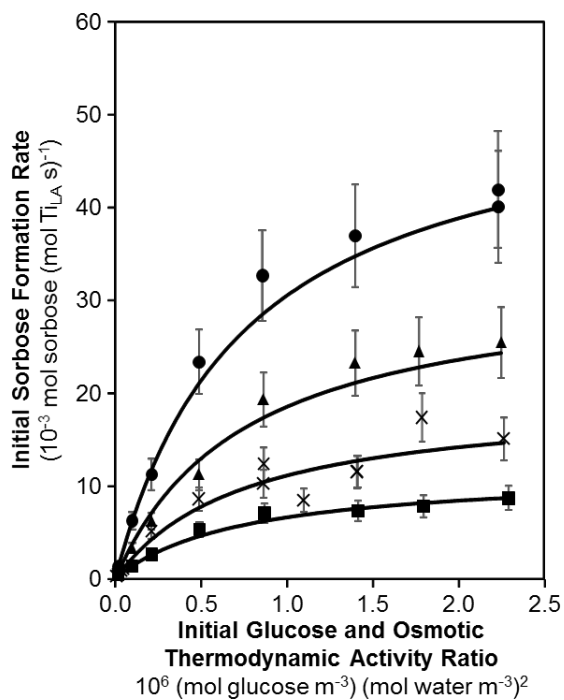


**Figure 6.48:** Dependence of initial sorbose formation rates (pH 3) on Ti-Beta-F-155 on initial glucose and osmotic thermodynamic activity ratio (corresponding to 1–50 wt% initial glucose concentration) at 368 (■), 373 (×), 378 (▲), and 383 K (●). Solid lines for all data represent modeled regressions of the experimental data to the overall rate equation given in Eq. 6.16 in the main text using activation enthalpies and entropies given in Table 6.4.

### 6.6.5.3 Comparison of fitted thermodynamic properties with activity coefficient sets and for multiple fitting strategies

The modeled behavior derived from the regression of Eq. 6.16 in the main text to the experimental data set leads to the apparent enthalpy and entropy values reported in Table 6.4 when the experimental data points are weighted by experimental rate values. This weighting scheme minimizes the natural tendency for higher measured rates at increased glucose activities and temperature, and therefore higher absolute error differences between the experimental data and the model, to dominate the regression and instill systematic errors in the regressed parameters. Other weighting methods were investigated and did affect regressed activation enthalpies and entropies but led to systematic errors in model regression leading to exaggeration of rate measurements at higher glucose activities and temperatures. The presence of systemic errors derived from regressed parameters were studied by quantifying percent residuals using the following equation:

$$\text{Percent Residual} = \frac{(r_{\text{exp}} - r_{\text{model}})}{r_{\text{exp}}} * 100 \quad (6.76)$$

Figures 6.47–6.50 show percent residuals as a function of glucose activity and temperature on both Ti-Beta-F-155 and Ti-Beta-OH-46 for both fructose and sorbose formation from rates given in Figures 6.44–6.46 and Figure 6.8 in the main text. Systematic trends are not observed as a function of initial glucose activity, indicating that the model is not introducing systematic errors derived from the chosen fitting method. We note that negligible differences in fitted apparent enthalpies and entropies are observed when ideality is assumed for all solution-phase species ( $\gamma_i \rightarrow 1$ ) and when activity coefficients are not adjusted for temperature changes. Glucose and water activities are therefore used throughout the main text.



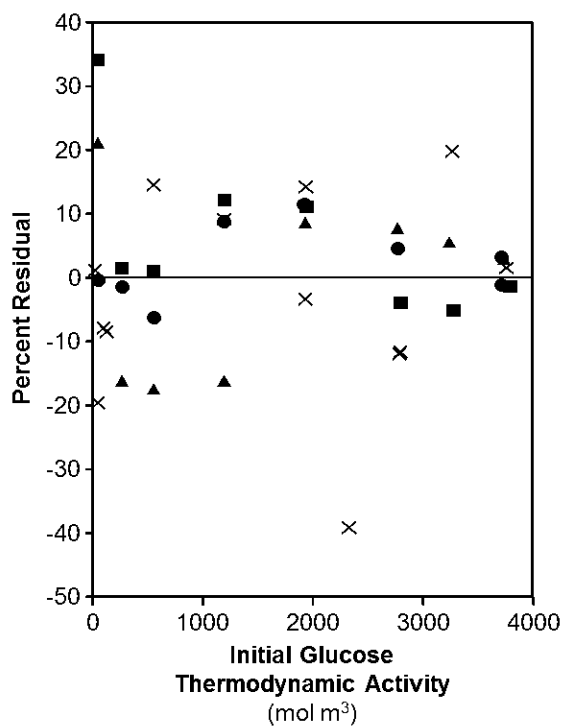


**Figure 6.50:** Percent residual plot of sorbose formation rates on Ti-Beta-F-155 as a function of initial glucose thermodynamic activity (corresponding to 1–50 wt% initial glucose concentration) at 368 (■), 373 (×), 378 (▲), and 383 K (●) comparing experimental rate measurements with modeled rate behavior from Eq. 6.16 from the main text. Percent residuals were obtained from Eq. 6.72.

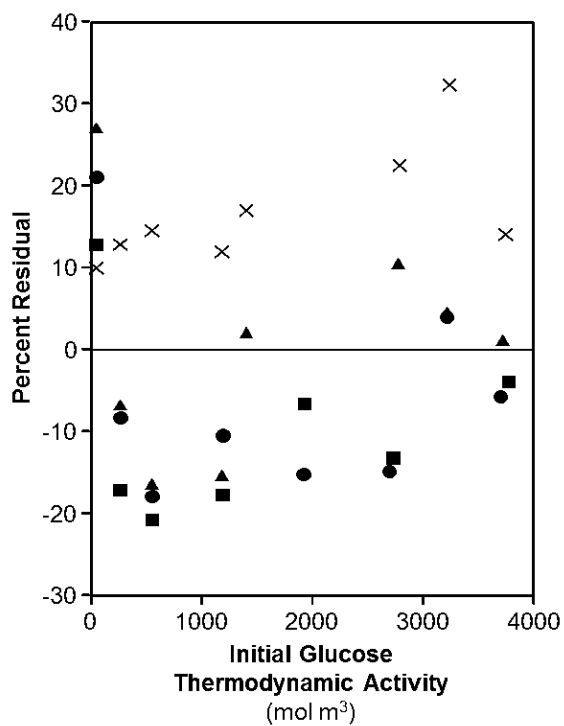


**Figure 6.51:** Percent residual plot of fructose formation rates on Ti-Beta-OH-46 as a function of initial glucose thermodynamic activity (corresponding to 1–50 wt% initial glucose concentration) at 368 (■), 373 (×), 378 (▲), and 383 K (●) comparing experimental rate measurements with modeled rate behavior from Eq. 6.16 from the main text. Percent residuals were obtained from Eq. 6.72.

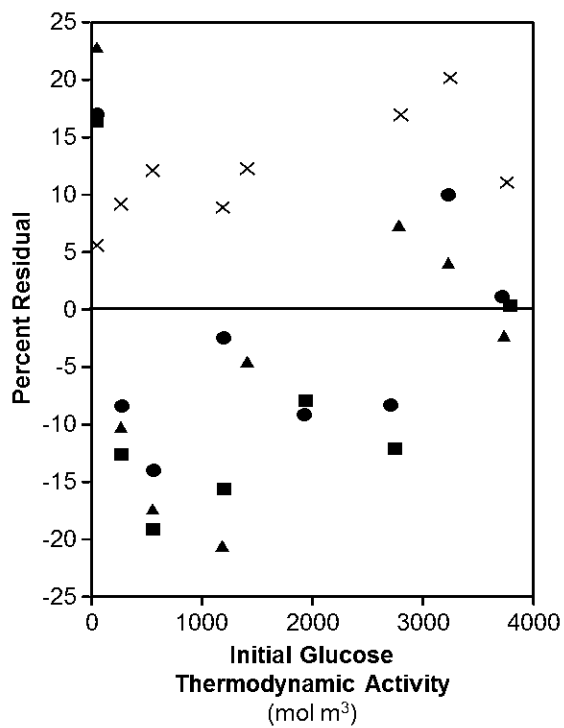


**Figure 6.52:** Percent residual plot of sorbose formation rates on Ti-Beta-OH-46 as a function of initial glucose thermodynamic activity (corresponding to 1–50 wt% initial glucose concentration) at 368 (■), 373 (×), 378 (▲), and 383 K (●) comparing experimental rate measurements with modeled rate behavior from Eq. 6.16 from the main text. Percent residuals were obtained from Eq. 6.72.

The regressed rates derived from the apparent enthalpies and entropies listed in Table 6.4 of the main text predict zero-order rate constants that are higher than the rates measured at high glucose activities where Lewis acidic Ti sites are covered with bound glucose MARIs as seen from ATR-IR spectra. These differences result from measured isomerization rates that are not precisely zero-order at high glucose activities at all temperatures as shown in Figure 6.52, but are less significant for measured first-order rate constants (Figure 6.51). First-order and zero-order rate constants can then be estimated from single rate measurements at low ( $a_G = 275 \text{ mol m}^{-3}$ ) and high ( $a_G = 3500 \text{ mol m}^{-3}$ ) glucose activities, respectively. Apparent activation enthalpies and entropies listed in Table 6.9 were determined from these measured rates at consistent glucose activities.

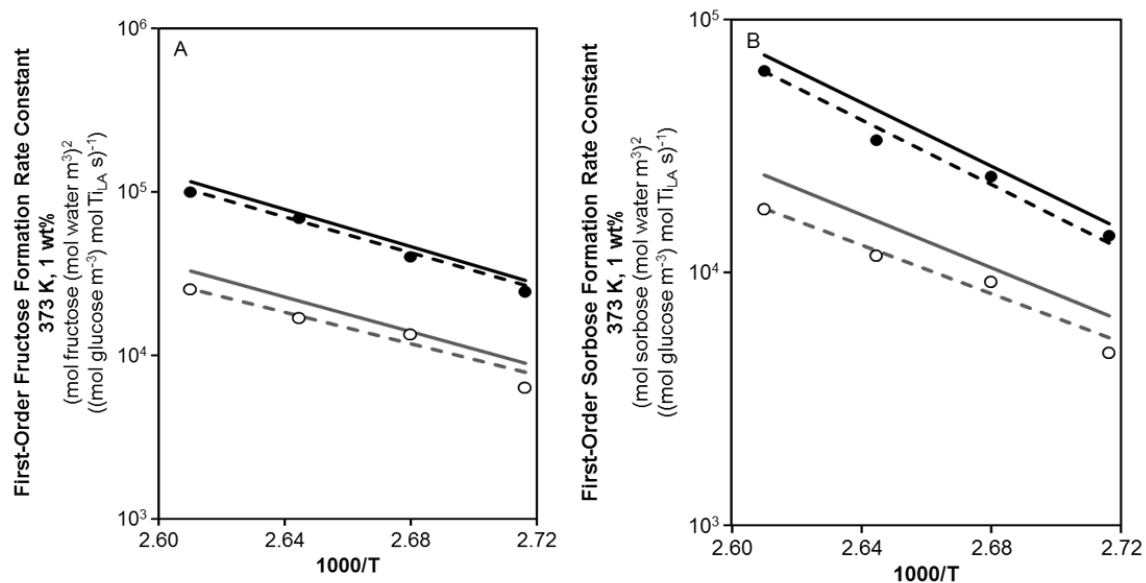


**Figure 6.53:** Arrhenius plot for apparent first-order fructose (A) and sorbose (B) formation rate constants (368–383 K, 5 wt%) on Ti-Beta-F-155 (●) and Ti-Beta-OH-46 (○). Solid lines represent the results of the regression of Eq. 6.16 and dashed lines represent regressions using rate measurements at 5 wt% on Ti-Beta-F-155 (black) and Ti-Beta-OH-46 (gray). Both regression lines follow the Eyring equation with activation enthalpies and entropies given in Table 6.4 of the main text and Table 6.9, respectively.

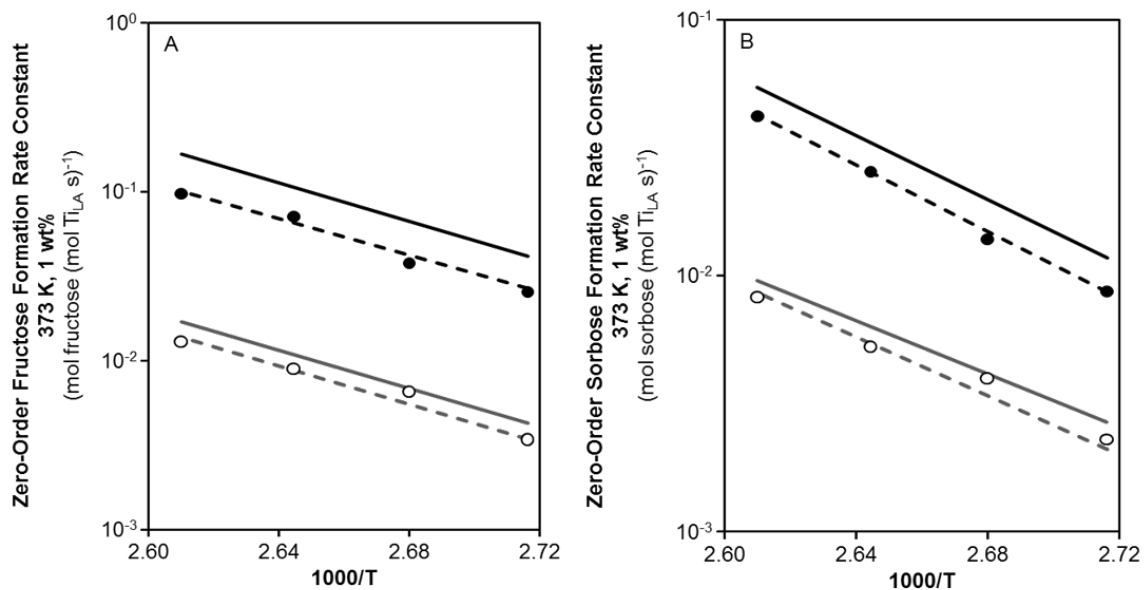


**Figure 6.54:** Arrhenius plot for apparent zero-order fructose (A) and sorbose (B) formation rate constants (368–383 K, 50 wt%) on Ti-Beta-F-155 (●) and Ti-Beta-OH-46 (○). Solid lines represent the results of the regression of Eq. 6.16 and dashed lines represent regressions using rate measurements at 50 wt% on Ti-Beta-F-155 (black) and Ti-Beta-OH-46 (gray). Both regressions follow the Eyring equation with activation enthalpies and entropies given in Table 6.4 of the main text and Table 6.9, respectively.

**Table 6.9:** Apparent enthalpies and entropies for first- and zero-order rate constants describing fructose and sorbose formation on Ti-Beta-F-155 and Ti-Beta-OH-46 derived from single rate measurements at 5 and 50 wt% corresponding to first-order and zero-order rates. Differences in apparent activation enthalpies ( $\Delta\Delta H_{\text{app}}$ ) and entropies ( $\Delta\Delta S_{\text{app}}$ ) are listed as the difference between Ti-Beta-F-155 and Ti-Beta-OH-46.

	$\Delta H_{\text{app}}$ (kJ mol <sup>-1</sup> )		$\Delta S_{\text{app}}$ (J mol <sup>-1</sup> K <sup>-1</sup> )		$\Delta\Delta H_{\text{app}}$ (kJ mol <sup>-1</sup> )		$\Delta\Delta S_{\text{app}}$ (J mol <sup>-1</sup> K <sup>-1</sup> )	
rate constant	Ti-Beta-F-155	Ti-Beta-OH-46	Ti-Beta-F-155	Ti-Beta-OH-46	Ti-Beta-F-155	Ti-Beta-OH-46	(F-OH) <sup>b</sup>	(F-OH) <sup>b</sup>
$k_{\text{zero,fructose}}$	100	105	4	0	-5	4		
$k_{\text{first,fructose}}$	102	89	124	78	13	46		
$K_{\text{comp,fructose}}$	-2	16	-120	-78	18	42		
$k_{\text{zero,sorbose}}$	122	106	53	0	16	53		
$k_{\text{first,sorbose}}$	119	89	163	76	30	87		
$K_{\text{comp,sorbose}}$	3	17	-90	-76	14	34		

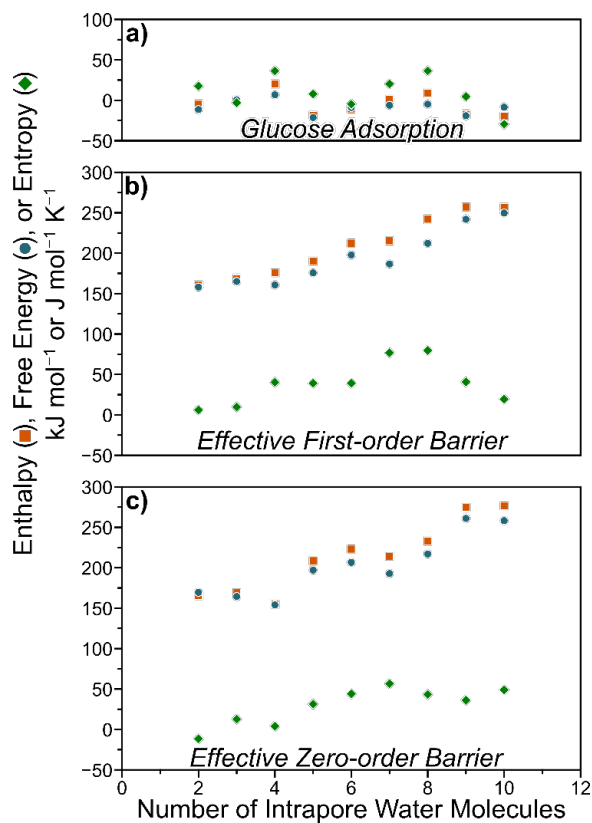


**Figure 6.55:** DFT-calculated glucose adsorption energies (a) and effective first- (b) and zero-order (c) energy barriers for glucose-fructose isomerization. Enthalpies (■) and free energies (●) are shown in  $\text{kJ mol}^{-1}$  and entropies (◆) in  $\text{J mol}^{-1} \text{K}^{-1}$  (373 K). The intrapore water molecule density was assumed to remain constant during glucose adsorption and reaction for first-order analyses yet water molecules were allowed to reorient into lowest energy configurations in all cases.

## 7. DEFECT-MEDIATED ORDERING OF CONDENSED WATER STRUCTURES IN MICROPOROUS ZEOLITES

### 7.1 Introduction

Microporous materials have long been known to influence the interaction of solvents with catalytic active sites. The structure of water around Brønsted acid sites in zeolites, for example, has been shown to influence catalytic conversion of biomass feedstocks [177] using both computation and spectroscopy [73]. However, molecular-level descriptions of such solvent interactions, how they are mediated by ubiquitous framework defects, and what their impact is on catalytic reactivity, remain largely unexplored. Development of a molecular understanding of these phenomena could, in turn, provide design principles to tune catalytic properties via manipulation of local solvent structure. Such tunability would be of interest in metal organic frameworks (MOFs) [347], carbon polymorphs [348–350], and zeolites [100], where the uptake of solvent into confining voids is directly related to the relative strengths of hydrophobic and hydrophilic interactions between solvent molecules and the solid [351]. Among these materials, the hydrothermal stability, high crystallinity, isolated Lewis acid sites, and synthetic control of point defects [103,104] in zeolites make them a particularly attractive class of materials for elucidating the molecular-level details of the relationship between defect structure, local solvent properties, and catalysis.

In Lewis acid zeolites, defects that influence solvent interactions can be broadly classified as either heteroatom substitutions to form Lewis acid sites (e.g.,  $\text{Sn}^{4+}$ ,  $\text{Ti}^{4+}$ ) or silanol groups formed through synthetic or post-synthetic treatments. The Beta zeolite framework, with intersecting 12-membered ring silica pores (Figure 7.1a,b), catalyzes reactions of oxygenated molecules when substituted with Sn in the presence of a polar solvent [16,102,106] and is the primary focus of the present study. Sn sites

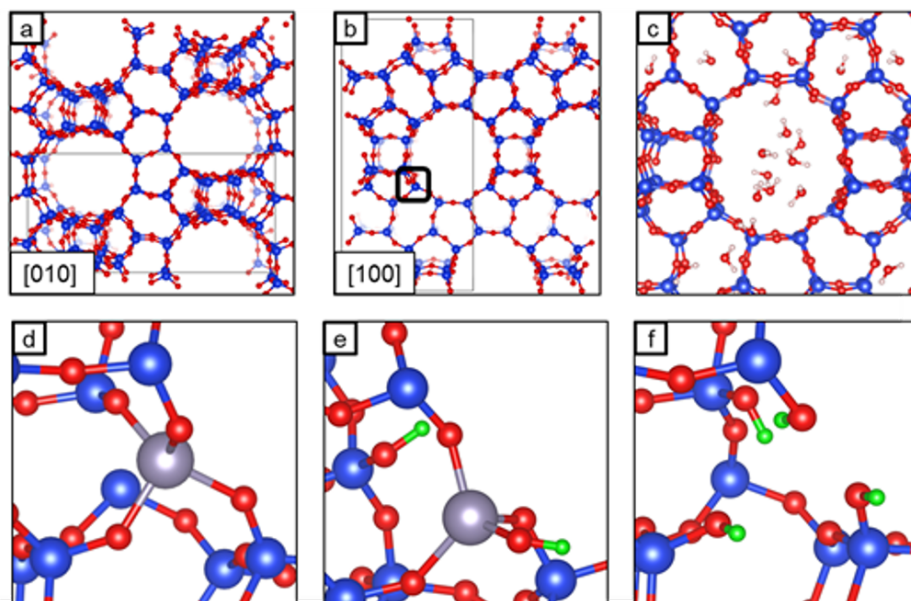


**Figure 7.1:** Zeolite Beta with intersecting pore structures (a,b). Water physisorbed in Si-Beta exploring parallel and perpendicular pore structures (c). Closed Sn (d), hydrolyzed open Sn (SnOH) (e), and silanol nests (OH<sub>4</sub>) (f) in the Si-Beta framework. Oxygen is red, silicon is blue, tin is grey, and hydrogen is green (at defects) or white (in water).

interconvert between tetravalent framework coordination (Sn, Figure 7.1d) and trivalent framework coordination with a hydroxyl ligand (SnOH, Figure 7.1e) [154, 180], introducing additional polar functionality to these sites. Polar silanol nest defects can be introduced through post-synthetic treatments [352] ((OH)<sub>4</sub>, Figure 7.1f). While some theoretical consideration has been given to condensation of water in defected zeolites, such as Silicalite-1 [42, 353, 354], the impact of the rich space of local defects on solvent structure and associated catalytic properties is not well understood.

Herein, we present a fully *ab-initio* determination, coupled with transmission infrared spectroscopic characterization, of the structural properties of localized water phases surrounding point defects and catalytic active sites in Sn-Beta, using defect-free Si-Beta as a reference case. We further identify the molecular-scale features of each site that control the local water structure and explicitly demonstrate the reaction conditions under which these phases are thermodynamically stable. Periodic

*ab-initio* molecular dynamics simulations (AIMD) elucidate the structure of water under standard conditions (room temperature) in contact with various defect and active site models. Temperature, volume, and water density are explicitly controlled in the simulations, and free energies are extracted from these simulations using quasi-harmonic vibrational density of states analyses. AIMD, in turn, provides a consistent treatment of interactions between water and defects with dissimilar chemical identity.

Defect-free Si Beta exhibits limited water adsorption at modest water partial pressures and ambient temperature, whereas tightly nucleated water clusters comprising 4–6 water molecules per unit cell ( $\text{H}_2\text{O u.c.}^{-1}$ ) chemisorb at tetrahedrally coordinated Sn sites and persist even at higher water densities ( $23 \text{ H}_2\text{O u.c.}^{-1}$ ). In contrast, the presence of  $(\text{OH})_4$  silanol nests nucleate hydrogen-bonding networks that contribute to greater amounts of water adsorption than are found in chain-like, weakly bound water molecules in purely siliceous frameworks [355–357]. These predicted trends are fully consistent with infrared measurements which reveal that zeolites with defect silanol nests exhibit perturbed OH stretches, indicating stronger hydrogen bonding interactions among solvent molecules than are found in Si-Beta.

## 7.2 Results and Discussion

Si-Beta provides a reference for understanding the dynamic structure of water in zeolites. As the water density per unit cell is increased from the lowest density possible in a single unit cell ( $1 \text{ H}_2\text{O u.c.}^{-1}$ ) to the approximate density of a bulk liquid in the accessible pore volume ( $23 \text{ H}_2\text{O u.c.}^{-1}$ , Figure 7.1f), water is observed to experience structural changes that are not observed in unconfined bulk water. At low water densities, between  $1\text{--}3 \text{ H}_2\text{O u.c.}^{-1}$ , molecules are weakly correlated and explore the full channel system. As the number of molecules is increased to approximately  $5\text{--}9 \text{ H}_2\text{O u.c.}^{-1}$ , uniformly dispersed chains form along a pore channel (Figure 7.2a), while occupation within perpendicular pore systems is negligible. At the highest water densities, above  $12 \text{ H}_2\text{O u.c.}^{-1}$ , chains begin to link across intersections and fill perpendicular pores (Figure 7.2b) [24, 358]. We note that filling in the [100] direction

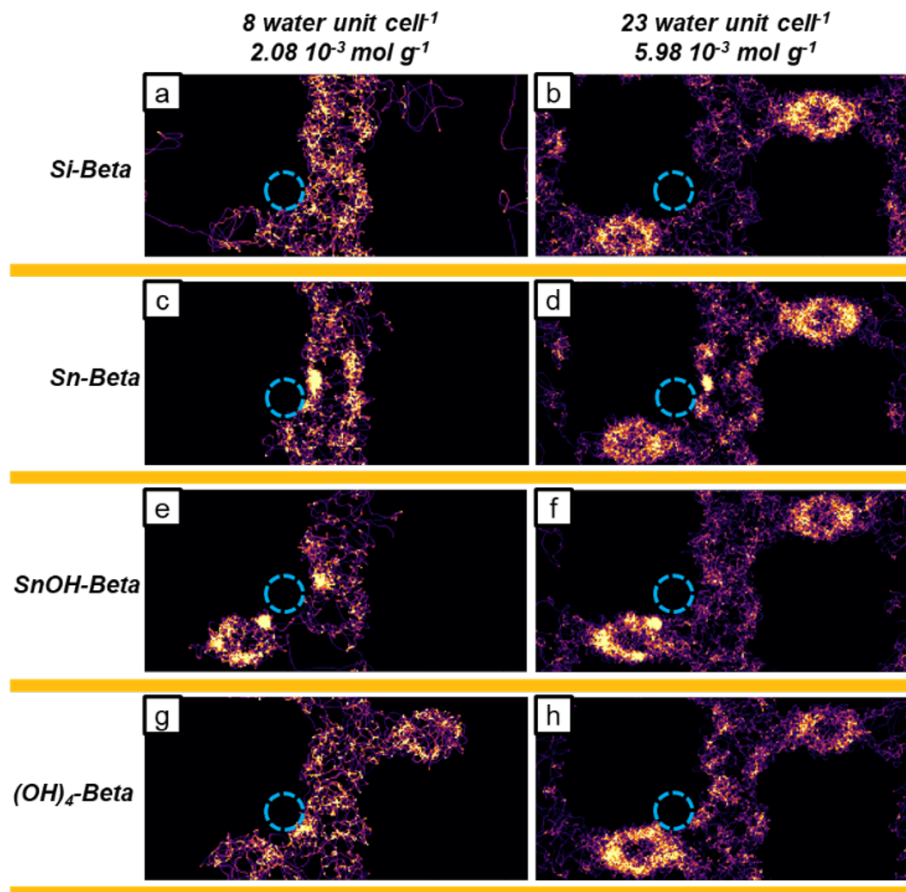


**Figure 7.2:** Time-averaged low (8 H<sub>2</sub>O per cell) and high (23 H<sub>2</sub>O per cell) densities in each Beta model, as viewed along the [010] plane. Intensities are normalized to the highest intensity of each simulation and are not directly comparable between images. Approximate location of the defects are indicated by blue circles. Orthogonal direction views are provided in the SI (section 7.5.3.2).

(perpendicular to Figure 7.2b) is observed in the lower left and upper right corners of the high density plots and does not correspond to localized clustering. Additional images are provided in the Supporting Information (7.5.3.2).

To quantify the organization of water at intermediate densities, between lower values where water chains are observed and the limit of the bulk liquid density, a dynamic clustering algorithm is developed based on network connectivity theory. While methods based on Voronoi tessellations [359] using grand canonical Monte Carlo techniques are extensively employed in molecular simulation studies to determine nonlo-

cal solvent structures [360], the limited system sizes associated with first principles methods preclude the use of these methods. In contrast, the connectivity method (see Supporting Information 7.5.1.4) directly evaluates the correlation between hydrogen bonds, permitting an analysis of clustering [361] that does not depend on the spatial positions of water molecules. Mean clustering coefficients reflect the degree to which water molecules are localized in networks of hydrogen bonds, with a coefficient of unity implying rigid hydrogen bonding interactions, as in a solid, where each water molecule is the center of an infinitely dispersed cluster. The mean clustering coefficients for defect-free Si-Beta (Figure 7.3a, in blue), for example, show an average coefficient close to unity at a density of  $8 \text{ H}_2\text{O u.c.}^{-1}$ . Note that this does not indicate that water molecules are immobile; but that they diffuse while maintaining a correlated network, as shown in Figure 7.2a. The other limit of clustering coefficients, zero, describes an ideal gas, where no hydrogen-bonding occurs. Intermediate values correspond to bonds that are transiently formed and broken, as is the case for bulk liquid water, which has a mean clustering coefficient of 0.74, as denoted by the dashed line in Figure 7.3a. Indeed, as water density increases, mean clustering coefficients in Si-Beta become like those of bulk liquid water, demonstrating that dynamic hydrogen bond restructuring is occurring, which in turn leads to enhanced linking of water between pores (Figure 7.2b). We note that the increase in the mean clustering coefficient at a density of  $15 \text{ H}_2\text{O u.c.}^{-1}$  coincides with densely packed network formation in a single pore, which then begins to crosslink to perpendicular pores at higher loadings.

The observed transition from isolated water chains into linked water networks across perpendicular pores with bulk liquid-like mean clustering coefficients can be further characterized by a thermodynamic phase diagram to identify stable aqueous phases within the Si-Beta pores. The extensive free energy, which can be considered as a Landau-type ensemble (defined as the calculated Helmholtz energy, minus the chemical potential of an external water reservoir multiplied by the number of water molecules), is minimized at the thermodynamically optimal water density for a given

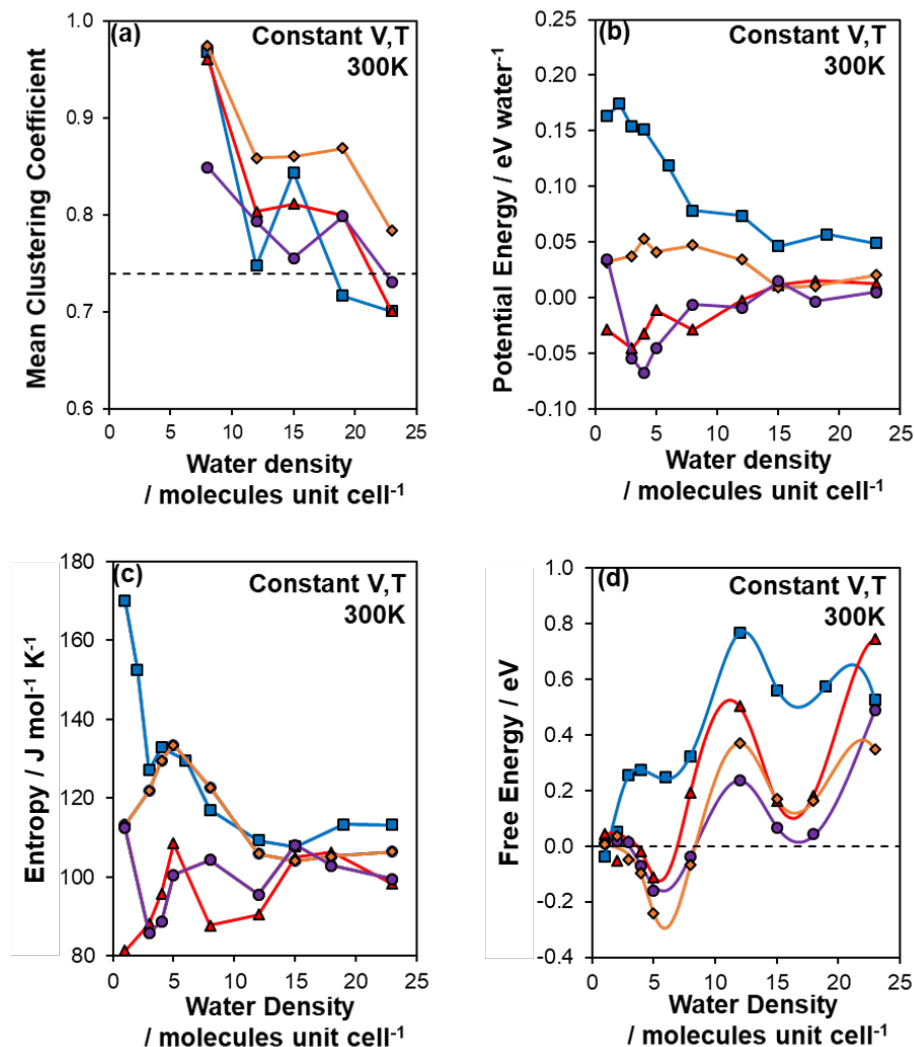


**Figure 7.3:** (a) Clustering coefficients, (b) potential energy, (c) entropy, and (d) free energy, defined as the calculated Helmholtz energy, minus the chemical potential of an external water reservoir multiplied by the number of water molecules (see text for details), as a function of water density for each considered defect in zeolite Beta. Blue squares are Si-Beta, red triangles denote Sn-Beta, purple circles correspond to SnOH-Beta, and orange diamonds are (OH)<sub>4</sub>-Beta.

chemical potential of the external reservoir (see Supporting Information, 7.5.2.2, for a full derivation). The Helmholtz energy, referenced, for convenience, to the calculated chemical potential of ideal gaseous water at 0.05 bar and 300 K, is then calculated from potential energies and entropies as determined using a vibrational density of states

analysis (Figure 7.3 and Supporting Information section 7.5.2.2). In Figure 7.3d, the chemical potential of water in an external reservoir, in equilibrium with the system, is also fixed at that of ideal gaseous water at 0.05 bar and 300 K. In Si-Beta, the global free energy minimum at this chemical potential corresponds to a water density of  $\sim 1 \text{ H}_2\text{O u.c.}^{-1}$ , a region where gas-like structure is observed. In addition, two local free energy minima are seen at densities of  $\sim 7 \text{ H}_2\text{O u.c.}^{-1}$ , where individual chains are observed, and at  $17\text{--}18 \text{ H}_2\text{O u.c.}^{-1}$ , corresponding to a liquid-like phase. As the reservoir chemical potential is increased, the free energy analysis demonstrates that higher water densities become favored, but the intermediate density phase with isolated water chains remains metastable and is never the thermodynamic ground state (see Figure 7.36 for examples of the dependence of the free energy on the chemical potential). The liquid-like phase is accessed only at higher pressures (water intrusion pressures for Si-Beta are observed at pressures greater than 500 bar [362]).

The combination of thermodynamic phase analysis, water density maps, and clustering coefficients, as described above, provides molecular-level insights into the behavior of water in a defect-free Si-Beta material. In what follows, we extend these complementary methods to explore the phase behavior of water in the presence of defects.

In Sn-Beta, chemisorbed water and dense hydrogen-bound water, comprising a cluster, are shown in Figure 7.2c for low average water densities ( $8 \text{ H}_2\text{O u.c.}^{-1}$ ). These structures are qualitatively different from corresponding geometries in defect-free Si-Beta, which exhibits delocalized chain-like structures at this water density (Supporting Information Figure 7.5, 7.6). Further, the entropy of water in Sn-Beta at this density is  $20 \text{ J mol}^{-1} \text{ K}^{-1}$  lower than that of water in Si-Beta (Figure 7.3c) due to localization around the framework Sn atom, and self-diffusion constants are also considerably lower (see SI, section 7.5.2.1). At higher densities, where the pore containing Sn retains a cluster of hyper-conjugated water near the Sn site (Figure 7.2d), water with reduced density occupies the surrounding pores. At this condition, the entropy of water is like that in Si-Beta (Figure 7.3c). Mean clustering coefficients

in Sn-Beta have values of  $\sim 0.8$  across a density range of  $\sim 8\text{--}18$   $\text{H}_2\text{O}$  u.c. $^{-1}$ , after which they approach the same bulk limit as Si-Beta, reflecting dense hydrogen bond coordination. The grand free energies for Sn-Beta show the existence of a stable phase of between  $5\text{--}6$   $\text{H}_2\text{O}$  u.c. $^{-1}$ , consistent with the localized hyper-conjugated water structure observed, while a liquid-like extended phase is stabilized at higher water densities ( $\sim 17$   $\text{H}_2\text{O}$  u.c. $^{-1}$ ) and higher chemical potentials (Figure 7.3d).

SnOH-Beta at low water densities ( $8$   $\text{H}_2\text{O}$  u.c. $^{-1}$ , Figure 7.2e) shows dense water clustering both within the main (parallel) pore and in a perpendicular pore due to interaction with a framework SnOH group and the proximal SiOH group (additional images provided in 7.5.3.1, 7.5.3.2). The entropy of water in SnOH-Beta is similar to that of Sn-Beta, where chemisorption and increased extents of hydrogen bonding reduce the total entropy as compared to Si-Beta. The mean clustering coefficient of SnOH-Beta at  $8$   $\text{H}_2\text{O}$  u.c. $^{-1}$  is lower than that of Si-Beta at the same conditions, which is due to the three adsorption sites (Sn heteroatom, framework silanol, and hydroxyl ligand) having similar adsorption energies, as evidenced by trajectories that show water molecules rapidly breaking and reforming hydrogen bonds between the different sites. As water density increases, chemisorbed water molecules are retained on the SnOH group in a perpendicular pore, where water molecules interact with the Sn center and hydroxyl ligand, but water clusters at the framework silanol group dissipate upon hydrogen bonding with other water molecules in the pores (see also 7.5.3.2). At higher water densities, the mean clustering coefficient of SnOH-Beta approaches a liquid-like limit, as is the case with Si-Beta and Sn-Beta. The grand free energy analysis identifies stable phases at water densities similar to those in Sn-Beta. A localized phase with two water clusters at the SnOH and SiOH hydroxyl groups is predicted at  $5\text{--}6$   $\text{H}_2\text{O}$  u.c. $^{-1}$ , while the SnOH cluster persists at higher densities and eventually transitions to the liquid-like extended phase at higher densities and water chemical potentials.

In contrast to the results for the two Sn defects, the  $(\text{OH})_4$ -silanol nest has no strongly chemisorbed water molecules at low water densities (Figure 7.2g). This result

resembles some of the observations for the SnOH defect, wherein SiOH moieties are observed to lose their water clusters more easily than SnOH groups, and is also likely due to the significant internal hydrogen bonding between hydroxyl moieties in the nests, which reduces their ability to hydrogen bond with additional water molecules. In addition, water molecules around silanol nests exhibit a greater range of molecular diffusion than in Si-Beta, and after saturation of the nest at densities below  $5 \text{ H}_2\text{O u.c.}^{-1}$  (7.5.3.1, Supporting Information), additional water molecules explore the perpendicular pores differently than is the case in Si-Beta. Mean clustering coefficients across the full range of densities are greater than for either Si-Beta or the Sn defects, indicating greater correlation in hydrogen bonding between water molecules, although the total entropy is very similar to that of water in Si-Beta. The stronger hydrogen bond networks are mobile and point to favorable water-zeolite interactions, which suggest an explanation for the observed hydrophilicity of Beta zeolites synthesized with a high density of silanol defects [173].

To provide additional evidence that silanol nest defects promote the formation of strongly correlated hydrogen bonding networks, transmission IR spectra of low-defect and high defect ( $\sim 1 \text{ Si-(OH)}_4$  nest per unit cell) Beta were measured as a function of water pressure. These samples were synthesized such that a direct relationship between the defect density and the hydrogen bonding could be measured and compared to corresponding computational analyses (see SI for additional details). In Figure 7.4, subtracted spectra reflect contributions from all adsorbed water and perturbed zeolite vibrations, and differential subtracted spectra reflect contributions relative to adsorbed structures at the next-lowest relative water pressure. Quantifying  $\delta(\text{OH})$  peak areas ( $1630 \text{ cm}^{-1}$ ) enables the relation of measured spectra to their adsorbed water content (Section 7.5.3.10, Supporting Information). Si-Beta-F adsorbs little water, with  $\nu(\text{OH})$  peak centers that are invariant with water pressure (Figure 7.4c), reflecting low extents of hydrogen bonding. Si-Beta-OH, in contrast, adsorbs more water, with  $\nu(\text{OH})$  peak centers that shift to lower wavenumbers with water pressure, consistent with greater extents of hydrogen bonding [38]. Analogous  $\nu(\text{OD})$  peak cen-

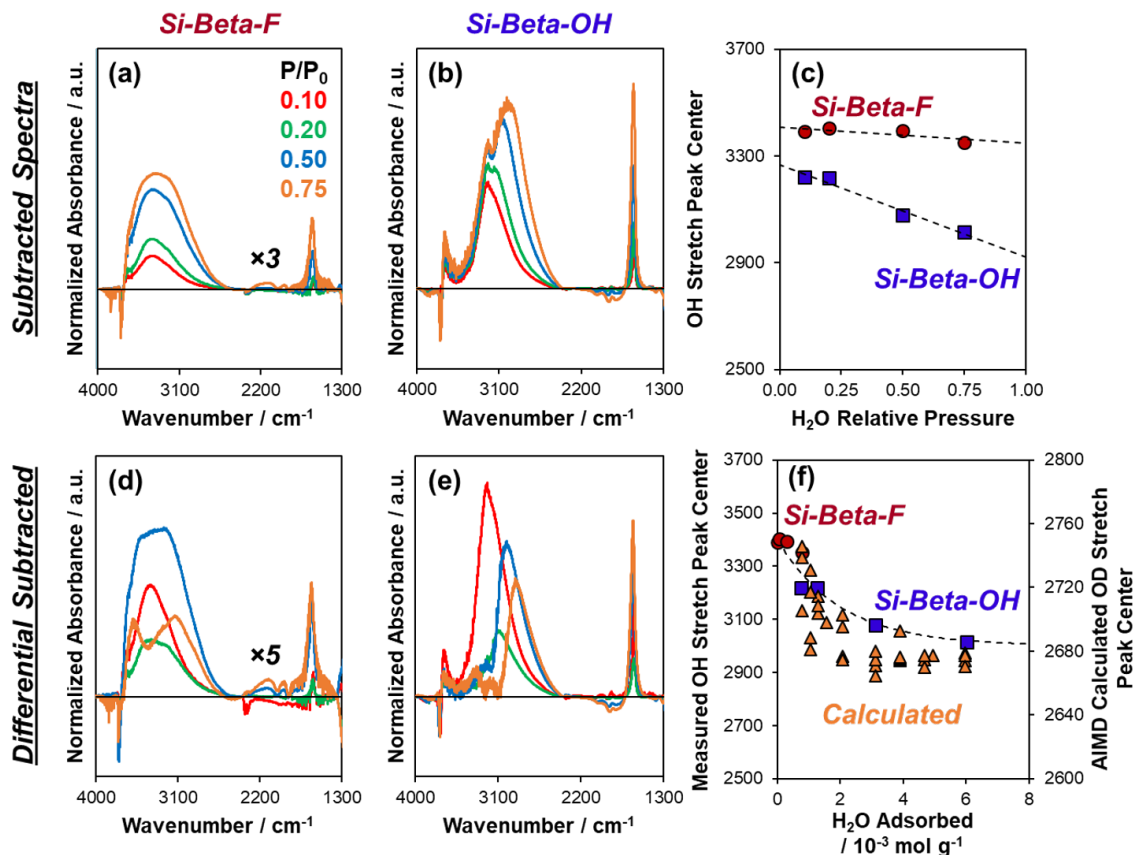


**Figure 7.4:** Difference infrared spectra of water adsorbed on low-defect Si-Beta-F (a,d; red) and high-defect Si-Beta-OH (b,e; blue) zeolites. Subtracted spectra are relative to the sample before water adsorption, and differential spectra are relative to the next-lowest  $\text{H}_2\text{O}$  pressure. Measured OH stretching peak centers versus  $\text{H}_2\text{O}$  adsorption (f), including AIMD-predicted OD peak shifts (f).

ters were calculated by AIMD (Figure 7.4f, Section 7.5.3.5, Supporting Information), indicating that the peak center shifts correlate with the strength of the hydrogen bonding network nucleated by silanol defects.

### 7.3 Conclusions

In summary, the combination of *ab-initio* molecular dynamics simulations, cluster network calculations, and comprehensive thermodynamic analysis reveals rich phase behavior for water entrained in Si-Beta micropores. Defect-free pores show hydropho-

bic behavior, with direct transitions from isolated chains to pore-filling water networks at high water chemical potentials. In contrast, framework Sn and hydrolyzed SnOH catalytic sites localize thermodynamically stable phases of clustered water at chemical potentials relevant to various catalytic chemistries. In the case of framework Sn, these localized clusters are preserved even as liquid-like water fills the surrounding pores, while for hydrolyzed Sn sites, clusters form around both the SnOH and SiOH groups, but only the former survive at higher densities. Finally, Si(OH)<sub>4</sub> defects do not nucleate tightly bound clusters of water, but rather stabilize more delocalized water networks, thus facilitating formation of delocalized water structures in Si-Beta pores at higher defect densities. These results not only shed light on the structure and thermodynamics of water phases in defected microporous networks, but also point to strategies whereby the impact of solvents on catalytic reactions in these micropores could be evaluated. In particular, the analysis identifies conditions where locally stable water clusters, surrounding catalytic active sites, provide a starting point for evaluating the impact of solvents on catalytic reactions and also points to more general types of defects, such as silanol nests, where delocalized water structure models may be appropriate.

#### 7.4 Acknowledgements

R.G. and J.B. acknowledge financial support from the Purdue Process Safety and Assurance Center (P2SAC), and a 3M Non-Tenured Faculty Award. B.B. and J.G. acknowledge support from the Department of Energy Office of Science, Office of Basic Energy Sciences, Chemical, Biological, and Geosciences Division under DE-SC0010379. Use of the Center for Nanoscale Materials, a U.S. Department of Energy, Office of Science, Office of Basic Energy Sciences User Facility under Contract No. DE-AC02-06CH11357, and of computational resources from the National Energy Research Scientific Computing Center, are gratefully acknowledged.

Reprinted with permission from *Angew. Chem. Int. Ed.* 2019, 58, 16422–16426. Copyright (2019) John Wiley and Sons.

## 7.5 Supporting Information

### 7.5.1 Methodology

#### 7.5.1.1 DFT calculations

Periodic self-consistent density functional theory (DFT) was performed using the Vienna Ab-initio Simulation Package (VASP) [132–135]. The computational parameters used here are consistent with our previous work in zeolite Beta [58, 180] and are described in detail below. The Bayesian error estimation functional (BEEF-vdW) [137] was chosen based on the inclusion of van der Waals interactions as well as its predictions of bulk lattice constants for Beta (reported to be within 3% [180] of that provided by the International Zeolite Association [142]). A single Beta unit cell was used in all simulations, with optimized lattice constants  $a, b = 12.67 \text{ \AA}$ ,  $c = 26.60 \text{ \AA}$ . We note the similarities between adsorption energies of oxygenate species to Lewis acid sites incorporated in zeolites between PBE-D3 and BEEF-vdW [113], and as will be shown later, bulk liquid entropies calculated with BEEF-vdW were reasonable. Parameterized force field models of water (such as TIP4P-Ew [363] and SPC/E [364] have found tremendous success in accurately predicting water-water interactions and hydrogen bonding; however, a DFT approach was chosen to capture the range of interactions with Sn in different ligand environments. This fundamentally reduces the accuracy in treating water-water interactions, as BEEF-vdW was not developed to treat such delicate interactions. For this reason, and also because of the model size which is constrained by AIMD, a conservative interpretation of the computed absolute entropies is adopted. In particular, we restrict ourselves to discussions of relative changes in water structuring and entropy, which will be indicative of general properties of water as they restructure in different confining environments.

All calculations, including AIMD, are performed at the same level of rigor as used previously to study catalysis in zeolite Beta. Spin-polarization is used with a cutoff energy of 520 eV. Forces are evaluated to an energetic cutoff of 0.1 meV, and ground state calculations are converged to a force cutoff of 30 meV /  $\text{\AA}$ . Gaussian smearing

is employed, and a single Gamma K-point is included due to the large unit cell structure and lack of non-covalent interactions. Projector Augmented Wave (PAW) pseudopotentials are used [136, 141].

#### 7.5.1.2 Ab-initio molecular dynamics simulations

All AIMD simulations were performed in VASP. A Nosé-Hoover thermostat [365] with a frequency of  $850\text{ cm}^{-1}$  was used to sample an NVT ensemble with a temperature of 350 K (for purposes of statistical analysis, this is considered to be room temperature, as is common practice in AIMD simulations – see also discussion below). All hydrogen atoms were deuterated to permit use of a reasonably large timestep (1 fs) without sacrificing numerical accuracy. Calculations were equilibrated for 5 ps before beginning production runs. All production runs had a minimum duration of 20 ps, subject to a criterion that fluctuations in the calculated water entropies (discussed below) are lower than  $3\text{ J mol}^{-1}\text{ K}^{-1}$  as compared at 19 ps and 20 ps (Section 7.5.3.4). Simulations exhibiting large fluctuations would imply non-equilibrium, requiring additional simulation time to more accurately sample configurations at equilibrium. Plots of temperature and total energy fluctuations over the simulation time for Si-Beta at a unit cell density of  $23\text{ H}_2\text{O u.c.}^{-1}$  are provided in Section 7.5.3.4. For simulations in which large entropy fluctuations were indeed observed, multiple initial water configurations were considered to gauge if these fluctuations were due to unstable and short-timespan configurations which would require longer simulation times to properly sample the ensemble of states. These additional calculations were used as a criterion to determine when additional equilibration time was necessary. Initial water configurations could be selected either as fully randomized structures or developed from addition or subtraction of water from converged structures. Initially, low density structures were fully randomized, but as intuition was developed about stable water configurations, differential changes in previous structures became preferred. To prevent biasing structures which may be metastable at the previous water density, velocities were randomized and a full 5 ps equilibration was performed

to reach equilibrium, with the constraint that entropy fluctuations reduce below  $3 \text{ J mol}^{-1} \text{ K}^{-1}$ . Entropy fluctuations were quantified by calculating the vibrational density of states as a function of simulation time, providing a criterion for estimating sensitivity to simulation time. The estimated total time sampled across 4 defects, 10 water densities plus a bare framework, with 25 ps equilibration and production runs, exceeds 1 ns. To help determine if the simulation times were sufficient to sample all of the void spaces in Beta, longer duration simulations (some in excess of 40 ps) were performed for lower unit cell densities of water, and no significant differences in the structuring of water was observed. While it is possible that even longer timescale dynamics in water structuring, such as cleavage and reformation of chains or clusters, could be revealed through longer simulation times, such phenomena are unlikely to alter trends in the properties of locally thermodynamically stable phases which are the primary focus of this study.

To simulate bulk water, 54 deuterated water molecules were confined in an  $18.8024 \text{ \AA}$  by  $9.3150 \text{ \AA}$  by  $9.3150 \text{ \AA}$  cubic cell, to yield a density of  $0.9972 \text{ g cm}^{-3}$  in close agreement with the reported density of water at 298 K [366]. As mentioned above, a simulation temperature of 350 K was chosen based on previous reports of PBE structuring of water at 298 K [367, 368]. A similar 5 ps equilibration and 20 ps of production runs were performed. A snapshot of bulk water supercell is shown in Section 7.5.3.3.

### 7.5.1.3 Entropy calculations

The calculation of water entropies was accomplished using an in-house build of the quasi-harmonic 2-phase theory (2PT) algorithm developed by Lin, Blanco, Pascal, Maiti, and Goddard [161, 162, 369]. We have previously applied this method to estimate differences in the entropy of adsorption for reactive intermediates for ethanol dehydration [180] and acetonitrile [58] in zeolite Beta. Our implementation is described below. Periodic trajectory files from VASP are converted into the .XYZ file format using the Atomic Simulation Environment (ASE) [370] with the zeolite

framework atoms removed. The trajectories are unwrapped across periodic boundary conditions and sorted by water molecule to infer molecular identity using the molecular dynamics toolbox TRAVIS [168]. From there, an in-house implementation of the 2PT theory is performed which includes decomposition of the molecular degrees of freedom into center of mass translation, rotation, and vibration. These are then individually passed through a Fourier transform filter and smoothed using a Savitzky-Golay filter producing Velocity Density of State (VDOS) functions for the translational, vibrational, and rotational modes.

The gas-like contributions to translational and rotational modes are approximated as a set of hard spheres. Thus, a VDOS for the gas-like diffusion, gas-like rotation, solid-like diffusion, and vibrations can be individually integrated to obtain entropies according to the general relation in equation 7.1:

$$S = k \left[ \int_0^\infty dv S^s (W_S^s(v)) W_S^s(v) + \int_0^\infty dv S^g(v) W_S^g(v) \right] \quad (7.1)$$

where  $S$  is the entropy of a given type of motion comprised of a solid-like VDOS,  $S^s(v)$ , and quantum harmonic weight function,  $W_S^s(v)$ , integrated over the range of frequencies  $v$ , and the corresponding VDOS for the gas-like component  $S^g(v)$  with weight function  $W_S^g(v)$  derived from the Carnahan-Starling equation of state for hard sphere gases, as discussed by Lin et al. [161, 162, 369] Entropies calculated from this method could be compared across a range of densities and compared to the entropy of the bulk water reservoir. While the method by Lin et al. has shown success in calculating absolute entropies, our small number of guest water molecules and use of the BEEF-vdW functional leads us to take the more conservative approach of comparing only relative entropies across the composition space.

#### 7.5.1.4 Hydrogen bonding network theory

The weighted clustering coefficients are calculated with the method by Barrat et al. [361], but the development of the water network connectivity diagrams requires

additional discussion. The time-averaged hydrogen bonds at each water density were calculated by the method of Durrant et al. [371] where both the distance between hydrogen bond donors and acceptors and the angle formed between hydrogen bond donors and acceptors are used as criteria to determine the existence of a hydrogen bond. A maximum noncovalent O-H bond distance of 3.5 Å, and maximum O-H-O bond angle of 30°, were used for cutoffs. Existence of hydrogen bonds between pairs of water molecules is summed for the duration of the calculation and normalized by the duration of the simulation. Thus, while each water molecule is free to donate and accept multiple hydrogen bonds at a given time, the individual hydrogen bond between a pair of water molecules is expressed as a fraction representing the time-averaged duration of the hydrogen bond. For example, a pair of waters perpetually hydrogen bound to each other would have a connectivity of 1. A pair of waters hydrogen bound to each other for half the duration of the simulation would have a connectivity of 0.5. Thus, an adjacency matrix  $a_{ij}$  can be written where if a hydrogen bond exists at any timestep between water molecules  $i$  and  $j$ ,  $a_{ij} = 1$  and is equal to zero if no hydrogen bonds are formed. A matrix of edge weights,  $w_{ij}$ , can also be constructed, which is equal to the time averaged hydrogen bond connectivity between water molecules  $i$  and  $j$ , which is bounded between 0 and 1. Heat maps of connectivity matrices are included in Section 7.5.3.6 which directly visualizes the correlations between water pairs.

From the adjacency and edge weight matrices, the weighted clustering coefficient as derived by Barrat et al. can be implemented, with the following equation:

$$c_i^w = \frac{1}{s_i(k_i - 1)} \sum_{j,h} \frac{(w_{i,j} + w_{i,h})}{2} a_{ij}a_{ih}a_{jh} \quad (7.2)$$

Here,  $k_i$  is the number of edges (hydrogen bonds) at a given vertex (water molecule), and  $s_i$  is the sum over all weights at a given edge. The weights of each pair of edges are expressed as  $w_{i,j} + w_{i,h}$ , with the product of edges between vertices  $i, j, h$  being nonzero if a triangle can connect all three vertices. Thus, the weighted clustering

coefficient of a given vertex  $i$ , is calculated as the sum of all triply connected vertices weighted by their hydrogen-bonding connectivity and normalized by the maximum connectivity of hydrogen bonds at a given water density.

From the weighted clustering coefficient for each vertex, the overall clustering coefficient as averaged over the network is also given by Barrat et al. [361]

$$C^w = N^{-1} \sum_i c_i^w \quad (7.3)$$

which is the arithmetic mean of clustering coefficients at each vertex normalized by the number of vertices,  $N$ . Higher order moments about the distribution of clustering coefficients at a given water density can also be considered.

#### 7.5.1.5 AIMD OD stretching peak center identification

To identify OD stretching peaks in the AIMD simulations, VDOS (described above) which include the spectrum of all water vibrational states, could be directly fitted. The advantage of using the VDOS, as opposed to a 0 K vibrational state calculation, is that the perturbations in OD stretches were averaged over all water molecules and sampled for the full duration, as well as approximately including temperature effects on vibrational frequencies. Peak positions were determined by performing a Gaussian fitting of the VDOS and reporting mean positions after using a Hanning filter to remove high frequency modes post-FFT. Plots of the vibrational spectra are included in Section 7.5.3.5.

#### 7.5.1.6 Synthesis of Beta zeolites

Si-Beta-F was synthesized using tetraethylammonium fluoride dihydrate (TEAF) as the structure-directing agent and fluoride source following reported procedures [106]. TEAF (Alfa Aesar, 97%, 5.1 g) was dissolved in deionized water (18.2 M $\Omega$  cm, 5.5 g) in a perfluoroalkoxy alkane (PFA) container with a Teflon stir bar. Tetraethyl orthosilicate (TEOS, Sigma Aldrich, 98%, 10.3 g) was added to the PFA container,

and the mixture was covered and homogenized overnight at ambient conditions to completely hydrolyze TEOS. Then, the mixture was uncovered until ethanol completely evaporated from the mixture, and some water. Deionized water was added to the mixture to achieve a gel with molar composition  $1 \text{ SiO}_2/0.55 \text{ TEAF}/6.7 \text{ H}_2\text{O}$ , and the mixture was transferred into a  $45 \text{ cm}^3$  Teflon-lined stainless steel autoclave and heated to 413 K for 11 days in an isothermal rotating oven (Yamato DKN-402C). The product solids were recovered by centrifugation and washed thoroughly with water and acetone, then dried overnight in a 373 K oven. The dried solids were treated in flowing air (Indiana Oxygen, UHP,  $1.67 \text{ cm}^3 (\text{g solid})^{-1} \text{ s}^{-1}$ ) to 853 K ( $0.0167 \text{ K s}^{-1}$ ) for 10 h.

H-Al-Beta-F was synthesized following the procedure of Cambor et al. [93] TEOS (10 g) was mixed with tetraethylammonium hydroxide (TEAOH, Sachem, 35%, 11 g) in a PFA container and homogenized while covered for 2 h. Aluminum isopropoxide powder ( $\text{Al}(\text{O-i-Pr})_3$ , Sigma Aldrich, 98%, 0.16 g) and excess deionized water (12.4 g) were added to the mixture, which was covered and stirred overnight to completely hydrolyze TEOS and  $\text{Al}(\text{O-i-Pr})_3$ . The mixture was uncapped in order to completely evaporate ethanol and isopropanol and partially evaporate water to reach the desired molar ratio. Then, hydrofluoric acid solution (Sigma Aldrich, 48%, 1.1 g) was added and the mixture was homogenized with a PTFE spatula to yield a thick gel with molar composition  $1 \text{ SiO}_2/0.56 \text{ TEAOH}/0.57 \text{ HF}/0.016 \text{ Al}/7 \text{ H}_2\text{O}$ . (Caution: when working with hydrofluoric acid, use appropriate personal protective equipment, ventilation, and other engineering controls.) The gel was loaded into a  $45 \text{ cm}^3$  Teflon-lined stainless steel autoclave and heated to 413 K for 7 days in an isothermal rotating oven. The product solids were recovered by centrifugation and washed thoroughly with water and acetone, then dried overnight in a 373 K oven. The dried solids were treated in flowing air (Indiana Oxygen, UHP,  $1.67 \text{ cm}^3 (\text{g solid})^{-1} \text{ s}^{-1}$ ) to 853 K ( $0.0167 \text{ K s}^{-1}$ ) for 10 h.

Si-Beta-OH was obtained via dealumination of H-Al-Beta-F following reported procedures [151]. Air-treated H-Al-Beta-F solids (1 g) were mixed in a PFA container

with  $\text{HNO}_3$  (Sigma Aldrich, 70%,  $20 \text{ cm}^3 (\text{g solid})^{-1}$ ), stirred at 400 rpm with a Teflon stir bar, and heated to 353 K in an oil bath for 20 h. The solids were recovered by centrifugation, washed 5 times with deionized water ( $\sim 35 \text{ cm}^3$  per wash), and dried overnight in a 373 K oven.

#### 7.5.1.7 Characterization of Beta zeolites

Powder X-ray diffraction (XRD) patterns were collected with a Rigaku Smartlab X-ray diffractometer with a  $\text{Cu K}\alpha$  X-ray source in the range of  $2\theta = 4\text{--}40^\circ$  with a step size of  $0.01^\circ$  and scan speed of  $0.005^\circ \text{ s}^{-1}$ .

$\text{N}_2$  and  $\text{H}_2\text{O}$  adsorption isotherms were collected on a Micromeritics ASAP 2020 instrument. Samples were pelleted and sieved to retain 180–250  $\mu\text{m}$  aggregates, and 0.010–0.040 g were degassed by heating to 393 K for 2 h then 623 K for 10 h under dynamic vacuum ( $<0.67 \text{ Pa}$ ) prior to adsorption measurements.  $\text{N}_2$  adsorption isotherms were collected at 77 K by immersion in a liquid  $\text{N}_2$  bath, and  $\text{H}_2\text{O}$  adsorption isotherms were collected at 293 K by immersion in a recirculating chiller bath held at 293 K.  $\text{H}_2\text{O}$  was introduced from the vapor phase generated from a flask held at 313 K containing deionized water, after degassing by three freeze-pump-thaw cycles.  $\text{N}_2$  micropore volumes were determined at the uptake corresponding to the minimum value of  $\partial V_{\text{ads}}/\partial \log(P/P_0)$ .

The bulk mass fraction of Al in Al-Beta-F was obtained by atomic absorption spectroscopy (AAS). 0.03 g of powder were digested with 2 g of HF (Sigma Aldrich, 48%) overnight, then diluted with 50 g of deionized water. Calibration standards were prepared by diluting a stock solution (Sigma Aldrich,  $1000 \pm 4 \text{ ppm Al}$ ) with deionized water. A PerkinElmer AAnalyst 300 instrument equipped with a lamp for Al (309.3 nm) was used to measure the absorbance of the standards and digested sample. The Si/Al ratio was calculated assuming the unit cell formula of Beta.

### 7.5.1.8 Infrared spectroscopy of adsorbed H<sub>2</sub>O

IR spectra of adsorbed H<sub>2</sub>O were collected using procedures similar to those in our previous reports [57]. Samples of Si-Beta-F and Si-Beta-OH (0.040–0.050 g) were pressed into self-supporting wafers with a 0.9 cm radius and loaded into a custom-built quartz cell with CaF<sub>2</sub> windows housed within an alumina silicate ceramic chamber (Purdue Research Machining Services) with a mineral-insulated resistive heating coil (ARi Industries) [184]. The temperature of the wafers was measured by two K-type thermocouples (Omega) within 2 mm of each side of the wafer. Spectra were collected on a Nicolet 4700 spectrometer with a Hg-Cd-Te detector (MCT, cooled to 77 K by liquid N<sub>2</sub>) as the average of 640 scans (600 s) to ensure temporal averaging of periodic fluctuations in gas-phase H<sub>2</sub>O pressure. Wafers were pretreated in flowing dry air (<1 ppm of CO<sub>2</sub>, 200 K water dew point, Parker Balston, 19–24 cm<sup>3</sup> g<sup>-1</sup> s<sup>-1</sup>) to 823 K (0.083 K s<sup>-1</sup>) for 1 h, then cooled in flowing He (UHP, Indiana Oxygen, 19–24 cm<sup>3</sup> g<sup>-1</sup> s<sup>-1</sup>) to 293 K. Temperature was controlled at 293 K by flowing H<sub>2</sub>O at 288 K through channels in the block with a recirculating chiller, and resistive heating.

A spectrum was collected of the wafer at 293 K under flowing He (19–24 cm<sup>3</sup> g<sup>-1</sup> s<sup>-1</sup>) to be used as a reference before H<sub>2</sub>O adsorption. Then, the same He flow was redirected through a heated (>363 K) line connected to a glass syringe (1 cm<sup>3</sup>, Hamilton) containing deionized water. Transfer lines after the syringe leading to the cell were heated to >363 K to prevent condensation. The flow rate of the liquid H<sub>2</sub>O was controlled via syringe pump (KD Scientific Legato 100) to give an H<sub>2</sub>O pressure of 0.2 kPa ( $P/P_0 = 0.1$ , 293 K). Care was taken to slowly introduce the liquid H<sub>2</sub>O through the dead volume ( $\sim 20\text{--}100 \times 10^{-3}$  cm<sup>3</sup>) connecting the syringe to the line to prevent exposing the wafer to a H<sub>2</sub>O partial pressure higher than 0.2 kPa. Spectra were collected continuously (600 s per scan), and the wafer was held at 293 K in the 0.2 kPa H<sub>2</sub>O stream for 4 h after H<sub>2</sub>O introduction to ensure equilibration, which was verified by invariant spectra collected at the end of this time period. The H<sub>2</sub>O flow rate was adjusted to give partial pressures of 0.5 kPa, 1.2 kPa, and 1.7 kPa,

corresponding to  $P/P_0 = 0.2, 0.5,$  and  $0.75$  (at 293 K), and 2 h were allowed at each condition for equilibration (verified by invariant spectra).

This procedure was first performed with an empty cell to obtain signals for gas-phase  $H_2O$  at each  $P/P_0$  value. A background spectrum of the empty cell before  $H_2O$  introduction was used as the reference for all other collected spectra. The processing of spectra is illustrated in Figure 7.33. The spectra for the empty cell at the corresponding  $H_2O$   $P/P_0$  values were subtracted from the wafer spectra to yield cell-corrected spectra (Figure 7.33a). Then, the cell-corrected spectra were normalized by the Si-O-Si overtone vibration ( $1750\text{--}2100\text{ cm}^{-1}$ ) peak area of the wafer before  $H_2O$  adsorption. The normalized, cell-corrected spectrum of the wafer before  $H_2O$  adsorption was subtracted from those measured at each  $H_2O$   $P/P_0$  value to give subtracted spectra (Figure 7.33b) that represent the signal for adsorbed  $H_2O$ , and any changes to the vibrations associated with the zeolite, e.g., perturbation of Si-OH groups. Spectra were also subtracted between incremental increases in  $H_2O$  pressure, denoted “differential subtracted,” in order to visualize the change in signal associated with the adsorption of additional  $H_2O$  molecules. Subtracted and differential subtracted spectra were further baseline-corrected with pivot points at  $4000, 2400,$  and  $1350\text{ cm}^{-1}$ , where no absorbance was detected.

## 7.5.2 Supplementary Discussions

### 7.5.2.1 Characterization of water trajectories

Qualitative differences in water trajectories, as observed during simulations, provide the first indication of unique water structures, which are included as characteristic snapshots (7.5.3.1), time averaged trajectory heat maps along two lattice vectors (7.5.3.2), and selected movies of simulations (online source). These depict the formation of water chains, hyper-conjugated clusters, and cross-linked networks which emerge among the defect types. It is important to keep in mind that the fixed unit cell size prevents size extensivity of low-density water structures which may agglomerate

into water dimers, trimers, and multi-mers at lower densities, especially in Si-Beta, where no nucleating defects exist. As a result, detailed characterization of the gas-phase low density limit (1-3 water molecules per unit cells) is difficult, as at a density of 1 water per unit cell, it is impossible to form water dimers without considering multiple unit cells. Thus, for Si-Beta at densities of 1-3 water molecules per unit cell, diffusing monomers, dimers, and trimers of water are observed. Beginning as low as 4 waters per unit cell, water molecules begin to disperse along the [100] pore direction. This is most apparent at a density of 8 waters per unit cell, where the heat density map of 7.5.3.2. shows the predominant density of water in a single [100] pore, with some diffusion of individual gas-phase water molecules in the surrounding space. This well-defined chain has been reported in previous classical MD literature on siliceous zeolites [355,357]. The self-diffusion coefficient of water at this condition is  $1.84 \times 10^{-8} \text{ m}^2 \text{ s}^{-1}$  (Table 7.2) as calculated with the TRAVIS [168] package from trajectory data. Despite appearing to uniformly fill the pore along [010], water molecules prefer configurations closer to the pore walls, with a noticeable decrease in density in the pore center, due to favorable van der Waals interactions. As water densities increase, filling of the perpendicular pore structure begins, while the [010] water chain persists. This crosslinking behavior has also been previously reported. Even at a density of 23 waters per unit cell, close to the expected bulk density of liquid water, non-uniform filling of pore space is still observed, where denser packing of water molecules as described by Siepmann [358] must result. The self-diffusion constant of water at this density is  $1.08 \times 10^{-8} \text{ m}^2 \text{ s}^{-1}$  (Table 7.2), qualitatively similar to that of bulk liquid water, which has been previously reported as attainable in cation-exchanged Faujasites [372]. While these results for Si-Beta are not in themselves new, they provide confidence in the use of BEEF-vdW to qualitatively capture the physical properties of confined water and demark a comparison with the more exotic defects.

The Sn-Beta defect material provides a marked contrast to Si-Beta, where low water densities are characterized by hyperconjugation of water molecules on the Lewis acidic Sn. It has been widely reported that adsorption of more than one

water molecule per Sn site is common in gas-phase catalysis, however, the degree of conjugation under a range of solvent conditions has not been examined. Up to a density of 5 waters per unit cell, there is no indication of chain formation as observed in Si-Beta, and even at 8 waters per unit cell, there is separation of water clusters between periodic boundary conditions, as evidenced by the snapshots. Density plots show nearly complete localization to the [010] pore with regions of high density at the image center, directly interacting with the Sn atom, indicating inviscid water molecules hyper-conjugated to the Sn center. The self-diffusion constant is also smaller by an order of magnitude than Si-Beta at the same density ( $1.84 \times 10^{-8} \text{ m}^2 \text{ s}^{-1}$  as compared to  $0.16 \times 10^{-8} \text{ m}^2 \text{ s}^{-1}$ ) reflecting the more localized chemisorbed water molecules comprising a cluster. As water density increases and the filling of perpendicular pores and crosslinking through intersections begins to occur, the higher density regions of localized water are still apparent at 23 waters per unit cell, and the self-diffusion constant increases to  $0.47 \times 10^{-8} \text{ m}^2 \text{ s}^{-1}$  which is nearly half that of Si-Beta at the same density ( $1.08 \times 10^{-8} \text{ m}^2 \text{ s}^{-1}$ ).

Hydrolysis of the Sn cation to form SnOH is accompanied with a framework silanol [113,154,180,373], which introduces both Lewis acid and weak Bronsted acid character at the same site. A hydroxyl ligand extends into the [100] pore, with framework silanol nestled in the [010] pore, with the metal cation accessible to both pores. Consequently, all three sites (hydroxyl ligand, exposed Sn cation, and framework silanol) adsorb water. Like Sn-Beta, formation of water chains is not observed until higher densities near 15 waters per unit cell, as hyperconjugation of water around the three binding sites is observed, again further evidenced by time-averaged plots which demonstrate higher density regions around the Sn. Two high density spots are seen, which correspond to the clustering of water around the hydroxyl ligand and framework silanol, which are in opposite pore environments, with additional interaction directly with the Sn cation. The water self-diffusion coefficient at  $8 \text{ H}_2\text{O}$  u.c.<sup>-1</sup> is like that of Sn-Beta ( $0.21 \times 10^{-8} \text{ m}^2 \text{ s}^{-1}$ ) indicating that while water molecules can bind at multiple sites, there is still a nucleated cluster of reduced diffusivity at

the defect site. These high density regions persist at a density of 23 waters per unit cell where hyperconjugation of water around the intersection spanned by the three binding sites is observed. The water self-diffusion coefficient at this higher density is  $0.32 \times 10^{-8} \text{ m}^2 \text{ s}^{-1}$ , nearly one third of the Si-Beta diffusivity.

Removal of the Sn site and terminating the four oxygens produces a silanol nest defect, which provides the most contrast to Sn-Beta and SnOH-Beta. At densities below 5 waters per unit cell, there is strong interaction of water with each silanol nest, which results in a high degree of localization in water structuring. Beyond saturation of the nest, a transition into chain-like water structures, like Si-Beta, with exploration of the [100] pores observed to a visibly greater degree than for Si-Beta. This greater degree of expansion may be due to silanols providing additional flexibility to the water network at this density, and allowing for fewer water molecules to form the [010] chain, effectively providing additional water molecules to the network. There is no visible clustering observed for the silanol nests, indicating that the silanol groups mediate transient hydrogen bonds that do not significantly localize water. It is noted, that uniform filling of the [100] pore is observed at a density of 8 waters per unit cell, which could indicate a higher density of water throughout the diameter of the pore, possible due to a larger hydrogen bond network which compensates the weaker van der Waals interactions with the pore walls. The water self-diffusion constant at 8 H<sub>2</sub>O u.c.<sup>-1</sup> is  $0.91 \times 10^{-8} \text{ m}^2 \text{ s}^{-1}$ , larger than either of the Sn speciations, but only half of the Si-Beta diffusivity, likely due to hydrogen bonding interactions with the silanol nest reducing diffusivity along the channel. This is; however, not observed at the highest density of 23 waters per unit cell, where the centers of the [010] and [100] pores are not uniformly filled, and no clustering is observed. In fact, the time averaged density plots of Si-Beta and (OH)<sub>4</sub>-Beta look nearly identical at a density of 23 waters per unit cell, indicating the strong interactions with silanol nests have been attenuated, and the water network has adopted a more transient dynamic structure. The water self-diffusion coefficient is  $0.61 \times 10^{-8} \text{ m}^2 \text{ s}^{-1}$ , which is more than half that of Si-Beta

at the same density, which reflects the attenuated effect of the silanol nest and lack of defined clustering.

While not rigorous in their own respect, a careful analysis of the physical trajectory data can provide insights and generate hypotheses which can be further tested through more quantitative characterization methods such as the thermodynamic, network approach, and connection to experiment through OH stretching peaks. The four Beta materials behave quite differently, with Si-Beta observing no formal clustering except the formation of transient dimers and trimers, Sn-Beta forming hyperconjugated water structures which persist at all water densities, SnOH-Beta which also forms persistent water structures at all adsorption sites, and finally (OH)<sub>4</sub>-Beta where initial strong interactions with silanol nests at low density are attenuated and begin to behave similarly to the transient nature of Si-Beta.

We note that, although the resolution of the sampling statistics and associated density fluctuations obtained from such AIMD-based approaches can be limited by accessible simulation time and small unit cell sizes, the vibrational densities of state are converged with respect to simulation time, and the results are consistent with trends seen in classical simulations of water in carbon nanotubes [350] and with other zeolite simulations [42, 355, 357] (see 7.5.2.1), as well as with our own experimental results.

#### 7.5.2.2 Free energy analysis

To calculate the potential energy of water in each zeolite, the ensemble averaged energy of the bare framework was subtracted from the zeolite including adsorbed water, which could then be normalized to an intensive property by dividing by the number of water molecules. This is referenced to an intensive energy of bulk water calculated at 350 K and 1 bar:

$$\widehat{E}_w = \frac{\langle E_{W+Z} \rangle - \langle E_Z \rangle}{N} - \widehat{E}_{\text{bulk}} \quad (7.4)$$

where  $\langle E_{W+Z} \rangle$  denotes the potential energy of the zeolite with adsorbed water averaged over the duration of the simulation and  $\langle E_Z \rangle$  denotes the potential energy of the bare zeolite averaged over the duration of the simulation.  $N$  is the number of water molecules, and  $\widehat{E}_{\text{bulk}}$  is the intensive potential energy of bulk water at 350 K and 1 bar. The resulting property has units of eV (water molecule)<sup>-1</sup>. The above relation is only reasonable in the limit where the vibrational states of the zeolite framework are uncoupled from the dynamics of water molecules. The vibrational spectrum of the zeolite framework was calculated at varying water densities, and as shown in Section 7.5.3.7, no peaks shift even in the presence of 45 water molecules per unit cell, indicating the energetic terms are approximately separable, as described above.

The intensive Helmholtz free energy of water in Beta is described relative to the chemical potential of water vapor at 300K and a  $P/P_0$  of 0.05. The Helmholtz free energy of the reference state is thus defined as:

$$a_{\text{ref}} \left( 300K, 0.05 \frac{P}{P_0} \right) = E_{\text{DFT}} + TS_{\text{I.G.}} - kT \ln \left( \frac{P}{P_0} \right) \quad (7.5)$$

where  $E_{\text{DFT}}$  is the total energy of a gas phase water molecule and  $S_{\text{I.G.}}$  is the ideal gas entropy obtained from partition functions (estimated to be 188 J mol<sup>-1</sup> K<sup>-1</sup>). The Helmholtz free energy of water in Beta is then described with the following expression

$$A_w \left( 300 K, 0.05 \frac{P}{P_0} \right) = (\langle E_{ZW} \rangle - \langle E_Z \rangle) - TS_{ZW} - a_{\text{ref}}N \quad (7.6)$$

where  $\langle E_{ZW} \rangle$  is the averaged total energy from AIMD of water and the zeolite and  $\langle E_Z \rangle$  is the averaged total energy from AIMD of the empty zeolite framework.  $S_{ZW}$  is the entropy of water and the zeolite, but the entropy of the zeolite upon loading with water is identical to the empty zeolite as evidenced by Section 7.5.3.7. Therefore  $S_{ZW} = S_W$ , which is the entropy of water in the framework calculated from the vibrational density of states. This is then referenced to the bulk chemical potential expressed as the pure-component Helmholtz free energy of water vapor.

The free energy criterion can be derived by considering equilibrium between the zeolite, with an extensive Helmholtz energy of  $A(N)$ , as calculated from the AIMD simulations, and an external reservoir of water with a chemical potential of  $\mu_{\text{res}}$ . At equilibrium between the system and the reservoir,  $\frac{\partial A(N)}{\partial N} = \mu_{\text{res}}$ . To refer these quantities to an (arbitrary) reference state, which we take as the chemical potential of ideal gaseous water at 0.05 bar and 300 K, we subtract  $\mu_{\text{reference}}$  from both sides of the equation yielding  $\frac{\partial[A(N)-N\mu_{\text{reference}}]}{\partial N} = \mu_{\text{res}} - \mu_{\text{reference}}$ . Absorbing  $N\mu_{\text{reference}}$  into the definitions of  $A(N)$  and  $\mu_{\text{res}}$ , we recover the original expression  $\frac{\partial[A(N)]}{\partial N} = \mu_{\text{res}}$  but with the modified reference state implied. If we make the further assumption that the reservoir is truly infinite in extent, then its chemical potential will not be affected by changes in number of molecules in the system, and we can move it into the derivative to obtain  $\frac{\partial[A(N)-\mu_{\text{res}}N]}{\partial N} = 0$ . Hence, at thermodynamic equilibrium, the quantity  $A(N)-\mu_{\text{res}}N$ , with both  $A(N)$  and  $\mu_{\text{res}}$  referenced to the indicated state, will be minimized with respect to  $N$ . Thus, to find the equilibrium number of water molecules in the zeolite pores for a given value of the reservoir chemical potential, one may plot  $A(N)-\mu_{\text{res}}N$  vs.  $N$  and identify the value of  $N$  that gives the lowest value. As shown in Section 7.5.3.11, as relative chemical potentials decrease, corresponding to lower pressures than that of the reference state described above, only water densities lower than 1 water per unit cell are stable for both Si-Beta and the defected Beta materials. As the relative chemical potentials increase, however, higher density water clusters become stable, and extended water structures in the defected Beta materials are observed.

### 7.5.2.3 Supplementary discussion of experimental data

Synthesis of crystalline Si-Beta-F, Al-Beta-F, and Si-Beta-OH zeolites was confirmed by XRD patterns (Section 7.5.3.8) and micropore volumes ( $0.21 \text{ cm}^3 \text{ g}^{-1}$ , Table 7.2) consistent with the Beta topology. Complete dealumination of Al-Beta-F to give Si-Beta-OH was verified by AAS signals for Al approaching the detection limit (Si/Al

> 1500, Table 7.2). Assuming one  $(\text{SiOH})_4$  nest is generated per Al removed, the Si-Beta-OH zeolite possesses approximately one  $(\text{SiOH})_4$  nest per unit cell.

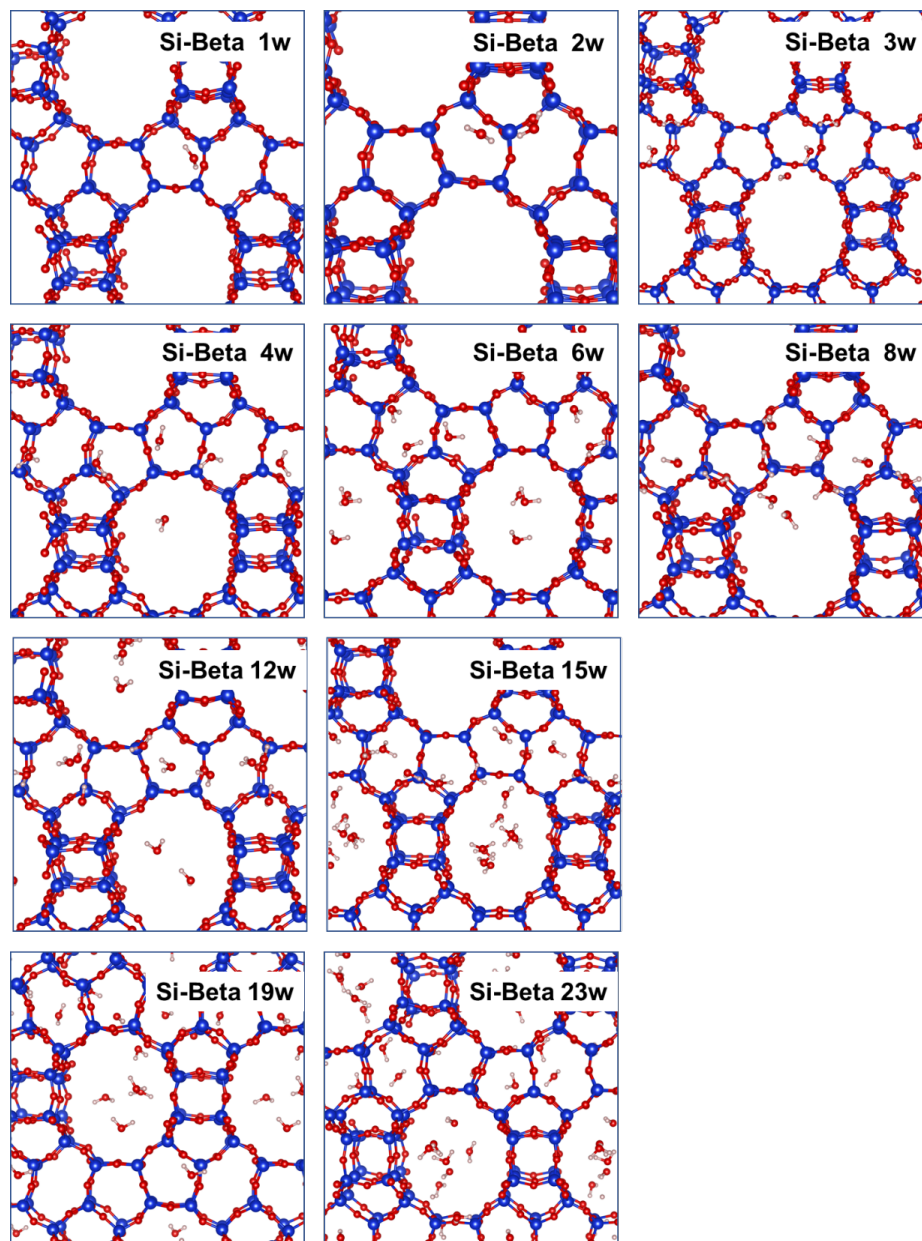
The bulk hydrophobic and hydrophilic character of the two Si-Beta samples is evident in their volumetric  $\text{H}_2\text{O}$  adsorption isotherms (Section 7.5.3.9), where  $\text{H}_2\text{O}$  adsorbs within Si-Beta-F with a Type III isotherm [199], where low uptakes at low  $P/P_0$  values indicate weak adsorbate-adsorbent interactions, and increased uptakes at higher  $P/P_0$  values indicate adsorption predominantly via adsorbate-adsorbate interactions, or at minority defect sites. Adsorption on Si-Beta-OH, in contrast, occurs by hydrogen-bonding interactions at Si-OH defects, leading to increasing water uptakes at low relative  $P/P_0$  values. The isotherm is not strictly Type I [199], however, where complete micropore filling would be observed, because there are still low-defect regions that do not provide favorable hydrogen-bonding interactions for  $\text{H}_2\text{O}$ . The uptakes at a  $P/P_0 = 0.2$  (selected because this value is characteristic of cyclohexane pore-filling in hydrophobic MOR zeolites [171]) on the Si-Beta-F and Si-Beta-OH (Table 7.2) are consistent with those expected for hydrophobic and hydrophilic zeolites, respectively [56], providing additional evidence for their respective defect densities inferred based on their synthetic histories.

The area of the  $\delta(\text{OH})$  peak at  $1630\text{ cm}^{-1}$  was quantified and linearly correlated in Figure 7.35 with the volumetrically-determined water uptakes at equivalent  $P/P_0$  values (Figure 7.32), providing a link between water uptakes and measured spectra (Figure 7.4f, Main Text). Differential subtracted IR spectra of the Si-OH stretching region on Si-Beta-F and Si-Beta-OH zeolites (Figure 7.34) indicate that between  $P/P_0 = 0.1\text{--}0.75$  on both zeolites,  $\text{H}_2\text{O}$  adsorbs at Si-OH groups, perturbing their OH stretching peaks as evidenced by negative peaks at  $3735\text{ cm}^{-1}$  and  $3745\text{ cm}^{-1}$  for internal and external Si-OH groups, respectively [329], with corresponding broad peaks centered at  $\sim 3400\text{ cm}^{-1}$  for hydrogen-bonded Si-OH groups (Figure 7.4, Main Text). The broad  $\nu(\text{OH})$  peaks in Figure 7.4 also include contributions at  $\sim 3570\text{ cm}^{-1}$  and  $3640\text{ cm}^{-1}$  assigned to loosely-bound water in one-dimensional chains previously observed in carbon nanotubes with diameters  $<1\text{ nm}$  [38], consistent with the

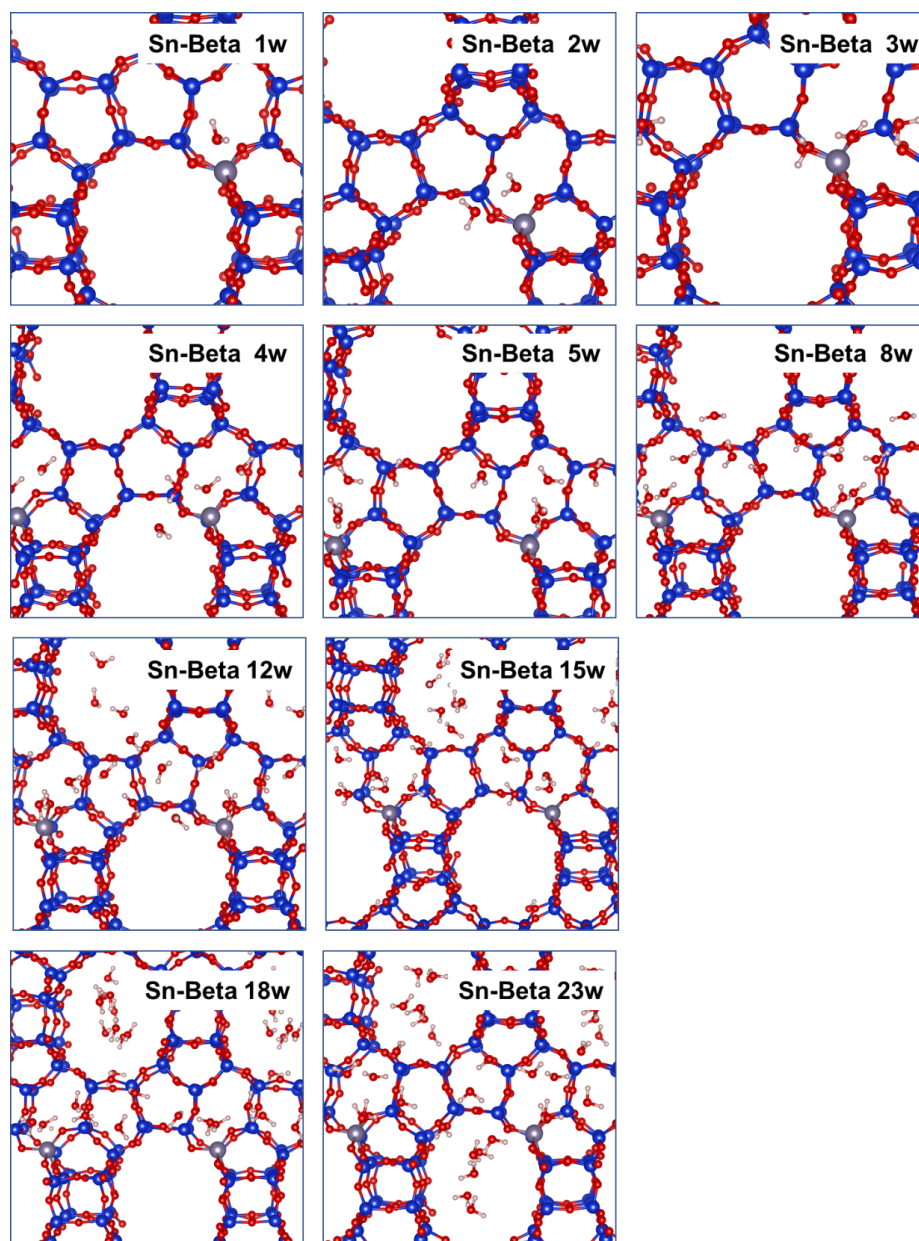
uniformly-dispersed chains observed in AIMD simulations in Si-Beta-F at 5–12 water molecules per unit cell.

### 7.5.3 Supplementary Figures

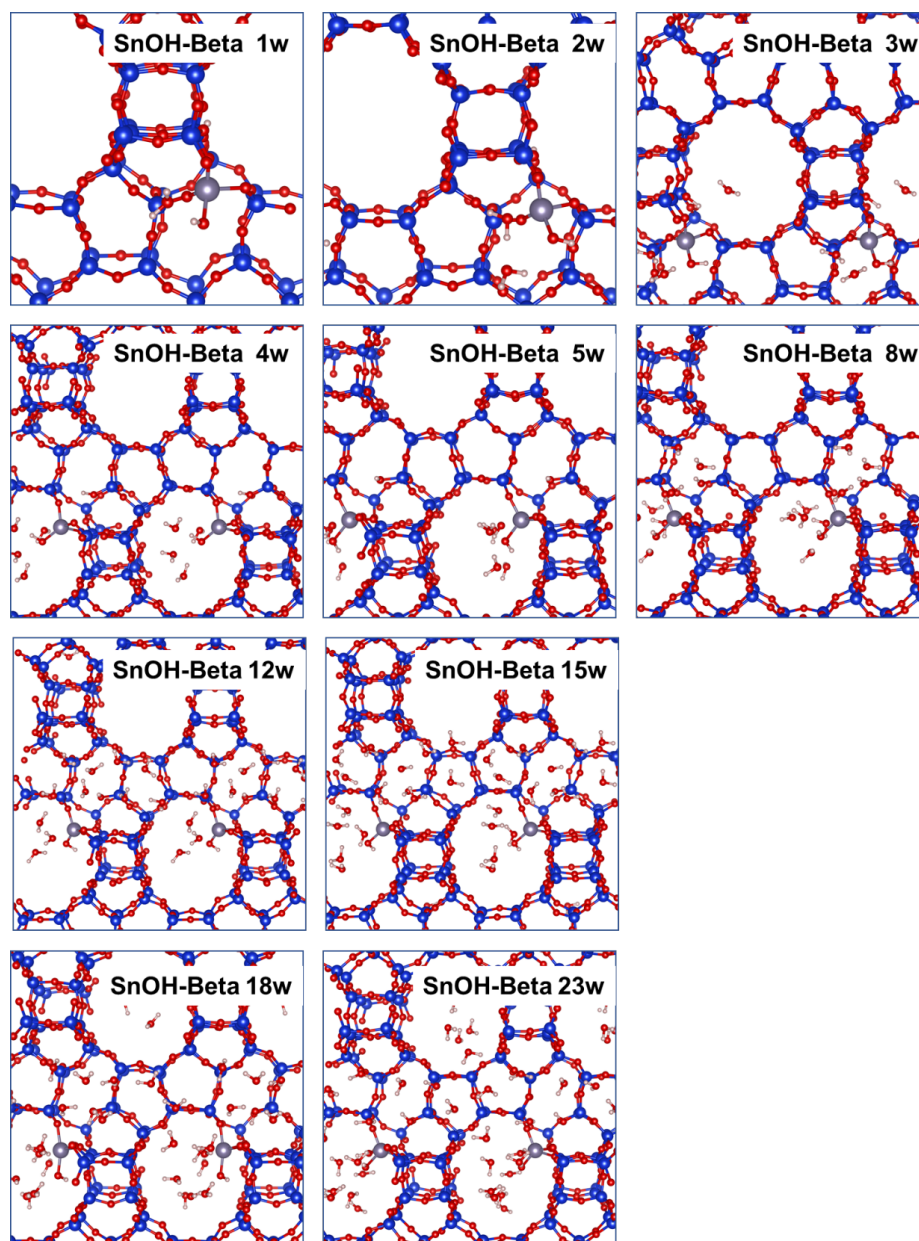
#### 7.5.3.1 Representative simulation images



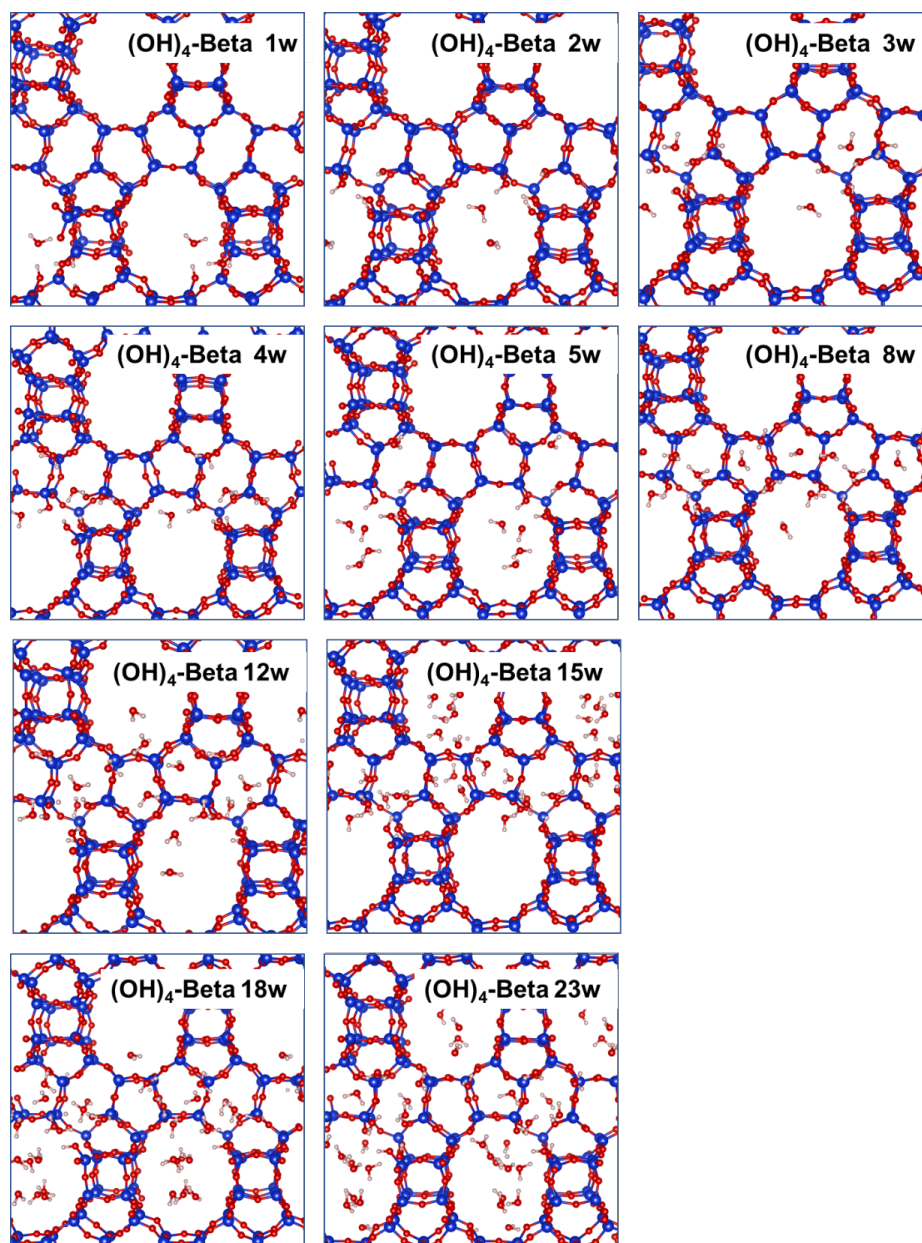
**Figure 7.5:** Representative snapshots of water structures obtained during production runs at varying density in Si-Beta.



**Figure 7.6:** Representative snapshots of water structures obtained during production runs at varying density in Sn-Beta.

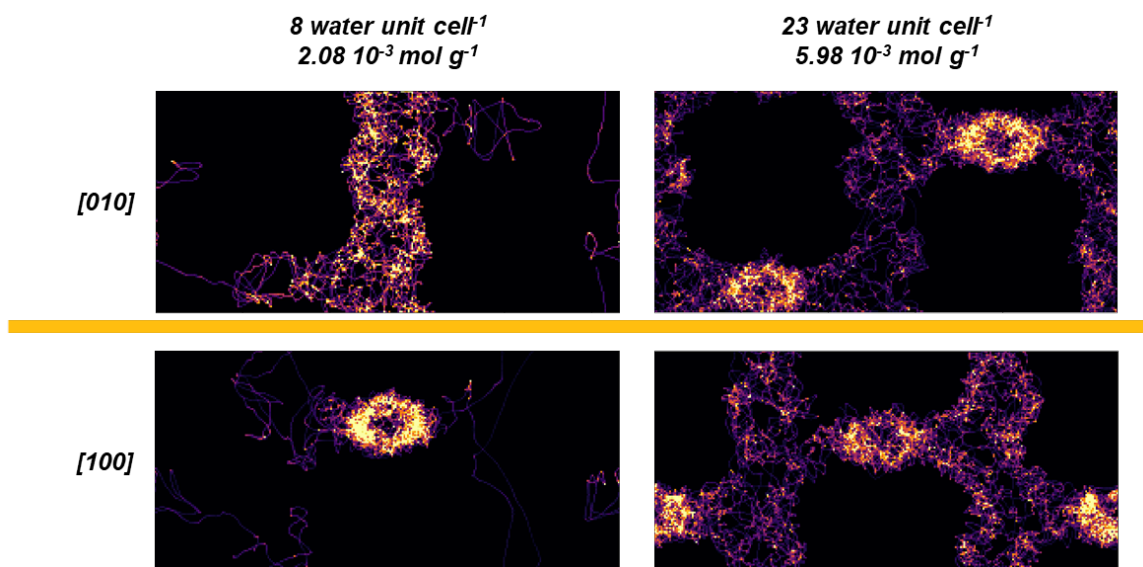


**Figure 7.7:** Representative snapshots of water structures obtained during production runs at varying density in SnOH-Beta.

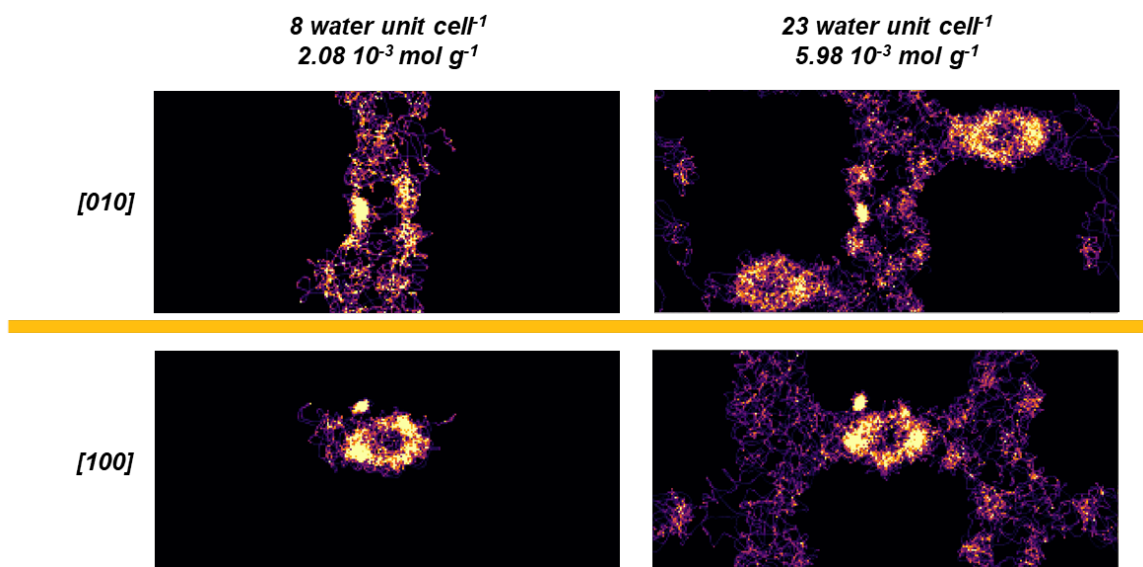


**Figure 7.8:** Representative snapshots of water structures obtained during production runs at varying density in  $(\text{OH})_4\text{-Beta}$ .

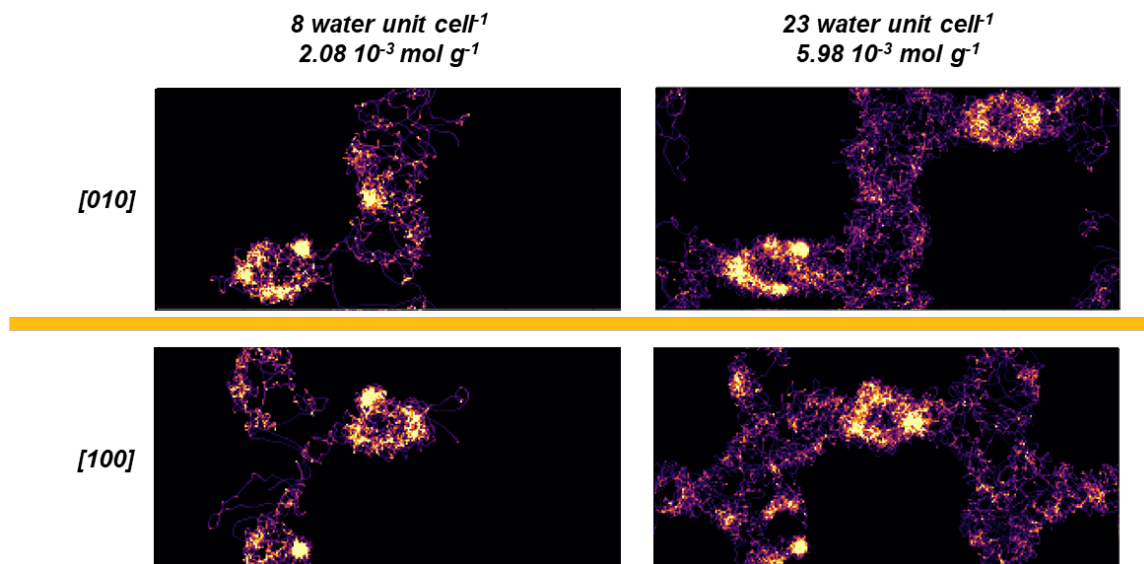
## 7.5.3.2 Time averaged density plots along [100]



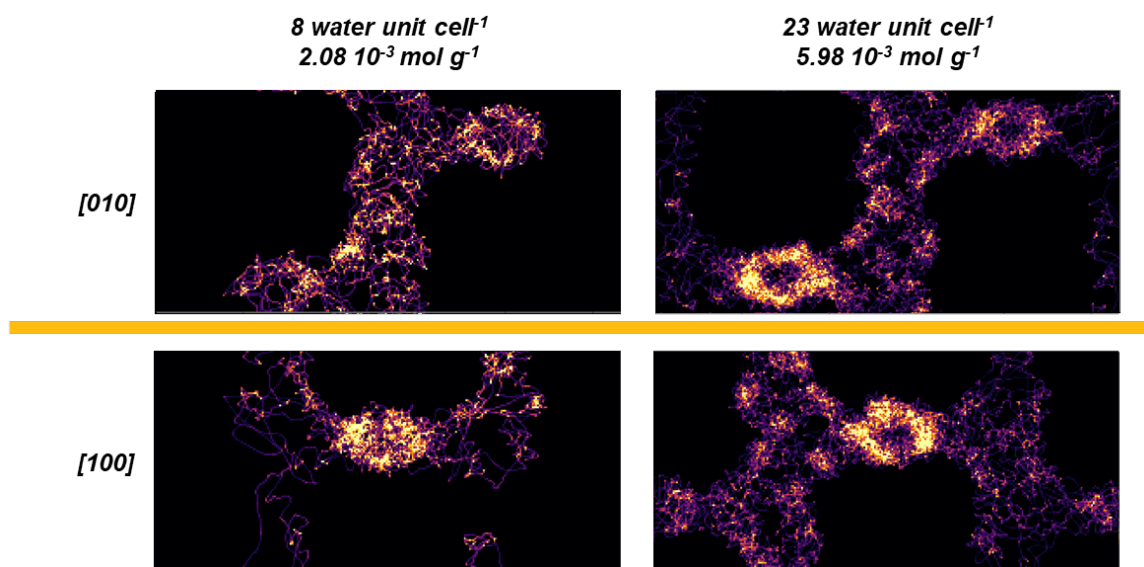
**Figure 7.9:** Time averaged density plot for Si-Beta along the [010] and [100] planes at low (8) and high (23) water densities (water unit cell<sup>-1</sup>).



**Figure 7.10:** Time averaged density plot for Sn-Beta along the [010] and [100] planes at low (8) and high (23) water densities (water unit cell<sup>-1</sup>).

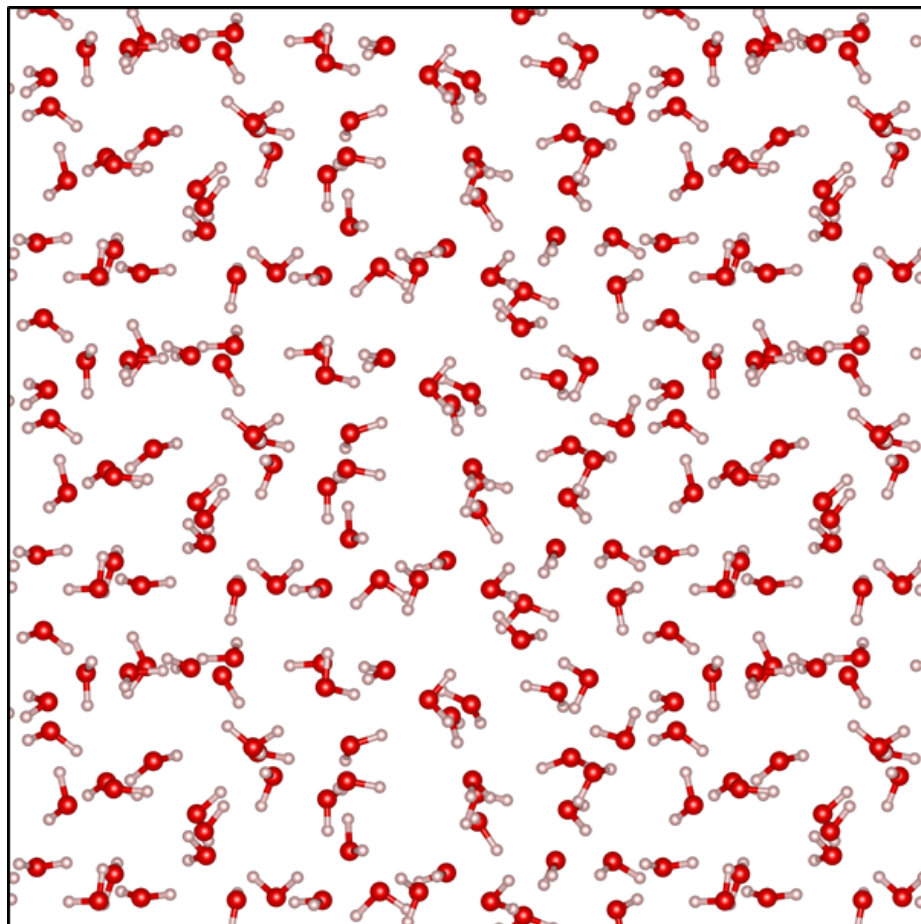


**Figure 7.11:** Time averaged density plot for SnOH-Beta along the [010] and [100] planes at low (8) and high (23) water densities (water unit cell<sup>-1</sup>).



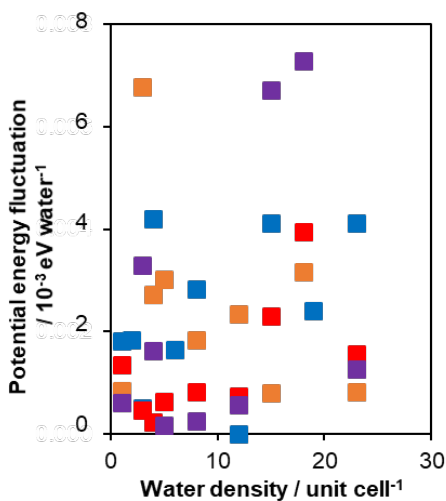
**Figure 7.12:** Time averaged density plot for (OH)<sub>4</sub>-Beta along the [010] and [100] planes at low (8) and high (23) water densities (water unit cell<sup>-1</sup>).

## 7.5.3.3 Bulk water structural image

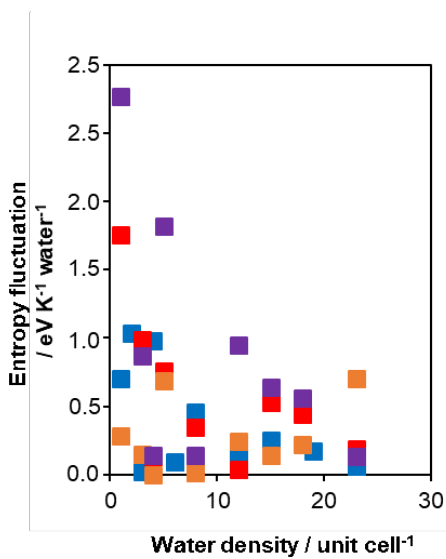


**Figure 7.13:** Supercell of bulk water simulated as a reference state.

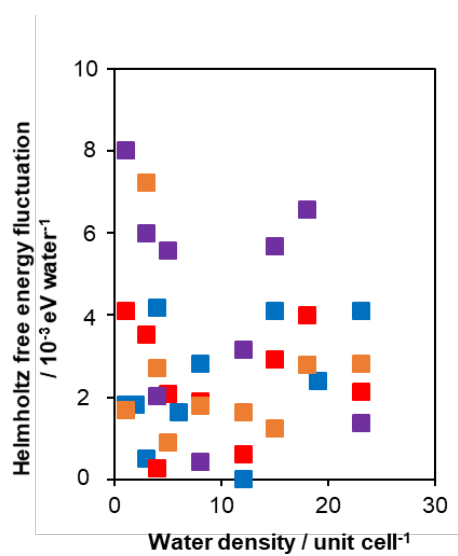
## 7.5.3.4 Fluctuations in averaged thermodynamic properties



**Figure 7.14:** Fluctuations in the potential energy predicted per water molecule for Si-beta (blue), Sn-Beta (red), SnOH-Beta (orange), and  $(\text{OH})_4$ -Beta (purple) at 19 ps and 20 ps.

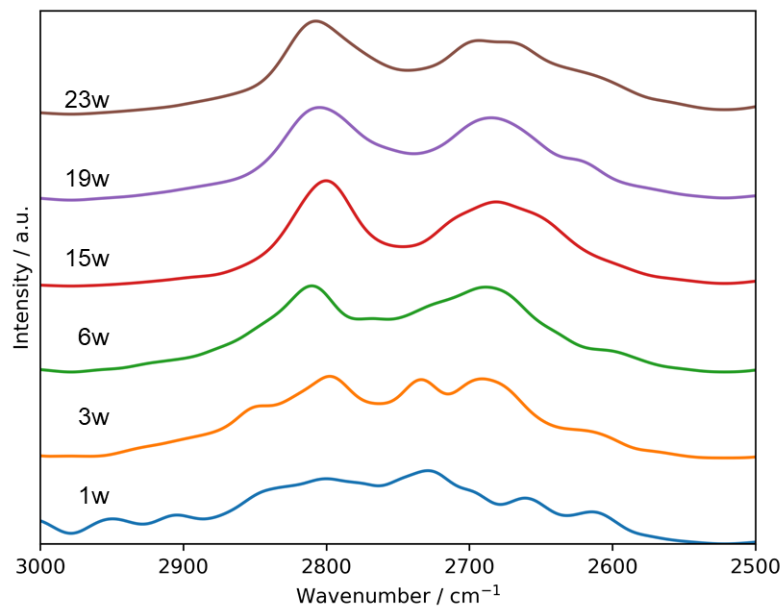


**Figure 7.15:** Fluctuations in the entropy predicted per water molecule for Si-beta (blue), Sn-Beta (red), SnOH-Beta (orange), and  $(\text{OH})_4$ -Beta (purple) at 19 ps and 20 ps.

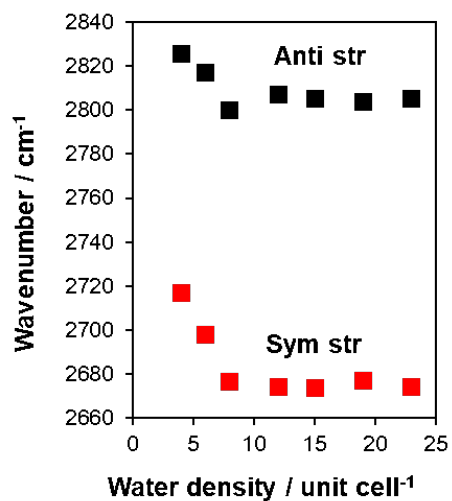


**Figure 7.16:** Fluctuations in the potential energy predicted per water molecule for Si-beta (blue), Sn-Beta (red), SnOH-Beta (orange), and (OH) $_4$ -Beta (purple) at 19 ps and 20 ps.

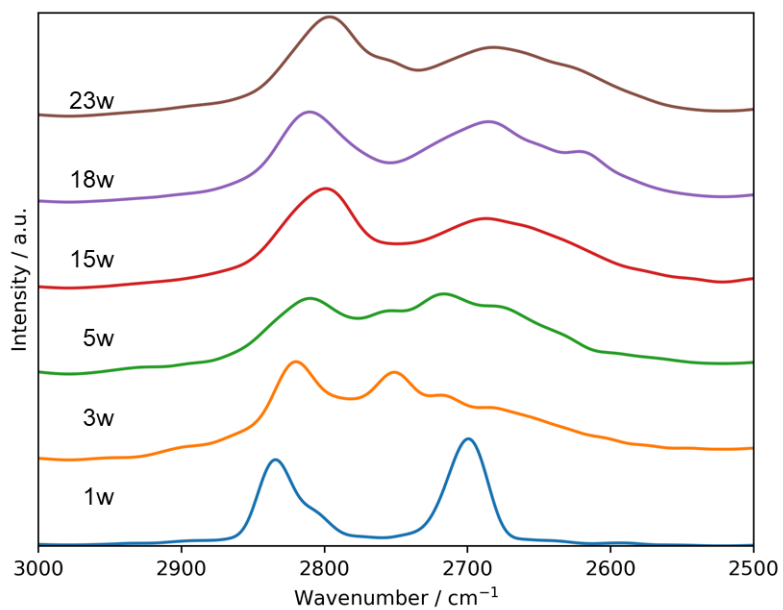
## 7.5.3.5 Computational OD stretching peaks



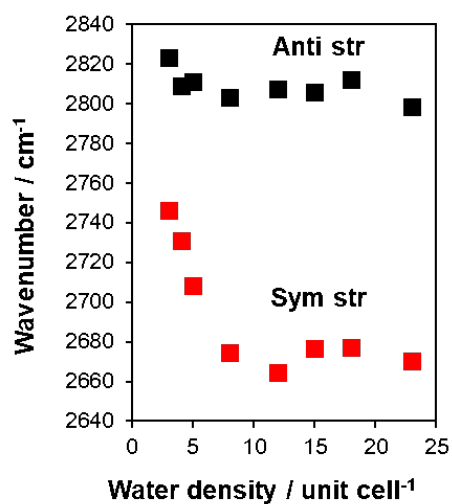
**Figure 7.17:** Calculated OD stretching peaks in Si-Beta. Spectra have been offset and normalized for clarity. Inset Xw denotes X number of water molecules per unit cell.



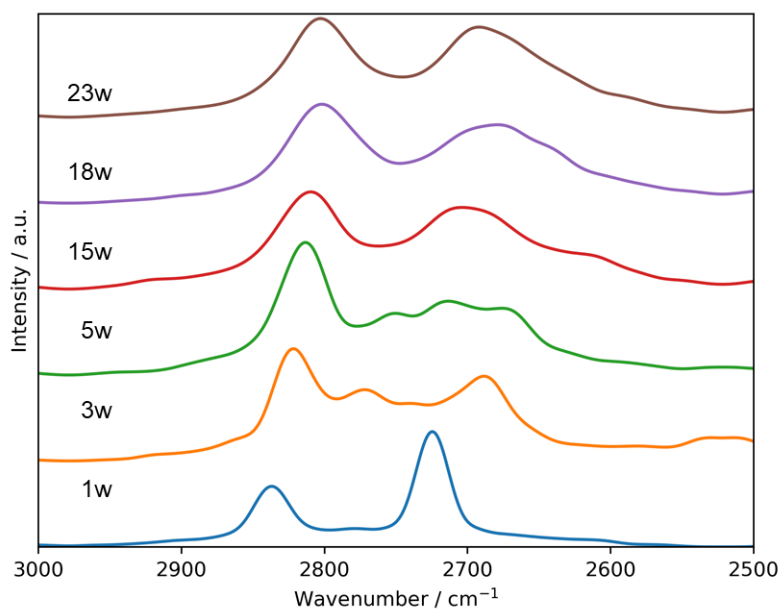
**Figure 7.18:** Calculated peak centers in Si-Beta.



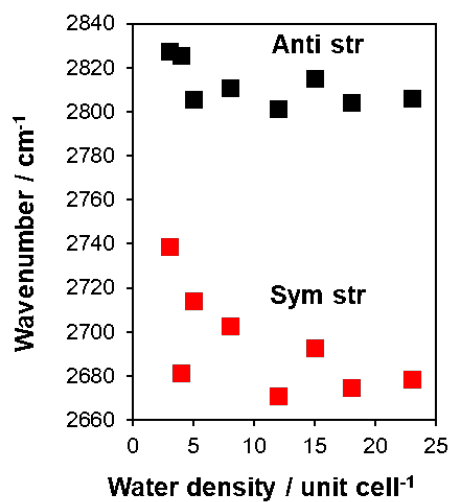
**Figure 7.19:** Calculated OD stretching peaks in Sn-Beta. Spectra have been offset and normalized for clarity. Inset Xw denotes X number of water molecules per unit cell.



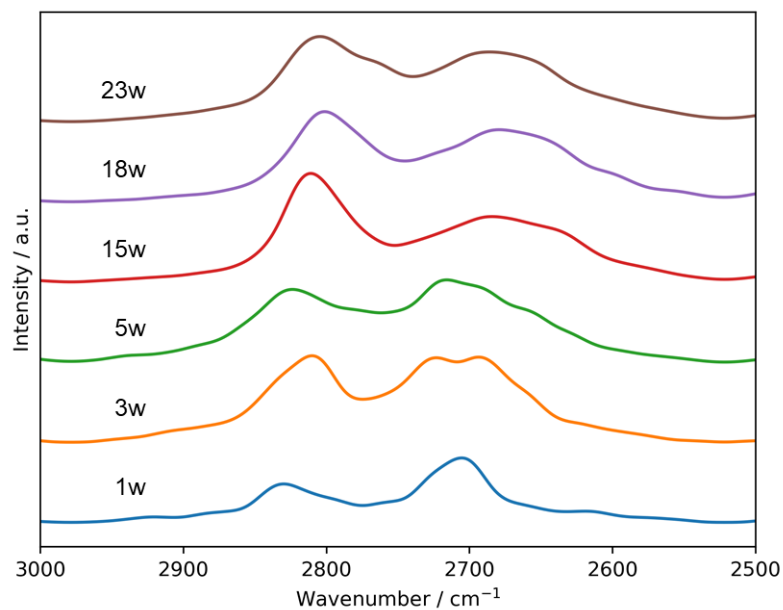
**Figure 7.20:** Calculated peak centers in Sn-Beta.



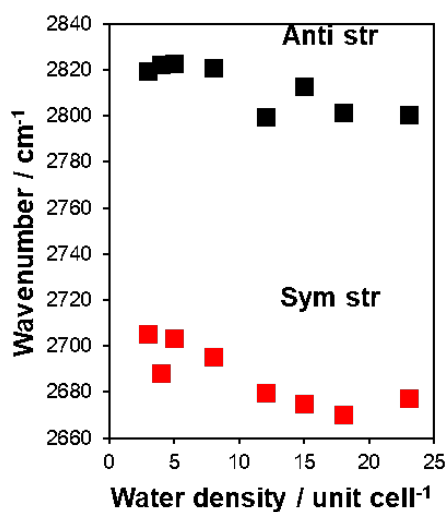
**Figure 7.21:** Calculated OD stretching peaks in SnOH-Beta. Spectra have been offset and normalized for clarity. Inset Xw denotes X number of water molecules per unit cell.



**Figure 7.22:** Calculated peak centers in SnOH-Beta.

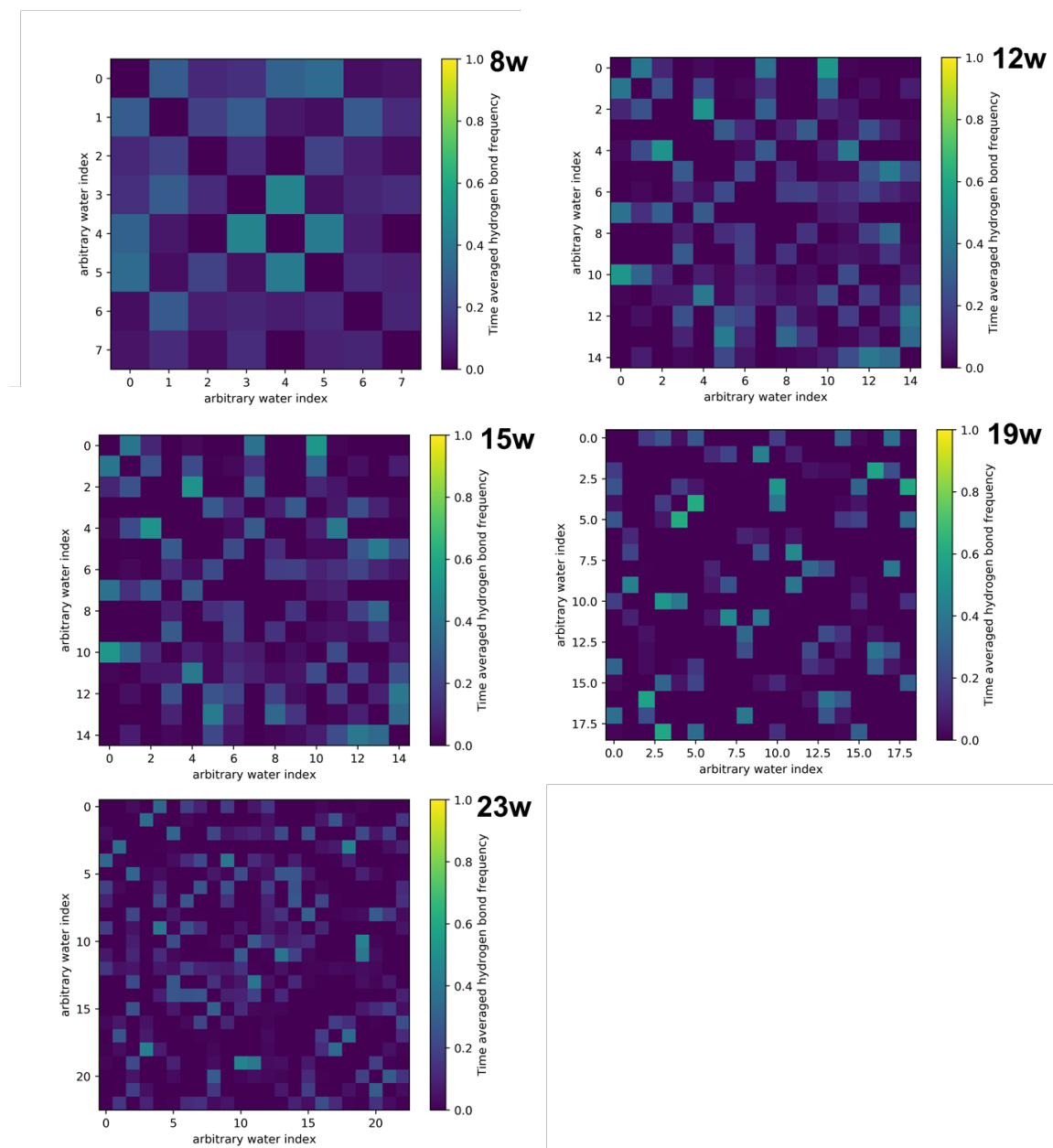


**Figure 7.23:** Calculated OD stretching peaks in  $(\text{OH})_4\text{-Beta}$ . Spectra have been offset and normalized for clarity. Inset Xw denotes X number of water molecules per unit cell.

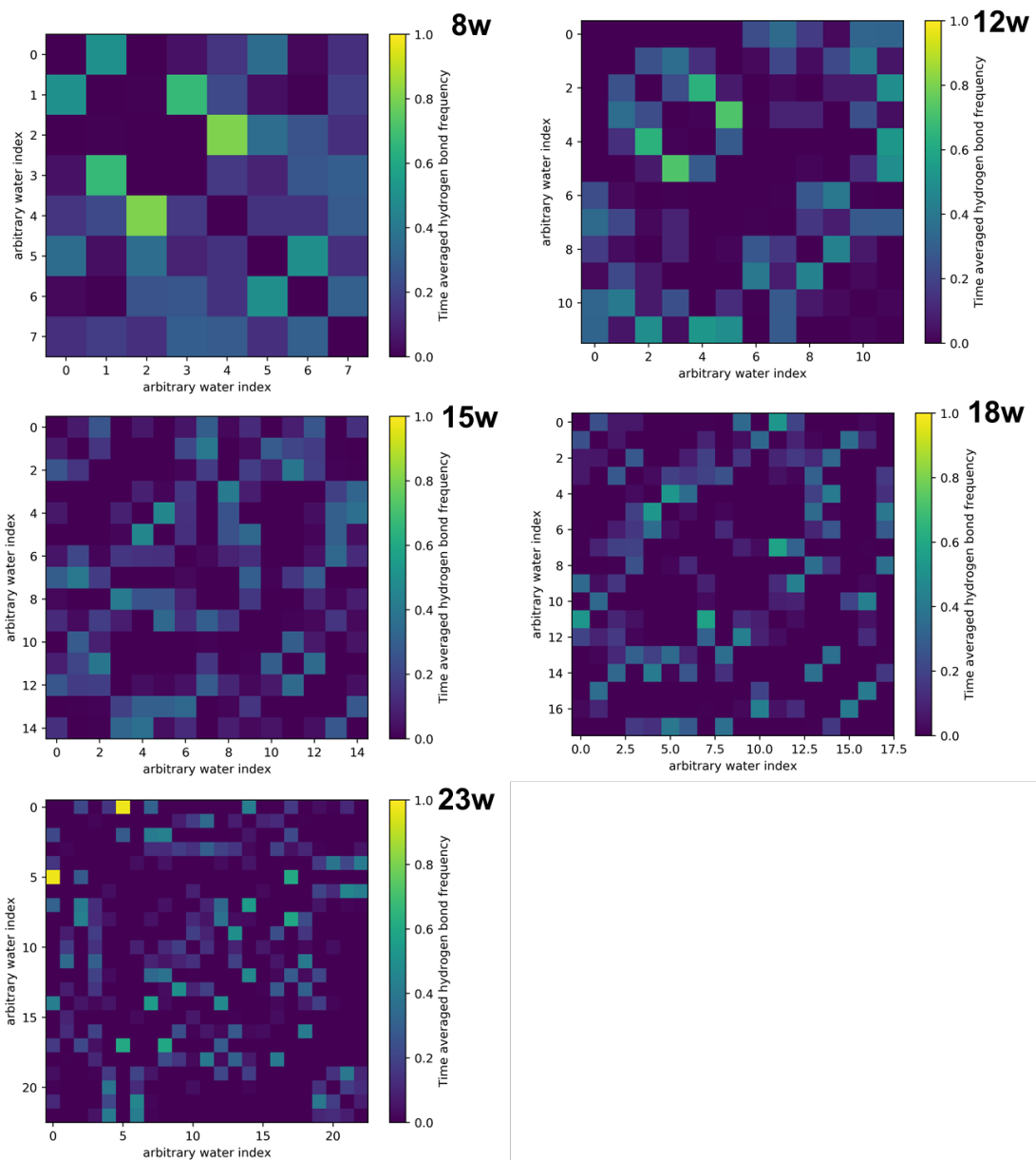


**Figure 7.24:** Calculated peak centers in  $\text{SnOH-Beta}$ .

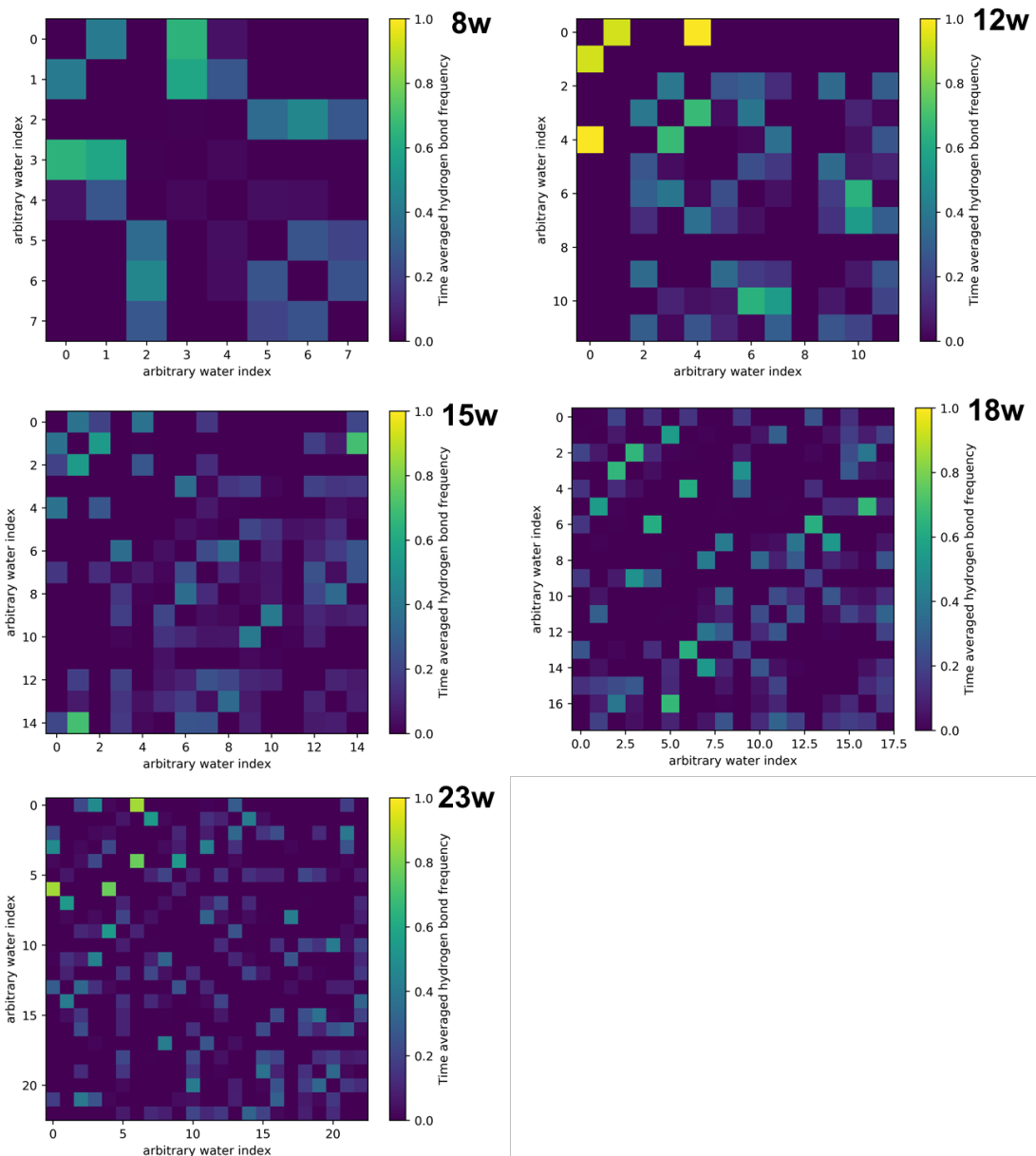
## 7.5.3.6 Hydrogen bond connectivity matrix



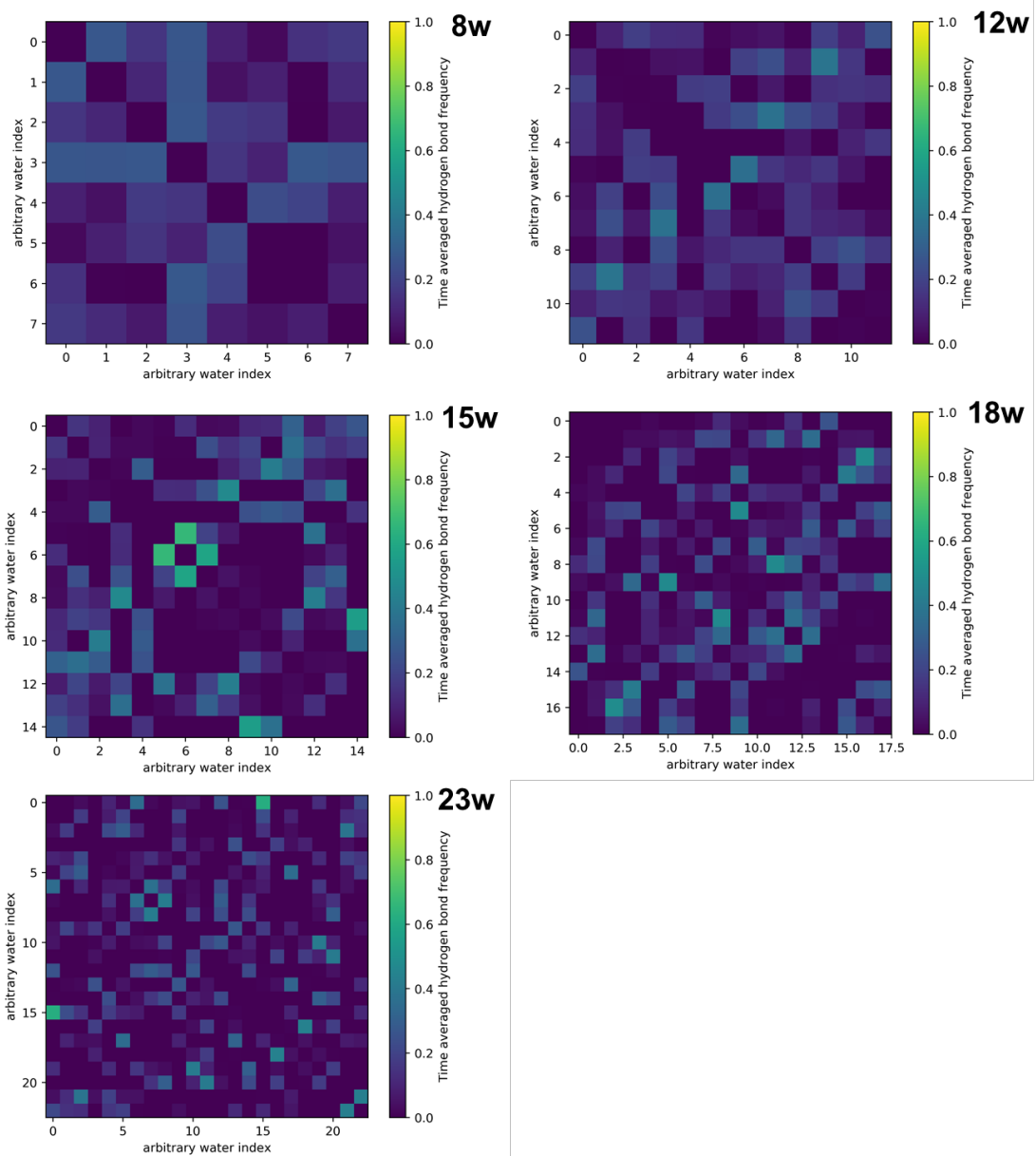
**Figure 7.25:** Hydrogen bonding graphs showing time averaged hydrogen bond frequency between water pairs in Si-Beta.



**Figure 7.26:** Hydrogen bonding graphs showing time averaged hydrogen bond frequency between water pairs in Sn-Beta.

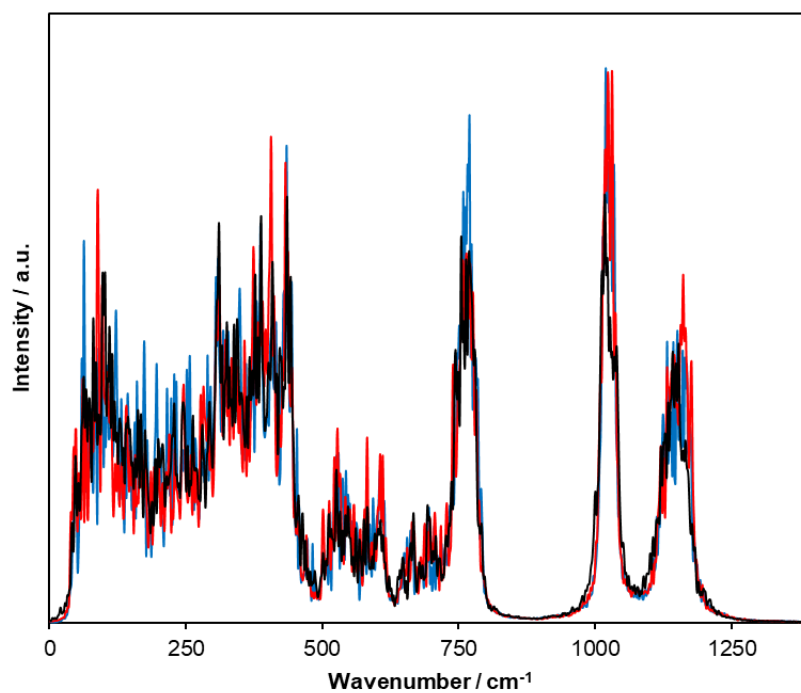


**Figure 7.27:** Hydrogen bonding graphs showing time averaged hydrogen bond frequency between water pairs in SnOH-Beta.



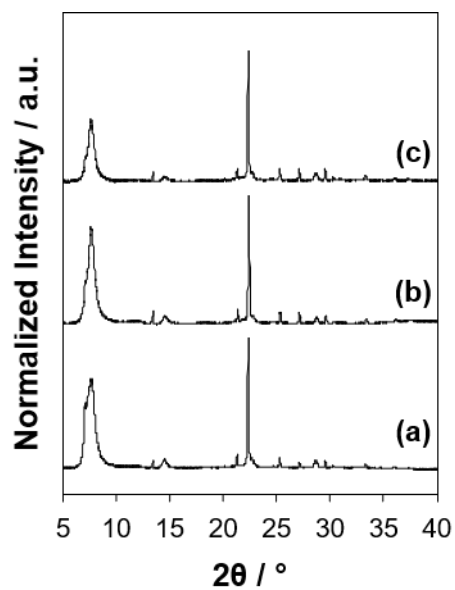
**Figure 7.28:** Hydrogen bonding graphs showing time averaged hydrogen bond frequency between water pairs in  $(\text{OH})_4\text{-Beta}$ .

## 7.5.3.7 Computational zeolite framework vibrational spectra

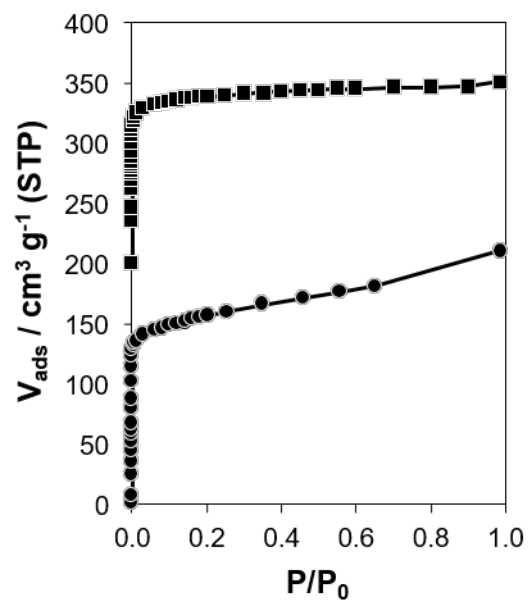


**Figure 7.29:** VDOS spectra of the Si-Beta framework at water densities of 0 (blue), 12 (red), and 45 (black) waters per unit cell.

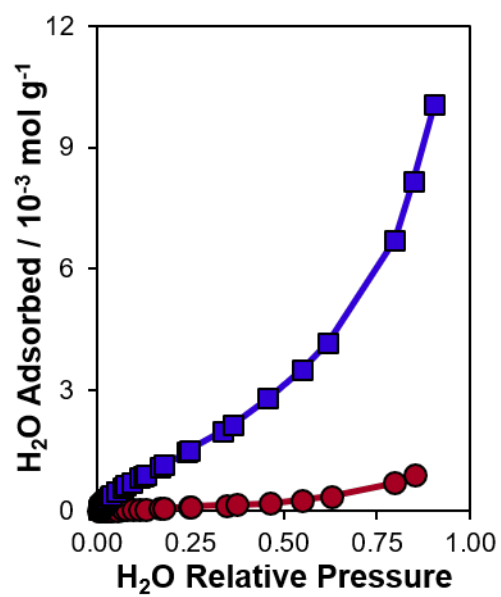
## 7.5.3.8 X-Ray diffraction patterns



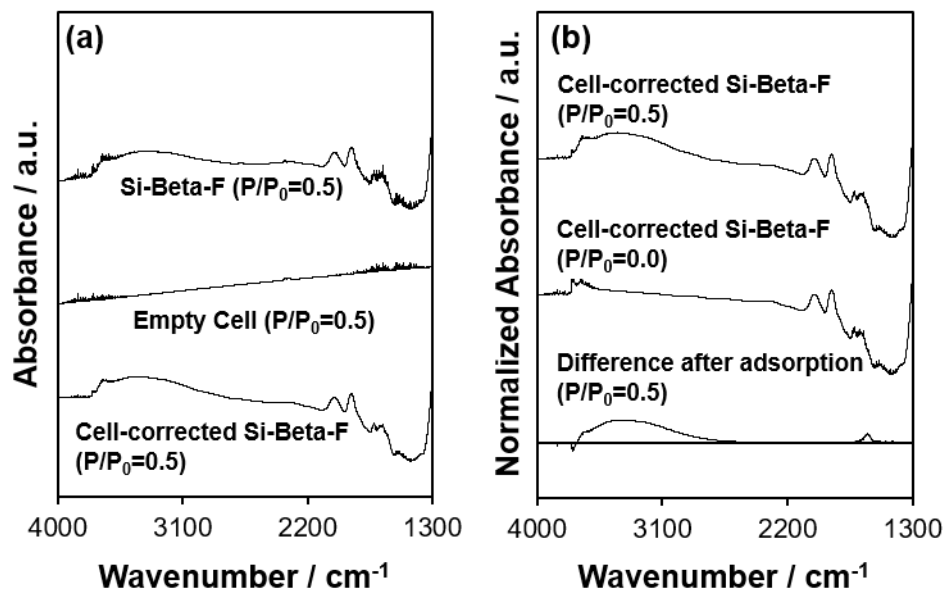
**Figure 7.30:** XRD patterns of (a) Si-Beta-F, (b) H-Al-Beta-F, and (c) Si-Beta-OH, normalized to maximum intensity.

7.5.3.9 N<sub>2</sub> and H<sub>2</sub>O adsorption isotherms

**Figure 7.31:** N<sub>2</sub> adsorption isotherms (77 K) on Si-Beta-F (●) and Si-Beta-OH (■). Isotherms are offset by 200 units for clarity.



**Figure 7.32:** H<sub>2</sub>O adsorption isotherms (293 K) on Si-Beta-F (●) and Si-Beta-OH (■).

7.5.3.10 Infrared spectra of adsorbed H<sub>2</sub>O

**Figure 7.33:** Illustration of processing of spectra under flowing H<sub>2</sub>O, using Si-Beta-F at  $P/P_0 = 0.5$  (293 K) as an example. (a) The signal from vapor-phase H<sub>2</sub>O in the empty cell is subtracted from the signal for Si-Beta-F under flowing vapor-phase H<sub>2</sub>O to yield a cell-corrected spectrum, then (b) the spectrum of the zeolite in flowing He before H<sub>2</sub>O adsorption is subtracted from this to give the difference after adsorption.

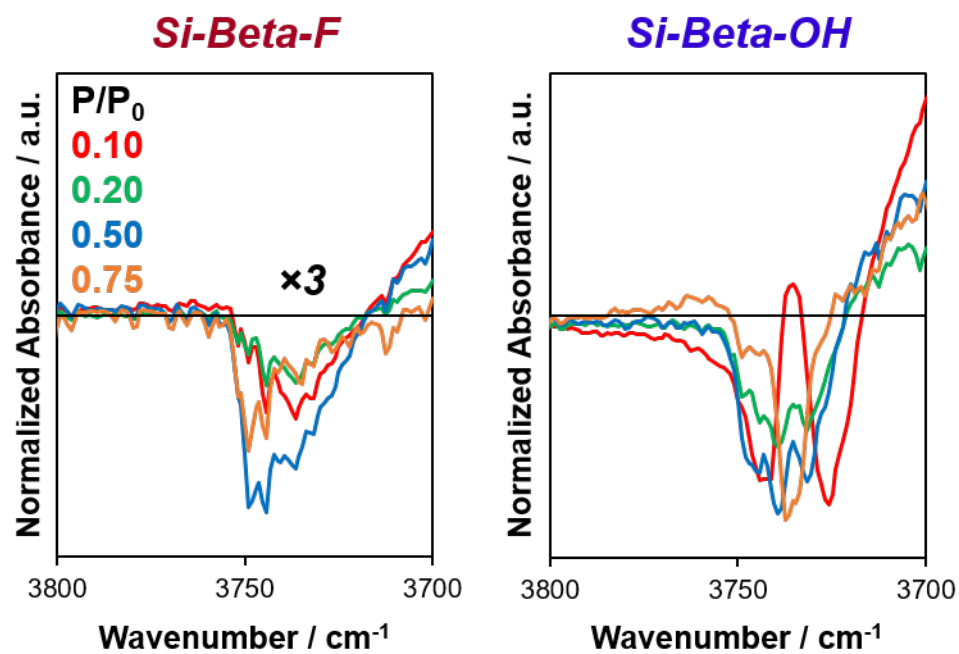


**Figure 7.34:** Differential subtracted IR spectra of H<sub>2</sub>O adsorbed at 293 K on Si-Beta-F (left) and Si-Beta-OH (right) at P/P<sub>0</sub> values of 0.1–0.75. Si-Beta-F spectra are multiplied by 3 for clarity.

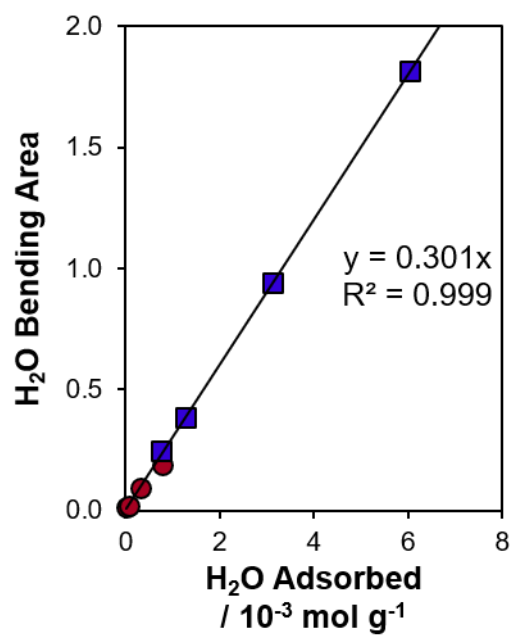


**Figure 7.35:** Correlation of  $\delta(\text{O-H})$  bending area ( $1630\text{ cm}^{-1}$ ) quantified from subtracted IR spectra in the range of  $P/P_0 = 0.1\text{--}0.75$  with the amount of adsorbed  $\text{H}_2\text{O}$  quantified at the same  $P/P_0$  value in volumetric adsorption isotherms on Si-Beta-F (●) and Si-Beta-OH (■).

## 7.5.3.11 Grand potential energy

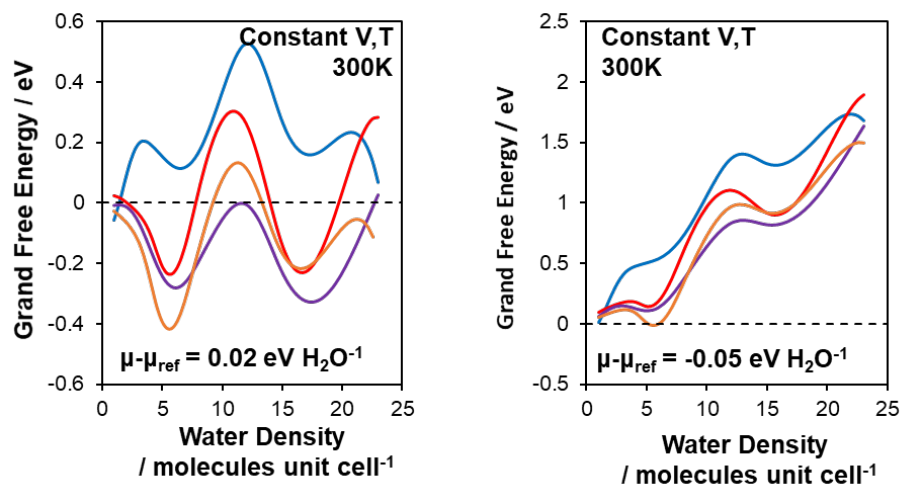


**Figure 7.36:** Grand potential energies referenced to the Helmholtz energy of water ( $\mu_{\text{ref}}$ , at  $P/P^{\circ} = 0.05$  and 300 K) for each defect. The curves shift systematically as the chemical potential is changed, with the mathematical dependence discussed in section 7.5.2.2. At any given value of the chemical potential, the value of  $N$  that minimizes the grand free energy corresponds to the thermodynamic equilibrium of the system. Blue, Si-Beta; red, Sn-Beta; purple, SnOH; orange,  $(\text{OH})_4$ -Beta.

## 7.5.3.12 Temperature and total energy fluctuations

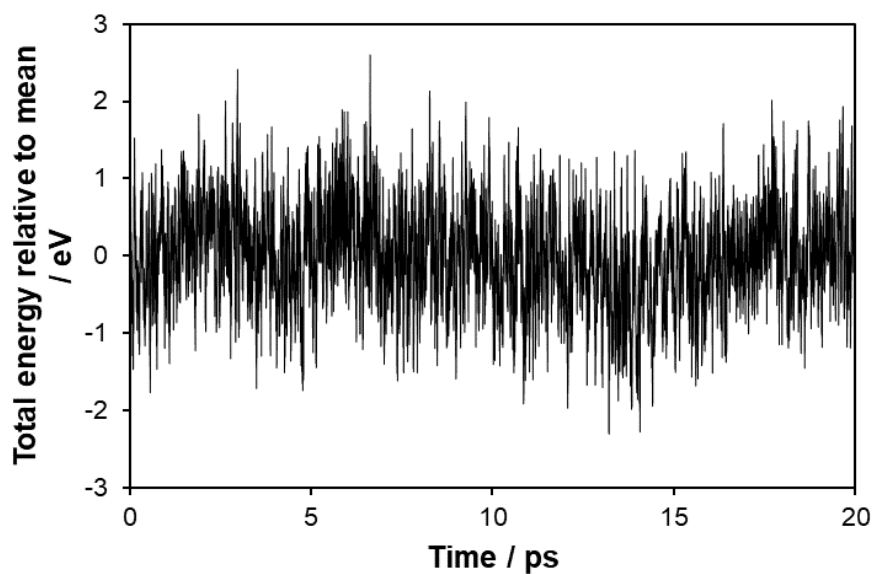


**Figure 7.37:** Fluctuations in total energy for Si-Beta at a unit cell energy of 23 H<sub>2</sub>O u.c.<sup>-1</sup>.

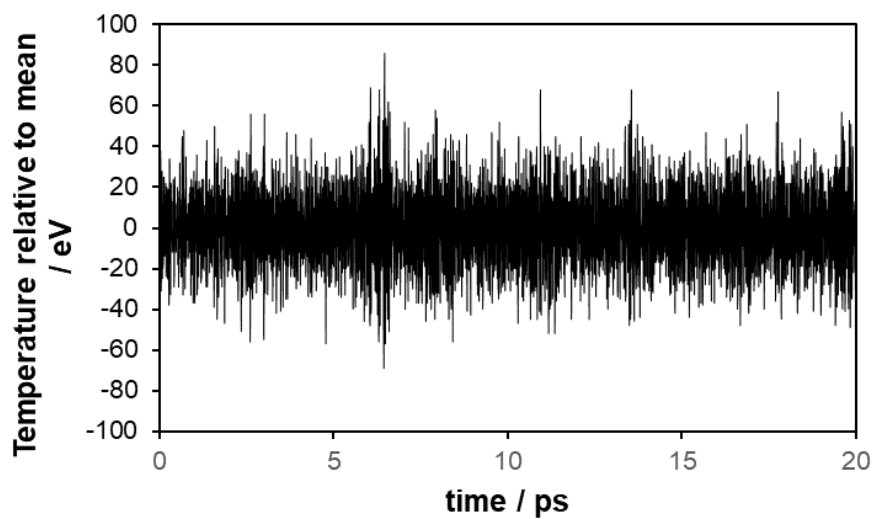


**Figure 7.38:** Fluctuations in temperature for Si-Beta at a unit cell energy of 23 H<sub>2</sub>O u.c.<sup>-1</sup>.

## 7.5.4 Supplementary Tables

**Table 7.1:** Al contents, micropore volumes, and water uptakes of zeolite Beta samples in this work.

Sample	Si/Al (Al wt%) <sup>a</sup>	$V_{\text{micro}}^{\text{b}} / \text{cm}^3 \text{g}^{-1}$	$V_{\text{ads,H}_2\text{O}}^{\text{c}} (P/P_0 = 0.2) / \text{cm}^3 \text{g}^{-1}$
Si-Beta-F	–	0.21	0.0016
H-Al-Beta-F	65 (0.7)	0.21	–
Si-Beta-OH	>1500	0.20	0.023

<sup>a</sup>Quantified by AAS<sup>b</sup>Determined by N<sub>2</sub> adsorption minimum in  $\partial V_{\text{ads}}/\partial \log(P/P_0)$ <sup>c</sup>Assuming the liquid density of H<sub>2</sub>O at 293 K**Table 7.2:** Self-diffusion coefficients calculated from the TRAVIS package at representative low and high water densities per unit cell for each defect identity.

Water density / H <sub>2</sub> O u.c. <sup>-1</sup>	Water self-diffusion constant / 10 <sup>-8</sup> m <sup>2</sup> s <sup>-1</sup>			
	Si-Beta	Sn-Beta	SnOH-Beta	(OH) <sub>4</sub> -Beta
8	1.84	0.16	0.21	0.91
23	1.08	0.47	0.32	0.61

## 8. STRUCTURE AND SOLVATION OF CONFINED WATER WITHIN MICROPOROUS BRØNSTED ACIDS AND ITS INFLUENCE ON ETHANOL DEHYDRATION KINETICS

### 8.1 Introduction

In heterogeneous catalysis, the interface between liquid or liquid-like solvating environments and active sites at solid surfaces introduces additional complexity to free energy landscapes, and its ubiquitous effects have been documented in electrocatalysis [374–378], aqueous-phase reactions on metal nanoparticles [344, 379–382], and gas-phase reactions at high-pressure conditions that cause condensation within porous solids (e.g., Fisher-Tropsch synthesis [383–385], alkene oligomerization [23, 386, 387]). In addition, the confinement of solvents within sub-nanometer spaces imposes constraints on their structure and the reactivity of moieties at active sites in their vicinity, as demonstrated by the breadth of water structures and dynamics within carbon nanotubes of different dimensions [38, 41, 388, 389], and the diverse function of enzymes with different hydrophobicity [288]. Inorganic, crystalline, microporous frameworks offer independent control of the density, chemical identity, and coordination of catalytic active sites, and the structure and polarity of the pores that confine them, which make zeolites and zeotype-molecular sieves an ideal platform to study fundamental principles underlying the catalytic behavior of confined solvents. Lewis acid zeolites containing framework  $\text{Ti}^{4+}$  or  $\text{Sn}^{4+}$  centers have been reported recently to show significant differences in reactivity for aqueous-phase olefin epoxidation [47, 48, 58, 308, 390] and sugar isomerization [53, 56, 57, 92, 151] in response to changes in active site structure and the stabilization or exclusion of extended water networks within microporous environments. The interplay between the solvated structures and reactivity of Brønsted acidic  $\text{H}^+$  sites associated with framework  $\text{Al}^{3+}$ , however, are less well-

understood because of the diversity of  $\text{H}^+$ , reactant, and transition state complexes engendered by solvating water within confining voids.

Zeolite frameworks are comprised largely of siloxane bonds that are non-polar and hydrophobic [171], but also contain hydrophilic binding sites in the form of  $\text{H}^+$  that charge-compensate framework  $\text{Al}^{3+}$  and defect Si-OH groups that both preferentially bind  $\text{H}_2\text{O}$  [171, 174, 175, 391].  $\text{H}_2\text{O}$  forms hydrogen-bonded complexes with  $\text{H}^+$  at low coverages ( $<1$   $\text{H}_2\text{O}$  per  $\text{H}^+$ ) [392], and hydronium ions ( $\text{H}_3\text{O}^+$ ) as additional  $\text{H}_2\text{O}$  molecules adsorb ( $>1$   $\text{H}_2\text{O}$  per  $\text{H}^+$ ) [393]. Vjunov et al. [71] reported IR spectra, DFT calculations, and Al K-edge XANES spectra that indicate  $\text{H}_2\text{O}$ -solvated  $\text{H}^+$  within H-Al-MFI zeolites form  $\text{H}^+(\text{H}_2\text{O})_n$  clusters analogous to gas-phase clusters, and delocalize positive charge more distant from charge-compensating framework  $[\text{AlO}_{4/2}]^-$ . The nuclearity of these clusters within a suite of H-Al-MFI samples (Si/Al = 15–110) was recently reported from vapor-phase  $\text{H}_2\text{O}$  adsorption isotherm measurements (298 K) to consist of 7–8  $\text{H}_2\text{O}$  (per  $\text{H}^+$ ), consistent with aqueous-phase cyclohexanol adsorption saturation values (298 K) that decreased with increasing  $\text{H}^+$  density as  $\text{H}^+(\text{H}_2\text{O})_n$  ( $n = 7,8$ ) clusters occupied higher fractions of void space [72]. The stoichiometry of 7–8  $\text{H}_2\text{O}$  per cluster was also corroborated by  $^1\text{H}$  and  $^1\text{H}$ - $^{29}\text{Si}$  CP MAS NMR of H-Al-MFI (Si/Al = 15, 40) samples as a function of  $\text{H}_2\text{O}$  coverage (at ambient temperature), and *ab initio* molecular dynamics (AIMD) simulations (300 K) [73]. These results highlight the distinct clustered structures of  $\text{H}_2\text{O}$  stabilized at  $\text{H}^+$  within zeolites, unlike the classical solution-phase Zundel ( $\text{H}_5\text{O}_2^+$ ) [394] and Eigen ( $\text{H}_9\text{O}_4^+$ ) [395] structures, or the  $\text{H}_{13}\text{O}_6^+$  cluster reported by Stoyanov et al. [396], and with more compressed structures and different proton-hopping dynamics from gas-phase clusters according to AIMD simulations [73]. Despite these detailed structural characterizations of  $\text{H}^+(\text{H}_2\text{O})_n$ , changes to their structure upon interacting with reactants under conditions relevant to catalysis, and the kinetic consequences of such solvated reactant and transition state complexes, are not as well-understood.

The effects of co-adsorbed solvents on gas-phase reactions catalyzed by  $\text{H}^+$  within zeolites have been studied at low solvent coverages. Haw and coworkers reported

that co-solvating nitromethane enhanced proton-transfer to  $^{13}\text{C}$ -labeled acetone detected by  $^{13}\text{C}$  NMR and increased the conversion of isopropanol [397]. These concepts can be extended to co-adsorbed  $\text{H}_2\text{O}$ , which enhances the rate of alkane C-H bond activation [398] and H-D exchange [399] in H-Al-MFI zeolites, and enables distinct  $\text{H}_3\text{O}^+$ -mediated pathways in hydrogenation of furanics [400] and aldol condensation of ketones [401]. In alcohol dehydration reactions,  $\text{H}_2\text{O}$  inhibits the rates of formation of both alkenes and ethers by unimolecular and bimolecular pathways, respectively [87].  $\text{H}_2\text{O}$  inhibition quantified by negative reaction orders is accurately described by reaction mechanisms that include inhibitory alcohol-water dimer species, as observed in alcohol dehydration catalyzed by Brønsted acidic Keggin-type polyoxometalate clusters [79] and Lewis acidic  $\gamma\text{-Al}_2\text{O}_3$  [88,181] and Sn-Beta zeolites [180,227]. Others have suggested that co-adsorbed  $\text{H}_2\text{O}$  inhibits alcohol dehydration by stabilizing adsorbed alcohols preferentially over transition states, in the case of 1-propanol dehydration on H-Al-MFI [177]. In the liquid phase, confinement of  $\text{H}_3\text{O}^+$  within H-Beta zeolite pores ( $\sim 0.7$  nm in diameter) leads to higher rates of cyclohexanol dehydration than in solution because of enhanced association of  $\text{H}_3\text{O}^+$  and reactants, and entropic destabilization of this precursor relative to the transition state [46]. Kinetic and adsorption measurements showed that increasing densities of  $\text{H}_3\text{O}^+$  resulted in lower reactant coverages at  $\text{H}_3\text{O}^+$  active sites in aqueous-phase alkylation of phenol in H-Al-MFI zeolites (523 K) [95], and *in operando* NMR measurements during glucose isomerization catalysis (403 K) on Na-FAU zeolites showed that tuning organic/aqueous solvent compositions could also change reactant coverages within the zeolite [50]. Turnover rates of homogeneously-catalyzed unimolecular dehydration reactions that reflect the stability of their elimination transition states relative to the solvated proton initial state indicate that the composition of the solvent mixture ( $\text{H}_2\text{O}$ -organic solvent) predominantly influences the free energy of the solvated proton, which is stabilized when solvated by water [44,51]. Other studies of co-solvents within zeolites have suggested based on IR spectra and catalytic isopropanol dehydration probe reactions that the protic nature of solvents (e.g., acetic acid) and co-existing cations (e.g., Na) can also

change the type, number, and strength of Brønsted acid sites in zeolites [402–404]. Bridging the gap in mechanistic understanding from that of molecular species and complexes prevalent during gas-phase studies at H<sub>2</sub>O pressures well below saturation, to those of extended solvent networks and condensed phases around active sites that are prevalent during liquid-phase studies, requires considering the clustered nature of alcohol-water intermediates and probing their interactions with active sites and solvating water confined within pores [306, 405]. In contrast to gas-phase studies, however, the scope of mechanistic investigations in heterogeneous catalysis is limited in liquid phases because aqueous solvent structures at the liquid-solid interface cannot be controlled independent of reactant or co-solvent concentrations.

Here, we use gas-phase kinetic measurements, *in situ* IR spectroscopy, and theoretical modeling in regimes approaching liquid condensation within micropores to gain insights into the structure and kinetic consequences of water networks confined within pores of different sizes and shapes. A suite of H-Al-Beta-F zeolites synthesized with a wide range of H<sup>+</sup> densities (0.11–2.0 per unit cell) confined within micropores that contain low densities of residual Si-OH defects provide a platform with well-defined active sites to quantitatively study the structures of adsorbed H<sub>2</sub>O. Turnover rates of ethanol dehydration to form diethyl ether (373 K, per H<sup>+</sup>) are measured across a wide range of H<sub>2</sub>O pressures (0.02–75 kPa) that encompass intrapore coverage regimes including alcohol-water dimers, alcohol-water-hydronium ion clusters, and liquid-like water networks that solvate them, and interpreted mechanistically to provide molecular-level insight into the various interactions of these water-reactant complexes that manifest as inhibitory effects of H<sub>2</sub>O. Rate constants (373 K, per H<sup>+</sup>) that are first-order in ethanol, which reflect surfaces covered by reactive intermediates containing one C<sub>2</sub>H<sub>5</sub>OH molecule and additional H<sub>2</sub>O molecules, are –1 order in H<sub>2</sub>O pressure because a second C<sub>2</sub>H<sub>5</sub>OH displaces H<sub>2</sub>O at H<sup>+</sup> to form the dehydration transition state, yet become more negative than –1 at higher H<sub>2</sub>O pressures (>10 kPa). The different H<sub>2</sub>O structures stabilized at H<sup>+</sup> and silanol groups within Beta zeolites are probed by volumetric adsorption isotherms, their isosteric

heats of adsorption, and *in situ* IR spectra at 293 K ( $\text{H}_2\text{O } P/P_0 = 0.1\text{--}0.75$ ) and under conditions relevant to catalysis (373 K, 10–75 kPa  $\text{H}_2\text{O}$ ), which reveal the stabilization of extended hydrogen-bonded  $\text{H}_2\text{O}$  networks by Si-OH groups, and surrounding  $(\text{H}_3\text{O}^+)(\text{H}_2\text{O})_6$  clusters and  $(\text{C}_2\text{H}_5\text{OH})(\text{H}_3\text{O}^+)(\text{H}_2\text{O})_n$  reactive intermediates. The identity of most abundant reactive intermediate species that consist of  $(\text{C}_2\text{H}_5\text{OH})(\text{H}_3\text{O}^+)(\text{H}_2\text{O})_{4-5}$  clusters at sufficiently high  $\text{H}_2\text{O}$  pressures ( $>10$  kPa) is confirmed by *ab initio* molecular dynamics simulations and *in situ* IR spectra. The kinetic relevance of transition states that require desorption of  $\text{H}_2\text{O}$  from  $\text{H}^+$ , but not additional solvating  $\text{H}_2\text{O}$ , is confirmed by a combination of static DFT calculations and metadynamics. These kinetic, spectroscopic, and theoretical insights are combined in a mechanistic framework that requires non-ideal activity coefficient formalisms to account for the different solvation of MARI species and transition states by extended  $\text{H}_2\text{O}$  networks, which lead to more severe  $\text{H}_2\text{O}$  inhibition than  $-1$  order dependences because transition states larger than MARI species disrupt their networks to greater extents. This approach is also extended to interrogate solid Brønsted acids with varying pore architectures, and highlight the role that the shapes of confining environments play in determining the structure and reorganization of solvents around reactive intermediates and transition states.

## 8.2 Results and Discussion

### 8.2.1 Kinetics of Brønsted Acid-catalyzed Ethanol Dehydration and Water Inhibition in Zeolites

Different densities of Brønsted acid  $\text{H}^+$  or Si-OH groups stabilize water networks within zeolites that are distinct in their clustered and extended hydrogen-bonded structures [71–73, 406], and have been reported to influence reactivity in different and sometimes contradictory ways, including different competitive adsorption of solvent(s) and reactants [50, 95], entropic gains when water networks are disrupted by transition states [58, 407], and entropic losses when transition states are disrupted by water networks [57]. Studying the intrapore structures of water and relating them to the

rate and equilibrium constants of a probe reaction, bimolecular ethanol dehydration to diethyl ether (DEE), requires interrogating H-zeolite samples with varying  $H^+$  and Si-OH density to disentangle their relative effects on intrapore solvent structure. Here, a suite of Brønsted acidic H-Al-Beta zeolites was synthesized in fluoride medium according to Cambor et al. [93] (denoted H-Al-Beta-F(X), where X is the number of  $H^+$  per unit cell (u.c.<sup>-1</sup>) determined by  $NH_3$  TPD, Table 8.1). The use of fluoride as the mineralizing agent enabled preparing zeolites containing a wide range of proton densities (0.1–2  $H^+$  u.c.<sup>-1</sup>) while minimizing the number of silanol defects ( $\sim 0.3$ – $0.6$  Si-OH u.c.<sup>-1</sup>, quantified by  $CD_3CN$  IR on Ti-Beta-F zeolites [57]) that otherwise form when hydroxide is used as the mineralizing agent ( $\sim 3$ – $5$  SiOH u.c.<sup>-1</sup>, quantified by  $CD_3CN$  IR on Ti-Beta-OH zeolites [57]), because anionic siloxy ( $Si-O^-$ ) defects form to balance the cationic charge of occluded tetraethylammonium cations in as-synthesized solids [35]. The H-Al-Beta-F samples in Table 8.1 therefore provide control of the density of  $H^+$  sites within otherwise hydrophobic siliceous zeolite channels, whereas an H-Al-Beta-OH sample was synthesized in hydroxide medium to contain a higher density of Si-OH defects within micropores.

Turnover rates (373 K, per  $H^+$ ) of ethanol dehydration to DEE were measured in differential reactors (details in Section 8.6.2.1, Supporting Information) on H-Al-Beta zeolites with  $H^+$  densities between 0.16–2.0 u.c.<sup>-1</sup> across a wide range of ethanol and water pressures ( $2 \times 10^{-3}$ –10 kPa  $C_2H_5OH$ , 0–75 kPa  $H_2O$ , Figure 8.1) in order to quantify the effects of co-fed  $H_2O$  pressure in terms of rate constants that reflect the stabilities of intermediates and transition states in accepted reaction mechanisms.  $H^+$  densities were quantified during ethanol dehydration catalysis by *in situ* poisoning with 2,6-di-*tert*-butylpyridine (DTBP) to enable accurate normalization of turnover rates [80, 408] (Figure 8.14–Figure 8.20, Supporting Information). In the absence of co-fed water, turnover rates increase linearly with ethanol pressure ( $< 0.01$  kPa) and approach constant values at higher ethanol pressures ( $\sim 0.05$  kPa, Figure 8.1a). This functional dependence is consistent with an associative mechanism for bimolecular ethanol dehydration to DEE [158, 218, 409, 410] depicted in Figure 8.2, in

**Table 8.1:** Elemental compositions, micropore volumes, and H<sup>+</sup> densities of H-Al-Beta-F zeolites and their dealuminated analogs.

Sample	Si/Al <sup>a</sup>	V <sub>micro</sub> <sup>b</sup> / cm <sup>3</sup> g <sup>-1</sup>	H <sup>+</sup> /Al (NH <sub>4</sub> <sup>+</sup> ) <sup>c</sup>	H <sup>+</sup> /Al (DTBP) <sup>d</sup>	H <sup>+</sup> /u.c. <sup>c</sup>	V <sub>micro</sub> <sup>b</sup> (de-Al) <sup>e</sup>
Si-Beta-F	--	0.21	--	--	0	--
H-Al-Beta-F(2.0)	23	0.22	0.75	0.54	2.0	0.22
H-Al-Beta-F(1.4)	34	0.18	0.78	--	1.4	0.21
H-Al-Beta-F(1.2)	45	0.20	0.84	0.79	1.2	0.21
H-Al-Beta-F(0.78)	65	0.21	0.79	--	0.78	0.20
H-Al-Beta-F(0.57)	93	0.23	0.84	--	0.57	0.22
H-Al-Beta-F(0.16)	220	0.20	0.54	1.1	0.16	--
H-Al-Beta-F(0.11)	500	0.20	0.84	--	0.11	--
H-Al-Beta-OH(1.7)	40	0.23	1.1	0.38	1.7	--

<sup>a</sup>Determined by AAS. <sup>b</sup>Determined by N<sub>2</sub> adsorption minimum in  $\partial V_{\text{ads}}/\partial \log(P/P_0)$ . <sup>c</sup>Determined by TPD of NH<sub>3</sub> after aqueous-phase ion exchange with 1 M NH<sub>4</sub>NO<sub>3</sub>, 24 h, 353 K. <sup>d</sup>Determined by *in situ* 2,6-di-*tert*-butylpyridine titration during ethanol dehydration catalysis (378 K, 5 kPa C<sub>2</sub>H<sub>5</sub>OH, 1 kPa H<sub>2</sub>O).

which H<sup>+</sup> sites are occupied by most abundant reactive intermediate (MARI) species consisting of hydrogen-bonded ethanol monomers (K<sub>1</sub>, Figure 8.2) and protonated ethanol-ethanol dimers (K<sub>2</sub>, Figure 8.2) that are in quasi-equilibrium with gaseous ethanol, and protonated dimers rearrange to form co-adsorbed DEE and water in the kinetically relevant step (k<sub>3</sub>, Figure 8.2) followed by product desorption in kinetically irrelevant steps to complete the catalytic cycle. The presence of protonated dimers has been inferred experimentally by the persistence of Evans windows in IR spectra of ethanol adsorbed on H-Al-MFI and H-MOR up to coverages of 2 per H<sup>+</sup> site [411], and corroborated theoretically by *ab initio* molecular dynamics simulations of vibrational densities of states consistent with measured IR spectra [127]. These mechanistic assumptions (steps 1–3, Figure 8.2) lead to a rate expression for the bimolecular dehydration turnover rate that captures the measured dependence on ethanol pressure:

$$\frac{r_{\text{DEE}}}{[H^+]} = \frac{k_3 K_2 P_{\text{C}_2\text{H}_5\text{OH}}}{1 + K_2 P_{\text{C}_2\text{H}_5\text{OH}}} \quad (8.1)$$

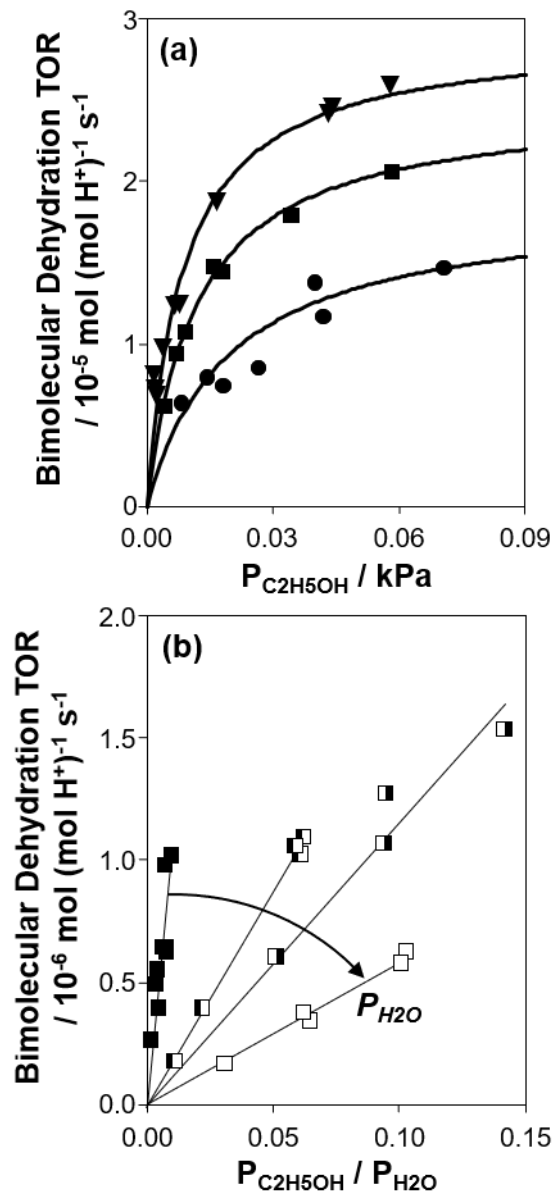


**Figure 8.1:** (a) Bimolecular ethanol dehydration turnover rate (per  $\text{H}^+$ , 373 K) as a function of  $\text{C}_2\text{H}_5\text{OH}$  pressure, without co-fed  $\text{H}_2\text{O}$ , on H-Al-Beta-F(1.2) (●), H-Al-Beta-F(2.0) (■), and H-Al-Beta-OH(1.7) (▼). Solid lines represent regression to Eq. 8.1. (b) Bimolecular ethanol dehydration turnover rate (per  $\text{H}^+$ , 373 K) on H-Al-Beta-F(2.0) as a function of the  $\text{C}_2\text{H}_5\text{OH}/\text{H}_2\text{O}$  pressure ratio, in the range 2–10 kPa  $\text{H}_2\text{O}$  (■), and at 40 kPa  $\text{H}_2\text{O}$  (◼), 50 kPa  $\text{H}_2\text{O}$  (◻), and 75 kPa  $\text{H}_2\text{O}$  (□).

where  $K_2$  is the equilibrium constant to form the protonated ethanol-ethanol dimer from the hydrogen-bonded ethanol monomer and gaseous ethanol ( $\text{kPa}^{-1}$ ),  $k_3$  is the

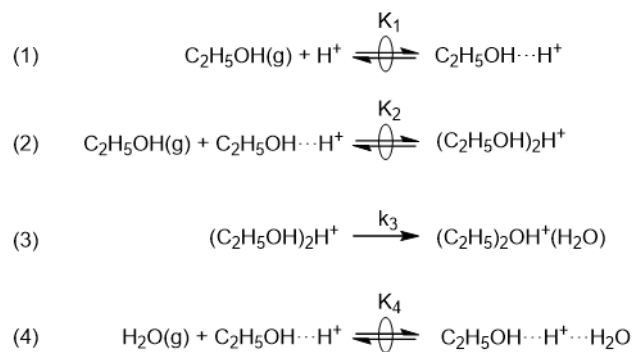


**Figure 8.2:** Series of elementary steps describing associative bimolecular ethanol dehydration at  $\text{H}^+$  sites in zeolites (steps 1–3), and the adsorption of water to form inhibitory ethanol-water dimers (step 4). Kinetically irrelevant DEE and water desorption steps are omitted for brevity.

intrinsic bimolecular dehydration rate constant ( $\text{mol}(\text{mol H}^+)^{-1} \text{s}^{-1}$ ), and  $P_{\text{C}_2\text{H}_5\text{OH}}$  is the ethanol pressure (kPa). The  $k_3$  and  $K_2$  values that result from this analysis (Table 8.3) are within a factor of  $\sim 2$  among the three H-Al-Beta samples, consistent with single-site catalysis at  $\text{H}^+$  sites accurately quantified by 2,6-di-*tert*-butylpyridine, and do not depend systematically on  $\text{H}^+$  density (Figure 8.22) indicating that measured rates are kinetically limited according to the Madon-Boudart criterion [196]. These  $k_3$  values ( $1.9\text{--}2.9 \times 10^{-5} \text{ mol}(\text{mol H}^+)^{-1} \text{ s}^{-1}$ , 373 K) are also consistent with those measured on an H-Al-MFI zeolite ( $\text{Si}/\text{Al} = 43$ ) by Chiang and Bhan [218] ( $1.7 \times 10^{-5} \text{ mol}(\text{mol H}^+)^{-1} \text{ s}^{-1}$ , 368 K), where  $\text{H}^+$  are proposed to reside in channel intersections [85, 412, 413] whose dimensions (0.64 nm diameter) are similar to those of Beta zeolite channels (0.67 nm diameter). The similar value of  $k_3$  quantified on the same commercially-sourced H-Al-MFI sample used by Chiang and Bhan ( $3.6 \times 10^{-5} \text{ mol}(\text{mol H}^+)^{-1} \text{ s}^{-1}$ , 373 K, Figure 8.23) provides additional data benchmarking our measurements. Chiang and Bhan also demonstrated that associative dehydration mechanisms prevail in MFI and MOR zeolites because DEE site-time yields (per  $\text{H}^+$ ) were independent of co-fed ethene pressure (0–2 kPa, 388–409 K), which would facilitate ethoxide-based pathways [218]. Measured kinetic data in the absence of co-fed water (Figure 8.1a) serve to benchmark experimental measurements made here to

prior literature reports [194] and validate the mechanistic assumptions used to interpret rate data, and set the stage for detailed investigations of the effects of water under conditions that approach capillary condensation and catalysis within liquid-like phases confined within microporous environments.

Bimolecular dehydration turnover rates (373 K, per  $H^+$ ) measured on H-Al-Beta-F(2.0) as a function of the ethanol/water pressure ratio (2–75 kPa  $H_2O$ ) are presented in Figure 8.1b. The inhibitory effects of water are consistent with the formation of an ethanol-water dimer species (step 4, Figure 8.2) invoked previously to account for inhibition of monomolecular 2-butanol dehydration rates by water on Brønsted acidic polyoxometalate clusters [79] (343 K, <0.5 kPa  $H_2O$ ). Including step 4 in bimolecular ethanol dehydration rate expressions, assuming quasi-equilibrated water adsorption, and including the ethanol-water dimer as a candidate MARI alongside ethanol monomer and ethanol-ethanol dimer species leads to a modified rate expression:

$$\frac{r_{DEE}}{[H^+]} = \frac{k_3 K_2 P_{C_2H_5OH}}{1 + K_2 P_{C_2H_5OH} + K_4 P_{H_2O}} \quad (8.2)$$

where  $K_4$  is the equilibrium constant to form the ethanol-water dimer from hydrogen-bonded ethanol monomer and a gaseous water molecule ( $kPa^{-1}$ ), and  $P_{H_2O}$  is the gas-phase water pressure (kPa). The functional form of Eq. 8.2 shows that an appreciable coverage of ethanol-ethanol dimers would lead to measured rates with fractional reaction orders in ethanol. The data in Figure 8.1b are restricted to kinetic regimes where rates were strictly first-order in ethanol ( $P_{C_2H_5OH}/P_{H_2O} < 0.15$ ), which require that the coverage of ethanol-ethanol dimers at  $H^+$  sites is negligible, as occurs in the limiting case where ethanol pressures are sufficiently low relative to co-fed water pressures:

$$\frac{r_{DEE}}{[H^+]} = \frac{k_3 K_2 P_{C_2H_5OH}}{1 + K_4 P_{H_2O}} \quad (8.3)$$

In the limiting case of excess water pressures, ethanol-water dimers are the sole MARI and rates depend linearly on the ethanol-to-water pressure ratio:

$$\frac{r_{\text{DEE}}}{[H^+]} = \frac{k_3 K_2}{K_4} \frac{P_{C_2H_5OH}}{P_{H_2O}} \quad (8.4)$$

Eq. 8.4 predicts the inhibitory effects of water at moderate pressures (2–10 kPa, filled data points in Figure 8.1b), which reflects the energetic penalty to displace water (reverse of Step 4, Figure 8.2) with ethanol (Step 2, Figure 8.2) at Brønsted acid sites en route to the bimolecular dehydration transition state (Step 3, Figure 8.2). The bimolecular dehydration turnover rate (373 K, per  $H^+$ ) is a single-valued function of ethanol/water pressure ratio in the range of 2–10 kPa of water (solid data points in Figure 8.1b,  $P_{C_2H_5OH}/P_{H_2O} = 0.002\text{--}0.01$ ), consistent with full coverage of  $H^+$  sites by ethanol-water dimer species. The conditions that lead to these prevalent surface intermediates (373 K,  $P_{C_2H_5OH}/P_{H_2O} = 0.002\text{--}0.01$ ) contrast those studied previously by Zhi et al. [177] for 1-propanol dehydration on H-Al-MFI (423 K), where no dependence on co-fed water pressure (0.53 and 2.5 kPa) was observed, likely because the higher 1-propanol pressures studied (0.075–4 kPa) led to surfaces partially covered by propanol-propanol dimers ( $P_{C_3H_7OH}/P_{H_2O} > 0.03$ ) that attenuated the effects of water inhibition (see Section 8.6.2.2 for additional discussion).

When the water pressure is increased above 10 kPa (partially filled and unfilled data points in Figure 8.1b), measured rates deviate from the single-valued function observed between 2–10 kPa and described by Eq. 8.4, but remain first-order in ethanol pressure, according to the empirical relationship:

$$\frac{r_{\text{DEE}}}{[H^+]} = k_{\text{first}} P_{C_2H_5OH} \quad (8.5)$$

where  $k_{\text{first}}$  is the apparent first-order rate constant in ethanol pressure (mol (mol  $H^+$ )<sup>-1</sup> (kPa  $C_2H_5OH$ )<sup>-1</sup> s<sup>-1</sup>). The value of  $k_{\text{first}}$  in the form of Eq. 8.5 also contains an unknown functional dependence on water pressure that is not described by Eq. 8.4, however, because turnover rates decrease systematically with water pressure in higher

pressure regimes ( $>10$  kPa  $\text{H}_2\text{O}$ , Figure 8.1b) at the same ethanol-to-water pressure ratio, indicating that water inhibits turnover rates more strongly than the inverse order predicted by kinetic models where active sites are saturated with ethanol-water dimers (Eq. 8.4). The value of  $k_{first}$  was quantified as a function of water pressure (0.02–75 kPa, see Figure 8.24, Supporting Information for rate data) to include regimes corresponding to partial and full coverage by ethanol-water dimers ( $\sim 0.02$ – $10$  kPa, described by Eq. 8.3) and the departure from the behavior described by Eq. 8.4 (10–75 kPa), as shown in Figure 8.3a. Combining Eqs. 8.3 and 8.5 gives an expression for the apparent first-order rate constant as a function of water pressure in regimes that include ethanol monomers and ethanol-water dimers as MARI species:

$$\frac{r_{\text{DEE}}}{[H^+] P_{\text{C}_2\text{H}_5\text{OH}}} = \frac{k_3 K_2}{1 + K_4 P_{\text{H}_2\text{O}}} = k_{\text{first}} \quad (8.6)$$

The solid lines in Figure 8.3a represent regression of  $k_{first}$  values ( $\sim 0.02$ – $10$  kPa  $\text{H}_2\text{O}$ ) to the functional form of Eq. 8.6, and give values for the lumped rate and equilibrium constant groups  $k_3 K_2$  and  $k_3 K_2 K_4^{-1}$  in the low and high water pressure limits, respectively (Table 8.4, Supporting Information). The value of  $k_3 K_2$  reflects the free energy of the confined bimolecular dehydration transition state relative to the free energy of the confined ethanol monomer and gas-phase ethanol, and  $k_3 K_2 K_4^{-1}$  reflects that of the confined transition state and gas-phase water relative to the confined ethanol-water dimer and gas-phase ethanol (derivation in Section 8.6.2.5, Supporting Information). Values of  $k_3 K_2$  quantified with co-fed water are systematically 2–4 $\times$  lower than those quantified in the absence of co-fed water (Table 8.3, Supporting Information). This difference corresponds to apparent activation free energies at 404 K that are 2–4 kJ mol $^{-1}$  higher with co-fed water, which qualitatively seems reasonable because physisorbed water can preferentially stabilize adsorbed alcohol intermediates over dehydration transition states, as suggested by Zhi et al. for experimentally measured 1-propanol dehydration activation enthalpies and entropies with and without co-fed  $\text{H}_2\text{O}$  (413–443 K, 0–2.5 kPa  $\text{H}_2\text{O}$ ) [177]. Additional variations in values of

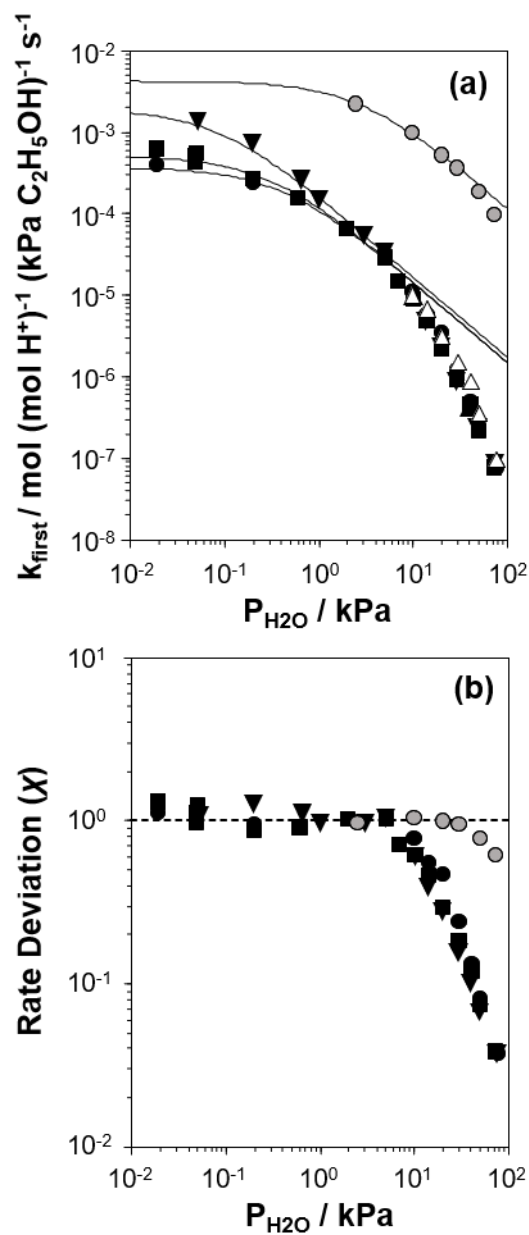


**Figure 8.3:** (a) Apparent first-order bimolecular ethanol dehydration rate constant (per  $\text{H}^+$ , 373 K) and (b) rate deviation ( $\chi$ ) from the functional dependence of Eq. 8.7, as a function of  $\text{H}_2\text{O}$  pressure on H-Al-Beta-F(0.16) ( $\Delta$ ), H-Al-Beta-F(1.2) ( $\bullet$ ,  $\circ$  at 423 K), H-Al-Beta-F(2.0) ( $\blacksquare$ ), and H-Al-Beta-OH(1.7) ( $\blacktriangledown$ ). Solid lines reflect regression to the functional form of Eq. 8.7.

$k_3K_2$  among the samples may also result from different proximity of Si-OH groups to  $H^+$  active sites, which have been reported to stabilize adsorbed water and alcohol intermediates and dehydration transition states to different extents in Lewis acid-catalyzed ethanol dehydration [180, 227]. Values of  $k_3K_2K_4^{-1}$  are essentially identical among the three H-Al-Beta samples ( $1.5\text{--}1.7 \times 10^{-4} \text{ mol (mol } H^+)^{-1} \text{ s}^{-1}$ , Table 8.4, Supporting Information), indicating that once  $H^+$  are saturated with ethanol-water dimer intermediates, the free energy difference required to replace adsorbed water with adsorbed ethanol at the transition state is insensitive to differences in Si-OH density or other sample heterogeneities.

The deviation of  $k_{first}$  values from those predicted by Eq. 8.6 at water pressures above  $\sim 10$  kPa (Figure 8.3a) was quantified as a function of water pressure up to 75 kPa. At 373 K, this range of water pressures corresponds to conditions where liquid-like water begins to condense within zeolite pores (see Section 8.2.2 below). This deviation can be expressed as a function of water pressure by combining Eq. 8.5 and Eq. 8.6:

$$\chi = k_{first} \left[ \frac{k_3K_2}{1 + K_4P_{H_2O}} \right]^{-1} \quad (8.7)$$

where values of  $k_3K_2$  and  $K_4$  are those estimated from rate data measured below 10 kPa  $H_2O$  corresponding to conditions in which Eq. 8.3 holds. By definition, values of  $\chi$  are unity in regimes where rate expressions involving ethanol monomers and ethanol-water dimers are MARI species ( $\sim 0.02\text{--}10$  kPa  $H_2O$ , Eq. 8.6). The value of  $\chi$  (Figure 8.3b) deviates sharply from values of unity at high water pressures ( $>10$  kPa) and systematically decreases with increasing water pressure to reach values  $<0.1$  at and above 50 kPa water; that is, measured turnover rates are more than one order of magnitude lower than predicted by Eq. 8.6 under these conditions. Prior to mechanistic interpretation of this phenomenon, the possibility that values of  $\chi$  below unity reflect the onset of intracrystalline mass transport limitations or a decrease in the number of active sites must be ruled out. Measured  $k_{first}$  values are insensitive to the density of  $H^+$  sites within Beta zeolites at high water pressures ( $0.2\text{--}2.0 H^+ \text{ u.c.}^{-1}$ , Figure 8.28, Supporting Information), consistent with kinetically

limited reaction rates according to the Madon-Boudart criterion [196], and the Mears criterion [203] also estimates that ethanol diffusion rates are orders of magnitude faster than measured reaction rates (Section 8.6.2.3, Supporting Information). The number of catalytically active protons also does not decrease with increasing water pressure, confirmed by quantifying the  $\text{H}^+$  density at 30 kPa of  $\text{H}_2\text{O}$  by *in situ* 2,6-di-tert-butylpyridine titration ( $0.66 \text{ H}^+/\text{Al}$ , Figure 8.15, Supporting Information) on H-Al-Beta-F(2.0), which was similar to that quantified at 1 kPa of  $\text{H}_2\text{O}$  ( $0.54 \text{ H}^+/\text{Al}$ , Table 8.1). Thus, the dependence of  $\chi$  on  $\text{H}_2\text{O}$  pressure is mechanistic in origin and may reflect differences in the MARI species, kinetically relevant steps, the identity of the active sites, or solvation of adsorbed intermediates and transition states.

Values of  $k_{first}$  at 423 K on H-Al-Beta-F(2.0) (Figure 8.3, ●) are accurately described by Eq. 8.6 between 2.5–30 kPa  $\text{H}_2\text{O}$  and are  $-1$  order in  $\text{H}_2\text{O}$  above 20 kPa  $\text{H}_2\text{O}$  (Eq. 8.4), in contrast to  $k_{first}$  values measured at 373 K that are  $-1$  order in  $\text{H}_2\text{O}$  above 2 kPa  $\text{H}_2\text{O}$ . The delayed onset of the inverse water order dependence to higher water pressures at 423 K is consistent with lower coverages of inhibitory ethanol-water dimer intermediates at higher temperature, and is reflected by a lower  $K_4$  value at 423 K (0.35, Table 8.5) than at 373 K (2.5, Table 8.5). In addition,  $\chi$  values quantified at 423 K deviate from unity only above 30 kPa of  $\text{H}_2\text{O}$ , whereas  $\chi$  values deviate from unity above 10 kPa  $\text{H}_2\text{O}$  at 373 K. The shift in the onset of sub-unity deviations in  $\chi$  values to higher  $\text{H}_2\text{O}$  pressures at higher temperatures is consistent with shifts in the same direction of the onset of the kinetic regime that is  $-1$  order in water in which the surface is saturated by ethanol-water dimers. By analogy, it is hypothesized that the dependence of  $\chi$  on water pressure is related to increasing coverages of water within micropores, which can be probed further using characterizations of the coverage and structure of intrapore  $\text{H}_2\text{O}$  under conditions relevant to catalysis.

## 8.2.2 Characterization of Intracrystalline Water Structures

The coverages and structures of  $\text{H}_2\text{O}$  prevalent during ethanol dehydration catalysis at 373 K were assessed using a combination of volumetric adsorption isotherms and

*in situ* infrared spectroscopy. The individual contributions of polar hydroxyl groups associated with both Brønsted acid sites ( $\text{H}^+$ ) and silanol nests were systematically varied using the suite of H-Al-Beta-F samples that contain varying densities of  $\text{H}^+$  u.c.<sup>-1</sup> (0.11–2.0, Table 8.1) and minimal densities of intracrystalline Si-OH defects (0.3–0.6 Si-OH u.c.<sup>-1</sup>, quantified by  $\text{CD}_3\text{CN}$  IR on Ti-Beta-F zeolites [57]) because they were prepared in fluoride media [93]. Complete dealumination in  $\text{HNO}_3$  (70%, 353 K) yielded deAl-Beta-F samples (residual Al u.c.<sup>-1</sup> < 0.04, below detection limit of AAS) that contained silanol nest densities approximately equal to the number of  $\text{H}^+$  u.c.<sup>-1</sup> before dealumination, as quantified by the integrated area for  $\nu(\text{OH})$  peaks of silanol nests in IR spectra (Figure 8.44, Supporting Information), without disruption to their crystalline structure according to similar micropore volume measurements (Table 8.1) and XRD patterns (Figure 8.11, Supporting Information). The non-zero intercept of the correlation of silanol nest  $\nu(\text{OH})$  peak area with silanol nests per unit cell (Figure 8.44, Supporting Information) indicates that a low density of Si-OH defects is unavoidable during fluoride-mediated crystallization of Beta zeolites, which should be taken into account when developing correlations between adsorbed quantities and the silanol nests generated by dealumination. Measured volumetric water adsorption isotherms (293 K, Figure 8.4a) indicate that the adsorbed amount of water systematically increases with the density of hydrophilic groups ( $\text{H}^+$ , silanol), consistent with prior reports [72, 173]. The adsorption isotherm on Si-Beta-F (symbol) is classified as Type III [199] and indicates weak adsorbate-adsorbent interactions where adsorption occurs by dispersive interactions of  $\text{H}_2\text{O}$  with non-polar siloxane bonds within micropores, and at Si-OH defects. The isotherm on Si-Beta-F was subtracted from those of H-Al-Beta-F and deAl-Beta-F to obtain isotherms that predominantly reflect  $\text{H}_2\text{O}$  adsorption at their defects ( $\text{H}^+$ , silanol nest), then these isotherms were normalized by the densities of  $\text{H}^+$  or silanol nests to interrogate whether adsorption at individual functional groups is influenced by their density within crystallites.

$\text{H}^+$ -normalized  $\text{H}_2\text{O}$  adsorption isotherms (Figure 8.4b, bottom) are invariant across the full range of  $\text{H}^+$  densities (0.11–2.0 u.c.<sup>-1</sup>) in H-Al-Beta-F zeolites at low rel-

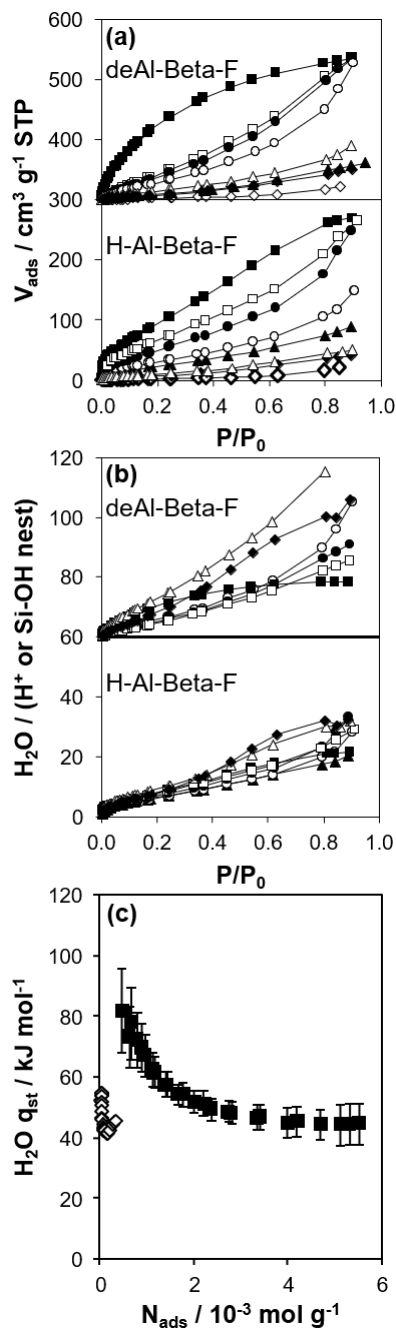


**Figure 8.4:** (a) Volumetric  $\text{H}_2\text{O}$  adsorption isotherms (293 K) on H-Al-Beta-F samples and their dealuminated analogs, with  $\text{H}^+$  (or Si-OH nest) u.c. $^{-1}$  = 0.11 ( $\blacklozenge$ ), 0.16 ( $\triangle$ ), 0.57 ( $\blacktriangle$ ), 0.78 ( $\circ$ ), 1.2 ( $\bullet$ ), 1.4 ( $\square$ ), 2.0 ( $\blacksquare$ ), and Si-Beta-F ( $\diamond$ ); and (b) after subtraction of Si-Beta-F isotherm and normalizing by  $\text{H}^+$  (or Si-OH nest). (c) Isosteric heat of adsorption of  $\text{H}_2\text{O}$  as a function of coverage on Si-Beta-F ( $\diamond$ ) and deAl-Beta-F(2.0) ( $\blacksquare$ ), determined in the range 283–302 K. deAl-Beta-F isotherms are offset for clarity by 300 units in (a) and 60 units in (b).

ative pressures ( $P/P_0 < \sim 0.2$ , 293 K), indicating that adsorption occurs preferentially at  $H^+$  sites and generates  $(H_3O^+)(H_2O)_n$  clusters of increasing size with increasing  $H_2O$  pressure, consistent with similar observations on H-Al-MFI zeolites [72, 73].  $H^+$ -normalized isotherms deviate among samples at higher relative pressures ( $P/P_0 > 0.2$ ), implying that  $(H_3O^+)(H_2O)_n$  clusters have reached their maximum size and  $H_2O$  instead adsorbs within void spaces that are not occupied by  $(H_3O^+)(H_2O)_n$  clusters, and at intracrystalline and extracrystalline Si-OH groups [73] that may be present in different amounts among samples. The saturation of  $(H_3O^+)(H_2O)_n$  clusters at  $P/P_0 \sim 0.2$  is also consistent with  $H_2O$  adsorption isotherms that are identical above  $P/P_0 = 0.2$  on H-Al-Beta-F(0.57) and Na-Al-Beta-F(0.57), but offset by the difference in size of clusters stabilized by the different cations (Figure 8.40). At a  $P/P_0$  value of 0.2, the average value of  $H_2O/H^+$  is  $7 \pm 1$  on H-Al-Beta-F samples with  $H^+$  u.c.<sup>-1</sup> varying from 0.11–2.0 (Table 8.6, Supporting Information). Clusters containing 7  $H_2O$  molecules have also been reported on H-Al-MFI zeolites by a similar volumetric isotherm approach [72], and by a combination of  $^1H$  and  $^1H$ - $^{29}Si$  CP MAS NMR that show that  $H_2O$  adsorbs at Si-OH rather than at  $H^+$  after  $\sim 7 H_2O/H^+$  [73]. These  $(H_3O^+)(H_2O)_6$  clusters are reported to be distinct in structure from those reported in the aqueous phase (i.e., Zundel ( $H_5O_2^+$ ) [394] and Eigen ( $H_9O_4^+$ ) [395] structures, or the  $H_{13}O_6^+$  cluster reported by Stoyanov et al. [396]) because of the spatial constraints imposed by the confining environment [72, 73]; however, the influence of different zeolite topologies is unclear.  $(H_3O^+)(H_2O)_6$  clusters of the same nuclearity in MFI and Beta zeolites are consistent with the similar size of Beta channels (0.67 nm) and MFI pore intersections (0.64 nm). Similar approaches using samples with systematically varying  $H^+$  density and minimal Si-OH defects would be required to probe whether clusters of different nuclearity are stabilized within different zeolite topologies.

$H_2O$  adsorption isotherms (293 K) normalized to the number of silanol nests in deAl-Beta-F samples (Figure 8.4b, top) show wider variation among samples than observed on H-Al-Beta-F samples, but adsorption behavior is consistent with prefer-

ential adsorption at silanol nests at low partial pressures ( $P/P_0 < \sim 0.1$ ) followed by formation of extended hydrogen-bonded water networks [57,406]. This adsorption behavior contrasts the more tightly bound  $(\text{H}_3\text{O}^+)(\text{H}_2\text{O})_n$  clusters localized at  $\text{H}^+$  sites that form initially in H-Al-Beta-F samples. The proportionality of water uptakes with silanol nest density indicates that the formation of extended hydrogen-bonded networks throughout the crystallite is limited by the density of Si-OH nest defects, in which micropore regions devoid of nest defects that are found in samples with lower defect densities (0.11–0.57 u.c.<sup>-1</sup>) behave as essentially hydrophobic, while higher silanol nest densities (0.78–2.0 u.c.<sup>-1</sup>) lead to hydrogen-bonded water networks that extend throughout crystallites, as indicated by similar water uptakes (per g) at high water pressures ( $P/P_0 = 0.9$ ). These data are consistent with simulations [37,178,414] and experiments [43] that indicate that the density and spatial distribution of hydrophilic binding sites on hydrophobic surfaces influence the structure and dynamics of water.

The preferential adsorption of  $\text{H}_2\text{O}$  at  $\text{H}^+$  and Si-OH nest defects was corroborated by obtaining isosteric heats of adsorption ( $q_{\text{st}}$ ) as a function of coverage from adsorption isotherms collected at different temperatures (283–302 K, Figure 8.4c and Figure 8.42–Figure 8.43, Supporting Information):

$$q_{\text{st}} = -R \left( \frac{\partial \ln P}{\partial \left( \frac{1}{T} \right)} \right)_{N_{\text{H}_2\text{O}}} \quad (8.8)$$

where  $q_{\text{st}}$  is calculated from a plot of  $-\text{Rln}(P)$  vs.  $1/T$  ( $\text{K}^{-1}$ ) where the  $P$  values (kPa) are obtained from adsorption isotherms at a given constant value of  $\text{H}_2\text{O}$  coverage ( $\text{mol g}^{-1}$ ). The calculation of  $q_{\text{st}}$  relies on the assumptions of reversible adsorption, an ideal gas phase, and negligible molar volume of the adsorbed phase relative to the gas phase [415,416]. The latter two assumptions are typically satisfied at low pressure and low coverage, but caution should be taken when interpreting high-coverage values [416]. On Si-Beta-F (Figure 8.4c,  $\diamond$ ), the isosteric heat of adsorption is initially 50–55  $\text{kJ mol}^{-1}$  (0.005–0.02  $\text{mmol g}^{-1}$ ), then rapidly decreases with increasing amounts of adsorbed water, becoming constant ( $\sim 45 \text{ kJ mol}^{-1}$ ) above  $\sim 0.2 \text{ mmol g}^{-1}$ . The

initial heat of adsorption of H<sub>2</sub>O measured calorimetrically at Si-OH defects present in low densities on an amorphous SiO<sub>2</sub> surface treated to 1073 K was a similar value (54 kJ mol<sup>-1</sup>, ~0.04 mmol g<sup>-1</sup>) [176], indicating that the initial q<sub>st</sub> on Si-Beta-F is consistent with preferential adsorption of H<sub>2</sub>O at a minority of Si-OH defect sites within micropores (0.03–0.2 mmol g<sup>-1</sup>, quantified by CD<sub>3</sub>CN IR on Ti-Beta-F zeolites [57]). Adsorption at higher coverages (>0.2 mmol g<sup>-1</sup>) occurs at extracrystalline locations at higher relative pressures (P/P<sub>0</sub>>0.6, 293 K) [56] with a q<sub>st</sub> of ~45 kJ mol<sup>-1</sup>, consistent with q<sub>st</sub> values (44 kJ mol<sup>-1</sup>) on a hydrophobic Si-MFI-F zeolite at similar coverages (0.1–0.2 mmol g<sup>-1</sup>) [417].

In contrast to Si-Beta, the q<sub>st</sub> for water on de-Al-Beta-F(2.0) (Figure 8.4c, ■) is 82 ± 14 kJ mol<sup>-1</sup> at low coverage (0.5 mmol g<sup>-1</sup> = ~1 H<sub>2</sub>O per Si-OH nest), in agreement with calorimetrically measured heats of adsorption of H<sub>2</sub>O at Si-OH groups on amorphous SiO<sub>2</sub> activated at 423 K (80 kJ mol<sup>-1</sup>) [418] and 473 K (73 kJ mol<sup>-1</sup>) [176], which indicates that H<sub>2</sub>O adsorption occurs preferentially at Si-OH nests in deAl-Beta-F zeolites. The value of q<sub>st</sub> decreases to 45 kJ mol<sup>-1</sup> above a coverage of ~3 mmol g<sup>-1</sup> (~6 H<sub>2</sub>O per Si-OH nest), after which adsorption likely occurs by adsorbate-adsorbate interactions energetically similar to those of liquid H<sub>2</sub>O (ΔH<sub>cond</sub> = 41 kJ mol<sup>-1</sup>), and similar to the value measured calorimetrically on H-Al-MFI zeolites after (H<sub>3</sub>O)<sup>+</sup>(H<sub>2</sub>O)<sub>6</sub> clusters are formed (45 kJ mol<sup>-1</sup>) [72]. Calorimetric [72] and isosteric [391] heats of adsorption measured on H-Al-MFI zeolites measure similarly high heats of adsorption at H<sup>+</sup> (~80 kJ mol<sup>-1</sup>) consistent with preferential formation of (H<sub>3</sub>O)<sup>+</sup>(H<sub>2</sub>O) at coverages between 1–2 H<sub>2</sub>O/H<sup>+</sup>. Taken together, volumetric adsorption isotherms and heats of adsorption of H<sub>2</sub>O indicate that H<sub>2</sub>O adsorbs preferentially at low coverages at hydrophilic binding sites (H<sup>+</sup>, Si-OH) within hydrophobic zeolite pores, then forms clustered (H<sub>3</sub>O)<sup>+</sup>(H<sub>2</sub>O)<sub>6</sub> clusters and extended hydrogen-bonded networks. Measured isotherms provide a quantitative relationship between H<sub>2</sub>O coverage and partial pressure that can be further related to the spectroscopic signatures of adsorbed H<sub>2</sub>O structures present at different H<sub>2</sub>O coverages.

Transmission infrared (IR) spectra were collected on the suite of H-Al-Beta-F and deAl-Beta-F zeolites at 293 K exposed to H<sub>2</sub>O pressures between 0.2–1.7 kPa ( $P/P_0 = 0.1$ – $0.75$ ). The spectrum of the zeolite prior to H<sub>2</sub>O adsorption and that of gas-phase H<sub>2</sub>O within the cell at the given  $P/P_0$  value were subtracted from measured spectra (as illustrated in Figure 8.45, Supporting Information) to provide difference spectra that reflect the vibrational signatures of adsorbed H<sub>2</sub>O and of zeolite functional groups that are perturbed after adsorption. Representative spectra on Si-Beta-F, H-Al-Beta-F(2.0), and deAl-Beta-F(2.0) are shown in Figure 8.5a and 8.5b (spectra on all samples can be found in Figure 8.46–Figure 8.60, Supporting Information). Figure 8.5b shows the peak centered between 1620–1630 cm<sup>-1</sup> that corresponds to the  $\delta(\text{HOH})$  scissoring mode of adsorbed H<sub>2</sub>O [328]. The position of the center of the  $\delta(\text{HOH})$  peak does not change significantly when H<sub>2</sub>O adsorbs at different functional groups (H<sup>+</sup>, Si-OH) or at different coverages, and its integrated area is proportional to the amount of water adsorbed at the same  $P/P_0$  value quantified by volumetric adsorption isotherms (Figure 8.4). The linear relationship between quantity adsorbed and  $\delta(\text{HOH})$  peak area is shown in Figure 8.5c and quantitatively predicts the amount adsorbed with a mean absolute error (MAE) of 0.3 mmol g<sup>-1</sup> averaged among fifteen samples with H<sup>+</sup>/Si-OH nests u.c.<sup>-1</sup> between 0–2.0, which enables measuring the amount of adsorbed H<sub>2</sub>O on zeolite wafers directly from IR spectra instead of estimating it from data collected at equivalent external water chemical potential ( $T$ ,  $P/P_0$ ) in equilibrium with zeolite powders in separate volumetric adsorption isotherm measurements.

The O-H stretching region in Figure 8.5a (2800–4000 cm<sup>-1</sup>) includes negative peaks at 3735 cm<sup>-1</sup> and 3745 cm<sup>-1</sup> associated with the perturbation of isolated Si-OH groups within pores and at crystallite surfaces, respectively [329, 419], a negative peak at 3600 cm<sup>-1</sup> associated with the perturbation or disappearance of Brønsted acidic H<sup>+</sup> coordinated to the zeolite framework ( $\nu(\text{OH})$  of Al-OH) [419, 420] in the case of H-Al-Beta-F(2.0), and a broad positive peak between  $\sim 2800$ – $3700$  cm<sup>-1</sup> that reflects a convolution of perturbed H<sup>+</sup>/Si-OH groups and adsorbed H<sub>2</sub>O molecules. The strong

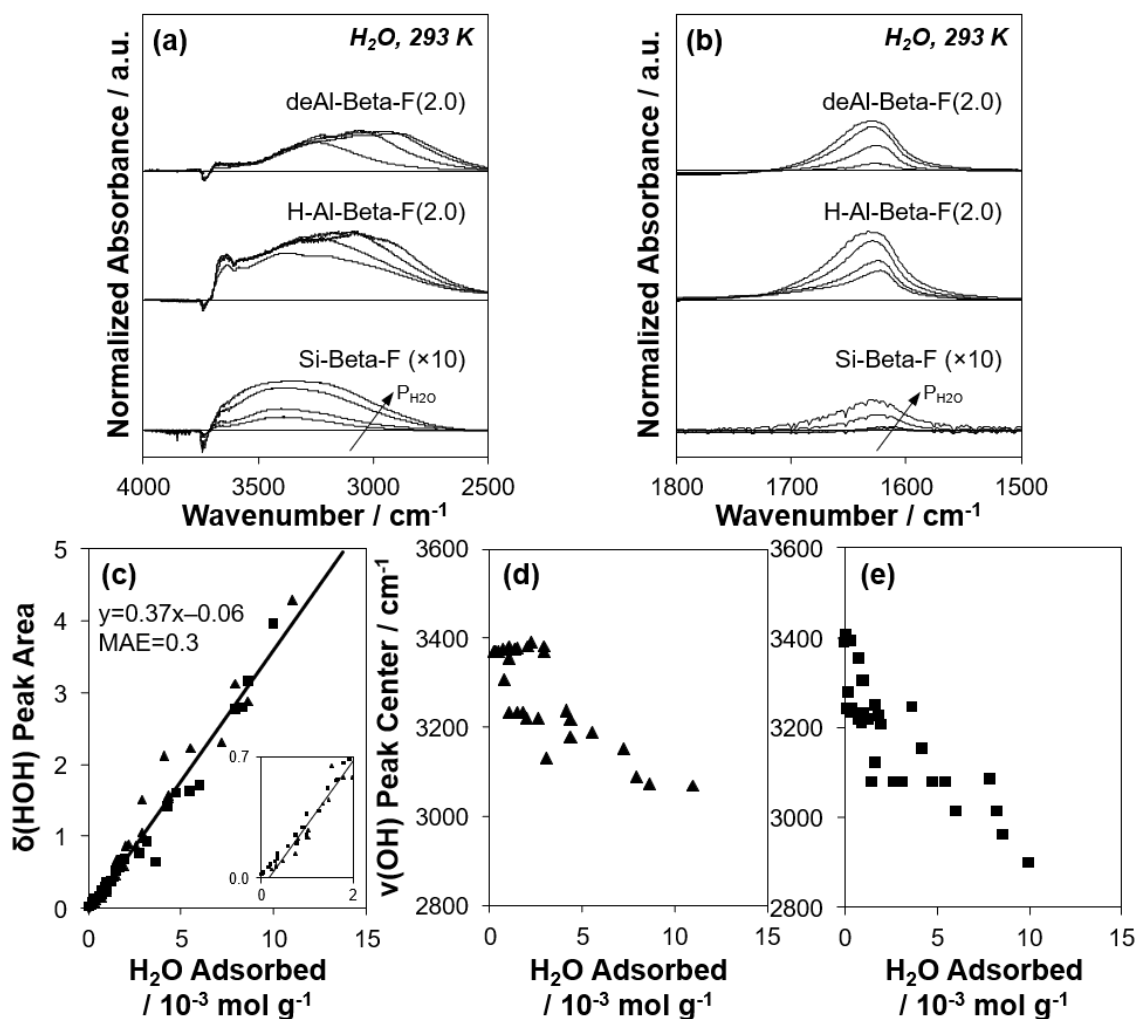


**Figure 8.5:** (a, b) Baseline-corrected difference IR spectra of  $\text{H}_2\text{O}$  adsorbed at 293 K on Si-Beta-F (bottom,  $\times 10$  for clarity), H-Al-Beta-F(2.0) (middle), and deAl-Beta-F(2.0) (top) at  $P/P_0$  values of 0.1, 0.2, 0.5, and 0.75 in (a) the  $\nu(\text{OH})$  stretching region and (b) the  $\delta(\text{HOH})$  scissoring region. Difference spectra reflect the subtraction of the spectrum of the dehydrated sample under flowing He prior to  $\text{H}_2\text{O}$  adsorption, and the spectrum of  $\text{H}_2\text{O}$  adsorbed within an empty IR cell. All spectra are normalized to the T–O–T overtone peak area (1750–2100  $\text{cm}^{-1}$ ) prior to adsorption. (c) Correlation of  $\delta(\text{HOH})$  area quantified from subtracted spectra on all H-Al-Beta-F ( $\blacktriangle$ ) and siliceous Beta samples (deAl-Beta-F, Si-Beta-F,  $\blacksquare$ ) found in Table 8.1 with the amount of  $\text{H}_2\text{O}$  adsorbed at the same  $P/P_0$  in volumetric isotherms (Figure 8.4). Solid line reflects line-of-best-fit. (d, e) Correlation of the  $\nu(\text{OH})$  peak center with the amount of  $\text{H}_2\text{O}$  adsorbed on (d) H-Al-Beta-F ( $\blacktriangle$ ) and (e) siliceous Beta samples (deAl-Beta-F, Si-Beta-F,  $\blacksquare$ ).

A,B,C triplet ( $\sim 2900$ ,  $\sim 2400$ , and  $\sim 1700$   $\text{cm}^{-1}$ ) generated by Fermi resonance between the  $\nu(\text{OH})$ ,  $\delta(\text{OH})$  and  $\gamma(\text{OH})$  fundamentals of the Al-OH group in hydrogen-bonded 1:1  $\text{H}_2\text{O}/\text{H}^+$  complexes [392, 421–423] is absent because all spectra are collected at higher coverages ( $P/P_0 \geq 0.1$ ) after  $\text{H}^+$  have been liberated from the framework as  $(\text{H}_3\text{O}^+)(\text{H}_2\text{O})_n$  clusters [71], consistent with complete disappearance of the  $3600$   $\text{cm}^{-1}$  peak at  $P/P_0 = 0.1$  (Figure 8.54b, Supporting Information). Isolated Si-OH groups ( $3735$   $\text{cm}^{-1}$ ,  $3745$   $\text{cm}^{-1}$ ) are perturbed by  $\text{H}_2\text{O}$  adsorbing throughout the entire  $P/P_0$  range on samples with  $\text{H}^+/\text{Si-OH}$  nest densities between 0–1.4, indicated by negative peaks in differential subtracted spectra (Figure 8.46b–Figure 8.60b insets), whereas these groups are fully perturbed above  $P/P_0$  values of 0.5 in H-Al-Beta-F(2.0) and deAl-Beta-F(2.0). The perturbation of isolated Si-OH groups throughout the  $P/P_0$  range is consistent with weaker adsorption at these groups concurrent with stronger adsorption at  $\text{H}^+$  or Si-OH nests, as inferred from volumetric adsorption isotherms and isosteric heats of adsorption (Figure 8.5). Full perturbation of Si-OH groups at lower relative pressures than expected for strictly isolated Si-OH groups may result from their closer proximity, on average, to Si-OH nests or  $\text{H}^+$  when such hydrophilic binding sites are present in higher density.

The positive  $\nu(\text{OH})$  peak (Figure 8.5a) is comprised of multiple components proposed to reflect O-H oscillators with increasing extents of hydrogen bonding as the wavenumber of the peak center decreases [38, 330, 406]. The peak between  $3600$ – $3700$   $\text{cm}^{-1}$  is reminiscent of a peak assigned to  $\text{H}_2\text{O}$  bound in one-dimensional chains within  $0.8$  nm diameter carbon nanotubes and to  $\text{H}_2\text{O}$  with non-hydrogen-bonded O-H groups pointing toward carbon nanotube walls in pores  $\geq 1.4$  nm in diameter ( $\nu(\text{OH}) = 3640$   $\text{cm}^{-1}$ ) [38]. A similar peak has been assigned recently to the  $\nu(\text{OH})$  of  $\text{H}_2\text{O}$  (liquid) with one O-H group ( $3660$   $\text{cm}^{-1}$ ) pointing toward a siloxane bridge on fused  $\text{SiO}_2$  surfaces with  $3.5$ – $4.5$  Si-OH  $\text{nm}^{-2}$  by vibrational sum frequency generation spectroscopy (vSFG) [424]. These literature assignments are consistent with interpretation of this peak in Si-Beta-F and deAl-Beta-F ( $3600$ – $3700$   $\text{cm}^{-1}$ ) to reflect weakly correlated  $\text{H}_2\text{O}$  molecules that explore the full hydrophobic channel system, as

identified previously in *ab initio* molecular dynamics (AIMD) simulations of defect-free Si-Beta ( $1\text{--}3 \text{ H}_2\text{O u.c.}^{-1}$ ) [406]. The  $\nu(\text{OH})$  peak at  $3600\text{--}3700 \text{ cm}^{-1}$  is present at higher intensity for H-Al-Beta-F(2.0) than for deAl-Beta-F(2.0) or Si-Beta-F, indicating that it is predominantly associated with non-hydrogen-bonded (“free”) O-H groups of  $\text{H}_2\text{O}$  molecules that are part of  $(\text{H}_3\text{O}^+)(\text{H}_2\text{O})_6$  clusters, consistent with assignments made for free O-H groups ( $3700 \text{ cm}^{-1}$ ) at the interface between water and air by vSFG [425], and in gas-phase  $\text{Cs}^+(\text{H}_2\text{O})_{20}$  clusters by cryogenic photofragmentation mass spectrometry [426].

At low relative pressure ( $P/P_0 = 0.1$ ), the dominant positive  $\nu(\text{OH})$  peak (Figure 8.5a) is centered at  $3390 \text{ cm}^{-1}$  on Si-Beta-F,  $3360\text{--}3380 \text{ cm}^{-1}$  on H-Al-Beta-F zeolites ( $0.11\text{--}2.0 \text{ H}^+ \text{ u.c.}^{-1}$ ), and  $3220\text{--}3320 \text{ cm}^{-1}$  on deAl-Beta-F zeolites ( $0.11\text{--}2.0 \text{ Si-OH nest u.c.}^{-1}$ ), and progressively shifts to lower wavenumbers as a function of coverage on both H-Al-Beta-F (Figure 8.5d) and deAl-Beta-F (Figure 8.5e). The  $\nu(\text{OH})$  peak on Si-Beta-F does not change its shape nor the position of its center significantly (within  $\sim 40 \text{ cm}^{-1}$ ) with increasing coverage, and contains contributions from hydrogen-bonded Si-OH groups ( $\sim 3400 \text{ cm}^{-1}$ ) [186] and from the O-H oscillators of the  $\text{H}_2\text{O}$  molecules bound at them. Bound  $\text{H}_2\text{O}$  lead to additional contributions that broaden the  $\nu(\text{OH})$  peak both above and below its center at  $\sim 3400 \text{ cm}^{-1}$ , and have been assigned to the hydrogen-bonded O-H group of water molecules in gas-phase  $\text{Cs}^+(\text{H}_2\text{O})_{20}$  clusters whose second O-H group is either hydrogen-bonded ( $\sim 3410\text{--}3570 \text{ cm}^{-1}$ ) or free ( $\sim 3080\text{--}3370 \text{ cm}^{-1}$ ), respectively [426]. Overtones of  $2\delta(\text{HOH})\sim 3200 \text{ cm}^{-1}$  also contribute in this region [426, 427]. The peak centered within a narrow range ( $3360\text{--}3380 \text{ cm}^{-1}$ ) at  $P/P_0 = 0.1$  on H-Al-Beta-F samples ( $0.11\text{--}2.0 \text{ H}^+ \text{ u.c.}^{-1}$ ) reflects predominantly  $(\text{H}_3\text{O}^+)(\text{H}_2\text{O})_n$  clusters of similar structure regardless of  $\text{H}^+$  density ( $n = 4$ , Table 8.7, Supporting Information), and is broader than the  $\nu(\text{OH})$  peak on Si-Beta-F because of higher intensity in both the  $3600\text{--}3700 \text{ cm}^{-1}$  region (free O-H) and  $\sim 3080\text{--}3370 \text{ cm}^{-1}$  region (hydrogen-bonded O-H in  $\text{H}_2\text{O}$  with free O-H), likely because the clustered structure of  $(\text{H}_3\text{O}^+)(\text{H}_2\text{O})_4$  leads to more free O-H groups than in  $\text{H}_2\text{O}$  hydrogen-bound at Si-OH groups in Si-Beta-F. The  $\nu(\text{OH})$  signal for  $\text{H}_2\text{O}$

adsorbed at Si-OH nests in deAl-Beta-F zeolites at  $P/P_0 = 0.1$  ( $\text{H}_2\text{O}/\text{Si-OH nest} = 5 \pm 2$ , Table 8.8, Supporting Information) contains contributions from the aforementioned OH groups belonging to  $\text{H}_2\text{O}$  and perturbed Si-OH groups, but is centered at lower wavenumbers (3220–3320  $\text{cm}^{-1}$ ). The lower wavenumber and broader range of the peak center reflects contributions from clustered hydrogen-bonded  $\text{H}_2\text{O}$  molecules with free O-H groups at Si-OH nest defects, but not from perturbation among OH groups within Si-OH nests already hydrogen-bonded prior to water adsorption, in contrast to  $\text{H}^+$  that become solvated as  $\text{H}_3\text{O}^+(\text{H}_2\text{O})_n$  after  $\text{H}_2\text{O}$  adsorption. Hydrogen-bonded clusters of  $\text{H}_2\text{O}$  molecules at Si-OH nests at lower coverages is consistent with AIMD simulations that show  $\text{H}_2\text{O}$  binding at the Si-OH nest at loadings between 1–5  $\text{H}_2\text{O}$  per nest [406].

As the coverage of  $\text{H}_2\text{O}$  increases at higher partial pressures ( $P/P_0 = 0.2$ – $0.75$ ), the  $\nu(\text{OH})$  peak centers on both H-Al-Beta-F and deAl-Beta-F zeolites decrease in wavenumbers (Figure 8.5d,e) because additional  $\text{H}_2\text{O}$  primarily leads to increased peak area in the 2800–3200  $\text{cm}^{-1}$  region (see peak centers of differential-subtracted spectra between  $P/P_0 = 0.2$ – $0.75$ , Figure 8.46b–Figure 8.60b, Supporting Information). These peaks are not associated with ice-like water structures [428] despite their similar wavenumbers to that of ice (3200  $\text{cm}^{-1}$ ) [429], but instead have been shown to result from Fermi resonance between  $2\delta(\text{HOH})$  modes and  $\nu(\text{OH})$  modes when  $\text{H}_2\text{O}$  molecules are coupled in extended hydrogen-bonded networks [427, 430, 431]. As the extent of hydrogen-bonding increases, the  $\nu(\text{OH})$  mode shifts to lower wavenumber and the splitting caused by Fermi resonance results in an apparent decrease in intensity above  $2\delta(\text{HOH})$  and an increase below it [427, 430, 431]. Isotopic  $\text{D}_2\text{O}/\text{HOD}/\text{H}_2\text{O}$  mixtures that are dilute in  $\text{H}_2\text{O}$  were used by prior researchers to identify this phenomenon because the  $\nu(\text{OH})$  mode is not split by the  $2\delta(\text{HOD}) = 2900 \text{ cm}^{-1}$  mode [427], and has been verified here using a 16:8:1  $\text{D}_2\text{O}:\text{HOD}:\text{H}_2\text{O}$  mixture [431] on Si-Beta-F and deAl-Beta-F(2.0), where the  $\nu(\text{OH})$  peak center does not shift to lower wavenumbers under the same coverage regimes (Figure 8.61–Figure 8.62). Although increased  $\nu(\text{OH})$  intensity between 2800–3200  $\text{cm}^{-1}$  does not quantitatively

correspond to a particular species or structure, it is indicative of the formation of extended hydrogen-bonded networks that have been identified in AIMD simulations of Beta zeolites containing one SiOH nest per unit cell [406]. These networks form in both H-Al-Beta-F and deAl-Beta-F zeolites at relative pressures above  $\sim 0.2$ , consistent with shifts in the overall  $\nu(\text{OH})$  peak center to lower wavenumbers with increasing coverage (Figure 8.5d,e), and with adsorption isotherms on H-Al-Beta-F zeolites that are proportional to  $\text{H}^+$  density up to  $P/P_0 \sim 0.2$  to generate  $(\text{H}_3\text{O}^+)(\text{H}_2\text{O})_6$  clusters, followed by formation of extended hydrogen-bonded networks that surround these clusters. These  $(\text{H}_3\text{O}^+)(\text{H}_2\text{O})_6$  clusters remain intact as  $\text{H}_2\text{O}$  networks surround them, in contrast to  $\text{H}_2\text{O}$  clusters at Si-OH nests that were observed to integrate into these extended hydrogen-bonded networks in AIMD simulations ( $>5 \text{ H}_2\text{O}$  u.c.<sup>-1</sup>), which is consistent with  $\nu(\text{OH})$  peak centers that represent the majority of  $\text{H}_2\text{O}$  molecules participating in extended networks and thus reach lower values in deAl-Beta-F zeolites (Figure 8.5e) than in H-Al-Beta-F zeolites (Figure 8.5d). The generation of extended hydrogen-bonded  $\text{H}_2\text{O}$  networks within H-Al-Beta-F zeolites under similar relative pressure regimes ( $P/P_0 = 0.2\text{--}0.75$ ) to those where kinetically measured  $\chi$  values deviate from unity is consistent with the hypothesis that such networks are responsible for more severe  $\text{H}_2\text{O}$  inhibition; however, a mechanistic basis that validates the identity of the assumed reaction intermediates (cf. Figure 8.2) is required.

*In situ* IR spectra were collected at 373 K on H-Al-Beta-F(2.0) under conditions analogous to those of turnover rate measurements to verify the formation of extended hydrogen-bonded networks in the presence of  $\text{C}_2\text{H}_5\text{OH}$  at reaction temperature.  $\text{H}_2\text{O}$  was fed at pressures of 10–75 kPa ( $P/P_0 = 0.1\text{--}0.75$ ) corresponding to the regime where  $\chi$  values deviate from unity (Figure 8.3b), and  $\text{C}_2\text{H}_5\text{OH}$  was additionally included at  $\text{C}_2\text{H}_5\text{OH}/\text{H}_2\text{O}$  ratios between 0.005–0.06 where  $k_{\text{first}}$  values were quantified on H-Al-Beta-F(2.0) (Figure 8.1b). The shape and position of  $\delta(\text{HOH})$  peaks at 373 K and 293 K are similar (Figure 8.6b) and their areas indicate that at 373 K, the coverage of  $\text{H}_2\text{O}$  within micropores quantified by the correlation in Figure 8.5c is similar to that quantified by volumetric adsorption isotherms at 293 K in the same relative

pressure regime ( $P/P_0 = 0.1\text{--}0.75$ ). Values of  $\text{H}_2\text{O}$  coverage were similar (within 20%) with and without co-fed  $\text{C}_2\text{H}_5\text{OH}$  (Table 8.10), indicating that under these conditions ( $\text{C}_2\text{H}_5\text{OH}/\text{H}_2\text{O} = 0.005\text{--}0.06$ ),  $\text{C}_2\text{H}_5\text{OH}$  does not significantly displace  $\text{H}_2\text{O}$  in the bulk adsorbed  $\text{H}_2\text{O}$  phase. Adsorbed  $\text{C}_2\text{H}_5\text{OH}$  can be identified in IR spectra by its  $\nu(\text{C-H})$  peaks at 2905 and 2980  $\text{cm}^{-1}$  (Figure 8.6a). Similar  $\nu(\text{C-H})$  peak areas (within a factor of 2, Figure 8.6d) quantified over a wide range of  $\text{C}_2\text{H}_5\text{OH}$  pressures (0.05–4.6 kPa) are consistent with saturation of sites with  $(\text{C}_2\text{H}_5\text{OH})(\text{H}^+)(\text{H}_2\text{O})_n$  MARI species that lead mechanistically to apparent first-order kinetics (in  $P_{\text{C}_2\text{H}_5\text{OH}}$ , Figure 8.1b). The shapes of the peaks in the  $\nu(\text{OH})$  region (Figure 8.6a) show similar increases in peak area (2800–3200  $\text{cm}^{-1}$ , see also differential subtracted spectra in Figure 8.63–Figure 8.64, Supporting Information) corresponding to the formation of extended hydrogen-bonded  $\text{H}_2\text{O}$  networks between 10–75 kPa  $\text{H}_2\text{O}$  at 373 K both with and without co-fed  $\text{C}_2\text{H}_5\text{OH}$ , reflected in shifts in the overall  $\nu(\text{OH})$  peak center (Figure 8.6e) from 3400  $\text{cm}^{-1}$  (10 kPa  $\text{H}_2\text{O}$ ) to 3220–3230  $\text{cm}^{-1}$  (75 kPa  $\text{H}_2\text{O}$ ). In summary, *in situ* IR spectra at 373 K under conditions corresponding to those where  $\chi$  values deviate from unity reveal concomitant formation of extended hydrogen-bonded  $\text{H}_2\text{O}$  structures that solvate clustered  $(\text{C}_2\text{H}_5\text{OH})(\text{H}^+)(\text{H}_2\text{O})_n$  MARI species at active sites within H-Al-Beta-F zeolites. The free energies of these intermediates and putative transition states can be interrogated by DFT calculations, *ab initio* molecular dynamics, and metadynamics.

### 8.2.3 Theoretical Calculations of Solvated Ethanol Dehydration Reaction Coordinates

The Gibbs free energies (373 K) of adsorbed intermediates and transition states involved in bimolecular ethanol dehydration reaction coordinates were calculated by DFT in the absence of  $\text{H}_2\text{O}$  to validate the assumption of associative mechanisms, and with one co-adsorbed  $\text{H}_2\text{O}$  molecule to explore its impact on transition state stability. The T9 site was selected as a representative location for Al based on the stability of adsorbed ethanol species, and the most stable configurations of adsorbates

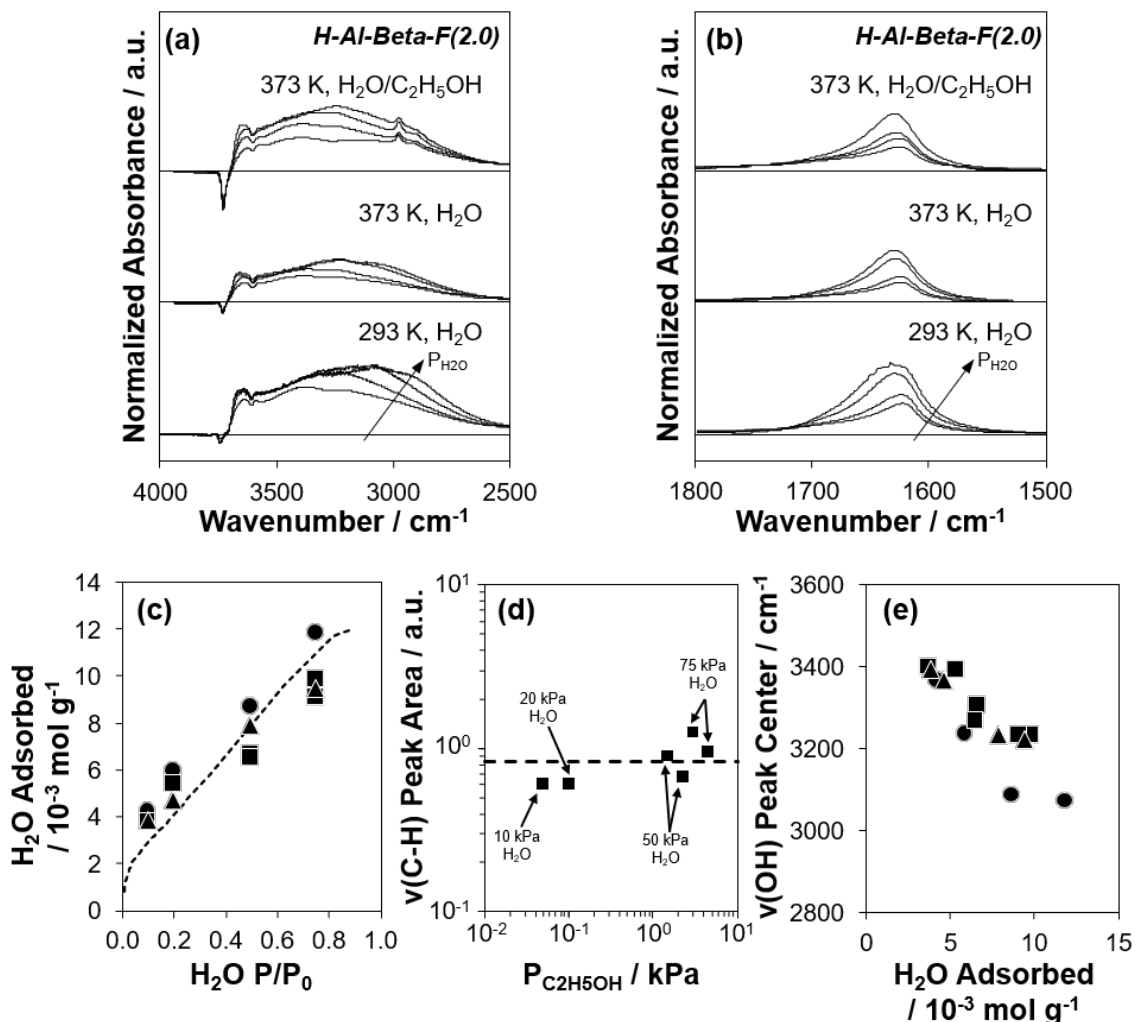


**Figure 8.6:** (a, b) Baseline-corrected difference IR spectra of adsorbed species on H-Al-Beta-F(2.5) at H<sub>2</sub>O P/P<sub>0</sub> values of 0.1, 0.2, 0.5, and 0.75 at 293 K (bottom), 373 K (middle), and 373 K with co-fed C<sub>2</sub>H<sub>5</sub>OH (top, C<sub>2</sub>H<sub>5</sub>OH/H<sub>2</sub>O = 0.005 (10, 20 kPa H<sub>2</sub>O) and 0.03 (50, 75 kPa H<sub>2</sub>O)) in (a) the  $\nu(\text{OH})$  stretching region and (b) the  $\delta(\text{HOH})$  scissoring region. Difference spectra reflect the subtraction of the spectrum of the dehydrated sample under flowing He prior to adsorption, and the spectrum of species adsorbed within an empty IR cell. All spectra are normalized to the T–O–T overtone peak area (1750–2100 cm<sup>-1</sup>) prior to adsorption. (c) Amount of H<sub>2</sub>O adsorbed determined from  $\delta(\text{HOH})$  scissoring areas and the correlation in Figure 8.5c at 293 K (●), 373 K (▲), and 373 K with co-fed C<sub>2</sub>H<sub>5</sub>OH (■). Dashed line corresponds to the volumetric adsorption isotherm of H<sub>2</sub>O at 293 K (Figure 8.4). (d) Variation in  $\nu(\text{CH})$  peak area with C<sub>2</sub>H<sub>5</sub>OH pressure on H-Al-Beta-F(2.5) at 373 K with co-fed H<sub>2</sub>O at 10, 20, 50, and 75 kPa. Dashed line represents the average value. (e) Correlation of the  $\nu(\text{OH})$  peak center with the amount of H<sub>2</sub>O adsorbed on H-Al-Beta-F(2.5) at 293 K (●), 373 K (▲), and 373 K with co-fed C<sub>2</sub>H<sub>5</sub>OH (0.05–4.6 kPa) (■).

reflect sampling of the configurational space at each of the four framework oxygen atoms bonded to the Al site. Both associative and dissociative pathways begin with adsorption of gas-phase ethanol to form a hydrogen-bound ethanol monomer at  $H^+$  ( $E^*$ ), with a calculated adsorption free energy of  $-49 \text{ kJ mol}^{-1}$  (Figure 8.7). In the dissociative pathway, the ethanol monomer eliminates  $H_2O$  to form a surface ethoxy group ( $E_x^*$ ) and gas-phase water with an intrinsic activation free energy of  $140 \text{ kJ mol}^{-1}$  (TS2). This is followed by adsorption of a second gas-phase ethanol molecule and rearrangement to form diethyl ether with an intrinsic activation free energy of  $104 \text{ kJ mol}^{-1}$  (TS3). In the associative pathway, a second gas-phase ethanol molecule co-adsorbs with the ethanol monomer to form a dimer species ( $EE^*$ ) whose protonated configuration is consistent with that calculated previously [127]. The ethanol-ethanol protonated dimer rearranges to form the  $S_N2$  transition state (TS1) that eliminates water and forms diethyl ether with an intrinsic activation free energy of  $125 \text{ kJ mol}^{-1}$ . Referenced to an ethanol monomer-covered surface, the apparent activation free energy for the associative pathway is  $26 \text{ kJ mol}^{-1}$  lower than that of the dissociative pathway in the absence of water, which is consistent with diethyl ether formation predominantly through associative pathways as shown previously on H-Al-MFI zeolites [218] (for additional discussion, see Section 8.6.2.4, Supporting Information).

Gas-phase water co-adsorbs with the ethanol monomer ( $E^*$ ) to form an ethanol-water dimer species ( $EW^*$ , Figure 8.7) with a differential adsorption free energy of  $+5 \text{ kJ mol}^{-1}$ . Adsorption of gas-phase ethanol to form an ethanol-ethanol-water trimer ( $EEW^*$ ) is endergonic ( $24 \text{ kJ mol}^{-1}$ ), and this species may form diethyl ether by an  $S_N2$  transition state (TS4, Figure 8.7) with an intrinsic activation free energy of  $73 \text{ kJ mol}^{-1}$ , or an apparent activation free energy of  $102 \text{ kJ mol}^{-1}$  relative to the ethanol monomer, gas-phase ethanol, and gas-phase water. This apparent activation free energy is comparable to that of the associative pathway with the same reference state (TS1,  $114 \text{ kJ mol}^{-1}$ ), indicating that as  $H^+$  become covered by  $(C_2H_5OH)(H^+)(H_2O)_n$  MARI species, corresponding transition states with co-adsorbed  $H_2O$  may become kinetically relevant. Volumetric adsorption isotherms that indicate  $(H_3O^+)(H_2O)_n$

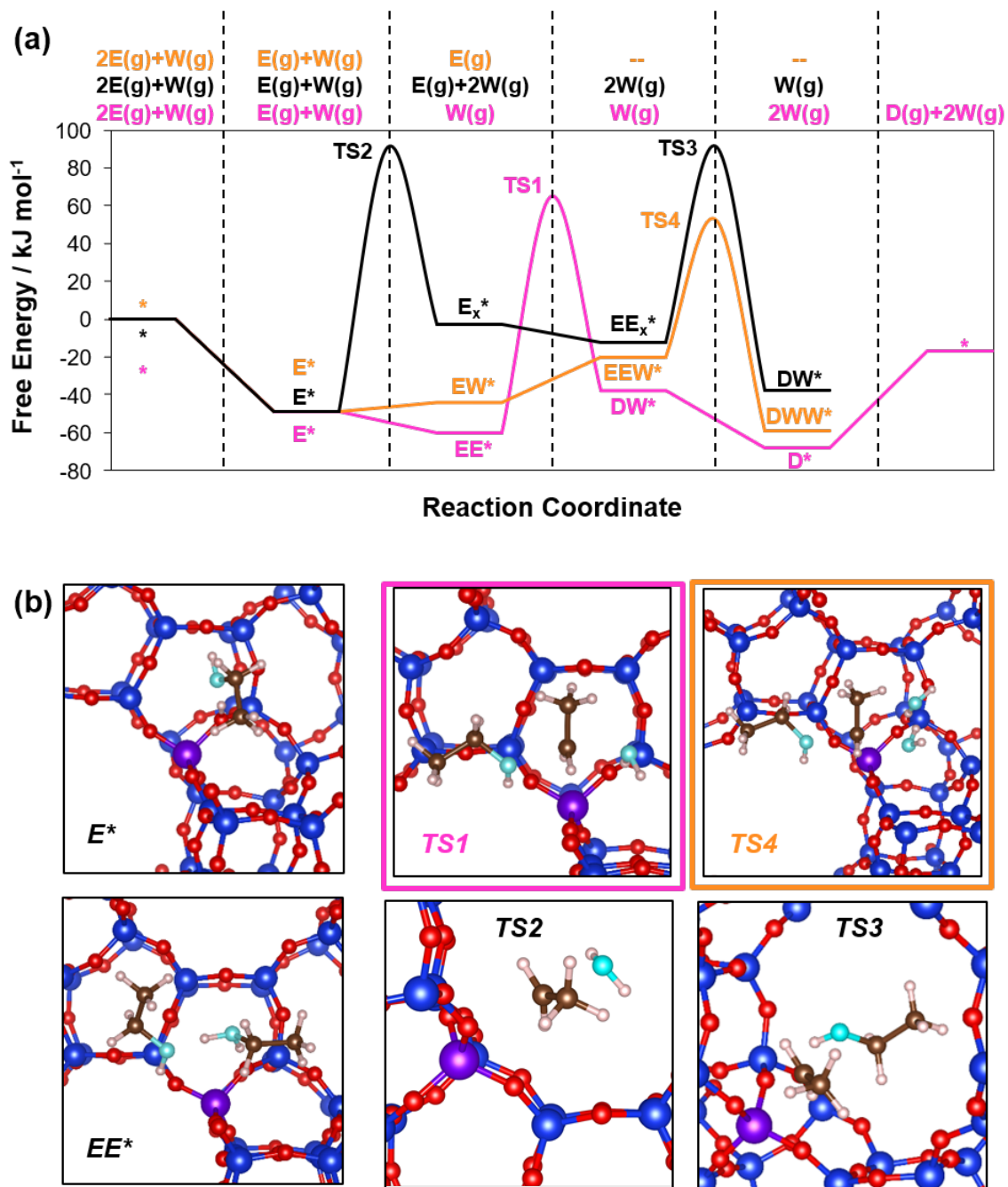


**Figure 8.7:** (a) Gibbs free energies of adsorbed intermediates and transition states within H-Al-Beta calculated by DFT, referenced to two gas-phase ethanol molecules and one water molecule, for diethyl ether formation through the dissociative pathway (black), the associative pathway (pink), and the associative pathway with one co-adsorbed  $\text{H}_2\text{O}$  molecule (orange). (b) Geometries of adsorbed intermediates and transition states.

clusters contain up to 7 H<sub>2</sub>O molecules (Figure 8.4b) [72,73] suggest that a similarly large configurational space exists for (C<sub>2</sub>H<sub>5</sub>OH)(H<sup>+</sup>)(H<sub>2</sub>O)<sub>n</sub> clusters, which lends itself to investigation by *ab initio* molecular dynamics (AIMD).

AIMD simulations were first conducted at 373 K with only H<sub>2</sub>O in H-Al-Beta (1 H<sup>+</sup> u.c.<sup>-1</sup>) to corroborate experimental identification of (H<sub>3</sub>O<sup>+</sup>)(H<sub>2</sub>O)<sub>n</sub> clusters. Loadings between 5–8 H<sub>2</sub>O u.c.<sup>-1</sup> were chosen based on the expected cluster size of 7 H<sub>2</sub>O from experiments, and because these loadings include the range where local clusters were observed in prior simulations of Sn-Beta and deAl-Beta zeolites [406]. Within this range, a local free energy minimum was found at 6 H<sub>2</sub>O u.c.<sup>-1</sup>, which corresponds to a (H<sub>3</sub>O<sup>+</sup>)(H<sub>2</sub>O)<sub>5</sub> cluster (W<sub>6</sub><sup>\*</sup>, Figure 8.8a), in reasonable agreement with experiment. In the simulations, the H<sup>+</sup> is solvated within the H<sub>2</sub>O cluster, consistent with the disappearance of  $\nu(\text{OH})$  stretches for Al-O(H)-Si groups in measured IR spectra. Shuttling of the H<sup>+</sup> among H<sub>2</sub>O molecules is facile, leading to complications in estimating entropy, which are discussed in detail in Section 8.6.2.6 of the Supporting Information. These simulations in the absence of reactant molecules (C<sub>2</sub>H<sub>5</sub>OH) successfully predict the structures of clustered (H<sub>3</sub>O<sup>+</sup>)(H<sub>2</sub>O)<sub>n</sub> that have been previously studied [71–73]; however, the effects of C<sub>2</sub>H<sub>5</sub>OH molecules on these structures are still unclear.

We simulated (C<sub>2</sub>H<sub>5</sub>OH)<sub>m</sub>(H<sup>+</sup>)(H<sub>2</sub>O)<sub>n</sub> clusters adsorbed in H-Al-Beta zeolites at 373 K by AIMD, where n was varied between 1–6 and m = 1, 2, corresponding to ethanol monomer and ethanol-ethanol dimer species with different degrees of solvation by H<sub>2</sub>O. The free energy of adsorption of these ethanol molecules was calculated from AIMD relative to gas-phase ethanol, and the same number of H<sub>2</sub>O molecules adsorbed within the zeolite:

$$\Delta G_{E_m,ads} = G_{E_m,solv} - mG_{E(g)} - G_{W_n,solv} \quad (8.9)$$

where  $G_{E_m,solv}$  is the total free energy of the system calculated by AIMD of the (C<sub>2</sub>H<sub>5</sub>OH)<sub>m</sub>(H<sup>+</sup>)(H<sub>2</sub>O)<sub>n</sub> cluster,  $G_{W_n,solv}$  is the total free energy of the system cal-

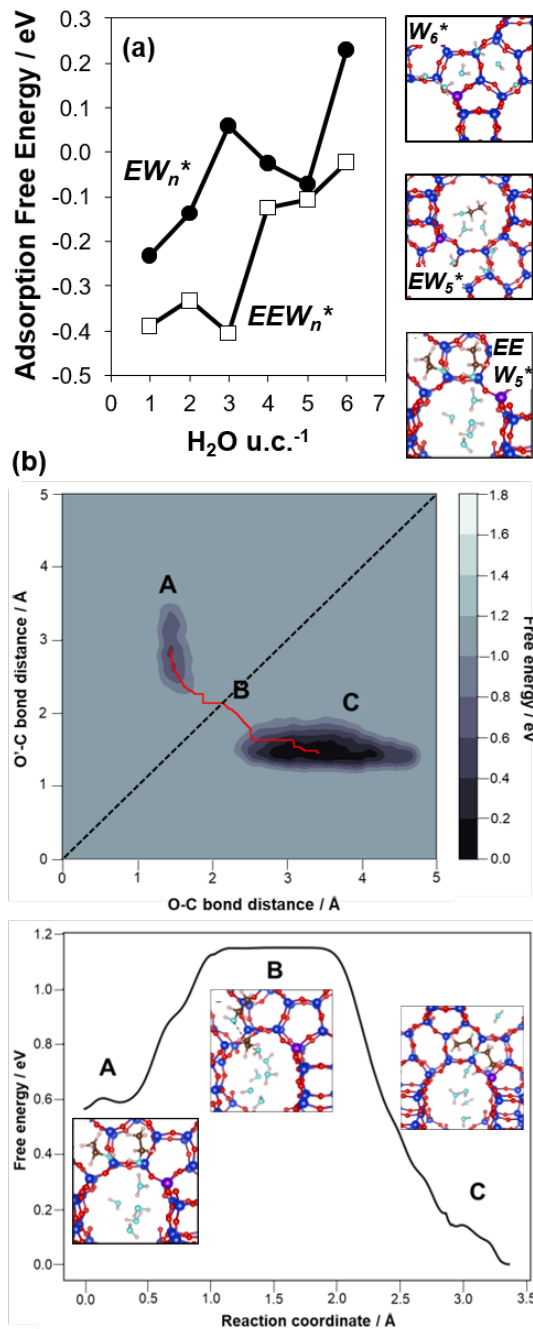


**Figure 8.8:** (a) Gibbs free energies of adsorption (373 K) of ethanol monomer and dimer species with 1–6 co-adsorbed H<sub>2</sub>O molecules calculated by *ab initio* molecular dynamics, referenced to gas-phase ethanol and the zeolite with the same number of adsorbed H<sub>2</sub>O molecules. (b) Gibbs free energy landscape (373 K) calculated by metadynamics, as a function of the collective variables which are the distances between the C<sub>α</sub> the ethanol molecule bound at H<sub>3</sub>O<sup>+</sup> in the EW<sub>5</sub><sup>\*</sup> cluster within H-Al-Beta (A), and the two O atoms that are involved in the nucleophile and leaving group at the transition state (B). The minimum free energy path including the transition state and representative images along the reaction coordinate are shown below.

culated by AIMD of the  $(\text{H}^+)(\text{H}_2\text{O})_n$  cluster, and  $G_{E(g)}$  is the free energy of gas-phase ethanol. The free energy of adsorption of gas-phase  $\text{C}_2\text{H}_5\text{OH}$  into  $(\text{C}_2\text{H}_5\text{OH})_m(\text{H}^+)(\text{H}_2\text{O})_n$  clusters is shown as a function of the number of  $\text{H}_2\text{O}$  molecules ( $n$ ) in Figure 8.8a. In general,  $\text{C}_2\text{H}_5\text{OH}$  adsorption to form  $(\text{C}_2\text{H}_5\text{OH})_m(\text{H}^+)(\text{H}_2\text{O})_n$  is less exergonic as the number of solvating  $\text{H}_2\text{O}$  molecules increases, because  $\text{C}_2\text{H}_5\text{OH}$  disrupts hydrogen bonds among  $\text{H}_2\text{O}$  molecules in clusters of increasing size. In the case of one  $\text{C}_2\text{H}_5\text{OH}$  molecule, a local minimum in free energy is observed at  $(\text{C}_2\text{H}_5\text{OH})(\text{H}^+)(\text{H}_2\text{O})_5$ , after which additional  $\text{H}_2\text{O}$  significantly increases the adsorption free energy by 0.3 eV, indicating that the largest stable  $(\text{C}_2\text{H}_5\text{OH})(\text{H}^+)(\text{H}_2\text{O})_n$  cluster occurs at  $n = 5$  ( $\text{EW}_5^*$ , Figure 8.8a), consistent with displacement of one  $\text{H}_2\text{O}$  molecule in the  $(\text{H}^+)(\text{H}_2\text{O})_6$  cluster by  $\text{C}_2\text{H}_5\text{OH}$ , which is found near the  $\text{H}_3\text{O}^+$  ion during the simulations. This  $(\text{C}_2\text{H}_5\text{OH})(\text{H}^+)(\text{H}_2\text{O})_5$  species is likely the MARI in experimentally-measured kinetics and IR spectra (373 K), which becomes increasingly solvated by extended hydrogen-bonded  $\text{H}_2\text{O}$  networks that surround it in  $\text{H}_2\text{O}$  pressure regimes (10–75 kPa) where  $\chi$  values deviate from unity. The local minimum for  $(\text{C}_2\text{H}_5\text{OH})_2(\text{H}^+)(\text{H}_2\text{O})_n$  species occurs at  $n = 3$ , indicating that adsorption of an additional ethanol prior to reaction further disrupts the hydrogen-bonding network of the  $\text{H}_2\text{O}$  cluster, such that at  $n = 5$  ( $\text{EEW}_5^*$ , Figure 8.8a) the second adsorbed ethanol molecule participates in hydrogen bonding only with the first  $\text{C}_2\text{H}_5\text{OH}$ , but not the remaining  $\text{H}_2\text{O}$  in the cluster. The  $\text{H}^+$  remains solvated as  $\text{H}_3\text{O}^+$ , rather than being shared between the two  $\text{C}_2\text{H}_5\text{OH}$  in a protonated dimer, which we hypothesize leads to additional free energy penalties to localize positive charge at the ethyl group in  $\text{S}_{\text{N}}2$  transition states that form diethyl ether and water.

The configurations of the bimolecular dehydration transition state in the presence of five  $\text{H}_2\text{O}$  molecules were explored further in metadynamics simulations. The  $(\text{C}_2\text{H}_5\text{OH})_2(\text{H}^+)(\text{H}_2\text{O})_5$  intermediate calculated in AIMD simulations was chosen as the starting point, and the collective variables were chosen as the distances between the C atom of the ethanol bound to  $\text{H}_3\text{O}^+$  and its O atom, which becomes the  $\text{H}_2\text{O}$  leaving group at the transition state, and that of the second ethanol molecule, O',

which is the nucleophilic O atom at the transition state. As such, at the initial state (A, Figure 8.8b), the O-C bond distance is constrained at  $\sim 1$  Å, while the O'-C distance explores a larger configurational space that is still limited to  $\sim 2$ – $3$  Å by the hydrogen-bonding interaction between the two ethanol molecules. The opposite is true at the final state (C, Figure 8.8b) where the O'-C bond has been fully formed in diethyl ether at a distance of  $\sim 1$  Å, while the leaving group H<sub>2</sub>O that determines the O-C distance may diffuse between 2–5 Å away from the product DEE.

Although the metadynamics simulation to find the transition state is not fully converged (more simulation time is required), one barrier recrossing has been observed, where the transition state (B, Figure 8.8b) resembles the S<sub>N</sub>2 configurations of TS1 and TS4 calculated with zero or one co-adsorbed H<sub>2</sub>O, respectively (Figure 8.7). The O-C and O'-C distances are approximately equivalent, where the C<sub>2</sub>H<sub>5</sub><sup>+</sup> group lies equidistant between the nucleophilic C<sub>2</sub>H<sub>5</sub>OH and the leaving group H<sub>2</sub>O. Here, charge has transferred from H<sub>3</sub>O<sup>+</sup> to the C<sub>2</sub>H<sub>5</sub><sup>+</sup> group, and thus five H<sub>2</sub>O molecules solvate the transition state, rather than the four that solvate the (C<sub>2</sub>H<sub>5</sub>OH)<sub>2</sub>H<sub>3</sub>O<sup>+</sup> precursor complex. The requirement to dissociate this bound H<sub>2</sub>O molecule from the H<sup>+</sup> active site en route to the bimolecular dehydration transition state results in the limiting case of  $-1$  reaction order in H<sub>2</sub>O. In contrast to TS1 and TS4, transition state B in Figure 8.8b is stabilized distant from the framework Al atom because of the delocalization of the H<sup>+</sup> charge as H<sub>3</sub>O<sup>+</sup> in its precursor state. This enables the transition state to more effectively maximize its van der Waals contacts with the surrounding pore environment than in the case where it is more electrostatically constrained near the framework Al. The transition state resides on the periphery of the H<sub>2</sub>O cluster rather than within it, indicating that under this coverage regime (up to 5 H<sub>2</sub>O per H<sup>+</sup>), the primary function of H<sub>2</sub>O is to solvate the H<sup>+</sup> active site as H<sub>3</sub>O<sup>+</sup>(H<sub>2</sub>O)<sub>n</sub>. This is reflected in the calculated intrinsic activation free energy of 60–70 kJ mol<sup>-1</sup>, which should not be overinterpreted because the simulation is not fully converged, but which is similar to the intrinsic activation free energy to form TS4 (73 kJ mol<sup>-1</sup>). The similarity of these values, and the location of the transition state on

the periphery of the H<sub>2</sub>O cluster, are consistent with kinetically relevant formation of DEE catalyzed by H<sub>3</sub>O<sup>+</sup> through transition states that do not require a reduction in the size of H<sub>2</sub>O clusters. In summary, the combined theoretical approaches here indicate that the structure of (C<sub>2</sub>H<sub>5</sub>OH)(H<sup>+</sup>)(H<sub>2</sub>O)<sub>n</sub> MARI species are analogous to those of (H<sup>+</sup>)(H<sub>2</sub>O)<sub>n</sub>, where one C<sub>2</sub>H<sub>5</sub>OH molecule displaces one H<sub>2</sub>O molecule, and that these MARI may access kinetically relevant DEE formation transition states after adsorption of a second ethanol and dissociation of one H<sub>2</sub>O molecule from the H<sup>+</sup> active site.

#### 8.2.4 Mechanistic Implications of Solvation by Condensed Water Structures

The thermodynamic accessibility of diethyl ether transition state free energies regardless of the number of H<sub>2</sub>O molecules in (C<sub>2</sub>H<sub>5</sub>OH)(H<sup>+</sup>)(H<sub>2</sub>O)<sub>n</sub> MARI is consistent with the elementary steps to form DEE in Figure 8.2, but with the additional complexity that increasing solvation of H<sup>+</sup> by H<sub>2</sub>O leads to new configurations of (C<sub>2</sub>H<sub>5</sub>OH)(H<sub>3</sub>O<sup>+</sup>)(H<sub>2</sub>O)<sub>1-5</sub> as MARI rather than (C<sub>2</sub>H<sub>5</sub>OH)(H<sup>+</sup>)(H<sub>2</sub>O) species, as revised in Figure 8.9. When  $n = 0$ , the elementary steps in Figure 8.9 are identical to those in Figure 8.2, so that addition of H<sub>2</sub>O to form (H<sub>3</sub>O<sup>+</sup>)(H<sub>2</sub>O)<sub>n</sub> does not impact the functional form of rate expressions. Clustered (C<sub>2</sub>H<sub>5</sub>OH)(H<sub>3</sub>O<sup>+</sup>)(H<sub>2</sub>O)<sub>1-5</sub> MARI must desorb one H<sub>2</sub>O molecule en route to transition states that localize positive charge at the ethyl group, recovering the -1 reaction order in H<sub>2</sub>O as the limiting case when surfaces are saturated by (C<sub>2</sub>H<sub>5</sub>OH)(H<sub>3</sub>O<sup>+</sup>)(H<sub>2</sub>O)<sub>4-5</sub> MARI (5 predicted by experiments, 4 by theory). Beyond the maximum cluster size, as shown by *in situ* IR spectra (293 K, 373 K), additional adsorbed water begins to solvate the MARI in extended hydrogen-bonded networks, which corresponds to regimes where  $\chi$  values deviate from unity. Rate expressions derived from steps 1-4 in Figure 8.9 that take this solvation into account, as Eq. 8.3 does not, are therefore required to provide a mechanistic basis for the increased inhibition by H<sub>2</sub>O when extended networks are formed. Within the formalism of transition state theory [432],

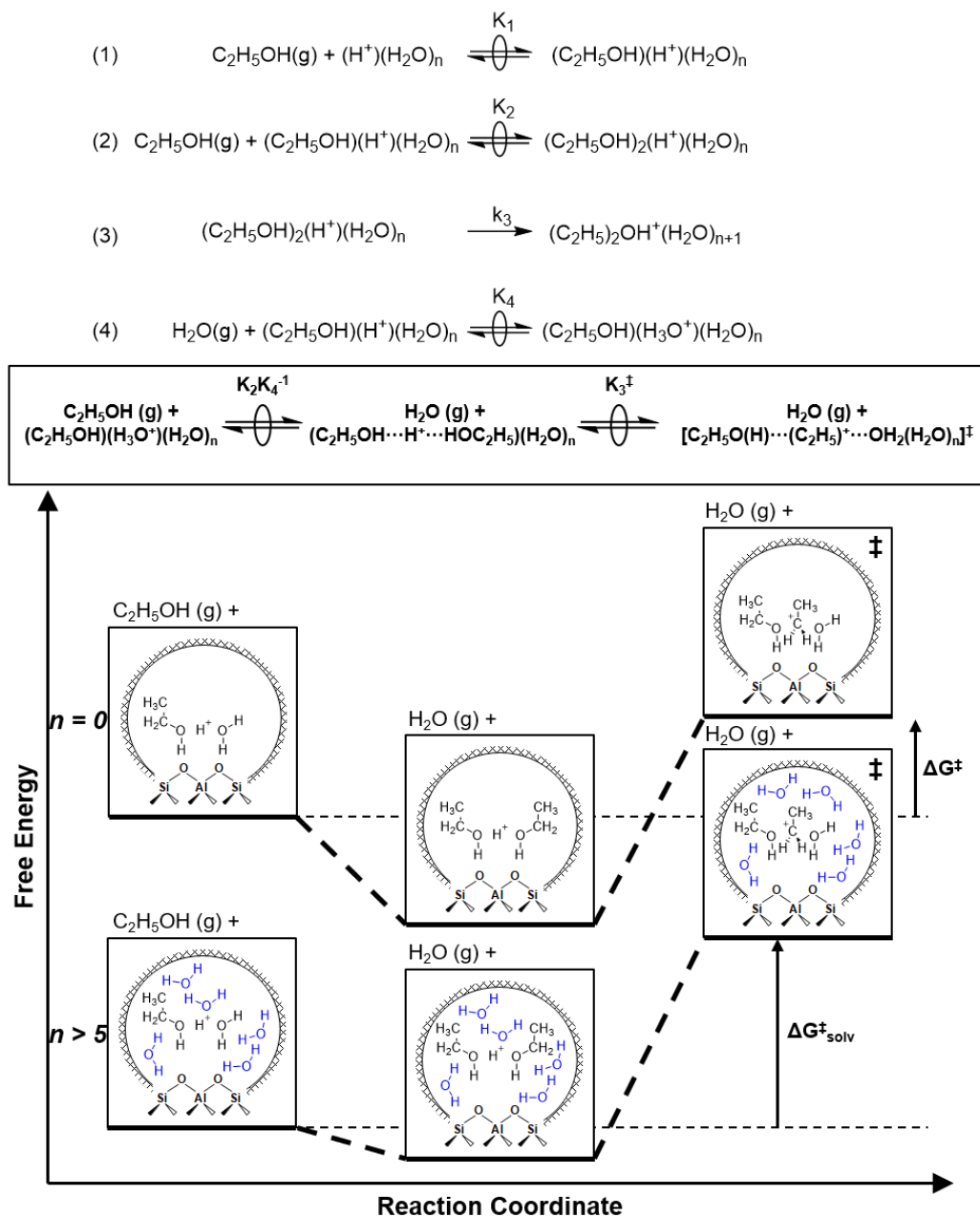


**Figure 8.9:** Series of elementary steps for ethanol dehydration catalyzed by solvated hydronium ions, and free energy diagram illustrating the effects of solvation by extended hydrogen-bonded  $\text{H}_2\text{O}$  networks.

$(\text{C}_2\text{H}_5\text{OH})(\text{H}_3\text{O}^+)(\text{H}_2\text{O})_n$  MARI and gas-phase  $\text{C}_2\text{H}_5\text{OH}$  are considered to be in equilibrium with  $[(\text{C}_2\text{H}_5\text{O}(\text{H})\cdots(\text{C}_2\text{H}_5)^+\cdots\text{OH}_2(\text{H}_2\text{O})_n)^\ddagger]$  and gas-phase  $\text{H}_2\text{O}$ :

$$\frac{r_{\text{DEE}}}{[\text{H}^+]} = \frac{k_{\text{B}}T}{h} C_{\ddagger} / [\text{H}^+] \quad (8.10)$$

where  $k_{\text{B}}$  is Boltzmann's constant,  $T$  is the temperature,  $h$  is Planck's constant, and  $C_{\ddagger}$  is the concentration [433] of the transition state, whose concentration can be expressed through  $K^\ddagger$ , the transition state equilibrium constant:

$$K^\ddagger = \frac{a_{\ddagger} a_{\text{H}_2\text{O}(g)}}{a_{\text{EW}_n} a_{\text{C}_2\text{H}_5\text{OH}(g)}} \quad (8.11)$$

where  $a_i$  is the thermodynamic activity of species  $i$ . Replacing activities with activity coefficients and concentrations ( $a_i = \gamma_i C_i$ ) in Eq. 8.11, solving for  $C_{\ddagger}$ , and substituting into Eq. 8.10 gives:

$$\frac{r_{\text{DEE}}}{[\text{H}^+]} = \frac{k_{\text{B}}T}{h} K^\ddagger \frac{\gamma_{\text{EW}_n}}{\gamma_{\ddagger}} \frac{\gamma_{\text{C}_2\text{H}_5\text{OH}(g)}}{\gamma_{\text{H}_2\text{O}(g)}} \frac{C_{\text{C}_2\text{H}_5\text{OH}(g)}}{C_{\text{H}_2\text{O}(g)}} \frac{C_{\text{EW}_n}}{[\text{H}^+]} \quad (8.12)$$

Eq. 8.12 can be simplified further by restricting its use to the conditions where experimental kinetics were collected with  $(\text{C}_2\text{H}_5\text{OH})(\text{H}_3\text{O}^+)(\text{H}_2\text{O})_n$  as the MARI (373 K,  $2 \times 10^{-3}$ –10 kPa  $\text{C}_2\text{H}_5\text{OH}$ , 0–75 kPa  $\text{H}_2\text{O}$ ), under which  $C_{\text{EW}_n}/[\text{H}^+] = 1$  because of the MARI assumption, and  $\gamma_{\text{C}_2\text{H}_5\text{OH}(g)}/\gamma_{\text{H}_2\text{O}(g)} = 1$  because the gas-phase activity coefficients of both  $\text{C}_2\text{H}_5\text{OH}$  and  $\text{H}_2\text{O}$  are nearly unity under these conditions far from their critical temperatures and pressures ( $\text{H}_2\text{O}$   $P_{\text{c}} = 22$  MPa,  $T_{\text{c}} = 647$  K;  $\text{C}_2\text{H}_5\text{OH}$   $P_{\text{c}} = 6.4$  MPa,  $T_{\text{c}} = 516$  K) [434]. Assumption of an ideal gas phase also enables converting the ratio of concentrations to one of pressures to arrive at an expression for the bimolecular ethanol dehydration turnover rate that is similar to Eq. 8.4 above:

$$\frac{r_{\text{DEE}}}{[\text{H}^+]} = \frac{k_{\text{B}}T}{h} K^\ddagger \frac{\gamma_{\text{EW}_n}}{\gamma_{\ddagger}} \frac{P_{\text{C}_2\text{H}_5\text{OH}}}{P_{\text{H}_2\text{O}}} \quad (8.13)$$

Upon relating the transition state equilibrium constant to those of elementary steps in Figure 8.9 (see Section 8.6.2.7, Supporting Information for full derivation):

$$\frac{r_{\text{DEE}}}{[H^+]} = \frac{k_3 K_2 \gamma_{EW_n} P_{C_2H_5OH}}{K_4 \gamma_{\ddagger} P_{H_2O}} \quad (8.14)$$

it is evident that under conditions where solvation of both the MARI and transition state are thermodynamically ideal (or more generally under any conditions where their activity coefficients fortuitously cancel [333], Eq. 8.14 is identical to Eq. 8.4. It therefore follows that:

$$\chi = \frac{\gamma_{EW_n}}{\gamma_{\ddagger}} \quad (8.15)$$

which provides a mechanistic basis to interpret deviations in  $\chi$  values below unity at increasing water pressures. As extended hydrogen-bonded  $H_2O$  networks form and solvate  $(C_2H_5OH)(H_3O^+)(H_2O)_{4-5}$  MARI and transition states, the activity coefficient of the transition state increases more rapidly than that of the MARI. This ratio effectively cancels in rate equations before the formation of extended  $H_2O$  networks because both MARI and transition states reside on the periphery of  $(H_3O^+)(H_2O)_n$  clusters, and only become solvated after these clusters have reached their maximum size, as indicated by AIMD and metadynamics. Inhibition by  $H_2O$  in the ideal regime (up to  $-1$  order,  $<10$  kPa  $H_2O$ ) is therefore accounted for by solvation of  $H^+$  within clusters of increasing nuclearity as  $H_3O^+$ , as shown previously in  $H_2O$ -organic solvent mixtures [44, 51]; however, extended hydrogen-bonded networks that solvate the MARI and transition state clusters after they are formed lead to more severe inhibition than that caused by stabilization of  $H^+$  alone.

The less effective solvation of the transition state that leads to more rapidly increasing values of  $\gamma_{\ddagger}$  relative to  $\gamma_{EW_n}$  is likely a consequence of the inability of the non-polar ethyl groups of ethanol molecules to participate in hydrogen bonding networks, as previously proposed to be the case for 1-octene alkyl groups that disrupt  $H_2O$  adsorbed at Si-OH nests in Ti-Beta zeolites during epoxidation catalysis (0.1 mM  $C_8H_{16}$ , 0.01 M  $H_2O_2$ , 0.039 M  $H_2O$  in  $CH_3CN$ , 313 K) [58]. The transition state

engages the hydroxyl groups of both  $C_2H_5OH$  molecules as nucleophile and leaving group, and thus both ethyl groups present at the transition state may disrupt hydrogen bonds in surrounding  $H_2O$  networks. In contrast, the  $(C_2H_5OH)(H_3O^+)(H_2O)_{4-5}$  MARI requires the solvation of only one non-polar ethyl group, which disrupts surrounding  $H_2O$  networks to a lesser extent than the two ethyl groups of the transition state. This analysis is conceptually similar to that of the activation volume [435–438] in liquid-phase reactions or the activation area on two-dimensional surfaces [170], where increasing pressures and concomitant increasing densification of the solvent phase destabilizes transition states with positive activation volume, according to the empirical equation [436]:

$$\left(\frac{\partial \ln(k)}{\partial P}\right)_T = \frac{-\Delta v^\ddagger}{RT} \quad (8.16)$$

where  $\Delta v^\ddagger$  is the (molar) activation volume of the transition state relative to its precursor(s). Here, the apparent activation volume is positive because transition states include two adsorbed  $C_2H_5OH$  molecules while the MARI species only includes one. The disruption of extended hydrogen-bonded networks by transition states has also been implicated in the destabilization of transition states for aqueous-phase glucose-fructose isomerization in Ti-Beta zeolites [57], where zeolites of different hydrophobicity enabled including or excluding  $H_2O$  networks, but not systematic variation of the intrapore structure of these networks between these two extremes. Here, we have demonstrated that gas-phase kinetic measurements and spectroscopic characterizations with co-fed solvent molecules under conditions that lead to intrapore condensation of extended liquid-like networks enable quantifying the thermodynamic nonidealities introduced by the solvation of kinetically relevant intermediates and transition states within confining environments, which are inaccessible to measurements in the liquid phase. With this approach, the role of the shape and size of confining pore environments in stabilizing water structures that in turn influence the solvation of reactive intermediates and transition states can be interrogated independent of other phenomena that also change concomitantly with pore architecture, such as reactant

coverage regimes or co-solvent interactions, that often complicate precise mechanistic interpretation of measured rate data.

### 8.2.5 Effects of Pore Topology on Solvation Effects

The generality of non-ideal solvation effects in confined liquid-like H<sub>2</sub>O networks and the effect of the topology of the pores that confine them was explored at 373 K in different zeolite frameworks (CHA, AEI, FAU, TON, MFI) and in a less-confined solid acid (H<sub>3</sub>PW<sub>12</sub>O<sub>40</sub>/Si-MCM-41), whose pore topologies and acid site densities are described in Table 8.2. The values of  $k_{first}$  were quantified at H<sub>2</sub>O pressures between 0.1–75 kPa and reported in Figure 8.10a. Regardless of confining environment, bimolecular ethanol dehydration turnover rates (373 K, per H<sup>+</sup>) on Brønsted acids were inhibited by H<sub>2</sub>O, and this inhibition could be described by Eq. 8.6 only at lower H<sub>2</sub>O pressures, which enabled quantifying  $k_3K_2K_4^{-1}$  values in regimes where  $k_{first}$  values were –1 order in H<sub>2</sub>O. These lumped rate and equilibrium constants reflect the free energy of the confined bimolecular dehydration transition state ( $[(C_2H_5O(H)\cdots(C_2H_5)^+\cdots OH_2(H_2O)_n]^\ddagger$ ) and gas-phase water with respect to the confined (C<sub>2</sub>H<sub>5</sub>OH)(H<sub>3</sub>O<sup>+</sup>)(H<sub>2</sub>O)<sub>n</sub> MARI and gas-phase ethanol (Figure 8.9). Gaseous species are insensitive to confinement within zeolite pores and their stabilities are unaffected by changes in topology, while the MARI and transition state are expected to be stabilized to different extents by van der Waals contacts within confining micropores of different dimensions [33]. The microporous voids where the MARI and transition state reside can be reasonably approximated by the diameter of the largest contained sphere within the zeolite,  $d_{LC}$  [6]. As shown in the inset of Figure 8.10a,  $k_3K_2K_4^{-1}$  values systematically decrease with increasing  $d_{LC}$ , consistent with the expectation that bimolecular dehydration transition states are preferentially stabilized within confining pore environments relative to (C<sub>2</sub>H<sub>5</sub>OH)(H<sub>3</sub>O<sup>+</sup>)(H<sub>2</sub>O)<sub>n</sub> MARI species, which are smaller in size and therefore benefit less from stronger van der Waals contacts (Figure 8.9). The HPW/Si-MCM-41 sample is not included in this correlation because POMs are stronger acids than zeolites (deprotonation energy

**Table 8.2:** Elemental compositions, micropore volumes, H<sup>+</sup> densities, and topological descriptors of Brønsted acidic solids.

Sample	Si/Al <sup>a</sup>	V <sub>micro</sub> <sup>b</sup> / cm <sup>3</sup> g <sup>-1</sup>	H <sup>+</sup> /Al (NH <sub>4</sub> <sup>+</sup> ) <sup>c</sup>	H <sup>+</sup> /Al (DTBP) <sup>d</sup>	d <sub>PL</sub> <sup>e</sup> / nm	d <sub>LC</sub> <sup>f</sup> / nm	Undulation Parameter <sup>g</sup>
H-Al-CHA	15	0.21 <sup>h</sup>	0.98	--	0.372	0.737	0.505
H-Al-AEI	9.5	0.20 <sup>h</sup>	0.85	--	0.384	0.733	0.524
H-Al-FAU	56	0.30	0.35	0.88	0.735	1.124	0.654
H-Al-MFI	43	0.13	0.85	--	0.470	0.636	0.739
H-Al-TON	43	0.05	0.77	--	0.511	0.571	0.895
H-Al-Beta-F(2.0)	23	0.22	0.75	0.54	0.595	0.668	0.891
HPW/Si-MCM-41	11 <sup>i</sup>	--	--	1.6 <sup>j</sup>	3.8 <sup>k</sup>	3.8 <sup>k</sup>	1.0

<sup>a</sup>Determined by AAS. <sup>b</sup>Determined by N<sub>2</sub> adsorption minimum in  $\partial V_{\text{ads}}/\partial \log(P/P_0)$ . <sup>c</sup>Determined by TPD of NH<sub>3</sub> after aqueous-phase ion exchange with 1 M NH<sub>4</sub>NO<sub>3</sub>, 24 h, 353 K. <sup>d</sup>Determined by *in situ* 2,6-di-*tert*-butylpyridine titration during ethanol dehydration catalysis (378 K, 5 kPa C<sub>2</sub>H<sub>5</sub>OH, 1 kPa H<sub>2</sub>O). <sup>e</sup>Pore-limiting diameter [6]. <sup>f</sup>Diameter of largest included sphere [6]. <sup>g</sup>Undulation parameter = d<sub>PL</sub> / d<sub>LC</sub>. <sup>h</sup>Determined by Ar adsorption minimum in  $\partial V_{\text{ads}}/\partial \log(P/P_0)$ . <sup>i</sup>W/P ratio quantified by ICP. <sup>j</sup>H<sup>+</sup>/POM. <sup>k</sup>Average of pore-size distribution determined by N<sub>2</sub> adsorption isotherm and NLDFT (Figure 8.39, Supporting Information).

(DPE) = 1087 kJ mol<sup>-1</sup> for HPW [78] <1201 ± 11 kJ mol<sup>-1</sup> for H-Al-zeolites [439]), whose acid strength is independent of topology [439]). Notably,  $k_3K_2K_4^{-1}$  values are similar in CHA, AEI, and Beta, indicating that reacting species are confined within the larger cages of CHA and AEI ( $d_{LC} = 0.73\text{--}0.74$  nm) that are similar in size to the channels of Beta ( $d_{LC} = 0.67$  nm), rather than their constrained 8-MR windows (pore-limiting diameter,  $d_{PL} = 0.37\text{--}0.38$  nm, Table 8.2). While the kinetic behavior of zeolites in regimes where  $\chi = 1$  is consistent with well-known principles of stabilization by attractive dispersion forces in confining environments, it is unclear whether the condensation of liquid-like water within micropores may attenuate or enhance the effects of confinement.

Measured values of  $\chi = \gamma_{EWn}/\gamma_{\ddagger}$  are shown as a function of H<sub>2</sub>O pressure (373 K) in Figure 8.10b. The Brønsted acid zeolite samples begin to deviate from  $\gamma_{EWn}/\gamma_{\ddagger}$  values of unity in the approximate range ~5–20 kPa H<sub>2</sub>O, and the HPW/Si-MCM-41 sample shows deviations in  $\gamma_{EWn}/\gamma_{\ddagger}$  starting at ~1 kPa of H<sub>2</sub>O. The earlier onset pressure of deviations observed on the HPW/Si-MCM-41 sample may be related to its higher acid strength, which we surmise would stabilize H<sub>3</sub>O<sup>+</sup> liberated from the conjugate anion at lower gas-phase H<sub>2</sub>O chemical potentials; a systematic study using POMs of different acid strength would provide clarification, but is beyond the scope of this investigation. The earlier onset of deviations in HPW/Si-MCM-41 has striking consequences for measured  $k_{first}$  values, which are more than one order of magnitude higher than H-Al-Beta zeolites in the  $\gamma_{EWn}/\gamma_{\ddagger} = 1$  regime, but decrease to similar values between 10–75 kPa H<sub>2</sub>O (Figure 8.10a), indicating that solvation by extended hydrogen-bonded H<sub>2</sub>O networks attenuates the benefits of acid strength. The presence of these networks was observed as increasing  $\nu(\text{OH})$  IR peak areas below 3200 cm<sup>-1</sup> on H-Al-zeolites and HPW/Si-MCM-41 at 373 K between 10–75 kPa H<sub>2</sub>O (Figure S53–Figure 8.69, Supporting Information), as observed on H-Al-Beta-F zeolites (Figure 8.6). Similar liquid-phase reactivity of solid acids of different strength was previously observed for dehydration of xylose to furfural (418 K, 0.15 M in H<sub>2</sub>O or  $\gamma$ -valerolactone solvent) with H-Al-Beta zeolites and H<sub>4</sub>SiW<sub>12</sub>O<sub>40</sub> clusters in solution [44].

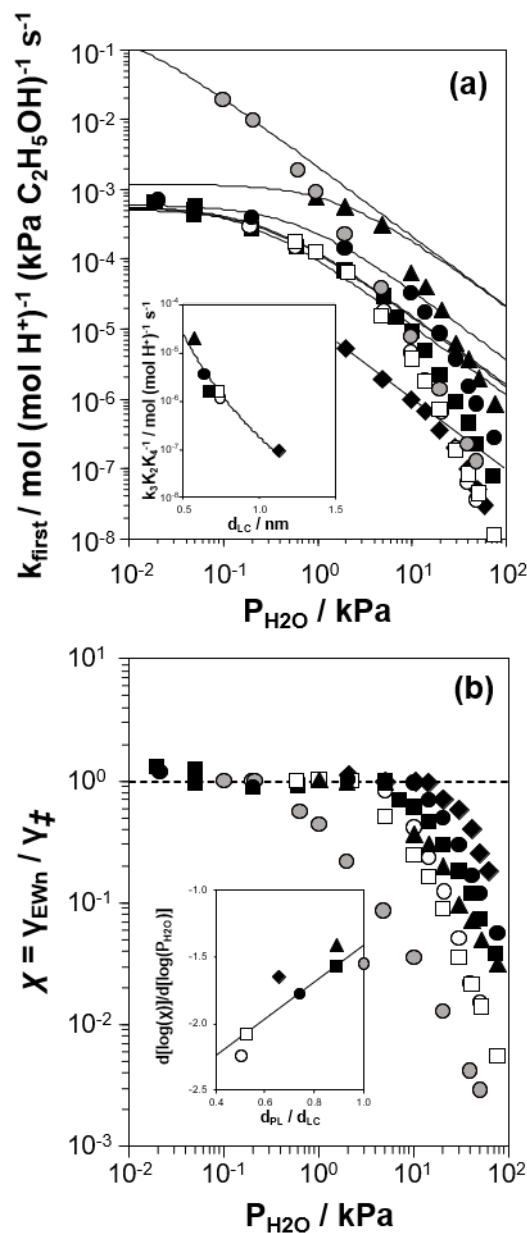


**Figure 8.10:** (a) Apparent first-order bimolecular ethanol dehydration rate constant (per  $\text{H}^+$ , 373 K) and (b) activity coefficient ratio ( $\chi = \gamma_{\text{EWn}}/\gamma_{\ddagger}$ ) from the functional dependence of Eq. 8.7, as a function of  $\text{H}_2\text{O}$  pressure on H-Al-Beta-F(2.0) ( $\blacksquare$ ), H-Al-TON ( $\blacktriangle$ ), H-Al-FAU ( $\blacklozenge$ ), H-Al-MFI ( $\bullet$ ), H-Al-AEI ( $\square$ ), H-Al-CHA ( $\circ$ ), and HPW/Si-MCM-41 ( $\odot$ ). Solid lines in (a) reflect regression of measured rate constants to Eq. 8.7. Inset (a): dependence of  $k_3K_2K_4^{-1}$  values on the largest included sphere diameter of zeolite pores. Inset (b): slopes of the data sets in (b) in the high water pressure limit, as a function of the channel undulation parameter ( $d_{\text{PL}}/d_{\text{LC}}$ ). Solid lines in both insets are to guide the eye.

In addition to the onset pressure of deviations in  $\gamma_{EWn}/\gamma_{\ddagger}$ , its dependence on H<sub>2</sub>O pressure was also compared among samples and quantified as the slope of the data in Figure 8.10b in the high pressure limit,  $d[\log(\chi)]/d[\log(P_{H_2O})]$ . The value of  $d[\log(\chi)]/d[\log(P_{H_2O})]$  is numerically equivalent to the reaction order of  $k_{first}$  in H<sub>2</sub>O plus one, because  $\gamma_{EWn}/\gamma_{\ddagger}$  reflects the deviation from an apparent  $-1$  kinetic order in water. The value of  $d[\log(\chi)]/d[\log(P_{H_2O})]$  was ca.  $-1.5$  for Beta, TON, and FAU zeolites, and HPW/MCM-41, while it was  $-1.8$  for MFI zeolites, and less than  $-2$  for CHA and AEI zeolites (Figure 8.10b inset). The values of  $d[\log(\chi)]/d[\log(P_{H_2O})]$  do not correlate with confinement ( $d_{LC}$ , Figure 8.37, Supporting Information) and are similar regardless of acid strength (cf. HPW/MCM-41, Beta, TON, FAU). In contrast, both CHA and AEI zeolites show  $\chi$  values that decrease more sharply with H<sub>2</sub>O pressure, and possess small-pore window-cage motifs different from the other structures characterized by channels (Beta, TON, MCM-41) or large-pore supercages (FAU). The MFI topology lies in between these two cases because it possesses channels ( $d_{PL} = 0.470$ ) that meet at less-confined intersections ( $d_{LC} = 0.636$ ). These topological differences have been described previously as the undulation parameter [440, 441], expressed as  $d_{PL}/d_{LC}$  (Table 8.2), which correlates with the values of  $d[\log(\chi)]/d[\log(P_{H_2O})]$  (Figure 8.10b inset). The undulation parameter has been invoked to account for the preferential retention of certain reaction products that can undergo additional reactions before egress from the crystallite because of the difficulty of egress through more confining windows [440, 441]. We hypothesize that  $\gamma_{EWn}/\gamma_{\ddagger}$  values that deviate more severely from unity within CHA and AEI zeolites than in channel-based topologies when extended H<sub>2</sub>O networks are formed at high  $P_{H_2O}$  reflect additional barriers to reorganize solvent into adjacent cages through confining windows. The different dependence of water inhibition on zeolite pore topology in regimes that approach liquid-phase catalysis (373 K, 10–75 kPa) and the deviation of  $k_{first}$  values from those expected based on measurements in low water-coverage regimes indicate that the structures of adsorbed solvents within micropores of different size and shape play a significant role in controlling their reactivity.

### 8.3 Conclusions

Ethanol dehydration turnover rates to form diethyl ether (373 K, per  $\text{H}^+$ ) are quantified on H-Al-Beta-F zeolites with 0.11–2.0  $\text{H}^+$  per unit cell under conditions that lead to  $\text{H}^+$  covered by most abundant reactive intermediate species consisting of one  $\text{C}_2\text{H}_5\text{OH}$  molecule and increasing amounts of  $\text{H}_2\text{O}$  ( $2 \times 10^{-3}$ –10 kPa  $\text{C}_2\text{H}_5\text{OH}$ , 0–75 kPa  $\text{H}_2\text{O}$ ), reflected in turnover rates that are first-order in  $\text{C}_2\text{H}_5\text{OH}$  and systematically decrease with  $\text{H}_2\text{O}$  pressure. First-order rate constants (373 K, per  $\text{H}^+$ ) reach  $-1$  order dependences on  $\text{H}_2\text{O}$  pressure ( $<10$  kPa  $\text{H}_2\text{O}$ ) because one water coordinated at  $\text{H}^+$  in MARI clusters must be displaced by ethanol to form the  $\text{S}_{\text{N}}2$  transition state that eliminates diethyl ether, but are inhibited more severely than this  $-1$  order dependence at higher  $\text{H}_2\text{O}$  pressures (10–75 kPa).

Volumetric  $\text{H}_2\text{O}$  isotherms, isosteric heats of adsorption, and *in situ* IR spectra (293 K,  $P/P_0 = 0.1$ –0.75) on H-Al-Beta-F zeolites and their dealuminated analogs indicate that silanol nests and  $\text{H}^+$  stabilize different water structures, where silanol nests predominantly stabilize extended hydrogen-bonded water networks, whereas  $\text{H}^+$  preferentially stabilize  $(\text{H}_3\text{O}^+)(\text{H}_2\text{O})_6$  clusters that then become solvated by extended  $\text{H}_2\text{O}$  networks. *In situ* IR spectra at 373 K under the catalytic conditions of severe  $\text{H}_2\text{O}$  inhibition (10–75 kPa  $\text{H}_2\text{O}$ , 0.05–4.6 kPa  $\text{C}_2\text{H}_5\text{OH}$ ) together with AIMD simulations are consistent with the stabilization of  $(\text{C}_2\text{H}_5\text{OH})(\text{H}_3\text{O}^+)(\text{H}_2\text{O})_{4-5}$  MARI species followed by hydrogen-bonded  $\text{H}_2\text{O}$  networks, and static DFT calculations and metadynamics simulations indicate that the corresponding transition states reside on the periphery of  $\text{H}_2\text{O}$  clusters and thus are accessed without desorbing  $\text{H}_2\text{O}$  from clusters beyond the one  $\text{H}_2\text{O}$  required to be replaced by  $\text{C}_2\text{H}_5\text{OH}$  at the transition state. These observations motivate using non-ideal thermodynamic formalisms to describe the different solvation of MARI and transition states by extended  $\text{H}_2\text{O}$  networks, which lead to severe inhibition of turnover rates because they are disrupted to a greater extent by transition states that contain additional ethyl moieties (than

the MARI) that are less effective at hydrogen bonding, in a manner reminiscent of liquid-phase reactions with positive activation volume [435–438].

The different solvation of reactive intermediates and transition states by water networks extends to Brønsted acid zeolites of different topology (FAU, TON, MFI, CHA, AEI), whose confining pore shapes influence the severity of H<sub>2</sub>O inhibition by changing the ease of solvent reorganization within channel or window-cage motifs. Similar extended hydrogen-bonded H<sub>2</sub>O structures have also been recently identified within the pores of hydrophilic metal-organic frameworks [442, 443], whose diverse topologies may provide an even broader range of solvent structures. Greater insights into the structure of solvents confined in liquid-like phases within microporous zeolite catalysts are provided by kinetics, spectroscopy, and theoretical calculations of gas-phase reaction coordinates under conditions that approach intrapore condensation, because these strategies enable systematic variation of their confined solvent structures. This study highlights the kinetic relevance of H<sub>2</sub>O clusters at H<sup>+</sup> active sites in Brønsted-acid-catalyzed aqueous reactions, and the extended hydrogen-bonded networks that surround them, which are disrupted to different extents by reacting moieties of different size and chemical functionality, and which reorganize differently within pores of different shape.

## 8.4 Experimental Section

### 8.4.1 Zeolite Synthesis and Post-synthetic Treatments

H-Al-Beta-F zeolites were hydrothermally synthesized in fluoride medium with a wide range of Al contents in the gel ( $\text{Si}/\text{Al}_{\text{gel}} = 20\text{--}400$ ) by adapting a procedure reported by Cambor et al. [93] An Al-Beta-OH zeolite sample was hydrothermally synthesized in hydroxide medium as reported by Chang et al. [183] Additional synthetic details are provided in Section 8.6.1.1 of the Supporting Information. These samples are denoted H-Al-Beta-X(Y), where X is the mineralizing agent in the gel (F, OH), and Y is the number of H<sup>+</sup> per unit cell quantified by temperature-programmed

desorption of  $\text{NH}_3$  (Section 8.6.1.5, Supporting Information). As-synthesized zeolites were recovered from synthesis gels by centrifugation, washed thoroughly with deionized water (18.2  $\text{M}\Omega$  cm) and acetone (Sigma-Aldrich,  $\geq 99.5\%$ ), and dried overnight in an oven at 353 K. The dried materials were then treated at 853 K ( $0.0167 \text{ K s}^{-1}$ ) for 10 h in air (UHP, Indiana Oxygen,  $1.67 \text{ cm}^3 \text{ s}^{-1} (\text{g zeolite})^{-1}$ ) in a muffle furnace (Nabertherm LE 6/11).

H-Al-Beta-F zeolites were dealuminated in concentrated nitric acid ( $\text{HNO}_3$ , Avantor, 69%). The zeolite was added to a PFA container, followed by  $\text{HNO}_3$  ( $25 \text{ cm}^3 (\text{g zeolite})^{-1}$ ), then the container was covered and stirred for 16 h at 353 K. The solids were recovered by centrifugation and washed thoroughly with deionized water until the pH of the supernatant was constant, then dried overnight in a 353 K oven. The Al AAS signal (see Section 8.6.1.4, Supporting Information for procedures) was below the detection limit for deAl-Beta-F(0.78), consistent with complete dealumination ( $\text{Si}/\text{Al} > 1500$ ;  $\text{H}^+ \text{ u.c.}^{-1} < 0.04$ ).

H-Al-TON ( $\text{Si}/\text{Al} = 43$ ) was purchased from ACS Materials (MSZ22H12) and used as-received. H-Al-FAU ( $\text{Si}/\text{Al} = 56$ ) was provided by Zeolyst (CBV780) and used as-received. H-Al-MFI ( $\text{Si}/\text{Al} = 43$ ) was provided by Zeolyst (CBV8014) and used as-received. The H-Al-CHA sample ( $\text{Si}/\text{Al} = 15$ ) was synthesized hydrothermally by Di Iorio and Gounder [444] and thoroughly characterized in previous work (SSZ-13(15,0) in Table 1 of Ref. [444]). The H-Al-AEI sample ( $\text{Si}/\text{Al} = 9.5$ ) was synthesized hydrothermally by Albarracin-Caballero et al. [445] and thoroughly characterized in that work (H-AEI in Table 2 of Ref. [445]).

Phosphotungstic acid polyoxometalate clusters were supported on Si-MCM-41 (Sigma-Aldrich #643645,  $0.98 \text{ cm}^3 \text{ g}^{-1}$  total pore volume) using incipient wetness impregnation. Si-MCM-41 was dried in a 353 K oven prior to use.  $\text{H}_3[\text{P}(\text{W}_3\text{O}_{10})_4] \cdot x\text{H}_2\text{O}$  (Sigma-Aldrich #P4006) was dissolved in deionized water to generate a 5 wt% solution. This solution was added dropwise to 1.11 g of dried Si-MCM-41 to the point of incipient wetness (1.15 g solution total). The resulting solid was dried overnight in an oven at 353 K and stored in a vial at ambient conditions prior to use.

#### 8.4.2 Characterization of Zeolites

Routine characterizations, including powder X-ray diffraction, N<sub>2</sub> and H<sub>2</sub>O adsorption, atomic absorption spectroscopy, inductively coupled plasma optical emission spectrometry (ICP-OES), and temperature-programmed desorption of NH<sub>3</sub>, are described in Section 8.6.1 of the Supporting Information.

Infrared spectra of H<sub>2</sub>O adsorbed within zeolites were collected as a function of relative pressure ( $P/P_0 = 0.1\text{--}0.75$ ) using procedures described previously [57, 406]. Spectra were collected at 293 K on a Nicolet 4700 spectrometer using a quartz cell and heated block assembly [184] described in our prior work [57, 406]. Si-Beta-F, H-Al-Beta-F, and deAl-Beta-F zeolites (0.020–0.050 g) were pressed into self-supporting wafers with a 0.9 cm radius, loaded into the IR cell, and pretreated in flowing dry air (<1 ppm of CO<sub>2</sub>, 200 K water dew point, Parker Balston, 18–45 cm<sup>3</sup> g<sup>-1</sup> s<sup>-1</sup>) to 823 K (0.083 K s<sup>-1</sup>) for 1 h, then cooled in flowing He (UHP, Indiana Oxygen, 18–45 cm<sup>3</sup> g<sup>-1</sup> s<sup>-1</sup>) to 293 K. Temperature was controlled at 293 K by flowing H<sub>2</sub>O at 288 K through channels in the block with a recirculating chiller, and resistive heating.

A spectrum was collected of the wafer at 293 K under flowing He (18–45 cm<sup>3</sup> g<sup>-1</sup> s<sup>-1</sup>) to be used as a reference before H<sub>2</sub>O adsorption. Then, the same He flow was redirected through a heated (>363 K) line connected to a glass syringe (1 cm<sup>3</sup>, Hamilton) containing deionized water. Transfer lines after the syringe leading to the cell were heated to >363 K to prevent condensation. The flow rate of the liquid H<sub>2</sub>O was controlled via syringe pump (KD Scientific Legato 100) to give an H<sub>2</sub>O pressure of 0.2 kPa ( $P/P_0 = 0.1$ , 293 K). Care was taken to slowly introduce the liquid H<sub>2</sub>O through the dead volume ( $\sim 20\text{--}100 \times 10^{-3}$  cm<sup>3</sup>) connecting the syringe to the line to prevent exposing the wafer to a H<sub>2</sub>O partial pressure higher than 0.2 kPa. Spectra were collected continuously (600 s per scan), and the wafer was held at 293 K in the 0.2 kPa H<sub>2</sub>O stream for 4 h after H<sub>2</sub>O introduction to ensure equilibration, which was verified by invariant spectra collected at the end of this time period. The H<sub>2</sub>O flow rate was adjusted to give partial pressures of 0.5 kPa, 1.2 kPa, and 1.7 kPa,

corresponding to  $P/P_0 = 0.2, 0.5,$  and  $0.75$  (at 293 K), and 2 h were allowed at each condition for equilibration (verified by invariant spectra). This procedure was first performed with an empty cell to obtain signals for gas-phase  $H_2O$  at each  $P/P_0$  value. A background spectrum of the empty cell before  $H_2O$  introduction was used as the reference for all other collected spectra. The processing of spectra to give the signal for adsorbed  $H_2O$ , and any changes to the vibrations associated with the zeolite, is illustrated in Figure 8.45.

Spectra were collected in separate experiments at 373 K on a Bruker Vertex 70 spectrometer using a low-dead-volume cell developed by Ribeiro and coworkers [446]. Self-supporting wafers of H-Al-zeolites (0.015–0.030 g) were loaded into a 304 stainless-steel sample holder with a 1.5 cm diameter hole through the center to allow the IR beam to pass through, and gas inlet and outlet channels that direct flow over the wafer. The sample holder is loaded within the cell body, followed by a retainer ring and  $CaF_2$  window. A custom-made graphite ferrule placed around the window in contact with the retainer ring is held in place by a ferrule backer with 8 screws tightened with a torque screwdriver to 14 in  $lb_f$ . The same  $CaF_2$  window-ferrule-backer assembly completes the seal on the reverse side of the cell. The cell is housed within an aluminum block equipped with cartridge heaters, and a thermocouple within the cell in contact with the sample holder is used for temperature control. Wafers were pretreated in flowing  $N_2$  (UHP, Indiana Oxygen,  $22\text{--}44\text{ cm}^3\text{ g}^{-1}\text{ s}^{-1}$ ) to 573 K ( $0.083\text{ K s}^{-1}$ ) for 1 h, then cooled to 373 K ( $0.033\text{ K s}^{-1}$ ). All transfer lines before and after the cell were heated to  $>383\text{ K}$  to prevent  $H_2O$  condensation. Two three-way valves were switched to redirect the  $N_2$  flow through lines connected at a tee to a  $50\text{ cm}^3$  syringe containing liquid  $H_2O$ , which was infused by syringe pump (Legato 100) to give a pressure of 10 kPa  $H_2O$ . The flow rate was adjusted to give pressures of 20, 50, and 75 kPa  $H_2O$ , and equilibration times, collection, and processing of spectra were identical to those described at 293 K. In some experiments, lower  $H_2O$  pressures were initially equilibrated over the sample (1–2 kPa). In a separate experiment,  $C_2H_5OH/H_2O$  mixtures were also loaded into the syringe while feeding

the same H<sub>2</sub>O pressures (C<sub>2</sub>H<sub>5</sub>OH/H<sub>2</sub>O = 0.005 (10, 20 kPa H<sub>2</sub>O) and 0.03 (50, 75 kPa H<sub>2</sub>O))).

### 8.4.3 Ethanol Dehydration Kinetics

The kinetics of bimolecular ethanol dehydration to diethyl ether were measured in a differential packed-bed reactor system described previously [227, 447]. Zeolites (0.020–0.199 g) were pelleted, crushed, and sieved to retain aggregates between 180–250 μm, and supported between two plugs of acid-washed quartz wool (W.R. Grace, washed with 1 M HNO<sub>3</sub> at ambient temperature for 16 h) within a tubular quartz reactor (7 mm i.d.). Zeolites were pretreated in flowing 5% O<sub>2</sub>/He (UHP, Indiana Oxygen, 16.67 cm<sup>3</sup> (g zeolite)<sup>-1</sup> s<sup>-1</sup>) at 773 K (0.0833 K s<sup>-1</sup>) for 4 h, then cooled to reaction temperature, typically 373 K (0.0333 K s<sup>-1</sup>), in flowing He (UHP, Indiana Oxygen, 16.67 cm<sup>3</sup> (g zeolite)<sup>-1</sup> s<sup>-1</sup>). Liquid C<sub>2</sub>H<sub>5</sub>OH (Sigma-Aldrich, anhydrous, >99.5%) and deionized water were loaded into glass syringes (1 cm<sup>3</sup>, 10 cm<sup>3</sup>, 50 cm<sup>3</sup>, Hamilton 1000 series) and fed via syringe pumps (KD Scientific Legato 100) into separate He streams (heated lines >383 K) flowing at approximately equal rates, and mixed at a tee upstream of the reactor. Reactant and product concentrations were measured by a gas chromatograph (Agilent 6890) equipped with a capillary column (HP-PLOT-Q, 30 m × 530 μm × 40 μm) and flame ionization detector. Diethyl ether was the only product detected under all conditions. Prior to reaction, the composition of the feed stream was verified from bypass injections while the zeolite was held in flowing He (16.67 cm<sup>3</sup> (g zeolite)<sup>-1</sup> s<sup>-1</sup>) at reaction temperature for 1 h. The pressures of C<sub>2</sub>H<sub>5</sub>OH (2 × 10<sup>-3</sup>–10 kPa) and H<sub>2</sub>O (0–75 kPa) were varied non-systematically over the course of the experiment. A period of 4–12 h was allowed at a given condition to reach a steady state, as verified by measured rates that did not systematically increase or decrease with time-on-stream. Reported rates represent an average of values over at least 1.5 h at steady state. No deactivation was detected over the course of kinetic measurements (~7–21 days), verified by periodically returning to a reference condition (5 kPa C<sub>2</sub>H<sub>5</sub>OH, 50 kPa H<sub>2</sub>O).

At the end of kinetic measurements on H-Al-Beta, H-Al-FAU, and HPW/Si-MCM-41 catalysts,  $H^+$  were titrated *in situ* with 2,6-di-*tert*-butylpyridine (DTBP, Sigma-Aldrich,  $\geq 97\%$ ) at 378 K. A solution of  $C_2H_5OH$  and deionized water with a  $C_2H_5OH/H_2O$  molar ratio of 5 was fed to the catalyst in flowing He to reach a measured steady-state rate at 5 kPa  $C_2H_5OH$  and 1 kPa  $H_2O$ . Simultaneously, a second feed stream was prepared in lines bypassing the reactor containing the same  $C_2H_5OH$  and  $H_2O$  pressures, and additionally  $0.5\text{--}2 \times 10^{-3}$  kPa of DTBP titrant. Prior to reaching steady-state in the reactor, the composition of the DTBP-containing stream was verified with GC injections. The pressure drop in the DTBP-containing stream was equalized with that of the reactor-to-GC stream with a metering valve in the bypass line. After reaching steady-state, the DTBP-containing stream was introduced to the reactor by switching a multi-position valve, and the cumulative uptake of DTBP was quantified by its disappearance relative to its measured bypass concentration while simultaneously quantifying the diethyl ether formation rate. After suppression of measured rates, the irreversibility of titration was confirmed by observing no recovery of measured rates or desorption of DTBP after returning the DTBP-free stream to the reactor. A titration was also performed at 0.7 kPa  $C_2H_5OH$  and 30 kPa  $H_2O$  on H-Al-Beta-F(2.0) by the same procedure, using liquid feeds of different composition.

#### 8.4.4 Theoretical Methods

Static DFT calculations were performed using VASP [133,134,136] and are similar to those we have reported previously [180]. The BEEF-vdW functional was used along with a 520 eV cutoff energy, and a force convergence criteria of 0.02 meV  $\text{\AA}^{-1}$ . The entropies of reactive intermediates were calculated using the Campbell-Sellers equation [163,448], where adsorbates were treated like a 2-D gas. From AIMD simulations adsorbates in H-Beta were found to have large diffusion distances, due in part to interaction with the acidic proton. The Campbell-Sellers equation may not be rigorously accurate for all adsorbed molecules, and additional AIMD and usage of the VDOS or decomposition of harmonic frequencies into translational and rotational

partition functions would be more accurate; however, the treatments used here are sufficient to identify the relevance of reactive intermediates and transition states under solvating conditions.

AIMD simulations were performed with VASP, with an NVT Nose-Hoover thermostat [365, 449]. Water structures were heated, and then equilibrated at 373 K for at least 10 ps at a timestep of 1 ps. Production runs were performed for 20 ps. All hydrogen atoms were deuterated. The same settings were used upon introducing ethanol to the system. The potential energy and temperature of the systems were monitored and found to fluctuate normally around the mean temperature and energy. The entropy of solvated water molecules was more complicated than reported previously in Sn-Beta [406]. The acidic proton could transfer among water molecules, preventing the participation of individual degrees of freedom for each water molecule. It was assumed that the proton entropy is constant, and so at each timestep the acidic proton was removed. This was performed in a python code that detects which water molecule is a hydronium, and then removes the hydrogen with the longest O-H bond length from the simulation. At most, only one proton exists in the simulation, so each water molecule is scanned to find the hydronium ion. The water molecules were partitioned and the root-mean-squared (RMS) diffusion of each water molecule was calculated according to the technique of Alexopoulos et al. [127] to yield the 3-D translational entropy of water. The same technique was used to calculate the translational entropy of ethanol molecules introduced into the system. See Section 8.6.2.6 in the Supporting Information for additional discussion of the entropy calculations.

Metadynamics simulations were performed in VASP using similar approaches as the AIMD. The thermostat and masses were the same as the AIMD calculations. The positions and trajectories from the AIMD thermodynamic calculations were used to ensure a well-equilibrated simulation. The control variables (CVs) were defined to be a carbon-oxygen bond distance of a carbon belonging to one ethanol and a carbon-oxygen bond distance of the same carbon and the oxygen atom of the second ethanol. Thus, at the transition state both C-O bond distances would be equivalent.

Both types of C-O bonds are constrained to a maximum bond distance of 5 Å as the primary interest is to study the structure of the transition state, and not an excessively large number of reactant and product states. The constraints are relaxed enough to allow for restructuring of solvent around the C-O bonds, which provides space for additional water molecules to participate in the transition states. Thus, the choice of control variables does not bias the mechanism by which C-O bonds are broken and reformed in the simulation. Gaussian hills were added every 70 fs with a height of 50 meV and width of 75 meV. These parameters were chosen based on test calculations in the gas phase where the approximate width and height of the barriers would ensure the Gaussians provided a slowly varying differential change in the free energy surface to ensure that an approximately canonical ensemble is preserved as the energy of the system is raised to the transition state. Convergence of the algorithm would occur when the potential energy surface is filled to become flat, which would be indicated by multiple crossings of the transition state. Analysis of the free energy surface is performed using a python code that maps each Gaussian from VASP into a matrix to be plotted. To identify the minimum energy path between basins, a modified version of Dijkstra's search algorithm was used. In short, the free energy surface is discretized into a graph data structure where points of a specified height are connected to neighboring points. By specifying a range of start and end nodes from basins in the free energy diagram, Dijkstra's algorithm is a shortest-path tree algorithm that then finds the minimum total energy path to connect the reactant and product basin. Dijkstra's algorithm can be generalized into higher-dimensional space by increasing the number of neighboring nodes.

## 8.5 Acknowledgements

J.B. and R.G. acknowledge financial support from the Ralph W. and Grace M. Showalter Research Trust and a 3M Non-Tenured Faculty Award. We thank John Di Iorio and Claire Nimlos for providing H-CHA and H-AEI zeolites, Juan-Carlos Vega-Vila for updating and maintaining *in situ* IR heating blocks, Claire Nimlos for

assistance with ICP-OES measurements, and Jamie Harris, John Di Iorio, Trevor Lardinois, and Siddarth Krishna for helpful technical discussions and feedback.

## 8.6 Supporting Information

### 8.6.1 Supplementary Methods

#### 8.6.1.1 Hydrothermal syntheses of zeolites

Si-Beta-F was synthesized using tetraethylammonium fluoride dihydrate (TEAF) as the structure-directing agent and fluoride source following reported procedures [106]. TEAF (Alfa Aesar, 97%, 5.1 g) was dissolved in deionized water (18.2 M $\Omega$  cm, 5.5 g) in a perfluoroalkoxy alkane (PFA) container with a Teflon stir bar. Tetraethyl orthosilicate (TEOS, Sigma Aldrich, 98%, 10.3 g) was added to the PFA container, and the mixture was covered and homogenized overnight at ambient conditions to completely hydrolyze TEOS. Then, the mixture was uncovered until ethanol completely evaporated from the mixture, and some water. Deionized water was added to the mixture to achieve a gel with molar composition 1 SiO<sub>2</sub>/0.55 TEAF/6.7 H<sub>2</sub>O, and the mixture was transferred into a 45 cm<sup>3</sup> Teflon-lined stainless-steel autoclave and heated to 413 K for 11 days in an isothermal rotating oven (Yamato DKN-402C).

H-Al-Beta-F zeolites were synthesized following the procedure of Cambor et al. [93] TEOS (10 g) was mixed with tetraethylammonium hydroxide (TEAOH, Sachem, 35%, 10.7–11.7 g) in a PFA container and homogenized while covered for 2 h. Aluminum isopropoxide powder (Al(O-*i*-Pr)<sub>3</sub>, Sigma Aldrich, 98%, 0.03–0.5 g) and excess deionized water (> 10 g) were added to the mixture, which was covered and stirred overnight to completely hydrolyze TEOS and Al(O-*i*-Pr)<sub>3</sub>. The mixture was uncapped in order to completely evaporate ethanol and isopropanol and partially evaporate water to reach the desired molar ratio. Then, hydrofluoric acid solution (Sigma Aldrich, 48%, 1.1 g) was added and the mixture was homogenized with a PTFE spatula to yield a thick gel with molar composition 1 SiO<sub>2</sub>/(0.54+x) TEAOH/(0.54+x) HF/x Al/(7+x) H<sub>2</sub>O, where  $x = 0.0025\text{--}0.05$  to achieve molar ratios of Si/Al = 20–500

in synthesis gels. (Caution: when working with hydrofluoric acid, use appropriate personal protective equipment, ventilation, and other engineering controls.) The gel was loaded into a 45 cm<sup>3</sup> Teflon-lined stainless-steel autoclave and heated to 413 K for 7 days in an isothermal rotating oven.

Al-Beta-OH was synthesized hydrothermally in hydroxide media as reported in the literature [183]. TEAOH (15.1 g) and Ludox HS-30 colloidal silica (Sigma Aldrich, 30%, 20 g) were added to a PFA container and stirred covered for 1 h at ambient conditions. Then, sodium hydroxide (NaOH, Avantor, 98%, 0.11 g) was dissolved in deionized water (4.4 g), and this mixture was added to the gel, followed by Al(O-*i*-Pr)<sub>3</sub> (0.21 g). The gel was stirred covered for 24 h at ambient conditions, then uncovered to completely evaporate isopropanol, and partially evaporate water to achieve the desired molar composition of 1 SiO<sub>2</sub>/0.01 Al<sub>2</sub>O<sub>3</sub>/13.24 H<sub>2</sub>O/0.18 TEAOH/0.014 Na<sub>2</sub>O. The gel was transferred into a 45 cm<sup>3</sup> Teflon-lined stainless-steel autoclave and heated statically in an isothermal oven at 413 K for 7 days.

As-synthesized zeolites were recovered and treated as described in the Main Text.

H-Al-Beta-F(0.57) (0.4 g) was exchanged with 1M NaCl (165 g solution (g zeolite)<sup>-1</sup>) for 24 h at ambient temperature in a stirred, sealed PFA container. The final pH of the exchange solution was 3.0. The solid was recovered by centrifugation and washed four times with deionized water (~35 cm<sup>3</sup> per wash), and dried overnight in a 353 K oven. The resulting solid is referred to as Na-Al-Beta-F(0.57).

#### 8.6.1.2 X-Ray diffraction

Powder X-ray diffraction (XRD) patterns were collected with a Rigaku Smartlab X-ray diffractometer with a Cu K $\alpha$  X-ray source in the range of  $2\theta = 4\text{--}40^\circ$  with a step size of  $0.01^\circ$  and scan speed of  $0.005^\circ \text{ s}^{-1}$ .

### 8.6.1.3 Volumetric N<sub>2</sub> and H<sub>2</sub>O adsorption isotherms

N<sub>2</sub> and H<sub>2</sub>O adsorption isotherms were collected on a Micromeritics ASAP 2020 instrument. Samples were pelleted and sieved to retain 180–250 μm aggregates, and 0.010–0.040 g were degassed by heating to 393 K for 2 h then 623 K for 10 h under dynamic vacuum (<0.67 Pa) before adsorption measurements. N<sub>2</sub> adsorption isotherms were collected at 77 K by immersion in a liquid N<sub>2</sub> bath, and H<sub>2</sub>O adsorption isotherms were collected at 283–302 K by immersion in a recirculating chiller bath held at 283–302 K. H<sub>2</sub>O was introduced from the vapor phase generated from a flask held at 313 K containing deionized water, after degassing by three freeze-pump-thaw cycles. N<sub>2</sub> micropore volumes were determined at the uptake corresponding to the minimum value of  $\partial V_{\text{ads}}/\partial \log(P/P_0)$ .

### 8.6.1.4 Atomic absorption spectroscopy and inductively coupled plasma optical emission spectrometry

The bulk mass fraction of Al in zeolite samples was obtained by atomic absorption spectroscopy (AAS). 0.03 g of powder were digested with 2 g of HF (Sigma Aldrich, 48%) overnight, then diluted with 50 g of deionized water. Calibration standards were prepared by diluting a stock solution (Sigma Aldrich, 1000 ± 4 ppm Al) with deionized water. A PerkinElmer AAnalyst 300 instrument equipped with a lamp for Al (309.3 nm) was used to measure the absorbance of the standards and digested samples. Si/Al ratios were calculated assuming the unit cell formula of each zeolite.

For ICP-OES, the same digestion procedures were performed, then in addition 1.5 g of HNO<sub>3</sub> (70%, Sigma-Aldrich) were added to the solutions. In some cases, these solutions were further diluted with deionized water to reach the desired concentration range of the calibration standards. ICP-OES measurements were performed on a Thermo Scientific iCAP 7000 Plus Series spectrometer. ICP-OES was used to quantify P (177.5 nm) and W (224.9 nm) in HPW/Si-MCM-41, and the mol POM g<sup>-1</sup> was assumed to be equivalent to the mol P g<sup>-1</sup>. Al (309.3 nm) was also quantified by ICP

on H-Al-FAU and H-Al-TON. All other reported elemental analyses were performed by AAS.

#### 8.6.1.5 Temperature-programmed desorption of $\text{NH}_3$

$\text{NH}_3$ -TPD was performed on H-Al-Beta samples after aqueous-phase ion-exchange at 353 K with 1 M  $\text{NH}_4\text{NO}_3$  in deionized water (24 h,  $100 \text{ cm}^3$  solution  $(\text{g zeolite})^{-1}$ ). All other zeolite topologies were exchanged at ambient temperature in aqueous 1 M  $\text{NH}_4\text{NO}_3$  (24 h,  $100 \text{ cm}^3$   $(\text{g zeolite})^{-1}$ ). Zeolites were recovered from ion-exchange solutions by centrifugation and washed thoroughly with deionized water, then dried in a 353 K oven overnight.  $\text{NH}_3$ -TPD was performed as described by Di Iorio et al. [450] In short, zeolites were supported between two quartz wool plugs within a U-shaped quartz tube, loaded into a Micromeritics Autochem II 2920, and heated in flowing He to 873 K ( $0.167 \text{ K s}^{-1}$ ). The  $\text{NH}_3$  evolved was detected using a Agilent 5975C mass selective detector, and quantified by the  $m/z = 17$  signal, after correction for the contribution from water present in a constant proportion to its signal at  $m/z = 18$ . A pulse of Ar ( $m/z = 40$ ) was used as an external standard for calibration to correct for drift in the MS signal over time.

### 8.6.2 Supplementary Discussion

#### 8.6.2.1 Validity of differential bed assumption in the absence of co-fed water

Figure 8.21 shows the fractional conversion of  $\text{C}_2\text{H}_5\text{OH}$  as a function of site-contact time on H-Al-Beta-F(2.0) and H-Al-Beta-OH(1.7) at 373 K without co-fed  $\text{H}_2\text{O}$ . Because they are not co-fed, both diethyl ether and  $\text{H}_2\text{O}$  gradients are present across the catalyst bed; however, linear dependences of conversion on site-contact time through the origin confirm the differential reactor bed assumption. In other words, varying the site-contact time effectively changes the average concentration of products within the bed, but does not affect the reaction rate because their concentrations are sufficiently small so as not to affect coverage terms in rate expressions. Rates were

collected on H-Al-Beta-F(1.2) at values of site-contact time and conversion lower than those verified here as differential, and are therefore also differential. Under these conditions,  $P_{\text{H}_2\text{O, outlet}} < 4 \times 10^{-4}$  kPa. In all experiments with co-fed water, the amount co-fed was in excess of that produced by the reaction, and conversions were <5%, consistent with the conditions of differential operation.

#### 8.6.2.2 Comparison with 1-propanol dehydration at 0.53 and 2 kPa of water

Figure 8.30 shows the bimolecular ethanol dehydration rate data measured as a function of ethanol and water pressure at 423 K on H-Al-Beta-F(1.2), and directly compares this with bimolecular 1-propanol dehydration to form di-*n*-propyl ether at 423 K on H-Al-MFI reported by Zhi et al. [177] Turnover rates are higher in the case of 1-propanol on H-Al-MFI, likely because the larger 1-propanol dehydration transition state is more effectively stabilized by van der Waals contacts with the confining pore environment than that of ethanol dehydration. Notably, Zhi et al. observed no dependence of turnover rates on co-fed H<sub>2</sub>O pressures between 0.53–2.0 kPa; however, the rate data in Figure 8.30 indicates that the reaction order in 1-propanol ranged between a maximum value of 0.5–0.7 ( $P_{\text{C}_3\text{H}_7\text{OH}} = 0.1\text{--}0.25$  kPa) and a minimum value of 0–0.1 ( $P_{\text{C}_3\text{H}_7\text{OH}} = 3\text{--}4$  kPa), meaning that under all conditions H<sup>+</sup> were partially covered by propanol-propanol dimer species. Under similar conditions, measured bimolecular ethanol dehydration turnover rates were invariant at 0.5 and 2.5 kPa H<sub>2</sub>O, and 0.5 kPa C<sub>2</sub>H<sub>5</sub>OH, consistent with the observations of Zhi et al. Yet, reaching first-order regimes in C<sub>2</sub>H<sub>5</sub>OH at 2.5 kPa of H<sub>2</sub>O required lowering the C<sub>2</sub>H<sub>5</sub>OH pressure to <0.01 kPa ( $P_{\text{C}_2\text{H}_5\text{OH}}/P_{\text{H}_2\text{O}} < 0.005$ ). Under conditions where H<sup>+</sup> in Beta zeolites were covered strictly by species involving only one ethanol, rates systematically decreased with increasing H<sub>2</sub>O pressure, suggesting that the lack of systematic dependence observed by Zhi et al. resulted from partial coverage by alcohol dimers ( $P_{\text{C}_3\text{H}_7\text{OH}}/P_{\text{H}_2\text{O}} > 0.03$ ), and that such a dependence would be recovered if the  $P_{\text{C}_3\text{H}_7\text{OH}}/P_{\text{H}_2\text{O}}$  ratio was lowered either by decreasing the 1-propanol pressure or increasing the H<sub>2</sub>O pressure.

### 8.6.2.3 Assessment of intraparticle transport corruptions

According to the Madon-Boudart criterion [196], measured reaction rates are free from transport corruptions when they are independent of active site density, and if the reaction is exothermic, this observation is required at two different temperatures. The latter prescription by Madon and Boudart stems from the expected dependence of the effectiveness factor on the Thiele modulus in the case where intraparticle temperature gradients are present; however, the low reactant conversions measured here (<0.2% between 10–75 kPa H<sub>2</sub>O at 373 K on H-Al-Beta-F(2.0)) and mildly exothermic enthalpy of reaction for bimolecular ethanol dehydration to diethyl ether and water (–24 kJ mol<sup>–1</sup>) make intraparticle temperature gradients unlikely. The values of  $k_{\text{first}}$  at 373 K on four different H-Al-Beta samples with H<sup>+</sup> densities spanning approximately  $1\text{--}4 \times 10^{-4}$  H<sup>+</sup> g<sup>–1</sup> (as quantified during catalysis by 2,6-di-*tert*-butylpyridine titrations) are shown at water pressures between 10–75 kPa in Figure 8.28. Under these conditions, where  $k_{\text{first}}$  values deviate from their expected dependence on water pressure,  $k_{\text{first}}$  values are invariant with H<sup>+</sup> density, which is consistent with kinetically limited rate measurements as described by the Madon-Boudart criterion.

Intraparticle transport corruptions were further assessed using the Mears criterion [203]. Measured reaction rates are kinetically limited when they are significantly lower than the estimated diffusion rate per catalyst particle:

$$\frac{Rr_p^2}{C_s D_e} < \frac{1}{|n|} \quad (8.17)$$

where R is the reaction rate (per particle volume) for an n<sup>th</sup> order reaction ( $R=kC_s^n$ ),  $r_p$  is the particle radius,  $C_s$  is the reactant concentration at the external surface of the particle, and  $D_e$  is the effective diffusivity of the reactant within the particle. The reaction rate per particle volume is computed using the measured reaction rate per mass, and assuming the framework density of zeolite Beta ( $15.3 \text{ Si } (1000 \text{ \AA}^3)^{-1} = 1.53 \times 10^6 \text{ g m}^{-3}$ ). The particle radius was conservatively estimated as 1.5 μm, because the largest crystallites observed in SEM images of H-Al-Beta-F samples by Cambior

et al. [93] were 3  $\mu\text{m}$  in diameter (belonging to a sample with Si/Al = 200, higher Al content samples had smaller crystallites). The surface concentration of  $\text{C}_2\text{H}_5\text{OH}$  was assumed to be equivalent to the bulk gas-phase concentration because large aggregates were not present in the catalyst bed (sieved to 180–250  $\mu\text{m}$  aggregates) and thus interparticle gradients are not expected. The effective diffusivity of  $\text{C}_2\text{H}_5\text{OH}$  was taken to be  $2 \times 10^{-11} \text{ m}^2 \text{ s}^{-1}$ , which was the minimum value calculated in molecular dynamics simulations of 50/50  $\text{C}_2\text{H}_5\text{OH}/\text{H}_2\text{O}$  mixtures in FAU zeolites at 300 K up to adsorbed densities commensurate with pore filling [204]. This is also a conservative estimate because diffusivities would be higher at 373 K. Taken together, the Mears criterion values calculated with these conservative estimates are  $< 10^{-2}$  under all water pressure conditions where measured  $k_{\text{first}}$  values deviated from their expected dependence ( $> 10 \text{ kPa H}_2\text{O}$ , Figure S19). Thus, these deviations are not a result of transport limitations.

#### 8.6.2.4 Derivation of the relative rates of dissociative and associative pathways

Refer to Figure 8.7 in the main text for the identity of each intermediate and transition state.

The rate of the dissociative pathway is assumed equal to the rate of ethoxy formation:

$$r_{\text{dissoc}} = k_d(E^*) \quad (8.18)$$

where  $k_d$  is the intrinsic rate constant that reflects the free energy of activation (TS2, Figure 8.7, Main Text) to form ethoxy from the ethanol monomer. The assumption of Eq. 8.18 is reasonable because the second step of the associative pathway (TS3) has an intrinsic free energy barrier that is 36  $\text{kJ mol}^{-1}$  lower than the first step. The rate of the associative pathway proceeds from ethanol-ethanol dimer species:

$$r_{\text{assoc}} = k_a(\text{EE}^*) \quad (8.19)$$

where  $k_a$  is the intrinsic rate constant that reflects the free energy of activation to form the  $S_N2$  elimination transition state (TS1, Figure 8.7, Main Text) from the ethanol-ethanol dimer. Assuming quasi-equilibrated adsorption of gas-phase ethanol to form the ethanol-ethanol dimer:

$$r_{\text{assoc}} = k_a K_D (E^*) P_{C_2H_5OH} \quad (8.20)$$

where  $K_D$  is the thermodynamic equilibrium constant to adsorb gas-phase ethanol at the ethanol monomer to form the ethanol-ethanol dimer. Dividing 8.18 by 8.20 gives:

$$\frac{r_{\text{dissoc}}}{r_{\text{assoc}}} = \frac{k_d}{k_a K_D P_{C_2H_5OH}} \quad (8.21)$$

The rate and equilibrium constants may be written in terms of the free energies of intermediates and transition states in Figure 8.7 of the Main Text:

$$k_d = \frac{k_B T}{h} \exp\left(\frac{-(\Delta G^\circ_{TS2} - \Delta G^\circ_{E^*})}{RT}\right) \quad (8.22)$$

$$k_a = \frac{k_B T}{h} \exp\left(\frac{-(\Delta G^\circ_{TS1} - \Delta G^\circ_{EE^*})}{RT}\right) \quad (8.23)$$

$$K_D = \exp\left(\frac{-(\Delta G^\circ_{EE^*} - \Delta G^\circ_{E^*} - \Delta G^\circ_{E(g)})}{RT}\right) \quad (8.24)$$

Combining 8.21 with 8.22–8.24 gives:

$$\frac{r_{\text{dissoc}}}{r_{\text{assoc}}} = \exp\left(\frac{\Delta G^\circ_{TS1} + \Delta G^\circ_{E(g)} - \Delta G^\circ_{TS2}}{RT}\right) P_{C_2H_5OH}^{-1} \quad (8.25)$$

where  $\Delta G^\circ_i$  are standard-state free energies of component  $i$  ( $\text{kJ mol}^{-1}$ ), and the units of  $P_{C_2H_5OH}$  are bar. The values of  $\Delta G^\circ_i$  from Figure 8.7 in the Main Text predict that the rate of the dissociative pathway in the absence of water exceeds that of the associative pathway at  $P_{C_2H_5OH} < 0.02$  kPa (Figure 8.70); however, the precise pressure at which this transition occurs is subject to error in DFT-calculated free

energies which can be on the order of 10 kJ mol<sup>-1</sup> [124, 451]. By analogy, the same relationship as in Eq. 8.25 exists for the dissociative and associative pathways with one co-adsorbed H<sub>2</sub>O molecule shown in Figure 8.71, whose transition states differ by an amount (25 kJ mol<sup>-1</sup>) almost identical to the water-free case (26 kJ mol<sup>-1</sup>), meaning that a similar transition point (0.02 kPa C<sub>2</sub>H<sub>5</sub>OH) would be predicted with co-adsorbed H<sub>2</sub>O.

Considering the reaction orders in ethanol measured experimentally, and the expected prevalent surface coverages brings clarity to the question of the dominant pathway. In either case with or without co-fed H<sub>2</sub>O, experimentally, rate data collected under conditions where P<sub>C<sub>2</sub>H<sub>5</sub>OH</sub> < 0.02 kPa are approximately first-order in C<sub>2</sub>H<sub>5</sub>OH, which would reflect either dominant associative pathways with an ethanol monomer-saturated surface, or dominant dissociative pathways with a completely vacant surface. If the adsorption free energy to form an ethanol monomer (E\*) is 49 kJ mol<sup>-1</sup>, as predicted by DFT, then this allows estimating its equilibrium constant:

$$K_{E^*} = \exp\left(\frac{-\left(\Delta G^\circ_{E^*} - \Delta G^\circ_* - \Delta G^\circ_{E(g)}\right)}{RT}\right) \quad (8.26)$$

which gives a value of 7 × 10<sup>6</sup> at 373 K. Assuming the MARI are (\*) and (E\*), the coverage of E\* is given by:

$$\theta_{E^*} = \frac{K_{E^*} P_{C_2H_5OH}}{1 + K_{E^*} P_{C_2H_5OH}} \quad (8.27)$$

where  $K_{E^*}$  is given by Eq. 8.25, and P<sub>C<sub>2</sub>H<sub>5</sub>OH</sub> has units of bar. Eq. 8.27 predicts that H<sup>+</sup> are not vacant under any experimentally-tested condition at 373 K (Figure 8.70b), but are rather covered by ethanol monomers (E\*) or (C<sub>2</sub>H<sub>5</sub>OH)(H<sup>+</sup>)(H<sub>2</sub>O)<sub>n</sub> species (Figure 8.6, Main Text). In this case, only associative mechanisms would give first-order kinetics, and so it is concluded that dissociative mechanisms are not kinetically relevant under the conditions of experimental rate measurements (373 K, 2 × 10<sup>-3</sup>–10 kPa C<sub>2</sub>H<sub>5</sub>OH, 0–75 kPa H<sub>2</sub>O).

### 8.6.2.5 Derivation of the apparent free energies of activation in different coverage regimes

The rate and equilibrium constants in this derivation correspond to those shown in Figure 8.2 in the Main Text, with the adsorbed intermediates abbreviated as:  $(\text{C}_2\text{H}_5\text{OH})_2\text{H}^+ = \text{EE}^*$ ,  $\text{C}_2\text{H}_5\text{OH}\cdots\text{H}^+ = \text{E}^*$ , and  $\text{C}_2\text{H}_5\text{OH}\cdots\text{H}^+\cdots\text{H}_2\text{O} = \text{EW}^*$ .

According to transition state theory,  $k_3$  can be written as:

$$k_3 = \frac{k_B T}{h} \exp\left(\frac{- (\Delta G^\circ_{TS3} - \Delta G^\circ_{EE^*})}{RT}\right) \quad (8.28)$$

The adsorption equilibrium constant  $K_2$  is defined as:

$$K_2 = \exp\left(\frac{- (\Delta G^\circ_{EE^*} - \Delta G^\circ_{E^*} - \Delta G^\circ_{E(g)})}{RT}\right) \quad (8.29)$$

Combining 8.28 and 8.29 gives:

$$k_3 K_2 = \frac{k_B T}{h} \exp\left(\frac{- (\Delta G^\circ_{TS3} - \Delta G^\circ_{E^*} - \Delta G^\circ_{E(g)})}{RT}\right) \quad (8.30)$$

which indicates that the value of  $k_3 K_2$  reflects the free energy of the confined bimolecular dehydration transition state relative to those of the confined ethanol monomer and gas-phase ethanol.

The adsorption equilibrium constant  $K_4$  is defined as:

$$K_4 = \exp\left(\frac{- (\Delta G^\circ_{EW^*} - \Delta G^\circ_{E^*} - \Delta G^\circ_{W(g)})}{RT}\right) \quad (8.31)$$

Combining 8.30 and 8.31 gives:

$$k_3 K_2 K_4^{-1} = \frac{k_B T}{h} \exp\left(\frac{- (\Delta G^\circ_{TS3} - \Delta G^\circ_{EW^*} + \Delta G^\circ_{W(g)} - \Delta G^\circ_{E(g)})}{RT}\right) \quad (8.32)$$

which indicates that  $k_3K_2K_4^{-1}$  reflects the free energy of the confined bimolecular dehydration transition state and gas-phase water relative to the confined ethanol-water dimer and gas-phase ethanol.

#### 8.6.2.6 Estimating entropy in AIMD simulations of ethanol and water in H-Al-Beta zeolites

Proton shuttling is facile, which complicates entropy calculations as each proton transfer is a collision causing the angular velocity to be discontinuous in the reference frame of individual water molecules. Therefore, the acidic mobile proton was eliminated from each simulation, and only the RMS diffusion of water molecules were included in entropy simulations. This implicitly assumes the entropy of the solvated proton is the same across water densities. This approximation is justified as the contribution of the individual proton entropy is small relative to the system entropy dominated by water diffusion. The RMS diffusion also assumes the rotational and vibrational degrees of freedom to be constant across the range of water densities. The similarity in vibrational degrees of freedom is also likely a good approximation across a narrow range of water densities, as vibrational state frequencies will shift in the gas phase and solid phase limits. As the phase diagrams provided here are across a smaller range of similarly solvated states, the vibrational degrees of freedom are similar across the range of conditions considered here. The consistency of rotational states is more contentious, as it is likely that even with small changes in density the rotational states may change more substantially. The discontinuity in rotation due to proton shuttling presents a complication in evaluating rotational degrees of freedom in the traditional AIMD methods such as the VDOS or non-rigid moments of inertia. One potential technique would be re-scaling of the moments of inertia before the collision, and translating the moment of inertia after each collision back to their initial configuration to smooth the moments of inertia and allow partition function methods for calculating rotational entropies.

8.6.2.7 Relating  $K^\ddagger$  to the rate and equilibrium constants for elementary steps

As defined in the main text,  $K^\ddagger$  reflects the free energy of the transition state and gas-phase water relative to that of  $(C_2H_5OH)(H_3O^+)(H_2O)_n$  and gas-phase ethanol:

$$\frac{k_B T}{h} K^\ddagger = \frac{k_B T}{h} \exp \left( \frac{- (\Delta G^\circ_{\ddagger} + \Delta G^\circ_{H_2O(g)} - \Delta G^\circ_{C_2H_5OH(g)} - \Delta G^\circ_{EW_n})}{RT} \right) \quad (8.33)$$

Within the exponential, we can add and subtract the free energies of both  $EW_{n-1}$  and  $EEW_{n-1}$  intermediates which are formed en route to the transition state in Figure 8.9, and group terms together into quantities that can be simplified to the rate and equilibrium constants of elementary steps:

$$\begin{aligned} \frac{k_B T}{h} K^\ddagger &= \frac{k_B T}{h} \exp \left( \frac{- (\Delta G^\circ_{\ddagger} - \Delta G^\circ_{EEW_{n-1}})}{RT} \right) \\ &\quad \exp \left( \frac{- (\Delta G^\circ_{EEW_{n-1}} - \Delta G^\circ_{C_2H_5OH(g)} - \Delta G^\circ_{EW_{n-1}})}{RT} \right) \\ &\quad \exp \left( \frac{- (\Delta G^\circ_{H_2O(g)} + \Delta G^\circ_{EW_{n-1}} - \Delta G^\circ_{EW_n})}{RT} \right) \end{aligned} \quad (8.34)$$

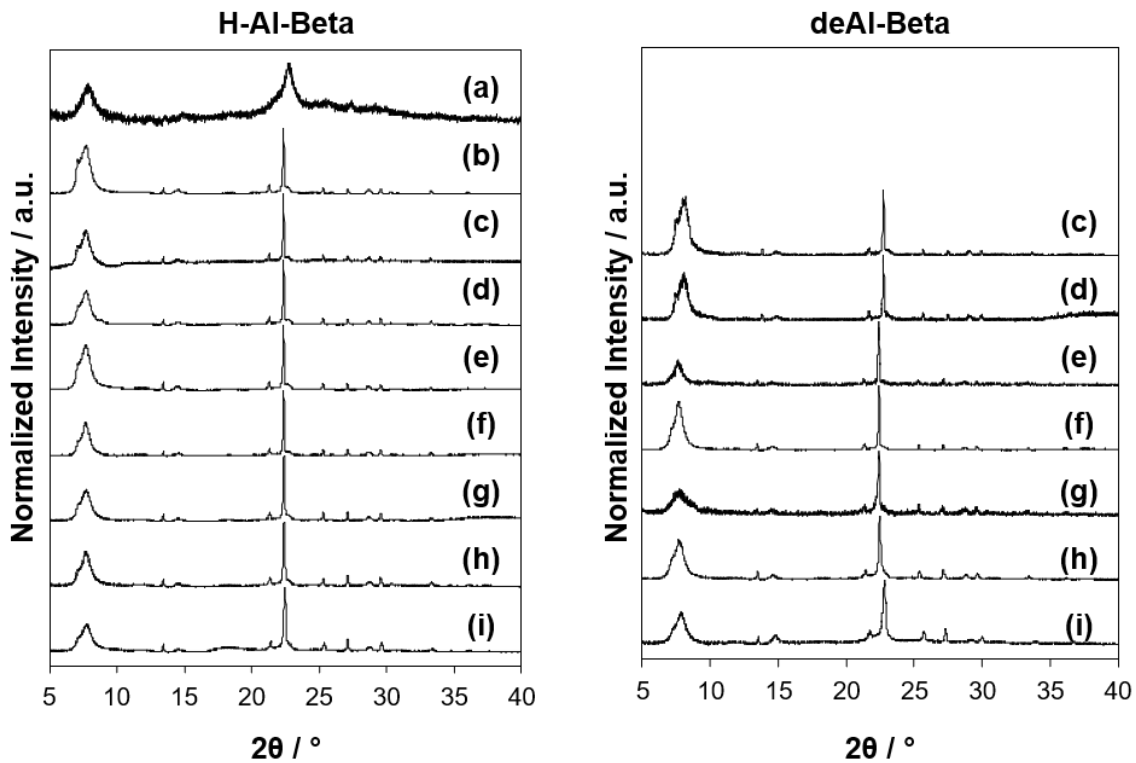
$$\frac{k_B T}{h} K^\ddagger = k_3 K_2 K_4^{-1} \quad (8.35)$$

Eq. 8.35 can then be substituted directly into Eq. 8.13 in the main text to give:

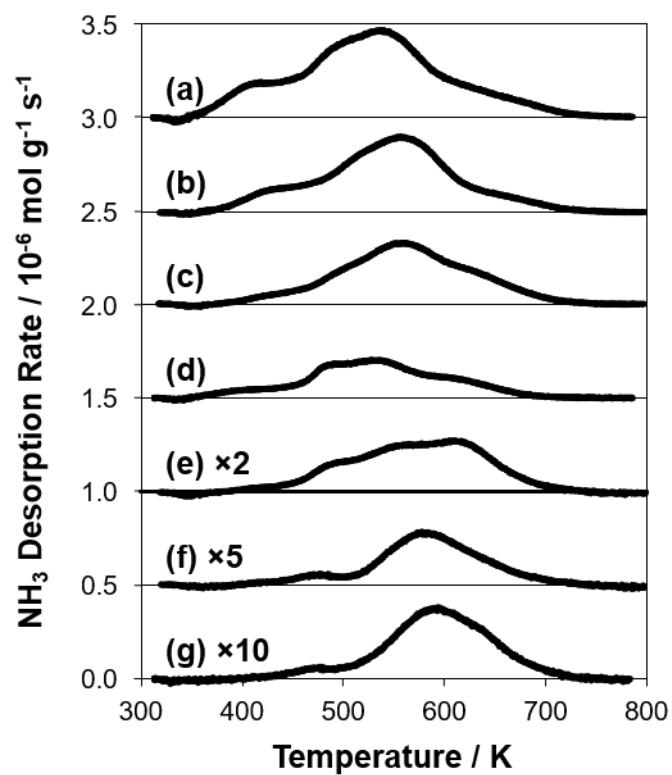
$$\frac{r_{DEE}}{[H^+]} = \frac{k_3 K_2}{K_4} \frac{\gamma_{EW_n}}{\gamma_{\ddagger}} \frac{P_{C_2H_5OH}}{P_{H_2O}} \quad (8.36)$$

## 8.6.3 Supplementary Figures

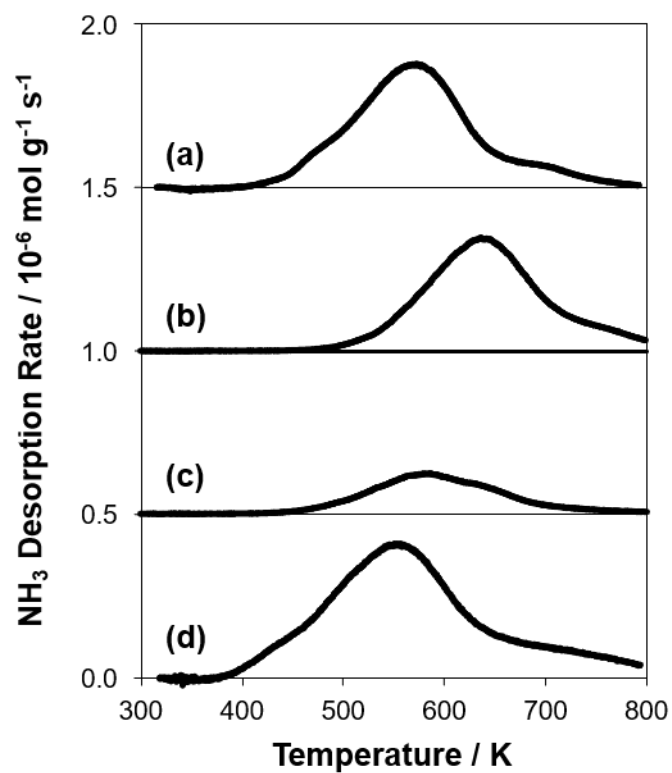
## 8.6.3.1 XRD patterns



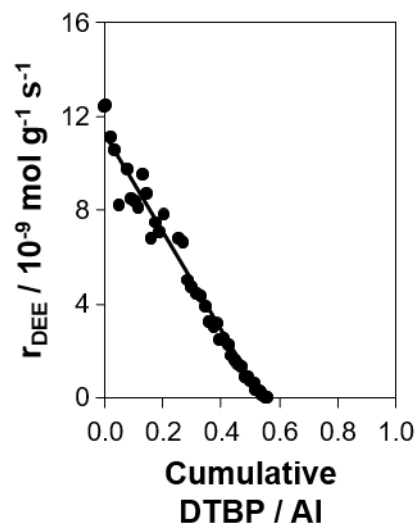
**Figure 8.11:** Left: XRD patterns of (a) H-Al-Beta-OH(1.7), (b) Si-Beta-F, and H-Al-Beta-F with  $H^+$  u.c. $^{-1}$  = (c) 0.11, (d) 0.16, (e) 0.57, (f) 0.78, (g) 1.2, (h) 1.4, (i) 2.0. Right: dealuminated analogs (deAl-Beta-F) of the samples at left. All XRD patterns are normalized to their highest peak intensity.

8.6.3.2  $\text{NH}_3$ -TPD data

**Figure 8.12:**  $\text{NH}_3$ -TPD profiles for H-Al-Beta-F zeolites with Si/Al = (a) 23, (b) 34, (c) 45, (d) 65, (e) 93, (f) 220, (g) 500. Offset by 0.5 units for clarity.



**Figure 8.13:**  $\text{NH}_3$ -TPD profiles for (a) H-Al-MFI, (b) H-Al-TON, (c) H-Al-FAU, (d) H-Al-Beta-OH(1.7). Offset by 0.5 units for clarity.

8.6.3.3 In situ 2,6-di-*tert*-butylpyridine titration data

**Figure 8.14:** Diethyl ether formation rate (per g catalyst, 378 K, 5 kPa C<sub>2</sub>H<sub>5</sub>OH, 1 kPa H<sub>2</sub>O) as a function of 2,6-di-*tert*-butylpyridine uptake (0.6 Pa DTBP) on H-Al-Beta-F(2.0) during catalysis. Solid line represents linear regression.

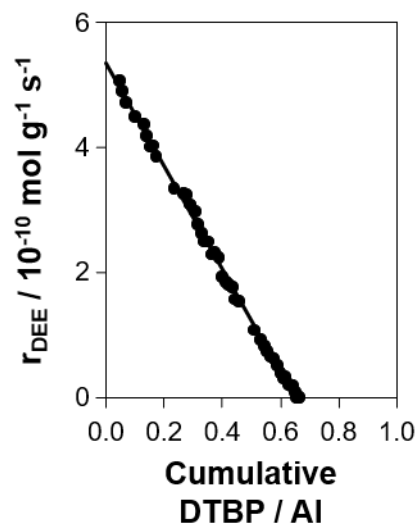


**Figure 8.15:** Diethyl ether formation rate (per g catalyst, 378 K, 0.7 kPa C<sub>2</sub>H<sub>5</sub>OH, 30 kPa H<sub>2</sub>O) as a function of 2,6-di-*tert*-butylpyridine uptake (1.4 Pa DTBP) on H-Al-Beta-F(2.0) during catalysis. Solid line represents linear regression.

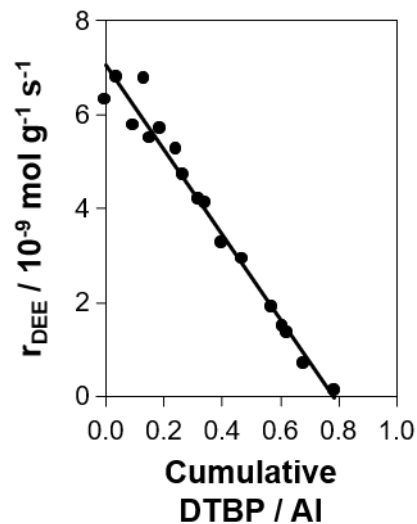


**Figure 8.16:** Diethyl ether formation rate (per g catalyst, 378 K, 4.5 kPa  $\text{C}_2\text{H}_5\text{OH}$ , 1 kPa  $\text{H}_2\text{O}$ ) as a function of 2,6-di-*tert*-butylpyridine uptake (1.8 Pa DTBP) on H-Al-Beta-F(1.2) during catalysis. Solid line represents linear regression.

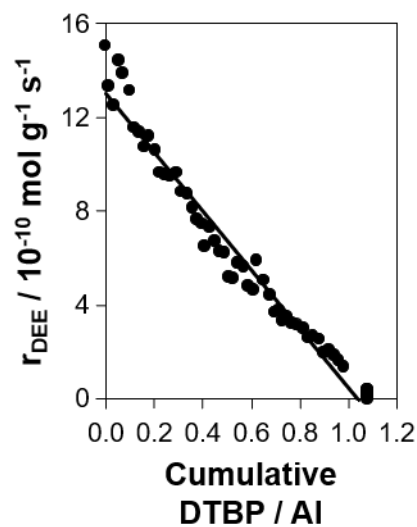


**Figure 8.17:** Diethyl ether formation rate (per g catalyst, 378 K, 4.5 kPa  $\text{C}_2\text{H}_5\text{OH}$ , 1 kPa  $\text{H}_2\text{O}$ ) as a function of 2,6-di-*tert*-butylpyridine uptake (0.5 Pa DTBP) on H-Al-Beta-F(0.16) during catalysis. Solid line represents linear regression.

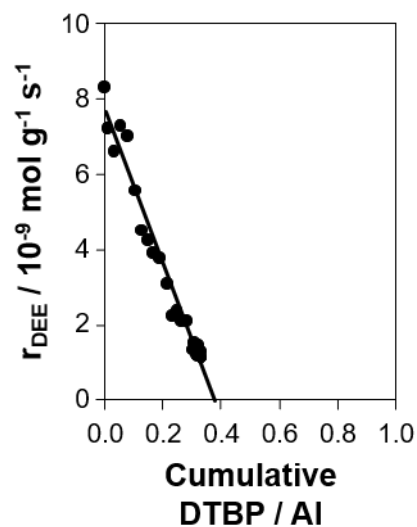


**Figure 8.18:** Diethyl ether formation rate (per g catalyst, 378 K, 4.4 kPa  $C_2H_5OH$ , 1 kPa  $H_2O$ ) as a function of 2,6-di-*tert*-butylpyridine uptake (1.9 Pa DTBP) on H-Al-Beta-OH(1.7) during catalysis. Solid line represents linear regression.

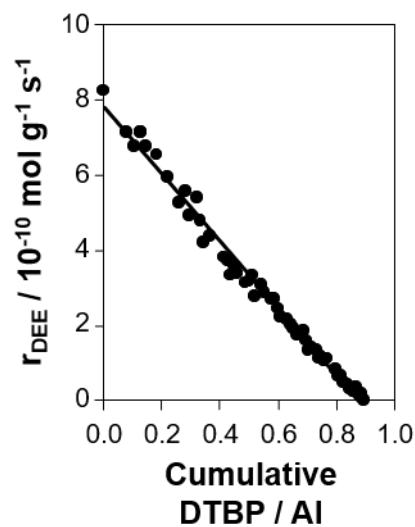


**Figure 8.19:** Diethyl ether formation rate (per g catalyst, 373 K, 4.7 kPa  $C_2H_5OH$ , 1 kPa  $H_2O$ ) as a function of 2,6-di-*tert*-butylpyridine uptake (0.9 Pa DTBP) on H-Al-FAU during catalysis. Solid line represents linear regression.

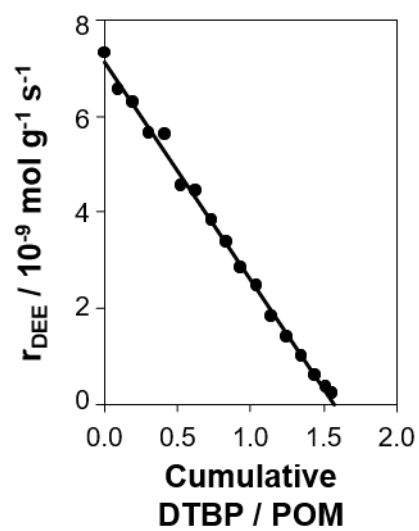


**Figure 8.20:** Diethyl ether formation rate (per g catalyst, 378 K, 4.5 kPa  $\text{C}_2\text{H}_5\text{OH}$ , 1 kPa  $\text{H}_2\text{O}$ ) as a function of 2,6-di-*tert*-butylpyridine uptake (0.4 Pa DTBP) on HPW/Si-MCM-41 during catalysis. Solid line represents linear regression.

## 8.6.3.4 Ethanol dehydration kinetic data

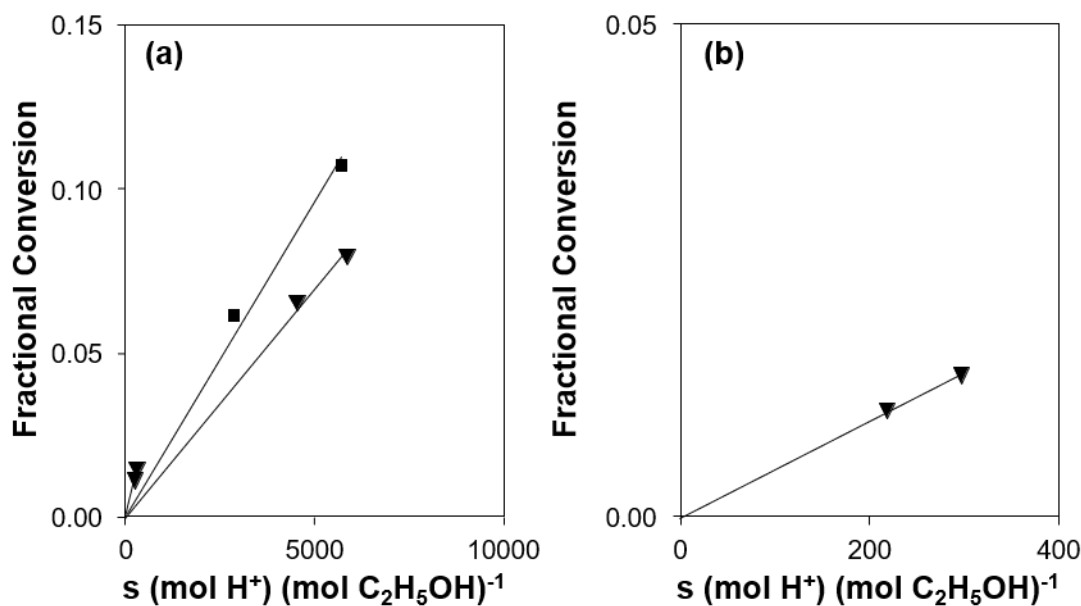


**Figure 8.21:** (a) Fractional conversion of  $\text{C}_2\text{H}_5\text{OH}$  as a function of site-contact time at 0.008 kPa  $\text{C}_2\text{H}_5\text{OH}$  on H-Al-Beta-F(2.0) (■), and at 0.04 kPa and 0.002 kPa  $\text{C}_2\text{H}_5\text{OH}$  on H-Al-Beta-OH(1.7) (▼), collected without co-fed  $\text{H}_2\text{O}$  at 373 K. (b) provides a better view of the data points near the origin in (a) at 0.04 kPa  $\text{C}_2\text{H}_5\text{OH}$  on H-Al-Beta-OH(1.7) (▼).

These measurements (Figure 8.23) give values of  $k_3 = 3.6 \times 10^{-5} \text{ mol } (\text{mol H}^+)^{-1} \text{ s}^{-1}$  and  $K_2 = 59 \text{ kPa}^{-1}$ . This value of  $k_3$  agrees well with that measured by Chiang and Bhan [218] on the same Zeolyst H-Al-MFI sample (CBV8014). Chiang and Bhan report (in the zero-order regime, at 368 K) a value of  $k = 1.7 \times 10^{-5} \text{ mol } (\text{mol H}^+)^{-1} \text{ s}^{-1}$ . Their reported  $k$  values as a function of temperature (368–409 K,  $E_{\text{app}} = 103 \text{ kJ mol}^{-1}$ ) can be used to interpolate this value at 373 K as  $k = 2.7 \times 10^{-5} \text{ mol } (\text{mol H}^+)^{-1} \text{ s}^{-1}$ . This value is 76% that quantified here (Figure 8.23), which is in reasonable agreement and thus provides a benchmark that validates the measurements reported using this reactor system.

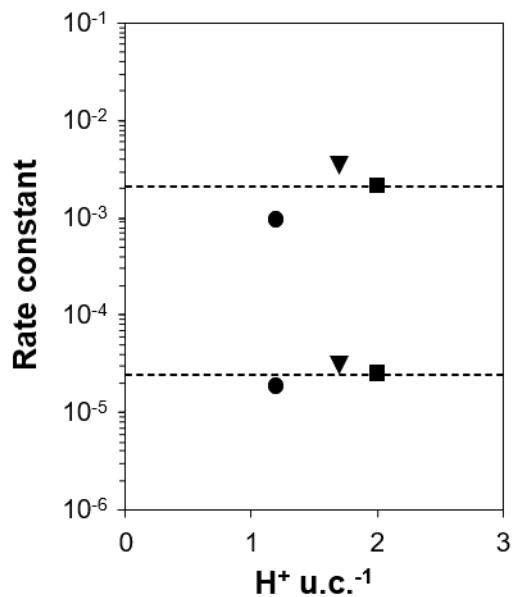


**Figure 8.22:** First-order ( $k_3K_2 / \text{mol} (\text{mol H}^+)^{-1} \text{kPa}^{-1} \text{s}^{-1}$ ) and zero-order ( $k_3 / \text{mol} (\text{mol H}^+)^{-1} \text{s}^{-1}$ ) dehydration rate constants (per  $\text{H}^+$ , 373 K) quantified on H-Al-Beta-F(1.2) (●), H-Al-Beta-F(2.0) (■), and H-Al-Beta-OH(1.7) (▼) as a function of  $\text{H}^+$  density. Dashed line represents the average value. Because intracrystalline transport limitations would lead to lower  $k_3$  values at higher  $\text{H}^+$  densities, these data are consistent with kinetically limited rates as described by the Madon-Boudart criterion [196].

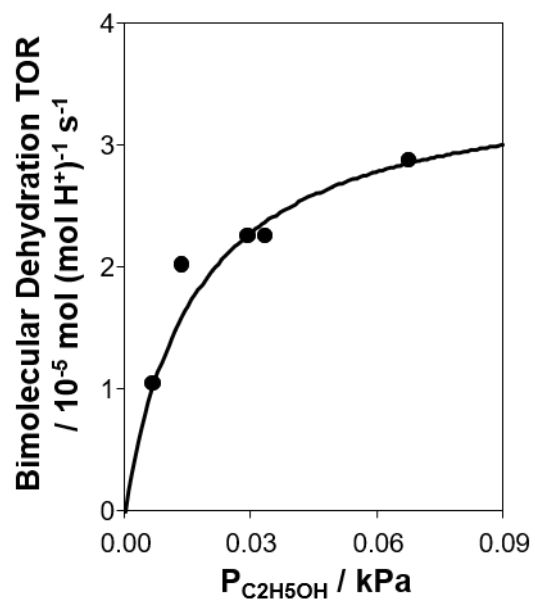


**Figure 8.23:** Bimolecular ethanol dehydration turnover rate (per  $H^+$ , 373 K) as a function of  $C_2H_5OH$  pressure, without co-fed  $H_2O$ , on H-Al-MFI. Solid line represents regression to Eq. 8.1 (Main Text).

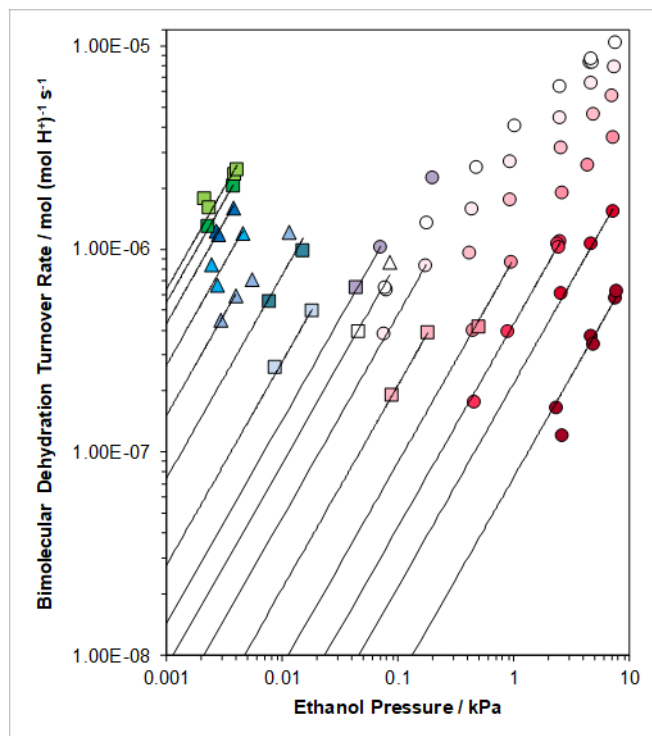


**Figure 8.24:** Bimolecular ethanol dehydration turnover rate (373 K, per H<sup>+</sup>) on H-Al-Beta-F(2.0) as a function of ethanol pressure at water pressures of 0.02, 0.05, 0.2, 0.6, 2, 5, 7, 10, 14, 20, 30, 40, 50, 75 kPa. Squares, triangles, and circles were measured in separate experiments. Solid lines reflect linear regression to data points in first-order regimes.

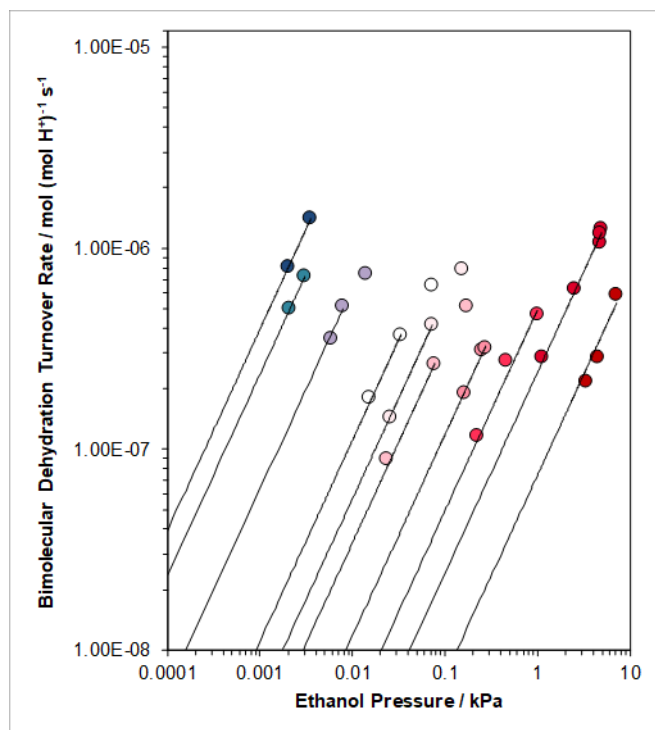


**Figure 8.25:** Bimolecular ethanol dehydration turnover rate (373 K, per H<sup>+</sup>) on H-Al-Beta-F(1.2) as a function of ethanol pressure at water pressures of 0.02, 0.2, 2, 10, 14, 20, 30, 40, 50, 75 kPa. Solid lines reflect linear regression to data points in first-order regimes.

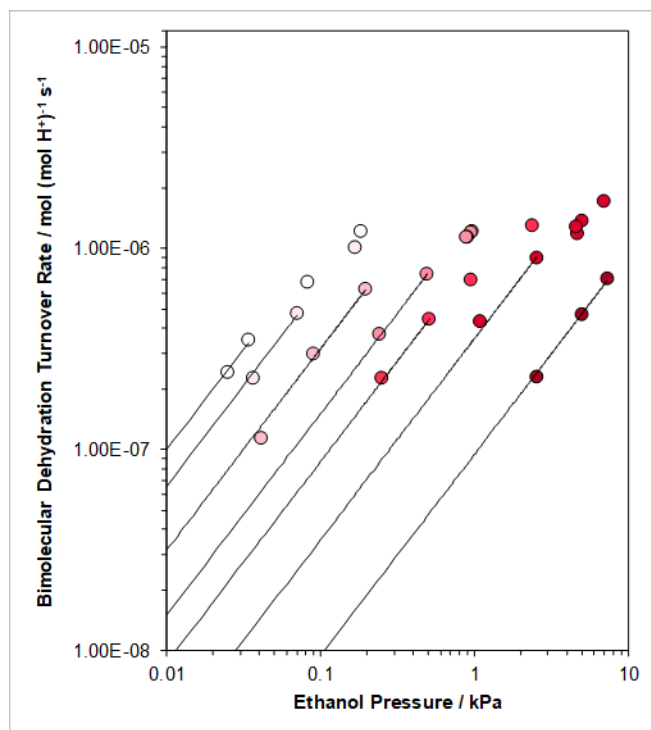


**Figure 8.26:** Bimolecular ethanol dehydration turnover rate (373 K, per H<sup>+</sup>) on H-Al-Beta-F(0.16) as a function of ethanol pressure at water pressures of 10, 14, 20, 30, 40, 50, 75 kPa. Solid lines reflect linear regression to data points in first-order regimes.

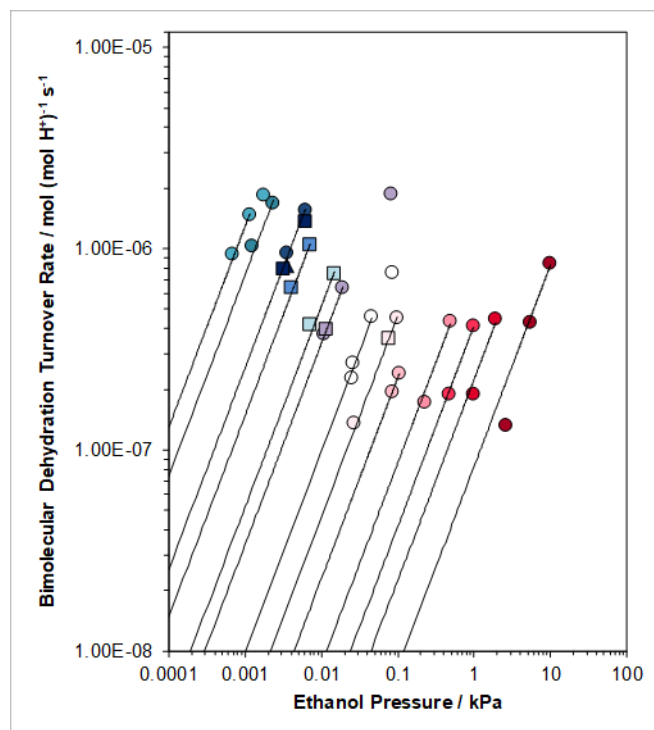


**Figure 8.27:** Bimolecular ethanol dehydration turnover rate (373 K, per H<sup>+</sup>) on H-Al-Beta-OH(1.7) as a function of ethanol pressure at water pressures of 0.05, 0.2, 0.6, 1, 2, 5, 10, 14, 20, 30, 40, 50, 75 kPa. Squares and circles were measured in separate experiments. Solid lines reflect linear regression to data points in first-order regimes.

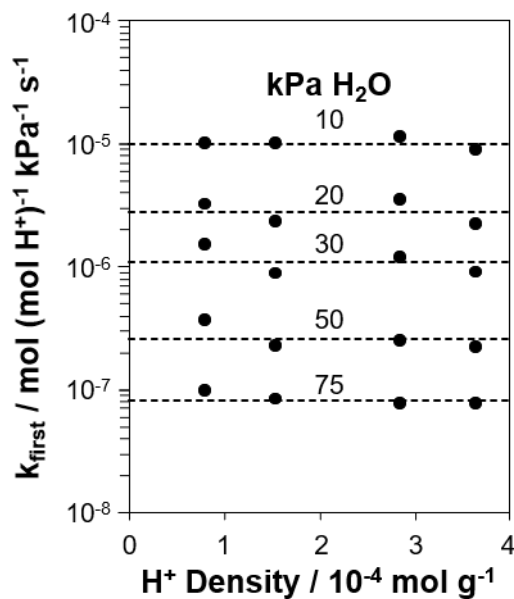


**Figure 8.28:** Apparent first-order rate constant for bimolecular ethanol dehydration (per  $\text{H}^+$ , 373 K) on H-Al-Beta samples as a function of  $\text{H}_2\text{O}$  pressure (10–75 kPa) and  $\text{H}^+$  density (quantified by *in situ* 2,6-di-*tert*-butylpyridine titration). Dashed lines represent averages at each  $\text{H}_2\text{O}$  pressure.

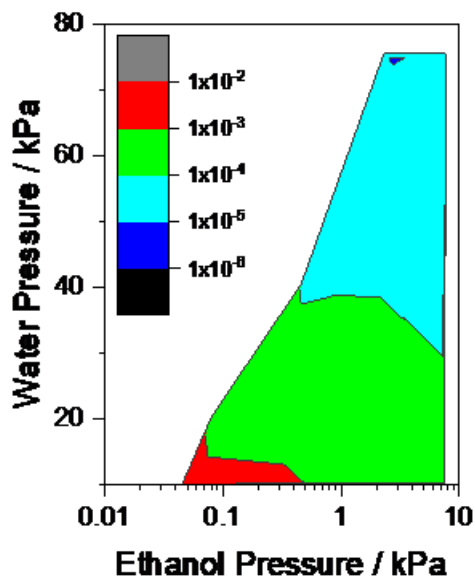


**Figure 8.29:** Mears criterion values calculated as a function of ethanol and water pressure on H-Al-Beta-F(2.0) at 373 K. Shaded regions correspond to Mears criterion values that fall in the range of values specified by the scale bar.

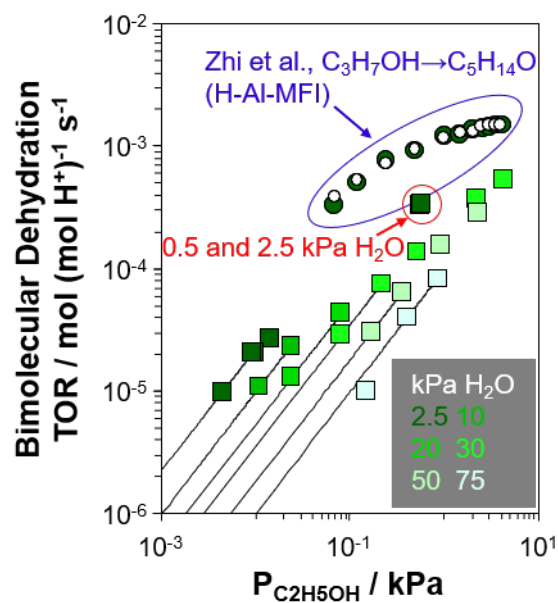


**Figure 8.30:** Bimolecular ethanol dehydration turnover rate (423 K, per  $\text{H}^+$ ) on H-Al-Beta-F(1.2) (boxes) as a function of ethanol pressure at water pressures between 2.5–75 kPa (see color legend in bottom right). Bimolecular 1-propanol dehydration turnover rates (423, per  $\text{H}^+$ ) on H-Al-MFI reported by Zhi et al. [177] are adapted from Figure 8.4S in their manuscript’s Supporting Information, where the filled circles were collected at 2.5 kPa  $\text{H}_2\text{O}$ , and the open circles were collected at 0.53 kPa  $\text{H}_2\text{O}$ .

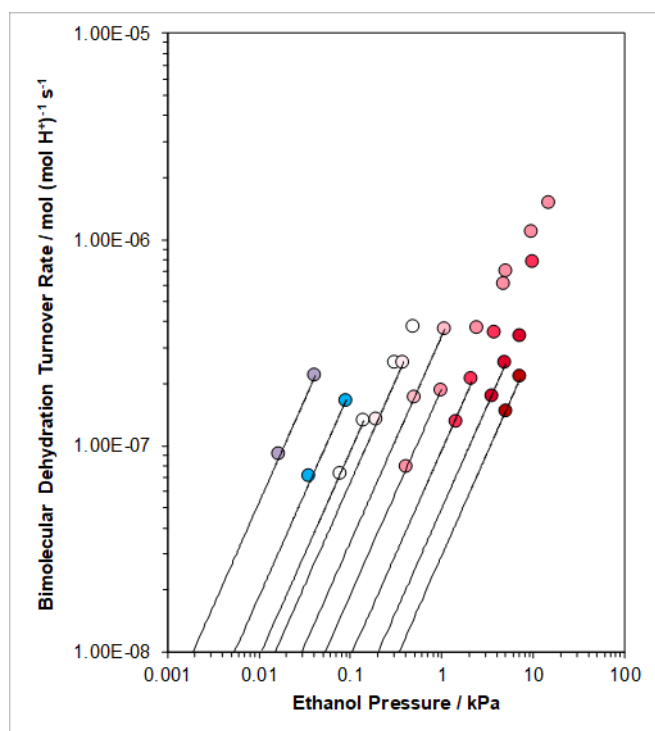


**Figure 8.31:** Bimolecular ethanol dehydration turnover rate (373 K, per H<sup>+</sup>) on H-Al-FAU as a function of ethanol pressure at water pressures of 2, 5, 10, 14, 20, 30, 40, 60 kPa. Solid lines reflect linear regression to data points in first-order regimes.

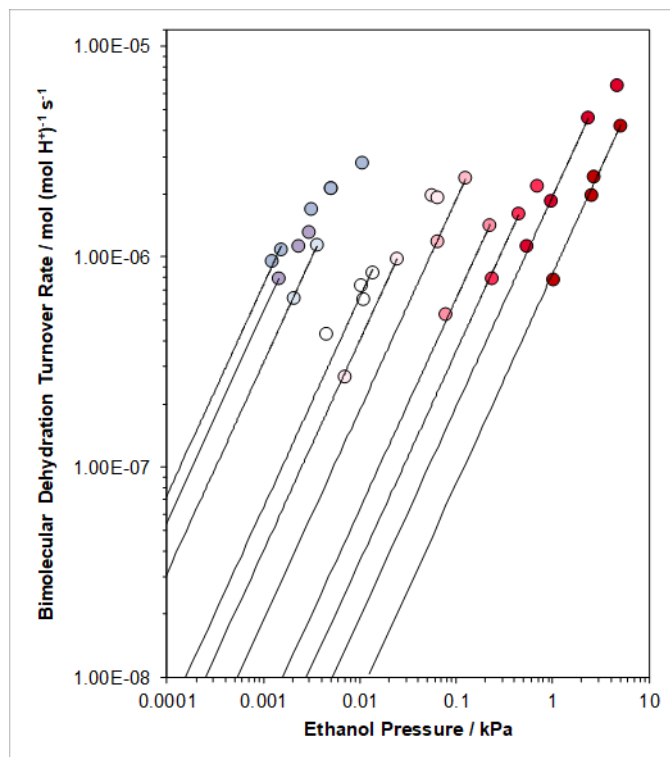


**Figure 8.32:** Bimolecular ethanol dehydration turnover rate (373 K, per H<sup>+</sup>) on H-Al-TON as a function of ethanol pressure at water pressures of 1, 2, 5, 10, 14, 20, 30, 40, 50, 75 kPa. Solid lines reflect linear regression to data points in first-order regimes.

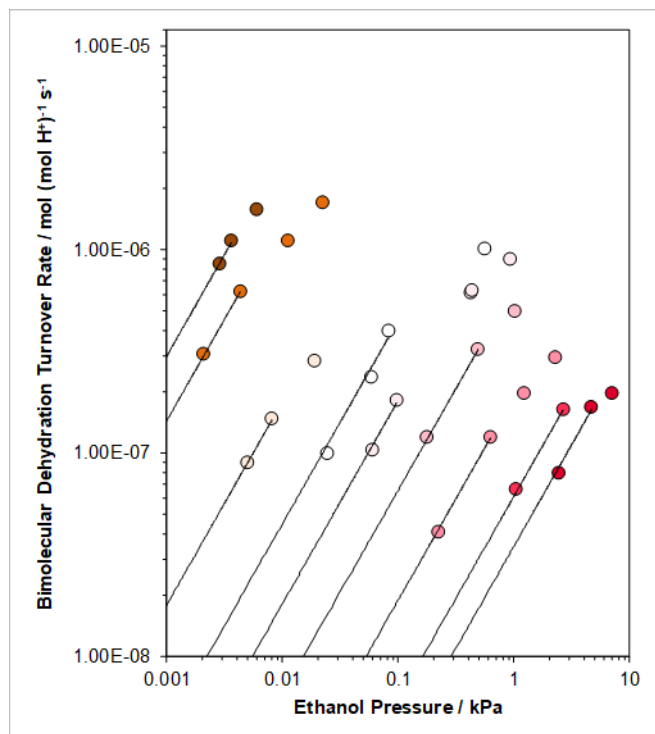


**Figure 8.33:** Bimolecular ethanol dehydration turnover rate (373 K, per H<sup>+</sup>) on H-Al-CHA as a function of ethanol pressure at water pressures of 0.2, 0.6, 5, 10, 14, 20, 30, 40, 50 kPa. Solid lines reflect linear regression to data points in first-order regimes.

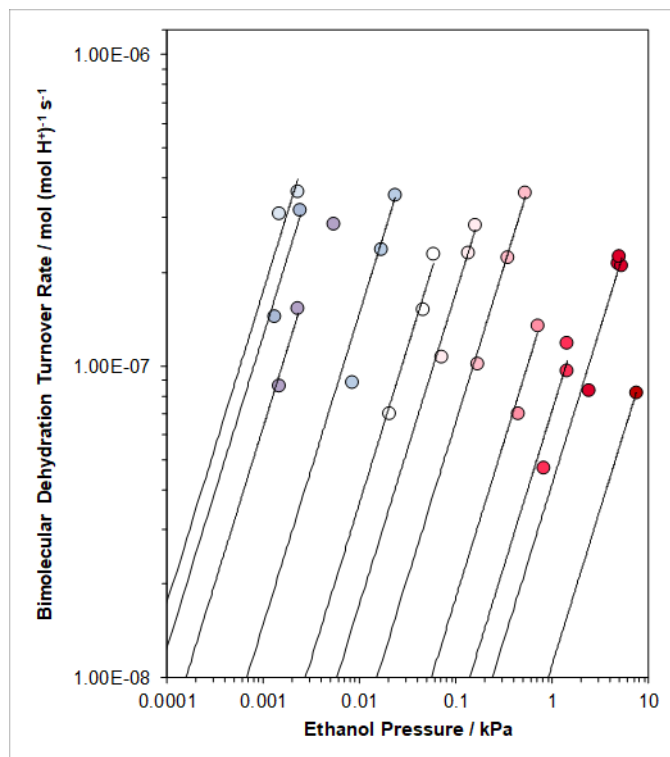


**Figure 8.34:** Bimolecular ethanol dehydration turnover rate (373 K, per H<sup>+</sup>) on H-Al-AEI as a function of ethanol pressure at water pressures of 0.6, 1, 2, 5, 10, 14, 20, 30, 40, 50, 75 kPa. Solid lines reflect linear regression to data points in first-order regimes.

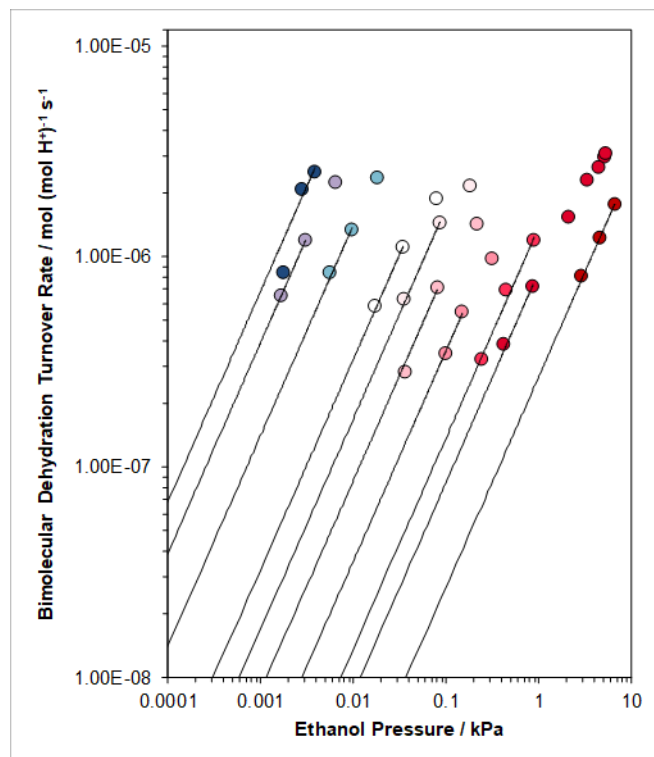


**Figure 8.35:** Bimolecular ethanol dehydration turnover rate (373 K, per H<sup>+</sup>) on H-Al-MFI as a function of ethanol pressure at water pressures of 0.02, 0.2, 2, 10, 14, 20, 30, 40, 50, 75 kPa. Solid lines reflect linear regression to data points in first-order regimes.

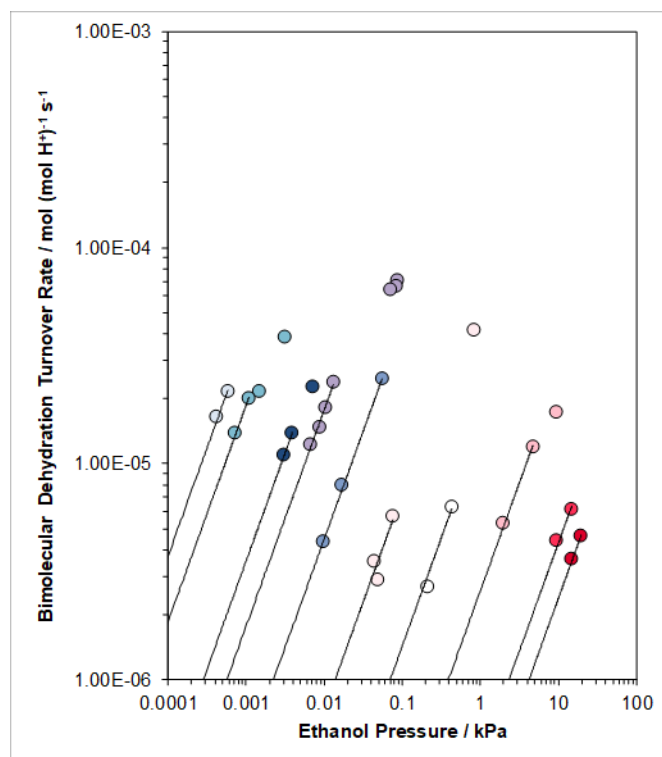


**Figure 8.36:** Bimolecular ethanol dehydration turnover rate (373 K, per H<sup>+</sup>) on HPW/Si-MCM-41 as a function of ethanol pressure at water pressures of 0.1, 0.2, 0.6, 1, 2, 5, 10, 20, 40, 50 kPa. Solid lines reflect linear regression to data points in the first-order regime.

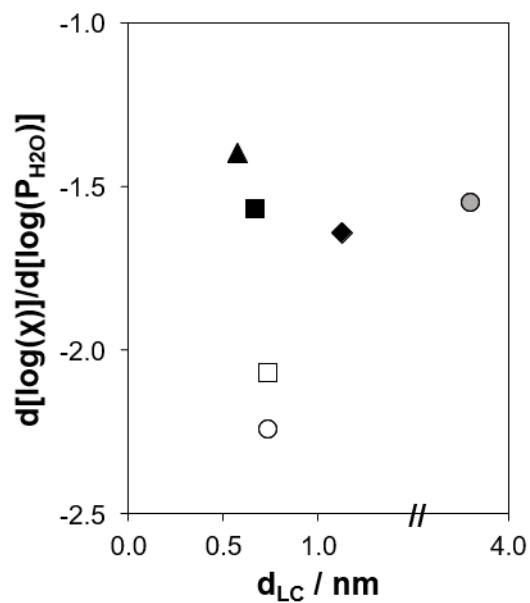


**Figure 8.37:** Dependence of activity coefficient ratios ( $\chi = \gamma_{EW_n}/\gamma_{\ddagger}$ ) on  $P_{H_2O}$  in the high water pressure limit, on H-Al-Beta-F(2.0) (■), H-Al-TON (▲), H-Al-FAU (◆), H-Al-AEI (□), H-Al-CHA (○), and HPW/Si-MCM-41 (●), as a function of the diameter of the largest included sphere within the pore topology ( $d_{LC}$ ).

## 8.6.3.5 Volumetric adsorption isotherms

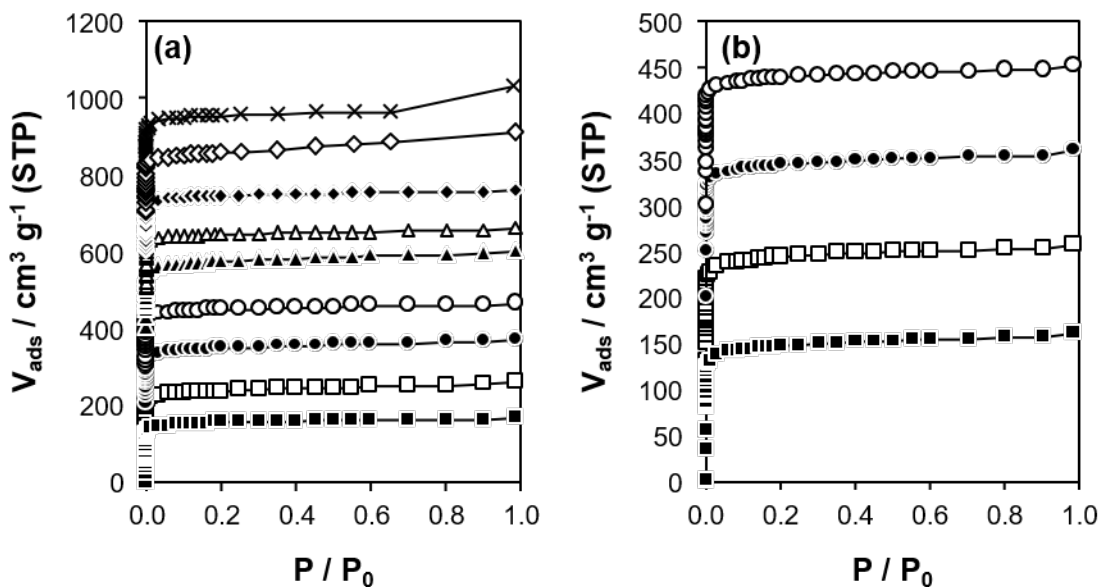


**Figure 8.38:** Volumetric  $N_2$  adsorption isotherms (77 K) measured on H-Al-Beta-F samples (a) and their dealuminated analogs (b), with  $H^+$  (or Si-OH nest) per unit cell = 0 ( $\diamond$ ), 0.11 ( $\blacklozenge$ ), 0.16 ( $\triangle$ ), 0.57 ( $\blacktriangle$ ), 0.78 ( $\circ$ ), 1.2 ( $\bullet$ ), 1.4 ( $\square$ ), and 2.0 ( $\blacksquare$ ), and on H-Al-Beta-OH(1.7) ( $\times$ ). Isotherms are offset by 100 units for clarity.

The mesopores of Si-MCM-41 are between 3.0–5.5 nm, with the maximum of the distribution at 3.9 nm. The mesopores of HPW/Si-MCM-41 are between 3.0–4.5 nm, with the maximum of the distribution at 3.8 nm. This indicates that the POM clusters are located within the mesopores and preferentially occupy the mesopores of larger diameter.

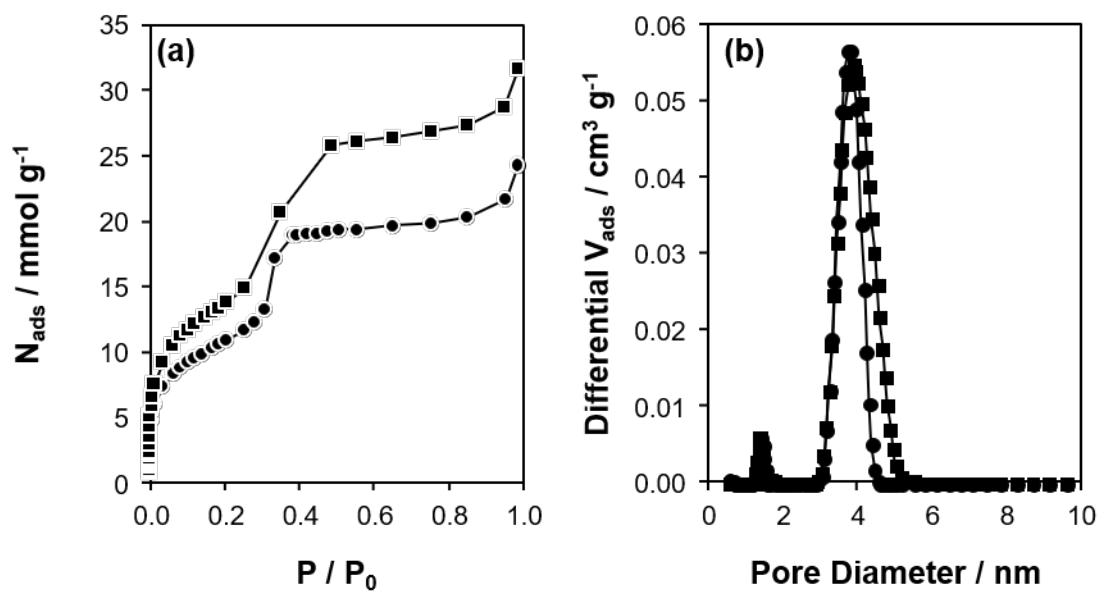


**Figure 8.39:** (a) Volumetric  $N_2$  adsorption isotherms (77 K) measured on Si-MCM-41 (■) and HPW/Si-MCM-41 (●), and (b) NLDFT-based pore-size distributions derived from the data.

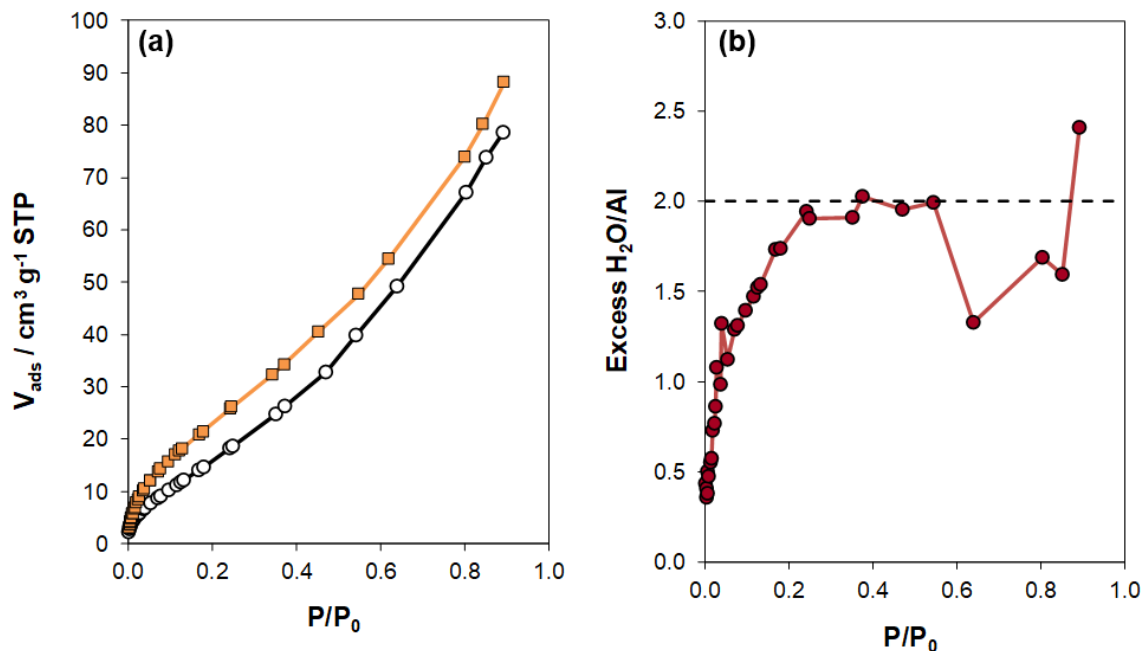


**Figure 8.40:** (a) Volumetric H<sub>2</sub>O adsorption isotherms (293 K) on H-Al-Beta-F(0.57) (orange squares) and Na-Al-Beta-F(0.57) (black circles). (b) Difference between H-Al-Beta-F(0.57) and Na-Al-Beta-F(0.57) isotherms in (a), normalized by the Al density. Dashed line represents approximate plateau value between  $P/P_0 = 0.2$ – $0.6$ , which implies that  $(\text{H}^+)(\text{H}_2\text{O})_n$  clusters are saturated at  $P/P_0 = 0.2$ , and that they contain 2 more H<sub>2</sub>O molecules than  $(\text{Na}^+)(\text{H}_2\text{O})_n$  clusters.

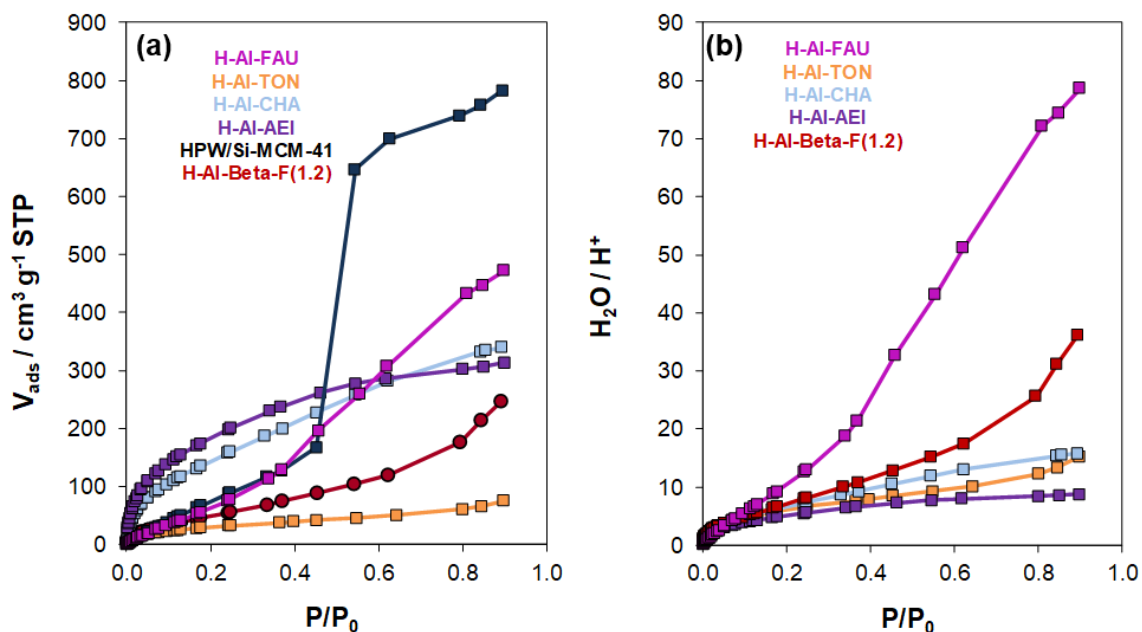


**Figure 8.41:** (a) H<sub>2</sub>O adsorption isotherms (293 K) on H-Al-FAU (pink), H-Al-TON (orange), H-Al-CHA (light blue), H-Al-AEI (purple), HPW/Si-MCM-41 (dark blue), and H-Al-Beta-F(1.2) (red), for comparison. (b) Calculated H<sub>2</sub>O adsorbed per H<sup>+</sup> on H-zeolite samples. H<sub>2</sub>O adsorbed within Si-Beta-F or any other siliceous analogs is not subtracted in this case, as it is in the main text on H-Al-Beta-F samples.

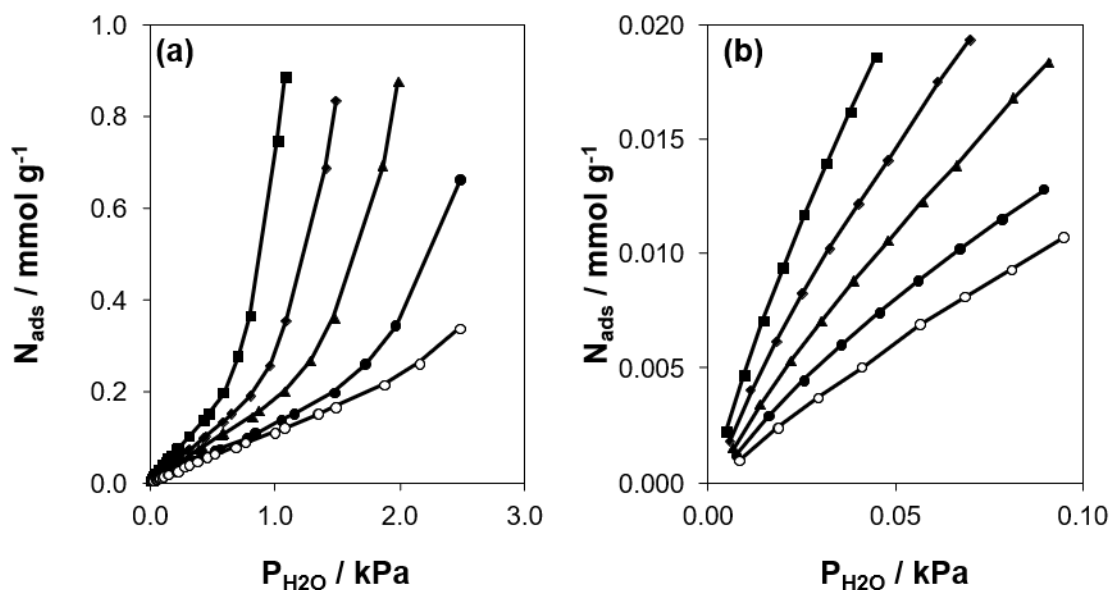


**Figure 8.42:** (a) Volumetric adsorption isotherms of H<sub>2</sub>O on Si-Beta-F at 283 K (■), 288 K (◆), 293 K (▲), 298 K (●), and 302 K (○), with low-coverage data shown in (b) for clarity.

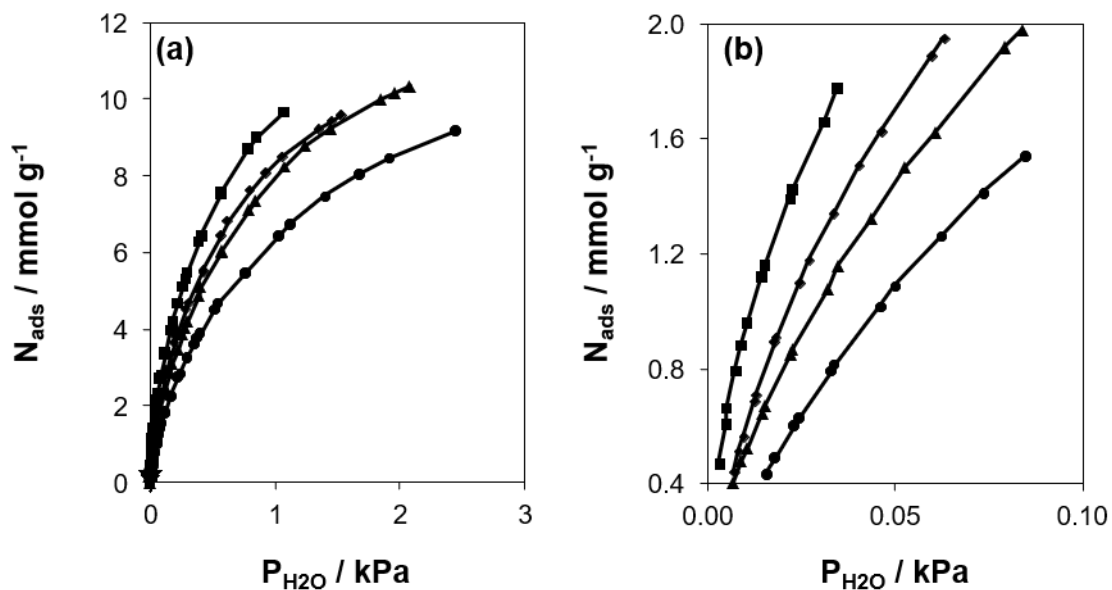


**Figure 8.43:** (a) Volumetric adsorption isotherms of H<sub>2</sub>O on deAl-Beta-F(2.0) at 283 K (■), 288 K (◆), 293 K (▲), and 298 K (●), with low-coverage data shown in (b) for clarity.

## 8.6.3.6 Infrared spectra collected at 293 K

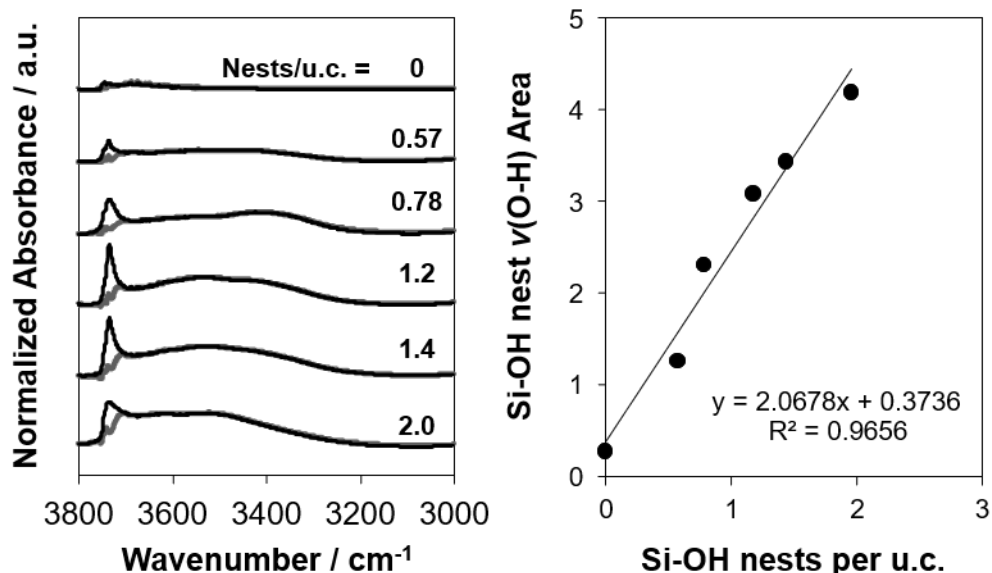


**Figure 8.44:** (a) Normalized (to T–O–T overtone peak area (1750–2100  $\text{cm}^{-1}$ )) IR spectra of Si-Beta-F and deAl-Beta-F zeolites at 293 K after treatment in flowing He to 823 K for 1 h. Grey traces represent deconvoluted signal for Si-OH nest peak areas. (b) Correlation of Si-OH nest  $\nu(\text{O-H})$  peak area with the number of Si-OH nests  $\text{u.c.}^{-1}$  generated by removal of framework Al.

The spectra for the empty cell at the corresponding  $\text{H}_2\text{O}$   $P/P_0$  values were subtracted from the wafer spectra to yield cell-corrected spectra (Figure 8.45a). Then, the cell-corrected spectra were normalized by the Si-O-Si overtone vibration (1750–2100  $\text{cm}^{-1}$ ) peak area of the wafer before  $\text{H}_2\text{O}$  adsorption. The normalized, cell-corrected spectrum of the wafer before  $\text{H}_2\text{O}$  adsorption was subtracted from those measured at each  $\text{H}_2\text{O}$   $P/P_0$  value to give subtracted spectra (Figure 8.45b) that represent the signal for adsorbed  $\text{H}_2\text{O}$ , and any changes to the vibrations associated with the zeolite, e.g., perturbation of Si-OH groups. Spectra were also subtracted between incremental increases in  $\text{H}_2\text{O}$  pressure, denoted “differential subtracted,” in order to visualize the change in signal associated with the adsorption of additional  $\text{H}_2\text{O}$  molecules. Subtracted and differential subtracted spectra were further baseline-corrected with pivot points at 4000, 2400, and 1350  $\text{cm}^{-1}$ , where no absorbance was detected.

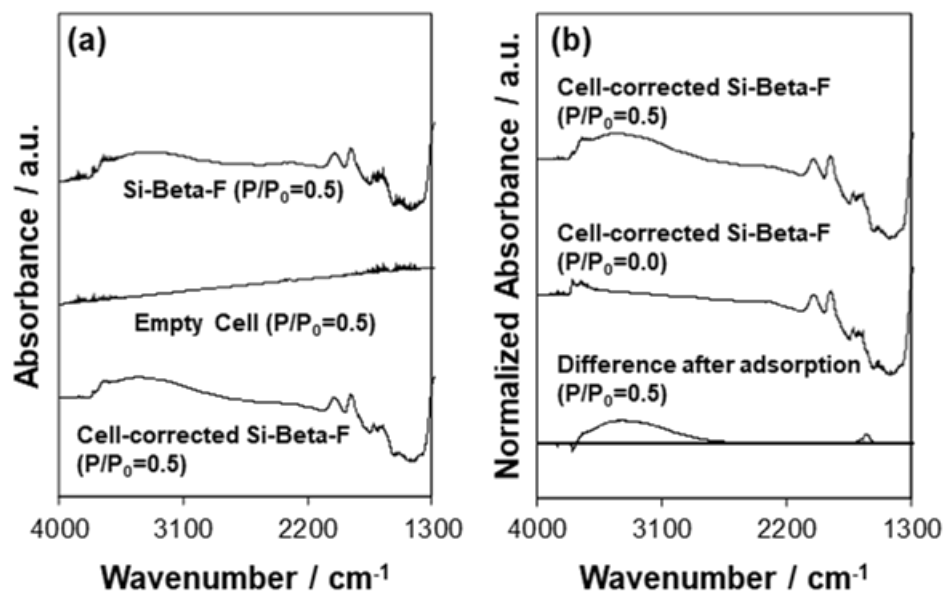


**Figure 8.45:** Illustration of processing of spectra under flowing H<sub>2</sub>O, using Si-Beta-F at  $P/P_0 = 0.5$  (293 K) as an example. (a) The signal from vapor-phase H<sub>2</sub>O in the empty cell is subtracted from the signal for Si-Beta-F under flowing vapor-phase H<sub>2</sub>O to yield a cell-corrected spectrum, then (b) the spectrum of the zeolite in flowing He before H<sub>2</sub>O adsorption is subtracted from this to give the difference after adsorption.

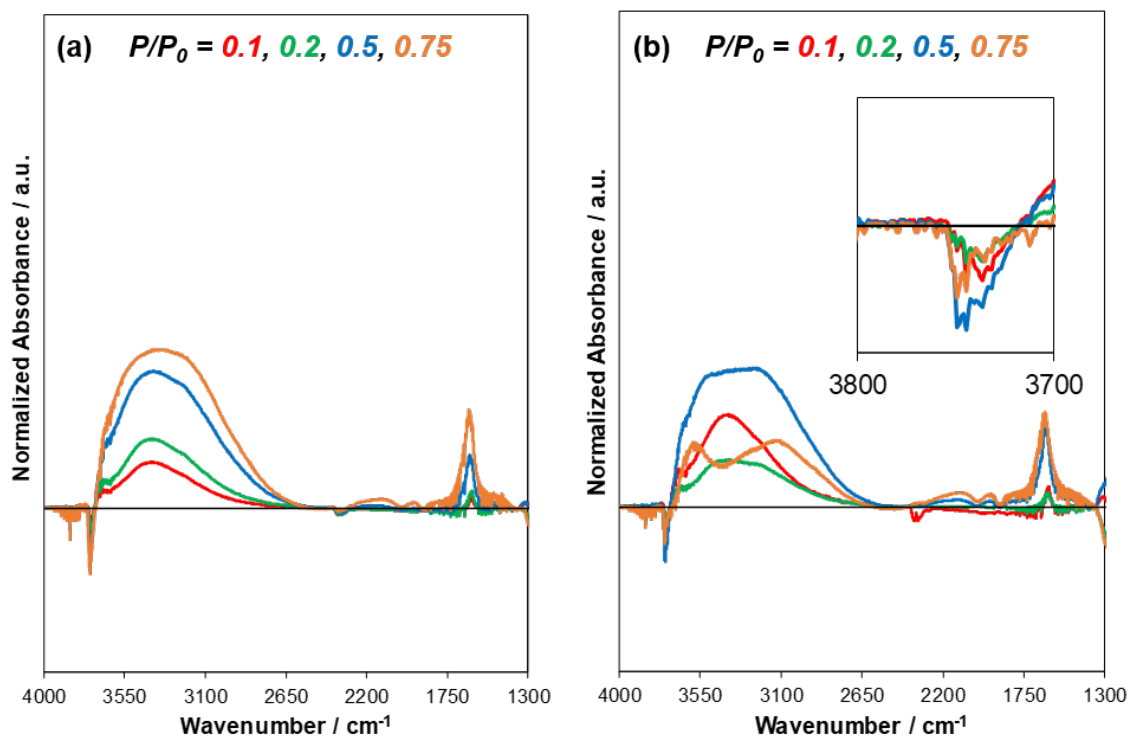


**Figure 8.46:** (a) Baseline-corrected difference IR spectra of H<sub>2</sub>O adsorbed at 293 K on Si-Beta-F at  $P/P_0$  values of 0.1 (red), 0.2 (green), 0.5 (blue), and 0.75 (orange). Difference spectra reflect the subtraction of the spectrum of the dehydrated sample under flowing He prior to H<sub>2</sub>O adsorption, and the spectrum of H<sub>2</sub>O adsorbed within an empty IR cell. (b) Differential-subtracted spectra reflect the difference between the spectrum at the given  $P/P_0$  value and the next-lowest  $P/P_0$  value. All spectra are normalized to the T–O–T overtone peak area (1750–2100 cm<sup>-1</sup>) prior to adsorption. The spectra on Si-Beta-F were originally reported in Ref. [406].

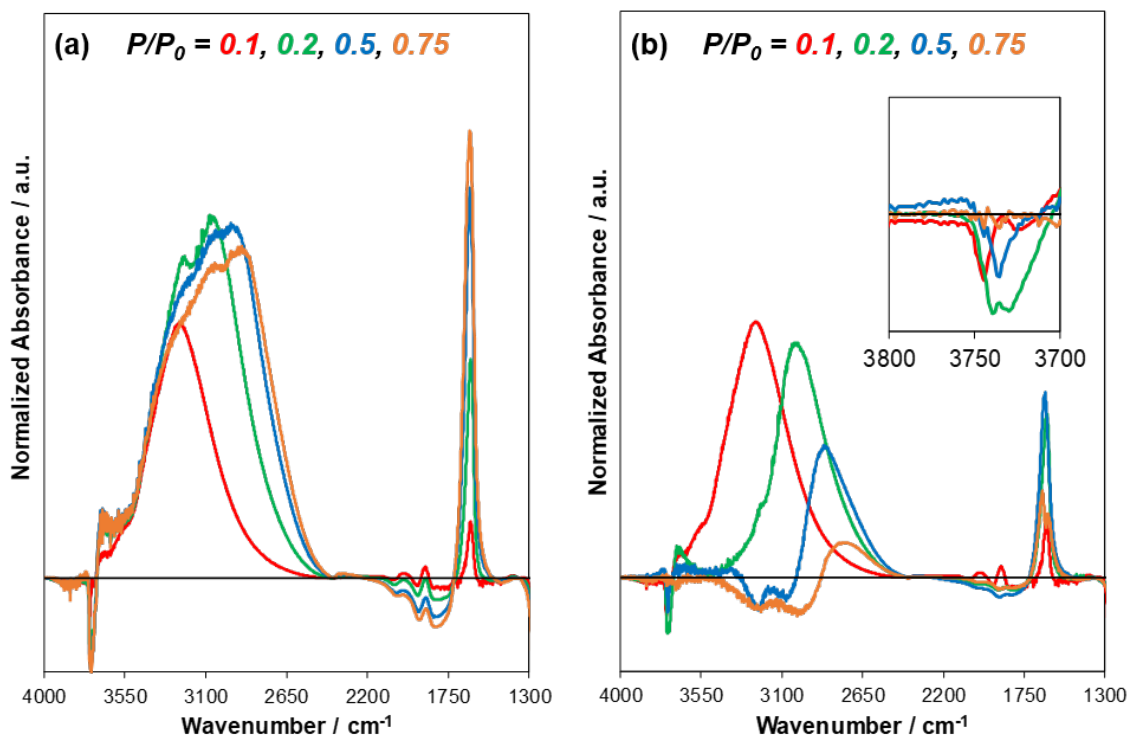


**Figure 8.47:** (a) Baseline-corrected difference IR spectra of H<sub>2</sub>O adsorbed at 293 K on deAl-Beta-F(2.0) at  $P/P_0$  values of 0.1 (red), 0.2 (green), 0.5 (blue), and 0.75 (orange). Difference spectra reflect the subtraction of the spectrum of the dehydrated sample under flowing He prior to H<sub>2</sub>O adsorption, and the spectrum of H<sub>2</sub>O adsorbed within an empty IR cell. (b) Differential-subtracted spectra reflect the difference between the spectrum at the given  $P/P_0$  value and the next-lowest  $P/P_0$  value. All spectra are normalized to the T–O–T overtone peak area (1750–2100 cm<sup>-1</sup>) prior to adsorption.

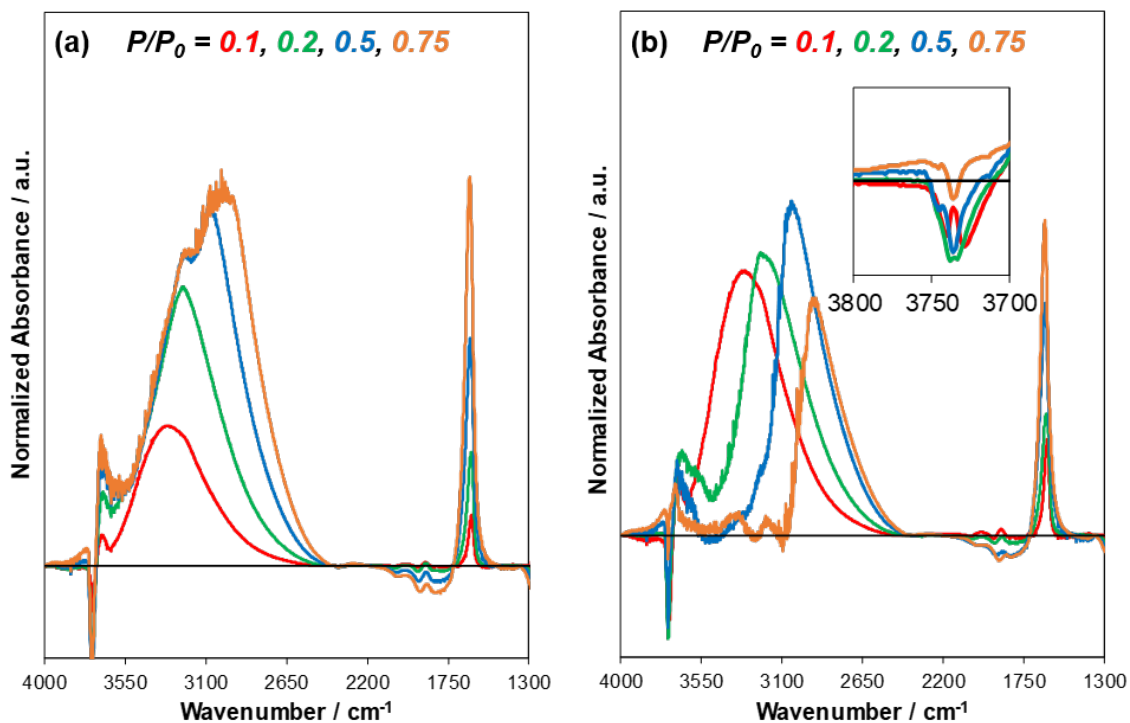


**Figure 8.48:** (a) Baseline-corrected difference IR spectra of H<sub>2</sub>O adsorbed at 293 K on deAl-Beta-F(1.4) at  $P/P_0$  values of 0.1 (red), 0.2 (green), 0.5 (blue), and 0.75 (orange). Difference spectra reflect the subtraction of the spectrum of the dehydrated sample under flowing He prior to H<sub>2</sub>O adsorption, and the spectrum of H<sub>2</sub>O adsorbed within an empty IR cell. (b) Differential-subtracted spectra reflect the difference between the spectrum at the given  $P/P_0$  value and the next-lowest  $P/P_0$  value. All spectra are normalized to the T–O–T overtone peak area (1750–2100 cm<sup>-1</sup>) prior to adsorption.

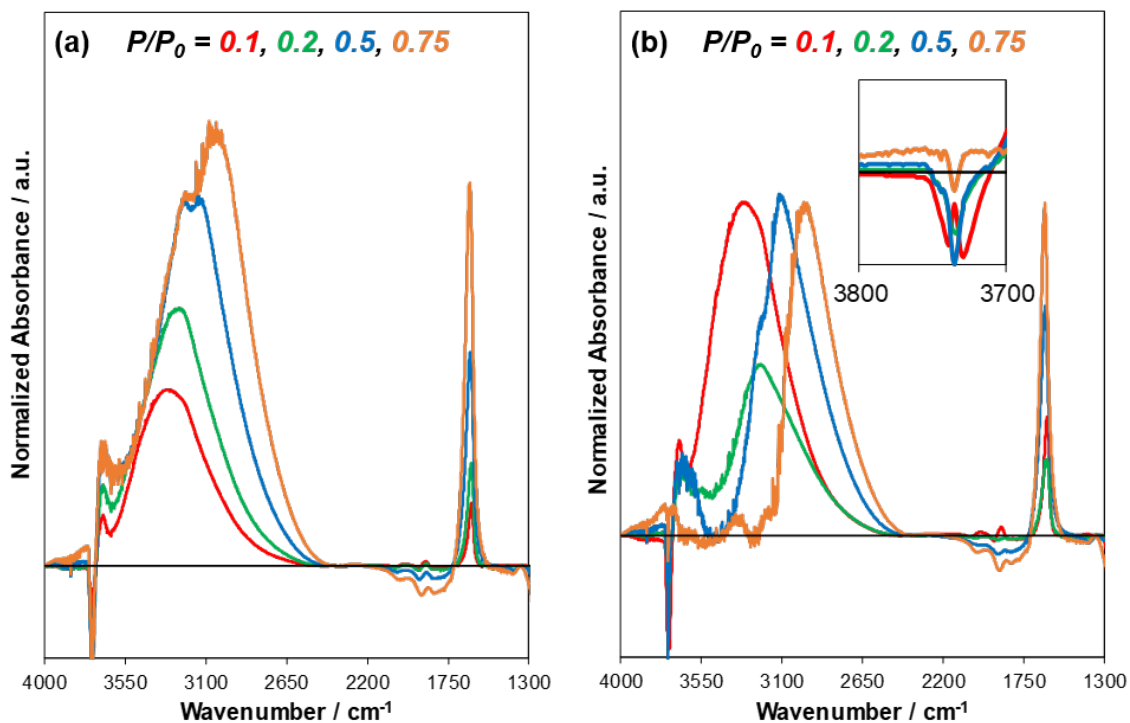


**Figure 8.49:** (a) Baseline-corrected difference IR spectra of H<sub>2</sub>O adsorbed at 293 K on deAl-Beta-F(1.2) at  $P/P_0$  values of 0.1 (red), 0.2 (green), 0.5 (blue), and 0.75 (orange). Difference spectra reflect the subtraction of the spectrum of the dehydrated sample under flowing He prior to H<sub>2</sub>O adsorption, and the spectrum of H<sub>2</sub>O adsorbed within an empty IR cell. (b) Differential-subtracted spectra reflect the difference between the spectrum at the given  $P/P_0$  value and the next-lowest  $P/P_0$  value. All spectra are normalized to the T–O–T overtone peak area (1750–2100 cm<sup>-1</sup>) prior to adsorption.

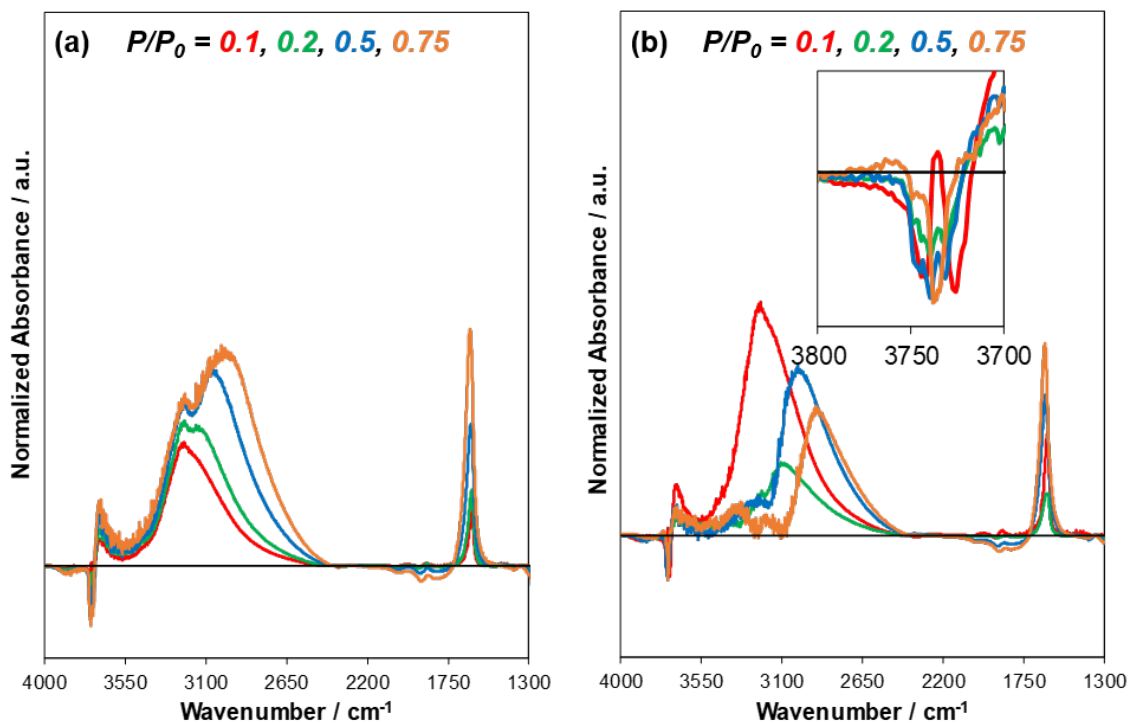


**Figure 8.50:** (a) Baseline-corrected difference IR spectra of H<sub>2</sub>O adsorbed at 293 K on deAl-Beta-F(0.78) at  $P/P_0$  values of 0.1 (red), 0.2 (green), 0.5 (blue), and 0.75 (orange). Difference spectra reflect the subtraction of the spectrum of the dehydrated sample under flowing He prior to H<sub>2</sub>O adsorption, and the spectrum of H<sub>2</sub>O adsorbed within an empty IR cell. (b) Differential-subtracted spectra reflect the difference between the spectrum at the given  $P/P_0$  value and the next-lowest  $P/P_0$  value. All spectra are normalized to the T–O–T overtone peak area (1750–2100 cm<sup>-1</sup>) prior to adsorption.

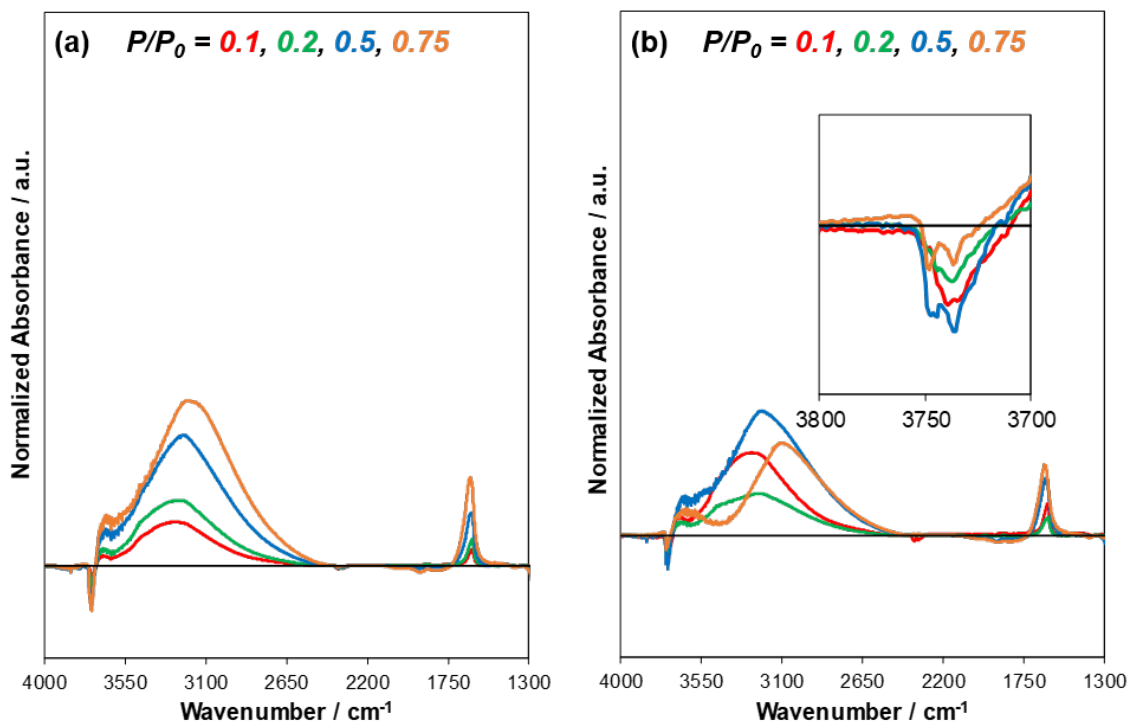


**Figure 8.51:** (a) Baseline-corrected difference IR spectra of H<sub>2</sub>O adsorbed at 293 K on deAl-Beta-F(0.57) at  $P/P_0$  values of 0.1 (red), 0.2 (green), 0.5 (blue), and 0.75 (orange). Difference spectra reflect the subtraction of the spectrum of the dehydrated sample under flowing He prior to H<sub>2</sub>O adsorption, and the spectrum of H<sub>2</sub>O adsorbed within an empty IR cell. (b) Differential-subtracted spectra reflect the difference between the spectrum at the given  $P/P_0$  value and the next-lowest  $P/P_0$  value. All spectra are normalized to the T–O–T overtone peak area (1750–2100 cm<sup>-1</sup>) prior to adsorption.

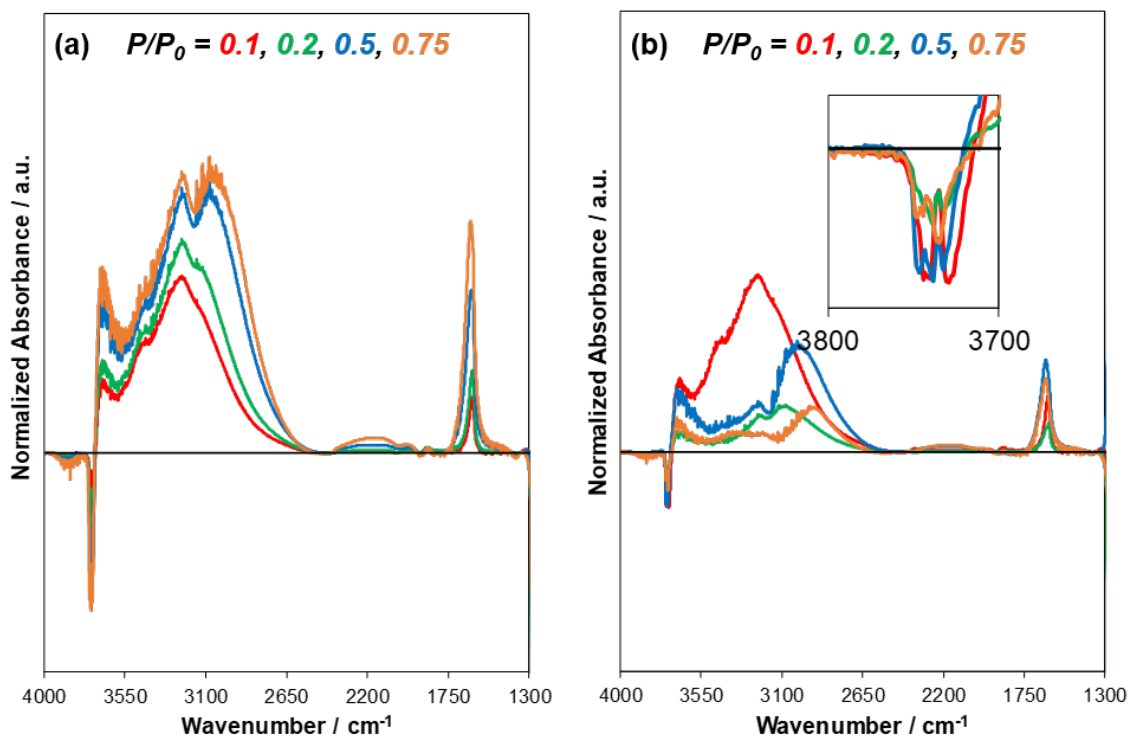


**Figure 8.52:** (a) Baseline-corrected difference IR spectra of H<sub>2</sub>O adsorbed at 293 K on deAl-Beta-F(0.16) at  $P/P_0$  values of 0.1 (red), 0.2 (green), 0.5 (blue), and 0.75 (orange). Difference spectra reflect the subtraction of the spectrum of the dehydrated sample under flowing He prior to H<sub>2</sub>O adsorption, and the spectrum of H<sub>2</sub>O adsorbed within an empty IR cell. (b) Differential-subtracted spectra reflect the difference between the spectrum at the given  $P/P_0$  value and the next-lowest  $P/P_0$  value. All spectra are normalized to the T–O–T overtone peak area (1750–2100 cm<sup>-1</sup>) prior to adsorption.

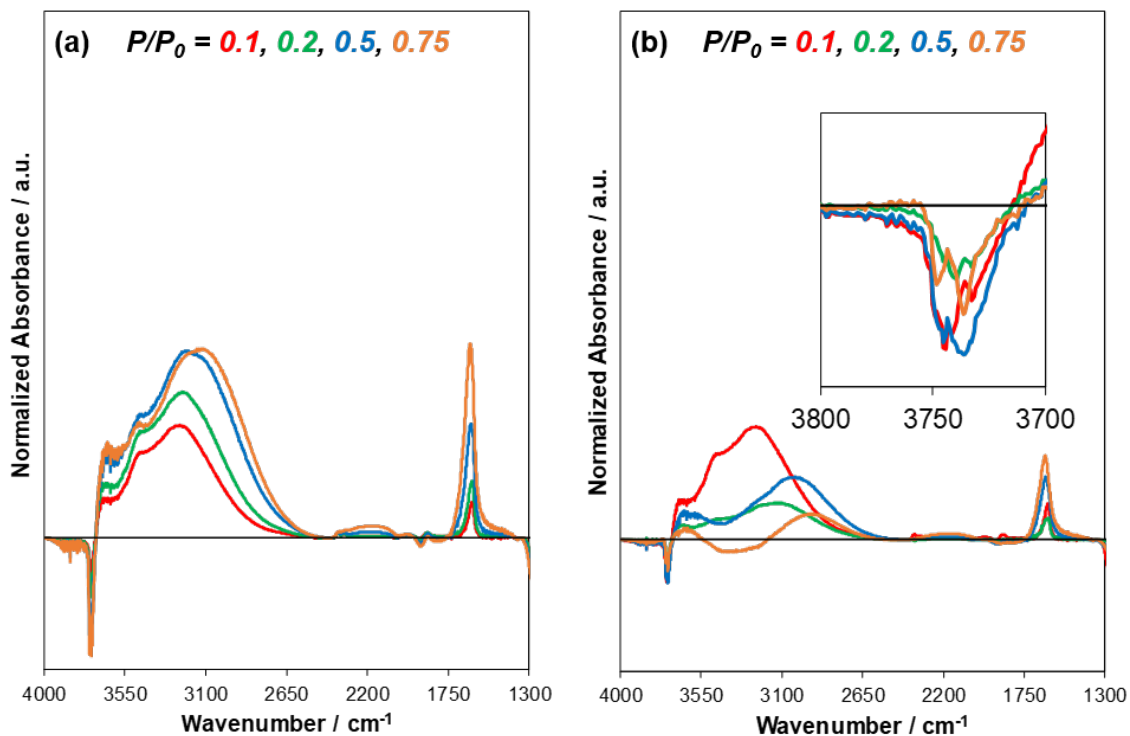


**Figure 8.53:** (a) Baseline-corrected difference IR spectra of H<sub>2</sub>O adsorbed at 293 K on deAl-Beta-F(0.11) at  $P/P_0$  values of 0.1 (red), 0.2 (green), 0.5 (blue), and 0.75 (orange). Difference spectra reflect the subtraction of the spectrum of the dehydrated sample under flowing He prior to H<sub>2</sub>O adsorption, and the spectrum of H<sub>2</sub>O adsorbed within an empty IR cell. (b) Differential-subtracted spectra reflect the difference between the spectrum at the given  $P/P_0$  value and the next-lowest  $P/P_0$  value. All spectra are normalized to the T–O–T overtone peak area (1750–2100 cm<sup>-1</sup>) prior to adsorption.

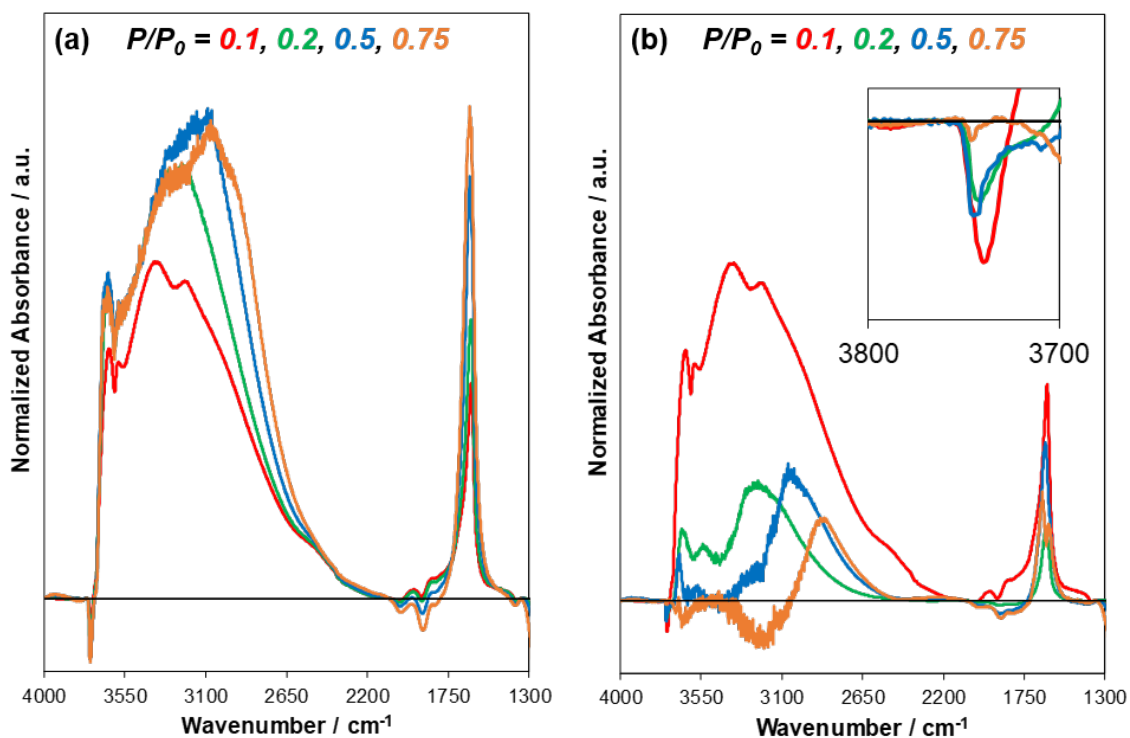


**Figure 8.54:** (a) Baseline-corrected difference IR spectra of H<sub>2</sub>O adsorbed at 293 K on H-Al-Beta-F(2.0) at  $P/P_0$  values of 0.1 (red), 0.2 (green), 0.5 (blue), and 0.75 (orange). Difference spectra reflect the subtraction of the spectrum of the dehydrated sample under flowing He prior to H<sub>2</sub>O adsorption, and the spectrum of H<sub>2</sub>O adsorbed within an empty IR cell. (b) Differential-subtracted spectra reflect the difference between the spectrum at the given  $P/P_0$  value and the next-lowest  $P/P_0$  value. All spectra are normalized to the T–O–T overtone peak area (1750–2100 cm<sup>-1</sup>) prior to adsorption.

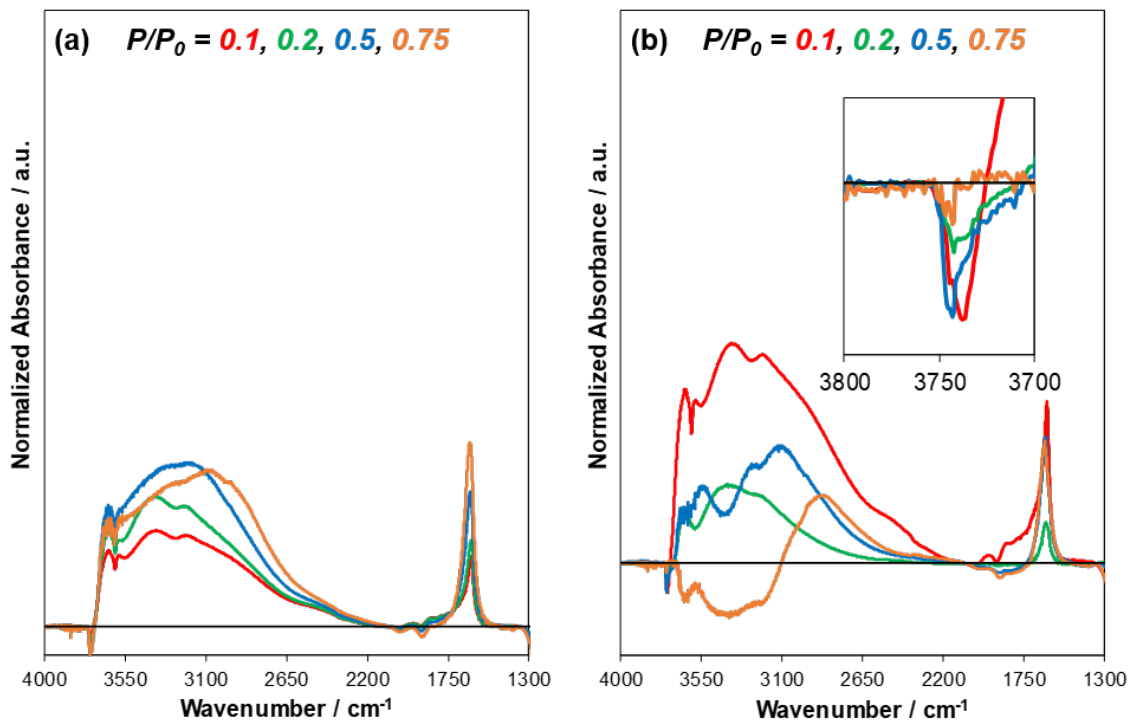


**Figure 8.55:** (a) Baseline-corrected difference IR spectra of H<sub>2</sub>O adsorbed at 293 K on H-Al-Beta-F(1.4) at  $P/P_0$  values of 0.1 (red), 0.2 (green), 0.5 (blue), and 0.75 (orange). Difference spectra reflect the subtraction of the spectrum of the dehydrated sample under flowing He prior to H<sub>2</sub>O adsorption, and the spectrum of H<sub>2</sub>O adsorbed within an empty IR cell. (b) Differential-subtracted spectra reflect the difference between the spectrum at the given  $P/P_0$  value and the next-lowest  $P/P_0$  value. All spectra are normalized to the T–O–T overtone peak area (1750–2100 cm<sup>-1</sup>) prior to adsorption.

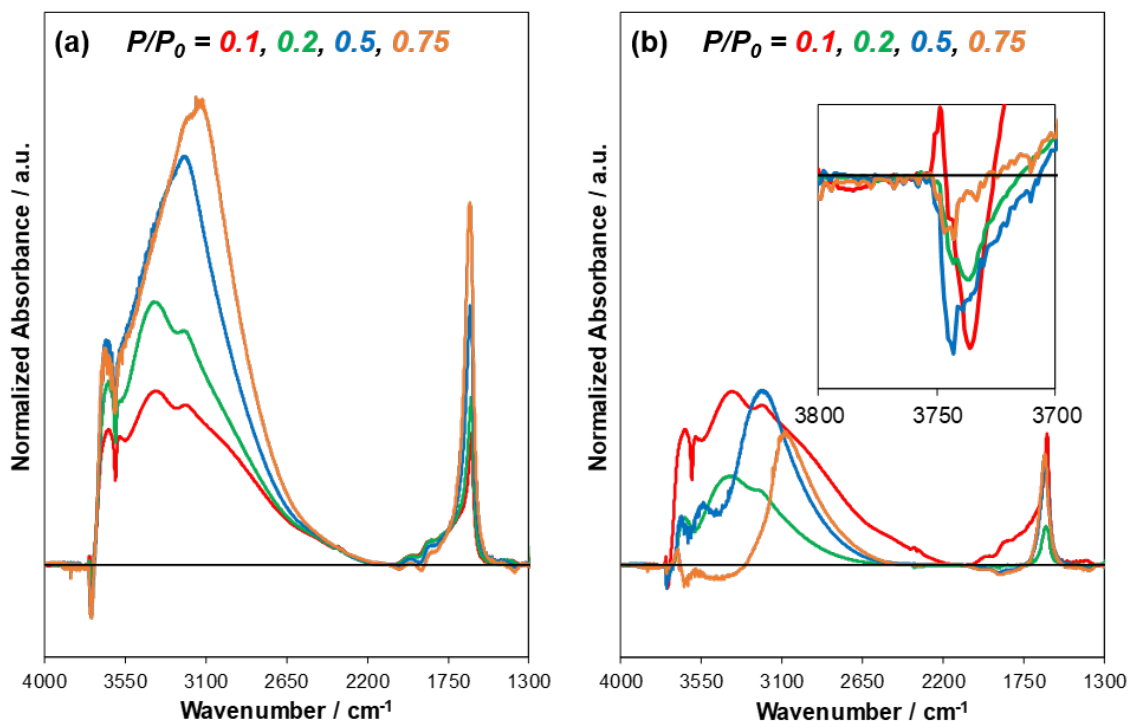


**Figure 8.56:** (a) Baseline-corrected difference IR spectra of H<sub>2</sub>O adsorbed at 293 K on H-Al-Beta-F(1.2) at  $P/P_0$  values of 0.1 (red), 0.2 (green), 0.5 (blue), and 0.75 (orange). Difference spectra reflect the subtraction of the spectrum of the dehydrated sample under flowing He prior to H<sub>2</sub>O adsorption, and the spectrum of H<sub>2</sub>O adsorbed within an empty IR cell. (b) Differential-subtracted spectra reflect the difference between the spectrum at the given  $P/P_0$  value and the next-lowest  $P/P_0$  value. All spectra are normalized to the T–O–T overtone peak area (1750–2100 cm<sup>-1</sup>) prior to adsorption.

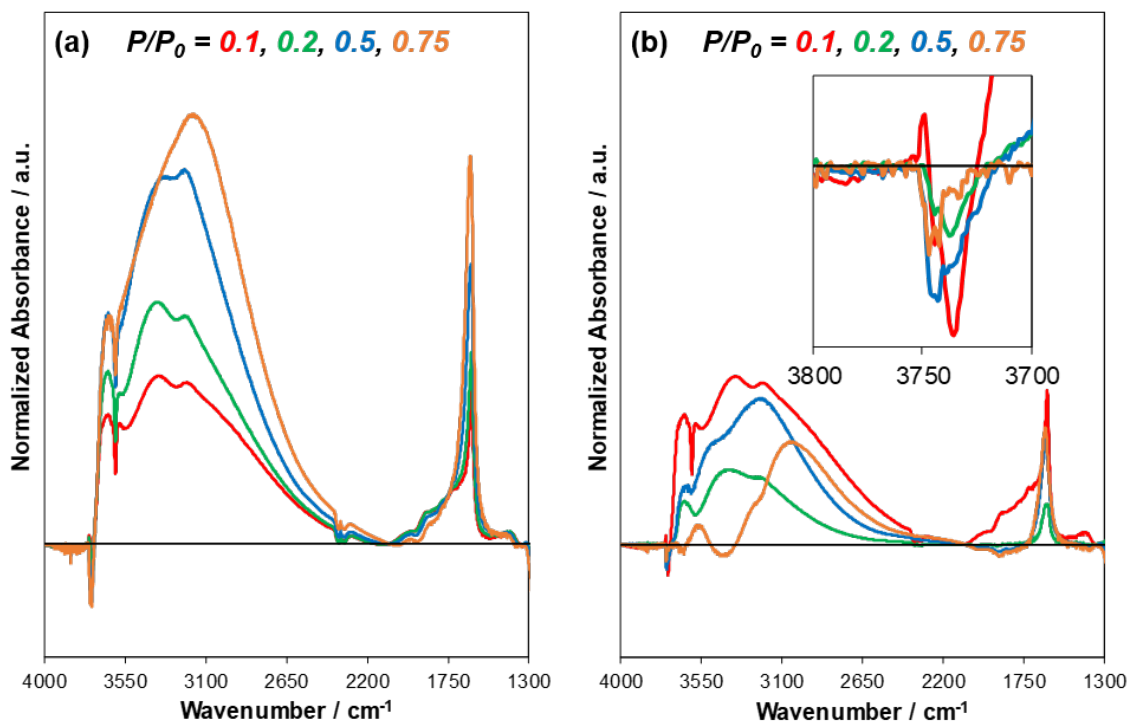


**Figure 8.57:** (a) Baseline-corrected difference IR spectra of H<sub>2</sub>O adsorbed at 293 K on H-Al-Beta-F(0.78) at  $P/P_0$  values of 0.1 (red), 0.2 (green), 0.5 (blue), and 0.75 (orange). Difference spectra reflect the subtraction of the spectrum of the dehydrated sample under flowing He prior to H<sub>2</sub>O adsorption, and the spectrum of H<sub>2</sub>O adsorbed within an empty IR cell. (b) Differential-subtracted spectra reflect the difference between the spectrum at the given  $P/P_0$  value and the next-lowest  $P/P_0$  value. All spectra are normalized to the T–O–T overtone peak area (1750–2100 cm<sup>-1</sup>) prior to adsorption.

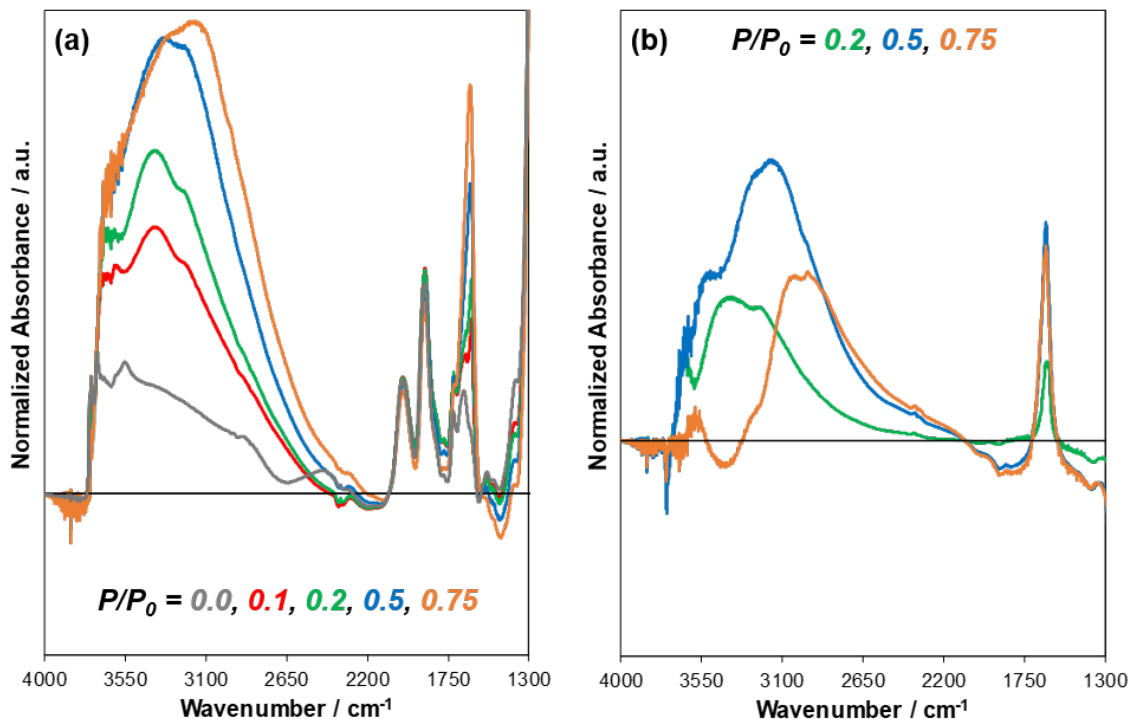


**Figure 8.58:** (a) Baseline-corrected IR spectra of  $\text{H}_2\text{O}$  adsorbed at 293 K on H-Al-Beta-F(0.57) at  $P/P_0$  values of 0.1 (red), 0.2 (green), 0.5 (blue), and 0.75 (orange). A small leak in the system led to  $\text{H}_2\text{O}$  entering the system during cooling to 293 K, and adsorbing at some of the  $\text{H}^+$  in 1:1 hydrogen-bonded complexes, evident in the A, B, C triplet seen in the grey spectrum, so difference spectra were not analyzed. (b) Differential-subtracted spectra reflect the difference between the spectrum at the given  $P/P_0$  value and the next-lowest  $P/P_0$  value. All spectra are normalized to the T–O–T overtone peak area ( $1750\text{--}2100\text{ cm}^{-1}$ ) prior to adsorption.

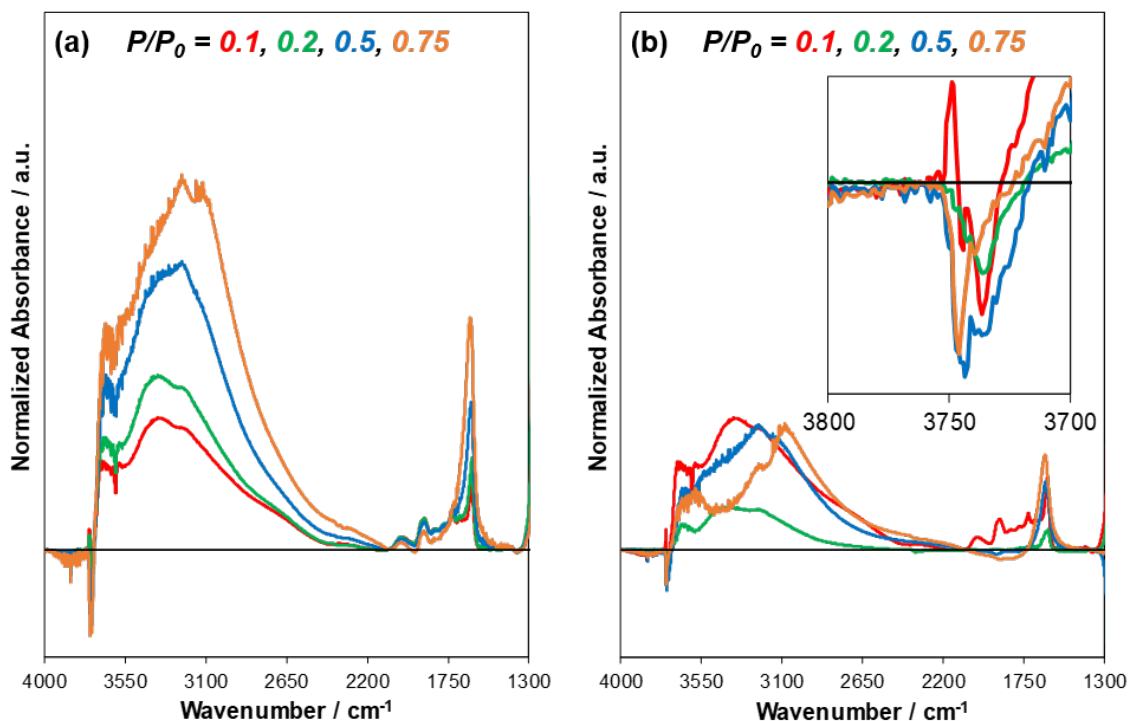


**Figure 8.59:** (a) Baseline-corrected difference IR spectra of H<sub>2</sub>O adsorbed at 293 K on H-Al-Beta-F(0.16) at  $P/P_0$  values of 0.1 (red), 0.2 (green), 0.5 (blue), and 0.75 (orange). Difference spectra reflect the subtraction of the spectrum of the dehydrated sample under flowing He prior to H<sub>2</sub>O adsorption, and the spectrum of H<sub>2</sub>O adsorbed within an empty IR cell. (b) Differential-subtracted spectra reflect the difference between the spectrum at the given  $P/P_0$  value and the next-lowest  $P/P_0$  value. All spectra are normalized to the T–O–T overtone peak area (1750–2100 cm<sup>-1</sup>) prior to adsorption.

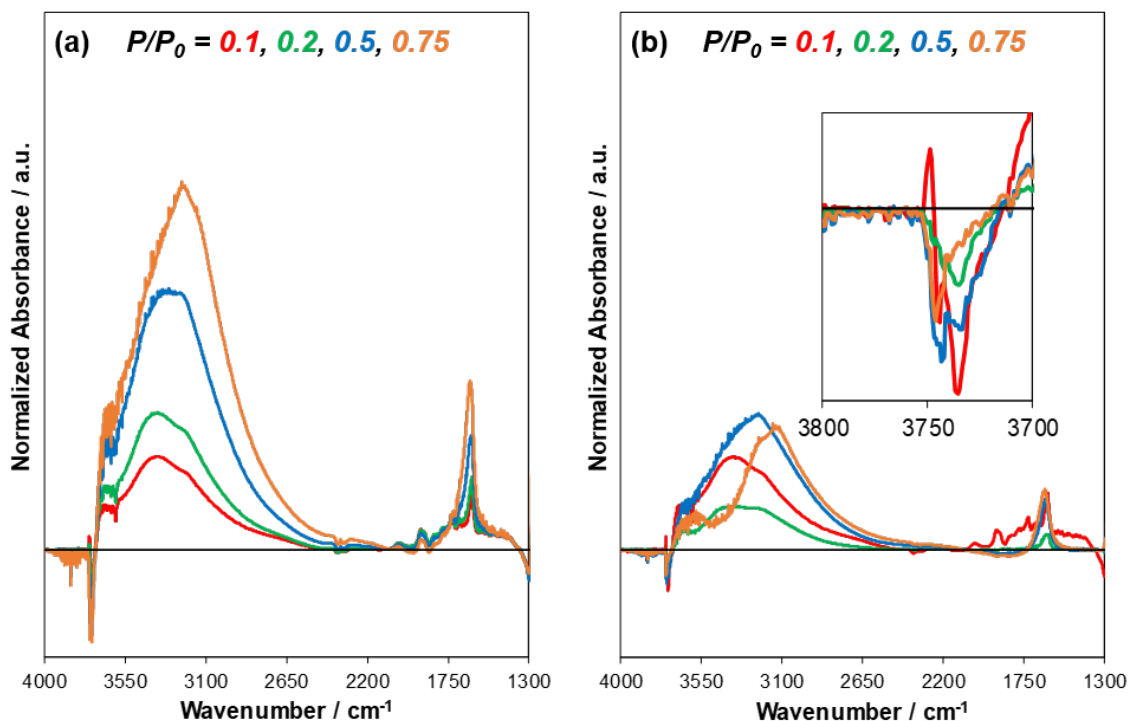


**Figure 8.60:** (a) Baseline-corrected difference IR spectra of H<sub>2</sub>O adsorbed at 293 K on H-Al-Beta-F(0.11) at  $P/P_0$  values of 0.1 (red), 0.2 (green), 0.5 (blue), and 0.75 (orange). Difference spectra reflect the subtraction of the spectrum of the dehydrated sample under flowing He prior to H<sub>2</sub>O adsorption, and the spectrum of H<sub>2</sub>O adsorbed within an empty IR cell. (b) Differential-subtracted spectra reflect the difference between the spectrum at the given  $P/P_0$  value and the next-lowest  $P/P_0$  value. All spectra are normalized to the T–O–T overtone peak area (1750–2100 cm<sup>-1</sup>) prior to adsorption.

### 8.6.3.7 Infrared spectra of D<sub>2</sub>O/HOD/H<sub>2</sub>O mixtures

The correlation of peak areas in Figure 8.62 with a regressed slope of 0.28 that closely matches the mole fraction of HOD in the 16:8:1 D<sub>2</sub>O:HOD:H<sub>2</sub>O stream (0.32) indicates that coverages and extents of hydrogen bonding between H(D)<sub>2</sub>O molecules are the same between pure H<sub>2</sub>O and the mixture experiments. Note that the  $\delta(\text{HOH})$  peak area was too small to quantify because of the low mole fraction of H<sub>2</sub>O in the mixture (0.04), and the  $\delta(\text{DOD})$  peak at 1210 cm<sup>-1</sup> could not be detected because it is obscured by the Si-O-Si modes of the zeolite framework (<1300 cm<sup>-1</sup>). At the same coverage values where in the pure-H<sub>2</sub>O experiment the  $\nu(\text{OH})$  peak center shifted to low wavenumbers with increasing coverages, when 96% of the mixture is D<sub>2</sub>O or HOD there is no shift in the  $\nu(\text{OH})$  peak center, because  $2\delta(\text{HOD})$  (2900 cm<sup>-1</sup>) and  $2\delta(\text{DOD})$  (2400 cm<sup>-1</sup>) do not generate Fermi resonance with  $\nu(\text{OH})$  when in extended hydrogen-bonded networks, because they lie at lower wavenumbers [427].

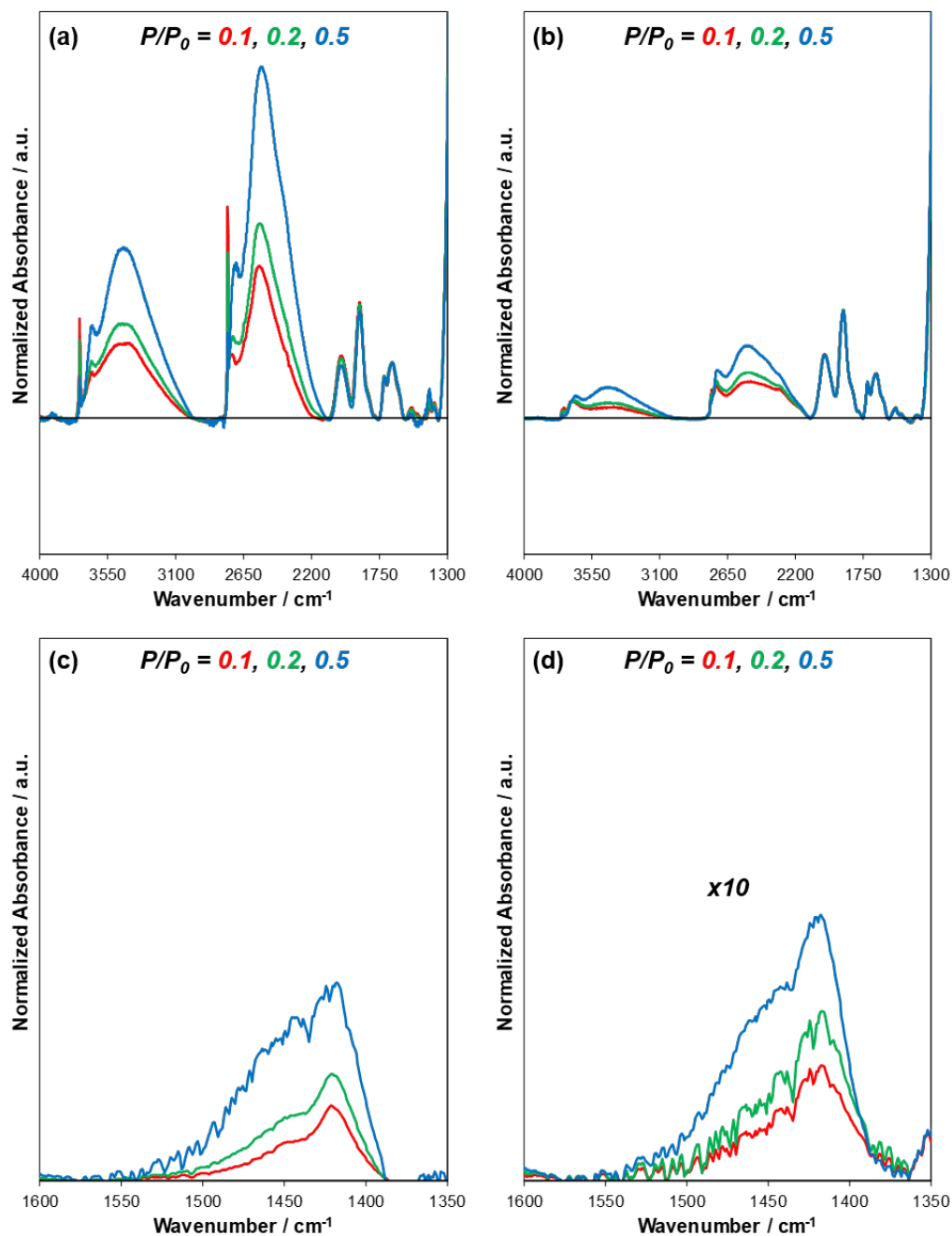


**Figure 8.61:** Baseline-corrected, gas-phase-corrected IR spectra of 16:8:1 D<sub>2</sub>O:HOD:H<sub>2</sub>O mixtures adsorbed at 303 K on (a) deAl-Beta-F(2.0) and (b) Si-Beta-F, at  $P/P_0$  values of 0.1 (red), 0.2 (green), and 0.5 (blue). All spectra are normalized to the T–O–T overtone peak area (1750–2100 cm<sup>-1</sup>) prior to adsorption. (c) and (d) show subtracted IR spectra of the  $\delta$ (HOD) peaks under the same conditions described for (a), (b) on (c) deAl-Beta-F(2.0) and (d) Si-Beta-F.

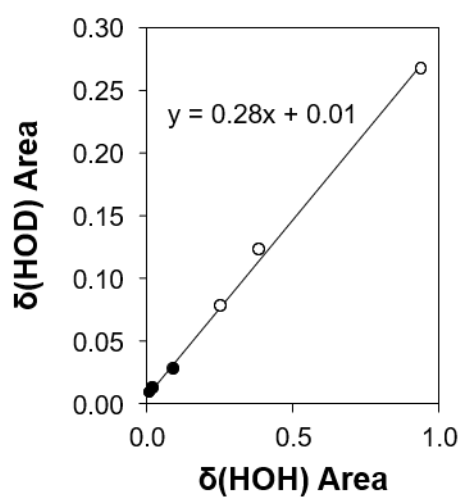


**Figure 8.62:**  $\delta(\text{HOD})$  peak areas quantified from Figure 8.61c,d correlated with the  $\delta(\text{HOH})$  peak areas quantified from Figure 8.46 and Figure 8.47 on Si-Beta-F (●) and deAl-Beta-F(2.0) (○) at the same  $P/P_0$  conditions (0.1, 0.2, 0.5).

## 8.6.3.8 Infrared spectra collected at 373 K

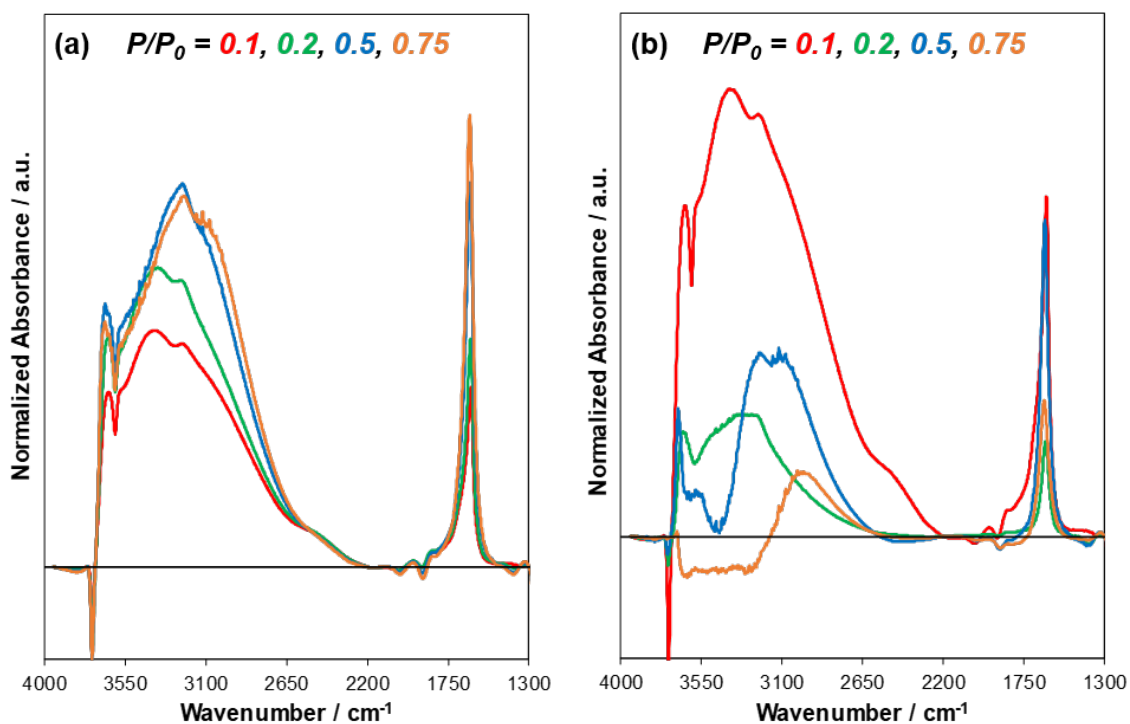


**Figure 8.63:** (a) Baseline-corrected difference IR spectra of  $\text{H}_2\text{O}$  adsorbed at 373 K on H-Al-Beta-F(2.0) at  $\text{H}_2\text{O}$  pressures of 10 (red), 20 (green), 30 (blue), and 75 kPa (orange) ( $P/P_0 = 0.1$ – $0.75$ ). Difference spectra reflect the subtraction of the spectrum of the dehydrated sample under flowing He prior to  $\text{H}_2\text{O}$  adsorption, and the spectrum of  $\text{H}_2\text{O}$  adsorbed within an empty IR cell. (b) Differential-subtracted spectra reflect the difference between the spectrum at the given  $P/P_0$  value and the next-lowest  $P/P_0$  value. All spectra are normalized to the T–O–T overtone peak area ( $1750$ – $2100 \text{ cm}^{-1}$ ) prior to adsorption.

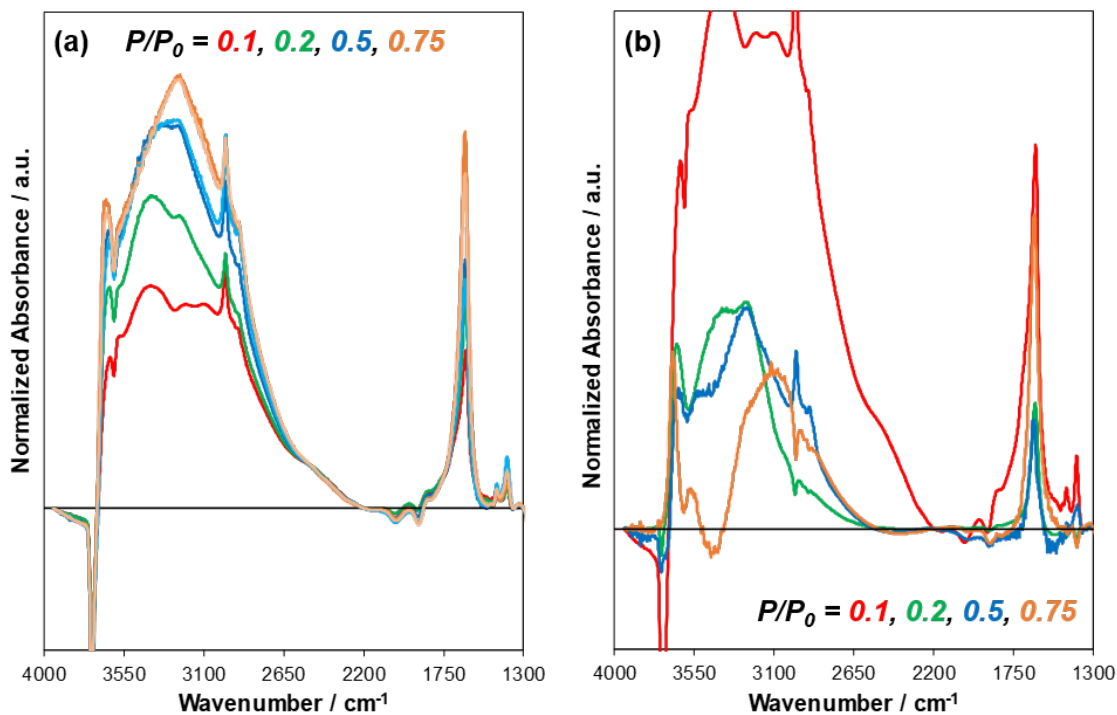


**Figure 8.64:** (a) Baseline-corrected difference IR spectra of  $\text{H}_2\text{O}/\text{C}_2\text{H}_5\text{OH}$  mixtures adsorbed at 373 K on H-Al-Beta-F(2.0) at  $\text{H}_2\text{O}$  pressures of 10 (red), 20 (green), 30 (blue), and 75 kPa (orange) ( $P/P_0 = 0.1$ – $0.75$ ). The colors shown in the legend correspond to  $\text{C}_2\text{H}_5\text{OH}/\text{H}_2\text{O}$  ratios of 0.005 (red, green) and 0.03 (blue, orange), and the lighter blue and orange spectra correspond to a  $\text{C}_2\text{H}_5\text{OH}/\text{H}_2\text{O}$  ratio of 0.06. Difference spectra reflect the subtraction of the spectrum of the dehydrated sample under flowing He prior to  $\text{H}_2\text{O}$  adsorption, and the spectrum of  $\text{H}_2\text{O}$  adsorbed within an empty IR cell. (b) Differential-subtracted spectra reflect the difference between the spectrum at the given  $P/P_0$  value and the next-lowest  $P/P_0$  value. All spectra are normalized to the T–O–T overtone peak area ( $1750$ – $2100\text{ cm}^{-1}$ ) prior to adsorption.

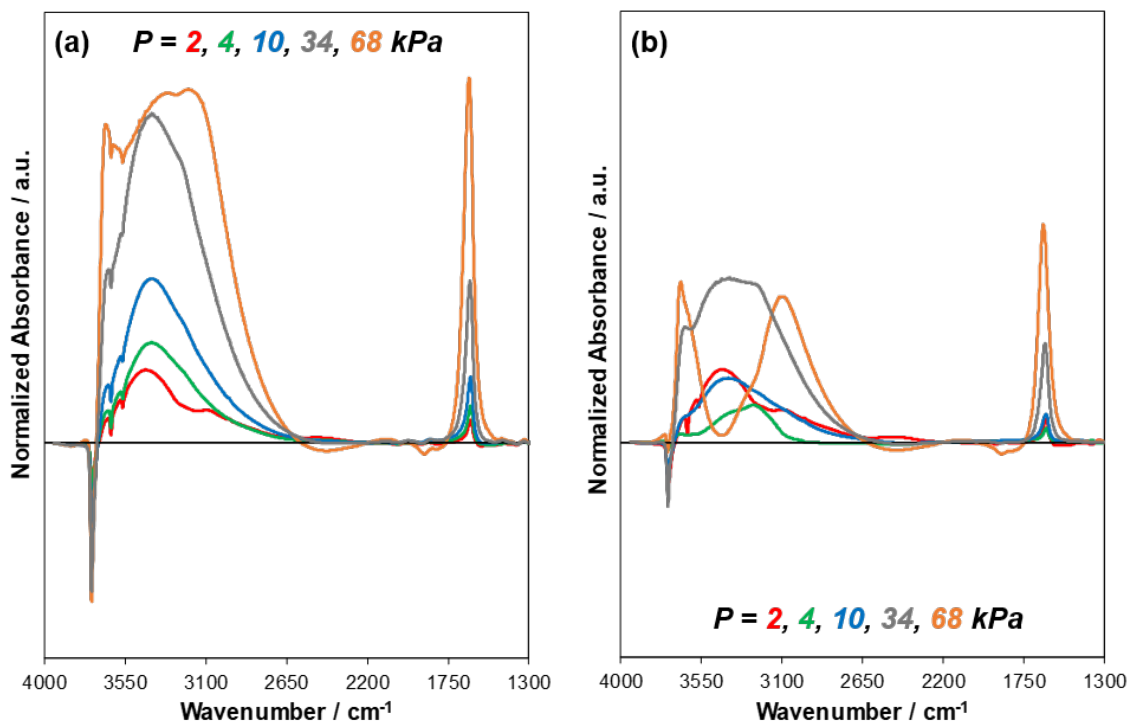


**Figure 8.65:** (a) Baseline-corrected difference IR spectra of H<sub>2</sub>O adsorbed at 373 K on H-Al-FAU at H<sub>2</sub>O pressures of 2 (red), 4 (green), 10 (blue), 34 (grey), and 68 kPa (orange) ( $P/P_0 = 0.02$ – $0.75$ ). Difference spectra reflect the subtraction of the spectrum of the dehydrated sample under flowing He prior to H<sub>2</sub>O adsorption, and the spectrum of H<sub>2</sub>O adsorbed within an empty IR cell. (b) Differential-subtracted spectra reflect the difference between the spectrum at the given  $P/P_0$  value and the next-lowest  $P/P_0$  value. All spectra are normalized to the T–O–T overtone peak area ( $1750$ – $2100$  cm<sup>-1</sup>) prior to adsorption.

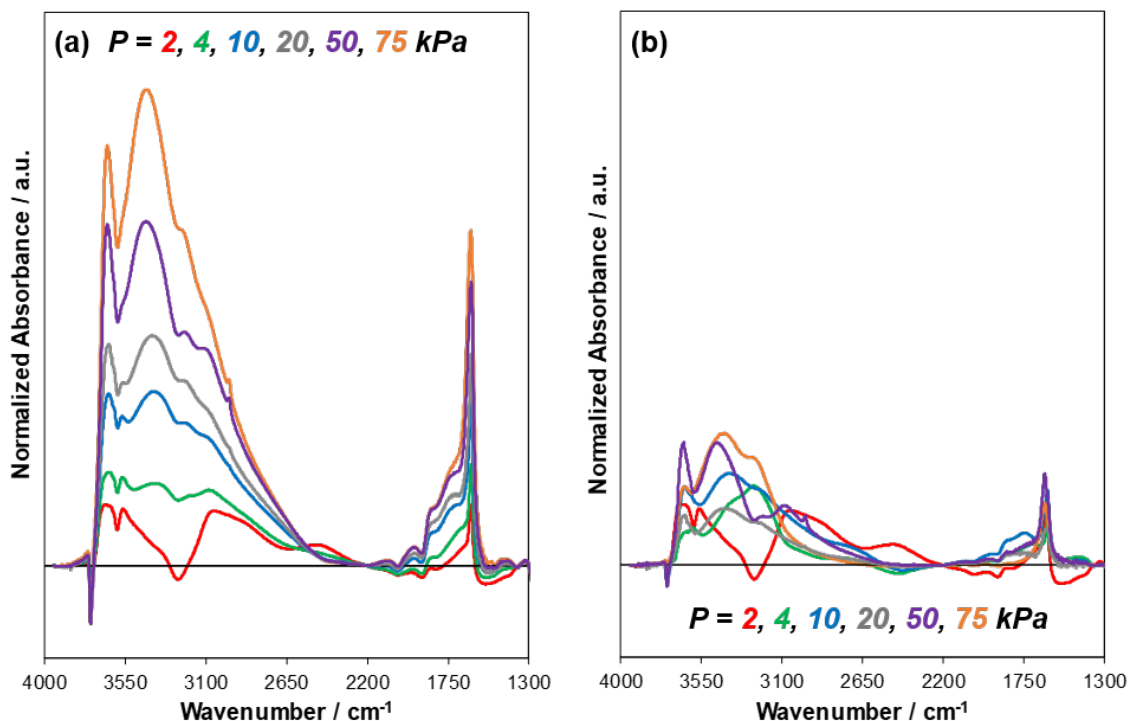


**Figure 8.66:** (a) Baseline-corrected difference IR spectra of H<sub>2</sub>O adsorbed at 373 K on H-Al-TON at H<sub>2</sub>O pressures of 2 (red), 4 (green), 10 (blue), 20 (grey), 50 (purple) and 75 kPa (orange) ( $P/P_0 = 0.02\text{--}0.75$ ). Difference spectra reflect the subtraction of the spectrum of the dehydrated sample under flowing He prior to H<sub>2</sub>O adsorption, and the spectrum of H<sub>2</sub>O adsorbed within an empty IR cell. (b) Differential-subtracted spectra reflect the difference between the spectrum at the given  $P/P_0$  value and the next-lowest  $P/P_0$  value. All spectra are normalized to the T–O–T overtone peak area (1750–2100 cm<sup>-1</sup>) prior to adsorption.

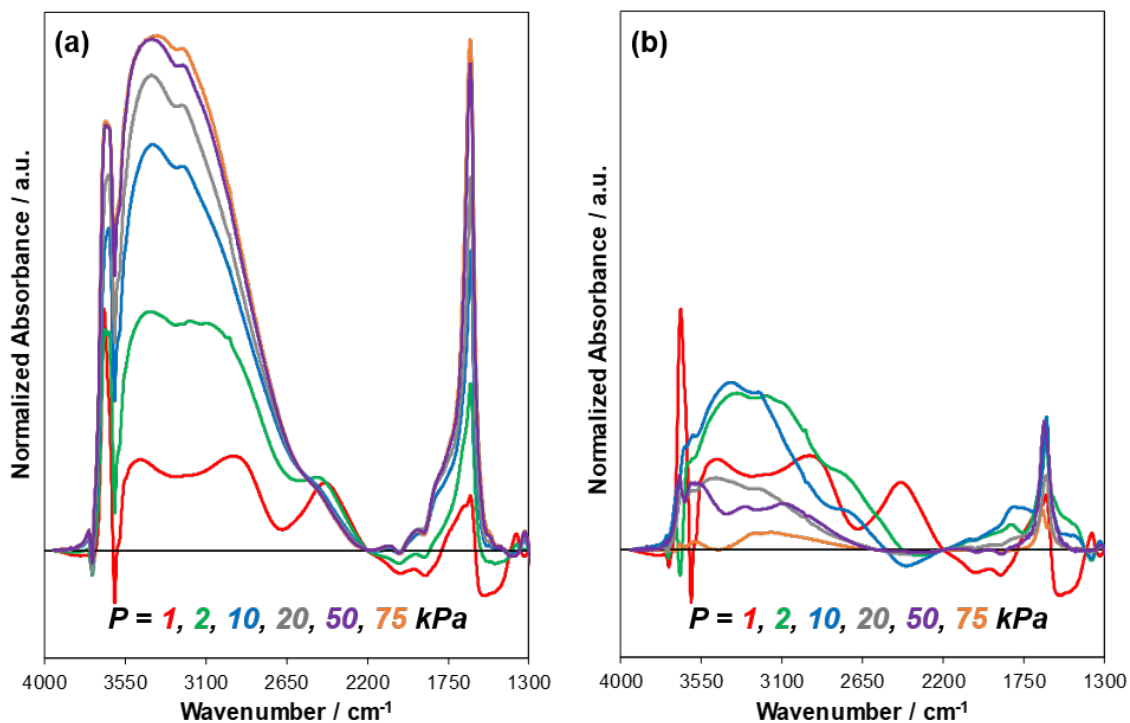


**Figure 8.67:** (a) Baseline-corrected difference IR spectra of H<sub>2</sub>O adsorbed at 373 K on H-Al-AEI at H<sub>2</sub>O pressures of 1 (red), 2 (green), 10 (blue), 20 (grey), 50 (purple) and 75 kPa (orange) ( $P/P_0 = 0.02$ – $0.75$ ). Difference spectra reflect the subtraction of the spectrum of the dehydrated sample under flowing He prior to H<sub>2</sub>O adsorption, and the spectrum of H<sub>2</sub>O adsorbed within an empty IR cell. (b) Differential-subtracted spectra reflect the difference between the spectrum at the given  $P/P_0$  value and the next-lowest  $P/P_0$  value. All spectra are normalized to the T–O–T overtone peak area ( $1750$ – $2100$  cm<sup>-1</sup>) prior to adsorption.

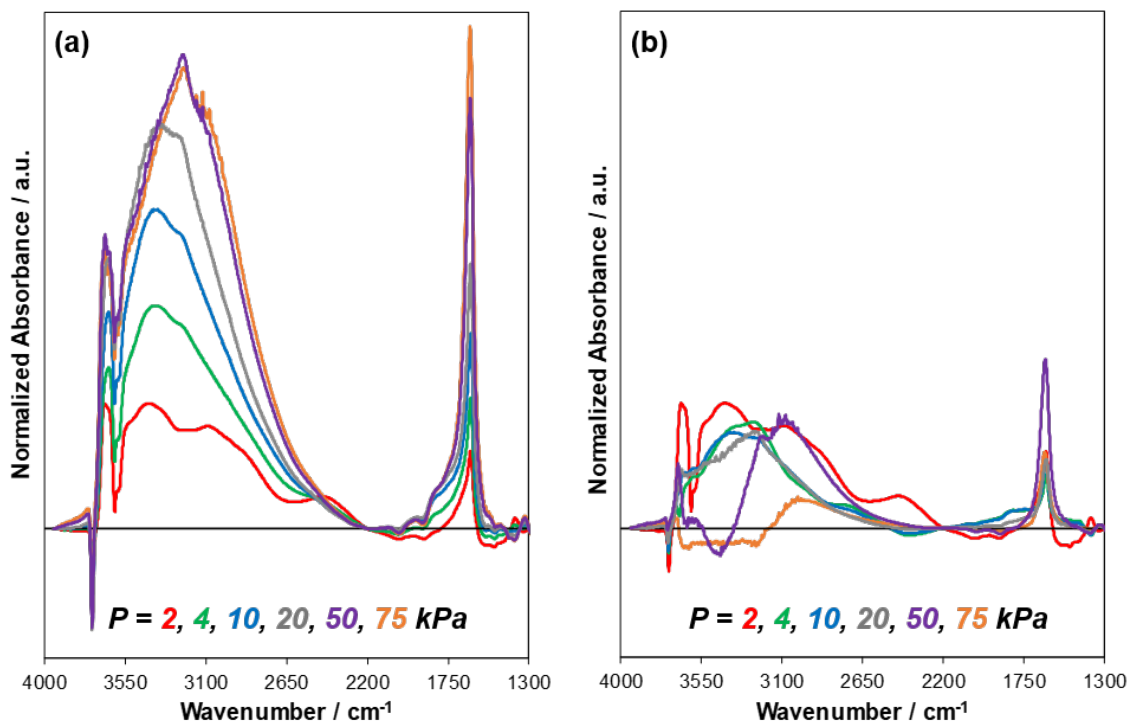


**Figure 8.68:** (a) Baseline-corrected difference IR spectra of H<sub>2</sub>O adsorbed at 373 K on H-Al-CHA at H<sub>2</sub>O pressures of 2 (red), 4 (green), 10 (blue), 20 (grey), 50 (purple) and 75 kPa (orange) ( $P/P_0 = 0.02$ – $0.75$ ). Difference spectra reflect the subtraction of the spectrum of the dehydrated sample under flowing He prior to H<sub>2</sub>O adsorption, and the spectrum of H<sub>2</sub>O adsorbed within an empty IR cell. (b) Differential-subtracted spectra reflect the difference between the spectrum at the given  $P/P_0$  value and the next-lowest  $P/P_0$  value. All spectra are normalized to the T–O–T overtone peak area ( $1750$ – $2100$  cm<sup>-1</sup>) prior to adsorption.

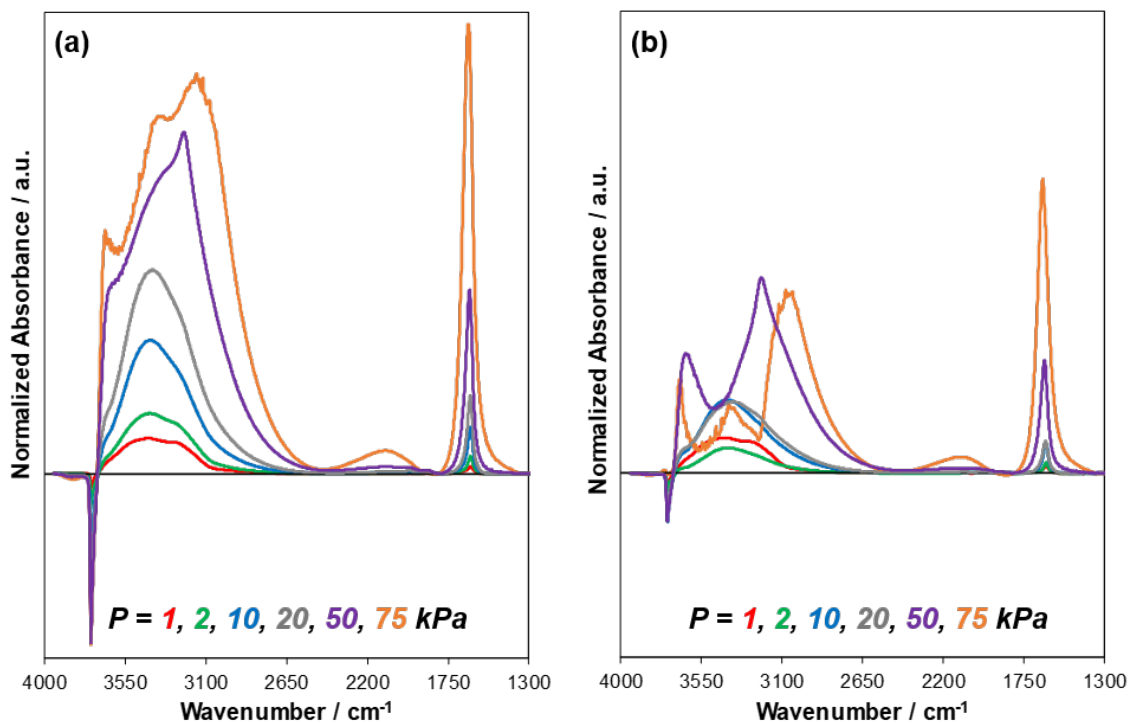


**Figure 8.69:** (a) Baseline-corrected difference IR spectra of H<sub>2</sub>O adsorbed at 373 K on HPW/Si-MCM-41 at H<sub>2</sub>O pressures of 1 (red), 2 (green), 10 (blue), 20 (grey), 50 (purple) and 75 kPa (orange) ( $P/P_0 = 0.02\text{--}0.75$ ). Difference spectra reflect the subtraction of the spectrum of the dehydrated sample under flowing He prior to H<sub>2</sub>O adsorption, and the spectrum of H<sub>2</sub>O adsorbed within an empty IR cell. (b) Differential-subtracted spectra reflect the difference between the spectrum at the given  $P/P_0$  value and the next-lowest  $P/P_0$  value. All spectra are normalized to the T–O–T overtone peak area ( $1750\text{--}2100\text{ cm}^{-1}$ ) prior to adsorption.

## 8.6.3.9 Theoretical calculations

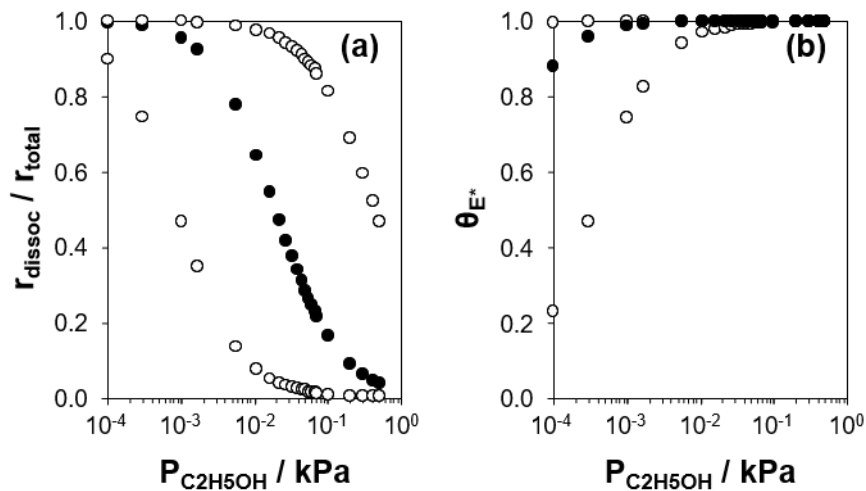


**Figure 8.70:** (a) Relative rates of dissociative and associative pathways to form diethyl ether (373 K) in the absence of co-fed water as a function of ethanol pressure on H-Al-Beta zeolites predicted from their DFT-calculated free energy barriers (Eq. 8.25), plotted as the fraction of the total rate ( $r_{total} = r_{dissoc} + r_{assoc}$ ). (b) Predicted coverage of ethanol monomers at H $^+$  in H-Al-Beta at 373 K as a function of ethanol pressure, based on the DFT-calculated adsorption free energy (Eq. 8.26–8.27). In both plots, the range of possible values introduced by a  $\pm 10$  kJ mol $^{-1}$  error in free energies is shown as the unfilled circles.

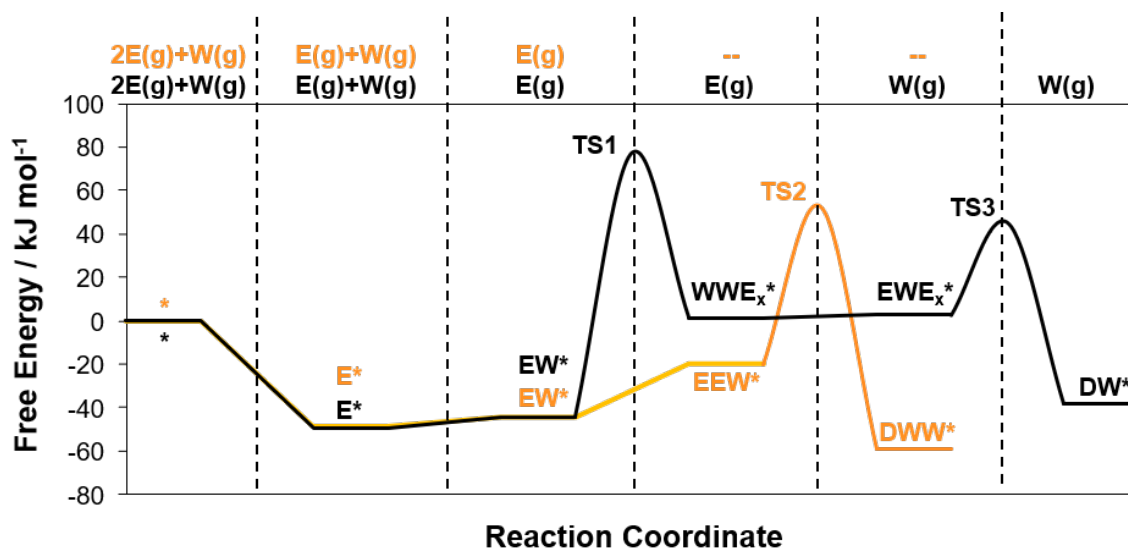


**Figure 8.71:** Gibbs free energies of adsorbed intermediates and transition states within H-Al-Beta calculated by DFT, referenced to two gas-phase ethanol molecules and one water molecule, for diethyl ether formation through the dissociative pathway with one co-adsorbed H<sub>2</sub>O molecule (black) and the associative pathway with one co-adsorbed H<sub>2</sub>O molecule (orange).

## 8.6.4 Supplementary Tables

**Table 8.3:** Ethanol dehydration rate and equilibrium constants on H-Al-Beta zeolites quantified in the absence of co-fed water at 373 K.

Sample	$k_3 / 10^{-5} \text{ mol (mol H}^+)^{-1} \text{ s}^{-1}$	$K_2 / \text{kPa}^{-1}$
H-Al-Beta-F(2.0)	2.5	84
H-Al-Beta-F(1.2)	1.9	51
H-Al-Beta-OH(1.7)	2.9	110

**Table 8.4:** Ethanol dehydration rate and equilibrium constants on H-Al-Beta zeolites quantified at 373 K in the water pressure regime described by Equation 6 in the main text ( $\sim 0.02$ – $10$  kPa).

Sample	$k_3 K_2 / 10^{-4a}$	$k_3 K_2 K_4^{-1} / 10^{-4b}$	$k_3 K_2 / 10^{-4a,c}$
H-Al-Beta-F(2.0)	5.2	1.5	21
H-Al-Beta-F(1.2)	3.8	1.5	9.5
H-Al-Beta-OH(1.7)	19	1.7	33

<sup>a</sup>units [=]  $\text{mol (mol H}^+)^{-1} \text{ s}^{-1} \text{ kPa}^{-1}$  <sup>b</sup>units [=]  $\text{mol (mol H}^+)^{-1} \text{ s}^{-1}$  <sup>c</sup>quantified without co-fed H<sub>2</sub>O (Table 8.3)

**Table 8.5:** Ethanol dehydration rate and equilibrium constants on H-Al-Beta-F(1.2) quantified in the water pressure regime described by Equation 6 in the main text.

Temperature / K	$k_3 K_2 / 10^{-4a}$	$k_3 K_2 K_4^{-1} / 10^{-4b}$	$K_4 / \text{kPa}^{-1}$
373	3.8	1.5	2.5
423	43	120	0.35

<sup>a</sup>units [=]  $\text{mol (mol H}^+)^{-1} \text{ s}^{-1} \text{ kPa}^{-1}$  <sup>b</sup>units [=]  $\text{mol (mol H}^+)^{-1} \text{ s}^{-1}$

**Table 8.6:** Data used to estimate  $\text{H}_2\text{O}/\text{H}^+$  on H-Al-Beta-F zeolites from volumetric adsorption isotherms at  $P/P_0=0.2$ .

Sample	mmol g <sup>-1</sup> H <sub>2</sub> O	Si-Beta-F correction <sup>b</sup>	H <sub>2</sub> O/H <sup>+</sup> <sup>b</sup>
Si-Beta-F	0.087	--	--
H-Al-Beta-F(0.11)	0.31	28%	7.9
H-Al-Beta-F(0.16)	0.46	19%	9.0
H-Al-Beta-F(0.57)	1.0	9%	6.2
H-Al-Beta-F(0.78)	1.4	6%	6.2
H-Al-Beta-F(1.2)	2.2	4%	6.8
H-Al-Beta-F(1.4)	2.9	3%	7.5
H-Al-Beta-F(2.0)	4.1	2%	7.0
Average	--	--	7 ± 1

<sup>a</sup>Percentage of total adsorbed amount subtracted when correcting for Si-Beta-F adsorbed amount <sup>b</sup>Corrected for Si-Beta mmol g<sup>-1</sup> <sup>c</sup>Error represents 95% confidence interval of data set

**Table 8.7:** Data used to estimate  $\text{H}_2\text{O}/\text{H}^+$  on H-Al-Beta-F zeolites from volumetric adsorption isotherms at  $P/P_0=0.1$ .

Sample	mmol g <sup>-1</sup> H <sub>2</sub> O	Si-Beta-F correction <sup>b</sup>	H <sub>2</sub> O/H <sup>+</sup> <sup>b</sup>
Si-Beta-F	0.051	--	--
H-Al-Beta-F(0.11)	0.22	23%	4.6
H-Al-Beta-F(0.16)	0.34	15%	6.1
H-Al-Beta-F(0.57)	0.76	7%	4.5
H-Al-Beta-F(0.78)	1.0	5%	4.6
H-Al-Beta-F(1.2)	1.6	3%	5.0
H-Al-Beta-F(1.4)	2.2	2%	5.5
H-Al-Beta-F(2.0)	3.1	2%	5.3
Average	--	--	5.1 ± 0.4

<sup>a</sup>Percentage of total adsorbed amount subtracted when correcting for Si-Beta-F adsorbed amount <sup>b</sup>Corrected for Si-Beta mmol g<sup>-1</sup> <sup>c</sup>Error represents 95% confidence interval of data set

**Table 8.8:** Data used to estimate  $\text{H}_2\text{O}/(\text{Si-OH nest})$  on deAl-Beta-F zeolites from volumetric adsorption isotherms at  $P/P_0=0.1$ .

Sample	mmol g <sup>-1</sup> H <sub>2</sub> O	Si-Beta-F correction <sup>b</sup>	H <sub>2</sub> O/H <sup>+</sup> <sup>b</sup>
Si-Beta-F	0.044	--	--
deAl-Beta-F(0.11)	0.17	25%	4.6
deAl-Beta-F(0.16)	0.37	12%	8.0
deAl-Beta-F(0.78)	0.75	6%	3.5
deAl-Beta-F(1.2)	0.94	5%	2.9
deAl-Beta-F(1.4)	1.0	4%	2.6
deAl-Beta-F(2.0)	3.6	1%	6.3
Average	--	--	5 ± 2

<sup>a</sup>Percentage of total adsorbed amount subtracted when correcting for Si-Beta-F adsorbed amount <sup>b</sup>Corrected for Si-Beta mmol g<sup>-1</sup> <sup>c</sup>Error represents 95% confidence interval of data set

**Table 8.9:** Data used to estimate  $\text{H}_2\text{O}/(\text{Si-OH nest})$  on deAl-Beta-F zeolites from volumetric adsorption isotherms at  $P/P_0=0.2$ .

Sample	mmol g <sup>-1</sup> H <sub>2</sub> O	Si-Beta-F correction <sup>b</sup>	H <sub>2</sub> O/H <sup>+</sup> <sup>b</sup>
Si-Beta-F	0.087	--	--
deAl-Beta-F(0.11)	0.32	27%	9.8
deAl-Beta-F(0.16)	0.61	14%	14
deAl-Beta-F(0.78)	1.3	7%	6.0
deAl-Beta-F(1.2)	1.6	5%	5.2
deAl-Beta-F(1.4)	1.8	5%	4.7
deAl-Beta-F(2.0)	5.5	2%	9.5
Average	--	--	8 ± 3

<sup>a</sup>Percentage of total adsorbed amount subtracted when correcting for Si-Beta-F adsorbed amount <sup>b</sup>Corrected for Si-Beta mmol g<sup>-1</sup> <sup>c</sup>Error represents 95% confidence interval of data set

**Table 8.10:** H<sub>2</sub>O coverages quantified by *in situ* IR at 373 K on H-Al-Beta-F(2.0).

P <sub>H<sub>2</sub>O</sub> / kPa	N <sub>H<sub>2</sub>O</sub> <sup>a</sup> / 10 <sup>-3</sup> mol g <sup>-1</sup>	P <sub>C<sub>2</sub>H<sub>5</sub>OH</sub> / kPa	N <sub>H<sub>2</sub>O</sub> <sup>b</sup> / 10 <sup>-3</sup> mol g <sup>-1</sup>	Ratio of H <sub>2</sub> O coverages <sup>c</sup>
10	3.8	0.05	3.7	0.99
20	4.7	0.1	5.4	1.15
50	7.9	1.5	6.6	0.84
50	7.9	3	6.5	0.83
75	9.5	2.3	9.8	1.04
75	9.5	4.6	9.1	0.96

<sup>a</sup>Quantified from  $\delta(\text{HOH})$  peak area in IR spectra at the H<sub>2</sub>O pressure specified in column 1. Error  $\pm 0.3 \times 10^{-3}$  mol g<sup>-1</sup>

<sup>b</sup>Quantified from  $\delta(\text{HOH})$  peak area in IR spectra at the H<sub>2</sub>O and C<sub>2</sub>H<sub>5</sub>OH pressures specified in columns 1 and 3. Error  $\pm 0.3 \times 10^{-3}$  mol g<sup>-1</sup>

<sup>c</sup>Ratio of H<sub>2</sub>O coverages with and without co-fed C<sub>2</sub>H<sub>5</sub>OH

## REFERENCES

## REFERENCES

- [1] F. A. Mumpton. La roca magica: Uses of natural zeolites in agriculture and industry. *Proceedings of the National Academy of Sciences*, 96(7):3463–3470, March 1999.
- [2] Shaobin Wang and Yuelian Peng. Natural zeolites as effective adsorbents in water and wastewater treatment. *Chemical Engineering Journal*, 156(1):11–24, January 2010.
- [3] Zhiping Lai, Griselda Bonilla, Isabel Diaz, Jose Geraldo Nery, Khristina Sujaoti, Miguel A. Amat, Efrosini Kokkoli, Osamu Terasaki, Robert W. Thompson, Michael Tsapatsis, and Dionisios G. Vlachos. Microstructural Optimization of a Zeolite Membrane for Organic Vapor Separation. *Science*, 300(5618):456–460, April 2003.
- [4] Pablo J. Bereciartua, ngel Cantn, Avelino Corma, Jos L. Jord, Miguel Palomino, Fernando Rey, Susana Valencia, Edward W. Corcoran, Pavel Kortunov, Peter I. Ravikovitch, Allen Burton, Chris Yoon, Yu Wang, Charanjit Paur, Javier Guzman, Adeana R. Bishop, and Gary L. Casty. Control of zeolite framework flexibility and pore topology for separation of ethane and ethylene. *Science*, 358(6366):1068–1071, November 2017.
- [5] Avelino Corma. From Microporous to Mesoporous Molecular Sieve Materials and Their Use in Catalysis. *Chemical Reviews*, 97(6):2373–2420, October 1997.
- [6] Ch. Baerlocher and L. B. McCusker. Database of Zeolite Structures, 2019.
- [7] Michael W. Deem, Ramdas Pophale, Phillip A. Cheeseman, and David J. Earl. Computational Discovery of New Zeolite-Like Materials. *The Journal of Physical Chemistry C*, 113(51):21353–21360, December 2009.
- [8] Ramdas Pophale, Phillip A. Cheeseman, and Michael W. Deem. A database of new zeolite-like materials. *Physical Chemistry Chemical Physics*, 13(27):12407–12412, 2011.
- [9] Mark E. Davis and Raul F. Lobo. Zeolite and molecular sieve synthesis. *Chemistry of Materials*, 4(4):756–768, July 1992.
- [10] Colin S. Cundy and Paul A. Cox. The Hydrothermal Synthesis of Zeolites: History and Development from the Earliest Days to the Present Time. *Chemical Reviews*, 103(3):663–702, March 2003.
- [11] CHARLES J. PLANK. The Invention of Zeolite Cracking Catalysts A Personal Viewpoint. In *Heterogeneous Catalysis*, volume 222 of *ACS Symposium Series*, pages 253–271. American Chemical Society, June 1983.

- [12] T. F. Degnan, G. K. Chitnis, and P. H. Schipper. History of ZSM-5 fluid catalytic cracking additive development at Mobil. *Microporous and Mesoporous Materials*, 3536:245–252, April 2000.
- [13] Marco Taramasso, Giovanni Perego, and Bruno Notari. Preparation of porous crystalline synthetic material comprised of silicon and titanium oxides, October 1983.
- [14] R.J. Saxton. Crystalline microporous titanium silicates. *Topics in Catalysis*, 9(1):43–57, July 1999.
- [15] Carlo Perego, Angela Carati, Patrizia Ingallina, Maria Angela Mantegazza, and Giuseppe Bellussi. Production of titanium containing molecular sieves and their application in catalysis. *Applied Catalysis A: General*, 221(1):63–72, November 2001.
- [16] Yuriy Romn-Leshkov and Mark E. Davis. Activation of Carbonyl-Containing Molecules with Solid Lewis Acids in Aqueous Media. *ACS Catalysis*, 1(11):1566–1580, 2011.
- [17] Stavros Caratzoulas, Mark E. Davis, Raymond J. Gorte, Rajamani Gounder, Raul F. Lobo, Vladimiro Nikolakis, Stanley I. Sandler, Mark A. Snyder, Michael Tsapatsis, and Dionisios G. Vlachos. Challenges of and Insights into Acid-Catalyzed Transformations of Sugars. *The Journal of Physical Chemistry C*, 118(40):22815–22833, 2014.
- [18] Thijs Ennaert, Joost Van Aelst, Jan Dijkmans, Rik De Clercq, Wouter Schutyser, Michiel Dusselier, Danny Verboekend, and Bert F. Sels. Potential and challenges of zeolite chemistry in the catalytic conversion of biomass. *Chemical Society Reviews*, December 2015.
- [19] Helen Y. Luo, Jennifer D. Lewis, and Yuriy Romn-Leshkov. Lewis Acid Zeolites for Biomass Conversion: Perspectives and Challenges on Reactivity, Synthesis, and Stability. *Annual Review of Chemical and Biomolecular Engineering*, 7(1):663–692, 2016.
- [20] Paola Ferrini, Jan Dijkmans, Rik De Clercq, Stijn Van de Vyver, Michiel Dusselier, Pierre A. Jacobs, and Bert F. Sels. Lewis acid catalysis on single site Sn centers incorporated into silica hosts. *Coordination Chemistry Reviews*, 343:220–255, July 2017.
- [21] Putla Sudarsanam, Elise Peeters, Ekaterina V. Makshina, Vasile I. Parvulescu, and Bert F. Sels. Advances in porous and nanoscale catalysts for viable biomass conversion. *Chemical Society Reviews*, 48(8):2366–2421, 2019.
- [22] Tae Hun Kim, Pedram Mehrabi, Zhong Ren, Adnan Sljoka, Christopher Ing, Alexandr Bezginov, Libin Ye, Rgis Poms, R. Scott Prosser, and Emil F. Pai. The role of dimer asymmetry and protomer dynamics in enzyme catalysis. *Science*, 355(6322):eaag2355, January 2017.
- [23] Iker Agirrezabal-Telleria and Enrique Iglesia. Stabilization of active, selective, and regenerable Ni-based dimerization catalysts by condensation of ethene with inordered mesopores. *Journal of Catalysis*, 352:505–514, August 2017.

- [24] Tiecheng Zhou, Peng Bai, J. Ilja Siepmann, and Aurora E. Clark. Deconstructing the Confinement Effect upon the Organization and Dynamics of Water in Hydrophobic Nanoporous Materials: Lessons Learned from Zeolites. *The Journal of Physical Chemistry C*, 121(40):22015–22024, October 2017.
- [25] Shuai Wang, Iker Agirrezabal-Telleria, Aditya Bhan, Dante Simonetti, Kazuhiro Takahashi, and Enrique Iglesia. Catalytic routes to fuels from C1 and oxygenate molecules. *Faraday Discussions*, February 2017.
- [26] P. B. Weisz and V. J. Frillette. INTRACRYSTALLINE AND MOLECULAR-SHAPE-SELECTIVE CATALYSIS BY ZEOLITE SALTS. *The Journal of Physical Chemistry*, 64(3):382–382, March 1960.
- [27] P. B. Weisz, V. J. Frillette, R. W. Maatman, and E. B. Mower. Catalysis by crystalline aluminosilicates II. Molecular-shape selective reactions. *Journal of Catalysis*, 1(4):307–312, August 1962.
- [28] Johan A. Martens, Mia Tielens, Peter A. Jacobs, and Jens Weitkamp. Estimation of the void structure and pore dimensions of molecular sieve zeolites using the hydroconversion of n-decane. *Zeolites*, 4(2):98–107, April 1984.
- [29] S. I. Zones and T. V. Harris. The Constraint Index test revisited: anomalies based upon new zeolite structure types. *Microporous and Mesoporous Materials*, 3536:31–46, April 2000.
- [30] Eric G. Derouane. Shape selectivity in catalysis by zeolites: The nest effect. *Journal of Catalysis*, 100(2):541–544, August 1986.
- [31] Aditya Bhan and Enrique Iglesia. A Link between Reactivity and Local Structure in Acid Catalysis on Zeolites. *Accounts of Chemical Research*, 41(4):559–567, April 2008.
- [32] Rajamani Gounder and Enrique Iglesia. The Roles of Entropy and Enthalpy in Stabilizing Ion-Pairs at Transition States in Zeolite Acid Catalysis. *Accounts of Chemical Research*, 45(2):229–238, 2011.
- [33] Rajamani Gounder and Enrique Iglesia. The catalytic diversity of zeolites: confinement and solvation effects within voids of molecular dimensions. *Chemical Communications*, 49(34):3491–3509, April 2013.
- [34] G. L. Woolery, L. B. Alemany, R. M. Dessau, and A. W. Chester. Spectroscopic evidence for the presence of internal silanols in highly siliceous ZSM-5. *Zeolites*, 6(1):14–16, January 1986.
- [35] Hubert Koller, Raul F. Lobo, Sandra L. Burkett, and Mark E. Davis. SiO<sub>2</sub>·nH<sub>2</sub>O Hydrogen Bonds in As-Synthesized High-Silica Zeolites. *The Journal of Physical Chemistry*, 99(33):12588–12596, August 1995.
- [36] Christopher W. Jones, Katsuyuki Tsuji, and Mark E. Davis. Organic-functionalized molecular sieves as shape-selective catalysts. *Nature*, 393(6680):52–54, May 1998.
- [37] Nicolas Giovambattista, Pablo G. Debenedetti, and Peter J. Rossky. Hydration Behavior under Confinement by Nanoscale Surfaces with Patterned Hydrophobicity and Hydrophilicity. *The Journal of Physical Chemistry C*, 111(3):1323–1332, January 2007.

- [38] Simona Dalla Bernardina, Erwan Paineau, Jean-Blaise Brubach, Patrick Judeinstein, Stphan Rouzire, Pascale Launois, and Pascale Roy. Water in Carbon Nanotubes: The Peculiar Hydrogen Bond Network Revealed by Infrared Spectroscopy. *Journal of the American Chemical Society*, 138(33):10437–10443, August 2016.
- [39] L. Fumagalli, A. Esfandiar, R. Fabregas, S. Hu, P. Ares, A. Janardanan, Q. Yang, B. Radha, T. Taniguchi, K. Watanabe, G. Gomila, K. S. Novoselov, and A. K. Geim. Anomalously low dielectric constant of confined water. *Science*, 360(6395):1339–1342, June 2018.
- [40] Samuel Faucher, Narayana Aluru, Martin Z. Bazant, Daniel Blankschtein, Alexandra H. Brozena, John Cumings, J. Pedro de Souza, Menachem Elimelech, Razi Epsztein, John T. Fourkas, Ananth Govind Rajan, Heather J. Kulik, Amir Levy, Arun Majumdar, Charles Martin, Michael McEldrew, Rahul Prasanna Misra, Aleksandr Noy, Tuan Anh Pham, Mark Reed, Eric Schwegler, Zuzanna Siwy, YuHuang Wang, and Michael Strano. Critical Knowledge Gaps in Mass Transport through Single-Digit Nanopores: A Review and Perspective. *The Journal of Physical Chemistry C*, 123(35):21309–21326, September 2019.
- [41] Tomonori Ohba. Size-Dependent Water Structures in Carbon Nanotubes. *Angewandte Chemie International Edition*, 53(31):8032–8036, July 2014.
- [42] M. Trzpit, M. Soulard, J. Patarin, N. Desbiens, F. Cailliez, A. Boutin, I. Demachy, and A. H. Fuchs. The Effect of Local Defects on Water Adsorption in Silicalite-1 Zeolite: A Joint Experimental and Molecular Simulation Study. *Langmuir*, 23(20):10131–10139, September 2007.
- [43] Alex M. Schrader, Jacob I. Monroe, Ryan Sheil, Howard A. Dobbs, Timothy J. Keller, Yuanxin Li, Sheetal Jain, M. Scott Shell, Jacob N. Israelachvili, and Songi Han. Surface chemical heterogeneity modulates silica surface hydration. *Proceedings of the National Academy of Sciences*, page 201722263, February 2018.
- [44] Max A. Mellmer, Canan Sener, Jean Marcel R. Gallo, Jeremy S. Luterbacher, David Martin Alonso, and James A. Dumesic. Solvent Effects in Acid-Catalyzed Biomass Conversion Reactions. *Angewandte Chemie International Edition*, 53(44):11872–11875, October 2014.
- [45] Hui Shi, Sebastian Eckstein, Aleksei Vjunov, Donald M. Camaioni, and Johannes A. Lercher. Tailoring nanoscopic confines to maximize catalytic activity of hydronium ions. *Nature Communications*, 8:15442, May 2017.
- [46] Yuanshuai Liu, Aleksei Vjunov, Hui Shi, Sebastian Eckstein, Donald M. Camaioni, Donghai Mei, Eszter Barth, and Johannes A. Lercher. Enhancing the catalytic activity of hydronium ions through constrained environments. *Nature Communications*, 8:14113, March 2017.
- [47] Gunther Langhendries, Dirk E. De Vos, Gino V. Baron, and Pierre A. Jacobs. Quantitative Sorption Experiments on Ti-Zeolites and Relation with -Olefin Oxidation by H<sub>2</sub>O<sub>2</sub>. *Journal of Catalysis*, 187(2):453–463, October 1999.
- [48] Mario G. Clerici. The role of the solvent in TS-1 chemistry: active or passive? An early study revisited. *Topics in Catalysis*, 15(2-4):257–263, June 2001.

- [49] Chen E. Ramachandran, Hongwei Du, Yoo Joong Kim, Mayfair C. Kung, Randall Q. Snurr, and Linda J. Broadbelt. Solvent effects in the epoxidation reaction of 1-hexene with titanium silicalite-1 catalyst. *Journal of Catalysis*, 253(1):148–158, January 2008.
- [50] Long Qi, Ricardo Alamillo, William A. Elliott, Amity Andersen, David W. Hoyt, Eric D. Walter, Kee Sung Han, Nancy M. Washton, Robert M. Rioux, James A. Dumesic, and Susannah L. Scott. Operando Solid-State NMR Observation of Solvent-Mediated Adsorption-Reaction of Carbohydrates in Zeolites. *ACS Catalysis*, 7(5):3489–3500, May 2017.
- [51] Max A. Mellmer, Chotitath Sanpitakseree, Benginur Demir, Peng Bai, Kaiwen Ma, Matthew Neurock, and James A. Dumesic. Solvent-enabled control of reactivity for liquid-phase reactions of biomass-derived compounds. *Nature Catalysis*, 1(3):199–207, March 2018.
- [52] T. Blasco, M. A. Camblor, A. Corma, P. Esteve, J. M. Guil, A. Martinez, J. A. Perdign-Meln, and S. Valencia. Direct Synthesis and Characterization of Hydrophobic Aluminum-Free TiBeta Zeolite. *The Journal of Physical Chemistry B*, 102(1):75–88, 1998.
- [53] Rajamani Gounder and Mark E. Davis. Monosaccharide and disaccharide isomerization over Lewis acid sites in hydrophobic and hydrophilic molecular sieves. *Journal of Catalysis*, 308:176–188, December 2013.
- [54] William N. P. van der Graaff, Christiaan H. L. Tempelman, Guanna Li, Brahim Mezari, Nikolay Kosinov, Evgeny A. Pidko, and Emiel J. M. Hensen. Competitive Adsorption of Substrate and Solvent in Sn-Beta Zeolite During Sugar Isomerization. *ChemSusChem*, 9(22):3145–3149, November 2016.
- [55] Sabrina Conrad, Patrick Wolf, Philipp Mller, Hailey Orsted, and Ive Hermans. Influence of Hydrophilicity on the Sn-Catalyzed BaeyerVilliger Oxidation of Cyclohexanone with Aqueous Hydrogen Peroxide. *ChemCatChem*, 9(1):175–182, January 2017.
- [56] James W. Harris, Michael J. Cordon, John R. Di Iorio, Juan Carlos Vega-Vila, Fabio H. Ribeiro, and Rajamani Gounder. Titration and quantification of open and closed Lewis acid sites in Sn-Beta zeolites that catalyze glucose isomerization. *Journal of Catalysis*, 335:141–154, March 2016.
- [57] Michael J. Cordon, James W. Harris, Juan Carlos Vega-Vila, Jason S. Bates, Sukhdeep Kaur, Mohit Gupta, Megan E. Witzke, Evan C. Wegener, Jeffrey T. Miller, David W. Flaherty, David D. Hibbitts, and Rajamani Gounder. Dominant Role of Entropy in Stabilizing Sugar Isomerization Transition States within Hydrophobic Zeolite Pores. *Journal of the American Chemical Society*, 140(43):14244–14266, October 2018.
- [58] Daniel T. Bregante, Alayna M. Johnson, Ami Y. Patel, E. Zeynep Ayla, Michael J. Cordon, Brandon C. Bukowski, Jeffrey Greeley, Rajamani Gounder, and David W. Flaherty. Cooperative Effects between Hydrophilic Pores and Solvents: Catalytic Consequences of Hydrogen Bonding on Alkene Epoxidation in Zeolites. *Journal of the American Chemical Society*, January 2019.

- [59] Philipp Mller, Patrick Wolf, and Ive Hermans. Insights into the Complexity of Heterogeneous Liquid-Phase Catalysis: Case Study on the Cyclization of Citronellal. *ACS Catalysis*, pages 2760–2769, March 2016.
- [60] William N. P. van der Graaff, Christiaan H. L. Tempelman, Evgeny A. Pidko, and Emiel J. M. Hensen. Influence of pore topology on synthesis and reactivity of Sn-modified zeolite catalysts for carbohydrate conversions. *Catalysis Science & Technology*, 2017.
- [61] Daniel T. Bregante, Nicholas E. Thornburg, Justin M. Notestein, and David W. Flaherty. Consequences of Confinement for Alkene Epoxidation with Hydrogen Peroxide on Highly Dispersed Group 4 and 5 Metal Oxide Catalysts. *ACS Catalysis*, 8(4):2995–3010, April 2018.
- [62] Taylor Hugh Stott. A theory of the catalytic surface. *Proceedings of the Royal Society of London. Series A, Containing Papers of a Mathematical and Physical Character*, 108(745):105–111, May 1925.
- [63] M. Boudart. Turnover Rates in Heterogeneous Catalysis. *Chemical Reviews*, 95(3):661–666, May 1995.
- [64] Robert Davis. Turnover rates on complex heterogeneous catalysts. *AIChE Journal*, 64(11):3778–3785, 2018.
- [65] Aleksei Vjunov, Mirosław A. Derewinski, John L. Fulton, Donald M. Camaioni, and Johannes A. Lercher. Impact of Zeolite Aging in Hot Liquid Water on Activity for Acid-Catalyzed Dehydration of Alcohols. *Journal of the American Chemical Society*, August 2015.
- [66] Lu Zhang, Kuizhi Chen, Banghao Chen, Jeffery L White, and Daniel E. Resasco. Factors that Determine Zeolite Stability in Hot Liquid Water. *Journal of the American Chemical Society*, August 2015.
- [67] Ryan M. Ravenelle, Florian Schuessler, Andrew D’Amico, Nadiya Danilina, Jeroen A. van Bokhoven, Johannes A. Lercher, Christopher W. Jones, and Carsten Sievers. Stability of Zeolites in Hot Liquid Water. *Journal of Physical Chemistry C*, 114(46):19582–19595, November 2010.
- [68] Ricardo Bermejo-Deval, Rajeev S. Assary, Eranda Nikolla, Manuel Moliner, Yuriy Romn-Leshkov, Son-Jong Hwang, Arna Palsdottir, Dorothy Silverman, Raul F. Lobo, Larry A. Curtiss, and Mark E. Davis. Metalloenzyme-like catalyzed isomerizations of sugars by Lewis acid zeolites. *Proceedings of the National Academy of Sciences*, 109(25):9727–9732, June 2012.
- [69] Neeraj Rai, Stavros Caratzoulas, and Dionisios G. Vlachos. Role of Silanol Group in Sn-Beta Zeolite for Glucose Isomerization and Epimerization Reactions. *ACS Catalysis*, 3(10):2294–2298, October 2013.
- [70] Guanna Li, Evgeny A. Pidko, and Emiel J. M. Hensen. Synergy between Lewis acid sites and hydroxyl groups for the isomerization of glucose to fructose over Sn-containing zeolites: a theoretical perspective. *Catalysis Science & Technology*, 4(8):2241–2250, July 2014.

- [71] Aleksei Vjunov, Meng Wang, Niranjana Govind, Thomas Huthwelker, Hui Shi, Donghai Mei, John L. Fulton, and Johannes A. Lercher. Tracking the Chemical Transformations at the Brønsted Acid Site upon Water-Induced Deprotonation in a Zeolite Pore. *Chemistry of Materials*, 29(21):9030–9042, November 2017.
- [72] Sebastian Eckstein, Peter H. Hintermeier, Ruixue Zhao, Eszter Barth, Hui Shi, Yue Liu, and Johannes A. Lercher. Influence of Hydronium Ions in Zeolites on Sorption. *Angewandte Chemie International Edition*, 58(11):3450–3455, 2019.
- [73] Meng Wang, Nicholas R. Jaegers, Mal-Soon Lee, Chuan Wan, Jian Zhi Hu, Hui Shi, Donghai Mei, Sarah D. Burton, Donald M. Camaioni, Oliver Y. Gutierrez, Vassiliki-Alexandra Glezakou, Roger Rousseau, Yong Wang, and Johannes A. Lercher. Genesis and Stability of Hydronium Ions in Zeolite Channels. *Journal of the American Chemical Society*, 141(8):3444–3455, February 2019.
- [74] Josef Macht, Robert T. Carr, and Enrique Iglesia. Functional assessment of the strength of solid acid catalysts. *Journal of Catalysis*, 264(1):54–66, May 2009.
- [75] M. Boudart. Catalysis by Supported Metals. In D. D. Eley, Herman Pines, and Paul B. Weisz, editors, *Advances in Catalysis*, volume 20, pages 153–166. Academic Press, January 1969.
- [76] John H. Sinfelt. Catalysis by alloys and bimetallic clusters. *Accounts of Chemical Research*, 10(1):15–20, January 1977.
- [77] Michel Boudart and G. Djga-Mariadassou. *Kinetics of Heterogeneous Catalytic Reactions*. Princeton University Press, 1984.
- [78] Josef Macht, Michael J. Janik, Matthew Neurock, and Enrique Iglesia. Catalytic Consequences of Composition in Polyoxometalate Clusters with Keggin Structure. *Angewandte Chemie International Edition*, 46(41):7864–7868, October 2007.
- [79] Josef Macht, Michael J. Janik, Matthew Neurock, and Enrique Iglesia. Mechanistic Consequences of Composition in Acid Catalysis by Polyoxometalate Keggin Clusters. *Journal of the American Chemical Society*, 130(31):10369–10379, August 2008.
- [80] Robert T. Carr, Matthew Neurock, and Enrique Iglesia. Catalytic consequences of acid strength in the conversion of methanol to dimethyl ether. *Journal of Catalysis*, 278(1):78–93, February 2011.
- [81] Andrew J. Jones, Robert T. Carr, Stacey I. Zones, and Enrique Iglesia. Acid strength and solvation in catalysis by MFI zeolites and effects of the identity, concentration and location of framework heteroatoms. *Journal of Catalysis*, 312:58–68, April 2014.
- [82] Prashant Deshlahra, Robert T. Carr, and Enrique Iglesia. Ionic and Covalent Stabilization of Intermediates and Transition States in Catalysis by Solid Acids. *Journal of the American Chemical Society*, 136(43):15229–15247, October 2014.
- [83] Prashant Deshlahra and Enrique Iglesia. Toward More Complete Descriptors of Reactivity in Catalysis by Solid Acids. *ACS Catalysis*, pages 5386–5392, July 2016.

- [84] Rajamani Gounder, Andrew J. Jones, Robert T. Carr, and Enrique Iglesia. Solvation and acid strength effects on catalysis by faujasite zeolites. *Journal of Catalysis*, 286:214–223, February 2012.
- [85] Andrew J. Jones, Stacey I. Zones, and Enrique Iglesia. Implications of Transition State Confinement within Small Voids for Acid Catalysis. *The Journal of Physical Chemistry C*, 118(31):17787–17800, August 2014.
- [86] Herman Pines and Werner O. Haag. Alumina: Catalyst and Support. IX.1 The Alumina Catalyzed Dehydration of Alcohols<sup>2,3</sup>. *Journal of the American Chemical Society*, 83(13):2847–2852, July 1961.
- [87] H. Knzinger. Dehydration of Alcohols on Aluminum Oxide. *Angewandte Chemie International Edition in English*, 7(10):791–805, 1968.
- [88] Joseph F. DeWilde, Hsu Chiang, Daniel A. Hickman, Christopher R. Ho, and Aditya Bhan. Kinetics and Mechanism of Ethanol Dehydration on -Al<sub>2</sub>O<sub>3</sub>: The Critical Role of Dimer Inhibition. *ACS Catalysis*, 3(4):798–807, April 2013.
- [89] Matthew A. Christiansen, Giannis Mpourmpakis, and Dionisios G. Vlachos. Density Functional Theory-Computed Mechanisms of Ethylene and Diethyl Ether Formation from Ethanol on -Al<sub>2</sub>O<sub>3</sub>(100). *ACS Catalysis*, 3(9):1965–1975, 2013.
- [90] Minje Kang, Joseph F. DeWilde, and Aditya Bhan. Kinetics and Mechanism of Alcohol Dehydration on -Al<sub>2</sub>O<sub>3</sub>: Effects of Carbon Chain Length and Substitution. *ACS Catalysis*, 5(2):602–612, 2014.
- [91] Yuriy RomnLeshkov, Manuel Moliner, Jay A. Labinger, and Mark E. Davis. Mechanism of Glucose Isomerization Using a Solid Lewis Acid Catalyst in Water. *Angewandte Chemie International Edition*, 49(47):8954–8957, November 2010.
- [92] Rajamani Gounder and Mark E. Davis. Titanium-Beta Zeolites Catalyze the Stereospecific Isomerization of d-Glucose to l-Sorbose via Intramolecular C5C1 Hydride Shift. *ACS Catalysis*, 3(7):1469–1476, 2013.
- [93] Miguel A. Camblor, Avelino Corma, and Susana Valencia. Synthesis in fluoride media and characterisation of aluminosilicate zeolite beta. *Journal of Materials Chemistry*, 8(9):2137–2145, January 1998.
- [94] Peter H. Hintermeier, Sebastian Eckstein, Donghai Mei, Mariefel V. Olarte, Donald M. Camaioni, Eszter Barth, and Johannes A. Lercher. Hydronium-Ion-Catalyzed Elimination Pathways of Substituted Cyclohexanols in Zeolite H-ZSM5. *ACS Catalysis*, 7(11):7822–7829, November 2017.
- [95] Sebastian Eckstein, Peter H. Hintermeier, Mariefel V. Olarte, Yue Liu, Eszter Barth, and Johannes A. Lercher. Elementary steps and reaction pathways in the aqueous phase alkylation of phenol with ethanol. *Journal of Catalysis*, 352:329–336, August 2017.
- [96] Zhenchao Zhao, Hui Shi, Chuan Wan, Mary Y. Hu, Yuanshuai Liu, Donghai Mei, Donald M. Camaioni, Jian Zhi Hu, and Johannes A. Lercher. Mechanism of Phenol Alkylation in Zeolite H-BEA Using In Situ Solid-State NMR Spectroscopy. *Journal of the American Chemical Society*, June 2017.

- [97] Yuanshuai Liu, Eszter Barth, Hui Shi, Jianzhi Hu, Donald M. Camaioni, and Johannes A. Lercher. Solvent-determined mechanistic pathways in zeolite-H-BEA-catalysed phenol alkylation. *Nature Catalysis*, 1(2):141–147, February 2018.
- [98] Avelino Corma, Laszlo T. Nemeth, Michael Renz, and Susana Valencia. Sn-zeolite beta as a heterogeneous chemoselective catalyst for BaeyerVilliger oxidations. *Nature*, 412(6845):423–425, July 2001.
- [99] Avelino Corma, Marcelo E. Domine, Laszlo Nemeth, and Susana Valencia. Al-Free Sn-Beta Zeolite as a Catalyst for the Selective Reduction of Carbonyl Compounds (MeerweinPonndorfVerley Reaction). *Journal of the American Chemical Society*, 124(13):3194–3195, April 2002.
- [100] Manuel Moliner, Yuriy Romn-Leshkov, and Mark E. Davis. Tin-containing zeolites are highly active catalysts for the isomerization of glucose in water. *Proceedings of the National Academy of Sciences*, 107(14):6164–6168, April 2010.
- [101] Yi-Pei Li, Martin Head-Gordon, and Alexis T. Bell. Analysis of the Reaction Mechanism and Catalytic Activity of Metal-Substituted Beta Zeolite for the Isomerization of Glucose to Fructose. *ACS Catalysis*, 4(5):1537–1545, 2014.
- [102] Mercedes Boronat, Patricia Concepcin, Avelino Corma, Michael Renz, and Susana Valencia. Determination of the catalytically active oxidation Lewis acid sites in Sn-beta zeolites, and their optimisation by the combination of theoretical and experimental studies. *Journal of Catalysis*, 234(1):111–118, August 2005.
- [103] Mercedes Boronat, Avelino Corma, Michael Renz, and Pedro M. Viruela. Predicting the Activity of Single Isolated Lewis Acid Sites in Solid Catalysts. *Chemistry A European Journal*, 12(27):7067–7077, 2006.
- [104] Helen Y. Luo, Daniel F. Consoli, William R. Gunther, and Yuriy Romn-Leshkov. Investigation of the reaction kinetics of isolated Lewis acid sites in Beta zeolites for the MeerweinPonndorfVerley reduction of methyl levulinate to -valerolactone. *Journal of Catalysis*, 320:198–207, December 2014.
- [105] Jennifer D. Lewis, Michelle Ha, Helen Luo, Alexandra Faucher, Vladimir K. Michaelis, and Yuriy Romn-Leshkov. Distinguishing Active Site Identity in Sn-Beta Zeolites Using 31p MAS NMR of Adsorbed Trimethylphosphine Oxide. *ACS Catalysis*, 8(4):3076–3086, February 2018.
- [106] Ricardo Bermejo-Deval, Marat Orazov, Rajamani Gounder, Son-Jong Hwang, and Mark E. Davis. Active Sites in Sn-Beta for Glucose Isomerization to Fructose and Epimerization to Mannose. *ACS Catalysis*, 4(7):2288–2297, 2014.
- [107] Patrick Wolf, Wei-Chih Liao, Ta-Chung Ong, Maxence Valla, James W. Harris, Rajamani Gounder, William N. P. van der Graaff, Evgeny A. Pidko, Emiel J. M. Hensen, Paola Ferrini, Jan Dijkmans, Bert Sels, Ive Hermans, and Christophe Copret. Identifying Sn Site Heterogeneities Prevalent Among Sn-Beta Zeolites. *Helvetica Chimica Acta*, 99(12):916–927, 2016.
- [108] Simon R. Bare, Shelly D. Kelly, Wharton Sinkler, John J. Low, Frank S. Modica, Susana Valencia, Avelino Corma, and Laszlo T. Nemeth. Uniform Catalytic Site in Sn--Zeolite Determined Using X-ray Absorption Fine Structure. *Journal of the American Chemical Society*, 127(37):12924–12932, September 2005.

- [109] Christian M. Osmundsen, Martin Spangenberg Holm, Sren Dahl, and Esben Taarning. Tin-containing silicates: structureactivity relations. *Proceedings of the Royal Society of London A: Mathematical, Physical and Engineering Sciences*, 468(2143):2000–2016, July 2012.
- [110] Timothy D. Courtney, Chun-Chih Chang, Raymond J. Gorte, Raul F. Lobo, Wei Fan, and Vladimiro Nikolakis. Effect of water treatment on Sn-BEA zeolite: Origin of 960cm<sup>1</sup> FTIR peak. *Microporous and Mesoporous Materials*, 210:69–76, July 2015.
- [111] Patrick Wolf, Maxence Valla, Francisco Nez-Zarur, Aleix Comas-Vives, Aaron J. Rossini, Connor Firth, Hana Kallas, Anne Lesage, Lyndon Emsley, Christophe Copret, and Ive Hermans. Correlating Synthetic Methods, Morphology, Atomic-Level Structure, and Catalytic Activity of Sn- Catalysts. *ACS Catalysis*, 6(7):4047–4063, July 2016.
- [112] Patrick Wolf, Maxence Valla, Aaron J. Rossini, Aleix Comas-Vives, Francisco Nez-Zarur, Bernard Malaman, Anne Lesage, Lyndon Emsley, Christophe Copret, and Ive Hermans. NMR Signatures of the Active Sites in Sn-Zeolite. *Angewandte Chemie International Edition*, 53(38):10179–10183, 2014.
- [113] Brandon C. Bukowski and Jeffrey Greeley. Scaling Relationships for Molecular Adsorption and Dissociation in Lewis Acid Zeolites. *The Journal of Physical Chemistry C*, 120(12):6714–6722, March 2016.
- [114] James W. Harris, Wei-Chih Liao, John R. Di Iorio, Alisa M. Henry, Ta-Chung Ong, Aleix Comas-Vives, Christophe Copret, and Rajamani Gounder. Molecular Structure and Confining Environment of Sn Sites in Single-Site Chabazite Zeolites. *Chemistry of Materials*, 29(20):8824–8837, October 2017.
- [115] R. E. Skyner, J. L. McDonagh, C. R. Groom, T. Mourik, and J. B. O. Mitchell. A review of methods for the calculation of solution free energies and the modelling of systems in solution. *Physical Chemistry Chemical Physics*, 17(9):6174–6191, February 2015.
- [116] G. M. Lari, P. Y. Dapsens, D. Scholz, S. Mitchell, C. Mondelli, and J. Prez-Ramrez. Deactivation mechanisms of tin-zeolites in biomass conversions. *Green Chemistry*, 18(5):1249–1260, February 2016.
- [117] Daniele Padovan, Charlie Parsons, Manuel Simplicio Grasiña, and Ceri Hammond. Intensification and deactivation of Sn-beta investigated in the continuous regime. *Green Chemistry*, 18(18):5041–5049, September 2016.
- [118] Sounak Roy, Giannis Mpourmpakis, Do-Young Hong, Dionisios G. Vlachos, A. Bhan, and R. J. Gorte. Mechanistic Study of Alcohol Dehydration on - Al<sub>2</sub>O<sub>3</sub>. *ACS Catalysis*, 2(9):1846–1853, 2012.
- [119] Carsten Stegelmann, Anders Andreasen, and Charles T. Campbell. Degree of Rate Control: How Much the Energies of Intermediates and Transition States Control Rates. *Journal of the American Chemical Society*, 131(23):8077–8082, June 2009.
- [120] Jochen Heyd, Gustavo E. Scuseria, and Matthias Ernzerhof. Hybrid functionals based on a screened Coulomb potential. *The Journal of Chemical Physics*, 118(18):8207, 2003.

- [121] Florian Gltl and Jrgen Hafner. Structure and properties of metal-exchanged zeolites studied using gradient-corrected and hybrid functionals. I. Structure and energetics. *The Journal of Chemical Physics*, 136(6):064501, February 2012.
- [122] Florian Gltl and Jrgen Hafner. Structure and properties of metal-exchanged zeolites studied using gradient-corrected and hybrid functionals. II. Electronic structure and photoluminescence spectra. *The Journal of Chemical Physics*, 136(6):064502, February 2012.
- [123] Florian Gltl and Jrgen Hafner. Structure and properties of metal-exchanged zeolites studied using gradient-corrected and hybrid functionals. III. Energetics and vibrational spectroscopy of adsorbates. *The Journal of Chemical Physics*, 136(6):064503, February 2012.
- [124] GiovanniMaria Piccini and Joachim Sauer. Effect of Anharmonicity on Adsorption Thermodynamics. *Journal of Chemical Theory and Computation*, 10(6):2479–2487, June 2014.
- [125] GiovanniMaria Piccini, Maristella Alessio, and Joachim Sauer. AbInitio Calculation of Rate Constants for MoleculeSurface Reactions with Chemical Accuracy. *Angewandte Chemie International Edition*, 55(17):5235–5237, April 2016.
- [126] G. M. Torrie and J. P. Valleau. Nonphysical sampling distributions in Monte Carlo free-energy estimation: Umbrella sampling. *Journal of Computational Physics*, 23(2):187–199, February 1977.
- [127] Konstantinos Alexopoulos, Mal-Soon Lee, Yue Liu, Yuchun Zhi, Yuanshuai Liu, Marie-Franoise Reyniers, Guy B. Marin, Vassiliki-Alexandra Glezakou, Roger Rousseau, and Johannes A. Lercher. Anharmonicity and Confinement in Zeolites: Structure, Spectroscopy, and Adsorption Free Energy of Ethanol in H-ZSM-5. *The Journal of Physical Chemistry C*, 120(13):7172–7182, April 2016.
- [128] Rasmus Y. Brogaard, Reynald Henry, Yves Schuurman, Andrew J. Medford, Poul Georg Moses, Pablo Beato, Stian Svelle, Jens K. Nrskov, and Unni Olsbye. Methanol-to-hydrocarbons conversion: The alkene methylation pathway. *Journal of Catalysis*, 314:159–169, May 2014.
- [129] Mikkel Jrgensen and Henrik Grnbeck. Adsorbate Entropies with Complete Potential Energy Sampling in Microkinetic Modeling. *The Journal of Physical Chemistry C*, 121(13):7199–7207, April 2017.
- [130] Ariana Beste. One-dimensional anharmonic oscillator: Quantum versus classical vibrational partition functions. *Chemical Physics Letters*, 493(13):200–205, June 2010.
- [131] Charles T. Campbell. The Degree of Rate Control: A Powerful Tool for Catalysis Research. *ACS Catalysis*, pages 2770–2779, March 2017.
- [132] G. Kresse and J. Furthmller. Efficiency of ab-initio total energy calculations for metals and semiconductors using a plane-wave basis set. *Computational Materials Science*, 6(1):15–50, July 1996.

- [133] G. Kresse and J. Furthmüller. Efficient iterative schemes for *ab initio* total-energy calculations using a plane-wave basis set. *Physical Review B*, 54(16):11169–11186, October 1996.
- [134] G. Kresse and J. Hafner. *Ab initio* molecular dynamics for liquid metals. *Physical Review B*, 47(1):558–561, January 1993.
- [135] G. Kresse and J. Hafner. *Ab initio* molecular-dynamics simulation of the liquid-metal<sup>21</sup> amorphous-semiconductor transition in germanium. *Physical Review B*, 49(20):14251–14269, May 1994.
- [136] G. Kresse and D. Joubert. From ultrasoft pseudopotentials to the projector augmented-wave method. *Physical Review B*, 59(3):1758–1775, January 1999.
- [137] Jess Wellendorff, Keld T. Lundgaard, Andreas Mgelhj, Vivien Petzold, David D. Landis, Jens K. Nrskov, Thomas Bligaard, and Karsten W. Jacobsen. Density functionals for surface science: Exchange-correlation model development with Bayesian error estimation. *Physical Review B*, 85(23), June 2012.
- [138] Jochen Heyd and Gustavo E. Scuseria. Efficient hybrid density functional calculations in solids: Assessment of the HeydScuseriaErnzerhof screened Coulomb hybrid functional. *The Journal of Chemical Physics*, 121(3):1187, 2004.
- [139] Stefan Grimme. Semiempirical GGA-type density functional constructed with a long-range dispersion correction. *Journal of Computational Chemistry*, 27(15):1787–1799, November 2006.
- [140] Stefan Grimme, Jens Antony, Stephan Ehrlich, and Helge Krieg. A consistent and accurate *ab initio* parametrization of density functional dispersion correction (DFT-D) for the 94 elements H-Pu. *The Journal of Chemical Physics*, 132(15):154104, April 2010.
- [141] P. E. Blchl. Projector augmented-wave method. *Physical Review B*, 50(24):17953–17979, December 1994.
- [142] Ch. Baerlocher and L. B. McCusker. Database of Zeolite Structures, 2017.
- [143] Graeme Henkelman and Hannes Jnsson. Improved tangent estimate in the nudged elastic band method for finding minimum energy paths and saddle points. *The Journal of Chemical Physics*, 113(22):9978–9985, December 2000.
- [144] Graeme Henkelman, Blas P. Uberuaga, and Hannes Jnsson. A climbing image nudged elastic band method for finding saddle points and minimum energy paths. *The Journal of Chemical Physics*, 113(22):9901–9904, December 2000.
- [145] Sren Smidstrup, Andreas Pedersen, Kurt Stokbro, and Hannes Jnsson. Improved initial guess for minimum energy path calculations. *The Journal of Chemical Physics*, 140(21):214106, June 2014.
- [146] R. A. Olsen, G. J. Kroes, G. Henkelman, A. Arnaldsson, and H. Jnsson. Comparison of methods for finding saddle points without knowledge of the final states. *The Journal of Chemical Physics*, 121(20):9776–9792, November 2004.

- [147] Amit A. Gokhale, Shampa Kandoi, Jeffrey P. Greeley, Manos Mavrikakis, and James A. Dumesic. Molecular-level descriptions of surface chemistry in kinetic models using density functional theory. *Chemical Engineering Science*, 59(2223):4679–4691, November 2004.
- [148] Tej Choksi and Jeffrey Greeley. Partial Oxidation of Methanol on MoO<sub>3</sub> (010): A DFT and Microkinetic Study. *ACS Catalysis*, 6(11):7260–7277, November 2016.
- [149] Stefan Maintz, Volker L. Deringer, Andrei L. Tchougreff, and Richard Dronskowski. LOBSTER: A tool to extract chemical bonding from plane-wave based DFT. *Journal of Computational Chemistry*, 37(11):1030–1035, April 2016.
- [150] W. Tang, E. Sanville, and G. Henkelman. A grid-based Bader analysis algorithm without lattice bias. *Journal of Physics: Condensed Matter*, 21(8):084204, 2009.
- [151] Juan Carlos Vega-Vila, James W. Harris, and Rajamani Gounder. Controlled insertion of tin atoms into zeolite framework vacancies and consequences for glucose isomerization catalysis. *Journal of Catalysis*, 344:108–120, December 2016.
- [152] Nawal Kishor Mal and Arumugamangalam V. Ramaswamy. Hydroxylation of phenol over Sn-silicalite-1 molecular sieve: solvent effects. *Journal of Molecular Catalysis A: Chemical*, 105(3):149–158, February 1996.
- [153] Ricardo Bermejo-Deval, Rajamani Gounder, and Mark E. Davis. Framework and Extraframework Tin Sites in Zeolite Beta React Glucose Differently. *ACS Catalysis*, 2(12):2705–2713, 2012.
- [154] Tyler R. Josephson, Glen R. Jenness, Dionisios G. Vlachos, and Stavros Caratzoulas. Distribution of open sites in Sn-Beta zeolite. *Microporous and Mesoporous Materials*, 245:45–50, June 2017.
- [155] Alexander V. Yakimov, Yury G. Kolyagin, Sren Tolborg, Peter N. R. Vennestrm, and Irina I. Ivanova. <sup>119</sup>sn MAS NMR Study of the Interaction of Probe Molecules with Sn-BEA: The Origin of Penta- and Hexacoordinated Tin Formation. *The Journal of Physical Chemistry C*, 120(49):28083–28092, December 2016.
- [156] W. A. Cowdrey, E. D. Hughes, C. K. Ingold, S. Masterman, and A. D. Scott. 257. Reaction kinetics and the Walden inversion. Part VI. Relation of steric orientation to mechanism in substitutions involving halogen atoms and simple or substituted hydroxyl groups. (0):1252–1271, January 1937.
- [157] Seung Seo Lee, Sung You Hong, James C. Errey, Atsushi Izumi, Gideon J. Davies, and Benjamin G. Davis. Mechanistic evidence for a front-side, S<sub>N</sub>i-type reaction in a retaining glycosyltransferase. *Nature Chemical Biology*, 7(9):631–638, September 2011.
- [158] William Knaeble and Enrique Iglesia. Kinetic and Theoretical Insights into the Mechanism of Alkanol Dehydration on Solid Brnsted Acid Catalysts. *The Journal of Physical Chemistry C*, 120(6):3371–3389, February 2016.

- [159] Zhi-Jian Zhao, Zhenglong Li, Yanran Cui, Houyu Zhu, William F. Schneider, W. Nicholas Delgass, Fabio Ribeiro, and Jeffrey Greeley. Importance of metal-oxide interfaces in heterogeneous catalysis: A combined DFT, microkinetic, and experimental study of water-gas shift on Au/MgO. *Journal of Catalysis*, 345(Supplement C):157–169, January 2017.
- [160] Anthony Plauck, Eric E. Stangland, James A. Dumesic, and Manos Mavrikakis. Active sites and mechanisms for H<sub>2</sub>O<sub>2</sub> decomposition over Pd catalysts. *Proceedings of the National Academy of Sciences*, 113(14):E1973–E1982, April 2016.
- [161] Shiang-Tai Lin, Prabal K. Maiti, and William A. Goddard. Two-Phase Thermodynamic Model for Efficient and Accurate Absolute Entropy of Water from Molecular Dynamics Simulations. *Journal of Physical Chemistry B*, 114(24):8191–8198, June 2010.
- [162] Shiang-Tai Lin, Mario Blanco, and William A. Goddard Iii. The two-phase model for calculating thermodynamic properties of liquids from molecular dynamics: Validation for the phase diagram of Lennard-Jones fluids. *The Journal of Chemical Physics*, 119(22):11792–11805, December 2003.
- [163] Charles T. Campbell and Jason R. V. Sellers. The Entropies of Adsorbed Molecules. *Journal of the American Chemical Society*, 134(43):18109–18115, 2012.
- [164] Zhi-Jian Zhao, Ambarish Kulkarni, Laia Vilella, Jens K. Nørskov, and Felix Studt. Theoretical Insights into the Selective Oxidation of Methane to Methanol in Copper-Exchanged Mordenite. *ACS Catalysis*, 6(6):3760–3766, June 2016.
- [165] Aliaksandr V. Krukau, Oleg A. Vydrov, Artur F. Izmaylov, and Gustavo E. Scuseria. Influence of the exchange screening parameter on the performance of screened hybrid functionals. *The Journal of Chemical Physics*, 125(22):224106, December 2006.
- [166] B. Silvi and A. Savin. Classification of chemical bonds based on topological analysis of electron localization functions. *Nature*, 371(6499):683–686, October 1994.
- [167] Richard Dronskowski and Peter E. Blochl. Crystal orbital Hamilton populations (COHP): energy-resolved visualization of chemical bonding in solids based on density-functional calculations. *The Journal of Physical Chemistry*, 97(33):8617–8624, August 1993.
- [168] Martin Brehm and Barbara Kirchner. TRAVIS - A Free Analyzer and Visualizer for Monte Carlo and Molecular Dynamics Trajectories. *Journal of Chemical Information and Modeling*, 51(8):2007–2023, August 2011.
- [169] Martin Thomas, Martin Brehm, Reinhold Fligg, Peter Vhringer, and Barbara Kirchner. Computing vibrational spectra from ab initio molecular dynamics. *Physical Chemistry Chemical Physics*, 15(18):6608, 2013.
- [170] Jianwei Liu, David Hibbitts, and Enrique Iglesia. Dense CO Adlayers as Enablers of CO Hydrogenation Turnovers on Ru Surfaces. *Journal of the American Chemical Society*, 139(34):11789–11802, August 2017.

- [171] N. Y. Chen. Hydrophobic properties of zeolites. *The Journal of Physical Chemistry*, 80(1):60–64, January 1976.
- [172] J. L. Guth, H. Kessler, J. M. Higel, J. M. Lamblin, J. Patarin, A. Seive, J. M. Chezeau, and R. Wey. Zeolite Synthesis in the Presence of Fluoride Ions. In *Zeolite Synthesis*, volume 398 of *ACS Symposium Series*, pages 176–195. American Chemical Society, July 1989.
- [173] Rajamani Gounder and Mark E. Davis. Beyond shape selective catalysis with zeolites: Hydrophobic void spaces in zeolites enable catalysis in liquid water. *AIChE Journal*, 59(9):3349–3358, 2013.
- [174] Michael Hunger, Jrg Krger, Harry Pfeifer, Jrgen Caro, Bodo Zibrowius, Martin Blow, and Ryszard Mostowicz. Investigation of internal silanol groups as structural defects in ZSM-5-type zeolites. *Journal of the Chemical Society, Faraday Transactions 1: Physical Chemistry in Condensed Phases*, 83(11):3459–3468, January 1987.
- [175] J. Stelzer, M. Paulus, M. Hunger, and J. Weitkamp. Hydrophobic properties of all-silica zeolite beta1. *Microporous and Mesoporous Materials*, 22(13):1–8, June 1998.
- [176] Di Wu, Xiaofeng Guo, Hui Sun, and Alexandra Navrotsky. Energy Landscape of Water and Ethanol on Silica Surfaces. *The Journal of Physical Chemistry C*, 119(27):15428–15433, July 2015.
- [177] Yuchun Zhi, Hui Shi, Linyu Mu, Yue Liu, Donghai Mei, Donald M. Camaioni, and Johannes A. Lercher. Dehydration Pathways of 1-Propanol on HZSM-5 in the Presence and Absence of Water. *Journal of the American Chemical Society*, 137(50):15781–15794, December 2015.
- [178] Benjamin Rotenberg, Amish J. Patel, and David Chandler. Molecular Explanation for Why Talc Surfaces Can Be Both Hydrophilic and Hydrophobic. *Journal of the American Chemical Society*, 133(50):20521–20527, December 2011.
- [179] Jennifer D. Lewis, Stijn VandeVyver, Anthony J. Crisci, William R. Gunther, Vladimir K. Michaelis, Robert G. Griffin, and Yuriy Romn-Leshkov. A Continuous Flow Strategy for the Coupled Transfer Hydrogenation and Etherification of 5-(Hydroxymethyl)furfural using Lewis Acid Zeolites. *ChemSusChem*, 7(8):2255–2265, August 2014.
- [180] Brandon C. Bukowski, Jason S. Bates, Rajamani Gounder, and Jeffrey Greeley. First principles, microkinetic, and experimental analysis of Lewis acid site speciation during ethanol dehydration on Sn-Beta zeolites. *Journal of Catalysis*, 365:261–276, September 2018.
- [181] Minje Kang and Aditya Bhan. Kinetics and mechanisms of alcohol dehydration pathways on alumina materials. *Catalysis Science & Technology*, 6(17):6667–6678, August 2016.
- [182] Alexander V. Yakimov, Yury G. Kolyagin, Sren Tolborg, Peter N. R. Vennestrm, and Irina I. Ivanova. Accelerated synthesis of Sn-BEA in fluoride media: effect of H<sub>2</sub>O content in the gel. *New Journal of Chemistry*, 40(5):4367–4374, May 2016.

- [183] Chun-Chih Chang, Zhuopeng Wang, Paul Dornath, Hong Je Cho, and Wei Fan. Rapid synthesis of Sn-Beta for the isomerization of cellulosic sugars. *RSC Advances*, 2(28):10475–10477, October 2012.
- [184] Viktor J. Cybulskis, James W. Harris, Yury Zvinevich, Fabio H. Ribeiro, and Rajamani Gounder. A transmission infrared cell design for temperature-controlled adsorption and reactivity studies on heterogeneous catalysts. *Review of Scientific Instruments*, 87(10):103101, October 2016.
- [185] Charles L. Angell and Maria V. Howell. Infrared spectroscopic investigation of zeolites and adsorbed molecules. IV. Acetonitrile. *The Journal of Physical Chemistry*, 73(8):2551–2554, August 1969.
- [186] A. G. Pelmeshnikov, R. A. van Santen, J. Janchen, and E. Meijer. Acetonitrile-d<sub>3</sub> as a probe of Lewis and Brønsted acidity of zeolites. *The Journal of Physical Chemistry*, 97(42):11071–11074, October 1993.
- [187] Jiesheng Chen, John Meurig Thomas, and Gopinathan Sankar. IR spectroscopic study of CD<sub>3</sub>CN adsorbed on ALPO-18 molecular sieve and the solid acid catalysts SAPO-18 and MeAPO-18. *Journal of the Chemical Society, Faraday Transactions*, 90(22):3455–3459, January 1994.
- [188] Vitaly L. Sushkevich, Irina I. Ivanova, and Alexander V. Yakimov. Revisiting Acidity of SnBEA Catalysts by Combined Application of FTIR Spectroscopy of Different Probe Molecules. *The Journal of Physical Chemistry C*, 121(21):11437–11447, June 2017.
- [189] Johannes A. Lercher and Andreas Jentys. Chapter 13 Infrared and raman spectroscopy for characterizing zeolites. In Herman van Bekkum, Avelino Corma and Ferdi Schth, editor, *Studies in Surface Science and Catalysis*, volume 168 of *Introduction to Zeolite Science and Practice*, pages 435–476. Elsevier, 2007.
- [190] J. M. Newsam, M. M. J. Treacy, W. T. Koetsier, and C. B. De Gruyter. Structural Characterization of Zeolite Beta. *Proceedings of the Royal Society of London A: Mathematical, Physical and Engineering Sciences*, 420(1859):375–405, December 1988.
- [191] Raymond J. Gorte. Design parameters for temperature programmed desorption from porous catalysts. *Journal of Catalysis*, 75(1):164–174, May 1982.
- [192] R. A. Demmin and R. J. Gorte. Design parameters for temperature-programmed desorption from a packed bed. *Journal of Catalysis*, 90(1):32–39, November 1984.
- [193] R. J. Gorte. Temperature-programmed desorption for the characterization of oxide catalysts. *Catalysis Today*, 28(4):405–414, September 1996.
- [194] Thomas Bligaard, R. Morris Bullock, Charles T. Campbell, Jingguang G. Chen, Bruce C. Gates, Raymond J. Gorte, Christopher W. Jones, William D. Jones, John R. Kitchin, and Susannah L. Scott. Toward Benchmarking in Catalysis Science: Best Practices, Challenges, and Opportunities. *ACS Catalysis*, 6(4):2590–2602, April 2016.

- [195] Enrique Iglesia. *Formic acid decomposition on copper, nickel, and copper-nickel alloys*. Thesis, Stanford University, 1981.
- [196] Rostam J. Madon and Michel Boudart. Experimental criterion for the absence of artifacts in the measurement of rates of heterogeneous catalytic reactions. *Industrial & Engineering Chemistry Fundamentals*, 21(4):438–447, November 1982.
- [197] Elangannan Arunan, Gautam R. Desiraju, Roger A. Klein, Joanna Sadlej, Steve Scheiner, Ibon Alkorta, David C. Clary, Robert H. Crabtree, Joseph J. Dannenberg, Pavel Hobza, Henrik G. Kjaergaard, Anthony C. Legon, Benedetta Mennucci, and David J. Nesbitt. Definition of the hydrogen bond (IUPAC Recommendations 2011). *Pure and Applied Chemistry*, 83(8):1637–1641, 2011.
- [198] Peter A. Kollman and Leland C. Allen. Theory of the hydrogen bond. *Chemical Reviews*, 72(3):283–303, June 1972.
- [199] Stephen Brunauer, Lola S. Deming, W. Edwards Deming, and Edward Teller. On a Theory of the van der Waals Adsorption of Gases. *Journal of the American Chemical Society*, 62(7):1723–1732, July 1940.
- [200] Paul E. Hathaway and Mark E. Davis. High resolution, quasi-equilibrium sorption studies of molecular sieves. *Catalysis Letters*, 5(4-6):333–347, July 1990.
- [201] Toshio Okuhara. Water-Tolerant Solid Acid Catalysts. *Chemical Reviews*, 102(10):3641–3666, October 2002.
- [202] H. Scott Fogler. *Elements of Chemical Reaction Engineering*. Prentice Hall, September 2005.
- [203] De Mears. Tests for Transport Limitations in Experimental Catalytic Reactors. *Industrial & Engineering Chemistry Process Design and Development*, 10(4):541–547, 1971.
- [204] Rajamani Krishna and Jasper M. van Baten. Hydrogen Bonding Effects in Adsorption of Water-Alcohol Mixtures in Zeolites and the Consequences for the Characteristics of the Maxwell-Stefan Diffusivities. *Langmuir*, 26(13):10854–10867, July 2010.
- [205] NIST Chemistry WebBook, 2017.
- [206] Michel Boudart. Kinetics on ideal and real surfaces. *AIChE Journal*, 2(1):62–64, March 1956.
- [207] John Jones, Haifeng Xiong, Andrew T. DeLaRiva, Eric J. Peterson, Hien Pham, Sivakumar R. Challa, Gongshin Qi, Se Oh, Michelle H. Wiebenga, Xavier Isidro Pereira Hernandez, Yong Wang, and Abhaya K. Datye. Thermally stable single-atom platinum-on-ceria catalysts via atom trapping. *Science*, 353(6295):150–154, July 2016.
- [208] H.-J. Qiu, Yoshikazu Ito, Weitao Cong, Yongwen Tan, Pan Liu, Akihiko Hirata, Takeshi Fujita, Zheng Tang, and Mingwei Chen. Nanoporous Graphene with Single-Atom Nickel Dopants: An Efficient and Stable Catalyst for Electrochemical Hydrogen Production. *Angewandte Chemie International Edition*, 54(47):14031–14035, 2015.

- [209] Wengang Liu, Leilei Zhang, Xin Liu, Xiaoyan Liu, Xiaofeng Yang, Shu Miao, Wentao Wang, Aiqin Wang, and Tao Zhang. Discriminating Catalytically Active Fe<sub>N</sub>x Species of Atomically Dispersed Fe<sub>N</sub>C Catalyst for Selective Oxidation of the CH Bond. *Journal of the American Chemical Society*, 139(31):10790–10798, August 2017.
- [210] Jiahan Xie, James D. Kammert, Nicholas Kaylor, Jonathan W. Zheng, Eunjin Choi, Hien N. Pham, Xiahan Sang, Eli Stavitski, Klaus Attenkofer, Raymond R. Unocic, Abhaya K. Datye, and Robert J. Davis. Atomically Dispersed Co and Cu on N-Doped Carbon for Reactions Involving CH Activation. *ACS Catalysis*, 8(5):3875–3884, May 2018.
- [211] Yong Wang, Jun Mao, Xianguang Meng, Liang Yu, Dehui Deng, and Xinhe Bao. Catalysis with Two-Dimensional Materials Confining Single Atoms: Concept, Design, and Applications. *Chemical Reviews*, 119(3):1806–1854, February 2019.
- [212] Jacklyn N. Hall and Praveen Bollini. Structure, characterization, and catalytic properties of open-metal sites in metal organic frameworks. *Reaction Chemistry & Engineering*, 4(2):207–222, February 2019.
- [213] Loredana Valenzano, Bartolomeo Civalieri, Sachin Chavan, Silvia Bordiga, Merete H. Nilsen, Sren Jakobsen, Karl Petter Lillerud, and Carlo Lamberti. Disclosing the Complex Structure of UiO-66 Metal Organic Framework: A Synergic Combination of Experiment and Theory. *Chemistry of Materials*, 23(7):1700–1718, April 2011.
- [214] Dong Yang, Manuel A. Ortuo, Varinia Bernales, Christopher J. Cramer, Laura Gagliardi, and Bruce C. Gates. Structure and Dynamics of Zr<sub>6</sub>O<sub>8</sub> MetalOrganic Framework Node Surfaces Probed with Ethanol Dehydration as a Catalytic Test Reaction. *Journal of the American Chemical Society*, 140(10):3751–3759, March 2018.
- [215] W. O. Haag, R. M. Lago, and P. B. Weisz. The active site of acidic aluminosilicate catalysts. *Nature*, 309(5969):589, June 1984.
- [216] Aditya Bhan, Ayman D. Allian, Glenn J. Sunley, David J. Law, and Enrique Iglesia. Specificity of Sites within Eight-Membered Ring Zeolite Channels for Carbonylation of Methyls to Acetyls. *Journal of the American Chemical Society*, 129(16):4919–4924, April 2007.
- [217] Rajamani Gounder and Enrique Iglesia. Catalytic Consequences of Spatial Constraints and Acid Site Location for Monomolecular Alkane Activation on Zeolites. *Journal of the American Chemical Society*, 131(5):1958–1971, February 2009.
- [218] Hsu Chiang and Aditya Bhan. Catalytic consequences of hydroxyl group location on the rate and mechanism of parallel dehydration reactions of ethanol over acidic zeolites. *Journal of Catalysis*, 271(2):251–261, May 2010.
- [219] Yang Zhang, Ruixue Zhao, Maricruz Sanchez-Sanchez, Gary L. Haller, Jianzhi Hu, Ricardo Bermejo-Deval, Yue Liu, and Johannes A. Lercher. Promotion of protolytic pentane conversion on H-MFI zeolite by proximity of extra-framework aluminum oxide and Brnsted acid sites. *Journal of Catalysis*, 370:424–433, February 2019.

- [220] Chenhai Song, Yueying Chu, Meng Wang, Hui Shi, Li Zhao, Xuefeng Guo, Weimin Yang, Jianyi Shen, Nianhua Xue, Luming Peng, and Weiping Ding. Cooperativity of adjacent Brønsted acid sites in MFI zeolite channel leads to enhanced polarization and cracking of alkanes. *Journal of Catalysis*, 349:163–174, May 2017.
- [221] John R. Di Iorio, Claire T. Nimlos, and Rajamani Gounder. Introducing Catalytic Diversity into Single-Site Chabazite Zeolites of Fixed Composition via Synthetic Control of Active Site Proximity. *ACS Catalysis*, 7(10):6663–6674, October 2017.
- [222] Steven Nystrom, Alexander Hoffman, and David Hibbitts. Tuning Brønsted Acid Strength by Altering Site Proximity in CHA Framework Zeolites. *ACS Catalysis*, 8(9):7842–7860, September 2018.
- [223] Yury G. Kolyagin, Alexander V. Yakimov, Sren Tolborg, Peter N. R. Vennestrm, and Irina I. Ivanova. Application of 119sn CPMG MAS NMR for Fast Characterization of Sn Sites in Zeolites with Natural 119sn Isotope Abundance. *The Journal of Physical Chemistry Letters*, pages 1249–1253, March 2016.
- [224] Guodong Qi, Qiang Wang, Jun Xu, Qinming Wu, Chao Wang, Xingling Zhao, Xiangju Meng, Fengshou Xiao, and Feng Deng. Direct observation of tin sites and their reversible interconversion in zeolites by solid-state NMR spectroscopy. *Communications Chemistry*, 1(1):22, April 2018.
- [225] Yury G. Kolyagin, Alexander V. Yakimov, Sren Tolborg, Peter N. R. Vennestrm, and Irina I. Ivanova. Direct Observation of Tin in Different T-Sites of Sn-BEA by One- and Two-Dimensional 119sn MAS NMR Spectroscopy. *The Journal of Physical Chemistry Letters*, 9(13):3738–3743, July 2018.
- [226] Jan Dijkmans, Michiel Dusselier, Wout Janssens, Maarten Trekels, Andr Vanomme, Eric Breynaert, Christine Kirschhock, and Bert F. Sels. An Inner-/Outer-Sphere Stabilized Sn Active Site in -Zeolite: Spectroscopic Evidence and Kinetic Consequences. *ACS Catalysis*, 6(1):31–46, January 2016.
- [227] Jason S. Bates and Rajamani Gounder. Influence of confining environment polarity on ethanol dehydration catalysis by Lewis acid zeolites. *Journal of Catalysis*, 365:213–226, September 2018.
- [228] Z. Qin, L. Lakiss, J.-P. Gilson, K. Thomas, J.-M. Goupil, C. Fernandez, and V. Valtchev. Chemical Equilibrium Controlled Etching of MFI-Type Zeolite and Its Influence on Zeolite Structure, Acidity, and Catalytic Activity. *Chemistry of Materials*, 25(14):2759–2766, July 2013.
- [229] Zhengxing Qin, Georgian Melinte, Jean-Pierre Gilson, Maguy Jaber, Krasimir Bozhilov, Philippe Boullay, Svetlana Mintova, Ovidiu Ersen, and Valentin Valtchev. The Mosaic Structure of Zeolite Crystals. *Angewandte Chemie International Edition*, 55(48):15049–15052, November 2016.
- [230] N. K. Mal, V. Ramaswamy, P. R. Rajamohanam, and A. V. Ramaswamy. Sn-MFI molecular sieves: synthesis methods, 29si liquid and solid MAS-NMR, 119sn static and MAS NMR studies. *Microporous Materials*, 12(46):331–340, December 1997.

- [231] Mercedes Boronat, Patricia Concepcin, Avelino Corma, Mara Teresa Navarro, Michael Renz, and Susana Valencia. Reactivity in the confined spaces of zeolites: the interplay between spectroscopy and theory to develop structureactivity relationships for catalysis. *11(16):2876–2884*, April 2009.
- [232] Miguel A. Camblor, Mara-Jos Daz-Cabaas, Joaquin Perez-Pariente, Simon J. Teat, William Clegg, Ian J. Shannon, Philip Lightfoot, Paul A. Wright, and Russell E. Morris. SSZ-23: An Odd Zeolite with Pore Openings of Seven and Nine Tetrahedral Atoms. *Angewandte Chemie International Edition*, 37(15):2122–2126, August 1998.
- [233] Guanqun Zhang, Pei Feng, Weiping Zhang, Hao Liu, Congxin Wang, Huaijun Ma, Donge Wang, and Zhijian Tian. Single isomerization selectivity of glucose in methanol over Sn-BEC zeolite of homogenous Sn distribution. *Microporous and Mesoporous Materials*, 247:158–165, July 2017.
- [234] Douglas L. Dorset, Karl G. Strohmaier, Chris E. Kliever, Avelino Corma, Mari J. Daz-Cabaas, Fernando Rey, and Christopher J. Gilmore. Crystal Structure of ITQ-26, a 3d Framework with Extra-Large Pores. *Chemistry of Materials*, 20(16):5325–5331, August 2008.
- [235] Paul A. Wright, Wuzong Zhou, Joaquin Prez-Pariente, and Mar Arranz. Direct Observation of Growth Defects in Zeolite Beta. *Journal of the American Chemical Society*, 127(2):494–495, January 2005.
- [236] Vitaly L. Sushkevich, Pavel A. Kots, Yury G. Kolyagin, Alexander V. Yakimov, Artem V. Marikutsa, and Irina I. Ivanova. Origin of Water-Induced Brnsted Acid Sites in Sn-BEA Zeolites. *The Journal of Physical Chemistry C*, 123(9):5540–5548, March 2019.
- [237] William R. Gunther, Vladimir K. Michaelis, Robert G. Griffin, and Yuriy Romn-Leshkov. Interrogating the Lewis Acidity of Metal Sites in Beta Zeolites with <sup>15</sup>n Pyridine Adsorption Coupled with MAS NMR Spectroscopy. *The Journal of Physical Chemistry C*, 120(50):28533–28544, December 2016.
- [238] Miguel A. Camblor, Philip A. Barrett, Mara-Jos Daz-Cabaas, Luis A. Villaescusa, Marta Puche, Teresa Boix, Eva Prez, and Hubert Koller. High silica zeolites with three-dimensional systems of large pore channels. *Microporous and Mesoporous Materials*, 48(1):11–22, November 2001.
- [239] L. Delmotte, M. Soulard, F. Guth, A. Seive, A. Lopez, and J. L. Guth. 19f MAS n.m.r. studies of crystalline microporous solids synthesized in the fluoride medium. *Zeolites*, 10(8):778–783, November 1990.
- [240] Yasuhide Goa, Peng Wu, and Takashi Tatsumi. Influence of Fluorine on the Catalytic Performance of TiBeta Zeolite. *The Journal of Physical Chemistry B*, 108(14):4242–4244, April 2004.
- [241] Michael J. Cordon, Jacklyn N. Hall, James W. Harris, Jason S. Bates, Son-Jong Hwang, and Rajamani Gounder. Deactivation of Sn-Beta zeolites caused by structural transformation of hydrophobic to hydrophilic micropores during aqueous-phase glucose isomerization. *Catalysis Science & Technology*, 9(7):1654–1668, April 2019.

- [242] Son-Jong Hwang, Rajamani Gounder, Yashodhan Bhawe, Marat Orazov, Ricardo Bermejo-Deval, and Mark E. Davis. Solid State NMR Characterization of Sn-Beta Zeolites that Catalyze Glucose Isomerization and Epimerization. *Topics in Catalysis*, 58(7-9):435–440, March 2015.
- [243] Rafael van Grieken, Carmen Martos, Manuel Snchez-Snchez, David P. Serrano, Juan A. Melero, Jos Iglesias, and Alvar G. Cubero. Synthesis of Snsilicalite from hydrothermal conversion of SiO<sub>2</sub>SnO<sub>2</sub> xerogels. *Microporous and Mesoporous Materials*, 119(13):176–185, March 2009.
- [244] Pavel A. Kots, Anna V. Zabilska, Evgeny V. Khramov, Yuriy V. Grigoriev, Yan V. Zubavichus, and Irina I. Ivanova. Mechanism of Zr Incorporation in the Course of Hydrothermal Synthesis of Zeolite BEA. *Inorganic Chemistry*, 57(19):11978–11985, October 2018.
- [245] German Sastre and Julian D. Gale. ZeoTsites: a code for topological and crystallographic tetrahedral sites analysis in zeolites and zeotypes. *Microporous and Mesoporous Materials*, 43(1):27–40, March 2001.
- [246] Avelino Corma, Marie T. Navarro, Fernando Rey, Jordi Rius, and Susana Valencía. Pure Polymorph C of Zeolite Beta Synthesized by Using Framework Isomorphous Substitution as a Structure-Directing Mechanism. *Angewandte Chemie International Edition*, 40(12):2277–2280, June 2001.
- [247] Xiaolong Liu, Ugo Ravon, and Alain Tuel. Fluoride Removal from Double Four-Membered Ring (D4r) Units in As-Synthesized Ge-Containing Zeolites. *Chemistry of Materials*, 23(22):5052–5057, November 2011.
- [248] Teresa Blasco, Avelino Corma, Ma Jos Daz-Cabaas, Fernando Rey, Jos A. Vidal-Moya, and Claudio M. Zicovich-Wilson. Preferential Location of Ge in the Double Four-Membered Ring Units of ITQ-7 Zeolite. *The Journal of Physical Chemistry B*, 106(10):2634–2642, March 2002.
- [249] German Sastre, Jose A. VidalMoya, Teresa Blasco, Jordi Rius, Jose L. Jord, Maria T. Navarro, Fernando Rey, and Avelino Corma. Preferential Location of Ge Atoms in Polymorph C of Beta Zeolite (ITQ-17) and Their Structure-Directing Effect: A Computational, XRD, and NMR Spectroscopic Study. *Angewandte Chemie International Edition*, 41(24):4722–4726, 2002.
- [250] R. Hoffmann, V. I. Minkin, and B. K. Carpenter. Ockham’s Razor and chemistry. *Bulletin de la Socit chimique de France*, 133(2):117–130, 1996.
- [251] R. Szostak, K. P. Lillerud, and M. Stocker. Properties of Tschernichite, the Aluminum-Rich Mineral Analog of Zeolite Beta. *Journal of Catalysis*, 148(1):91–99, July 1994.
- [252] Rosemarie Szostak, Ming Pan, and Karl Petter Lillerud. High-resolution TEM imaging of extreme faulting in natural zeolite tschernichite. *The Journal of Physical Chemistry*, 99(7):2104–2109, February 1995.
- [253] B. Mihailova, V. Valtchev, S. Mintova, A.-C. Faust, N. Petkov, and T. Bein. Interlayer stacking disorder in zeolite beta family: a Raman spectroscopic study. *Physical Chemistry Chemical Physics*, 7(14):2756–2763, July 2005.

- [254] Mercedes Boronat, Avelino Corma, and Michael Renz. Mechanism of the Meerwein-Ponndorf-Verley-Oppenauer (MPVO) Redox Equilibrium on Sn and Zr-Beta Zeolite Catalysts. *The Journal of Physical Chemistry B*, 110(42):21168–21174, 2006.
- [255] Mercedes Boronat, Patricia Concepcion, Avelino Corma, and Michael Renz. Peculiarities of Sn-Beta and potential industrial applications. *Catalysis Today*, 121(12):39–44, March 2007.
- [256] Jennifer D. Lewis, Stijn VandeVyver, and Yuriy RomnLeshkov. Acid-Base Pairs in Lewis Acidic Zeolites Promote Direct Aldol Reactions by Soft Enolization. *Angewandte Chemie International Edition*, 54(34):9835–9838, 2015.
- [257] Lewis B. Young. Preparing phenylalkanes, November 1981.
- [258] Rene B. LaPierre, Randall D. Partridge, Nai Y. Chen, and Steven S. Wong. Catalytic dewaxing process, December 1983.
- [259] Rene B. LaPierre, Randall D. Partridge, Nai Y. Chen, and Stephen S. Wong. Hydrotreating/isomerization process to produce low pour point distillate fuels and lubricating oil stocks, May 1985.
- [260] Nai Yuen Chen and Tracy J. Huang. Hydroprocessing catalyst, June 1987.
- [261] Mercedes Boronat, Avelino Corma, Michael Renz, Germn Sastre, and Pedro M. Viruela. A Multisite Molecular Mechanism for Baeyer-Villiger Oxidations on Solid Catalysts Using Environmentally Friendly H<sub>2</sub>O<sub>2</sub> as Oxidant. *Chemistry A European Journal*, 11(23):6905–6915, November 2005.
- [262] Sharan Shetty, Sourav Pal, Dilip G. Kanhere, and Annick Goursot. Structural, Electronic, and Bonding Properties of Zeolite Sn-Beta: A Periodic Density Functional Theory Study. *Chemistry A European Journal*, 12(2):518–523, 2006.
- [263] Nicholas E. Thornburg, Anthony B. Thompson, and Justin M. Notestein. Periodic Trends in Highly Dispersed Groups IV and V Supported Metal Oxide Catalysts for Alkene Epoxidation with H<sub>2</sub>O<sub>2</sub>. *ACS Catalysis*, pages 5077–5088, July 2015.
- [264] MG CLERICI, G. BELLUSSI, and U. ROMANO. SYNTHESIS OF PROPYLENE-OXIDE FROM PROPYLENE AND HYDROGEN-PEROXIDE CATALYZED BY TITANIUM SILICALITE. *Journal of Catalysis*, 129(1):159–167, May 1991.
- [265] Mark E. Davis. Heterogeneous Catalysis for the Conversion of Sugars into Polymers. *Topics in Catalysis*, 58(7-9):405–409, April 2015.
- [266] Rajamani Gounder. Hydrophobic microporous and mesoporous oxides as Brønsted and Lewis acid catalysts for biomass conversion in liquid water. *Catalysis Science & Technology*, 4(9):2877–2886, August 2014.
- [267] Andrey Y. Kovalevsky, Leif Hanson, S. Zoe Fisher, Marat Mustyakimov, Sax A. Mason, V. Trevor Forsyth, Matthew P. Blakeley, David A. Keen, Trixie Wagner, H. L. Carrell, Amy K. Katz, Jenny P. Glusker, and Paul Langan. Metal Ion Roles and the Movement of Hydrogen during Reaction Catalyzed by D-Xylose Isomerase: A Joint X-Ray and Neutron Diffraction Study. *Structure*, 18(6):688–699, June 2010.

- [268] S. H. Bhosale, M. B. Rao, and V. V. Deshpande. Molecular and industrial aspects of glucose isomerase. *Microbiological Reviews*, 60(2):280–+, June 1996.
- [269] Hong Je Cho, Paul Dornath, and Wei Fan. Synthesis of Hierarchical Sn-MFI as Lewis Acid Catalysts for Isomerization of Cellulosic Sugars. *Acs Catalysis*, 4(6):2029–2037, June 2014.
- [270] Sebastian Proding, Hui Shi, Sebastian Eckstein, Jian Zhi Hu, Mariefel V. Olarte, Donald M. Camaioni, Mirosław A. Derewinski, and Johannes A. Lercher. Stability of Zeolites in Aqueous Phase Reactions. *Chemistry of Materials*, 29(17):7255–7262, September 2017.
- [271] Paula A. Zapata, Yi Huang, Miguel A. Gonzalez-Borja, and Daniel E. Resasco. Silylated hydrophobic zeolites with enhanced tolerance to hot liquid water. *Journal of Catalysis*, 308:82–97, December 2013.
- [272] Sebastian Proding, Hui Shi, Huamin Wang, Mirosław A. Derewinski, and Johannes A. Lercher. Impact of structural defects and hydronium ion concentration on the stability of zeolite BEA in aqueous phase. *Applied Catalysis B: Environmental*, 237:996–1002, December 2018.
- [273] Paula A. Zapata, Jimmy Faria, M. Pilar Ruiz, Rolf E. Jentoft, and Daniel E. Resasco. Hydrophobic Zeolites for Biofuel Upgrading Reactions at the Liquid-Liquid Interface in Water/Oil Emulsions. *Journal of the American Chemical Society*, 134(20):8570–8578, May 2012.
- [274] Daniele Padovan, Sren Tolborg, Luca Botti, Esben Taarning, Irantzu Sadaba, and Ceri Hammond. Overcoming catalyst deactivation during the continuous conversion of sugars to chemicals: maximising the performance of Sn-Beta with a little drop of water. *Reaction Chemistry & Engineering*, 3(2):155–163, April 2018.
- [275] William N. P. van der Graaf, Christiaan H. L. Tempelman, Frank C. Hendriks, Javier Ruiz-Martinez, Sara Bals, Bert M. Weckhuysen, Evgeny A. Pidko, and Erniel J. M. Hensen. Deactivation of Sn-Beta during carbohydrate conversion. *Applied Catalysis a-General*, 564:113–122, August 2018.
- [276] William N. P. van der Graaff, Guanna Li, Brahim Mezari, Evgeny A. Pidko, and Erniel J. M. Hensen. Synthesis of Sn-Beta with Exclusive and High Framework Sn Content. *ChemCatChem*, pages n/a–n/a, February 2015.
- [277] F. Gu, S. F. Wang, C. F. Song, M. K. Lu, Y. X. Qi, G. J. Zhou, D. Xu, and D. R. Yuan. Synthesis and luminescence properties of SnO<sub>2</sub> nanoparticles. *Chemical Physics Letters*, 372(3-4):451–454, April 2003.
- [278] Pierre Y. Dapsens, Cecilia Mondelli, Jakub Jagielski, Roland Hauert, and Javier Perez-Ramirez. Hierarchical Sn-MFI zeolites prepared by facile top-down methods for sugar isomerisation. *Catalysis Science & Technology*, 4(8):2302–2311, 2014.
- [279] Irantzu Sadaba, Manuel Lopez Granados, Anders Riisager, and Esben Taarning. Deactivation of solid catalysts in liquid media: the case of leaching of active sites in biomass conversion reactions. *Green Chemistry*, 17(8):4133–4145, 2015.

- [280] Sounak Roy, Kevin Bakhmutsky, Eyas Mahmoud, Raul F. Lobo, and Raymond J. Gorte. Probing Lewis Acid Sites in Sn-Beta Zeolite. *ACS Catalysis*, 3(4):573–580, 2013.
- [281] Miguel A. Camblor, Avelino Corma, and Susana Valencia. Spontaneous nucleation and growth of pure silica zeolite- free of connectivity defects. *Chemical Communications*, (20):2365–2366, January 1996.
- [282] Daniele Padovan, Luca Botti, and Ceri Hammond. Active site hydration governs the stability of Sn-Beta during continuous glucose conversion. *ACS Catalysis*, June 2018.
- [283] Luca Botti, Ricardo Navar, Sren Tolborg, Juan S. Martinez-Espin, Daniele Padovan, Esben Taarning, and Ceri Hammond. Influence of Composition and Preparation Method on the Continuous Performance of Sn-Beta for Glucose-Fructose Isomerisation. *Topics in Catalysis*, November 2018.
- [284] Alyssa M. Love, Carlos A. Carrero, Alessandro Chiericato, Joseph T. Grant, Sabrina Conrad, Rene Verel, and Ive Hermans. Elucidation of Anchoring and Restructuring Steps during Synthesis of Silica-Supported Vanadium Oxide Catalysts. *Chemistry of Materials*, 28(15):5495–5504, August 2016.
- [285] Mark H. Tucker, Ricardo Alamillo, Anthony J. Crisci, Gretchen M. Gonzalez, Susannah L. Scott, and James A. Dumesic. Sustainable Solvent Systems for Use in Tandem Carbohydrate Dehydration Hydrogenation. *Acs Sustainable Chemistry & Engineering*, 1(5):554–560, May 2013.
- [286] Kuizhi Chen, Jarred Kelsey, Jeffery L. White, Lu Zhang, and Daniel Resasco. Water Interactions in Zeolite Catalysts and Their Hydrophobically Modified Analogues. *ACS Catalysis*, pages 7480–7487, November 2015.
- [287] Jeremy M. Berg, John L. Tymoczko, Lubert Stryer, and Lubert Stryer. *Biochemistry*. W.H. Freeman, New York, 5th ed edition, 2002.
- [288] Phillip W. Snyder, Matthew R. Lockett, Demetri T. Moustakas, and George M. Whitesides. Is it the shape of the cavity, or the shape of the water in the cavity? *The European Physical Journal Special Topics*, 223(5):853–891, April 2014.
- [289] R. U. Lemieux. How water provides the impetus for molecular recognition in aqueous solution. *Accounts of Chemical Research*, 29(8):373–380, August 1996.
- [290] Tjelvar S. G. Olsson, John E. Ladbury, Will R. Pitt, and Mark A. Williams. Extent of enthalpy-entropy compensation in protein-ligand interactions. *Protein Science*, 20(9):1607–1618, September 2011.
- [291] W. KAUZMANN. SOME FACTORS IN THE INTERPRETATION OF PROTEIN DENATURATION. *Advances in Protein Chemistry*, 14:1–63, 1959.
- [292] Benjamin Breiten, Matthew R. Lockett, Woody Sherman, Shuji Fujita, Mohammad Al-Sayah, Heiko Lange, Carleen M. Bowers, Annie Heroux, Goran Krilov, and George M. Whitesides. Water Networks Contribute to Enthalpy/Entropy Compensation in ProteinLigand Binding. *Journal of the American Chemical Society*, 135(41):15579–15584, October 2013.

- [293] Sudip Chakraborty, Hemant Kumar, Chandan Dasgupta, and Prabal K. Maiti. Confined Water: Structure, Dynamics, and Thermodynamics. *Accounts of Chemical Research*, 50(9):2139–2146, September 2017.
- [294] M. Majumder, N. Chopra, R. Andrews, and B. J. Hinds. Nanoscale hydrodynamics - Enhanced flow in carbon nanotubes. *Nature*, 438(7064):44–44, November 2005.
- [295] J. K. Holt, H. G. Park, Y. M. Wang, M. Stadermann, A. B. Artyukhin, C. P. Grigoropoulos, A. Noy, and O. Bakajin. Fast mass transport through sub-2-nanometer carbon nanotubes. *Science*, 312(5776):1034–1037, May 2006.
- [296] Ralph K. Iler. *The chemistry of silica: solubility, polymerization, colloid and surface properties, and biochemistry*. Wiley, New York, 1979.
- [297] OI VINOGRADOVA. DRAINAGE OF A THIN LIQUID-FILM CONFINED BETWEEN HYDROPHOBIC SURFACES. *Langmuir*, 11(6):2213–2220, June 1995.
- [298] E. Bonaccorso, H. J. Butt, and V. S. J. Craig. Surface roughness and hydrodynamic boundary slip of a newtonian fluid in a completely wetting system. *Physical Review Letters*, 90(14):144501, April 2003.
- [299] OI VINOGRADOVA, NF BUNKIN, NV CHURAEV, OA KISELEVA, AV LOBEYEV, and BW NINHAM. SUBMICROCAVITY STRUCTURE OF WATER BETWEEN HYDROPHOBIC AND HYDROPHILIC WALLS AS REVEALED BY OPTICAL CAVITATION. *Journal of Colloid and Interface Science*, 173(2):443–447, August 1995.
- [300] D. F. Shantz, JSAD Gunne, H. Koller, and R. F. Lobo. Multiple-quantum H-1 MAS NMR studies of defect sites in as-made all-silica ZSM-12 zeolite. *Journal of the American Chemical Society*, 122(28):6659–6663, July 2000.
- [301] D. F. Shantz, C. Fild, H. Koller, and R. F. Lobo. Guest-host interactions in As-made Al-ZSM-12: Implications for the synthesis of zeolite catalysts. *Journal of Physical Chemistry B*, 103(49):10858–10865, December 1999.
- [302] SA AXON and J. KLINOWSKI. SYNTHESIS AND CHARACTERIZATION OF DEFECT-FREE CRYSTALS OF MFI-TYPE ZEOLITES. *Applied Catalysis a-General*, 81(1):27–34, January 1992.
- [303] JM CHEZEAU, L. DELMOTTE, JL GUTH, and M. SOULARD. HIGH-RESOLUTION SOLID-STATE SI-29 AND C-13 NMR ON HIGHLY SILICEOUS MFI-TYPE ZEOLITES SYNTHESIZED IN NONALKALINE FLUORIDE MEDIUM. *Zeolites*, 9(1):78–80, January 1989.
- [304] Elodie Bourgeat Lami, Francois Fajula, Didier Anglerot, and Thierry Des Courieres. Single step dealumination of zeolite beta precursors for the preparation of hydrophobic adsorbents. *Microporous Materials*, 1(4):237–245, July 1993.
- [305] R. DERUITER, APM KENTGENS, J. GROOTENDORST, JC JANSEN, and H. VANBEKKUM. CALCINATION AND DEBORONATION OF [B]-MFI SINGLE-CRYSTALS. *Zeolites*, 13(2):128–138, February 1993.

- [306] Donghai Mei and Johannes A. Lercher. Mechanistic insights into aqueous phase propanol dehydration in H-ZSM-5 zeolite. *AIChE Journal*, 63(1):172–184, January 2017.
- [307] C. B. Khouw, C. B. Dartt, J. A. Labinger, and M. E. Davis. Studies on the Catalytic-Oxidation of Alkanes and Alkenes by Titanium Silicates. *Journal of Catalysis*, 149(1):195–205, September 1994.
- [308] Nicols A. Grosso-Giordano, Christian Schroeder, Alexander Okrut, Andrew Solovyov, Christian Schttle, Walter Chass, Neboja Marinkovi, Hubert Koller, Stacey I. Zones, and Alexander Katz. Outer-Sphere Control of Catalysis on Surfaces: A Comparative Study of Ti(IV) Single-Sites Grafted on Amorphous versus Crystalline Silicates for Alkene Epoxidation. *Journal of the American Chemical Society*, 140(15):4956–4960, April 2018.
- [309] Hong Zhao, Toshiyuki Yokoi, Junko N. Kondo, and Takashi Tatsumi. Hydrophobicity enhancement of Ti-MWW catalyst and its improvement in oxidation activity. *Applied Catalysis A: General*, 503:156–164, August 2015.
- [310] Gang Yang, Evgeny A. Pidko, and Emiel J. M. Hensen. The Mechanism of Glucose Isomerization to Fructose over Sn-BEA Zeolite: A Periodic Density Functional Theory Study. *ChemSusChem*, 6(9):1688–1696, 2013.
- [311] Samir H. Mushrif, Jithin J. Varghese, and Chethana B. Krishnamurthy. Solvation dynamics and energetics of intramolecular hydride transfer reactions in biomass conversion. *Physical Chemistry Chemical Physics*, 17(7):4961–4969, February 2015.
- [312] John P. Perdew, Kieron Burke, and Matthias Ernzerhof. Generalized Gradient Approximation Made Simple. *Physical Review Letters*, 77(18):3865–3868, October 1996.
- [313] Y. K. Zhang and W. T. Yang. Comment on "Generalized gradient approximation made simple". *Physical Review Letters*, 80(4):890–890, January 1998.
- [314] B. Hammer, L. B. Hansen, and J. K. Norskov. Improved adsorption energetics within density-functional theory using revised Perdew-Burke-Ernzerhof functionals. *Physical Review B*, 59(11):7413–7421, March 1999.
- [315] Stefan Grimme, Stephan Ehrlich, and Lars Goerigk. Effect of the Damping Function in Dispersion Corrected Density Functional Theory. *Journal of Computational Chemistry*, 32(7):1456–1465, May 2011.
- [316] HJ MONKHORST and JD PACK. SPECIAL POINTS FOR BRILLOUIN-ZONE INTEGRATIONS. *Physical Review B*, 13(12):5188–5192, 1976.
- [317] Hannes Jnsson, Greg Mills, and Karsten W. Jacobsen. Nudged elastic band method for finding minimum energy paths of transitions. In *Classical and Quantum Dynamics in Condensed Phase Simulations*, pages 385–404, LERICI, Villa Marigola, June 1998. WORLD SCIENTIFIC.
- [318] G. Henkelman and H. Jonsson. A dimer method for finding saddle points on high dimensional potential surfaces using only first derivatives. *Journal of Chemical Physics*, 111(15):7010–7022, October 1999.

- [319] Atsushi Urakawa, Thomas Brgi, and Alfons Baiker. Sensitivity enhancement and dynamic behavior analysis by modulation excitation spectroscopy: Principle and application in heterogeneous catalysis. *Chemical Engineering Science*, 63(20):4902–4909, October 2008.
- [320] Daniel T. Bregante, Pranjali Priyadarshini, and David W. Flaherty. Kinetic and spectroscopic evidence for reaction pathways and intermediates for olefin epoxidation on Nb in \*BEA. *Journal of Catalysis*, 348:75–89, April 2017.
- [321] T. Ressler. WinXAS: a Program for X-ray Absorption Spectroscopy Data Analysis under MS-Windows. *Journal of Synchrotron Radiation*, 5(2):118–122, March 1998.
- [322] M. A. Camblor, A. Corma, and S. Valencia. Characterization of nanocrystalline zeolite Beta. *Microporous and Mesoporous Materials*, 25(1-3):59–74, December 1998.
- [323] M. A. Camblor, A. Corma, A. Mifsud, J. PerezPariente, and S. Valencia. Synthesis of nanocrystalline zeolite Beta in the absence of alkali metal cations. In H. Chon, S. K. Ihm, and Y. S. Uh, editors, *Progress in Zeolite and Microporous Materials, Pts a-C*, volume 105, pages 341–348. 1997.
- [324] F. Bonino, A. Damin, S. Bordiga, C. Lamberti, and A. Zecchina. Interaction of CD3cn and pyridine with the Ti(IV) centers of TS-1 catalysts: a spectroscopic and computational study. *Langmuir*, 19(6):2155–2161, March 2003.
- [325] V. Eroshenko, R. C. Regis, M. Soulard, and J. Patarin. The heterogeneous systems 'water-hydrophobic zeolites': new molecular springs. *Comptes Rendus Physique*, 3(1):111–119, February 2002.
- [326] Istvan Halasz, Song Kim, and Bonnie Marcus. Uncommon Adsorption Isotherm of Methanol on a Hydrophobic Y-zeolite. *The Journal of Physical Chemistry B*, 105(44):10788–10796, November 2001.
- [327] Michelle E. Dose, Ke Zhang, Joshua A. Thompson, Johannes Leisen, Ronald R. Chance, William J. Koros, Benjamin A. McCool, and Ryan P. Lively. Effect of Crystal Size on Framework Defects and Water Uptake in Fluoride Mediated Silicalite-1. *Chemistry of Materials*, 26(15):4368–4376, 2014.
- [328] Patricia A. Thiel and Theodore E. Madey. The interaction of water with solid surfaces: Fundamental aspects. *Surface Science Reports*, 7(6):211–385, October 1987.
- [329] Johannes A. Lercher and Andreas Jentys. INFRARED AND RAMAN SPECTROSCOPY FOR CHARACTERIZING ZEOLITES. In J. Cejka, H. V. Bekkum, A. Corma, and F. Schuth, editors, *Introduction to Zeolite Science and Practice*, volume 168, pages 435–476. 2007.
- [330] C. P. Lawrence and J. L. Skinner. Vibrational spectroscopy of HOD in liquid D<sub>2</sub>O. III. Spectral diffusion, and hydrogen-bonding and rotational dynamics. *The Journal of Chemical Physics*, 118(1):264–272, December 2002.
- [331] David S Eisenberg. *The structure and properties of water*. Clarendon P., Oxford, 1969.

- [332] Jeffrey R. Christianson, Stavros Caratzoulas, and Dionisios G. Vlachos. Computational Insight into the Effect of Sn-Beta Na Exchange and Solvent on Glucose Isomerization and Epimerization. *ACS Catalysis*, July 2015.
- [333] Rostam J. Madon and Enrique Iglesia. Catalytic reaction rates in thermodynamically non-ideal systems. *Journal of Molecular Catalysis A: Chemical*, 163(12):189–204, December 2000.
- [334] K. MIYAJIMA, M. SAWADA, and M. NAKAGAKI. STUDIES ON AQUEOUS-SOLUTIONS OF SACCHARIDES .1. ACTIVITY-COEFFICIENTS OF MONOSACCHARIDES IN AQUEOUS-SOLUTIONS AT 25-DEGREES-C. *Bulletin of the Chemical Society of Japan*, 56(6):1620–1623, 1983.
- [335] Milo D. Koretsky. *Engineering and chemical thermodynamics*. Wiley, Hoboken, NJ, 2nd edition edition, 2013.
- [336] Coblenz Society, Inc. *Evaluated Infrared Reference Spectra*. NIST Chemistry WebBook, NIST Standard Reference Database Number 69. National Institute of Standards and Technology, Gaithersburg MD, 20899.
- [337] M. HINENO. IR-SPECTRA AND NORMAL VIBRATIONS OF BETA-D-GLUCOPYRANOSE. *Carbohydrate Research*, 56(2):219–227, 1977.
- [338] JJ CAEL, JL KOENIG, and BLACKWEL.J. INFRARED AND RAMAN-SPECTROSCOPY OF CARBOHYDRATES .4. IDENTIFICATION OF CONFIGURATION-SENSITIVE AND CONFORMATION-SENSITIVE MODES FOR D-GLUCOSE. *Carbohydrate Research*, 32(1):79–91, 1974.
- [339] HA WELLS and RH ATALLA. AN INVESTIGATION OF THE VIBRATIONAL-SPECTRA OF GLUCOSE, GALACTOSE AND MANNOSE. *Journal of Molecular Structure*, 224:385–424, July 1990.
- [340] M. MATHLOUTHI and DV LUU. LASER-RAMAN SPECTRA OF D-GLUCOSE AND SUCROSE IN AQUEOUS-SOLUTION. *Carbohydrate Research*, 81(2):203–212, 1980.
- [341] M. Ibrahim, M. Alaam, H. El-Haes, A. F. Jalbout, and A. de Leon. Analysis of the structure and vibrational spectra of glucose and fructose. *Ecletica Quimica*, 31(3):15–21, 2006.
- [342] Peng Bai, J. Ilja Siepmann, and Michael W. Deem. Adsorption of glucose into zeolite beta from aqueous solution. *Aiche Journal*, 59(9):3523–3529, September 2013.
- [343] D. Chandler. Interfaces and the driving force of hydrophobic assembly. *Nature*, 437(7059):640–647, September 2005.
- [344] Neil M. Wilson and David W. Flaherty. Mechanism for the Direct Synthesis of H<sub>2</sub>O<sub>2</sub> on Pd Clusters: Heterolytic Reaction Pathways at the Liquid/Solid Interface. *Journal of the American Chemical Society*, 138(2):574–586, January 2016.
- [345] Dieter Baurecht and Urs Peter Fringeli. Quantitative modulated excitation Fourier transform infrared spectroscopy. *Review of Scientific Instruments*, 72(10):3782–3792, October 2001.

- [346] Francois Farges, Gordon E. Brown, and John J. Rehr. Coordination chemistry of Ti(IV) in silicate glasses and melts: I. XAFS study of titanium coordination in oxide model compounds. *Geochimica et Cosmochimica Acta*, 60(16):3023–3038, August 1996.
- [347] Chuan-De Wu and Wenbin Lin. Highly Porous, Homochiral MetalOrganic Frameworks: Solvent-Exchange-Induced Single-Crystal to Single-Crystal Transformations. *Angewandte Chemie International Edition*, 44(13):1958–1961, March 2005.
- [348] Kenichiro Koga, G. T. Gao, Hideki Tanaka, and X. C. Zeng. Formation of ordered ice nanotubes inside carbon nanotubes. *Nature*, 412(6849):802–805, August 2001.
- [349] Naotoshi Nakashima, Yasuhiko Tomonari, and Hiroto Murakami. Water-Soluble Single-Walled Carbon Nanotubes via Noncovalent Sidewall-Functionalization with a Pyrene-Carrying Ammonium Ion. *Chemistry Letters*, 31(6):638–639, June 2002.
- [350] G. Hummer, J. C. Rasaiah, and J. P. Noworyta. Water conduction through the hydrophobic channel of a carbon nanotube. *Nature*, 414(6860):188–190, November 2001.
- [351] Kenneth K. S. Lau, Jos Bico, Kenneth B. K. Teo, Manish Chhowalla, Gehan A. J. Amaratunga, William I. Milne, Gareth H. McKinley, and Karen K. Gleason. Superhydrophobic Carbon Nanotube Forests. *Nano Letters*, 3(12):1701–1705, December 2003.
- [352] Jan Dijkmans, Jan Demol, Kristof Houthoofd, Shuigen Huang, Yiannis Pontikes, and Bert Sels. Post-synthesis Sn: An exploration of synthesis parameters and catalysis. *Journal of Catalysis*, 330:545–557, October 2015.
- [353] Jol Puibasset and Roland J.-M. Pellenq. Grand Canonical Monte Carlo Simulation Study of Water Adsorption in Silicalite at 300 K. *The Journal of Physical Chemistry B*, 112(20):6390–6397, May 2008.
- [354] Fabien Cailliez, Mickael Trzpit, Michel Soulard, Isabelle Demachy, Anne Boutin, Jol Patarin, and Alain H. Fuchs. Thermodynamics of water intrusion in nanoporous hydrophobic solids. *Physical Chemistry Chemical Physics*, 10(32):4817–4826, August 2008.
- [355] Pierfranco Demontis, Giovanna Stara, and Giuseppe B. Suffritti. Behavior of Water in the Hydrophobic Zeolite Silicalite at Different Temperatures. A Molecular Dynamics Study. *The Journal of Physical Chemistry B*, 107(18):4426–4436, May 2003.
- [356] Pierfranco Demontis, Giovanna Stara, and Giuseppe B. Suffritti. Dynamical behavior of one-dimensional water molecule chains in zeolites: Nanosecond time-scale molecular dynamics simulations of bikitaite. *The Journal of Chemical Physics*, 120(19):9233–9244, April 2004.
- [357] P. Demontis, J. Guln-Gonzlez, M. Masia, and G. B. Suffritti. The behaviour of water confined in zeolites: molecular dynamics simulations versus experiment. *Journal of Physics: Condensed Matter*, 22(28):284106, 2010.

- [358] Chun-Hung Wang, Peng Bai, J. Ilja Siepmann, and Aurora E. Clark. Deconstructing Hydrogen-Bond Networks in Confined Nanoporous Materials: Implications for Alcohol/Water Separation. *The Journal of Physical Chemistry C*, 118(34):19723–19732, August 2014.
- [359] F Dehne and H Noltemeier. Voronoi trees and clustering problems. *Information Systems*, 12(2):171–175, January 1987.
- [360] Witold Brostow, Mieczyslaw Chybicki, Robert Laskowski, and Jaroslaw Rybicki. Voronoi polyhedra and Delaunay simplexes in the structural analysis of molecular-dynamics-simulated materials. *Physical Review B*, 57(21):13448–13458, June 1998.
- [361] A. Barrat, M. Barthlemy, R. Pastor-Satorras, and A. Vespignani. The architecture of complex weighted networks. *Proceedings of the National Academy of Sciences of the United States of America*, 101(11):3747–3752, March 2004.
- [362] Valentin Eroshenko, Robert-Charles Regis, Michel Soulard, and Jol Patarin. Energetics: A New Field of Applications for Hydrophobic Zeolites. *Journal of the American Chemical Society*, 123(33):8129–8130, August 2001.
- [363] Hans W. Horn, William C. Swope, Jed W. Pitera, Jeffry D. Madura, Thomas J. Dick, Greg L. Hura, and Teresa Head-Gordon. Development of an improved four-site water model for biomolecular simulations: TIP4p-Ew. *The Journal of Chemical Physics*, 120(20):9665–9678, May 2004.
- [364] H. J. C. Berendsen, J. R. Grigera, and T. P. Straatsma. The missing term in effective pair potentials. *The Journal of Physical Chemistry*, 91(24):6269–6271, November 1987.
- [365] The Nose-Hoover thermostat. *The Journal of Chemical Physics*, 83(8):4069–4074, October 1985.
- [366] William M. Haynes and David R. Lide, editors. *CRC handbook of chemistry and physics: a ready-reference book of chemical and physical data*. CRC Press, Boca Raton, Fla., 93. ed., 2012 - 2013 edition, 2012.
- [367] Katrin Forster-Tonigold and Axel Gro. Dispersion corrected RPBE studies of liquid water. *The Journal of Chemical Physics*, 141(6):064501, August 2014.
- [368] Andreas Mgelhj, Andr K. Kelkkanen, K. Thor Wikfeldt, Jakob Schitz, Jens Jrgen Mortensen, Lars G. M. Pettersson, Bengt I. Lundqvist, Karsten W. Jacobsen, Anders Nilsson, and Jens K. Nrskov. Ab Initio van der Waals Interactions in Simulations of Water Alter Structure from Mainly Tetrahedral to High-Density-Like. *The Journal of Physical Chemistry B*, 115(48):14149–14160, December 2011.
- [369] Tod A. Pascal, Shiang-Tai Lin, and William A. Goddard III. Thermodynamics of liquids: standard molar entropies and heat capacities of common solvents from 2pt molecular dynamics. *Phys. Chem. Chem. Phys.*, 13(1):169–181, 2011.
- [370] Ask Hjorth Larsen, Jens Jrgen Mortensen, Jakob Blomqvist, Ivano E. Castelli, Rune Christensen, Marcin Du\lak, Jesper Friis, Michael N. Groves, Bjrk Hammer, Cory Hargus, Eric D. Hermes, Paul C. Jennings, Peter Bjerre Jensen, James Kermode, John R. Kitchin, Esben Leonhard Kolsbjerg, Joseph Kubal,

- Kristen Kaasbjerg, Steen Lysgaard, Jn Bergmann Maronsson, Tristan Maxson, Thomas Olsen, Lars Pastewka, Andrew Peterson, Carsten Rostgaard, Jakob Schitz, Ole Schtt, Mikkel Strange, Kristian S. Thygesen, Tejs Vegge, Lasse Villhelmsen, Michael Walter, Zhenhua Zeng, and Karsten W. Jacobsen. The atomic simulation environmenta Python library for working with atoms. *Journal of Physics: Condensed Matter*, 29(27):273002, June 2017.
- [371] Jacob D. Durrant and J. Andrew McCammon. HBonanza: A computer algorithm for molecular-dynamics-trajectory hydrogen-bond analysis. *Journal of Molecular Graphics and Modelling*, 31:5–9, November 2011.
- [372] Carlo Parravano, J. D. Baldeschwieler, and Michel Boudart. Diffusion of Water in Zeolites. *Science*, 155(3769):1535–1536, 1967.
- [373] Tyler R. Josephson, Robert F. DeJaco, Swagata Pahari, Limin Ren, Qiang Guo, Michael Tsapatsis, J. Ilja Siepmann, Dionisios G. Vlachos, and Stavros Caratzoulas. Cooperative Catalysis by Surface Lewis Acid/Silanol for Selective Fructose Etherification on Sn-SPP Zeolite. *ACS Catalysis*, 8(10):9056–9065, October 2018.
- [374] Joaquin Resasco, Leanne D. Chen, Ezra Clark, Charlie Tsai, Christopher Hahn, Thomas F. Jaramillo, Karen Chan, and Alexis T. Bell. Promoter Effects of Alkali Metal Cations on the Electrochemical Reduction of Carbon Dioxide. *Journal of the American Chemical Society*, 139(32):11277–11287, August 2017.
- [375] Zachary K. Goldsmith, Yan Choi Lam, Alexander V. Soudackov, and Sharon Hammes-Schiffer. Proton Discharge on a Gold Electrode from Triethylammonium in Acetonitrile: Theoretical Modeling of Potential-Dependent Kinetic Isotope Effects. *Journal of the American Chemical Society*, 141(2):1084–1090, January 2019.
- [376] Megan N. Jackson, Michael L. Pegis, and Yogesh Surendranath. Graphite-Conjugated Acids Reveal a Molecular Framework for Proton-Coupled Electron Transfer at Electrode Surfaces. *ACS Central Science*, May 2019.
- [377] Megan N. Jackson, Onyu Jung, Hamish C. Lamotte, and Yogesh Surendranath. Donor-dependent promotion of interfacial proton-coupled electron transfer in aqueous electrocatalysis. *ACS Catalysis*, March 2019.
- [378] Xuan Yang, Jared Nash, Nicholas Oliveira, Yushan Yan, and Bingjun Xu. Understanding the pH Dependence of Underpotential Deposited Hydrogen on Platinum. *Angewandte Chemie International Edition*, 58(49):17718–17723, 2019.
- [379] Bhushan N. Zope, David D. Hibbitts, Matthew Neurock, and Robert J. Davis. Reactivity of the Gold/Water Interface During Selective Oxidation Catalysis. *Science*, 330(6000):74–78, October 2010.
- [380] Johnny Saavedra, Christopher J. Pursell, and Bert D. Chandler. CO Oxidation Kinetics over Au/TiO<sub>2</sub> and Au/Al<sub>2</sub>O<sub>3</sub> Catalysts: Evidence for a Common Water-Assisted Mechanism. *Journal of the American Chemical Society*, 140(10):3712–3723, March 2018.
- [381] Daniel Muoz-Santiburcio, Matteo Farnesi Camellone, and Dominik Marx. Solvation-Induced Changes in the Mechanism of Alcohol Oxidation at Gold/Titania Nanocatalysts in the Aqueous Phase versus Gas Phase. *Angewandte Chemie International Edition*, 57(13):3327–3331, March 2018.

- [382] Guoju Yang, Sneha A. Akhade, Xi Chen, Yue Liu, Mal-Soon Lee, Vassiliki-Alexandra Glezakou, Roger Rousseau, and Johannes A. Lercher. The Nature of Hydrogen Adsorption on Platinum in the Aqueous Phase. *Angewandte Chemie International Edition*, 58(11):3527–3532, 2019.
- [383] Enrique Iglesia. Design, synthesis, and use of cobalt-based Fischer-Tropsch synthesis catalysts. *Applied Catalysis A: General*, 161(1):59–78, November 1997.
- [384] Ajay K. Dalai, Tapan K. Das, Karuna V. Chaudhari, Gary Jacobs, and Burtron H. Davis. Fischer-Tropsch synthesis: Water effects on Co supported on narrow and wide-pore silica. *Applied Catalysis A: General*, 289(2):135–142, August 2005.
- [385] David D. Hibbitts, Brett T. Loveless, Matthew Neurock, and Enrique Iglesia. Mechanistic Role of Water on the Rate and Selectivity of Fischer-Tropsch Synthesis on Ruthenium Catalysts. *Angewandte Chemie International Edition*, 52(47):12273–12278, 2013.
- [386] Yong Tae Kim, Joseph P. Chada, Zhuoran Xu, Yomaira J. Pagan-Torres, Devon C. Rosenfeld, William L. Winniford, Eric Schmidt, and George W. Huber. Low-temperature oligomerization of 1-butene with H-ferrierite. *Journal of Catalysis*, 323:33–44, March 2015.
- [387] Iker Agirrezabal-Telleria, Ignacio Luz, Manuel A. Ortuño, Mikel Oregui-Bengoechea, Iaki Gandarias, Nria Lopez, Marty A. Lail, and Mustapha Soukri. Gas reactions under intrapore condensation regime within tailored metalorganic framework catalysts. *Nature Communications*, 10(1):2076, May 2019.
- [388] S. Ghosh, K. V. Ramanathan, and A. K. Sood. Water at nanoscale confined in single-walled carbon nanotubes studied by NMR. *EPL (Europhysics Letters)*, 65(5):678, March 2004.
- [389] Qiang Chen, Julie L. Herberg, Gregory Mogilevsky, Hai-Jing Wang, Michael Stadermann, Jason K. Holt, and Yue Wu. Identification of Endohedral Water in Single-Walled Carbon Nanotubes by 1h NMR. *Nano Letters*, 8(7):1902–1905, July 2008.
- [390] Nicols A. Grosso-Giordano, Adam S. Hoffman, Alexey Boubnov, David W. Small, Simon R. Bare, Stacey I. Zones, and Alexander Katz. Dynamic Reorganization and Confinement of  $\text{Ti}^{\text{iv}}$  Active Sites Controls Olefin Epoxidation Catalysis on Two-Dimensional Zeotypes. *Journal of the American Chemical Society*, 141(17):7090–7106, May 2019.
- [391] D. H Olson, W. O Haag, and W. S Borghard. Use of water as a probe of zeolitic properties: interaction of water with HZSM-5. *Microporous and Mesoporous Materials*, 3536:435–446, April 2000.
- [392] Adriano Zecchina, Francesco Geobaldo, Giuseppe Spoto, Silvia Bordiga, Gabriele Ricchiardi, Roberto Buzzoni, and Guido Petrini. FTIR Investigation of the Formation of Neutral and Ionic Hydrogen-Bonded Complexes by Interaction of H-ZSM-5 and H-Mordenite with  $\text{CH}_3\text{cn}$  and  $\text{H}_2\text{o}$ : Comparison with the H-NAFION Superacidic System. *The Journal of Physical Chemistry*, 100(41):16584–16599, January 1996.

- [393] L. Smith, A. K. Cheetham, R. E. Morris, L. Marchese, J. M. Thomas, P. A. Wright, and J. Chen. On the Nature of Water Bound to a Solid Acid Catalyst. *Science*, 271(5250):799–802, February 1996.
- [394] G. Zundel. Hydration Structure and Intermolecular Interaction in Polyelectrolytes. *Angewandte Chemie International Edition in English*, 8(7):499–509, 1969.
- [395] M. Eigen. Proton Transfer, Acid-Base Catalysis, and Enzymatic Hydrolysis. Part I: ELEMENTARY PROCESSES. *Angewandte Chemie International Edition in English*, 3(1):1–19, 1964.
- [396] Evgenii S. Stoyanov, Irina V. Stoyanova, and Christopher A. Reed. The Structure of the Hydrogen Ion ( $\text{H}_3\text{O}^+$ ) in Water. *Journal of the American Chemical Society*, 132(5):1484–1485, February 2010.
- [397] James F. Haw, Teng Xu, John B. Nicholas, and Patrick W. Goguen. Solvent-assisted proton transfer in catalysis by zeolite solid acids. *Nature*, 389(6653):832–835, October 1997.
- [398] Kuizhi Chen, Joshua Damron, Carlie Pearson, Daniel Resasco, Lu Zhang, and Jeffery L. White. Zeolite Catalysis: Water Can Dramatically Increase or Suppress Alkane CH Bond Activation. *ACS Catalysis*, 4(9):3039–3044, September 2014.
- [399] Kuizhi Chen, Abhishek Gumidyala, Maryam Abdolrhamani, Cameron Villines, Steven Crossley, and Jeffery L. White. Trace water amounts can increase benzene H/D exchange rates in an acidic zeolite. *Journal of Catalysis*, 351:130–135, July 2017.
- [400] Zheng Zhao, Reda Bababrik, Wenhua Xue, Yaping Li, Nicholas M. Briggs, Dieu-Thy Nguyen, Umi Nguyen, Steven P. Crossley, Sanwu Wang, Bin Wang, and Daniel E. Resasco. Solvent-mediated charge separation drives alternative hydrogenation path of furanics in liquid water. *Nature Catalysis*, 2(5):431–436, May 2019.
- [401] Gengnan Li, Bin Wang, Banghao Chen, and Daniel E. Resasco. Role of water in cyclopentanone self-condensation reaction catalyzed by MCM-41 functionalized with sulfonic acid groups. *Journal of Catalysis*, 377:245–254, September 2019.
- [402] Nicholas S. Gould and Bingjun Xu. Effect of liquid water on acid sites of NaY: An in situ liquid phase spectroscopic study. *Journal of Catalysis*, 342:193–202, October 2016.
- [403] Nicholas S. Gould and Bingjun Xu. Quantification of acid site densities on zeolites in the presence of solvents via determination of extinction coefficients of adsorbed pyridine. *Journal of Catalysis*, 358:80–88, February 2018.
- [404] Brian M. Murphy, Jingcheng Wu, Hong Je Cho, Juliana Soreo, Chenguang Wang, Longlong Ma, and Bingjun Xu. Nature and Catalytic Properties of In-Situ-Generated Brønsted Acid Sites on NaY. *ACS Catalysis*, 9(3):1931–1942, March 2019.

- [405] Donghai Mei and Johannes A Lercher. Effects of Local Water Concentrations on Cyclohexanol Dehydration in H-BEA Zeolite. *The Journal of Physical Chemistry C*, September 2019.
- [406] Brandon C. Bukowski, Jason S. Bates, Rajamani Gounder, and Jeffrey Greeley. Defect-Mediated Ordering of Condensed Water Structures in Microporous Zeolites. *Angewandte Chemie International Edition*, 58(46):16422–16426, November 2019.
- [407] Daniel T Bregante and David W. Flaherty. Impact of Specific Interactions Among Reactive Surface Intermediates and Confined Water on Epoxidation Catalysis and Adsorption in Lewis Acid Zeolites. *ACS Catalysis*, October 2019.
- [408] Chelsey D. Baertsch, Kenny T. Komala, Yong-Hwee Chua, and Enrique Iglesia. Genesis of Brnsted Acid Sites during Dehydration of 2-Butanol on Tungsten Oxide Catalysts. *Journal of Catalysis*, 205(1):44–57, January 2002.
- [409] Solange R. Blaszkowski and Rutger A. van Santen. The Mechanism of Dimethyl Ether Formation from Methanol Catalyzed by Zeolitic Protons. *Journal of the American Chemical Society*, 118(21):5152–5153, January 1996.
- [410] Cory B. Phillips and Ravindra Datta. Production of Ethylene from Hydrous Ethanol on H-ZSM-5 under Mild Conditions. *Industrial & Engineering Chemistry Research*, 36(11):4466–4475, November 1997.
- [411] Adriano Zecchina, Silvia Bordiga, Giuseppe Spoto, Domenica Scarano, Guido Span, and Francesco Geobaldo. IR spectroscopy of neutral and ionic hydrogen-bonded complexes formed upon interaction of  $\text{CH}_3\text{OH}$ ,  $\text{C}_2\text{H}_5\text{OH}$ ,  $(\text{CH}_3)_2\text{O}$ ,  $(\text{C}_2\text{H}_5)_2\text{O}$  and  $\text{C}_4\text{H}_8\text{O}$  with H-Y, H-ZSM-5 and H-mordenite: comparison with analogous adducts formed on the H-Nafion superacidic membrane. *Journal of the Chemical Society, Faraday Transactions*, 92(23):4863–4875, 1996.
- [412] Michele L. Sarazen, Eric Duskocil, and Enrique Iglesia. Catalysis on solid acids: Mechanism and catalyst descriptors in oligomerization reactions of light alkenes. *Journal of Catalysis*, 344:553–569, December 2016.
- [413] Gina Noh, Zhichen Shi, Stacey I. Zones, and Enrique Iglesia. Isomerization and -scission reactions of alkanes on bifunctional metal-acid catalysts: Consequences of confinement and diffusional constraints on reactivity and selectivity. *Journal of Catalysis*, 368:389–410, December 2018.
- [414] Jacob I. Monroe and M. Scott Shell. Computational discovery of chemically patterned surfaces that effect unique hydration water dynamics. *Proceedings of the National Academy of Sciences*, 115(32):8093–8098, August 2018.
- [415] Stephen Brunauer. *The Adsorption Of Gases And Vapors Vol I*. Oxford University Press., 1943.
- [416] Huanhua Pan, James A. Ritter, and Perla B. Balbuena. Examination of the Approximations Used in Determining the Isothermic Heat of Adsorption from the ClausiusClapeyron Equation. *Langmuir*, 14(21):6323–6327, October 1998.
- [417] Ke Zhang, Ryan P. Lively, James D. Noel, Michelle E. Dose, Benjamin A. McCool, Ronald R. Chance, and William J. Koros. Adsorption of Water and Ethanol in MFI-Type Zeolites. *Langmuir*, 28(23):8664–8673, 2012.

- [418] Vera Bolis, Claudia Busco, and Piero Ugliengo. Thermodynamic Study of Water Adsorption in High-Silica Zeolites. *The Journal of Physical Chemistry B*, 110(30):14849–14859, August 2006.
- [419] I. Kiricsi, C. Flego, G. Pazzuconi, W. O. Jr. Parker, R. Millini, C. Perego, and G. Bellussi. Progress toward Understanding Zeolite .beta. Acidity: An IR and 27al NMR Spectroscopic Study. *The Journal of Physical Chemistry*, 98(17):4627–4634, April 1994.
- [420] A. Corma, V. Fornas, F. Melo, and J. Prez-Pariente. Zeolite Beta: Structure, Activity, and Selectivity for Catalytic Cracking. In *Fluid Catalytic Cracking*, volume 375 of *ACS Symposium Series*, pages 49–63. American Chemical Society, September 1988.
- [421] M. F. Claydon and N. Sheppard. The nature of A,B,C-type infrared spectra of strongly hydrogen-bonded systems; pseudo-maxima in vibrational spectra. *Journal of the Chemical Society D: Chemical Communications*, 0(23):1431–1433, January 1969.
- [422] A. G. Pelmenchikov, R. A. van Santen, J. H. M. C. van Wolput, and J. Jnchen. The IR transmission windows of hydrogen bonded complexes in zeolites: a new interpretation of IR data of acetonitrile and water adsorption on zeolitic Bronsted sites. In J. Weitkamp, H. G. Karge, H. Pfeifer, and W. Hlderich, editors, *Studies in Surface Science and Catalysis*, volume 84 of *Zeolites and Related Microporous Materials: State of the Art 1994 - Proceedings of the 10th International Zeolite Conference, Garmisch-Partenkirchen, Germany, 17-22 July 1994*, pages 2179–2186. Elsevier, January 1994.
- [423] A. G. Pelmenchikov, J. H. M. C. van Wolput, J. Jaenchen, and R. A. van Santen. (A,B,C) Triplet of Infrared OH Bands of Zeolitic H-Complexes. *The Journal of Physical Chemistry*, 99(11):3612–3617, March 1995.
- [424] Jene D. Cyran, Michael A. Donovan, Doris Vollmer, Flavio Siro Brigiano, Simone Pezzotti, Daria R. Galimberti, Marie-Pierre Gageot, Mischa Bonn, and Ellen H. G. Backus. Molecular hydrophobicity at a macroscopically hydrophilic surface. *Proceedings of the National Academy of Sciences*, 116(5):1520–1525, January 2019.
- [425] Jan Schaefer, Ellen H. G. Backus, Yuki Nagata, and Mischa Bonn. Both Inter- and Intramolecular Coupling of OH Groups Determine the Vibrational Response of the Water/Air Interface. *The Journal of Physical Chemistry Letters*, 7(22):4591–4595, November 2016.
- [426] Nan Yang, Chinh H. Duong, Patrick J. Kelleher, Anne B. McCoy, and Mark A. Johnson. Deconstructing waters diffuse OH stretching vibrational spectrum with cold clusters. *Science*, 364(6437):275–278, April 2019.
- [427] Maria Sovago, R. Kramer Campen, George W. H. Wurpel, Michiel Mller, Huib J. Bakker, and Mischa Bonn. Vibrational Response of Hydrogen-Bonded Interfacial Water is Dominated by Intramolecular Coupling. *Physical Review Letters*, 100(17), April 2008.
- [428] E. A. Raymond, T. L. Tarbuck, and G. L. Richmond. Isotopic Dilution Studies of the Vapor/Water Interface as Investigated by Vibrational Sum-Frequency

- Spectroscopy. *The Journal of Physical Chemistry B*, 106(11):2817–2820, March 2002.
- [429] P. B. Miranda and Y. R. Shen. Liquid Interfaces: A Study by Sum-Frequency Vibrational Spectroscopy. *The Journal of Physical Chemistry B*, 103(17):3292–3307, April 1999.
- [430] Satoshi Nihonyanagi, Shoichi Yamaguchi, and Tahei Tahara. Water Hydrogen Bond Structure near Highly Charged Interfaces Is Not Like Ice. *Journal of the American Chemical Society*, 132(20):6867–6869, May 2010.
- [431] Anton Myalitsin, Shu-hei Urashima, Satoshi Nihonyanagi, Shoichi Yamaguchi, and Tahei Tahara. Water Structure at the Buried Silica/Aqueous Interface Studied by Heterodyne-Detected Vibrational Sum-Frequency Generation. *The Journal of Physical Chemistry C*, 120(17):9357–9363, May 2016.
- [432] Henry Eyring. The Activated Complex in Chemical Reactions. *The Journal of Chemical Physics*, 3(2):107–115, February 1935.
- [433] Ca Eckert and M. Boudart. On the Use of Fugacities in Gas Kinetics. *Chemical Engineering Science*, 18(2):144–147, 1963.
- [434] Stanley I. Sandler. *Chemical, biochemical, and engineering thermodynamics*. John Wiley, Hoboken, N.J, 4th ed edition, 2006.
- [435] K. J. Laidler and David Chen. The influence of pressure on the kinetics of the alkaline hydrolysis of esters and amides. *Transactions of the Faraday Society*, 54:1026, 1958.
- [436] R. A. Grieger and C. A. Eckert. Solvent effects on the activation volume of a Diels-Alder reaction. *Transactions of the Faraday Society*, 66(0):2579–2584, January 1970.
- [437] K. F. Wong and C. A. Eckert. Solution thermodynamics and kinetic solvent effects on a Diels-Alder reaction. *Transactions of the Faraday Society*, 66(0):2313–2319, January 1970.
- [438] Geoffrey A. Lawrance and Donald R. Stranks. Role of activation volume in the elucidation of reaction mechanisms in octahedral coordination complexes. *Accounts of Chemical Research*, 12(11):403–409, November 1979.
- [439] Andrew J. Jones and Enrique Iglesia. The Strength of Brnsted Acid Sites in Microporous Aluminosilicates. *ACS Catalysis*, pages 5741–5755, August 2015.
- [440] Michele L. Sarazen, Eric Dorskocil, and Enrique Iglesia. Effects of Void Environment and Acid Strength on Alkene Oligomerization Selectivity. *ACS Catalysis*, pages 7059–7070, September 2016.
- [441] Gina Noh, Stacey I. Zones, and Enrique Iglesia. Isomer sieving and the selective formation of terminal methyl isomers in reactions of linear alkanes on one-dimensional zeolites. *Journal of Catalysis*, 377:255–270, September 2019.
- [442] Adam J Rieth, Ashley M. Wright, Grigorii Skorupskii, Jenna L. Mancuso, Christopher H. Hendon, and Mircea Dinca. Record-Setting Sorbents for Reversible Water Uptake by Systematic Anion-Exchanges in Metal-Organic Frameworks. *Journal of the American Chemical Society*, August 2019.

- [443] Adam J. Rieth, Kelly M. Hunter, Mircea Dinc, and Francesco Paesani. Hydrogen bonding structure of confined water templated by a metal-organic framework with open metal sites. *Nature Communications*, 10(1):4771, December 2019.
- [444] John R. Di Iorio and Rajamani Gounder. Controlling the Isolation and Pairing of Aluminum in Chabazite Zeolites Using Mixtures of Organic and Inorganic Structure-Directing Agents. *Chemistry of Materials*, 28(7):2236–2247, April 2016.
- [445] Jonatan D. Albarracin-Caballero, Ishant Khurana, John R. Di Iorio, Arthur J. Shih, Joel E. Schmidt, Michiel Dusselier, Mark E. Davis, Aleksey Yezerets, Jeffrey T. Miller, Fabio H. Ribeiro, and Rajamani Gounder. Structural and kinetic changes to small-pore Cu-zeolites after hydrothermal aging treatments and selective catalytic reduction of NO<sub>x</sub> with ammonia. *Reaction Chemistry & Engineering*, 2(2):168–179, April 2017.
- [446] Jun Wang, Vincent F. Kispersky, W. Nicholas Delgass, and Fabio H. Ribeiro. Determination of the Au active site and surface active species via operando transmission FTIR and isotopic transient experiments on 2.3wt.% Au/TiO<sub>2</sub> for the WGS reaction. *Journal of Catalysis*, 289:171–178, May 2012.
- [447] Jason S. Bates, Brandon C. Bukowski, James W. Harris, Jeffrey Greeley, and Rajamani Gounder. Distinct Catalytic Reactivity of Sn Substituted in Framework Locations and at Defect Grain Boundaries in Sn-Zeolites. *ACS Catalysis*, 9(7):6146–6168, July 2019.
- [448] Charles T. Campbell and Jason R. V. Sellers. Enthalpies and Entropies of Adsorption on Well-Defined Oxide Surfaces: Experimental Measurements. *Chemical Reviews*, 113(6):4106–4135, June 2013.
- [449] Shuichi Nos. A unified formulation of the constant temperature molecular dynamics methods. *The Journal of Chemical Physics*, 81(1):511–519, July 1984.
- [450] John R. Di Iorio, Shane A. Bates, Anuj A. Verma, W. Nicholas Delgass, Fabio H. Ribeiro, Jeffrey T. Miller, and Rajamani Gounder. The Dynamic Nature of Brønsted Acid Sites in CuZeolites During NO<sub>x</sub> Selective Catalytic Reduction: Quantification by Gas-Phase Ammonia Titration. *Topics in Catalysis*, 58(7-9):424–434, April 2015.
- [451] GiovanniMaria Piccini, Maristella Alessio, Joachim Sauer, Yuchun Zhi, Yuan-shuai Liu, Robin Kolvenbach, Andreas Jentys, and Johannes A. Lercher. Accurate Adsorption Thermodynamics of Small Alkanes in Zeolites. Ab initio Theory and Experiment for H-Chabazite. *The Journal of Physical Chemistry C*, 119(11):6128–6137, March 2015.
- [452] John R. Di Iorio, Alexander J. Hoffman, Claire T. Nimlos, Steven Nystrom, David Hibbitts, and Rajamani Gounder. Mechanistic origins of the high-pressure inhibition of methanol dehydration rates in small-pore acidic zeolites. *Journal of Catalysis*, October 2019.
- [453] Andrew J. Jones and Enrique Iglesia. Kinetic, Spectroscopic, and Theoretical Assessment of Associative and Dissociative Methanol Dehydration Routes in Zeolites. *Angewandte Chemie International Edition*, 53(45):12177–12181, November 2014.

- [454] Anton N. Mlinar, Paul M. Zimmerman, Fuat E. Celik, Martin Head-Gordon, and Alexis T. Bell. Effects of Brnsted-acid site proximity on the oligomerization of propene in H-MFI. *Journal of Catalysis*, 288:65–73, April 2012.
- [455] Christopher Paolucci, Atish A. Parekh, Ishant Khurana, John R. Di Iorio, Hui Li, Jonatan D. Albarracin Caballero, Arthur J. Shih, Trunojoyo Anggara, W. Nicholas Delgass, Jeffrey T. Miller, Fabio H. Ribeiro, Rajamani Gounder, and William F. Schneider. Catalysis in a Cage: Condition-Dependent Speciation and Dynamics of Exchanged Cu Cations in SSZ-13 Zeolites. *Journal of the American Chemical Society*, 138(18):6028–6048, May 2016.
- [456] Sichi Li, Hui Li, Rajamani Gounder, Anthony Debellis, Imke B. Mller, Subramanian Prasad, Ahmad Moini, and William F. Schneider. First-Principles Comparison of Proton and Divalent Copper Cation Exchange Energy Landscapes in SSZ-13 Zeolite. *The Journal of Physical Chemistry C*, 122(41):23564–23573, October 2018.
- [457] J. Ddeek, Z. Sobalk, and B. Wichterlov. Siting and Distribution of Framework Aluminium Atoms in Silicon-Rich Zeolites and Impact on Catalysis. *Catalysis Reviews*, 54(2):135–223, April 2012.
- [458] Claire Nimlos, Young Gul Hur, John R. Di Iorio, and Rajamani Gounder. Synthesis Methods to Influence Aluminum Location and Proximity in MFI Zeolites and Catalytic Consequences for Methanol Dehydration, June 2019.
- [459] Young Gul Hur, Philip M. Kester, Claire T. Nimlos, YoonRae Cho, Jeffrey T. Miller, and Rajamani Gounder. Influence of Tetrapropylammonium and Ethylenediamine Structure-Directing Agents on the Framework Al Distribution in BA1MFI Zeolites. *Industrial & Engineering Chemistry Research*, June 2019.

## APPENDICES

## A. BIMOLECULAR DEHYDRATION OF ETHANOL-METHANOL MIXTURES AS A PROBE OF INTRAPORE ALKANOL STRUCTURE IN BRØNSTED ACID ZEOLITES

### A.1 Motivation

Observed inhibition of methanol dehydration turnover rates to dimethyl ether (415 K, per  $\text{H}^+$ ) at high methanol pressures ( $> 10$  kPa  $\text{CH}_3\text{OH}$ ) in H-CHA [221] has been recently shown to reflect the formation of methanol clusters as MARI consisting of 3–5  $\text{CH}_3\text{OH}$  as estimated by volumetric adsorption isotherms, which must desorb 0–2  $\text{CH}_3\text{OH}$  molecules to access the kinetically preferred methanol trimer intermediate (with one spectating methanol) whose associative transition state to eliminate dimethyl ether contains the lowest apparent free energy barrier (among those from other methanol intermediates) according to DFT calculations [452]. In contrast, condensed water within H-CHA (373 K, 10–75 kPa  $\text{H}_2\text{O}$ ) inhibits bimolecular ethanol dehydration turnover rates (per  $\text{H}^+$ ) with reaction orders that are more negative than  $-1$  because of the formation of extended hydrogen-bonded networks of water that require non-ideal thermodynamic formalisms to describe their different stabilization of MARI and transition states, as described in Chapter 8. It was hypothesized that more extensive pore-filling by methanol may be required to approach regimes requiring non-ideal thermodynamic treatments, which may be realized at lower temperatures.

### A.2 Results and Discussion

Methanol co-feeds were introduced to H-CHA ( $\text{Si}/\text{Al} = 15$ ,  $\sim 0\%$  Al in 6-MR pairs as quantified by  $\text{Co}^{2+}$  titration) during ethanol dehydration experiments (373 K), at first with the intent to measure diethyl ether formation rates as a function of co-fed methanol pressure in regimes dilute in ethanol to assess whether methanol

also inhibits diethyl ether (DEE) formation with inhibition similar to that caused by  $\text{H}_2\text{O}$ . Initially, the ethanol pressure was varied over a wide range (0.05–5 kPa) with a constant 4 kPa co-feed of methanol (E/M ratios of 0.01–1), to quantify reaction orders that should enable inferring the MARI and mechanistic pathways that lead to formation of products. Under these conditions, DEE, methyl ethyl ether (MEE), and dimethyl ether (DME) can be quantified as products whose formation rates depend differently on the  $P_{\text{C}_2\text{H}_5\text{OH}}/P_{\text{CH}_3\text{OH}}$  ratio (Figure A.1a). The simplest series

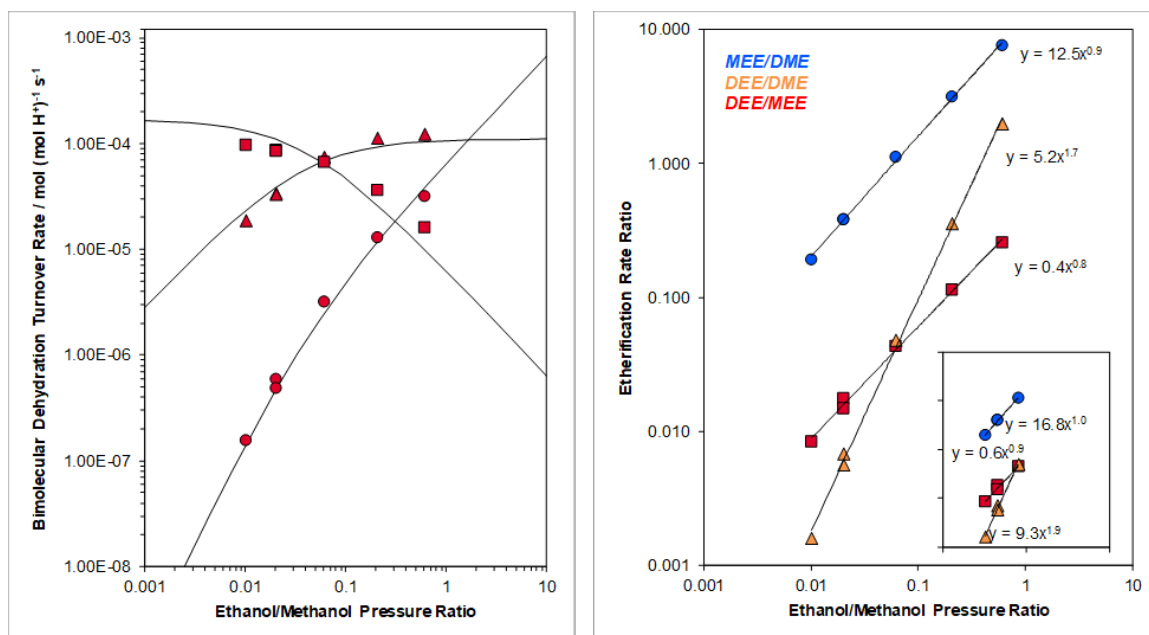


**Figure A.1:** (a) DME (square), MEE (triangle), and DEE (circle) turnover rates (per  $\text{H}^+$ , 373 K) on H-CHA ( $\text{Si}/\text{Al} = 15$ , 0% Al in 6-MR pairs) as a function of the ethanol/methanol pressure ratio, at constant  $P_{\text{CH}_3\text{OH}} = 4\text{ kPa}$ . Solid lines represent fits to the rate expressions in Table A.1. (b) Etherification rate ratios calculated from the data in the left graph. Blue:  $r_{\text{MEE}}/r_{\text{DME}}$ , orange:  $r_{\text{DEE}}/r_{\text{DME}}$ , red:  $r_{\text{DEE}}/r_{\text{MEE}}$ , with fits to data from  $\alpha = 0.01$ – $0.06$  in the inset.

of elementary steps that capture the measured dependences in Figure A.1a is summarized in Figure A.2. At this methanol pressure (4 kPa) and in the limit of low ethanol pressure, methanol-methanol dimer species ( $\text{MM}^*$ ) would be expected as the dominant MARI species (DME reaction orders in methanol are near zero under these

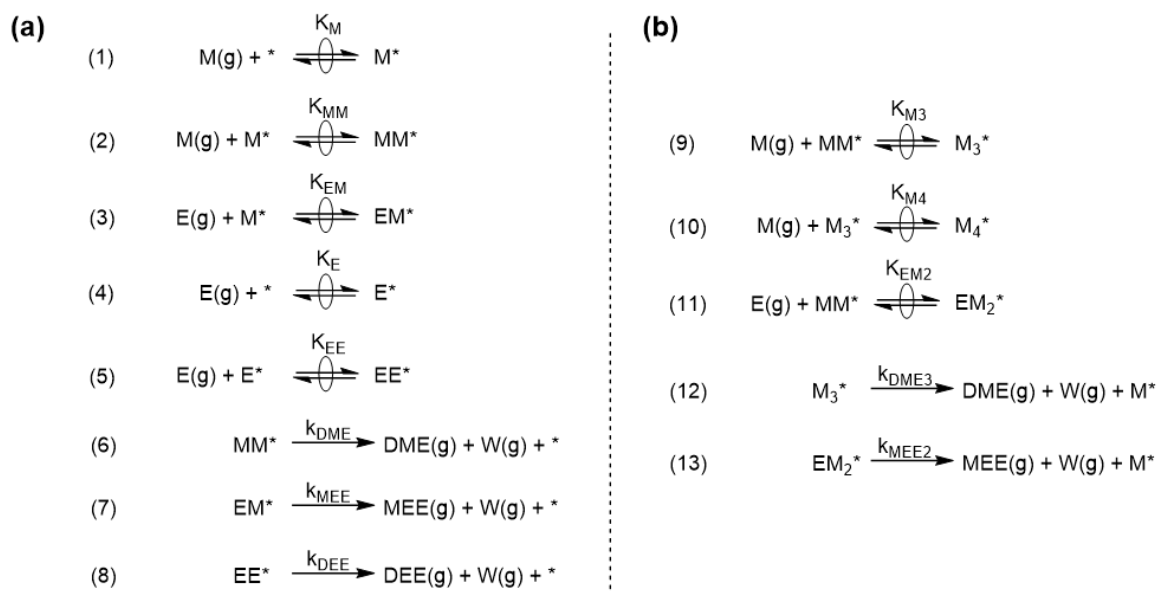


**Figure A.2:** (a) Series of elementary steps to form DME, MEE, and DEE by associative mechanisms through transition states involving dimeric surface intermediates with no co-adsorbed spectator alcohol molecules. (b) Additional plausible elementary steps to rationalize high-pressure methanol inhibition of DME and MEE turnover rates.

conditions, Figure A.3, *vide infra*), which may compete with ethanol-methanol dimers ( $\text{EM}^*$ ) at active sites as the co-fed ethanol pressure is increased. Assuming all ether products are formed by analogous associative dehydration pathways (kinetic irrelevance of alkoxide-based pathways is discussed in Section A.3.2), mechanism-derived rate expressions for each product contain identical denominator terms for  $\text{H}^+$  coverage, but different dependences in numerator terms reflecting the preferred protonated dimer intermediate to form such products and thus in turn on the  $P_{\text{C}_2\text{H}_5\text{OH}}/P_{\text{CH}_3\text{OH}}$  ratio (defined as  $\alpha$  hereafter) in the limiting cases of coverage by ( $\text{MM}^*$ ) or ( $\text{EM}^*$ ) MARI, summarized in Table A.1. These rate equations also predict that the rate ratios  $r_{\text{MEE}}/r_{\text{DME}}$ ,  $r_{\text{DEE}}/r_{\text{DME}}$ , and  $r_{\text{DEE}}/r_{\text{MEE}}$  depend on  $\alpha^n$ , where  $n = 1, 2,$  and  $1$ , respectively, which is the case for  $\alpha$  values between 0.01–0.06 (Figure A.1b). Deviations at higher  $\alpha$  values (0.2–0.6) may reflect kinetically relevant parallel ether formation pathways not accurately described by the assumptions in Figure A.2, but

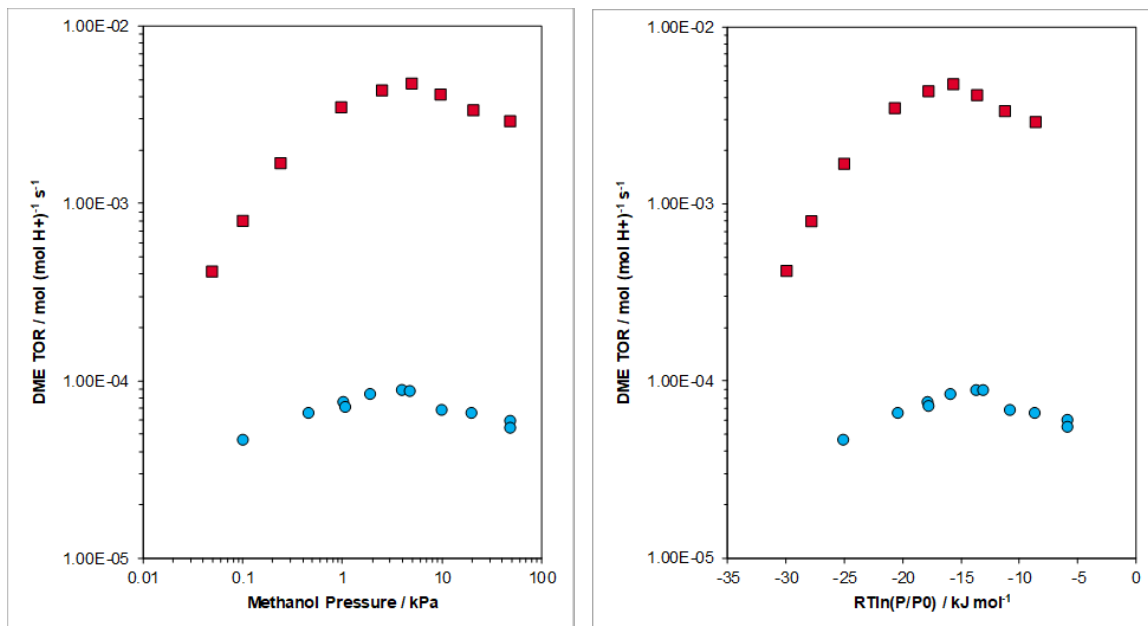


**Figure A.3:** (a) (blue circles) DME turnover rate (373 K, per H<sup>+</sup>) on H-CHA (Si/Al = 15) as a function of methanol pressure, at constant (M)/(E) ratio = 100. (red squares) DME turnover rate (403 K, per H<sup>+</sup>) measured by Di Iorio et al. [452] without co-fed ethanol. (b) The same data as in (a), but as a function of the CH<sub>3</sub>OH Gibbs free energy, RTln(P/P<sub>sat</sub><sup>-1</sup>) [452].

**Table A.1:** Rate expressions for bimolecular dehydration products given the series of elementary steps in Figure A.2 and different MARI species.

Rate <sup>a</sup>	MM*, EM*	MARI MM*	EM*	Lumped Expression <sup>b</sup>
$\frac{r_{DME}}{(L)} =$	$\frac{k_{DME}K_{MM}}{K_{MM}+K_{EM}\alpha}$	$k_{DME}$	$\frac{k_{DME}K_{MM}}{K_{EM}}\alpha^{-1}$	$\frac{A}{1+\beta\alpha}$
$\frac{r_{MEE}}{(L)} =$	$\frac{k_{MEE}K_3\alpha}{K_{MM}+K_{EM}\alpha}$	$\frac{k_{MEE}K_3}{K_{MM}}\alpha$	$k_{MEE}$	$\frac{B\beta\alpha}{1+\beta\alpha}$
$\frac{r_{DEE}}{(L)} =$	$\frac{k_{DEE}K_EK_{EE}K_M^{-1}\alpha^2}{K_{MM}+K_{EM}\alpha}$	$\frac{k_{DEE}K_EK_{EE}}{K_MK_{MM}}\alpha^2$	$\frac{k_{DEE}K_EK_{EE}}{K_MK_{EM}}\alpha$	$\frac{C\alpha^2}{1+\beta\alpha}$

<sup>a</sup>The parameter  $\alpha$  is the (E)/(M) ratio

<sup>b</sup> $\beta = K_{EM}/K_{MM}$ ,  $A = k_{DME}$ ,  $B = k_{MEE}$ ,  $C = k_{DEE}K_EK_{EE}K_M^{-1}K_{MM}^{-1}$

is beyond the scope of this study as we will ultimately focus on interpreting kinetics at low  $\alpha$  values (0.005–0.02).

The dependence of measured rates of all three ether products on  $\alpha$  can be reasonably fit (Figure A.1a, solid lines) using a single value of the equilibrium constant ratio  $\beta = K_{EM}/K_{MM}$  (Table A.1), and three separate values for the intrinsic or apparent rate constant for each product (A, B, C; Table A.1), consistent with their formation from the same pool of intermediates at  $H^+$  sites. The regressed value of  $\beta$  ( $26 \pm 0.4$ , Table A.2) reflects the relative preference for forming  $EM^*$  over  $MM^*$  from an adsorbed methanol monomer (Steps 2 and 3, Figure A.2), likely because the larger  $EM^*$  dimeric intermediate is stabilized by van der Waals interactions when confined within CHA. The values of  $k_{DME}$  ( $1.69 \times 10^{-4} \text{ mol (mol } H^+)^{-1} \text{ s}^{-1}$ , Table A.2) and

**Table A.2:** Rate parameters used to fit the data in Figure A.1 using the expressions in Table A.1.

Parameter	$\beta^a$	$A^b / 10^{-4}$	$B^b / 10^{-4}$	$C^b / 10^{-3}$
Value <sup>c</sup>	$26 \pm 0.4$	$1.69 \pm 0.02$	$1.11 \pm 0.01$	$1.75 \pm 0.08$

<sup>a</sup>unitless

<sup>b</sup>units [=]  $\text{mol (mol } H^+)^{-1} \text{ s}^{-1}$

<sup>c</sup>Reported uncertainties represent 95% marginal highest posterior density intervals from Athena Visual Studio

$k_{MEE}$  ( $1.11 \times 10^{-4} \text{ mol (mol } H^+)^{-1} \text{ s}^{-1}$ , Table A.2) fit by the model are within a factor of two, and reflect the intrinsic barriers to form DME (Step 6, Figure A.2) and MEE (Step 7, Figure A.2) from their respective dimeric precursors, suggesting that these ether formation transition states are stabilized by confinement to similar extents as their precursors (indicated by  $\beta$ ) of similar size. The value of the apparent rate constant  $C = k_{DEE}K_EK_{EE}K_M^{-1}K_{MM}^{-1}$  reflects the free energy of the transition state that eliminates DEE relative to sites covered by methanol-methanol dimers ( $MM^*$ ). The value of  $C$  ( $1.75 \times 10^{-3} \text{ mol (mol } H^+)^{-1} \text{ s}^{-1}$ , Table A.2) is approximately one order of magnitude higher than  $k_6$ , where the ratio  $C/k_{DME}$  reflects the relative free energies of the DEE and DME transition states, respectively, because both are in reference to the same  $MM^*$ -covered surface. Similar to the interpretation of the value of  $\beta$ ,  $C/k_{DME}$  likely reflects the preferential stabilization of the larger DEE transition state

relative to the smaller DME transition state by more effective van der Waals contacts with the CHA pore.

The kinetics measured in Figure A.1 indicate that if the mechanistic assumptions of Figure A.2 hold, then the turnover rates of all products should be the same function of  $\alpha$  in regimes where the methanol pressure is sufficient to saturate  $H^+$  sites with methanol-methanol dimers, and increasing ethanol pressures only lead to a shift to ethanol-methanol dimer-covered surfaces. To avoid the complication of needing to account for mixed ethanol-methanol species as MARI in further analyses at different methanol pressures, turnover rates (373 K, per  $H^+$ ) were measured at  $\alpha^{-1}$  values between 50–200. Under these low ethanol pressure conditions, DEE formation rates were often undetectable, but MEE and DME formation rates were. The kinetics of methanol dehydration to DME (373 K,  $\alpha^{-1} = 50\text{--}200$ ) were verified to behave similar to those measured by Di Iorio et al. between 398–415 K (without co-fed  $C_2H_5OH$ ) [452], where measured turnover rates (Figure A.3a) first increase with increasing methanol pressure (0.1–2 kPa  $CH_3OH$ ), reach a zero-order regime (2–5 kPa  $CH_3OH$ ), and then decrease (5–50 kPa  $CH_3OH$ ). These data are consistent with kinetically relevant formation of DME through methanol trimer intermediates ( $M_3^*$ , Step 12, Figure A.2b) at high methanol pressures (5–50 kPa  $CH_3OH$ ) at  $H^+$  partially covered by methanol tetramer species ( $M_4^*$ , Step 10, Figure A.2b) that lead to the apparent inhibition [452]. Converting the gas-phase methanol pressure to a Gibbs free energy ( $RT\ln(P_{CH_3OH}/P_{sat})$ ) indicates that decreasing the temperature to 373 K enabled extending the upper value of free energies explored from  $-9$  to  $-6$   $\text{kJ mol}^{-1}$ , which was likely not a sufficient enough change to populate sites with a different set of higher-nuclearity methanol clusters. The lower value of the apparent reaction order in methanol at 373 K ( $\sim 0.2$ ) than at 403 K ( $\sim 0.6$ ) in the low methanol pressure regime (0.1–1 kPa) reflects higher coverages of methanol-methanol dimers at lower temperatures because adsorption of gaseous methanol at surface monomers is exothermic ( $-50$   $\text{kJ mol}^{-1}$ , as quantified from kinetic data of H-MFI [453] and H-CHA [221]) and leads to a strong dependence of  $K_{MM}$  on temperature.

Ethanol co-feeds that do not lead to measurable coverages of  $C_2H_5OH$  at  $H^+$  sites ( $\alpha^{-1} = 50\text{--}200$ ) provide additional information to further validate mechanistic assumptions. Formation of MEE from the same pool of intermediates at  $H^+$  sites enables quantifying  $r_{DME}/r_{MEE}$  rate ratios that rigorously eliminate the dependence of measured rates on coverage terms that appear in the denominators of rate expressions for each product in isolation. The  $r_{DME}/r_{MEE}$  rate ratio was quantified as a function of  $\alpha^{-1}$  at constant values of  $CH_3OH$  pressure between 0.1–50 kPa, shown in Figure A.4. In the limit of low  $P_{CH_3OH}$ ,  $r_{DME}/r_{MEE}$  is expected to depend linearly on  $\alpha^{-1}$

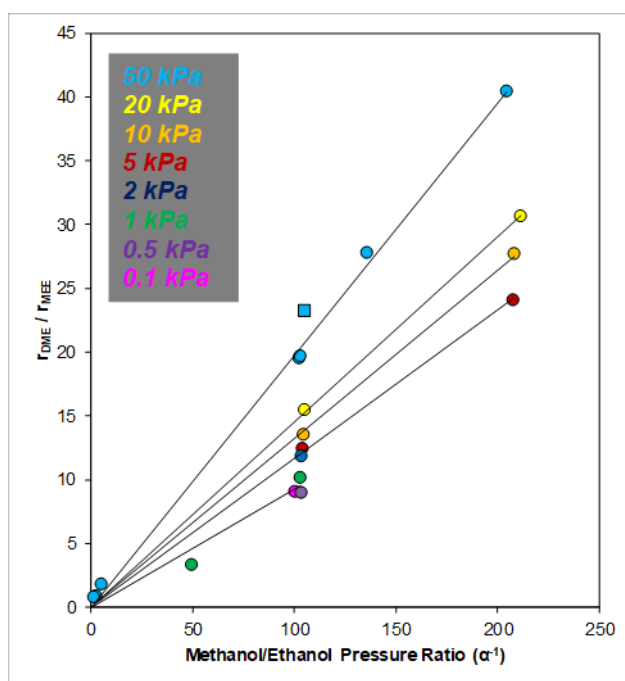


**Figure A.4:** DME/MEE rate ratio as a function of the  $P_{CH_3OH}/P_{C_2H_5OH}$  ratio ( $\alpha^{-1}$ ) on H-CHA (Si/Al = 15) at 373 K at methanol pressures between 0.1–50 kPa. Solid lines obtained by linear regression constrained to go through the origin.

according to the equation (see Section A.3.1 for complete derivation):

$$\frac{r_{DME}}{r_{MEE}} = \frac{k_{DME}}{k_{MEE}K_{EM}K_{MM}^{-1}} \frac{P_{CH_3OH}}{P_{C_2H_5OH}} = \frac{k_{DME}K_{MM}}{k_{MEE}K_{EM}} \alpha^{-1} = \chi \alpha^{-1} \quad (A.1)$$

Equation A.1 holds between 0.1–1 kPa  $CH_3OH$ , quantifying a value of  $\chi = 0.09$  (unitless).  $\chi$  reflects the relative free energies of the DME and MEE transition states,

and indicates that at 373 K the MEE transition state is 7 kJ mol<sup>-1</sup> lower in free energy than the DME transition state, likely because of confinement, as discussed above. The value of  $\chi$  independently fit from the data in Figure A.1, collected at 4 kPa CH<sub>3</sub>OH but across a wider range of  $\alpha^{-1}$  values (1–100) that leads to coverage regimes that include EM\*, is  $0.06 \pm 0.01$  (AB<sup>-1</sup> $\beta^{-1}$ , Table A.2), and is in reasonable agreement with the value of  $0.09 \pm 0.01$  determined at lower CH<sub>3</sub>OH pressure.

The data in Figure A.4, however, indicate that at methanol pressures between 2–50 kPa, Equation A.1 is insufficient to describe that data because the  $r_{\text{DME}}/r_{\text{MEE}}$  ratio is no longer a single-valued function of  $\alpha^{-1}$ . The measured dependence of the DME formation rate (Figure A.3) on methanol pressure reflects the kinetically relevant formation of DME through methanol trimer-mediated pathways [452], indicating that Equation A.1 must be revised to include coverage terms for (M<sub>3</sub>\*) because it introduces a new term to the numerator of the  $r_{\text{DME}}$  rate expression, even though it rigorously cancels in the denominator terms of the  $r_{\text{DME}}/r_{\text{MEE}}$  ratio. Including this parallel DME formation pathway leads to a new expression for the  $r_{\text{DME}}/r_{\text{MEE}}$  ratio (see Section A.3.1 for complete derivation):

$$\frac{r_{\text{DME}}}{r_{\text{MEE}}} = (1 + k_{\text{DME}3}k_{\text{DME}}^{-1}K_{\text{M}3}P_{\text{CH}_3\text{OH}}) \chi\alpha^{-1} \quad (\text{A.2})$$

where Equation A.2 reduces to Equation A.1 in the limit of low  $P_{\text{CH}_3\text{OH}}$ , but adds an additional dependence on  $P_{\text{CH}_3\text{OH}}$  at higher pressures because of the kinetic relevance of Step 13 in Figure A.2. At a constant value of  $P_{\text{CH}_3\text{OH}}$ ,  $r_{\text{DME}}/r_{\text{MEE}}$  should still depend linearly on  $\alpha^{-1}$ , which has been verified at CH<sub>3</sub>OH pressures between 5–50 kPa (Figure A.4). In qualitative agreement with Equation A.2, the linear slope systematically increases above values of  $\chi$  with increasing CH<sub>3</sub>OH pressure. This predicted dependence and the mechanistic assumptions underlying it can be quantitatively assessed by rearranging Equation A.2:

$$\frac{r_{\text{DME}}}{r_{\text{MEE}}}\alpha\chi^{-1} = 1 + k_{\text{DME}3}k_{\text{DME}}^{-1}K_{\text{M}3}P_{\text{CH}_3\text{OH}} \quad (\text{A.3})$$

where the value of  $\chi$  was taken as 0.09 (quantified from data measured between 0.1–1 kPa CH<sub>3</sub>OH), and  $r_{\text{DME}}/r_{\text{MEE}}\alpha$  reflects the slopes of the lines in Figure A.4. The value of  $\frac{r_{\text{DME}}}{r_{\text{MEE}}}\alpha\chi^{-1}$  is plotted as a function of the CH<sub>3</sub>OH pressure in Figure A.5, and depends linearly on  $P_{\text{CH}_3\text{OH}}$  with an intercept of unity as predicted by Equation A.3, consistent with the mechanistic assumptions used to derive Equation A.3 that also account for the inhibition of DME rates at high CH<sub>3</sub>OH pressures (5–50 kPa) [452]. The value of the slope of the linear regression ( $3 \text{ bar}^{-1}$ ,  $k_{\text{DME}3}K_{\text{M}3}k_{\text{DME}}^{-1}$ ) reflects

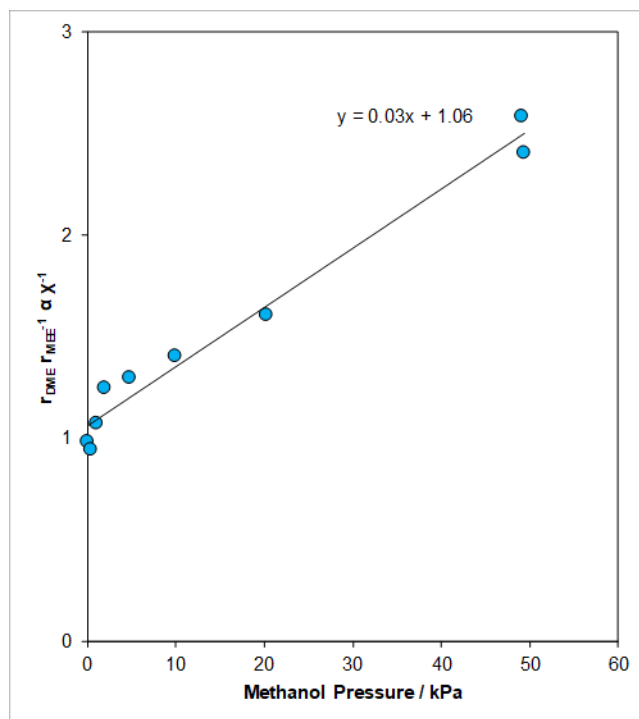


**Figure A.5:** Dependence of  $r_{\text{DME}}/r_{\text{MEE}}\alpha\chi^{-1}$  (373 K, as quantified according to Equation A.1 at  $\alpha^{-1}$  values between 50–200 in Figure A.4) on the CH<sub>3</sub>OH pressure. Solid line obtained by linear regression.

the free energy of the trimer-mediated DME elimination transition state relative to the dimer-mediated DME elimination transition state, and predicts that the trimer-mediated transition state is 3 kJ mol<sup>-1</sup> more stable in free energy than the dimer-mediated transition state. This is not as large as that predicted by DFT calculations in Di Iorio et al. [452] (34 kJ mol<sup>-1</sup>, extrapolated from the data in Figure 15); however, it is in the right direction. Errors in DFT-calculated enthalpies are often on the order

of  $\sim 10$  kJ mol<sup>-1</sup> based on choice of functional, and the addition of errors in free energies of 10–20 kJ mol<sup>-1</sup> introduced by the unreliable approximation of replacing low-frequency vibrational modes with 60 cm<sup>-1</sup> to calculate vibrational entropies [124, 125, 180] is sufficient to explain this discrepancy.

Lastly, Equation A.3 assumes that MEE formation from ethanol-methanol-methanol trimer species does not contribute to MEE turnover rates (Step 13, Figure A.2), which would otherwise lead to  $r_{\text{DME}}/r_{\text{MEE}}$  values that plateau in the limit of high CH<sub>3</sub>OH pressures (Equation A.13, Supporting Information). The linearity of Figure A.5 indicates that this parallel MEE formation pathway is not kinetically relevant under the conditions explored (373 K, 0.1–50 kPa CH<sub>3</sub>OH,  $\alpha^{-1} = 50$ –200). Corroborating evidence for this assumption could be supplied by theoretical calculations of these reaction coordinates. It can be speculated that the MEE transition state may be destabilized by spectating methanol because this methanol-methanol-ethanol arrangement may prefer protonation of the two methanol molecules rather than the mixed methanol-ethanol dimer. Evidence that MEE can also form through kinetically relevant multimer-based pathways (in addition to methanol-ethanol dimers) would require additional mechanistic revisions to the above discussion.

### A.3 Supporting Information

#### A.3.1 Derivation of DME/MEE rate ratio expression

Assuming the steps in both Figure A.2a and b are kinetically relevant,

$$r_{\text{DME}} = k_{\text{DME}}(MM^*) + k_{\text{DME3}}(M_3^*) \quad (\text{A.4})$$

$$r_{\text{MEE}} = k_{\text{MEE}}(EM^*) + k_{\text{MEE2}}(EM_2^*) \quad (\text{A.5})$$

and using the assumption of quasi-equilibrated adsorption steps to arrive at the same surface intermediate terms:

$$r_{\text{DME}} = k_{\text{DME}}K_{\text{MM}}(M^*)P_{\text{CH}_3\text{OH}} + k_{\text{DME3}}K_{\text{MM}}K_{\text{M3}}(M^*)P_{\text{CH}_3\text{OH}}^2 \quad (\text{A.6})$$

$$r_{\text{MEE}} = k_{\text{MEE}} K_{\text{EM}} (M^*) P_{\text{C}_2\text{H}_5\text{OH}} + k_{\text{MEE}2} K_{\text{MM}} K_{\text{EM}2} (M^*) P_{\text{CH}_3\text{OH}} P_{\text{C}_2\text{H}_5\text{OH}} \quad (\text{A.7})$$

Factoring  $(M^*)$ ,  $K_{\text{MM}}$ , and pressure terms out of both equations and dividing A.6 by A.7 gives:

$$\frac{r_{\text{DME}}}{r_{\text{MEE}}} = \frac{k_{\text{DME}} + k_{\text{DME}3} K_{\text{M}3} P_{\text{CH}_3\text{OH}}}{k_{\text{MEE}} K_{\text{EM}} K_{\text{MM}}^{-1} + k_{\text{MEE}2} K_{\text{EM}2} P_{\text{CH}_3\text{OH}}} \frac{P_{\text{CH}_3\text{OH}}}{P_{\text{C}_2\text{H}_5\text{OH}}} \quad (\text{A.8})$$

In the low  $P_{\text{CH}_3\text{OH}}$  limit, A.8 becomes:

$$\frac{r_{\text{DME}}}{r_{\text{MEE}}} = \frac{k_{\text{DME}}}{k_{\text{MEE}} K_{\text{EM}} K_{\text{MM}}^{-1}} \frac{P_{\text{CH}_3\text{OH}}}{P_{\text{C}_2\text{H}_5\text{OH}}} = \frac{k_{\text{DME}} K_{\text{MM}}}{k_{\text{MEE}} K_{\text{EM}}} \alpha^{-1} = \chi \alpha^{-1} \quad (\text{A.9})$$

where  $\alpha$  is the ethanol/methanol pressure ratio as defined in the Main Text. This equation is linear in the methanol/ethanol pressure ratio. If step 12 is kinetically relevant, as employed by Di Iorio et al. [452], but step 13 is not, then the expression becomes:

$$\frac{r_{\text{DME}}}{r_{\text{MEE}}} = \frac{k_{\text{DME}} K_{\text{MM}}}{k_{\text{MEE}} K_{\text{EM}}} \left(1 + k_{\text{DME}3} k_{\text{DME}}^{-1} K_{\text{M}3} P_{\text{CH}_3\text{OH}}\right) \alpha^{-1} \quad (\text{A.10})$$

Rewriting using the definition in A.9 yields:

$$\frac{r_{\text{DME}}}{r_{\text{MEE}}} = \left(1 + k_{\text{DME}3} k_{\text{DME}}^{-1} K_{\text{M}3} P_{\text{CH}_3\text{OH}}\right) \chi \alpha^{-1} \quad (\text{A.11})$$

or,

$$\frac{r_{\text{DME}}}{r_{\text{MEE}}} \alpha \chi^{-1} = 1 + k_{\text{DME}3} k_{\text{DME}}^{-1} K_{\text{M}3} P_{\text{CH}_3\text{OH}} \quad (\text{A.12})$$

Lastly, if both steps 12 and 13 are kinetically relevant, in the high  $\text{CH}_3\text{OH}$  pressure limit Equation A.8 reduces to:

$$\frac{r_{\text{DME}}}{r_{\text{MEE}}} = \frac{k_{\text{DME}3} K_{\text{M}3}}{k_{\text{MEE}2} K_{\text{EM}2}} \alpha^{-1} \quad (\text{A.13})$$

### A.3.2 Alkoxide-mediated DEE and MEE formation

Alkoxide-mediated pathways to form DEE and MEE would require kinetically relevant alkoxide formation followed by kinetically irrelevant ether formation from the bound alkoxide, as was found for methanol dehydration [452]. Kinetically relevant

alkoxide formation leads to ether formation rates equivalent to alkoxide formation rates from adsorbed monomeric alkanol species  $A^*$ :

$$r_{\text{ether}} = r_{\text{alkoxide}} = k_{\text{alk}}(A^*) \quad (\text{A.14})$$

where  $k_{\text{alk}}$  is the rate constant for the kinetically relevant alkoxide formation step. With quasi-equilibrated adsorption to form alkanol monomers from vacant sites (\*) and gas-phase alkanol (A):

$$\frac{r_{\text{ether}}}{(L)} = k_{\text{alk}} K_A P_A \frac{(*)}{(L)} \quad (\text{A.15})$$

where  $P_A$  is the pressure of the alkanol (kPa),  $K_A$  is the equilibrium constant for the adsorption step ( $\text{kPa}^{-1}$ ), and  $(L)/(*)$  reflects the site balance that can take various forms assuming different MARI.

In the case of DEE, Equation A.15 implies that second-order dependences on  $P_{\text{C}_2\text{H}_5\text{OH}}$  ( $\alpha = 0.01\text{--}0.02$  at constant  $P_{\text{CH}_3\text{OH}} = 4$  kPa, Figure A.1) can not be described by alkoxide-mediated pathways, and thus DEE must be formed via an associative pathway through protonated dimer species, and that there are no ethanol-derived intermediates involved in site balances under these conditions.

If MEE is formed by alkoxide-mediated pathways, then Equation A.15 could be re-written in terms of  $(M^*)$  as:

$$r_{\text{MEE}} = k_{\text{alk}} K_E P_{\text{C}_2\text{H}_5\text{OH}} K_M^{-1} P_{\text{CH}_3\text{OH}}^{-1} (M^*) \quad (\text{A.16})$$

Using Equation A.6, the expression for  $r_{\text{MEE}}$  in A.16 would result in:

$$\frac{r_{\text{DME}}}{r_{\text{MEE}}} = \frac{k_{\text{DME}} + k_{\text{DME}3} K_{M3} P_{\text{CH}_3\text{OH}} \frac{P_{\text{CH}_3\text{OH}}^2}{P_{\text{C}_2\text{H}_5\text{OH}}}}{k_{\text{alk}} K_E K_M^{-1}} \quad (\text{A.17})$$

This expression does not describe the measured dependence of  $r_{\text{DME}}/r_{\text{MEE}}$  on  $\alpha^{-1}$  (Figure A.4), indicating that MEE is also not formed via alkoxide-mediated pathways.

## B. EFFECTS OF PROTON PROXIMITY ON ETHANOL DEHYDRATION CATALYSIS IN CHA AND MFI ZEOLITES

### B.1 Motivation

The proximity of protons in Brønsted acid zeolites has been reported to influence the catalytic behavior of different hydrocarbon chemistries in H-MFI zeolites [219,454], but on a series of MFI zeolites lacking independent and systematic control of the convoluting effects of  $H^+$  density, which can lead to different diffusion-mediated selectivity in intrinsically diffusion-limited secondary reaction pathways [413,440,441], and  $H^+$  location between confining channels ( $\sim 0.47$  nm diameter) and less-confined channel intersections ( $\sim 0.64$  nm diameter), which influences the free energies of reaction intermediates and transition states by van der Waals forces [33]. Recently our group studied methanol dehydration (415 K) on a suite of H-CHA zeolites (Si/Al = 15) with  $H^+$  at the same crystallographically unique Al T-sites and thus within the same confining environments, which enabled concluding that proximal  $H^+$  sites increased methanol dehydration turnover rates in both first-order and zero-order kinetic regimes by stabilizing methoxy-based pathways over associative dehydration pathways [221]. In that case, proximal  $H^+$  sites were known to be located in next-next-nearest neighbor configurations across 6-membered rings based on DFT calculations [455,456] and  $^{29}\text{Si}$  NMR spectra that did not detect  $Q^2$  Si atoms for next-nearest-neighbor Al configurations [444], and could be quantified by titrations with divalent  $\text{Co}^{2+}$  cations. MFI zeolites, in contrast, possess a variety of proximal Al sites with a potentially wide range of proximity to one another and bond connectivity within the framework [457], and whose selective titration by  $\text{Co}^{2+}$  is ambiguous. MFI zeolites synthesized with constant Si/Al = 50 and systematically varying Co/Al values (0.1–0.4) possessed zero-order methanol dehydration rate constants that were

invariant with the number of Co-titratable sites, in contrast to CHA zeolites [458]. We hypothesized (perhaps naively) that if Co-titratable sites were more distant from one another within MFI than in CHA, then a probe reaction with larger adsorbed intermediates and transition states may be more sensitive to their proximity. Here, ethanol dehydration kinetics (415 K) are measured on H-CHA (Si/Al = 15) and H-MFI (Si/Al = 50) zeolites to interrogate this hypothesis.

## B.2 Results and Discussion

### B.2.1 Ethanol dehydration is not sensitive to H<sup>+</sup> proximity in MFI zeolites

The H-CHA and H-MFI zeolites studied here are summarized in Table B.1. Sam-

**Table B.1:** H-CHA and H-MFI zeolites studied.<sup>a</sup>

Zeolite Name	H <sup>+</sup> density <sup>b</sup> / 10 <sup>-4</sup> mol g <sup>-1</sup>	H <sup>+</sup> /Al <sup>b</sup>	Co/Al <sup>c</sup>	H <sup>+</sup> <sub>pair</sub> /H <sup>+</sup> <sub>tot</sub> <sup>d</sup>	Sample Code <sup>a</sup>
H-CHA(0.44)	8.4	1.00	0.22	0.44	CN1-004
H-CHA(0.23)	11	1.02	0.12	0.23	SBLB2P21
H-CHA(0)	9.6	0.98	0	0	JD1-093
H-MFI(0.12)	3.3	1.01	0.062	0.12	YH1-148
H-MFI(0.23)	3.3	1.01	0.12	0.23	YH1-049
H-MFI(0.39)	3.2	1.13	0.22	0.39	YH1-150
H-MFI(0.46)	2.9	0.97	0.22	0.46	YH1-152

<sup>a</sup>Zeolite synthesis and characterization courtesy of John Di Iorio, Claire Nimlos, and Young Gul Hur. Characterization data on these CHA zeolites has been reported in the literature [221, 444, 455]. Sample codes are provided for ease of reference by co-workers.

<sup>b</sup>Quantified by NH<sub>3</sub>-TPD

<sup>c</sup>Quantified by AAS after aqueous-phase ion-exchange saturation as reported for CHA [444] and MFI [459] zeolites

<sup>d</sup>H<sup>+</sup><sub>pair</sub> reflects H<sup>+</sup> titrated by Co<sup>2+</sup> in 6-MR in CHA zeolites. We refer to this quantity as H<sup>+</sup><sub>prox</sub> in the case of MFI because of the unknown locations of Co<sup>2+</sup>.

ples are referred to as H-ZEO(X), where X is the fraction of total H<sup>+</sup> in proximal

configurations titrated by  $\text{Co}^{2+}$ . Ethanol dehydration turnover rates (per  $\text{H}^+$ ) to form both diethyl ether (DEE) were quantified on H-MFI zeolites at 415 K and  $\text{C}_2\text{H}_5\text{OH}$  pressures between 0.02–60 kPa, shown in Figure B.1. DEE was the only product

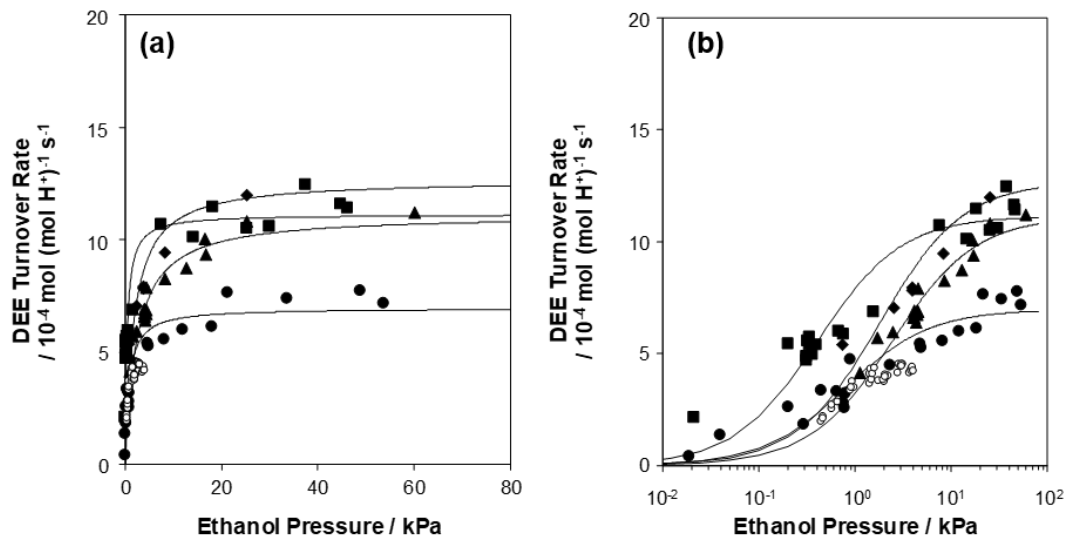


**Figure B.1:** DEE turnover rate (415 K, per  $\text{H}^+$ ) as a function of ethanol pressure on H-MFI(0.12) ( $\blacktriangle$ ), H-MFI(0.23) ( $\bullet$ ), H-MFI(0.39) ( $\blacklozenge$ ), and H-MFI(0.46) ( $\blacksquare$ ) on a linear scale (a) and a semi-log scale (b). Solid lines represent regression to Equation B.2. Unfilled data points are adapted from Chiang and Bhan [218] (409 K, H-MFI Si/Al = 43, Zeolyst CBV8014).

detected under these conditions. Measured turnover rates are approximately zero-order at high ethanol pressures (20–60 kPa), and approach first-order dependences at lower ethanol pressures ( $<1$  kPa). In the interest of benchmarking [194], these data closely resemble data collected by Chiang and Bhan on an H-MFI zeolite (Si/Al = 43, Zeolyst CBV8014, 409 K, 0.3–6 kPa) at a temperature  $\sim 6$  K lower (Figure B.1, open circles) [218]. As shown previously by Chiang and Bhan [218], measured DEE formation rates on H-MFI zeolites reflect associative dehydration mechanisms where  $\text{H}^+$  become covered first by hydrogen-bonded ethanol monomer intermediates (Step 1, Figure B.2), followed by protonated ethanol-ethanol dimer intermediates (Step 2, Figure B.2). The protonated dimer species form diethyl ether and water in the sole

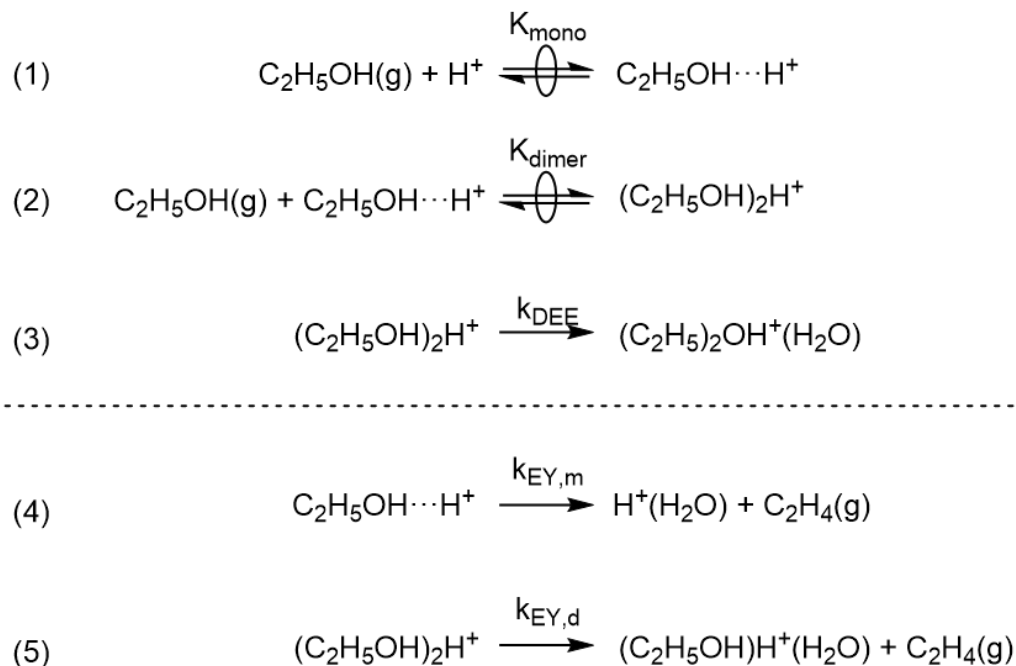


**Figure B.2:** Plausible series of elementary steps (1–3) that describe the dependence of DEE formation rates on ethanol pressure on H-MFI and H-CHA zeolites. Below the dashed line, steps (4–5) are proposed to describe EY formation rates on H-CHA zeolites.

kinetically relevant step (Step 3, Figure B.2) via an associative transition state. The full rate expression is:

$$r_{\text{DEE}} = \frac{k_{\text{DEE}}K_{\text{mono}}K_{\text{dimer}}P_{\text{C}_2\text{H}_5\text{OH}}^2}{1 + K_{\text{mono}}P_{\text{C}_2\text{H}_5\text{OH}} + K_{\text{mono}}K_{\text{dimer}}P_{\text{C}_2\text{H}_5\text{OH}}^2} \quad (\text{B.1})$$

which can be simplified further assuming the most abundant reactive intermediate (MARI) species are ethanol monomers and ethanol-ethanol dimers:

$$r_{\text{DEE}} = \frac{k_{\text{DEE}}K_{\text{dimer}}P_{\text{C}_2\text{H}_5\text{OH}}}{1 + K_{\text{dimer}}P_{\text{C}_2\text{H}_5\text{OH}}} \quad (\text{B.2})$$

where  $k_{\text{DEE}}$  is the zero-order rate constant in the limiting case of high  $P_{\text{C}_2\text{H}_5\text{OH}}$ , which reflects the free energy of the associative dehydration transition state referenced to the ethanol-ethanol dimer, and  $k_{\text{DEE}}K_{\text{dimer}}$  is the apparent first-order rate constant

in the limiting case of low  $P_{\text{C}_2\text{H}_5\text{OH}}$ , which reflects the free energy of the associative dehydration transition state referenced to the ethanol monomer and gas-phase ethanol. Eq. B.2 accurately describes the measured rate data on H-MFI zeolites (solid lines in Figure B.1), and provides values of  $k_{\text{DEE}}$  and  $k_{\text{DEE}}K_{\text{dimer}}$  that can be further interpreted in terms of the location and proximity of  $\text{H}^+$  in these samples.

Apparent first-order and zero-order rate constants for methanol dehydration to dimethyl ether have been shown previously to depend both on proton location within confining voids of different size [85], and their proximity (in the 6-MR of CHA zeolites) [221]. By analogy to these cases, we expect  $k_{\text{DEE}}K_{\text{dimer}}$  values to depend more strongly on confining environment dimensions than  $k_{\text{DEE}}$ , because it is referenced to a MARI species (ethanol monomer) that differs in size from its transition state. Proximity, in contrast affects both the first-order and zero-order rate constants because it stabilizes methoxy-based mechanisms in CHA zeolites, and thus we would expect it to affect the values of both  $k_{\text{DEE}}$  and  $k_{\text{DEE}}K_{\text{dimer}}$ . The regressed values of these apparent rate constants are shown in Figure B.3 as a function of  $\text{H}^+_{\text{prox}}/\text{H}^+_{\text{total}}$  on the H-MFI zeolites tested here, and summarized in Table B.2. The zero-order rate constants

**Table B.2:** Regressed ethanol dehydration rate and equilibrium constants on H-MFI zeolites.<sup>a</sup>

Zeolite Name	$k_{\text{DEE}} / 10^{-4\text{b}}$	$K_{\text{dimer}} / \text{kPa}^{-1}$	$k_{\text{DEE}}K_{\text{dimer}} / 10^{-4\text{c}}$
H-MFI(0.12)	$11 \pm 1$	$0.41 \pm 0.10$	$4.5 \pm 1.1$
H-MFI(0.23)	$7.0 \pm 0.6$	$1.2 \pm 0.5$	$8.6 \pm 3.3$
H-MFI(0.39)	$13 \pm 1$	$0.56 \pm 0.22$	$7.1 \pm 2.9$
H-MFI(0.46)	$11 \pm 1$	$2.4 \pm 0.7$	$27 \pm 8$

<sup>a</sup>Regressed in Athena Visual Studio to the data sets on each sample using Equation B.2

<sup>b</sup>units [=]  $\text{mol} (\text{mol H}^+)^{-1} \text{ s}^{-1}$  <sup>c</sup>units [=]  $\text{mol} (\text{mol H}^+)^{-1} \text{ kPa}^{-1} \text{ s}^{-1}$

( $k_{\text{DEE}}$ ) are essentially invariant (within a factor of 2) among these four samples ( $7\text{--}13 \times 10^{-4} \text{ mol} (\text{mol H}^+)^{-1} \text{ s}^{-1}$ ) and do not systematically depend on  $\text{H}^+_{\text{prox}}/\text{H}^+_{\text{total}}$ , indicating that Co-titrated sites ( $\text{H}^+_{\text{prox}}$ ) in MFI zeolites do not stabilize alternative

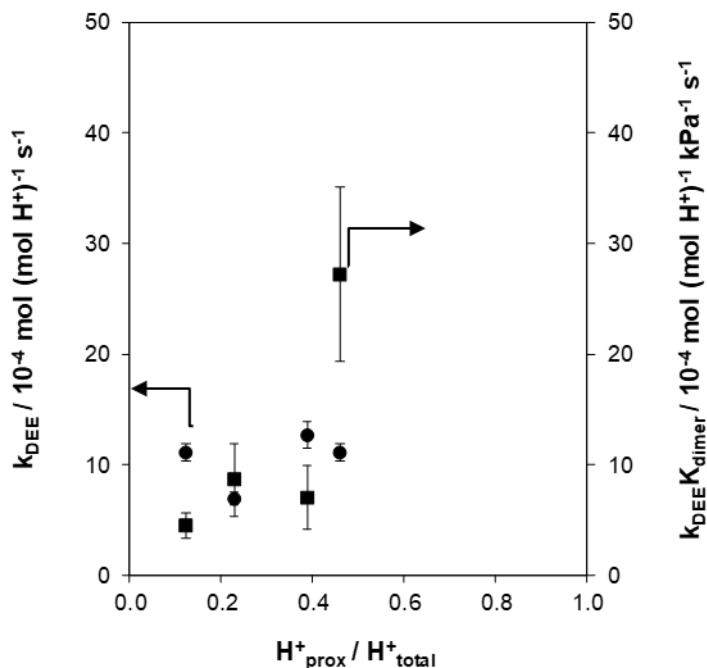


**Figure B.3:** First-order ( $k_{\text{DEE}}K_{\text{dimer}}$ , ■, right axis) and zero-order ( $k_{\text{DEE}}$ , ●, left axis) rate constants to form DEE on MFI zeolites as a function of proximal  $H^+$  fraction (titrated by  $\text{Co}^{2+}$ ).

dissociative pathways with higher turnover rates as reported for CHA zeolites. H-MFI does contain 6-MR motifs, but other ring structures (e.g., 5-MR) leave open the possibility that this set of samples exchanges  $\text{Co}^{2+}$  but does not possess the same Al configurations titrated by  $\text{Co}^{2+}$  in H-CHA that stabilize dissociative dehydration pathways. A second possibility is that ethanol dehydration is not sensitive to  $H^+$  proximity in any zeolite, which is disproved below in Section B.2.2. We thus conclude that the  $H^+_{\text{prox}}$  sites titrated by  $\text{Co}^{2+}$  in MFI are distinct from those titrated in CHA, and that the site requirements for stabilizing dissociative dehydration pathways are more narrow than only the ability to exchange divalent  $\text{Co}^{2+}$  cations. The apparent first-order rate constants ( $k_{\text{DEE}}K_{\text{dimer}}$ ), which are sensitive to confinement, provide some evidence that  $H^+$  location may be changing in these samples. In Figure B.3,  $k_{\text{DEE}}K_{\text{dimer}}$  values show a wider scatter ( $\sim 6\times$ ), where specifically the H-MFI(0.46) sample is the outlier with a 3–6 $\times$  higher value than the others. This sample may have

a higher fraction of  $H^+$  within confining channel environments, and the validity of this hypothesis can be initially checked by comparing with first-order rate constants for  $CH_3OH$  dehydration. Next, we show that  $H^+_{\text{pair}}$  sites in CHA increase the turnover rates of ethanol dehydration analogous to their effect on methanol dehydration, with additional consequences for ethene formation.

### B.2.2 Ethanol dehydration is sensitive to $H^+$ proximity in CHA zeolites

Three H-CHA samples were studied here spanning  $H^+_{\text{pair}}/H^+_{\text{tot}}$  values from 0–0.44 in order to probe the influence of proximity on ethanol dehydration catalysis. Ethanol dehydration site-time yields (STY, per  $H^+$ ) to form both diethyl ether (DEE, Figure 4) and ethene (EY, Figure B.4) were quantified on H-CHA zeolites at 415 K and  $C_2H_5OH$  pressures between 0.05–69 kPa. EY was observed at all  $C_2H_5OH$  pressures

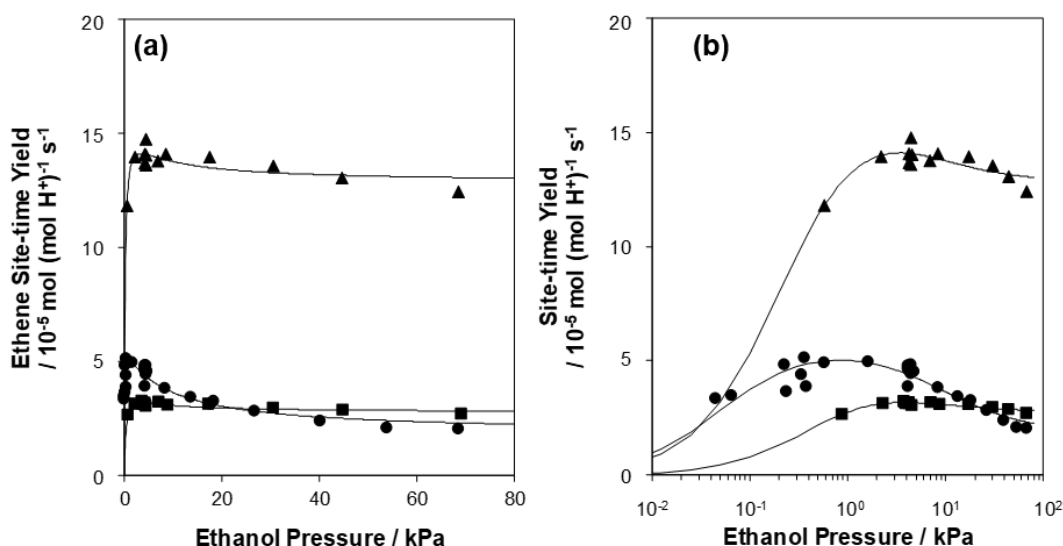


**Figure B.4:** EY STY (415 K, per  $H^+$ ) as a function of ethanol pressure on H-CHA(0) (●), H-CHA(0.23) (■), and H-CHA(0.44) (▲) on a linear scale (a) and a semi-log scale (b). Solid lines represent regression to Equation B.5.

tested at this temperature, contrasting undetectable EY formation rates on MFI and FER zeolites at 409 K [218], but consistent with detectable EY formation rates on

H-MOR zeolites at 409 K [218], which Chiang and Bhan rationalized as the ability of confined 8-MR side pockets to stabilize EY formation transition states, which these authors attributed to ethoxy-based pathways. The DEE STY is accurately described by Eq. B.1 (solid lines in Figure B.5). Vacant sites were left as a MARI species

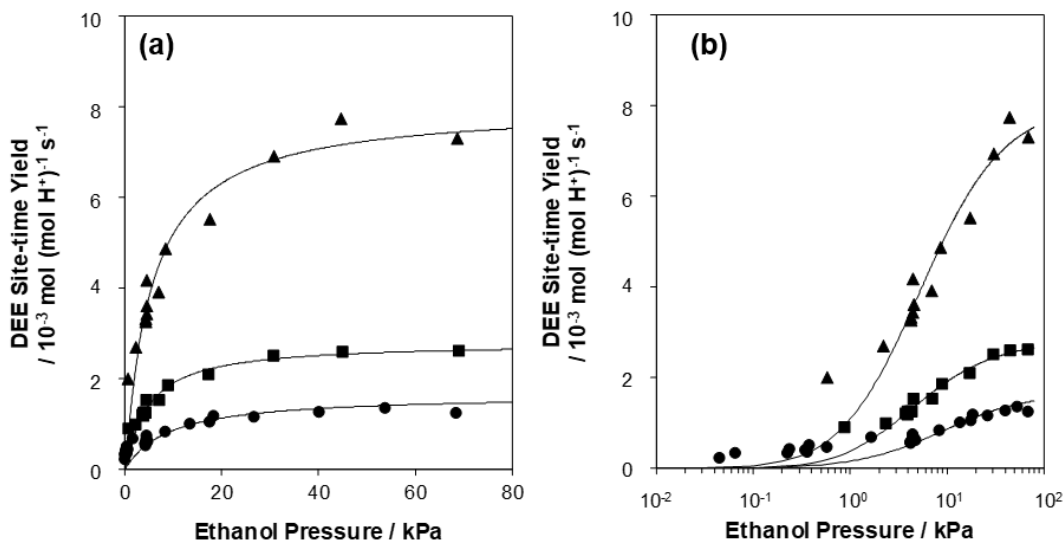


**Figure B.5:** DEE STY (415 K, per H<sup>+</sup>) as a function of ethanol pressure on H-CHA(0) (●), H-CHA(0.23) (■), and H-CHA(0.44) (▲) on a linear scale (a) and a semi-log scale (b). Solid lines represent regression to Equation B.1.

for completeness, but are not present at detectable coverages under the majority of experimental conditions, reflected in fit values of  $K_{mono}$  with large errors (Table B.3).

Rate expressions for EY formation developed in the literature reflect kinetically relevant unimolecular dehydration steps from the ethanol monomer species to form either ethene directly (Figure 2, step 4) [79] or to form a surface-bound ethoxy that goes on to form ethene in kinetically-irrelevant steps [218] that make this pathway kinetically indistinguishable from the direct pathway, and so it is omitted for brevity. Assuming ethene is formed solely in step 4 (Figure B.2), the ratio  $r_{DEE}/r_{EY}$  is:

$$\frac{r_{DEE}}{r_{EY}} = \frac{k_{DEE}K_{dimer}}{k_{EY,m}}P_{C_2H_5OH} \quad (B.3)$$

**Table B.3:** Regressed ethanol dehydration rate and equilibrium constants on H-CHA zeolites.

Zeolite Name	$K_{\text{mono}} / \text{kPa}^{-1}$	$K_{\text{dimer}} / \text{kPa}^{-1}$	$k_{\text{DEE}} / 10^{-4\text{a}}$	$k_{\text{EY,m}} / 10^{-5\text{a}}$	$k_{\text{EY,d}} / 10^{-5\text{a}}$
H-CHA(0.44) <sup>b</sup>	$5.1 \pm 3.6$	$0.19 \pm 0.05$	$80 \pm 7$	$16 \pm 1$	$24 \pm 1$
H-CHA(0.23) <sup>b</sup>	$2.5 \pm 0.7$	$0.22 \pm 0.06$	$28 \pm 2$	$3.9 \pm 0.2$	$6.2 \pm 0.1$
H-CHA(0) <sup>b</sup>	$20 \pm 10$	$0.11 \pm 0.07$	$17 \pm 4$	$5.6 \pm 0.5$	$2.1 \pm 0.6$
$\text{H}^+_{\text{iso}}$ <sup>c</sup>	$8.3 \pm 6.3$	$0.24 \pm 0.48$	$9.0 \pm 5.7$	$4.5 \pm 2.9$	$1.1 \pm 2.3$
$\text{H}^+_{\text{pair}}$ <sup>c</sup>	indeterminate	$0.17 \pm 0.07$	$150 \pm 20$	$19 \pm 8$	$25 \pm 7$
Pair/iso ratio <sup>d</sup>	--	$0.7 \pm 1$	$17 \pm 11$	$4 \pm 3$	$23 \pm 50$

<sup>a</sup>units [=]  $\text{mol} (\text{mol H}^+)^{-1} \text{s}^{-1}$

<sup>b</sup>Regressed in Athena Visual Studio separately to the data sets on each sample using Equations B.1 and B.5

<sup>c</sup>Regressed in Athena Visual Studio to all data at the same time using Equations B.6 and B.7, errors represent 95% marginal highest posterior density intervals

<sup>d</sup>Errors derived from propagation of errors in individual rate and equilibrium constants used to calculate the ratio

where  $k_{\text{DEE}}K_{\text{dimer}}$  has been defined above, and  $k_{\text{EY,m}}$  reflects the free energy of the ethene formation transition state relative to the adsorbed ethanol monomer species. Eq. B.3 predicts that the  $r_{\text{DEE}}/r_{\text{EY}}$  ratio is linear in  $P_{\text{C}_2\text{H}_5\text{OH}}$ , but instead the DEE/EY ratio (Figure B.6) shows a non-linear dependence that has been previously ascribed to the kinetic relevance of multiple parallel pathways to form either DEE or EY in kinetic measurements on polyoxometalate clusters [158].

The apparent non-linear dependence of  $r_{\text{DEE}}/r_{\text{EY}}$  on  $P_{\text{C}_2\text{H}_5\text{OH}}$  is primarily a consequence of the high-pressure kinetic dependence of the EY STY on  $P_{\text{C}_2\text{H}_5\text{OH}}$ , which approaches a zero-order regime (Figure B.4), whereas rate expressions based on monomolecular ethene formation steps would predict a limiting  $-1$  order dependence on  $P_{\text{C}_2\text{H}_5\text{OH}}$  when surfaces are saturated with ethanol-ethanol dimers. This zero-order

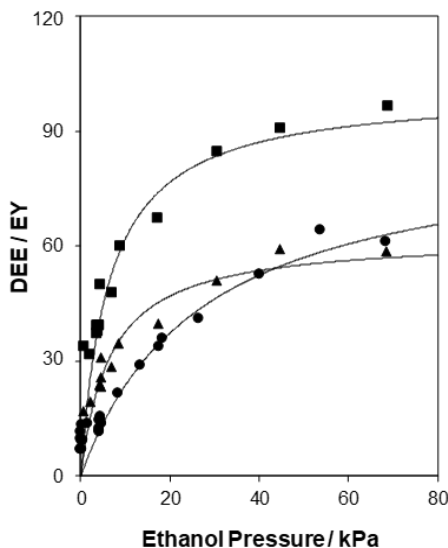


**Figure B.6:** Ratio of DEE / EY formation rates (415 K, per  $\text{H}^+$ ) as a function of ethanol pressure on H-CHA(0) ( $\bullet$ ), H-CHA(0.23) ( $\blacksquare$ ), and H-CHA(0.44) ( $\blacktriangle$ ). Solid lines represent regression to Equations B.1 and B.5.

limiting behavior was also observed by Chiang and Bhan on H-MOR, who took this as evidence that  $\text{H}^+$  confined within 8-MR side pockets were unable (at  $P_{\text{C}_2\text{H}_5\text{OH}} < 6$  kPa) to stabilize ethanol-ethanol dimer species, leading to rate expressions with two terms:

$$r_{\text{EY}} = x_{12\text{MR}} \frac{k_{\text{EY},m}}{1 + K_{\text{dimer}} P_{\text{C}_2\text{H}_5\text{OH}}} + x_{8\text{MR}} k_{\text{DEY},8\text{MR}} \quad (\text{B.4})$$

where  $x_{y\text{MR}}$  are the fractions of  $\text{H}^+$  confined within  $y$ -MR environments. This explanation may be plausible within MOR, where certain T-sites may be embedded within confining side pockets and constrain reactive intermediates to reside within them, but in CHA zeolites, every T-site (there is only one crystallographically unique T-site) is accessible within the less-confined CHA cage ( $\sim 0.7$  nm largest included sphere [6]). An alternative explanation, which leads to the same functional dependence on  $P_{\text{C}_2\text{H}_5\text{OH}}$  as in Eq. B.4, has been suggested by Zhi et al. [177] to describe measured 1-propanol dehydration rates (per  $\text{H}^+$ ) to form propylene with H-MFI zeolites (413–443 K, 0.075–4 kPa 1-propanol), where propanol-propanol dimers are capable of stabilizing elimination transition states that form propylene. Such an elementary

step is described in Step 5 of Figure B.2, and leads to rate expressions for ethene formation that are zero-order at high  $P_{C_2H_5OH}$ :

$$r_{EY} = \frac{k_{EY,m}K_{\text{mono}}P_{C_2H_5OH} + k_{EY,d}K_{\text{mono}}K_{\text{dimer}}P_{C_2H_5OH}^2}{1 + K_{\text{mono}}P_{C_2H_5OH} + K_{\text{mono}}K_{\text{dimer}}P_{C_2H_5OH}^2} \quad (\text{B.5})$$

where  $k_{EY,d}$  reflects the free energy of the ethene formation transition state, with one co-adsorbed ethanol molecule, referenced to the ethanol-ethanol dimer. Eq. B.5 provides reasonable fits to the dependence of both  $r_{EY}$  (Figure B.4) and  $r_{DEE}/r_{EY}$  (Figure B.6) on  $P_{C_2H_5OH}$ , when Eq. B.5 and Eq. B.1 are fit simultaneously to the data in Figure B.5–Figure B.6, to give values of  $k_{DEE}$ ,  $k_{DEE}K_{\text{dimer}}$ ,  $k_{EY,m}$ , and  $k_{EY,d}$  that can be compared among samples with different  $H^+_{\text{pair}}/H^+_{\text{total}}$  values.

The dependences of  $k_{DEE}$  and  $k_{DEE}K_{\text{dimer}}$  on  $H^+_{\text{pair}}/H^+_{\text{total}}$  are shown in Figure B.7a. On these three samples, the values of both first-order and zero-order DEE formation rate constants systematically increase with the fraction of paired  $H^+$  in CHA 6-MR. The dependence is approximately linear (solid lines in Figure B.7a), as would be expected for two discrete pools of sites operating with different turnover rates. The extrapolated values of both apparent rate constants on  $H^+_{\text{pair}}$  are over one order of magnitude higher than those measured on the fully-isolated sample, consistent with findings for methanol dehydration on a larger suites of CHA zeolites that included these three samples [221]. The intrinsic rate constants for ethene formation ( $k_{EY,m}$ ,  $k_{EY,d}$ , Figure B.7b) also depend on the fraction of paired  $H^+$ , but with more scatter than in the case of DEE, and with similar regression line slopes that suggest that mechanistic change that increases the rates of both pathways affects them to a similar extent.

Rather than use linear regression from the values fit individually on each sample (solid lines in Figure B.7) the entire data set on all samples was fit using Athena Visual Studio, assuming distinct sets of rate constants on the two site types  $H^+_{\text{pair}}$  and  $H^+_{\text{iso}}$ :

$$r_{DEE} = x_{\text{pair}}r_{DEE,\text{pair}} + (1 - x_{\text{pair}})r_{DEE,\text{iso}} \quad (\text{B.6})$$

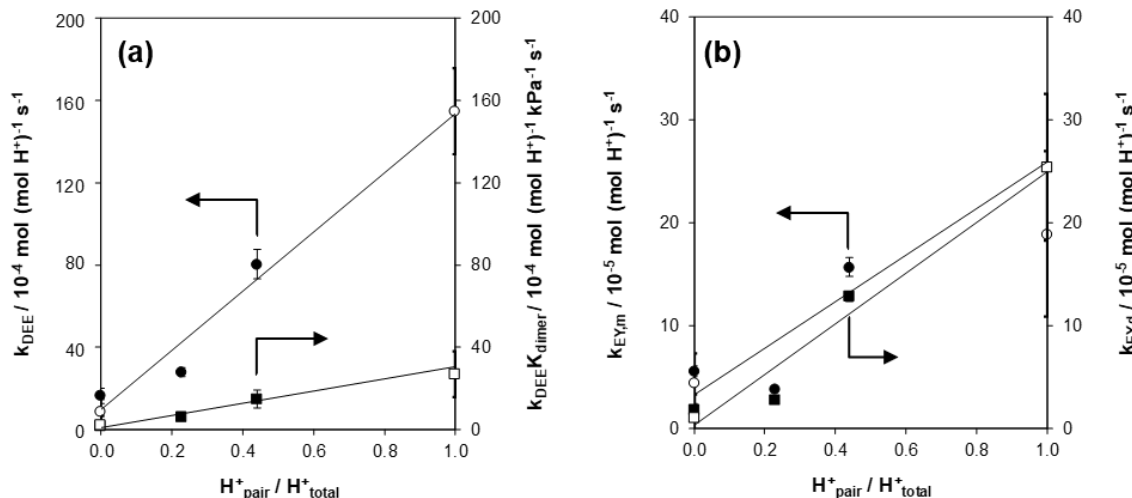


**Figure B.7:** (a) First-order ( $k_{\text{DEE}}K_{\text{dimer}}$ ,  $\blacksquare$ , right axis) and zero-order ( $k_{\text{DEE}}$ ,  $\bullet$ , left axis) rate constants to form DEE on CHA zeolites as a function of paired  $\text{H}^+$  fraction. (b) Intrinsic rate constants to form ethene from ethanol monomer precursors ( $k_{\text{EY},\text{m}}$ ,  $\bullet$ , left axis) and ethanol-ethanol dimer precursors ( $k_{\text{EY},\text{d}}$ ,  $\blacksquare$ , right axis) on CHA zeolites as a function of paired  $\text{H}^+$  fraction. Solid symbols were fit by regression of Equations B.1 and B.5 to data on collected on each sample, and the solid lines represent a linear regression to the solid symbols. Unfilled symbols and their associated error bars represent regression of the entire data set to the same rate equation as a function of paired  $\text{H}^+$  fraction (Equations B.6 and B.7).

$$r_{\text{EY}} = x_{\text{pair}}r_{\text{EY},\text{pair}} + (1 - x_{\text{pair}})r_{\text{EY},\text{iso}} \quad (\text{B.7})$$

where  $x_{\text{pair}}$  is defined as  $\text{H}^+_{\text{pair}}/\text{H}^+_{\text{total}}$  (Table B.1),  $r_{\text{DEE}}$  is defined according to Eq. B.1, with different equilibrium and rate constants for paired and isolated sites, and  $r_{\text{EY}}$  is defined according to Eq. B.5, with different equilibrium and rate constants for paired and isolated sites. The results of fitting the entire data set are shown in the last two lines of Table B.3, and as the open symbols in Figure B.7, whose error bars reflect 95% marginal highest posterior density intervals calculated from Bayesian nonlinear regression in Athena Visual Studio. Despite having only three samples, the error bars indicate that the values of all apparent rate constants that were fit for both DEE and EY are higher at paired  $\text{H}^+$  than at isolated  $\text{H}^+$ , and that the values fit for  $\text{H}^+_{\text{iso}}$  are within error of those fit only for H-CHA(0). The similarity of the

magnitude of rate enhancement at  $\text{H}^+_{\text{pair}}$  for DEE formation pathways and both EY formation pathways suggests that the new mechanistic pathways opened up to form both products share the same reactive intermediates that are stabilized at  $\text{H}^+_{\text{pair}}$  sites. The stabilization of sequential ethoxy-based routes would be consistent with this behavior, in analogy to the case of methanol dehydration, where this interpretation was supported by the detection of methoxy intermediates under the conditions of methanol dehydration catalysis by *in situ* IR spectroscopy. In this case, attempts to detect ethoxy intermediates were unsuccessful because their C-O vibration at  $\sim 1150 \text{ cm}^{-1}$  [214] is obscured by strong Si-O-Si modes in transmission IR spectra.

VITA

## VITA

Jason Bates was born in Plano, TX, and grew up in Overland Park, KS. He attended Brookwood Elementary, Mission Valley Middle School, and went on to high school at Shawnee Mission East (SME). During high school he was active in the youth group at Village Presbyterian Church, participating in various social activities and trips, and spending each spring break on the yearly mission trip to build a school and distribute medical supplies in the Dominican Republic. At SME he joined the tennis team, playing on varsity for three years, and joined a smaller community of students in the International Baccalaureate program, receiving the IB diploma after graduation. He developed an aptitude for and enjoyment of math and science, inspired by the teaching of Rick Royer (Calculus) and Steven Appier (Chemistry). The IB program's emphasis on independent projects led him to write a history paper on the life of Fritz Haber, which, together with lectures in Appier's Chem II IB class on Haber's fascinating ammonia synthesis process, sowed the seeds that grew into his lifelong passion for catalysis science.

Studying chemical engineering at the University of Kansas from 2010–2014, Jason joined a diverse group of students living in Pearson Scholarship Hall, whose cooperative living setup instilled a strong sense of solidarity. Jason lived in Pearson for all four years that he attended KU, giving back to the hall in various service roles (social chair, basketball camping sports chair), and was recognized by his hallmates as a Distinguished Resident in 2014. Throughout college, he took on various roles that solidified an appreciation for teaching in various modes, including a job as a summer camp counselor at Heartland Center in 2011, tutoring peers in calculus, acting as an undergraduate teaching assistant for General Chemistry II lab, and writing opinion columns in the University Daily Kansan. Jason's interest in catalysis was re-awakened

when he spent the summer of 2012 working in Bob Davis' lab at the University of Virginia as part of the Center for Biorenewable Chemicals REU program, where he learned the fundamental principles of catalysis science and hypothesis-driven research. Back at KU, he deepened his experience in catalysis working with Bala Subramaniam as part of the Center for Environmentally Beneficial Catalysis, where he spent the remainder of his undergraduate career studying alcohol dehydration to alkenes on mesoporous solid Lewis acids. Continuing to pursue catalysis, he spent the summer of 2014 prior to starting graduate school at the National Renewable Energy Laboratory working with Josh Schaidle studying supported nanoparticles used in the hydrodeoxygenation of biomass-derived oxygenates.

Jason arrived at Purdue in the fall of 2014 and, with Juan Carlos Vega-Vila and Phil Kester, nearly doubled the size of the Gounder group. In the Gounder group, Jason built a fully automated gas flow reactor for alcohol dehydration kinetic measurements and served in various roles, including shared gas purchaser and lab manager. Outside the lab, he enjoyed reading, playing guitar with friends, traveling near and far to see live music, and camping and hiking in many of Indiana's state parks. In January 2020, Jason will begin a postdoctoral appointment at the University of Wisconsin–Madison working with Shannon Stahl.